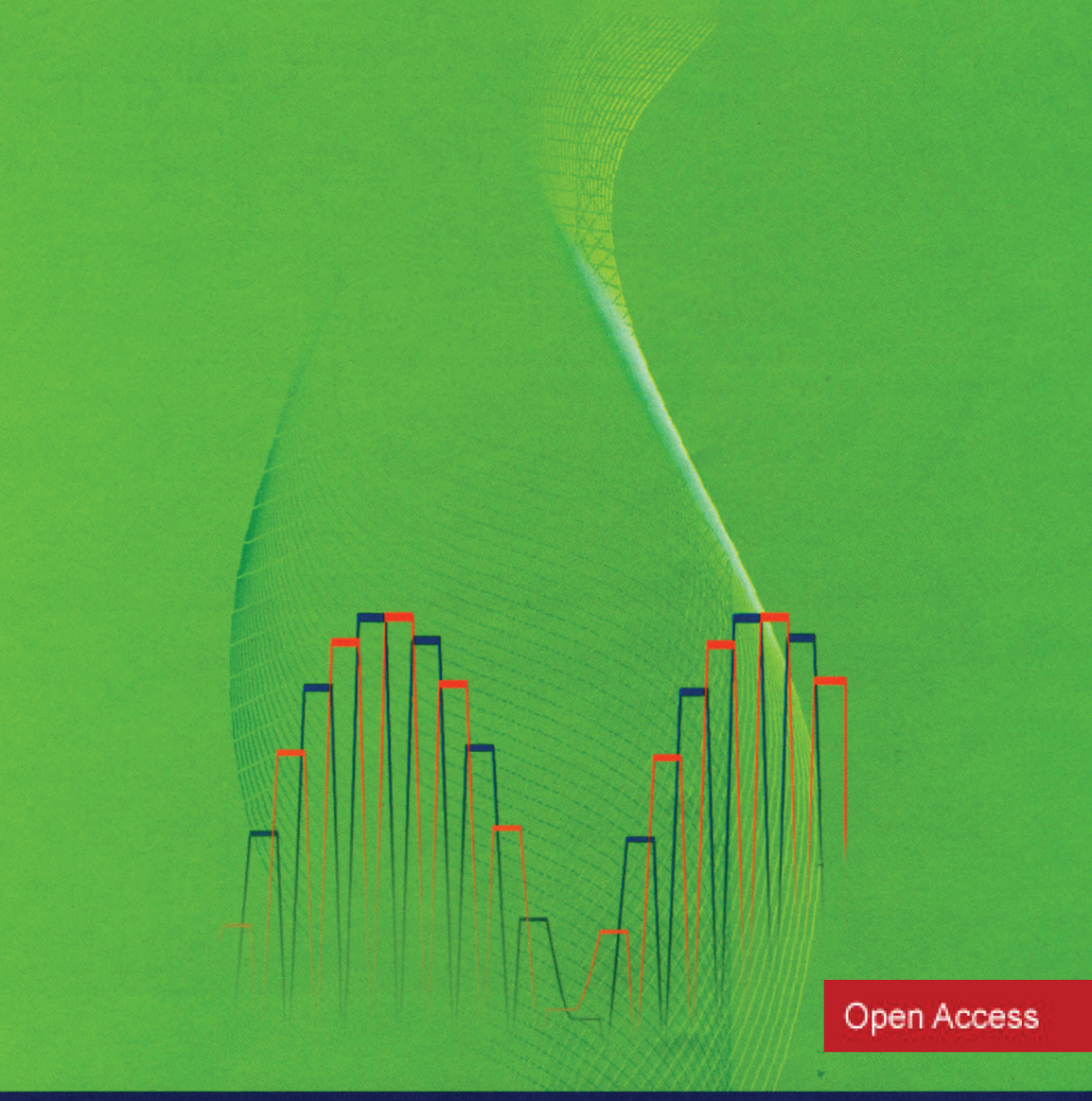


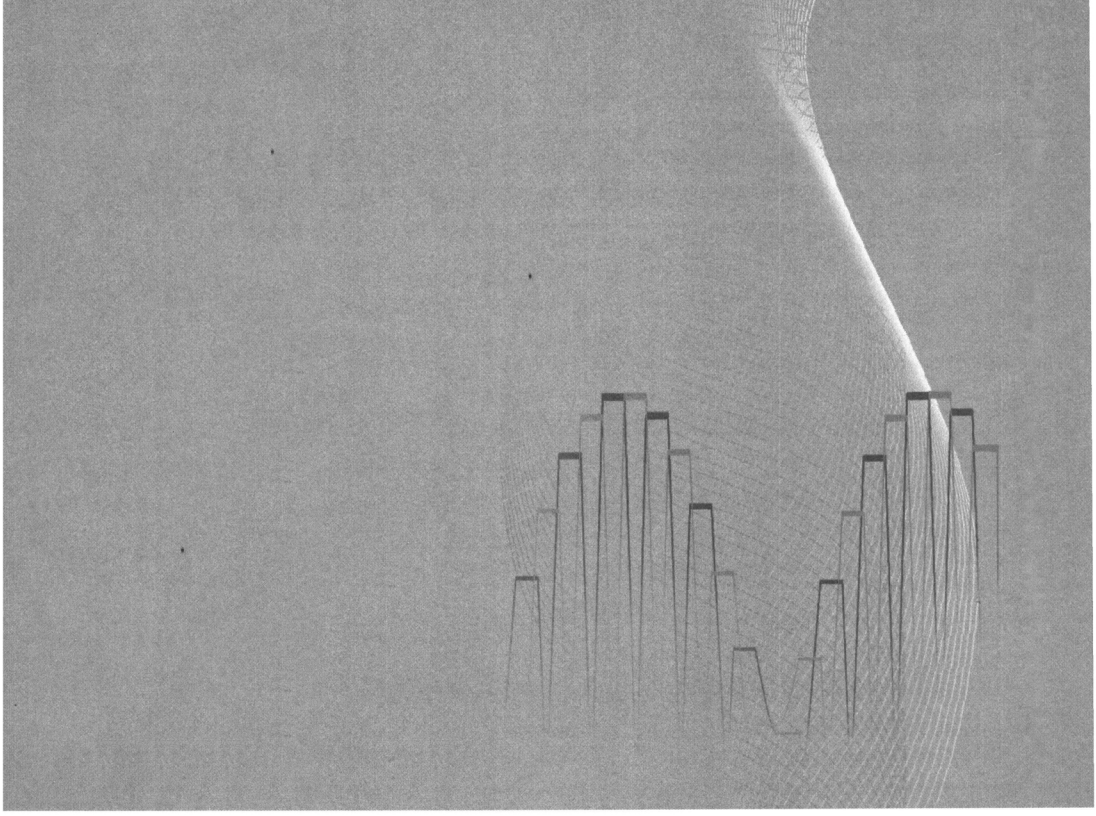
Open Access

Physics of Intensity Dependent Beam Instabilities

K. Y. Ng

Physics of Intensity Dependent Beam Instabilities

This page intentionally left blank



Physics of Intensity Dependent Beam Instabilities

K. Y. Ng

Fermi National Accelerator Laboratory, USA

World Scientific

NEW JERSEY • LONDON • SINGAPORE • BEIJING • SHANGHAI • HONG KONG • TAIPEI • CHENNAI

Published by

World Scientific Publishing Co. Pte. Ltd.

5 Toh Tuck Link, Singapore 596224

USA office: 27 Warren Street, Suite 401-402, Hackensack, NJ 07601

UK office: 57 Shelton Street, Covent Garden, London WC2H 9HE

British Library Cataloguing-in-Publication Data

A catalogue record for this book is available from the British Library.

PHYSICS OF INTENSITY DEPENDENT BEAM INSTABILITIES





Open Access funded by SCOAP³

Copyright © 2025 The Editor(s) (if applicable) and The Author(s)

This ebook was converted to Open Access in 2025 through the sponsorship of SCOAP3, licensed under the terms of the Creative Commons Attribution-NonCommercial 4.0 International License (https://creativecommons.org/licenses/by-nc/4.0/), which permits use, sharing, adaptation, distribution and reproduction in any medium or format, as long as you give appropriate credit to the original author(s) and the source, provide a link to the Creative Commons license and is used for non-commercial purposes.

Copyright © 2006 by World Scientific Publishing Co. Pte. Ltd.

ISBN: 9789812563422 (print)

ISBN: 9789812703392 (ebook for institutions)

ISBN: 9789814480321 (ebook for individuals)

For any available supplementary material, please visit
https://www.worldscientific.com/worldscibooks/10.1142/5835#t=suppl

Printed in Singapore

To my dearest wife Ruth and my children Julia and Enrico

This page intentionally left blank

2025 © The Author(s). This is an Open Access chapter published by World Scientific Publishing Company, licensed under the terms of the Creative Commons Attribution-NonCommercial 4.0 International License (CC BY-NC 4.0).

Preface

Our knowledge of the properties of intensity-dependent beam instabilities has grown tremendously in the last several decades, owing to the introduction of more precise instrumentation and very much faster digital computers. Every few years, a new beam instability is discovered and an ingenious new method to cure an instability is proposed. Here, I am having the pleasure of introducing them to my readers and sharing with them my personal views and understanding.

The subject on intensity dependent instabilities is important in the field of accelerator physics. The thresholds and growth rates of these instabilities very often determine the upper limit of the particle beam intensity, the lower limit of the bunch sizes, the minimum aperture of the vacuum chamber, the smoothness of the chamber walls, and have a lot of influence on the design of all the beam-related elements such as diagnosis detectors, kickers, beam separators, beam collimators, etc. The understanding of how instabilities are generated and the various ways to contain them has become an essential part of operating an existing accelerator and in the design of future machines.

The first chapter is devoted to a review of the basic concept of wake potentials and coupling impedances in the vacuum chamber, which enables the formulation of the static and dynamic contributions to the equations of motion. Static solutions are then given, followed by the consequence of beam instabilities and the result of possible beam loss. The dynamic solutions lead to intensity-dependent instabilities, some of which are collective effects and some are not. While some of these instabilities exhibit thresholds, some do not. Special emphasis are made separately on proton and electron machines, because these two categories are so different in lattice design, in beam storage operation, and in beam structure. Other special topics of interest covered include Landau damping, Balakin–Novokhatsky–Smirnov damping, Sacherer's integral equations, Landau cavity, saw-tooth instability, Robinson stability criteria, beam loading, transition

crossing, two-stream instabilities, and collective instability issues of isochronous rings.

The readers will find this book theory oriented, because the basic features of the instabilities are laid out by mathematics. However, we try every means to minimize the use of mathematics, especially at the beginning, so that the readers can grasp the mechanism of the instabilities rather than become lost in the jungle of formulas and equations. For example, Sacherer's integral equation is not introduced and derived until Chapter 8, while its formal solution in terms of orthogonal polynomials is delayed until Chapter 9. Except for some geometrical concepts that may be accepted intuitively, the presentation here is intended to be rigorous and self-contained. Nearly all the formulas and equations employed in the book are derived or given guidelines to be derived in the exercises at the end of each chapter. The introduction of an instability is mostly followed by a thorough description of one or more experimental observations together with different methods of cures.

This book is an outgrowth from the lecture notes of two courses "Physics of Collective Beam Instabilities" and "Physics of Intensity Dependent Instabilities" given in the 2000 and 2002 at the U.S. Particle Accelerator School. I wish to thank my colleagues and students for countless helpful remarks. The material in this book can serve as subject matter for a graduate physics course in accelerator physics. A preliminary background in classical electrodynamics and basic knowledge of accelerator physics will be required.

Because the book is composed of a number of lectures, there has been an initial intention of writing each chapter as independent as possible. Although such an intention does not materialize completely, however, I do have some formulas depicted more than once, some notations defined more than once, and some concepts construed more than once throughout the book. While some consider it long-winded, I consider it a merit, because the readers may find it convenient when they wish to jump into a chapter or a section without the necessity of starting from the first page of the book.

To conclude, I would like to express both regret and pleasure. The range of topics discussed and the pace of their development have made the writing of an adequate bibliography impossible. I have therefore chosen to refer primarily to those papers from which I happened to have learned certain things. Consequently, inadequate recognition is frequently given to the originators of certain ideas, fundamental or technical, and apologies are undoubtedly due to a number of my colleagues. Inevitably there will be errors in the manuscript coming both from careless typos and something beyond my present understanding. Comments and corrections are welcome and can be sent to NG@FNAL.GOV.

The pleasure comes from the opportunity to express appreciation to those contributed to the existence and final form of the book. My utmost thanks go to Dr. P. Colestock, Professor S.Y. Lee, and Dr. M. Syphers, who provided the necessary encouragement for the writing of the book. Particular appreciation goes to Dr. C. Ankenbrandt who carefully read the manuscripts of my 2000 lecture notes and 2002 lecture notes of the U.S. Accelerator School, which form the basis of this book. I am grateful to many of my colleagues for numerous discussions and final clarification of many ambiguities, paradoxes, and difficulties that popped up in the course of writing the book. To mention a few, they include Professor A. W. Chao, Professor R. Gluckstern, Dr. G. Lambertson, Dr. F. Ostiguy, Dr. T.S. Wang, Dr. B. Zotter, and many others. Ultimately, my greatest thanks go to my wife whose constant understanding, encouragement, and support have been essential to the completion of the book.

K.Y. Ng
Batavia, Illinois
September 2005

This page intentionally left blank

2025 © The Author(s). This is an Open Access chapter published by World Scientific Publishing Company, licensed under the terms of the Creative Commons Attribution-NonCommercial 4.0 International License (CC BY-NC 4.0).

Contents

Preface vii

1 Wakes and Impedances 1

1.1 Wake Fields . . . 1
1.1.1 Two Approximations . . . 2
1.1.2 Panofsky–Wenzel Theorem . . . 3
1.1.3 Cylindrically Symmetric Chamber . . . 6
1.2 Coupling Impedances . . . 11
1.3 Parasitic Loss . . . 19
1.3.1 Coherent Loss . . . 19
1.3.2 Incoherent Loss . . . 22
1.4 Exercises . . . 26
1.5 Appendix: A Collection of Wakes and Impedances . . . 29

2 Potential-Well Distortion 37

2.1 Longitudinal Phase Space . . . 37
2.1.1 Momentum Compaction . . . 37
2.1.2 Equations of Motion . . . 40
2.2 Mode Approach . . . 47
2.2.1 Vlasov Equation . . . 48
2.2.2 Coasting Beams . . . 49
2.3 Static Solution . . . 50
2.4 Reactive Force . . . 52
2.4.1 Space-Charge Impedance . . . 53
2.4.2 Other Distributions . . . 55

2.5 Bunch-Shape Distortion 58
2.5.1 Haissinski Equation 58
2.5.2 Elliptical Phase-Space Distribution 61
2.6 Synchrotron Tune Shift 64
2.6.1 Incoherent Synchrotron Tune Shift 64
2.6.2 Coherent Synchrotron Tune Shift 68
2.7 Potential-Well Distortion Compensation 69
2.7.1 Space-Charge Cancellation 69
2.7.2 Ferrite Insertion 71
2.8 Potential-Well Distortion in Barrier RF 75
2.8.1 RF Barriers 76
2.8.2 Asymmetric Beam Profile 76
2.9 Exercises 80

3 Betatron Tune Shifts 89
3.1 Static Transverse Forces 89
3.1.1 Electric Image Forces 91
3.1.2 Magnetic Image Forces 93
3.2 Space-Charge Self-Force 96
3.2.1 Incoherent Self-Force Tune Shift 96
3.2.2 Tune-Shift Distribution 101
3.2.3 Incoherence versus Coherence 106
3.3 Tune Shift for a Beam 107
3.3.1 Image Formation 107
3.3.2 Coasting Beams 109
3.3.3 Bunched Beams 110
3.4 Other Vacuum Chamber Geometries 112
3.4.1 Circular Vacuum Chamber 113
3.4.2 Elliptical Vacuum Chamber 114
3.4.3 Rectangular Vacuum Chamber 117
3.4.4 Closed Yoke 120
3.5 Connection with Impedance 121
3.5.1 Impedance from Images 121
3.5.2 Impedance from Self-Force 124
3.6 Exercises 127

4 Envelope Equation 133

4.1 The Integer Resonance 133
4.2 The Kapchinsky–Vladimirsky Equation 136
4.2.1 Least-Square Value 139
4.2.2 One Dimension 139
4.2.3 Two Dimensions 141
4.3 Collective Oscillations of Beams 144
4.3.1 One Dimension 144
4.3.2 Two Dimensions 148
4.4 Simulations 152
4.4.1 One Dimension 152
4.4.2 Two Dimensions 153
4.5 Application to Synchrotrons 156
4.6 Exercises 157

5 Longitudinal Microwave Instability for Coasting Beams 159
5.1 Microwave Instability 159
5.1.1 Dispersion Relation 162
5.1.2 Stability Curve and Keil–Schnell Criterion 166
5.1.3 Landau Damping 170
5.1.4 Self-Bunching 170
5.1.5 Overshoot 173
5.2 Observation and Cure 174
5.3 Ferrite Insertion and Instability 177
5.3.1 Microwave Instability 177
5.3.2 Cause of Instability 179
5.3.3 Heating the Ferrite 183
5.3.4 Application at the PSR 187
5.4 Exercises 190

6 Longitudinal Microwave Instability for Short Bunches 193
6.1 Bunch Modes 193
6.1.1 A Particle in Synchrotron Oscillation 193
6.1.2 Coherent Azimuthal Modes 199
6.1.3 Measurement of Coherent Modes 201
6.2 Collective Instability 203
6.2.1 Dispersion Relation of a Sideband 203
6.2.2 Landau Damping of a Sideband 208

6.2.3 Stability of a Bunch 213
6.3 Coupling of Azimuthal Modes 219
6.4 Bunch Lengthening and Scaling Law 224
6.5 Sawtooth Instability 228
6.5.1 Possible Cure 233
6.6 Exercises 237

7 Beam-Loading and Robinson's Instability 241
7.1 Equivalent Circuit 241
7.2 Beam-Loading in an Accelerator Ring 247
7.2.1 Steady-State Compensation 249
7.3 Robinson's Stability Criteria 257
7.3.1 Phase Stability at Low Intensity 257
7.3.2 Phase Stability at High Intensity 258
7.3.3 Robinson's Damping 262
7.4 Transient Beam-Loading 263
7.4.1 Fundamental Theorem of Beam-Loading 264
7.4.2 From Transient to Steady State 266
7.4.3 Transient Beam-Loading of a Bunch 270
7.4.4 Transient Compensation 278
7.5 Examples 284
7.5.1 Fermilab Main Ring 284
7.5.2 Fermilab Booster 285
7.5.3 Fermilab Main Injector 286
7.5.4 Proposed Prebooster 288
7.6 Exercises 296

8 Longitudinal Coupled-Bunch Instabilities 301
8.1 Sacherer's Integral Equation 301
8.1.1 Frequency Domain 304
8.1.2 Synchrotron Tune Shift 308
8.1.3 Robinson's Instability 309
8.2 Time Domain Derivation 315
8.3 Observation and Cures 321
8.3.1 Higher-Harmonic Cavity 324
8.3.2 Passive Landau Cavity 326
8.3.3 Rf-Voltage Modulation 336

8.3.4 Uneven Fill 339
8.4 Exercises 352

9 Transverse Instabilities 359
9.1 Transverse Focusing and Transverse Wake 359
9.2 Betatron Fast and Slow Waves 361
9.3 Separation of Transverse and Longitudinal Motions 364
9.4 Sacherer's Integral Equation 366
9.5 Solution of Sacherer's Integral Equations for Radial Modes . . 370
9.5.1 Chebyshev Modes 372
9.5.2 Legendre Modes 373
9.5.3 Hermite Modes 374
9.5.4 Longitudinal Integral Equation 375
9.6 Frequency Shifts and Growth Rates 376
9.6.1 Broadband Impedance 376
9.6.2 Narrowband Impedance 380
9.7 Approximate Solutions and Effective Impedances 381
9.7.1 Sacherer's Sinusoidal Modes 383
9.8 Chromaticity Frequency Shift 386
9.9 Exercises 389

10 Transverse Coupled-Bunch Instabilities 393
10.1 Resistive-Wall Instabilities 393
10.1.1 Resistive-Wall Impedance at Low Frequencies 398
10.1.2 Bypass Inductance 400
10.2 Derivation of Resistive-Wall Impedance 407
10.2.1 Wave Equations 407
10.2.2 Source Fields 411
10.2.3 Thin-Wall Model 414
10.2.4 Thick-Wall Model 418
10.2.5 Layered Wall 426
10.2.6 Laminations 427
10.3 Applications 428
10.3.1 Fermilab Booster 428
10.3.2 Bench Measurement 437
10.4 Narrow Resonances 439
10.5 Exercises 441

11 Mode-Coupling Instabilities 445
11.1 Transverse Mode-Coupling 445
11.2 Space-Charge and Mode-Coupling 451
11.3 Two-Particle Model 456
11.4 Longitudinal Mode-Coupling 459
11.4.1 Long Bunches 460
11.4.2 Short Bunches 462
11.5 TMCI for Long Bunches 464
11.5.1 High Energy Accelerators 464
11.5.2 TMCI Threshold for Present Proton Machines 467
11.5.3 Possible Observation 468
11.6 Exercises 470

12 Head-Tail Instabilities 473
12.1 Transverse Head-Tail 473
12.1.1 Two-Particle Model 474
12.1.2 For a Bunch 478
12.1.3 Application to the Tevatron 481
12.2 Longitudinal Head-Tail 489
12.3 Exercises 495

13 Landau Damping 499
13.1 Harmonic Beam Response 500
13.2 Shock Response 503
13.3 Landau Damping 507
13.4 Transverse Bunched Beam Instabilities 510
13.5 Longitudinal Bunched Beam Instabilities 516
13.6 Transverse Unbunched Beam Instabilities 519
13.6.1 Resistive-Wall Instabilities 523
13.7 Longitudinal Unbunched Beam Instabilities 533
13.8 Beam Transfer Function and Impedance Measurements 537
13.9 Decoherence versus Landau damping 543
13.9.1 Landau damping of a beam 545
13.9.2 Longitudinal Decoherence 550
13.10 Exercises 555

14 Beam Breakup 557

14.1 Two-Particle Model 558
14.2 Long Bunch 561
14.2.1 Balakin–Novokhatsky–Smirnov Damping 561
14.2.2 Autophasing 563
14.3 Linac 567
14.3.1 Adiabatic Damping 567
14.3.2 Detuned Cavity Structure 569
14.3.3 Multi-Bunch Breakup 573
14.3.4 Analytic Treatment 575
14.3.5 Misaligned Linac 587
14.4 Quadrupole Wake 593
14.4.1 Two-Particle Model 596
14.4.2 Observation 599
14.5 Exercises 602

15 Two-Stream Instabilities 609

15.1 Trapped Electrons 609
15.1.1 Single-Electron Mechanics 612
15.1.2 Electron Bounce Frequency 612
15.1.3 Coupled-Centroid Oscillation 619
15.1.4 Production of Electrons 628
15.1.5 Discussion and Conclusion 641
15.2 Fast Beam-Ion Instability 643
15.2.1 The Linear Theory 644
15.2.2 Application to Electron/Positron Rings 657
15.2.3 Application to Fermilab Linac 662
15.2.4 Application to Fermilab Designed Damping Ring . . . 672
15.3 Half-Integer Stopband 679
15.4 Exercises 684

16 Instabilities Near and Across Transition 691

16.1 Bunch Shape Near Transition 692
16.1.1 Nonadiabatic Time 692
16.1.2 Simple Estimation 694
16.1.3 More Sophisticated Approximation 698
16.2 Space-Charge Mismatch 707

16.2.1 Mathematical Formulation 710
16.2.2 Transition Jump 713
16.3 Negative-Mass Instability 714
16.3.1 Growth at Cutoff 715
16.3.2 Schottky-Noise Model 726
16.3.3 Self-Bunching Model 741
16.4 Instability of Isochronous Rings 744
16.4.1 Higher-Order Momentum Compaction 745
16.4.2 η_1-Dominated Bucket 748
16.4.3 η_2-Dominated Bucket 751
16.4.4 Microwave Instability Near Transition 753
16.5 Exercises 764

Index 771

2025 © The Author(s). This is an Open Access chapter published by World Scientific Publishing Company, licensed under the terms of the Creative Commons Attribution-NonCommercial 4.0 International License (CC BY-NC 4.0).

Chapter 1

Wakes and Impedances

1.1 Wake Fields

A positively charged particle at rest has static electric field going out radially in all directions. In motion with velocity v, magnetic field is generated. As the particle velocity approaches c, the velocity of light, the electric and magnetic fields are pancake-like, the electric field is radial and magnetic field azimuthal (the Liénard–Wiechert fields [1]) with an open angle of about $1/\gamma$, where $\gamma = (1 - v^2/c^2)^{-1/2}$. It is interesting to point out that no matter how far away, this pancake is always perpendicular to the path of motion. In other words, the fields move with the test particle without any lagging behind as illustrated in Fig. 1.1. Such a field pattern does not necessarily violate causality because it is a steady-state solution, which may require a long time to establish.

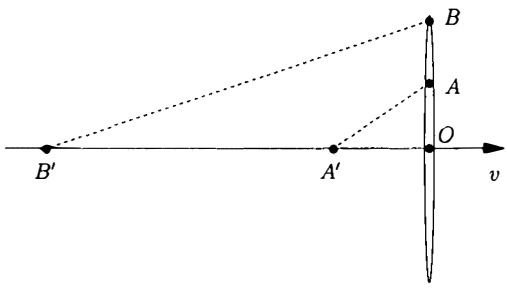


Fig. 1.1 Schematic drawing of pancake electromagnetic fields emitted by an ultra-relativistic particle traveling with velocity v. The pancake is always perpendicular to the path of the particle and travels in pace with the particle no matter how far away the fields are from the particle. There is no violation of causality because fields at points A and B come from the particle at different locations, respectively, from A' at a time OA'/v ago and from B' at a time OB'/v ago.

When placed inside a perfectly conducting beam pipe, the pancake of fields is trimmed by the beam pipe. A ring of negative charges will be formed on the walls of the beam pipe where the electric field ends, and these image charges will travel at the same pace with the particle, creating the so-called *image current*. If the

wall of the beam pipe is not perfectly conducting or contains discontinuities, the movement of the image charges will be slowed down, thus leaving electromagnetic fields behind. For example, upon coming across a cavity, the image current will flow into the walls of the cavity, exciting fields trapped inside the cavity. These fields left behind by the particle are called *wake fields*, which are important because they influence the motion of the particles that follow.

In addition to the wake fields, the electromagnetic fields experienced by the beam particle also consist of the external fields from the guiding and focusing magnets, rf cavities, etc. The electric field $\vec{E}$ and magnetic flux density $\vec{B}$ can be written as

$$(\vec{E},\vec{B})_{\substack{\text{seen by}\\ \text{particles}}} = (\vec{E},\vec{B})_{\substack{\text{external, from}\\ \text{magnets, rf, etc.}}} + (\vec{E},\vec{B})_{\substack{\text{wake}\\ \text{fields}}}, \tag{1.1}$$

where

$$(\vec{E},\vec{B})_{\substack{\text{wake}\\ \text{fields}}} \begin{cases} \propto \text{ beam intensity,} \\ \ll (\vec{E},\vec{B})_{\text{external}}. \end{cases}$$

Note that the last restriction, which is certainly not true in plasma physics, allows the wake fields inside the vacuum chamber to be treated as perturbation. This perturbation, however, will break down when potential-well distortion is large. In that case, the potential-well distortion has to be included into the non-perturbative part. What we need to compute are the wake fields at a distance z behind the source particle and their effects on the test or witness particles that make up the beam. The computation of the wake fields is nontrivial. Two approximations are therefore introduced.

1.1.1 *Two Approximations*

At high energies, the particle beam is rigid and the following two approximations apply:*

(1) **The rigid-beam approximation**, which says that the beam traverses the discontinuities of the vacuum chamber rigidly and the wake-field perturbation does not affect the motion of the beam during the traversal of the discontinuities. This is a good approximation even in the presence of synchrotron oscillations, because the longitudinal distance between two beam particles changes negligibly in a revolution turn relative to the bunch length. This implies that the distance z of the test particle behind some source particle as shown in Fig. 1.2 does not change.

*This approach to the Panofsky–Wenzel Theorem was first presented by A. W. Chao at the OCPA Accelerator School, Hsinchu, Taiwan, August 3–12, 1998.

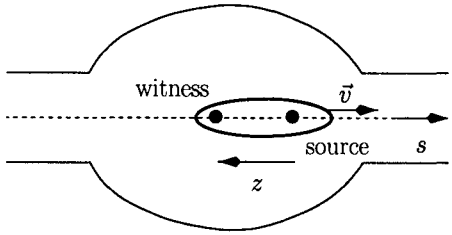


Fig. 1.2 Schematic drawing of a witness particle at a distance z behind some source particle in a beam. Both particles are traveling along the direction s with velocity $\vec{v}$.

(2) **The impulse approximation.** Although the test particle carrying a charge q sees a wake force $\vec{F}$ coming from $(\vec{E}, \vec{B})$, what it cares for is the impulse

$$\Delta\vec{p} = \int_{-\infty}^{\infty} dt\ \vec{F} = \int_{-\infty}^{\infty} dt\ q(\vec{E} + \vec{v} \times \vec{B}), \tag{1.2}$$

as it completes the traversal through the discontinuities at its fixed velocity $\vec{v}$. Note that MKS units have been used in Eq. (1.2) and will be adopted throughout the rest of the book. We will therefore be coming across the electric permitivity of free space $\epsilon_0 = 10^7/(4\pi c^2)$ farads/m and the magnetic permeability of free space $\mu_0 = 4\pi \times 10^{-7}$ henry/m. These two quantities are related to the free-space impedance Z_0 and velocity of light c by

$$Z_0 = \sqrt{\frac{\mu_0}{\epsilon_0}} = 2.99792458 \times 40\pi = 376.730313 \text{ Ohms}, \tag{1.3}$$

$$c = \frac{1}{\sqrt{\mu_0 \epsilon_0}} = 2.99792458 \times 10^8 \text{ m/s}. \tag{1.4}$$

Both $\vec{E}$, $\vec{B}$ and $\vec{F}$ are difficult to compute even at high beam energies. However, the impulse $\Delta\vec{p}$ has great simplifying properties through the Panofsky–Wenzel theorem, which forms the basis of wake potentials and impedances.

1.1.2 *Panofsky–Wenzel Theorem*

Maxwell equations for a particle in the beam are

$$\begin{cases} \vec{\nabla}\cdot\vec{E} = \dfrac{\rho}{\epsilon_0} & \text{Gauss's law for electric charge,} \\ \vec{\nabla}\times\vec{B} - \dfrac{1}{c^2}\dfrac{\partial\vec{E}}{\partial t} = \mu_0\beta c\rho\hat{s} & \text{Ampere's law,} \\ \vec{\nabla}\cdot\vec{B} = 0 & \text{Gauss's law for magnetic charge,} \\ \vec{\nabla}\times\vec{E} + \dfrac{\partial\vec{B}}{\partial t} = 0 & \text{Faraday's \& Lenz law.} \end{cases} \tag{1.5}$$

We have replaced the current density with $\vec{j} = \beta c \rho \hat{s}$ where ρ is the charge density of the beam. The beam particle velocity $|\vec{v}| = \beta c$ will be treated as a constant, which is the result of the rigid-beam approximation, and is certainly true at high energies when $\beta \approx 1$. Note that we have been denoting the s-axis as the direction of motion of the beam, while reserving z as the distance the witness particle is *ahead of* the source particle. For a circular ring, the s-axis constitutes the axis of symmetry of the vacuum chamber. Together with the horizontal and vertical coordinates, x and y, they form a local right-handed Cartesian coordinate system. Thus, the above wake fields $\vec{E}$ and $\vec{B}$ as well as wake force $\vec{F}$ are functions of x, y, s, t. The charge distribution ρ in above consists of actually only the source and test particles. From the rigid-beam approximation, the location of the test particle, s, is not independent, but is related to t by $s = z + \beta ct$, where z is regarded as time-independent and the location of the source particle is given by $s_{\text{source}} = \beta ct$. Since we are looking at the field behind a source, z is negative.†

The Lorentz force on the test particle of charge q is $\vec{F} = q(\vec{E} + \beta c \hat{s} \times \vec{B})$. Here the rigid-beam approximation has been used by requiring that the test particle has the same velocity as all other beam particles. It follows that

$$\vec{\nabla} \cdot \vec{F} = \frac{q\rho}{\epsilon_0 \gamma^2} - \frac{q\beta}{c} \frac{\partial E_s}{\partial t}, \tag{1.6}$$

$$\vec{\nabla} \times \vec{F} = -q \left(\frac{\partial}{\partial t} + \beta c \frac{\partial}{\partial s} \right) \vec{B}. \tag{1.7}$$

We are only interested in the impulse

$$\Delta \vec{p}(x, y, z) = \int_{-\infty}^{\infty} dt \; \vec{F}(x, y, z + \beta ct, t); \tag{1.8}$$

i.e., the integration of $\vec{F}$ along a rigid path with z being held fixed. Applying the curl to both sides,

$$\underset{\substack{\uparrow \\ \text{this } \vec{\nabla} \text{ refers} \\ \text{to } x, y, z}}{\vec{\nabla} \times \Delta \vec{p}(x, y, z)} = \int_{-\infty}^{\infty} dt \; \underset{\substack{\uparrow \\ \text{this } \vec{\nabla} \text{ refers} \\ \text{to } x, y, s}}{\left[\vec{\nabla} \times \vec{F}(x, y, s, t) \right]_{s = z + \beta ct}}, \tag{1.9}$$

we obtain

† z will be made positive later after a change of convention.

$$\vec{\nabla}\times\Delta\vec{p} = -q\int_{-\infty}^{\infty} dt\ \left[\left(\frac{\partial}{\partial t}+\beta c\frac{\partial}{\partial s}\right)\vec{B}(x,y,s,t)\right]_{s=z+\beta ct}$$
$$= -q\int_{-\infty}^{\infty} dt\ \frac{d\vec{B}}{dt} = -q\vec{B}(x,y,z+\beta ct,t)\Big|_{t=-\infty}^{\infty} = 0, \tag{1.10}$$

which is the Panofsky–Wenzel theorem. It is important to note that so far no boundary conditions have been imposed. The Panofsky–Wenzel theorem is valid for any boundaries! The only needed inputs are the two approximations: the rigid-bunch approximation and the impulse approximation. The Panofsky–Wenzel theorem even does not require $\beta = 1$. It just requires $\beta \approx 1$ so that β can remain constant. Thus, the Panofsky–Wenzel theorem is very general.

The Panofsky–Wenzel theorem can be decomposed into a component parallel to $\hat{s}$ and another perpendicular to $\hat{s}$. The decomposition is obtained by taking dot product and cross product of $\hat{s}$ with Eq. (1.10):

$$\vec{\nabla}\cdot(\hat{s}\times\Delta\vec{p}) = 0, \tag{1.11}$$

$$\frac{\partial}{\partial z}\Delta\vec{p}_\perp = \vec{\nabla}_\perp\Delta p_s. \tag{1.12}$$

Equation (1.11) says something about the transverse components of $\Delta\vec{p}$, which becomes, in Cartesian coordinates,

$$\frac{\partial\Delta p_x}{\partial y} = \frac{\partial\Delta p_y}{\partial x}. \tag{1.13}$$

On the other hand, Eq. (1.12) relates $\Delta\vec{p}_\perp$ and $\Delta\vec{p}_s$, that the transverse gradient of the longitudinal impulse is equal to the longitudinal gradient of the transverse impulse. Thus, the Panofsky–Wenzel theorem strongly constraints the components of $\Delta\vec{p}$.

There is an important supplement to the Panofsky–Wenzel theorem, which states:

$$\beta = 1 \longrightarrow \vec{\nabla}_\perp\cdot\Delta\vec{p}_\perp = 0. \tag{1.14}$$

Proof:

$$\vec{\nabla}\cdot\Delta\vec{p} = \int_{-\infty}^{\infty} dt\left[\vec{\nabla}\cdot\vec{F}(x,y,s,t)\right]_{s=z+ct} = -\frac{q}{c}\int_{-\infty}^{\infty} dt\left[\frac{\partial E_s}{\partial t}\right]_{s=z+ct}$$
$$= q\int_{-\infty}^{\infty} dt\left[\frac{\partial E_s}{\partial s}\right]_{s=z+ct} = \frac{\partial}{\partial z}\Delta p_s,$$

where we have used the fact that the longitudinal component of the wake force is independent of the magnetic flux density. For the second last step, use has been made of

$$\frac{\partial}{\partial t}E_s(s,t) = \frac{d}{dt}E_s(s,t) - \frac{ds}{dt}\frac{\partial}{\partial s}E_s(s,t). \tag{1.15}$$

It is important to note that $4\pi q\rho/\gamma^2$, the space-charge term of $\vec{\nabla}\cdot\vec{F}$ in Eq. (1.7) has been omitted because $\beta = 1$.

1.1.3 *Cylindrically Symmetric Chamber*

When the beam of cylindrical cross section is inside a cylindrically symmetric vacuum chamber, naturally cylindrical coordinates will be used. Some differential operators in the cylindrical coordinates are listed in Table 1.1. The Panofsky–Wenzel theorem, Eq. (1.10), and the supplemental theorem, Eq. (1.14), are rewritten as [3]

$$\begin{cases} \dfrac{\partial}{\partial r}(r\Delta p_\theta) = \dfrac{\partial}{\partial \theta}\Delta p_r, \\ \dfrac{\partial}{\partial z}\Delta p_r = \dfrac{\partial}{\partial r}\Delta p_s, \\ \dfrac{\partial}{\partial z}\Delta p_\theta = \dfrac{1}{r}\dfrac{\partial}{\partial \theta}\Delta p_s, \\ \dfrac{\partial}{\partial r}(r\Delta p_r) = -\dfrac{\partial}{\partial \theta}\Delta p_\theta \qquad (\beta = 1). \end{cases} \tag{1.16}$$

Now, this set of equations for $\Delta\vec{p}$ becomes surprisingly simple. It does not contain any source terms and is completely independent of boundaries, which can be conductors, resistive wall, dielectric, or even plasma. This result solely arises from the Maxwell equations plus the two approximations.

Table 1.1 Differential operators in the cylindrical coordinates. Here $\vec{A}$ is a vector and ϕ is a scalar.

$$\vec{\nabla}\cdot\vec{A} = \frac{1}{r}\frac{\partial}{\partial r}(rA_r) + \frac{1}{r}\frac{\partial A_\theta}{\partial \theta} + \frac{\partial A_s}{\partial s}$$

$$\vec{\nabla}\times\vec{A} = \hat{r}\left(\frac{1}{r}\frac{\partial A_s}{\partial \theta} - \frac{\partial A_\theta}{\partial s}\right) + \hat{\theta}\left(\frac{\partial A_r}{\partial s} - \frac{\partial A_s}{\partial r}\right) + \hat{s}\left(\frac{1}{r}\frac{\partial (rA_\theta)}{\partial r} - \frac{1}{r}\frac{\partial A_r}{\partial \theta}\right)$$

$$\nabla^2\phi = \frac{1}{r}\frac{\partial}{\partial r}\left(r\frac{\partial \phi}{\partial r}\right) + \frac{1}{r^2}\frac{\partial^2\phi}{\partial \theta^2} + \frac{\partial^2\phi}{\partial s^2}$$

There is no loss of generality to let $\Delta p_z \sim \cos m\theta$ with $m \geq 0$. Then, the three components of the impulse become

$$\Delta p_s = \Delta \tilde{p}_s \cos m\theta, \quad \Delta p_r = \Delta \tilde{p}_r \cos m\theta, \quad \text{and} \quad \Delta p_\theta = \Delta \tilde{p}_\theta \sin m\theta, \tag{1.17}$$

where $\Delta \tilde{p}_s$, $\Delta \tilde{p}_r$, and $\Delta \tilde{p}_\theta$ are θ-independent. The set of equations for $\Delta \vec{\tilde{p}}$ becomes

$$\begin{cases} \dfrac{\partial}{\partial r}(r\Delta \tilde{p}_\theta) = -m\Delta \tilde{p}_r, \\ \dfrac{\partial}{\partial z}\Delta \tilde{p}_r = \dfrac{\partial}{\partial r}\Delta \tilde{p}_s, \\ \dfrac{\partial}{\partial z}\Delta \tilde{p}_\theta = -\dfrac{m}{r}\Delta \tilde{p}_s, \\ \dfrac{\partial}{\partial r}(r\Delta \tilde{p}_r) = -m\Delta \tilde{p}_\theta \qquad (\beta = 1). \end{cases} \tag{1.18}$$

From the first and last equations, we must have, for $m = 0$,

$$\Delta \tilde{p}_\theta = 0 \qquad \text{and} \qquad \Delta \tilde{p}_r = 0, \tag{1.19}$$

otherwise they will be proportional to r^{-1} which is singular at $r = 0$. From the same two equations, we get, for $m \neq 0$,

$$\frac{\partial}{\partial r}\left[r\frac{\partial}{\partial r}(r\Delta \tilde{p}_r)\right] = m^2 \Delta \tilde{p}_r, \tag{1.20}$$

and therefore

$$\Delta p_r(r, \theta, z) \sim r^{m-1} \cos m\theta. \tag{1.21}$$

Now the whole solution can be written as, for all $m \geq 0$,

$$\begin{cases} v\Delta \vec{p}_\perp = -q\mathcal{Q}_m W_m(z) m r^{m-1}\left(\hat{r}\cos m\theta - \hat{\theta}\sin m\theta\right), \\ v\Delta p_s = -q\mathcal{Q}_m W'_m(z) r^m \cos m\theta. \end{cases} \tag{1.22}$$

In above, $W_m(z)$ is called the *transverse wake function of azimuthal* m and $W'_m(z)$ the *longitudinal wake function of azimuthal* m. The latter is the derivative of the former. They are related because of the Panofsky–Wenzel theorem. The wake functions are functions of one variable z only, and are the only remaining unknowns. They are the only quantities that are dependent on the boundary conditions, and must be solved independently. Recall that the complicated Maxwell–Vlasov equation that involves $\vec{E}$, $\vec{B}$, and sources has been reduced drastically to solving just for $W_m(z)$.

More comments about Eq. (1.22) are in order. The original solution in the top line of Eq. (1.22) was for $m \neq 0$ only. However, we can always define a $W_0(z)$ which is the anti-derivative of $W_0'(z)$ so that the solution holds for all m. Although $W_0(z)$ has no physical meaning, yet it will be helpful in discussions below. In Eq. (1.22), q is the charge of the test particle and $\mathcal{Q}_m$ is the electric mth multipole of the source particle. For a source particle of charge e at an offset a from the axis of the cylindrical beam pipe, $\mathcal{Q}_m = ea^m$. Thus, W_m' has the dimension of force per charge square per length$^{(2m-1)}$ or Volts/Coulomb/m^{2m}, while W_m has the dimension of force per charge square per length^{2m} or Volts/Coulomb/m^{2m-1}. The negative signs on the right sides arise just from a convention. For example, we want the longitudinal wake $W_m'(z)$ to be positive when the impulse acting on the test particle is decelerating.

Sometimes the wake functions are listed in the CGS units in literature, and W_m has the CGS dimension of length^{-2m}. The conversion consists of simply multiplying the wake functions in the CGS units by the factor $Z_0 c/(4\pi) = 0.898755 \times 10^{10}$. Thus a dipole transverse wake of $W_1 = 1 \times 10^5$ m^{-2} corresponds to $W_1 = 0.898755 \times 10^{15}$ V/(Coulomb-m).

Recall that we have been looking at the wake force on a particle traveling at $s = z + vt$ behind a source particle traveling at $s = vt$. Thus $z < 0$. When $v \to c$, causality has to be imposed that $W_m(z) = 0$ when $z > 0$. For our discussions below, we will continue to use v instead of c in most places, because we would like to derive stability conditions and growth rates also for machines that are not ultra-relativistic. However, strict causality will be imposed as if the velocity is c. So far, the derivation has been in the time domain. All variables, like the charge distribution ρ, the electromagnetic fields $\vec{E}$ and $\vec{B}$, the wake force $\vec{F}$, the impulse $\Delta\vec{p}$, etc, are real quantities. Thus the wake functions $W_m(z)$'s are also real functions.

Immediately behind a source particle, the test particle should receive a retarding force, otherwise a particle will continue to gain energy as it is traveling down the vacuum chamber in direct violation of the conservation of energy. This implies that $W_m'(z) > 0$ when $|z|$ is small, recalling that the $W_m'(z)$ is defined in Eq. (1.22) with a negative sign on the right side. This is illustrated in Fig. 1.3. It will be proved later in Chapter 7 that a particle sees half of its own wake. For the transverse wake $W_m(z)$, it starts out from zero[‡] and goes negative as $|z|$ increases, as required by the Panofsky–Wenzel theorem. Thus, when the source particle is deflected, a transverse wake force is created in the direction that it will deflect particles immediately following in the *same* direction of the deflection of the source. Again, special attention should be paid to the negative

[‡]Although it cannot be proved that $W_m(0) = 0$, however, most wakes do have this property.

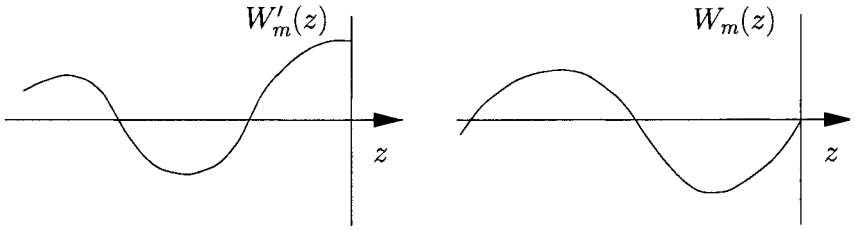


Fig. 1.3 The longitudinal wake $W'_m(z)$ vanishes when $z > 0$ and is positive definite when $|z|$ is small. The transverse wake $W_m(z)$ starts out from zero and goes negative as z decreases when $|z|$ is small.

sign on the right side of the definition of $W_m(z)$ in Eq. (1.22). The transverse wake W_m vanishes at $z = 0$ implies that a particle will not see its own transverse wake at all. This leads to the important conclusion that a shorter bunch will be preferred if the transverse wake dominates, and a longer bunch will be preferred if the longitudinal wake dominates.

When $m = 0$ or the monopole, we have $\Delta p_\perp = 0$ while Δp_s is independent of (r, θ) and depends only on z. Thus, particles in a thin transverse slice of the beam will see the same impulse in the s-direction according to the dependence of W'_0 on z, as shown in Fig. 1.4. This impulse can lead to self-bunching or microwave instability.

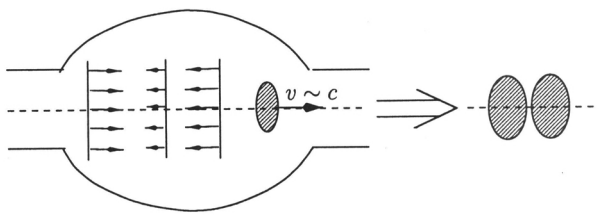


Fig. 1.4 All particles in a vertical slice of the beam see exactly the same monopole wake impulse ($m = 0$) from the source according to the slice position z behind the source. This longitudinal variation of impulse effect on the slices can lead to longitudinal microwave instability.

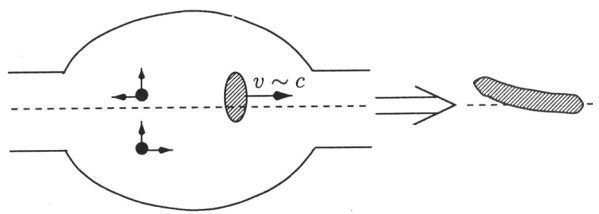


Fig. 1.5 Transverse kicks for all the particles in a vertical slice from the dipole wake impulse have the same magnitude; however, the longitudinal kicks point to forward or backward direction depending on whether the particles are above or below the axis of symmetry.

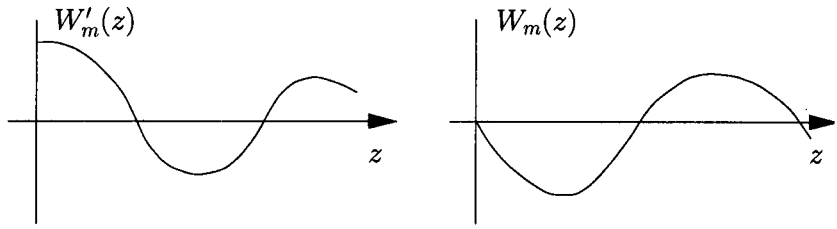


Fig. 1.6 This is a different convention that the wake functions $W_m(z)$ vanish when $z < 0$. Since the physics is the same, the wake functions are the same as in Fig. 1.3 and just the direction of z has been changed. In this convention, the interpretation $W'_m(z) \equiv -\frac{d}{dz}W_m(z)$ is required.

For $m = 1$, we have from Eq. (1.22) that $\Delta p_\perp$ is independent of (r, θ) but depends on z only. All particles in a vertical slice of the beam suffer exactly the same vertical kick from the dipole wake impulse ($m = 1$) which depends only on how far the slice is behind the dipole source, and will be kicked in the same transverse direction, as is shown in Fig. 1.5. Such an impulse can lead to the tilting of the tail of the bunch into a banana shape. Particle loss will occur when the tilted bunch hits the vacuum chamber. This is the cause of beam breakup. On the other hand, the dipole longitudinal impulse Δp_s ($m = 1$) is proportional to the offset of the test particle in the x-direction. Thus particles on opposite sides of the axis of the vacuum chamber will be driven longitudinally in the opposite directions.

For the sake of convenience, many authors do not like to work with a negative z for the particles that are following. There is another convention that $W_m(z) = 0$ when $z < 0$. This does not change the physics and the direction of the wake forces will not be changed. Thus, instead of Fig. 1.3, we have Fig. 1.6 instead. A price has to be paid for this convention. We must interpret the connection between the longitudinal and transverse wakes as

$$W'_m(z) \equiv -\frac{d}{dz}W_m(z). \tag{1.23}$$

This convention will be used for the rest of the book.[§] Fortunately, we will not be using Eq. (1.23) much below, because most longitudinal instabilities are driven dominantly by the monopole longitudinal wake W'_0 and most transverse instabilities are driven dominantly by the dipole transverse wake W_1. We will have a brief investigation of the quadrupole wake function in Chapter 14.

[§]The readers should be aware of yet another convention in the literature that $W_m(z)$ and $W'_m(z)$ are defined in Eq. (1.22) *without* the negative signs on the right sides. The wake functions, however, will have just the opposite signs of what are depicted in Fig. 1.6.

1.2 Coupling Impedances

Beam particles form a current, of which the component with frequency $\omega/(2\pi)$ is[†] $I(s,t) = \hat{I}e^{-i\omega(t-s/v)}$, where $\hat{I}$ may be complex. Let us concentrate on a very short section Δs_1 of the cylindrical vacuum chamber at s_1 and assume that the vacuum chamber does not generate any wake outside this section. A test particle at location s_1 at time t will be affected by the wake left behind by the preceding charge element $I(s_1, t-z/v)dz/v$ that passes the point s_1 at time $t-z/v$ earlier. The *accelerating* voltage seen (or energy gained per unit test charge) is

$$V(s_1,t) = -\int_{-\infty}^{\infty} \hat{I}e^{-i\omega[t-(s_1+z)/v]} \left[W_0'(z)\right]_1 \frac{dz}{v} = -I(s_1,t)\int_{-\infty}^{\infty} e^{i\omega z/v} \left[W_0'(z)\right]_1 \frac{dz}{v}, \tag{1.24}$$

where $[W_0'(z)]_1$ is wake function for the small section of the vacuum chamber at s_1. If we write the potential across the section at s_1 as $V(s_1,t) = \hat{V}_1 e^{-i\omega(t-s_1/v)}$, the above simplifies to

$$\hat{V}_1 = -\hat{I}\int_{-\infty}^{\infty} e^{i\omega z/v} \left[W_0'(z)\right]_1 \frac{dz}{v}. \tag{1.25}$$

Thus, we can identify the *longitudinal coupling impedance* of this small section of the vacuum chamber at s_1 as

$$\left[Z_0^{\parallel}(\omega)\right]_1 = \int_{-\infty}^{\infty} e^{i\omega z/v} \left[W_0'(z)\right]_1 \frac{dz}{v}, \tag{1.26}$$

where the lower limit has been extended to $-\infty$ because of the causal property of the wake function. This definition is the same as the ordinary impedance in a circuit. Notice that $q\hat{V}_1 = F^{\parallel}(s_1)\Delta s_1$, and the latter is just the integrated longitudinal wake force across the small section at s_1. Unlike the integrated wake force (or the longitudinal impulse Δp_s), however, $V(s_1,t)$ in general complex. This is because we have been using a current wave as the source in the complex representation.

Next let us consider the adjacent section of the vacuum chamber at s_2 and assume the rest of the vacuum chamber does not generate any wake. We then obtain the potential $V(s_2,t) = \hat{V}_2 e^{-i\omega(t-s_2/v)}$ across this section as

$$\hat{V}_2 = -\hat{I}\left[Z_0^{\parallel}(\omega)\right]_2, \tag{1.27}$$

[†] We are going to use the physicist convention of frequency dependence $e^{-i\omega t}$, which leads to the results that the capacitive impedance is positive imaginary while the inductive impedance is negative imaginary. The opposite is true in the engineer convention of $e^{j\omega t}$.

where $\left[Z_0^{\parallel}(\omega)\right]_2$, given by Eq. (1.26) with the subscript 1 replaced by 2, is the coupling impedance for this small section at s_2. When all these small sections are added up, $\sum_i [W_0'(z)]_i = W_0'(z)$, which is the wake function of the whole vacuum chamber, and $Z_0^{\parallel}(\omega) = \sum_i \left[Z_0^{\parallel}(\omega)\right]_i$, or

$$Z_0^{\parallel}(\omega) = \int_{-\infty}^{\infty} e^{i\omega z/v} W_0'(z) \frac{dz}{v} \tag{1.28}$$

becomes the longitudinal coupling impedance of the whole vacuum chamber.

We have here much more than in a circuit because, unlike a current in a resistive wire, the beam current possesses transverse distribution thus leading to higher multipoles, for example, when the current is displaced horizontally by a from the axis of symmetry of the cylindrical vacuum chamber. Let us concentrate now on the mth multipole of the current

$$\mathcal{P}_m(s,t) = I(s,t)a^m = \hat{\mathcal{P}}_m e^{-i\omega(t-s/v)}, \tag{1.29}$$

where $\hat{\mathcal{P}}_m = \hat{I}a^m$. Consider a test particle of charge q at $x = a$ in the beam traveling with velocity v in the s-direction. Its charge density is given by

$$\begin{aligned}\rho(r,\theta,s;t) &= \frac{q}{a}\delta(r-a)\delta(\theta)\delta(s-vt) \\ &= \sum_{m=0}^{\infty} \frac{\mathcal{Q}_m}{(1+\delta_{m0})\pi a^{m+1}} \delta(r-a)\cos m\theta \int_{-\infty}^{\infty} \frac{d\omega}{2\pi v} e^{-i\omega(t-s/v)},\end{aligned} \tag{1.30}$$

where $\mathcal{Q}_m = qa^m$ denotes the electric mth multipole of the test particle. Again assume that the vacuum chamber does not generate any wake fields except for a short section of length Δs_i at s_i. At location s_i and time t, the test particle will see the wake left behind by the preceding charge mth-multipole element in the beam, $\mathcal{P}(s_i, t - z/v)dz/v$, that passes the location s_i at time $t - z/v$. The total accelerating voltage seen by the test particle across this small section is, according to the longitudinal wake force in Eq. (1.22),

$$V(s_i,t) = -\int_{-\infty}^{\infty} \frac{dz}{v} \mathcal{P}_m(s_i, t-z/v) \left[W_m'(z)\right]_i \int r dr d\theta\, r^m \cos m\theta \frac{\delta(r-a)\delta(\theta)}{a}, \tag{1.31}$$

where $[W_m'(z)]_i$ is the mth-multipole wake function for this small section of the vacuum chamber at s_i, and the charge density of the test particle has been inserted. For consistency, it is easy to check that Eq. (1.31) reduces to Eq. (1.24) when $m = 0$. Obviously, only the mth multipole of the charge density contributes

and we obtain after integrating over r and θ,

$$\hat{V}_1 = -\frac{\hat{\mathcal{P}}_m \mathcal{Q}_m}{q} \int_{-\infty}^{\infty} \frac{dz}{v} e^{-i\omega z/v} \left[W'_m(z)\right]_i . \tag{1.32}$$

Summing up the contribution of all small sections of the vacuum chamber, we obtain the total potential difference, $\hat{V} = \sum_i \hat{V}_i$, across the whole vacuum chamber in terms of the total mth-multipole wake function $W'_m(z) = \sum_i \left[W'_m(z)\right]_i$,

$$\hat{V} = -\frac{\hat{\mathcal{P}}_m \mathcal{Q}_m}{q} \int_{-\infty}^{\infty} \frac{dz}{v} e^{-i\omega z/v} W'_m(z). \tag{1.33}$$

Following Eq. (1.28), we identify

$$Z_m^{\parallel}(\omega) = \int_{-\infty}^{\infty} e^{i\omega z/v} W'_m(z) \frac{dz}{v} \tag{1.34}$$

as the longitudinal coupling impedance of the vacuum chamber in the mth multipole. Physically, this is equal to the decelerating voltage seen by one unit of test charge multipole $\mathcal{Q}_m$ in a beam of unit current mth multipole $\mathcal{P}_m$. Correspondingly, the *transverse coupling impedance of the mth multipole* is defined as

$$Z_m^{\perp}(\omega) = \frac{i}{\beta} \int_{-\infty}^{\infty} e^{i\omega z/v} W_m(z) \frac{dz}{v}. \tag{1.35}$$

Recalling that $W'_m(z) = -dW_m(z)/dz$, we have therefore $Z_m^{\parallel}(\omega) = \omega Z_m^{\perp}(\omega)/c$. Since $\mathcal{R}e\, Z_1^{\perp}(\omega) > 0$ when $\omega > 0$ is required by the Panofsky–Wenzel theorem [see Eq. (1.49)], the oscillatory motion of the multipole $\mathcal{P}_m$ is seeing a transverse wake force $F_m^{\perp}$ that opposes its motion. Thus $F_m^{\perp}$ must lag the dipole by $\pi/2$ in order to dissipate its energy, and hence the the factor $-i$ in Eq. (1.43).[‡] The Lorentz factor $\beta = v/c$ is inserted to cancel the velocity in the Lorentz force.[§]

We learn from the above derivation that the longitudinal impedance in the mth multipole corresponds essentially to the energy lost to the mth multipole current when the mth-multipole wake force is encountered. In fact, we can write

$$q\hat{V} = \sum_i \left[F_m^{\parallel}\right]_i \Delta s_i = \int_0^L F_m^{\parallel}(s) ds, \tag{1.36}$$

where $\left[F_m^{\parallel}\right]_i$ is the mth-multipole wake force experienced at the small section at s_i with the factor $e^{-i\omega(t-s_i/v)}$ removed. Since the mth multipole wake force has

[‡]In the $e^{-i\omega t}$ convention, phase advances clockwise as time progresses. Thus a phase lead/lag implies $e^{-i\psi}$ with $\psi \gtrless 0$.

[§]Some authors define the transverse impedance without the factor β in the denominator.

a transverse distribution proportional to $r^m \cos m\theta$, its evaluation in Eq. (1.36) should be at $r = a$ and $\theta = 0$, the offset position of the original beam current or the test particle. Instead, Eq. (1.36) can be rewritten more conveniently as

$$q\hat{V} = \frac{1}{\hat{I}} \int_0^L F_m^{\parallel}(s, r, \theta) J_m^* dV, \tag{1.37}$$

where ¶

$$J_m(r, \theta, s; t) = \frac{\hat{\mathcal{P}}_m}{(1 + \delta_{m0})\pi a^{m+1}} \delta(r - a) \cos m\theta \, e^{-i\omega(t - s/v)} \tag{1.38}$$

is the mth-multipole current density in the same longitudinal direction of the longitudinal wake force, and the volume integral is performed with $dV = rdrd\theta ds$ ranging over the cross section and the length of the vacuum chamber.

Following Eq. (1.31), the coupling impedance $Z_m^{\parallel}(\omega)$ can be expressed as in terms of the wake force $F^{\parallel}(s, r, \theta)$ experienced by a test particle along the vacuum chamber,

$$Z_m^{\parallel}(\omega) = -\frac{1}{q\hat{\mathcal{P}}_m^2} \int_0^L F_m^{\parallel} J_m^* dV, \tag{1.39}$$

in a form which can be used more easily in computation. In above, and wake force $F_m^{\parallel}$ is allowed to include the exponential factor $e^{-i\omega(t - s/v)}$ and this factor is cancelled when it is multiplied by the complex conjugate of J_m. The transverse impedance in the mth multipole is then given by

$$Z_m^{\perp}(\omega) = -\frac{c}{\omega q \hat{\mathcal{P}}_m^2} \int_0^L F_m^{\parallel} J_m^* dV. \tag{1.40}$$

In Eqs. (1.39) and (1.40), q is the charge of a test particle, so that $F_m^{\parallel}(r, \theta, s; t)/q = E^{\parallel}(r, \theta, s; t)$ is the longitudinal electric field experienced by the beam particle. It is important to point out that in Eq. (1.39) or Eq. (1.40), the integration over ds covers just the length L of the beam pipe and in the case of a circular ring, L is usually taken as the ring circumference C. Thus, the integral represents an average of the wake force around the circumference of the ring. On the other hand, in Eq. (1.28), (1.34) or (1.35), the longitudinal integration is over z, the distance behind the source particle, and the upper limit has to be taken to $+\infty$ unless the wake is short.

¶Here we consider J_m to have the dimension of current density. If it is considered as a frequency Fourier component instead, so that the total current density is $\int d\omega J_m$, it carries the dimension of current density multiplied by time, and Eqs. (1.37), (1.39), and (1.40) will require suitable adjustment.

The transverse impedance can also be expressed in terms of the transverse wake force, because there Panofsky–Wenzel theorem relates the longitudinal and transverse wake forces. Let us concentrate on the dipole contribution ($m = 1$). For an infinitesimal offset ($a \to 0$), the dipole current density can be written as[‖]

$$J_1(r,\theta,s;t) = \frac{\mathcal{P}_1}{2a}\big[\delta(x-a) - \delta(x+a)\big]e^{-i\omega(t-s/v)}. \tag{1.41}$$

Then the dipole impedance in the horizontal direction is

$$\begin{aligned} Z_1^x(\omega) &= -\frac{c}{\omega q \mathcal{P}_1}\int_0^L F_1^{\parallel}\frac{\big[\delta(x-a)-\delta(x+a)\big]}{2a}\,\delta(y)\,e^{i\omega(t-s/v)}dV \\ &= -\frac{c}{\omega q \mathcal{P}_1}\int_0^L \frac{\partial F_1^{\parallel}}{\partial x}\,e^{i\omega(t-s/v)}dz, \end{aligned} \tag{1.42}$$

where $F_1^{\parallel}$, evaluated at $x = a$ and $y = 0$, is the longitudinal dipole wake force in the s-direction including the factor $e^{-i\omega(t-s/v)}$. Finally, employing Panofsky–Wenzel theorem in the form of Eq. (1.12), we obtain

$$Z_1^{\perp}(\omega) = -\frac{i}{\beta q \mathcal{P}_1}\int_0^L F_{1x}e^{i\omega(t-s/v)}dz, \tag{1.43}$$

where F_{1x} is the horizontal wake force. Thus the transverse dipole impedance is just the average integrated transverse wake force generated by a unit dipole current experienced by a particle of unit charge.

The transverse dipole impedance can also be derived directly from the transverse dipole wake force $F_1^{\perp}$ without going into the longitudinal wake force $F_1^{\parallel}$. When the current is displaced transversely by a from the axis of symmetry of the beam pipe, the *deflecting* transverse force acting on a current particle is obtained by summing the charge element $I(s,t-z/v)dz/v$ passing s at time $t-z/v$,

$$\begin{aligned} \langle F_1^{\perp}(s,t)\rangle &= -\frac{qa}{L}\int_{-\infty}^{\infty}\hat{I}e^{-i\omega[t-(s+z)/v]}W_1(z)\frac{dz}{v} \\ &= -\frac{qa}{L}I(s,t)\int_{-\infty}^{\infty}e^{i\omega z/v}W_1(z)\frac{dz}{v}, \end{aligned} \tag{1.44}$$

where $\langle F_1^{\perp}(s,t)\rangle$ is the transverse force of frequency ω in the direction of the displacement averaged over a length L covering the discontinuity of the vacuum chamber, and is therefore equal to $v\Delta p_{\perp}/L$, with $\Delta p_{\perp}$ being the transverse impulse studied in the previous section. With the definition of the dipole transverse

[‖] Essentially, as $a \to 0$, we have $\frac{1}{\pi a^2}\delta(r-a)\cos\theta = \frac{1}{2a}\big[\delta(x-a)-\delta(x+a)\big]\delta(y)$. The dipole moment results when multiplied by qx and integrated over the cross-sectional area.

coupling impedance of the vacuum chamber given by Eq. (1.35), we get back Eq. (1.43).

We learn that the coupling impedances are the Fourier transforms of the corresponding wake functions. The wake functions can be written in terms of the impedances as inverse Fourier transforms:

$$W_m(z) = -\frac{i\beta}{2\pi}\int_{-\infty}^{\infty} Z_m^{\perp}(\omega)e^{-i\omega z/v}d\omega, \tag{1.45}$$

$$W_m'(z) = \frac{1}{2\pi}\int_{-\infty}^{\infty} Z_m^{\parallel}(\omega)e^{-i\omega z/v}d\omega, \tag{1.46}$$

where the path of integration in both cases is above all the singularities of the impedances so as to guarantee causality.

Note that the longitudinal impedance is mostly the monopole ($m = 0$) impedance and the transverse impedance is mostly the dipole ($m = 1$) impedance, if the beam pipe cross section is close to circular and the particle path is close to the pipe axis. They have the dimensions of Ohms and Ohms/length, respectively. The impedances have the following properties:**

1. $Z_m^{\parallel}(-\omega) = \left[Z_m^{\parallel}(\omega)\right]^*$ and $Z_m^{\perp}(-\omega) = -\left[Z_m^{\perp}(\omega)\right]^*$. (1.47)
2. $Z_m^{\parallel}(\omega)$ and $Z_m^{\perp}(\omega)$ are analytic with poles only in the lower half ω-plane. (1.48)
3. $Z_m^{\parallel}(\omega) = \frac{\omega}{c}Z_m^{\perp}(\omega)$, for cylindrical geometry and each azimuthal harmonic including $m = 0$. (1.49)
4. $\mathcal{R}e\, Z_m^{\parallel}(\omega) \geq 0$ and $\mathcal{R}e\, Z_m^{\perp}(\omega) \geq 0$ when $\omega > 0$, if the beam pipe has the same entrance cross section and exit cross section. (1.50)
5. $\int_0^{\infty} d\omega\, \mathcal{I}m\, Z_m^{\perp}(\omega) = 0$, and $\int_0^{\infty} d\omega\, \frac{\mathcal{I}m\, Z_m^{\parallel}(\omega)}{\omega} = 0$. (1.51)

The first follows because the wake functions are real, the second from the causality of the wake functions, and the third from the Panofsky–Wenzel theorem [2] between transverse and longitudinal electromagnetic forces. $\mathcal{R}e\, Z_m^{\parallel}(\omega) \geq 0$ is the result of the fact that the total energy of a particle or a bunch cannot be increased after passing through a section of the vacuum chamber where there is no accelerating external forces, while $\mathcal{R}e\, Z_m^{\perp}(\omega) \geq 0$ when $\omega > 0$ follows from

**In Property 2, if we adopt the $e^{j\omega t}$ convention instead, all the singularities will be in the upper half plane. In Property 3, $Z_0^{\perp}$ may not have any physical meaning. But it is a well-defined quantity mathematically.

the Panofsky–Wenzel theorem. The fifth property follows from the assumption that $W_m(0) = 0$.

For a pure resistance R, the longitudinal wake is $W_0'(z) = R\delta(z/v)$. At low frequencies, the wall of the beam pipe is inductive. This wake function is $W_0'(z) = \mathcal{L}\delta'(z/v)$, where $\mathcal{L}$ is the inductance.

For a nonrelativistic beam of radius a inside a circular beam pipe of radius b, the longitudinal space-charge impedance for $m = 0$ is[††]

$$Z_0^{\parallel}(\omega) = i\frac{\omega}{\omega_0}\frac{Z_0}{2\gamma^2\beta}\left(1 + 2\ln\frac{b}{a}\right), \tag{1.52}$$

where $Z_0 = \sqrt{\mu_0/\epsilon_0} \approx 377\ \Omega$ is the impedance of free space, μ_0 and ϵ_0 are, respectively, the magnetic permeability and electric permitivity of free space, $\omega_0/(2\pi)$ is the revolution frequency of the beam particle with Lorentz factors γ and β. Although this impedance is capacitive, however, it appears in the form of a negative inductance. The corresponding wake function is

$$W_0'(z) = -\delta'(z/v)\frac{1}{\omega_0}\frac{Z_0}{2\gamma^2\beta}\left(1 + 2\ln\frac{b}{a}\right). \tag{1.53}$$

The $m = 1$ transverse space-charge impedance for a length L of the circular beam pipe is

$$Z_1^{\perp}(\omega) = i\frac{Z_0 L}{2\pi\gamma^2\beta^2}\left[\frac{1}{a^2} - \frac{1}{b^2}\right], \tag{1.54}$$

and the corresponding transverse wake function is

$$W_1(z) = \frac{Z_0 cL}{2\pi\gamma^2}\left[\frac{1}{a^2} - \frac{1}{b^2}\right]\delta(z). \tag{1.55}$$

The space-charge impedances will be derived in Chapter 2.

An important impedance is that of a resonant cavity. Near the resonant frequency $\omega_r/(2\pi)$, the mth multipole longitudinal impedances can be approximated by a RLC-parallel circuit:

$$Z_m^{\parallel}(\omega) = \frac{R_{ms}}{1 + iQ\left(\dfrac{\omega_r}{\omega} - \dfrac{\omega}{\omega_r}\right)}, \tag{1.56}$$

where the resonant angular frequency is $\omega_r = (\mathcal{L}_m C_m)^{-1/2}$ and quality factor is $Q = R_{ms}\sqrt{C_m/\mathcal{L}_m}$. Here, for the mth multipole, the shunt impedance R_{ms}

[††]This expression will be derived in Sec. 2.4. Here, the space-charge force is seen by beam particles at the beam axis. If the force is averaged over the cross section of the beam with a uniform transverse cross section, the first term in the brackets becomes $\frac{1}{2}$ instead of 1.

is in Ohms/m^{2m}, the inductance $\mathcal{L}_m$ in henry/m^{2m}, and the capacitance C_m in farad-m^{2m}. The transverse impedance can now be obtained from the Panofsky–Wenzel theorem of Eq. (1.49):

$$Z_m^{\perp}(\omega) = \frac{c}{\omega} \frac{R_{ms}}{1 + iQ\left(\frac{\omega_r}{\omega} - \frac{\omega}{\omega_r}\right)}. \tag{1.57}$$

Another example is the longitudinal impedance for a length L of the resistive beam pipe:

$$Z_0^{\parallel}(\omega) = [1 - i\,\mathrm{sgn}(\omega)] \frac{L}{2\pi b \sigma_c \delta_{\mathrm{skin}}}, \tag{1.58}$$

where b is the radius of the cylindrical beam pipe, σ_c is the conductivity of the pipe wall,

$$\delta_{\mathrm{skin}} = \sqrt{\frac{2c}{Z_0 \mu_r \sigma_c |\omega|}} \tag{1.59}$$

is the skin-depth at frequency $\omega/(2\pi)$, and μ_r is the relative magnetic permeability of the pipe wall. The transverse impedance is

$$Z_1^{\perp}(\omega) = [1 - i\,\mathrm{sgn}(\omega)] \frac{Lc}{\pi \omega b^3 \sigma_c \delta_{\mathrm{skin}}}, \tag{1.60}$$

and is related to the longitudinal impedance by

$$Z_1^{\perp}(\omega) = \frac{2c}{b^2 \omega} Z_0^{\parallel}(\omega). \tag{1.61}$$

The above relation has been used very often to estimate the transverse impedance from the longitudinal. However, we should be aware that this relation holds only for resistive impedances of a cylindrical beam pipe. The monopole longitudinal impedance and the dipole transverse impedance belong to different azimuthals; therefore they should not be related. An example that violates Eq. (1.61) is the longitudinal and transverse space-charge impedances stated in Eqs. (1.52) and (1.54).

The expression of the transverse resistive-wall impedance as given by Eq. (1.60) is not quite correct because it indicates a divergency as $\omega^{-1/2}$ at low frequencies. Actually, $\mathcal{I}m\, Z_1^{\perp}$ approaches a constant as $\omega \to 0$ while $\mathcal{R}e\, Z_1^{\perp}$ bends around and approaches zero. These behaviors have important bearing on transverse coupled-bunch instabilities, which we will address in Chapter 10.

More expressions for wakes and impedances resulting from various types of discontinuity in the vacuum chamber are listed in the Appendix. [4] Readers that have interest in deriving these and other expressions of impedances should

consult the books or articles written by Chao, Gluckstern, as well as Zotter and Kheifets. [3, 15, 16]

1.3 Parasitic Loss

A beam particle inside a vacuum chamber loses energy in three ways: through synchrotron radiation when its path is bent by the magnetic dipole fields of the accelerator lattice, through interaction with the wake fields left by preceding beam particles, and through interaction with the residual gas molecules. In this section, we are going to concentrate on the energy loss through wake fields. This loss is also known as parasitic loss.

1.3.1 *Coherent Loss*

Consider a bunch having linear distribution $\lambda(\tau)$ that is normalized to unity,

$$\int_{-\infty}^{\infty} \lambda(\tau) d\tau = 1. \tag{1.62}$$

A beam particle is referenced by τ, its time of arrival at a designated point in the accelerator ring ahead of the synchronous particle (see Sec. 2.1.1). The bunch is considered stationary and its time dependency has therefore been omitted in this consideration. The energy *gained* experienced by this particle in a revolution turn is, according to Eq. (1.22),

$$\Delta\mathcal{E}(\tau) = -e^2 N_b \int_{-\infty}^{\tau} d\tau' W_0'(\tau - \tau')\lambda(\tau'), \tag{1.63}$$

where N_b is the total number of beam particles in the bunch. In the frequency space, with*

$$\tilde{\lambda}(\omega) = \frac{1}{2\pi} \int_{-\infty}^{\infty} d\tau \lambda(\tau) e^{-i\omega\tau}, \tag{1.64}$$

the energy gained by the beam particle can be represented by

$$\Delta\mathcal{E}(\tau) = -e^2 N_b \int_{-\infty}^{\infty} d\omega \tilde{\lambda}(\omega) Z_0^{\parallel}(\omega) e^{-i\omega\tau}, \tag{1.65}$$

where Eq. (1.46) has been used. We see that particles at different arrival time τ gain energy differently. When averaged over all the particles in the bunch, the

*The reader should be aware that the definition of the Fourier transform, with or without the factor $(2\pi)^{-1}$ in front of the integral, will affect the expressions for energy gain below.

average energy gain per particle per turn is given by

$$\overline{\Delta\mathcal{E}} = \int_{-\infty}^{\infty} d\tau \lambda(\tau)\mathcal{E}(\tau) = -2\pi e^2 N_b \int_{-\infty}^{\infty} d\omega \left|\tilde{\lambda}(\omega)\right|^2 Z_0^{\parallel}(\omega). \tag{1.66}$$

Notice that

$$\begin{aligned}\left|\tilde{\lambda}(\omega)\right|^2 &= \frac{1}{(2\pi)^2}\int_{-\infty}^{\infty} d\tau \int_{-\infty}^{\infty} d\tau' \lambda(\tau)\lambda(\tau')e^{-i\omega(\tau-\tau')} \\ &= \frac{1}{(2\pi)^2}\int_{-\infty}^{\infty} d\tau \int_{-\infty}^{\infty} d\tau' \lambda(\tau)\lambda(\tau')\cos[\omega(\tau-\tau')].\end{aligned} \tag{1.67}$$

Since $\left|\tilde{\lambda}(\omega)\right|^2$ is real and is symmetric in ω, only $\mathcal{R}e\, Z_0^{\parallel}$ contributes in Eq. (1.66). For a bunch in a circular beam pipe of radius b and Gaussian distributed linearly with rms length σ_τ, the parasitic energy gained per revolution turn can be computed straightforwardly using the longitudinal resistive-wall impedance given in Eq. (1.58), and the result is

$$\Delta\mathcal{E}_{\text{bunch}} = -\frac{e^2 N_b^2 R\Gamma\left(\frac{3}{4}\right)}{2\pi b\sigma_\tau^{3/2}}\left(\frac{Z_0\mu_r}{2\sigma_c c}\right)^{1/2}, \tag{1.68}$$

where μ_r and σ_c are, respectively, the relative magnetic permeability and electric conductivity of the beam pipe, R is the mean radius of the accelerator ring, and $\Gamma\left(\frac{3}{4}\right) = 1.22542$ is the Gamma function.

The Fourier transform of the linear density has not been performed correctly. [5] In the absence of focusing by the rf system, the linear density $\lambda(\tau)$ is periodic in τ with period $T_0 = 2\pi/\omega_0$. The Fourier transform is therefore discrete. The correct Fourier expansion should be

$$\lambda(\tau) = \frac{2\pi}{T_0}\sum_{n=-\infty}^{\infty} \tilde{\lambda}_n e^{in\omega_0\tau}. \tag{1.69}$$

Instead of Eq. (1.64), the Fourier transform is

$$\tilde{\lambda}_n = \frac{1}{2\pi}\int_{-T_0/2}^{T_0/2} d\tau\, \lambda(\tau)e^{-in\omega_0\tau}, \tag{1.70}$$

with the energy gain per turn

$$\Delta\mathcal{E}(\tau) = -e^2 N_b\omega_0 {\sum_{n=-\infty}^{\infty}}' \lambda_n Z_0^{\parallel}(n\omega_0)e^{in\omega_0\tau}, \tag{1.71}$$

where the primed summation runs over all nonzero integer n and the exclusion of $n = 0$ will be explained below. An unconventional constant has been placed

in front of the summation in the harmonic expansion of Eq. (1.69) so that the discrete Fourier transform $\tilde{\lambda}_n$ of Eq. (1.70) has similar definition as the non-periodic transform $\tilde{\lambda}(\omega)$ of Eq. (1.64). This also results in the average energy gain per particle per turn

$$\overline{\Delta\mathcal{E}} = -2\pi e^2 N_b \omega_0 \sum_{n=-\infty}^{\infty}{}' \left|\tilde{\lambda}_n\right|^2 \mathcal{R}e\, Z_0^{\parallel}(n\omega_0), \tag{1.72}$$

which is very similar to the corresponding one, Eq. (1.66), in the non-periodic expansion.

When the bunch is short, there is not much difference between Eqs. (1.66) and (1.72), because the spectrum of the bunch extends to very high frequencies and therefore many harmonics. However, for very long bunches, the difference can become very big. This is reflected by the fact that the Fourier transform of the linear density in Eq. (1.64) is clearly invalid mathematically when the bunch nearly fills up the ring longitudinally. As an example, a long bunch of length τ_0 in the Fermilab Recycler Ring confined between two barrier waves usually has sharp edges longitudinally and may occupy over 80% of the ring. In this case, only very few low harmonics will contribute. If the linear density is represented by

$$\lambda(\tau) = \begin{cases} \dfrac{1}{\tau_0} & |\tau| < \dfrac{\tau_0}{2}, \\ 0 & \text{otherwise}, \end{cases} \tag{1.73}$$

the power spectrum is, for any integer n from $-\infty$ to $+\infty$,

$$\left|\tilde{\lambda}_n\right|^2 = \frac{1}{(2\pi)^2}\left(\frac{\sin n\omega_0\tau_0/2}{n\omega_0\tau_0/2}\right)^2. \tag{1.74}$$

Let us examine the lower harmonics. First, the zero harmonic (or dc component) does not contribute to the parasitic loss even if $\mathcal{R}e\, Z_0^{\parallel} \neq 0$. The $n = 0$ component of a beam is static because there is no time dependency.[†] As a result, electric field and magnetic field in the Maxwell equations are separated. There is no more Faraday's law. Thus, the static magnetic field of the beam's dc component does not induce any electric field on the surface or inside the wall of the beam pipe. In other words, there is no image current corresponding to the dc component of the beam, resulting in zero energy loss. For the dc component, what is present in the wall of the beam pipe is just static (nonmoving) image charges. For the

[†] One may argue that the dc component is also time varying because the revolution frequency of the beam is changing when the rf voltage is turned off. However, this change is extremely slow, for example, only 0.032 Hz in an hour in the Fermilab Recycler Ring.

other low harmonics, the argument of sine,

$$\frac{n\omega_0\tau_0}{2} = n\pi\frac{\tau_0}{T_0} \tag{1.75}$$

is close to $n\pi$ if the bunch length is nearly as long as the circumference of the ring. Thus, the energy loss per turn will be very small. For example, if $\tau_0/T_0 = 0.82$, $\left|\tilde{\lambda}_n\right|^2 = 0.00110, 0.00078, 0.00042, 0.00014, \cdots$, respectively, for $n = \pm 1, \pm 2, \pm 3, \pm 4, \cdots$, indicating that only a few low harmonics are important. On the other hand, if the non-periodic expression of Eq. (1.66) is used instead, the large $\sin x/x$ peak will have been partially included in an incorrect way, even with a $\mathcal{R}e\, Z_0^{\parallel}$ that goes to zero at zero frequency. Notice that, as the bunch length continues to increase to fill up the whole ring, the power spectrum $\left|\tilde{\lambda}_n\right|$ falls to zero except for $n = 0$, implying that the parasitic loss approaches zero. On the other hand, in the non-periodic expansion, the parasitic loss given by Eq. (1.65) will never go to zero.

1.3.2 *Incoherent Loss*

The energy loss expressions derived above are for *coherent* energy loss, implying that only the loss due to the coherent spectrum has been taken into account. This can be understood by realizing that we have been referring to the power spectrum of a bunch but not the spectrum of the individual particles. For this reason, the total energy loss by the bunch is proportional to N_b^2 and the per particle energy loss is proportional to N_b.

For a true coasting beam, the arrival time of a beam particle at a designated point of the accelerator ring is random. The image current will be the *incoherent sum* of the image current coming from each individual beam particle. As will be shown below, the energy loss of the whole beam is incoherent, because it is proportional to N, the total number of beam particles in the beam rather than N^2. [6, 7, 8]

In the time domain, each particle induces an image pulse of rms width (Exercise 1.4)

$$\sigma_\tau = \frac{b}{\sqrt{2}\gamma\beta c} \tag{1.76}$$

in the wall of the beam pipe, where b is the radius of the beam pipe in the cylindrical approximation. Suppose for simplicity that all particles have the same revolution period T_0. If the nth particle induces an image pulse current $i_n(t) = i_0(t - t_n)$, where $t = t_n$ is the arrival time of the particle at a particular point of the ring ($0 \leq t_n < T_0$), the total image current on the beam pipe

becomes

$$I(t) = \sum_{n=1}^{N} i_n(t) - i_{dc}. \tag{1.77}$$

In above, i_{dc} denotes the dc component of the beam and its subtraction reflects its inability to induce image current. In the frequency domain, the spectrum of the image current is,

$$\tilde{I}(\omega) = \begin{cases} 0 & \omega = 0, \\ \sum_{n=1}^{N} \tilde{i}_n(\omega) & \omega \neq 0, \end{cases} \tag{1.78}$$

where $\tilde{i}_n(\omega) = \tilde{i}_0(\omega) e^{-i\omega t_n}$ and [9]

$$\tilde{i}_0(\omega) = \frac{1}{2\pi} \int_{-\infty}^{\infty} i_0(t) e^{-i\omega t} dt = -\frac{e}{2\pi I_0(x)} \tag{1.79}$$

is the Fourier transform of $i_0(t)$, with e being the particle charge, $I_0(x)$ being the modified Bessel function of order zero, and $x = \sqrt{2}\sigma_\tau \omega$ (Exercise 1.4).

It is clear that

$$\left\langle \tilde{I}(\omega) \right\rangle = 0, \tag{1.80}$$

because a perfect coasting beam should not have any nonzero frequency component. However, the expectation of the square is nonvanishing. Actually, we have

$$\left\langle \left| \tilde{I}(\omega) \right|^2 \right\rangle = \sum_{n=1}^{N} \left\langle \left| \tilde{i}_n(\omega) \right|^2 \right\rangle = N \left| \tilde{i}_0(\omega) \right|^2. \tag{1.81}$$

The parasitic mode gain per particle per turn is therefore

$$\overline{\Delta \mathcal{E}} = -2\pi \int_{-\infty}^{\infty} \left| \tilde{i}_0(\omega) \right|^2 \mathcal{R}e\, Z_0^{\parallel}(\omega)\, d\omega = -\frac{e^2}{\pi} \int_0^{\infty} \frac{\mathcal{R}e\, Z_0^{\parallel}(\omega)}{I_0(x)^2}\, d\omega. \tag{1.82}$$

When there is a small spread in revolution frequency in the beam particles, Eq. (1.82) gives the mean energy loss per particle per turn. The presence of the impedance perturbs the image pulse $i_0(t)$ of the single particle and alters its frequency distribution $\tilde{i}_0(\omega)$. However, this effect is of higher order and is therefore neglected in Eq. (1.82).

We notice that first, the parasitic mode loss is a single-particle effect that a particle is affected only by its own wake, and second, the parasitic mode loss receives contribution from very high frequencies because of the tiny size

of the image pulse. The single-particle effect of this problem has been verified experimentally at the CERN ISR, where the energy loss of coasting beams at 31.4 GeV/c with intensity varying for almost four orders of magnitude, from 4 mA to 32 A, was monitored and the per particle loss was found to be practically the same.

Let us take the Fermilab Recycler Ring as an illustration. It has an elliptic beam pipe of major and minor diameters 3.806″ and 1.75″. If we take the average and let $b = 3.528$ cm be the radius of the effective cylindrical approximate, the image pulse of a beam particle has the rms length $\sigma_\tau = 8.78$ ps (2.62 mm)[‡] according to Eq. (1.76), and its rms frequency spread is $1/(2\pi\sigma_\tau) = 18.11$ GHz. Thus the knowledge of the coupling impedance up to several tens GHz will be required. It is extremely difficult to compute the coupling impedance up to these frequencies, because every variation of the vacuum chamber of the size of a millimeter has to be taken into account.

Lots of theoretical work have been performed to understand the behavior of the coupling impedance at high frequencies. It has been concluded that if the vacuum chamber is not composed of periodic cavities, the impedance at high frequencies comes mostly from the variation in cross section of the vacuum chamber. Then, the diffraction model should apply and coupling impedance $Z_0^\parallel$ should roll off as $1/\sqrt{\omega}$ at high frequencies. [10] Experimental verification has been made at the CERN ISR by monitoring the energy loss of a coasting beam with its momentum centered at 3.6 GeV/c, 15.4 GeV/c, and 31.4 GeV/c. [11]

As a result, it appears to be reasonable to introduce a simple impedance model for the accelerator ring: in addition to the resistive wall impedance, there is a real part of the impedance which has a constant $Z_0^\parallel/n = (Z/n)_c$ below the cutoff frequency of $f_c = \omega_c/(2\pi) = 2.405c/(2\pi b)$, which amounts to 3.25 GHz

[‡]One may raise the following paradox: For a beam of the Recycler Ring of intensity 0.876×10^{11}, there are on the average 6.91×10^4 particles within one rms image-pulse length ($\sigma_\tau = 8.78$ ps or 2.62 mm). The image pulse of each particle, after deducting the dc part, will be composed of waves $\exp[ins/R - i\omega(t - t_0)]$ going around the ring. For these 6.91×10^4 particles that are clustered within the 2.62 mm, their waves will add up coherently for wavelength longer than 2.62 mm, because their times of arrival (or phases) t_0 will differ by less than 8.78 ps, in the same way as the occurrence of coherent synchrotron radiation in wavelengths longer than the bunch length. The solution to the paradox is simple. The waves moving around the ring in a particular frequency are generated not only by the 6.91×10^4 particles clustered within the 2.62 mm. If we look at the waves of a particular frequency at a particular location around the ring, we will be seeing in total 0.876×10^{11} waves generated by all the 0.876×10^{11} particles in the coasting beam. Since these 0.876×10^{11} particles have completely random phases, these waves tend to cancel each other, which is just Eq. (1.80). The only component that can add up to a nonzero value is the dc component, which is not present in the image current. The situation in coherent synchrotron radiation is quite different. Only those particles inside the short bunch contribute.

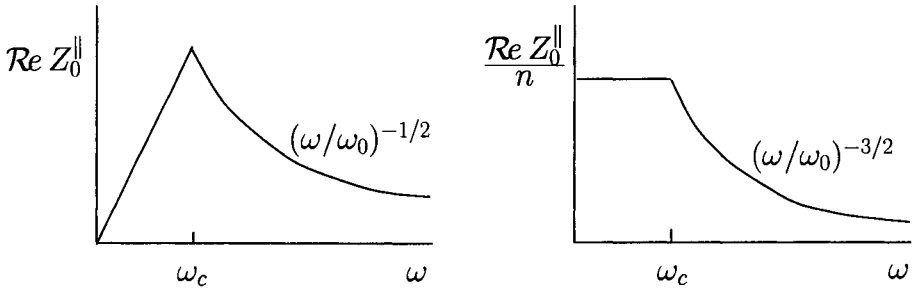


Fig. 1.7 Schematic drawing of the simplest impedance model to be used in the estimation of parasitic mode loss, showing the $\omega^{-1/2}$ asymptotic behavior of $\mathcal{R}e\, Z_0^{\parallel}$ at high frequencies and constant $\mathcal{R}e\, Z_0^{\parallel}/n$ below cutoff frequency.

for the Recycler Ring, and the impedance rolls off as $1/\sqrt{\omega}$ above cutoff as illustrated in Fig. 1.7, i.e., $\mathcal{R}e\, Z_0^{\parallel}/n = (Z/n)_c(\omega_c/\omega)^{3/2}$ when $\omega > \omega_c$.

Monitoring the per particle energy loss of a coasting beam can reveal the impedance of accelerator ring, specially at high frequencies. As energy is lost, the beam spiral inwards resulting in an increase in revolution frequency. Thus, by monitoring the change in revolution frequency, the energy loss can be inferred from the momentum-compaction factor of the ring (see Sec. 2.1.1). Usually this change in revolution frequency is small because the energy loss is small. The energy loss due to synchrotron radiation can be easily separated because it can be computed rather accurately from the lattice of the ring and is usually very small for most hadron rings. The energy loss due to interaction with residual gas can be big or small depending on whether the residual-gas pressure in the vacuum chamber is high or low. If the beam starts off with a symmetric distribution in revolution frequency, interaction with residual gas will result in an asymmetric distribution which is calculable when the gas species and gas pressure is known. [12, 13, 14] On the other hand, interaction with wake fields will only shifts the whole distribution in revolution frequency to lower frequencies. This difference provides a way to separate the parasitic energy loss from the energy loss due to residual gas, so that the coupling impedance of the vacuum chamber can be derived. An example is shown in Fig. 1.8 for a coasting beam consisting of 0.088×10^{11} protons in the Fermilab Recycler Ring. The beam intensity was chosen to be extremely low so that increase in beam emittances and energy spread would not be significant during the long duration when distribution in revolution frequency was monitored. The left plot shows the frequency distribution at start recorded by a 1.75-GHz Schottky detector. The plot on the right shows the distribution

becoming asymmetric after 46 min. Careful separation of the effects of parasitic loss and loss due to residual gas gives a shift in revolution frequency by 0.024 Hz out of the nominal revolution frequency of 89813 Hz. This corresponds to a per particle parasitic energy loss of 0.36 MeV per hour or 1.5 meV per revolution turn.

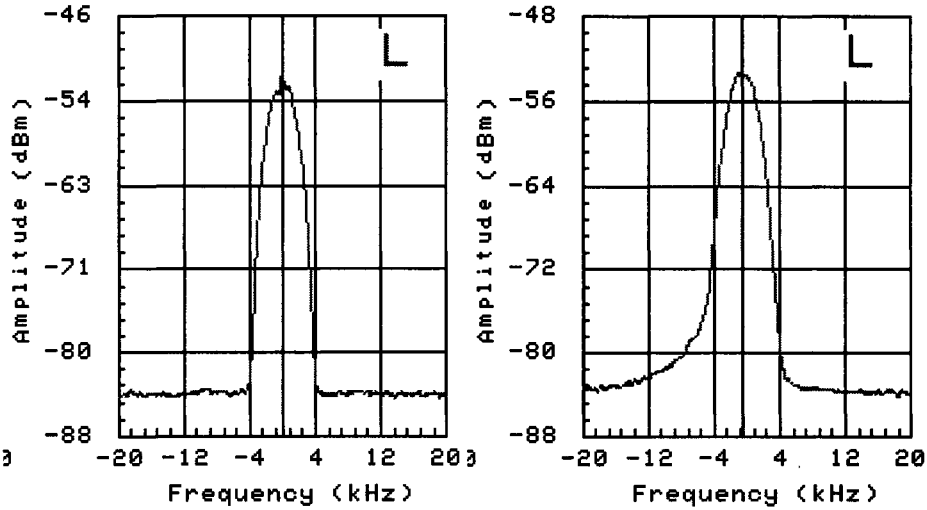


Fig. 1.8 Digitized 1.75 GHz Schottky signals at the low intensity of 0.088×10^{11} protons. Comparison of the center of the initial signal at 11.41 (left) and the peak of the final signal at 12:27 (right) gives a shift of the revolution frequency of 0.024 Hz or 0.031 Hz per hour.

1.4 Exercises

1.1 Prove the properties of the impedances in Eqs. (1.47)–(1.50).

1.2 Using a RLC-parallel circuit, derive the longitudinal impedance in Eq. (1.56) by identifying $R_{0s} = R$, $\omega_r = 1/\sqrt{\mathcal{L}C}$, and $Q = R\sqrt{C/\mathcal{L}}$. Then show that the wake function is $W_0' = 0$ for $z < 0$ and

$$W_0'(z) = \frac{\omega_r R_{0s}}{Q} e^{-\alpha z/v} \left[\cos \frac{\bar{\omega} z}{v} - \frac{\alpha}{\bar{\omega}} \sin \frac{\bar{\omega} z}{v} \right], \tag{1.83}$$

for $z > 0$ with $\alpha = \omega_r/(2Q)$ and $\bar{\omega} = \sqrt{\omega_r^2 - \alpha^2}$. Similarly, show that

$$W_1(z) = -\frac{R_{1s} v \omega_r}{Q \bar{\omega}_r} e^{-\alpha z/v} \sin \frac{\bar{\omega} z}{v}, \tag{1.84}$$

for $z > 0$ and zero otherwise.

1.3 Show that the wake functions corresponding to the longitudinal resistive wall impedance of Eq. (1.58) and the transverse resistive wall impedance of Eq. (1.60) for a length L are, respectively,

$$W_0'(z) = -\frac{\beta^{3/2} cL}{4\pi b z^{3/2}} \sqrt{\frac{Z_0 \mu_r}{\pi \sigma_c}}, \tag{1.85}$$

$$W_1(z) = -\frac{\beta^{3/2} cL}{\pi b^3 z^{1/2}} \sqrt{\frac{Z_0 \mu_r}{\pi \sigma_c}}, \tag{1.86}$$

where b is the beam pipe radius, σ_c is the conductivity and μ_r the relative magnetic permeability of the beam pipe walls. The above are only approximates and are valid for $b\chi^{1/3} \ll z \ll b/\chi$, where $\chi = 1/(b\sigma_c Z_0)$. When $z \ll b\chi^{1/3}$, $W_0'(z)$ should have the proper positive sign.

1.4 Fill in all the missing steps in the derivation of Eq. (1.79) outlined below. [9]
(1) Consider a point particle carrying charge e at position $r = a$ and $\theta = \theta_0$ moving with velocity v longitudinally inside a cylindrical beam pipe of radius $r = b$. The charged density is

$$\begin{aligned} \rho(r, \theta, s, t) &= \frac{e}{a} \delta(s - vt)\delta(r - a)\delta(\theta - \theta_0) \\ &= \sum_{m=0}^{\infty} \int d\omega \rho_m \delta(r - a) \cos m(\theta - \theta_0) e^{-i\omega(t - s/v)}, \end{aligned} \tag{1.87}$$

with

$$\rho_m = \frac{e}{2\pi^2 a v (1 + \delta_{m0})}. \tag{1.88}$$

(2) In a frame at rest with the charged particle under the Lorentz transformation

$$s^* = \gamma(s - vt) \quad \text{with } \gamma = \frac{1}{\sqrt{1 - v^2/c^2}}, \tag{1.89}$$

the charge density becomes static and is given by

$$\rho^*(r, \theta, s^*) = \frac{\rho(r, \theta, s, t)}{\gamma} = \sum_{m=0}^{\infty} \int d\omega \, \rho_m^* \delta(r - a) \cos m(\theta - \theta_0) e^{-i\omega s^*/(\gamma v)}, \tag{1.90}$$

with

$$\rho_m^* = \frac{\rho_m}{\gamma} = \frac{e}{2\pi^2 a \gamma v (1 + \delta_{m0})}. \tag{1.91}$$

We have marked all the variables in the frame at rest with the charge particle with an asterisk.

(3) In this frame at rest with the charged particle, the electrostatic potential $\phi^*(r,\theta,s^*)$ satisfies the Poisson's equation

$$\nabla^{*2}\phi^*(r,\theta,s^*) = -\frac{\rho^*(r,\theta,s^*)}{\epsilon_0}\ . \tag{1.92}$$

Expand the potential according to

$$\phi^*(r,\theta,s^*) = \sum_{m=0}^{\infty}\int d\omega\,\phi_m^*(r)\cos m(\theta-\theta_0)e^{-i\omega s^*/(\gamma v)}, \tag{1.93}$$

and the Poisson equation reduces to

$$\left[\frac{1}{r}\frac{\partial}{\partial r}\left(r\frac{\partial}{\partial r}\right) - \left(\frac{m^2}{r^2}+\frac{\omega^2}{\gamma^2 v^2}\right)\right]\phi_m^*(r) = -\frac{\rho_m^*}{\epsilon_0}\,\delta(r-a). \tag{1.94}$$

(4) For perfectly conducting beam-pipe walls, the solution is

$$\phi_m^*(r) = \begin{cases} A_m\left[I_m(xr/b)K_m(x) - K_m(xr/b)I_m(x)\right] & a<r<b, \\ A_m' I_m(xr/b)K_m(x) & 0<r<a, \end{cases} \tag{1.95}$$

where $x = \omega b/(\gamma v)$, and I_m and K_m are, respectively, the modified Bessel function and Hankel function of order m. Continuity of $E_z^*(r,\theta,s^*) = -\partial\phi^*(r,\theta,s^*)/\partial s^*$ at $r=a$ gives

$$\frac{A_m'}{A_m} = 1 - \frac{K_m(xa/b)I_m(x)}{I_m(xa/b)K_m(x)}. \tag{1.96}$$

By encircling the charge distribution inside a thin shell at $a_- < r < a_+$ and $0_- < s^* < 0_+$, the divergence theorem leads to

$$A_m = -\frac{e}{2\pi^2 e\epsilon_0\gamma v(1+\delta_{m0})}\frac{I_m(xa/b)}{I_m(x)}. \tag{1.97}$$

(5) The radial electric field at the wall of the beam pipe is

$$E_r^*(b,\theta,s^*) = -\frac{\partial}{\partial r}\phi(r,\theta,s^*)\bigg|_{r=b} = -\sum_{m=0}^{\infty}\int d\omega\frac{A_m}{b}\cos m(\theta-\theta_0)e^{i\omega s^*/(\gamma v)}, \tag{1.98}$$

and the surface charge density at the wall of the beam pipe is

$$\sigma^*(\theta,s^*) = -\epsilon_0 E_r^*(b,\theta,s^*). \tag{1.99}$$

We are not interested in the image charge distribution as a function of θ. We thus transform back to the laboratory frame and integrate over θ to arrive at the linear image charge density,

$$\bar{\lambda}(s,t) = -\int d\omega\, e^{-i\omega(t-s/v)}\, \frac{eI_m(xa/b)}{2\pi v I_0(x)}, \tag{1.100}$$

where only the monopole ($m = 0$) contributes. We next transform the variable to arrival time $\tau = t - s/v$ and obtain the linear image charge density

$$\lambda(\tau) = -\int d\omega\, e^{-i\omega\tau}\, \frac{e}{2\pi I_0(x)}, \tag{1.101}$$

which is normalized to the particle image charge when integrated over τ. We have also moved the beam towards the axis of the beam pipe ($a \to 0$) so that $I_m(xa/b)$ disappears from the numerator.
(6) The rms spread of the distribution can be obtained by performing the integration

$$\sigma_\tau^2 = \int d\tau \int d\omega\, e^{-i\omega\tau}\, \frac{\tau^2}{2\pi I_0(x)}, \tag{1.102}$$

which can be rewritten as

$$\sigma_\tau^2 = -\int d\tau \int d\omega\, e^{-i\omega\tau}\, \frac{d^2}{d\omega^2}\left[\frac{1}{2\pi I_0(x)}\right], \tag{1.103}$$

and can be evaluated easily because the integration over τ just gives the Dirac δ-function.

1.5 Appendix: A Collection of Wakes and Impedances

Below is a collection of coupling impedances and wake functions for various elements of the vacuum chamber. These are taken from Sec. 3.2.5 of *Handbook of Accelerator Physics and Engineering*, edited by A. W. Chao and M. Tigner, World Scientific, 1998. [4] All known errors and typos have been corrected. The first expression concerning wall resistivity on the next page has been generalized so that it is valid even when the frequency approaches zero. The relative permeability μ_r of the wall of the beam pipe has also been included.

3.2.5 Explicit Expressions of Impedances and Wake Functions

K.Y. Ng, FNAL

General Remarks and Notations:

W'_m denotes mth azimuthal longitudinal wake function as a function of distance z for $z<0$. When $z>0$, $W'_m(z)=0$ and $W'_m(0)=\lim_{z\to 0-} W'_m(z)$. Similar for transverse wake W_m.

The mth azimuthal longitudinal impedance $Z^{\parallel}_m(\omega) = \int e^{-i\omega z/v} W^{\parallel}_m(z)dz/v$ is related to the transverse impedance of the same azimuthal $Z^{\perp}_m(\omega) = \int e^{-i\omega z/v} W^{\perp}_m(z)idz/(\beta v)$ by $Z^{\parallel}_m = (\omega/c)Z^{\perp}_m$ (valid when $m \neq 0$). In many cases, $\beta=v/c$ has been set to 1.

Unless otherwise stated, round beam pipe of radius b is assumed. $C = 2\pi R$ is the ring circumference and n is the revolution harmonic. $Z_0 \approx 377\ \Omega$ is the free-space impedance. ϵ_0 and μ_0 are the free-space dielectric constant and magnetic permeability.

Description	Impedances	Wakes
Space-charge: [1] beam radius a in a length L of perfectly conducting beam pipe of radius b.	$\frac{Z^{\parallel}_0}{n} = i\frac{Z_0 L}{2C\beta\gamma^2}\left[1+2\ln\frac{b}{a}\right]$ $Z^{\perp}_{m\neq 0} = i\frac{Z_0 L}{2\pi\beta^2\gamma^2 m}\left[\frac{1}{a^{2m}}-\frac{1}{b^{2m}}\right]$	$W'_0 = \frac{Z_0 cL}{4\pi\gamma^2}\left[1+2\ln\frac{b}{a}\right]\delta'(z)$ $W_{m\neq 0} = \frac{Z_0 cL}{2\pi\gamma^2 m}\left[\frac{1}{a^{2m}}-\frac{1}{b^{2m}}\right]\delta(z)$
Resistive Wall: [1] pipe length L, wall thickness t, conductivity σ_c, skin depth $\delta_{\rm skin}$.	$\frac{Z^{\parallel}_m}{L} = \frac{\omega}{c}\frac{Z^{\perp}_m}{L} = \frac{Z_0 c/(\pi b^{2m})}{[1+\mathrm{sgn}(\omega)i](1+\delta_{m0})bc\sqrt{\frac{\sigma_c Z_0 c}{2\lvert\omega\rvert}} - \frac{ib^2\omega}{m+1} + \frac{imc^2}{\omega}}$ $t \gg \delta_{\rm skin} = \sqrt{2c/(\lvert\omega\rvert Z_0\sigma_c)}, \quad \lvert\omega\rvert \gg c\chi/b, \quad \chi = 1/(Z_0\sigma_c b)$	
For $t \gg \delta_{\rm skin}$ and $b/\chi \gg \lvert z\rvert \approx c/\lvert\omega\rvert \gg b\chi^{1/3}$.	$Z^{\parallel}_m = \frac{\omega}{c}Z^{\perp}_m$ $Z^{\parallel}_m = \frac{1-\mathrm{sgn}(\omega)i}{1+\delta_{0m}}\frac{L}{\pi\sigma_c\delta_{\rm skin}b^{2m+1}}$	$W_m = -\frac{c}{\pi b^{2m+1}(1+\delta_{m0})}\sqrt{\frac{Z_0}{\pi\sigma_c}}\frac{L}{\lvert z\rvert^{1/2}}$ $W'_m = -\frac{c}{2\pi b^{2m+1}(1+\delta_{m0})}\sqrt{\frac{Z_0}{\pi\sigma_c}}\frac{L}{\lvert z\rvert^{3/2}}$
For $t \ll \delta_{\rm skin}$ or very low freq., and $b/\chi \gg \lvert z\rvert \approx c/\lvert\omega\rvert \gg \sqrt{bt}$.	$\frac{Z^{\parallel}_0}{L} = -\frac{iZ_0 t\omega}{2\pi bc}, \quad \frac{Z^{\perp}_1}{L} = -\frac{iZ_0 t}{\pi b^3}$	$\frac{W'_0}{L} = -\frac{Z_0 tc}{2\pi b}\delta'(z), \quad \frac{W_1}{L} = -\frac{Z_0 tc}{\pi b^3}\delta(z)$
A *pair* of strip-line BPM's: [2] length L, angle each subtending to pipe axis ϕ_0, forming transmission lines of characteristic impedance Z_c with pipe.	$Z^{\parallel}_0 = 2Z_c\left[\frac{\phi_0}{2\pi}\right]^2\left[2\sin^2\frac{\omega L}{c} - i\sin\frac{2\omega L}{c}\right]$ $Z^{\perp}_1 = \left[\frac{Z^{\parallel}_0}{\omega}\right]_{\rm pair}\frac{c}{b^2}\left[\frac{4}{\phi_0}\right]^2\sin^2\frac{\phi_0}{2}$	$W'_0 = 2Z_c c\left[\frac{\phi_0}{2\pi}\right]^2[\delta(z)-\delta(z+2L)]$ $W_1 = \frac{8Z_c c}{\pi^2 b^2}\sin^2\frac{\phi_0}{2}[H(z)-H(z+2L)]$
	The strip-lines are assumed to terminate with impedance Z_c at the upstream end.	
Heifets inductive impedance: [3] low freq. pure inductance $\mathcal{L}$. $Z^{\parallel}_0$ rolls off as $\omega^{-1/2}$.	$Z^{\parallel}_0 = -\frac{i\omega\mathcal{L}}{(1-i\omega a/c)^{3/2}} \longrightarrow -i\omega\mathcal{L}$ as $a\to 0$	$W'_0 = \frac{c^2\mathcal{L}}{a\sqrt{\pi az}}\left[1+\frac{2z}{a}\right]e^{z/a} \longrightarrow c^2\mathcal{L}\delta'(z)$ as $a\to 0$
Pill-box cavity at low freq.: length g, radial depth $h+b$, where $g \leq h \ll b$. [6]	$Z^{\parallel}_0 = -i\frac{\omega Z_0}{2\pi cb}\left[gh-\frac{g^2}{2\pi}\right]$ $Z^{\perp}_1 = -i\frac{Z_0}{\pi b^3}\left[gh-\frac{g^2}{2\pi}\right]$	$W'_0 = -\frac{Z_0 c}{2\pi b}\left[gh-\frac{g^2}{2\pi}\right]\delta'(z)$ $W_1 = -\frac{Z_0 c}{\pi b^3}\left[gh-\frac{g^2}{2\pi}\right]\delta(z)$

<table>
<tr><th>Description</th><th>Impedances</th><th>Wakes</th></tr>
<tr><td>Pill-box cavity at low freq.: length g, radial depth $h+b$, where $h \ll g \ll b$. [6]</td><td>$Z_0^{\parallel} = -i\dfrac{\omega Z_0 h^2}{\pi^2 cb}\left[\ln\dfrac{2\pi g}{h}+\dfrac{1}{2}\right]$
$Z_1^{\perp} = -i\dfrac{2Z_0 h^2}{\pi^2 b^3}\left[\ln\dfrac{2\pi g}{h}+\dfrac{1}{2}\right]$</td><td>$W_0' = -\dfrac{Z_0 ch^2}{\pi^2 b}\left[\ln\dfrac{2\pi g}{h}+\dfrac{1}{2}\right]\delta'(z)$
$W_1 = -\dfrac{2Z_0 ch^2}{\pi^2 b^3}\left[\ln\dfrac{2\pi g}{h}+\dfrac{1}{2}\right]\delta(z)$</td></tr>
<tr><td>Pill-box cavity: length g, radial depth d. At freq. $\omega \gg c/b$, diffraction model applies. [1]</td><td>$Z_m^{\parallel} = \dfrac{[1+\mathrm{sgn}(\omega)i]Z_0}{(1+\delta_{m0})\pi^{3/2}b^{2m+1}}\sqrt{\dfrac{cg}{|\omega|}}$
$Z_m^{\parallel} = \dfrac{\omega}{c}Z_m^{\perp}$</td><td>$W_m = -\dfrac{2Z_0 c\sqrt{2g}}{(1+\delta_{m0})\pi^2 b^{2m+1}}|z|^{1/2}$
$W_m' = \dfrac{Z_0 c\sqrt{2g}}{(1+\delta_{m0})\pi^2 b^{2m+1}}|z|^{-1/2}$</td></tr>
<tr><td>Optical model: [7] A series of cavities of periodic length L. Each cavity has width g, high Q resonances of freq. $\omega_n/(2\pi)$ and loss factor $k_n^{(m)}$ for azimuthal mode m.</td><td colspan="2">$\mathrm{Re}Z_m^{\parallel} = \sum_{n=1}^{N}\pi k_n^{(m)}\delta(\omega-\omega_n) + \dfrac{2\pi C_{\mathrm{SV}}G(\bar\nu)F(\nu)}{(1+\delta_{m0})b^{2m}}H(\omega-\omega_N)$
$W_m' = \sum_{n=1}^{N}2k_n^{(m)}\cos\dfrac{\omega_n z}{c} + \dfrac{2C_{\mathrm{SV}}G(\bar\nu)}{(1+\delta_{m0})b^{2m}}\int_{\omega_N}^{\infty}d\omega F(\nu)\cos\dfrac{\omega z}{c}$
where $C_{\mathrm{SV}} = 2Z_0 j_{m1}^2/(\pi^2\zeta^2\beta) \approx 650\ \Omega$ for $m=0$ and $1650\ \Omega$ for $m=1$, j_{m1} is first zero of Bessel function J_m, $\zeta = 0.8237$.
$G(\bar\nu) = \bar\nu^2 K_1^2(\bar\nu),\ F(\nu) = \dfrac{\sqrt{\nu}+1}{(\nu+2\sqrt{\nu}+2)^2},\ \bar\nu = \dfrac{\omega b}{\beta\gamma c},\ \nu = \dfrac{\omega}{\omega_{\mathrm{SV}}} = \dfrac{4b^2\omega}{\zeta^2 c\sqrt{gL}}$</td></tr>
<tr><td>Formulas for computation of W_m'. erfc(x) is the complementary error function.</td><td colspan="2">$\int_{\hat\omega}^{\infty}d\omega F(\nu)\cos\dfrac{\omega z}{c} = \omega_{\mathrm{SV}}\tilde F_0(z/c) - \int_0^{\hat\omega}d\omega F(\nu)\cos\dfrac{\omega z}{c}$
$\tilde F_0(x) = \int_0^{\infty}d\omega F(\nu)\cos\omega x = \dfrac{\pi}{4}(1+4x)e^{2x}\mathrm{erfc}(\sqrt{2x}) - \sqrt{\dfrac{\pi x}{2}}$</td></tr>
<tr><td>Resonator model for the mth azimuthal, with shunt imp. $R_s^{(m)}$, resonant freq. $\omega_r/(2\pi)$, quality factor Q. [1]</td><td>$Z_m^{\parallel} = \dfrac{R_s^{(m)}}{1+iQ(\omega_r/\omega-\omega/\omega_r)}$
$Z_m^{\perp} = \dfrac{c}{\omega}\dfrac{R_s^{(m)}}{1+iQ(\omega_r/\omega-\omega/\omega_r)}$</td><td>$W_m = \dfrac{R_s^{(m)}c\omega_r}{Q\bar\omega_r}e^{\alpha z/c}\sin\dfrac{\bar\omega_r z}{c}$
where $\alpha = \omega_r/(2Q)$
$\bar\omega_r = \sqrt{\lvert\omega_r^2-\alpha^2\rvert}$</td></tr>
<tr><td>Res. freq. $\omega_{mnp}/(2\pi)$ and shunt impedance $(R_s)_{mnp}$ of a pill-box cavity for nth radial and pth longitudinal modes. Radial depth d and length g. x_{mn} is nth zero of Bessel function J_m. [8]</td><td colspan="2">$\dfrac{\omega_{mnp}^2}{c^2} = \dfrac{x_{mn}^2}{d^2} + \dfrac{p^2\pi^2}{g^2}$
$\left[\dfrac{R_s}{Q}\right]_{0np} = \dfrac{Z_0}{x_{0n}^2 J_0'^2(x_{0n})}\dfrac{8c}{\pi g\omega_{0np}}\begin{cases}\sin^2\dfrac{g\omega_{0np}}{2\beta c}\times\dfrac{1}{1+\delta_{0p}} & p \text{ even}\\ \cos^2\dfrac{g\omega_{0np}}{2\beta c} & p \text{ odd}\end{cases}$
$\left[\dfrac{R_s}{Q}\right]_{1np} = \dfrac{Z_0}{J_1'^2(x_{1n})}\dfrac{2c^2}{\pi g d^2\omega_{1np}^2}\begin{cases}\sin^2\dfrac{g\omega_{1np}}{2\beta c} & p\neq 1 \text{ and even}\\ \cos^2\dfrac{g\omega_{1np}}{2\beta c} & p \text{ odd}\end{cases}$</td></tr>
</table>

Description	Impedances	Wakes
Low-freq. response of a pill-box cavity: [4] length g, radial depth d. When $g \gg 2(d-b)$, replace g by $(d-b)$. Here, $S = d/b$.	$\frac{Z_0^{\parallel}}{n} = -i\frac{Z_0 g}{2\pi R}\ln S$ $Z_1^{\perp} = -i\frac{Z_0 g}{\pi b^2}\frac{S^2-1}{S^2+1}$	$W_0' = -\frac{Z_0 c g}{2\pi}\ln S\,\delta'(z)$ $W_1 = -\frac{Z_0 c g}{\pi b^2}\frac{S^2-1}{S^2+1}\delta(z)$
	Effect will be one half for a step in the beam pipe from radius b to radius d, or vice versa, when $g \gg 2(d-b)$.	
Iris of half elliptical cross section at low freq.: width $2a$, maximum protruding length h. [5]	$Z_0^{\parallel} = -i\frac{\omega Z_0 h^2}{4cb}$ $Z_1^{\perp} = -i\frac{Z_0 h^2}{2b^3}$	$W_0' = -\frac{Z_0 c h^2}{4b}\delta'(z)$ $W_1 = -\frac{Z_0 c h^2}{2b^3}\delta(z)$
Pipe transition at low freq.: tapering angle θ, transition height h. γ is Euler's constant and ψ is the psi-function. [6]	$Z_0^{\parallel} = \frac{\omega b^2 Z_1^{\perp}}{2c} = -i\frac{\omega Z_0 h^2}{2\pi^2 cb}\left\{\ln\left[\frac{b\theta}{h} - 2\theta\cot\theta\right] + \frac{3}{2} - \gamma - \psi\left(\frac{\theta}{\pi}\right) - \frac{\pi}{2}\cot\theta - \frac{\pi}{2\theta}\right\}$ $W_0' = -\left\lvert\frac{Z_0^{\parallel}}{\omega}\right\rvert c^2\delta'(z), \quad W_1 = -\left\lvert Z_1^{\perp}\right\rvert c\delta(z), \quad h\cot\theta \ll b$	
Pipe transition at low frequencies with transition height $h \ll b$. [6]	$Z_0^{\parallel} = \frac{\omega b^2}{2c}Z_1^{\perp} = -i\frac{\omega Z_0 h^2}{2\pi^2 cb}\left(\ln\frac{2\pi b}{h} + \frac{1}{2}\right)$ $W_0' = -\left\lvert\frac{Z_0^{\parallel}}{\omega}\right\rvert c^2\delta'(z), \quad W_1 = -\left\lvert Z_1^{\perp}\right\rvert c\delta(z)$	
Kicker with window-frame magnet: [9] width a, height b, length L, beam offset x_0 horizontally, and all image current carried by conducting current plates.	$Z_0^{\parallel} = \frac{\omega^2\mu_0^2 L^2 x_0^2}{4a^2 Z_k}$ $Z_1^{\perp} = \frac{c\omega\mu_0^2 L^2}{4a^2 Z_k}$	$W_0' = -\frac{c^3\mu_0^2 L^2 x_0^2}{4a^2 Z_k}\delta_0''(z)$ $W_1 = -\frac{c^3\mu_0^2 L^2}{4a^2 Z_k}\delta'(z)$
	$Z_k = -i\omega\mathcal{L} + Z_g$ with $\mathcal{L} \approx \mu_0 bL/a$ the inductance of the windings and Z_g the impedance of the generator and the cable. If the kicker is of C-type magnet, x_0 in $Z_0^{\parallel}$ should be replaced by $(x_0 + b)$.	
Traveling-wave kicker with characteristic impedance Z_c for the cable, and a window magnet of width a, height b, and length L. [9]	$Z_0^{\parallel} = \frac{Z_c}{4}\left[2\sin^2\frac{\theta}{2} - i(\theta - \sin\theta)\right], \quad Z_1^{\perp} = \frac{Z_c L}{4ab}\left[\frac{1-\cos\theta}{\theta} - i\left(1 - \frac{\sin\theta}{\theta}\right)\right]$ $W_0' = \frac{Z_c c}{4}\left[\delta(z) - \delta\left(z - \frac{Lc}{v}\right) - \frac{Lc}{v}\delta'(z)\right]$ $W_1 = \frac{Z_c v}{4ab}\left[H(z) - H\left(z - \frac{Lc}{v}\right) - \frac{Lc}{v}\delta(z)\right]$ $\theta = \omega L/v$ denotes the electrical length of the kicker windings and $v = Z_c ac/(Z_0 b)$ is the matched transmission-line phase velocity of the capacitance-loaded windings.	
Bethe's electric and magnetic moments of a hole of radius a in beam pipe wall. [10]	Electric and magnetic dipole moments when wavelength $\gg a$: $\vec{d} = -\frac{2\epsilon_0}{3}a^3\vec{E}, \quad \vec{m} = -\frac{4}{3\mu_0}a^3\vec{B}$ $\vec{E}$ and $\vec{B}$ are electric and magnetic flux density at hole when hole is absent. This is a diffraction solution for a thin-wall pipe.	

<table>
<tr><th>Description</th><th>Impedances</th><th>Wakes</th></tr>
<tr><td rowspan="2">Small obstacle [5, 11] on beam pipe, size $\ll$ pipe radius, freq. below cutoff. α_e and α_m are electric polarizability and magnetic susceptibility of the obstacle.</td><td>$Z_0^{\parallel} = -i\dfrac{\omega Z_0}{c}\dfrac{\alpha_e+\alpha_m}{4\pi^2 b^2}$
$Z_1^{\perp} = -i\dfrac{Z_0(\alpha_e+\alpha_m)}{\pi^2 b^4}\cos\Delta\varphi$</td><td>$W_0' = -Z_0 c\dfrac{\alpha_e+\alpha_m}{4\pi^2 b^2}\,\delta'(z)$
$W_1 = -Z_0 c\dfrac{\alpha_e+\alpha_m}{\pi^2 b^4}\cos\Delta\varphi\,\delta(z)$</td></tr>
<tr><td colspan="2">$\Delta\varphi$ is the azimuthal angle between the obstacle and the direction concerning $Z_1^{\perp}$ and W_1.</td></tr>
<tr><td colspan="3">Polarizabilities for various geometry: beam pipe radius is b and wall thickness is t.</td></tr>
<tr><td>Elliptical hole: major and minor radii are a and d. $K(m)$ and $E(m)$ are complete elliptical functions of the first and second kind, with $m = 1-m_1$ and $m_1 = (d/a)^2$. For long ellipse $\perp$ beam, major axis $a \ll b$, beam pipe radius, because the curvature of the beam pipe has been neglected here. [12]</td><td colspan="2">$\alpha_e+\alpha_m = \begin{cases} \dfrac{\pi a^3 m_1^2[K(m)-E(m))]}{3E(m)[E(m)-m_1K(m)]} \\ \dfrac{\pi a^3[E(m)-m_1K(m)]}{3[K(m)-E(m)]} \end{cases} \overset{\substack{m\to 1 \\ \text{long} \\ \text{ellipse}}}{\Longrightarrow} \begin{cases} \dfrac{\pi d^4[\ln(4a/d)-1]}{3a} & \parallel \text{beam}\ d \ll b \\ \dfrac{\pi a^3}{3\,[\ln(4a/d)-1]} & \perp \text{beam}\ a \ll b \end{cases}$
$\alpha_e+\alpha_m \overset{\substack{\text{circular} \\ m\to 0}}{\Longrightarrow} \dfrac{2a^3}{3}$ circular hole $a = d \ll b$
Above are for $t \ll a$, $\times 0.56$ (circular) or $\times 0.59$ (long ellipse) when $t \geq a$.
For higher frequency correction, add to $\alpha_e+\alpha_m$ the extra term,
$+\dfrac{2\pi a^3}{3}\left[\dfrac{11\omega^2 a^2}{30c^2}\right]$ circular, $\begin{cases} -\dfrac{\pi a d^2}{3}\left[\dfrac{\omega^2 a^2}{5c^2}\right] & \parallel \text{beam, long ellipse} \\ +\dfrac{2\pi a^3}{3}\left[\dfrac{2\omega^2 a^2}{5c^2[\ln(4a/d)-1]}\right] & \perp \text{beam, long ellipse} \end{cases}$</td></tr>
<tr><td>Rectangular slot: length L, width w.</td><td colspan="2">$\alpha_e+\alpha_m = w^3(0.1814 - 0.0344w/L)$ $\quad t \ll a$, $\quad \times 0.59$ when $t \geq a$</td></tr>
<tr><td>Rounded-end slot: length L, width w.</td><td colspan="2">$\alpha_e+\alpha_m = w^3(0.1334 - 0.0500w/L)$ $\quad t \ll a$, $\quad \times 0.59$ when $t \geq a$</td></tr>
<tr><td>Annular-ring-shaped cut: inner and outer radii a and $d = a+w$ with $w \ll d$.</td><td colspan="2">$\alpha_e+\alpha_m = \dfrac{\pi^2 d^2 a}{2\ln(32d/w)-4} - \dfrac{\pi^2 w^2(a+d)}{16}$ $\quad t \ll d$
$\alpha_e+\alpha_m = \pi d^2 w - \frac{1}{2}w^2(a+d)$ $\quad t \geq d$</td></tr>
<tr><td>Half ellipsoidal protrusion with semi axes h radially, a longitudinally, and d azimuthally. ${}_2F_1$ is the hypergeometric function.</td><td colspan="2">$\alpha_e+\alpha_m = 2\pi a h d\left[\dfrac{1}{I_b}+\dfrac{1}{I_c-3}\right]$
$I_b = {}_2F_1\left(1,1;\frac{5}{2};1-\frac{h^2}{a^2}\right)$, $\quad I_c = {}_2F_1\left(1,\frac{1}{2};\frac{5}{2};1-\frac{a^2}{h^2}\right)$, $\quad$ if $a = d$
$\alpha_e+\alpha_m = \pi a^3$ if $a = d = h$, $\quad \dfrac{2\pi h^3}{3[\ln(2h/a)-1]}$ if $a = d \ll h$
$\alpha_e+\alpha_m = \dfrac{8h^3}{3}\left[1+\left(\dfrac{4}{\pi}-\dfrac{\pi}{4}\right)\dfrac{a}{h}\right]$ if $a \ll h = d$
$\alpha_e+\alpha_m = \dfrac{8\pi h^4}{3a}\left[\ln\dfrac{2a}{h}-1\right]$ if $a \gg h = d$</td></tr>
</table>

<table>
<tr>
<td>Array of pill-boxes, box spacing L, each with gap width g, beam pipe radius b. Gluckstern–Yokoya–Bane formula [15] at high freq. to order $(kg)^{-1}$:</td>
<td colspan="2">For each cavity of length L with $k = \omega/c$,
$$Z_0^{\parallel} = \frac{iZ_0L}{\pi kb^2}\left\{1 + [1 + i\,\mathrm{sgn}(k)]\frac{\alpha L}{b}\sqrt{\frac{\pi}{|k|g}}\right\}^{-1}$$
with $k = \omega/c$. $\alpha = 1$ when $g/L \ll 1$ and $\alpha = \alpha_1 = 0.4648$ when $g/L = 1$, the limiting case of infinitely thin irises. In general, with $\Upsilon = g/L$, $\alpha(\Upsilon) = 1 - \alpha_1\Upsilon^{1/2} - (1 - 2\alpha_1)\Upsilon + \mathcal{O}(\Upsilon^{3/2})$.</td>
</tr>
<tr>
<td rowspan="2">The above pill-box array with radial depth d generates a single-frequency resonance impedance at $\omega_r = c\left(\frac{2L}{bgd}\right)^{1/2}$. [16, 17]</td>
<td>$$Z_0^{\parallel} = \frac{Z_0cL}{2\pi b^2}\sum_{\omega'=\pm\omega_r}\left[\pi\delta(\omega-\omega') + \frac{i}{\omega-\omega'}\right]$$
$$Z_1^{\perp} = \frac{2cL}{b^2\omega}Z_0^{\parallel}$$</td>
<td>$$W_0'(z) = \frac{Z_0cL}{\pi b^2}\cos\frac{\omega_r z}{c}$$
$$W_1(z) = \frac{2Z_0L}{\pi b^4\omega_r}\sin\frac{\omega_r z}{c}$$</td>
</tr>
<tr>
<td colspan="2">The corresponding resonator per pill box has $\frac{R_s^{(0)}\omega_r}{Q} = \frac{Z_0cL}{\pi b^2}$.</td>
</tr>
<tr>
<td>Smooth toroidal b and $R = \frac{1}{2}(a + b)$. As the Lorentz factor $\gamma \to \infty$, (ultra-relativistic beam), a curvature contribution remains for the longitudinal impedance. [18]</td>
<td colspan="2">Valid from zero frequency up to just below synchronous resonant modes, i.e., $0 < \nu < \sqrt{R/h}$ with $\nu = \omega h/c$,
$$\frac{Z_0^{\parallel}}{n} = iZ_0\left(\frac{h}{\pi R}\right)^2\left\{\left[1 - e^{-2\pi(b-R)/h} - e^{-2\pi(R-a)/h}\right]\left[1 - 3\left(\frac{\nu}{\pi}\right)^2\right] + 0.05179 - 0.01355\left(\frac{\nu}{\pi}\right)^2\right\} + \rho$$
$$\approx iZ_0\left(\frac{h}{\pi R}\right)^2\left[A - 3B\left(\frac{\nu}{\pi}\right)^2\right].$$
where ρ is quadratic in ν. As $(b-a)/h$ increases, ρ vanishes exponentially and $A \approx B \approx 1$. In general, $A/B \approx 1$ implying $\mathrm{Im}Z_0^{\parallel}$ changes sign (a node) near $\nu = \pi/\sqrt{3}$.</td>
</tr>
<tr>
<td>Rf cage: beam of radius a surrounded by a cylindrical cage or array of N wires of radius ρ_w, length L at radial distance r_w from beam center. Wire filling factor is $f_w = N\rho_w/(\pi r_w)$. Formulas are valid at low frequencies, $0 < n < R/r_w$ and $N \gg 1$.</td>
<td colspan="2">$$\frac{Z_0^{\parallel}}{n} = \frac{iZ_0L}{4\pi R\beta\gamma^2}\left[1 + 2\ln\frac{r_w}{a} + C_{\parallel}\right], \quad Z_1^{\perp} = \frac{iZ_0L}{2\pi\beta^2\gamma^2}\left[\frac{1}{a^2} - \frac{1 - C_{\perp}}{r_w^2}\right]$$
Without metallic beam pipe outside wire array or cage, [19]
$$C_{\parallel} = -\frac{2\ln(nr_w/R)\ln(\pi f_w)}{N\ln(nr_w/R) + \ln(\pi f_w)}, \quad C_{\perp} = -\frac{2\ln(\pi f_w)}{N - 2\ln(\pi f_w)}$$
With infinitely conducting metallic beam pipe, radius $b > r_w$, [20]
$$C_{\parallel} = 2\ln\frac{b}{r_w} - \frac{2N[\ln(b/r_w)]^2}{N\ln(b/r_w) - \ln(\pi f_w) + \ln[1-(r_w/b)^{2N}]}$$
$$C_{\perp} = \frac{[1-(r_w/b)^2][(r_w/b)^2 + (b/r_w)^2]\{\ln[1-(r_w/b)^{2N}] - 2\ln(\pi f_w)\}}{N[1-(r_w/b)^2] + [(r_w/b)^2 + (b/r_w)^2]\ln[1-(r_w/b)^{2N}] - 2\ln(\pi f_w)}$$
A ceramic layer between the wires and metallic beam pipe has negligible effect on the impedances.</td>
</tr>
</table>

Wall roughness [13] 1-D axisymmetric bump, $h(z)$ or 2-D bump $h(z,\theta)$. Valid for low frequency $k = \omega/c \ll$ (bump length or width)$^{-1}$, $h \ll b$, pipe radius, and $\|\nabla h\| \ll 1$.	1-D: $Z_0^{\parallel} = -\frac{2ikZ_0}{b}\int_0^{\infty} \kappa \|\tilde{h}(\kappa)\|^2 d\kappa$ with spectrum $\tilde{h}(k) = \frac{1}{2\pi}\int_{-\infty}^{\infty} h(z)e^{-ikz}dz$ 2-D: $Z_0^{\parallel} = -\frac{4ikZ_0}{b}\sum_{m=-\infty}^{\infty}\int_{-\infty}^{\infty}\frac{\kappa^2}{\sqrt{\kappa^2+m^2/b^2}}\|\tilde{h}_m(\kappa)\|^2 d\kappa$ with spectrum $\tilde{h}_m(k) = \frac{1}{(2\pi)^2}\int_0^{2\pi} d\theta \int_{-\infty}^{\infty} dz\, h(z,\theta)e^{-ikz-im\theta}$
Heifets and Kheifets formulas for tapered steps and tapered cavity at high frequencies. [14]	
Taper in from radius h to $b\,(<h)$, out from radius b to h; tapering angle α. Tapering inefficient for a bunch of rms length σ, if $2(h-b)\tan\alpha \gg \sigma$. All formulas here and below are valid for *positive* $k = \omega/c$ only.	$\mathrm{Re}Z_0^{\parallel} = \pm\frac{Z_0}{2\pi}\ln\frac{h}{b} + \left(Z_0^{\parallel}\right)_{\rm step}$, $\mathrm{Re}Z_1^{\perp} = \pm\frac{Z_0 b}{4\pi}\left(\frac{1}{b^2}-\frac{1}{h^2}\right) + \left(Z_1^{\perp}\right)_{\rm step}$ $\begin{cases}+\text{in}\\-\text{out}\end{cases}$ $\left(Z_0^{\parallel}\right)_{\rm step} = \frac{Z_0}{2\pi}\ln\frac{h}{b}$, $\tan\alpha > \frac{h-b}{kb^2}$, $\left(Z_0^{\parallel}\right)_{\rm step} = \frac{Z_0}{4}kb\tan\alpha$, $\tan\alpha \ll \frac{1}{kb}$ $\left(Z_1^{\perp}\right)_{\rm step} = \frac{Z_0}{4\pi b}\left[1 - \frac{1}{(1+kb)^2}\,{}_2F_1\left(1,\frac{3}{2},3,\frac{4bh}{(b+h)^2}\right)\right]$, $\tan\alpha > \frac{h-b}{kb^2}$, $kb \gg 1$ $\left(Z_1^{\perp}\right)_{\rm step} = \frac{Z_0 b}{4\pi}\left(\frac{1}{b^2}-\frac{1}{h^2}\right)$, $\tan\alpha > \frac{h-b}{kb^2}$, $kb \gg 1$, $h \gg b$ $\left(Z_1^{\perp}\right)_{\rm step} = \frac{Z_0}{16b}(kb)^3\tan\alpha$, $\tan\alpha \ll \frac{1}{kb}$

References

[1] A. W. Chao, *Physics of Collective Beam Instabilities in High Energy Accelerators*, (Wiley, 1993), ch.2.

[2] K. Y. Ng, *Part. Accel.* **23**, 93 (1988).

[3] S.A. Heifets, G. Sabbi, SLAC/AP-104 (1996).

[4] E. Keil, B. Zotter, *Part. Accel.* **3**, 11 (1972); K. Y. Ng, Fermilab Report FN-389 (1981).

[5] S. S. Kurennoy, *Phys. Rev.* **E55**, 3529 (1997); S. S. Kurennoy, R. L. Gluckstern, *Phys. Rev.* **E55**, 3533 (1997).

[6] S. S. Kurennoy, G. V. Stupakov, *Part. Accel.* **45**, 95 (1994).

[7] A. M. Sessler, unpublished citation in E. Keil, *Nucl. Instr. Method* **100**, 419 (1972); L. A. Veinshtein, *Sov. Phys. JETP* **17**, 709 (1963); D. Brandt, B. Zotter, CERN-ISR/TH/82-13 (1982)

[8] C. C. Johnson, *Field and Wave Electrodynamics*, (McGraw-Hill), Ch.6.

[9] G. Nassibian, F. Sacherer, *Nucl. Instr. Method* **59**, 21 (1971); G. Nassibian, CERN/PS 84-25 (BR) (1984); CERN 85-68 (BR) (1986).

[10] M. Sands, SLAC note PEP-253 (1977); H.A. Bethe, *Phys. Rev.* **66**, 163 (1944).

[11] S. S. Kurennoy, *Part. Accel.* **39**, 1 (1992); *Part. Accel.* **50**, (1995) 167; R. L. Gluckstern, *Phys. Rev.* **A46**, 1106, 1110 (1992); S. S. Kurennoy, R. L. Gluckstern, G. V. Stupakov, *Phys. Rev.* **E52**, 4354 (1995).

[12] A. Fedotov, PhD Thesis, U. Maryland (1997)

[15] R. Gluckstern, *Phys. Rev.* **D39**, 2773, 2780 (1989); G. Stupakov, PAC 95 3303, K. Yokoya and K. Bane, PAC 99, p.1725.

[16] A. Novokhatski, A. Mosnier, PAC 97, p.1661.

[17] K. L. F. Bane, A. Novokhatski, SLAC Report AP-117 (1999).

[18] K. Y. Ng and R. Warnock, PAC 89, p.798, *Phys. Rev.* **D40**, 231 (1989).

[19] T. S. Wang, AIP Conf. Proc. 448, 286 (1998).

[20] T. S. Wang and R. Gluckstern, PAC 99, p.2876.

[13] G. V. Stupakov, SLAC-PUB-7908 (1998), *Phys. Rev. ST AB* **1**, 064401 (1998).

[14] S. A. Heifets, *Phys. Rev.* **D40**, 3097 (1989); S. A. Heifets, S. A. Kheifets, *Rev. Mod. Phys.* **63**, 631 (1990).

Bibliography

[1] See for example, J. D. Jackson, *Classical Electrodynamics, 3rd edn.* (John Wiley & Sons, 1999), Chapter 14.

[2] W. K. H. Panofsky and W. A. Wenzel, *Rev. Sci. Instrum.* **27**, 967 (1956).

[3] A. W. Chao, *Physics of Collective Beam Instabilities in High Energy Accelerators* (John Wiley & Sons, 1993), p. 251.

[4] *Handbook of Accelerator Physics and Engineering*, eds. A. W. Chao and M. Tigner (World Scientific, 1999).

[5] K. Y. Ng, *Coherent Parasitic Energy Loss of the Recycler Beam*, Fermilab Report TM-2249, 2004.

[6] J. Arnold, T. Bohl, H. Burkhardt, R. Cornali, K. Cornelis, G. Engelmann, R. Giachino, A. Hofmann, M. Jonker, T. Linnecar, M. Meddahi, L. Normann, E. Shaposhnikova, A. Wagner, and B. Zotter, *Energy Loss of proton and Lead Beams in the CERN-SPS*, Proc. 1997 Part. Accel. Conf., eds. M. Comyn, M. K. Craddock, M. Reiser, and J. Thomson (Vancouver, Canada, May 12–16, 1997), p.1813.

[7] A. Hofmann and T. Risselada, *Measuring the ISR Impedance at Very High Frequencies by Observing the Energy Loss of a Coasting Beam, IEEE Trans. Nucl. Sci.* **NS-30**(4), 2400 (1983).

[8] K. Y. Ng and J. Marriner, *Energy Loss of a Coasting Beam inside the Recycler Ring*, Fermilab Report FN-0740, 2003.

[9] J. H. Cupérus, *Nucl. Instrum. Methods* **145**, 219 (1977).

[10] S. A Heifets and S. A. Kheifets, *High-Frequency Limit of the Longitudinal Impedance, Part. Accel. Special Issue: Impedance Beyond Cutoff,* **25**(2–4), 61 (1990).

[11] A. Hofmann, T. Risselada, and B. Zotter, *Measurement of Asymptotic Behavior of the High Frequency Impedance*, Proc. 4th Advanced ICFA Beam Dynamics Workshop on Collective Effects in Short Bunches (KEK, Japan, 24–29 Sept. 1990), p. 138.

[12] L. Livingston and H. Bethe, *Rev. Mod. Phys.* **9**, 245 (1937); J. D. Jackson, *Classical Electrodynamics*, 3rd edn., (John Wiley & Son, 1999), Chapter 13.

[13] L. D. Landau, *On the Energy Loss of Fast Particles by Ionization, J. Exp. Phys. (USSR)* **8**, 201 (1944); *Collected Papers of L.D. Landau*, ed. D. ter Haar, (Gordon and Breach, 1965), p. 416.

[14] P. V. Vavilov, *Ionization Losses of High-Energy Heavy Particles, Soviet Physics JETP* **5**, 749 (1957).

[15] R. Gluckstern, *Analytic Methods for Calculating Coupling Impedances*, CERN Report CERN-2000-011, 2000.

[16] B. W. Zotter and S. A. Kheifets, *Impedances and Wakes in High-Energy Particle Accelerators* (World Science, 1997).

2025 © The Author(s). This is an Open Access chapter published by World Scientific Publishing Company, licensed under the terms of the Creative Commons Attribution-NonCommercial 4.0 International License (CC BY-NC 4.0).

Chapter 2

Potential-Well Distortion

2.1 Longitudinal Phase Space

2.1.1 *Momentum Compaction*

A bunch of charged particles has an unavoidable spread of energy because of many reasons, for example, random quantum excitations which change the energy of the particles randomly (for electrons and ultra-high energy protons only), intrabeam scattering that is just Coulomb scattering among the particles, Touschek scattering [1] which is large-angle Coulomb scattering that converts the transverse momentum of a particle into longitudinal. But most important of all, an amount of energy spread must be present in a beam as a means to counter collective instabilities through Landau damping. In an accelerator ring or storage ring, particles with different energies have different closed orbits, with their lengths given by

$$C = C_0 \left[1 + \alpha_0 \delta + \mathcal{O}(\delta^2)\right], \tag{2.1}$$

where δ is the fractional spread in momentum and C_0 is the orbit length of the so-called *on-momentum* particle. The proportionality constant α_0 is called the *momentum-compaction factor* of the accelerator ring and is a property of the lattice of the ring. The fractional momentum spread δ is related to the lowest order fractional energy spread $\Delta E/E_0$ by

$$\delta = \frac{\Delta p}{p_0} \approx \frac{1}{\beta_0^2} \frac{\Delta E}{E_0}, \tag{2.2}$$

where p_0, E_0, and $v_0 = \beta_0 c$ are the momentum, energy, and longitudinal velocity of the on-momentum particle. The momentum-compaction factors of most accelerators and storage rings have the property that $\alpha_0 > 0$, implying that particles with higher energies travel along longer closed orbits with more radial

excursions. A longer closed orbit may imply relatively longer revolution period T. On the other hand, a higher energy particle travels with higher velocity v and the period of revolution will be relatively shorter. The result is a slip in revolution time ΔT (either positive or negative) every turn with respect to the on-momentum particle. The particles inside the bunch will therefore spread out longitudinally and the bunch will disintegrate unless there is some longitudinal focusing force like the rf voltage. Since $T = C/v$, a *slip factor* η can be defined by

$$\frac{\Delta T}{T_0} = \frac{\Delta C}{C_0} - \frac{\Delta v}{v_0} \equiv \eta\delta, \tag{2.3}$$

where T_0 is the revolution period of the on-momentum particle. Thus, to the lowest order in the fractional momentum spread, we have

$$\eta = \alpha_0 - \frac{1}{\gamma_0^2}, \tag{2.4}$$

where $E_0 = \gamma_0 mc^2$ and m is the rest mass of the particle. Higher orders of the slip factor will be discussed in Sec. 16.4.

For most electron rings and high energy proton rings, the particle velocity v is extremely close to c, the velocity of light, so that the revolution-time slip is dominated by the increase in orbit length. We therefore have $\eta \approx \alpha_0$ and we call the operation *above the transition energy.* For low-energy hadron rings, the velocity term in Eq. (2.4) may dominate making $\eta < 0$ and we call the operation *below the transition energy*, implying that the velocity change of an off-momentum particle is more important than the change in orbit length. The higher-momentum particle, having a larger velocity, will complete a revolution turn in less time than the on-momentum particle, resulting in a forward slip. Obviously, transition occurs when the velocity change is just as important as the change in orbit length, or $\eta = 0$. The transition energy is defined as $E_t = \gamma_t mc^2$ with $\gamma_t = \alpha_0^{-1/2}$. There are also rings, like the 1.2 GeV CERN Low Energy Antiproton Ring (LEAR) and many newly designed ones [2] that have *negative* momentum-compaction factors or $\alpha_0 < 0$. In these rings, lower momentum particles have longer closed orbits or larger radial excursions than higher momentum particles. Negative momentum-compaction implies an imaginary γ_t and the slip factor will always be negative, indicating that the ring will be always below transition. Some believe that such rings will be more stable against collective instabilities. [3] Design and study of negative momentum-compaction rings have been an active branch of research in accelerator physics lately. [4]

In order to have the particles bunched, a longitudinal focusing force will be required. This is done by the introduction of rf cavities. Consider three

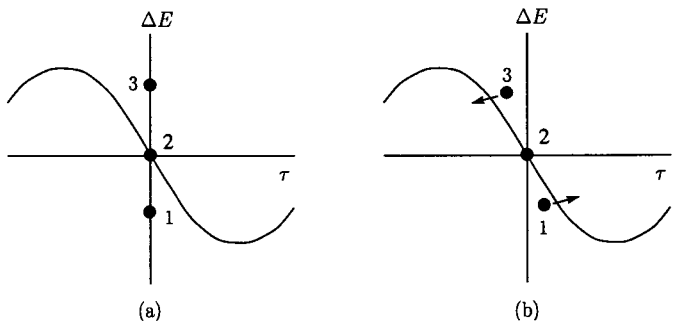


Fig. 2.1 Three particles are shown in the longitudinal phase planes. (a) Initially, they are all at the rf phase of 180° and do not gain or lose any energy. (b) One turn later, the on-momentum particle, denoted by 2, arrives with the same phase of 180° without any change in energy. The particle with lower energy, denoted by 1, arrives earlier and gains energy from the positive part of the rf voltage wave at phase < 180°. The particle with higher energy, denoted by 3, arrives late and loses energy because it sees the rf voltage wave at phase > 180°.

particles arriving in the first turn at exactly the same time at a cavity gap, where the rf sinusoidal gap voltage wave is at 180°, as shown in Fig. 2.1(a). All three particles are seeing zero rf voltage and are not gaining any energy from the rf wave. The drawing of the rf voltage wave implies that the rf voltage at the cavity gap was positive a short time ago and will be negative a short time later. Assume that the ring is above transition or $\eta > 0$. One turn later, the on-momentum particle, denoted by 2 in the figure, arrives at the cavity gap at exactly the time when the rf sinusoidal voltage curve is again at 180° and gains no energy. At this moment, the positions of the three particles and the rf wave are shown in Fig. 2.1(b). The lower energy particle, denoted by 1, arrives at the gap earlier by τ_1, which we call *time slip*. It sees the positive part of the rf voltage and gains energy. For the second turn, it arrives at the gap earlier by $\tau_1 + \tau_2$, where $\tau_2 < \tau_1$ because the particle energy has been raised during the second passage of the cavity gap. This particle will continue to gain energy from the rf every turn and its turn-by-turn additional time slip diminishes. Eventually, this particle will have an energy higher than the on-momentum particle and starts to arrive at the cavity gap later turn after turn, or its turn-by-turn time slip becomes negative. Similar conclusion can be drawn for the particle, denoted by 3 in the figure, that has initial energy higher than the on-momentum particle. With the rf voltage wave, the off-momentum particles therefore oscillate around the on-momentum particle, thus forming a bunch. In reality, the particles lose an amount of energy U_s every turn due to synchrotron radiation and another amount U_{wake} due to interaction with the coupling impedance of the vacuum

chamber. This is compensated by shifting the rf phase slightly from 180° to $\phi_s = \sin^{-1}[(U_s + U_{\rm wake})/eV_{\rm rf}]$, where $V_{\rm rf}$ is the rf voltage (the peak value of the sinusoidal rf wave), so that the on-momentum particle will see the rf voltage at the phase ϕ_s in the amount $V_{\rm rf}\sin\phi_s$, when traversing the cavity gap. This particle is also known as the *synchronous* particle.

2.1.2 *Equations of Motion*

To measure the charge distribution in a bunch, we choose a fixed reference point s_0 along the ring and put a detector there. A particle in a bunch is characterized longitudinally by τ, the time it arrives at s_0 ahead of the synchronous particle. We record the amount of charge arriving when the time advance is between τ and $\tau + d\tau$. The result is $e\lambda(\tau)d\tau$, where $\lambda(\tau)$ is a measure of the particle linear distribution* and e is the particle charge. The actual linear particle density per unit length† is $\bar{\lambda}(s) = \lambda(\tau)/v_0$ and is normalized to unity upon integration over s, where v_0 is the velocity of the synchronous particle. Note that this charge distribution is measured at a fixed point but at different times. Therefore, it is *not* a periodic function of τ. In one turn, the change in time advance is

$$\Delta\tau = -\eta T_0 \delta. \tag{2.5}$$

The negative sign comes about because the revolution period of a higher-momentum particle is larger above transition ($\eta > 0$) and therefore its time of arrival slips. During that turn, the energy gained by the particle relative to the synchronous particle is

$$\Delta E = eV_{\rm rf}(\sin\phi - \sin\phi_s) - [U_s(\delta) - U_{s0}] + C\langle F_0^{\parallel}(\tau; s)\rangle - C_0\langle F_{0s}^{\parallel}\rangle_{\rm stat}, \tag{2.6}$$

where the subscript s stands for synchronous particle. The first term on the right is the sinusoidal rf voltage and the second term is the radiation energy. The third is the average wake force‡ defined in the previous section coming from all the beam particles ahead and can be written as, according to Fig. 2.2,

$$\langle F_0^{\parallel}(\tau; s)\rangle = -\frac{e^2}{C}\int_{\tau}^{\infty} d\tau' \lambda(\tau'; s) W_0'(\tau' - \tau), \tag{2.7}$$

*In Chapter 1, ρ represents the volume charge density. Here, λ represents particle number linear density so that $\int \lambda(\tau)d\tau = N_b$, the total number of particles in the bunch. The linear charge density becomes $eN_b\lambda$. However, care must be exercised that $\lambda(\tau)$ is normalized to unity later in this chapter and also in other chapters.

†The notation $\bar{\lambda}(s)$ is used to distinguish it from $\lambda(\tau)$ which is a function of arrival time τ. For convenience, however, the bar will be omitted when there is no confusion.

‡Recall that the word *average* and the symbol $\langle\cdots\rangle$ actually imply that $\langle F_0^{\parallel}\rangle$ is the wake force on the test particle assuming that the impedance is distributed uniformly along the ring.

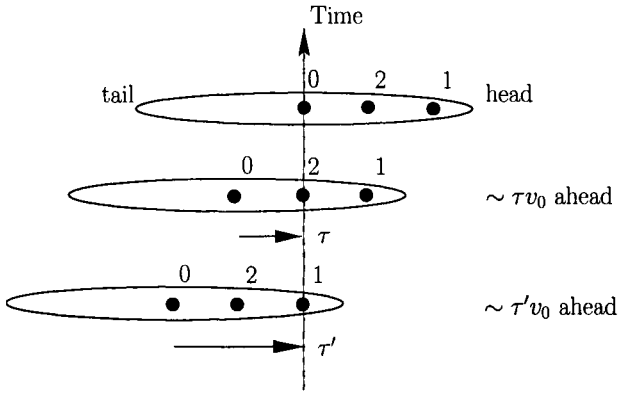


Fig. 2.2 The synchronous particle 0 arrives at location s at the ring (top). The test particle 2 with a time advance τ arrives at s earlier and sees the wake left by source particle 1 (middle), which arrives at s with a time advance τ' (bottom). Thus test particle 2 is $z \sim v_0(\tau' - \tau)$ behind source particle 1. The total wake force acting on test particle 2 is the superposition of the wake forces contributed by all particles in the bunch with time advances $\tau' \geq \tau$.

where the linear density of the bunch consists of a stationary part that is time-independent and an oscillating part that is time- or s-dependent, which is also known as the *dynamic part.* Notice that we have written, for convenience, the wake function as a function of time advance $(\tau' - \tau)$ instead of distance $z \sim v_0(\tau' - \tau)$, with v_0 denoting the velocity of the synchronous particle. There is an approximation here because the particles inside the bunch travel with slightly different velocities, and therefore the distance between particles 1 and 2 is not a constant. The error, which is less then $\Delta v/v_0 = \delta/\gamma_0^2$, is small, where Δv is the maximum velocity spread in the bunch. Its neglect is just the rigid-bunch approximation. In the same approximation, we do not distinguish between C and C_0, the path length of an off-momentum particle and that of the synchronous particle. The signs in Eq. (2.7) and in front of $\langle F_0^{\parallel}(\tau)\rangle$ in Eq. (2.6) can be checked by seeing whether there is an energy loss when substituting the wake of, for example, a real resistance $W_0'(\tau) = R\delta(\tau)$.

The synchronous particle has dynamic evolution and participates in the instability of the bunch. This explains why we allow for only $\langle F_{0s}^{\parallel}\rangle_{\text{stat}}$, the *static* part of the average wake force experienced by the synchronous particle to be subtracted in Eq. (2.6) but not the dynamic part. It is easy to see that $\langle F_{0s}^{\parallel}\rangle_{\text{stat}}$ can be obtained from Eq. (2.7) by substituting the static part of the linear beam density and letting $\tau = 0$, thus retaining only the time-independent portion of the wake force experienced by the synchronous particle. In this way, the dynamic features of the synchronous particle can still be probed in the same way as the other beam particles in the beam through the equations of motion. The

synchronous phase ϕ_s in Eq. (2.6) is a parameter chosen to satisfy the equation

$$eV_{\rm rf}\sin\phi_s - U_s + C_0\langle F_{0s}^{\parallel}\rangle_{\rm stat} = U_{\rm acc}, \tag{2.8}$$

where $U_{\rm acc}$ is the energy imparted to the beam particle to increase its energy. For a storage ring when the beam is maintained at a fixed energy, the right side of Eq. (2.8) vanishes ($U_{\rm acc} = 0$). The time advance τ of a particle is measured with respect to the synchronous particle that is stationary at $\phi = \phi_s$. There will be a phase loop that makes correction to the synchronous angle so as to maintain the correct energy of the beam as time progresses.

The two equations of motion are related because the momentum spread is related to the energy spread by $\delta = \Delta E/(\beta_0^2 E_0) + \mathcal{O}(\Delta E^2/E_0^2)$, and the rf phase seen is related to the time advance,

$$\phi - \phi_s = -h\omega_0\tau, \tag{2.9}$$

where $\omega_0/(2\pi) = 1/T_0$ is the revolution frequency of the ring for the synchronous particle and h is the rf harmonic, which is the number of oscillations the rf wave makes during one revolution period. The negative sign on the right side of Eq. (2.9) comes about because when the particle arrives *earlier* ($\tau > 0$), it sees an rf phase *earlier* than the synchronous phase ϕ_s (see Fig. 2.1).[§] Writing as *discrete* differential equations, they become

$$\frac{d\tau}{dn} = -\frac{\eta T_0}{\beta_0^2}\frac{\Delta E}{E_0}, \tag{2.10}$$

$$\frac{d\Delta E}{dn} = eV_{\rm rf}\Big[\sin(\phi_s - h\omega_0\tau) - \sin\phi_s\Big] - [U(\delta) - U_s] + C_0\Big[\langle F_0^{\parallel}\rangle - \langle F_{0s}^{\parallel}\rangle_{\rm stat}\Big]. \tag{2.11}$$

To simplify future mathematical derivations, a continuous independent variable is desired instead of the discrete turn number n. Time is not a good variable here because particles with different energies complete one revolution turn in different time intervals. Even for one particle, its energy oscillates with synchrotron motion and so is the revolution time for consecutive turns. We choose instead s, the distance measured along the closed orbit of the synchronous particle, because the increase in s per revolution turn is always the length of the closed orbit[¶] C_0 of the synchronous particle, regardless of the momentum offset of the beam particle under consideration. This transition from discrete turn number n to the continuum is a good approximation, because in reality it takes a particle many

[§]To avoid the negative sign, some authors prefer to define τ as the arrival time *lagging behind* the synchronous particle (rather than ahead of).

[¶]In subsequent chapters, the subscript '0' in C_0, E_0, v_0, β_0, γ_0, etc. for the synchronous particle may be omitted in order to simplify the notation.

($\sim$ 50 to 100 in electron rings and $\sim$ 200 to 1000 in proton rings) revolution turns to complete a synchrotron oscillation, and it takes the beam a large number of turns for an instability to develop.

With τ and ΔE as the canonical variables,[‖] the equations of motion for a particle in a small bunch become

$$\frac{d\tau}{ds} = -\frac{\eta}{v_0 \beta_0^2 E_0}\,\Delta E, \tag{2.12}$$

$$\frac{d\Delta E}{ds} = \frac{eV_{\rm rf}}{C_0}\Big[\sin(\phi_s - h\omega_0\tau) - \sin\phi_s\Big] - \frac{U_s(\Delta E) - U_{s0}}{C_0} + \langle F_0^{\parallel}(\tau; s)\rangle - \langle F_{0s}^{\parallel}\rangle_{\rm stat}. \tag{2.13}$$

Although one may also use $t = s/v_0$ as the independent variable, we want to emphasize that this t is the time describing the synchronous particle and is *not* the time variable for the off-energy particle whose equations of motion we are studying. Thus, the independent variable s is quite different from the true time variable of the particle under consideration.

As we said before, $eV_{\rm rf}\sin\phi_s$ consists of three components: to supply the acceleration-required energy, to compensate for the radiation loss U_s, and to compensate for the loss due to wake fields $\langle F_{0s}^{\parallel}\rangle_{\rm stat}$ (also known as *parasitic loss*). Out of the three contributions to the synchronous phase, the third one, the loss due to wake fields is usually small and can be treated as a perturbation. In that case, we first solve Eq. (2.8) and obtain an unperturbed synchronous angle ϕ_{s0} with $\langle F_{0s}^{\parallel}\rangle_{\rm stat}$ omitted. Then the time advance τ of a particle will be with respect to the *unperturbed* synchronous particle at $\phi = \phi_{s0}$. In Eq. (2.13), the term $\sin\phi_s$ consists of $\sin\phi_{s0}$ plus a part counteracting the loss from the wake fields. Thus when $\sin\phi_s$ is replaced by $\sin\phi_{s0}$, the last term, $\langle F_{0s}^{\parallel}\rangle_{\rm stat}$, should be removed also. We can address this apparent complication in another way. Since ϕ_s represents the synchronous phase with the influence of static part of the wake force taken into account already, the static part of the wake experienced by the synchronous particle should not appear in the the equation of motion anymore. Thus $\langle F_{0s}^{\parallel}\rangle_{\rm stat}$ must be subtracted from the total wake force $\langle F_0^{\parallel}(\tau; s)\rangle$ experienced by the particle under consideration. When ϕ_s is replaced by the unperturbed synchronous phase ϕ_{0s}, however, the static part of the wake experienced by the synchronous particle has not been taken into account yet, and, as a result, it must be retained inside the total wake force $\langle F_0^{\parallel}(\tau; s)\rangle$ and therefore the subtraction $-\langle F_{0s}^{\parallel}\rangle_{\rm stat}$ must be omitted. Now if we solve the equations of motion using ϕ_{0s} instead of ϕ_s as the synchronous phase,

[‖] This set of canonical variables should not be used if the accelerator is ramping. Instead the set with τ/ω_0 and $\Delta E/\omega_0$ is preferred.

the solution for τ will automatically include a synchronous phase shift because of the presence of the wake fields. We will address the solution of this problem later in Sec. 2.6.

2.1.2.1 *Synchrotron Oscillation*

Let us first neglect the dynamical part of the wake potential and also the small difference between the energy lost by the off-momentum particle $U(\delta)$ and the energy lost by the on-momentum particle U_s. For small-amplitude oscillations, the two equations combine to give

$$\frac{d^2\tau}{ds^2} - \frac{2\pi\eta he V_{\rm rf}\cos\phi_s}{C_0^2\beta_0^2 E_0}\tau = 0. \tag{2.14}$$

Therefore, the bunch particles are oscillating with the angular frequency $\omega_s = \nu_s\omega_0$, where

$$\nu_s = \sqrt{-\frac{\eta he V_{\rm rf}\cos\phi_s}{2\pi\beta_0^2 E_0}} \tag{2.15}$$

is called the small-amplitude *synchrotron tune* or the number of longitudinal oscillations a particle makes in one revolution turn when the oscillation amplitude is small, and $\omega_s = \nu_s\omega_0$ the *synchrotron angular frequency.* This is the synchrotron tune with the static part of the wake force taken into account. Without the static part of the wake force, the unperturbed or *bare* synchrotron tune ν_{s0} is also given by Eq. (2.15), but with the perturbed synchronous phase ϕ_s replaced by the unperturbed synchronous phase ϕ_{s0}. The negative sign inside the square root implies that ϕ_s should be near 180° in the second quadrant above transition ($\eta > 0$), but near 0° in the first quadrant below transition ($\eta < 0$). Synchrotron motion is slow and the synchrotron tune is usually of the order of 0.001 to 0.01. When the oscillation amplitude becomes larger, the nonlinear contribution of the rf sine wave comes in. The focusing force is smaller and the synchrotron tune ν_s for maximum phase excursion $\hat{\phi}$ becomes smaller as is shown in Fig. 2.3 according to (Exercise 2.3)

$$\nu_s(\hat{\phi}) = \frac{\pi\nu_{s0}}{2K(\sin\frac{1}{2}\hat{\phi})}, \tag{2.16}$$

where

$$K(x) = \int_0^{\pi/2} \frac{du}{\sqrt{1 - x^2\sin^2 u}} \tag{2.17}$$

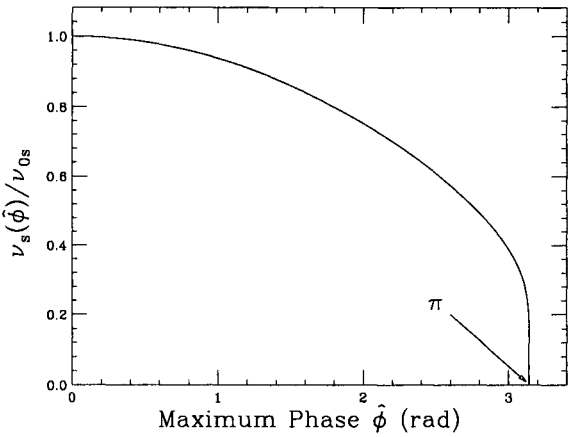


Fig. 2.3 Plot showing the synchrotron frequency decreasing to zero at the edge of the rf bucket. (Courtesy Huang *et al.* [5])

is the complete elliptic integral of the first kind. This amplitude-dependency has been verified experimentally at the Indiana University Cyclotron Facility (IUCF) Cooler Ring. [5] In the small-amplitude approximation, we have $\nu_s(\hat{\phi}) = \nu_{s0}\left(1 - \frac{1}{16}\hat{\phi}^2\right)$, which can be derived easily by a small-argument expansion of $K(x)$. In other words, there will be a spread in the synchrotron tune among the particles in the bunch, which will be important to the Landau damping of the collective instabilities to be discussed later. As the oscillation amplitude continues to increase, a point will be reached when there is no more focusing available from the rf voltage anymore. This boundary in the τ-ΔE phase space provides the maximum possible bunch area allowed and is called the *rf bucket* holding the bunch. Particles that go outside the bucket will be lost, because they will continue to drift around the accelerator ring and will be picked up as *dc beam* by the current monitor. The equation of motion is, in fact, exactly that of a pendulum, whose frequency of oscillation decreases with amplitude. If we start the pendulum motion at its rest position with too large a kinetic energy, the pendulum will no longer be in oscillatory motion. It will wrap around the point of support performing librations instead.** This critical angular amplitude of the pendulum is $\pm\pi$, exactly the same for the rf bucket. Figure 2.4 illustrates some stationary buckets (when the synchronous phase $\phi_s = 180°$ above transition) and moving or accelerating buckets (when ϕ_s is between 90° and 180°). The figure also shows the trajectories of libration outside the buckets. The horizontal axis is the rf phase ϕ (instead of the time advance used in Fig. 2.1); the trajectories therefore move clockwise (instead of counter-clockwise in Fig. 2.1).

If the radiation energy is neglected, the two equations of motion are derivable

**Libration implies periodic motion in the phase space, similar to a sine wave going from $-\infty$ to $+\infty$. Rotation motion in phase space implies to-and-fro oscillatory motion.

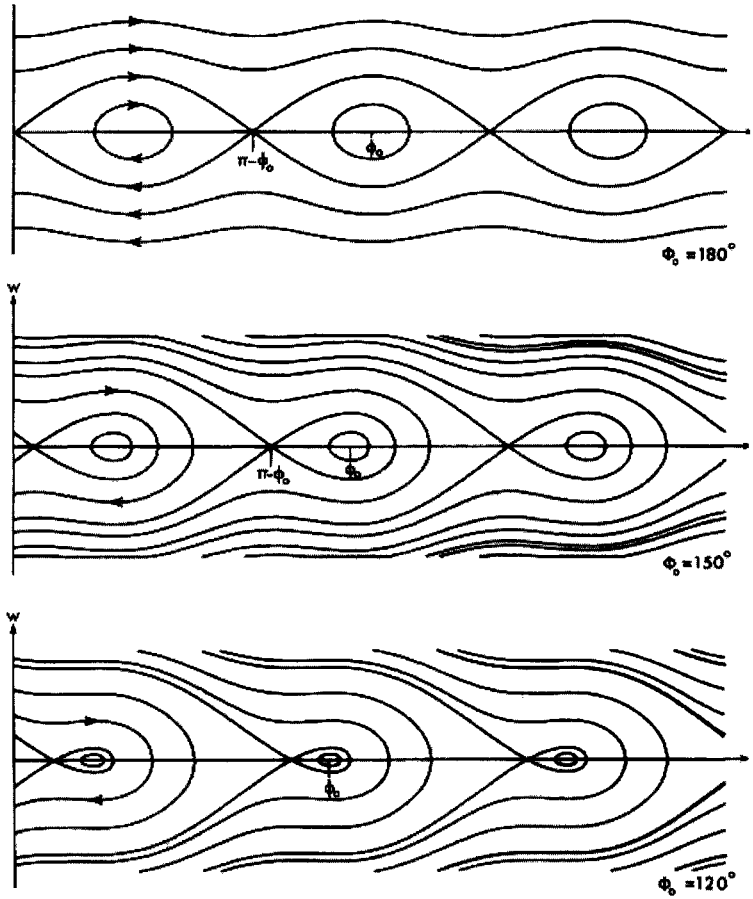


Fig. 2.4 The trajectories in the longitudinal phase space above the transition energy. Top: stationary buckets when the synchronous phase $\phi_0 = 180°$. Middle and lower: moving or accelerating buckets when the synchronous phases are, respectively, $\phi_0 = 150°$ and $120°$. The moving buckets shrink when the synchronous phase decreases from 180° towards 90°. Notice that the horizontal axis is the rf phase (instead of arrival time in Fig. 2.1); the directions of the trajectories are therefore clockwise above transition. (Courtesy Montague. [6])

from the Hamiltonian

$$H = -\frac{\eta \Delta E^2}{2v_0\beta_0^2 E_0} - \frac{eV_{\mathrm{rf}}}{C_0 h\omega_0}\left[\cos(\phi_s - h\omega_0\tau) - \cos\phi_s - h\omega_0\tau\sin\phi_s\right] + U_{\mathrm{wake}}(\tau; s), \tag{2.18}$$

with the aid of the Hamilton's equations

$$\begin{cases} \dfrac{d\tau}{ds} = \dfrac{\partial H}{\partial \Delta E}, \\ \dfrac{d\Delta E}{ds} = -\dfrac{\partial H}{\partial \tau}. \end{cases} \tag{2.19}$$

The potential of the wake force is given by

$$\begin{aligned} U_{\text{wake}}(\tau; s) &= -\int_0^\tau d\tau' \left[\langle F_0^{\parallel}(\tau; s) \rangle - \langle F_{0s}^{\parallel} \rangle_{\text{stat}} \right] \\ &= \frac{e^2}{C_0} \int_0^\tau d\tau'' \left[\int_{-\infty}^{\infty} d\tau' \lambda(\tau'; s) W_0'(\tau' - \tau'') - \int_{-\infty}^{\infty} d\tau' \lambda_0(\tau') W_0'(\tau') \right], \end{aligned} \tag{2.20}$$

where $\lambda_0(\tau)$ is the unperturbed part of the linear density, and its contribution to the second term in the squared brackets denotes the energy lost by synchronous particle due to the static part of the wake force $\langle F_{0s}^{\parallel} \rangle_{\text{stat}}$. In Eq. (2.18), the $\cos\phi_s$ term is added to adjust the rf potential to zero for synchronous particles ($\tau = 0$). For small-amplitude oscillations, the Hamiltonian simplifies to

$$H = -\frac{\eta \Delta E^2}{2v_0 \beta_0^2 E_0} - \frac{\omega_s^2 \beta_0^2 E_0}{2\eta v_0} \tau^2 + U_{\text{wake}}(\tau; s), \tag{2.21}$$

where $\omega_s = \nu_s \omega_0$, the synchrotron angular frequency for small amplitudes, is given by Eq. (2.15).

In an electron ring, synchrotron radiation may provide damping to many collective instabilities. Because this damping force is dissipative in nature, strictly speaking a Hamiltonian formalism does not apply. However, the synchrotron radiation damping time is usually very much longer than the synchrotron period. The fast growing instabilities very often evolve to their full extent before the damping mechanism becomes materialized. We are most interested in studying those instabilities that grow within one radiation damping time of the ring. For a time period much less than the radiation damping time, radiation can be neglected and the Hamiltonian formalism therefore applies.

2.2 Mode Approach

We would like to study the evolution of a bunch that contains, say, 10^{12} particles. The Hamiltonian in Eq. (2.18) has to be modified to include 10^{12} sets of canonical variables in order to fully describe the bunch. The description of the motion of a collection of 10^{12} particles is known as the *particle approach*, and is

often tackled in the time domain. However, what are of interest to us are the collective behaviors of the bunch like the motion of its centroid, the evolution of the particle distribution, the increase in emittances, etc. In other words, we are studying here the evolution of various modes of motion of these collective variables. For 10^{12} particles, there are 10^{12} modes of motion in each direction. However, we will never be interested in those modes whose wavelengths are of the order of the separation between two adjacent particles inside the bunch, because they correspond to motions of very high frequencies, and those motions are microscopic in nature. What we would like to study are the macroscopic modes of the bunch, or those having wavelengths of the same order as the length of the bunch or the radius of the vacuum chamber. Sometimes, we may even want to study modes with wavelengths one tenth or one hundredth of the bunch length or beam pipe radius, but definitely not down to the microscopic size like the distance between two neighboring beam particles. In other words, we go to the frequency domain and look at the different modes of motion of oscillation of the bunch as a whole. Our interest is on those few modes that have the lowest frequencies or longest wavelengths. This direction of study is known as the *mode approach.*

2.2.1 *Vlasov Equation*

When collisions are neglected, the basic mathematical tool for the mode approach is the Vlasov equation or the Liouville theorem. [7] It states that if we follow the motion of a representative particle in the longitudinal or τ-ΔE phase space, the density of particles in its neighborhood is constant. In other words, the distribution of particles $\psi(\tau, \Delta E; s)$ moves in the longitudinal phase space like an incompressible fluid. Mathematically, the Vlasov equation reads

$$\frac{d\psi}{ds} = \frac{\partial\psi}{\partial s} + \frac{d\tau}{ds}\frac{\partial\psi}{\partial\tau} + \frac{d\Delta E}{ds}\frac{\partial\psi}{\partial\Delta E} = 0. \tag{2.22}$$

In terms of the Hamiltonian, it becomes

$$\frac{\partial\psi}{\partial s} + [\psi, H] = 0, \tag{2.23}$$

where $[,]$ denotes the Poisson bracket. Here, the time of early arrival τ and the energy offset ΔE are the set of canonical variables chosen. The Poisson bracket is therefore

$$[\psi, H] = \frac{\partial\psi}{\partial\tau}\frac{\partial H}{\partial\Delta E} - \frac{\partial\psi}{\partial\Delta E}\frac{\partial H}{\partial\tau}. \tag{2.24}$$

Together with the Hamilton's equations of Eq. (2.19), Eq. (2.22) is reproduced.

If radiation is included in the discussion, one must extend the Vlasov equation to the Fokker–Planck equation [8]

$$\frac{d\psi}{ds} = A\frac{\partial(\psi\Delta E)}{\partial\Delta E} + \frac{D}{2}\frac{\partial^2\psi}{\partial\Delta E^2}, \tag{2.25}$$

where A and D are related, respectively, to the damping and diffusion coefficients.

2.2.2 *Coasting Beams*

A coasting beam is not bunched. There is no rf voltage and therefore no synchrotron oscillation. Thus, there is no synchronous particle. For the longitudinal position, we can make reference with respect to a designated point in the accelerator ring. For the energy offset, we can make reference with respect to the average energy of all the on-momentum particles. Here, we cannot talk about bunch modes. Instead, the linear density of an excitation of the beam can be described much better by an harmonic wave,

$$f_1(\theta;t) \sim e^{i(n\theta-\Omega t)}, \tag{2.26}$$

where θ is the azimuthal angle around the ring measured from the point of reference, n is a revolution harmonic or n modulations of the longitudinal linear density when viewed from the top of the accelerator ring at a fixed time t, and Ω is the angular velocity of the wave. The harmonic $n = 0$ should be excluded because it violates charge conservation since the integral of f_1 over the whole ring does not vanish when $n = 0$. The excitation of Eq. (2.26) is a *snap-shot* view, similar to taking a picture of the beam above the accelerator ring. Thus the linear density is a periodic function of θ with period 2π. The linear density can therefore be expanded as a Fourier series and the excitation $f_1(s;t)$ is just a Fourier component. To describe a beam particle, we use the canonical variable z and ΔE, where $z = R\theta$ with $R = C_0/(2\pi)$ being the mean radius of the on-momentum closed orbit. Here, z is just the longitudinal distance ahead of the point of reference at time t and ΔE is the energy offset. Since we are using snap-shot description, the real time t can be used as the continuous independent variable. The equations of motion are

$$\frac{dz}{dt} = -\frac{\eta\Delta E}{v_0\beta_0^2 E_0}, \tag{2.27}$$

$$\frac{d\Delta E}{dt} = -\frac{U-U_s}{T_0} + v_0\langle F_0^{\parallel}(z;t)\rangle, \tag{2.28}$$

where v_0 and T_0 are, respectively, the velocity and revolution period of the on-momentum particle, $\langle F_0^{\parallel}(z;t)\rangle$ is the average longitudinal wake force acting on the beam particle under consideration. Notice that $\langle F_{0s}^{\parallel}(t)\rangle$ is absent because there is no synchronous particle to act as a reference in a coasting beam.

When synchrotron radiation is neglected, the equations of motion can be derived from the Hamiltonian

$$H = -\frac{\eta \Delta E^2}{2v_0\beta_0^2 E_0} + \int_0^z \langle F_0^{\parallel}(z';t)\rangle v_0 dz'. \tag{2.29}$$

For the beam distribution $\psi(z, \Delta E; t)$ in the longitudinal phase space, the Vlasov equation becomes

$$\frac{\partial \psi}{\partial t} + \frac{dz}{dt}\frac{\partial \psi}{\partial z} + \frac{d\Delta E}{dt}\frac{\partial \psi}{\partial \Delta E} = 0, \tag{2.30}$$

where dz/dt and $d\Delta E/dt$ are given by the equations of motion. It is important to realize that dz/dt is *not* the longitudinal velocity v of the particle having energy offset ΔE. Instead, it represents the phase slip (in length) per revolution period T_0. Thus $dz/dt = 0$ for the on-momentum particles.

2.3 Static Solution

The wake potential affects the particle bunch in two ways. Static perturbation changes the shape of the bunch, while time-dependent perturbation leads to instability of the bunch. This is analogous to quantum mechanics, where time-independent perturbation shifts the energy levels while time-dependent perturbation causes transition. In this chapter, we are going to study stationary bunch distributions, or distributions influenced by the time-independent perturbation of the wake potential. This alteration of bunch distribution is called *potential-well distortion.*

From the Vlasov equation depicted in Eq. (2.22), it is evident that the solution for the stationary particle distribution $\psi(\tau, \Delta E)$ in the longitudinal phase space must satisfy

$$[\psi, H_{\text{stat}}] = 0, \tag{2.31}$$

or it is sufficient that ψ is a function of H_{stat}, the static part of Hamiltonian,

$$\psi = \psi(H_{\text{stat}}). \tag{2.32}$$

Recall that the Hamiltonian of a particle with small-amplitude synchrotron oscillations is

$$H = -\frac{\eta \Delta E^2}{2v\beta^2 E_0} - \frac{\omega_{s0}^2 \beta^2 E_0}{2\eta v}\tau^2 + U_{\text{wake}}(\tau; s), \tag{2.33}$$

which describes the motion of a beam particle in the potential

$$U(\tau; s) = -\frac{\omega_{s0}^2 \beta^2 E_0}{2\eta v}\tau^2 + U_{\text{wake}}(\tau; s), \tag{2.34}$$

where ΔE and τ are the energy offset and time advance of the beam particle, while the synchronous particle has energy E_0, velocity[††] $v = \beta c$, bare synchrotron angular frequency ω_{s0}, and slip factor η. The static part of the Hamiltonian H_{stat} receives contribution from the static part of the wake potential [Eqs. (2.7), (2.13), and (2.19)], or[‡‡]

$$U_{\text{wake}}(\tau; s)\Big|_{\text{stat}} = \frac{e^2}{C_0}\int_0^\tau d\tau'' \int_{\tau''}^\infty d\tau' \lambda_0(\tau') W_0'(\tau' - \tau''), \tag{2.35}$$

where C_0 is the length of the designed closed orbit, W_0' is the longitudinal monopole wake function, and $\lambda_0(\tau)$ is the unperturbed linear particle density under the influence of the wake. Notice that here we approach the problem from Eq. (2.33) with the bare synchrotron frequency ω_{s0} in the Hamiltonian and consider the wake potential as a perturbation. Thus the potential arising from $\langle F_{0s}^{\parallel}\rangle_{\text{stat}}$ should not be subtracted [*cf.* Eq. (2.20)]. This explains why Eq. (2.35) is obtained as the static part of the wake potential. When the effects of the wake potential are removed, this is just a parabolic potential well. In the presence of the wake potential, the potential well is distorted and the distribution of the beam particle in the longitudinal phase space is therefore modified. As will be seen below, a purely reactive wake potential, meaning that the coupling impedance is either inductive or capacitive, will modify the parabolic potential in such a way that the potential well remains symmetric. Correspondingly, the distorted particle distribution will also be head-tail symmetric, assuming that the original particle distribution in the rf potential alone is symmetric. A wake potential with a resistive component, however, will affect the symmetry of the parabolic potential well so that the bunch distribution will no longer be head-tail symmetric. Before going into the detail, let us first make a detour and study the reactive force acting on the beam particles.

[††]Here, we drop the subscript "0" for v and β for the sake of convenience.

[‡‡]Here, we start with the bare tune ν_{s0} and treat the time-independent part of the wake force as the perturbation. Thus, unlike Eq. (2.20), no subtraction of $\langle F_{0s}^{\parallel}\rangle_{\text{stat}}$ is necessary.

2.4 Reactive Force

Consider a particle beam with linear density† $\bar{\lambda}(s;t)$ traveling in the positive s-direction with velocity v inside a cylindrical beam pipe of radius b with infinitely-conducting walls. The axis of the beam coincides with the axis of the beam pipe. The beam is assumed to be rigid; therefore $\bar{\lambda}(s;t) = \bar{\lambda}(s-vt)$. We are interested in the longitudinal electric field E_s seen by the beam particles at the axis of the beam at a location where its transverse distribution is uniform within a radius a. To compute that, we invoke Faraday's law,

$$\vec{\nabla} \times \vec{E} = -\frac{\partial}{\partial t}\vec{B}, \tag{2.36}$$

or in the integral form,

$$\oint \vec{E}\cdot\vec{d\ell} = -\frac{\partial}{\partial t}\oint \vec{B}\cdot d\vec{A}. \tag{2.37}$$

In above, the closed path of integration of the electric field $\vec{E}$ is along two radii of the beam pipe at s and $s+ds$ together with two length elements at the beam axis and the wall of the beam pipe, as illustrated in Fig. 2.5. The area of integration of the magnetic flux density $\vec{B}$ is the area enclosed by the closed path. Now, the left side of Eq. (2.37) becomes

$$\oint \vec{E}\cdot\vec{d\ell} = E_s ds + \frac{e\bar{\lambda}(s+ds-vt)}{2\pi\epsilon_0}\left[\int_0^a \frac{rdr}{a^2} + \int_a^b \frac{dr}{r}\right] - \frac{e\bar{\lambda}(s-vt)}{2\pi\epsilon_0}\left[\int_0^a \frac{rdr}{a^2} + \int_a^b \frac{dr}{r}\right], \tag{2.38}$$

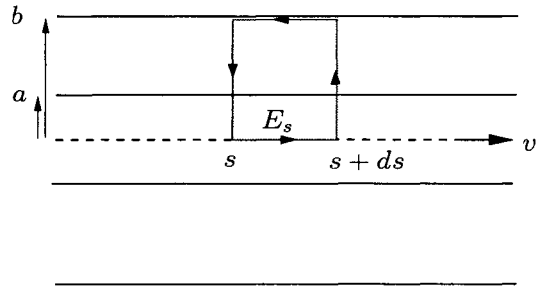


Fig. 2.5 Derivation of the space-charge longitudinal electric field E_s experienced by a beam particle in a beam of radius a in an infinitely conducting beam pipe of radius b.

†We introduce $\bar{\lambda}(s;t)$, which is normalized to the total number of particles N when integrated over s, to distinguish it from $\lambda(\tau;t)$, which is normalized to the same N when integrated over τ. Sometimes the overhead bar may be omitted for convenience.

while the right side

$$-\frac{\partial}{\partial t}\oint \vec{B}\cdot d\vec{A} = -\frac{\partial}{\partial t}\frac{\mu_0 e\bar{\lambda}(s-vt)v}{2\pi}\left[\int_0^a \frac{rdr}{a^2} + \int_a^b \frac{dr}{r}\right] ds. \tag{2.39}$$

Assumption has been made that the open angle $1/\gamma$ of the radial electric field is small compared with the distance ℓ over which the linear density changes appreciably, or $b/\gamma \ll \ell$. Here, $\gamma = E_0/(mc^2)$ and m is the rest mass of the beam particle. In terms of the square-bracketed expressions in Eqs. (2.38) and (2.39), we can define

$$g_0 = 2\left[\int_0^a \frac{rdr}{a^2} + \int_a^b \frac{dr}{r}\right] = 1 + 2\ln\frac{b}{a}, \tag{2.40}$$

which is a geometric factor depending on the geometry of the beam and the beam pipe, and it will deviate from Eq. (2.40) if we relax, for example, the restriction of the transverse uniformity of the particle distribution. Combining the above, we arrive at

$$E_s + \frac{eg_0}{4\pi\epsilon_0}\frac{\partial\bar{\lambda}}{\partial s} = v^2\frac{e\mu_0 g_0}{4\pi}\frac{\partial\bar{\lambda}}{\partial s}, \tag{2.41}$$

or

$$E_s = -\frac{eg_0}{4\pi\epsilon_0\gamma^2}\frac{\partial\bar{\lambda}}{\partial s}, \tag{2.42}$$

which is the longitudinal space-charge force experienced by a particle in a beam. In the reduction from Eq. (2.40) to Eq. (2.42), use has been made of the relation $\epsilon_0\mu_0 = c^{-2}$.

2.4.1 *Space-Charge Impedance*

The first application is a longitudinal harmonic wave

$$\bar{\lambda}_1(s;t) \propto e^{i(ns/R-\Omega t)}, \tag{2.43}$$

perturbing a coasting beam of uniform linear density $\bar{\lambda}_0$, where n is a revolution harmonic, R is the radius of the accelerator ring, and Ω is the frequency of the wave. It will be shown in Chapter 5 that $\Omega \approx n\omega_0 = nv/R$; the difference comes from the perturbation of the coupling impedance. Thus, $\bar{\lambda}_1$ is roughly a function of $s - vt$. Substitution into Eq. (2.42) results in the voltage

$$V = -E_s C_0 = \frac{ineZ_0 cg_0}{2\gamma^2}\bar{\lambda}_1 \tag{2.44}$$

seen by a beam particle per accelerator turn. The perturbation wave constitutes a perturbation current $I_1 = e\bar{\lambda}_1 v$. Therefore, the space-charge impedance per harmonic seen is

$$\left.\frac{Z_0^{\parallel}}{n}\right|_{\text{sp ch}} = \frac{iZ_0 g_0}{2\gamma^2\beta}, \tag{2.45}$$

which is to be compared with Eq. (1.52). From Eq. (2.42), the space-charge force experienced by a beam particle at position s and time t becomes

$$F(s;t) = \frac{ie^2 v}{2\pi}\left.\frac{Z_0^{\parallel}}{n}\right|_{\text{reactive}} \frac{\partial\bar{\lambda}(s;t)}{\partial s}. \tag{2.46}$$

Since an inductive impedance can be viewed as a negative space-charge impedance, we have replaced in above the space-charge impedance by the more general reactive impedance. When the position of the beam particle is measured in terms of time advanced τ ahead of the synchronous particle, the particle linear distribution $\lambda(\tau;s)$, which is normalized to the total number of beam particles, is related to $\bar{\lambda}(s;t)$ by

$$\bar{\lambda}(s;t)ds = \lambda(\tau;s)d\tau \qquad \text{or} \qquad \frac{\partial\bar{\lambda}(s;t)}{\partial s} = \frac{1}{v^2}\frac{\partial\lambda(\tau;s)}{\partial\tau}. \tag{2.47}$$

The reactive force exerted on a beam particle becomes

$$F(\tau;s) = \frac{ie^2}{2\pi v}\left.\frac{Z_0^{\parallel}}{n}\right|_{\text{reactive}} \frac{\partial\lambda(\tau;s)}{\partial\tau}. \tag{2.48}$$

Of course, the above expression can also be obtained by substituting the reactive wake function

$$W_0'(\tau) = \delta'(\tau)\left[\frac{i}{\omega_0}\frac{Z_0^{\parallel}}{n}\right]_{\text{reactive}} \tag{2.49}$$

directly into Eq. (2.7).

The second application is on potential-well distortion. For a bunch, the head has a negative slope or $\partial\lambda/\partial\tau < 0$, while the tail has a positive slope or $\partial\lambda/\partial\tau > 0$. For a space-charge impedance, the head of the bunch is therefore accelerated and gains energy, while the tail decelerated and loses energy. Below transition, the head arrives earlier after one turn while the tail arrives later, resulting in the spreading out of the bunch. The space-charge force therefore distorts the rf potential by counteracting the rf focusing force, while an inductive force enhances the rf focusing. The opposite is true above transition.

2.4.2 *Other Distributions*

The above derivation has been for a beam with transverse uniform distribution. For a round beam with a some other transverse distribution inside a cylindrical beam pipe, the geometric factor g_0 or the space-charge impedance can be derived in the same way. We first derive the electric field in the radial direction and then integrate it from the beam axis to the surface of the beam pipe in exactly the same manner as before. The resulting geometric factors for some common transverse distributions are listed in Table 2.1 (Exercise 2.5). [9]

Table 2.1 Geometric factors for longitudinal space-charge impedance. evaluated for various transverse beam distributions. $\gamma_e = 0.55721$ is Euler's constant and H is the Heaviside step function.

	Phase space distribution	Geometric factor g_0	a_{eff}
Uniform	$\frac{1}{\pi\hat{r}^2} H(\hat{r}-r)$	$1+2\ln\frac{b}{\hat{r}}$	$\hat{r}$
Elliptical	$\frac{3}{2\pi\hat{r}}\left(1-\frac{r^2}{\hat{r}^2}\right)^{1/2} H(\hat{r}-r)$	$\frac{8}{3}-2\ln 2+2\ln\frac{b}{\hat{r}}$	$0.8692\hat{r}$
Parabolic	$\frac{1}{2\pi\hat{r}^2}\left(1-\frac{r^2}{\hat{r}^2}\right) H(\hat{r}-r)$	$\frac{3}{2}+2\ln\frac{b}{\hat{r}}$	$0.7788\hat{r}$
Cosine-square	$\frac{2\pi}{\pi^2-4}\cos^2\frac{\pi r}{2\hat{r}} H(\hat{r}-r)$	$1.9212+2\ln\frac{b}{\hat{r}}$	$0.6309\hat{r}$
Bi-Gaussian	$\frac{1}{2\pi\sigma_r^2} e^{-r^2/(2\sigma_r^2)}$	$\gamma_e+2\ln\frac{b}{\sqrt{2}\sigma_r}$	$1.747\sigma_r$

If the geometric factor is to be written in the format of Eq. (2.40), an effective or equivalent uniform-distributed beam radius a_{eff} can be defined. These a_{eff}'s for the various distributions are listed in the last column of the table. Note that g_0 for bi-Gaussian distribution in the table is only an approximate. The exact expression is given in Exercise 2.5.

The definition of g_0 in Eq. (2.40) involves the line integral of the electric field, and therefore represents the electric potential ϕ_{sp}, called *space-charge* potential, between the center of the beam and the wall of the beam pipe. More concretely, from Eq. (2.38),

$$\phi_{\text{sp}} = \frac{e\bar{\lambda}}{4\pi\epsilon_0} g_0, \tag{2.50}$$

where $\bar{\lambda}$ is the linear density at the longitudinal position under consideration and is normalized to the total number of beam particles when integrated over s. Thus the derivation of the longitudinal space-charge effects or g_0 reduces to the computation of the space-charge potential between the beam center and the walls

of the vacuum chamber. Such a computation involves the solution of the Poisson equation with the beam particles distributed inside the vacuum chamber. It is well-known that this problem is nontrivial because it depends not only on the distribution of the particles in the beam but also the cross-sectional boundary of the vacuum chamber.[‡] The situation of a cylindrical beam at the center of a cylindrical beam pipe has been simple because the equipotential surfaces of a cylindrical beam are cylindrical and the beam pipe just coincides with one of them. Besides this special situation, we are not aware of any that can provide a simple analytic formula.[§]

Although most of the time numerical solution is required to evaluate the space-charge potential, however, there exists some semi-analytic approximations. One of them is for a rectangular beam inside a rectangular beam pipe derived by Gröbner and Hübner. [10] Here, the beam pipe is at $x = 0$ to $2w$ and $|y| = h$. The particle distribution is uniform in the y-direction between $\pm a_y$, but is not restricted in the x-direction. When the transverse density of the beam is expanded as a sine series

$$\rho(x,y) = \frac{\bar{\lambda}}{4a_y w} \sum_{n=1}^{\infty} g_n \sin \eta_n x \, H(a_y^2 - y^2), \tag{2.51}$$

with $\eta_n = n\pi/(2w)$ and $H(a_y^2 - y^2)$ is Heaviside step function, the space-charge potential at the center of the beam is (Exercise 2.6)

$$\phi_{\rm sp} = \frac{e\bar{\lambda}}{4\epsilon_0 a_y w} \sum_{n=1}^{\infty} \left[1 - \frac{\cosh \eta_n (h - a_y)}{\cosh \eta_n h}\right] \frac{g_n \sin \eta_n w}{\eta_n^2}. \tag{2.52}$$

For a uniformly distributed beam within $w - a_x < x < w + a_x$ and $|y| < a_y$, the spectrum g_n is given by

$$g_n = \frac{1}{\eta_n a_x}\Big[\cos \eta_n (w - a_x) - \cos \eta_n (w + a_x)\Big] = \frac{2}{a_x \eta_n} \sin \eta_n w \sin \eta_n a_x. \tag{2.53}$$

Thus the geometric factor g_0 can be expressed as

$$g_0 = \frac{4\pi}{a_x a_y w} \sum_{n=1,3,\cdots} \frac{\sin \eta_n a_x \sinh \frac{1}{2}\eta_n a_y \, \sinh \eta_n (h - \frac{1}{2}a_y)}{\eta_n^3 \cosh \eta_n h}. \tag{2.54}$$

[‡]Even in the cylindrically symmetric case, g_0 depends on the beam size a and the radius of the beam pipe b through $\ln(b/a)$, unlike the transverse dipole space-charge impedance to be discussed in Chapter 3, where the parts involving a and b are separated.

[§]The potential of a one-dimension beam (planar beam with only variation vertically) between two horizontal parallel plates can be solved exactly. However, this problem may not be of interest in practice, because the horizontal width of a beam is usually not very much larger than the separation between the plates making the one-dimension approximation invalid.

In particular, g_0 for a rectangular beam inside a squared beam pipe is computed and is shown in the top plot of Fig. 2.6 for various aspect ratios of the beam as functions of h/a_y. We see that when the beam is square, g_0 is almost indis-

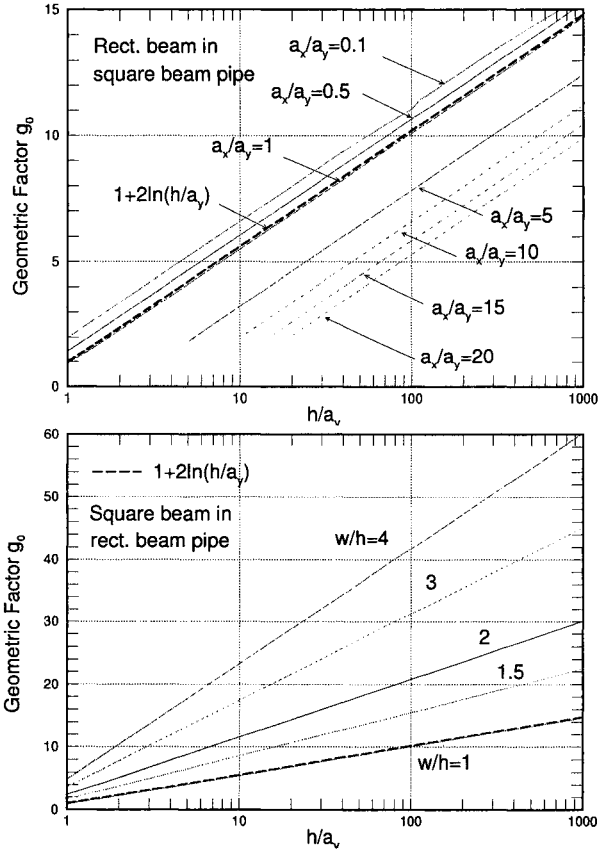


Fig. 2.6 Top: A rectangular beam at the center of a squared beam pipe. We see that g_0 is almost indistinguishable from $1+2\ln(h/a_y)$ (plotted in dashes) when the beam is square, but decreases as the beam spreads out horizontally, because the charges spread out and the vertical electric field becomes less intense. However, the $2\ln(h/a_y)$ behavior is preserved, where h and a_y are half heights of, respectively, the beam pipe and the beam. Bottom: A squared beam at the center of a rectangular beam pipe. As ratio of width to height w/h of the beam pipe increases, g_0 increases and deviates from the $2\ln(h/a_y)$ behavior, because the electric field from the beam is more concentrated.

tinguishable from that of a circular beam inside a circular beam pipe, which is also plotted in dashes for comparison. As the beam spreads out horizontally, g_0 decreases. However, its $2\ln(h/a_y)$ behavior is unchanged. The reduction in g_0 is due to the fact that the charges spread out horizontally so that the electric field becomes relatively smaller.

The situation of a square beam at the center of a rectangular beam pipe is shown in the bottom plot. As mentioned before, when the beam pipe is square ($w/h = 1$), g_0 is almost indistinguishable from $1+2\ln(h/a_y)$, the g_0 of a circular beam inside a circular beam pipe, which is plotted in dashes for comparison.

We see that as the beam pipe is elongated horizontally, g_0 increases because the electric field coming from the beam becomes more concentrated vertically. We also note that g_0 no longer follows the $2\ln(h/a_y)$ behavior. For example, $g_0 \approx 2.5 + 4\ln(h/a_y)$ when $w/h = 2$, and $g_0 \approx 5 + 7.8\ln(h/a_y)$ when $w/h = 4$.

2.5 Bunch-Shape Distortion

2.5.1 *Haissinski Equation*

For an electron bunch, because of the random quantum radiation and excitations, the stationary distribution should have a Gaussian distribution in ΔE, or

$$\psi(\tau, \Delta E) = \frac{1}{\sqrt{2\pi}\sigma_E} \exp\left(-\frac{\Delta E^2}{2\sigma_E^2}\right) \lambda(\tau), \tag{2.55}$$

where σ_E is the rms beam energy spread determined by synchrotron radiation. Noting Eq. (2.32) and the Hamiltonian in Eq. (2.33), we must have

$$\psi(\tau, \Delta E) \propto \exp\left(\frac{v\beta^2 E_0}{\eta\sigma_E^2} H_{\text{stat}}\right). \tag{2.56}$$

The linear density or distribution $\lambda(\tau)$ is obtained by an integration over ΔE. Since Hamiltonian H_{stat} depends on $\lambda(\tau)$ [see, for example, Eqs. (2.20) and (2.21)], we finally arrive at a self-consistent equation for the linear density,

$$\lambda(\tau) = \lambda(0) \exp\left[-\left(\frac{\omega_{s0}\beta^2 E_0}{\eta\sigma_E}\right)^2 \frac{\tau^2}{2} + \frac{e^2\beta^2 E_0}{\eta T_0 \sigma_E^2} \int_0^\tau d\tau'' \int_{\tau''}^\infty d\tau' \lambda(\tau') W_0'(\tau' - \tau'')\right]. \tag{2.57}$$

This is called the *Haissinski equation*, [11] where the constant $\lambda(0)$ is obtained by normalizing to N_b, the total number of particles in the bunch,

$$\int d\tau \lambda(\tau) = N_b. \tag{2.58}$$

The solution will give a linear distribution that deviates from the Gaussian form, and we call this *potential-well distortion.* Since the rf voltage is modified, the angular synchrotron frequency also changes from ω_{s0} to the perturbed incoherent ω_s accordingly.

For a purely resistive impedance $Z_0^{\parallel}(\omega) = R_s$ with the wake function $W_0'(z) = R_s\delta(z/v)$, the equation can be solved analytically giving the solution

(Exercise 2.10) [13]

$$\lambda(\tau) = \frac{\sqrt{2/\pi}e^{-\tau^2/(2\sigma_\tau^2)}}{\alpha_R\sigma_\tau\{\coth(\alpha_R N_b/2) - \mathrm{erf}[\tau/(\sqrt{2}\sigma_\tau)]\}}, \tag{2.59}$$

where

$$\sigma_\tau = \frac{|\eta|\sigma_E}{\beta^2\omega_{s0}E_0}, \quad \alpha_R = \frac{e^2\beta^2E_0R_s}{\eta T_0\sigma_E^2}, \tag{2.60}$$

and

$$\mathrm{erf}(x) = \frac{2}{\sqrt{\pi}}\int_0^x e^{-t^2}dt \tag{2.61}$$

is the error function. For a weak beam with $|\alpha_R|N_b \lesssim 1$, the peak beam density occurs at

$$\tau = \frac{\alpha_R N_b}{\sqrt{2\pi}}\sigma_\tau. \tag{2.62}$$

This peak moves forward above transition ($\alpha_R > 0$) and backward below transition ($\alpha_R < 0$) as the beam intensity increases. The effect comes from the parasitic loss of the beam particle which is largest at the peak of the linear density $\lambda(\tau)$ and smallest at the two ends. Those particles losing energy will arrive earlier/later than the synchronous particle in time above/below transition and the distribution will therefore lean forward/backward. Such bunch profiles are plotted in Fig. 2.7 for $\alpha_R N_b = -10$, -5, 0, 5, and 10. In the figure, the linear density is normalized to $\sigma_\tau\sqrt{\pi/2}$ when integrated over τ.

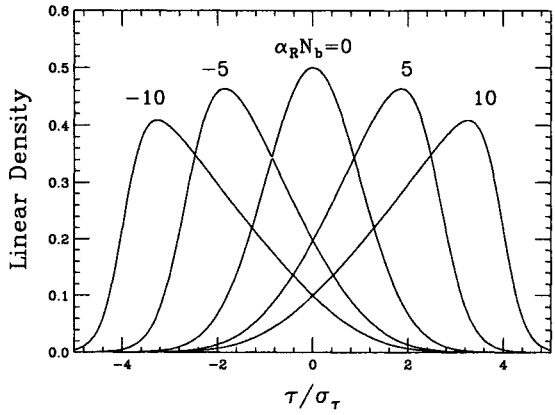


Fig. 2.7 Plot of bunch profiles between $\pm 5\sigma_\tau$'s for $\alpha_R N_b = -10$, -5, 0, 5, and 10, according to the solution of the Haissinski equation when the impedance is purely resistive. These profiles are normalized to $\sigma_\tau\sqrt{\pi/2}$ when integrated over τ. It is evident that the profile leans forward above transition ($\alpha_R > 0$) and backward below transition ($\alpha_R < 0$).

When the longitudinal impedance is purely inductive, $W_0'(z) = \mathcal{L}\delta'(z/v)$, the double integrals can be performed and the Haissinski equation becomes

$$\lambda(\tau) = ke^{-\tau^2/(2\sigma_\tau^2)-\alpha_L\lambda(\tau)}, \tag{2.63}$$

where k is a positive constant and $\alpha_L = e^2\beta^2 E_0\mathcal{L}/(\eta T_0\sigma_E^2)$. The above can be rewritten as

$$\lambda(\tau)e^{\alpha_L\lambda(\tau)} = ke^{-\tau^2/(2\sigma_\tau^2)}. \tag{2.64}$$

The right side is an even function of τ and so must be the left side, $\lambda e^{\alpha_L\lambda}$. Thus, it appears that the distorted distribution λ is also an even function of τ. The linear distribution will remain left-right symmetric. Therefore, the reactive part of the impedance will either lengthen or shorten the bunch, while the resistive part will cause the bunch to lean forward or backward. When $|\alpha_L|N_b \lesssim 1$, we can iterate,

$$\lambda \approx ke^{-\tau^2/(2\sigma_\tau^2)}\left[1 - k\alpha_L e^{-\tau^2/(2\sigma_\tau^2)}\right]. \tag{2.65}$$

Without the impedance term, k in Eq. (2.63) represents the particle density at the center of the bunch. Now with $\alpha_L > 0$, Eq. (2.65) says that effectively k becomes smaller. In other words, the distribution spreads out, or the effective rms bunch length becomes larger than σ_τ. This is the situation of either a repulsive inductive impedance force above transition or a repulsive capacitive force ($\mathcal{L} < 0$) below transition. On the other hand, for an attractive inductive force below transition or an attractive capacitive force above transition, $\alpha_L < 0$. The bunch will be shortened.

For a general wake function, the Haissinski equation can only be solved numerically. The equation, however, can be cast into the more convenient form (Exercise 2.7)

$$\lambda(\tau) = \xi \exp\left[-\left(\frac{\omega_{s0}\beta^2 E_0}{\eta\sigma_E}\right)^2\frac{\tau^2}{2} - \frac{e^2\beta^2 E_0}{\eta T_0\sigma_E^2}\int_0^\infty d\tau'\lambda(\tau+\tau')\int_0^{\tau'} d\tau'' W_0'(\tau'')\right]. \tag{2.66}$$

Notice that $\lambda(\tau)$ on the left side depends only on the λ on the right side evaluated in front of τ. We can therefore solve for λ at successive slices of the bunch by assigning zero or some arbitrary value to λ at the very first slice (the head) and some value to the constant ξ. The value of ξ is varied until the proper normalization of λ is obtained.

The longitudinal wake potential of the damping rings at the SLAC Linear Collider (SLC) has been calculated carefully. Using it as input, the Haissinski equation is solved numerically at various beam intensities. The results are shown

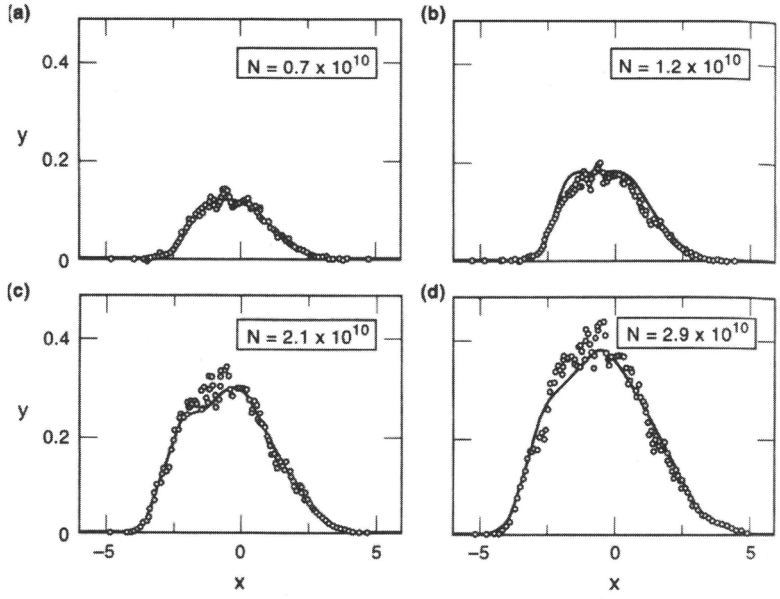


Fig. 2.8 Potential-well distortion of bunch shape for various beam intensities for the SLAC SLC damping ring. Solid curves are solution of the Haissinski equation and open circles are measurements. The horizontal axis is in units of unperturbed rms bunch length σ_{z0}, while the vertical scale gives $y = 4\pi e\lambda(z)/[V'_{\rm rf}(0)\sigma_{z0}]$. The beam is going to the left. (Courtesy Banes. [12])

as solid curves in Fig. 2.8 along with the actual measurements. The agreement has been very satisfactory. [12]

2.5.2 *Elliptical Phase-Space Distribution*

An easier way to compute the bunch length distorted by the reactive impedance is to consider the elliptical phase-space distribution

$$\psi(\tau, \Delta E) = \frac{3N_b|\eta|\sqrt{\kappa}}{2\pi\beta^2\omega_{s0}E_0\hat{\tau}_0^3}\sqrt{\hat{\tau}_0^2 - \left(\frac{\eta}{\beta^2\omega_{s0}E_0}\right)^2\Delta E^2 - \kappa\tau^2}, \tag{2.67}$$

where $\hat{\tau}_0$ is the unperturbed half bunch length (in time advance). The distribution vanishes when the expression inside the square root of Eq. (2.67) becomes negative. This distribution is for an electron bunch, because the maximum half-

energy spread $\widehat{\Delta E}$ derived from Eq. (2.67),

$$\widehat{\Delta E} = \frac{\beta^2 \omega_{s0} E_0 \hat{\tau}_0}{|\eta|}, \tag{2.68}$$

exactly that given by the phase equation (2.12), is a constant determined by synchrotron radiation. The half width of the bunch can be derived from Eq. (2.67),

$$\hat{\tau} = \frac{\hat{\tau}_0}{\sqrt{\kappa}}, \tag{2.69}$$

and is determined by the parameter κ. This distribution when integrated over ΔE gives the normalized parabolic linear distribution

$$\lambda(\tau) = \frac{3N_b\sqrt{\kappa}}{4\hat{\tau}_0^3}\left(\hat{\tau}_0^2 - \kappa\tau^2\right). \tag{2.70}$$

With the reactive wake function $W_0'(z) = \mathcal{L}\delta'(z/v)$, the static part of the Hamiltonian in Eq. (2.21) can therefore be written as a quadratic in ΔE and τ:

$$H_{\text{stat}} = -\frac{\eta}{2v\beta^2 E_0}(\Delta E)^2 - \frac{\omega_{s0}^2 \beta^2 E_0}{2\eta v}\tau^2 - \frac{e^2\mathcal{L}}{C_0}\lambda(\tau). \tag{2.71}$$

Substituting for the linear density $\lambda(\tau)$, the Hamiltonian becomes

$$H_{\text{stat}} = \frac{\omega_{s0}^2 \beta^2 E_0}{2\eta v}\left[-\left(\frac{\eta}{\beta^2\omega_{s0}E_0}\right)^2 \Delta E^2 - \tau^2(1 - D\kappa^{3/2})\right], \tag{2.72}$$

where

$$D = \frac{3e^2 N_b \eta v \mathcal{L}}{2\omega_{s0}^2 \beta^2 E_0 C_0 \hat{\tau}_0^3}, \tag{2.73}$$

and the constant term involving $\hat{\tau}_0$ has been dropped. To be self-consistent, the expression of ψ in Eq. (2.67) must be a function of the Hamiltonian. Comparing Eq. (2.67) with Eq. (2.72), we arrive at

$$\kappa = 1 - D\kappa^{3/2} \tag{2.74}$$

or

$$\left(\frac{\hat{\tau}}{\hat{\tau}_0}\right)^3 = \left(\frac{\hat{\tau}}{\hat{\tau}_0}\right) + D. \tag{2.75}$$

This cubic can be solved by iteration. First we put $\hat{\tau}/\hat{\tau}_0 = 1$ on the right side. If $D > 0$, we find $\hat{\tau}/\hat{\tau}_0 > 1$ or the bunch is lengthened. If $D < 0$, it is shortened. The former corresponds to either an inductive force above transition or a

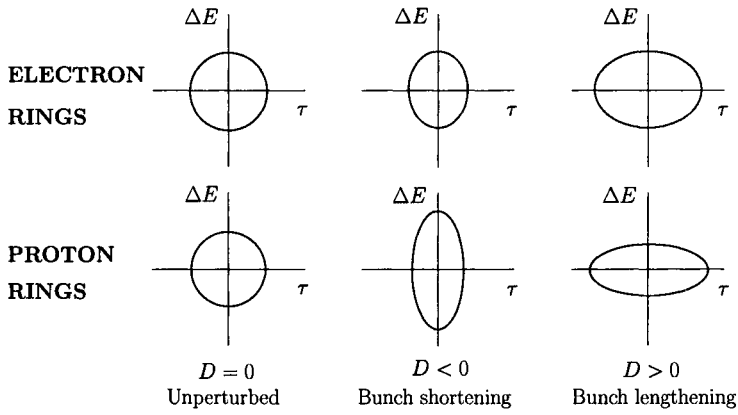


Fig. 2.9 Potential-well distortion of the bunch shape in the longitudinal phase space. $D > 0$ corresponds to either an inductive perturbation above transition or a capacitive perturbation below transition, while $D < 0$ implies either an inductive perturbation below transition or a capacitive perturbation above transition. Top row is for electron bunches where the energy spread remains constant as a result of radiation damping. Bottom row is for proton bunches where the bunch area is constant.

capacitive force below transition. The latter corresponds to either an inductive force below transition or a capacitive force above transition. This is illustrated in the first row of Fig. 2.9, where we notice that the energy spread of the bunch is unchanged for various types of perturbation.

For a proton bunch, the energy spread is also modified but the bunch area remains constant. The phase-space distribution has to be rewritten as

$$\psi(\tau, \Delta E) = \frac{3N_b|\eta|}{2\pi\beta^2\omega_{s0}E_0\hat{\tau}_0^3}\sqrt{\hat{\tau}_0^2 - \frac{1}{\kappa}\left(\frac{\eta}{\beta^2\omega_{s0}E_0}\right)^2\Delta E^2 - \kappa\tau^2}. \tag{2.76}$$

Now we have (Exercise 2.11)

$$\hat{\tau} = \frac{\hat{\tau}_0}{\sqrt{\kappa}} \qquad \text{and} \qquad \widehat{\Delta E} = \sqrt{\kappa}\widehat{\Delta E}_0, \tag{2.77}$$

so that the bunch area is unchanged. Integrating over ΔE, we obtain the same linear density as in Eq. (2.70) and therefore the same Hamiltonian H_{stat} as in Eq. (2.72). However, comparing the phase-space distribution $\psi(\tau, \Delta E)$ with the Hamiltonian, we arrive at the quartic equation

$$\left(\frac{\hat{\tau}}{\hat{\tau}_0}\right)^4 = 1 + D\left(\frac{\hat{\tau}}{\hat{\tau}_0}\right), \tag{2.78}$$

from which the bunch lengthening can be solved. This is illustrated in the bottom row of Fig. 2.9.

2.6 Synchrotron Tune Shift

2.6.1 *Incoherent Synchrotron Tune Shift*

When the potential well is distorted, the frequency of oscillation will be changed also. For an elliptical bunch distribution in the longitudinal phase space, the synchrotron oscillation frequency shift can be easily extracted from the Hamiltonian in Eq. (2.72). We get

$$\left(\frac{\omega_s}{\omega_{s0}}\right)^2 = \left(1 + \frac{\Delta\omega_s}{\omega_{s0}}\right)^2 = 1 - D\kappa^{3/2}, \tag{2.79}$$

which is true for both electron and proton bunches. As a first approximation, the synchrotron frequency shift $\Delta\omega_s$ or synchrotron tune shift $\Delta\nu_s$ is given by

$$\frac{\Delta\omega_s}{\omega_{s0}} = \frac{\Delta\nu_s}{\nu_{s0}} \approx -\frac{D}{2} = -\frac{3e^2 N_b \eta v \mathcal{L}}{4\omega_{s0}^2 \beta^2 E_0 C_0 \hat{\tau}_0^3}, \tag{2.80}$$

where $\omega_{s0}/(2\pi)$ is the *bare* or *unperturbed* synchrotron frequency and $\nu_{s0} = \omega_{s0}/\omega_0$ is the *bare* or *unperturbed* synchrotron tune. We see that an inductive vacuum chamber will lower/increase the synchrotron tune above/below transition. For the longitudinal space-charge self-force, the synchrotron tune will be shifted upward/downward above/below transition. This is the tune shift for an individual particle and is called the *incoherent* synchrotron tune shift.

For a more general bunch distribution and a more general impedance, we resort to the equations of motion [Eqs. (2.12) and (2.13)]. In the absence of the wake force, let the *unperturbed* synchronous angle required to counteract radiation beam loss be ϕ_{s0}. Let τ be the time advance of a particle measured from the *unperturbed* synchronous particle. Now the wake force is introduced as a perturbation on the right side of the equation of motion:†

$$\frac{d^2\tau}{ds^2} + \frac{\nu_{s0}^2}{R^2}\tau = -\frac{\eta}{v\beta^2 E_0}\langle F_0^{\parallel}(\tau; s)\rangle, \tag{2.81}$$

†Here we start with the bare tune ν_{s0} and treat the wake force as a perturbation. Thus the subtraction of $\langle F_{0s}^{\parallel}\rangle_{\text{stat}}$, the static wake force experienced by the synchronous particle, is omitted [see discussion following Eq. (2.13)].

with the wake force given by

$$\langle F_0^{\parallel}(\tau;s)\rangle = -\frac{e^2N_b}{C_0}\int_{-\infty}^{\infty} d\tau'\lambda(\tau';s)W_0'(\tau'-\tau), \tag{2.82}$$

where we have explicitly separated out N_b, the number of particles in the bunch, so that $\lambda(\tau;s)$ will now be normalized to unity when integrated over τ. Since we are studying the static effects of the wake, we must use only the unperturbed linear bunch density $\lambda_0(\tau)$, which implies the linear density is stationary in the bottom of the rf potential well. What we mean is that although particles continue to make synchrotron oscillations, however, the linear density remains time independent.[‡] Substituting for the Fourier transform of the wake and that of the linear density,

$$\lambda_0(\tau) = \int_{-\infty}^{\infty} d\omega\tilde{\lambda}_0(\omega)e^{i\omega\tau}, \tag{2.83}$$

we obtain

$$\langle F_0^{\parallel}(\tau;s)\rangle_{\text{stat}} = -\frac{e^2N_b}{C_0}\int_{-\infty}^{\infty} d\omega Z_0^{\parallel}(\omega)\tilde{\lambda}_0(\omega)e^{i\omega\tau}. \tag{2.84}$$

We can write $\tau = \hat{\tau}\cos\phi$, where $\hat{\tau}$ is the amplitude of synchrotron oscillation of the particle and ϕ is the instantaneous synchrotron-oscillation phase. Next, expand into azimuthal harmonics in the longitudinal phase space with the aid of

$$e^{i\omega\hat{\tau}\cos\phi} = \sum_{m=-\infty}^{\infty} i^m J_m(\omega\hat{\tau})\cos m\phi, \tag{2.85}$$

where J_m is the Bessel function of order m. To study the effect to the synchrotron tune, we only need to retain up to the dipole terms, thus the equation of motion becomes[§]

$$\frac{d^2\tau}{ds^2} + \frac{\nu_{s0}^2}{R^2}\tau = \frac{\eta e^2N_b}{v\beta^2E_0C_0}\int_{-\infty}^{\infty} d\omega\tilde{\lambda}_0(\omega)Z_0^{\parallel}(\omega)\left[J_0(\omega\hat{\tau}) + \frac{iJ_1(\omega\hat{\tau})}{\hat{\tau}/2}\tau\right]. \tag{2.86}$$

Notice that the right side is real because we started with a real wake potential and a real linear density. Notice also that when the linear distribution $\lambda_0(\tau)$

[‡]Strictly speaking, this is possible only when there are infinite number of particles in the bunch.

[§]We perform multipole expansion in the longitudinal phase space rather than power series expansion in τ, because dipole synchrotron oscillation corresponds to $e^{i(\phi-\omega_s t)}$, quadrupole oscillation corresponds to $e^{i2(\phi-\omega_s t)}$, etc.

is left-right symmetric, the Fourier transform $\tilde{\lambda}_0(\omega)$ is real.[¶] We can therefore write

$$\frac{d^2\tau}{ds^2} + \frac{\nu_{s0}^2}{R^2}\tau = \frac{\nu_{s0}^2}{R^2}\xi\left[\frac{\mathcal{Z}_0}{\omega_0} - \mathcal{Z}_1\tau\right], \tag{2.87}$$

where [14]

$$\mathcal{Z}_0 = 2\pi\int_{-\infty}^{\infty}\frac{d\omega}{\omega_0}\tilde{\lambda}_0(\omega)\,\mathcal{R}e\,Z_0^{\parallel}(\omega)J_0(\omega\hat{\tau}), \tag{2.88}$$

$$\mathcal{Z}_1 = 2\pi\int_{-\infty}^{\infty}\frac{d\omega}{\omega_0}\tilde{\lambda}_0(\omega)\,\mathcal{I}m\,Z_0^{\parallel}(\omega)\frac{J_1(\omega\hat{\tau})}{\omega_0\hat{\tau}/2}, \tag{2.89}$$

both of them have the dimension of monopole impedance. In above, the scaling factor is defined as

$$\xi = -\frac{eI_b}{hV_{\rm rf}\cos\phi_{s0}} = \frac{\eta eI_b}{2\pi\beta^2E_0\nu_{s0}^2}, \tag{2.90}$$

positive above transition and negative below transition, where $I_b = eN_b\omega_0/(2\pi)$ is the average bunch current and $\nu_{s0} = \sqrt{-\eta he V_{\rm rf}\cos\phi_{s0}/(2\pi\beta^2E_0)}$ is the unperturbed synchrotron tune. In this definition, ξ has the dimension of inverse monopole impedance.

The solution to Eq. (2.87) is

$$\tau = \xi\frac{\mathcal{Z}_0}{\omega_0} + \hat{\tau}\cos\nu_s\omega_0 s/v, \tag{2.91}$$

where ν_s is the incoherent synchrotron tune with the perturbation of the wake fields included and is given by

$$\nu_s^2 = \nu_{s0}^2(1 + \xi\mathcal{Z}_1), \tag{2.92}$$

which also gives the dependency on amplitude $\hat{\tau}$. Thus the second term in the solution indicates a shift of the synchrotron frequency, while the first term indicates a shift of the equilibrium position of synchrotron oscillation. Below transition ($\xi < 0$), a particle losing energy from $\mathcal{R}e\,Z_0^{\parallel}$ arrives a bit later at the cavity gap in order to regain the energy from the rf system, which explains why

[¶]At a finite synchronous angle $\phi_s \neq 0$, the rf potential is not symmetric about the synchronous point and $\lambda_0(\tau)$ is not left-right symmetric. However, this asymmetry should be small if the bunch is short. Therefore the more accurate expression for $\mathcal{Z}_0$ will involve a small contribution of $\mathcal{I}m\,Z_0^{\parallel}$ and the expressions for $\mathcal{Z}_1$ will involve a small contribution of $\mathcal{R}e\,Z_0^{\parallel}$.

$\xi \mathcal{Z}_0/\omega < 0$ on the right side of Eq. (2.91). The result constitutes the shifting of the synchronous phase by a positive value

$$\Delta\phi_s = -\xi h \mathcal{Z}_0. \tag{2.93}$$

For a purely inductive impedance $\mathcal{I}m\, Z_0^{\parallel}(\omega) = -\omega\mathcal{L}$ where $\mathcal{L}$ is the inductance (or a space-charge-like capacitive impedance with $\mathcal{L} < 0$), $\mathcal{Z}_1$ can be evaluated exactly to give [15]

$$\mathcal{Z}_1 = \frac{4\mathcal{L}}{\omega_0^2 \hat{\tau}} \int_0^{\pi} d\theta \cos\theta \frac{d\lambda_0(\tau)}{d\tau}\Big|_{\tau=\hat{\tau}\cos\theta}. \tag{2.94}$$

This arises with the aid of the inverse Fourier transform of the linear distribution $\lambda_0(\tau)$ and the integral representation of the Bessel function

$$i\pi J_1(z) = \int_0^{\pi} d\theta\, \cos\theta\, e^{iz\cos\theta}. \tag{2.95}$$

It is worthwhile to point out that, because the beam is inside an accelerator ring, a more correct formulation of the wake force of Eq. (2.82) should include the contribution of the wake left by the beam in previous turns (see Chapter 8). The result is the replacement of the integral over ω in Eqs. (2.88) and (2.89) by a discrete sum over all the revolution harmonic frequency $p\omega_0$ with $p = 0,\ 1,\ 2,\ \cdots$. Miraculously, this procedure arrives back to exactly the same expression for $\mathcal{Z}_1$ in Eq. (2.94).

For a parabolic distribution,

$$\lambda_0(\tau) = \frac{3}{4\hat{\tau}}\left(1 - \frac{\tau^2}{\hat{\tau}^2}\right), \tag{2.96}$$

for $|\tau| < \hat{\tau}$, the synchrotron tune shift is

$$\frac{\Delta\nu_s}{\nu_{s0}} \approx \frac{\xi\mathcal{Z}_1}{2} = -\frac{3\pi\mathcal{L}\xi}{2\omega_0^2\hat{\tau}^3}, \tag{2.97}$$

agreeing with the previous solution in Eq. (2.80). For a Gaussian linear distribution with rms bunch length σ_τ,

$$\lambda_0(\tau) = \frac{1}{\sqrt{2\pi}\sigma_\tau} e^{-\tau^2/(2\sigma_\tau^2)}, \tag{2.98}$$

the integral can be performed analytically to give

$$\mathcal{Z}_1 = -\frac{\sqrt{2\pi}\mathcal{L}}{\omega^2\sigma_\tau^3} e^{-z}\left[I_0(z) - I_1(z)\right], \tag{2.99}$$

where $z = \hat{\tau}^2/(4\sigma_\tau^2)$ and the integral representation of the modified Bessel function

$$I_n(z) = \frac{(-1)^n}{2\pi} \int_0^{2\pi} d\theta \, \cos n\theta \, e^{-z\cos\theta}, \tag{2.100}$$

has been used. Thus, for a small synchrotron oscillation amplitude $\hat{\tau} \ll \sigma_\tau$, the incoherent synchrotron tune shift is

$$\frac{\Delta\nu_s}{\nu_{s0}} \approx \frac{\xi \mathcal{Z}_1}{2} = -\frac{\sqrt{2\pi}\mathcal{L}\xi}{2\omega_0^2\hat{\tau}^3}\left(1 - \frac{3\hat{\tau}^2}{8\sigma_\tau^2}\right). \tag{2.101}$$

2.6.2 *Coherent Synchrotron Tune Shift*

If we average Eq. (2.87) over all beam particles, we obtain the equation of motion for the center-of-mass of the bunch and arrive at exactly the same synchrotron tune shift in Eq. (2.92). Since this concerns the center of the bunch, we obtain the conclusion that the *coherent* synchrotron tune shift of the bunch due to potential-well distortion is exactly the same as the *incoherent* synchrotron tune shift. However, there is another contribution to this coherent tune shift from the dynamic part of the perturbation which we are going into later (see Secs. 6.2.1 and 8.1.2). This dynamic contribution will cancel the potential-well contribution, resulting in no coherent synchrotron tune shift in the dipole mode when the bunch intensity is weak and the wake is no longer than the bunch spacing. Physically, this dipole mode is a rigid rotation of the bunch in the longitudinal phase space. The wake-field pattern, and therefore the potential-well distortion, moves with the bunch. Thus the motion of the bunch as a whole is not affected by the wake fields at all. On the other hand, the picture for incoherent motion is about a beam particle moving inside the bunch with the bunch center at rest. An individual particle can therefore sample the variation of the wake fields while executing synchrotron oscillation. Thus, to demonstrate the effect of space-charge impedance or inductive impedance, the coherent quadrupole mode of the synchrotron oscillation should be measured. If the incoherent synchrotron tune is desired, a Schottky scan of the beam will be necessary.

The synchrotron tune shift from potential-well distortion, $\Delta\nu_s$, obtained above is usually moved to the left side of the equation of motion and combined with the bare tune coming from the rf focusing to form a perturbed synchrotron tune ν_s. The equation of motion then becomes

$$\frac{d^2\tau}{ds^2} + \frac{\nu_s^2}{R^2}\tau = \cdots, \tag{2.102}$$

where

$$\nu_s = \nu_{s0} + \Delta\nu_s \tag{2.103}$$

and the right side contains dynamic effect of the wake only and no more potential-well distortion. As demonstrated in Eqs. (2.89) and (2.92) above, ν_s is, in general, not a constant, but a function of the position of the particle in the beam, because of a possible spread in synchrotron tune shift among the beam particles. This will be the equation of motion we will be using in later chapters.

2.7 Potential-Well Distortion Compensation

Potential-well distortion can often be a serious problem in the operation of an accelerator or storage ring. If the distortion opposes the rf bunching, a much larger rf voltage and hence rf power will be required to counteract the distortion. Even when such a higher compensating rf voltage is available, the rf bucket may have been so much distorted that its useful area has very much been reduced. An example is the Los Alamos Proton Storage Ring (PSR), which stores an intense proton beam at the kinetic energy of 797 MeV. The ring has a transition gamma of $\gamma_t = 3.1$, implying that the operation of the ring is below transition. The longitudinal space-charge force is therefore repulsive in nature and tends to lengthen the bunch. This longitudinal repulsive force will counteract the rf bunching force. Let us study how serious the potential-well distortion is and a possible way to cure the problem.

2.7.1 *Space-Charge Cancellation*

The PSR has a circumference of 90.2 m. It receives chopped proton beams from a linac cumulatively in 1000 to 2000 turns. The beam is bunched by an rf buncher to the desired length and is then extracted for experimental use. The rf buncher is of rf harmonic $h = 1$, or there is only one bunch. The revolution frequency and the rf frequency are both 2.796 MHz. A typical store consists of a bunch consisting of typically 3.2×10^{13} protons, of typical half length $\hat{\tau} = 133.5$ ns, occupying roughly two-third of ring, and a typical half-energy spread of $\widehat{\Delta E/E_0} = 0.005$. If space-charge is neglected, to keep such a bunch matched to the rf bucket, the synchrotron tune is

$$\nu_{s0} = \frac{|\eta|\widehat{\Delta E_0}}{\omega_0 \beta^2 E_0 \hat{\tau}} = 0.000402, \tag{2.104}$$

and the required rf voltage is

$$V_{\rm rf} = \frac{2\pi\beta^2 E_0 \nu_{s0}^2}{e|\eta|h} = 6.60\ kV. \tag{2.105}$$

Now let us estimate the space-charge effect. [16] The 95% normalized transverse emittance is $50 \times 10^{-6}\pi$ m. From this and the ring lattice, the g_0 factor has been estimated to be

$$g_0 = 1 + 2\ln\frac{b}{a} \approx 3.0, \tag{2.106}$$

where a is the beam radius and b is the beam pipe radius. The longitudinal space-charge impedance is therefore

$$\left(\frac{Z_0^{\parallel}}{n}\right)_{\rm spch} = i\frac{Z_0 g_0}{2\gamma^2\beta} \approx i196\ \Omega. \tag{2.107}$$

According to Eq. (2.48), a particle with an arrival time τ ahead of the synchronous particle sees an electric field

$$E_{s\,\rm spch} = -\frac{eN_b}{2\pi\beta c}\left|\frac{Z_0^{\parallel}}{n}\right|_{\rm spch}\frac{d\lambda}{d\tau}, \tag{2.108}$$

where N_b is the number particles in the bunch and $\lambda(\tau)$ is the linear particle density normalized to unity when integrated over τ. This electric field comes from the longitudinal space-charge effect and is in the direction of the motion of the bunch. It is positive in the head half of the bunch ($\tau > 0$) and negative in the tail half ($\tau < 0$). It is therefore repulsive. Assume a parabolic linear distribution,

$$\lambda(\tau) = \frac{3N_b}{4\hat{\tau}}\left(1 - \frac{\tau^2}{\hat{\tau}^2}\right), \tag{2.109}$$

so that the electric field becomes linear in τ. The particle will gain in a turn the potential

$$V_{\rm spch} = E_{s\,\rm spch} C_0 = \frac{3eN_b}{2\omega_0\hat{\tau}^2}\left|\frac{Z_0^{\parallel}}{n}\right|_{\rm spch}\frac{\tau}{\hat{\tau}} = 4.82\frac{\tau}{\hat{\tau}}\ \text{kV}, \tag{2.110}$$

according to its position in the bunch. This potential would be of roughly the same size as the rf voltage required if there were no space-charge. Thus, in the presence of space-charge, we need to increase $V_{\rm rf}$ from 6.60 kV to approximately $6.60 + 4.82 = 11.42$ kV; nearly 42% of the rf voltage has been spent to counteract the space-charge force. One must realize that the rf buncher at PSR was capable

to deliver only 12 kV in 1997. Although the rf buncher has been upgraded later to about 18 kV, there is also a goal to increase the beam intensity to 5×10^{13} protons as well. It is important to point out that rf compensation to space-charge can never be exact, because the rf force is sinusoidal while the space-charge force is linear if the linear distribution is parabolic. Although the space-charge force may become sinusoidal-like if the unperturbed linear beam distribution is Gaussian, the frequency content is still very different from the rf focusing force.

2.7.2 *Ferrite Insertion*

It has been proposed that if ferrite rings (also called cores) are installed inside the vacuum chamber, the proton beam will see an extra inductive impedance from the ferrite, and hopefully this inductive impedance would cancel the capacitive space-charge impedance of the beam. [17, 18] Toshiba M_4C_{21A} ferrite rings were used, each having an inside diameter $d_i = 12.7$ cm, outside diameter $d_o = 20.3$ cm, and thickness $t = 2.54$ cm. The relative magnetic permeability is $\mu' \approx 70$ at the PSR rotation frequency, 2.796 MHz. With n_f ferrite rings stacked together, the impedance per harmonic is

$$\left.\frac{Z_0^{\parallel}}{n}\right|_{\text{ferrite}} = -i\frac{Z_0\omega_0 t n_f}{2\pi c}\mu' \ln\frac{d_o}{d_i} = 2.93 n_f\ \Omega. \tag{2.111}$$

Thus, to cancel a space-charge impedance per harmonic of $\sim$ 300 Ω, about $n_f = 102$ will be needed. Three ferrite inserts were assembled. Each consisted of a stainless-steel pill-box cavity having an inner diameter of 20.3 cm and inner length of 75.5 cm, so that 30 ferrite cores could be packed inside. To prevent charge buildup on the inner surface of the cores, each of the cores were treated with a very thin (1 MΩ per square)[‖] conductive coating (Heraeus R8261) baked on the inner and outer surfaces. Additional radial conducting 'spokes' were added to provide conductivity from the inner surface to the outer wall of the chamber. Solenoidal wiring was wound outside the stainless steel container so that the magnetic permeability of the ferrite could be controlled.

Two such ferrite tuners or inserts were installed in the PSR in 1997. To study space-charge compensation caused by the installed inductance, two experiments, using different bunch lengths, were performed. The designated charge configurations were injected into the PSR and the longitudinal profiles (bunch length and shape) were observed, digitized, and recorded using signals from a

[‖] *Impedance per square* of a surface, also known as surface impedance, implies $\rho_c/\delta_{\text{skin}}$ where ρ_c is the resistivity and δ_{skin} is the skin-depth into the surface. When multiplied by the length and divided by width, one obtains the impedance of the surface.

wideband wall current monitor at the end of each 625-μs injection period. The experiments were performed for two bunch lengths: $\sim$ 50 ns (half length) with 4.0×10^{12} particles and $\sim$ 150 ns (half length) with 1.2×10^{13} particles. The rf voltage was set to 7 kV in both cases. The resulting waveforms are compared with detailed particle-tracking simulations in Fig. 2.10 for the two bunch lengths. The solid curve in the top-left plot represents the bunch shape with the full effect of the inserted inductance (zero bias). The dotted curve corre-

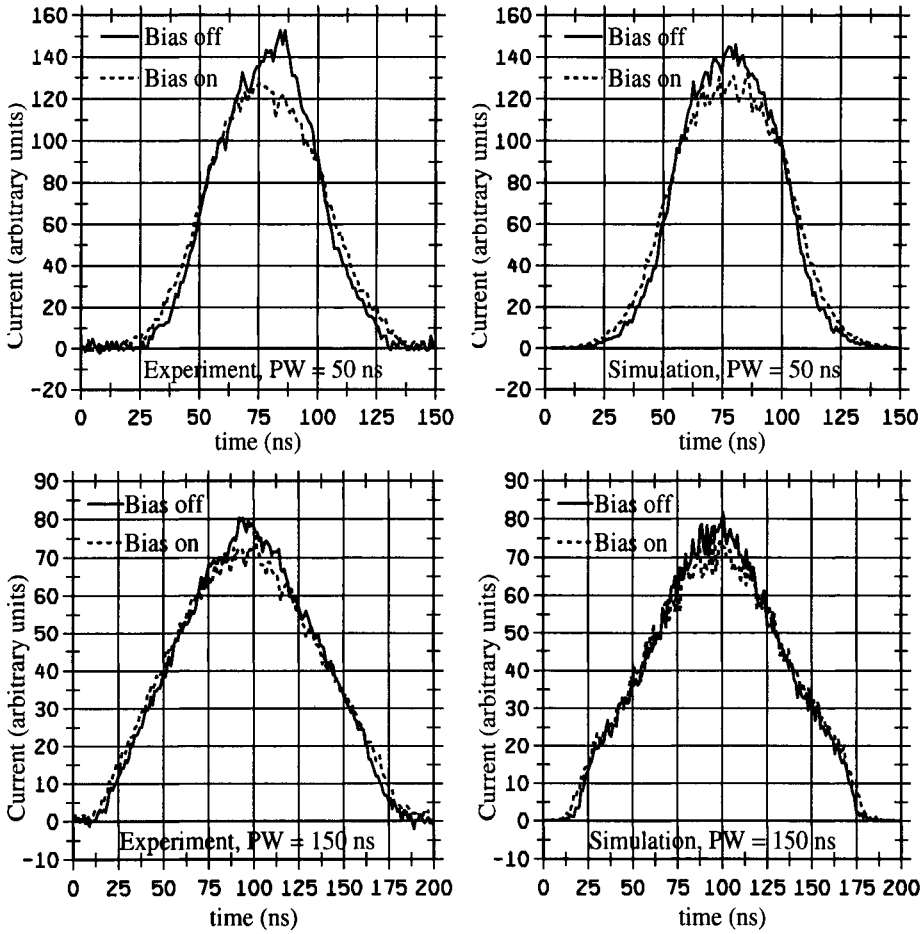


Fig. 2.10 Measured (left) and simulated (right) pulse shapes after 625 μs, for injected pattern widths of 50 ns with 4.0×10^{12} protons (top) and 150 ns with 1.2×10^{13} protons (bottom). In both cases, $V_{\rm rf} = 7.5$ kV. Solid: no bias, dotted: 900-A bias with a reduction of μ' by factor or 34%. (Courtesy Plum *et al.* [18])

sponds to data with the effect of the inductance diminished by the 900-A dc bias. The difference of peak heights is about 16%. Simulations performed with assumed injection half-momentum spread $\Delta p/p = 0.08\%$ are shown in the top-right plot. They predict an rms bunch length of 19 ns, but increasing to 22 ns when the ferrite bias current is raised to 900 A with the inductance reduced to 34% of its unbiased value. The experiment measurements are consistent with the simulation predictions. Similar conclusion can be drawn for the long-bunch-length situation shown in bottom plots of Fig. 2.10. We see that bunch lengths have been reduced with the ferrite insertion, indicating that the space-charge impedance has been cancelled to a certain extent.

It is unfortunate that the change in synchrotron frequency could not be measured to give another demonstration of the cancellation of space-charge. This is mainly due to the slow synchrotron oscillation in the PSR. During the whole accumulation and storage time, the beam particles usually make less than one synchrotron oscillation. A similar space-charge compensation experiment had also been performed at the KEK PS Main Ring, but with a much lower intensity of 2 to 9×10^{11} protons per bunch. [19] The beam kinetic energy was 500 MeV with a space-charge impedance $Z_0^{\parallel}/n = i310\ \Omega$. Instead of ferrite, the inductor inserts or tuners were loaded with a Met-Glass-like material called Finemet. Since the coherent synchrotron frequency in the dipole mode is not affected by space-charge, the coherent frequency of the quadrupole synchrotron oscillation was measured instead as a function of bunch intensity. The inductor tuners were not equipped with biased current coil to control the permeability of the Finemet. In order to alleviate the effect of the Finemet when required, mechanical copper shorts were installed across the inductor tuners instead. As shown in Fig. 2.11, with several inductor tuners installed, the coherent frequency was less dependent on intensity without the mechanical shorts than with the mechanical shorts, indicating that the space-charge force had been partially cancelled by the Finemet cores.

The second experiment at the PSR is to measure the onset of vertical instability using a short-stripline beam-position monitor. With a 3.0×10^{13}-proton beam stored, the rf voltage was lowered until vertical instability was registered. This signal came about when the rf bucket was not large enough to hold the bunch so that some protons spills out into the bunch gap. These protons in the gap trapped electrons preventing them to be cleared and causing a transverse *e-p* instability (see Chapter 15). Many previous performance points represented by squares are plotted in Fig. 2.12 as the required buncher voltage versus beam intensity. The historical performance is roughly represented by the dashed line. The results of this experiment are indicated by triangles. It was found that less

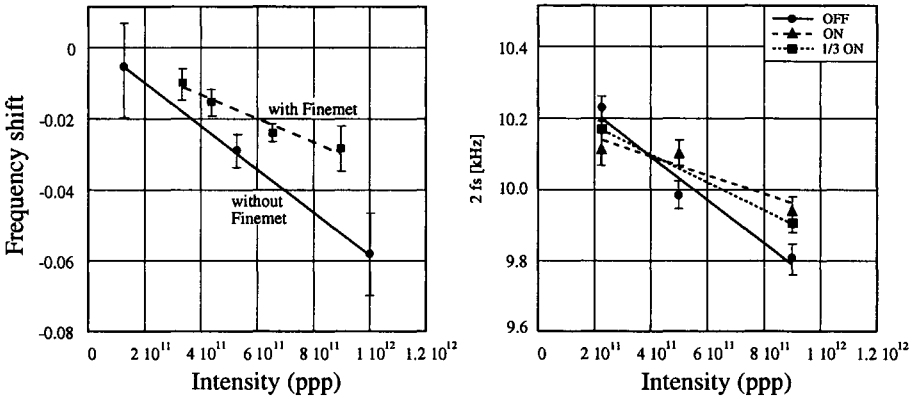


Fig. 2.11 Left: Measured frequency shifts of the quadrupole oscillations versus beam intensity at the KEK PS with and without Finemet insertion. Right: New KEK results of quadrupole oscillation frequency versus beam intensity with Finemet tuners on, one-third on, and off. (Courtesy Koba *et al.* [19])

buncher voltage was required to sustain the beam in the presence of the inductor inserts. For example, at the highest intensity that could be reached during the experiment, 3×10^{10} protons in the beam, only 6.9 kV was required, which amounted to a $\sim 30\%$ reduction of what had previously been necessary to maintain stability. This result indicates that the space-charge impedance has been compensated to a certain extent by the ferrite cores in the two tuners installed in the vacuum chamber. At the same time, it was found that the bunch gap was the cleanest ever observed.

This experiment, however, has far from being perfect. First, there are only a few points measured (the triangles in Fig. 2.12); the indication is therefore not very convincing. Second, the bunch lengthening when the solenoidal bias was turned on had only been minimal and not spectacular (see Fig. 2.10), leaving behind the question of the efficiency about the inserts—how much space-charge had actually been compensated. Third and worst of all, a longitudinal instability had been observed, although at the intensity of 3.2×10^{13} protons, this instability had been small and appeared to be tolerable. Because of these and other reasons, the ferrite inserts were removed during the upgrade. After the upgrade, when the machine was turned on, however, the performance was very poor as is indicated by the dot-dashed line in Fig. 2.12. In order to improve the performance, the inductor inserts were once again installed. With the upgraded beam intensity, however, the small longitudinal instability had become so intense that the beam profiles became heavily distorted and there was a considerable of beam loss. This instability together with its eventual cure will be discussed in detail in Sec. 5.3.

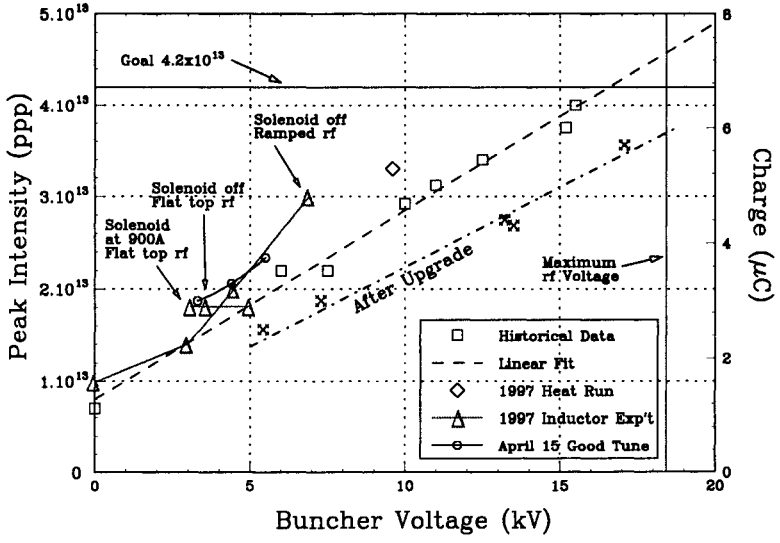


Fig. 2.12 The performance of the PSR: the required buncher voltage plotted against the intensity of the beam. The dashed line shows roughly the historical performance before upgrade. The triangles are results of the experiment discussed here. For example, with the ferrite insertion without solenoidal bias, only 6.9 kV is required to hold a bunch containing 3×10^{13} protons, which is about $\frac{1}{3}$ less than the historical value.

2.8 Potential-Well Distortion in Barrier RF

In the presence of a purely resistive impedance R_s, the Haissinski equation describing the potential-well distorted bunch profile of an electron bunch, $\lambda(\tau)$, can be rewritten as

$$\lambda(\tau) = \lambda_0 \exp\left[-\frac{\tau^2}{2\sigma_\tau^2} + \alpha_R \int_0^\tau N_b \lambda(\tau')d\tau'\right], \tag{2.112}$$

where λ_0 is the profile at $\tau = 0$, N_b is the number of particles in the bunch, and α_R, given by Eq. (2.60), is proportional to R_s. Here $\lambda(\tau)$ is normalized to unity upon integration over τ. Notice that the first term in the exponent of Eq. (2.112), $U_{\rm rf}(\tau) = -\tau^2/(2\sigma_\tau^2)$, represents the linearized sinusoidal rf potential and is an even function of the particle arrival time τ, while the second term, $\sim \alpha_R \lambda_0 \tau$, the cause of the asymmetric solution, is an odd function of τ, representing the perturbation to the rf potential arising from the interaction of the beam with the resistive impedance. The reactive part of the coupling impedance, on the other hand, distorts the rf potential symmetrically and therefore contributes only to the lengthening and shortening of the beam. The longitudinal asymmetry of the

beam is only significant, however, when the second term is comparable to the first term. Proton beams are usually long and the bunch spectra roll off before they reach the broadband resonance part of $\mathcal{R}e\, Z_0^{\|}$. In other words, proton beams can hardly see the real part of the impedance. Thus the effective $\alpha_R N_b/\sqrt{2\pi}$ is usually very small and, as a result, no significant head-tail asymmetry has ever been reported. However, at the Fermilab Recycler Ring where rf barriers are used, [20] the rf potential experienced by most part of the beam is essentially zero. For this reason, head-tail asymmetry of the beam profile has been observed.

2.8.1 *RF Barriers*

Broadband cavities are employed to create barriers of opposite polarities to confine antiprotons in the Recycler Ring. [21] Some of the merits are:

(1) The beam can spread out uniformly, as indicated in the left-top plot of Fig. 2.13, so that the space-charge force becomes smaller.
(2) Two batches can be merged easily by placing them in two separate barrier buckets close together and then annihilating the two central barriers, as indicated in the left-lower plot of Fig. 2.13.
(3) The length of a batch can be compressed by moving the two barriers closer together slowly.
(4) The whole batch can be moved from one location to another by moving the two confining barriers slowly in the same direction.

The are four 50 Ω broadband ferrite-loaded rf stations in the rf system of the Recycler Ring. [21] The amplifiers are of 3.5 kW from 10 kHz to 100 MHz, capable of supplying a total of ± 2 kV. The rf waveform generated is determined by the amplitude and phase of each of the 588 revolution harmonics (or up to 52.8 MHz).

When the baseline between the two barrier pulses is nonzero, as shown in dashes in the top-right plot of Fig. 2.13, the barrier potential becomes slanting, as shown in dashes in the lower-right plot. Such nonzero baseline can come from either rf errors or the coupling impedance of the vacuum chamber. Here, we are talking about a deviation of ~ 10 V from zero, out of a peak barrier voltage of $V_0 = \pm 2$ kV, or $\sim 0.5\%$.

2.8.2 *Asymmetric Beam Profile*

There is a linearization compensation program that makes sure that baseline voltage has been adjusted to zero by noting that the beam profile is flat at low

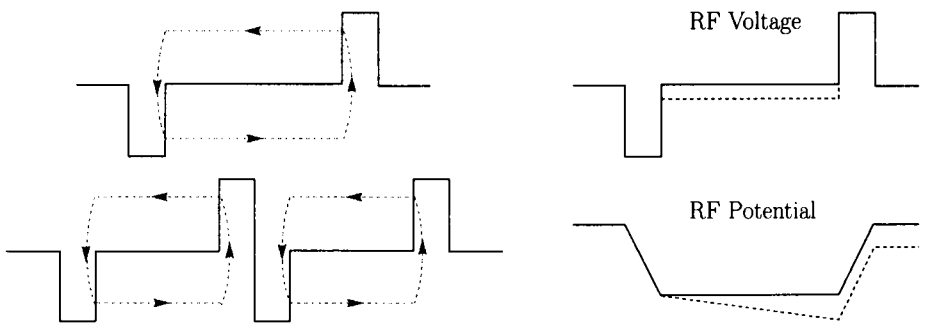


Fig. 2.13 Left: The trajectory of a proton inside a barrier bucket set up by two barrier waves with equal and opposite polarities (top). Two barrier buckets set up by four barrier waves (bottom) are prepared side by side. When the two central barrier waves annihilate each other, the two buckets merge into one. Right: When the baseline voltage (top) inside a barrier bucket set up by two barrier waves of opposite polarities is different from zero (dashed), the rf potential well (bottom) no longer has a flat bottom. A beam inside the potential well therefore no longer has a head-tail symmetric linear density.

beam intensity ($N_b \sim 1 \times 10^{11}$). However, at higher intensities, the beam profile was seen slanting. An example is shown in the left plot of Fig. 2.14 at the intensity of 6.4×10^{11}, where the tail lags behind the head. Since the Recycler Ring is a permanent-magnet storage ring at 8.9383 GeV operating below transition, this asymmetry may come from the interaction with the resistive part of the longitudinal impedance.

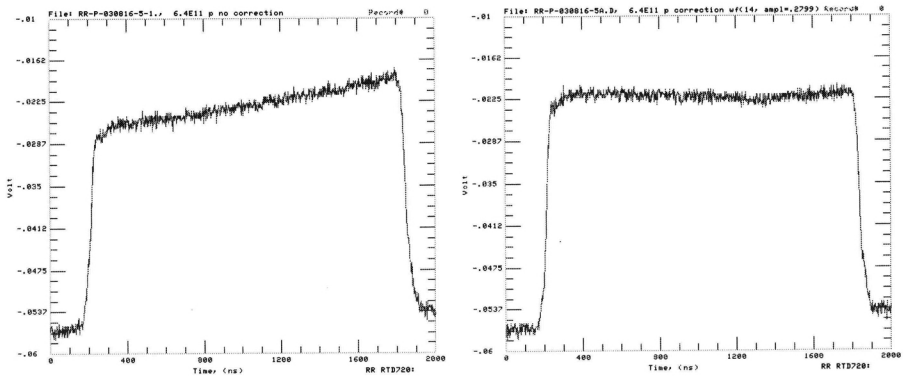


Fig. 2.14 Left: A beam of intensity $N_b = 6.4 \times 10^{11}$ inside a barrier bucket of width ~ 1.59 μs exhibits head-tail asymmetry, after response linearization is implemented. The beam going to the right lags backwards in agreement with energy loss due to resistive impedance. Right: The asymmetry of the beam profile is compensated by adding ~ 8.82 V to the region between the barriers.

Recall in Eq. (2.9) that the arrival time ahead of the synchronous particle τ and the rf phase ϕ with respect to the synchronous phase have opposite signs. In order to avoid a negative argument in the rf voltage, we re-define τ in this section as the arrival time *lagging behind* the synchronous particle. Then the equations of motion for a beam particle become

$$\begin{aligned}\frac{d\tau}{d\theta} &= \frac{\eta \Delta E}{\omega_0 \beta^2 E_0}, \\ \frac{d\Delta E}{d\theta} &= \frac{eV(\tau)}{2\pi} - \frac{e^2 N_b}{2\pi} \int_0^\tau W_0'(\tau - \tau')\lambda(\tau'; \theta) d\tau', \end{aligned} \tag{2.113}$$

where $V(\tau)$ represents the rf voltage experienced by the beam particle, N_b the number of particles in the beam, and the independent variable has been chosen as θ, the azimuthal angle around the ring, which advances by 2π in a revolution turn. Note the sign differences when compared with Eqs (2.12) and (2.13), where τ represents the arrival time ahead of the synchronous particle. The plots in Fig. 2.13 have been drawn with this new definition of τ, and, as a result, the trajectories revolve anticlockwise instead below transition ($\eta < 0$). For the Recycler Ring the impedance is mostly resistive and the wake function can therefore be written as $W_0'(\tau) = R_s \delta(\tau)$. Thus the static part of the Hamiltonian is

$$H_{\text{stat}} = \frac{\eta \Delta E^2}{2\omega_0 \beta^2 E_0} - \frac{e}{2\pi} \int_0^\tau V(\tau') d\tau' + \frac{e^2 R_s N_b}{2\pi} \int_0^\tau \lambda(\tau') d\tau', \tag{2.114}$$

including only the static part of the linear distribution. The Hamiltonian can be rewritten as

$$H_{\text{stat}} = -\frac{\eta \sigma_E^2}{\omega_0 \beta^2 E_0} \left[-\frac{\Delta E^2}{2\sigma_E^2} + \frac{e\beta^2 E_0}{\eta T_0 \sigma_E^2} \int_0^\tau V(\tau') d\tau' - \alpha_R N_b \int_0^\tau \lambda(\tau') d\tau' \right], \tag{2.115}$$

where σ_E is the rms energy offset of the beam, and the dimensionless parameter α_R, proportional to R_s, has been defined in Eq. (2.60). If we assume a Gaussian distribution for the energy offset, the distribution of the beam in the longitudinal phase space must take the form

$$\psi(\Delta E, \tau) \sim \exp\left[-\frac{\Delta E^2}{2\sigma_E^2} + \frac{e\beta^2 E_0}{\eta T_0 \sigma_E^2} \int_0^\tau V(\tau') d\tau' - \alpha_R N_b \int_0^\tau \lambda(\tau') d\tau' \right]. \tag{2.116}$$

Upon integrating over the energy offset, we obtain the linear distribution

$$\lambda(\tau) = \lambda(0) \exp\left[\frac{e\beta^2 E_0}{\eta T_0 \sigma_E^2} \int_0^\tau V(\tau') d\tau' - \alpha_R N_b \int_0^\tau \lambda(\tau') d\tau' \right], \tag{2.117}$$

which is the Haissinski equation. When the rf voltage is the usual sinusoidal wave or $V(\tau) = V_{\rm rf} \sin h\omega_0\tau$, it is easy to show that the negative of the rf potential $-U_{\rm rf}$, first term in the exponent of Eq. (2.117), becomes $-\tau^2/(2\sigma_\tau^2)$ for small τ and Eq. (2.117) reduces to Eq. (2.112) exactly. In the rf system of the Recycler Ring, however, the rf wave consists of two square waves of magnitude $\pm V_0$ and width T_1 separated by T_2 as illustrated in the top-right plot of Fig. 2.13. Mathematically, it can be represented by

$$\frac{V(\tau)}{V_0} = -H\left(\tau+T_1+\tfrac{1}{2}T_2\right) + H\left(\tau+\tfrac{1}{2}T_2\right) + H\left(\tau-\tfrac{1}{2}T_2\right) - H\left(\tau-T_1-\tfrac{1}{2}T_2\right), \quad (2.118)$$

where $H(\tau)$ is the Heaviside step function. In between the two rf barriers $|\tau| < \frac{1}{2}T_2$, the rf potential vanishes. There, the exponent in the Haissinski equation is contributed completely by the resistive-impedance term, which is asymmetric in τ, thus giving rise to to observed asymmetry in the beam profile.

The four broadband rf cavities have a total resistive impedance $Z_0^{\|} = 200\ \Omega$. When the shunt impedances at the amplifiers are taken into account, the impedance visible to be beam is about $Z_0^{\|} = 130\ \Omega$ up to ~ 52.8 MHz (or up to revolution harmonics 588). Comparatively, the resistive-wall impedance of the vacuum chamber can be neglected because its real part is only $\mathcal{R}e\, Z_0^{\|} = 12.0\ \Omega$ at the revolution harmonic. This can also viewed as beam-loading and contributes negatively to the potential experienced by the beam particle ($\alpha_R < 0$ since $\eta < 0$). When substituted into the Haissinski equation, the numerical solution results in a beam profile closely resembling observation, as depicted as solid in Fig. 2.15.

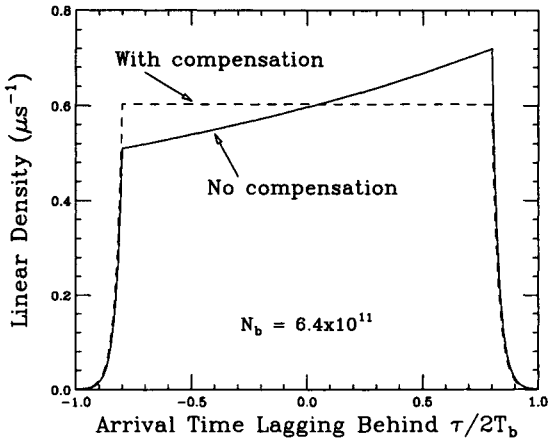


Fig. 2.15 Solution of the Haissinski equation with barrier waves, a resistive impedance $R_s = 130\ \Omega$, and beam intensity $N_b = 6.4 \times 10^{11}$ reproduces the observed beam profile with head-tail asymmetry shown in the left plot of Figure 2.14. A compensating voltage, 8.82 V, restores the head-tail symmetry (dashes). Here $T_b = 1.59\ \mu$s is the total bunch length.

The asymmetric beam profile can be compensated by adding some rf voltages in the originally rf-free region. After the compensation, the resistive-impedance term in the exponent of the Haissinski equation is linear in τ because $\lambda(\tau)$ will have been flat. Thus the compensation consists of adding a constant voltage equally in the region between the two barriers in the amount

$$V_b = \frac{\eta \sigma_E^2 T_0}{2\beta^2 E_0 T_2} \alpha_R N_b = \frac{e N_b R_s}{T_2}, \tag{2.119}$$

where the definition of α_R has been used. This compensation can be interpreted as the local beam current eN_b/T_2 multiplied by the resistivity R_s, or the beam-loading voltage, or the energy dissipated by the beam encountering the resistivity of the vacuum chamber. With $T_2 \approx 1.59$ μs as the distance between the inner edges of the two barriers, the required compensating voltage is $V_b = 8.39$ V. As expected, the head-tail asymmetry disappears (dashes) in Fig. 2.15 with the addition of such a voltage. Experimentally, we also see that slant of the beam profile goes away in the right plot of Fig. 2.14 after adding $\sim$ 8.82 V to the region between the barriers.

The beam profile computed in Fig. 2.15 is not exactly linear. In fact, the beam profile can be solved analytically by transforming the Haissinski integral equation into a differential equation. In between the two barrier waves or the rf-free region, the beam profile turns out to be (Exercise 2.13),

$$\lambda(\tau) = \frac{\lambda_0}{1 + \alpha_R N_b \lambda_0 \tau}. \tag{2.120}$$

We can see clearly that the beam profile is, in fact, hyperbolic. However, when the resistive impedance is small ($|\alpha_R N_b| \ll T_2/2$), the beam profile appears to be linear. The hyperbolic beam profile was derived by assuming that the energy distribution is Gaussian. The beam profile can also be solved analytically when the energy distribution is elliptical-like, as demonstrated in Exercise 2.13.

2.9 Exercises

2.1 The Hamiltonian of Eq. (2.18) describes motion in the longitudinal phase space. With the effects of the wake potential $U_{\text{wake}}(\tau, s)$ neglected, find the fixed points of the Hamiltonian above and below transition, and determine whether they are stable or not. The separatrices are the contours of fixed Hamiltonian values that pass through the unstable fixed points. They separate the region of libration motion from rotation motion. Plot the separatrices.

2.2 The canonical variables τ_0 and ΔE_0 evaluated at 'time' $s = 0$ become τ_1 and ΔE_1 at an infinitesimal time step Δs later according to

$$\tau_1 = \tau_0 + \frac{\partial H}{\partial \Delta E_0}\Delta s, \qquad \Delta E_1 = \Delta E_0 - \frac{\partial H}{\partial \tau_0}\Delta s. \tag{2.121}$$

Consider the small phase-space area element $d\tau_0 d\Delta E_0 = J d\tau_1 d\Delta E_1$. Show that the Jacobian $J = 1$ to the first order in Δs, implying that the area surrounding a given number of particles does not change in time, which is Liouville Theorem. It is possible to prove $J = 1$ to all orders in Δs using canonical transformation. [23]

2.3 Starting from the Hamiltonian in Eq. (2.18) with the synchronous phase $\phi_s = 0$ or π but in the absence of the wake potential, derive the synchrotron tune, Eq. (2.16), of a particle having an rf phase amplitude $\hat{\phi}$. Repeat the derivation for any arbitrary synchronous phase.
Hint: From the first Hamilton's equation of Eq. (2.19), one gets

$$ds = \frac{v_0 \beta_0^2 E_0}{\eta h \omega_0 \Delta E} d\phi, \tag{2.122}$$

where from the Hamiltonian in Eq. (2.18) with $\phi_s = 0$,

$$\Delta E = \sqrt{-\frac{2 v_0 \beta_0^2 E_0 e V_{\rm rf}}{C_0 \eta h \omega_0}(\cos\phi - \cos\hat{\phi})}. \tag{2.123}$$

Integrating over one-quarter of a synchrotron period from $\phi = 0$ to $\hat{\phi}$, the left side is $C_0/(4\nu_s)$. The integral on the right side,

$$\int_0^{\hat{\phi}} \frac{d\phi}{\sqrt{\cos\phi - \cos\hat{\phi}}} = \frac{1}{\sqrt{2}} \int_0^{\hat{\phi}} \frac{d\phi}{\sqrt{\sin^2 \frac{1}{2}\hat{\phi} - \sin^2 \frac{1}{2}\phi}} \tag{2.124}$$

can be shown equal to $\sqrt{2}K(\sin \frac{1}{2}\hat{\phi})$ with the integration variable changed form ϕ to θ via the substitution $\sin \frac{1}{2}\phi = \sin \frac{1}{2}\hat{\phi} \sin\theta$.

2.4 Show that the space-charge geometric factor defined in Eq. (2.40) for the longitudinal space-charge impedance becomes

$$g_0 = \frac{1}{2} + 2 \ln \frac{b}{a}, \tag{2.125}$$

when the longitudinal electric field opposing the beam is averaged over all the beam particles. In above, b is the radius of the beam pipe and a is the transverse radius of the beam.

2.5 (1) Show that the geometric factor g_0 for a beam of linear density λ and cylindrically symmetric transverse particle distribution density $\rho(r)$ is given by

$$\frac{g_0}{2} = \int_0^{r_e} \frac{dr}{r} \int_0^{r} \frac{\rho(r)}{\lambda} 2\pi r' dr' + \int_{r_e}^{b} \frac{dr}{r}, \tag{2.126}$$

where r_e is the radius of the transverse beam edge.
(2) For a beam with transverse bi-Gaussian distribution truncated at $m\sigma_r$, show that the space-charge geometric factor is

$$g_0 = \frac{\gamma_e + 2\ln \dfrac{b}{\sqrt{2}\sigma_r} + E_1\left(\frac{1}{2}m^2\right)}{1 - e^{-m^2/2}}, \tag{2.127}$$

where the denominator shows the normalization of the truncated bi-Gaussian distribution, $\gamma_e = \lim_{n\to\infty}\left[1 + \frac{1}{2} + \frac{1}{3} + \frac{1}{4} + \cdots + \frac{1}{m} - \ln m\right] = 0.57721$ is Euler's constant, and the exponential integral is defined as

$$E_n(z) = \int_1^{\infty} \frac{e^{-zt}}{t^n}\, dt, \tag{2.128}$$

with the asymptotic expansion

$$E_n(z) = \frac{e^{-z}}{z}\left[1 - \frac{n}{z} + \frac{n(n+1)}{z^2} - \frac{n(n+1)(n+2)}{z^3} + \cdots\right]. \tag{2.129}$$

Thus, the geometric factor can be written as

$$g_0 = \frac{\gamma_e + 2\ln \dfrac{b}{\sqrt{2}\sigma_r} + \dfrac{e^{-m^2/2}}{m^2}\left[1 - \dfrac{2}{m^2} + \mathcal{O}(m^{-4})\right]}{1 - e^{-m^2/2}}. \tag{2.130}$$

Notice that with the truncation at 3σ's, terms involving $e^{-m^2/2}$ can be neglected with an error of approximately 1% only.
(3) Derive the geometric factors for the elliptical and parabolic distributions as given in Table 2.1.

2.6 (1) Solve the Poisson equation

$$\nabla^2\phi(x,y) = -\frac{e\rho(x,y)}{\epsilon_0}, \tag{2.131}$$

with a beam distribution $\rho(x,y)$ given by Eq. (2.51) and the potential vanishing on a rectangular vacuum chamber defined by $x = 0$ to $2w$ and $|y| = h$.
(2) Show that the space-charge potential is given by Eq. (2.52).

(3) Verify Eq. (2.54), the geometric factor g_0 of a square beam in a rectangular vacuum chamber.

2.7 Transform the Haissinski equation (2.57) according to the following:

(1) Notice that the integral over τ'' can be rewritten as

$$\int_0^{\tau} d\tau'' \rightarrow -\int_{\tau}^{\infty} d\tau'' + \text{ constant}, \tag{2.132}$$

where the constant can be absorbed into the normalization constant $\lambda(0)$ which is renamed as ξ.

(2) The integration in the τ'-τ'' space is in the 0° to 45° quadrant between the lines $\tau'' = \tau$ and $\tau'' = \tau'$. Translate the τ' and τ'' axes so that the region of integration is now between the τ'-axis and the 45° line $\tau'' = \tau'$.

(3) Integrate over τ'' first from 0 to τ'; then integrate over τ'.

(4) Change the variable τ'' to $\tau' - \tau''$. Now the Haissinski equation takes the more convenient form of Eq. (2.66), or

$$\lambda(\tau) = \xi \exp\left[-\left(\frac{\omega_{s0}\beta^2 E_0}{\eta\sigma_E}\right)^2 \frac{\tau^2}{2} - \frac{e^2\beta^2 E_0}{\eta T_0 \sigma_E^2}\int_0^{\infty} d\tau' \lambda(\tau+\tau')\int_0^{\tau'} d\tau'' W_0'(\tau'')\right]. \tag{2.133}$$

2.8 The bunch in the Fermilab Tevatron contains $N_b = 2.7 \times 10^{11}$ protons and has a designed half length of $\hat{\tau} = 2.75$ ns. The ring main radius is $R = 1$ km and the slip factor is $\eta = 0.0028$ at the injection energy of $E_0 = 150$ GeV. The rf harmonic is $h = 1113$ and the rf voltage is $V_{\text{rf}} = 1.0$ MV. Assume a broadband impedance centered at $\omega_r/(2\pi) \approx 3$ GHz, quality factor $Q = 1$, and shunt impedance $R_s = 250$ kΩ.

(1) Show that the frequencies the bunch samples are much lower than the resonant frequency of the broadband, so that the asymmetric beam distortion driven by $\mathcal{R}e\, Z_0^{\parallel}$ can be neglected.

(2) Using only the inductive part of the impedance at low frequencies, compute from Eq. (2.78) the equilibrium bunch length as a result of potential-well distortion.

(3) Electron bunches are usually very short. If an electron bunch of rms bunch length 2 cm is injected into the Tevatron, show that its spectrum will sample the resonant peak of $\mathcal{R}e\, Z_0^{\parallel}$ and asymmetric distortion will result. Compute the asymmetric factor $\alpha_R N_b$ given by Eq. (2.59) and determine whether the asymmetry is large or not.

2.9 From Eq. (2.75) for an electron bunch, show that there are two solutions for the perturbed bunch length due to distortion by a capacitive impedance when $-2/3^{3/2} < D < 0$. Which one is physical? When $D < -2/3^{3/2}$, there

is no solution. At this critical situation, the bunch shortening ratio is $3^{-1/2}$. Hint: Transform Eq. (2.75) to

$$4x^3 - 3x = \frac{3^{3/2}}{2} D \tag{2.134}$$

and substitute for $x = \sin\theta$. What is the right side in terms of θ?

2.10 When the coupling impedance is purely resistive,
(1) derive the potential-well distorted linear distribution, Eq. (2.59).
(2) Show that when the intensity of the bunch is weak, the peak of the distribution is given by Eq. (2.62).
Hint: Transform the Haissinski equation to a differential equation,

$$\lambda' + \frac{\tau}{\sigma_\tau^2}\lambda - \alpha_R \lambda^2 = 0. \tag{2.135}$$

Solve the equation and determine $\lambda(0)$.

2.11 Starting from Eq. (2.76) and filling in the missing steps, derive the quartic equation (2.78) for the proton half-bunch length under the influence of a purely reactive longitudinal impedance.

2.12 The beam profile $\lambda(\tau)$ inside a barrier bucket can be solved more easily by converting the Haissinski integral equation into a differential equation. In between the barriers, where barrier rf potential is zero, show that the beam profile satisfies the differential equation

$$\lambda' = -\alpha_R N_b \lambda^2. \tag{2.136}$$

Show that the solution gives

$$\lambda(\tau) = \frac{\lambda(0)}{1 + \alpha_R N_b \lambda(0)\tau}, \tag{2.137}$$

which is just the solution of the Haissinski equation in the region between the barrier waves.

2.13 The beam profile $\lambda(\tau)$ inside a barrier bucket can also be derived with the energy distribution is elliptical-like instead of Gaussian. In the absence of any rf and coupling impedance, the distribution in the longitudinal phase space is

$$\psi(\tau, \Delta E) = A\left[\widehat{\Delta E}_0^2 - \Delta E^2\right]^n, \tag{2.138}$$

where $\widehat{\Delta E}_0$ is the half-energy spread, A is a normalization constant, and n is a number that need not be an integer or half integer. In the presence of the two barriers and a pure resistive impedance, R_s,

(1) Show that the distribution in the longitudinal phase space is still given by Eq. (2.138), but with $\widehat{\Delta E}_0$ replaced by $\widehat{\Delta E}(\tau)$, where

$$\widehat{\Delta E}^2(\tau) = \widehat{\Delta E}_0^2\left[1 + bU_{\rm rf}(\tau) - a\int_0^\tau \lambda(\tau')d\tau'\right], \tag{2.139}$$

with

$$a = \frac{2\beta^2 e^2 N E_0 R_s}{-\eta T_0 \widehat{\Delta E}_0^2} \quad \text{and} \quad b = \frac{2\beta^2 E_0 e V_0 T_1}{-\eta T_0 \widehat{\Delta E}_0^2}, \tag{2.140}$$

$U_{\rm rf}$ being the barrier rf potential of unit voltage and duration T_1, and τ being the arrival time lagging behind the synchronous particle at the center of the bucket. Hint: Use the fact that $\psi(\tau, \Delta E)$ must be a function of the Hamiltonian,

$$H_{\rm stat} = -\frac{\eta(\Delta E)^2}{2\beta^3 c E_0} - \frac{eV_0T_1}{\beta c T_0}U_{\rm rf}(\tau) + \frac{e^2R_sN}{\beta c T_0}\int_0^\tau d\tau'\lambda(\tau'). \tag{2.141}$$

(2) Integrating over energy offset, show that the beam profile is

$$\lambda(\tau) = 2A\left[\widehat{\Delta E}^2(\tau)\right]^{n+\frac{1}{2}}\int_0^1 (1-t^2)^n dt = 2\gamma_n A\left[\widehat{\Delta E}^2(\tau)\right]^{n+\frac{1}{2}}, \tag{2.142}$$

with

$$\gamma_n = \int_0^1 (1-t^2)^n dt = \frac{\pi\Gamma(2n+2)}{2^{2n+1}\Gamma^2\left(n+\frac{3}{2}\right)}. \tag{2.143}$$

(3) In the region $-\frac{1}{2}T_2 \le \tau \le \frac{1}{2}T_2$ where the barrier potential $U_{\rm rf}(\tau) = 0$ with T_2 representing the separation between the inner edges of the barriers, show that the beam profile satisfies

$$\lambda' = -\frac{2n+1}{2}\, a\lambda_0^{\frac{2}{2n+1}}\lambda^{\frac{4n}{2n+1}}, \tag{2.144}$$

where $\lambda_0 = 2\gamma_n A\left(\widehat{\Delta E}_0^2\right)^{n+\frac{1}{2}}$ is the linear density at $\tau = 0$.

(4) Solve the differential equation to obtain the beam profile in the rf-free region,

$$\lambda(\tau) = \lambda_0\left[1 + \frac{2n-1}{2}\, a\lambda_0\tau\right]^{-\frac{2n+1}{2n-1}}. \tag{2.145}$$

The beam profile becomes exponential when $n = \frac{1}{2}$ and this situation should be treated separately.

2.14 Instead of doing a perturbation, if we start off with the synchronous angle ϕ_s that has taken into account of the wake fields, the equation of motion is

$$\frac{d^2\tau}{ds^2} + \frac{\nu_{s0}^2}{R^2}\tau = -\frac{\eta}{v\beta^2 E_0}\left[\langle F_0^{\parallel}(\tau, s)\rangle_{\text{stat}} - \langle F_0^{\parallel}(0, s)\rangle_{\text{stat}}\right], \tag{2.146}$$

where the time advance τ is measured with respect to the particle synchronized at $\phi = \phi_s$, but the synchrotron tune ν_{s0} still has not included the effects of the wake fields.

(1) Show that the solution no longer involves a shift of the synchronous angle.

(2) Show that the synchrotron tune shift of a particle with amplitude $\hat{\tau}$ is given by Eq. (2.92) with ξ defined by Eq. (2.90).

(3) For small τ, Eq. (2.146) can be expressed in terms of the differential of the wake potential. For a purely inductive wake with inductance $\mathcal{L}$, show that the synchrotron tune shift seen by the synchronous particle is given by

$$\nu_s^2 = \nu_{s0}^2\left[1 + \frac{2\pi\mathcal{L}\xi\lambda''(0)}{\omega_0^2}\right]. \tag{2.147}$$

Bibliography

[1] C. Bernardine, *et al.*, *Phys. Rev. Lett.* **10**, 407 (1963).

[2] *JHP Accelerator Design Study Report*, KEK Report 97-16, JHF-97-10, 1997; K. Y. Ng, D. Trbojevic and S. Y. Lee, Proc. 1991 IEEE Part. Accel. Conf., ed. L. Lizama (San Francisco, May 6–9, 1991), p. 159; C. Ankenbrandt, *et al.*, *Status of Muon Collider Research and Development and Future Plans*, *Phys. Rev. ST Accel. Beams* **2**, 081001 (1999).

[3] S. X. Fang, K. Oide, K. Yokoya, B. Chen and J. Q. Wang, Proc. 1995 IEEE Part. Accel. Conf., ed. L. Gennari (Dallas, May 1–5, 1995), p. 3064.

[4] S. Y. Lee, K. Y. Ng and D. Trbojevic, *Phys. Rev.* **E4**, 3040 (1993); S. Y. Lee, K. Y. Ng and D. Trbojevic, Fermilab Report FN-595, 1992.

[5] H. Huang, M. Ball, B. Brabson, J. Budnick, D. D. Caussyn, A. W. Chao, J. Collins, V. Derenchuk, S. Dutt, G. East, M. Ellison, D. Friesel, B. Hamilton, W. P. Jones, S. Y. Lee, D. Li, M. G. Minty, S. Nagaitsev, K. Y. Ng, X. Pei, A. Riabko, T. Sloan, M. Syphers, L. Teng, Y. Wang, Y. T. Yan and P. L. Zhang, *Experimental Determination of the Hamiltonian for Synchrotron Motion with RF Phase Modulation*, *Phys. Rev.* **E48**, 4678 (1993).

[6] B. W. Montague, *Single-Particle Dynamics—RF Acceleration*, Proc. First Course of Int. School of part. Accel., ed. M. H. Blewett (Erice, Nov. 10–22, 1976), CERN 77-13, 1977.

[7] A. A. Vlasov, *J. Phys. USSR* **9**, 25 (1945).

[8] H. Risken, *The Fokker–Planck Equation*, 2nd edn. (Springer-Verlag, N.Y., 1989).

[9] K. Y. Ng, *Space-Charge Impedances of Beams with Non-uniform Transverse Distribution*, Fermilab Report FN-0756, 2004.

[10] O. Gröbnerand K.Hübner, *Computation of the Electrostatic Beam Potential in Vacuum Chambers of Rectangular Cross-Section*, CERN Report CERN/ISR-TH-VA/75-27, 1975.

[11] J. Haissinski, *Nuovo Cimento* **18B**, 72 (1973).

[12] K. L. F. Bane and R. D. Ruth, Proc. of 1989 IEEE Part. Accel. Conf., eds. F. Bennett and J. Kopta (Chicago, March 20–23, 1989), p. 789.

[13] A. G. Ruggiero, *Theory of Longitudinal Instability for Bunched Electron Beams, IEEE Trans. Nucl. Sci.* **NS-24**, 1205 (1977).

[14] B. Zotter, *Potential-Well Bunch Lengthening*, CERN Report CERN SPS/81-14 (D1), 1981.

[15] B. Zotter, *Longitudinal Stability of Bunched Beams Part II: Synchrotron Frequency Spread*, CERN Report CERN SPS/81-19 (D1), 1981.

[16] K. Y. Ng and Z. Qian, *Instabilities and Space-Charge Effects of the High-Intensity Proton Driver*, Fermilab Report FN-659, 1997, AIP Conf. Proc. 435, Workshop on Physics at the First Muon Collider and at the Front End of the Muon Collider, eds. S. Geer and R. Raja (Batavia, IL, Nov. 6–9, 1997), p. 841.

[17] J. E. Griffin, K. Y. Ng, Z. B. Qian and D. Wildman, *Experimental Study of Passive Compensation of Space Charge Potential Well Distortion at the Los Alamos National laboratory Proton Storage Ring*, Fermilab Report FN-661, 1997.

[18] M. A. Plum, D. H. Fitzgerald, J. Langenbrunner, R. J. Macek, F. E. Merrill, F. Neri, H. A. Thiessen, P. L. Walstrom, J. E. Griffin, K. Y. Ng, Z. B. Qian, D. Wildman and B. A. Jr. Prichard, *Phys. Rev. ST Accel. Beams* **2**, 064201 (1999).

[19] K. Koba, S. Machida and Y. Mori, KEK Note, 1997 (unpublished); K. Koba, *et al.*, Proc. 1995 IEEE Part. Accel. Conf. ed. L. Gennari (Dallas, May 1–5, 1995), p. 1653; K. Koba, *et al.*, *Phys. Sci. Instrum.* **70**, 2988 (1999).

[20] J. Griffin, C. Ankenbrandt, J. A. MacLachlan and A. Moretti, *IEEE Trans. Nucl. Sci.* **NS-30**, 3502 (1983); V. K. Bharadwaj, J. E. Griffin, D. J. Harding, and J. A. MacLachlan, *IEEE Trans. Nucl. Sci.* **NS-34**, 1025 (1987).

[21] J. E. Dey and D. W. Wildman, *Wideband Rf System for the Fermilab Recycler Ring*, Proc. 1999 Part. Accel. Conf., eds. A. Luccio and W. MacKay (New York, March 27–April 2, 1999), p. 869.

[22] C. M. Bhat and K. Y. Ng, *Potential-Well Distortion in Barrier RF*, Proc. 30th Advanced ICFA Beam Dynamics Workshop on High Luminosity e^+e^- Collisions (e^+e^- Factories 2003) (Stanford, CA, Oct. 13–16, 2003).

[23] See, for example, H. Goldstein, *Classical Mechanics*, (Addison-Wesley 1959), Sec. 8-3.

This page intentionally left blank

2025 © The Author(s). This is an Open Access chapter published by World Scientific Publishing Company, licensed under the terms of the Creative Commons Attribution-NonCommercial 4.0 International License (CC BY-NC 4.0).

Chapter 3

Betatron Tune Shifts

3.1 Static Transverse Forces

The vertical motion of a particle inside a coasting beam obeys the equation of motion

$$\frac{dp_y}{dt} = F_{\text{ext}}(y) + F_{\text{beam}}(y, \bar{y}), \tag{3.1}$$

where $p_y = \gamma m dy/dt$ is the vertical momentum of the particle and m its rest mass. Since we want to study the motion of small vertical displacement y, the Lorentz factor γ can therefore be taken out of the derivative. Here, $F_{\text{ext}}(y)$ is the force due to the magnets outside the vacuum chamber and it gives rise to betatron oscillations, while $F_{\text{beam}}(y, \bar{y})$ is the force coming from the electromagnetic fields of the beam and it is dependent on the particle vertical displacement y and the beam vertical center at $\bar{y}$. For example, with quadrupole focusing,

$$F_{\text{ext}}(y) = \frac{B'_y}{B\rho}\, y, \tag{3.2}$$

where $B'_y = dB_y/dx$ is the gradient of the quadrupole magnetic flux density, $B\rho$ is the rigidity of the beam, and y is measured from the centers of the quadrupoles. We assume uniform betatron focusing along the accelerator ring. Remarks will be given and remedy made when this approximation fails. We can therefore make the replacement

$$\langle F_{\text{ext}}(y) \rangle \longrightarrow -(\nu_{0y}\omega_0)^2 y, \tag{3.3}$$

where ν_{0y} is the number of vertical oscillations the particle makes in a turn or what we usually call the *bare* vertical betatron tune, while $\omega_0/(2\pi)$ is the revolution frequency. Notice that the average of the external force is proportional to the impulse in one accelerator turn. Now the transverse equation of motion

becomes

$$\frac{d^2y}{ds^2} + \frac{\nu_{0y}^2}{R^2}\, y = \frac{\langle F_{\text{beam}}(y,\bar{y})\rangle}{\gamma m v^2}, \tag{3.4}$$

where R is the mean radius of the ring. In above, the rigid-bunch and impulse approximations have been applied to the F_{beam}, and we have replaced d/dt by vd/ds with $v = \beta c$ being the nominal velocity of the beam, c the velocity of light, and s the distance measured along the longitudinal path in the ring. In this chapter, we are going to study the steady-state effects of the transverse wake potential on the beam. Therefore, there is no explicit time dependency in $\langle F_{\text{beam}}\rangle$. As will be shown below, the steady-state effects of the wake potential contribute to betatron tune shifts, while the time-dependent effects may excite instabilities.

Since we are interested only in small amount of motion in the vertical direction, the beam force can be Taylor expanded to obtain

$$\frac{d^2y}{ds^2} + \frac{\nu_{0y}^2}{R^2} y = \frac{1}{\gamma m v^2}\left(\left.\frac{\partial\langle F_{\text{beam}}\rangle}{\partial y}\right|_{\bar{y}=0} y + \left.\frac{\partial\langle F_{\text{beam}}\rangle}{\partial \bar{y}}\right|_{y=0} \bar{y} \right). \tag{3.5}$$

The first term on the right side is proportional to the vertical displacement of the witness particle; it therefore constitutes a shift of the vertical betatron tune ν_{0y} to become $\nu_{y\,\text{incoh}}$. When the shift is small,* we write $\nu_{y\,\text{incoh}}^2 = \nu_{0y}^2 + 2\nu_{0y}\Delta\nu_{y\,\text{incoh}}$ with

$$\Delta\nu_{y\,\text{incoh}} = -\frac{R^2}{2\nu_{0y}\gamma m v^2} \left.\frac{\partial\langle F_{\text{beam}}\rangle}{\partial y}\right|_{\bar{y}=0}. \tag{3.6}$$

Since this shift affects an individual beam particle, $\Delta\nu_{y\,\text{incoh}}$ is called the vertical *incoherent tune shift.* Thus, the incoherent tune shift can be computed by setting $\bar{y} = 0$ or without any displacement of the center of the whole beam.

Let us come back to Eq. (3.5), the transverse equation of motion. We can write one such equation for each beam particle. Perform an average by adding up these equations and dividing by the total number of beam particles. The result is

$$\frac{d^2\bar{y}}{ds^2} + \frac{\nu_{0y}^2}{R^2} \bar{y} = \frac{1}{\gamma m v^2}\left(\left.\frac{\partial\langle F_{\text{beam}}\rangle}{\partial y}\right|_{\bar{y}=0} \bar{y} + \left.\frac{\partial\langle F_{\text{beam}}\rangle}{\partial \bar{y}}\right|_{y=0} \bar{y} \right). \tag{3.7}$$

This equation describes the vertical motion of the center of the beam, or the *coherent motion* of the beam, which is just a simple harmonic motion. The

*When the tune shift is large, $\Delta\nu_{y\,\text{incoh}}$ on the left side of Eq. (3.6) should be replaced by $\Delta\nu_{y\,\text{incoh}}^2/(2\nu_{0y})$. The same applies to Eqs. (3.8), (3.13), (3.16), (3.19), etc.

vertical betatron tune of the center of the beam, or the *coherent* vertical betatron tune of the beam, is now $\nu_{y\,\mathrm{coh}} = \nu_{0y} + \Delta\nu_{y\,\mathrm{coh}}$. When the perturbation is small, the coherent tune shift becomes

$$\Delta\nu_{y\,\mathrm{coh}} = -\frac{R^2}{2\nu_{0y}\gamma m v^2}\left(\left.\frac{\partial\langle F_{\mathrm{beam}}\rangle}{\partial y}\right|_{\bar{y}=0} + \left.\frac{\partial\langle F_{\mathrm{beam}}\rangle}{\partial\bar{y}}\right|_{y=0}\right). \tag{3.8}$$

Because we keep only the linear terms of the Taylor expansion in Eq. (3.5), we have included only the dipole parts of the wake force. As a result, these tune shifts should be called dipole coherent tune shift and dipole incoherent tune shift.

Let us assume here that the vacuum chamber is completely smooth and infinitely conducting. Then the force on a beam particle from the beam comes from only two sources: (1) electromagnetic interaction of the beam particle with all other beam particles in the beam, which we call *self-force*, (2) reflection of electromagnetic fields from the walls of the vacuum chamber, which we call *image forces.*

3.1.1 *Electric Image Forces*

The image forces certainly depends on the geometry of the vacuum chamber. Let us consider the simple case when the vacuum chamber consists of two infinite horizontal plates at location $y = \pm h$ as illustrated in Fig. 3.1. The beam of say positive charges is displaced by $\bar{y}_1$ vertically and the witness particle is at

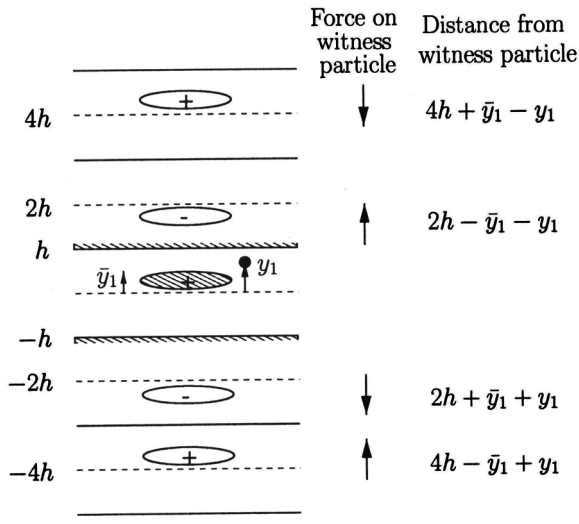


Fig. 3.1 Illustration showing the electric forces from the images of a beam, off centered vertically by $\bar{y}_1$, acting on a witness particle a location y_1 inside the beam between two infinite horizontal conducting parallel plates separated vertically by distance $2h$.

y_1. We wish to consider the electric force on the witness particle coming from reflection by the top and bottom walls of the vacuum chamber. In order that the horizontal electric field at the top wall vanishes, there must be an image of the beam with negative charges at position $y = 2h - \bar{y}_1$ or at a distance $2h - \bar{y}_1 - y_1$ from the witness particle. In order that the horizontal electric field at the bottom wall vanishes, this image will have another image of positive charges from the bottom wall at $y = -(4h - \bar{y}_1)$ or $4h - \bar{y}_1 + y_1$ from the witness particle. This secondary image will have a third image of negative charges from the top wall, a fourth image of positive charges from the bottom wall, etc.

Similarly, the beam has an image of negative charges first from the bottom wall at $y = -(2h + \bar{y}_1)$ or $2h + \bar{y}_1 + y_1$ from the witness particle. This image will form another image of positive charges through the top wall with positive charges at $y = 4h + \bar{y}_1$ or $4h + \bar{y}_1 - y_1$ from the witness particle, etc. Summing up, the vertical electric field acting on the witness particle is, according to Gauss's law,†

$$E_y = \frac{e\lambda}{2\pi\epsilon_0}\left[+\frac{1}{2h-\bar{y}_1-y_1} - \frac{1}{2h+\bar{y}_1+y_1} + \frac{1}{6h-\bar{y}_1-y_1} - \frac{1}{6h+\bar{y}_1+y_1} + \cdots \right.$$
$$\left. - \frac{1}{4h+\bar{y}_1-y_1} + \frac{1}{4h-\bar{y}_1+y_1} - \frac{1}{8h+\bar{y}_1-y_1} + \frac{1}{8h-\bar{y}_1+y_1} + \cdots\right], \tag{3.9}$$

where λ is the linear particle density per unit length along the ring, normalized to the number of particles in the beam upon integration from $s = 0$ to $2\pi R$. Every two adjacent terms are grouped together giving

$$E_y = \frac{e\lambda}{2\pi\epsilon_0}\left[+\frac{2(\bar{y}_1+y_1)}{(2h)^2-(\bar{y}_1+y_1)^2} + \frac{2(\bar{y}_1+y_1)}{(6h)^2-(\bar{y}_1+y_1)^2} + \cdots \right.$$
$$\left. + \frac{2(\bar{y}_1-y_1)}{(4h)^2-(\bar{y}_1-y_1)^2} + \frac{2(\bar{y}_1-y_1)}{(8h)^2-(\bar{y}_1-y_1)^2} + \cdots\right]. \tag{3.10}$$

Since we consider only small vertical motion, only terms linear in $\bar{y}_1 + y_1$ and $\bar{y}_1 - y_1$ are kept leading to

$$E_y = \frac{e\lambda}{\pi\epsilon_0 h^2}\left[(\bar{y}_1+y_1)\left(\frac{1}{2^2}+\frac{1}{6^2}+\frac{1}{10^2}+\cdots\right) + (\bar{y}_1-y_1)\left(\frac{1}{4^2}+\frac{1}{8^2}+\frac{1}{12^2}+\cdots\right)\right]$$
$$= \frac{e\lambda}{\pi\epsilon_0 h^2}\left[(\bar{y}_1+y_1)\frac{\pi^2}{32} + (\bar{y}_1-y_1)\frac{\pi^2}{96}\right]. \tag{3.11}$$

†According to the notation in the previous chapter, the linear beam density should be written as $\bar{\lambda}$. The bar is omitted here just for convenience.

In the literature, there is a standard way to write these image contributions following the work of Laslett: [1, 2, 3]

$$E_y = \frac{e\lambda}{\pi\epsilon_0}\frac{\epsilon_{1y}}{h^2}y_1 \qquad \text{and} \qquad \frac{e\lambda}{\pi\epsilon_0}\frac{\xi_{y1}}{h^2}\bar{y}_1, \tag{3.12}$$

where ϵ_{1y} and ξ_{1y} are called, respectively, the incoherent and coherent *electric image coefficients.* For the situation of two parallel plates, we have $\epsilon_{1y} = \pi^2/48$ and $\xi_{1y} = \pi^2/16$. Attention should be paid that in deriving the coherent image coefficient, y_1 has been replaced by $\bar{y}_1$ in Eq. (3.9) or (3.10) or (3.11). According to Eqs. (3.6) and (3.8), the coherent and incoherent vertical tune shifts due to electric images are:

$$\Delta\nu_{y\,\text{incoh}} = -\frac{Nr_0R}{\pi\gamma\beta^2\nu_{0y}}\frac{\epsilon_{1y}}{h^2} \qquad \text{and} \qquad \Delta\nu_{y\,\text{coh}} = -\frac{Nr_0R}{\pi\gamma\beta^2\nu_{0y}}\frac{\xi_{1y}}{h^2}, \tag{3.13}$$

where we have replaced the linear particle density of the coasting beam by $\lambda = N/(2\pi R)$ with N being the total number of particles in the beam, and introduced the classical radius of the particle $r_0 = e^2/(4\pi\epsilon_0 mc^2)$.

Notice that there is a negative sign in front of each of the tune shift expressions in Eq. (3.13). This implies that a positive image coefficient will contribute a downward shifting to the betatron tune.

3.1.2 *Magnetic Image Forces*

Unlike the electric field that cannot penetrate the metallic vacuum chamber at any frequency, the effect of the magnetic field is more complex. The magnet field has an ac component and a dc component. The ac component has its component parallel to the wall of the vacuum chamber converted into eddy current. In other words, the ac magnetic field *cannot* penetrate the wall of the vacuum chamber. There the boundary condition is $B_\perp = 0$, or the magnetic flux density B is parallel to the wall of the vacuum chamber. To accomplish this, the first image from a boundary wall gives an image current that flows in the opposite direction to that the beam. The total force from these magnetic images acting on the witness charge current at position y_1 is illustrated in Fig. 3.2 and is very similar to Eq. (3.9) except for some changes in the direction of each force component. We have

$$\begin{aligned}\frac{F_y^{\text{mag}}}{e} = -\frac{e\mu_0\lambda v^2}{2\pi}\Bigg[&\left(+\frac{1}{2h-\bar{y}_1-y_1}-\frac{1}{2h+\bar{y}_1+y_1}\right)+\left(2\to 6\right)+\cdots\\ &\left(-\frac{1}{4h+\bar{y}_1-y_1}+\frac{1}{4h-\bar{y}_1+y_1}\right)+\left(4\to 8\right)+\cdots\Bigg].\end{aligned} \tag{3.14}$$

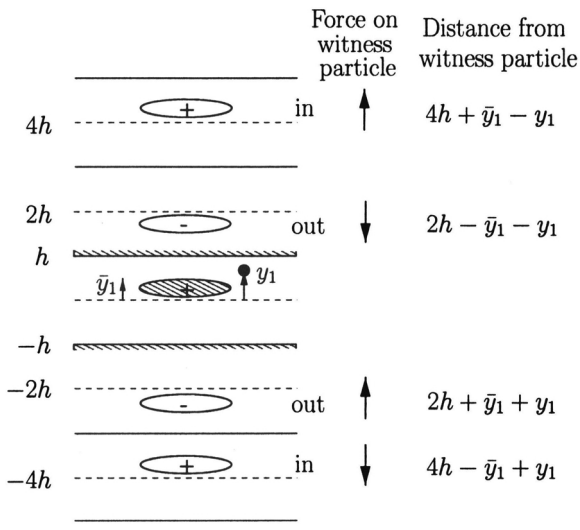


Fig. 3.2 Illustration showing magnetic forces from images of a beam, $\bar{y}_1$ off-centered vertically, acting on a witness current at location y_1 inside the beam between two infinite horizontal conducting parallel plates separated by $2h$. The normal components of the nonpenetrating magnetic fields vanish at the plates. The beam or image current directions into or out of the paper are labeled "in" or "out".

There is the factor v^2 outside the square brackets on the right side. One v comes from the source beam current and the other v comes from the Lorentz force. It is interesting to see that the factor outside the square brackets is equal to $-e\lambda\beta^2/(2\pi\epsilon_0)$. Thus, the force due to the ac magnetic images are equal to the force due to the electric images multiplied by the factor $-\beta^2$. Keeping up to the dipole contribution, this leads to

$$\frac{F_y^{\text{mag}}}{e} = -\frac{e\lambda\beta^2}{2\pi\epsilon_0 h^2}\left[(\bar{y}_1 + y_1)\frac{\pi^2}{32} + (\bar{y}_1 - y_1)\frac{\pi^2}{96}\right]. \tag{3.15}$$

Following Eq. (3.13), tune shifts due to ac magnetic images can be expressed as terms of the former electric image coefficients ϵ_{1y} and ξ_{1y}:

$$\Delta\nu_{y\,\text{incoh}} = \frac{Nr_0R}{\pi\gamma\nu_{0y}}\frac{\epsilon_{1y}}{h^2} \qquad \text{and} \qquad \Delta\nu_{y\,\text{coh}} = \frac{Nr_0R}{\pi\gamma\nu_{0y}}\frac{\xi_{1y}}{h^2}, \tag{3.16}$$

and no new image coefficients need to be introduced separately.

There is always a dc part of the magnetic field that can penetrate the wall of the beam pipe and land on the pole faces of the magnet as if the vacuum chamber were not there. The boundary condition on the magnet pole faces is now $B_\perp$ continuous and $B_\parallel = 0$. In order to accommodate this, all the image currents must flow in exactly the same direction of the source beam, as illustrated in Fig. 3.3. The force on the witness particle is now

$$\frac{F_y^{\text{mag}}}{e} = \frac{e\mu_0\lambda v^2}{2\pi}\left[\left(+\frac{1}{2g-\bar{y}_1-y_1}-\frac{1}{2g+\bar{y}_1+y_1}\right)+\left(2\to 6\right)+\cdots\right.$$
$$\left.\left(+\frac{1}{4g+\bar{y}_1-y_1}-\frac{1}{4g-\bar{y}_1+y_1}\right)+\left(4\to 8\right)+\cdots\right], \qquad (3.17)$$

where the magnetic pole faces are at $y = \pm g$ or the magnets have a vertical gap $2g$ between the poles faces. It is important to note the slight difference between Eqs. (3.14) and (3.17). Here we obtain

$$\frac{F_y^{\text{mag}}}{e} = +\frac{e\lambda\beta^2}{2\pi\epsilon_0 g^2}\left[(\bar{y}_1+y_1)\frac{\pi^2}{32}-(\bar{y}_1-y_1)\frac{\pi^2}{96}\right], \qquad (3.18)$$

as compared to Eq. (3.15). Following Laslett, we write the tune shifts due to dc magnetic images as

$$\Delta\nu_{y\,\text{incoh}} = -\frac{Nr_0R}{\pi\gamma\nu_{0y}}\frac{\epsilon_{2y}}{g^2} \qquad \text{and} \qquad \Delta\nu_{y\,\text{coh}} = -\frac{Nr_0R}{\pi\gamma\nu_{0y}}\frac{\xi_{2y}}{g^2}, \qquad (3.19)$$

where ϵ_{2y} and ξ_{2y} are called, respectively, the vertical incoherent and coherent dc *magnetic image coefficients.* For the special case of two parallel plates, they assume the values $\epsilon_{2y} = \pi^2/24$ and $\xi_{2y} = \pi^2/16$.

There is also a set of horizontal image coefficients: ϵ_{1x}, ϵ_{2x}, ξ_{1x}, and ξ_{2x}. Because the image forces acting on the witness particle come directly from the individual images, the electric field and magnetic flux density from the images at the location of the witness particle satisfy source-free electric and magnetic

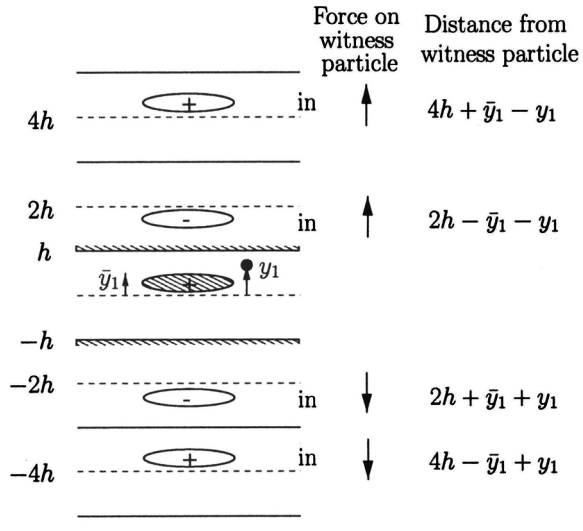


Fig. 3.3 Illustration showing magnetic forces from images of a beam, $\bar{y}_1$ off centered vertically, acting on a witness current at location y_1 inside the beam between two infinite horizontal parallel pole faces separated by $2g$. The parallel components of the penetrating magnetic fields vanish at the pole faces. Here, the beam and all image currents flow into the paper.

Gauss's laws, or $\vec{\nabla} \cdot \vec{E} = 0$ and $\vec{\nabla} \cdot \vec{B} = 0$. We therefore always have

$$\epsilon_{1x} = -\epsilon_{1y} \qquad \text{and} \qquad \epsilon_{2x} = -\epsilon_{2y}. \tag{3.20}$$

On the other hand, there is no definite relationship between the horizontal and vertical coherent electric image coefficients. In the special case of two parallel plates, it is obvious that $\xi_{1x} = 0$ and $\xi_{2x} = 0$, which is the result of translational invariance. For a beam pipe with circular cross section or square cross section, $\epsilon_{1x} = 0$ and $\epsilon_{2x} = 0$ because of symmetry between the horizontal and vertical.

It is important to point out that electric and magnetic image coefficients are always defined with reference to the square of the *half vertical* vacuum chamber h or the square of the *half vertical* magnetic pole gap g, independent of whether we are talking about the vertical or horizontal tune shifts. For the example of a rectangular beam pipe of half height h and half width w, only h^2 will enter into the denominators but never w^2, such as in Eqs. (3.13), (3.16), or (3.19). In the same way, for an elliptical beam pipe of vertical radius b and horizontal radius a, the image coefficients will be defined with reference to $h = b$ but not a. It is because of such a dedicated reference that the relations in Eq. (3.20) hold.

3.2 Space-Charge Self-Force

3.2.1 *Incoherent Self-Force Tune Shift*

The interaction of a beam particle with other beam particles in the beam depends on the transverse distribution of the beam. Let us first consider a uniformly distributed coasting beam of circular cross section and radius a. The witness particle inside the beam at $y = y_1$ sees, in the y-direction, an electric force[‡]

$$F_y^{\text{elect}} = \frac{e^2\lambda}{2\pi\epsilon_0 a^2}(y_1 - \bar{y}_1), \tag{3.21}$$

and a magnetic force

$$F_y^{\text{mag}} = -\frac{e^2\mu_0\lambda v^2}{2\pi a^2}(y_1 - \bar{y}_1) = -\frac{e^2\lambda\beta^2}{2\pi\epsilon_0 a^2}(y_1 - \bar{y}_1), \tag{3.22}$$

or a total force of

$$F_y = \frac{e^2\lambda}{2\pi\epsilon_0\gamma^2 a^2}(y_1 - \bar{y}_1), \tag{3.23}$$

[‡]The vertical electric and magnetic forces in Eqs. (3.21) and (3.22) are true for any particle inside the beam at a vertical distance $y = y_1$ above the center of the beam and are independent of the particle horizontal position.

where $\bar{y}_1$ is vertical position of the center of the beam. This self-force is a space-charge force. Because of the repulsive nature, it counteracts the focusing force of the external quadrupoles. According to Eq. (3.6), it leads to a space-charge tune shift of

$$\Delta\nu_{y,x\,\mathrm{incoh}}^{\mathrm{spch}} = -\frac{Nr_0R}{2\pi\gamma^3\beta^2a^2\nu_{0y,x}}. \tag{3.24}$$

It is clear from Eq. (3.23) that the coherent space-charge tune shifts in both transverse directions are zero. This is understandable, because the center of the beam does not see its own space-charge force. We can also define the self-field or space-charge coefficients in the vertical and horizontal directions, $\epsilon_{y,x}^{\mathrm{spch}} = \frac{1}{2}$, such that

$$\Delta\nu_{y,x\,\mathrm{incoh}}^{\mathrm{spch}} = -\frac{Nr_0R}{\pi\gamma^3\beta^2\nu_{0y,x}}\frac{\epsilon_{y,x}^{\mathrm{spch}}}{a^2B}. \tag{3.25}$$

The space-charge coefficients take care of the transverse shape of the beam and how the beam particles are distributed. In the above, we have also introduced the single-bucket bunching factor B to take care of the fact the the beam may be longitudinally bunched. The single-bucket bunching factor is defined as

$$B = \frac{I_{\mathrm{av}}}{I_{\mathrm{pk}}}, \tag{3.26}$$

where I_{av} and I_{pk} are, respectively, the current of a bunch averaged over a *single* rf bucket and its peak current, or the ratio of the average current to the peak current assuming that all the buckets are filled.

Now consider a beam with uniform transverse distribution but elliptical cross section with vertical and horizontal radii a_y and a_x. In defining the space-charge coefficients, we follow the same convention of the Laslett image coefficients that the a^2 in the denominator of Eq. (3.25) is always a_y^2, independent of whether we are referring to the vertical or horizontal space-charge tune shift. The vertical and horizontal space-charge coefficients are then (Exercise 3.3)

$$\epsilon_y^{\mathrm{spch}} = \frac{a_y}{a_y + a_x} \qquad \text{and} \qquad \epsilon_x^{\mathrm{spch}} = \frac{a_y^2}{a_x(a_y + a_x)}. \tag{3.27}$$

These coefficients become $\frac{1}{2}$ when $a_y = a_x$ as expected.

Next let us consider a beam with cylindrical cross section but with transverse bi-Gaussian distribution,

$$f(x,y) = \frac{\lambda}{2\pi\sigma^2}e^{-(x^2+y^2)/(2\sigma^2)}, \tag{3.28}$$

where σ is the rms transverse spread of the beam and $\lambda = N/(2\pi R)$ is the linear density. A particle at $y = y_1$ vertically above the center of the beam sees an electric repulsive force in the y direction,

$$F_y^{\text{elect}} = \frac{e^2}{2\pi\epsilon_0 y_1}\frac{\lambda}{\sigma^2}\int_0^{y_1} e^{-r^2/(2\sigma^2)} r dr = \frac{e^2\lambda}{2\pi\epsilon_0 y_1}\left[1 - e^{-y_1^2/(2\sigma^2)}\right]. \tag{3.29}$$

For small offset, $y_1 \ll \sigma$, this force can be Taylor expanded. Keeping the lowest order, we have

$$F_y^{\text{elect}} = \frac{e^2\lambda}{4\pi\epsilon_0\sigma^2} y_1. \tag{3.30}$$

The magnetic force is the same except for the extra multiplication by $-\beta^2$. Summing up the electric and magnetic contributions, the incoherent space-charge tune shift is therefore

$$\Delta\nu_{y,x\,\text{incoh}}^{\text{spch}} = -\frac{Nr_0 R}{4\pi\gamma^3\beta^2\sigma^2\nu_{0y,x}}. \tag{3.31}$$

In general, if the beam has an elliptical cross section with vertical rms beam size σ_y and horizontal rms beam size σ_x, the space-charge coefficients for a beam particle, defined in Eq. (3.25), can be represented by

$$\epsilon_y^{\text{spch}} = \frac{f\sigma_y}{\sigma_y + \sigma_x} \quad \text{and} \quad \epsilon_x^{\text{spch}} = \frac{f\sigma_y^2}{\sigma_x(\sigma_y + \sigma_x)}, \tag{3.32}$$

where the form factor f comes about because each particle in a transverse slice of the beam receives different tune shifts. For the bi-Gaussian distribution, if we consider only the particles at the center of the beam where the tune shifts are largest, $f = 3$. Thus the tune shift is three times as large as the tune shift for a uniform distribution in Eq. (3.34). This is because particles are mostly concentrated near the bunch center in a bi-Gaussian distribution and the linear particle density at the bunch center is therefore much larger. However, the tune shift for those particles with transverse offsets will be much smaller. If we make a rough model by assuming those particles within one sigma of the beam core to have the maximum tune shift while those outside do not experience any space-charge force, we obtain some sort of average for the particles in the cross sectional slice, $f = 3(1 - e^{-1/2}) = 1.180$, which is only slightly larger than that for a uniformly distributed beam.

We can also express the incoherent space-charge tune shift in term of the

normalized emittance of the beam[§]

$$\epsilon_{Ny,x} = \gamma\beta\frac{a_{y,x}^2}{\beta_{y,x}}, \tag{3.33}$$

which has the merit that it is an invariant, although both the beam radius $a_{y,x}$ and the betatron function $\beta_{y,x}$ vary along the accelerator ring. We therefore have for uniform transverse distribution,

$$\Delta\nu_{y,x\,\mathrm{incoh}}^{\mathrm{spch}} = -\frac{Nr_0}{\pi\gamma^2\beta\sqrt{\epsilon_{Ny,x}}\left(\sqrt{\epsilon_{Ny,x}} + \sqrt{\epsilon_{Nx,y}\langle\beta_{x,y}\rangle/\langle\beta_{y,x}\rangle}\right)B}, \tag{3.34}$$

where the smooth approximation $\langle\beta_{y,x}\rangle = R/\nu_{0y,x}$ has been made. For the bi-Gaussian distribution, the 95% normalized transverse emittance $\epsilon_{N95y,x}$ of the beam which encloses 95% of the beam particles is used. This corresponds to a radius r_{95} given by

$$\frac{1}{2\pi\sigma^2}\int_0^{r_{95}} e^{-r^2/(2\sigma^2)}2\pi r dr = 95\%, \tag{3.35}$$

which results in $r_{95} \approx \sqrt{6}\sigma$. Thus

$$\epsilon_{N95y,x} = \gamma\beta\frac{r_{95}^2}{\beta_{y,x}} \approx \gamma\beta\frac{6\sigma^2}{\beta_{y,x}}. \tag{3.36}$$

The maximum incoherent space-charge tune shift is therefore

$$\Delta\nu_{y,x\,\mathrm{incoh}}^{\mathrm{spch}} = -\frac{3Nr_0}{\pi\gamma^2\beta\sqrt{\epsilon_{N95y,x}}\left(\sqrt{\epsilon_{N95y,x}} + \sqrt{\epsilon_{N95x,y}\langle\beta_{x,y}\rangle/\langle\beta_{y,x}\rangle}\right)B}, \tag{3.37}$$

where again the substitution $\langle\beta_{y,x}\rangle = R/\nu_{0y,x}$ has been made.

However, expressions in Eqs. (3.34) and (3.37) are often not very useful, because (1) the horizontal beam size a_x has another contribution from the horizontal dispersion D_x (the vertical dispersion is zero for most rings), and (2) the beta functions $\beta_{y,x}$ vary along the accelerator ring. To solve the first problem, we must write, for the uniform distribution,

$$a_x = \sqrt{\frac{\beta_x\epsilon_{Nx}}{\gamma\beta} + (D_x\delta)^2}, \tag{3.38}$$

[§]The *unnormalized emittances* are defined without the factor $\gamma\beta$, and are not constants of motion during an acceleration. It is common to assume that the transverse emittance is expressed in πmm-mr. Thus, the factor of π is left out in the definition of Eq. (3.33). This can be confusing because the longitudinal emittance of bunch area is usually defined with the factor of π.

where δ is the half-momentum spread of the beam. We add the two contributions in quadrature, because momentum distribution is independent of the location along the ring. For the bi-Gaussian distribution,

$$\sigma_x = \sqrt{\frac{\beta_x \epsilon_{Nx\,\mathrm{rms}}}{\gamma\beta} + (D_x\sigma_\delta)^2}, \tag{3.39}$$

is used instead, where σ_δ is the rms fractional spread of momentum.

To solve the second problem, we must do an integration around the ring using the Twiss parameters of the lattice. For example, the vertical incoherent space-charge tune shift in the uniform distribution should take the form,

$$\Delta\nu_{y\,\mathrm{incoh}}^{\mathrm{spch}} = -\frac{Nr_0}{\pi\gamma^3\beta^2 B}\left\langle \frac{\beta_y}{a_y(a_y+a_x)} \right\rangle, \tag{3.40}$$

and similarly for the horizontal tune shift, where $\langle\cdots\rangle$ represents taking the average around the ring. For the bi-Gaussian distribution, we have

$$\Delta\nu_{y,x\,\mathrm{incoh}}^{\mathrm{spch}} = -\frac{Nr_0}{\pi\gamma^3\beta^2 B}\left\langle \frac{\beta_{y,x}\epsilon_{y,x}^{\mathrm{spch}}}{\sigma_y^2} \right\rangle, \tag{3.41}$$

where the space-charge coefficients $\epsilon_{y,x}^{\mathrm{spch}}$ are given by Eq. (3.32), the rms beam radii $\sigma_y = \sqrt{\beta_y\epsilon_{Ny\,\mathrm{rms}}/(\gamma\beta)}$ and σ_x given by Eq. (3.39). For most rings when dispersion is not the main contribution to the horizontal beam size, the estimated incoherent tune shifts using averages do not differ very much from the one obtained by integration around the ring, because σ_y and σ_x contribute a factor $\sqrt{\beta_y\beta_x}$ to counteract β_y in the numerator of Eq. (3.41) so that the averaging is roughly $\langle\sqrt{\beta_y/\beta_x}\rangle$. However, when the contribution of dispersion overwhelms that of the horizontal emittance in Eq. (3.39), the averaging becomes $\langle\sqrt{\beta_y}/D_x\rangle$ instead. In the case, the incoherent tune shift obtained by integration around the ring can be more than a factor of two larger than when averages are used in the estimation. An example is the Fermilab designed damping ring for the International Linear Collider. The vertical space-charge tune shift computed by integration over the ring gives $\Delta\nu_{y\,\mathrm{incoh}}^{\mathrm{spch}} = -0.0654$. However, in the smooth approximation, it is only -0.0311 (Exercise 3.6).

One may be tempted to obtain Eq. (3.41) from Eq. (3.31) or Eq. (3.37) by substituting $R/\nu_{0y} = \beta_y$ and then perform the averaging around the ring. In fact, Eq. (3.41) *cannot* be derived from Eq. (3.4) where smooth focusing has already been assumed. We must first start off from the Hill's equation. The best derivation is to use the Hamiltonian formalism in the action-angle variables and perform first-order perturbation (Exercise 3.7).

3.2.2 *Tune-Shift Distribution*

The spread in space-charge tune shift among particles inside the beam is important because this spread can be a source of Landau damping to counteract collective instabilities. One may have the wrong understanding that only the spread of the tune shift is important but not the average shift, because the latter can be corrected by changing the bare tune of the machine. This is incorrect, since the tune spread will not be able to Landau damp collective instabilities if it is shifted outside the coherent betatron tune. For this reason, it is important to study the distribution in betatron tune shift.

For a distribution of finite extent, the space-charge tune spread is always less than the maximum space-charge tune spread, which occurs at the center of the beam for most distributions. For a transverse bi-Gaussian distribution that extends to infinity, the space-charge tune shift of a particle infinitely far away from the beam axis is zero, and therefore the space-charge tune spread is equal to the maximum space-charge tune shift. However, as we shall see the rms spread is much smaller.

For simplicity, we consider a round beam with the same *bare* betatron tune ν_0 in both the x- and y-directions. The Hamiltonian describing the transverse motion of a particle inside the round coasting beam is

$$H = \frac{p_x^2 + p_y^2}{2} + \frac{\nu_0^2}{R^2}\frac{x^2 + y^2}{2} - U_{\text{spch}}(r), \tag{3.42}$$

where R is the main radius of the accelerator ring. The space-charge potential of the transverse bi-Gaussian distributed beam is given by

$$U_{\text{spch}}(r) = \int_0^r F_{\text{spch}}(r')dr', \tag{3.43}$$

where the space-charge force at the distance $r = \sqrt{x^2 + y^2}$ in the radial direction can be written as

$$F_{\text{spch}}(r) = \frac{e^2\lambda}{2\pi\sigma^2\gamma^3 mv^2}\frac{1}{2\pi\epsilon_0 r}\int_0^r e^{-r'^2/(2\sigma^2)}2\pi r'dr'. \tag{3.44}$$

The independent variable is s, the distance measured along the accelerator ring.

To derive the betatron tune in the presence of the space-charge force, it is best to go to action-angle variables. Since the space-charge force is usually much smaller than the external focusing force, the space-charge potential will be treated as a perturbation.

Solution of the unperturbed horizontal motion can be written as[¶]

$$\begin{cases} x = \sqrt{2J_x\bar{\beta}}\cos\psi_x, \\ p_x = -\sqrt{\dfrac{2J_x}{\bar{\beta}}}\sin\psi_x, \end{cases} \tag{3.45}$$

where J_x and ψ_x are the horizontal action-angle variables. Here, we have introduced the average betatron function $\bar{\beta} = R/\nu_0$. Since $p_x = dx/ds$, we find that $d\psi/ds = 1/\bar{\beta}$ is also satisfied. Including the vertical components, the unperturbed Hamiltonian is therefore

$$H_0 = \frac{p_x^2 + p_y^2}{2} + \frac{\nu_0^2}{R^2}\frac{x^2 + y^2}{2} = \frac{\nu_0}{R}(J_x + J_y). \tag{3.46}$$

From the Hamilton equations of motion,

$$\frac{d\psi_{x,y}}{ds} = \frac{\partial H}{\partial J_{x,y}}, \tag{3.47}$$

the betatron tunes including space-charge effect can be conveniently derived

$$\frac{\nu_{x,y}}{R} = \frac{\partial\langle H\rangle}{\partial J_{x,y}}, \tag{3.48}$$

where $\langle H\rangle$ is the Hamiltonian averaged over the angle variables ψ_x and ψ_y. This derivation is correct because the betatron tune is defined as the average number of betatron oscillations per revolution turn in the accelerator.

Let us first derive the small-amplitude tunes. For this, the space-charge potential is linearized to obtain

$$\Delta H = -U_{\text{spch}}(r) = -\frac{r_0\lambda R}{2\nu_0\gamma^3\beta^2\sigma^2}\Big(2J_x\cos^2\psi_x + 2J_y\cos^2\psi_y\Big), \tag{3.49}$$

[¶]The canonical transformation can be derived from the generating function

$$F_1(x,\psi_x) = \int_0^x p_x\,dx = -\frac{x^2}{2\bar{\beta}}\tan\psi_x,$$

where

$$p_x = -\frac{x}{\bar{\beta}}\tan\psi_x,$$

obtained from Eqs. (3.45) by eliminating J_x, has been substituted. The canonical transformation is then given by the above expression for p_x and

$$J_x = -\frac{\partial F_1}{\partial\psi_x} = \frac{x^2}{2\bar{\beta}}\sec^2\psi_x = \frac{x^2}{2\bar{\beta}}\left(1 + \frac{\bar{\beta}^2p_x^2}{x^2}\right) = \bar{\beta}H_0.$$

where the substitution of x and y in term of the action-angle variables has been made. After averaging over the angle variables, the space-charge tune shifts are obtained according to Eq. (3.48),

$$\Delta\nu_{x,y} = -\frac{r_0\lambda R^2}{2\nu_0\gamma^3\beta^2\sigma^2}, \tag{3.50}$$

which is the same incoherent space-charge tune shift $\Delta\nu^{\text{spch}}_{x,y\,\text{incoh}}$ obtained in Eq. (3.31) as expected. For the sake of convenience, $\Delta\nu_{x,y}$ is just a short-hand notation. We denote these small-amplitude tune shifts by $\Delta\nu^{\text{max}}_{\text{spch}}$, because these are the largest space-charge tune shifts the particle experiences since the particle is seeing the largest space-charge force at the center of the beam. Because the linearized space-charge potential has been used, $\Delta\nu^{\text{max}}_{\text{spch}}$ is also known as the linearized incoherent space-charge tune shift.

In terms of the small-amplitude space-charge tune shift $\Delta\nu^{\text{max}}_{\text{spch}}$, the space-charge potential of Eq. (3.43) becomes

$$\Delta H = -U_{\text{spch}}(r) = -\int_0^r dr' \frac{4\nu_0|\Delta\nu^{\text{max}}_{\text{spch}}|\sigma^2}{R^2 r'}\left[1 - e^{-r'^2/(2\sigma^2)}\right], \tag{3.51}$$

where

$$r^2 = x^2 + y^2 = 2J_x\bar{\beta}\cos^2\psi_x + 2J_y\bar{\beta}\cos^2\psi_y. \tag{3.52}$$

Actually, it is more convenient to express the space-charge potential defined in Eq. (3.43) in the form

$$U_{\text{spch}}(r) = \frac{1}{\gamma^3 m v^2}\frac{e^2\lambda}{4\pi\epsilon_0}\int_0^\infty dt \frac{e^{-(x^2+y^2)/(2\sigma^2+t)}}{2\sigma^2+t}. \tag{3.53}$$

The merit of this representation is that the variables x and y become separable. The implication is that the angle variables can now be integrated. For example,

$$\begin{aligned}\int_0^{2\pi} e^{-x^2/(2\sigma^2+t)}\frac{d\psi_x}{2\pi} &= \int_0^{2\pi} e^{-2J_x\bar{\beta}\cos^2\psi_x/(2\sigma^2+t)}\frac{d\psi_x}{2\pi} \\ &= e^{-J_x\bar{\beta}/(2\sigma^2+t)}\int_0^{2\pi} e^{-J_x\bar{\beta}\cos 2\psi_x/(2\sigma^2+t)}\frac{d\psi_x}{2\pi} \\ &= e^{-J_x\bar{\beta}/(2\sigma^2+t)} I_0\left(\frac{J_x\bar{\beta}}{2\sigma^2+t}\right),\end{aligned} \tag{3.54}$$

where I_n is the modified Bessel function of order n. We therefore obtain the

space-charge potential averaged over angle variables:

$$\langle U_{\rm spch}(J_x,J_y)\rangle = \frac{2\nu_0\sigma^2|\Delta\nu_{\rm spch}^{\rm max}|}{R^2} \times \int_0^\infty \frac{dt}{2\sigma^2+t} I_0\!\left(\frac{J_x\bar\beta}{2\sigma^2+t}\right) I_0\!\left(\frac{J_y\bar\beta}{2\sigma^2+t}\right) e^{-(J_x+J_y)\bar\beta/(2\sigma^2+t)}, \tag{3.55}$$

where $\Delta\nu_{\rm spch}^{\rm max}$, the maximum space-charge tune shift of Eq. (3.50) has been substituted. Obviously, this representation will be beneficial if an extension to a bi-Gaussian distribution with unequal horizontal and vertical spreads is desired.

The tune shift in the x-direction is given by

$$\frac{\Delta\nu_x}{R} = -\frac{\partial}{\partial J_x}\langle U_{\rm spch}(r)\rangle \tag{3.56}$$

where $\langle\cdots\rangle$ implies averaging over the angle variables. We obtain

$$\frac{\Delta\nu_x}{|\Delta\nu_{\rm spch}^{\rm max}|} = \int_0^1 dz\, e^{-\frac{1}{2}s_x z-\frac{1}{2}s_y z} I_0\!\left(\tfrac{1}{2}s_y z\right)\left[I_0\!\left(\tfrac{1}{2}s_x z\right) - I_1\!\left(\tfrac{1}{2}s_x z\right)\right], \tag{3.57}$$

with the introduction of the variables

$$s_{x,y} = \frac{J_{x,y}\bar\beta}{\sigma^2} \qquad \text{and} \qquad z = \frac{2\sigma^2}{2\sigma^2+t}. \tag{3.58}$$

To study the distribution in space-charge tune shift, first we must write down the distribution of the transverse particle offset in the beam. Let us concentrate on the distribution of the horizontal offset. Since the distribution density must be a function of the Hamiltonian, a Gaussian distribution density can be written as

$$f(H_0) = \frac{1}{2\pi(\sigma^2/\bar\beta)} e^{-\bar\beta^2 H_0/\sigma^2} = \frac{1}{2\pi(\sigma^2/\bar\beta)} e^{-x^2/(2\sigma^2)-p_x^2/(2\sigma^2/\bar\beta)}, \tag{3.59}$$

which is normalized to unity via integration over x and p_x. Since we are after the distribution in amplitude, we need to go to action-angle variables, or

$$f(H_0) = \frac{1}{2\pi(\sigma^2/\bar\beta)} e^{-J_x/(\sigma^2/\bar\beta)}. \tag{3.60}$$

The distribution density of J_x is obtained by an integration over ψ_x. Including the vertical components, we arrive at the distribution density

$$f(J_x,J_y) = \frac{e^{-(J_x+J_y)/(\sigma^2/\bar\beta)}}{(\sigma^2/\bar\beta)^2}. \tag{3.61}$$

Including the distribution in J_x and J_y of Eq. (3.61), the average horizontal space-charge tune shift becomes

$$\frac{\langle \Delta\nu_x \rangle}{|\Delta\nu_{\text{spch}}^{\max}|} = \int_0^1 dz \int_0^\infty ds_x \int_0^\infty ds_y e^{-s_x(1+\frac{1}{2}z)-s_y(1+\frac{1}{2}z)} \times I_0\left(\tfrac{1}{2}s_y z\right)\left[I_0\left(\tfrac{1}{2}s_x z\right) - I_1\left(\tfrac{1}{2}s_x z\right)\right]. \tag{3.62}$$

Since the integrals over the action variables decoupled, we can integrate over s_x and s_y separately and finally do the integration over z to obtain

$$\frac{\langle \Delta\nu_x \rangle}{|\Delta\nu_{\text{spch}}^{\max}|} = \ln \frac{64}{\left(1+\sqrt{2}\right)^4} = 0.633389. \tag{3.63}$$

For the second moment, the integral cannot be performed analytically and numerical method is required, giving the rms incoherent horizontal space-charge tune spread

$$\left(\frac{\Delta\nu_x}{\Delta\nu_{\text{spch}}^{\max}}\right)_{\text{rms}} = \sqrt{\left\langle \left(\frac{\Delta\nu_x}{\Delta\nu_{\text{spch}}^{\max}}\right)^2 \right\rangle - \left\langle \frac{\Delta\nu_x}{\Delta\nu_{\text{spch}}^{\max}} \right\rangle^2} = 0.1678. \tag{3.64}$$

The distribution of the space-charge tune shift can be obtained numerically using a statistical method. [4] One trillion particles are populated in the beam cross section at random according to the bi-Gaussian distribution. The space-charge tune shift of each of these particles can be computed using Eq. (3.57). The tune-shift distribution is then derived by putting the particles into 1000 bins of equal width so that the fractional rms statistical fluctuation is only 0.1%. The result is plotted in Fig. 3.4. We see that the distribution density starts from

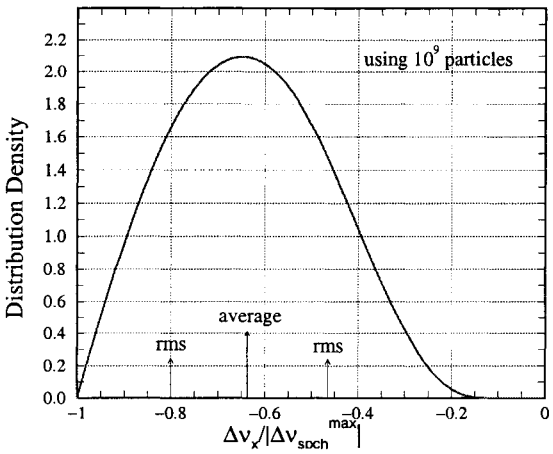


Fig. 3.4 Distribution density of particles with incoherent horizontal space-charge tune shift $\Delta\nu_x$, in units of the maximum $|\Delta\nu_{\text{spch}}^{\max}|$. Shown here is the numerical computation using one trillion particles populated in the beam cross section according to the bi-Gaussian distribution. The average and rms spread of the distribution are marked.

zero at the maximum tune shift $\Delta\nu_{\text{spch}}^{\text{max}}$. This is expected, because only those few particles at the center of the beam will have tune shift equal to $\Delta\nu_{\text{spch}}^{\text{max}}$. The distribution is skew with a peak near $\Delta\nu_x/|\Delta\nu_{\text{spch}}^{\text{max}}| \sim -0.65$, although the average tune shift is 0.63 of $\Delta\nu_{\text{spch}}^{\text{max}}$. This distribution of incoherent tune shift can now be employed in the dispersion relation to determine whether a certain transverse beam dynamic effect can be Landau-stabilized or not.

3.2.3 *Incoherence versus Coherence*

We now understand that the space-charge self-force of a bunch acting on the individual beam particles constitutes vertical and horizontal tune spreads. Usually, people say that large incoherent space-charge tune spreads will encompass a lot of parametric resonances in the ν_x-ν_y tune space and lead to instability. For this reason, the beam intensities in low-energy synchrotrons are limited by the horizontal and vertical space-charge tune spreads. The common rule of thumb is that incoherent self-field tune spreads should not exceed ~ 0.40 for a low-energy proton booster ring. At the same time, the widths of important stopbands should also be minimized by corrections made to the ring lattice. However, these self-field tune spreads at injection have never been well-measured beam parameters. It is difficult to measure because low-energy rings are usually ramped very rapidly. Thus, the self-field tune spreads diminish very quickly as the energy of the beam increases. Most low-energy rings that have large space-charge tune spreads are ramped by resonators. To measure the self-field tune spreads, we must disconnect the magnet-winding currents from the resonator so as to provide a longer interval for which the beam energy does not change. This is not always possible, because the beam will generally become unstable if it is allowed to stay at such low energy for a long time. If the condition is available, however, the tune spreads can be measured using a Schottky scan which shows the tunes of individual particles. The coherent tune shifts, on the other hand, can be measured very accurately by a technique called rf knockout. A narrow-band rf dipole signal is used to excite the beam. The betatron oscillation amplitude of the beam will increase linearly when the knockout frequency is equal to the coherent betatron frequency of the beam. If the knockout perturbation continues, the whole beam will be lost eventually.

As we shall see in Chapter 4, it is the *coherent* rather than the *incoherent* tune shifts that determine the instability of a beam. In fact, this is quite reasonable. When the bunch is oscillating at an integer coherent tune, we have the usual integer resonance. This leads to an instability because the center of the beam is performing betatron oscillations with a tune component that is at an

integer. The whole beam will become unstable. Although the dipole coherent space-charge tune shift vanishes because the beam moves rigidly, there are other coherent motion of the beam, for example, when the beam size oscillates without the beam center being moved. Some of these modes will be derived in Chapter 4 after introducing the envelope equation.

One may argue that if the incoherent tune spread covers an integer or half-integer resonance, *a small amount* of particles are hitting the resonance, and this small amount of the beam will be unstable. It will be shown in Chapter 4 that even this statement is incorrect, because the space-charge self-force decouples when the incoherent motion of the beam particles hit a resonance. Then why should we study the incoherent space-charge tune shift if the resonances have nothing to do with incoherent motion? The answer is: the higher-multipole coherent space-charge tune shifts depend on the incoherent space-charge tune shift. Thus, if the incoherent space-charge tune shift can be controlled, say by blowing up the transverse beam size, the higher-multipole coherent space-charge tune shifts will become smaller. In this way, a higher intensity beam will be possible before hitting the parametric resonances.

3.3 Tune Shift for a Beam

In this section, we want to derive the general expressions of incoherent and coherent tune shifts for a beam, unbunched or bunched, in terms of Laslett image coefficients and the self-force coefficients. These expressions are complicated by the fact that the magnetic field may or may not penetrate the vacuum chamber.

3.3.1 *Image Formation*

Let us recall how images of the beam are formed in the walls of the vacuum chamber or in the magnetic pole faces. For the electric field, because the parallel component vanishes on the walls of the vacuum chamber which we assume to be infinitely conducting, images will always be formed in the walls of the vacuum chamber. We therefore say that electric field is always *non-penetrating*. In this discussion, *penetrating* or *non-penetrating* always implies penetrating or non-penetrating the vacuum chamber.

The magnetic field is quite different. All low-frequency magnetic field will penetrate the vacuum chamber and form images in the magnet pole faces. If no magnet pole faces are present, we assume that magnetic field will go to infinity and will no longer affect the test particle. All high-frequency magnetic field will not penetrate the vacuum chamber and form images in the walls of the vacuum

chamber.

Before proceeding further, there is an important rule that is worth mentioning. For images in the walls of the vacuum chamber, the *electric* image coefficient $\epsilon_{1y,x}$ or $\xi_{1y,x}$ is always used, depending on whether it is incoherent or coherent, not only for electric images but also for magnetic images. The only difference is that, for magnetic images, we write $-\beta^2\epsilon_{1y,x}$ or $-\beta^2\xi_{1y,x}$. This is because the actual contribution of magnetic field from the images in the walls of the vacuum chamber is exactly the same as the electric field. The factor β^2 comes about because we need a factor of β from the magnetic part of the Lorentz force and another factor of β from the source which is the beam current. The negative sign comes about because the magnetic force on a beam is always in opposite direction to the electric force. As for images formed in the magnet pole faces, they can only be magnetic images, because electric field cannot penetrate the vacuum chamber. Their contributions will be $\beta^2\epsilon_{2y,x}$ or $\beta^2\xi_{2y,x}$, respectively, when the tune shifts are incoherent or coherent. Here, we have the same factor of β^2. However, there is *no negative sign*, which is just a convention. In other words, one may consider the negative sign to have been absorbed into the definition of $\beta^2\epsilon_{2y,x}$ or $\beta^2\xi_{2y,x}$. We can also say that electric image coefficients are for images in the walls of the vacuum chamber independent of whether the effect is electric or magnetic, while magnetic image coefficients are for images in the magnet pole faces. All these considerations are summarized in Table 3.1, where we also separate the coherent tune shift in Eq. (3.8) into two parts: the dc part $\partial\langle F_{\rm beam}\rangle/\partial y|_{\bar{y}=0}$ when the center of the beam is stationary and the ac part $\partial\langle F_{\rm beam}\rangle/\partial\bar{y}|_{y=0}$ when the center of the beam is oscillating.

Table 3.1 Relation of each component of the beam force to the image coefficients with images formed in the vacuum chamber or magnetic pole faces.

Beam force components	Images in vacuum chamber		Images in pole faces	Comments
	electric	magnetic	magnetic	
$\left.\frac{\partial\langle F_{\rm beam}\rangle}{\partial y}\right\|_{\bar{y}=0}$	$\frac{\epsilon_{1y,x}}{h^2}$	$-\beta^2\frac{\epsilon_{1y,x}}{h^2}$	$\beta^2\frac{\epsilon_{2y,x}}{g^2}$	incoherent dc coherent
$\left.\frac{\partial\langle F_{\rm beam}\rangle}{\partial y}\right\|_{\bar{y}=0}+\left.\frac{\partial\langle F_{\rm beam}\rangle}{\partial\bar{y}}\right\|_{y=0}$	$\frac{\xi_{1y,x}}{h^2}$	$-\beta^2\frac{\xi_{1y,x}}{h^2}$	$\beta^2\frac{\xi_{2y,x}}{g^2}$	coherent
$\left.\frac{\partial\langle F_{\rm beam}\rangle}{\partial\bar{y}}\right\|_{y=0}$		$-\beta^2\frac{\xi_{1y,x}-\epsilon_{1y,x}}{h^2}$	$\beta^2\frac{\xi_{2y,x}-\epsilon_{2y,x}}{g^2}$	ac coherent

3.3.2 *Coasting Beams*

Now we are ready to express the betatron tune shifts in terms of image coefficients. First, let us study the simpler case of a coasting beam, where the only ac magnetic field comes from betatron oscillations. The frequency of the magnetic field will be low when the betatron tune is close to an integer and the magnetic field may be penetrating. On the other hand, the frequency will be high when the betatron tune is close to a half integer and the magnetic field may be non-penetrating. The incoherent betatron tune shifts are:

$$\Delta\nu_{y,x\,\mathrm{incoh}} = -\frac{Nr_0R}{\pi\gamma\beta^2\nu_{0y,x}}\left[\frac{\epsilon_{1y,x}}{h^2} + \mathcal{F}\beta^2\frac{\epsilon_{2y,x}}{g^2} + (1-\beta^2)\frac{\epsilon_{y,x}^{\mathrm{spch}}}{a_y^2}\right]. \tag{3.65}$$

↑ electric image in vacuum chamber; ↑ magnetic image in magnet poles; ↑ self-field, $(1-\beta^2)$ gives balance between $\vec{E}$ and $\vec{H}$

Here, the first term comes from the electric images in the vacuum chamber since electric field is always non-penetrating and therefore the incoherent electric image coefficient $\epsilon_{1y,x}/h^2$ has been used. The second term comes the magnetic images in the magnet pole faces and therefore the incoherent magnetic image coefficient $\epsilon_{2y,x}$ has been used, together with the factor β^2 in front and g^2 in the denominator. The factor $\mathcal{F}$ represents the fraction of the ring circumference where the beam is sandwiched between magnetic pole faces. As stated before, the incoherent beam force comes from the images of the beam center which is not displaced or $\bar{y} = 0$. These images are not moving and the beam force is therefore static or dc, and the magnetic field is therefore landing on the magnet pole faces. The last term is just the space-charge contribution, where the 1 denotes the electric part and $-\beta^2$ the magnetic part, while a_y represents the half vertical height of the beam.

For the coherent tune shifts of a coasting beam, if the magnetic field is penetrating, we just have simply,

$$\Delta\nu_{y,x\,\mathrm{coh}} = -\frac{Nr_0R}{\pi\gamma\beta^2\nu_{0y,x}}\left[\frac{\xi_{1y,x}}{h^2} + \mathcal{F}\beta^2\frac{\xi_{2y,x}}{g^2}\right], \tag{3.66}$$

↑ electric image in vacuum chamber; ↑ magnetic image in magnet poles

where all the magnetic field penetrates the vacuum chamber and forms images in the magnet pole faces. Thus only the coherent image coefficients are present. Note that there is no space-charge term because the center of the beam does not see the self-force among beam particles.

When the magnetic field is non-penetrating, we have instead

$$\Delta\nu_{y,x\,\mathrm{coh}} = -\frac{Nr_0R}{\pi\gamma\beta^2\nu_{0y,x}}\left[\underset{\substack{\uparrow\\ \text{electric image}\\ \text{in vacuum chamber}}}{\frac{\xi_{1y,x}}{h^2}} + \mathcal{F}\beta^2\underset{\substack{\uparrow\\ \text{magnetic image}\\ \text{in magnet poles}}}{\frac{\epsilon_{2y,x}}{g^2}} - \beta^2\underset{\substack{\uparrow\\ \text{ac magnetic image}\\ \text{in vacuum chamber}}}{\frac{\xi_{1y,x}-\epsilon_{1y,x}}{h^2}}\right]. \tag{3.67}$$

To understand this expression, recall the magnetic part of beam force on the right side of Eq. (3.5). The ac magnetic field comes from the betatron oscillation of the whole beam and has its source coming from the second term on the right side only, since we require a moving beam center or $\bar{y} \neq 0$. According to Table 3.1, the contribution is therefore $-\beta^2(\xi_{1y,x}-\epsilon_{1y,x})/h^2$. The dc part of the coherent magnet beam force is the first term on the right side of Eq. (3.5). Since this dc field produces images in the magnet pole faces, we have therefore the second term of Eq. (3.67). The first term comes from the electric component of the coherent beam force. After re-arrangement, the coherent tune shift with penetrating fields reads

$$\Delta\nu_{y,x\,\mathrm{coh}} = -\frac{Nr_0R}{\pi\gamma\beta^2\nu_{0y,x}}\left[\frac{(1-\beta^2)\xi_{1y,x}}{h^2} + \beta^2\frac{\epsilon_{1y,x}}{h^2} + \mathcal{F}\beta^2\frac{\epsilon_{2y,x}}{g^2}\right]. \tag{3.68}$$

3.3.3 *Bunched Beams*

For bunched beam, we would like to compute the maximum betatron tune shifts when the beam current is at its local maximum. We therefore divide by the bunching factor B suitably so that the bunch intensity will be properly enhanced. Notice that ac magnetic field now comes from two sources: transverse betatron oscillation of the bunch and longitudinal or axial bunching of the beam. Although both effects are ac, their frequencies are in general very different. The frequency of transverse betatron oscillation is $(n-\nu_{0y,x})\omega_0/(2\pi)$, where n is the revolution harmonic closest to the tune. These frequencies are therefore only fractions of the revolution frequency. On the other hand, the axial bunch frequency is a $h\omega_0/(2\pi)$ with h the rf harmonic, which is often many times revolution frequency. For this reason, it is reasonable to consider the ac magnetic fields arising from axial bunching *always non-penetrating*, while the ac magnetic fields arising from betatron oscillation sometimes non-penetrating and sometimes penetrating.

In the expressions below, we try also to include the effect of trapped particles that carry charges of the opposite sign. Take a proton beam, for example, electrons can be trapped, giving a neutralization coefficient χ_e, which is defined as the ratio of the total number of trapped electrons to the total number of

protons. (For an antiproton beam, the particles trapped are positively charged ions.) The trapped electrons will not travel longitudinally. Therefore, they only affect the electric force but not the magnetic force. In other words, for electric contributions, we replace 1 by $(1-\chi_e)$.

The incoherent tune shift for a bunched beam is expressed as

$$\Delta\nu_{y,x\,\mathrm{incoh}} = -\frac{Nr_0R}{\pi\gamma\beta^2\nu_{0y,x}}\left[\frac{1-\chi_e}{B}\frac{\epsilon_{1y,x}}{h^2} + \mathcal{F}\beta^2\frac{\epsilon_{2y,x}}{g^2} - \right.$$
$$\left. -\beta^2\left(\frac{1}{B}-1\right)\frac{\epsilon_{1y,x}}{h^2} + (1-\chi_e-\beta^2)\frac{1}{B}\frac{\epsilon^{\mathrm{spch}}_{y,x}}{a_y^2}\right]. \qquad (3.69)$$

($\epsilon_{2y,x}$: magnetic image in magnet poles; $\epsilon_{1y,x}$: electric image in vacuum chamber; $\left(\frac{1}{B}-1\right)\frac{\epsilon_{1y,x}}{h^2}$: ac magnetic image in axial bunching; $\frac{1}{B}\frac{\epsilon^{\mathrm{spch}}_{y,x}}{a_y^2}$: self-field)

The second term represents magnetic fields of a stationary beam and its images and therefore the usual incoherent magnetic image coefficient $\epsilon_{2y,x}$, which describes dc magnetic fields penetrating the vacuum chamber and landing at the magnet poles. Here, there is no division by the bunching factor B, because we are talking about the dc fields coming from the *average* beam current.

The third term is for the ac magnetic fields generated from axial bunching and a division by B is therefore necessary. Since the ac magnetic fields are non-penetrating, their contribution is the same as that of the incoherent electric field and therefore the factor $-\beta^2\epsilon_{1y,x}$. We must remember that there is a dc part that lands on the magnet pole faces which we have considered already and must not be included here again. For this reason, we need to replace B^{-1} by $B^{-1}-1$. The accuracy of this term can be inferred by noticing its disappearance when we let $B \to 1$, or the bunched beam becomes totally unbunched. After re-arrangement, this incoherent tune shift becomes

$$\Delta\nu_{y,x\,\mathrm{incoh}} = -\frac{Nr_0R}{\pi\gamma\beta^2\nu_{0y,x}}\left[\left(\frac{1-\chi_e-\beta^2}{B}+\beta^2\right)\frac{\epsilon_{1y,x}}{h^2}+\mathcal{F}\beta^2\frac{\epsilon_{2y,x}}{g^2}+(1-\chi_e-\beta^2)\frac{\epsilon^{\mathrm{spch}}_{y,x}}{Ba_y^2}\right]. \qquad (3.70)$$

For coherent motion with penetrating magnetic fields from betatron oscillation, we have

$$\Delta\nu_{y,x\,\mathrm{coh}} = -\frac{Nr_0R}{\pi\gamma\beta^2\nu_{0y,x}}\left[\frac{1-\chi_e}{B}\frac{\xi_{1y,x}}{h^2} + \mathcal{F}\beta^2\frac{\xi_{2y,x}}{g^2} - \beta^2\left(\frac{1}{B}-1\right)\frac{\xi_{1y,x}}{h^2}\right]. \qquad (3.71)$$

($\xi_{1y,x}$: electric image in vacuum chamber; $\xi_{2y,x}$: magnetic image in magnet poles; $\left(\frac{1}{B}-1\right)\frac{\xi_{1y,x}}{h^2}$: ac magnetic image from axial bunching)

where the third term is contributed by the magnetic field of bunching frequencies, which cannot penetrate the vacuum chamber. The magnetic fields divide into the dc part and the ac part in exactly the same way as Eq. (3.69), the expression for incoherent tune shift. Because we are talking about coherent tune shifts, the coefficients $\epsilon_{2y,x}$ and $\epsilon_{1y,x}$ are replaced, respectively, by $\xi_{2y,x}$ and $\xi_{1y,x}$. After re-arrangement, the coherent tune shifts with penetrating magnetic fields from betatron oscillation becomes

$$\Delta\nu_{y,x\,\mathrm{coh}} = -\frac{Nr_0R}{\pi\gamma\beta^2\nu_{0y,x}}\left[\left(\frac{1-\chi_e-\beta^2}{B}+\beta^2\right)\frac{\xi_{1y,x}}{h^2}+\mathcal{F}\beta^2\frac{\xi_{2y,x}}{g^2}\right]. \tag{3.72}$$

Finally, we come to ac magnetic fields that are non-penetrating coming from both axial bunching and betatron oscillation. The coherent tune shifts are

$$\Delta\nu_{y,x\,\mathrm{coh}} = -\frac{Nr_0R}{\pi\gamma\beta^2\nu_{0y,x}}\left[\frac{1-\chi_e}{B}\frac{\xi_{1y,x}}{h^2}+\mathcal{F}\beta^2\frac{\epsilon_{2y,x}}{g^2} -\beta^2\frac{\xi_{1y,x}-\epsilon_{1y,x}}{h^2}-\beta^2\left(\frac{1}{B}-1\right)\frac{\xi_{1y,x}}{h^2}\right]. \tag{3.73}$$

electric image in vacuum chamber; magnetic image in magnet poles; ac magnetic image from transverse motion; ac magnetic image from axial bunching

Here, the axial bunching parts are very exactly the same as in Eq. (3.71) because they describe exactly the same ac magnetic fields coming from axial bunching. As for the dc magnetic fields, the contribution in Eq. (3.71) comes from both terms of the beam force on the right side of Eq. (3.5) and contributes the coefficient $\xi_{2y,x}$. Here the dc magnetic fields come from only the first term of the beam force and contribute $\epsilon_{1y,x}$ instead, for exactly the same reason as in Eq. (3.65). The part of the second term that comes from betatron oscillation of the beam gives rise to the second last term of Eq. (3.73), for exactly the same reason as in Eq. (3.65). After re-arrangement, this coherent tune shift takes the form

$$\Delta\nu_{y,x\,\mathrm{coh}} = -\frac{Nr_0R}{\pi\gamma\beta^2\nu_{0y,x}}\left[\frac{1-\chi_e-\beta^2}{B}\frac{\xi_{1y,x}}{h^2}+\mathcal{F}\beta^2\frac{\epsilon_{2y,x}}{g^2}+\beta^2\frac{\epsilon_{1y,x}}{h^2}\right]. \tag{3.74}$$

3.4 Other Vacuum Chamber Geometries

The electric and magnetic image coefficients have been computed for other geometries of the vacuum chamber: circular cross section, elliptical cross section, [2, 3, 5] rectangular cross section, [6] and even with the beam off-centered.

The computations for the rectangular and elliptical cross sections involve one or more than one conformal mappings and the results are given in terms of elliptical functions.

3.4.1 *Circular Vacuum Chamber*

The situation of circular cross section with an on-center beam is rather simple. Consider a line charge of linear density λ_1 at location $x = 0$ and $y = \bar{y}_1$ inside the cylindric beam pipe of radius b with infinitely-conducting walls. We place an image line charge of linear density λ_2 at location $x = 0$ and $y = \bar{y}_2$ as shown in left plot of Fig. 3.5.

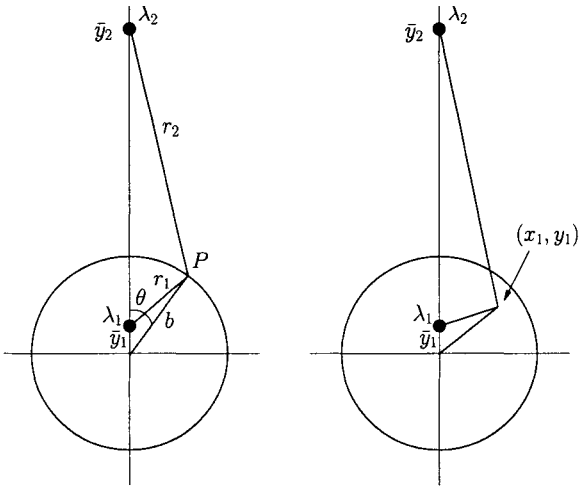


Fig. 3.5 Left plot illustrates a line charge density λ_1 inside a cylindrical beam pipe offset vertically by $\bar{y}_1$. There is an image line charge density λ_2 at $\bar{y}_2$ such that the electric potential vanishes at every point P at the beam pipe. Right plot shows the combined electric force acting on a witness line charge at (x_1, y_1).

The electric potential at point P on a chamber wall at an angle θ is given by

$$V_P = -\frac{e\lambda_1}{2\pi\epsilon_0} \ln r_1 - \frac{e\lambda_2}{2\pi\epsilon_0} \ln r_2, \tag{3.75}$$

where

$$\begin{cases} r_1^2 = \bar{y}_1^2 + b^2 - 2\bar{y}_1 b \cos\theta, \\ r_2^2 = \bar{y}_2^2 + b^2 - 2\bar{y}_2 b \cos\theta. \end{cases} \tag{3.76}$$

Two assertions are made:

$$\bar{y}_2 = \frac{b^2}{\bar{y}_1} \qquad \text{and} \qquad \lambda_2 = -\lambda_1. \tag{3.77}$$

We obtain from the first assertion that $r_2^2 = r_1^2(b^2/\bar{y}_1^2)$. Then the second assertion ensures that the electric potential V_P vanishes aside from a constant for any point on the wall of the cylindrical vacuum chamber.

To compute the image force, place a witness line charge at $x = x_1$ and $y = y_1$, as illustrated in the right plot of Fig. 3.5. The electric force exerted on the witness charge by the image has the y component

$$\frac{F_y^{\text{elec}}}{e} = \frac{e\lambda_1}{2\pi\epsilon_0} \frac{\dfrac{b^2}{\bar{y}_1} - y_1}{x_1^2 + \left(\dfrac{b^2}{\bar{y}_1} - y_1\right)^2} \longrightarrow \frac{e\lambda_1}{2\pi\epsilon_0} \frac{\bar{y}_1}{b^2}, \tag{3.78}$$

where in the last step only terms linear in y_1 and $\bar{y}_1$ are retained. According to Eq. (3.13),

$$\Delta\nu_{y\,\text{incoh}} = -\frac{Nr_0R}{\pi\gamma\beta^2\nu_{0y}} \frac{\epsilon_{1y}}{b^2} \qquad \text{and} \qquad \Delta\nu_{y\,\text{coh}} = -\frac{Nr_0R}{\pi\gamma\beta^2\nu_{0y}} \frac{\xi_{1y}}{b^2}, \tag{3.79}$$

we immediately obtain the incoherent and coherent electric image coefficients for a circular beam pipe:

$$\epsilon_{1y} = 0 \qquad \text{and} \qquad \xi_{1y} = \frac{1}{2}. \tag{3.80}$$

Because of the cylindrical symmetry, we also have

$$\epsilon_{1x} = 0 \qquad \text{and} \qquad \xi_{1x} = \frac{1}{2}. \tag{3.81}$$

It is not surprising to see the incoherent electric image coefficients vanish. This is because at the point of observation of the witness charge, $\vec{\nabla} \cdot \vec{E} = 0$, leading to $\epsilon_{1x} + \epsilon_{1y} = 0$.

3.4.2 *Elliptical Vacuum Chamber*

Off-Centered Beam

The elliptical cross section of the vacuum chamber has *half width* w and *half height* $h < w$. They are also known as the major and minor radii. The focal points are on the horizontal axis at distance $\varepsilon = \sqrt{w^2 - h^2}$ from the center. Consider a line beam on the horizontal axis at distance x from the center. The image coefficients can be obtained by performing two conformal mappings, transforming the elliptical beam pipe into a plane. [2, 3, 5] The derivations are rather involved. Here, we only present the results. When

the beam is inside the focal points† or $0 < x < \varepsilon$,

$$\epsilon_{1y} = -\epsilon_{1x} = \frac{h^2}{12W^2}\left[A\left(\frac{2K}{\pi\,\mathrm{cn}\,\mathrm{dn}}\right)^2 + \frac{6Kk'^2 x\,\mathrm{sn}}{\pi W\,\mathrm{cn}\,\mathrm{dn}} - \frac{4\varepsilon^2 + 5x^2}{2W^2}\right], \tag{3.82}$$

$$\xi_{1y} = \frac{h^2}{4W^2}\left[\left(\frac{2K\,\mathrm{dn}}{\pi\,\mathrm{cn}}\right)^2 + \frac{2Kk'^2 x\,\mathrm{sn}}{\pi W\,\mathrm{cn}\,\mathrm{dn}} - \frac{\varepsilon^2 + x^2}{W^2}\right], \tag{3.83}$$

$$\xi_{1x} = -\frac{h^2}{4W^2}\left[(1 - k^2\mathrm{sn}^4)\left(\frac{2Kk'}{\pi\,\mathrm{cn}\,\mathrm{dn}}\right)^2 + \frac{2Kk'^2 x\,\mathrm{sn}}{\pi W\,\mathrm{cn}\,\mathrm{dn}} - \frac{\varepsilon^2 + x^2}{W^2}\right], \tag{3.84}$$

where

$$A = (2 - k^2) - \tfrac{1}{2}(1 + k^2)^2\mathrm{sn}^2 - k^2(1 - 2k^2)\,\mathrm{sn}^4, \tag{3.85}$$

and

$$W^2 = \varepsilon^2 - x^2 = w^2 - h^2 - x^2. \tag{3.86}$$

In above, sn, cn, and dn are the Jacobian elliptic functions. Their arguments are

$$\left(\frac{2K(k)}{\pi}\sin^{-1}\frac{x}{\varepsilon},\, k\right), \tag{3.87}$$

where $K = K(k)$ is the complete elliptical function of the first kind and k is called the *modulus.*‡ The complementary modulus k' is given by

$$k' = \sqrt{1 - k^2}. \tag{3.88}$$

We first compute the *nome*, defined as

$$q = \exp\left[-\frac{\pi K'(k)}{K(k)}\right], \tag{3.89}$$

using the expression

$$q = \frac{w - h}{w + h}, \tag{3.90}$$

†These expressions are presented from Eqs. (74) to (76) in Ref. [3]. The expression following Eq. (74) is incorrect that the factor $(1 + k^2 + k^4)$ in the middle term should have been $(1 + 2k^2 + k^4)$. The first factor in Eq. (76) after the opening square bracket, $(1 - k^2S^2)$, should have been $(1 - k^2S^4)$.

‡Some authors also define the *parameter* $m = k^2$ and the *complementary parameter* $m' = k'^2 = 1 - m$.

then the complementary modulus k' using[§]

$$k'^{\frac{1}{2}} = \frac{1 + 2\sum_{s=1}^{\infty}(-1)^s q^{s^2}}{1 + 2\sum_{s=1}^{\infty} q^{s^2}}, \tag{3.91}$$

and finally the modulus k through Eq. (3.88).

Notice that each term in Eqs. (3.82), (3.83), and (3.84) becomes singular when the beam approaches the focal points of the elliptic cross section. However, the singularities cancel each other in each expression to arrive at a finite value as $x \to \varepsilon$. For this reason double precision must be used in the evaluation of these expressions. Right at the focal points the image coefficients are given by the expressions:[¶]

$$\epsilon_{1y} = -\epsilon_{1x} = \frac{h^2}{360\varepsilon^2}\left[(1-16k^2+k^4)\left(\frac{2K}{\pi}\right)^4 + 10(1+k^2)\left(\frac{2K}{\pi}\right)^2 - 11\right], \tag{3.92}$$

$$\xi_{1y} = \frac{h^2}{180\varepsilon^2}\left[(2+13k^2+2k^4)\left(\frac{2K}{\pi}\right)^4 + 5(1+k^2)\left(\frac{2K}{\pi}\right)^2 - 7\right], \tag{3.93}$$

$$\xi_{1x} = \frac{-h^2}{180\varepsilon^2}\left[2(1-16k^2+k^4)\left(\frac{2K}{\pi}\right)^4 + 5(1+k^2)\left(\frac{2K}{\pi}\right)^2 - 7\right]. \tag{3.94}$$

When the beam is outside the focal points or $x > \varepsilon$, the image coefficients assume the form[‖]

$$\epsilon_{1y} = -\epsilon_{1x} = \frac{h^2}{12W^2}\left[B_1\left(\frac{2K}{\pi \operatorname{sn}\operatorname{cn}}\right)^2 + \frac{6Kx\operatorname{dn}}{\pi W \operatorname{sn}\operatorname{cn}} - \frac{4\varepsilon^2 + 5x^2}{2W^2}\right], \tag{3.95}$$

$$\xi_{1y} = \frac{h^2}{4W^2}\left[\left(\frac{2K\operatorname{cn}}{\pi \operatorname{sn}}\right)^2 + \frac{2Kx\operatorname{dn}}{\pi W \operatorname{sn}\operatorname{cn}} - \frac{\varepsilon^2 + x^2}{W^2}\right], \tag{3.96}$$

[§]This formula was stated wrongly in Eq. (6) of Ref. [6].

[¶]in Ref. [3], in Appendix D(f), the first term of ξ_{1y} was $(2 - 13k^2 + 2k^4)$ which has a wrong sign preceding $13k^2$ as compared with our Eq. (3.93). In Ref. [5], Table II, Part (c), the expression for $\epsilon_{1y,x}$ when $x = \varepsilon$, has an overall incorrect sign.

[‖]In Ref. [3], Appendix D(e), the expressions for ϵ_{1y}, ξ_{1y}, and ξ_{1x} all have negative signs in front of the middle terms inside the square brackets. They should be all positive as given by Eqs. (3.95), (3.96), and (3.97). The expression for B_1 in Ref. [3] has the typo that S in the second term on the right side should have been S^2.

$$\xi_{1x} = -\frac{h^2}{4W^2}\left[B_2\left(\frac{2K}{\pi\,\mathrm{sn}\,\mathrm{cn}}\right)^2 + \frac{2Kx\,\mathrm{dn}}{\pi W\,\mathrm{sn}\,\mathrm{cn}} - \frac{\varepsilon^2+x^2}{W^2}\right], \tag{3.97}$$

where

$$B_1 = \tfrac{3}{2} - \tfrac{1}{2}\left(8-k'^2\right)\mathrm{sn}^2 + \left(1+k'^2\right)\mathrm{sn}^4, \qquad B_2 = 1 - 2\,\mathrm{sn}^2 + k'^2\mathrm{sn}^4. \tag{3.98}$$

Unlike the situation when the beam is inside the focal points, here

$$W^2 = x^2 - \varepsilon^2 = x^2 - w^2 + h^2, \tag{3.99}$$

and the Jacobian elliptic functions sn, cn, and dn have arguments

$$\left(\frac{2K(k)}{\pi}\cosh^{-1}\frac{x}{\varepsilon},\, k'\right). \tag{3.100}$$

However, the nome q, modulus k, and complementary modulus k' are the same as given by Eqs. (3.90), (3.88), and (3.91), independent of whether the beam is inside or outside the focal points.

Centered Beam

When the beam is right at the center of the vacuum chamber, $x = 0$. The arguments of the elliptic functions in Eq. (3.87) simplify to $(0, k)$ and we have $\mathrm{sn} = 0$, $\mathrm{cn} = \mathrm{dn} = 1$. The expressions for the image coefficients in Eqs. (3.82), (3.83), and (3.84) simplify readily to

$$\epsilon_{1y} = -\epsilon_{1x} = \frac{h^2}{12\varepsilon^2}\left[\left(1+k'^2\right)\left(\frac{2K}{\pi}\right)^2 - 2\right], \tag{3.101}$$

$$\xi_{1y} = \frac{h^2}{4\varepsilon^2}\left[\left(\frac{2K}{\pi}\right)^2 - 1\right], \qquad \xi_{1x} = \frac{h^2}{4\varepsilon^2}\left[1 - \left(\frac{2Kk'}{\pi}\right)^2\right]. \tag{3.102}$$

3.4.3 *Rectangular Vacuum Chamber*

Off-Centered Beam

To conform with the elliptical beam pipe, let h and w be, respectively, the *half height* and *half width* of the rectangular cross section.** Conformal mapping is employed to open up the rectangular beam pipe into a plane. Here, we omit the derivation and give only the results. When the beam is on the horizontal

**Note that in Ref. [6], h and w are the *full height* and *full width* of the rectangular cross section.

axis but with fractional offset g (or at distance gw from the center), the image coefficients are[††]

$$\epsilon_{1y} = -\epsilon_{1x} = \frac{K^2(k)}{4}\left[\frac{k'^4 \mathrm{sn}^2\,\mathrm{cn}^2}{2\,\mathrm{dn}^2} - \frac{k'^2(1-2\,\mathrm{sn}^2)}{3} - \frac{\mathrm{dn}^2\,(3-4\,\mathrm{sn}^2+4\,\mathrm{sn}^4)}{6\,\mathrm{sn}^2\,\mathrm{cn}^2}\right], \tag{3.103}$$

$$\xi_{1y} = \frac{K^2(k)}{4}\,\frac{k'^4 \mathrm{sn}^2\,\mathrm{cn}^2}{\mathrm{dn}^2}, \tag{3.104}$$

$$\xi_{1x} = \frac{K^2(k)}{4}\left[k'^2(1-2\,\mathrm{sn}^2) + \frac{\mathrm{dn}^2}{\mathrm{sn}^2\,\mathrm{cn}^2}\right]. \tag{3.105}$$

The arguments of the elliptic functions sn, cn, dn are

$$\left(\frac{K(k)y_0}{h},\, k'\right) = \left(\frac{K(k)w}{h}(1-g),\, k'\right), \tag{3.106}$$

where $y_0 = (1-g)w$ is the position of the beam measured from one vertical wall of the vacuum chamber, and $K(k)$ is the complete elliptical function of the first kind. Note that this argument is very different from those for the elliptical beam pipe. Here, the nome is computed according to

$$q = e^{-2\pi w/h}, \tag{3.107}$$

which is also quite different from the one used in Eq. (3.90) for the elliptical beam pipe. After obtaining the nome, the complementary modulus k' can next be computed from Eq. (3.91), from which the modulus k can be obtained via Eq. (3.88).

Centered Beam

For a centered beam, $g = 0$, the arguments of the elliptical functions become

$$\left(\frac{K(k)w}{h},\, k'\right) = \left(\tfrac{1}{2}K'(k),\, k'\right) = \left(\tfrac{1}{2}K(k'),\, k'\right). \tag{3.108}$$

Notice that the periods of sn, cn, dn with modulus k' are $4K(k')$. The elliptical functions simplify to [7]

$$\mathrm{sn}\left(\frac{K(k')}{2}, k'\right) = \frac{1}{\sqrt{1+k}},\quad \mathrm{cn}\left(\frac{K(k')}{2}, k'\right) = \frac{\sqrt{k}}{\sqrt{1+k}},\quad \mathrm{dn}\left(\frac{K(k')}{2}, k'\right) = \sqrt{k}. \tag{3.109}$$

[††]Equation (3.103) was reported in Eq. (53) of Ref. [6] with a wrong sign in front of sn_{10}^4 inside the last term in the curly brackets.

The electric image coefficients simplify to

$$\epsilon_{1y} = -\epsilon_{1x} = \frac{K^2(k)}{12}\left(1 - 6k + k^2\right), \tag{3.110}$$

$$\xi_{1y} = \frac{K^2(k)}{4}\left(1 - k\right)^2, \qquad \xi_{1x} = K^2(k)\, k, \tag{3.111}$$

which involve only the complete elliptical function of the first kind, while all the Jacobian elliptical functions disappear.

Comments

(1) Since q decreases exponentially as w/h increases, very accurate value of k' can be computed with Eq. (3.91). For example, even for $1 \geq w/h \geq 0.2$, 14-figure accuracy can be readily obtained for k' when the summations in the numerator and denominator are extended to $s = 5$. Next, with the aid of Eq. (3.88), very accurate value of k^2 can be acquired. In fact, for centered beam, there is no need to go to $w/h < 1$, because we can interchange the role of w and h.

(2) When $w/k > 1$, q becomes very small and k' is very close to 1. (For example, $k^2 = 2.9437 \times 10^{-3}$, 5.5796×10^{-5} and 1.0420×10^{-7}, respectively, when $w/h = 1$, 2 and 3.) Equation (3.88) can no longer to used to give accurate result for k. To preserve accuracy, we must expand k^2 as power series in q instead with the aid of Eqs. (3.88) and (3.91):

$$\begin{aligned} k^2 =& 16q\Big(1 - 8q + 44q^2 - 192q^3 + 718q^4 - 2400q^5 \\ &+ 7352q^6 - 20992q^7 + 56549q^8 - \cdots\Big), \end{aligned} \tag{3.112}$$

from which 14-figure accuracy can be obtained when $w/k \geq 1$.

(3) Because $k^2 \ll 1$ when $w/h > 1$, Eqs. (3.110) and (3.111) can be viewed as expansions from values for the infinite horizontal plates. In fact, with

$$K(k) = \frac{\pi}{2}\left[1 + \frac{1}{4}k^2 + \frac{9}{64}k^4 + \mathcal{O}\left(k^6\right)\right], \tag{3.113}$$

we can write

$$\epsilon_{1y} = -\epsilon_{1x} = \frac{\pi^2}{48}\left[1 - 6k + \frac{3}{2}k^2 - 3k^3 + \frac{27}{32}k^4 - \frac{33}{16}k^5 + \mathcal{O}\left(k^6\right)\right], \tag{3.114}$$

$$\xi_{1y} = \frac{\pi^2}{16}\left[1 - 2k + \frac{3}{2}k^2 - k^3 + \frac{27}{32}k^4 - \frac{11}{16}k^5 + \mathcal{O}\left(k^6\right)\right], \tag{3.115}$$

$$\xi_{1x} = \frac{\pi^2}{4} k \left[1 + \frac{1}{2}k^2 + \frac{11}{32}k^4 + \mathcal{O}(k^6)\right]. \tag{3.116}$$

3.4.4 *Closed Yoke*

So far the image coefficients are derived using ideal boundary conditions; i.e., the beam pipe has infinitely conducting walls while the magnetic material has infinite relative permeability. Mathematically, it is impossible to compute the magnetic image coefficients for a closed cylindrical iron yoke that has infinite relative permeability. In fact, no solution exists for a closed iron yoke of any geometry. This is because Ampere's law requires

$$\oint \vec{H} \cdot d\vec{\ell} = I. \tag{3.117}$$

For a beam of current I, the component of magnetic field $\vec{H}$ along the inner surface of the iron yoke is therefore nonzero. Thus, the magnetic flux density $\vec{B}$ inside the yoke becomes infinite. Speaking in the reverse order, if the magnetic flux density inside the yoke is finite, the magnetic field $\vec{H}$ along the inner surface must vanish. From Ampere's law, one gets $I = 0$, or no current is allowed to flow through the yoke.

For a normal-temperature magnet, we like to operate in the linear region of the B-$\mu_0 H$ hysteresis curve, for example at Point N in Fig. 3.6, in order to take advantage of the large relative magnetic permeability, $\mu_r \sim 1000$. Then, most of the magnetic flux density across the pole gap is supplied by μ_r and only a few percents come from the winding current. Such operation limits the magnetic flux density to $B_{\max} \sim 1.8$ T. This explains why the iron yoke is mostly made

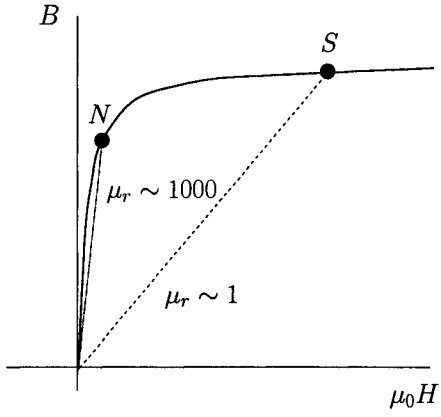


Fig. 3.6 B-$\mu_0 H$ hysteresis plot showing the operation of normal temperature magnet at Point N where the relative magnetic permeability μ_r is large. The operation of superconducting magnet is at Point S where the iron yoke is at saturation and $\mu_r \approx 1$.

up of two pieces glued together with some medium. In that case, $\mu_0 \vec{H}$ will only be large in the medium but relatively small inside the yoke and a much larger beam current will be allowed.

The story for superconducting magnets is quite different. Here, the magnetic flux density is mostly supplied by the high winding current, while the iron yoke is always saturated. The operation point in the hysteresis curve is now at S of Fig. 3.6 in the large $\mu_0 H$ region where the local slope is 1. Thus the relative permeability μ_r becomes close to 1 and is very much less than the linear region of the hysteresis curve. If a closed iron yoke is used, the maximum beam current allowed by Ampere's law becomes $\mu_r \sim 1000$ times larger at operation point S than at operation point N.

When the relative permeability is finite, the Laplace equation can still be solved using the image method, provided there is sufficient symmetry in the geometry. Readers with interest are referred to, for example, the book by Binns and Lawrenson. [8]

In Table 3.2, we tabulate the self-field coefficients for uniformly charged beams and image coefficients for centroid beams. [9]

3.5 Connection with Impedance

3.5.1 *Impedance from Images*

In Eq. (3.5), the term proportional to y on the right side is absorbed into the betatron tune shift so that the bare tune ν_{0y} becomes the incoherent tune ν_y. The equation becomes

$$\frac{d^2y}{ds^2} + \frac{\nu_y^2}{R^2} y = \frac{1}{\gamma m v^2} \left. \frac{\partial \langle F_{\text{beam}}(y, \bar{y}) \rangle}{\partial \bar{y}} \right|_{y=0} \bar{y}. \tag{3.118}$$

The coherent force on the right is related to the transverse wake function and therefore the transverse impedance. The connection can be easily made using Eq. (1.43), which says

$$\left. \frac{\partial \langle F_{\text{beam}}(y, \bar{y}) \rangle}{\partial \bar{y}} \right|_{y=0} \bar{y} = \frac{ieZ_1^{\perp} \beta I \bar{y}}{C} = \frac{ie^2 Z_1^{\perp} \beta^2 c \lambda \bar{y}}{C}, \tag{3.119}$$

where C is the circumference of the accelerator ring. On the other hand, in Eq. (3.12), according to the the definition of the image coefficient,

$$eE_y(y, \bar{y})|_{y=0} = \frac{e^2 \lambda Z_0 c}{\pi} \frac{\xi_{1y} - \epsilon_{1y}}{h^2} \bar{y}. \tag{3.120}$$

Table 3.2 Self-field coefficients for uniformly charged beam and image coefficients for centered beam.

Coeff.	Circular	Elliptical	Rectangular	Parallel Plates
ϵ_y^{spch}	$\frac{1}{2}$	$\frac{a_y}{a_x+a_y}$		
ϵ_x^{spch}	$\frac{1}{2}$	$\frac{a_y^2}{a_x(a_x+a_y)}$		
ϵ_{1y}	0	$\frac{h^2}{12\varepsilon^2}\left[(1+k'^2)\left(\frac{2K}{\pi}\right)^2-2\right]$	$\frac{K^2(k)}{12}(1-6k+k^2)$	$\frac{\pi^2}{48}$
ϵ_{1x}	0	$\frac{-h^2}{12\varepsilon^2}\left[(1+k'^2)\left(\frac{2K}{\pi}\right)^2-2\right]$	$\frac{-K^2(k)}{12}(1-6k+k^2)$	$-\frac{\pi^2}{48}$
ϵ_{2y}	*	*	*	$\frac{\pi^2}{24}$
ϵ_{2x}	*	*	*	$-\frac{\pi^2}{24}$
ξ_{1y}	$\frac{1}{2}$	$\frac{h^2}{4\varepsilon^2}\left[\left(\frac{2K}{\pi}\right)^2-1\right]$	$\frac{K^2(k)}{4}(1-k)^2$	$\frac{\pi^2}{16}$
ξ_{1x}	$\frac{1}{2}$	$\frac{h^2}{4\varepsilon^2}\left[1-\left(\frac{2Kk'}{\pi}\right)^2\right]$	$K^2(k)k$	0
ξ_{2y}	*	*	*	$\frac{\pi^2}{16}$
ξ_{2x}	*	*	*	0

*ϵ_2 and ξ_2 for closed magnetic boundary (e.g., circular, elliptic, or rectangular) cannot be calculated when the relative permeability $\mu_r \to \infty$, since the induced magnetic field would not permit a charged beam to pass through because the field energy would become infinite. Closed magnetic yokes are used in superconducting magnets, but there the coefficients $\epsilon_2 = \xi_2 \to 0$, since the magnetic material is driven completely into saturation ($\mu_r \to 1$).

$K(k)$ is the complete elliptic integral of the first kind. k is determined from $(w-h)/(w+h) = \exp(-\pi K'/K)$ for the elliptical cross section but $w/h = K'/(2K)$ for the rectangular cross section, where w and h are the half width and half height, with $\varepsilon = \sqrt{w^2-h^2}$, and $K' = K(k')$ with $k' = \sqrt{1-k^2}$.

As a result, we obtain

$$Z_1^{y,x} = -i\frac{Z_0 C}{\pi\gamma^2\beta^2}\frac{\xi_{1y,x}-\epsilon_{1y,x}}{h^2}. \tag{3.121}$$

For a circular beam pipe, $\xi_{1y,x} = \frac{1}{2}$ and $\epsilon_{1y,x} = 0$. This is just exactly the second half of the transverse space-charge impedance in Eq. (1.54). Thus, the transverse space-charge impedance can be interpreted as the summation of two parts: the

part proportional to $a_{y,x}^{-2}$ is the self-field contribution, with $a_{y,x}$ denoting the vertical/horizontal radius of the beam, and the part proportional to h^{-2} is the wall image contribution, with h denoting the half height of the vacuum chamber. We can therefore rewrite the expression in a more general form

$$Z_1^{y,x} = i\frac{Z_0 C}{\pi\gamma^2\beta^2}\left[\frac{\epsilon_{y,x}^{\text{spch}}}{a_y^2} - \frac{\xi_{1y,x}-\epsilon_{1y,x}}{h^2}\right]. \tag{3.122}$$

It is important to distinguish the difference between the force generating the coherent tune shift and the force generating the transverse impedance. The former involves the ξ_1 coefficient while the latter involves $\xi_1 - \epsilon_1$. The coherent tune shift is the result of all forces acting on the center of the beam at $\bar{y}$, while the transverse impedance comes from the force generated by the center motion of the beam on an individual particle. In other words,

$$\Delta\nu_{y\,\text{coh}} \propto \left.\frac{\partial\langle F_{\text{beam}}(y,\bar{y})\rangle}{\partial y}\right|_{\bar{y}=0} + \left.\frac{\partial\langle F_{\text{beam}}(y,\bar{y})\rangle}{\partial \bar{y}}\right|_{y=0},$$

$$Z_1^y \propto \left.\frac{\partial\langle F_{\text{beam}}(y,\bar{y})\rangle}{\partial \bar{y}}\right|_{y=0}. \tag{3.123}$$

Thus, the results can be very different. Take the example of a beam between two infinite horizontal conducting planes. Because of horizontal translational invariance, the horizontal image force acting at the center of the beam vanishes independent of whether the beam is oscillating horizontally or vertically. The horizontal coherent tune shift therefore vanishes and has been verified by measurement in the CERN SPS in Fig. 3.7. We see that over a wide range of beam intensity, the horizontal coherent tune shift is equal to zero to a high precision, while the vertical coherent tune shift decreases linearly with beam intensity.

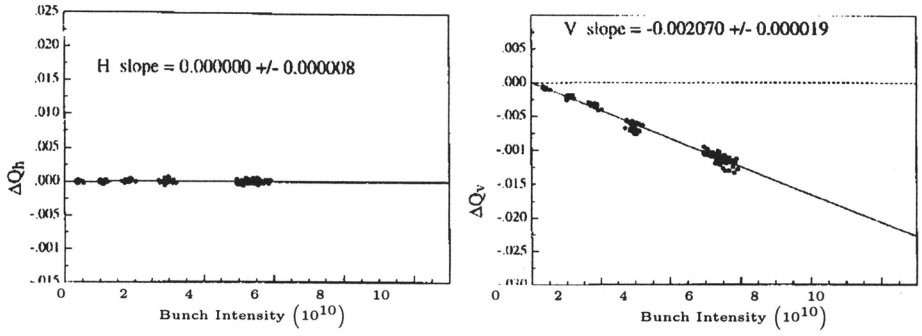


Fig. 3.7 Single bunch tune shift measurements in the CERN SPS. (Courtesy Gareyte. [10].)

On the other hand, the horizontal motion of the center of mass of the beam does provide a horizontal force on an individual particle, which may not be moving with the center of mass. That individual particle will therefore see a nonvanishing horizontal impedance.

3.5.2 *Impedance from Self-Force*

Now let us review the first term of Eq. (3.122), which gives the transverse dipole impedance coming from space-charge self-force for a beam with transverse uniform distribution and radius a. Let us derive this expression. When the beam is at rest, the volume charge distribution is

$$\rho(r) = \frac{e\lambda}{\pi a^2} H(a-r), \tag{3.124}$$

where λ is the linear particle distribution and $H(a-r)$ is the Heaviside step function. To create a dipole beam, let us displace it by an infinitesimal amount Δ in the horizontal direction. The dipole charge density is given by the differential of $\rho(r)$; for example,

$$\Delta\rho(r) = -\frac{\partial\rho(\vec{r})}{\partial x}\Delta = \frac{e\lambda\Delta\cos\theta}{\pi a^2}\delta(a-r), \tag{3.125}$$

which describes a hollow cylinder of charges of radius a with $\cos\theta$ variation, as illustrated in Fig. 3.8. The electric force acting on a test particle at the center of the *unperturbed beam* is in the x-direction and is given by

$$F_{\text{elec}} = \int_0^{2\pi} d\theta \int_0^{\infty} r dr \frac{e^2\lambda\Delta\cos\theta}{\pi a^2}\delta(a-r)\frac{\cos\theta}{2\pi\epsilon_0 r} = \frac{e^2\lambda\Delta Z_0 c}{2\pi a^2}, \tag{3.126}$$

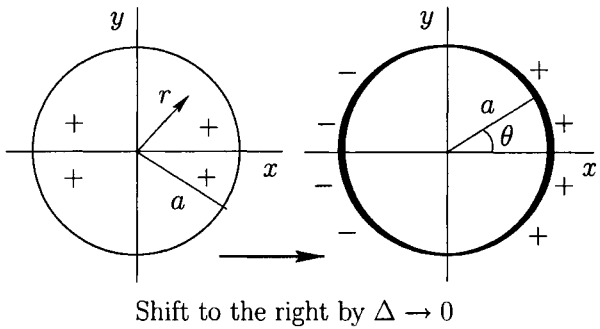


Fig. 3.8 A beam of uniform transverse density and radius a is shifted by an infinitesimal amount Δ horizontally to create a dipole beam of hollow cylinder of charges of radius a.

where Z_0 is the free-space impedance. We now take into account that the beam is moving at a velocity βc forming a current $\lambda\beta c$. A hollow cylinder of current with $\cos\theta$ distribution becomes a dipole current $\lambda\Delta\beta c$. The magnetic force on the test particle at the center of the beam is the same as the electric force except that it is multiplied by $-\beta^2$. One of these β's comes from the Lorentz force while the other comes from the velocity of the test particle. The total integrated force observed by the test particle in a revolution turn is therefore

$$\int_0^C F_{\text{spch}} ds = \frac{e^2\lambda\Delta c Z_0 R}{\gamma^2\beta^2 a^2}. \tag{3.127}$$

From the definition in Eq. (1.43), we obtain the transverse dipole impedance due to space-charge self-force

$$Z_1^{\perp}\big|_{\text{self-force}} = i\frac{Z_0 R}{\gamma^2\beta^2}\frac{1}{a^2}. \tag{3.128}$$

The a^{-2} dependency in this expression appears to resemble the incoherent space-charge tune shift. In fact, this is true. The dipole impedance arises from the space-charge force acting on the center of the *unperturbed beam* and is related to the difference between the coherent tune shift and the incoherent tune shift. The coherent tune shift arises from the space-charge self-force acting on the center of the *perturbed beam.* Since the center of the perturbed beam moves with the beam, the self-force on the beam center vanishes. Thus the coherent tune shift vanishes. As a result, the space-charge self-force part of the transverse space-charge impedance is proportional to the incoherent tune shift. In fact, by comparing Eq. (3.128) and Eq. (3.24), we can write

$$Z_1^{\perp}\big|^{y,x}_{\text{self-force}} = -i\frac{2\pi Z_0\gamma\nu_{0y,x}}{N r_0}\Delta\nu^{\text{spch}}_{y,x\,\text{incoh}}, \tag{3.129}$$

where N is the number of beam particles whose classical radius is r_0, and $\nu_{0y,x}$ is the bare vertical/horizontal betatron tune.

Following the procedure laid out above, the transverse space-charge impedance for any cylindrical transverse distribution $\rho(r)$ can be derived. However, a closer examination shows that the derivation can, in fact, be made much simpler. [12] The shifted dipole density is

$$\Delta\rho(r) = -\frac{\partial\rho(r)}{\partial y}\Delta = -\frac{d\rho(r)}{dr}\cos\theta\,\Delta. \tag{3.130}$$

When substituted in Eq. (3.126), the dipole electric force in the horizontal di-

rection can be written more generally as

$$F_{\rm elec} = -\Delta \int_0^{2\pi} d\theta \int_0^{\infty} r dr \left[-e^2 \frac{d\rho(r)}{dr} \right] \frac{\cos^2\theta}{2\pi\epsilon_0 r} = -\frac{e^2\rho(0)\Delta}{2\epsilon_0}, \tag{3.131}$$

where we have used the fact that $\rho(r)$ vanishes when evaluated at the upper limit or the transverse edge of the beam.‡‡ The space-charge self-force part of the transverse impedance is therefore

$$Z_1^{\perp}\Big|_{\rm self\text{-}force} = i\frac{Z_0 R}{\gamma^2\beta^2}\frac{\pi\rho(0)}{\lambda}. \tag{3.132}$$

In other words, the self-force part of the transverse impedance of a coasting beam with cylindrical transverse distribution is just proportional to the distribution density at $r = 0$. Or the equivalent uniform-distribution-radius is just

$$a_{\rm eff} = \sqrt{\frac{\lambda}{\pi\rho(0)}}. \tag{3.133}$$

In Table 3.3, we list the results for several common transverse distributions. The result of the bi-Gaussian distribution is approximate. Suppose that the distribution is truncated at $r = m\sigma_r$, where m need not be an integer, although we must require $m\sigma_r < b$ so that the beam pipe will be large enough to hold the beam. The volume particle distribution density is

$$\rho(r) = \frac{A_N\lambda}{2\pi\sigma_r^2} e^{-r^2/(2\sigma_r^2)}\, H(m\sigma_r - r), \tag{3.134}$$

with H being the Heaviside step function and

$$A_N = \frac{1}{1 - e^{-m^2/2}}, \tag{3.135}$$

so that it is properly normalized to λ when integrated over the transverse coordinates. Thus the equivalent uniform-density radius is

$$a_{\rm eff} = \frac{\sqrt{2}\sigma_r}{\sqrt{1 - e^{-m^2/2}}}. \tag{3.136}$$

‡‡For a distribution density like that of the uniform distribution, $\rho(r) = \lambda/(\pi a^2)$ for $r < a$, that is not continuous at the edge of the beam, one may be confused whether we should use $\rho(a+) = 0$ or $\rho(a-) = \lambda/(\pi a^2)$ at the beam edge. However, looking into the integration of Eq. (3.126), it is clear that we must use $r = a+$ as the edge, otherwise the contribution of the δ-function will not be included.

However, the approximation $a_{\text{eff}} \approx \sqrt{2}\sigma_r$ is usually accurate enough. For example, with a truncation at $3\sigma_r$, the error in the transverse space-charge self-force impedance is only 1%.

Table 3.3 Transverse dipole space-charge impedance for some common transverse distributions written in the form of Eq. (3.128) with and effective beam radius a_{eff}. H is the Heaviside step function.

	Phase space distribution	a_{eff}
Uniform	$\frac{1}{\pi\hat{r}^2}H(\hat{r}-r)$	$\hat{r}$
Elliptical	$\frac{3}{2\pi\hat{r}}\left(1-\frac{r^2}{\hat{r}^2}\right)^{1/2}H(\hat{r}-r)$	$\sqrt{\frac{2}{3}}\hat{r}$
Parabolic	$\frac{1}{2\pi\hat{r}^2}\left(1-\frac{r^2}{\hat{r}^2}\right)H(\hat{r}-r)$	$\frac{1}{\sqrt{2}}\hat{r}$
Cosine-square	$\frac{2\pi}{\pi^2-4}\cos^2\frac{\pi r}{2\hat{r}}H(\hat{r}-r)$	$\frac{\sqrt{\pi^2-4}}{\sqrt{2}\pi}\hat{r}$
Bi-Gaussian	$\frac{1}{2\pi\sigma_r^2}e^{-r^2/(2\sigma_r^2)}$	$\sqrt{2}\sigma_r$

3.6 Exercises

3.1 Consider a beam with bi-parabolic or semi-circular distribution

$$\rho(r) = \frac{2e\lambda}{\pi\hat{r}^2}\left(1-\frac{r^2}{\hat{r}^2}\right), \tag{3.137}$$

where $\hat{r}$ is the radial extent of the beam and λ is the linear particle density.
(1) Compute the self-field or space-charge incoherent tune shift at the center of the beam where it is maximal and show that the space-charge coefficient defined in Eq. (3.25) is $\epsilon^{\text{spch}} = 1$.
(2) Explain how one can understand that ϵ^{spch} for this distribution is in between $\epsilon^{\text{spch}} = \frac{1}{2}$ for uniform distribution and $\epsilon^{\text{spch}} \approx \frac{3}{2}$ for bi-Gaussian distribution.

3.2 The horizontal betatron tune shift due to a quadrupole gradient error $\Delta k(s) = \Delta B_y'/(B\rho)$ at location s along the accelerator ring is

$$\Delta\nu_{\beta_x} = \frac{1}{4\pi}\int_0^C \beta_x(s)\Delta k(s)ds, \tag{3.138}$$

where β_x is the betatron function, C is the circumference of the ring, $\Delta B_y'$ is the vertical quadrupole gradient error, and $(B\rho)$ is the magnetic rigid-

ity. Consider the space-charge self-force as a quadrupole gradient error, derive, using the above formula, the incoherent dipole space-charge tune shift, Eq. (3.24), inside a beam of uniform transverse distribution.

3.3 Consider a beam with elliptic cross section and uniform particle distribution.
(1) Show that the electric potential

$$U(x,y) = -\frac{e\lambda}{2\pi\epsilon_0}\frac{1}{a_x+a_y}\left(\frac{x^2}{a_x^2}+\frac{y^2}{a_y^2}\right) \tag{3.139}$$

for $x^2/a_x^2 + y^2/a_y^2 \leq 1$ and 0 otherwise, satisfies the Laplace equation

$$\nabla^2 U(x,y) = -\frac{e\lambda}{\pi\epsilon_0 a_x a_y}, \tag{3.140}$$

where λ is the linear particle density of the beam.
(2) Show that inside the beam, the transverse electric fields are

$$E_x = \frac{e\lambda}{\pi\epsilon_0}\frac{x}{a_x(a_x+a_y)},$$

$$E_y = \frac{e\lambda}{\pi\epsilon_0}\frac{y}{a_y(a_x+a_y)}. \tag{3.141}$$

(3) Comparing with the electric field components inside a cylindrically symmetric beam of radius a, show that the space-charge tune shift coefficients, defined in Eq. (3.25), inside this beam of elliptic cross section are

$$\epsilon_x^{\text{spch}} = \frac{a_y^2}{a_x(a_x+a_y)} \quad \text{and} \quad \epsilon_y^{\text{spch}} = \frac{a_y}{a_x+a_y}. \tag{3.142}$$

3.4 We are going to derive the electric potential $U(x,y,z)$ for a 3-dimensional charge distribution,

$$\rho(x,y,z) = \frac{eN}{(2\pi)^{3/2}\sigma_x\sigma_y\sigma_z}\exp\left[-\frac{x^2}{2\sigma_x^2}-\frac{y^2}{2\sigma_y^2}-\frac{z^2}{2\sigma_z^2}\right], \tag{3.143}$$

following the method of Takayama, [11] where N is the total number of particles.
(1) Show that the Green function of the Laplace equation can be written as

$$G(\vec{r},\vec{\xi}) = \frac{1}{4\pi|\vec{r}-\vec{\xi}|} = \frac{1}{2\pi^{3/2}}\int_0^\infty dq\, e^{-|\vec{r}-\vec{\xi}|^2 q^2}. \tag{3.144}$$

In other words, $G(\vec{r},\vec{\xi})$ satisfies

$$\nabla^2 G(\vec{r},\vec{\xi}) = -\delta(\vec{r}-\vec{\xi}). \tag{3.145}$$

(2) Changing the variable of integration to $t = q^{-2}$, show that the electric potential can be written as

$$U(x,y,z) = \frac{1}{4\pi^{3/2}\epsilon_0}\int_0^\infty \frac{dt}{t^{3/2}}\int_{-\infty}^{\infty} d\vec{\xi}\,\rho(\vec{\xi})e^{-|\vec{r}-\vec{\xi}|^2/t}. \tag{3.146}$$

(3) With ρ given by Eq. (3.143), derive the electric potential

$$U(x,y,z) = \frac{eN}{4\pi^{3/2}\epsilon_0}\int_0^\infty dt\,\frac{\exp\left[-\frac{x^2}{(2\sigma_x^2+t)}-\frac{y^2}{(2\sigma_y^2+t)}-\frac{z^2}{(2\sigma_z^2+t)}\right]}{\sqrt{(2\sigma_x^2+t)(2\sigma_y^2+t)(2\sigma_z^2+t)}}. \tag{3.147}$$

3.5 Consider a beam with bi-Gaussian transverse charge distribution,

$$\rho(x,y) = \frac{e\lambda}{2\pi\sigma_x\sigma_y}\exp\left(-\frac{x^2}{2\sigma_x^2}-\frac{y^2}{2\sigma_y^2}\right), \tag{3.148}$$

where σ_x and σ_y are the rms width and height, and λ is the linear particle density.

(1) From Eq. (3.147), show that the electric potential is

$$U(x,y) = \frac{e\lambda}{4\pi\epsilon_0}\int_0^\infty dt\,\frac{\exp\left[-\frac{x^2}{(2\sigma_x^2+t)}-\frac{y^2}{(2\sigma_y^2+t)}\right]}{\sqrt{(2\sigma_x^2+t)(2\sigma_y^2+t)}}. \tag{3.149}$$

(2) Show that the transverse electric fields are

$$E_x = \frac{e\lambda x}{2\pi\epsilon_0}\int_0^\infty dt\,\frac{\exp\left[-\frac{x^2}{(2\sigma_x^2+t)}-\frac{y^2}{(2\sigma_y^2+t)}\right]}{(2\sigma_x^2+t)\sqrt{(2\sigma_x^2+t)(2\sigma_y^2+t)}},$$

$$E_y \to E_x \quad \text{with} \quad x \to y, \quad y \to x. \tag{3.150}$$

(3) The self-field or space-charge tune shifts are at their maxima at the center of the beam, or $x \to 0$ and $y \to 0$. Show that they are given by Eq. (3.31) with

$$\begin{aligned} \sigma^2 &\to \frac{\sigma_x(\sigma_x+\sigma_y)}{2} \text{ for } \Delta\nu^{\text{spch}}_{x\,\text{incoh}}, \\ \sigma^2 &\to \frac{\sigma_y(\sigma_x+\sigma_y)}{2} \text{ for } \Delta\nu^{\text{spch}}_{y\,\text{incoh}}. \end{aligned} \tag{3.151}$$

3.6 A 5.066-GeV damping ring for the TESLA linear collider was designed at Fermilab, which has the smaller ring circumference of 6114.0 m rather than the 17 km TESLA damping ring. [13, 14] The bare betatron tunes are $\nu_{0y,x} = 41.62/56.58$ and average dispersion is 0.2571 m. The beam has normalized rms emittances $\epsilon_{Ny,x\,\mathrm{rms}} = 0.020/8.00$ πmm-mr and an rms momentum spread $\sigma_\delta = 1.5 \times 10^{-3}$. Using these numbers, show that the vertical incoherent space-charge tune shift is $\Delta\nu_{y\,\mathrm{incoh}}^{\mathrm{spch}} = -0.0311$. When the Twiss parameters of the lattice are used in an integration around the ring, we find $\Delta\nu_{y\,\mathrm{incoh}}^{\mathrm{spch}} = -0.0654$, which is more than twice larger than the estimate using averages. The big difference come from the overwhelming contribution from the dispersion to the horizontal beam size rather than from the horizontal emittance. This can be checked by excluding dispersion contribution. Then the vertical incoherent space-charge tune shift using averages becomes -0.102 while the computation with integration around the ring becomes -0.109. Although the tune shifts are much larger now because of the smaller horizontal beam size, however their difference is only 6.5%.

3.7 The Hamiltonian representing the transverse motion of a particle with horizontal and vertical offsets X and Y in the presence of space-charge is

$$H_1 = \frac{P_x^2 + K_x(s)X^2}{2} + \frac{P_y^2 + K_y(s)Y^2}{2} - U_{\mathrm{spch}}(X, Y), \tag{3.152}$$

where $K_x(s)$ and $K_y(s)$ are the restoring force gradients from the quadrupoles around the ring, and

$$U_{\mathrm{spch}}(X, Y) = \frac{1}{\gamma^3 m v^2} \frac{e^2\lambda}{4\pi\epsilon_0} \int_0^\infty dt \, \frac{\exp\left[-\frac{X^2}{(2\sigma_x^2+t)} - \frac{Y^2}{(2\sigma_y^2+t)}\right]}{\sqrt{(2\sigma_x^2+t)(2\sigma_y^2+t)}}, \tag{3.153}$$

as given by Eq. (3.149) when bi-Gaussian transverse distribution is assumed.
(1) Using the generating function

$$G_1(x, P_x, y, P_y; s) = \sum_{u=x,y} \left[-\left(\frac{\beta_u}{\beta_0}\right)^{1/2} P_u u + \frac{\beta_u'}{4\beta_0} u^2 \right], \tag{3.154}$$

derive the new Hamiltonian in the normalized form

$$H_2 = \sum_{u=x,y} \frac{R}{2\beta_u} \left(\beta_0 p_u^2 + \frac{u^2}{\beta_0} \right) - R U_{\mathrm{spch}}(X, Y), \tag{3.155}$$

with

$$X = x\sqrt{\frac{\beta_x}{\beta_0}} \qquad Y = y\sqrt{\frac{\beta_y}{\beta_0}}. \tag{3.156}$$

Here, the independent variable has been changed from s to $\theta = s/R$. In the above, β_0 is just some reference betatron function so that x and y retain the dimension of length, and use has been made of the relation

$$\frac{1}{2}\beta_u\beta_u'' - \frac{1}{4}\beta_u'^2 + K_u\beta_u^2 = 1, \tag{3.157}$$

which defines the beta-functions in terms of K_x and K_y.
(2) Using the generating function

$$G_2(\phi_x, p_x, \phi_y, p_y; \theta) = \sum_{u=x,y} \frac{1}{2}\beta_0 p_u^2 \cot\phi_u, \tag{3.158}$$

derive the transformation

$$\begin{aligned} u &= (2J_u\beta_0)^{1/2}\cos\phi_u, \\ \beta_0 p_u &= -(2J_u\beta_0)^{1/2}\sin\phi_u, \end{aligned} \tag{3.159}$$

and the new Hamiltonian

$$H_3 = \nu_{0x}J_x + \nu_{0y}J_y - RU_{\text{spch}}(X, Y), \tag{3.160}$$

where the betatron tune ν_{0x} and ν_{0y} are obtained from

$$\nu_{0x} = \left.\frac{\partial H_3}{\partial J_x}\right|_{U_{\text{spch}}=0} \qquad \nu_{0y} = \left.\frac{\partial H_3}{\partial J_y}\right|_{U_{\text{spch}}=0}. \tag{3.161}$$

(3) The space-charge part of the Hamiltonian now becomes

$$U_{\text{spch}}(X, Y) = \frac{1}{\gamma^3 m v^2}\frac{e^2\lambda}{4\pi\epsilon_0}\int_0^\infty dt\, \frac{\exp\left[-\frac{2J_x\beta_x\cos^2\phi_x}{(2\sigma_x^2+t)} - \frac{2J_y\beta_y\sin^2\phi_x}{(2\sigma_y^2+t)}\right]}{\sqrt{(2\sigma_x^2+t)(2\sigma_y^2+t)}}. \tag{3.162}$$

Compute the vertical incoherent space-charge tune shift via

$$\Delta\nu_y^{\text{spch}} = \frac{\partial RU_{\text{spch}}(X, Y)}{\partial J_y}. \tag{3.163}$$

The final vertical incoherent space-charge tune shift expressed in Eq. (3.41) is obtained by (1) letting $J_x = J_y = 0$ because we are after the tune shift of those particles at the center of the beam, (2) averaging over the angle

variables $\phi_{x,y}$ because the betatron tune is defined as the average number of betatron oscillations per revolution turn, and finally (3) averaging around ring by integrating over $\theta/(2\pi)$ to take care of the variations in betatron functions and dispersion.

Bibliography

[1] L. J. Laslett, Proc. 1963 Summer Study on Storage Rings, BNL-Report 7534, p. 324; L. J. Laslett and L. Resegotti, Proc. VI Int. Conf. on High Energy Accel. (Cambridge, MA, 1967), p. 150.

[2] B. W. Zotter, *Tune Shifts of Excentric Beams in Elliptic Vacuum Chamber*, *IEEE Trans. Nucl. Sci.* **NS-22**(3), 1451 (1975); CERN Reports ISR-TH/72-8 (1972); IST-TH/74-38 (1974); ISR-TH/75-17 (1975).

[3] B. Zotter, *Nucl. Instrum. Meth.* **129**, 377 (1975).

[4] K. Y. Ng, *Distribution of Incoherent Space-Charge Tune Shift of a Bi-Gaussian Beam*, Fermilab Report TM-2241, 2004.

[5] B. Zotter, CERN Report ISR-TH/74-11 (1974).

[6] K. Y. Ng, *Part. Accel.* **16**, 63 (1984).

[7] See, for example, Abramowitz and Stegun, *Handbook of Mathematical Functions* (Dover, 1965), Table 16.5, p. 571.

[8] K. J. Binns and P. J. Lawrenson, *Analysis and Computation of Electric and Magnetic Field Problems*, 2nd edn. (Pergamon Press, 1973).

[9] G. Guignard, CERN Report CERN 77-10 (1977).

[10] J. Gareyte, *Impedances: Measurements and Calculations for Non-symmetric Structures*, Proc. EPAC 2002 (Paris, June 3–7, 2002), p. 89.

[11] K. Takayama, *Lett. Al Nuovo Cimento* **34**, 190 (1982).

[12] K. Y. Ng, *Space-Charge Impedances of Beams with Non-uniform Transverse Distributions*, Fermilab Report FN-0756, 2004.

[13] *TESLA Technical Design Report—The Superconducting Electron-Positron Linear Collider with an Integrated X-Ray Laser Laboratory, Part II The Accelerator*, eds. R. Brinkmann, K. Flöttmann, J. Rossbach, P. Schmüser, N. Walker, H. Weise, DESY Report DESY-2001-011, 2001.

[14] Shekhar Mishra, David Neuffer, K. Y. Ng, Franois Ostiguy, Nikolay Solyak, Aimin Xiao, George D. Gollin, Guy Bresler, Keri Dixon, Thomas R. Junk, and Jeremy B. Williams, *Studies Pertaining to a Small Damping Ring for the International Linear Collider*, Fermilab Report FERMI-TM-2272, 2004.

2025 © The Author(s). This is an Open Access chapter published by World Scientific Publishing Company, licensed under the terms of the Creative Commons Attribution-NonCommercial 4.0 International License (CC BY-NC 4.0).

Chapter 4

Envelope Equation

We often read that when the linear part of the space-charge force is added to the linear equation of motion, it produces an incoherent tune shift, which if large enough can place individual particles onto low-order betatron resonant lines, resulting in an instability. This picture, although appealing, is very misleading. In fact, the resonant driving force drives the beam to resonance only when the *coherent* space-charge tune shift lands the coherent betatron tune of the beam onto the resonance lines. We are going to show that resonant driving force of any order will *not* affect an individual particle when the space-charge force shifts its betatron tune onto the resonance line of that order.

4.1 The Integer Resonance

In this section, we are going to study the effects on beam particles under the influence of errors in the dipoles. We will find that although the beam center is able to see the force from the dipole errors, it will not see the self-fields among the beam particles. On the other hand, a single particle sees the self-fields and has its betatron tunes shifted. However, a single particle oscillating at an integer tune will be not be driven by the dipole-error force. We shall follow a discussion by Baartman. [1]

The integer resonance is driven by errors in the dipoles around the accelerator ring. The transverse motion of a beam particle is governed by

$$\frac{d^2X}{d\psi_x^2} + \nu_{0x}^2 X = F_x^{\text{spch}} + F_x^{\text{ext}}(\psi_x), \tag{4.1}$$

where

$$\psi_x = \int_0^s \frac{ds}{\nu_{0x}\beta_x(s)} \tag{4.2}$$

is the transverse Floquet phase which advances by 2π per turn, X is the normalized transverse offset (actual offset x divided by square root of the betatron function β_x), and ν_{0x} is the bare betatron tune. The *force** due to errors in dipoles in the x-direction is represented by $F_x^{\text{ext}}(\psi_x)$, which is periodic in ψ_x and is X-independent. The space-charge force F_x^{spch}, if linear, can be written as

$$F_x^{\text{spch}} = -2\nu_{0x}\Delta\nu_x^{\text{spch}}(X - \langle X\rangle), \tag{4.3}$$

where $\langle X\rangle$ is the transverse offset of the center of charge of the beam and $\Delta\nu_x^{\text{spch}}$ is the incoherent space-charge tune shift depicted in, for example, Eq. (3.24). The equation of motion becomes

$$\frac{d^2X}{d\psi_x^2} + \nu_{0x}^2 X = -2\nu_{0x}\Delta\nu_x^{\text{spch}}(X - \langle X\rangle) + F_x^{\text{ext}}(\psi_x). \tag{4.4}$$

Taking the average, we obtain the equation of motion for the center of the beam,

$$\frac{d^2\langle X\rangle}{d\psi_x^2} + \nu_{0x}^2\langle X\rangle = F_x^{\text{ext}}(\psi_x). \tag{4.5}$$

Here, we assume $\Delta\nu_x^{\text{spch}}$ to be the same for every particle, for example, in a parabolic distribution. The space-charge term disappears, indicating that the motion of the center-of-charge is not affected by the space-charge self-force. Physically, the beam transverse motion is rigid and therefore the center cannot see any change in the pattern of the space-charge self-field. In other words, there is no coherent dipole space-charge tune shift. However, we do see that the center of the beam is driven by the dipole force due to lattice error. The beam will be unstable if the coherent tune ν_{0x}, or just bare tune here, is equal to an integer. Another way of saying the same thing is that as the coherent tune approaches an integer, the closed-orbit distortion, being kicked in the same direction in every turn, increases without limit. To show this more clearly, let us write the nth-harmonic component of the periodic lattice-error force as $F_x^{\text{ext}}(\psi_x) = f_n e^{in\psi_x}$. The particular solution of Eq. (4.5) is

$$\langle X\rangle = \frac{f_n e^{in\psi_x}}{\nu_{0x}^2 - n^2}, \tag{4.6}$$

which is indeed unstable when the $\nu_{0x} = n$.

The incoherent motion is obtained by subtracting Eq. (4.5) from Eq. (4.4),

$$\frac{d^2}{d\psi_x^2}(X - \langle X\rangle) + \left(\nu_{0x}^2 + 2\nu_{0x}\Delta\nu_x^{\text{spch}}\right)(X - \langle X\rangle) = 0, \tag{4.7}$$

*Here, F_x^{spch} and F_x^{ext} do not have the dimension of a force. They should be forces divided by appropriate variables. But for simplicity, we just call them forces.

showing that an individual particle is making betatron motion about the center of the beam with the incoherent betatron tune $\nu_{x\,\mathrm{incoh}} = \nu_{0x} + \Delta\nu_x^{\mathrm{spch}}$. It is important to notice that the incoherent equation of motion contains no driving terms for the integer resonance. Therefore, incoherent motion is not affected by dipole errors. This means that the incoherent tune can be equal to an integer with no adverse effects. It is worth re-emphasizing: A particle which is shifted by direct space-charge to a tune of exactly an integer, turn by turn sees the same dipole errors at the same betatron phase, and yet is not even slightly affected compared with other particles which do not have an integer tune. This is not due to space-charge stabilizing the resonance, as claimed by Ref. [2], because in this example of linear space-charge, there is no incoherent tune spread to generate Landau damping. The correct answer is simply no driving term for incoherent motion.

One may argue that both X_i and $\langle X\rangle$ are driven by the dipole force $F_x^{\mathrm{ext}}(\psi_x)$ according to Eqs. (4.4) and (4.5). Equation (4.7) does not contain the dipole force only when the particle position is measured with respect to the center of the beam. In practice, however, one bothers about the particle position X_i but not its offset from the beam center $X_i - \langle X\rangle$, because the former is what the beam-position monitor picks up or what one records in a numerical simulation. For this reason, a single particle is affected by the dipole force and will be driven into resonance. This argument is completely correct. The important ingredient is: the single particle is not driven into resonance at its own oscillating tune $\nu_{x\,\mathrm{incoh}} = \nu_{0x} + \Delta\nu_x^{\mathrm{spch}}$, which is the incoherent tune, but is driven into resonance only at ν_{0x}, the oscillating tune of the beam center of the coherent tune of the whole beam.

The same concept can be extended easily to any nonlinear space-charge force. For the ith particle, the equation of motion is

$$\frac{d^2X_i}{d\psi_x^2} + \nu_{0x}^2 X_i = {\sum_j}' F_{ij} + F_x^{\mathrm{ext}}, \tag{4.8}$$

where F_{ij} is the force of the jth particle acting on the ith particle, and $\sum_j'$ implies a summation over j but with $j = i$ excluded. Thus, $\sum_j' F_{ij}$ is just the space-charge force from all other particles acting on the ith particle. We now take the average of Eq. (4.8) by summing over i, giving exactly Eq. (4.5) again. This result is obtained because of Newton's third law: $F_{ij} = -F_{ji}$ when $i \neq j$. Subtracting Eq. (4.5) from Eq. (4.8), we arrive at the incoherent equation

$$\frac{d^2}{d\psi_x^2}\left(X - \langle X\rangle\right) + \nu_{0x}^2\left(X_i - \langle X\rangle\right) = {\sum_j}' F_{ij}. \tag{4.9}$$

Again, there is no dipole driving force for the equation of incoherent motion. The space-charge self-force, being nonlinear, does not just reduce to a simple incoherent tune shift. The incoherent tune will be different for each different particle depending on its amplitude and the transverse beam distribution. However, whatever the incoherent tune is, even at an integer, the individual particle will not be affected by the dipole lattice error at all.

4.2 The Kapchinsky–Vladimirsky Equation

Now let us come to the errors in the quadrupoles. This force, denoted by $XF(\psi_x)$ is responsible for the half-integer resonance. Sometimes it is also called the linear error force, because quadrupoles are linear elements of the accelerator lattice. The equation of transverse motion for a particle is

$$\frac{d^2X}{d\psi_x^2} + \nu_{0x}^2 X = -2\nu_{0x}\Delta\nu_x^{\text{spch}}(X - \langle X\rangle) + XF(\psi_x), \tag{4.10}$$

where a linear space-charge force $-2\nu_{0x}\Delta\nu_x^{\text{spch}}(X - \langle X\rangle)$ has been assumed. Coherent motion is obtained by averaging Eq. (4.10),

$$\frac{d^2\langle X\rangle}{d\psi_x^2} + \nu_{0x}^2\langle X\rangle = \langle X\rangle F(\psi_x), \tag{4.11}$$

and the difference gives the incoherent motion,

$$\frac{d^2}{d\psi_x^2}(X - \langle X\rangle) + \left(\nu_{0x}^2 + 2\nu_{0x}\Delta\nu_x^{\text{spch}}\right)(X - \langle X\rangle) = (X - \langle X\rangle)\,F(\psi_x). \tag{4.12}$$

It appears in Eq. (4.12) that the incoherent motion is driven by the quadrupole-error force so that the particle will experience an instability at the half integer. This conclusion is incorrect, although there is nothing wrong with the derivation from Eqs. (4.10) to (4.12). A quadrupole in the lattice will change the size of the particle beam and so will the quadrupole-error force. The incoherent space-charge tune shift depends on the beam size, which is a function of the quadrupole error force $XF(\psi_x)$. Actually, the effect of the quadrupole-error force inside the incoherent space-charge tune shift just cancels the quadrupole-error force on the right side of Eq. (4.12), leaving behind an incoherent motion not affected by the quadrupole-error force. To demonstrate this, we need to study the equation of motion governing the beam size or beam envelope.

The dipole coherent tune shifts are zero because the beam center does not experience any variation of the forces between beam particles, when the beam is executing rigid dipole oscillations as a whole. Thus, the space-charge forces do

not affect the restoring force of rigid oscillation and therefore do not affect the dipole coherent tunes. However, there are other collective modes of oscillation in a beam. Examples are the breathing mode, where the transverse beam size expands and contracts without the beam center being moved, and the mode when the breathing in the two transverse directions are 180° out of phase. The restoring forces of these modes of oscillation do depend on the forces between the beam particles. Thus, their frequencies of oscillation are affected by the space-charge forces. To study these modes, we need to resort to the equations of motion governing the beam envelope.

The envelope equation was first derived by Kapchinsky and Vladimirsky [3] for a coasting beam with uniform charge density and elliptical cross section. It was later generalized by Sacherer [4] to include any distribution when the beam envelope $\hat{x}$ is replaced by the rms beam size $\tilde{x} = \sqrt{\langle x^2 \rangle}$ of the beam. We are going to follow Sacherer's approach.

Consider a particle in an ensemble that obeys the single-particle equations

$$\begin{aligned} x' &= p_x, \\ p_x' &= F_x(x, s), \end{aligned} \tag{4.13}$$

where x is the transverse offset, p_x is the canonical momentum, and the prime denotes derivative with respect to time s, the distance along the designed orbit of the accelerator. The total force[†] in the x-direction,

$$F_x(x, s) = F_x^{\text{spch}} + F_x^{\text{ext}}, \tag{4.14}$$

includes the space-charge self-force F_x^{spch} and the external force F_x^{ext}. Averaging over the particle distribution $f(x, p, s)$, we obtain the equations of motion for the center of the beam:

$$\begin{aligned} \langle x \rangle' &= \langle p_x \rangle, \\ \langle p_x \rangle' &= \langle F_x(x, s) \rangle = \langle F_x^{\text{ext}} \rangle, \end{aligned} \tag{4.15}$$

where the last equation follows from $\langle F_x^{\text{spch}} \rangle = 0$ because of Newton's third law. Note that the order of the averaging and differentiation with respect to s is immaterial and can be interchanged if one wishes. For a linear machine, for example with only dipoles and quadrupoles in the ring, the external force is linear. We can write $F_x^{\text{ext}} = -K_x(s)x$, and the equation of motion governing the center of the beam becomes

$$\langle x \rangle'' + K_x(s)\langle x \rangle = 0, \tag{4.16}$$

[†]We call them forces, although $F_x(x, s)$, F_x^{spch}, and F_x^{ext} do not have the dimension of a force. Note that they have a different dimension from the forces introduced in Eq. (4.1).

which involves only first moments and is independent of the space-charge force or the detailed form of the beam distribution.

The second moments satisfy the equations

$$\begin{aligned}
\langle x^2\rangle' &= 2\langle xx'\rangle = 2\langle xp_x\rangle,\\
\langle xp_x\rangle' &= \langle x'p_x\rangle + \langle xp_x'\rangle = \langle p_x^2\rangle - K_x(s)\langle x^2\rangle + \langle xF_x^{\text{spch}}\rangle,\\
\langle p_x^2\rangle' &= 2\langle p_xp_x'\rangle = -2K_x(s)\langle xp_x\rangle + 2\langle p_xF_x^{\text{spch}}\rangle.
\end{aligned} \tag{4.17}$$

Notice that this set of equations is not closed because $\langle xF_x^{\text{spch}}\rangle$ and $\langle pF_x^{\text{spch}}\rangle$ are usually functions of the higher moments like $\langle x^n\rangle$, $\langle x^np_x\rangle$, etc.

To study space-charge effects, we are interested in the position and momentum offsets of the particle from their respective averages, i.e.,

$$\Delta x = x - \langle x\rangle, \quad \Delta p_x = p_x - \langle p_x\rangle. \tag{4.18}$$

Since $\langle F_x^{\text{spch}}\rangle = 0$, it is straightforward to demonstrate that $\langle \Delta x^2\rangle'$, $\langle \Delta x\Delta p_x\rangle'$, and $\langle \Delta p_x^2\rangle'$ satisfy exactly the same expressions as in Eq. (4.17) but with the substitutions $x \to \Delta x$ and $p_x \to \Delta p_x$.

Let us introduce the rms emittance

$$\mathcal{E}_x = \sqrt{\langle \Delta x^2\rangle\ \langle \Delta p_x^2\rangle - \langle \Delta x\Delta p_x\rangle^2}. \tag{4.19}$$

If we assume that the rms emittance is either time-invariant or its time dependency is known *a priori*, $\langle \Delta p_x^2\rangle$ can be expressed in terms of $\langle \Delta x^2\rangle$, $\langle \Delta x\Delta p_x\rangle$, and $\mathcal{E}_x$. Then, the expressions for $\langle \Delta x^2\rangle'$ and $\langle \Delta x\Delta p_x\rangle'$ can be combined to give a K–V type envelope equation

$$\tilde{x}'' + K(s)\tilde{x} - \frac{\mathcal{E}_x^2}{\tilde{x}^3} - \frac{\langle \Delta xF_x^{\text{spch}}\rangle}{\tilde{x}} = 0, \tag{4.20}$$

where $\tilde{x} = \sqrt{\langle \Delta x^2\rangle}$ is the rms beam size. Unfortunately, this equation is not closed in the sense that $\langle \Delta xF_x^{\text{spch}}\rangle$ depends on higher moments.

Using the rate of change in the second moments in Eq. (4.17), the rate of change of the rms emittance along the accelerator is

$$\mathcal{E}_x' = \frac{\langle \Delta x^2\rangle\langle \Delta p_xF_x^{\text{spch}}\rangle - \langle \Delta x\Delta p_x\rangle\langle \Delta xF_x^{\text{spch}}\rangle}{\mathcal{E}_x}. \tag{4.21}$$

Thus, the rms emittance is an invariant provided that the space-charge force is linear, or when it can be written as $F_x^{\text{spch}} = \epsilon(s)\Delta x$, the rms emittance is an invariant and then Eq. (4.20) becomes a closed envelope equation without involvement of higher moments. Unfortunately, the space-charge force is not linear. As will be demonstrated below, however, if the self-force is derivable from the free-space Poisson equation, $\langle \Delta xF_x^{\text{spch}}\rangle$ depends mainly on up to the

second moments and very little, if at all, on the higher moments. Before going into further discussions, let us express the envelope equation in terms of the static electric field E_x of the space-charge self-force in the x-direction and put back all the missing factors. The envelope equation in the MKS units now reads

$$\tilde{x}'' + K(s)\tilde{x} - \frac{\mathcal{E}_x^2}{\tilde{x}^3} - \frac{e}{m\gamma^3\beta^2c^2}\frac{\langle \Delta x E_x \rangle}{\tilde{x}} = 0, \tag{4.22}$$

where m is the mass of the beam particles. In the denominator, we have the Lorentz factor $\gamma\beta^2$ because of Newton's second law and the other γ^2 because of the presence of the magnetic field of the beam in the laboratory frame, as demonstrated in Eqs. (3.23) and (3.24).

4.2.1 *Least-Square Value*

The space-charge term has an interesting interpretation. If we define the linear part of the space-charge force F_x^{spch} as $\varepsilon(s)\Delta x$, where $\varepsilon(s)$ is determined by minimizing at a fixed time

$$D = \int \left[\varepsilon(s)\Delta x - F_x^{\text{spch}}\right]^2 n(\Delta x, s)dx, \tag{4.23}$$

where the linear distribution is

$$n(\Delta x, s) = \int f(\Delta x, \Delta p_x; s)d\Delta p_x, \tag{4.24}$$

and the phase-space distribution is $f(\Delta x, \Delta p_x; s)$, then we obtain

$$\varepsilon(s)\Delta x = \frac{\langle \Delta x F_x^{\text{spch}} \rangle}{\tilde{x}^2}\Delta x. \tag{4.25}$$

In other words, the rms envelope equation depends only on the linear part of the space-charge force determined by least square.

4.2.2 *One Dimension*

Consider a very long beam traveling in the z-direction with very wide width in the y-direction. The situation can be approximated by a one-dimensional beam having space-charge self-force only in the x-direction and we assume that its distribution is symmetric with respect to the $x = 0$ plane. In this way, we can simplify the writing by having $\Delta x \to x$. The static electric field E_x in the x-direction is given by Poisson equation

$$\frac{\partial E_x}{\partial x} = \frac{e}{\epsilon_0} n(x; s), \tag{4.26}$$

from which

$$E_x = \frac{e}{\epsilon_0}\int_0^x n(x';s)dx'. \tag{4.27}$$

Here, $n(x,s)$ is the particle distribution per unit volume. Therefore, when integrated over x from $-\infty$ to $+\infty$, it is normalized to σ, the particle density per unit area in the y-z plane. Since the electric field is proportional to the fraction of particles it encloses between $\pm x$, we must have

$$\frac{\langle xE_x\rangle}{\tilde{x}} = \frac{e}{\epsilon_0}\frac{\displaystyle\int_{-\infty}^{\infty} x\,\frac{n(x)}{\sigma}dx\int_0^x n(x')dx'}{\left[\displaystyle\int_{-\infty}^{\infty} x^2\frac{n(x)}{\sigma}dx\right]^{1/2}} = \frac{e\sigma}{2\epsilon_0}\,\varrho, \tag{4.28}$$

where we have defined the dimensionless parameter

$$\varrho = \frac{2\displaystyle\int_{-\infty}^{\infty} xh(x)dx\int_0^x h(x')dx'}{\left[\displaystyle\int_{-\infty}^{\infty} x^2h(x)dx\right]^{1/2}}. \tag{4.29}$$

We have introduced a new distribution function $h(x) = n(x)/\sigma$ so that σ, the particle number per unit area in the y-z plane, is factored out and $h(x)$ is normalized to unity. It is important to point out that while ϱ is dimensionless, $h(x)$ can be scaled to anything that is convenient. For example, in a uniform distribution, we can choose the edges as ± 1, and in a Gaussian distribution, we can choose the rms spread as 1. Substituting in Eq. (4.22), the one-dimensional envelope equation now becomes

$$\tilde{x}'' + K(s)\tilde{x} - \frac{\mathcal{E}_x^2}{\tilde{x}^3} - \frac{2\pi r_0\sigma}{\gamma^3\beta^2}\varrho = 0, \tag{4.30}$$

where $r_0 = e^2/(4\pi\epsilon_0 mc^2)$ is the classical radius of the beam particles.

For a uniform distribution in one dimension, the half widths of the beam is $\hat{x} = \sqrt{3}\tilde{x}$. The full emittance is $\epsilon_x = 3\mathcal{E}_x$, since we also have $\hat{p}_x = \sqrt{3}\sqrt{\langle p_x^2\rangle}$. Thus the envelope equation for the half beam width in one dimension becomes

$$\hat{x}'' + K(s)\hat{x} - \frac{\epsilon_x^2}{\hat{x}^3} - \frac{2\pi r_0\sigma}{\gamma^3\beta^2} = 0, \tag{4.31}$$

where $\varrho = 1/\sqrt{3}$ has been substituted.

Table 4.1 shows the values of ϱ for four distributions. We see that for a wide range of distributions that are likely to be encountered, the variation of ϱ is less then 2.3%. Thus the one-dimension rms envelope equation will be accurately described by Eq. (4.30) with $\varrho = 1/\sqrt{3}$.

Table 4.1 The values of the dimensionless parameter ϱ for a wide range of distributions. They are all close to $1/\sqrt{3}$. H is the Heaviside step function.

Distribution	$h(x)$	$\sqrt{3}\varrho$
Uniform	$\frac{1}{2}H(1-\|x\|)$	1.000
Parabolic	$\frac{3}{4}(1-x^2)H(1-\|x\|)$	0.996
Gaussian	$\frac{1}{\sqrt{2\pi}}e^{-x^2/2}$	0.977
Hollow	$\frac{1}{\sqrt{2\pi}}x^2e^{-x^2/2}$	0.987

4.2.3 *Two Dimensions*

With the absence of cross-correlations and coupling terms, the rms envelope equations in the two transverse directions are given by Eq. (4.22) and the two space-charge terms $\langle xF_x^{\text{spch}}\rangle$ and $\langle yF_y^{\text{spch}}\rangle$ depend on the particle distribution. It will be shown below that $\langle xF_x^{\text{spch}}\rangle$ and $\langle yF_y^{\text{spch}}\rangle$ depend only on second moments if the distribution has the elliptical symmetry

$$n(x,y;s) = n\left(\frac{x^2}{a^2}+\frac{y^2}{b^2};\, s\right), \tag{4.32}$$

which when integrated over x and y gives the linear particle density λ. Here, we assume for simplicity, $\langle x\rangle = \langle y\rangle = 0$. Thus, x and y in above actually imply $\Delta x = x - \langle x\rangle$ and $\Delta y = y - \langle y\rangle$. Corresponding to this distribution, the static electric field in the x-direction at a fixed location s can be written as

$$E_x = \frac{eabx}{2\epsilon_0}\int_0^\infty \frac{n(T)}{a^2+u}\,\frac{du}{D(u)}, \tag{4.33}$$

where

$$D(u) = \sqrt{(a^2+u)(b^2+u)} \tag{4.34}$$

and

$$T = \frac{x^2}{a^2+u}+\frac{y^2}{b^2+u}. \tag{4.35}$$

The validity of Eq. (4.33) can be verified by computing the divergence of the electric field. We get

$$\frac{\partial E_x}{\partial x} = \frac{eab}{2\epsilon_0}\int_0^\infty \frac{du}{D(u)}\left[\frac{n(T)}{a^2+u}+\frac{2x^2n'(T)}{(a^2+u)^2}\right]. \tag{4.36}$$

Changing variable of integration from u to T,

$$dT = -\left[\frac{x^2}{(a^2+u)^2} + \frac{y^2}{(b^2+u)^2}\right] du \tag{4.37}$$

and noting that

$$\frac{d\ln D(u)}{du} = \frac{1}{2}\left(\frac{1}{a^2+u} + \frac{1}{b^2+u}\right), \tag{4.38}$$

we arrive at

$$\vec{\nabla}\cdot\vec{E} = \frac{eab}{2\epsilon_0}\left[\int_0^\infty \frac{du}{D(u)}\, 2n(T)\frac{d\ln D(u)}{du} - \int_{u=0}^{u=\infty} dT\, \frac{2n'(T)}{D(u)}\right]. \tag{4.39}$$

The variable in the first integral can now be easily changed from u to T, and we obtain

$$\vec{\nabla}\cdot\vec{E} = \frac{eab}{\epsilon_0}\int_{u=0}^{u=\infty} dT\, \left[\frac{n(T)}{D^2}\,\frac{dD}{dT} - \frac{n'(T)}{D}\right]$$

$$= -\frac{eab}{\epsilon_0}\int_{u=0}^{u=\infty} dT\, \frac{d}{dT}\left[\frac{n}{D}\right] = \frac{e}{\epsilon_0}\, n\left(\frac{x^2}{a^2} + \frac{y^2}{b^2}\right), \tag{4.40}$$

as required by Gauss's law. In passing, we give also the electric potential

$$\Phi(x,y) = -\frac{eab}{4\epsilon_0}\int_0^\infty \frac{du}{D(u)}\int_0^T dT'\, n(T'). \tag{4.41}$$

Now we are ready to compute $\langle xE_x\rangle$ and $\langle yE_y\rangle$. By definition,

$$\langle xE_x\rangle = \frac{eab}{2\epsilon_0\lambda}\int_0^\infty \frac{du}{D(u)}\int_{-\infty}^\infty \frac{x^2dx}{a^2+u}\int_{-\infty}^\infty dy\, n(T)\, n\left(\frac{x^2}{a^2} + \frac{y^2}{b^2}\right). \tag{4.42}$$

This suggests the change of variables from x and y to the circular coordinates r and θ,

$$r\cos\theta = \frac{x}{\sqrt{a^2+u}}, \quad r\sin\theta = \frac{y}{\sqrt{b^2+u}} \longrightarrow \frac{dxdy}{D(u)} = rdrd\theta. \tag{4.43}$$

The integration variable u is now changed to r' with

$$r'^2 = \frac{x^2}{a^2} + \frac{y^2}{b^2} = r^2\left[\frac{a^2+u}{a^2}\cos^2\theta + \frac{b^2+u}{b^2}\sin^2\theta\right], \tag{4.44}$$

$$2r'dr' = \frac{r^2}{a^2b^2}\left(a^2\sin^2\theta + b^2\cos^2\theta\right)du, \tag{4.45}$$

and the integration limits from $u = 0$ to ∞ changed to $r' = r$ to ∞. All these changes convert Eq. (4.42) to

$$\langle xE_x \rangle = \frac{ea^3b^2}{2\pi\epsilon_0\lambda(a+b)} \int_0^\infty n\left(r^2\right) 2\pi r dr \int_r^\infty n(r'^2) 2\pi r' dr', \tag{4.46}$$

where the integration over θ has been performed with the help of

$$\int_0^{2\pi} \frac{\cos^2\theta}{a^2\sin^2\theta + b^2\cos^2\theta}\, d\theta = \frac{2\pi}{b(a+b)}. \tag{4.47}$$

Note that the variables r and r' carry no dimension. With the newly defined function

$$Q(r) = ab \int_0^r n(r'^2) 2\pi r' dr' \qquad \text{with} \quad Q(\infty) = \lambda, \tag{4.48}$$

Eq. (4.46) can be integrated to give

$$\langle xE_x \rangle = \frac{ea}{2\pi\epsilon_0\lambda(a+b)} \int_0^\infty dr\, \frac{dQ(r)}{dr} [\lambda - Q(r)] = \frac{ea\lambda}{4\pi\epsilon_0(a+b)}. \tag{4.49}$$

Since $\tilde{x} = \sqrt{\langle x^2 \rangle} \propto a$ and $\tilde{y} = \sqrt{\langle y^2 \rangle} \propto b$, we obtain the final rms envelope equation in two dimension:

$$\begin{aligned} \tilde{x}'' + K_x(s)\tilde{x} - \frac{\mathcal{E}_x^2}{\tilde{x}^3} - \frac{r_0\lambda}{\gamma^3\beta^2} \frac{1}{\tilde{x}+\tilde{y}} &= 0, \\ \tilde{y}'' + K_y(s)\tilde{y} - \frac{\mathcal{E}_y^2}{\tilde{y}^3} - \frac{r_0\lambda}{\gamma^3\beta^2} \frac{1}{\tilde{x}+\tilde{y}} &= 0. \end{aligned} \tag{4.50}$$

For a uniform distribution with elliptical symmetry in two dimensions, the half widths of the beam are $\hat{x} = 2\tilde{x}$ and $\hat{y} = 2\tilde{y}$. The emittance is $\epsilon_{x,y} = 4\mathcal{E}_{x,y}$, since we also have $\hat{p}_{x,y} = 2\sqrt{\langle p_{x,y} \rangle}$. The envelope equation becomes

$$\begin{aligned} \hat{x}'' + K_x(s)\hat{x} - \frac{\epsilon_x^2}{\hat{x}^3} - \frac{4r_0\lambda}{\gamma^3\beta^2} \frac{1}{\hat{x}+\hat{y}} &= 0, \\ \hat{y}'' + K_y(s)\hat{y} - \frac{\epsilon_y^2}{\hat{y}^3} - \frac{4r_0\lambda}{\gamma^3\beta^2} \frac{1}{\hat{x}+\hat{y}} &= 0. \end{aligned} \tag{4.51}$$

These are just the well-known K–V equations. However, the rms envelope equations depicted in Eq. (4.50) are not restricted to the uniform K–V distribution and are valid for any distribution with elliptical symmetry.

Two comments are in order. First, the distribution with elliptical symmetry represented by Eq. (4.32) is a very general distribution. Nearly all practical beam distributions fall into this category. Therefore, Sacherer's conclusion that $\langle xE_x \rangle$

in Eq. (4.49) does not involve moments higher than second order is remarkable. Second, the rate of change of the beam emittance E_x, Eq. (4.21), depends on both $\langle xE_x \rangle$ and $\langle p_x E_x \rangle$, and will vanish if both of them do not involve moments higher than second order. Unfortunately, $\langle p_x E_x \rangle$ does depend on moments of the beam higher than second order. As a result, the emittance introduced in Eq. (4.19) is time-dependent and this renders the rms envelope equations not a closed system. The set of rms envelope equations is only closed when the distribution is uniform. It can be shown that the rate of increase of emittance is proportional to the energy of the part of the space-charge self-field that is nonlinear. [5, 6, 7]

4.3 Collective Oscillations of Beams

4.3.1 *One Dimension*

The one-dimension envelope equation for uniform beam, Eq. (4.30), contains the external focusing term $K_x(s)$, which includes both the ideal quadrupole focusing force and the gradient errors. We first eliminate the rapidly varying part of $K_x(s)$ from the envelope equation by introducing the Floquet phase advance ψ_x, which increases by 2π each revolution turn,

$$\psi_x = \int_0^s \frac{ds}{\nu_{0x}\beta_x(s)}, \tag{4.52}$$

where ν_{0x} is the bare tune and β_x is the betatron function defined in the absence of the space-charge self-force. Next, introduce the dimensionless half beam size

$$\hat{X} = \frac{\hat{x}}{\sqrt{\epsilon_x \beta_x}}, \tag{4.53}$$

where the full emittance ϵ_x, defined via Eq. (4.19) with $\langle x \rangle = 0$ and $\langle p_x \rangle = 0$,

$$\epsilon_x = 3\sqrt{\langle x^2 \rangle \langle p_x^2 \rangle - \langle x p_x \rangle^2}, \tag{4.54}$$

is a constant of motion because the distribution is now uniform and the space-charge force is therefore linear [see Eq. (4.21)]. The envelope equation for a uniform beam in one dimension now becomes (Exercise 4.1)

$$\frac{d^2\hat{X}}{d\psi_x^2} + \nu_{0x}^2 \hat{X} - \frac{\nu_{0x}^2}{\hat{X}^3} - \frac{2\pi r_0 \sigma}{\gamma^3 \beta^2} \frac{\nu_{0x}^2 \beta_x^{3/2}}{\sqrt{\epsilon_x}} = 0. \tag{4.55}$$

The last term on the left side depends on s through the betatron function β_x. Because β_x is periodic in s or the phase advance ψ_x, we can expand it as a Fourier

series. The part oscillatory in ψ_x is x-independent and is therefore similar to the force due to dipole errors which we have studied earlier in Sec. 4.1. Since it will drive only integer resonance and we are interested in half-integer resonance only in this section, this oscillatory part is discarded. The non-oscillatory part is related to the incoherent space-charge tune shift $\Delta\nu_x^{\text{spch}}$, or (Exercise 4.2)

$$2\nu_{0x}\Delta\nu_x^{\text{spch}} = -\frac{2\pi r_0\sigma}{\gamma^3\beta^2}\,\frac{\nu_{0x}^2\bar{\beta}_x^{3/2}}{\sqrt{\epsilon_x}}, \tag{4.56}$$

where $\bar{\beta}_x$ is the betatron function averaged over the Floquet phase ψ and is equal to R/ν_{0x}, with R being the mean radius of the accelerator ring. In terms of $\Delta\nu_x^{\text{spch}}$, the one-dimension envelope equation now takes the simple form[‡]

$$\frac{d^2\hat{X}}{d\psi_x^2} + \left(\nu_{0x}^2 + 2\nu_{0x}\Delta\nu_{\text{stop}}\cos n\psi_x\right)\hat{X} - \frac{\nu_{0x}^2}{\hat{X}^3} + 2\nu_{0x}\Delta\nu_x^{\text{spch}} = 0, \tag{4.57}$$

where we have included the part in $K(s)$ that corresponds to quadruple gradient errors as a force possessing nth harmonic and total *stopband width* $\Delta\nu_{\text{stop}}$.

When space-charge is absent, the *static* solution (s or ψ_x independent) of the envelope equation is just $\hat{X} = 1$. Here, *static* is just mathematically true for the normalized beam size $\hat{X}$. In fact, this solution is not physically static, because it corresponds to the beam size

$$\hat{x} = \sqrt{\epsilon_x\beta_x}, \tag{4.58}$$

and β_x is a function of s. We can also see how the normalization process simplifies the analysis of the envelope equation. The solution in Eq. (4.58) says nothing more than the fact that $\sqrt{\beta_x}$ is the beam radius when the beam is *matched* to the lattice. In fact, the envelope equation, Eq. (4.30), before normalizing, is the equation satisfied by $\sqrt{\beta_x}$.

In the presence of space-charge, the 'static' solution becomes

$$\hat{X} = 1 + \xi_x, \tag{4.59}$$

which can be solved as a power series in

$$\Delta_x = \frac{\Delta\nu_x^{\text{spch}}}{\nu_{0x}}. \tag{4.60}$$

[‡]The incoherent space-charge tune shift is negative. Many authors prefer to denote $\Delta\nu_x^{\text{spch}}$ as the absolute value of the tune shift. In that convention, the sign in front of the last term on the left side of Eq. (4.57) will be negative instead.

We obtain

$$\xi_x = -\frac{\Delta_x}{2} + \frac{3\Delta_x^2}{8} + \mathcal{O}\left(\Delta_x^3\right). \tag{4.61}$$

Since $\Delta\nu_x^{\text{spch}} < 0$, the beam size is therefore larger due to the repulsive nature of the space-charge force. This can be viewed as an increase in the betatron function due to space-charge by

$$\beta_x \longrightarrow \frac{\beta_x \nu_{0x}}{\nu_{0x} + \Delta\nu_x^{\text{spch}}}. \tag{4.62}$$

Now we are ready to solve the envelope equation around the 'static' solution, for which we let

$$\hat{X} = 1 + \xi_x + \delta_x(\psi_x). \tag{4.63}$$

Here, δ_x represents the amplitude of oscillation of the beam width about the equilibrium value $1 + \xi_x$. We only need δ_x to be infinitesimal. Therefore, we perform the power series expansion according to

$$\delta_x \ll \xi_x \ll 1, \tag{4.64}$$

and keep only the first order in δ_x. We require only an infinitesimal driving force, because this is what it needs to drive a particle into instability. Thus, we will consider the width of the stopband $\Delta\nu_{\text{stop}}/\nu_{0x}$ to be of the same order as δ_x. This consideration leads to the equation

$$\frac{d^2\delta_x}{d\psi_x^2} + \left(4\nu_{0x}^2 + 6\nu_{0x}\Delta\nu_x^{\text{spch}}\right)\delta_x = -2\nu_{0x}\Delta\nu_{\text{stop}}\cos n\psi_x. \tag{4.65}$$

It is now easy to see that the beam envelope oscillates with the natural coherent tune $2\left(\nu_{0x} + \frac{3}{4}\Delta\nu_x^{\text{spch}}\right)$, and resonance occurs when

$$n^2 = 4\nu_{0x}^2 + 6\nu_{0x}\Delta\nu_x^{\text{spch}} \quad \text{or} \quad \frac{n}{2} \approx \nu_{0x} - \frac{3}{4}\left|\Delta\nu_x^{\text{spch}}\right| = \nu_{x\,\text{incoh}} + \frac{1}{4}\left|\Delta\nu_x^{\text{spch}}\right|. \tag{4.66}$$

The incoherent tune $\nu_{x\,\text{incoh}} = \nu_{0x} + \Delta\nu_x^{\text{spch}}$ can therefore be depressed beyond the half-integer $\frac{n}{2}$ by $\frac{1}{4}|\Delta\nu_x^{\text{spch}}|$, a quarter of the incoherent tune shift before hitting the resonance as is illustrated in Fig. 4.1. Solution of Eq. (4.65) gives

$$\hat{X} = 1 - \frac{\Delta\nu_x^{\text{spch}}}{2\nu_{0x}} - \frac{2\nu_{0x}\Delta\nu_{\text{stop}}\cos n\psi_x}{4\nu_{0x}^2 + 6\nu_{0x}\Delta\nu_x^{\text{spch}} - n^2}, \tag{4.67}$$

where only the lowest order of $\Delta\nu_x^{\text{spch}}/\nu_{0x}$ has been included. Clearly, this solution reflects the resonance depicted in Eq. (4.66), although the solution is

perturbative and is not valid near the resonance. We also see the beam envelope oscillate and that represents a quadrupole breathing mode, which is a coherent mode or collective mode because all beam particles have to participate collectively to produce this pattern of motion. This is in contrast to the incoherent motion, where a single beam particle executes betatron oscillations regardless of what the rest are doing.

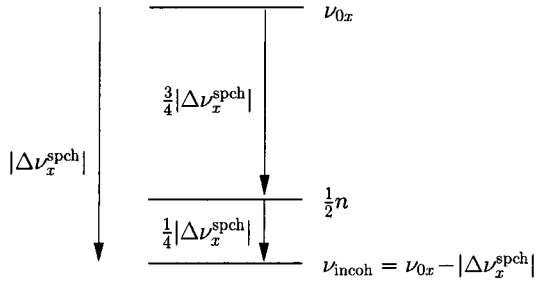


Fig. 4.1 Plot showing that the incoherent tune of a one-dimensional beam, $\nu_{\rm incoh} = \nu_{0x} - |\Delta\nu_x^{\rm spch}|$, can be depressed to pass the half-integer $\frac{1}{2}n$ before the coherent quadrupole tune $\nu_{\rm coh} = \nu_{0x} - \frac{3}{4}|\Delta\nu_x^{\rm spch}|$ reaches the half-integer instability.

Now we are in the position to study whether the force due to quadrupole errors will drive a single particle unstable at the half-integer resonance. Let us return to Eq. (4.12), the equation of motion of a single particle, which we rewrite as

$$\frac{d^2X}{d\psi_x^2} + \left(\nu_{0x}^2 + 2\nu_{0x}\Delta\nu_{\rm stop}\cos n\psi_x\right) X + 2\nu_{0x}\Delta\nu_x^{\rm spch}\frac{X}{\hat{X}} = 0, \tag{4.68}$$

where X and $\hat{X}$ are, respectively, the x-coordinate of the particle and the beam half width normalized by $\sqrt{\beta_x\epsilon_x}$. The quantity $\Delta\nu_x^{\rm spch}$, as given by Eq. (4.56), is the commonly quoted incoherent space-charge tune shift without consideration of the beam being driven by the gradient errors of the quadrupole. The correct incoherent space-charge tune shift is actually given by $\Delta\nu_x^{\rm spch}/\hat{X}$ because of the increase in beam size (see Exercise 4.2). Since we are not interested in the rigid motion of the beam, the beam center $\langle X\rangle$ can be set to zero. When the perturbative solution $\hat{X}$ of the beam envelope in Eq. (4.67) is substituted, Eq. (4.68) becomes

$$\frac{d^2X}{d\psi_x^2} + \left(\nu_{0x}+\Delta\nu_x^{\rm spch}\right)^2 X + 2\nu_{0x}\Delta\nu_{\rm stop}\cos n\psi_x\left[1+\frac{2\nu_{0x}\Delta\nu_x^{\rm spch}}{4\nu_{0x}^2+6\nu_{0x}\Delta\nu_x^{\rm spch}-n^2}\right]X = 0, \tag{4.69}$$

where non-resonant free oscillations have not been included. At the particle intensity which shifts the betatron tune to half-integer, namely $\nu_{0x} + \Delta\nu_x^{\rm spch} = n/2$, the two terms inside the square brackets cancel, and the single-particle

equation of motion reduces to

$$\frac{d^2X}{d\psi_x^2} + \left(\frac{n}{2}\right)^2 X = 0. \tag{4.70}$$

We see that when the incoherent tune of a particle is shifted to half-integer, the driving force due to gradient errors cancels exactly. Thus, no resonance occurs for the particle.

The above proof appears to be overly approximated.§ The reader can pursuit this proof to another order of the incoherent tune shift.

4.3.2 *Two Dimensions*

Similar to the one-dimensional case, we normalize the two-dimensional envelope equations with uniformly distributed elliptic cross section in the same way by introducing the phase advances

$$\psi_x = \int_0^s \frac{ds}{\nu_{0x}\beta_x(s)} \qquad \text{and} \qquad \psi_y = \int_0^s \frac{ds}{\nu_{0y}\beta_y(s)}, \tag{4.71}$$

and the dimensionless half beam radii

$$\hat{X} = \frac{\hat{x}}{\sqrt{\epsilon_x\beta_x}} \qquad \text{and} \qquad \hat{Y} = \frac{\hat{y}}{\sqrt{\epsilon_y\beta_y}}, \tag{4.72}$$

where ν_{0x} and ν_{0y} are the bare tunes and β_x and β_y are the betatron functions in the x and y directions, respectively, defined in the absence of the space-charge self-force. Equation (4.51) that governs the motion of the beam radii takes the form,

$$\begin{aligned}
&\frac{d^2\hat{X}}{d\psi_x^2} + \left(\nu_{0x}^2 + 2\nu_{0x}\Delta\nu_{sx}\cos n_x\psi_x\right)\hat{X} - \frac{\nu_{0x}^2}{\hat{X}^3} + 2\nu_{0x}\Delta\nu_x^{\text{spch}}\frac{a+b}{a\hat{X}+b\hat{Y}} = 0,\\
&\frac{d^2\hat{Y}}{d\psi_y^2} + \left(\nu_{0y}^2 + 2\nu_{0y}\Delta\nu_{sy}\cos n_y\psi_y\right)\hat{Y} - \frac{\nu_{0y}^2}{\hat{Y}^3} + 2\nu_{0y}\Delta\nu_y^{\text{spch}}\frac{a+b}{a\hat{X}+b\hat{Y}} = 0,
\end{aligned} \tag{4.73}$$

where $a = \sqrt{\epsilon_x\bar{\beta}_x}$ and $b = \sqrt{\epsilon_y\bar{\beta}_y}$ are the beam radii defined through the average betatron functions $\bar{\beta}_x$ and $\bar{\beta}_y$,

$$\Delta\nu_x^{\text{spch}} = -\frac{2\lambda r_0 R^2}{\gamma^3\beta^2\nu_{0x}a(a+b)} \qquad \text{and} \qquad \Delta\nu_y^{\text{spch}} = -\frac{2\lambda r_0 R^2}{\gamma^3\beta^2\nu_{0y}b(a+b)} \tag{4.74}$$

§The more accurate condition for envelope instability is $\nu_{0x}^2 - \frac{3}{2}\left|\nu_{0x}\Delta\nu_x^{\text{spch}}\right| = \left(\frac{n}{2}\right)^2$. So the more accurate condition for "incoherent resonance" is $\nu_{0x}^2 - 2\left|\nu_{0x}\Delta\nu_x^{\text{spch}}\right| = \left(\frac{n}{2}\right)^2$. Use of these conditions make the driving term vanish to a more accurate degree.

are the incoherent space-charge tune shifts. Apparently, the coupling of the two envelope equations originates from the transverse space-charge force. We have also included the forces due to gradient errors at harmonics n_x and n_y. The magnitudes of these forces are just the widths of the half-integer stopbands $\Delta\nu_{sx}$ and $\Delta\nu_{sy}$.

In exactly the same way as for the one-dimensional envelope equation, we first solve for the *static* beam radii

$$\hat{X} = 1 + \xi_x \quad \text{and} \quad \hat{Y} = 1 + \xi_y \tag{4.75}$$

in terms of the incoherent space-charge tune shifts $\Delta\nu_x^{\text{spch}}$ and $\Delta\nu_y^{\text{spch}}$ via the two parameters,

$$\Delta_x = \frac{\Delta\nu_x^{\text{spch}}}{\nu_{0x}} \quad \text{and} \quad \Delta_y = \frac{\Delta\nu_y^{\text{spch}}}{\nu_{0y}}. \tag{4.76}$$

Up to the second order, we get

$$\xi_x = -\frac{\Delta_x}{2} + \frac{\Delta_x^2}{4} - \frac{\Delta_x\Delta_y}{8} \quad \text{and} \quad \xi_y = -\frac{\Delta_y}{2} + \frac{\Delta_y^2}{4} - \frac{\Delta_x\Delta_y}{8}. \tag{4.77}$$

Next, the infinitesimal displacements δ_x and δ_y are included:

$$\hat{X} = 1 + \xi_x + \delta_x \quad \text{and} \quad \hat{Y} = 1 + \xi_y + \delta_y. \tag{4.78}$$

The derivation becomes very lengthy and uninteresting. Readers with interest should consult the thesis of Sacherer. [8] For the sake of simplicity, we study instead the special case of a round beam with $a = b$ and obtain the equations for small-amplitude oscillations:

$$\frac{d^2\delta_x}{d\psi_x^2} + (4 + 5\Delta_x)\,\nu_{0x}^2\delta_x - \nu_{0x}^2\Delta_x\delta_y = -2\nu_{0x}^2\Delta\nu_x^{\text{spch}}\cos n_x\psi_x, \tag{4.79}$$

$$\frac{d^2\delta_y}{d\psi_y^2} + (4 + 5\Delta_y)\,\nu_{0y}^2\delta_y - \nu_{0y}^2\Delta_y\delta_x = -2\nu_{0y}^2\Delta\nu_y^{\text{spch}}\cos n_y\psi_y. \tag{4.80}$$

This is just a set of driven coupled simple-harmonic oscillators. For a round beam, we expect the incoherent space-charge tune shifts in the two transverse directions to be equal, i.e., $\Delta\nu_x^{\text{spch}} = \Delta\nu_y^{\text{spch}}$. The eigentunes ν can be found by solving the eigenvalues of the matrix

$$\begin{pmatrix} 4\nu_{0x}^2 + 5\nu_{0x}\Delta\nu_x^{\text{spch}} & -\nu_{0x}\Delta\nu_x^{\text{spch}} \\ -\nu_{0y}\Delta\nu_x^{\text{spch}} & 4\nu_{0y}^2 + 5\nu_{0y}\Delta\nu_x^{\text{spch}} \end{pmatrix}, \tag{4.81}$$

from which we get

$$\nu^2 = 2\left(\nu_{0x}^2+\nu_{0y}^2\right)+\frac{5}{2}(\nu_{0x}+\nu_{0y})\Delta\nu_x^{\text{spch}} \pm\sqrt{4\left(\nu_{0x}^2-\nu_{0y}^2\right)^2+\nu_{0x}\nu_{0y}\left(\Delta\nu_x^{\text{spch}}\right)^2+10(\nu_{0x}-\nu_{0y})^2(\nu_{0x}+\nu_{0y})\Delta\nu_x^{\text{spch}}}. \tag{4.82}$$

When the two bare tunes are close so that $|\nu_{0x}-\nu_{0y}| \ll |\nu_{0x}\Delta\nu_x^{\text{spch}}|$, the two coherent tunes are

$$\nu^2 = \begin{cases} 4\bar{\nu}^2 - 4\left|\nu_{0x}\Delta\nu_x^{\text{spch}}\right| \\ 4\bar{\nu}^2 - 6\left|\nu_{0y}\Delta\nu_x^{\text{spch}}\right| \end{cases} \quad \text{or} \quad \nu \approx \begin{cases} 2\left(\bar{\nu}-\frac{1}{2}\left|\Delta\nu_x^{\text{spch}}\right|\right), \\ 2\left(\bar{\nu}-\frac{3}{4}\left|\Delta\nu_x^{\text{spch}}\right|\right), \end{cases} \tag{4.83}$$

where $2\bar{\nu}^2 = \nu_{0x}^2+\nu_{0y}^2$. This represents that the two transverse directions are tightly coupled. The eigenfunctions are $\sim(\delta_x+\delta_y)$ for the upper solution and $\sim(\delta_x-\delta_y)$ for the lower solution. Thus, the upper solution is the symmetric breathing mode where the oscillations are in phase in both transverse directions and the tune is $\bar{\nu}-\frac{1}{2}|\Delta_x^{\text{spch}}|$. The lower solution is the antisymmetric mode where the beam envelope oscillates out of phase in the two transverse directions with tune $\bar{\nu}-\frac{3}{4}|\Delta_x^{\text{spch}}|$.

If the tune split is large so that $|\nu_{0x}-\nu_{0y}| \gg |\nu_{0x}\Delta\nu_x^{\text{spch}}|$, the oscillations in the two transverse directions are almost uncoupled. The envelope oscillations in the two transverse directions are just two independent oscillators. The two coherent tunes becomes

$$\nu^2 = \begin{cases} 4\nu_{0x}^2 - 5\left|\nu_{0x}\Delta\nu_x^{\text{spch}}\right| \\ 4\nu_{0y}^2 - 5\left|\nu_{0y}\Delta\nu_y^{\text{spch}}\right| \end{cases} \quad \text{or} \quad \nu \approx \begin{cases} 2\left(\nu_{0x}-\frac{5}{8}\left|\Delta\nu_x^{\text{spch}}\right|\right), \\ 2\left(\nu_{0y}-\frac{5}{8}\left|\Delta\nu_y^{\text{spch}}\right|\right). \end{cases} \tag{4.84}$$

Let us come back to the situation of no tune split. Suppose that the bare tunes $\nu_{0x}\sim\nu_{0y}\sim\bar{\nu}$ are above a half-integer or integer by the amount $\Delta\nu$. We try to increase the beam intensity and the incoherent tune shift $|\Delta\nu_x^{\text{spch}}|$ increases accordingly. We will first meet with the condition $\frac{3}{4}|\Delta\nu_x^{\text{spch}}| = \Delta\nu$ and the antisymmetric mode becomes unstable. However, the incoherent tune, $\nu_{0x}-|\Delta\nu_x^{\text{spch}}|$ has passed the half integer already by a factor of $\frac{4}{3}$. The symmetric mode will meet with the half-integer and become unstable much later when $|\Delta\nu_x^{\text{spch}}| = 2\Delta\nu$.

Similar to the one-dimensional case, the oscillatory solutions for the envelope radii can be solved. When substituted back into the single-particle equations of motion, we can verify that the driving force vanishes when the incoherent equations are at half integers, showing that the incoherent motion of individual particles can have their tunes right at half-integers without instability. The derivation is tedious but straightforward, and will be left as an exercise for the readers (Exercise 4.4).

4.3.2.1 *Equivalent-Uniform-Beam*

Other distributions can be analyzed in the same way. Notice that, for a round beam of uniform transverse distribution, the space-charge tune shift $\Delta\nu_x^{\text{spch}}$ in the last terms of the two-dimensional envelope equations in Eq. (4.73) is, according to Eq. (4.74),

$$\Delta\nu_x^{\text{spch}} = -\frac{Nr_0}{2\pi\gamma^3\beta^2\epsilon} = -\frac{Nr_0}{8\pi\gamma^3\beta^2\epsilon_{\text{rms}}}, \tag{4.85}$$

where $N = 2\pi R\lambda$ is the total number of particles in the beam. We have substituted ϵ, the full emittance of the uniform distributed beam, by the rms emittance $\epsilon_{\text{rms}} = \epsilon/4$. Now rewrite Eq. (4.85) as

$$\Delta\nu_x^{\text{spch}} = \frac{1}{2}\left[-\frac{Nr_0}{4\pi\gamma^3\beta^2\epsilon_{\text{rms}}}\right], \tag{4.86}$$

where the square-bracketed term is the maximum incoherent space-charge tune shift of a bi-Gaussian distributed round beam. Thus what we need to remember is that the factor $\Delta\nu_x^{\text{spch}}$ in the envelope equation represents one half of the maximum incoherent space-charge tune shift for bi-Gaussian distribution. We mentioned before that for the case of strong coupling, the tune depression of the antisymmetric mode is $\frac{3}{4}|\Delta\nu_x^{\text{spch}}|$ and the incoherent tune shift can exceed that needed for coincidence with a half integer resonance by a factor of $\frac{4}{3}$. Now for the case of the bi-Gaussian distribution, the tune depression of this mode becomes $\frac{3}{4} \times \frac{1}{2}$ of the maximum incoherent space-charge tune shift for the bi-Gaussian distributed beam, and therefore the incoherent tune can exceed that needed for coincidence with a half-integer resonance by as much as a factor of $\frac{8}{3}$. For this reason, we define a parameter G, such that Eq. (4.85) can be written as

$$\Delta\nu_x^{\text{spch}} = \frac{1}{G}\left[\begin{array}{l}\text{max incoherent}\\ \text{sp ch tune shift}\end{array}\right]. \tag{4.87}$$

Then, the incoherent space-charge tune shift for the distribution considered will exceed the tune depression of a particular collective quadrupole mode G times better than if the distribution is uniform. Here, $G = \frac{1}{2}$ for a bi-Gaussian distributed beam.

If we neglect the time dependency of the emittances, the rms envelope equations, Eq. (4.50), say that the space-charge effects of all beams are the same if they have the same rms widths and emittances. These beams are called *equivalent* beams. For example, an *equivalent-uniform-beam* implies that the beam has the same rms dimensions as a uniform beam. This concept can also be extended to a nonround beam.

4.4 Simulations

4.4.1 *One Dimension*

Baartman [1] performed simulations with up to 50,000 particles according to the equation of motion:

$$x'' + \nu_{0x}^2 x = \alpha x^{m-1} \cos(n\theta) + F_x^{\text{spch}}. \tag{4.88}$$

Here, the driving force leads to resonances whenever the tune ν satisfies $m\nu = n$. The space-charge self-force F_x^{spch} on a particular particle in the simulations is simply equal to an intensity parameter multiplied by the difference between the number of particles to its left and to its right.

For a sextupole force ($m = 3$) and bare tune equals $\nu_{0x} = 2.45$, the relevant resonance is at $\frac{n}{m} = \frac{7}{3} = 2.3333$. We expect to see the beam in resonance when the coherent tune $\nu_{x\,\text{coh}} = \nu_{0x} - C_{33}|\Delta\nu_x^{\text{spch}}| = \frac{7}{3}$, where $\Delta\nu_x^{\text{spch}}$ is the incoherent space-charge tune shift and $C_{33} = \frac{7}{8}$ by solving the envelope equation in one dimension. This corresponds to an incoherent space-charge tune shift of $|\Delta\nu_x^{\text{spch}}| = (2.45 - 2.333)/C_{33} = 0.1334$ or the incoherent tune of $2.45 - 0.1334 = 2.3167$. The simulations were performed for a beam with transverse Gaussian distribution. The results are plotted in Fig. 4.2 as the fraction of particles inside a given betatron amplitude versus the incoherent tune of the stationary beam of the same rms size. The incoherent tune is chosen because it serves as a measure of the beam intensity. Larger incoherent tune implies lower beam intensity. The thick curve in the center is the rms beam size. We clearly see that it passes the incoherent tune of $\frac{7}{3}$ with nothing happening. However, there is a sharp threshold at the expected incoherent tune 2.3167. This verifies the fact that it is the coherent tune but not the incoherent tune that determines the arrival of a resonance. The horizontal curves in the figure represent the fraction of particles inside a fixed emittance for the Gaussian distribution. They step downwards as particles are driven to larger amplitudes. The stepdown occurs when a horizontal curve meets the curve connecting the + symbols. These + symbols represent the emittance at which the incoherent tune is on resonance. If we examine the figure more closely, we find that only those horizontal curves representing more than 50% of particles step downwards, and also the stepdowns are more appreciable only when the particle amplitude becomes larger. This phenomenon happens because of some halo particles residing at the very edges of the beam. They behave like a separate beam and feel the space-charge force from the core of the beam as an external force. Since this is not the space-charge self-force of the beam halo, our discussion of the irrelevance of the incoherent tune does not apply to these particles.

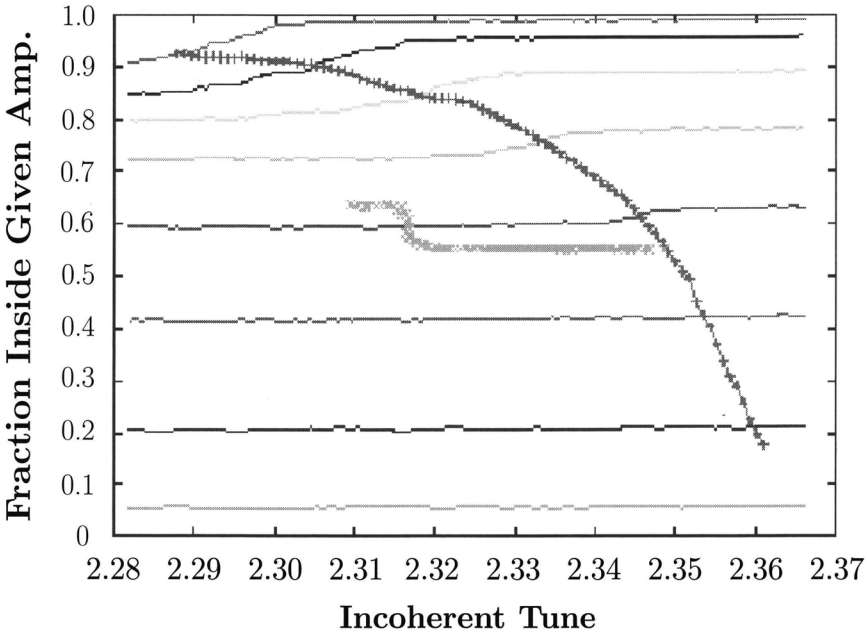


Fig. 4.2 Plot of the rms size (thick curve at center) of the simulated one-dimensional beam of Gaussian distribution as a function of the incoherent tune, which is used here as a measure of the beam intensity. Obviously, there is no effect on the beam when the incoherent tune crosses the $\frac{7}{3}$ resonance. But the rms beam size increases very suddenly when the incoherent tune reaches 2.3167 corresponding to the $\frac{7}{3}$ resonance of the coherent tune. See text for the other curves. (Courtesy Baartman. [1])

4.4.2 *Two Dimensions*

Machida [9] performed two-dimensional space-charge simulations of the Low Energy Booster of the Superconducting Super Collider (SSC) by including quadrupole error forces. The horizontal bare tune was fixed at $\nu_{0x} = 11.87$ while the vertical bare tune ν_{0y} varied from 11.95 to 11.55. The maximum incoherent space-charge self-force tune shift was kept fixed at $|\Delta\nu_y^{\text{spch}}| = 0.33$ initially. The beam simulated had a bi-Gaussian distribution. The emittance initially at 0.5 πmm-mr was found to grow when the vertical bare tune was below ~ 11.66 as indicated in the left plot of Fig. 4.3. This vertical bare tune was much less than $11.83 (= 11.50 + 0.33)$ when the incoherent tune passed the half-integer resonance of 11.50 with a stopband of 0.02. Since there is not any exhibition of emittance increase in Fig. 4.3 when the bare tune is around $\nu_{0y} = 11.83$, the conclusion can be drawn that emittance growth is not determined by the incoherent tune.

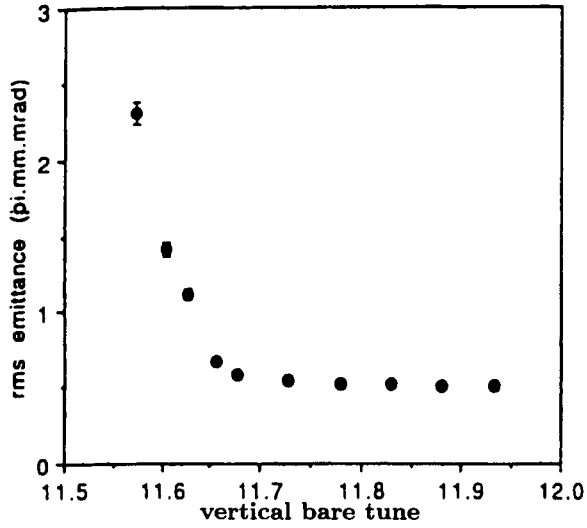


Fig. 4.3 Vertical emittance versus vertical bare tune. Emittance starts to grow when the bare vertical tune is less than $\nu_{0y} = 11.66$. The bare horizontal tune is at $\nu_{0x} = 11.87$ and the maximum initial incoherent space-charge tune shift is $|\Delta\nu_y^{\text{spch}}| = 0.33$. It is clear that there is not any emittance change at $\nu_{0y} = 11.83$ when the incoherent vertical tune $\nu_{y\,\text{incoh}} = 11.83 - 0.33 = 11.50$ crosses the half-integer stopband. (Courtesy Machida. [9])

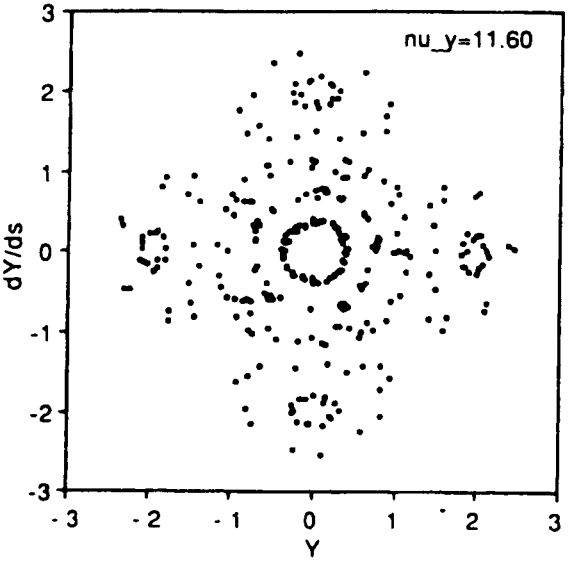


Fig. 4.4 Poincaré map of a test particle for 32 turns when the vertical bare tunes is 11.60. This coherent quadrupole resonance occurs when the vertical coherent tune hits the half-integer tune 2×11.50, thus initiating an emittance growth. (Courtesy Machida. [9])

An incoherent tune shift of 0.33 for a bi-Gaussian distributed beam is the same as an incoherent tune shift of 0.33/2=0.165 of an equivalent-uniform-beam. With $\nu_{0x} = 11.87$, $\nu_{0y} = 11.66$, and $|\Delta\nu_y^{\text{spch}}| = 0.165$ substituted, the two coherent quadrupole tunes of the equivalent-uniform-beam are, according to Eq. (4.82), 2×11.768 and 2×11.54. The approximated result in Eq. (4.83)

is not accurate enough because the two transverse bare tunes are not exactly equal. We see that one of the coherent quadrupole tunes is close to the half-integer stopband at 11.50. In fact, it will become 2×11.768 and 2×11.500 when the bare tune is chosen to be $\nu_{0x} = 11.87$ and $\nu_{0y} = 11.605$. Thus the emittance growth is probably the result of hitting this half-integer tune by the coherent quadrupole mode. This is further verified by the exhibition of the fourth order resonance in the simulation Poincaré plot shown in Fig. 4.4.

In other two-dimensional simulations, Machida and Ikegami [10] also demonstrated that it was the *coherent* rather than the *incoherent* tune shifts that determine the instability of a beam. Some results are illustrated in Fig. 4.5. In the simulations, the horizontal coherent quadrupole tune hits the integer 13 when the beam intensity reaches $\sim$ 15 A. We do see that the horizontal emittance increases rapidly around the beam intensity of 15 A. The vertical coherent quadrupole tune hits the integer 11 when the beam intensity is raised to around

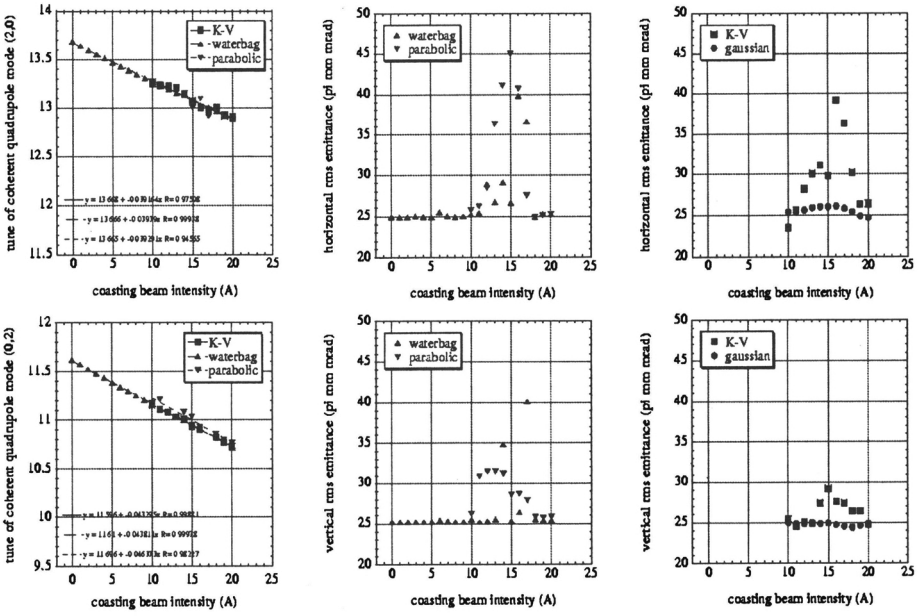


Fig. 4.5 Tune of coherent quadrupole mode (left) and rms emittance at 512 turns after injection (center and right) versus beam intensity. Upper figures show results in the horizontal plane while lower ones show results in the vertical plane. Rms emittance growth is observed when either the horizontal or vertical coherent quadrupole tune crosses an integer. (Courtesy Machida and Ikegami. [10])

13 to 15 A. Around those intensities, large increase in vertical emittance is evident in the plots. However, no growth of emittance has been observed when the incoherent quadrupole tunes, either vertical or horizontal, cross half integers. The simulations were performed using beams with the water-bag distribution, the K–V distribution, and the parabolic distribution. As is seen in the plots, the results do not depend much on the beam distribution.

4.5 Application to Synchrotrons

Let us apply what we have learned to some low-energy synchrotrons. For the Fermilab Booster with an injection energy of 400 MeV and round beam, the bare tunes derived from the lattice are $\nu_{0x} = 6.70$ and $\nu_{0y} = 6.80$. The nearest half-integer is 6.5. Thus, if the half-integer resonance arises from the incoherent motion of the beam particles, the largest incoherent space-charge tune shift allowed will be $|\Delta\nu_x^{\text{spch}}| = 0.20$. If the resonance comes from one of the coherent quadrupole envelope modes hitting the half-integer, the largest incoherent space-charge tune shift allowed becomes[¶] $|\Delta\nu_x^{\text{spch}}| = 0.296$ or $|\Delta\nu_y^{\text{spch}}| = 0.291$. These numbers are obtained from the matrix in Eq. (4.81) by substituting $\frac{1}{2}\nu = 6.5$ for the eigentune and solving for $|\Delta\nu_x^{\text{spch}}|$. On the other hand, from the experimentally measured beam size, the calculated incoherent space-charge tune shift is 0.40, which definitely exceeds the result from incoherent motion and agrees more or less with the result from the coherent mode. So far the estimation has been based on uniform distribution. If the distribution were bi-Gaussian, the largest incoherent space-charge tune shift allowed would become $|\Delta\nu_x^{\text{spch}}| = 2 \times 0.296 = 0.592$ or $|\Delta\nu_y^{\text{spch}}| = 2 \times 0.291 = 0.582$ instead for particles at the center of the beam with small amplitude betatron oscillations.

Similar computations are performed for various low-energy synchrotrons, for which the beams are mostly round and the distribution uniform. The results are tabulated in Table 4.2. We see that for all the synchrotrons listed, the space-charge tune shifts computed from experimentally measured beam sizes exceed those derived from incoherent particle motion and are close to those derived from the coherent modes.

[¶]We can also make the rough estimate of assuming the two betatron bare tunes are equal, i.e., $\nu_{0x} \sim \nu_{0y} \sim 6.70$. Then the incoherent space-charge tune shift according to Eq. (4.83) is $|\Delta\nu_x^{\text{spch}}| \sim |\Delta\nu_x^{\text{spch}}| \sim \frac{4}{3} \times 0.2 = 0.267$.

Table 4.2 Estimated incoherent space-charge tune shifts for various low-energy synchrotrons. The incoherent space-charge tune shifts are derived from the experimentally measured beam size (third column), the assumption that the half-integer resonance comes from the incoherent motion of the beam particles (fourth column), and the assumption that the half-integer resonance comes from a coherent envelope mode (fifth column). We see that the values from experiments exceed those from incoherent motion and agree mostly with those from the coherent modes.

		$\lvert\Delta\nu_x^{\text{spch}}\rvert/\lvert\Delta\nu_y^{\text{spch}}\rvert$		
Synchrotron	Bare tunes ν_{0x}/ν_{0y}	from experiment	from incoh motion	from coherent motion
KEK Booster	2.17/2.30	0.23	0.17	0.25/0.24
FNAL Booster	6.70/6.80	0.40	0.20	0.30/0.29
ISIS	3.70/4.20	0.40	0.20	0.31/0.27
AGS	8.75/8.75	0.58	0.25	0.33/0.33
AGS Booster	4.80/8.75	0.50	0.30	0.46/0.25
CERN PS	6.22/6.22	0.27	0.22	0.29/0.29
CERN PS-2	6.22/6.28	0.36	0.22	0.31/0.31

4.6 Exercises

4.1 Supply the missing steps in transforming the one-dimension envelope equation from Eq. (4.31) to the normalized form of Eq. (4.55). You may need the definition of the betatron function

$$\frac{\beta_x\beta_x''}{2} - \frac{\beta_x'^{\,2}}{4} + \beta_x^2 K_x(s) - 1 = 0, \tag{4.89}$$

where the prime denotes derivative with respect to s, the distance along the accelerator ring, and $K_x(s)$ is the focusing strength of the external quadrupoles.

4.2 Show that the incoherent space-charge tune shift $\Delta\nu_x^{\text{spch}}$ of a one-dimension beam uniformly distributed in the x direction and infinite in the y and s directions is given by

$$2\nu_{0x}\Delta\nu_x^{\text{spch}} = \frac{2\pi r_0 \sigma R^2}{\gamma^3\beta^2\hat{x}}, \tag{4.90}$$

where the beam has extent between $\pm\hat{x}$, σ is the particle density per unit area in the y-s plane, r_0 is the classical particle radius, γ and β are the Lorentz parameters, and R is the mean radius of the accelerator ring.

4.3 Verify the expression for $\langle xE_x\rangle$ given by Eq. (4.49) by computing this quantity for a round beam with (1) uniform distribution and (2) bi-Gaussian distribution.

4.4 Similar to the one-dimensional case, verify in the two-dimensional case that the parametric-resonance driving force vanishes when the incoherent equations are at half integers, showing that the incoherent motion of individual particles can have their tunes right at half-integers without instability.

4.5 Derive the incoherent space-charge tune shifts for the various synchrotrons listed in the last column of Table 4.2 when the intensity of the beam having uniform distribution is increased so that the first coherent envelope mode reaches the half-integer resonance.

Bibliography

[1] R. Baartman, *Betatron Resonances with Space Charge*, Proc. Int. Workshop on Emittance in Circular Accelerators (KEK, Japan, Nov. 1994), KEK Report 95-7, p. 273; R. Baartman, *Betatron Resonances with Space Charge*, Proc. Workshop on Space Charge Physics in High Intensity Hadron Rings, eds. A. U. Luccio and W. T. Weng (Shelter Island, New York, May 4–7, 1998) p. 56.

[2] W. T. Weng, *Space Charge Effects — Tune Shifts and Resonances*, AIP Conf. Proc. **153**, 1987, p. 43.

[3] I. M. Kapchinsky and V. V. Vladimirsky, *Limitations of Proton Beam Current in a Strong Focusing Linear Accelerator Associated with the Beam Space Charge*, Proc. Int. Conf. on High Energy Accel., ed. L. Kowarski (Geneva, Sept. 14–19, 1959), p. 274.

[4] F. Sacherer, *RMS Envelope Equations with Space Charge*, *IEEE Trans. Nucl. Sci.* **NS-18**, 1105 (1971). See also the longer report of the same title in CERN Report CERN-SI-Int.-DL/70-12, Nov., 1970.

[5] P. M. Lapostolle, *Possible Emittance Increase Through Filamentation due to Space Charge*, *IEEE Trans. Nucl. Sci.* **NS-20**, 1101 (1971).

[6] T. P. Wangler, K. R. Crandall, R. S. Mills, and M. Reiser, *Relation Between Field Energy and RMS Emittance in Intense Particle Beams*, *IEEE Trans. Nucl. Sci.* **NS-32**, 2196 (1985).

[7] I. Hoffmann, *Space Charge Dominated Beams Transport*, CERN Accelerator School for Advanced Accelerator Physics, (Oxford, England, Sept. 16–27, 1985), p. 327.

[8] F. J. Sacherer, *Transverse Space-Charge Effects in Circular Accelerators*, Thesis, University of California, Berkeley, Report UCRL-18454, 1968.

[9] S. Machida, *Space Charge Effects in Low Energy Proton Synchrotrons*, *Nucl. Instrum. Meth.* **A309**, 43 (1991).

[10] S. Machida and M. Ikegami, *Simulation of Space-Charge Effects in a Synchrotron*, Proc. of Workshop on Space Charge Physics in High Intensity Hadron Rings, eds. A. U. Luccio and W. T. Weng, (Shelter Island, New York, May 4–7, 1998), p. 73.

2025 © The Author(s). This is an Open Access chapter published by World Scientific Publishing Company, licensed under the terms of the Creative Commons Attribution-NonCommercial 4.0 International License (CC BY-NC 4.0).

Chapter 5

Longitudinal Microwave Instability for Coasting Beams

5.1 Microwave Instability

According to Eq. (2.11), a beam particle inside a bunch changes its energy per turn relative to the synchronous particle according to

$$\frac{d\Delta E}{dn} = eV_{\rm rf}\Big[\sin(\phi_s - h\omega_0\tau) - \sin\phi_s\Big] - \Big[U_s(\delta) - U_{s0}\Big] + C_0\langle F_0^{\parallel}(\tau;s)\rangle_{\rm dyn}, \quad (5.1)$$

where the first two terms on the right represent, respectively, the rf focusing and radiation damping, with ϕ_s being the synchronous phase taking into account potential-well distortion. The last term denotes the dynamic part of the longitudinal wake force [Eq. (2.7)]:

$$\begin{aligned}\langle F_0^{\parallel}(\tau;s)\rangle_{\rm dyn} &= \langle F_0^{\parallel}(\tau;s)\rangle - \langle F_0^{\parallel}(\tau;s)\rangle_{\rm stat} \\ &= -\frac{e^2}{C_0}\left[\int_{-\infty}^{\infty} d\tau'\lambda(\tau';s)W_0'(\tau'-\tau) - \int_{-\infty}^{\infty} d\tau'\lambda_0(\tau')W_0'(\tau'-\tau)\right],\end{aligned} \quad (5.2)$$

where $\lambda(\tau;s)$ is the linear particle density of the beam for a particle that arrives at time τ earlier than the synchronous particle, and $\lambda_0(\tau)$ is the potential-well distorted static linear distribution. Consider a small bump developed along the beam as illustrated in Fig. 5.1. For a purely inductive wake potential $W_0'(\tau) = \mathcal{L}\delta'(\tau)$ when $\tau \geq 0$ with $\mathcal{L} > 0$ being the inductance, the energy gained per turn becomes

$$\frac{d\Delta E}{dn} = e^2\mathcal{L}\lambda_{\rm bump}'(\tau;s), \quad (5.3)$$

where the prime denotes differentiation with respect to τ and the radiation damping terms have been neglected. In above,

$$\lambda_{\rm bump}(\tau;s) = \lambda(\tau;s) - \lambda_0(\tau), \quad (5.4)$$

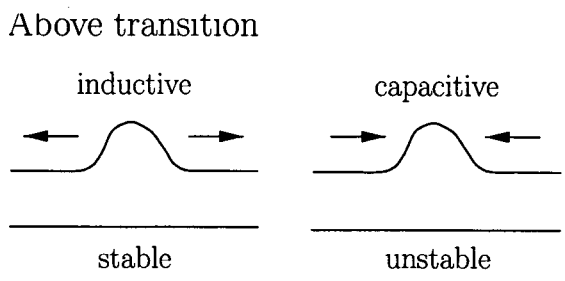


Fig. 5.1 Above transition, an inductive force will smooth out any bump (left) stabilizing the beam against bump formation. However, a capacitive force will continue to enhance bump formation (right) making the beam unstable. Below transition, the opposite is true.

is the time-dependent linear distribution describing the small bump, which is actually the *dynamic part* of the linear distribution $\lambda(\tau; s)$ while $\lambda_0(\tau)$ is the static part. Particles at the front of the bump lose energy because $\lambda'_{\text{bump}}(\tau; s) < 0$, and particles at the rear of the bump gain energy because $\lambda'_{\text{bump}}(\tau; s) > 0$. Above transition ($\eta > 0$), particles at the front arrive earlier and particles at the rear arrive later. Thus the bump will be smoothed out, as illustrated in the left drawing in Fig. 5.1. The result will be the same if the beam sees a capacitive wake ($\mathcal{L} < 0$) and is below transition. However, for capacitive wake above transition, particles at the front of the bump gain energy and will arrive later while those at the rear of the bump lose energy and will arrive earlier, thus enhancing the bump. The situation is the same for an inductive wake below transition. In other words, the beam is unstable against small nonuniformity in the linear distribution.

So far the momentum spread of particles in the beam has not been considered. In order for the bump to grow, the growth rate must be faster than phase-drifting rate coming from the momentum spread of the beam particles, otherwise the bump will be smeared. This damping process is called *wake-driven decoherence*, which is also known as* *Landau damping.* [1] The impedance driving the instability need not be purely reactive. It can be the real part of the impedance. Especially for a sharp bump, the driving frequency will be very high.

This same consideration can also be applied to a bunch provided that the growth must be faster than synchrotron frequency otherwise the bump will be smeared out. Needless to say, the size of the bump is much less than the length of the bunch. The driving impedance must therefore have a wavelength less than the length of the bunch. This growth at high frequencies is called *microwave instability.* This discussion is very similar to that in Sec. 2.4. There, the concern is about the enhancement or partial cancellation of the rf focusing force at rf

*A discussion concerning the relation between decoherence and Landau damping is given in Sec. 13.9.

frequency; therefore an inductive force below transition or a capacitive force above transition is preferred to prevent bunch lengthening. Here, the concern is the evolution of a small bump at high frequencies. In order that a small bump will not grow, the opposite conclusion is obtained. In other words, to smooth out a bump, a capacitive force below transition or an inductive force above transition is preferred.

Because of the random quantum excitation in an electron bunch, there is a finite probability of having electrons jumping outside the bucket and getting lost. To increase the *quantum lifetime* of an electron bunch, a large rf bucket is necessary. Touschek scattering will also convert transverse momentum spread of electrons into longitudinal. [2] In order that those electrons are not lost, the rf bucket has to be large. For this reason, the bucket in an electron machine is in general very much larger than the size of the electron bunch, usually the height of the bucket is more than ten times the rms energy spread of the bunch, in contrast with only about three times or less in proton machines. To achieve this, the rf voltage $V_{\rm rf}$ for an electron ring will be relatively much larger than that in a proton ring of the same energy. Another reason of a high $V_{\rm rf}$ in an electron machine is to compensate for the energy loss due to synchrotron radiation. For example, in the high-energy ring of the SLAC PEP II storing 9 GeV electrons, $V_{\rm rf} = 18.5$ MV is required. On the other hand, $V_{\rm rf}$ for the Fermilab Tevatron storing 1 TeV protons is only 2.16 MV. As a result, the synchrotron tunes for electron rings, $\nu_s \sim 0.01$, are usually an order of magnitude larger than those for proton rings, $\nu_s \sim 0.001$. For this reason, in the consideration of collective instabilities, the synchrotron period of the protons is sometimes much longer than the instability growth times. The wavelength of the perturbation or instability driving force is often of the same size as the radius or diameter of the vacuum chamber, which is usually much shorter than the length of a proton bunch. Thus, the proton bunches can be viewed locally as coasting beams in many instability considerations, and each individual revolution harmonic can therefore be considered as an independent mode. On the other hand, the electron bunch is mostly short, of the same size or even shorter than the diameter of the vacuum chamber. In other words, the electron bunch length can be of the same order or even shorter than the wavelength of the instability driving force. Therefore, for electron bunches, their bunch structure must be considered when studying their instabilities. Individual revolution harmonics are no longer independent and we need to study bunch modes instead. In this chapter, we are going to study the longitudinal instabilities of a coasting beam, or a bunch so long that it can be viewed locally as a coasting beam, leaving the longitudinal instabilities of short bunches to be discussed in the next chapter.

5.1.1 *Dispersion Relation*

Let us first study the dispersion relation governing the longitudinal instability of a proton beam, from which a criterion for stability will be obtained. Consider a coasting beam with mean energy E_0 and mean velocity v_0. The unperturbed distribution in the longitudinal phase-space is

$$\psi_0(\Delta E) = \frac{N}{C_0} f_0(\Delta E), \tag{5.5}$$

where the energy-spread distribution $f_0(\Delta E)$ is normalized to unity when integrated over the energy offset ΔE. The phase-space distribution $\psi_0(\Delta E)$ is normalized to the number of particle N in the beam when integrated over ΔE and distance s along the closed orbit of the on-momentum orbit. Since the linear distribution of a coasting beam is uniform, ψ_0 does not depend on the location s. It is also time-independent in the unperturbed stable mode. The length of the beam can be considered as equal to the circumference C_0 of the accelerator ring. Note that here we are using time t as the independent variable, because we are using a snap-shot description. The variables s and ΔE have been the canonical variables used to describe the beam in the longitudinal phase space.

This stationary distribution is perturbed by an infinitesimal longitudinal density wave ψ_1 which is position-dependent and evolves in time. In the snap-shot description, the particle distribution around the ring is a periodic function in s. At time t, we therefore postulate the ansatz

$$\psi_1(s, \Delta E; t) = \hat{\psi}_1(\Delta E) e^{i(ns/R - \Omega t)}, \tag{5.6}$$

where $R = C_0/(2\pi)$ is the mean radius of the closed orbit of an on-momentum particle, and $\Omega/(2\pi)$ the collective frequency of oscillation to be determined. Here, n denotes the revolution harmonic and can be either positive or negative. However, $n = 0$ must be excluded, otherwise charge conservation will be violated. By ansatz, we mean a postulation of the solution which must be verified to be consistent at the end of the derivation. In fact, Eq. (5.6) can be considered as just one term of a Fourier series expansion. In other words, our postulation is the independence of each revolution harmonic or the revolution harmonics are good eigennumbers. When integrated over ΔE, we get the perturbation line density at time t,

$$\lambda_1(s; t) = \hat{\lambda}_1 e^{i(ns/R - \Omega t)}. \tag{5.7}$$

A monitor at the fixed location s records the perturbation wave passing through. A particle at s experiences a wake force due to all beam particles that pass the

location at an earlier time. This force, with the coupling impedance averaged over the ring circumference, can be expressed as

$$\langle F_0^{\parallel}(s;t)\rangle - \langle F_0^{\parallel}\rangle_{\text{stat}} = -\frac{e^2}{C_0}\int_0^{\infty} dz\, \lambda_1\left(s; t-\frac{z}{v_0}\right) W_0'(z) = -\frac{e^2 v_0}{C_0}\,\lambda_1(s;t) Z_0^{\parallel}(\Omega), \tag{5.8}$$

where $Z_0^{\parallel}(\Omega)$ is the longitudinal impedance of the vacuum chamber evaluated at the collective frequency. As was indicated in Eq. (5.1), only the dynamical or time-dependent part of the linear distribution is involved. The static part, $\lambda_0 = N/C_0$, belongs to the effect of potential-well distortion and has been considered already when the synchronous phase ϕ_s is chosen. In fact, we cannot even talk about potential-well distortion here because there is no longitudinal potential in a coasting beam. This 'static' term, which is proportional to to $\lambda_0 Z_0^{\parallel}(0)$, vanishes because† $Z_0^{\parallel}(0) = 0$.

Notice that the impedance samples the coherent frequency of the perturbation and has no knowledge of the revolution harmonic dependency. This is because the impedance is a localized quantity at a fixed point along the ring. However, as we shall see below, the coherent frequency Ω does contain a harmonic content. The particle energy will be perturbed according to the equation of motion Eq. (5.1),

$$\frac{d\Delta E}{dt} = -\frac{e^2 v_0}{T_0} Z_0^{\parallel}(\Omega)\hat{\lambda}_1 e^{i(ns/R-\Omega t)}, \tag{5.9}$$

where $T_0 = C_0/v_0$ is the revolution period of the on-momentum particles.

Now let us pull out the Vlasov equation in its first order,

$$\frac{\partial \psi_1}{\partial t} + \frac{\partial \psi_1}{\partial s}\frac{ds}{dt} + \frac{\partial \psi_0}{\partial \Delta E}\frac{d\Delta E}{dt} = 0. \tag{5.10}$$

Substitution leads to

$$-i(\Omega - n\omega)\psi_1 = \frac{e^2 v_0 Z_0^{\parallel}(\Omega)}{T_0}\frac{d\psi_0}{d\Delta E}\hat{\lambda}_1 e^{i(ns/R-\Omega t)}, \tag{5.11}$$

where $\omega = v/R$ and v are, respectively, the angular revolution frequency and velocity of the test beam particle with energy offset ΔE. Next we have

$$\psi_1(s, \Delta E, t) = \frac{ie^2 v_0 Z_0^{\parallel}(\Omega)}{T_0}\frac{d\psi_0}{d\Delta E}\frac{\hat{\lambda}_1 e^{i(ns/R-\Omega t)}}{\Omega - n\omega}. \tag{5.12}$$

† At zero frequency, there is no Ampere's law and therefore no dc image current induced in the wall of the vacuum chamber. What is at the wall of the vacuum chamber are only static charges. Thus the dc component of the wake force and therefore $Z_0^{\parallel}(0)$ vanish exactly.

Integrate both sides over ΔE. From Eq. (5.7), the left side is just the perturbation linear density which cancels $\hat{\lambda}_1$ and the exponential on the right side, leaving behind

$$1 = \frac{ie^2 N Z_0^{\parallel}}{T_0^2} \int \frac{f_0'(\Delta E)}{\Omega - n\omega}\, d\Delta E, \tag{5.13}$$

where the unperturbed distribution f_0 in Eq. (5.5) that is normalized to unity has been used, and the prime is derivative with respect to ΔE. An integration by part leads to the dispersion relation

$$1 = \frac{ieI_0\eta n Z_0^{\parallel}(\Omega)\omega_0^2}{2\pi\beta^2 E_0} \int \frac{f_0(\Delta E)}{(\Omega - n\omega)^2}\, d\Delta E, \tag{5.14}$$

where use has been made to the relation

$$\frac{d\omega}{d\Delta E} = -\frac{\eta\omega_0}{\beta^2 E_0}, \tag{5.15}$$

and $I_0 = eN/T_0$ is the mean current of the beam. The negative sign on the right side of Eq. (5.15) comes about because the revolution frequency decreases as energy increases above transition. An immediate conclusion of Eq. (5.14) is that our ansatz for ψ_1 in Eq. (5.6) is correct and all revolution harmonics are decoupled.[‡] Equation (5.14) is called a dispersion relation because it provides the relation of the collective frequency Ω to the wave number n/R. This collective frequency is to be solved from the dispersion relation for each revolution harmonic. If Ω has an imaginary part that is positive, the solution reveals a growth and there is a collective instability.

If there is no energy spread, the collective frequency can be solved easily. The collective frequency of oscillation is

$$\Omega = n\omega_0 + \omega_0 \sqrt{\frac{eI_0\eta n^2}{2\pi\beta^2 E_0} \left[\frac{i\,\mathcal{R}e\, Z_0^{\parallel}(\Omega)}{n} - \frac{\mathcal{I}m\, Z_0^{\parallel}(\Omega)}{n}\right]_{\Omega\approx n\omega_0}}, \tag{5.16}$$

of which the positive imaginary part is the growth rate. Writing it this way, there is no growth above transition ($\eta > 0$) only when $Z_0^{\parallel}$ is purely inductive,

$$\frac{\mathcal{I}m\, Z_0^{\parallel}(n\omega_0)}{n} < 0, \tag{5.17}$$

independent of whether n is positive or negative, as postulated at the beginning of this chapter. By the same token, the beam is stable below transition if the

[‡]This is true when only the linear terms are included in the Vlasov equation. For the inclusion of the lowest nonlinear terms, see Refs. [11, 12].

impedance is purely capacitive. For a low-energy machine, the space-charge impedance per harmonic is frequency-independent and rolls off only at very high frequencies (see Sec. 16.3.1). Therefore above transition, the growth rate is directly proportional to n or frequency. This is the source of *negative-mass instability* for a proton machine just above transition. The terminology comes about because the space-charge force appears to be attractive above transition in binding particles together to form clumps as if the mass of the particles is negative. From Eq. (5.16), we can define

$$\omega_G = \omega_0 \sqrt{-\frac{i\eta e I_0 n Z_0^{\parallel}}{2\pi\beta^2 E_0}} \tag{5.18}$$

as the growth rate without damping due to energy spread. Close examination reveals some similarity of this definition with the expression of synchrotron angular frequency ω_s. We can therefore interpret ω_G as the synchrotron angular frequency inside a bucket created by the interaction of the beam current I_0 with the longitudinal coupling impedance $Z_0^{\parallel}$ at the revolution harmonic n. The factor $-i$ takes care of the fact that the voltage created has to be 90° out of phase with the current so that a bucket can be formed. More about negative-mass instability will be addressed in Chapter 16.

Now let us consider a realistic beam that has an energy spread. Since ω is a function of the energy offset ΔE, define a revolution frequency distribution $g_0(\omega)$ for the unperturbed beam such that

$$g_0(\omega)d\omega = f_0(\Delta E)d\Delta E. \tag{5.19}$$

Substituting into Eq. (5.14) and integrating by part, we obtain

$$1 = -\frac{ieI_0\eta Z_0^{\parallel}(\Omega)\omega_0^2}{2\pi\beta^2 E_0} \int \frac{g_0'(\omega)}{\Omega - n\omega}\, d\omega. \tag{5.20}$$

Given the frequency distribution $g_0(\omega)$ of the unperturbed beam and the impedance $Z_0^{\parallel}$ of the ring at roughly $n\omega_0$, the collective frequency Ω can be solved from the dispersion equation. For a given revolution harmonic n, there can be many solutions for Ω. However, we are only interested in those that have positive imaginary parts. This is because if there is one such unstable solution, the system will be unstable independent of how many stable solutions there are. However, there is a subtlety in dealing with solution on the edge of stability, that is, when Ω is real. The dispersion relation will blow up when $n\omega = \Omega$ during the integration. This subtlety can be resolved if the problem is formulated as an initial value problem, which we will discuss in Chapter 13 on Landau damping. It

will be shown that Eq. (5.20), as it stands, is defined only in the upper half Ω/n-plane and is certainly discontinuous across $\mathcal{I}m\,\Omega/n = 0$. To have the dispersion relation defined analytically (except for isolated poles) in the whole Ω/n-plane, one must perform an analytic continuation from the upper half Ω/n-plane to the lower half Ω/n-plane. The easiest way to accomplish this is to follow a contour of integration from $\omega = -\infty$ to $+\infty$ and go *under* the Ω/n pole as illustrated in Fig. 5.2. If we are only interested in solving for the threshold of instability, we can simply make the replacement

$$\frac{\Omega}{n} \longrightarrow \frac{\Omega}{n} + i\epsilon, \tag{5.21}$$

where ϵ is an infinitesimal positive real number and integrate along the real ω-axis.

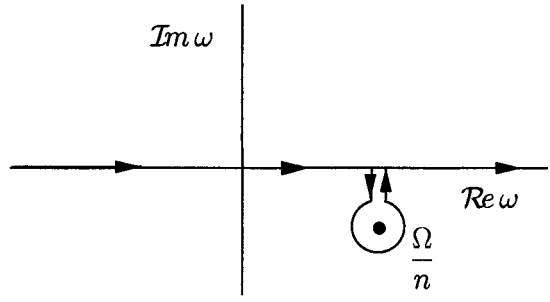


Fig. 5.2 In order that the dispersion relation is an analytic function except for isolated poles, the path of integration must go *under* the Ω/n-pole.

5.1.2 *Stability Curve and Keil–Schnell Criterion*

For a Gaussian distribution, the integral in the dispersion relation is related to the complex error function and an analytic solution can be written down (Exercise 5.3). For other distributions, one has to resort to numerical method. For a given growth rate or $\mathcal{I}m\,\Omega$, we perform the integral for various values of $\mathcal{R}e\,\Omega$ and read off $\mathcal{R}e\,Z_0^{\parallel}$ and $\mathcal{I}m\,Z_0^{\parallel}$ from the dispersion equation. Thus, we can plot a contour in the complex $Z_0^{\parallel}$-plane corresponding to a fixed growth rate. This plot for the Gaussian distribution below transition is shown in Fig. 5.3. What are plotted are the real part U' and imaginary part V' of

$$U' + iV' = \frac{eI_0\beta^2(Z_0^{\parallel}/n)}{|\eta|E_0(\Delta E/E)^2_{\text{FWHM}}} \tag{5.22}$$

at fixed growth rates. From outside to inside, the contours in the figure correspond to growth rates 0.25 to -0.25 in steps of -0.05 in units of full-width-at-

half-maximum (FWHM) of the frequency spread, where negative values imply damping. The contour corresponding to the stability threshold is drawn in dot-dashes and the area inside it is stable. The expression for the contours is given in Eq. (5.47) in Exercise 5.3 below. For a purely reactive impedance, it is clear that a particle beam with Gaussian distribution can be unstable when the impedance is larger than a capacitive threshold. On the other hand, the beam is completely stable no matter how inductive the impedance is. The latter is not completely true because a highly inductive vacuum chamber coupled with a small resistive part of the impedance can easily throw the beam outside the stability region. Figure 5.3 can also be used for a beam below transition by simply flipping the contours upside down.

Note that the positive V'-axis is a cut and those damping contours continue into other Riemann sheets after passing through the cut. Therefore, for each (U', V') outside the stability region bounded by the dot-dashed curve, there can also be one or more stable solutions. However, since there is at least one unstable solution, this outside region is termed unstable.

Obviously, these contours depend on the distribution $g_0(\omega)$ assumed. In Fig. 5.4, we plot the stability contours for various frequency distributions below transition. They are for frequency distributions, from inside to outside, $f(x) = \frac{3}{4}(1-x^2)$, $\frac{8}{3\pi}(1-x^2)^{3/2}$, $\frac{15}{16}(1-x^2)^2$, $\frac{315}{32}(1-x^2)^4$, and $\frac{1}{\sqrt{2\pi}}e^{-x^2/2}$. The innermost one is the parabolic distribution with discontinuous density slopes at

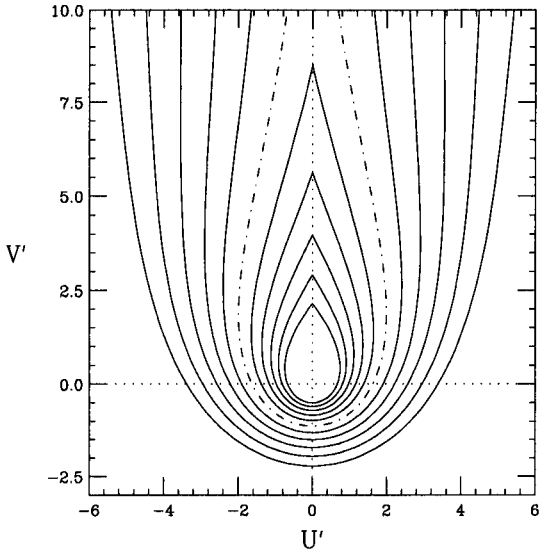


Fig. 5.3 The growth contours for a Gaussian distribution in revolution frequency or energy spread below transition. The abscissa U' and ordinate V' are, respectively, real and imaginary parts of $eI_0\beta^2(Z_0^{\parallel}/n)/[|\eta| E_0(\Delta E/E)^2_{\rm FWHM}]$. From outside to inside, the contours correspond to growth rates 0.25 to −0.25 in steps of −0.05 in units of FWHM of the frequency spread, where negative values imply damping. The contour corresponding to the stability threshold is drawn in dot-dashes and the area inside it is stable. Above transition, the contours should be flipped upside down.

the edges and we see that the stability contour curves towards the origin in the positive V' region. The contour next to it corresponds to continuous density slopes at the edges and it does not dip downward in the positive V' region. As the edges become smoother or with higher derivatives that are continuous, the contour shoots up higher in the upper half plane. For all distributions with a finite spread, the contours end with finite values at the positive V'-axis. For the Gaussian distribution which has infinite spread and continuous derivatives up to infinite orders, the contour only approach the positive V'-axis without intersecting it.

We note in Fig. 5.4 that, regardless the form of distribution, all contours cut the negative V'-axis at ~ -1. Therefore, it is reasonable to approximate the stability region by a unit circle in the U'-V' plane, so that a stability criterion can be written analytically. This is the *Keil–Schnell criterion* which reads [4] (Exercise 5.1)

$$\left|\frac{Z_0^{\parallel}}{n}\right| < F\frac{|\eta|E_0}{eI_0\beta^2}\left(\frac{\Delta E}{E_0}\right)^2_{\text{FWHM}}, \tag{5.23}$$

where F is a distribution-dependent form factor and is equal to the negative V'-intersection of the contour. For all the distributions discussed here, $F \approx 1$. (See Exercise 5.1 below).

For a bunch beam, if the disturbance has a wavelength much less than the

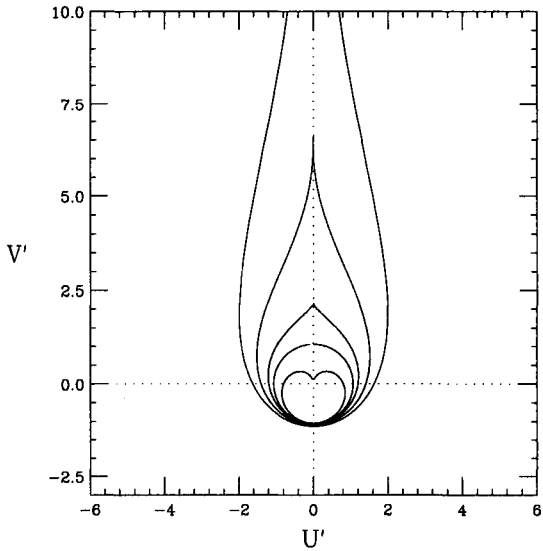


Fig. 5.4 Stability contours for various distributions of revolution frequency or energy spread below transition. The abscissa U' and ordinate V' are, respectively, real and imaginary parts of $eI_0\beta^2(Z_0^{\parallel}/n)/[|\eta|E_0\,(\Delta E/E)^2_{\text{FWHM}}]$. From inside to outside, they correspond to unperturbed distribution density of revolution frequency $f(x) = \frac{3}{4}(1-x^2)$, $\frac{8}{3\pi}(1-x^2)^{3/2}$, $\frac{15}{16}(1-x^2)^2$, $\frac{315}{32}(1-x^2)^4$, and $\frac{1}{\sqrt{2\pi}}e^{-x^2/2}$. Note that all contours cut the V'-axis at about -1. When the stability contours are flipped upside down, they apply to beams above transition.

bunch length, we can view the bunch locally as a coasting beam. Boussard [5] suggested to apply the same Keil–Schnell stability criterion to a bunch beam by replacing the coasting beam current I_0 with the peak current $I_{\rm pk}$ of the bunch. Krinsky and Wang [7] performed a vigorous derivation of the microwave stability limit for a bunch beam with a Gaussian energy spread and found the stability criterion

$$\left|\frac{Z_0^{\parallel}}{n}\right| < \frac{2\pi|\eta|E_0}{eI_{\rm pk}\beta^2}\left(\frac{\Delta E}{E_0}\right)^2_{\rm rms}. \tag{5.24}$$

Comparing with Eq. (5.23), the Krinsky–Wang criterion corresponds to the Keil–Schnell criterion with a form factor of $\pi/(4\ln 2) = 1.133$, which is exactly the negative V'-intersect (see Exercise 5.1.) We want to point out that it is necessary for the Keil–Schnell criterion of Eq. (5.23) to be defined in terms of the *full-width-at-half-maximum* (FWHM) of the energy spread. Only such a reference will give a form factor F that is close to unity for all reasonable distributions of the energy spread. This is because particles of the whole beam including the tail participate in Landau damping and not just those particles at the center of the distribution. Mathematically, it is the gradient of the distribution that appears in the dispersion relation. In this sense, obviously the FWHM provides us with a more accurate measurement of the spread than the rms value. As an example, in terms of FWHM according to Eq. (5.23), the form factors for the Gaussian and the parabolic distributions are, respectively, $F = \pi/(4\ln 2) = 1.133$ and $F = \pi/3 = 1.0472$. On the other hand, since $\Delta E_{\rm FWHM} = 2\sqrt{2\ln 2}\Delta E_{\rm rms}$ for the Gaussian distribution and $\Delta E_{\rm FWHM} = \sqrt{10}\Delta E_{\rm rms}$ for parabolic distribution, if we express the stability criterion in terms of the rms energy spread as in Eq. (5.24), the form factors become $F = 1$ for the Gaussian distribution and $F = 5/3 = 1.67$ for the parabolic distribution.

The stability of a space-charge dominated beam below transition (or inductive-impedance dominated above transition) is not governed by the Keil–Schnell criterion and the stability contours should be consulted. Suppose the distribution is parabolic to start with and the Keil–Schnell limit has been exceeded. The stability contour is heart-shaped as given in Fig. 5.4. Since the gradient of the distribution is discontinuous at the two ends, the instability first takes place there. The result is the smoothing out of the sharp edges of the parabolic distribution into something like $f(x) = \frac{8}{3\pi}(1-x^2)^{3/2}$. The instability will propagate inwards from the smoothened edges to where the gradient of the distribution is largest. This will drive more particles towards the tails resulting in a distribution similar to $(1-x^2)^m$ with larger m. At the same time the stability region increases as illustrated in Fig. 5.4. This process continues and

the eventual distribution may have long and smooth tails resembling those of the Gaussian. For this reason, whatever the distribution is at the beginning, a space-charge dominated beam below transition will have its edges smoothed out and become stable even if the Keil–Schnell criterion has been exceeded severalfold. Thus, to determine the stability criterion driven by the longitudinal space-charge force, the threshold contour for the Gaussian distribution should be consulted.

5.1.3 *Landau Damping*

Keil–Schnell Criterion can be rearrange to read, for $n > 0$,

$$n\omega_0\sqrt{\frac{e|\eta||Z_0^{\parallel}/n|I_0}{2\pi\beta^2E_0}} < n\omega_0\sqrt{\frac{F}{2\pi}}\frac{|\eta|\Delta E|_{\text{FWHM}}}{\beta^2E_0}. \tag{5.25}$$

The left side is the growth rate without damping as discussed in Eq. (5.18) with I_0 replaced by I_{pk} in the case of a bunch. The right side can therefore be considered as the Landau damping rate coming from energy spread or frequency spread. Stability is maintained if Landau damping is large enough. The theory of Landau damping is rather profound, for example, involving the exchange of energy between particles and waves, the mechanism of damping, the contour around the poles in Eq. (5.14), etc. These will be studied in detail in Chapter 13. The readers are also referred to the papers by Landau and Jackson, [1, 8] and also a very well-written chapter in Chao's book. [3] It is interesting to point out that the growth rate without damping on the left side of Eq. (5.25) is proportional to $\sqrt{|\eta|}$, while the damping rate on the right side is proportional to $|\eta|$. Thus a stable beam will eventually become unstable when transition is approached as $|\eta| \to 0$.

5.1.4 *Self-Bunching*

Neglecting the effect of the wake function, the Hamiltonian for particle motion can be written as

$$H = -\frac{\eta}{2v\beta^2E_0}(\Delta E)^2 + \frac{eV_{\text{rf}}}{2\pi vh}\cos(h\omega_0\tau), \tag{5.26}$$

where the synchronous angle has been put to zero and the small-bunch approximation has been relaxed. It is easy to see that the height of the bucket is

$$\Delta E|_{\text{bucket}} = \sqrt{\frac{eE_0V_{\text{rf}}}{\pi h|\eta|}}. \tag{5.27}$$

Keil–Schnell criterion can now be rearranged to read

$$\sqrt{\frac{eE_0 I_0 |Z_0^{\parallel}|}{\pi n |\eta|}} < \sqrt{\frac{F}{\pi \beta^2}} \Delta E_{\text{FWHM}} \tag{5.28}$$

Comparing with Eq. (5.27), the left side can be viewed as the height of a bucket created by an induced voltage $I_0 \left|Z_0^{\parallel}\right|$ while the right side represents roughly the half full-energy spread of the beam. This induced voltage will bunch the beam just as an rf voltage does. If the self-bunched bucket height is less than the half full energy spread of the beam, the bunching effect will not be visible and beam remains coasting. Otherwise, the beam breaks up into bunchlets of harmonic n, and we call it unstable. This mechanism is known as *self-bunching.*

In fact, self-bunching is not so simple. The image current of the beam is rich in frequency components. For the component at the resonant frequency of the impedance, the voltage induced, called *beam-loading voltage*, is in phase with the image current, or more correctly in opposite direction of the beam.[§] Such voltage will not create any rf-like bucket at all, and therefore cannot produce self-bunching. Remember that when the beam is in the storage mode inside an accelerator ring, the rf voltage is at 90° to the beam current and the bucket created will be of maximum size—the so-called *stationary bucket* with synchronous angle $\phi_s = 0$ when the operation is below transition. As the synchronous angle ϕ_s increases, the angle between the beam-loading voltage (which acts as the rf voltage here) and the beam, or the *detuning angle* $\psi = \frac{\pi}{2} - \phi_s$, defined in Eq. (5.31) below, decreases and so is the bucket area—the so-called *moving bucket.*

When the rf voltage is in phase with the beam, the synchronous angle $\phi_s = \frac{\pi}{2}$ and the bucket area shrinks to zero. In order for the beam image current to develop spontaneous self-bunching, the fields developed must be of such a phase and amplitude as to develop a real bucket of sufficient area to contain the beam. Although a small beam-loading angle or a large synchronous angle will result in a small bucket area, however, as the beam frequency moves away too far from the resonance frequency, the beam-loading voltage induced by the resonance impedance decreases also because the resonant impedance rolls off when the detuning is large. Consequently, there is a frequency deviation between the beam Fourier component and the resonance frequency at which the developed bucket area passes through a maximum. Some may argue that it is not the bucket area but the bucket height that sets the instability threshold, and the

[§]Readers who are not familiar with beam-loading may postpone this subsection until after going over Chapter 7.

bucket height also goes through a maximum in between $\phi_s = 0$ and $\frac{\pi}{2}$. It is this bucket height that should enter into Eq. (5.27) for the stability criterion.

The impedance of a resonance is

$$Z_0^{\parallel}(\omega) = \frac{R_s}{1 - iQ\left(\frac{\omega}{\omega_r} - \frac{\omega_r}{\omega}\right)}, \tag{5.29}$$

where R_s is the shunt impedance, Q the quality factor, and ω_r the angular resonant frequency. When the frequency ω of the image current is close to the resonant frequency, we can write

$$Z_0^{\parallel}(\omega) \approx R_s \cos\psi \, e^{-i\psi}, \tag{5.30}$$

with the detuning angle defined as

$$\tan\psi = 2Q\,\frac{\omega_r - \omega}{\omega_r}. \tag{5.31}$$

Therefore, the beam-loading voltage induced by the image current of frequency component ω will be proportional to $\cos\psi$ and at an angle ψ from the image current. Since $\psi = \frac{\pi}{2} - \phi_s$ and both the bucket area and height are proportional to the square root of the voltage, we have,

$$\begin{aligned} \text{induced bucket area} &\propto \alpha(\Gamma)\sqrt{\Gamma}, \\ \text{induced bucket height} &\propto \beta(\Gamma)\sqrt{\Gamma}, \end{aligned} \tag{5.32}$$

where $\Gamma = \sin\phi_s = \cos\psi$. The parameter $\alpha(\Gamma)$ is the ratio of the moving bucket area to the stationary bucket area (when $\Gamma = 0$), and the parameter $\beta(\Gamma)$ is the ratio of the moving bucket height to the stationary bucket height, [9] both of which can be derived straightforwardly from a Hamiltonian, like the one in Eq. (5.26) with a nonzero synchronous angle or the one in Eq. (2.18) with the wake potential removed. The induced bucket area and bucket height area are plotted against Γ in Fig. 5.5. We see that the induced bucket area has a maximum when $\Gamma = 0.25$ or the detuning angle $\psi = 76°$, while the induced bucket height has a maximum when $\Gamma = 0.39$ or the detuning angle $\psi = 67°$. From these results, the most probable frequency at which self-bunching takes place can be inferred.

There are two comments. First, our discussion above is for an accelerator operating below transition. The detuning angle is positive implying that the frequency shift is towards the inductive or low-frequency side of ω_r. When the accelerator is above transition, the detuning will be towards the capacitive or high-frequency side of ω_r. This can be easily understood in a phasor-diagram description, which we will pursue in Chapter 7. Second, the synchronous angle

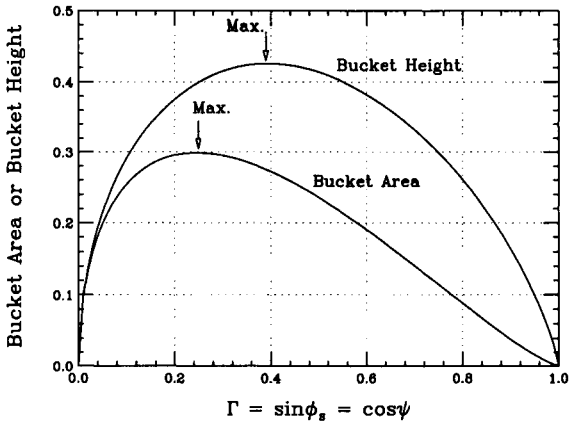


Fig. 5.5 Plot showing the area and height of the bucket created by image current interacting with a resonant impedance. At a certain detuning ψ, describing the frequency offset of the image current Fourier component from the resonant frequency of the impedance, the induced bucket area or bucket height passes through a maximum. Self-bunching is most probable when the bucket area or bucket height is maximized.

ϕ_s that we reference in this subsection is in fact the negative of the usual synchronous angle. This is because the beam-loading voltage is essentially in the opposite direction of the beam current. Therefore the beam-loading voltage will decelerate the beam instead of the usual acceleration by the rf voltage. However, the sign of ϕ_s does not affect the area or height of the induced bucket.

5.1.5 *Overshoot*

When the current is above the microwave threshold, the self-bunching concept tells us that there will be an increase in energy spread of the beam. The increase continues until it is large enough to stabilize the beam again according to the Keil–Schnell criterion. For a proton beam, experimental observation indicates that there will be an overshoot. Let ΔE_i be the initial energy spread which is below the threshold energy spread ΔE_{th} postulated by the Keil–Schnell criterion. The final energy spread ΔE_f was found to be given empirically by [10]

$$\Delta E_i \Delta E_f = \Delta E_{\text{th}}^2. \tag{5.33}$$

Thus the final energy spread is always larger than the threshold energy spread. Overshoot formulas similar to but not exactly the same as Eq. (5.33) have been derived by Chin and Yokoya, [11] and Bogacz and Ng. [12] The derivation involves the Vlasov equation in the second order of the perturbation. It is the nonlinear effect of the perturbation that leads to the overshoot effect. For a bunch, the rf voltage introduces synchrotron oscillations. Thus, an increase in energy spread implies also eventual increase in bunch length. At the same time, the bunch area will be increased also.

The situation is quite different for electron bunches and no overshoot has

ever been reported. A possible reason is the presence of radiation damping. The evolution of electron bunches above the stability threshold will be discussed in Chapter 6.

5.2 Observation and Cure

In order for a bunch to be microwave unstable, the growth rate has to be much faster than the synchrotron frequency. For the Fermilab Main Ring, the synchrotron period was typically about 100 to 200 turns or 2 to 4 ms. A naive way to observe the microwave growth is to view the spectrum of the bunch over a large range of frequencies at a certain moment. However, the bunch spectrum produced by a network analyzer is usually via a series of frequency filters of narrow width, starting from low frequencies and working its way towards high frequencies. This process is time consuming. As soon as the filtering reaches the frequencies concerned, typically a few GHz, the microwave growth may have been stabilized already through bunch dilution, and therefore no growth signals will be recorded. The correct way is to set the network analyzer at a narrow frequency span and look at the beam signal as a function of time. The frequency span is next set to an adjacent narrow frequency interval and the observation repeated until the frequency range of a few GHz has been covered. Besides, we must make sure that the network analyzer is capable of covering the high frequency of a few GHz for the microwave growth signals. The cable from the beam detector to the network analyzer must also be thick enough so that high-frequency attenuation is not a problem in signal propagation. Such an observation was made at the CERN Intersecting Storage Ring (ISR) which is a coasting beam machine. [13] The network analyzer was set at zero span at 0.3 GHz. The beam current was at 55 mA. The signal observed from injection for 0.2 s is shown at the lower left corner of Fig. 5.6 in a linear scale. We see the signal rise sharply and decade very fast, implying an instability which saturates very soon. The beam current was next increased by steps to 190 mA and the observation repeated. We notice that with a higher beam current, the instability starts sooner and stays on longer. The center frequency of the network analyzer was next increased in steps of 0.2 GHz and the observation repeated. The observation reveals an instability driven by a broadband impedance centering roughly at 1.2 GHz. Microwave instability can also be revealed in monitoring the longitudinal beam profiles, sometimes known as mountain ranges, via a wall resistance monitor. An example is shown in Fig. 5.8. From the ripples, the frequency of the driving impedance can be determined.

One way to induce microwave instability is to lower the rf voltage adiabatically. As the momentum spread of the bunch becomes lower than the Keil–

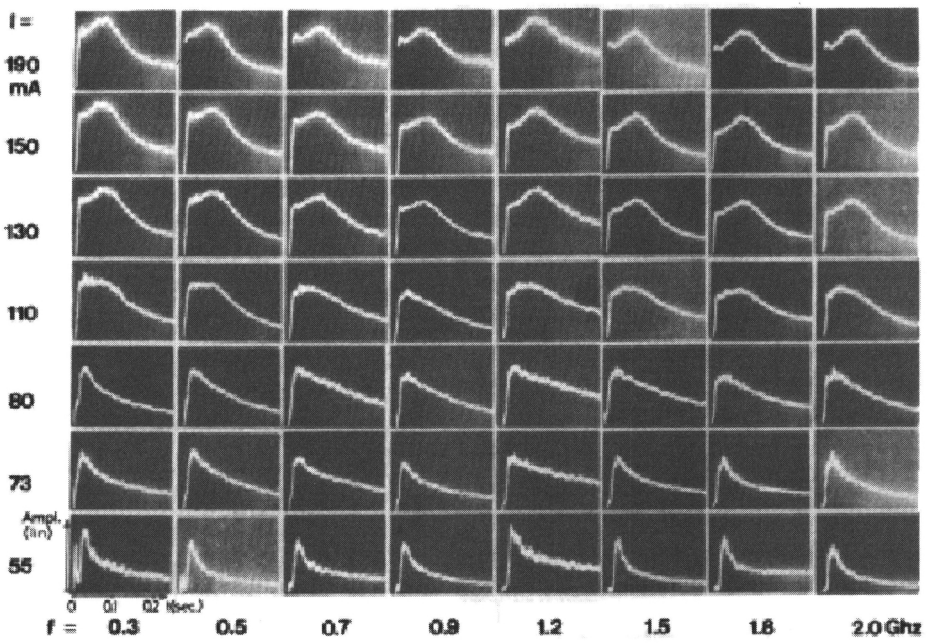


Fig. 5.6 Pick-up signal after injection in the CERN ISR, for different observation frequencies but at zero span and different values of beam current. For high beam current, the signal grows before it decays. (Courtesy Hereward. [13])

Schnell criterion, microwave instability will develop. From the critical rf voltage, the momentum spread of the bunch can be computed and the impedance of the vacuum chamber driving the instability can be inferred. The rf voltage of the cavities in a proton synchrotron cannot be very much reduced, otherwise multipactoring will occur. The total voltage of the rf system can, however, be reduced by adjusting the phases between the cavities. For example, if the phase between two cavities is 180°, the voltages in these two cavities will be canceled. This is called paraphasing. For this reason, it is not possible to know the rf voltage exactly. Small errors in the paraphasing angles will bring about a large uncertainty in the tiny paraphased voltage. As a result, the impedance determined by this method may not be accurate.

Another way to observe microwave instability is through debunching. The rf voltage is turned off abruptly and beam starts to debunch. During debunching, the local momentum spread decreases. When the latter is small enough, microwave instability occurs. From the time the instability starts, the impedance of the vacuum chamber can be inferred with the help of the Keil–Schnell criterion. In performing this experiment, the rf cavities must be shorted mechanically

after the rf voltage is turned off. Otherwise, the beam will excite the cavities, a process called beam-loading. The excited fields inside the cavities can bunch the beam developing high-frequency signals resembling signals of microwave instability. In addition, the beam-loading voltage will bunch the beam, not allowing the debunching process to continue. Such an experiment has been performed at the CERN Proton Synchrotron (CPS) and the observation is displayed in Fig. 5.7. [5] The figure shows the time development at 2 ms per division. The top trace shows the rf voltage which is turned off at 4 ms point. The network analyzer was set at a span from 1.5 to 1.8 GHz and the beam pick-up signal of the beam is shown in the lower trace. We see high-frequency beam signal start developing about 1 ms after the rf voltage is turned off. The signal grows for a few ms before it subsides. The shortcoming of this method of impedance measurement is the difficulty in determining the exact time when the microwave instability starts to develop. One must understand that the growth of the signal amplitude is exponential; therefore the very initial growth may not be visible.

Since microwave instability occurs so fast, it is difficult to use a damper system to cure it. One way to prevent the instability is to blow up the bunch so that the energy spread is large enough to provide the amount of Landau damping needed. Another way is to reduce the total longitudinal coupling impedance of the ring by smoothing out the discontinuities of the vacuum chamber. For negative-mass instability driven by the space-charge impedance just after transition, one can try to modify the ramp curve so that transition can be crossed faster. Of course, a γ_t-jump mechanism will certainly be very helpful.

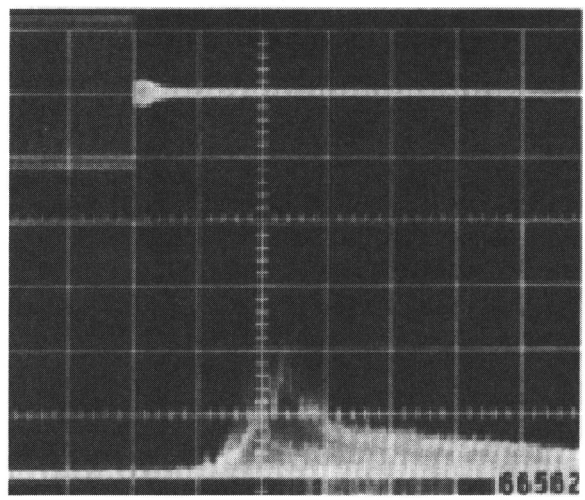


Fig. 5.7 Microwave signal observed during debunching in the CERN CPS after the rf voltage (top trace) is turned off. The lower trace shows the beam signal at 1.5 to 1.8 GHz. The sweep is 2 ms per division. (Courtesy Boussard. [5])

5.3 Ferrite Insertion and Instability

In Sec. 2.7, we discuss an experiment at the Los Alamos PSR where the space-charge repulsive force is large compared with the available rf bunching force. Ferrite rings enclosed inside two pill-box cavities were installed into the vacuum chamber so that the beam would see an amount of inductive force from the ferrite, hoping that the space-charge repelling force would be compensated. The experimental results indicate that this additional inductive force did cancel an appreciable amount of the space-charge force of the intense proton beam to a certain extent. This is evident because the bunch lengths were shortened in the presence of the ferrite inserts with zero bias of the solenoidal current windings outside the ferrite tuners, and lengthened when the ferrite rings were biased. Also, the rf voltage required to keep the protons bunched to the required length had been lowered by about one-third in the presence of the ferrite insertion. At the same time the gap between successive proton beams was the cleanest ever seen, indicating that the rf buncher was able to keep the beam within the space-charge distorted but ferrite compensated rf buckets so that no proton would leak out. However, the space-charge compensation of the potential-well distortion had not been perfect. The ferrite insertion did lead to serious instabilities when two ferrite tuners were installed. We are going to discuss below the instabilities and how they were finally alleviated.

5.3.1 *Microwave Instability*

The PSR was upgraded in 1998. The two previous ferrite tuners together with an additional one were installed in order to compensate for the space-charge force of the higher intensity beam. However, an instability was observed. [14] With the rf buncher off, the maintain-range plot in Fig. 5.8 shows two consecutive turns of a chopped coasting beam accumulated for 125 μs and stored for 500 μs. The signals were recorded by a wideband wall-gap monitor. The ripples at the beam profile indicate that a longitudinal microwave instability has occurred. The fast Fourier transform spectrum in Fig. 5.9 shows that the instability is driven at 72.7 MHz or the 26th revolution harmonic. The instability had also been observed in bunched beam. Ripples also show up at the rear half of a bunch, as recorded by the wall-gap monitor in Fig. 5.10. The left plot is two successive turns of a $\sim$ 250-ns (full width) bunch. Apparently, the instability is tolerable because ripples do not distort the shape of the bunch by too much. However, the $\sim$ 100-ns (full width) bunch on the right plot is totally disastrous. The instability lengthens the bunch to almost 200 ns with very noticeable head-tail

asymmetry. Although longitudinal microwave instabilities have been observed in many accelerators, however, all of them were above transition. The instabilities at the PSR might have been the first microwave instabilities that occurred below transition. Because microwave instabilities have always been associated with beams above transition, some accelerator physicists are even reluctant to identify the PSR instabilities that took place below transition by the same category of microwave instabilities. Nevertheless, the theory that has been developed so far never makes any distinction whether the beam is above or below transition.

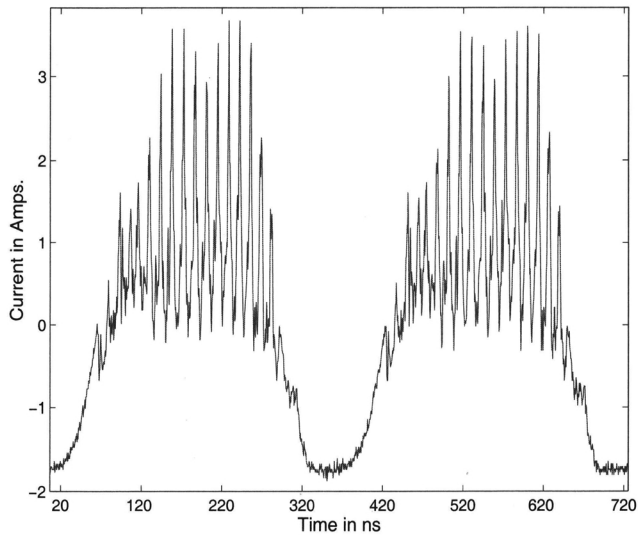


Fig. 5.8 Beam profile of two consecutive turns of a chopped coasting beam recorded in a wall-gap monitor after storage of $\sim$ 500 μs. The ripples show that a longitudinal microwave instability has occurred. (Courtesy Macek. [15])

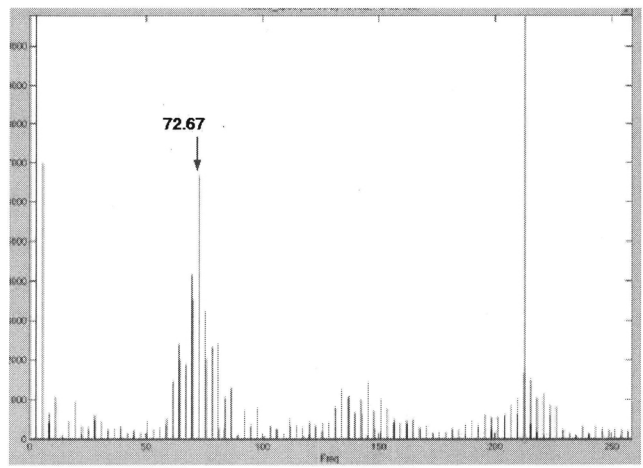


Fig. 5.9 Spectrum of the longitudinal instability signal of a chopped coasting beam showing the driving frequency is at 72.7 MHz. (Courtesy Macek. [15])

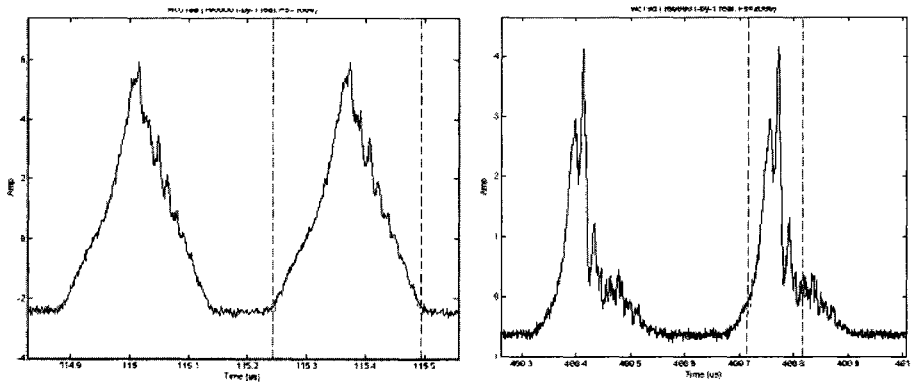


Fig. 5.10 Instability perturbation on profiles of bunches with full width 250 ns (left) and 100 ns (right). The effect on the 250 ns bunch may be tolerable, but certainly not on the 100 ns bunch, which has lengthened almost to 200 ns. (Courtesy Macek. [15])

5.3.2 *Cause of Instability*

In order to understand the reason behind the instability, let us first construct a simple model for the ferrite tuner. To incorporate loss, the relative permeability of the ferrite can be made complex:[¶] $\mu_s \to \mu_s' + i\mu_s''$, where both μ_s' and μ_s'' are real. The impedance of a ferrite core of outer/inner diameter d_o/d_i and thickness t is therefore

$$Z_0^{\parallel} = -i(\mu_s' + i\mu_s'')\omega\mathcal{L}_0, \tag{5.34}$$

where $\mathcal{L}_0 = \mu_0 t \ln(d_0/d_i)$ denotes the geometric contribution of the ferrite inductance, i.e., when the relative permeability $\mu_s = 1$. It is clear that μ_s' and μ_s'' must be frequency-dependent, because the impedance, being an analytic function, satisfies a dispersion relation. Their general behaviors are shown in Fig. 5.11. For the Toshiba M_4C_{21A} ferrite, μ_s' is roughly constant at ~ 50 to 70 at low frequencies and starts to roll off around $\omega_r/(2\pi) \sim 50$ MHz, while μ_s'', being nearly zero at low frequencies, reaches a maximum near $\omega_r/(2\pi)$. The simplest model for a piece of ferrite consists of an *ideal* inductance $\mathcal{L}_p$ and an *ideal* resistor R_p in parallel, as indicated in Fig. 5.12(a).

The impedance of the ferrite core is

$$Z_0^{\parallel}(\omega) = -i\omega\mathcal{L}_p \frac{1 - j\omega/\omega_r}{1 + \omega^2/\omega_r^2}, \tag{5.35}$$

[¶]The subscript 's' signifies that the permeabilities are defined as if an inductor and a resistor are *in series*.

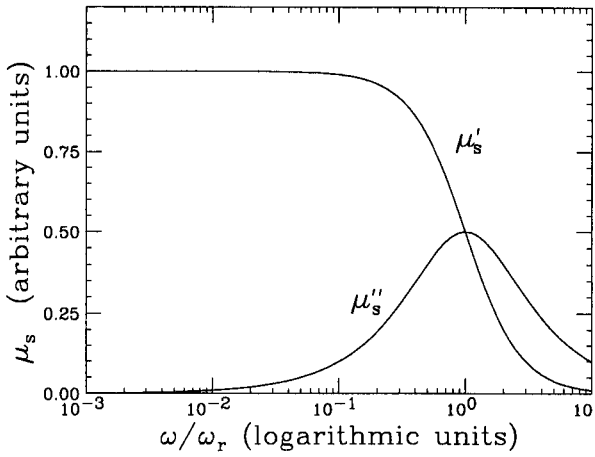


Fig. 5.11 Plot of μ_s' and μ_s'' as functions of frequency in the two-parameter model. These are the typical properties of μ' and μ'' for most ferrites.

with a resonance at

$$\omega_r = \frac{R_p}{\mathcal{L}_p}, \tag{5.36}$$

and

$$\mu_s' = \frac{\mathcal{L}_p}{\mathcal{L}_0}\frac{1}{1+\omega^2/\omega_r^2}, \qquad \mu_s'' = \frac{\mathcal{L}_p}{\mathcal{L}_0}\frac{\omega/\omega_r}{1+\omega^2/\omega_r^2}. \tag{5.37}$$

We see that the series μ_s' is relatively constant at low frequencies and starts to roll off when approaches ω_r, while μ_s'' increases as ω at low frequencies and resonates at ω_r. The corresponding longitudinal wake potential is, for $\tau > 0$,

$$W_0'(\tau) = R_p\,[\,\delta(\tau) - \omega_r e^{-\omega_r \tau}\,]. \tag{5.38}$$

When the ferrite is biased, $\mathcal{L}_p$ decreases so that μ_s' decreases. In this model, this is accomplished by a rise in the resonant frequency ω_r. Actually, measurements

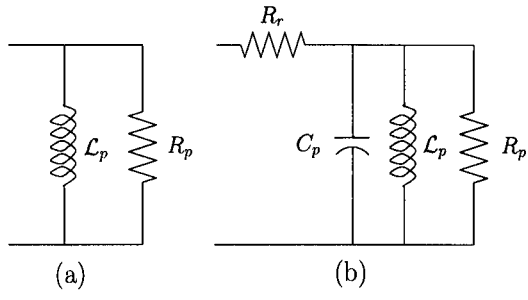


Fig. 5.12 (a) Two-element model of ferrite. (b) Three-element model of ferrite cores enclosed in a pill-box cavity.

show that the resonant frequency of μ_s'' does increase when the ferrite is biased. As a result, this simple two-parameter model gives a very reasonable description of the ferrite.

With the ferrite cores enclosed in a pill-box cavity, a three-parameter broad-band parallel-RLC resonance model, as indicated in Fig. 5.12(b), appears to be more appropriate for the ferrite tuner as a whole. We therefore have, for the inductive insert,

$$Z_0^{\parallel}(\omega) = \frac{R_p}{1 - iQ\left(\dfrac{\omega}{\omega_r} - \dfrac{\omega_r}{\omega}\right)}, \tag{5.39}$$

where the resonant frequency is $\omega_r = (\mathcal{L}_p C_p)^{-1/2}$ and the quality factor is $Q = R_p\sqrt{C_p/\mathcal{L}_p}$. Sometimes there may also be an additional residual resistance R_r which we neglect for the time being.

For a space-charge dominated beam, the actual area of beam stability in the complex $Z_0^{\parallel}/n$-plane (or the traditional U'-V' plane) is somewhat different from the commonly quoted Keil–Schnell estimation. [4, 5] In Fig. 5.13, the heart-shape solid curve, denoted by 1, is the threshold curve for parabolic distribution in momentum spread, where the momentum gradient is discontinuous at the ends of the spread. Instability develops and a smooth momentum gradient will result at the ends of the spread, changing the threshold curve to that of a

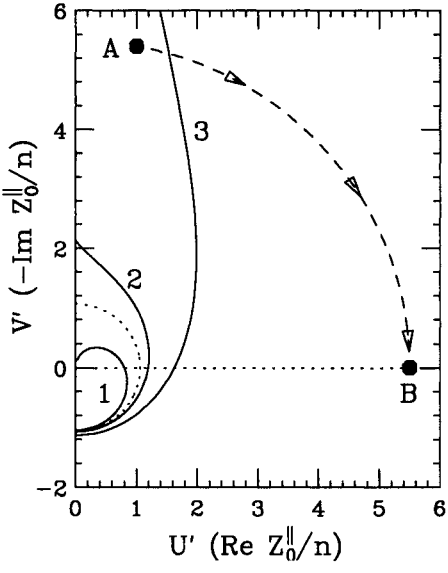


Fig. 5.13 Microwave instability threshold curves in the complex $Z_0^{\parallel}$- (or U'-V'-) plane, for (1) parabolic momentum distribution, (2) distribution with a continuous momentum gradient, and (3) Gaussian momentum distribution. The commonly quoted Keil–Schnell threshold criterion is denoted by the circle in dots. An intense space-charge dominated beam may have impedance at Point A outside the Keil–Schnell circle and is stable. A ferrite tuner compensating the space-charge completely will have a resistive impedance roughly at Point B and is therefore unstable.

distribution represented by 2, for example, $\frac{15}{16}(1-\delta^2/\hat{\delta}^2)^2$, where δ is the fractional momentum spread and $\hat{\delta}$ the half momentum spread. Further smoothing of the momentum gradient at the ends of the spread to a Gaussian distribution will change the threshold curve to 3. On the other hand, the commonly known Keil–Schnell threshold is denoted by the circle of unit radius in dots. This is the reason why in many low-energy machines the Keil–Schnell limit has been significantly overcome by a factor of about 5 to 10. [6] In this case, the space charge is almost the only source of the impedance, the real part of the impedance can be typically orders of magnitude smaller. As an example, if the impedance of the Los Alamos PSR is at Point A, the beam is within the microwave stable region if the momentum spread is Gaussian-like, although it exceeds the Keil–Schnell limit. Now, if we compensate the space-charge potential-well distortion by the ferrite inductance, the ferrite required will have an inductive impedance at low frequency equal to the negative value of the space-charge impedance at A, for example, about -5.5 units according to Fig. 5.13. However, the ferrite also has a resistive impedance or $\mathcal{R}e\, Z_0^{\|}$ coming from μ_s''. Although $\mathcal{R}e\, Z_0^{\|}/n$ is negligible at low frequencies (for example, the rf frequency of 2.796 MHz of the PSR), it reaches a peak value near $\omega_r/(2\pi)$ (about 50 to 80 MHz for the Toshiba M_4C_{21A} inside the pill-box container) with the peak value the same order of magnitude as the low-frequency $\mathcal{I}m\, Z_0^{\|}$. Actually, according to the *RLC* model discussed above, we get approximately

$$\frac{\mathcal{R}e\, Z_0^{\|}/n|_{\mathrm{pk}}}{\mathcal{I}m\, Z_0^{\|}/n|_{\omega\to 0}} \approx \frac{Q^2+Q+1}{Q+2} = \left\{\begin{array}{l} Q \text{ if } Q \gg 1 \\ 1 \text{ if } Q \sim 1 \\ \frac{1}{2} \text{ if } Q \ll 1 \end{array}\right\} \geq \frac{1}{2}. \tag{5.40}$$

The *RL* model gives the same impedance ratio of $\frac{1}{2}$ as the low-Q case of Eq. (5.40). Thus the ferrite will contribute a resistive impedance denoted roughly by Point B (~ 5.5 units) when $Q \sim 1$ or at least one half of it when $Q \ll 1$. This resistive impedance of the ferrite insert will certainly exceed the threshold curve and we believe that the longitudinal instability observed at the Los Alamos PSR is a result of this consideration. It follows from here that such low-frequency compensation of an intense space-charge induced potential-well distortion will result in the microwave instability at high frequencies, $\omega \simeq \omega_r$. The conclusion appears to be that strong space-charge potential-well distortion can only be compensated by the ferrite inductance to some extent to ensure that the resistive part of the ferrite insertion is kept below the microwave instability threshold. However, Eq. (5.40) is only correct when the *RLC* circuit is composed of an *ideal* resistor, an *ideal* inductor, and an *ideal* capacitor. In reality, the ferrite cores are much more complicated. To represent the inductor insert, many of these

elements are frequency-dependent. Thus, if one chooses the right ferrite in the construction of the inductive insert, it is possible to have the ratio of $\mathcal{R}e\, Z_0^{\parallel}/n|_{\rm pk}$ to $\mathcal{I}m\, Z_0^{\parallel}/n|_{\omega\to 0}$ much less than $\frac{1}{2}$. Such a ferrite will be the best candidate for space-charge compensation.

5.3.3 *Heating the Ferrite*

One way to avoid the longitudinal microwave instability driven by the compensating ferrite is to choose a ferrite having the properties of high μ_s' at low frequencies and low loss[‖] at high frequencies. Their ratio should be at least or larger than ~ 10. Past experience indicates that when a piece of ferrite is heated up, μ_s' will increase and hopefully the loss at high frequencies will decrease, thus having exactly the same properties that we are looking for.

A measurement of the temperature dependency of the ferrite has been made on a ferrite insert similar to those manufactured for the PSR was used, but much shorter containing only several ferrite cores. [16] A sinusoidal wave was introduced from one end of the ferrite tuner via an antenna while the transmitted wave was received with another antenna at the other end. What was measured was S_{21}, the forward transmission through the network (in this case cavity), or the attenuation of a passive network. The results are shown in Fig. 5.14 and reveal that the resonant loss peak drops by a factor of about 8 when the ferrite cores are heated from the room temperature of 23°C to 100°C.

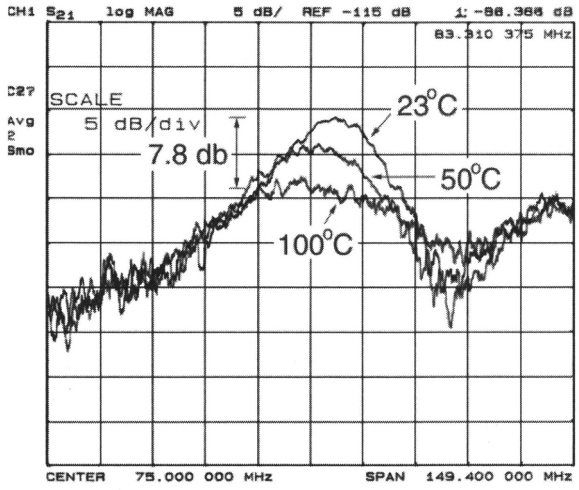


Fig. 5.14 An antenna at one end of the ferrite tuner sends out a sinusoidal wave to be picked up by another antenna at the other end of the tuner, and the loss is recorded. As the ferrite cores are heated from room temperature to 100°C, the loss has reduced by almost 8 times. (Courtesy Popovic. [16])

[‖]Low loss does not imply low μ_s''. Whenever ferrite is used, for example in the inductor insert, there will be inevitably capacitance involved. Thus low loss actually implies low R_p.

A measurement of the permeability of the ferrite has also been made on a single Toshiba M_4C_{21A} ferrite core as a function of core temperature. [17] To provide both a good electrical circuit path and a uniform core temperature, the core was encased in an aluminum test fixture before being placed on a hot plate. The top half of the test fixture consisted of a machined aluminum disk, 9 in in diameter and 1.25 in thick. The inner section of the disk was machined out 0.005 in undersize to accommodate the ferrite core. The disk was then heated and the core was slipped into the disk. Upon cooling, the aluminum disk contracted and made a good thermal contact with one side and the outer edge of the ferrite core. The aluminum fixture and core were then flipped over onto a flat aluminum plate so that only the inner edge of the core was exposed. A good electrical connection between the aluminum disk and flat plate was made using strips of adhesive backed copper tape. The test fixture was placed on a hot plate and covered with two fire bricks. The test fixture was then heated to 175°C and allowed to cool slowly.

The impedance measurement was made by placing the probe of an HP4193A vector-impedance meter directly across the inner edge of the ferrite core. Impedances were measured from 10 MHz to 110 MHz in 10-MHz-steps from 150°C to 25°C. The temperature of the core was monitored by a Fluke 80T-150U temperature probe inserted into a small hole in the aluminum disk portion of the test fixture.

In order to make an electrical model of the entire core and test fixture structure, it was necessary to obtain the equivalent parallel capacitance of the test set-up as depicted in Fig. 5.12(b). The capacitor C_p was determined by adding additional fixed 100-pf capacitors across the inner edge of the ferrite core and observing the change in the resonant frequency of the structure from 41 to 28 MHz, a frequency range in which the μ_s' of the ferrite is known to be relatively constant. In this manner, a capacitance of $C_p = 75$ pf was chosen to represent the equivalent parallel capacitance of the test circuit. There was also a series residual resistance of $R_r = 0.55\ \Omega$ in the probe. This residual resistance introduces a large error at low frequencies (below $\sim$ 10 Hz) when the resistive part of the RLC circuit is small. From the measurements of the input impedance, R_p and $\mathcal{L}_p$ were computed. From Eq. (5.37), the relative permeability, μ_s' and μ_s'' were inferred. These are plotted in Figs. 5.15. We see that from 23°C to 150°C, μ_s' at low frequencies has almost been doubled, implying that the inductance $\mathcal{L}_p$ at low frequencies has been doubled according to Eq. (5.37). The loss component μ_s'' also increases with temperature with its peak moves towards lower frequencies. This is obvious in the two-element model of a ferrite, because Eq. (5.37) says that the peak of μ_s'' is proportional to $\mathcal{L}_p$ and independent of R_p.

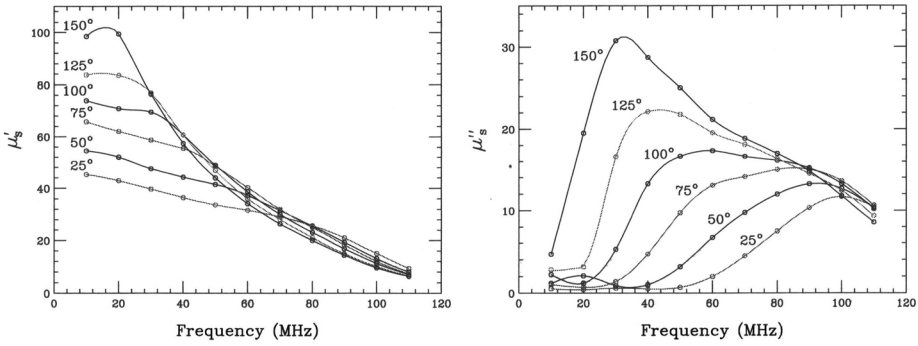


Fig. 5.15 Measured real (left) and imaginary (right) parts of the series magnetic permeability, μ_s' and μ_s'', of a single Toshiba M_4C_{21A} ferrite core up to 110 MHz at 25°, 50°, 75°, 100°, 125°, and 150°C. Measured points are denoted by circles. (Courtesy Wildman. [17])

There is always a capacitance accompanied the ferrite insert. For a pill-box enclosing a single ferrite core, the capacitance measured was $C_p = 75$ pF, which is not too different from the computed value of 93 pF where a relative dielectric $\epsilon_r = 13$ is assumed for the ferrite. The real part of the impedance of the ferrite insert per ferrite core, $\mathcal{R}e\, Z_0^{\parallel}$, is shown in the left plot of Fig. 5.16. The resonant peaks are actually represented by the element R_p in the RLC circuit. The measured values of R_p as a function of frequency and temperature is shown in the right plot of Fig. 5.16. We see that R_p depends very much on frequency and exhibits resonant peaks, which diminishes and moves to lower frequencies

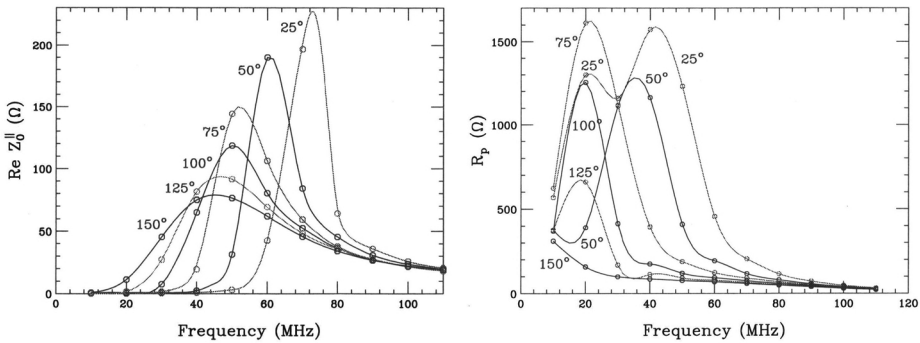


Fig. 5.16 Measured real part of the impedance (left) and the resistance of the resistor R_p (right) in the RL model of a single Toshiba M_4C_{21A} ferrite core inside an enclosing pill-box cavity up to 110 MHz at 25°, 50°, 75°, 100°, 125°, and 150°C. Measured points are denoted by circles.

as the temperature increases. Thus the loss at high frequencies has been very much reduced by heating the ferrite. For a coasting beam, the energy lost to the ferrite core is proportional to the area under the $\mathcal{R}e\, Z_0^{\|}$ curve. Although both R_p and $\mathcal{L}_p$ vary tremendously with temperature, we find out that this loss is in fact temperature-independent within 10% from 23°C to 150°C. However, the impedance becomes broader and broader and the resonant frequency shifts lower as the temperature increases.

The threshold microwave instability, depicted in Fig. 5.13, is determined by the impedance per unit PSR revolution harmonic, $Z_0^{\|}/n$, whose real and imaginary parts are shown, respectively, in Fig. 5.17. We now see that the resonant peak of $\mathcal{R}e\, Z_0^{\|}/n$ decreases with increasing temperature (except at 25°C). This explains why microwave instability can be alleviated by heating the ferrite cores.

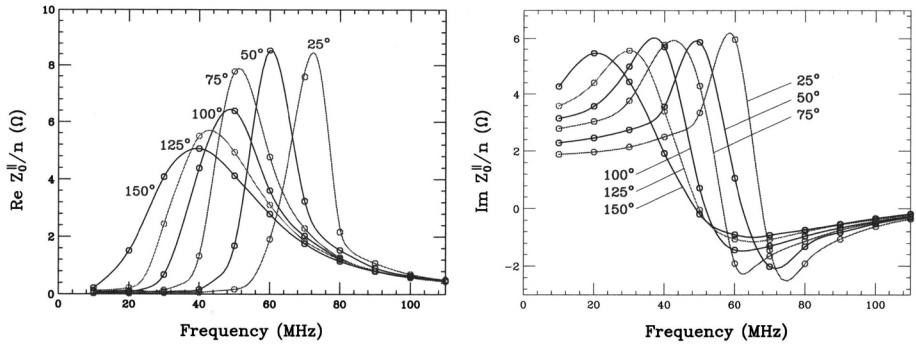


Fig. 5.17 Measured real (left) and imaginary (right) parts of the impedance per revolution harmonic of a single Toshiba M_4C_{21A} ferrite core inside an enclosing pill-box cavity up to 110 MHz at 25°, 50°, 75°, 100°, 125°, and 150°C. Measured points are denoted by circles.

The properties of the heated ferrite can be understand as follows. A piece of ferrite consists of domains with magnetization. The total magnetization is the vector sum of the magnetization of the domains. When the temperature increases, the domain magnetizations are freer to move. They tend to line up resulting in higher magnetic permeability μ_s', which is what we has been observing. However, if the temperature becomes too high, the spins of individual atoms or molecules become random and the total magnetization will drop and reach zero at the Curie temperature.

The magnetic permeability of the ferrite core had also been measured at different temperatures at Los Alamos Laboratory. [18] The numerical code MAFIA [19] was used to simulate the measured voltages with the correct geometry of the ferrite core inside the jig holding the core taken into account. [20]

From the simulations, the real and imaginary parts of the magnetic permeability at various temperatures were extracted. Next, MAFIA was used to compute the longitudinal impedance experienced by the beam passing through the pill-box tune assembly housing the ferrite cores. The calculated impedances appear to differ significantly from those depicted in Fig. 5.17. However, the qualitative features of having the resonant peak of $\mathcal{R}e\, Z_0^{\|}$ broadened and the low-frequency $\mathcal{I}m\, Z_0^{\|}$ enhanced at higher temperatures are essentially the same.

5.3.4 *Application at the PSR*

Later in 1999, the solenoids of the ferrite inserts for PSR were removed, the outside of the inserts were wound with heating tapes, and two modules were reinstalled in the PSR. When the ferrite is heated to 130°C, as recorded in Fig. 5.18, the longitudinal microwave instability, reported formerly in in 100-ns bunch in Fig. 5.10, disappears. The profile of the 100-ns bunch in the presence of the heated ferrite tuners, is no longer distorted and the bunch has not been lengthened. Further beam studies with the heated ferrites carried out during the remainder of 1999 demonstrated other benefits of the inductors without unmanageable operational impacts.

Two effects of the ferrite inserts are thought to contribute to improving the instability threshold possibly in two ways. One is the effect of a cleaner bunch gap that will trap fewer electrons during gap passage. This will improve the threshold of transverse *e-p* coupled-centroid instability (Chapter 15). The

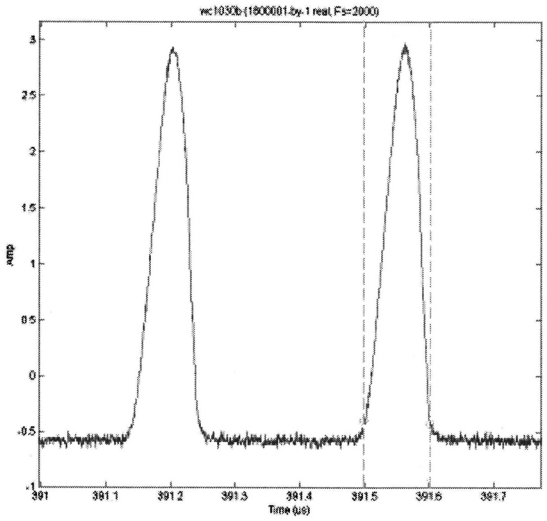


Fig. 5.18 With two ferrite tuners installed and heated to 130°C, the instability ripples disappear from the profile of the 100 ns bunch. (Courtesy Macek. [15])

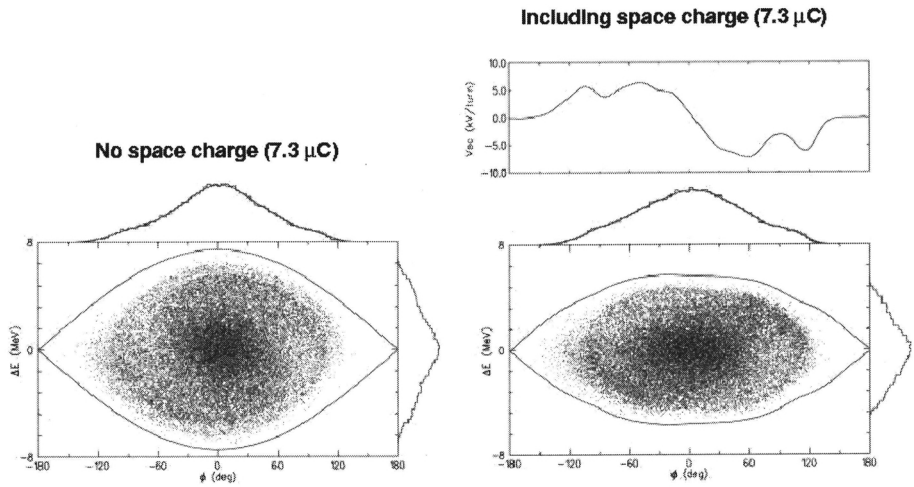


Fig. 5.19 Simulation of a PSR bunch with an intensity of 7.3 μC at the buncher voltage of 13 kV using the code ACCSIM. [21] The left plot is the result without space-charge while the right plot is the result with space-charge included. Notice that in the presence of space-charge the bucket height is reduced by 23%, implying a cancellation of the rf voltage by 41%. The top curve on the right shows the space-charge voltage per turn proportional to the spatial derivative of the proton linear density.

other is the increased momentum spread from the removal of the space-charge depression of the bucket height. This will increase Landau damping and improve the threshold of longitudinal microwave instability. The latter increase in momentum spread is illustrated in Fig. 5.19 which shows plots from ACCSIM simulations. [21] The simulations show the effect of longitudinal space-charge on the rf bucket height and momentum spread for a beam of 7.3 μC/pulse with 13-kV rf voltage. The left plot shows the bunch and the bucket without longitudinal space-charge or the equivalent to full compensation by the inductive inserts. The right plot shows the bunch and bucket subject to the longitudinal space-charge force. For this case, the space-charge effect reduces the bucket height by $\sim$23%. In the absence of space-charge, the bucket height scales by the square root of the rf voltage and would imply a reduction $\sim$41% in rf voltage to reach the same bucket height as with space-charge. This argument implies that with inductors a $\sim$41% reduction in rf voltage would reach the same momentum spread as obtained in their absence. This is in reasonable agreement with the observed effect of $\sim$35%. Thus, it appears that Landau damping explains much of the effect of the ferrite inserts on the instability. With the increase in bucket height after the compensation of the space-charge force by the inductive inserts, the bucket is able to hold the beam particles inside without leakage into the gap

region. Thus, the ferrite inserts improve the thresholds of both the longitudinal microwave instability as well as the transverse two-stream coupled-centroid instability.

Comparable reductions in threshold curves have been obtained with other means of Landau damping such as the use of a skew quadrupole (coupled Landau damping), sextupoles and octupoles. It has also been observed that the effects of these on the instability threshold add with that of the inductors. An additional sextupole was installed in the upgrade. It is surprising that this sextupole has an important bearing on the beam stability. Turning on this sextupole current to $+20$ A and optimizing the former four sextupoles and two octupoles in the ring can help to improve the threshold curve by $\sim$ 25% as is shown in Fig. 5.20. It is understandable that the sextupoles and octupoles introduce tune spread which can provide Landau damping of the vertical coupled *e-p* instability once protons leak into the bunch gap and prevent the electrons from clearing. However, why just one sextupole has this much effect is not clear at all.

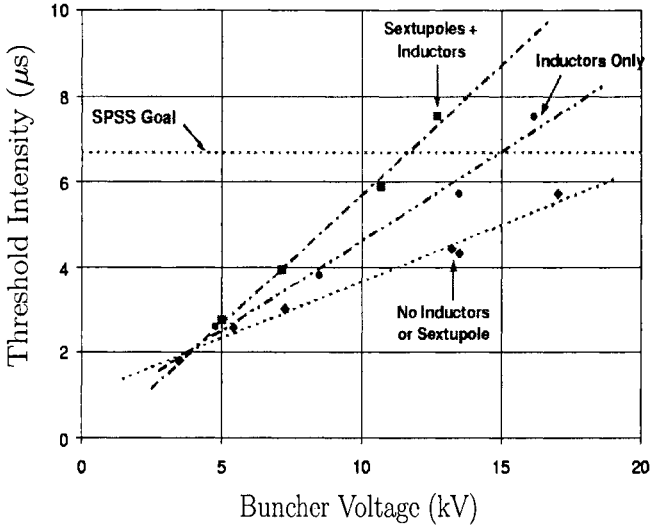


Fig. 5.20 After the upgrade, the PSR operating without the ferrite insert had a lower bunch intensity versus buncher voltage, depicted in dots, than the historical, depicted in dashes.

In late 1999, the combined effect of heated ferrites and a skew quadrupole enabled the accumulation and store at the PSR up to a record 9.7 μC/pulse, which is all that the linac could deliver. For this demonstration, the accumulation time was 1225 μs, the maximum obtainable at 1 Hz from the linac. The ferrite inserts were heated to 190°C, which over compensates longitudinal space-charge by $\sim$50%. The rf buncher was at the maximum of 18 kV. In addition, the bunch width was stretched out to 305 ns leaving behind a small gap of $\sim$ 60 ns,

something never been accomplished before without reducing the threshold intensity. Beam losses were high (~5%), which would be prohibitive at the repetition rate of 20 Hz. There was, no doubt, significant emittance growth that could be attributed to transverse space-charge effects from the very high peak beam current of 82 A observed in this demonstration.

Engineered versions of the heated ferrites were installed in the fall of 2000 and have been used in production running ever since. A bunch length of 290 ns instead of the 250 has reduced the accumulation time accordingly thereby saving ~$15k per month in linac power costs. At the present, the PSR with two heated-ferrite modules can operate stably at an intensity of 8 μC/pulse for low repetition rates for beam studies and single-pulse users. Thus, the peak intensity goal of the upgrade has been surpassed. The remaining challenge is to reduce beam losses so that routine operation at 20 Hz is possible with acceptable activation of the ring.

5.4 Exercises

5.1 The dispersion relation of Eq. (5.20) can be rewritten in a simpler form. let us measure revolution angular frequency in terms of $2S$, the FWHM spread, which is related to the FWHM energy spread by

$$2S \equiv \omega - \omega_0\big|_{\text{FWHM}} = -\frac{\eta\omega_0}{\beta^2}\left.\frac{\Delta E}{E_0}\right|_{\text{FWHM}}. \tag{5.41}$$

We can then introduce a dimensionless reduced angular frequency x such that

$$n\omega - n\omega_0 = nxS \qquad \text{and} \qquad \Omega - n\omega_0 = nx_1S, \tag{5.42}$$

where we have used the fact the the collective angular frequency Ω in Eq. (5.16) is close to $n\omega_0$. The frequency distribution function $g_0(\omega)$ is now transformed to a distribution $f(x)$ which is normalized to unity when integrated over x. We have

$$\frac{dg_0(\omega)}{d\omega}d\omega = \frac{df(x)}{dx}\frac{dx}{d\omega}dx = \frac{1}{S}\frac{df(x)}{dx}dx. \tag{5.43}$$

(1) Show that the dispersion relation (5.20) becomes

$$1 = -\frac{i2\,\text{sgn}(\eta)}{\pi}(U' + iV')\int\frac{f'(x)}{x_1 - x}dx, \tag{5.44}$$

where U' and V' are defined in Eq. (5.22).

(2) When the beam current is just above threshold, the reduced collective angular frequency is written as $x_1 = x_{1R} + i\epsilon$, where x_{1R} is real and ϵ is an infinitesimal positive number. Show that the stability curve can be obtained from

$$1 = -\frac{i2\,\mathrm{sgn}(\eta)}{\pi}(U' + iV')\left[\wp\int \frac{f'(x)}{x_{1R} - x}dx - i\pi f'(x_{1R})\right] \tag{5.45}$$

by varying x_{1R}, where $\wp$ denotes the principal value of the integral.
(3) Show that the negative V'-intersect or the lowest point of the bell-shaped stability curve V'_{in} is given by

$$1 = -\frac{2\,\mathrm{sgn}(\eta)V'_{\mathrm{in}}}{\pi}\wp\int \frac{f'(x)}{x}dx, \tag{5.46}$$

and the form factor in the Keil–Schnell criterion is given by $F = |V'_{\mathrm{in}}|$.
(4) The form factor F's in the Keil–Schnell criterion for various frequency-distribution functions are listed in Table 5.1. Verify the results.

Table 5.1 Form factors in the Keil–Schnell criterion for various distributions. For the first four, the distributions reside only inside the region $|\Delta\omega| \le \widehat{\Delta\omega}$. When normalized to the HWHM, the domain becomes $|x| \le a$.

Frequency Distribution				Form Factor
$g_0(\omega)$ $[\Delta\omega = \omega - \omega_0]$	$f(x)$			F
$\frac{3}{4\widehat{\Delta\omega}}\left(1-\frac{\Delta\omega^2}{\widehat{\Delta\omega}^2}\right)$	$\frac{3}{4a}\left(1-\frac{x^2}{a^2}\right)$	$a^2 = 2$		$\frac{\pi a^2}{6} = 1.0472$
$\frac{8}{3\pi\widehat{\Delta\omega}}\left(1-\frac{\Delta\omega^2}{\widehat{\Delta\omega}^2}\right)^{3/2}$	$\frac{8}{3\pi a}\left(1-\frac{x^2}{a^2}\right)^{3/2}$	$a^2 = \frac{1}{1-2^{-2/3}}$		$\frac{\pi a^2}{8} = 1.0612$
$\frac{15}{16\widehat{\Delta\omega}}\left(1-\frac{\Delta\omega^2}{\widehat{\Delta\omega}^2}\right)^{2}$	$\frac{15}{16a}\left(1-\frac{x^2}{a^2}\right)^{2}$	$a^2 = \frac{1}{1-2^{-1/2}}$		$\frac{\pi a^2}{10} = 1.0726$
$\frac{315}{256\widehat{\Delta\omega}}\left(1-\frac{\Delta\omega^2}{\widehat{\Delta\omega}^2}\right)^{4}$	$\frac{315}{256a}\left(1-\frac{x^2}{a^2}\right)^{4}$	$a^2 = \frac{1}{1-2^{-1/4}}$		$\frac{\pi a^2}{18} = 1.0970$
$\frac{1}{\sqrt{2\pi}\sigma}\exp\left(-\frac{\Delta\omega^2}{2\sigma^2}\right)$	$\frac{1}{\sqrt{2\pi}a}\exp\left(-\frac{x^2}{2a^2}\right)$	$a^2 = \frac{1}{2\ln 2}$		$\frac{\pi a^2}{2} = 1.1331$

5.2 Using Eq. (5.45), plot the bell-shaped stability contours for the distributions listed in Table 5.1 as illustrated in Fig. 5.4.

5.3 Using Eq. (5.44), show that the constant-growth contours for the Gaussian distribution are given by

$$1 = \frac{i\,\mathrm{sgn}(\eta)4\ln 2}{\pi}(U' + iV')\left[1 + i\sqrt{\pi\ln 2}\; x_1\, w(\sqrt{\ln 2}\, x_1)\right], \tag{5.47}$$

where use has been made of the integral representation of the complex error function:

$$w(z) = \frac{i}{\pi} \int_{-\infty}^{\infty} \frac{e^{-t^2}}{z-t} dt \qquad \text{for } \mathcal{I}m\, z > 0. \tag{5.48}$$

Plot the contours in Fig. 5.3.

Bibliography

[1] L. D. Landau, *J. Phys. USSR* **10**, 25 (1946).
[2] C. Bernardine, *et al.*, *Phys. Rev. Lett.* **10**, 407 (1963).
[3] A. W. Chao, *Physics of Collective Beam Instabilities in High Energy Accelerators*, (John Wiley & Sons, 1993), p. 251.
[4] E. Keil and W. Schnell, CERN Report TH-RF/69-48 (1969); V. K. Neil and A. M. Sessler, *Rev. Sci. Instrum.* **36**, 429 (1965).
[5] D. Boussard, CERN Report CERN-LAB II/RF/Int./75-2 (1975).
[6] J. Bosser, C. Carli, M. Chanel, N. Madsen, S. Maury, D. Möhl, G. Tranquille, *Nucl. Instrum. Meth.* **A441**, 1 (2000).
[7] S. Krinsky and J. M. Wang, *Part. Accel.* **17**, 109 (1985).
[8] J. D. Jackson, *Plasma Phys.* **C1**, 171 (1960).
[9] See for example, C. Bovet, *et al.*, *A Selection of Formulae and Data Useful for the Design of A.G. Synchrotron*, CERN/MPS-SI/Int. DL/70/4, 23 April, 1970.
[10] R. A. Dory, Thesis, MURA Report 654, 1962.
[11] Y. Chin and K. Yokoya, *Phys. Rev.* **D28**, 2141 (1983).
[12] S. A. Bogacz and K. Y. Ng, *Phys. Rev.* **D36**, 1538 (1987).
[13] A. Hofmann, *ISR Performance report*, CERN Report, August 17, 1976.
[14] K. Y. Ng, J. E. Griffin, D. Wildman, M. Popovic, A. Browman, D. Fitzgerald, R. Macek, M. Plum, and T. Spickermann, *Recent Experience with Inductive Insert at PSR*, Proc. 2001 Part. Accel. Conf., eds. P. Lucas and S. Webber (Chicago, June 18–22, 2001), p. 2890.
[15] R. Macek, private communication.
[16] M. Popovic, private communication.
[17] D. Wildman, private communication.
[18] A. Brownman, Meno to R. Macek, Apr. 2001, `http://lansce2-serv.atdiv.lanl.gov/browman/CY2001/`.
[19] CST, *MAFIA Manual 4.00*, `http://www.cst.de`, Jan. 1997.
[20] C. Beltran, *Study of the Longitudinal Space Charge Compensation and Longitudinal Instability of the Ferrite Inductive Inserts in the Los Alamos Proton Storage Ring*, PhD Thesis, Indiana University, 2003.
[21] F. W. Jones, G. H. Mackenzie, and H. Schönauer, *ACCSIM — A program to Simulate the Accumulation of Intense Proton Beams*, Proc. 14th Int. Conf. on High Energy Accelerators, *Part. Accel.* **31**, 199 (1990).

2025 © The Author(s). This is an Open Access chapter published by World Scientific Publishing Company, licensed under the terms of the Creative Commons Attribution-NonCommercial 4.0 International License (CC BY-NC 4.0).

Chapter 6

Longitudinal Microwave Instability for Short Bunches

In the previous chapter, microwave instability for a coasting beam was discussed. The theory can also be extended to a bunch provided that two criteria are satisfied: (1) the bunch is much longer than the wavelength of the perturbation and (2) the growth time is shorter than or of the order of a synchrotron oscillation period. These criteria are mostly satisfied by hadron bunches, but not by electron or positron bunches, which are usually shorter than or of the order of the beam pipe radius. Another theory of longitudinal instability is therefore necessary for short bunches.

6.1 Bunch Modes

6.1.1 *A Particle in Synchrotron Oscillation*

For electron bunches, the synchrotron period is usually much shorter than the collective instability growth times. Thus, synchrotron oscillation cannot be neglected in the investigation of longitudinal instabilities of the beam. As a result, the revolution harmonics can no longer be studied individually; they are no longer good eigennumbers. Here, we must analyze the different modes of oscillation inside a bunch.

Because the beam particles execute synchrotron oscillations, it is more convenient to employ instead, circular coordinates (r, ϕ) in the longitudinal phase space. We define the coordinates of a beam particle by

$$\begin{cases} \tau = r\cos\phi, \\ p_\tau = r\sin\phi = \dfrac{\eta\delta}{\omega_{sc}}, \end{cases} \tag{6.1}$$

where τ is the arrival time of the beam particle ahead of the synchronous particle

and p_τ is its conjugate momentum. In above, ω_{sc} is the *incoherent* angular synchrotron frequency of those particles at the center of the bunch, and is equal to*

$$\omega_{sc} = \omega_{s0} + \Delta\omega_{s\,\mathrm{incoh}}, \tag{6.2}$$

where ω_{s0} is the bare angular synchrotron frequency and $\Delta\omega_{s\,\mathrm{incoh}}$ is the incoherent angular frequency shift at the bunch center due to potential-well distortion studied in Chapter 2. We have chosen the incoherent angular synchrotron frequency as the normalization in Eq. (6.1) with the intention of letting the particle trajectories remain circular near the center of the bunch. A few azimuthal modes are shown in Fig. 6.1. One type of oscillation is azimuthal in ϕ, such as $\cos m\phi$. For example, $m = 1$ corresponds to a rigid-dipole oscillation which we usually observe when the bunch is injected with a phase error. Mode $m = 2$ corresponds to a quadrupole oscillation when there is a mismatch between the bunch and the rf bucket so that the oscillation appears to be twice as fast. The drawings show the motion of the bunch perturbed by the mth azimuthal mode. To isolate the mth azimuthal mode itself, the stationary distribution must be subtracted. For example, for the $m = 1$ mode with infinitesimal amplitude, after subtracting the stationary distribution, we obtain a ring with positive charges on the right and negative charges on the left. The best description will be $\cos\phi$, and there are two nodes at $\phi = \pm\frac{\pi}{2}$. The $m = 2$ mode assumes the shape of $\cos 2\phi$ with four nodes at $\phi = \pm\frac{\pi}{4}$ and $\pm\frac{3\pi}{4}$. For the mth mode, the shape is $\cos m\phi$ with

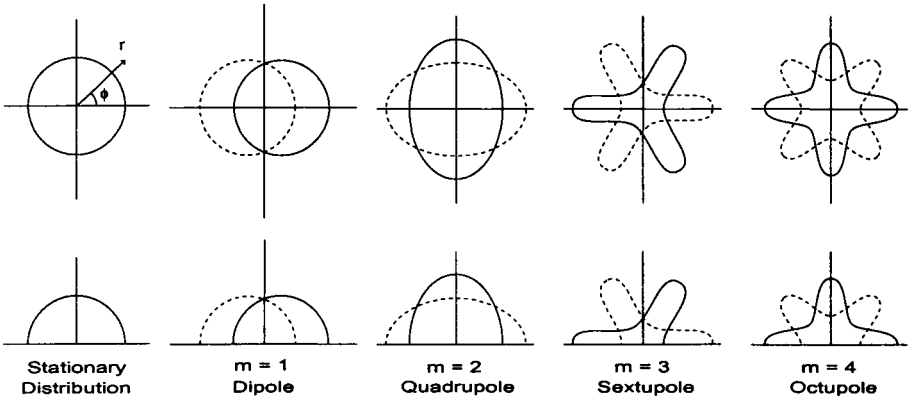


Fig. 6.1 Azimuthal synchrotron modes of a bunch in the longitudinal phase space (top) and as linear density (bottom).

*For convenience, sometimes we may just address it as ω_s instead.

$2m$ nodes in the longitudinal phase space (upper row of Fig. 6.1). As will be demonstrated below, these are just the azimuthal eigenmodes in the absence of wake field. The projection on the phase axis is the linear distribution, which exhibits m nodes in the mth mode not including the ends (lower row of Fig. 6.1).

It is clear that to drive the higher azimuthal modes, longitudinal impedance of higher frequencies will be required. These modes can be understood mathematically if we follow a particle and record its time of arrival at a fixed location along the accelerator ring turn after turn. First assume a point particle. The current signal recorded by a wall-gap monitor at location $\theta_{\text{wall}} = 0$ is

$$I_e(\hat{\tau}, \phi; s) = ev \sum_{k=-\infty}^{\infty} \delta \left[s + R\theta_0 - kC_0 - v\hat{\tau} \cos\left(\frac{\omega_{sc} s}{v} + \phi\right)\right], \tag{6.3}$$

where C_0 is the length of closed orbit of the synchronous particle whose velocity is v, and R is the mean radius of the closed orbit. For the particle under study, the turn number is denoted by k, the amplitude of synchrotron oscillation or the maximum arrival time ahead of the synchronous particle is $\hat{\tau}$, and the initial synchrotron phase is represented by ϕ. In addition, there is an initial phase θ_0 designating the location of the particle along the accelerator ring at $s = 0$. For the sake of convenience, however, this phase will be omitted in the following derivation. It is safe to substitute $s = kC_0$ inside the argument of cosine because the amplitude of synchrotron oscillation is very much smaller than the circumference of the ring ($\hat{\tau} \ll C_0/v$). To proceed, the Dirac δ-function is written as an integral

$$I_e(\hat{\tau}, \phi; s) = \frac{e}{2\pi} \int_{-\infty}^{\infty} d\omega \sum_{k=-\infty}^{\infty} e^{-i[s - kC_0 - \hat{\tau} v \cos(k\omega_{sc} C_0/v + \phi)]\omega/v}. \tag{6.4}$$

The mathematic formula for the expansion of an exponential in terms of the Bessel functions,

$$e^{-ix\cos\phi} = \sum_{m=-\infty}^{\infty} i^{-m} J_m(x)\, e^{im\phi}, \tag{6.5}$$

is then employed to obtain

$$I_e(\hat{\tau}, \phi; s) = \frac{e}{2\pi} \int_{-\infty}^{\infty} d\omega \sum_{k=-\infty}^{\infty} \sum_{m=-\infty}^{\infty} i^m J_m(\omega\hat{\tau}) e^{-i(s - kC_0)\omega/v} e^{-im(k\omega_{sc} C_0/v + \phi)}. \tag{6.6}$$

The terms involving k can now be grouped and the summation over k can be

performed using the Poisson formula,

$$\frac{1}{2\pi}\sum_{k=-\infty}^{\infty} e^{ik\theta} = \sum_{n=-\infty}^{\infty} \delta(\theta - 2\pi n), \tag{6.7}$$

to arrive at

$$\begin{aligned} I_e(\hat{\tau},\phi;s) &= \frac{e}{T_0}\int_{-\infty}^{\infty} d\omega \sum_{n=-\infty}^{\infty}\sum_{m=-\infty}^{\infty} i^m J_m(\omega\hat{\tau})\delta(\omega - n\omega_0 - m\omega_{sc}) e^{-im\phi} e^{-im\omega s/v} \\ &= \frac{e}{T_0}\sum_{n=-\infty}^{\infty}\sum_{m=-\infty}^{\infty} i^m J_m[(n\omega_0 + m\omega_{sc})\hat{\tau}]\, e^{-im\phi} e^{-i(n\omega_0+m\omega_{sc})s/v}, \end{aligned} \tag{6.8}$$

where $\omega_0/(2\pi) = v/C_0$ is the revolution frequency of the synchronous particle, and $T_0 = 2\pi/\omega_0$ is the revolution period. We now see all the azimuthal modes as sidebands of revolution harmonic. The Bessel functions in the summation determines the amplitude of the sidebands. The synchrotron amplitude $\hat{\tau}$ is usually very much smaller than the revolution period. In this case, the lowest sideband $m = 1$ dominates. The revolution harmonics ($m = 0$) have roughly the same amplitude under the envelope of J_0 while the amplitudes of the $m = 1$ sidebands increase linearly with frequency under the envelope of J_1. If $\hat{\tau}$ is getting larger, however, the higher order sidebands ($m > 1$) will be observed. The $m = 2$ sidebands can have larger amplitudes than the revolution harmonics ($m = 0$) and the $m = 1$ sidebands when J_2 assumes a maximum. This is illustrated in Fig. 6.2, where, for simplicity, only the positive frequency part has been shown. In order to illustrate the sidebands clearly, we have been taking $\omega_0\hat{\tau} = 0.4$, which is more than a hundred times larger than that in real accelerator rings. Let us take the Fermilab Tevatron as an example, the revolution period is $T_0 = 20.9$ μs and a particle at the edge of a bunch of rms length $\sigma_\tau = 1.33$ ns can have a synchrotron amplitude of $\hat{\tau} \approx 2\sigma_\tau$, giving $\omega_0\hat{\tau} \approx 8.0 \times 10^{-4}$. In this case, the lowest sidebands $m = 1$ dominate at low frequencies. The revolution harmonics ($m = 0$) having amplitudes bounded by J_0 start dropping appreciably near harmonic $n \sim 800$, while the amplitudes of the $m = 1$ sidebands increase first linearly with frequency under the envelope of J_1 and peak at the revolution harmonics ~ 2250 or 107 MHz $\left[J_1(z)\right.$ peaks at $\left.z \sim 1.8\right]$. The $m = 2$ sidebands increase with frequency quadratically under the envelope of J_2 and peak at the revolution harmonics ~ 3880 or 185 MHz $\left[J_2(z)\right.$ peaks at $\left.z \sim 3.1\right]$. Electron and positron rings behave differently. An electron ring like the Advance Photon Source (APS) at the Argonne National Laboratory has much shorter bunches at $\sigma_\tau \sim 30$ ps. Its revolution period is 3.68 μs, giving $\omega_0\hat{\tau} \sim 1.02 \times 10^{-4}$, so that the $m = 1$ sidebands peak near 4.78 GHz while the

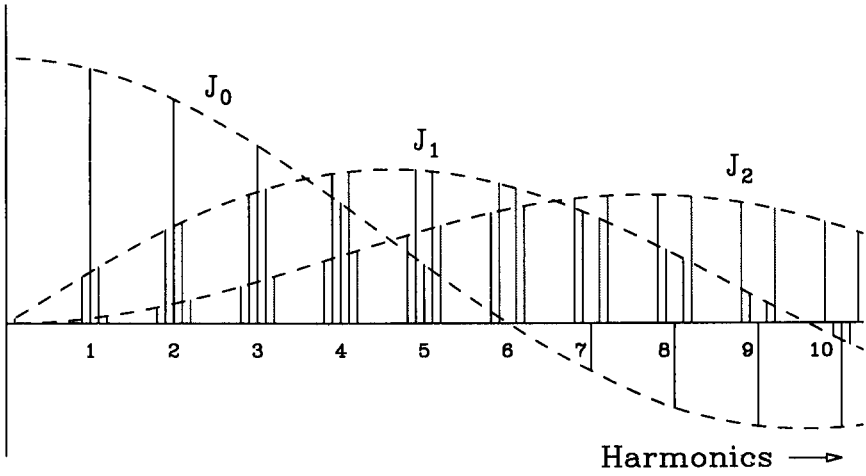


Fig. 6.2 Spectrum of a beam particle with synchrotron motion. Only the positive frequency is shown. The revolution harmonics ($m = 0$) are bounded by Bessel function of order zero, the first synchrotron sidebands ($m = 1$) are bounded by Bessel function of order one, and the second synchrotron sidebands ($m = 2$) are bounded by Bessel function of order two. For clarity, the plot has been made with $\omega_0 \hat{\tau} = 0.4$, which is unusually large.

$m = 2$ sidebands peak near 8.22 GHz.

It is important to point out that the Bessel functions have nothing to do with the linear distribution of the bunch and here we are dealing with only a point particle. The Bessel functions just reflect the synchrotron motion of the point particle. If we wish to know the signal from a bunch of particles, we need to multiply Eq. (6.8) by the particle distribution $psi(\hat{\tau}, \phi)$ in the synchrotron phase ϕ and the synchrotron oscillation amplitude $\hat{\tau}$, and perform an integration over $\hat{\tau}$ and ϕ. For example, if $psi(\hat{\tau}, \phi)$ is random in ϕ, the integral vanishes for all azimuthals except for $m = 0$, or just the revolution harmonics. This is understandable because the bunch is smooth azimuthally. The revolution harmonics will be visible, however, because a bunch is localized. For the azimuthal sidebands to be excited, the distribution inside the bunch must be nonuniform in the synchrotron phase. We also see from the derivation that the sidebands have zero width if they are excited, even if we are gathering signals from an ensemble of particles. This is not true in reality. The sidebands will be broadened because of the small spread in energy among the particles. Particles at slightly different energies will have slightly different revolution time because of the slip factor η. The sidebands will also be broadened, when the beam particles interact with the coupling impedance of the vacuum chamber. When excited below transition and

an instability occurs, as we shall see below, the lower synchrotron sidebands are unstable while the upper synchrotron sidebands are stable, and the other way around above transition.

Of course, to describe a bunch completely, there will also be radial modes, where the bunch oscillates with nodes at certain radii r. Nevertheless, we would like to restrict ourselves to only one radial mode per azimuthal in this chapter, the one that is most easily excited. At zero beam intensity, the azimuthal modes are separated by the synchrotron frequency $\omega_{sc}/(2\pi)$; for example, the mth mode exhibits as a sideband $m\omega_{sc}/(2\pi)$ away from a revolution harmonic line. This implies that at low intensities, the azimuthal modes are good eigenmodes. The radial eigenmodes, however, depend on the radial distribution of the unperturbed bunch. If the intensity of the bunch is increased, the spacings of the sidebands will change.

Here, we wish to study the collective motion of the bunch, implying that it will oscillate with a coherent frequency $\Omega/(2\pi)$. The time-dependent part is written as

$$\sum_{n=-\infty}^{\infty} F_n e^{-i(n\omega_0+\Omega)s/v}, \tag{6.9}$$

where F_n is some spectral factor depending on n and $\omega_0/(2\pi)$ is the revolution frequency. Suppose that the synchrotron dipole mode is excited, we will have[†] $\Omega \approx +\omega_{sc}$, provided that the intensity of the bunch is not too large. Therefore, the spectrum of the bunch will consist of only *upper* synchrotron sidebands at a distance ω_{sc} above the harmonic lines, as shown in the top plot of Fig. 6.3. Of course, not all the sidebands will be excited equally. The excitation will depend on the frequencies of the driving impedance and also the bunch shape. All these are grouped into the factor F_n. However, in an oscilloscope or network analyzer, we can see only *positive* frequencies. This is equivalent to folding the spectrum about the zero frequency point, the upper synchrotron sidebands corresponding to the negative harmonics will appear as lower synchrotron sidebands for the positive frequencies, as depicted in the lower plot of Fig. 6.3. When the driving impedance is a narrow resonance, we may happen to have $\Omega \approx -\omega_{sc}$, a lower sideband, excited instead. Suppose the narrow resonance is at frequency $\omega_r = n\omega_0 - \omega_{sc}$ with $n > 0$. Since $\mathcal{R}e\, Z_0^{\parallel}(\omega)$ is symmetric about $\omega = 0$, this narrow resonance is also driving the negative frequency $-\omega_r = n'\omega_0 + \omega_{sc}$ where $n' = -n$, which is the upper sideband of a negative harmonic. In other words, because of the definite symmetries of $\mathcal{R}e\, Z_0^{\parallel}(\omega)$ and $\mathcal{I}m\, Z_0^{\parallel}(\omega)$ together with the symmetry of the synchrotron-oscillation spectrum about $\omega = 0$ in Eq. (6.8), it is

[†]The coherent dipole synchrotron frequency is close to the bare synchrotron frequency.

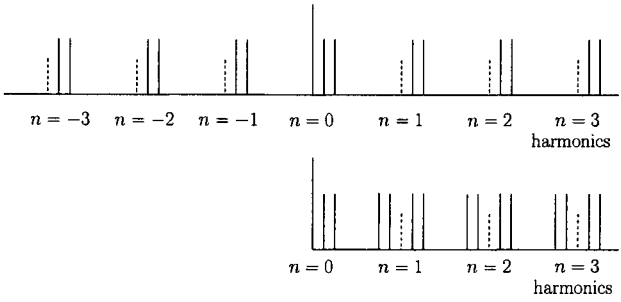


Fig. 6.3 Top: Revolution harmonics in dashes and synchrotron *upper* sidebands in solid for both positive and negative frequencies. Bottom: With negative harmonics folded onto positive harmonics, one sees both upper and lower sidebands for each revolution harmonic.

possible for us to study only half the sidebands in the language of positive and negative revolution harmonics, either the upper ($\Omega \approx \omega_{sc}$) or ($\Omega \approx -\omega_{sc}$) lower. Studying the upper sidebands alone will yield exactly the same results as studying the lower sidebands alone. For this reason, we can assume all the excited synchrotron sidebands to be only upper sidebands (and neglect the lower sidebands) in the language of having both positive and negative frequencies. This analysis, however, is not correct for transverse collective motion, because the synchrotron sidebands are around the tune lines which are not symmetric about the zero-frequency point.

We would like to emphasize here that the spectrum of beam particles performing synchrotron motion is very different from the spectrum of the coherent motion of beam particles. In the former, Eq. (6.8), we see all the possible modes as depicted in Fig. 6.2. However, in the latter, only some of those modes are excited coherently. We are looking at the coherent modes one at a time, because usually we have interest only in the one that has the fastest growth rate.

6.1.2 *Coherent Azimuthal Modes*

The modes observed in a bunch of particles are called coherent modes. For a smooth bunch, the distribution function is $\psi(\hat{\tau}, \phi) = \psi_0(\hat{\tau})$. The current signal of this N_b-particle bunch picked up by a gap monitor is

$$I_b(s) = N_b \int I_e(\hat{\tau}, \phi; s)\psi_0(\hat{\tau})\hat{\tau}d\hat{\tau}d\phi. \tag{6.10}$$

Substituting Eq. (6.8) for $I_e(\hat{\tau}, \phi; s)$, the current of the bunch can be written as

$$I_b(s) = I_0 \sum_{n=-\infty}^{\infty} A_{n0} e^{-in\omega_0 s/v}, \tag{6.11}$$

where $I_0 = eN_b f_0$ is the average beam current and f_0 is the revolution frequency. The amplitudes of the revolution harmonic signals A_{n0} are the Hankel transforms

of ψ_0,

$$A_{n0} = 2\pi \int_0^\infty J_0(n\omega_0\hat{\tau})\psi_0(\hat{\tau})\hat{\tau}d\hat{\tau}. \tag{6.12}$$

If one measures the amplitudes of all the revolution harmonics, one can reconstruct the distribution $\psi_0(\hat{\tau})$ from the inverse Hankel transform.

With the mth azimuthal mode excited, the bunch distribution becomes

$$\psi(\hat{\tau}, \phi; s) = \psi_0(\hat{\tau}) + \Delta\psi(\hat{\tau}, \phi; s), \tag{6.13}$$

where

$$\Delta\psi(\hat{\tau}, \phi; s) = \psi_m(\hat{\tau})e^{im\phi - i\Omega s/v}, \tag{6.14}$$

and Ω is the coherent frequency. The signals of the bunch current become

$$I_b(s) = I_0(s) + \Delta I_b(s), \tag{6.15}$$

with the coherent current signal

$$\Delta I_b(s) = N_b \int I_e(\hat{\tau}, \phi; s)\Delta\psi(\hat{\tau}, \phi; s)\hat{\tau}d\hat{\tau}d\phi = I_0 \sum_{n=-\infty}^{\infty} A_{nm}e^{-i(n\omega_0 + m\omega_{sc} + \Omega)s/v}. \tag{6.16}$$

In above, the amplitude of the excited sideband,[‡] A_{nm}, is the mth order Hankel transform of ψ_m,

$$A_{nm} = 2\pi \int_0^\infty i^m J_m(n\omega_0\hat{\tau})\psi_m(\hat{\tau})\hat{\tau}d\hat{\tau}. \tag{6.17}$$

Again, the collective perturbed distribution ψ_m can be reconstructed through inverse Hankel transform when all mth-azimuthal sideband amplitudes are measured by tuning a spectrum analyzer to each sideband. We can also obtain A_{nm} by taking the fast Fourier transform spectrum of the longitudinal beam profile digitized at fixed times during the onset of the coherent mode instability, for which a digital oscilloscope with a sizeable memory will be required.

To illustrate this, let us study the coherent synchrotron modes of a kicked beam. First assume a Gaussian equilibrium distribution and express it as a function of τ and $\dot{\tau}/\omega_{sc}$,

$$\psi_0(\hat{\tau}) = \frac{1}{2\pi\sigma_\tau^2}e^{-\hat{\tau}^2/(2\sigma_\tau^2)} = \frac{1}{2\pi\sigma_\tau^2}\exp\left[-\frac{\tau^2 + (\dot{\tau}/\omega_{sc})^2}{2\sigma_\tau^2}\right], \tag{6.18}$$

[‡]The phase i^m is unimportant, since it is the same for all A_{nm}'s.

where σ_τ is the rms bunch length. The beam is now kicked longitudinally by the amount τ_k. The initial distribution is obtained by substituting τ by $\tau + \tau_k$, or

$$\psi\left(\tau, \frac{\dot{\tau}}{\omega_{sc}}\right) = \frac{1}{2\pi\sigma_\tau^2} \exp\left(-\frac{\tau_k^2}{2\sigma_\tau^2} - \frac{\hat{\tau}^2}{2\sigma_\tau^2} - \frac{\hat{\tau}\tau_k}{\sigma_\tau^2}\cos\phi\right), \tag{6.19}$$

where $\hat{\tau}^2 = \tau^2 + (\dot{\tau}/\omega_{sc})^2$ and $\tau = \hat{\tau}\cos\phi$ have been used. Next invoke the identity

$$e^{-x\cos\phi} = \sum_{m=-\infty}^{\infty} (-1)^m I_m(x) e^{im\phi} \tag{6.20}$$

to obtain

$$\psi\left(\tau, \frac{\dot{\tau}}{\omega_{sc}}\right) = \frac{1}{2\pi\sigma_\tau^2} \exp\left(-\frac{\tau_k^2}{2\sigma_\tau^2} - \frac{\hat{\tau}^2}{2\sigma_\tau^2}\right) \sum_{m=-\infty}^{\infty} (-1)^m I_m\left(\frac{\hat{\tau}_k}{\sigma_\tau^2}\right) e^{im\phi}\ , \tag{6.21}$$

where I_m is the modified Bessel function of order m having the property $I_{-m} = I_m$. We can now identify

$$\psi_m(\hat{\tau}) = \frac{1}{2\pi\sigma_\tau^2} \exp\left(-\frac{\tau^2}{2\sigma_\tau^2} - \frac{\hat{\tau}_k^2}{2\sigma_\tau^2}\right) (-1)^m I_m\left(\frac{\hat{\tau}_k}{\sigma_\tau^2}\right), \tag{6.22}$$

and the coherent mode integral in Eq. (6.17) becomes[§]

$$\begin{aligned} A_{nm} &= \frac{2\pi i^m}{2\sigma_\tau^2} e^{-\tau_k^2/(2\sigma_\tau^2)} \int_0^\infty e^{-\hat{\tau}^2/(2\sigma_\tau^2)} I_m\left(\frac{\hat{\tau}\tau_k}{\sigma_\tau^2}\right) J_m(n\omega_0\hat{\tau})\hat{\tau}d\hat{\tau} \\ &= i^m e^{-\frac{1}{2}(n\omega_0\tau_k)^2(\sigma_\tau/\tau_k)^2} J_m(n\omega_0\tau_k). \end{aligned} \tag{6.23}$$

6.1.3 *Measurement of Coherent Modes*

An experimental measurement of coherent synchrotron modes was performed at the Cooler Ring of the Indiana University Cyclotron Facility (IUCF) in 1994 when holding the US Accelerator School. The ring had a revolution frequency of $f_0 = 1.03168$ Hz, a rf harmonic $h = 1$, and a phase slip factor $\eta = -0.86$. The bunched beam contained about 5×10^8 protons at a kinetic energy of 45 MeV and a rms length of about 20 ns. The cycle time was 5 s while the injected beam was electron-cooled for about 3 s. The beam was kicked longitudinally by phase-shifting the rf cavity wave form. The response time of the step phase shifts was limited primarily by the inertia of the rf cavities, which had a quality factor

[§]Gradskteyn and Ryzhik 6.633.4:
$\int_0^\infty e^{-\alpha x^2} I_m(\beta x) J_m(\gamma x) dx = \frac{1}{2\alpha} e^{(\beta^2-\gamma^2)/(4\alpha)} J_m\left(\frac{\beta\gamma}{2\alpha}\right)$ if $\mathcal{R}e\,\alpha > 0$ and $\mathcal{R}e\,m > -1$.

of about $Q = 40$. The first kick was $\tau_k = 90$ ns, or equivalently $\omega_0 \tau_k = 0.58$. The synchrotron sideband power was observed from a spectrum analyzer tuned to the sideband. The sideband power of the first harmonic $f_0 - f_s$, proportional to $|A_{11}|^2$, is shown in the upper trace of Fig. 6.4 and the sixth harmonic $6f_0 - f_s$, proportional to $|A_{61}|^2$, is shown in lower trace. The lower synchrotron sidebands were chosen because they are the more unstable ones below transition (see Sec. 6.2.3).

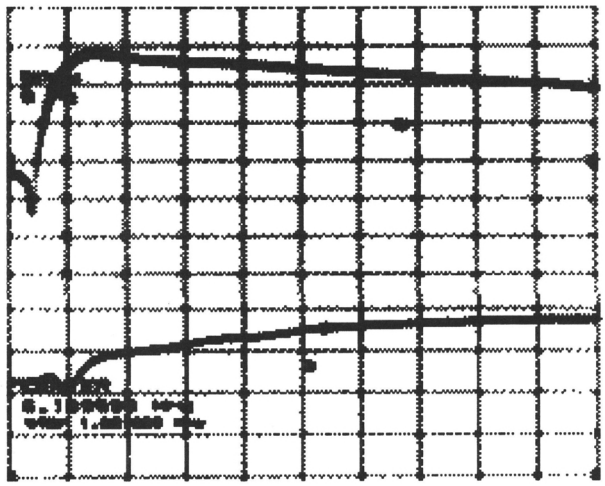


Fig. 6.4 The synchrotron sideband power of the fundamental harmonic (top trace) and that of the 6th harmonic (lower trace), as measured by a spectrum analyzer tuned to the sidebands. The sidebands were excited by shifting the rf phase by $\tau_k = 90$ ns. The amplitude of synchrotron oscillation was damped by electron cooling. (Courtesy S. Y. Lee [1].)

According to Eq. (6.23), the phase kick contributes

$$A_{11} \sim e^{-0.0083} J_1(0.58) \quad \text{and} \quad A_{61} \sim e^{-0.299} J_1(3.48) \,. \tag{6.24}$$

As a result, the sideband power of the fundamental harmonic is larger than that of the 6th harmonic by a factor of six, as is observed in the figure. As time goes on, the amplitude of synchrotron oscillation, initially at $\tau_a = \tau_k$, was damped by electron cooling. We see that the sideband power of the fundamental harmonic decreases and that of the 6th harmonic increases just as expected, because J_1 has its first maximum at 1.841 and its first zero at 3.832. The rf phase was then shifted to various values and the synchrotron side band power associated to each revolution harmonic was measured. Figure 6.5 shows the synchrotron sideband power as functions of frequency ($\omega \tau_k = n\omega_0 \tau_k$) for $\tau_k = 53$, 90, 100, and 150 ns. All data are normalized to the first peak ($n\omega_0 \tau_k \approx 1.8$ when $\tau_k = 53$ and $n = 1$). Solid curves are $|A_{n1}|^2$ from Eq. (6.23) normalized to the peak. There are no other adjustable parameters. Satisfactory agreement of measurement with theory is observed.

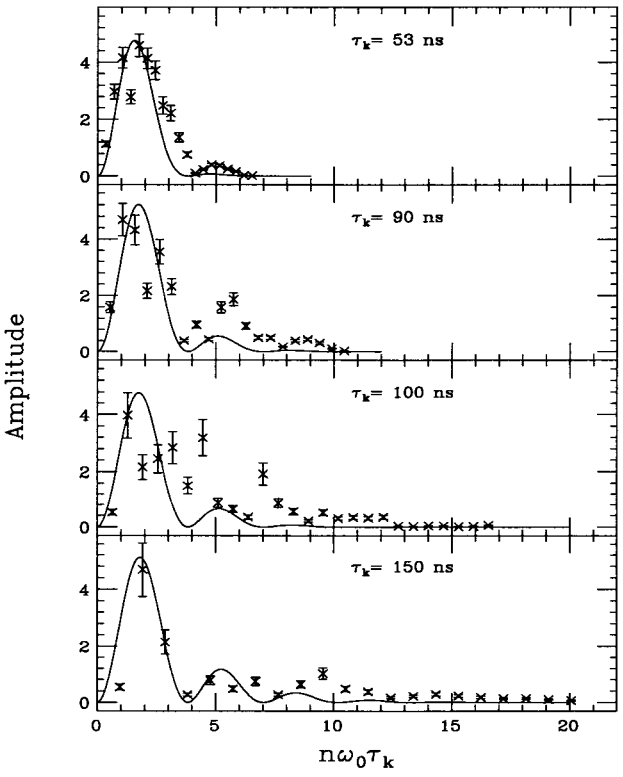


Fig. 6.5 The initial synchrotron sideband power as functions of frequency $\omega\tau_k = n\omega_0\tau_k$ after rf phase shifts of τ_k = 53m 90, 100, and 150 ns. The solid curves are the theoretical expectation normalized to the first peaks of the data. There are no other adjustable parameters. (Courtesy S. Y. Lee [1].)

6.2 Collective Instability

6.2.1 *Dispersion Relation of a Sideband*

Parallel to what we studied about the stability criterion for a coasting beam in the previous chapter, we are going to do the same for a bunched beam here. The important difference is that the revolution harmonics are no longer eigenstates and bunch modes must be used. The discussion here follows those of Sacherer and Zotter. [2, 3] With the circular coordinates defined in Eq. (6.1) and following Eq. (2.13), the two equations of motion in the longitudinal phase space can be written down easily,

$$\begin{cases} \dfrac{d\tau}{ds} = -\dfrac{\omega_{sc}}{v}\, p_\tau, \\ \dfrac{dp_\tau}{ds} = \dfrac{\omega_{sc}}{v}\tau + \dfrac{\eta}{E_0\omega_{sc}\beta^2}\langle F_0^{\parallel}(\tau;s)\rangle_{\rm dyn}. \end{cases} \tag{6.25}$$

They become more symmetric. In the absence of the wake force $\langle F_0^{\parallel}(\tau;s)\rangle_{\rm dyn}$, the trajectory of a beam particle is just a circle in the longitudinal phase space. In above, η is the slip factor, and $v=\beta c$ is the velocity, and E_0 the energy of the synchronous particle. The dynamic part of the wake force is defined as

$$\langle F_0^{\parallel}(\tau;s)\rangle_{\rm dyn} = \langle F_0^{\parallel}(\tau;s)\rangle - \langle F_0^{\parallel}(\tau;s)\rangle_{\rm stat}, \tag{6.26}$$

following Eq. (5.1), and only the *dynamic* or time-dependent part of the linear density of the bunch will contribute. The static part of the linear density has already been taken care of by solving the problem of potential-well distortion so that we have the incoherent synchrotron frequency ω_{sc} used in the Vlasov equation below instead of the bare synchrotron frequency ω_{s0}.

The phase-space distribution ψ of a bunch can be separated into the unperturbed or stationary part ψ_0 and the perturbed part ψ_1:

$$\psi(\tau,\Delta E;s) = \psi_0(\tau,\Delta E) + \psi_1(\tau,\Delta E;s), \tag{6.27}$$

where $\psi_0(\tau,\Delta E)$ is obtained from solving the problem of potential-well distortion. The linearized Vlasov equation becomes

$$\frac{\partial\psi_1}{\partial s} - \frac{\omega_{sc}}{v}p_x\frac{\partial\psi_1}{\partial x} + \frac{\omega_{sc}}{v}x\frac{\partial\psi_1}{\partial p_x} + \frac{\partial\psi_0}{\partial p_x}\frac{\eta}{E_0\omega_{sc}\beta^2}\langle F_0^{\parallel}(\tau;s)\rangle_{\rm dyn} = 0, \tag{6.28}$$

and, in the circular coordinates, it simplifies to

$$\frac{\partial\psi_1}{\partial s} + \frac{\omega_{sc}}{v}\frac{\partial\psi_1}{\partial\phi} + \frac{\eta}{E_0\omega_{sc}\beta^2}\frac{d\psi_0}{dr}\sin\phi\langle F_0^{\parallel}(\tau;s)\rangle_{\rm dyn} = 0. \tag{6.29}$$

The perturbed distribution can be expanded azimuthally in the longitudinal phase space,

$$\psi_1(r,\phi;s) = \sum_m \alpha_m R_m(r) e^{im\phi - i\Omega s/v}, \tag{6.30}$$

where $R_m(r)$ are functions corresponding to the mth azimuthal, α_m are the expansion coefficients, and $\Omega/(2\pi)$ is the collective frequency to be determined. In above, $m=0$ has been excluded because it has been included in the stationary part ψ_0, otherwise charge conservation will be violated. The Vlasov equation becomes

$$(\Omega - m\omega_{sc})\alpha_m R_m(r)e^{-i\Omega s/v} = -\frac{iv\eta}{E_0\omega_{sc}\beta^2}\frac{d\psi_0}{dr}\int_{-\pi}^{\pi}\frac{d\phi}{2\pi}e^{-im\phi}\sin\phi\langle F_0^{\parallel}(\tau;s)\rangle_{\rm dyn}. \tag{6.31}$$

The wake force acting on a beam particle at location s, with arrival time advance τ relative to the synchronous particle, due to all preceding particles passing

through s earlier can be expressed as

$$\langle F_0^{\parallel}(\tau;s)\rangle_{\rm dyn} = -\frac{e^2}{C_0}\int_{-\infty}^{\infty} d\tau' K(\tau'-\tau)\lambda_1(\tau';s), \tag{6.32}$$

where the translational-invariant kernel $K(\tau'-\tau)$ is exact for continuous interactions such as space-charge or resistive-wall (assuming smooth walls), and retains the average effect of localized structures such as cavities. For a broadband impedance the kernel is the same as the longitudinal monopole wake potential, or $K(\tau) = W_0'(\tau)$. Since $\lambda_1(\tau;s)$ is equal to the projection of $\psi_1(\tau,\Delta E;s)$ onto the τ-axis, Eq. (6.31) becomes an eigen-equation in the $R_m(r)$ after substituting the azimuthal expansion of Eq. (6.30).

We now make the approximation that the perturbation is small so that $\Omega - m\omega_{sc} \ll \omega_{sc}$, implying that the coupling between different azimuthal modes can be neglected. This simplifies the Vlasov equation to one involving only one azimuthal mode m,

$$(\Omega - m\omega_{sc})R_m(r) = -\frac{d\phi_0}{dr}\int_0^{\infty} G_m(r,r')R_m(r')r'dr', \tag{6.33}$$

where the interaction matrix is

$$G_m(r,r') = -\frac{ie^2v}{2\pi C_0}\int_0^{2\pi} d\phi \int_0^{2\pi} d\phi' K(r'\cos\phi' - r\cos\phi)\sin\phi\, e^{im(\phi'-\phi)}. \tag{6.34}$$

and the transformation of integration variables from $d\tau' d\Delta E$ to $r'dr'd\phi'$ has been made via

$$d\tau' d\Delta E = \frac{\omega_{sc}\beta^2 E_0}{\eta} r'dr'd\phi'. \tag{6.35}$$

Equation (6.33) is the simplified form of the Sacherer's integral equation [9] which we are going to study in more detail in subsequent chapters. Given a longitudinal wake and an unperturbed distribution, the coherent frequency of excitation Ω can be solved. Unfortunately, analytic solutions are only possible for some particular $\psi_0(r)$, especially when there is a spread in the incoherent synchrotron frequency, such as inside an rf bucket. In order to obtain some useful information concerning the stability of the particle beam, we resort to the method of *synthetic kernel*, which involves the substitution of the kernel of longitudinal dipole wake by a simple function. To study dipole motion, we assume the wake force to be proportional to the longitudinal position of the bunch center, an assumption which should be true only when the bunch is rigid.

Looking at Eq. (6.32), we can readily set the kernel as

$$K(\tau' - \tau) = A(\tau' - \tau) = A(r' \cos\phi' - r\cos\phi), \tag{6.36}$$

where A is a constant. We obtain immediately

$$G_m(r, r') = -\frac{\pi e^2 v A}{2} r' \delta_{m1}, \tag{6.37}$$

or only the $m = 1$ dipole mode will contribute as expected. Substitution into Eq. (6.33) gives

$$R_1(r) = \frac{\pi e^2 v A}{2} C_1 \frac{\psi_0'(r)}{\Omega - \omega_{sc}}, \tag{6.38}$$

where the prime denotes derivative with respect to r and

$$C_1 = \int_0^\infty R_1(r') r'^2 dr' \tag{6.39}$$

is a constant. Landau damping is introduced by allowing a spread in the incoherent synchrotron frequency, making it a function of r such that $\omega_s(0) = \omega_{sc}$. Thus multiplying both sides by r^2 and integrating over r lead to the dispersion relation

$$1 = -\pi \Delta\omega_{s\,\mathrm{dyn}} \int_0^\infty \frac{\psi_0'(r) r^2}{\Omega - \omega_s(r)} dr, \tag{6.40}$$

where $\Delta\omega_{s\,\mathrm{dyn}} = -e^2 v A/2$. Actually $\Delta\omega_{s\,\mathrm{dyn}}$ has a physical meaning. When there is no spread in the incoherent synchrotron frequency, the denominator of the integrand can be moved to the left side. It is then easy to verify that $\Delta\omega_{s\,\mathrm{dyn}} = \Omega - \omega_{sc}$, or $\Delta\omega_{s\,\mathrm{dyn}}$ is the dynamical shifting of the incoherent synchrotron frequency ω_{sc} towards the coherent frequency Ω. Combining Eq. (6.2), we arrive at

$$\Delta\omega_{s\,\mathrm{dyn}} = (\Omega - \omega_{s0}) - \Delta\omega_{s\,\mathrm{incoh}}, \tag{6.41}$$

implying that $\Delta\omega_{s\,\mathrm{dyn}}$ is the difference between the *coherent frequency shift* and *incoherent frequency shift*. We refer to $\Delta\omega_{s\,\mathrm{dyn}}$ as the *dynamic frequency shift* arising from the dynamic effects of the wake fields. As an example, let us consider the elliptical distribution

$$\psi_0(r) = \frac{3}{2\pi\hat{\tau}^2} \sqrt{1 - \frac{r^2}{\hat{\tau}^2}}, \tag{6.42}$$

when $r < \hat{\tau}$ and zero otherwise. When projected onto the τ-axis, this distribution leads to the parabolic linear distribution

$$\lambda_0(\tau) = \frac{3}{4\hat{\tau}}\left(1 - \frac{\tau^2}{\hat{\tau}^2}\right), \tag{6.43}$$

when $|\tau| < \hat{\tau}$ and zero otherwise. Let us first neglect the synchrotron frequency spread in the sinusoidal rf potential. In the presence of a constant $\mathcal{I}m\, Z_0^{\parallel}/n$ such as space-charge below transition, every particle in the bunch including the one at the bunch center has the same self-force frequency shift, according to Eq. (2.80),

$$\Delta\omega_{s\,\mathrm{incoh}} = \frac{3e^2 N_b \eta\, \mathcal{I}m\, Z_0^{\parallel}/n}{8\pi\beta^2 E_0 \omega_{s0}\hat{\tau}^3}, \tag{6.44}$$

which is negative. Now because of the dynamic effects of the wake fields, the coherent frequency at which the center of the bunch is oscillating receives an additional dynamical shift $\Delta\omega_{s\,\mathrm{dyn}}$. Thus the coherent synchrotron frequency of the bunch is

$$\Omega = \omega_{s0} + \Delta\omega_{s\,\mathrm{incoh}} + \Delta\omega_{s\,\mathrm{dyn}}. \tag{6.45}$$

Because the wake-field pattern and therefore the potential-well distortion moves with the bunch in this rigid-dipole mode, the bunch center will not be affected by the wake field at all. For this reason, we must have in this case the cancellation of the dynamic frequency shift and the incoherent frequency shift so that the coherent frequency Ω is just equal to the bare synchrotron frequency. As will be demonstrated below, however, this is true only when there is no spread in the incoherent synchrotron frequency.

Before ending this subsection, let us give some more comments about what the synthetic kernel has done to the problem physically. There is only one rigid-dipole mode (with $m = 1$), which is generated by displacing the unperturbed bunch distribution ψ_0 from the equilibrium position of the rf potential so that the distribution rotates rigidly with the synchrotron frequency. However, there are infinite number of nonrigid dipole modes with $m = 1$. For example, we can imagine the bunch as an elastic sheet in the longitudinal phase space and has only its center part displaced from the equilibrium position of the rf potential but leaving the edge part of the distribution undisturbed. The perturbation now rotates with synchrotron frequency but with a particular distribution radially. The same applies to the quadrupole modes ($m = 2$), sextupole modes ($m = 3$), etc. In other words, there are infinite number of radial modes associated with each azimuthal mode. The synthetic kernel just singles out the most easily

excited radial mode (the one with the least frequency shift) for each azimuthal, thus reducing the two-fold infinity of modes to only one series of modes.

6.2.2 *Landau Damping of a Sideband*

We learn from above that a capacitive or space-charge impedance below transition (or an inductive impedance above transition) shifts the incoherent synchrotron frequency downwards while the coherent synchrotron frequency remains at the value of the bare frequency in the elliptical distribution. Now let us turn on synchrotron frequency spread as a result of the sinusoidal rf potential. This provides the incoherent synchrotron frequency with a spread also in the downwards direction. Thus the coherent synchrotron frequency appears always to be *not covered* by the incoherent spread at all, and therefore there would not be any Landau damping. An illustration is shown in Fig. 6.6. We are going to show that this statement is incorrect and there will be Landau damping provided that the incoherent spread is large enough. [4] The reason is that the coherent synchrotron frequency is shifted from the bare frequency in the presence of an incoherent synchrotron spread.

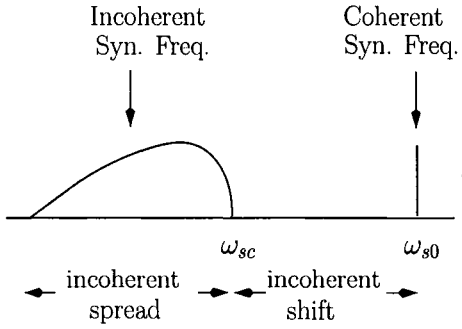


Fig. 6.6 Schematic drawing showing the incoherent spread of the synchrotron frequency in the sinusoidal rf potential shifted away from the coherent synchrotron frequency Ω which remains at the bare frequency ω_{s0}, thus not being able to provide Landau damping.

In the elliptical distribution, the only spread of incoherent synchrotron frequency comes from the sinusoidal rf potential well. With small half bunch length $\hat{\tau}$, this spread is given by

$$\omega_{s\,\mathrm{incoh}}(\hat{\tau}) = \omega_{sc} - S\hat{\tau}^2, \tag{6.46}$$

where ω_{sc} is the incoherent angular synchrotron frequency of particles at the center of the bunch and the spread S can be approximated by [2]

$$S = \left(\frac{h\omega_0}{4}\right)^2 \frac{1+\sin^2\phi_s}{1-\sin^2\phi_s}, \tag{6.47}$$

where h is the rf harmonic. The dependence on the synchronous angle ϕ_s is the result of a fitting with numerical computation. Here, the expression for S, quoted for the sake of completeness, will not be used in the discussion below. However, it is important to point out that this spread of synchrotron frequency, as defined in Eq. (6.46) is measured from ω_{sc}, the incoherent frequency at the center of the bunch.

For the rigid-dipole mode ($m = 1$), the dispersion relation now takes the form

$$1 = -\pi \Delta\omega_{s\,\mathrm{dyn}} \int_0^\infty \frac{\psi_0'(r) r^2}{\Omega - \omega_{sc} + S r^2}\, dr. \tag{6.48}$$

Let us introduce the dimensionless variable

$$z = \frac{\omega_{sc} - \Omega}{S}, \tag{6.49}$$

and change the variable of integration to $t = r^2$. The dispersion relation becomes

$$1 = -\frac{\pi \Delta\omega_{s\,\mathrm{dyn}}}{S} \int_0^\infty \frac{\psi_0'(t) t}{t - z + i\epsilon}\, dt, \tag{6.50}$$

where $\psi_0'(t) = d\psi_0(r)/dr^2|_{r^2=t}$, and an infinitesimal imaginary part $i\epsilon$ with $\epsilon > 0$ has been added to represent the situation just above threshold when z is real. Now the explicit expression for the elliptical distribution, Eq. (6.42), is substituted and the dispersion integral is evaluated to arrive at the threshold curve:

$$\left(\frac{\Delta\omega_{s\,\mathrm{dyn}}}{S}\right)^{-1} = \begin{cases} \dfrac{3}{4}\left[2 + \dfrac{z}{\sqrt{1-z}} \ln \dfrac{\sqrt{1-z}+1}{\sqrt{1-z}-1}\right] & z < 0, \\ \dfrac{3}{4}\left[2 + \dfrac{z}{\sqrt{1-z}} \ln \dfrac{1+\sqrt{1-z}}{1-\sqrt{1-z}} - i\pi \dfrac{z}{\sqrt{1-z}}\right] & 0 < z < 1, \\ \dfrac{3}{4}\left[2 - \dfrac{2z}{\sqrt{z-1}} \tan^{-1} \dfrac{1}{\sqrt{z-1}}\right] & 1 < z, \end{cases} \tag{6.51}$$

where, for the sake of convenience, we have set the half bunch length to $\hat{\tau} = 1$. The stability curve is depicted in the complex $(\Delta\omega_{s\,\mathrm{dyn}}/S)$-plane in the left plot of Fig. 6.7. On the right, we have plotted $\Delta\omega_{s\,\mathrm{dyn}}/S$ as a function of z to facilitate our discussion below. As defined in the previous subsection, $\mathcal{R}e\,\Delta\omega_{s\,\mathrm{dyn}}$ is the *dynamic part* of the coherent synchrotron tune shift of the bunch in the absence of synchrotron frequency spread ($S = 0$). It is equal to the incoherent synchrotron frequency shift $\Delta\omega_{s\,\mathrm{incoh}}$ and is therefore a measure of the reactive

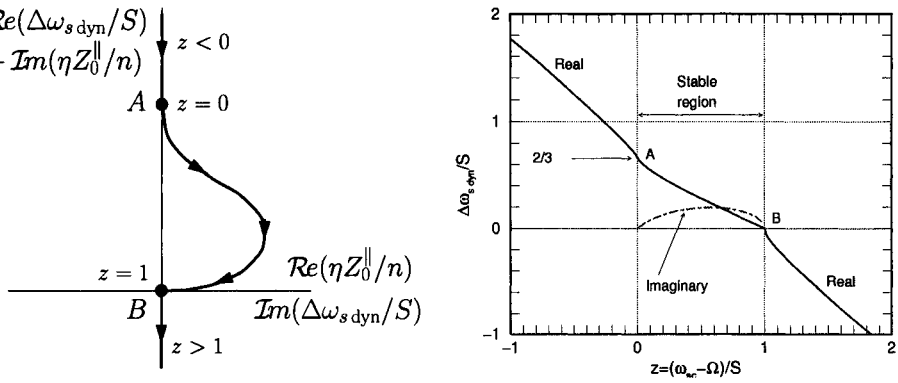


Fig. 6.7 Left: Stability curve for elliptical distribution, showing the direction z increasing (Ω decreasing). Right: $\Delta\omega_{s\,\mathrm{dyn}}/S$ as a function of $z=(\omega_{sc}-\Omega)/S$ in the stability contour.

impedance per harmonic of the vacuum chamber. When z is negative, the *dynamic part of the coherent frequency shift*[¶] $\Delta\omega_{s\,\mathrm{coh}}^{\mathrm{dyn}}=\Omega-\omega_{sc}$ in the presence of synchrotron frequency spread ($S>0$) is real and positive and is measured from the frequency ω_{sc}. Thus, the coherent synchrotron frequency is away from the incoherent synchrotron frequency spread. There is no Landau damping and the bunch is unstable in the presence of any small $\mathcal{R}e\,Z_0^{\parallel}$. When $z=0$, there is no dynamic coherent frequency shift or the coherent synchrotron frequency is right at ω_{sc}, just at the edge of stability. In the plot, this corresponds to $\Delta\omega_{s\,\mathrm{dyn}}/S=\frac{2}{3}$ or Point A. As z turns positive, the dynamic coherent synchrotron frequency shift $\Delta\omega_{s\,\mathrm{coh}}^{\mathrm{dyn}}$ becomes negative when measured from ω_{sc}. The beam is now inside the stability region. This is the region between Points A and B in stability plot. As the reactive impedance of the vacuum chamber becomes smaller and smaller ($\Delta\omega_{s\,\mathrm{dyn}}/S\to 0$), Point B is approached with $z\to 1-$. When the reactive impedance changes sign ($\eta\,\mathcal{I}m\,Z_0^{\parallel}/n$ going from negative to positive), $z>1$, Landau damping vanishes and the beam becomes unstable again.

The corresponding linear density of the particle bunch as a function of synchrotron frequency is shown schematically in Fig. 6.8. The top plot is for the situation when $\eta\,\mathcal{I}m\,Z_0^{\parallel}/n<0$. In this plot, when $\Delta\omega_{s\,\mathrm{coh}}^{\mathrm{dyn}}=-0.26S$ ($z=0.26$), $\mathcal{R}e\,\Delta\omega_{s\,\mathrm{dyn}}=-\Delta\omega_{s\,\mathrm{incoh}}=0.429S$ and $\mathcal{I}m\,\Delta\omega_{s\,\mathrm{dyn}}=0.146S$ on the stability

[¶]Here, $\Delta\omega_{s\,\mathrm{coh}}^{\mathrm{dyn}}$ is the *dynamic* part of the coherent shift and is measured from ω_{sc}. The *total* coherent shift is measured from the bare frequency ω_{s0} and contains, in addition to this dynamical part, a *static* part which is equal to the incoherent shift $\Delta\omega_{s\,\mathrm{incoh}}=\omega_{sc}-\omega_{s0}$. On the other hand $\Delta\omega_{s\,\mathrm{dyn}}$ represents the same dynamic part of the coherent shift measured from ω_{sc} only in the absence of incoherent synchrotron frequency spread.

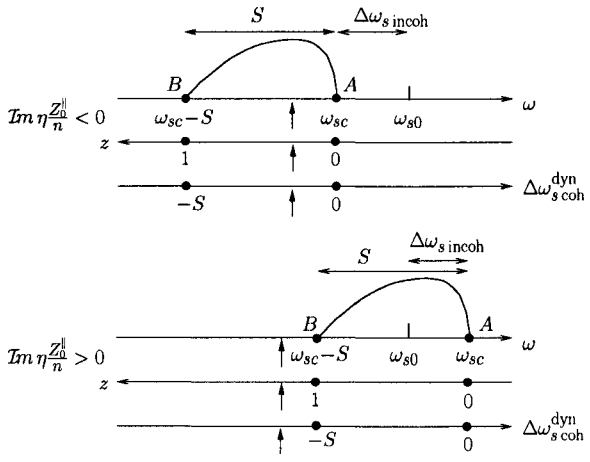


Fig. 6.8 Plot of linear bunch density as functions of synchrotron frequency ω, z, and the dynamical part of the coherent synchrotron frequency shift $\Delta\omega_{s\,\mathrm{coh}}^{\mathrm{dyn}}$ when (top) $\eta\,\mathcal{I}m\,Z_0^{\parallel}/n < 0$ and (bottom) $\eta\,\mathcal{I}m\,Z_0^{\parallel}/n > 0$. The vertical arrows point to the coherent synchrotron frequency of the bunch. Thus, when $\mathcal{R}e\,Z_0^{\parallel}$ is small, the bunch is stable in the top plot, but unstable in the bottom plot. Points A and B correspond to the same Points A and B in the threshold plot of Fig. 6.7.

contour, which are obtained by solving the dispersion relation or Eq. (6.51). The coherent synchrotron frequency is depicted by the vertical arrows between Points A and B. We see that the coherent synchrotron frequency now lies inside the incoherent frequency spread which provides Landau damping. Of course, the beam will become unstable if $\mathcal{I}m\,\Delta\omega_{s\,\mathrm{dyn}} > 0.146S$ (or $\mathcal{R}e\,Z_0^{\parallel}$ becomes larger) and z will have a negative imaginary part (Ω will have a positive imaginary part). Let us imagine that the incoherent frequency spread S is getting smaller and smaller while $\Delta\omega_{s\,\mathrm{incoh}}$ is held fixed. In another words, $\mathcal{R}e\,\Delta\omega_{s\,\mathrm{dyn}}/S$ becomes larger and larger. From the right plot of Fig. 6.7, z decreases or the dynamic coherent synchrotron frequency shift $\Delta\omega_{s\,\mathrm{coh}}^{\mathrm{dyn}}$ becomes less negative until it reaches zero ($z = 0$) arriving at Point A when $S = \frac{3}{2}\Delta\omega_{s\,\mathrm{dyn}} = -\frac{3}{2}\Delta\omega_{s\,\mathrm{incoh}}$. As S continues to shrink, $\Delta\omega_{s\,\mathrm{coh}}^{\mathrm{dyn}}$ becomes positive and goes outside the incoherent frequency spread. As $S \to 0$, we know from Fig. 6.7 and Eq. (6.51) that $z \to -\infty$. Solving Eqs. (6.49) and (6.51), one finds[‖] $\Delta\omega_{s\,\mathrm{coh}}^{\mathrm{dyn}} \to -\Delta\omega_{s\,\mathrm{inoch}}$ or the coherent synchrotron frequency goes back to the unperturbed value of ω_{s0} as expected. On the other hand, we can fix the incoherent frequency spread S and reduce $\Delta\omega_{sc}$ or $\mathcal{R}e\,\omega_{s\,\mathrm{dyn}}$ instead until it reaches zero. The coherent synchrotron frequency will shift towards Point B. It reaches Point B when $\Delta\omega_{s\,\mathrm{incoh}}$ reaches zero (z reaches $+1$). Thus, when $\eta\,\mathcal{I}m\,Z_0^{\parallel}/n < 0$, z varies from $-\infty$ to $+1$.

The bottom plot of Fig. 6.8 is for the situation when $\eta\,\mathcal{I}m\,Z_0^{\parallel}/n > 0$. Now the incoherent frequency shift $\Delta\omega_{s\,\mathrm{incoh}}$ in the absence of incoherent frequency spread becomes positive and the incoherent frequency spread may encompass

[‖] As $z \to -\infty$, Eq. (6.51) becomes $\Delta\omega_{s\,\mathrm{dyn}}/S \to 1 - z$. With $z = -\Delta\omega_{s\,\mathrm{coh}}^{\mathrm{dyn}}/S$, we obtain $\Delta\omega_{s\,\mathrm{coh}}^{\mathrm{dyn}} \to \Delta\omega_{s\,\mathrm{dyn}} - S \to -\Delta\omega_{s\,\mathrm{incoh}}$.

the unperturbed synchrotron frequency ω_{s0} as illustrated in the plot. However, there is no Landau damping, because under this situation $z > 1$ (see right plot of Fig. 6.7 when $\Delta\omega_{s\,\mathrm{dyn}} = -\Delta\omega_{s\,\mathrm{incoh}} < 0$). In other words, the dynamic coherent synchrotron frequency shifts negatively from ω_{sc} and the shift must be larger than $\omega_{sc} - S$, which is towards the right side of Point B. This plot shows $\Delta\omega_{s\,\mathrm{dyn}} = -0.40S$. Solution of Eq. (6.51) gives $z = 1.27$. This value of coherent synchrotron frequency is depicted by the vertical arrows. It is easy to see that no matter how large or small the incoherent frequency shift is, the coherent synchrotron frequency is always outside the incoherent frequency spread between Points A and B, or the beam is always unstable independent of how small $\mathcal{R}e\, Z_0^{\parallel}$ is.

6.2.2.1 *Equi-Growth Contours*

With a purely inductive wall above transition or a purely capacitive space-charge force below transition, the incoherent synchrotron frequency shift $\Delta\omega_{s\,\mathrm{incoh}}$ in an elliptical distribution without any frequency spread from the nonlinearity of the rf potential is given by Eq. (6.44) and is negative. We have shown in the above that this is equal to the negative of $\mathcal{R}e\,\Delta\omega_{s\,\mathrm{dyn}}$, real part of the dynamical frequency shift (in the absence of incoherent synchrotron frequency spread). It is easy to understand that the incoherent frequency shift in the absence of frequency spread is always real even when the coupling impedance contains a real part. This is because the incoherent frequency shift is obtained by linearizing the driving force on the right side of Eq. (2.81), which consists of the convolution of the wake potential and the linear beam distribution and both of them are real. However, $\Delta\omega_{s\,\mathrm{dyn}}$ as defined in Eq. (6.48) is in general, complex. Since $\mathcal{R}e\,\Delta\omega_{s\,\mathrm{dyn}}$ is well-defined and is proportional to $\mathcal{I}m\, Z_0^{\parallel}/n$, $\Delta\omega_{s\,\mathrm{dyn}}$, being analytic in frequency, can be defined easily by analytic continuation. In other words, we can write

$$\Delta\omega_{s\,\mathrm{dyn}} \sim -\mathcal{I}m(\eta Z) \longrightarrow -\mathcal{I}m(\eta Z) + i\,\mathcal{R}e(\eta Z). \tag{6.52}$$

This explains why $\mathcal{R}e(\eta Z)$ and $\mathcal{I}m(\Delta\omega/S)$ are in the same direction in the left plot of Fig. 6.7, while $\mathcal{I}m(\eta Z)$ and $\mathcal{R}e(\Delta\omega/S)$ are in the opposite directions. Thus, in the absence of incoherent frequency spread,

$$\mathcal{I}m\,\Omega = \frac{2c^2 N_b}{3\pi\beta^2 E_0 \omega_{s0}\hat{\tau}^3}\left(\eta\frac{\mathcal{R}e\, Z_0^{\parallel}}{n}\right), \tag{6.53}$$

and the solution is unstable/stable depending on $\eta\,\mathcal{R}e\, Z_0^{\parallel}/n \gtrless 0$. Therefore in the $(\Delta\omega_{s\,\mathrm{dyn}}/S)$-space such as in the left plot of Fig. 6.7, the left half is stable

and the right half unstable in the absence of incoherent synchrotron frequency spread, and the stability contour is just the $\mathcal{R}e\,\Delta\omega_{s\,\mathrm{dyn}}/S$ coordinate axis. When there is finite incoherent synchrotron frequency spread, the stability contour is pushed towards the right so that a solution with $\eta\,\mathcal{R}e\,Z_0^{\parallel}/n > 0$ can still be stable provided that it falls to the left side of the stability contour. The equi-growth contours and equi-damping contours can be easily computed by letting z complex in Eq. (6.51). The result is shown in the left plot of Fig. 6.9. The thick contour is the stability contour. To the right, the equi-growth contours correspond to growth rates in steps of $0.1S$. To the left, the equi-damping contours correspond to damping rates in steps of $0.1S$. It is clear that Points A and B ($z = 0$ and 1) are two branch points and the straight line AB is a branch cut.

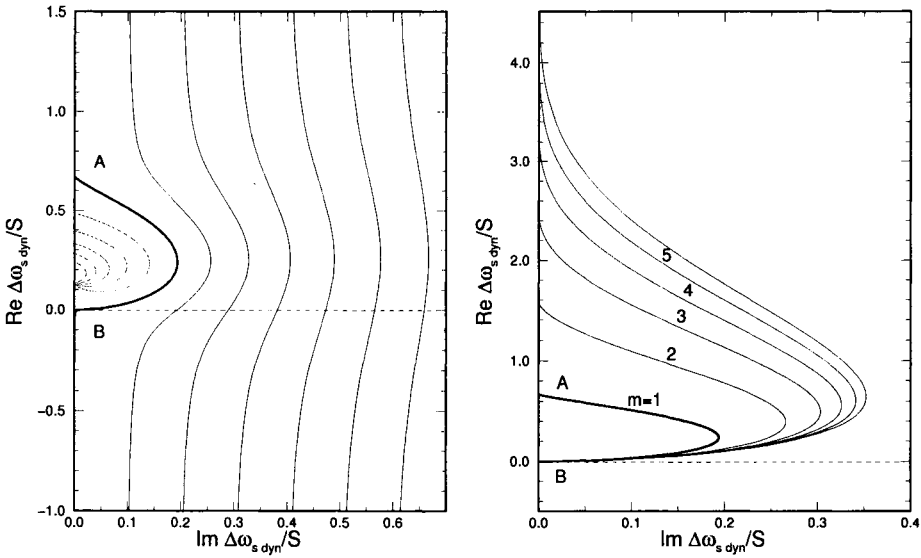


Fig. 6.9 Left: Equi-growth contours of the elliptical distribution $\frac{3}{2\pi}\sqrt{1-r^2}$, with growth rate increasing by steps of $0.1S$ to the right of the stability contour (darker curve) and damping rate increasing by steps of $0.1S$ to the left. Right: Stability contours for the elliptical distribution for azimuthal $m = 1$ to 6.

6.2.3 *Stability of a Bunch*

The upper and lower synchrotron sidebands flanking a positive revolution harmonic correspond to the upper sidebands associated with, respectively, the positive and negative revolution harmonics. Since $\mathcal{R}e\,Z_0^{\parallel}/n$ is an odd function of

frequency, $\eta\, \mathcal{R}e\, Z_0^{\parallel}/n$ is positive for the upper sidebands and negative for the lower sidebands above transition ($\eta > 0$). As a result, all the upper sidebands are stable, while all the lower sidebands are unstable unless there is sufficient Landau damping, such as the damping depicted in the left plot of Fig. 6.7. The opposite will be true below transition. The stability that we studied above is for a single azimuthal mode only, for example, either the upper or lower dipole synchrotron sideband in the language of only positive frequency. The spectrum of a bunch mode covers quite a number of synchrotron sidebands, some of which are stable and some unstable. To determine whether the bunch mode is stable or not, we need to sum up all the synchrotron sidebands of the bunch mode with $\eta\, \mathcal{R}e\, Z_0^{\parallel}/n$ as weights because all of them will be excited unless the impedance happens to vanish at those frequencies.

As an example, for mth azimuthal mode, the growth rate can be expressed as

$$\begin{aligned}\frac{1}{\tau_m} &\propto \sum_{n=-\infty}^{\infty} \eta h_m(n\omega_0+m\omega_s)\frac{\mathcal{R}e\, Z_0^{\parallel}}{n}(n\omega_0+m\omega_s) \\ &= \sum_{n=0}^{\infty} \eta h_m(n\omega_0+m\omega_s)\left[\frac{\mathcal{R}e\, Z_0^{\parallel}}{n}(n\omega_0+m\omega_s) - \frac{\mathcal{R}e\, Z_0^{\parallel}}{n}(n\omega_0-m\omega_s)\right]. \quad (6.54)\end{aligned}$$

The power spectrum of the bunch $h_m(\omega) = |p_m(\omega)|^2$ enters into the expression with p_m being the mth azimuthal Fourier component of the linear bunch density because $p_m(\omega)Z_0^{\parallel}(\omega)/n$ gives the longitudinal wake field, which must be integrated over the bunch to get the total force. The first line of Eq. (6.54) addresses the upper sidebands associated with both positive and negative frequency, while the second line corresponds to folding the negative-frequency sidebands onto the positive-frequency sidebands. The second line therefore expresses the difference in longitudinal impedance at the upper and lower synchrotron sidebands flanking the positive revolution harmonic n. For a broadband impedance, this difference is close to zero. In other words, the contributions of the upper and lower sidebands flanking each revolution harmonic cancel each other even if there is no incoherent frequency spread. In the presence of incoherent frequency spread, Landau damping will lead to an additional amount of damping when all sidebands are summed. The conclusion is that, when coupling of different azimuthal modes is unimportant, a bunch is always stable if the driving impedance is broadband. This is quite different from the longitudinal instability of a coasting beam. Here, synchrotron oscillation plays an important role having the two components it creates, a growing sideband and a damping sideband, cancel each other. This conclusion does not exclude the possibility of the Keil–

Schnell type of microwave instability studied in Chapter 5. This is because the bunch can be treated as a coasting beam when the wavelength of the instability is much less than the bunch length and when the growth time of instability is much smaller than the synchrotron oscillation period. In that case, there will not be any synchrotron sidebands established.

Equation (6.54), however, still leaves the option of a bunched-beam instability. The only possible instability that can occur in a bunch is when only one upper synchrotron sideband in Eq. (6.54) contributes essentially above transition (one lower sideband below transition). This happens when the impedance is a narrow resonance of the width of or less than the synchrotron frequency leaning more towards an upper synchrotron sideband than the accompanied lower sideband and the other way around below transition. This explains why the fundamental mode of an rf cavity is usually detuned slightly downward from a revolution harmonic above transition and slightly upward below transition in order to guarantee stability. This is the so-called Robinson stability criterion [10] which manifests itself because of the fine tuning of the resonance frequency. We will study more about the Robinson stability criterion in Chapters 7 and 8.

6.2.3.1 *Higher Azimuthal Modes*

For higher azimuthal modes, such as the quadrupole modes ($m = 2$), sextupole modes ($m = 3$), etc. the dispersion relation can be derived in the same way as the dipole modes. Again we include only the most easily excited radial modes using synthetic kernels, which can be inferred easily from Eq. (6.34). Remembering that the mth multipole kernel $K_m(r, r')$ is nothing more than the mth multipole wake function, we must have

$$K_m(r, r') \propto r^m r'^{m-1}. \tag{6.55}$$

The mth multipole interaction matrix is therefore $G_m(r, r') = C_m r^m r'^{m-1}$ where C_m is a constant. From the simplified Sacherer's integral equation in Eq. (6.33), it is easy to derive the dispersion relation,

$$1 = \frac{\Delta\omega_m}{W_m} \int \frac{\psi_0'(r) r^{2m}}{\Omega - m\omega_{sc} + mSr^2}\, dr, \tag{6.56}$$

where the spread S in incoherent synchrotron frequency has been included and $C_m = -\Delta\omega_m / W_m$. We have introduced

$$W_m = \int_0^\infty \psi_0'(r) r^{2m} dr, \tag{6.57}$$

so that in the absence of incoherent spread ($S = 0$), $\Delta\omega_m = \Omega - m\omega_{sc}$ is the dynamic part of the mth azimuthal coherent frequency shift. We further define

$$z = \frac{\omega_{sc} - \Omega/m}{S}, \tag{6.58}$$

and change the variable of integration to $t = r^2$. The dispersion relation finally takes the form

$$1 = \frac{\Delta\omega_m}{mSW_m} \int_0^\infty \frac{\psi_0'(t)t^m}{t - z}\, dr, \tag{6.59}$$

where we have used the short-hand notation $\psi_0'(t) \equiv \left[d\psi_0(r)/dr^2\right]_{r^2=t}$. In above, $\Delta\omega_m = C_m/(\pi S)$ with $\Delta\omega_1 = \Delta\omega_{s\,\mathrm{dyn}}$, the dynamic part of the coherent synchrotron frequency shift in the absence of an incoherent synchrotron frequency spread. It is convenient to define

$$\mathcal{G}_m(t) = \frac{t^m\psi_0'(t)}{mW_m}, \tag{6.60}$$

so that the dispersion relation simplifies to

$$1 = \frac{\Delta\omega_m}{S} \int_0^\infty \frac{\mathcal{G}_m(t)dt}{t - z}. \tag{6.61}$$

The stability threshold curve can then be readily solved and is given by

$$1 = \frac{\Delta\omega_m}{S}\Big[\mathcal{H}_m(z) - i\pi\mathcal{G}_m(z)\Big], \tag{6.62}$$

where

$$\mathcal{H}(z) = \wp \int_0^\infty \frac{\mathcal{G}_m t dt}{t - z}. \tag{6.63}$$

For the elliptical distribution, it is easy to obtain the solution:

$$\begin{aligned}
\mathcal{G}_m(z) &= -\frac{3z^m}{4\pi m W_m\sqrt{1-z}}, \\
\mathcal{H}_m(z) &= \frac{1}{mI_m}\left[\sum_{n=0}^{m-1} I_{m-n-1}z^n + \frac{z^m}{2\sqrt{1-z}}\ln\left|\frac{\sqrt{1-z}+1}{\sqrt{1-z}-1}\right|\right], \\
W_m &= -\frac{3I_m}{2\pi} \quad \text{and} \quad I_m = \int_0^1 (1-u^2)^m du = \frac{2^m m!}{(2m+1)!!},
\end{aligned} \tag{6.64}$$

when $0 < |z| < 1$, and zero otherwise. The stability contours for the higher azimuthal modes are depicted in the right plot of Fig. 6.9.

6.2.3.2 *Coherent Shift from Mean Incoherent Frequency*

Consider an impedance which has an inductive part and a resistive part and is well inside the stability region ($0 < z < 1$). The dynamic coherent synchrotron frequency shift on a beam above transition must therefore be negative. However, without any synchrotron frequency spread, the dynamic coherent synchrotron frequency shift is positive for an inductive impedance. Is there a contradiction? Our conclusion is that in the absence of a synchrotron frequency spread, when the unperturbed distribution is elliptical, every particle has its synchrotron frequency shifted by the same amount and so is the center of the bunch. Therefore the static shift of the coherent synchrotron frequency is downward or $\Delta\omega_{s\,\mathrm{coh}}^{\mathrm{static}} = \Delta\omega_{s,\,\mathrm{incoh}} = \omega_{sc} - \omega_{s0} < 0$. Since all particles execute synchrotron oscillation with exactly the same frequency, the bunch is rigid. The wake-field pattern moves with the bunch. Thus the motion of the bunch as a whole cannot be affected by the wake field at all. In other words, the dynamic coherent shift $\Delta\omega_{s\,\mathrm{coh}}^{\mathrm{dyn}}$ must be upward and is equal exactly to $\Delta\omega_{s\,\mathrm{coh}}^{\mathrm{static}}$. In the presence of a synchrotron frequency spread, the picture is different. The bunch will see the change in wake-field pattern and the bunch center will be affected by the wake. As a result, the coherent synchrotron frequency will be affected by the wake and the dynamic coherent synchrotron frequency shift will be different from $\Delta\omega_{s\,\mathrm{coh}}^{\mathrm{static}}$.

In the presence of a synchrotron frequency spread, the mean incoherent synchrotron frequency of the bunch due to the static effect of the impedance is less than ω_{sc}. This can be estimated by finding the rms of the synchrotron frequency of the individual particle because the synchrotron frequency appears as square in the equation of motion. We have

$$\langle\omega_s^2\rangle = \int (\omega_{sc} - Sr^2)^2 \psi_0 r\,dr\,d\theta. \tag{6.65}$$

For the elliptical distribution, the result is

$$\langle\omega_s^2\rangle = \omega_{sc}^2 \left[1 - \frac{4}{5}\frac{S}{\omega_{sc}} + \frac{8}{35}\frac{S^2}{\omega_{sc}^2}\right], \tag{6.66}$$

where the last term can be neglected because usually $S/\omega_{sc} \ll 1$. Thus, in the presence of a large spread, the average synchrotron frequency of the beam particles is roughly $\omega_{sc} - \frac{2}{5}S$ from the static effect of the impedance. Suppose the impedance introduces $\Delta\omega_{s\,\mathrm{dyn}}/S = \frac{1}{2}$, or the spread in synchrotron frequency is twice the static coherent shift without spread, the dispersion relation gives a dynamic coherent shift of $\Delta\omega_{s\,\mathrm{coh}}^{\mathrm{dyn}} = -0.209S$. This shift is negative because it is measured from ω_{sc}. However, this shift becomes $+0.191S$, which is positive, when measured from $\omega_{sc} - \frac{2}{5}S$, the average synchrotron frequency with the static

effect included only. This is illustrated schematically in Fig. 6.10.

On the other hand, $\Delta\omega_{s\,\mathrm{dyn}}$ shifts from ω_{sc} in the negative direction when $\eta\,\mathcal{I}m\,Z_0^{\parallel}/n < 0$ (dynamical coherent shift in the absence of spread) according to Fig. 6.8. Now in the presence of an incoherent frequency spread S, the average incoherent synchrotron frequency is no longer at ω_{sc}, but becomes somewhere in between ω_{sc} and ω_{sc}–S. Thus an additional coherent shift from the dynamical effects in the negative direction can easily land the coherent synchrotron frequency outside the incoherent frequency spread (more negative than $\omega_{sc}-S$). This may explain why there will not be any Landau damping when $\eta\,\mathcal{I}m\,Z_0^{\parallel}/n < 0$.

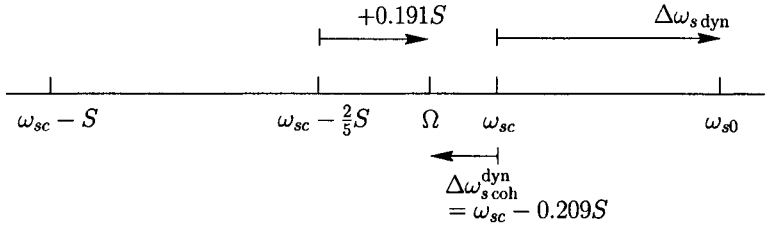


Fig. 6.10 In the absence of incoherent synchrotron frequency spread ($S = 0$), the dynamic frequency shift $\Delta\omega_{s\,\mathrm{dyn}}$ is upwards bringing the coherent frequency back towards the unperturbed synchrotron frequency ω_{s0}. In the presence a finite spread S, the dynamic shift $\Delta\omega_{s\,\mathrm{coh}}^{\mathrm{dyn}} = \omega_{sc} - 0.209S$ is downwards from ω_{sc} towards Ω. If we consider the this dynamic shift to be from the *average* incoherent synchrotron frequency of the bunch $\sim \omega_{sc} - \frac{2}{5}S$, this shift, $+0.191S$, is upward.

6.2.3.3 *Bi-Gaussian Distribution*

It will be nice to repeat the above argument with the bunch in other distributions as well. However, the investigation becomes much more involved, because besides the incoherent synchrotron frequency spread coming from the sinusoidal rf potential which is intensity independent, there is now also the incoherent synchrotron frequency spread coming from the nonlinear longitudinal self-force which is intensity dependent. The general method to tackle the problem is to move this intensity dependent synchrotron frequency spread from the left side of Eq. (6.33) to the right side, so that the interaction matrix now consists of the original wake-force part plus the new synchrotron-frequency-spread part. Although the interaction matrix becomes more complex, however, the left side contains only the same synchrotron-frequency spread coming from the rf potential. Thus all investigation can proceed as before and we envision to arrive at the same conclusion as in the elliptical distribution.

As an addendum, we are going to give the equi-growth contours and the

stability threshold contours for higher azimuthal modes in the bi-Gaussian distribution

$$\psi_0(r) = \frac{1}{2\pi} e^{-r^2/2}, \tag{6.67}$$

where the rms spread of the bunch has been normalized to unity. However, we shall ignore the incoherent synchrotron frequency spread due to nonlinear self-field effects, because their inclusion will lead to nonanalytic expressions.

The solution is given by the same expression in Eq. (6.62) with S equal to the rms incoherent frequency spread, and

$$\begin{aligned} \mathcal{G}_m(z) &= \frac{z^m e^{z/2}}{2^{m+1} m m!}, \\ \mathcal{H}_m(z) &= \frac{1}{2mm!} \left[\sum_{n=0}^{m-1} (m-n-1)! \left(\frac{z}{2}\right)^n + \left(\frac{z}{2}\right)^m e^{-z/2} E_1\left(-\frac{z}{2}\right) \right], \end{aligned} \tag{6.68}$$

where

$$W_m = -\frac{2^m m!}{2\pi}, \tag{6.69}$$

and

$$E_1(u) = \int_u^\infty \frac{e^{-t} dt}{t} \tag{6.70}$$

is the exponential integral. The stability contour and equi-growth contours are depicted in the left plot of Fig. 6.11 with growth rates in steps of S. In the right plot, we show the stability contours for the higher azimuthal modes.

6.3 Coupling of Azimuthal Modes

We learn from the previous section that when each azimuthal m is a good eigennumber, a single bunch is always stable in a broadband impedance. However, the picture will be changed when two azimuthals couple.

Assume a broadband impedance resonating at ω_r. The impedance will be inductive when $\omega < \omega_r$ and capacitive when $\omega > \omega_r$. If the rms length of the bunch $\sigma_\tau > \omega_r^{-1}$, the bunch particles are seeing mostly the inductive part of the impedance. We can assume that the accelerator ring is operated above the transition energy because the electrons, having small masses, are traveling at almost the velocity of light. This inductive force is repulsive opposing the focusing force of the rf voltage, thus lengthening the bunch and lowering the synchrotron frequency. Therefore, all azimuthal modes will be shifted downward,

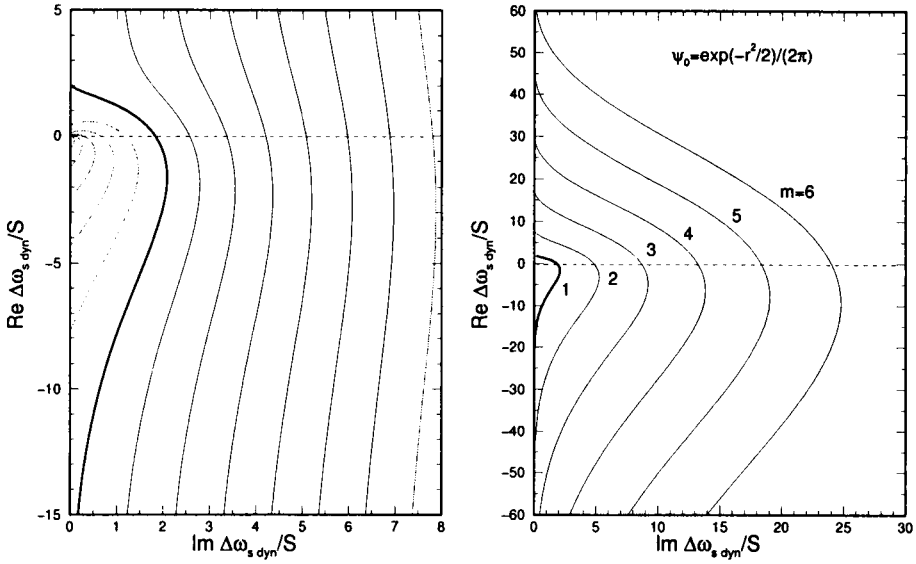


Fig. 6.11 Left: Equi-growth contours of the bi-Gaussian distribution $\psi_0(r) = e^{-r^2/2}/(2\pi)$, with growth rate increasing by steps of $0.1S$ to the right of the stability contour (darker curve) and damping rate increasing by steps of $0.1S$ to the left, where S is the rms spread of the incoherent synchrotron frequency. Right: Stability contours for the bi-Gaussian distribution for azimuthal modes $m = 1$ to 6.

except for the dipole mode $m = 1$ at least when the beam intensity is low. The $m = 1$ mode does not shift (from ω_{s0}) because this is a rigid-dipole motion and the inductive force acting on a beam particle is proportional to the gradient of the linear density as is demonstrated in Sec. 2.4. The centroid of the bunch does not see any linear density gradient and is therefore not affected by the inductive impedance. This is very similar to the space-charge self-field force. In fact, the inductive impedance is just the negative of a capacitive impedance. When the bunch intensity is large enough, the $m = 2$ mode will collide with the $m = 1$ mode, and an instability will occur if the frequencies corresponding to these two modes fall inside the resonant peak of $\mathcal{R}e\, Z_0^{\|}$. The interaction between the two modes is given by the overlap integral of the two mode spectra with $\mathcal{R}e\, Z_0^{\|}$ of the resonant peak. Mathematically, the frequency shifts of the two modes become complex. Since one solution is the complex conjugate of the other, one mode is damped while the other one grows. Thus the bunch becomes unstable. This is called *longitudinal mode-mixing* instability. Sometimes it is also known as *mode-coupling* or *mode-colliding* instability. An illustration is shown in Fig. 6.12 for a bunch of full length τ_L with parabolic linear density interacting with a broadband

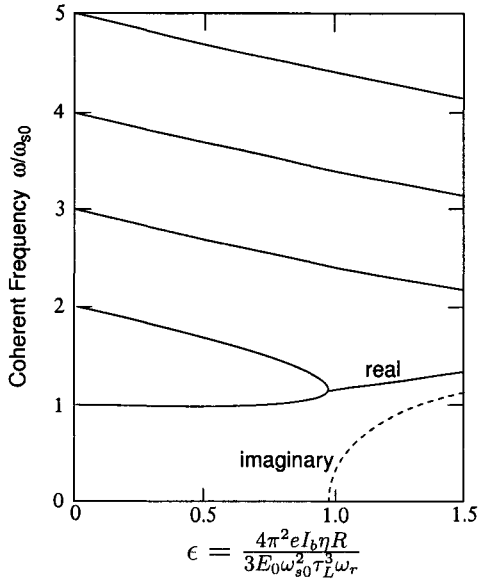


Fig. 6.12 Plot showing longitudinal mode-mixing instability of a parabolic bunch of full length τ_L interacting with a broadband impedance resonating with impedance R at frequency $\omega_r/(2\pi)$. The bunch length τ_L is much longer than ω_r^{-1} so that the bunch particles are seeing the inductive part of the impedance. Thus, all modes, except for $m = 1$, shift downward.

impedance resonating with impedance R at frequency $\omega_r/(2\pi)$. It is important to see that the coherent synchrotron frequency in vertical axis is normalized to the *bare* synchrotron frequency ω_{s0}.

A more thorough derivation will be given after we study Sacherer's integral of instability in later chapters. Here, we try to give a rough estimate of the threshold and discuss some points of interest. Just as a space-charge impedance will counteract the rf focusing force below transition, here an inductive impedance will counteract the rf focusing force above transition. According to Eq. (2.110), the extra voltage seen per turn by an electron at an arrival advance τ from the effect of the inductive impedance is

$$V_{\rm ind} = \frac{3eN_b}{2\omega_0\hat{\tau}^2}\left|\frac{Z_0^{\parallel}}{n}\right|_{\rm ind}\frac{\tau}{\hat{\tau}}, \tag{6.71}$$

where a parabolic linear distribution for the electron bunch of half length $\hat{\tau}$ has been assumed and N_b is the number of particles in the bunch. Although a parabolic distribution for electron bunches is not realistic, it does provide a linear potential and ease the mathematics. The synchrotron frequency is proportional to the square root of the potential gradient, $dV_{\rm ind}/d\phi$, where $\phi = -h\omega_0\tau + \phi_s$ is the rf phase of the particle at time advance τ, h is the rf harmonics, and ϕ_s is the synchronous phase. This extra voltage will shift the incoherent synchrotron

tune downward. If the beam intensity is low, the shift can be obtained by perturbation, giving

$$\frac{\Delta\nu_s}{\nu_{s0}} \approx \frac{1}{2}\frac{dV_{\rm ind}/d\phi}{dV_{\rm rf}/d\phi} = \frac{3e^2N_b\eta}{8\pi\omega_{s0}^2\hat{\tau}^3\beta^2E_0}\left|\frac{Z_0^{\parallel}}{n}\right|_{\rm ind}, \tag{6.72}$$

where $\nu_{s0}^2 = -e\eta h(dV_{\rm rf}/d\phi)/(2\pi\beta^2E_0)$ has been used. All the azimuthal modes will have their frequencies shifted downward coherently by roughly this amount also except for the $m = 1$ mode. The threshold can therefore be estimated roughly by equating the shift to the synchrotron tune. Because this shift is now large, the perturbative result of Eq. (6.72) cannot apply. Instead we equate the gradient of the extra voltage from the inductive impedance directly to the gradient of the rf voltage to obtain the threshold

$$\frac{3e^2N_b|\eta|}{4\pi\omega_{s0}^2\hat{\tau}^3\beta^2E_0}\left|\frac{Z_0^{\parallel}}{n}\right|_{\rm ind} \lesssim 1. \tag{6.73}$$

For a broadband impedance of quality factor $Q \approx 1$, it is easy to show at low frequencies,

$$\left|\frac{Z_0^{\parallel}}{n}\right|_{\rm ind} \approx \frac{R_s}{n_r}, \tag{6.74}$$

where R_s is the shunt impedance at the resonant angular frequency $\omega_r = n_r\omega_0$. Written in terms of the dimensionless current parameter ϵ in Fig. 6.12, the threshold of Eq. (6.73) translates into

$$\frac{4\pi^2eI_b|\eta|R_s}{3E_0\omega_s^2\tau_L^3\omega_r} \lesssim \frac{\pi^2}{9}, \tag{6.75}$$

which agrees with the point of coupling in Fig. 6.12 very well, where $\tau_L = 2\hat{\tau}$ is the full bunch length. It can also be rewritten as

$$\frac{R_s}{n_r} \lesssim \frac{8|\eta|E_0}{9eI_{\rm pk}\beta^2}\left(\frac{\Delta E}{E_0}\right)^2_{\rm FWHM}. \tag{6.76}$$

This is almost identical to the Keil–Schnell criterion in Eq. (5.23) with the average current replaced by the peak current. For this reason, this longitudinal mode-mixing threshold is often also referred to as the Keil–Schnell threshold. However, as will be shown later in Chapter 11, unlike the Keil–Schnell criterion, the left side of Eq. (6.76) is not the usual $|Z_0^{\parallel}/n|$ of a broad resonance. Because

this concerns the stability of a bunch mode, the broadband impedance should be replaced by the bunch-mode-weighted *effective impedance*:

$$\left|\frac{Z_0^{\parallel}}{n}\right| \longrightarrow \left.\frac{Z_0^{\parallel}}{n}\right|_{\text{eff}} = \frac{\int d\omega \dfrac{Z_0^{\parallel}(\omega)}{\omega}\omega_0 h_m(\omega)}{\int d\omega h_m(\omega)}, \tag{6.77}$$

where $h_m(\omega)$ is the power spectrum of the mth azimuthal mode depicted in Fig. 6.1. For Sacherer's approximate sinusoidal modes (see Sec. 9.7.1), the power spectra of some lower azimuthal modes are shown in Fig. 6.13. As will be shown in Chapter 13 that Landau damping has not been included in the stability limit of Eq. (6.76). In fact, the stability curve is bell-shaped and does not resemble the thermometer-bulb shape one for coasting beam derived in the last chapter. It is important to point out that it is the reactive part of the impedance that shifts the frequencies of the different azimuthal modes and the resistive part of the impedance that drive the stability. Unlike the coasting beam, pure reactive impedance is not able to drive longitudinal instability of the bunch. In the absence of a resistive part in the impedance, although two modes may collide with each other when the reactive part is large enough, the two modes just cross each other without interaction and no instability will result. This concept can be verified mathematically (see Chapter 13 and Exercise 11.3).

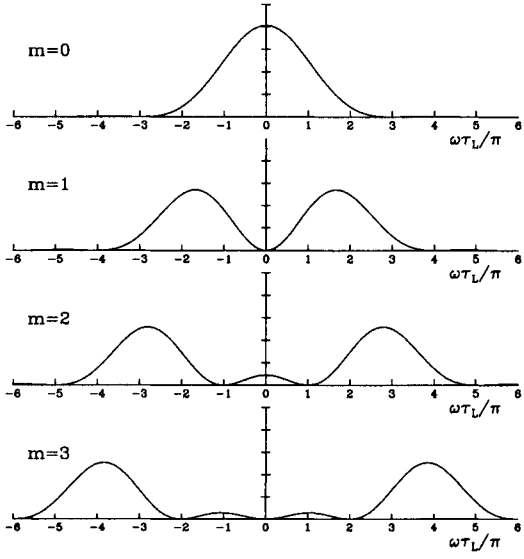


Fig. 6.13 Power spectra $h_m(\omega)$ of some lower azimuthal modes, $m = 0$ to 3, for a bunch with sinusoidal linear distribution, the so-called Sacherer's sinusoidal modes. (See Sec. 9.7.1).

According to Fig. 6.13, for the azimuth $m = 1$ to mix with azimuth $m = 2$, the peak of the resonance must have frequency between the peak of the power spectra of the two modes, or

$$\omega_r \sim \frac{2\pi}{\tau_L}. \tag{6.78}$$

In fact, this is expected, because with one or two oscillations in the linear density of the bunch, the wavelength of this instability must therefore have wavelength comparable to or shorter than the bunch length. The signal measured should correspond roughly to the rms frequency of the bunch spectrum, which is also in the microwave region (0.3–30 GHz), because an electron bunch is often shorter than the transverse size of the vacuum chamber. This is another reason why this instability is also referred to as microwave instability in the electron communities. Because an electron bunch has Gaussian distribution in energy spread, rather than Eq. (6.76), the stability limit

$$\left|\frac{Z_0^{\parallel}}{n}\right|_{\text{eff}} \lesssim \frac{2\pi|\eta|E_0}{eI_{\text{pk}}\beta^2}\left(\frac{\Delta E}{E_0}\right)^2_{\text{rms}} \tag{6.79}$$

is often used. It is worthwhile to point out that the above is only an empirical expression. Although this stability criterion is exactly the same as the one derived by Krinsky and Wang [5] depicted in Eq. (5.24) when the effective impedance is replaced just by the impedance, nevertheless, the derivation of Krinsky and Wang has nothing to do with the coupling of two azimuthal modes.

6.4 Bunch Lengthening and Scaling Law

In Fig. 6.12, the dashed curve denotes the growth rate of the instability. It is evident that the growth rate increases very rapidly as soon as the threshold is exceeded. We see that even when the bunch current exceeds the threshold by 20%, the growth rate reaches $\tau^{-1} \sim \omega_s$, or the growth time is of the order of a synchrotron period.** This means that the effect radiation damping and the use of conventional feedback systems may not be effective in damping the instability.

One way to avoid instability is to push the threshold to a higher value. For example, if the bunch is short enough so that $\sigma_\tau < \omega_r^{-1}$, the bunch particles will sample mostly the capacitive part of the broadband impedance. The frequencies of the azimuthal modes will shift upward instead. But the real part of the

**Theoretically, mode coupling instability cannot occur in a time span much shorter than a synchrotron period, because synchrotron oscillation is required for the formation of the azimuthal modes, which are separated by the synchrotron frequency.

impedance will eventually bend the mode downward. However, it will become harder for the $m = 2$ and $m = 1$ modes to collide, resulting in pushing the threshold to a higher value.

In reality, this instability is not devastating. The growth rate shown in Fig. 6.12 only applies when the bunch length and energy spread of the bunch are kept unchanged. As soon as the threshold is past, the bunch will be lengthened and the energy spread increased to such an extent that stability is regained again. Unlike proton bunches no overshoot is observed in electron bunches, probably because of the smoothing effect of synchrotron oscillation. Probably radiation damping also plays a role. Typical plots of the bunch length and energy spread are shown in Fig. 6.14. Note that because of the balancing of synchrotron radiation and random quantum excitations, there is a *natural* momentum spread σ_{δ_0} and the corresponding natural bunch length σ_{τ_0} is determined by the rf voltage. This is what we see below the threshold. For a short bunch with $\sigma_{\delta 0} < \omega_r^{-1}$, we will see the bunch length decreases as the bunch intensity increases, because the bunch samples the *attractive* capacitive impedance. This is called *potential-well distortion* which has been discussed in Chapter 2. However, the momentum spread is still determined by its natural value and is not changed. Above threshold, both the bunch length and energy spread are seen to increase. For each beam intensity, they increase to such values so that the stability criterion is satisfied again. As mentioned before, such feature does not manifest itself in a

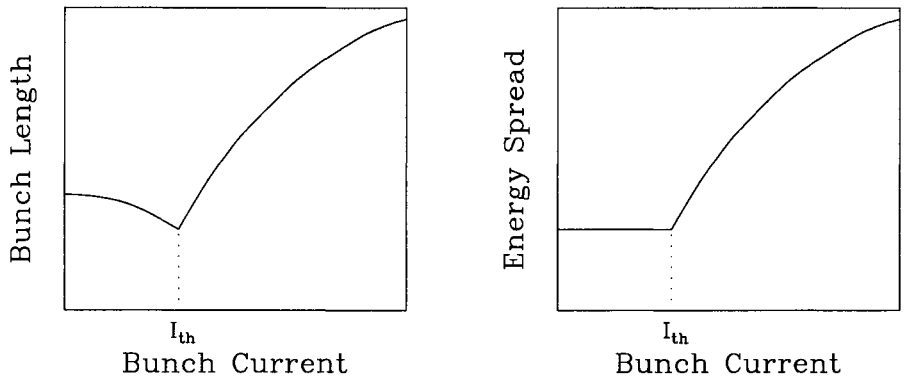


Fig. 6.14 Both the bunch length and energy spread begin to grow after the bunch current exceeds its microwave instability threshold $I_{\rm th}$. Left: The bunch length starts with its natural value at zero current and becomes shortened due to the capacitive potential-well distortion, if the natural bunch length is short enough so that the capacitive part of the impedance is sampled. Right: Below the instability threshold, the energy spread is always at its natural value unaffected by the effect of potential-well distortion.

proton bunch. If the threshold of microwave instability is exceeded by a small amount, overshoot occurs. If the threshold is exceeded by a large amount, the whole proton can often be lost.

One way to observe this instability is to measure the increase in bunch length. We can also monitor the synchrotron sidebands and see the $m = 2$ sideband move towards the $m = 1$ sideband. This frequency shift, which is a coherent shift, as a function of beam intensity is a measure of the reactive impedance of the ring. An accurate measurement of the frequency shift of the $m = 2$ mode may sometimes be difficult. An alternate and more accurate determination of the frequency shift can be made by monitoring the phase shift in the beam transfer function to be discussed in Chapter 13.

Above the instability threshold, the bunch-length lengthening and energy-spread increase depicted in Fig. (6.14) can be computed using the threshold condition. Chao and Gareyte [6] derived a scaling law which says that the bunch length is a function of one scaling parameter

$$\xi = \frac{\eta I_b}{\nu_s^2 E_0}, \tag{6.80}$$

where I_b is the average beam current of the bunch. In addition, when the part of the impedance sampled by the bunch behaves like

$$Z_0^{\parallel} \propto \omega^a, \tag{6.81}$$

the rms bunch length σ_τ above threshold has the behavior

$$\sigma_\tau \propto \xi^{1/(2+a)}. \tag{6.82}$$

This scaling law has been verified experimentally in the storage ring SPEAR at SLAC. The results are plotted in Fig. 6.15. The scaling law can be proved by first substituting the frequency-dependency of the impedance in Eq. (6.81) into the effective impedance per harmonic of Eq. (6.77). Noting that the power spectrum $h(\omega)$ can be made dimensionless because it is actually a function of $\omega\sigma_\tau$, we conclude readily that the effective impedance per harmonic is proportional to σ_τ^{1-a} (Exercise 6.3). Next, the Boussard-modified Keil–Schnell or Krinsky–Wang threshold condition of microwave instability [Eq. (5.23), (5.24), or just Eq. (6.76)] is rewritten in terms of σ_τ by eliminating the energy spread. When $|Z_0^{\parallel}/n|$ on the left side of the threshold condition is replaced by the effective impedance per harmonic, the scaling law results. A similar proof will be given later in Sec. 11.4 below.

For a bunch that is much longer than the radius of the beam pipe, the beam particles sample mostly the inductive part of the broadband impedance,

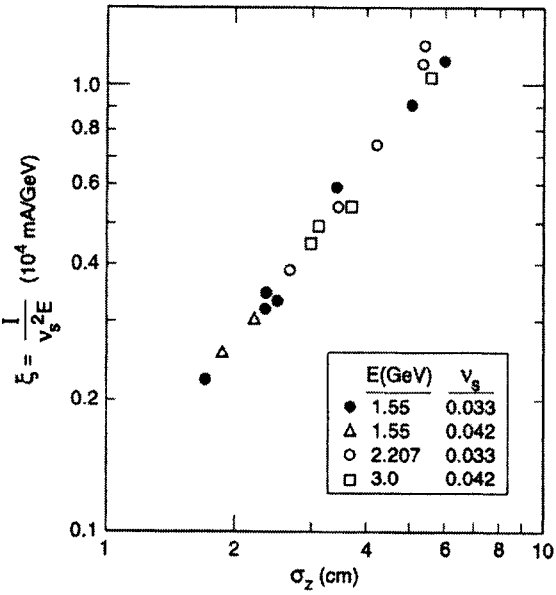


Fig. 6.15 RMS bunch length σ_z versus the scaling parameter ξ for the electron storage ring SPEAR. The momentum compaction factor has been kept constant. The measurement results indicate that $\sigma_z \propto \xi^{1/(2+a)}$ with $a = -0.68$. (Courtesy Chao and Gareyte. [6].)

resulting in $(Z_0^{\parallel}/n)_{\text{eff}}$ frequency-independent or $a = 1$, Thus the bunch length follows $\sigma_\tau \propto \xi^{1/3} \propto N_b^{1/3}$. When the bunch is much shorter than the radius of the beam pipe, the beam samples the frequencies higher than the peak of the broadband so picking up the capacitive part of the impedance. At such high frequencies,†† $(Z_0^{\parallel})_{\text{eff}} \propto \omega^{-1}$ or $a = -1$. Thus the bunch length follows $\sigma_\tau \propto \xi \propto N_b$. For SPEAR, measurements point to $\sigma_\tau \propto \xi^{0.76}$ or $a = -0.68$ (see Fig. 6.15), implying that the SPEAR bunches are short enough to sample the capacitive part of the impedance at frequencies higher than that of the broadband resonance. This is reasonable because the bunches at SPEAR have lengths slightly less than the radius of the beam pipe.

Proton bunches exhibit overshoot once the threshold of microwave instability is exceeded and therefore cannot be described by this scaling law. However, we still expect the scaling law to hold when the threshold is slightly exceeded so that overshoot is minimal. Since the peak current $I_{\text{pk}} \propto N_b/\sigma_\tau$ and the energy spread $\sigma_E \propto \sigma_\tau$, Keil–Schnell stability criterion implies $\sigma_\tau \propto N_b^{1/3}$ and more accurately $\sigma_\tau \propto \xi^{1/3}$, which corresponds to $a = 1$ or the impedance per harmonic experienced by the beam is roughly frequency independent. This is exactly what

†† Although $Z_0^{\parallel} \sim \omega^{-1/2}$ as $\omega \to \infty$, a result of the diffraction model, however, at frequencies not much higher than the frequency of the broadband resonance peak, the impedance rolls off according to $Z_0^{\parallel} \sim \omega^{-1}$.

the Keil–Schnell criterion is supposed to describe for a long proton beam, which samples mostly the inductive part with frequency much less than the peak of the broadband impedance. The discussion clearly demonstrates that the Keil–Schnell criterion is only suitable for long bunches which sample the inductive part of the broadband impedance, and cannot be used in an electron machine where the bunch length is so short that the capacitive part of the impedance is often sampled.

As mentioned before, this mode-coupling instability in the longitudinal phase space is not a devastating instability, because it results only in the blowup of the bunch area. In fact, many storage rings, especially collider rings, operate above this threshold, because a much higher beam intensity and therefore luminosity can be attained. However, this may not be the situation for a light source, where we always want to have shorter bunches so as to have smaller spot sizes for the synchrotron light. In order to accomplish this, the electron ring must be carefully designed so that the impedance is as small as possible. On the other hand, it is very difficult to reduce the impedance in a ring already built. For example, some capacitive structures were placed in the SLAC damping rings, so as to reduce the inductive impedance of the rings. After this modification, the threshold of the mixing of the $m = 2$ and $m = 1$ mode has been pushed much higher value. However, the beam particles are now seeing mostly the real part of the impedance, which distorts the bunch asymmetrically bringing out the importance of other radial excitation modes. These radial modes actually collide at a threshold much lower than the previous threshold before the modification. Fortunately, this instability due to the mixing of radial modes is tolerable because it is much weaker than the instability due to the mixing of azimuthal modes. [8]

6.5 Sawtooth Instability

Before the modification of the vacuum chambers in the SLAC Linear Collider (SLC) damping rings, a new form of longitudinal instability coupling with synchrotron radiation damping was observed. Upon the injection of a bunch, the bunch length decreased rapidly with a longitudinal damping time of the order of 2 ms. When the bunch length passed below a threshold, a sudden blowup in bunch length occurred in a time span comparable to or shorter than the 10 μs synchrotron period, as illustrated schematically in Fig. 6.16. This process was self-limiting because of the nonlinear nature of the short-range wake fields responsible for blowing up the bunch. Once the blowup ceased, the bunch was damped down until the threshold was reached again in about a synchrotron

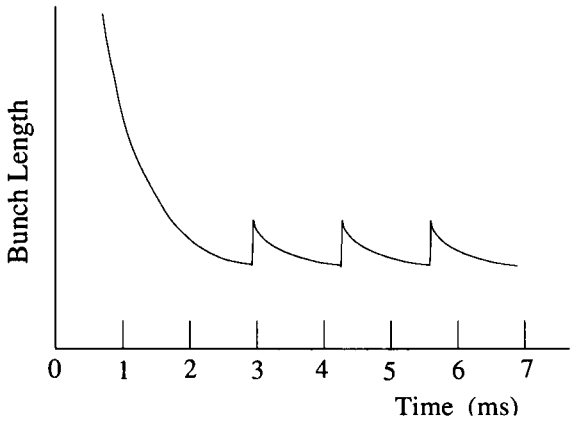


Fig. 6.16 Plot of bunch length versus time at the injection of the SLAC Damping Ring with an intensity of 3×10^{10} per bunch. The bunch length was damped rapidly in the first 2 ms after injection to a point where it was unstable. Rapid growth of the bunch length took place until the bunch was self-stabilized. After that it was damped by synchrotron radiation to below the instability threshold. This repetition has the shape of sawteeth.

damping time of $\sim$ 1.3 ms. Thus, a cyclical repetition of the instability was observed and termed according to its shape *sawtooth instability.* [11]

The time-dependent nature was seen in the bunch-length signal from the beam-position-monitor (BPM) electrodes and the bunch-phase signal from the synchronous-phase monitor. The bunch phase can be referenced to either the 714 MHz rf of the damping ring or to the 2856 MHz S-band rf of the linac. The synchronous beam phase angle is given by $\phi_s = \sin^{-1}(U_s/V_{\rm rf})$, where U_s is the energy loss per turn as a result of synchrotron radiation. The higher-order mode losses of a bunch are functions of the linear charge density and are inversely proportional to the bunch length. As the bunch blew up, the higher-order losses decreased and the beam phase shifted by about 0.5° at 714 MHz during a sawtooth. This translated into a 2° jump at the S-band in the linac. This magnitude of phase error was big enough to cause a problem with the rf bunch-length compressor in the ring-to-linac beam line. When this instability took place, the bunch would be incorrectly launched into the linac and might eventually be lost on the downstream collimators, causing the linac to trip the machine protection circuits. For some consequences, see Exercises 6.4 and 6.5.

There is a threshold for this instability, which occurred at around 3×10^{10} particles per bunch a nominal rf voltage of 1 MV. At higher intensities, the sawteeth appeared closer together in time. The process could be viewed as a relaxation oscillator where the period is a function of the bunch-length damping time and the trigger threshold. The damping time is constant but the bunch length at which the bunch went unstable increased at higher intensities. When the bunch intensity was increased to 4×10^{10} particles, a transition occurred to a second regime with "continuous sawteeth."

The longitudinal monopole impedance of the vacuum chamber was the first

to blame. Efforts had been made to reduce the inductive impedance hoping to reduce the downward shifting of azimuthal mode $m = 2$ and as a result the instability threshold would be pushed to a higher value. A new vacuum chamber was designed. With the installation of new SLC damping-ring vacuum chamber, however, the sawtooth instability did not go away as it was expected by simulations. On the contrary, the threshold went down from 3×10^{10} to $1.5\text{–}2 \times 10^{10}$ particles per bunch. The new instability has a similar sawtooth behavior, but it apparently is very much milder and does not affect the phase mismatch of the linac downstream as severely as the old instability.

An intense investigation has been going on to study this instability even after the installation of the new vacuum chamber. Podobedov and Siemann [12] tried to measure the longitudinal density bunch profiles from the synchrotron light with a high-resolution Hamamatsu streak camera during the instability. The phase of oscillation of the bunch density was obtained from the high-frequency BPM signals, processed and digitized by an oscilloscope. The 295 chosen profiles were binned according to their phases. The $+\frac{\pi}{2} \pm \frac{\pi}{4}$ phase bin implies near maximum deviation, while the $-\frac{\pi}{2} \pm \frac{\pi}{4}$ phase bin implies near minimum deviation. The average shapes for the two phase bins and the overall average profile are shown in the top plot of Fig. 6.17. The wavelength of oscillation is about 30 ps.

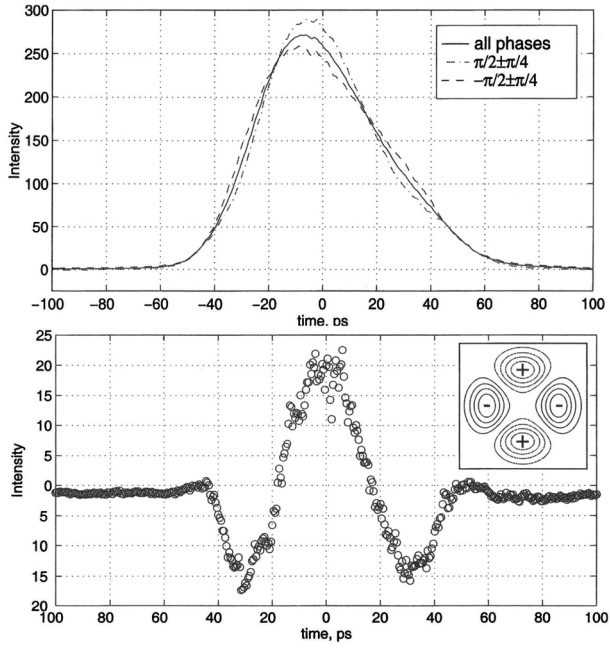


Fig. 6.17 Top: Beam density profiles during an instability burst captured by streak camera. The average is in solid. Those with the phase $+\frac{\pi}{2} \pm \frac{\pi}{4}$ are in dot-dashes and those with phase $-\frac{\pi}{2} \pm \frac{\pi}{4}$ are in dashes. Bottom: Bunch density oscillation with the average distribution subtracted. The structure resembles the projection of the azimuthal $m = 2$ oscillation. (Courtesy Podobedov and Siemann. [12].)

The oscillating part of the unperturbed linear density was next filtered out using

$$\delta\lambda(\tau) = \left\langle \frac{\lambda_k(\tau) - \lambda_0(\tau)}{\sin\phi_k} \right\rangle, \tag{6.83}$$

where λ_k are all the profiles with the phases ϕ_k ($k = 1, 2, \cdots, 295$), λ_0 is the phase-averaged profile, and the angle brackets denote the median value. The structure obtained is shown in the bottom plot of Fig. 6.17. This linear density resembles the $m = 2$ quadrupole mode in Fig 6.1 with the stationary distribution subtracted. The structure in the longitudinal phase space is shown in the corner of the figure. The ratio of the positive peak area to the negative peak area is about 3%, which measures the amount of redistributed particles creating the quadrupole structure. The conclusion is that the quadrupole mode ($m = 2$) had been excited. However, whether the instability arose from the coupling of the quadrupole mode to the dipole mode requires further investigation.

The instability was later pursued in the frequency domain by Podobedov and Siemann. [13] A bunch containing 3.5×10^{10} positrons was scanned in the SLC positron damping ring for the whole store of several minutes, during which the bunch intensity decayed by roughly a factor of two. The signal processing system consisted of a square-law detector which demodulated the instability signal from the sidebands to high-frequency revolution harmonics. This signal was subsequently amplified and the higher-order mixing products were removed by a low-pass filter. A typical spectrum at bunch intensity 3×10^{10} around the 1149th revolution harmonic (9.77 GHz) is shown in Fig. 6.18. We see the excitation of the quadrupole mode. The quadrupole sidebands are displaced from the harmonic by about 160 kHz, roughly 10% lower than twice the zero-

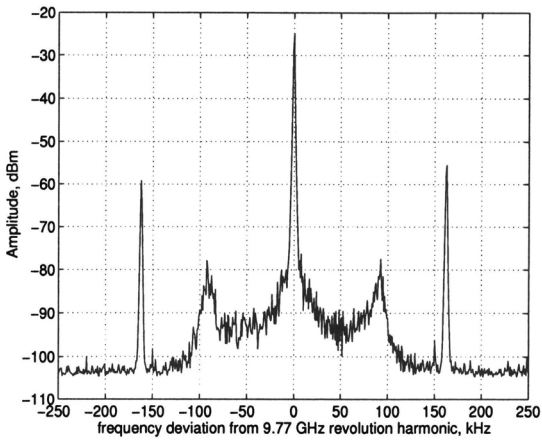


Fig. 6.18 Typical spectrum at 3×10^{10} ppb around the 1149th revolution harmonic (9.77 GHz) in the SLC positron damping ring after the installation of the new vacuum chamber. The quadrupole mode sidebands are excited and are displaced $\sim$ 160 kHz from the harmonic, about 10% less than twice the zero-current synchrotron frequency at 690 kV rf. (Courtesy Podobedov and Siemann. [13].)

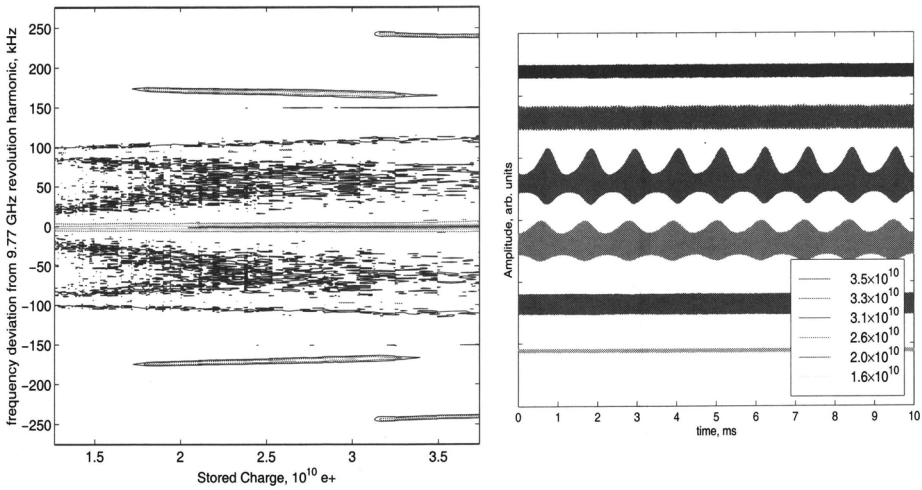


Fig. 6.19 Left: Contour plot of all the spectrum analyzer sweeps for a store of positron bunches in the SLC damping ring. The bunch intensity decays from 3.5×10^{10} to almost half near the end of the store. Sextupole mode instability is first seen and switches to quadrupole mode instability around $3.2\text{–}3.4 \times 10^{10}$ ppb. All instabilities stop below the intensity of 1.7×10^{10} ppb. Right: Oscilloscope traces of the instability signal from different values of the stored positron bunch. Sawtooth bursts occur near the intensity of $2.6\text{–}3.1 \times 10^{10}$ ppb when the mode of excitation is purely quadrupole. (Courtesy Podobedov and Siemann. [13].)

current synchrotron frequency at the rf voltage of 690 kV. The contour plot in Fig. 6.19 shows all the spectrum analyzer sweeps for the whole store. One can see how the instability jumps from the sextupole mode to the quadrupole mode around the intensity of $3.2\text{–}3.4 \times 10^{10}$ particles per bunch (ppb). The quadrupole mode threshold is about 1.7×10^{10} ppb with its frequency linearly decreasing at a rate of ~ 5 kHz/10^{10} ppb. Such a behavior is usually attributed to the inductive portion of the ring impedance. However, we do not see the crossing of the quadrupole and sextupole modes or the crossing of the quadrupole and dipole modes. This indicates that the instabilities may arise from the mixing of radial modes belonging to the same azimuthal, as postulated by Chao. [14] Unfortunately, we are not able to understand the sawtooth bursts before the modification of the vacuum chamber. Some believe that the instability, which was very much stronger, did arise from the mixing of two azimuthal modes, the dipole and the quadrupole, or the quadrupole and the sextupole. However, there is still the possibility that the bursts were the classic Keil–Schnell type microwave instabilities of a coasting beam. This is because, the bursts took place, as mentioned earlier, in a time span comparable or shorter than a synchrotron period, so that a coasting beam treatment may be justified. In any case, the

physics behind the sawtooth instability is still not completely understood.

Along with the spectrum analyzer data, right plot of Fig. 6.19 shows some oscilloscope traces taken concurrently. The top trace at 3.5×10^{10} ppb corresponds to a constant amplitude sextupole mode. The next trace corresponds to the case when both sextupole and quadrupole modes coexist. At even smaller current, 2.6–3.1 $\times$ 10^{10} ppb, the two traces in the middle show the sawtooth bursting behavior of the instability and correspond to pure quadrupole mode. Finally, below 2.5×10^{10} ppb, the bursts disappear and the quadrupole mode oscillates with constant amplitude.

Longitudinal sawtooth instability has also been observed at the Synchrotron Ultraviolet Radiation Facility (SURF III), the electron storage ring at the National Institute of Standards and Technology (NIST). Recently horizontal sawtooth instability has also been reported at the Advance Photon Source at ANL. Many simulations have been performed to reproduce the experimental observations in both the longitudinal and transverse planes and the results have been successful to a certain degree. [15, 16, 17]

6.5.1 *Possible Cure*

Before the modification of the vacuum chamber of the SLC damping ring, lowering the rf voltage has been a means of increasing the equilibrium bunch length and extending the intensity threshold. This is because the Landau damping from the energy spread, which is determined by synchrotron radiation, is unchanged, but lengthening the bunch reduces the local peak current and brings the bunch below the Keil–Schnell threshold according to Eq. (6.76) or (6.79). A low rf voltage, however, is not suitable for efficient injection and extraction for the damping ring. Before the installation of the new vacuum chamber into the damping ring, the rf voltage was ramped down from 1 MV to 0.25 MV approximately 1 ms after injection, as illustrated schematically in Fig. 6.20. It was ramped up back to 1 MV 0.5 ms before extraction. In this way the onset of sawtooth instability could be suppressed up to an intensity of 3.5×10^{10} per bunch.

Here, we want to mention another difference between electron and proton bunches. Although lowering the rf voltage may stabilize an electron bunch, this certainly will not work for a proton bunch. This is because for an electron bunch, the energy spread is determined by synchrotron radiation and will not change as the rf voltage is lowered. On the other hand, for a proton bunch, the bunch area conserves. Thus, lowering the rf voltage will diminish the energy spread instead, although the local linear density is decreased. Recall the Boussard-modified

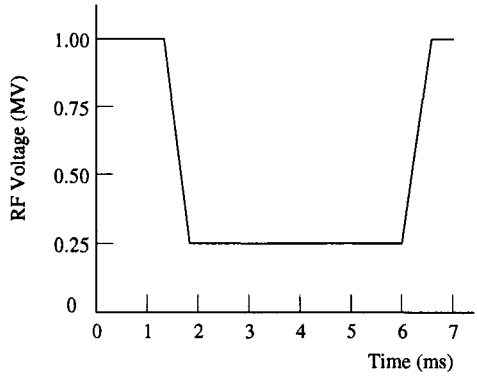


Fig. 6.20 The rf voltage was lowered in the SLAC damping ring after injection and before extraction, thus lengthening the bunch and reducing the local charge density. This raised the microwave instability threshold and prevented the sawtooth instability.

Keil–Schnell criterion [7] or the Krinsky–Wang criterion [5] of Eq. (5.24) for Gaussian energy spread distribution. Assuming also a Gaussian linear distribution, the peak current is $I_{\rm pk} = eN_b/(\sqrt{2\pi}\sigma_\tau)$, where σ_τ is the rms bunch length in time. Constant bunch area of a proton bunch implies constant $\sigma_\tau\sigma_E$, where σ_E is the rms energy spread. Thus, the threshold impedance per harmonic is directly proportional to the energy spread σ_E and is inversely proportional to the bunch length σ_τ. Reducing the rf voltage will make the proton bunch more susceptible to microwave instability. Such instability is very often seen when an rf rotation is perform to obtain a narrow proton bunch. The rf voltage is first lowered adiabatically in order to lengthen the bunch to as long as possible. The rf voltage is then raised suddenly to its highest possible value. The long and small-energy-spread bunch will rotate after a quarter of a synchrotron oscillation to a narrow bunch with large energy spread. Because it takes a lot of time to reduce the rf voltage adiabatically, the beam will often suffer from microwave instability when the momentum spread is small. To avoid this instability, one way is to snap the rf voltage down suddenly so that the rf bucket changes from Fig. 6.21(a) to 6.21(b). The bunch will be lengthened after a quarter synchrotron

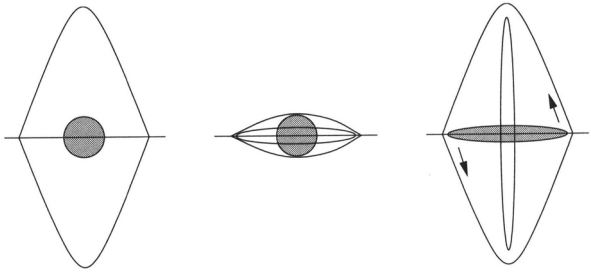


Fig. 6.21 Bunch shortening is performed by snapping down the rf voltage $V_{\rm rf}$, rotating for $\frac{1}{4}$ synchrotron oscillation, snapping up $V_{\rm rf}$, and rotating for another $\frac{1}{4}$ synchrotron oscillation.

oscillation. The rf voltage is then snapped up again as in Fig. 6.21(c) so that the lengthened bunch rotates into a narrow bunch as required. Since snapping the rf voltage is much faster than lowering it adiabatically, this may prevent the evolution of microwave instability. Such a method has also been used in bunch coalescence at Fermilab Main Injector.

6.5.1.1 *Precaution at The Next Linear Collider (NLC)*

In the design of the SLAC Next Linear Collider (NLC), extra attention has been paid to make sure that phase error in the damping ring due to, for example saw-tooth instability, will have minimal effects on the bunch length and bunch center in the main linac, as well as on the average energy and energy spread at the interaction point. After the damping ring, the bunch at 2 GeV must be compressed from the rms length of 5 mm to 0.09 mm, if not acceleration in the linac will be impossible because of the nonlinear rf force and the adverse effects of the wake fields. If a single strong compressor is employed, the energy spread will go up to more than 5% making preservation of transverse emittance difficult. Space-charge will pose a problem for such a short bunch at 2 GeV. In addition, coherent synchrotron radiation will become significant. Another problem is the 180° turn-around arc reserved for future upgrade. With more than 5% energy spread, the beam will become depolarized after passing through the arc. For all these reasons, a two-stage bunch compressor is proposed. [18]

The two-stage compressor is shown schematically in Fig. 6.22. The first stage is the L-band rf with a an rf slope k_1 followed by a wiggler with momentum compaction α_1. The second stage consists of the S-band pre-linac with with an rf slope k_2 followed by the 180° arc having momentum compaction α_2 and the S-band post-arc rf with slope k_3 followed by a chicane of momentum compaction α_3. After the first compression stage, essentially, bunch-center error and energy-center error are interchanged. However, one must make sure that this energy-center error will not introduce phase error in the main linac. In other words,

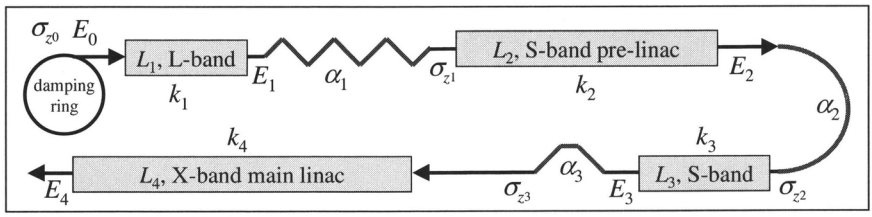


Fig. 6.22 The two-stage bunch compression system of the SLAC NLC with some symbol definitions indicated: α_i and k_i are the momentum compaction and rf-slope, respectively.

one would like to have the transfer-matrix element R_{56} for the second stage to vanish. The two-by-two transfer matrix for the longitudinal drift Δz and energy-spread δ for the second stage can be expressed as

$$R^{(1\to 3)} = \begin{pmatrix} 1 & \alpha_3 \\ 0 & 1 \end{pmatrix} \begin{pmatrix} 1 & 0 \\ k_3 & E_2/E_3 \end{pmatrix} \begin{pmatrix} 1 & \alpha_2 \\ 0 & 1 \end{pmatrix} \begin{pmatrix} 1 & 0 \\ k_2 & E_1/E_2 \end{pmatrix}, \tag{6.84}$$

where E_i represents the energy at each location. Thus the no-error-transfer requirement becomes

$$\alpha_2 = -\frac{E_2}{E_3}\frac{\alpha_3}{1+\alpha_3 k_3}. \tag{6.85}$$

As functions of the phase error at the extraction of the damping ring, the variations of the mean energy, energy spread, bunch center, and bunch length at the interaction point are obtained by tracking and are shown in Fig. 6.23. It is evident that the two-stage compression together with the no-error-transfer requirement does make these variations minimal.

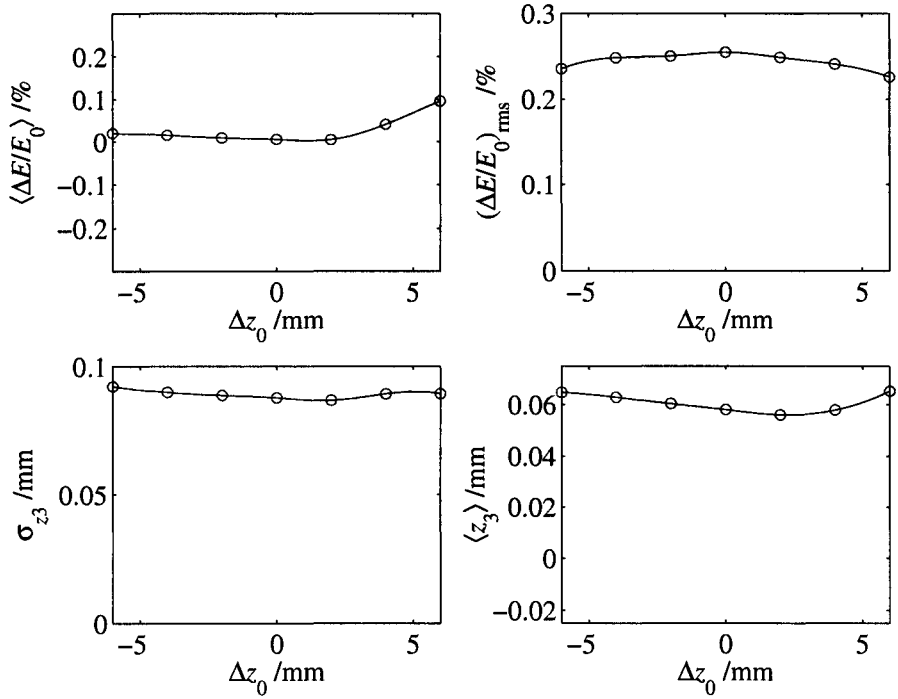


Fig. 6.23 At the interaction point of the SLAC NLC, the variations of mean energy, energy spread, bunch center, and bunch length versus initial phase error at the damping ring extraction.

6.6 Exercises

6.1 Derive the incoherent synchrotron tune shift in Eq. (6.72) driven by an inductive impedance.

6.2 (1) Derive the mode-mixing threshold, Eq. (6.73), by equating the synchrotron tune shift to the synchrotron mode separation.
(2) Rearrange the result to obtain the Keil–Schnell like criterion of Eq. (6.76).

6.3 Prove the scaling law about bunch length dependency using dimension argument as outlined in the text.

6.4 There is a difference in energy loss between the head and tail of a bunch in a linac because of the longitudinal wake. Take the SLAC linac as an example. It has a total length of $L = 3$ km and rf cavity cell period $L_0 = 3.5$ cm. The bunch consists of $N_b = 5 \times 10^{10}$ electrons and is of rms length $\sigma_z = 1.0$ mm. The longitudinal wake per cavity period is $W_0' = 6.29$ V/pC at $z = 0^+$ mm and 4.04 V/pC at $z = 1$ mm.
(1) Consider the bunch as one macro-particle, find the total energy loss by a particle traveling through the whole linac, taking into account the fundamental theorem of beam-loading (proved in Sec. 7.4.1 below) that a particle sees exactly one half of its own wake.
(2) Consider the bunch as made up of two macro-particles each containing $\frac{1}{2}N_b$ electrons, separated by the distance σ_z. Find the energy lost by a particle in the head and a particle in the tail as they traverse the whole linac.

6.5 A more detailed computation gives 1.2 GeV and 2.1 GeV as the energy lost by a particle $\frac{1}{2}\sigma_z$ ahead and behind the bunch center. This energy spread needs to be corrected to ensure the success of final focus at the interaction point of the SLAC Linear Collider. The rf voltage is 600 kV per cavity period and the rf frequency is 2.856 GHz.
(1) Explain why we cannot compensate for the energy spread by just placing the tail of the bunch ($\frac{1}{2}\sigma_z$ behind bunch center) at the crest of the rf wave so that the tail can gain more energy than the head.
(2) The correct way to eliminate this energy spread is to place the center of the bunch at an rf phase angle ϕ ahead the crest of the rf wave such that the gradient of the rf voltage is equal to the gradient of the energy loss along the bunch. Show that the suitable phase is $\phi = 17.3°$ for the bunch center.
(3) The accelerating gradient will decrease with this rf phase offset. A compromise phase offset is $\phi = 12°$. Compute the head-tail energy spread with this phase offset and compare the effective accelerating gradients in the two

situations.

(4) Assume that the sawtooth instability adds a $\pm 2°$ uncertainty in rf phase error, implying that ϕ now becomes $10°$ to $14°$. Compute the head-tail energy spread and the center energy uncertainty under this condition. Repeat the computation if the rf phase jitter is $\pm 5°$ instead.

Bibliography

[1] S. Y. Lee, *Accelerator Physics*, (World Scientific, 1999), Sec. VII.1.

[2] F. J. Sacherer, *A Longitudinal Stability Criterion for Bunched Beams*, CERN Report CERN/MPS/BR 73-1, 1973; *IEEE Trans. Nucl. Sci.* **NS 20**(3), 825 (1973).

[3] B. Zotter, *Longitudinal Stability of Bunched Beams Part II: Synchrotron Frequency Spread*, CERN Report CERN SPS/81-19 (D1), 1981.

[4] K. Y. Ng, *Comments on Landau Damping due to Synchrotron Frequency Spread*, Fermilab Report FERMILAB-FN-0762-AD, 2004.

[5] S. Krinsky and J. M. Wang, *Part. Accel.* **17**, 109 (1985).

[6] A. W. Chao and J. Gareyte, *Part. Accel.* **25**, 229 (1990).

[7] E. Keil and W. Schnell, CERN Report TH-RF/69-48 (1969); V. K. Neil and A. M. Sessler, *Rev. Sci. Instrum.* **36**, 429 (1965); D. Boussard, CERN Report Lab II/RF/Int./75-2 (1975).

[8] K. Bane, *et al.*, *High-Intensity Single Bunch Instability Behavior in the New SLC Damping Ring Vacuum Chamber*, Proc. 1995 IEEE Part. Accel. Conf., ed. L. Gennari (Dallas, May 1–5, 1995), p. 3109.

[9] F. J. Sacherer, *Methods for Computing Bunched-Beam Instabilities*, CERN Report CERN/SI-BR/72-5, 1972.

[10] P. B. Robinson, *Stability of Beam in Radiofrequency System*, Cambridge Electron Accel. Report CEAL-1010, 1964.

[11] P. Krejcik, K. Bane, P. Corredoura, F. J. Decker, J. Judkins, T. Limberg, M. Minty, R. H. Siemann, and F. Pedersen, *High Intensity Bunch Length Instabilities in the SLC Damping Ring*, Proc. 1993 Part. Accel. Conf., ed. S. T. Corneliussen, (Washington, D.C., May 17–20, 1993), p. 3240.

[12] B. Podobedov and R. Siemann, Proc. 1997 Part. Accel. Conf., eds. M. Comyn, M. K. Craddock, M. Reiser, and J. Thomson (Vancouver, Canada, May 12–16, 1997), p. 1629.

[13] B. Podobedov and R. Siemann, *Signals from Microwave Unstable Beams in the SLC Damping Rings*, Proc. 1999 Part. Accel. Conf., eds. A. Luccio and W. MacKay (New York, March 27–April 2, 1999), p. 146.

[14] A. Chao, B. Chen, and K. Oide, *A Weak Microwave Instability with Potential Well Distortion and Radial Mode Coupling*, Proc. 1995 IEEE Part. Accel. Conf., ed. L. Gennari (Dallas, May 1–5, 1995) p. 3040.

[15] K. Harkay, K.-J. Kim, N. Sereno, U. Arp, and T. Lucatorto, *Simulation Investigations of the Longitudinal Sawtooth Instability at SURF*, Proc. 2001 Part. Accel. Conf., eds. P. Lucas and S. Webber (Chicago, June 18–22, 2001), p. 1918.

[16] L. Harkay, Z. Huang, E. Lessner, and B. Yang, *Transverse Sawtooth Instability*

at the Advanced Photon Source, Proc. 2001 Part. Accel. Conf., eds. P. Lucas and S. Webber (Chicago, June 18–22, 2001), p. 1915.

[17] Yong-Chul Chae, *The Impedance Database and its Application to the APS Storage Ring*, Proc. 2003 Part. Accel. Conf., eds. J. Chew, P. Lucas and S. Webber (Portland, Oregon, May 12–16, 2003, 2001), p. 3017.

[18] P. Emma, SLAC Report, SLAC LCC-0021, 1999.

This page intentionally left blank

2025 © The Author(s). This is an Open Access chapter published by World Scientific Publishing Company, licensed under the terms of the Creative Commons Attribution-NonCommercial 4.0 International License (CC BY-NC 4.0).

Chapter 7

Beam-Loading and Robinson's Instability

Klystron or tetrodes* are employed to drive the rf cavities. When a klystron or tetrode is coupled to an rf cavity, electromagnetic fields are generated inside the cavity. The electric field across the gap of the cavity provides the required power to compensate for the energy lost to synchrotron radiation and coupling impedance, and to supply the necessary acceleration to the particle beam. However, the particle beam, when passing through the gap of the rf cavity, also excites electromagnetic fields inside the cavity in the same way as the klystron or the rf source. This excitation of the cavity by the particle beam is called *beam-loading*. beam-loading has two effects on the rf system. First, the electric field from beam-loading generates a potential, called the *beam-loading voltage*, across the cavity gap and opposes the accelerating voltage delivered by the klystron. Thus more power has to be supplied to the rf cavity in order to overcome the effect of beam-loading. Second, to optimize the power of the klystron, the cavity needs to be detuned. The detuning has to be performed correctly. If not, the power delivered by the klystron will not be efficient. Worst of all, an incorrect detuning will excite instability of the phase oscillation. We first study the steady-state beam-loading and derive the criterion for phase stability. Later, transient beam-loading will be addressed. The general methods to suppress and compensate beam-loading are reviewed. There are very good lecture notes and reviews on this subject written by Wilson, [1] Wiedemann, [2] and Boussard. [3]

7.1 Equivalent Circuit

The rf system can be represented by an equivalent circuit as shown in the top diagram of Fig. 7.1. The rf cavity is represented by a RLC circuit with angular

*Klystrons are usually used in electron rings where the rf frequencies are high while tetrodes are usually used in proton rings where the rf frequencies are low. In this chapter, there is no intention to distinguish between the two, and we often use the terminology *rf generator* instead.

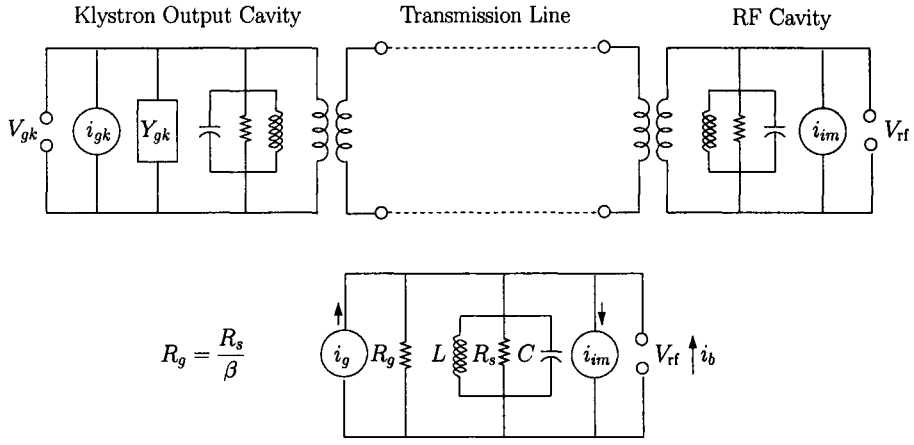


Fig. 7.1 Top: Circuit model representing an rf generator current source i_g driving an rf cavity with a beam-loading current i_{im}. Bottom: A simplified equivalent model.

resonant frequency

$$\omega_r = \frac{1}{\sqrt{\mathcal{L}C}}, \tag{7.1}$$

where $\mathcal{L}$ and C are the equivalent inductance and capacitance of the rf cavity. The klystron or tetrode is also represented by a RLC circuit with the angular resonant frequency $\omega_{\rm rf}$, which is the *rf frequency* of the accelerator ring and is slightly different from ω_r. The klystron/tetrode is connected to the rf cavity by waveguides or transmission lines via transformers as illustrated. The problem can be simplified considerably by assuming that there is a circulator or isolator just before the rf cavity, so that any power which is reflected from the cavity and travels back towards the klystron will be absorbed. Such an assumption leads to the equivalent circuit in the lower diagram of Fig. 7.1. The resistor R_s is called the *unloaded shunt impedance* of the rf system, because it is the impedance of the isolated cavity at its resonant frequency. The image current of the particle beam is represented by a current source i_{im}. This is a valid representation from the rigid-bunch approximation, because the velocities and therefore the current of the beam particles are assumed roughly constant when the beam passes through the cavity gap. We reference image current here instead of the beam current i_b, because it is the image current that flows across the cavity gap and also into the cavity. The image current is in opposite direction to the beam current.

On the other hand, the situation is different for the klystron. The velocities of the electrons as they pass through the the gap of the output cavity of the klystron

can change in response to the cavity fields of the klystron. As a consequence, the rf source is represented by a current source i_g in parallel to the *loading resistor* R_g or admittance $Y_g = 1/R_g$. The latter is written in terms of the *shunt admittance* Y_s or shunt impedance R_s of the rf cavity as

$$Y_g = \beta Y_s = \frac{\beta}{R_s}, \tag{7.2}$$

where β is the *coupling coefficient* still to be defined. The generator or klystron current i_g and the loading admittance Y_g in the lower equivalent circuit diagram are equivalent values and are different from the actual generator current i_{gk} and actual loading admittance Y_{gk} in the klystron circuit in the top circuit of Fig. 7.1. For example, in the rf system of the Fermilab Main Injector, $i_{gk} = 12 i_g$.

The rf generator outputs a generator current i_g in order to produce the rf gap voltage $V_{\rm rf}$ for the beam. The total *required* output power[†] is

$$P_{\rm total} = \frac{1}{2}\frac{i_g^2}{Y_g + Y_{\rm load}}, \tag{7.3}$$

where $Y_{\rm load}$ is called the *load-cavity admittance*, which includes the admittance of the cavity $Y_s = 1/R_s$ and also all the contribution from the particle beam. An explicit expression will be given in Eq. (7.43) below. In the situation of a very weak beam ($i_b \to 0$), $Y_{\rm load} \to Y_s$. The total power can be rewritten as

$$P_{\rm total} = \frac{1}{2}\frac{Y_g i_g^2}{(Y_g + Y_{\rm load})^2} + \frac{1}{2}\frac{Y_{\rm load} i_g^2}{(Y_g + Y_{\rm load})^2}. \tag{7.4}$$

The first term on the right is the power dissipated at the generator. The second term is the power required to be transferred to the cavity and the beam, and we denote it by P_g, which is usually referred to loosely as the *generator power*. We wish to obtain the condition for which this power delivered to the cavity and beam is a maximum by equating its derivative with respect to $Y_{\rm load}$ to zero. The condition is

$$Y_{\rm load} = Y_g = \beta Y_s. \tag{7.5}$$

[†]This is the power *required* to transfer a certain energy per unit time to the cavity and the beam, and is different from the power *available* to the beam and cavity. The latter is given by $\frac{1}{2}\tilde{i}_g \cdot \tilde{V}_{\rm rf}$ and becomes zero when the load angle $\theta_L = \pi/2$, as indicated in Eq. (7.38) below. On the other hand, the required power is inversely proportional to $\cos^2\theta_L$. When $\theta_L \to \pi/2$, most of the energy is being transferred to the cavity as stored energy and very little is given to the beam. Therefore to satisfy the requirement of the beam, an infinite required power by the generator becomes necessary.

This is just the usual matching of the input impedance to the output impedance. The maximized generator power is then

$$P_g = \frac{i_g^2}{8\beta Y_s} = \frac{R_s i_g^2}{8\beta}. \tag{7.6}$$

Notice that in the situation of an extremely weak beam, this matched condition is just $Y_g = Y_s$ with the coupling coefficient $\beta = 1$. Equation (7.6) will be used repeatedly below and whenever the generator power P_g is referenced; we always imply the matched condition satisfying Eq. (7.5).

We can also consider that the generator shunt impedance R_g is matched to a transmission line of characteristic impedance R_g. Thus one half of the generator current i_g flows through R_g while the other half flows into the transmission line. Then it is easy to see that the *forward power* P_f in the line (i.e., power flowing from the generator plus circulator towards the cavity) is given by P_g in Eq. (7.6). In general, there is also a current flowing backward in the transmission line from the cavity towards the generator. Thus the total power supplied to the transmission line will be more than P_f. If the load impedance $1/Y_{\text{load}}$ at the other end of the transmission line, that is the cavity shunt impedance together with the load of the beam, is equal to R_g there will not be any backward-flowing current in the line, and the total power supplied to the transmission line or the load from the generator is just the forward power P_f, which is the same as Eq. (7.6).

Here, all the currents and voltages referenced are the magnitudes of sinusoidally varying currents and voltages at the rf angular frequency ω_{rf} (not the cavity resonant angular frequency ω_r). Their corresponding *phasors* always have an overhead tilde. For example, i_{im} is the magnitude of the Fourier component of the image current phasor $\tilde{i}_{im}$ that flows into the cavity at the rf frequency. Thus, for a *short bunch*, we have (Exercise 7.1),

$$i_{im} = 2I_0, \tag{7.7}$$

with I_0 being the *dc current* of the beam. As phasors, however, they are in the opposite direction. It will be shown later, the image current phasor $\tilde{i}_m$ may not be equal to the negative beam current phasor $\tilde{i}_b$ because of possible feed-forward. In that case, I_0 in Eq. (7.7) will be the dc image current instead. For this reason, we try to make reference to the image current that actually flows into the cavity instead of the beam current.

In high energy electron linacs, bunches are usually accelerated at the peak or crest of the rf voltage wave in order to achieve maximum possible energy gain. As a result, the klystron is operated at exactly the same frequency as the

resonant frequency of the rf cavities, i.e., $\omega_{\rm rf} = \omega_r$. Without the rf generator, the beam or image current sees the *unloaded shunt impedance* R_s in the cavity and the *unloaded quality factor* Q_0, which can easily be found to be

$$Q_0 = \omega_r C R_s, \tag{7.8}$$

where C denotes the equivalent capacitance of the cavity. With the rf generator attached, however, the beam image current source sees an effective shunt impedance R_L in the cavity, which is the parallel combination of the generator shunt impedance R_g and the cavity shunt impedance R_s. This is called the cavity *loaded shunt impedance* in contrast with the cavity unloaded shunt impedance R_s. We therefore have

$$R_L = (Y_s + Y_g)^{-1} = \frac{R_s}{1+\beta}. \tag{7.9}$$

Correspondingly, the beam image current sees a *loaded quality factor* in the cavity, which is

$$Q_L = \omega_r C R_L = \frac{Q_0}{1+\beta}. \tag{7.10}$$

Notice that

$$\frac{R_s}{Q_0} = \frac{R_L}{Q_L}, \tag{7.11}$$

independent of whether it is loaded or unloaded. In fact, R_s/Q_0 is just a geometric factor of the cavity.

The beam-loading voltage is the voltage generated by the image current, and is given by

$$V_{br} = \frac{i_{im}}{Y_g + Y_s} = \frac{i_{im}}{Y_s(1+\beta)}, \tag{7.12}$$

while the voltage produced by the generator is

$$V_{gr} = \frac{i_g}{Y_g + Y_s} = \frac{i_g}{Y_s(1+\beta)}, \tag{7.13}$$

where the subscript "r" implies that the operation is at the resonant frequency, so that the currents and voltages are in phase, although they may have sign difference. In terms of the generator power P_g in Eq. (7.6), the generator voltage at resonance becomes

$$V_{gr} = \frac{\sqrt{8\beta}}{1+\beta}\sqrt{R_s P_g}. \tag{7.14}$$

It is clear that the beam-loading voltage is in the opposite direction of the generator voltage. Thus, the net accelerating voltage is

$$V_{\rm rf} = V_{gr} - V_{br} = \sqrt{R_s P_g}\left[\frac{\sqrt{8\beta}}{1+\beta}\left(1 - \frac{K}{2\sqrt{\beta}}\right)\right], \tag{7.15}$$

where

$$K^2 = \frac{i_{im}^2 R_s}{2P_g} \tag{7.16}$$

plays the role of the ratio of the beam-loading power to the generator power. Since the shunt impedance R_s of a superconducting cavity is very high, beam-loading becomes much more important. The fraction of generator power delivered to the beam is

$$\eta = \frac{i_{im} V_{\rm rf}}{2P_g} = \frac{2\sqrt{\beta}}{1+\beta} K\left(1 - \frac{K}{2\sqrt{\beta}}\right). \tag{7.17}$$

The power dissipated in the cavity is

$$P_c = \frac{V_{\rm rf}^2}{2R_s} = P_g\left(\frac{2\sqrt{\beta}}{1+\beta}\right)^2\left(1 - \frac{K}{2\sqrt{\beta}}\right)^2. \tag{7.18}$$

From the conservation of energy, we must have

$$P_g = \eta P_g + P_c + P_r, \tag{7.19}$$

where P_r is the power reflected back to the generator and is given by

$$\frac{P_r}{P_g} = \left(\frac{\beta - 1 - K\sqrt{\beta}}{1+\beta}\right)^2. \tag{7.20}$$

So far we have not said anything about the coupling coefficient β. Now we can choose β so that the generator power is delivered to the cavity and the beam without any reflection, or from Eq. (7.20), the *optimum coupling coefficient* is

$$K = \frac{\beta_{\rm op} - 1}{\sqrt{\beta_{\rm op}}}. \tag{7.21}$$

Notice that this optimization is also a maximization of the accelerating voltage $V_{\rm rf}$, as can be verified by differentiating Eq. (7.15) with respect to β.

7.2 Beam-Loading in an Accelerator Ring

In a synchrotron ring or storage ring, it is necessary to operate the rf system off the crest of the accelerating voltage waveform in order to have a sufficient large bucket area to hold the bunched beam and to insure stability of phase oscillation. The klystron or rf generator is operating at the *rf frequency* $\omega_{\rm rf}/(2\pi) = h\omega_0/(2\pi)$, where h is an integer called the *rf harmonic*, and $\omega_0/(2\pi)$ is the revolution frequency of the *synchronized* beam particles. Notice that this rf frequency will be the frequency the beam particles experienced at the cavity gap and is different from the intrinsic resonant frequency of the cavity $\omega_r/(2\pi)$ given by Eq. (7.1). According to the circuit diagram of Fig. 7.1, the impedance of the cavity seen by the particle at rf frequency $\omega_{\rm rf}/(2\pi)$ can be written as

$$Z_{\rm cav} = \frac{R_L}{1 + iQ_L\left(\dfrac{\omega_r}{\omega_{\rm rf}} - \dfrac{\omega_{\rm rf}}{\omega_r}\right)} = R_L \cos\psi\, e^{-i\psi}, \tag{7.22}$$

where ψ is called the *rf detuning angle* or just *detuning*. As will be shown below, detuning is an essential mechanism to make the beam particle motion stable under the influence of the rf system. It is important to point out that loaded values have been used here, because those are what the image current sees. From Eq. (7.22), the detuning angle is defined as

$$\tan\psi = Q_L\left(\frac{\omega_r}{\omega_{\rm rf}} - \frac{\omega_{\rm rf}}{\omega_r}\right). \tag{7.23}$$

When the deviation of $\omega_{\rm rf}$ from ω_r is small, an approximation gives

$$\tan\psi = 2\,Q_L\frac{\omega_r - \omega_{\rm rf}}{\omega_r}. \tag{7.24}$$

Phasors, as illustrated in Fig. 7.2, are represented by overhead tildes rotating clockwise with angular frequency $\omega_{\rm rf}$ if there is only one bunch in the ring.[‡] If there are n_b equal bunches in the ring separated equally by $h_b = h/n_b$ rf buckets, we can imagine the phasors to be rotating at angular frequency $\omega_{\rm rf}/h_b$. They are therefore the Fourier components at the rf frequency or $\omega_{\rm rf}/h_b$. This implies that we are going to see the same phasor plot for each passage of a bunch through the rf cavity. In order to be so, the beam-loading voltage should have

[‡]The phasors rotates clockwise because of the time-dependent factor $e^{-i\omega t}$ in our convention. They would rotate counterclockwise if $e^{j\omega t}$ were adopted instead. However, in both conventions, the voltage phasor $\tilde{V}_b$ in Eq. (7.26) always *leads in time* the image current phasor $\tilde{i}_{im}$. For convenience, we also say that $\tilde{V}_b$ *leads* $\tilde{i}_{im}$ *in phase* in Eq. (7.26) when $\psi > 0$.

negligible decay during the time interval $T_b = 2\pi h_b/\omega_{\rm rf}$ between two successive bunches. In other words, we require $T_b \ll T_f$ in this discussion, where

$$T_f = \frac{2Q_L}{\omega_r} \tag{7.25}$$

is the *fill time* of the cavity.

Most of the time, the image current phasor $\tilde{i}_{im}$ has the same magnitude as that of the beam current phasor $\tilde{i}_b$, although in the opposite direction. When the image current $\tilde{i}_{im}$ interacts with the loaded cavity, according to Eq. (7.22), a beam-loading voltage phasor $\tilde{V}_b$ will be produced and is given by

$$\tilde{V}_b = \tilde{i}_{im} R_L \cos\psi e^{-i\psi}, \tag{7.26}$$

and

$$V_b = V_{br} \cos\psi, \tag{7.27}$$

where V_{br} is the beam-loading voltage when there is no detuning, or when $\omega_{\rm rf} = \omega_r$. Thus the voltage phasor always leads the current phasor *in time* by the detuning phase ψ and the magnitude of the phasor $\tilde{V}_b$ is less than its value at the cavity resonant frequency V_{br} by the factor $\cos\psi$. If one likes, one can also introduce the phasor $\tilde{V}_{br}$ which is in phase with the current phasor $\tilde{i}_{im}$ and has the magnitude given by V_{br} in Eq. (7.27). This is illustrated in Fig. 7.2.

Some comments are necessary. Here, we start from only one Fourier component $\tilde{i}_{im}$ (the one at frequency $\omega_{\rm rf}$ or $\omega_{\rm rf}/h_b$) of the image current. The beam-loading voltage $\tilde{V}_b$ experienced by the beam is also a Fourier component at the same frequency. Since we are investigating the problem in the frequency domain, this is equivalent to a very long interval in the time domain. In other words, the result describes a steady-state problem, implying that the beam has passed by the rf cavities many many times already. The beam-loading voltage $\tilde{V}_b$ is therefore a sinusoidal wave in time. However, this is not exactly what we observe from a cavity. The beam-loading voltage decays exponentially as

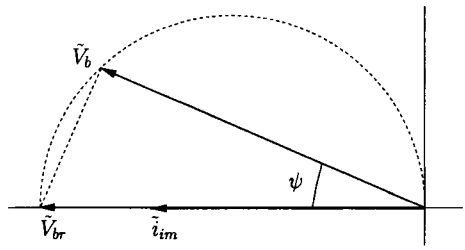


Fig. 7.2 Phasor plot showing the beam-loading voltage phasor $\tilde{V}_b$ induced in the rf cavity by the image current phasor $\tilde{i}_{im}$, which lags $\tilde{V}_b$ by the detuning angle ψ. Also plotted is the beam-loading voltage phasor $\tilde{V}_{br}$, with $V_b = V_{br}\cos\psi$ when the beam current is at the crest of the rf wave with no detuning.

soon as the beam leaves the rf cavity. It is charged up again like a step function when the beam passes by again. Thus, the time-dependent behavior of the beam-loading voltage is more like a sawtooth rather than sinusoidal. Putting it in another way, more than one Fourier component will be necessary to fully describe the beam-loading picture. However, if the exponential decay is slow, the beam-loading wave will behave more like sinusoidal. Therefore, our description of the beam-loading problem here is valid only when the cavity decay time constant (or fill time) $T_f = 2Q_L/\omega_r$ is very much longer than the interval T_b between successive beam passages. We will address a more accurate description later.

There are good reasons for detuning being necessary. The first one is for the compensation of beam-loading, which we describe in the next subsection. One may argue why we do not just employ an extra generator current equal and opposite to the image current for a simple 100% compensation. This requires the generator to deliver unnecessarily large current at a phase angle other than that of the rf voltage. Needless to say, this will result in a degradation of the efficiency of the rf excitation system and an increase in cost. The second reason is phase stability. When the center of the beam deviates from its proper rf phase, proper detuning will damp the deviation and guarantee phase stability. This will be addressed later in the section on Robinson's stability.

7.2.1 *Steady-State Compensation*

In Fig. 7.3, the total current phasor $\tilde{i}_t$ inside the cavity is the vector sum of the image current phasor $\tilde{i}_{im}$ and the generator current phasor $\tilde{i}_g$. The rf voltage phasor $\tilde{V}_{\rm rf}$, which is also known as the *cavity-gap voltage* is just gap voltage, is at the synchronous angle ϕ_s and leads the total current phasor by the detuning

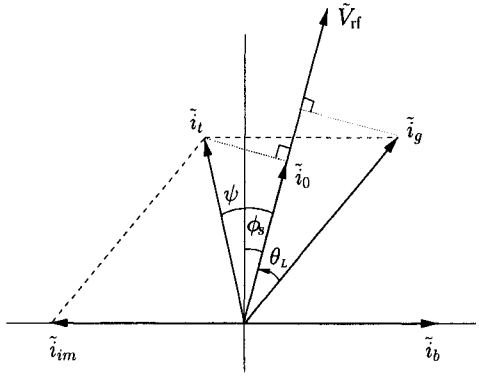


Fig. 7.3 Phasor plot showing the vector addition of the image current phasor $\tilde{i}_{im}$ and the generator current phasor $\tilde{i}_g$ to give the total current phasor $\tilde{i}_t$. The latter lags the rf voltage phasor $\tilde{V}_{\rm rf}$ at the synchronous phase ϕ_s by the detuning angle ψ. Note that the generator current phasor is, in general, not in phase with the rf voltage phasor. It lags $\tilde{V}_{\rm rf}$ by the load angle θ_L.

angle ψ. The current phasor $\tilde{i}_0$ is the projection of $\tilde{i}_t$ along $\tilde{V}_{\rm rf}$. Thus, $\tilde{i}_0$ is the generator current required to set up the rf voltage when the cavity is at resonance and when there is no beam current. In other words, $i_0 = V_{\rm rf}/R_L = (1+\beta)V_{\rm rf}/R_s$, where β is the coupling coefficient of the generator to the rf cavity and R_s is the unloaded shunt impedance.

We want to solve for the *load angle* θ_L that the the generator current phasor lags the rf voltage phasor. Since $\tilde{i}_g = \tilde{i}_t - \tilde{i}_{im}$, by projecting along and perpendicular to the rf voltage phasor, one obtains

$$\tan\theta_L = \frac{i_0 \tan\psi - i_{im}\cos\phi_s}{i_0 + i_{im}\sin\phi_s}, \tag{7.28}$$

and

$$i_g = \frac{i_0 + i_{im}\sin\phi_s}{\cos\theta_L}. \tag{7.29}$$

To optimize the efficiency of the generator, the generator current phasor $\tilde{i}_g$ and the rf voltage phasor $\tilde{V}_{\rm rf}$ should be in the same direction, because in this way the load will appear real to the generator and the stored energy will be reduced to a minimum. Substituting for $\theta_L = 0$, we obtain the in-phase conditions

$$\tan\psi = \frac{i_{im}\cos\phi_s}{i_0} \tag{7.30}$$

and

$$i_g = i_0 + i_{im}\sin\phi_s. \tag{7.31}$$

Figure 7.4 shows the voltage phasors inside the cavity with the rf voltage phasor $\tilde{V}_{\rm rf}$ in phase with the generator current phasor $\tilde{i}_g$. Here, we see that the beam-loading voltage phasor $\tilde{V}_b$ is ahead of the image current phasor $\tilde{i}_{im}$ by the detuning angle ψ. The generator voltage phasor $\tilde{V}_g$ is also ahead of the

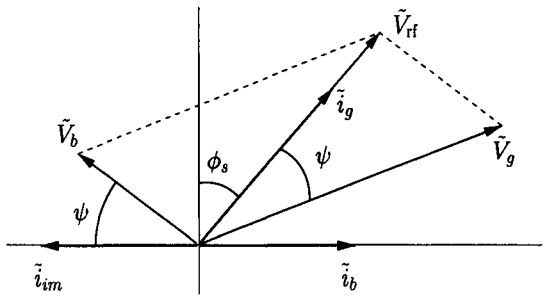


Fig. 7.4 Phasor plot showing the vector addition of the generator voltage phasor $\tilde{V}_g$ and the beam-loading voltage phasor $\tilde{V}_b$ to give the gap voltage phasor $\tilde{V}_{\rm rf}$ in an rf cavity. Note the detuning angle ψ which puts the generator current phasor $\tilde{i}_g$ in phase with the gap voltage phasor.

generator current phasor $\tilde{i}_g$ by the detuning angle ψ. These two voltage phasors add up to give the gap voltage phasor $\tilde{V}_{\rm rf}$ which is at the synchronous angle ϕ_s. The in-phase condition can also be obtained from this phasor diagram. Since the voltage components perpendicular to $\tilde{i}_g$ must add up to zero, $V_g \sin\psi = V_b \sin(\frac{\pi}{2} + \phi_s - \psi)$. After dividing by $R_L \cos\psi$, we get

$$i_g \sin\psi = i_{im} \sin(\tfrac{\pi}{2} + \phi_s - \psi). \tag{7.32}$$

Next, resolve the current contributions along $\tilde{i}_g$ and we obtain Eq. (7.31). Finally, eliminate i_g and arrive at the in-phase condition of Eq. (7.30).

Notice that steady-state beam-loading has been compensated by the introduction of a suitable generator current. This compensation scheme with detuning is much more efficient than the one without, because part of the beam-loading voltage has been utilized in the rf voltage and the generator current is in phase with the rf voltage. In other words, the generator power required will be smaller than when there is no detuning. Actually, it can be readily shown by differentiating Eq. (7.35) below with respect to the detuning angle ψ that the generator power is the smallest when the in-phase condition is met between the generator current phasor and the rf voltage phasor. In the event that the beam intensity is very high, the beam-loading voltage V_b can become much larger than the required gap voltage $V_{\rm rf}$. Needless to say, to balance such a large beam-loading voltage, a very high power amplifier will be necessary to generate the required generator current $\tilde{i}_g$. When this happens, low-level rf feedback can be installed to reduce the effective cavity impedance as observed by the beam. A low-level rf feed-forward is also possible to cancel partly or completely the image current. These methods will be discussed later in Sec. 7.4.4.

The generator power P_g can be computed with the aid of Eq. (7.14), namely,

$$P_g = \frac{(1+\beta)^2 V_{gr}^2}{8\beta R_s}, \tag{7.33}$$

where V_{gr} is the generator voltage at the cavity resonant frequency, and is related to the generator voltage V_g at the rf frequency by $V_g = V_{gr}\cos\psi$. Using the cosine law for the triangle made up from $\tilde{V}_g$, $\tilde{V}_b$, and $\tilde{V}_{\rm rf}$, it is easy to obtain

$$V_g^2 = V_b^2 + V_{\rm rf}^2 - 2V_b V_{\rm rf} \sin(\psi - \phi_s), \tag{7.34}$$

or

$$V_{gr}^2 = V_{br}^2 + V_{\rm rf}^2(1 + \tan^2\psi) - 2V_{br}V_{\rm rf}(\tan\psi\cos\phi_s - \sin\phi_s), \tag{7.35}$$

where $V_{br} = V_b/\cos\psi$ is the beam-loading voltage at the cavity resonant frequency. From Eq. (7.14), the required generator power for the cavity and beam

can be expressed as

$$P_g = \frac{R_s}{8\beta}\left[(i_0 + i_{im}\sin\phi_s)^2 + (i_0\tan\psi - i_{im}\cos\phi_s)^2\right], \tag{7.36}$$

where

$$V_{br} = \frac{V_b}{\cos\psi} = \frac{i_{im}R_s}{1+\beta} \tag{7.37}$$

is the beam-loading voltage at the cavity resonant frequency, and the definition of i_0 in Eq. (7.31) has been used. If the correct detuning is made so that $\tilde{i}_g$ and $\tilde{V}_{\rm rf}$ are in phase, the second term on the right-hand side vanishes and the expression is very much simplified. On the other hand, we notice that the two terms on the right side resemble the denominator and numerator on the right side of Eq. (7.28). We can therefore rewrite the generator power in terms of the load angle θ_L,

$$P_g = \frac{R_s}{8\beta}\frac{(i_0 + i_{im}\sin\phi_s)^2}{\cos^2\theta_L}, \tag{7.38}$$

which recovers the situation of in-phase detuning when $\theta_L = 0$. The factor $\cos^2\theta_L$ is important. It tells us that when the load angle $\theta_L \to \pi/2$, an infinite generator power is required. This is because only the fraction $\cos^2\theta_L$ of the power goes into the beam and the majority, $\sin^2\theta_L$, goes into charging the cavity.

With the in-phase condition satisfied, we still have a coupling coefficient β as a free parameter. We now optimize the generator power by differentiating Eq. (7.38) with respect to β, noting that $i_0 = (1+\beta)V_{\rm rf}/R_s$. The optimized coupling coefficient turns out to be

$$\beta_{\rm op} = 1 + \frac{i_{im}R_s\sin\phi_s}{V_{\rm rf}} = 1 + \frac{P_b}{P_c}, \tag{7.39}$$

where

$$P_c = \frac{V_{\rm rf}^2}{2R_s} \tag{7.40}$$

is the power dissipated in the walls of the cavity and

$$P_b = \tfrac{1}{2}\, i_{im}V_{\rm rf}\sin\phi_s = I_0 V_{\rm rf}\sin\phi_s \tag{7.41}$$

is the power spent on accelerating the beam, since $V_{\rm rf}\sin\phi_s$ is the accelerating voltage. Here, we have used Eq. (7.7), the fact that the Fourier component image current at the rf frequency (or at $\omega_{\rm rf}/h_b$) is nearly twice the dc beam current

I_0 when the bunch is short. At the optimized coupling constant, the generator power becomes

$$P_{g\,\mathrm{op}} = \frac{V_{\mathrm{rf}}^2}{2R_g} = \frac{V_{\mathrm{rf}}^2}{2R_s}\beta_{\mathrm{op}} = P_b + P_c, \tag{7.42}$$

which just states that the power is transmitted to the cavity completely without any reflected. Here, we can identify the *load-cavity admittance* $Y_{\mathrm{load}} = \beta Y_s$ defined in earlier in Eq. (7.4) as

$$Y_{\mathrm{load}} = \frac{i_{im}\sin\phi_s}{V_{\mathrm{rf}}} + \frac{1}{R_s}, \tag{7.43}$$

where the first term on the right is admittance of the beam and the second term is the admittance of the cavity. This optimized coupling coefficient should be compared with that of Eq. (7.21) in a linac. Although they are different in the two different situations, however, they do share the same physical implication.

Usually there is a servo-tuner which measures the phase difference between the generator current phasor and rf gap voltage phasor, and controls the cavity resonant frequency through a mechanical plunger or ferrite bias, so that the phase difference vanishes. At the equilibrium of the servo-tuner, Eqs. (7.30) and (7.31) are automatically satisfied, and the cavity detuning corresponds to

$$\Delta\omega = \omega_r - \omega_{\mathrm{rf}} = \frac{\omega_r R_L i_{im}\cos\phi_s}{2Q_L V_{\mathrm{rf}}}. \tag{7.44}$$

Recall that the generator power P_g that we refer to here is actually the power spent in accelerating the beam particles, compensating synchrotron radiation and wake-field loss to the vacuum chamber, as well as energy dissipated in the cavity system through the shunt impedance R_s which may include possible ferrite tuners. This is the second term defined in Eq. (7.4). The first term is the loss to the resistor R_g of the generator which is defined as $R_g = R_s/\beta$. Let us denote this power as P_G, which equals βP_c. We also recall the condition $P_G = P_g$, when the power delivered to the cavity and beam is at a maximum. We have now Eq. (7.42) at the optimal choice the coupling coefficient. The power dissipated at the load, R_g and R_s, or the loaded shunt impedance, is

$$P_L = P_G + P_c = (1 + \beta_{\mathrm{op}})P_c. \tag{7.45}$$

The ratio of the power supplied to be beam and the total power loss to the load is therefore

$$\frac{P_b}{P_L} = \frac{P_b/P_c}{1 + P_b/P_c} < 1. \tag{7.46}$$

We will see in the next section that this satisfies the criteria of Robinson's stability.

Let us address the magnitude of $\beta_{\rm op}$ by going into some examples. One of the future Fermilab booster designs consists of two rings. [4, 5] The low-energy ring has a circumference of 158.07 m ($\frac{1}{3}$ of present booster), cycles at 15 Hz, and accelerates four proton bunches, $N_b = 2.5\times10^{13}$ protons each, from kinetic energy 1 GeV to 3 GeV. The ten accelerating cavities have an rf frequency span of 6.638 to 7.368 MHz, and require a total peak voltage of $\sim 190\,\text{kV}$, or $\sim 20\,\text{kV}$ each. For such a small ring, small cavities are preferred, making the high-field Finemet very appealing. Finemet is a met-glass-like material developed in Japan. Ferrite is ceramic in nature and is manufactured by baking in an oven. Therefore, large ferrite cores are difficult to produce. On the other hand, Finemet is in the form of a tape which can be wound into a core over 1 m in diameter, making very high magnetic flux possible. Figure 7.5 shows the $\mu_p' Qf$ curves of Finemet and ferrite as functions of magnetic flux density, which is essentially the plot of the inverse shunt impedance; a smaller value of $\mu_p' Qf$ implies a bigger loss.[§] We see that the loss in Ni-Zn ferrite increases rapidly when the magnetic flux density penetrating it is more than a few Gauss. Even the Ni-Zn (CO) ferrite will not hold more than $\sim$ 100 G. On the other hand, Finemet has its $\mu_p' Qf$ level until more than 2 kG. However, there is a shortcoming, the relative parallel permeability μ_p' starts to drop at a much lower frequency of $\sim$ 2 MHz and the quality factor is low, $Q \sim 1$. This implies that Finemet is more lossy than ferrite with large power consumption. Fortunately, this lossy disadvantage can be improved by cutting the Finemet core into two semicircular halves. The air space in between lowers the capacitance and is able to boost the quality factor to $Q \sim 8$ and the

[§]Here, the relative *parallel* permeability $\mu_p' + i\mu_p''$ is used instead of the relative *series* one $\mu_s' + i\mu_s''$ in Sec. 5.3.2. In the former, the ferrite or Finemet is modeled as a parallel combination of a resistance and a reactance, $R = \omega\mu_p''\mathcal{L}_0$ and $X = \omega\mu_p'\mathcal{L}_0$, where $\mathcal{L}_0$ is the geometric contribution of the inductance (with permeability equal to unity), giving the impedance

$$Z_0^{\parallel} = \frac{-i\omega\mathcal{L}_0}{\frac{1}{\mu_p''} - \frac{1}{i\mu_p'}}. \tag{7.47}$$

The series representations is the series combination of $R = \omega\mu_s''\mathcal{L}_0$ and $X = \omega\mu_s'\mathcal{L}_0$, giving

$$Z_0^{\parallel} = -i\omega\mathcal{L}_0(\mu_s' + i\mu_s''). \tag{7.48}$$

The relation between the two representations is therefore

$$\mu_s' = \frac{\frac{1}{\mu_p'}}{\frac{1}{\mu_p'^2} + \frac{1}{\mu_p''^2}} \quad \text{and} \quad \mu_s' = \frac{\frac{1}{\mu_p''}}{\frac{1}{\mu_p'^2} + \frac{1}{\mu_p''^2}}. \tag{7.49}$$

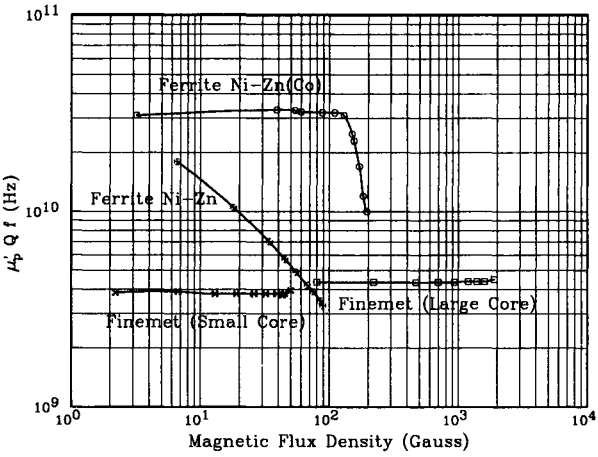


Fig. 7.5 Plots showing the $\mu_p' Qf$ properties of ferrite and Finemet as a function of magnetic flux density B, showing that ferrite becomes very lossy at $B \gtrsim 10$ Gauss for Ni-Zn ferrite and $B \gtrsim 100$ Gauss for Ni-Zn (CO) ferrite, but Finemet can hold up to 2 kG.

operating frequency to ~ 8 MHz.

The FT3M Finemet cores considered here have inner and outer radii 10 and 50 cm, respectively, while the Philips 4M2 ferrite cores have inner and outer radii 10 and 25 cm. Both cores have thickness 2.54 cm. The Finemet cores are cut with an air separation of 4.6 cm in order to boost the unloaded quality

Table 7.1 Properties of a Finemet and a ferrite cavity in a damping ring for the superconducting linear collider.

	Finemet	Ferrite
Inner radius r_i (cm)	10.00	10.00
Outer radius r_o (cm)	50.00	25.00
Core width t (cm)	2.54	2.54
Flux area $A_f = (r_o - r_i)t$ (cm^2)	101.6	38.10
Core volume $V_c = \pi(r_o^2 - r_i^2)t$ (cm^3)	19151	4189
Rf frequency $f_{\rm rf}$ (MHz)	7.37	7.37
Unloaded quality factor Q_0	11.4	45
$\mu_p' Qf$ at $f_{\rm rf}$ (GHz)	6.00	61.0
Permeability ($\mathcal{R}e$) μ_p'	71.43	183.9
Permeability ($\mathcal{I}m$) $\mu_p'' = Q_0 \mu_p'$	814.1	8277
Inductance $\mathcal{L}$ (μH)	0.5839	0.8561
Resistance $R = Q_0 \omega_{\rm rf} \mathcal{L}$ (Ω)	308.2	1784
Capacitance $C = 1/(\omega_{\rm rf}^2 \mathcal{L})$ (pF)	798.7	544.7
Gap voltage per cavity $V_{\rm rf}$ (kV)	20	20
Total flux density if one core $B_{\rm rf}$ (G)	425.1	1134
Suitable flux density per core (G)	250	100
Number of cores required n	2	11
Power lost per core P_1 (kW)	162.2	0.9166
Power lost for n cores $P = nP_1$ (kW)	324.4	10.19
Power per volume P_1/V_c (W/cm^3)	8.47	0.221

factor to $Q_0 = 11.4$. [6] The details are listed in Table 7.1. If there were only one core, the flux density would be $B_{\rm rf} = V_{\rm rf}/(\omega_{\rm rf} A_f)$, where A_f is the magnetic flux area. To limit dissipation to below the usual manageable 10 W/cm^3, at least two Finemet cores are required per cavity. Allowing ~ 2.54 cm separation between cores for air cooling, the length of a cavity can be made as short as ~ 13 cm. However, we do assume in this estimation that the quality factor and capacitance remain unchanged in view of the cooling space. The power loss is $nP_1 = V_{\rm rf}^2/(2nR) = 324$ kW per cavity, where $V_{\rm rf}$ is the gap voltage of the cavity consisting of n Finemet cores and R is the resistance per core. On the other hand, if ferrite is used, we need 11 cores with a total cavity length ~ 28 cm to satisfy its flux density limitation. Here, core spacing is not required because the total power loss for the whole cavity is only 10.2 kW. Although longitudinal space is saved in the Finemet cavities, power loss will be 31.8 times larger, totaling $P_c = 3.24$ MW for ten cavities. Assuming the acceleration of 1×10^{14} particles takes place in 1/30 of a second, the average power delivered to the particles is only $P_b = 0.961$ MW. Thus, we obtain the optimized coupling coefficients $\beta_{\rm op} = 1.30$ if Finemet is used and 10.43 if ferrite is used. The corresponding loaded quality factors are $Q_L = 4.96$ for Finemet and 3.94 for ferrite. As a result, we obtain the same wideband cavities independent of whether Finemet or ferrite is employed.

As another example, let us discuss the rf system of a damping ring designed for the superconducting version of a linear collider. [7] The ring has a circumference of 6113.97 m.

There are 60 trains each containing 47 bunches with 2×10^{10} electrons per bunch at 5.066 GeV. The bunch spacing is 6 ns and the empty gap between two consecutive trains is 64 ns. The average beam current is $I_0 = 0.443$ A and the image current at the rf frequency is $i_{im} = 0.866$ A. The rf system is to be at 500 MHz supplying a total rf gap voltage $V_{\rm rf} = 27.2$ MV. The average radiation loss per turn is 7.726 MV so that a synchronous angle of $\phi_s = \pi - 0.288$ is required. Thus the power required to be delivered to the beam is $P_b = \frac{1}{2} i_{im} V_{\rm rf} \sin\phi_s = 3.42$ MW. Room temperature cavities something like those at the PEP-II B-factory have been considered, although about 60 cells will be required to supply the required gap voltage. If one chooses superconducting cavities like those at the KEK B-factory, 12 cells will be required. The properties of the two types of cavities pertaining to the damping ring are listed in Table 7.2. We see that the two types of cavities are very different. The optimized coupling coefficient for the room-temperature rf system is $\beta_{\rm op} = 1.85$ and is small. On the other hand, $\beta_{\rm op} = 5.00 \times 10^4$ for the superconducting rf system, thus de-Qing the cavities tremendously from 1×10^{10} to 2×10^5. The beam-loading

voltages seen by a bunch are on the average $V_b = 20.1$ and 27.2 MV, respectively, for the room-temperature and super-conducting systems. If it were not of the huge $\beta_{\rm op}$ in the super-conducting rf, the beam-loading voltage would have been many orders of magnitudes larger than the rf gap voltage. The near equality of V_b and $V_{\rm rf}$ in the superconducting rf system is not accidental, but is the consequence of the huge optimum coupling coefficient $\beta_{\rm op}$. It is easy to show that this near equality shifts the generator voltage phasor $\tilde{V}_g$ in phase with beam current (see Exercise 7.3). As will be demonstrated in the next section, all possible Robinson's phase stability will be forfeited. Phase oscillation can only be maintained by radiation damping. In the absence of sufficient radiation damping, such as in hadron rings, a fast rf feedback and phase loop must be installed.

Table 7.2 Comparison of room-temperature and superconducting cavities.

	Room temperature	Super conducting
R/Q (Ω)	60	45
Unloaded quality factor Q_0	2.55×10^4	1×10^{10}
Number of cells required	60	12
Unloaded shunt impedance (MΩ)	91.8	5.4×10^6
Rf gap voltage (MV)	27.2	27.2
Power supplied to beam P_b (MW)	3.42	3.42
Power dissipated in cavities P_c (MW)	4.03	6.85×10^{-5}
Optimized coupling coefficient $\beta_{\rm op}$	1.85	5.00×10^4
Loaded quality factor Q_L	8949	2.00×10^5
Loaded shunt impedance R_L (MΩ)	32.2	108

7.3 Robinson's Stability Criteria

7.3.1 *Phase Stability at Low Intensity*

We are now in the position to discuss the conditions for phase stability, i.e., stable synchrotron oscillation. Suppose that center of the bunch has the same energy as the synchronous particle, but is at a small phase advance $\phi_{\rm rf} = \epsilon > 0$, as depicted by Point 1 in the synchrotron oscillation and the phasor $\tilde{i}_b$ in the phasor plot in Fig. 7.6. This implies that the phasor $\tilde{i}_b$ arrives earlier ahead of the x-axis by a small angle $\epsilon > 0$. Thus the accelerating voltage it sees at the cavity gap will be $V_{\rm rf} \sin(\phi_s - \epsilon)$ instead of $V_{\rm rf} \sin \phi_s$, or an extra decelerating voltage of $\epsilon V_{\rm rf} \cos \phi_s$ if $0 < \phi_s < \frac{1}{2}\pi$. Receiving less energy from the rf voltage than the synchronous particle will slow the bunch. If the beam is below transition, this implies the reduction of its revolution frequency, so that after the next h

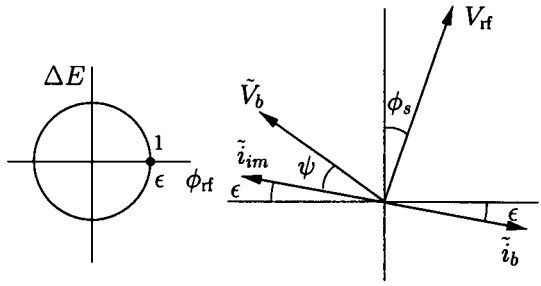


Fig. 7.6 With bunch center at Point 1 in the synchrotron oscillation, beam current phasor $\tilde{i}_b$ arrives earlier ahead of the x-axis by a small angle $\epsilon > 0$ in the phasor plot. The bunch sees a smaller rf voltage $V_{\rm rf}\sin(\phi_s - \epsilon)$ if the synchronous phase $0 < \phi_s < \frac{1}{2}\pi$ and receives an extra deceleration. Below transition, it arrives not so early in the next turn and phase stability is therefore established.

rf periods its arrival ahead of the synchronous particle will be smaller or ϵ will become smaller. As a result, the motion is therefore stable. Thus, to establish stable phase oscillation when beam-loading is small and can be neglected, one requires

$$\begin{cases} 0 < \phi_s < \frac{\pi}{2} & \text{below transition,} \\ \frac{\pi}{2} < \phi_s < \pi & \text{above transition.} \end{cases} \tag{7.50}$$

This is exactly the same condition for stable phase oscillation we conclude from the expression for the synchrotron tune in Eq. (2.15). Notice that this is just the condition of phase stability and there is no damping at all. Here, the derivation relies on the fact that the rf voltage phasor $\tilde{V}_{\rm rf}$ is unperturbed and this is approximately correct when the beam intensity and therefore the beam-loading voltage is small.

7.3.2 *Phase Stability at High Intensity*

When the beam current is very intense, we can no longer neglect the contribution of the beam-loading voltage. The condition of phase stability in Eq. (7.50) requires modification. Now, go back to Fig. 7.6 when the beam current phasor arrives at an angle $\epsilon > 0$ ahead of the x-axis but is at the same energy as the synchronous particle, the image current phasor $\tilde{i}_{im}$ will also advance by the same angle ϵ. Therefore, there will be an extra beam-loading voltage phasor $\epsilon i_{im} R_L \cos\psi\, e^{i(\pi/2-\psi)}$, which constitutes the perturbation of the rf voltage phasor $\tilde{V}_{\rm rf}$. If $\psi < 0$, this phasor will point into the second quadrant and decelerate the particle in concert with $\epsilon V_{\rm rf}\cos\phi_s$ in slowing the beam, thus causing no instability below transition. On the other hand, if $\psi > 0$, this phasor will point into the first quadrant and accelerate the particle instead. To be stable, the extra accelerating voltage on the beam from the beam-loading must be less than

the amount of decelerating voltage $\epsilon V_{\rm rf}\cos\phi_s$, or

$$\left[V_{\rm rf}\sin(\phi_s-\epsilon)-V_{\rm rf}\sin\phi_s\right]+\epsilon\, i_{im}R_L\cos\psi\sin\psi\approx$$
$$-\epsilon V_{\rm rf}\cos\phi_s+\epsilon V_{br}\cos\psi\sin\psi<0. \tag{7.51}$$

As a result, we require for phase stability,

$$\frac{V_{br}}{V_{\rm rf}}<\frac{\cos\phi_s}{\sin\psi\cos\psi}\qquad\begin{cases}\psi>0 \text{ below transition},\\ \psi<0 \text{ above transition},\end{cases} \tag{7.52}$$

which is called Robinson's *high-intensity criterion* of stability. In above, $V_{br}=i_{im}R_L$ is the *in-phase* beam-loading voltage when the beam is in phase with the loaded cavity impedance.

Notice that this Robinson's high-intensity criterion of stability is only a criterion of phase stability similar to the phase stability condition of Eq. (7.50). Satisfying this criterion just enables stable-oscillation-like motion inside a stable potential well. Violating this criterion will place the particle in an unstable potential well so that phase oscillation will not be possible. To include damping or antidamping due to the interaction of the beam with the cavity impedance, another criterion of Robinson stability, Eq. (7.62) below, must also be satisfied.

We can also look at the phase stability problem in another way. In order that the beam can execute stable phase oscillation, it must see a linear restoring force when the beam deviates from its equilibrium position. This force comes from change in the rf voltage $\tilde{V}_{\rm rf}$ seen by the beam when the beam is at a phase offset. This explains why we have the gradient of the rf accelerating voltage or $V_{\rm rf}\cos\phi_s$ in Eq. (2.15), the expression of the synchrotron tune. Now the rf voltage phasor $\tilde{V}_{\rm rf}$ is the sum of the beam-loading voltage phasor $\tilde{V}_b$ and the generator voltage phasor $\tilde{V}_g$, or

$$\tilde{V}_{\rm rf}=\tilde{V}_b+\tilde{V}_g. \tag{7.53}$$

Notice that the beam-loading voltage phasor $\tilde{V}_b$ moves with the beam and therefore will not provide any force gradient or restoring force to the beam. In other words, $d\tilde{V}_b/d\epsilon=0$. Thus only the generator voltage phasor $\tilde{V}_g$ can provide such a restoring force. Therefore, we should compute $d\tilde{V}_g/d\epsilon$. If this gradient enhances the displacement of the beam from the synchronous position, the system is unstable; otherwise, it is stable. When the generator voltage phasor is in phase with the beam as illustrated in Fig. 7.7, it is clear that for any small variation of time arrival ϵ of the beam, the beam will not see any variation of the generator voltage phasor $\tilde{V}_g$ in the direction of the beam, or $d\tilde{V}_g/d\epsilon=0$ in the direction of the beam. In other words, there is no restoring force to alter the energy of

the beam so as to push it back to its equilibrium position. For this reason, the configuration in Fig. 7.7 constitutes the Robinson's limit of phase stability. From the figure, it is evident that the projection of $\tilde{V}_{\rm rf}$ and $\tilde{V}_b$ perpendicular to the beam must be the same or the stability limit is

$$V_{\rm rf}\cos\phi_s = i_{im}R_L\cos\psi\sin\psi, \tag{7.54}$$

which is exactly the same as Eq. (7.52).

Now let us impose the condition that the generator current $\tilde{i}_g$ is in phase with the rf voltage $\tilde{V}_{\rm rf}$. First, we have $i_0 = V_{\rm rf}/R_L$, so that Robinson's criterion of phase stability in Eq. (7.52) can be rewritten as

$$\frac{i_{im}}{i_0} < \frac{\cos\phi_s}{\sin\psi\cos\psi} \qquad \begin{cases} \psi > 0 \text{ below transition}, \\ \psi < 0 \text{ above transition}. \end{cases} \tag{7.55}$$

Second, the in-phase condition implies Eq. (7.30), which simplifies the above to

$$\frac{i_{im}}{i_0} < \frac{1}{\sin\phi_s}, \tag{7.56}$$

after eliminating the detuning. If we further optimize the generator power by choosing the coupling constant $\beta_{\rm op}$ given by Eq. (7.39), it is easy to show that

$$\frac{i_{im}\sin\phi_s}{i_0} = \frac{\beta_{\rm op}-1}{\beta_{\rm op}+1} < 1. \tag{7.57}$$

In other words, the Robinson's phase stability criterion will always be satisfied when the generator current phasor $\tilde{i}_g$ and the rf voltage phasor $\tilde{V}_{\rm rf}$ are in phase and the coupling between the generator and the rf cavities is optimized.

When the generator current phasor and the rf voltage phasor are in phase, Fig. 7.7 immediately gives the phase stability limiting criterion for the detuning

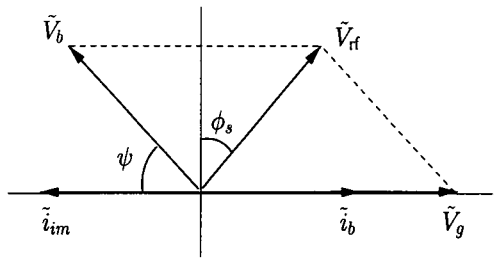


Fig. 7.7 When the generator voltage phasor $\tilde{V}_g$ becomes in phase with the beam current phasor $\tilde{i}_b$, it provides no force gradient to the beam in the direction of the beam. Since the restoring force vanishes for an infinitesimal offset of the beam arrival time, the beam is on the edge of instability in phase oscillation.

as

$$\psi = \frac{\pi}{2} - \phi_s. \tag{7.58}$$

Substituting into the in-phase condition of Eq. (7.30) reproduces the stability criterion of Eq. (7.56). The stability criterion can also be rewritten as

$$\tfrac{1}{2} V_{\rm rf} i_{im} \sin\phi_s < \tfrac{1}{2} V_{\rm rf} i_0, \tag{7.59}$$

where the right side is P_L, the power dissipated in the cavities and the generator, while the left side is P_b, the power supplied to the beam for acceleration and/or compensation of energy lost to radiation and impedance. Thus, Robinson's phase stability criterion can also be reworded as

$$P_b < P_L, \tag{7.60}$$

or the power allocated to dissipation is larger than the power delivered to the beam.

The Robinson's limit of phase stability is correct only if there is no other stabilizing mechanism available. In an accelerator ring, there is usually a loop that monitors the beam-loading and feedbacks onto the generator current so as to maintain the required rf gap voltage and synchronous phase. This correction, however, is not instantaneous, because it takes time for the new generator voltage to establish inside the rf cavity. This time delay, however, can be made shorter than the cavity fill time $T_f = 2Q_L/\omega_r$ of the cavity by having a high gain for the feedback. In any case, if the time delay is short compared with the synchrotron period, phase stability can be established, even if the criterion $P_b < P_L$ is violated. The former Fermilab Main Ring at its peak intensity of $N_p = 3.25 \times 10^{13}$ protons/pulse (about 3.25×10^{10} per bunch for 1000 bunches) serves as an example. The ring had a mean radius of 1 km and therefore a revolution frequency $f_0 = 47.7$ kHz at total energy $E = 150$ GeV. The dc beam current was $I_0 = eN_p f_0 = 0.245$ A or the image current was $i_{im} = 2I_0 = 0.490$ A assuming that the bunches are short. With 15 working cavities each supplying 213 kV, the total rf voltage was $V_{\rm rf} = 3.20$ MV. The acceleration rate was 125 GeV/s or 2.62 MeV/turn. Thus, $\sin\phi_s = 0.819$ and $i_{im}\sin\phi_0 = 0.407$ A. Each cavity had a loaded shunt impedance of 0.60 MΩ, or the total loaded shunt impedance was $R_L = 9.00$ MΩ. The current required to set up the rf voltage turned out to be $i_0 = V_{\rm rf}/R_L = 0.355$ A, which is less than $i_{im}\sin\phi_0$. Thus, Robinson's phase stability criterion had been violated [Eq. (7.56)]. There was a servo-tuner that guaranteed the generator current phasor to be in-phase with with rf voltage phasor. There were also rf voltage magnitude and phase loops to maintain the the proper rf voltage and synchronous phase. The rf cavities were

of $\omega_r/(2\pi) = 53.1$ MHz with a loaded quality factor $Q_L \approx 5000$. The cavity fill time was then $T_f = 30.0$ μs or about 1.43 revolution turns, small compared with the synchrotron period of ~ 2.1 ms (~ 100 turns). The modification of the detuning is usually the slowest part of the feedback procedure, but it is definitely faster than the synchrotron frequency. As a result, phase stability was maintained even when Robinson's stability criterion was not fulfilled.

7.3.3 *Robinson's Damping*

Next, we consider the interaction of the beam with the impedance of the rf system. As we will see, proper detuning damps synchrotron oscillations while improper detuning leads to an oscillation with increasing amplitude. During half of a synchrotron period, the center of the bunch is at an energy higher than the synchronous particle. Let us choose the particular moment when the phase of bunch center is just in phase with the synchronous particle, so that the phasor $\tilde{i}_b$ is exactly along the x-axis. This is illustrated in Fig. 7.8 by Point 2 in the synchrotron oscillation and by the beam current phasor being in phase with the x-axis in the accompanying phasor plot. Below transition, however, higher energy implies higher revolution frequency ω_0. The detuning ψ, which is defined by

$$\tan\psi = 2Q_L \frac{\omega_r - \omega_{\rm rf}}{\omega_r}, \tag{7.61}$$

appears effectively smaller from the view of the bunch center, when we consider the effective rf frequency as $\omega_{\rm rf} = h\omega_0$. The energy loss per turn, $i_{im}|Z_{\rm cav}|\cos\psi$, will be larger than if the bunch center were synchronous. For the other half of the synchrotron period, the beam particle has an energy smaller than the synchronous particle and revolves with a lower frequency, and therefore sees a larger effective detuning. Again we choose the moment when the phase of the bunch center is just in phase with synchronous particle, or Point 3 in the syn-

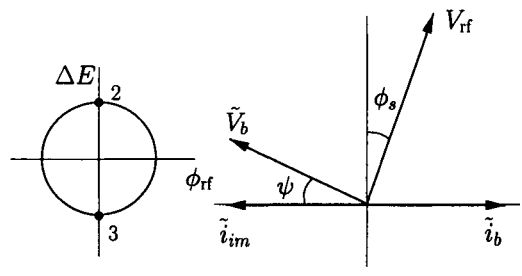


Fig. 7.8 With bunch center at Point 2 in the longitudinal phase space, current phasor $\tilde{i}_b$ is in phase with the x-axis in the phasor plot. Below transition, higher energy implies higher effective rf frequency $\omega_{\rm rf}$. The bunch sees a smaller effective detuning angle and loses more energy per turn than at the synchronous position. The synchrotron oscillation amplitude is therefore damped.

chrotron oscillation. The bunch will lose less energy than if it were synchronous. The result is a gradual decrease in the energy offset oscillation after oscillation. This reduction of synchrotron oscillation amplitude is called *Robinson damping.* Notice that if the detuning is in the other direction below transition, $\psi < 0$, the beam particle will lose less energy when its energy is higher than synchronous and lose more energy when its energy is less. The oscillation amplitude will increase turn after turn and the beam will become Robinson unstable. The opposite is true if the beam is above transition. We therefore have the criterion of Robinson stability:

$$\begin{cases} \psi > 0 \quad \text{or} \quad \omega_r > \omega_{\text{rf}} & \text{below transition,} \\ \psi < 0 \quad \text{or} \quad \omega_r < \omega_{\text{rf}} & \text{above transition.} \end{cases} \tag{7.62}$$

So far we have not imposed any optimization condition on the rf system. If the cavity detuning is adjusted in such a way that the generator current $\tilde{i}_g$ is in phase with the rf voltage $\tilde{V}_{\text{rf}}$ so that the beam-cavity impedance appears to be real as demonstrated in Fig. 7.4, the beam will always be Robinson stable, because the detuning will always satisfy Eq. (7.62) according to Eq. (7.30).

7.4 Transient Beam-Loading

By transient we mean that the fill time of the cavity T_f is not necessarily much longer than the time interval T_b for successive bunches to pass through the cavity. In other words, the beam-loading voltage from the first bunch will have significant decay before the successive bunch arrives.

First, let us understand how the transient beam-loading occurs. As the bunch of charge $q > 0$ passes through the cavity gap, a negative charge equal to that carried by the bunch will be left by the image current at the upstream end of the cavity gap. Since the negative image current will resume at the downstream end of the cavity gap following the bunch, an equal amount of positive charge will accumulate there. Thus, a voltage will be created at the gap opposing the beam current and this is the transient beam-loading voltage as illustrated in Fig. 7.9. For an infinitesimally short bunch, this transient voltage is

$$V_{b0} = \frac{q}{C} = \frac{q\omega_r R_s}{Q_0}, \tag{7.63}$$

where C is the equivalent capacitance across the gap of the cavity. Notice that we will arrive at the same value if the loaded shunt impedance R_L and the loaded quality factor Q_L are used instead. Due to the finite quality factor Q_0, this induced voltage across the gap starts to decay immediately, hence the name

transient beam-loading. We will give concrete example about the size of the voltage later. The next question is how much of this beam-loading voltage will be seen by the bunch. This question is answered by the fundamental theorem of beam-loading first derived by P. Wilson. [1]

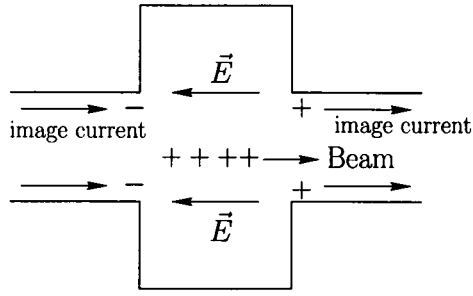


Fig. 7.9 As a positively charged bunch passes through a cavity, the image current leaves a negative charge at the upstream end of the cavity gap. As the image current resumes at the downstream side of the cavity, a positive charge is created at the downstream end of the gap because of charge conservation, thus setting up an electric field $\vec{E}$ and therefore the induced beam-loading voltage.

7.4.1 *Fundamental Theorem of Beam-Loading*

We would like to investigate whether a particle will see its own wake. Consider a particle of charge q passes through a cavity that is lossless (infinite R_s and infinite Q_0 but R_s/Q_0 held finite). It induces a voltage V_{b0} which will start to oscillate with the resonant frequency of the cavity. Suppose that the particle sees a fraction f of V_{b0}, which opposes its motion. After half an oscillation of induced field inside the cavity, a second particle of charge q passes through the cavity. The first induced voltage left by the first is now in the direction of the motion of the second particle and accelerates the particle. At the same time, this second particle will induce another retarding voltage $\bar{V}_{b0}$ which it will see as a fraction f. This second retarding voltage will cancel exactly the first one inside the cavity, since the cavity is assumed to be lossless. In other words, no field will be left inside the cavity after the passage of the two particles. The net energy gained by the second particle is

$$\Delta\mathcal{E}_2 = qV_{b0} - fqV_{b0}, \tag{7.64}$$

while the first particle gains

$$\Delta\mathcal{E}_1 = -fqV_{b0}. \tag{7.65}$$

Conservation of energy requires that the total energy gained by the two particles must be zero. This implies $f = \frac{1}{2}$. In other words, the particle sees one-half of

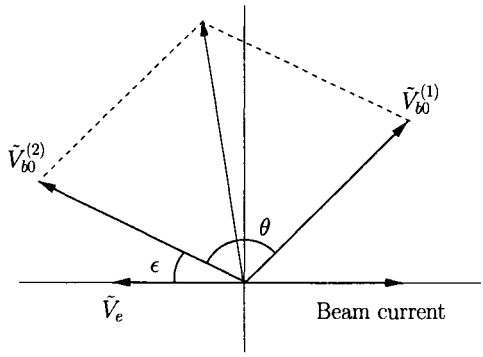


Fig. 7.10 Phasor plot showing the instant just after the second passage of the charged particle through the lossless cavity. The induced beam-loading voltage phasors for the two passages are labeled as $V_{b0}^{(1)}$ and $V_{b0}^{(2)}$, respectively.

its transient beam-loading voltage, which is the fundamental theorem of beam-loading.

The following is a more general proof by Wilson. The first particle induces a voltage phasor $\tilde{V}_{b0}^{(1)}$ in the lossless cavity which may lie at an angle ϵ with respect to the voltage $\tilde{V}_e$ seen by that particle. As before, we suppose the particle sees a fraction f of its own wake and thus loses an amount of energy. We have $V_e = fV_{b0}$, where V_e and V_{b0} are the magnitudes of, respectively, $\tilde{V}_e$ and $\tilde{V}_{b0}^{(1)}$. Some time later when the cavity phase changes by θ, the same particle returns via bending magnets or whatever and passes through the cavity again. It now induces a second beam-loading voltage phasor $\tilde{V}_{b0}^{(2)}$. It also experiences the voltage phasor $\tilde{V}_{b0}^{(1)}$ left by its previous passage. But this phasor $\tilde{V}_{b0}^{(1)}$ has now rotated to a new position as illustrated in Fig. 7.10. The particle loses the same energy to beam-loading as in its first passage together with an additional loss to the induced voltage left inside the cavity before. The net energy lost by the particle on the two passes is

$$\Delta\mathcal{E} = 2fqV_{b0}\cos\epsilon + qV_{b0}\cos(\epsilon+\theta). \tag{7.66}$$

The cavity, however, gains energy because of the beam-loading fields left behind. The energy inside a cavity is proportional to the square of the gap voltage. If the cavity is free of any field to start with, the final energy stored there becomes

$$\Delta\mathcal{E}_c = \alpha\left(2V_{b0}\cos\frac{\theta}{2}\right)^2 = 2\alpha V_{b0}^2(1+\cos\theta), \tag{7.67}$$

where α is a proportionality constant. From the conservation of energy, we get

$$2fqV_{b0}\cos\epsilon + qV_{b0}(\cos\epsilon\cos\theta - \sin\epsilon\sin\theta) - 2\alpha V_{b0}^2(1+\cos\theta) = 0. \tag{7.68}$$

Since θ is an arbitrary angle, we obtain

$$\begin{aligned} qV_{b0}\sin\epsilon &= 0, \\ qV_{b0}\cos\epsilon &= 2\alpha V_{b0}^2, \\ 2fqV_{b0}\cos\epsilon &= 2\alpha V_{b0}^2. \end{aligned} \tag{7.69}$$

The first equation gives $\epsilon = 0$ implying that the transient beam-loading voltage must have a phase such as to maximally oppose the motion of the inducing charge. Clearly $\epsilon = \pi$ will not be allowed because this leads to the unphysical situation of the particle gaining energy from nowhere. Solving the other two equations, we obtain $f = \frac{1}{2}$.

7.4.2 *From Transient to Steady State*

Let the bunch spacing be h_b rf buckets or T_b in time. The cavity time constant or filling time is $T_f = 2Q_L/\omega_r$ and the e-folding voltage decay decrement between two successive bunch passages is $\delta_L = T_b/T_f$. During this time period, the phase of the rf fields changes by $\omega_r T_b$ and the rf phase by $\omega_{\rm rf} T_b = 2\pi h_b$. The phasors therefore rotate by the angle $\Psi = \omega_r T_b - 2\pi h_b$, which can also be written in terms of the detuning angle ψ as

$$\Psi = (\omega_r - \omega_{\rm rf})T_b = \delta_L \tan\psi, \tag{7.70}$$

where Eq. (7.24) has been used. The transient beam-loading voltage left by the first passage of a short bunch carrying charge q is $V_{b0} = q/C = q\omega_r R_L/Q_L$. The total beam-loading voltage V_b seen by a short bunch is obtained by adding up vectorially the beam-loading voltage phasors for all previous bunch passages. The result is

$$V_b = \tfrac{1}{2}V_{b0} + V_{b0}\left(e^{-\delta_L}e^{-i\Psi} + e^{-2\delta_L}e^{-i2\Psi} + \cdots\right), \tag{7.71}$$

where the $\frac{1}{2}$ in the first term on the right side is the result of Wilson's fundamental theorem of beam-loading, which states that a particle sees only one-half of its own induced voltage. It is worth pointing out that these voltages are excitations of the cavity and are therefore oscillating at the cavity resonant frequency (all higher-order modes of the cavity are neglected). This infinite series of induced voltage phasors is illustrated in Fig. (7.11). The summation can be performed exactly giving the result

$$V_b = V_{b0}\Big[F_1(\delta_L,\psi) - iF_2(\delta_L,\psi)\Big], \tag{7.72}$$

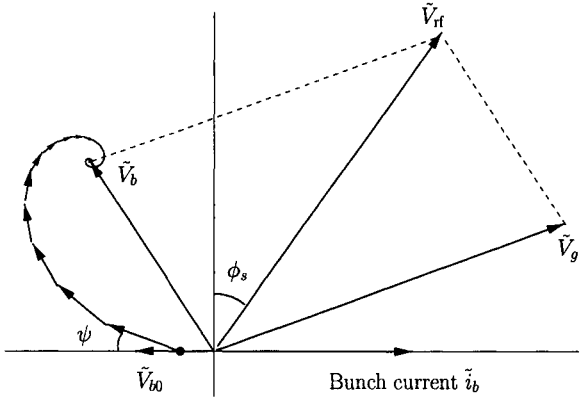


Fig. 7.11 Transient beam-loading voltages from equally spaced bunches. Each preceding voltage phasor has a decay $e^{-\delta_L}$ and a phase advance ψ because of detuning. Note that the bunch that is just passing by sees only half of its induced voltage $\tilde{V}_{b0}$. These voltage phasors add up to the total beam-loading voltage phasor $\tilde{V}_b$. Together with the generator voltage $\tilde{V}_g$, the cavity gap voltage results at the synchronous angle ϕ_s.

with

$$F_1 = \frac{1 - e^{-2\delta_L}}{2D}, \qquad F_2 = \frac{e^{-\delta_L} \sin(\delta_L \tan\psi)}{D}, \tag{7.73}$$

$$D = 1 - 2e^{-\delta_L} \cos(\delta_L \tan\psi) + e^{-2\delta_L}. \tag{7.74}$$

In terms of the coupling constant β and detuning angle ψ, we have

$$\tan\psi = 2Q_L \frac{\omega_r - \omega_{\rm rf}}{\omega_r}, \quad Q_L = \frac{Q_0}{1+\beta}, \quad \delta_L = \delta_0(1+\beta), \tag{7.75}$$

where we have defined $\delta_0 = T_b/T_{f0}$ with $T_{f0} = 2Q_0/\omega_{\rm rf}$ being the filling time of the unloaded cavity. Then the single bunch induced beam-loading voltage becomes

$$V_{b0} = 2I_0 R_s \delta_0, \tag{7.76}$$

where use has been made of the approximation for short bunches, so that the Fourier component of the current of a bunch at frequency $\omega_{\rm rf}/h_b$ is equal to twice its dc value or $i_b = 2I_0$ with $I_0 = q/T_b$. Putting things together, we get

$$V_b = 2I_0 R_s \delta_0 \Big[F_1(\delta_0, \beta, \psi) - iF_2(\delta_0, \beta, \psi) \Big], \tag{7.77}$$

with

$$F_1(\delta_0, \beta, \psi) = \frac{1 - e^{-\delta_0(1+\beta)}}{2D}, \quad F_2(\delta_0, \beta, \psi) = \frac{e^{-\delta_0(1+\beta)} \sin[\delta_0(1+\beta)\tan\psi]}{D},$$

$$D = 1 - 2e^{-\delta_0(1+\beta)} \cos[\delta_0(1+\beta)\tan\psi] + e^{-2\delta_0(1+\beta)}. \tag{7.78}$$

Some comments are in order. Figure 7.11 shows the transient nature of beam-loading if the beam-loading voltage phasors, that rotate by the angle Ψ and have their magnitudes diminished by the factor $e^{-\delta_L}$ for each successive time period, are excitations of *one* short bunch. However, what we consider is in fact the diminishing beam-loading voltage phasors coming from successive bunches that pass through the cavity at successive time periods nT_b earlier with $n = 1, 2, \cdots$. For this reason, what Fig. 7.11 shows is actually the steady-state situation of the beam-loading voltages, because for each time interval T_b later, we will see exactly the same spiraling beam-loading phasor plot and the same total beam-loading voltage phasor $\tilde{V}_b$. Therefore, we can add into the plot the generator voltage phasor $\tilde{V}_g$ in the same way as the plot in Fig. 7.4. In fact, the plot in Fig. 7.4 provides only an approximate steady-state plot, because the beam-loading voltage phasor there does attenuate a little bit after a 2π rotation of the phasors, although a high Q_L has been assumed. However, such attenuation has already been taken care of in Fig. 7.11, resulting in the plotting of an exact steady state. When the bunch arrives, the beam-loading voltage phasor is $\tilde{V}_b$ as indicated in Fig. 7.11. It rotates clockwise and its magnitude decreases because of the finite quality factor of the cavity. Just before the arrival of the next bunch, the beam-loading voltage phasor becomes $\tilde{V}_b - \frac{1}{2}\tilde{V}_{b0}$. Notice that the beam-loading voltage phasor rotates for more than 2π, since $\omega_r > \omega_{\rm rf}$ or the detuning angle ψ is positive in Fig. 7.11. As soon as the next bunch arrives, it jumps by $\frac{1}{2}\tilde{V}_{b0}$ and goes back to $\tilde{V}_b$. Therefore, the beam-loading voltage phasor is not sinusoidal and does not rotate at the speed of $\omega_{\rm rf}$ or $\omega_{\rm rf}/h_b$. It approaches sinusoidal only when the jump of the transient beam-loading voltage $\frac{1}{2}\tilde{V}_{b0}$ is small and that happens when the loaded quality factor Q_L is large, or when the cavity filling time $T_f = 2Q_L/\omega_r$ is much larger than the time interval T_b between successive bunch passages. On the other hand, the beam-loading voltage phasor $\tilde{V}_b$ seen by the bunch in Fig. 7.4 is sinusoidal because it is induced by a sinusoidal component of the beam. In fact, over there, we allow for only one Fourier component.

Using Eq. (7.14), the generator power P_g can now be computed:

$$P_g = \frac{(1+\beta)^2 V_{\rm rf}^2}{8\beta R_s \cos^2\psi}\left\{\left[\sin\phi_s - \frac{i_b R_s \delta_0}{V_{\rm rf}} F_1(\delta_0, \beta, \psi)\right]^2 + \left[\cos\phi_s + \frac{i_b R_s \delta_0}{V_{\rm rf}} F_2(\delta_0, \beta, \psi)\right]^2\right\}. \tag{7.79}$$

In the situation when the generator current $\tilde{i}_g$ is in phase with the rf voltage $\tilde{V}_{\rm rf}$, the generator power can be minimized so that there will not be any reflection. Similarly, the generator power can also be optimized by choosing a suitable coupling coefficient β. Unfortunately, these optimized powers cannot be written

as simple analytic expressions.

7.4.2.1 *Limiting Case with* $\delta_0 \to 0$

When the bunch spacing T_b is short compared to the unloaded cavity filling time T_{f0}, simplified expressions can be written for the total beam-loading voltage V_b. One gets

$$F_1(\delta_0, \beta, \psi) = \frac{1}{\delta_0(1+\beta)(1+\tan^2\psi)}, \quad F_2(\delta_0, \beta, \psi) = \frac{\tan\psi}{\delta_0(1+\beta)(1+\tan^2\psi)}, \tag{7.80}$$

so that

$$V_b = \frac{i_b R_s}{1+\beta} \frac{1}{1+i\tan\psi}. \tag{7.81}$$

Notice that this is exactly the same expression in Eq. (7.26). In fact, this is to be expected, because we are again in the situation of $T_b \ll T_f$, the case of a high Q_L resonating cavity.

In the absence of detuning, the beam-loading voltages left by previous bunches just added up to give

$$V_b = \frac{V_{b0}}{2} \frac{1+e^{-\delta_L}}{1-e^{-\delta_L}}. \tag{7.82}$$

For a high-Q_L cavity, this becomes

$$V_b = \frac{V_{b0}}{\delta_L} = i_b R_L, \tag{7.83}$$

which is the maximum beam-loading voltage seen by the beam.

When $\delta_0 \to 0$, the phase angle $\Psi = \delta_0(1+\beta)\tan\psi \to 0$, although the detuning ψ may be finite. Thus, the transient beam-loading voltage $\tilde{V}_{b0}$ will not decay and would apparently line up for successive former bunch passages, leading to an infinite total beam-loading voltage V_b seen by the bunch. However, $\delta_0 \to 0$ implies letting $Q_0 \to \infty$ while keeping the shunt impedance fixed. The instantaneous beam-loading voltage $V_{b0} = q/C = q\omega_r R_s/Q_0 = 2I_0 R_s \delta_0$ also goes to zero, implying that the summation has to be done with care. For successive V_{b0}'s to wrap around in a circle, one needs approximately $2\pi/\Psi$ V_{b0}'s. The radius of this circle will be V_{b0}/Ψ. As $\delta_0 \to 0$, this radius becomes

$$\lim_{\delta_0 \to 0} \frac{V_{b0}}{\Psi} = \frac{2I_0 R_s}{\tan\psi}, \tag{7.84}$$

which is finite. In fact, this is roughly the same as the total beam-loading voltage V_b as $\delta_0 \to 0$.

During bunch-to-bunch injection, the transient beam-loading voltage in the cavity will add up gradually as is indicated in the spiral in Fig. 7.11. Thus, if the decay decrement is small, the total beam-loading voltage will reach a maximum value up to twice the voltage given by Eq. (7.77) before spiraling to its limiting value. The maximum beam-loading voltage will be twice the value given by Eq. (7.81) as if the shunt impedance has been doubled.

7.4.2.2 *Limiting Case with $T_b \gg T_f$*

This is the situation when the instantaneous beam-loading voltage decays to zero before a second bunch comes by. It is easy to see that $F_1(\delta_0, \beta, \psi) \to \frac{1}{2}$ and $F_2(\delta_0, \beta, \psi) \to 0$. From Eq. (7.79), it is clear that the generator power increases rapidly as the square of δ_0. This is easy to understand, because the rf power that is supplied to the cavity gets dissipated rapidly. A pulse rf system will then be desirable. In such a system, the power is applied to the cavity for about a filling time preceding the arrival of the bunch. For most of the time interval between bunches, there is no stored energy in the cavity at all and hence no power dissipation.

7.4.3 *Transient Beam-Loading of a Bunch*

When a bunch of linear density $\lambda(\tau)$ passes through a cavity gap, electromagnetic fields are excited. The beam-loading retarding voltage seen by a beam particle at the cavity gap is just the wake potential left by all other particles in the bunch that pass the cavity earlier. At the arrival time τ ahead of the bunch center, the beam-loading voltage is therefore given by

$$V(\tau) = \int_{\tau}^{\infty} q\lambda(\tau')W_0'(\tau' - \tau)d\tau', \tag{7.85}$$

where q is the total charge in the bunch, $\lambda(\tau)$ is normalized to unity when integrated over τ, and $W_0'(\tau)$ is the wake potential left by a point charge passing through the cavity gap at a time τ ago. If we approximate the cavity as a RLC parallel circuit with angular resonant frequency ω_r, loaded quality factor Q_L, and loaded shunt impedance R_L, the wake function can be expressed analytically as, for $\tau > 0$,

$$W_0'(\tau) = \frac{\omega_r R_L}{Q_L} e^{-\alpha\tau} \left[\cos\bar{\omega}\tau - \frac{\alpha}{\bar{\omega}} \sin\bar{\omega}\tau\right], \tag{7.86}$$

and $W_0'(\tau) = 0$ for $\tau < 0$ because of causality. For $\tau = 0$, we have $W_0'(\tau) = \omega_r R_L/(2Q_L)$, a result of the fundamental theorem of beam-loading. In above,

the e-folding decay rate α and the shifted resonant angular frequency $\bar{\omega}$ are given by

$$\alpha = \frac{\omega_r}{2Q_L} \qquad \text{and} \qquad \bar{\omega} = \sqrt{\omega_r^2 - \alpha^2}. \tag{7.87}$$

Notice that this is exactly the same wake potential we studied in Eq. (1.85) of Exercise 1.3. For the convenience of derivation, we introduce the loss angle θ which is defined as[¶]

$$\cos\theta = \frac{\bar{\omega}}{\omega_r} \qquad \text{and} \qquad \sin\theta = \frac{\alpha}{\omega_r}. \tag{7.88}$$

With this introduction, the wake potential can be conveniently rewritten as

$$W_0'(\tau) = \frac{\omega_r R_L}{Q_L \cos\theta}\, \mathcal{R}e\, e^{i(e^{i\theta}\omega_r\tau + \theta)}. \tag{7.89}$$

The first application is for a point bunch with distribution $\lambda(\tau) = \delta(\tau)$. Substitution into Eq. (7.85) gives $V(\tau) = qW_0'(-\tau)$, or

$$V(\tau) = \begin{cases} 0 & \tau > 0, \\ \dfrac{q\omega_r R_L}{2Q_L} & \tau = 0, \\ \dfrac{q\omega_r R_L}{Q_L \cos\theta}\, \mathcal{R}e\, e^{i(e^{i\theta}\omega_r\tau + \theta)} & \tau < 0. \end{cases} \tag{7.90}$$

Thus, the head of the bunch ($\tau = 0+$) sees no beam-loading voltage. The tail of the bunch ($\tau = 0-$) sees the transient beam-loading voltage $V_{b0} = q/C$ as given by Eq. (7.63). The center of the bunch sees one half of V_{b0}.

7.4.3.1 *Gaussian Distribution*

Consider a Gaussian distributed bunch of rms length σ_τ. The linear density is

$$\lambda(\tau) = \frac{1}{\sqrt{2\pi}\sigma_\tau} e^{-\tau^2/(2\sigma_\tau^2)}. \tag{7.91}$$

The beam-loading voltage experienced by a beam particle at distance τ ahead the bunch center is (Exercise 7.7)

$$V(\tau) = \frac{q\omega_r R_L}{2Q_L \cos\theta}\, \mathcal{R}e\; e^{i\theta - \tau^2/(2\sigma_\tau^2)}\, w\!\left(\frac{\sigma_\tau \omega_r e^{i\theta}}{\sqrt{2}} + \frac{i\tau}{\sqrt{2}\sigma_\tau}\right), \tag{7.92}$$

[¶]If one prefers, this angle can also be defined as $\cos\theta = \alpha/\omega_r$ and $\sin\theta = \bar{\omega}/\omega_r$.

where q is the total charge in the bunch and w is the complex error function defined as

$$w(z) = e^{-z^2}\left[1 + \frac{2i}{\sqrt{\pi}}\int_0^z e^{t^2}dt\right]. \tag{7.93}$$

It can be readily shown that as the bunch length shortens to zero, the head, center, and tail of the bunch are seeing the transient beam-loading voltage (Exercise 7.7)

$$V(\tau) = \begin{cases} 0 & \tau = 0+ \quad \text{(head)}, \\ \dfrac{q\omega_r R_L}{2Q_L} & \tau = 0 \quad \text{(center)}, \\ \dfrac{q\omega_r R_L}{Q_L} & \tau = 0- \quad \text{(tail)}, \end{cases} \tag{7.94}$$

exactly the same result for a point bunch. In fact, Eq. (7.94) just serves as another proof of the fundamental theorem of beam-loading that the test charge sees one half of its own beam-loading voltage. This proof is more general than those presented in the previous subsection, because it involves a lossy cavity or a cavity with a finite quality factor Q_L.

The beam-loading voltages of a Gaussian bunch are plotted in Fig. 7.12. They are all normalized to $q\omega_r R_L/Q_L$, which is the beam-loading voltage when the bunch is contracted to a point. Each curve is identified by two parameters: (Q_L, F), where $F = \sqrt{6}\omega_r\sigma_\tau/\pi$ is roughly the fraction of the rf wavelength occupied by the bunch, since we usually equate the half 95% Gaussian bunch length to $\sqrt{6}\sigma_\tau$. The horizontal coordinate is the distance that the test particle

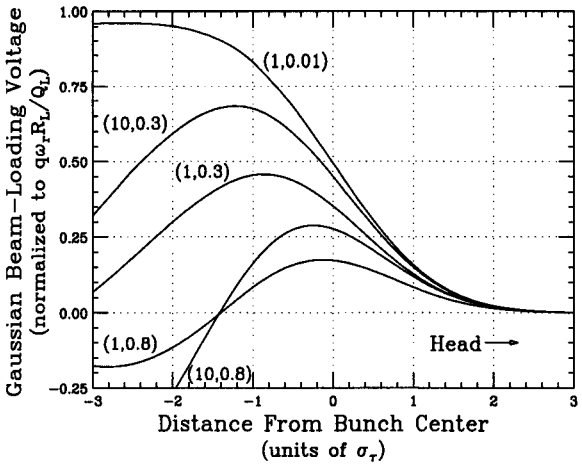


Fig. 7.12 The transient beam-loading voltage, normalized to $q\omega_r R_L/Q_L$, of a bunch with Gaussian distribution seen by a particle at distance τ/σ_τ ahead the bunch center, σ_τ being the bunch rms length and q the total charge in the bunch. Each curve is labeled by two parameters (Q_L, F), $F = \sqrt{6}\omega_r\sigma_\tau/\pi$ being the fraction of the rf wavelength occupied by the bunch, and Q_L, R_L, and $\omega_r/(2\pi)$, respectively, the loaded quality factor, loaded shunt impedance, and resonant frequency of the cavity.

is ahead of the bunch center in units of σ_τ, the rms bunch length. We notice that as the bunch becomes shorter, the beam-loading voltage becomes larger. When it becomes very short, the curve with (1,0.01), we recover the results in Eq. (7.94) that a particle at the center of the bunch sees one half of the bunch beam-loading voltage. As the bunch length increases, we find the transient beam-loading voltage decreases rapidly. This is because the charges spread out along the beam lowering the linear charge density and therefore lowering the beam-loading voltage. When the quality factor of the cavity becomes larger, the beam-loading voltage does not decay as fast and its reduced amplitude is therefore closer to unity. This feature is evident when the transient beam-loading voltages corresponding to (10,0.3) and (1,0.3) are compared. The same conclusion results when the transient beam-loading voltages corresponding to (10,0.8) and (1,0.8) are compared. We also notice that the beam-loading voltage seen by each particle in the bunch varies along the bunch. This result is important, because it tells us that it will be difficult to compensate for the beam-loading voltage to every point along the bunch.

7.4.3.2 *Parabolic Distribution*

Consider a bunch with parabolic distribution,

$$\lambda(\tau) = \frac{3}{4\hat{\tau}}\left(1 - \frac{\tau^2}{\hat{\tau}^2}\right) \qquad |\tau| \le \hat{\tau}, \tag{7.95}$$

where $\hat{\tau}$ is the half bunch length. As the bunch of total charge q passes through a cavity, the transient beam-loading voltage seen by a particle at a distance T behind the head of the bunch is (Exercise 7.8), for $T \le 2\hat{\tau}$,

$$V(T) = \frac{q\omega_r R_L}{Q_L}\frac{3p^2}{2\pi^2\cos\theta}\left\{\frac{p}{\pi}\left[\omega_r(\hat{\tau}-T)\cos\theta + \sin 2\theta\right]\right.$$
$$\left. + e^{-\alpha T}\left[\sin(\bar{\omega}T - 2\theta) - \frac{p}{\pi}\cos(\bar{\omega}T - \theta)\right]\right\}, \tag{7.96}$$

and for $T > 2\hat{\tau}$,

$$V(T) = \frac{q\omega_r R_L}{Q_L}\frac{3p^2}{2\pi^2\cos\theta}\left\{e^{-\alpha(T-2\hat{\tau})}\left[\frac{p}{\pi}\sin\left(\bar{\omega}(T-2\hat{\tau}) - 2\theta\right)\right.\right.$$
$$\left.\left. - \cos\left(\bar{\omega}(T-2\hat{\tau}) - \theta\right)\right] + e^{-\alpha T}\left[\sin(\bar{\omega}T - 2\theta) - \frac{p}{\pi}\cos(\bar{\omega}T - \theta)\right]\right\}, \tag{7.97}$$

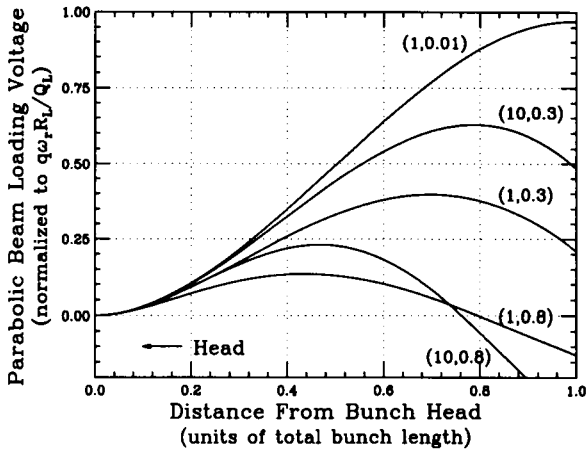


Fig. 7.13 The transient beam-loading voltage, normalized to $q\omega_r R_L/Q_L$, of a bunch with parabolic distribution seen by a particle at distance $T/(2\hat{\tau})$ behind of the head of the bunch, where $2\hat{\tau}$ is the total bunch length and q the total charge in the bunch. Each curve is labeled by (Q_L, F), where $F = \omega_r\hat{\tau}/\pi$ is the fraction of the rf wavelength occupied by the bunch, and Q_L, R_L, and $\omega_r/(2\pi)$ are, respectively, the loaded quality factor, loaded shunt impedance, and resonant frequency of the cavity.

where

$$p = \frac{\pi}{\omega_r\hat{\tau}}. \tag{7.98}$$

Beside the normalization factor $q\omega_r R_L/Q_L$, the beam-loading voltage depends on two parameters: $\omega_r\hat{\tau}$ and the loaded quality factor Q_L.

Figure 7.13 shows the beam-loading voltage seen by a bunch with parabolic distribution. The normalization is also to $q\omega_r R_L/Q_L$. The horizontal coordinate is the fractional distance $T/(2\hat{\tau})$ of the test particle behind the head of the bunch. Each voltage curve is labeled by the two parameters (Q_L, F), where $F = \omega_r\hat{\tau}/\pi = 1/p$ is the ratio of the total bunch length to the rf wavelength. All the comments of the beam-loading voltage of the Gaussian bunch apply here also.

7.4.3.3 *Cosine-Square Distribution*

Consider a bunch with cosine-square linear distribution,

$$\lambda(\tau) = \frac{1}{\hat{\tau}}\cos^2\frac{\pi\tau}{2\hat{\tau}} \qquad |\tau| \le \hat{\tau}, \tag{7.99}$$

where $\hat{\tau}$ is the half bunch length. Since Gaussian distribution carries an infinite tail at each end of the bunch, for proton bunches, sometimes the cosine-squire distribution may constitute a more realistic representation. As the bunch of total charge q passes through a cavity, the transient beam-loading voltage seen by a particle at a distance T behind the head of the bunch is (Exercise 7.8), for

$T \leq 2\hat{\tau}$,

$$V(T) = \frac{q\omega_r R_L}{Q_L} \frac{p^2}{2\pi D \cos\theta} \Bigg\{ (1-p^2) \sin \frac{\pi(\hat{\tau}-T)}{\hat{\tau}} \cos\theta + p \cos \frac{\pi(\hat{\tau}-T)}{\hat{\tau}} \sin 2\theta + p^3 e^{-\alpha T} \sin \bar{\omega} T - p e^{-\alpha T} \sin(\bar{\omega} T - 2\theta) \Bigg\}, \quad (7.100)$$

and for $T > 2\hat{\tau}$,

$$V(T) = \frac{q\omega_r R_L}{Q_L} \frac{p^2}{2\pi D \cos\theta} \Bigg\{ p e^{-\alpha(T-2\hat{\tau})} \sin \left[\bar{\omega}(T-2\hat{\tau}) - 2\theta\right] - p^3 e^{-\alpha(T-2\hat{\tau})} \sin \bar{\omega}(T-2\hat{\tau}) + p^3 e^{-\alpha T} \sin \bar{\omega} T - p e^{-\alpha T} \sin(\bar{\omega} T - 2\theta) \Bigg\}, \quad (7.101)$$

where p is given by Eq. (7.98) and

$$D = 1 - 2p^2 \cos 2\theta + p^4. \quad (7.102)$$

Besides the factor outside the curly brackets, the beam-loading voltage depends on two parameters: $\omega_r \hat{\tau}$ and the loaded quality factor Q_L.

Figure 7.14 shows the beam-loading voltage seen by a bunch with cosine-square distribution. The normalization is also to $q\omega_r R_L/Q_L$. The test particle is at the fractional distance $T/(2\hat{\tau})$ behind the head of the bunch. We label each reduced beam-loading voltage curve by (Q_L, F), where $F = \omega_r \hat{\tau}/\pi = 1/p$ is the ratio of the total bunch length to the rf wavelength. All the comments concerning the beam-loading voltage of the Gaussian bunch apply here as well.

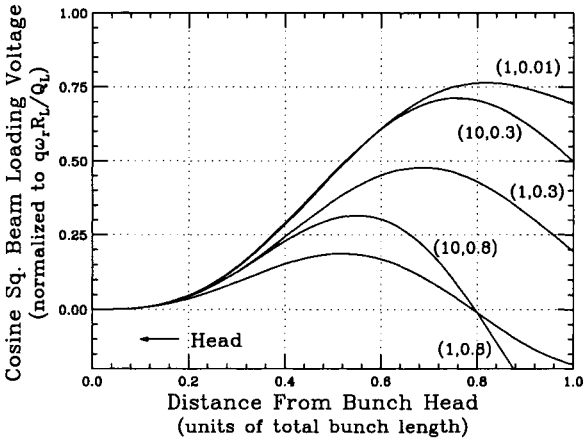


Fig. 7.14 The transient beam-loading voltage, normalized to $q\omega_r R_L/Q_L$, of a bunch with cosine-square distribution seen by a particle at distance $T/(2\hat{\tau})$ behind the head of the bunch, where $2\hat{\tau}$ is the total bunch length. Each curve is labeled by (Q_L, F), where $F = \omega_r \hat{\tau}/\pi$ is the fraction of the rf wavelength occupied by the bunch, and Q_L, R_L, and $\omega_r/(2\pi)$ are, respectively, the loaded quality factor, loaded shunt impedance, and resonant frequency of the cavity.

7.4.3.4 *Cosine Distribution*

Consider a bunch with cosine linear distribution,

$$\lambda(\tau) = \frac{\pi}{4\hat{\tau}} \cos\frac{\pi\tau}{2\hat{\tau}} \qquad |\tau| \le \hat{\tau}, \tag{7.103}$$

where $\hat{\tau}$ is the half bunch length. A proton bunch may better be represented by the cosine distribution rather than the parabolic distribution because the latter possesses abrupt discontinuation of the profile gradients at the two ends. As the bunch of total charge q passes through a cavity, the transient beam-loading voltage seen by a particle at a distance T behind the head of the bunch is (Exercise 7.8), for $T \le 2\hat{\tau}$,

$$V(T) = \frac{q\omega_r R_L}{Q_L \cos\theta} \frac{p^2}{8D} \left\{ \left(1 - \frac{p^2}{4}\right) \cos\frac{\pi T}{2\hat{\tau}} \cos\theta + \frac{p}{2} \sin\frac{\pi T}{2\hat{\tau}} \sin 2\theta \right.$$
$$\left. + e^{-\alpha T} \left[\frac{p^2}{4} \cos(\bar{\omega}T + \theta) - \cos(\bar{\omega}T + \theta) \right] \right\}, \tag{7.104}$$

and for $T > 2\hat{\tau}$,

$$V(T) = \frac{q\omega_r R_L}{Q_L \cos\theta} \frac{p^2}{8D} \left\{ e^{-\alpha(T-2\hat{\tau})} \left[\frac{p^2}{4} \cos\left(\bar{\omega}(T-2\hat{\tau}) + \theta\right) - \cos\left(\bar{\omega}(T-2\hat{\tau}) - \theta\right) \right] \right.$$
$$\left. + e^{-\alpha T} \left[\frac{p^2}{4} \cos(\bar{\omega}T + \theta) - \cos(\bar{\omega}T + \theta) \right] \right\}. \tag{7.105}$$

where p and D are given by Eqs. (7.98) and (7.102). Besides the factor outside the curly brackets, the beam-loading voltage depends on two parameters: $\omega_r\hat{\tau}$ and the loaded quality factor Q_L.

Figure 7.15 shows the beam-loading voltage seen by a bunch with cosine distribution when the test particle is at the fractional distance $T\omega_r/(2\pi)$ behind the head of the bunch, or the time is normalized to an rf wavelength. The beam-loading voltage is normalized to $q\omega_r R_L/Q_L$. We label each reduced beam-loading voltage curve by (Q_L, F), where $F = \omega_r\hat{\tau}/\pi = 1/p$ is the ratio of the total bunch length to the rf wavelength. All the comments concerning the beam-loading voltage of the Gaussian bunch apply here as well. Both curves are for the high quality factor $Q_L = 5000$. For the example of $F = 0.3$, the normalized transient beam-loading voltage has a maximum of 0.681 within the bunch length and later rings for a long time at the frequency $\omega_r/(2\pi)$ of the cavity with an amplitude 0.918 decaying very slowly. This amplitude is roughly equal to $I_1/(2I_0)$, where I_1 is the rf component of the bunch current and I_0 is the average bunch current.

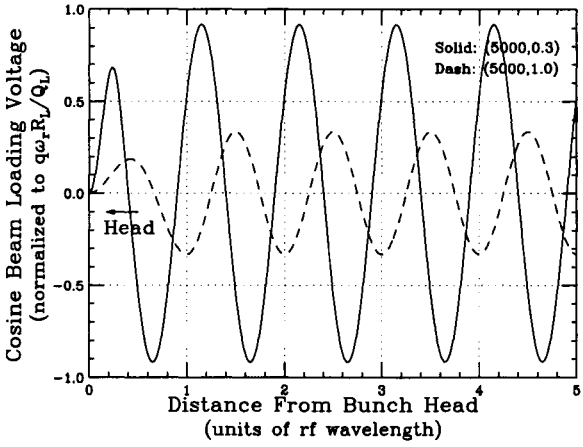


Fig. 7.15 The transient beam-loading voltage, normalized to $q\omega_r R_L/Q_L$, of a bunch with cosine distribution seen by a particle at distance T (normalized to the rf wavelength) behind the head of the bunch. Each curve is labeled by (Q_L, F), where $F = \omega_r \hat{\tau}/\pi$ is the fraction of the rf wavelength occupied by the bunch, and Q_L, R_L, and $\omega_r/(2\pi)$ are, respectively, the loaded quality factor, loaded shunt impedance, and resonant frequency of the cavity.

Because the e-folding decaying time is Q_L/π rf buckets, the bunch is seeing these ringing amplitudes left by its predecessors. For a ring with all buckets occupied, the long-term or steady-state beam-loading voltage seen by a bunch in the absence of rf detuning can be expressed as

$$V_b = \frac{q\omega_r R_L}{Q_L}\left[A + B\left(1 + e^{-\delta_L} + e^{-2\delta_L} + \cdots\right)\right], \tag{7.106}$$

where $\delta_L = \pi/Q_L$ is the decay decrement in the time interval of one rf wavelength. Here, A denotes the portion of the beam-loading voltage excited instantaneously by the bunch crossing the cavity gap while B denotes whatever left by the previous crossings. Compared with Eq. (7.71) for a point bunch ($F = 0$) where $A = \frac{1}{2}$ and $B = 1$, we have for a bunch of finite extent, for example $F = 0.3$ in the cosine distribution, $A = 0.681$ and $B = I_1/(2I_0) = 0.918$. For a high Q_L, it is the second term that dominates. We can conclude that compared with a point bunch, a distributed bunch of finite length will have its beam-loading voltage lowered only by a small amount, i.e., by the fraction $I_1/(2I_0)$.

The situation of $F = 1$ is very special and is represented by the dashed curve. Here, the bunch is as long as the rf wavelength. In fact, the situation corresponds to a bunch filling the rf bucket uniformly. Although the first maximum is $A \sim 0.2$, the actual ringing amplitude is roughly $B \approx 0.33$. It is easy to show that $I_1/(2I_0) = 1/3$. In other words, even when the bunch fills up the bucket, the beam-loading voltage is decreased by a factor of three only.

We plot in Fig. 7.16 $I_1/(2I_0)$ as functions of F, the total bunch length in units of rf wavelength, for various bunch distribution. We see that when the bunch is short, $I_1/(2I_0)$ is just slightly smaller than unity and depends on dis-

tribution rather weakly. The depression from unity becomes very much larger for a longer bunch and its dependence on distribution becomes more significant. When the total bunch length equal the bucket length or $F = 1$, $I_1/(2I_0) = 1/2$, $\exp(-\pi^2/16)$, $1/3$, and $3/\pi^2$, respectively, for the cosine-square, Gaussian, cosine, and parabolic distribution.

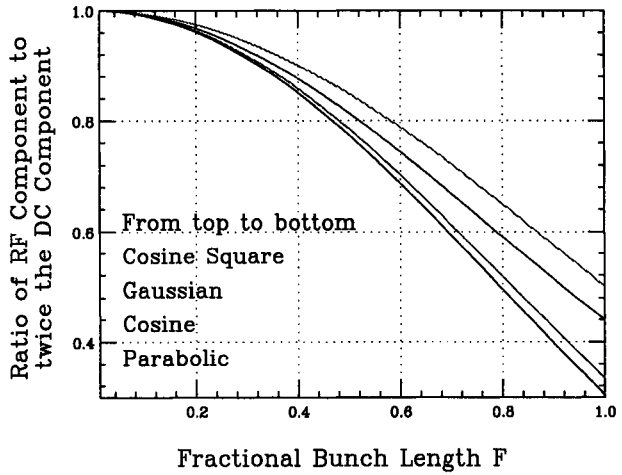


Fig. 7.16 Ratio of the rf component of the bunch to two times the dc component, $I_1/(2I_0)$, as functions of F, total bunch length in units of bucket length, for, from top to bottom, cosine-square, Gaussian, cosine, and parabolic distributions.

7.4.4 *Transient Compensation*

We are going to give a short overview of some methods to cope with transient beam-loading. The serious readers are referred to the references for further reading.

For a ring in the storage mode with all rf buckets filled with bunches of equal charges, each bunch is seeing exactly the same beam-loading voltage, except for the influence of its small amount of synchrotron motion. We say that the beam-loading is in the steady state and compensation can be made by detuning the cavity if the beam intensity is not too high.

However, the beam-loading in many circumstances is in the transient state when there is a sudden change in beam intensity. One example is injection when bunches are injected one by one. The beam-loading voltage inside the rf cavity will increase linear with time, and the beam-loading voltage seen by a bunch depends on time as well as its location along the ring. Obviously, slow extraction of an intense beam will also lead to sudden changes in the beam-loading voltage. Another example is a gap left in an accelerator ring to allow for

the firing of the injection and extraction kickers. Such a gap is also beneficial to clearing particles of opposite charge trapped inside the beam in order to eliminate collective two-stream instabilities. In the presence of such a gap, the total beam-loading voltage experienced at a cavity will be different during different bunch passages. For example, the bunch just after the gap will see the smallest beam-loading voltage and the bunch just preceding the gap will see the most. As a result, the last bunch in the bunch train or batch will always see a lower effective rf voltage than the first bunch. At best, there will be a synchronous phase difference between the bunches leading to increase in longitudinal bunch area. At worst, the final bunches of the batch will not have enough voltage for stability. Strictly speaking, the word *transient* has been used wrongly for the problem of a gap, because such an effect occurs even when the stored beam is in the steady state. The uneven beam-loading voltage experienced by the different bunches in the batch is a result of having many frequency components in the beam-loading voltage besides the ones at the rf frequency and its multipoles. Because of this, the term *transient beam-loading* should be defined as effects at frequencies other than the fundamental rf, its multiples, and their synchrotron sidebands.

One way to reduce beam-loading, either steady-state or transient, is to reduce the loaded shunt impedance R_L of the cavity seen by the beam. [13] An obvious method is to add a resistance in parallel. Although this reduces the voltage created by both the beam and the power amplifier, however, the power requirements of the amplifier are increased. If the power amplifiers are already operating at their capacity, this is not an applicable solution.

Another possibility for reducing the beam-loading voltage generated by the beam is to have another power amplifier to supply an additional generator current i_g equal and opposite to the beam image current. These two currents cancel each other at the cavity gap, making the cavity look like a short-circuit to the beam. This method is very fast because there is no need to fight against the filling time of the cavity since there is no net current flowing across the cavity gap at all and therefore no additional fields created inside the cavity. This is a powerful but expensive solution due to the extra amplifier required. It is called *high-level feed-forward* compensation and is applicable for fixed rf frequency only. It was added to the CERN Intersecting Storage Ring (ISR) rf system not so much to improve stability but due to a power limitation in the rf power amplifier. It can be shown [3] that the extra power required can become halved if the cavity is half-pretuned before the injection so that the peak powers before and after injection are the same. In other words, the power is unmodulated even when the beam is fully modulated. The required power can be lowered by a factor of

two again if there is optimum matching between the rf generator and the cavity. This can be accomplished by having a circulator inserted between the rf power and the cavity so that the additional current for the beam-loading compensation means also real power.

To avoid high power consumption, there are also methods for *low-level compensation.* One technique is referred to as *feed-forward.* [14] The bunch current at a location preceding the cavity in the accelerator ring is measured and the signal is added to the low-level rf drive of the power amplifier so that an additional generator current I_g equal and opposite beam current is generated at the time the bunch crosses the cavity gap, as illustrated in Fig. 7.17. Experience and analysis show a dramatic increase in the instability threshold. This scheme has been successfully applied in the CERN Proton Synchrotron (PS) and the CERN Proton Synchrotron Booster (PSB). The instability threshold can probably be raised an order of magnitude. This is because the cavity voltage is completely decoupled from the beam signal, which nullifies the Robinson's instability. However, it is difficult to apply when the rf frequency is varying. The feedback path through the beam response is fairly weak, so the risk of creating an unstable system response is low. However, with a weak feedback, any errors in the system will not be compensated, so it is very important that the delay and phase advance of the systems are properly tuned for beam cancellation. In practice, maintaining an error-free system is very difficult when large amounts of impedance reduction is required.

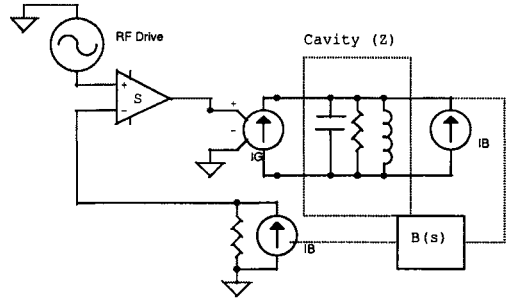


Fig. 7.17 Block diagram of direct rf feed-forward, where $B(s)$ is the beam response and S is the transconductance of the amplifier. (Courtesy J. Steimel. [13])

A second technique of reducing the cavity impedance is amplifier feedback. The voltage in the cavity is measured, amplified and added to the low-level rf drive, as is illustrated in Fig. 7.18. To compute the impedance seen by the beam, the input at the generator is turned off. The cavity voltage is amplified to GV_{rf} where G is the gain. It is then transformed into a current $-SGV_{\mathrm{rf}}$ through the transconductance S. This current is next fed through the generator and produces the additional gap voltage $-SGV_{\mathrm{rf}}Z$, giving a total gap voltage of

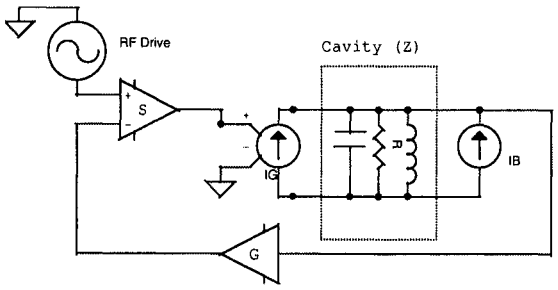


Fig. 7.18 Block diagram of direct rf feedback, where the amplifier gain is G and the transconductance is S. The effective impedance seen by the beam is reduced from R_L to $R_L/(1 + SGR_L)$. (Courtesy J. Steimel. [13])

$V_{\rm rf} = V_b - SGV_{\rm rf}Z$, where $V_b = R_L i_b$ is the beam-loading voltage produced by the beam current i_b in the absence of the feedback loop. The effective impedance experienced by the beam becomes

$$R_{\rm eff} = \frac{R_L}{1 + SGR_L}, \tag{7.107}$$

where $H = SGR_L$ is called the open-loop gain. Thus, by increasing the gain, the shunt impedance can be largely reduced. The main feedback path for this system no longer includes the beam response, and it is much stronger. The low-level feedback is very fast and the delay just depends on the length of the cables of the feedback loop. This is the most powerful method known and can be applied even for varying rf frequency. It has been applied to the CERN ISR at 9.5 MHz with $H = 60$, the CERN Antiproton Accumulator at 1.85 MHz with $H = 120$, and the CERN PSB at 6 to 16 MHz with $H = 5$ to 12.

In addition, there are a number of feedback loops in an rf accelerating system to assure that the particle beam will be accelerated according to the prescribed ramp design and to guarantee stability even when the Robinson's stability limit is exceeded. In the rf system of the former Fermilab Main Ring, for example, there are five feedback loops: [15]

(1) Rf frequency control loop, which compares the beam bunch phase versus rf phase comparator and output an error signal. It is dc coupled with very low bandwidth.

(2) Beam radial position control loop, which controls the radial position of the beam by making small adjustment to the synchronous phase angle. It is dc coupled with bandwidth about 10 kHz.

(3) Correction loop for cavity gap voltage phase versus generator voltage phase. It is ac coupled with 5 MHz bandwidth and is capable of fast adjustment of cavity excitation phase to compensate for transient beam-loading effects.

(4) Cavity voltage amplitude control loop, which adjusts the generator current such that the rf voltage amplitude developed at the cavity gap equals to its

prescribed value. It has a very high dc gain ($\sim$ 60 db) and corner frequency 5 Hz.
(5) Detuning loop, which monitors the load angle between the generator current and the cavity gap voltage and adjusts the cavity tuning through ferrite biasing so that the load impedance presented to the generator appears to be real. It has a high dc gain ($\sim$ 60 db) with low bandwidth and corner frequency 1 Hz.
Among these, the second and third loops are the fastest, while the detuning loop is the slowest. These loops are not only limited by their gains, because they are only independent when the beam intensity is low. As the beam intensity increases, they become coupled and gradually lose their function.

For large rf systems, long delays may be unavoidable and the conventional rf feedback would have too restricted a bandwidth, which may be much smaller than the cavity bandwidth itself. However, in the spectrum of transient beam-loading, it is only those revolution harmonic lines that require nullification, and there is nothing in between the harmonics. With a return path transfer function having a comb-filter shape with maxima at every revolution harmonic, this condition can be satisfied. The overall delay of the system must be extended to exactly one machine turn to ensure the correct phase at the harmonics. Nullifying the beam signals at the revolution harmonics other than the fundamental rf frequency cures the transient beam-loading.

7.4.4.1 *Coupled-Bunch Instabilities*

As will be discussed in Chapter 8, narrow resonances located at the synchrotron sidebands may excite longitudinal coupled-bunch instabilities. Although these narrow resonances originate mostly from the higher-order modes of the cavities, some may also come from the revolution harmonics of the beam-loading voltage excited because of having asymmetric fill in the stored beam. These harmonic lines have finite widths, due to the large-amplitude (and therefore large energy spread) phase oscillations of fractions of the beam, and can be large enough to cover the synchrotron sidebands and thus drive coupled-bunch instabilities. To avoid this unwelcome effect, the transient beam-loading at multipoles of the revolution harmonic must be corrected. One possibility is to employ a comb-filter shape feedback that has large gain only in the vicinity of the revolution harmonics where the beam current components and therefore transient beam-loading components exist.

Even for a ring of bunches with symmetric gaps, the detuning of the cavities may also drive coupled-bunch instabilities. This happens for a large machine where the revolution frequency f_0 is low. Detuning can very often shift the peak

of the intrinsic resonant frequency of the cavities by more than one or more revolution harmonics. Here, we use a design of the former Superconducting Super Collider (SSC) as an example. [9] The average beam current is $I_0 = 0.073$ A and a 374.7-MHz rf system is chosen. There are in the design, eight cavities, each having a shunt impedance $R_L = 2.01$ MΩ and $R_L/Q_L = 125$ Ω, or $Q_L = 1.608 \times 10^4$. At storage, the rf gap voltage per cavity is $V_{\rm rf} = 0.5$ MV. Thus, using the in-phase criterion of Eq. (7.30), the required detuning is given by

$$2Q_L \frac{\omega_r - \omega_{\rm rf}}{\omega_r} = \tan\psi = \frac{i_{im}\cos\phi_s}{i_0}, \tag{7.108}$$

where $i_0 = V_{\rm rf}/R_L$. At $\phi_s \approx \pi$ and using short-bunch approximation, we obtain

$$\frac{\omega_r - \omega_{\rm rf}}{\omega_r} = -\frac{i_{im}R_L}{2V_{\rm rf}Q_L} = -0.183 \times 10^{-4}, \tag{7.109}$$

or a detuning of $\Delta f_r = -6.84$ kHz. The half bandwidth of the loaded cavity is $\Delta f = f_r/(2Q_L) = 11.68$ kHz. However, the revolution frequency of the collider ring is only $f_0 = 3.614$ kHz. In other words, the resonant impedance of the cavities would occur at a frequency slightly greater than $f_{\rm rf} - 2f_0$ and have a spread covering about ten revolution harmonics. Such impedance could drive longitudinal coupled-bunch instabilities with considerable strength. If we compute the same with the Fermilab Main Ring at a total of 3.25×10^{13} protons in the ring, we find that $|\Delta f_r/f_{\rm rf}| = 1.33 \times 10^{-4}$ or $|\Delta f_r| = 7.1$ kHz during acceleration, while the half bandwidth of the cavities is ~ 4.4 kHz. These numbers are very much less than the revolution frequency $f_0 = 47.7$ kHz. On the other hand, the 200-MHz traveling-wave accelerating structures in the CERN Super Proton Synchrotron (SPS) have a considerable bandwidth so that the impedance at $f_{\rm rf} \pm nf_0$ for small n is appreciable. Coupled-bunch instabilities arising from this impedance have been reported. [10] This also happens in the Low Energy Ring (LER) of the SLAC B-factory. Matching the klystron to the rf cavities requires the cavity be detuned to a frequency near $f_{\rm rf} - 1.5f_0$, thus driving longitudinal coupled-bunch instabilities [11] in modes -1 and -2. Longitudinal coupled-bunch instabilities are usually alleviated by damping passively the driving resonances in the cavity or employing a mode damper. Here, the problem is quite different. First, we cannot damp this fundamental mode passively because we require it to supply energy to the beam. Second, the higher-order resonances that usually drive the coupled-bunch instabilities are much weaker than the fundamental. However, it is the fundamental that drives the coupled-bunch instabilities here. In other words, a very much powerful damper will be necessary to remove the instabilities. Because of this complication, a solution

to this problem proposed in the SSC Conceptual Design Report is to partially detune or even not to detune the cavities at the expense of violating the in-phase condition and thus increasing the required rf power.

7.5 Examples

7.5.1 *Fermilab Main Ring*

Once the former Fermilab Main Ring operated above transition in $M = 567$ consecutive bunches with total intensity 5×10^{13} protons. The ring consisted of $h = 1113$ rf buckets and the rf frequency was $\omega_r/(2\pi) = 53.09$ MHz. There were 15 rf cavities, each of which had a loaded shunt impedance of $R_L = 500$ kΩ and the loaded quality factor was $Q_L = 5000$.

At steady state, the kth bunch in a bunch train of M bunches sees a beam-loading voltage of (Exercise 7.9)

$$V_{bk} = V_0 e^{-(k-1)\delta_L} + V_{b0}\left(\tfrac{1}{2} + e^{-\delta_L} + \cdots + e^{-(k-1)\delta_L}\right), \tag{7.110}$$

where $\delta_L = \pi/Q_L$ is the decay decrement,

$$V_{b0} = \frac{qB\omega_r R_L}{Q_L} \tag{7.111}$$

is the transient beam-loading voltage left by a bunch carrying charge q, B is a parameter defined in Eq. (7.106) to take care of the fact that the bunch has a finite length, and is equal to the current component at the rf frequency divided by twice the dc current, and

$$V_0 = V_{b0}\frac{e^{-(h-M+1)\delta_L} - e^{-(h+1)\delta_L}}{(1 - e^{-\delta_L})(1 - e^{-h\delta_L})} \tag{7.112}$$

is the beam-loading voltage seen by the first bunch due to the excitation by earlier passages of the beam. Detuning has been omitted. The difference in beam-loading voltage experienced by the last and the first bunch is therefore (see Exercise 7.9)

$$\Delta V_b = V_{b0}\frac{e^{-\delta_L}[1 - e^{-(M-1)\delta_L}][1 - e^{-(h-M)\delta_L}]}{(1 - e^{-\delta_L})(1 - e^{-h\delta_L})}. \tag{7.113}$$

For the operation of the Fermilab Main Ring with $B = 0.872$, we obtain $V_{b0} = 0.411$ kV and $\Delta V_b = 113$ kV for one cavity. In the storage mode the gap voltage per cavity was $V_{\rm rf} = 66$ kV. Thus, if the generator current I_g is in phase with the gap voltage and the synchronous angle was exactly $\phi_s = \pi$ at the passage of

the first bunch through the cavity, the last bunch will see a synchronous angle $\phi_s = \tan^{-1}(\Delta V_b / V_{\rm rf}) \approx \frac{1}{3}\pi$. Such a large shift is intolerable. Even if this shift was reduced to one-half by choosing the synchronous angle of $\phi = \pi$ for the middle of the bunch train instead, the head and tail bunches would execute synchrotron oscillations with an amplitude of $\frac{1}{6}\pi$ and finally result in a large growth of the longitudinal emittances. There was a correction loop in the rf system that was capable of adding plus or minus quadrature currents up to $\sqrt{3}$ times the existing generator current to the input of the power amplifier. [15] With such an addition the synchronous angle goes back to π. The response time was $\sim$ 300 ns, about 16 bunch periods, and was limited by the length of the cable loop. During such time, a maximum synchrotron phase shift of only 2.8° could develop and was tolerable.

Equation (7.113) shows that ΔV_b is small when there are only a small number of consecutive bunches in the ring ($M \to 1$). This is expected because it just gives the sum of the beam-loading voltages of these few bunches. On the other hand, if the ring is almost filled ($M \to h$), ΔV_b is also small, because this is close to a symmetric filling of the ring. It is easy to show that the maximum ΔV_b occurs when the ring is half filled, or when the length of the gap is equal to the length of the bunch train.

7.5.2 *Fermilab Booster*

The injection into the Fermilab Booster from the Fermilab Linac is continuous for up to 12 (or even more) Booster turns. After that the beam is bunched by adiabatic capture, which takes place in about 150 μs while the rf voltage increases to 100 kV. During the injection, the beam is coasting and does not contain any component of the rf frequency. However, during adiabatic capture, both the rf voltage and the rf component of the current increase. The rf voltage during adiabatic capture in the Booster is maintained through counter-phasing. This is accomplished by dividing the 18 cavities into two groups. The required voltage amplitude and synchronous angle are obtained by varying the relative phase between the two groups. Thus the gap voltage in each cavity is not small and individually Robinson's stability is satisfied in each cavity. Counter-phasing is essential during adiabatic capture: First, maintaining too low a gap voltage inside a cavity will cause multi-pactoring. Second, the response of raising rf voltage during the capture through varying the generator current is slow because one has to fight the quality factor of the cavities, whereas controlling the rf voltage through varying the relative phase is fast. Since the beam-loading voltage always points in the same direction aside from a detuning angle, to achieve

counter-phasing, the generator current must be different in the two sets of cavities. The implication is that it will not be possible to have the generator current in phase with the gap voltage. Thus extra rf power will be required. [16]

In the present booster cycle, the maximum power delivered to the beam is $P_b = 265$ kW at $V_{\rm rf} = 864$ kV, while the maximum power lost to the ferrite is $P_L = 830$ kW. Since $P_b < P_L$ all the time, phase stability is guaranteed. To ensure that the beam accelerates according to the designed ramp curve, there is a slow low-level feedback loop which keeps the beam at the correct radial position in the aperture of the vacuum chamber by adjusting the synchronous phase angle. There is also a fast low-level feedback loop which damps phase oscillations. At extraction, since all bunches are extracted at the same location in one revolution turn, the bunches will not see any transient beam-loading voltage at all.

Most of the time, there are usually only $M = 80$ bunches in the ring of rf harmonic $h = 84$, and four bunch spaces are reserved for the extraction kicker. At the intensity of 6×10^{10} protons per bunch, the transient beam-loading voltage excited in each of the 18 cavities by one bunch at passage is $V_{b0} = q\omega_r R_L/Q_L = 37.9$ V where $R_L/Q_L \sim 13\ \Omega$ per cavity. According to Eq. (7.113), the difference in beam-loading voltages experienced between the last and first bunch is $\Delta V_b = 3.76 V_{b0} = 142$ V. The beam gap is created near the end of the ramp, where the rf voltage has the lowest value of 305 kV at extraction, or 16.9 kV per cavity. This amounts to an rf phase error of only 0.48°. Typically, a bunch at extraction has a half width of 2.8 ns or 54°. Thus the phase error is comparatively small and so is the increase in bunch area due to dilution. For this reason, no action is necessary to compensate for this gap-induced beam-loading.

7.5.3 *Fermilab Main Injector*

A batch of 84 bunches is extracted from the Fermilab Booster and injected into the Fermilab Main Injector. The rf frequency is $\omega_r/(2\pi) = 52.8$ MHz and the rf harmonic is $h = 588$. Each bunch contains 6×10^{10} particles. At injection, at the rf voltage of 1.2 MV and a bunch area of 0.15 eV-s, the half length is 2.83 ns. There are 18 rf cavities with a total $R_L/Q_L = 1.872\ \text{k}\Omega$ and $Q_L = 5000$. At the passage of the first bunch across the cavities, the transient beam-loading voltage excited in all the cavities is $V_b = qB\omega_r R_L/Q_L = 5.46$ kV, where we have taken $B = 0.915$ by assuming a parabolic distribution [see Eq. (7.106)]. At the passage of the last bunch of the batch, the total beam-loading voltage excited becomes $V_b = 444$ kV, where we have taken into account the decay decrement

but the detuning has been set to zero. If there is a second batch transferred from the Booster, this will take place after one Booster cycle or 66.7 ms. During this time interval, steady-state has already reached, since the fill time of the cavities is $2Q_L/\omega_r = 30$ μs (about 2.7 turns). Figure 7.19 shows the beam-loading voltages experienced by the 84 bunches in the batch in their first, second, and third passages through the cavities. The top trace represents the voltages seen when steady-state is reached. The difference in beam-loading voltages seen by last and first bunch can be read out from the figure. It can also be computed analytically from Eq. (7.113) to be $\Delta V_b = 388$ kV. Actually, this difference is not much different from that experienced even in the first revolution turn because of the large quality factor of the cavities. The designed rf voltage at injection is $V_{\rm rf} = 1.2$ MV. If the designed synchronous phase $\phi_s = 0$ is synchronized to the middle bunch of the batch, the phase error introduced becomes $\Delta\phi_s = \pm 9.18°$ for the first and last bunches. This large difference in beam-loading voltage, however, will not lead to energy difference along the bunches. The off-phase bunches will be driven into synchrotron motion instead. The first and last bunch will have amplitudes of oscillation $\Delta\phi_s = \pm 9.18°$. Eventually, the bunch area will increase. Measured in rf phase, the half width of the bunch at injection is 53.8°. Thus, the bunch length will increase linearly from the middle bunch towards the front and the rear of the batch, with a maximum fractional increase of 9.18/53.8=17%. Such an increase is tolerable at the moment. There is a fast feedback loop with a delay of only 16 bunch spacings (300 ns), implying that the maximum difference in beam-loading voltage before the feedback becomes effective will only be $\sim$ 88 kV and the phase error introduced will only be

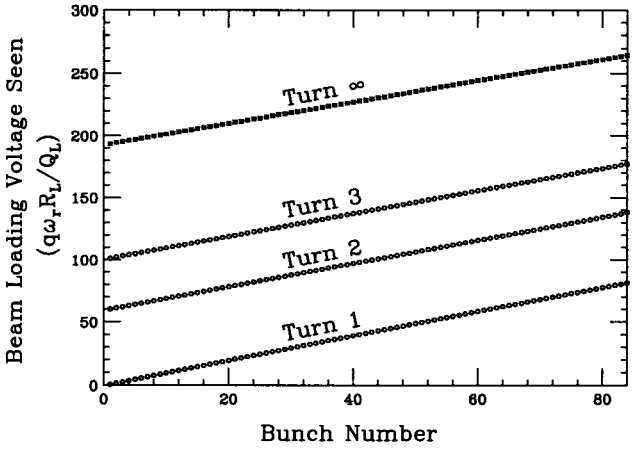


Fig. 7.19 Beam-loading voltages experienced by the 84 bunches in the batch at their first, second, and third passages of the Main Injector rf cavities. The top trace shows the beam-loading voltages after many revolution turns when steady state is reached. In the computation, cavity detuning has been set to zero.

$\sim \pm 2.1°$. Unfortunately, this feedback loop has not been working most of the time.

Notice that proper detuning does not help here if we want to keep the generator current in phase with the rf voltage for the middle bunch. For half of the batch (42 bunches), the accumulated phase shift due to detuning is of the order of 1° so that the transient beam-loading voltages of individual bunches still add up almost in a straight line (Exercise 7.11).

There is an upgrade plan that increases the bunch intensity by a factor of five. The transient beam-loading will then become intolerable, because the phase error can be as large as $\Delta\phi_s = \pm 58°$. One proposal of compensation is feedforward. Another proposal is to replace all the cavities with ones that have the same Q_L, but with R_L/Q_L reduced by a factor of five. The beam-loading effects will be the same as before. However, reducing the shunt impedance R_L five times implies the requirement of a larger generator current ($\sqrt{5} = 2.2$ times) in order to supply the same rf power.

There is a plan to slip-stack two Booster batches and capture them into 84 bunches of double intensity. [12] In order that two series of rf buckets can fit into the momentum aperture of the Main Injector, the rf voltage employed to sustain the bunches will have to decrease to less than 100 kV. Relatively, the transient beam-loading problem becomes very severe. To control beam-loading, the followings are planned:

1. Using only two or four of the 18 cavities to produce the required rf voltage and de-Qing the remaining cavities. One simple technique that may de-Q the cavities by a factor of three is to turn off the screen voltage to reduce the tube plate resistance.
2. Feed-forward the signal of the wall current monitored at a resistive-wall gap to the cavity drivers. Experience at the Main Ring expects to achieve a tenfold reduction in the effective wall current flowing into the cavities.
3. Feedback on all the cavities. A signal proportional to the gap voltage is amplified, inverted, and applied to the driver amplifier. Based on experience in the Main Ring and results achieved elsewhere, a 100-fold reduction can be achieved.

7.5.4 *Proposed Prebooster*

Let us look into the design of a proposed Fermilab prebooster which has a circumference of 158.07 m. It accelerates 4 bunches each containing 0.25×10^{14} protons from the kinetic energy 1 to 3 GeV. Because of the high intensity of the beam, the problems of space charge and beam-loading must be addressed.

We wish to examine the issues of beam-loading and Robinson instabilities based on a preliminary rf system proposed by Griffin. [17] To avoid passing through transition, the lattice adopted will be made up of flexible momentum-compaction modules. The transition gamma becomes imaginary and the beam will always be below transition. [18]

7.5.4.1 *The Ramp Curve*

Because of the high beam intensity, the longitudinal space-charge impedance per harmonic is $Z_{\|}/n|_{\text{spch}} \sim i100\ \Omega$. But the beam pipe discontinuity will contribute only about $Z_{\|}/n|_{\text{ind}} \sim -i20\ \Omega$ of inductive impedance. The space-charge force will be a large fraction of the rf-cavity gap voltage that intends to focus the bunch. A proposal is to insert ferrite rings into the vacuum chamber to counteract this space-charge force. [19] An experiment of ferrite insertion was performed at the Los Alamos Proton Storage Ring and the result has been promising. [20] Here we assume such an insertion will over-compensate all the space-charge force leaving behind about $Z_{\|}/n|_{\text{ind}} \approx -i25\ \Omega$ of inductive impedance. An over-compensation of the space charge will help bunching so that the required rf voltage needed will be smaller.

The acceleration from kinetic energy 1 to 3 GeV in four buckets at a repetition rate of 15 Hz is to be performed by resonant ramping. In order to reduce the maximum rf voltage required, about 3.75% of second harmonic is added. A typical ramp curve, with bucket area increasing quadratically with momentum,

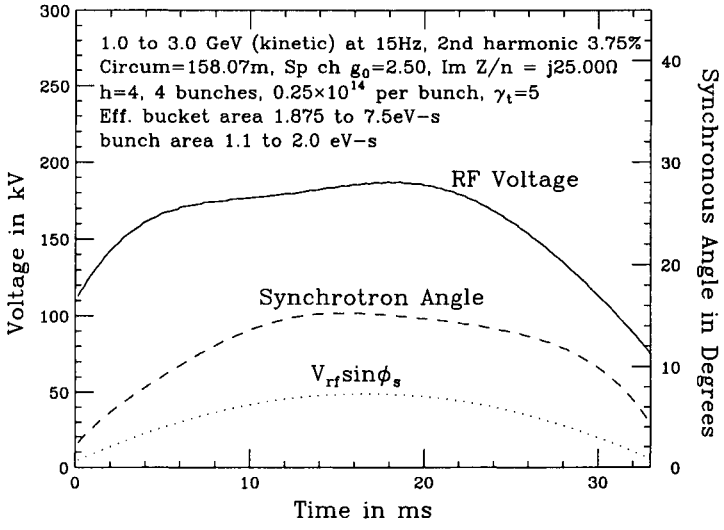


Fig. 7.20 A typical ramp curve for a design of the future Fermilab prebooster.

is shown in Fig. 7.20, which will be used as a reference for the analysis below. If the present choice of initial and final bucket areas and bunch areas is relaxed, the fraction of second harmonic can be increased. However, when the second harmonic is beyond $\sim 12.5\%$, it will only flatten the rf gap voltage in the ramp but will not decrease the maximum significantly.

7.5.4.2 *The RF System*

According to the ramp curve in Fig. 7.20, the peak voltage of the rf system is $V_{\rm rf} \approx 185$ kV. Griffin proposed ten cavities, [17] each delivering a maximum of 19.0 kV. Each cavity contains 26.8 cm of ferrite rings with inner and outer radii 20 and 35 cm, respectively. The ferrite has a relative magnetic permeability of $\mu_r = 21$. The inductance and capacitance of the cavity are $\mathcal{L} \sim 0.630$ μH and $C \sim 820$ pF. Assuming an average ferrite loss of 134 kW/m^3, the dissipation in the ferrite and wall of the cavity will be $P_c \sim 14.2$ kW. The mean energy stored is $W \sim 0.15$ J. Therefore each cavity has a quality factor $Q \sim 459$ and a shunt impedance $R_s \sim 12.7$ kΩ.

Because each bunch contains $q = 4.005$ μC, the transient beam-loading is large. For the passage of one bunch, 4.005 μC of positive charge will be left at downstream end of the cavity gap creating a transient beam-loading voltage of $V_{b0} \sim q/C = 5.0$ kV, where $C = 820$ pF is the gap capacitance. We note from Fig. 7.20 that the accelerating gap voltages at both ends of the ramp are only about or less than 10 kV in each cavity. If the wakes due to the bunches ahead do not die out, we need to add up the contribution due to all previous bunch passages. Assuming a loaded quality factor of $Q_L = 45$, we find from Eq. (7.77) that the accumulated beam-loading voltage can reach a magnitude of $V_b = 73$ kV when the detuning angle is zero (see Fig. 7.25).

A feed-forward system is suggested which will deliver via a tetrode the same amount of negative charge to the downstream end of the gap so as to cancel the positive charge created there as the beam passes by. Without the excess positive charge, there will not be any more transient beam-loading. This is illustrated in Fig. 7.21.

Here, we are in a situation where the image current i_{im} passing through the cavity gap is not equal to the beam current i_b. However, either at zero detuning or nonzero detuning, Eqs. (7.17) and (7.41) indicate that the portion of generator power transmitted to the acceleration of the beam is directly proportional to the magnitude of the image current. If the image current goes to zero in this feed-forward scheme, this implies that the rf generator is not delivering any power to the particle beam at all, although the beam is seeing an accelerating gap voltage. Then, how can the particle beam be accelerated? The answer is simple,

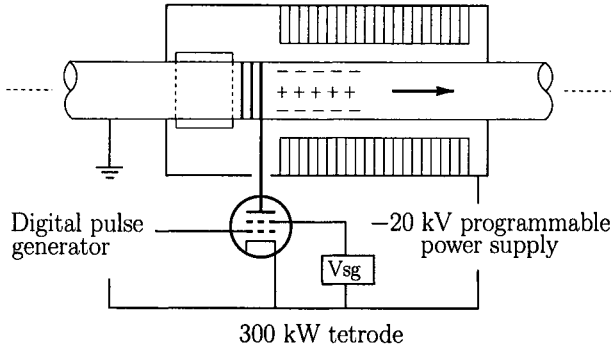


Fig. 7.21 Transient beam-loading power tetrode connected directly to an rf cavity gap to feed-forward the same amount of negative charge to the downstream end of the cavity gap so as to cancel the positive charge created there as the beam passes by. (Courtesy J. Griffin. [15])

the power comes from the tetrode that is doing the feed-forward. This explains why the tetrode has to be of high power.

Actually, the feed-forward system is not perfect and we assume that the cancellation is 85 %. For a δ-function beam, the component at the fundamental rf frequency is 56.0 A. Therefore, the remaining image current across the gap is $i_{im} = 8.4$ A. To counter this remaining 15% of beam-loading in the steady state, the cavity must be detuned according to Eq. (7.30) by the angle

$$\psi = \tan^{-1}\left(\frac{i_{im}\cos\phi_s}{i_0}\right), \tag{7.114}$$

where ϕ_s is the synchronous angle and $i_0 = V_{\rm rf}/R_s$ is the cavity current *in phase* with the cavity gap voltage $V_{\rm rf}$. For the high quality factor of $Q = 459$ which is accompanied by a large shunt impedance, the detuning angle will be large. Corresponding to the ramp curve of Fig. 7.20, the detuning angle is plotted as dashes in Fig. 7.22 along with the synchronous angle and maximum cavity gap voltage. We see that the detuning angle is between 80° and 86°, which is too large. If a large driving tube is installed with anode (or cathode follower) dissipation at $\sim$ 131 kW, the quality factor will be reduced to the loaded value of $Q_L \sim 45$ and the shunt impedance to the loaded value of $R_L \sim 1.38$ kΩ. The detuning angle then reduces to $\psi \sim 29°$ at the center of the ramp and to $\sim 40°$ or $\sim 56°$ at either end. This angle is also plotted in Fig. 7.22 as a dot-dashed curve for comparison. Then, this rf system becomes workable.

7.5.4.3 *Fixed-Frequency RF Cavities*

Now we want to raise the question whether it is possible to have a fixed resonant frequency for the cavity. A fixed-frequency cavity can be a very much simpler device because it may not need any biasing current at all. Thus the amount of

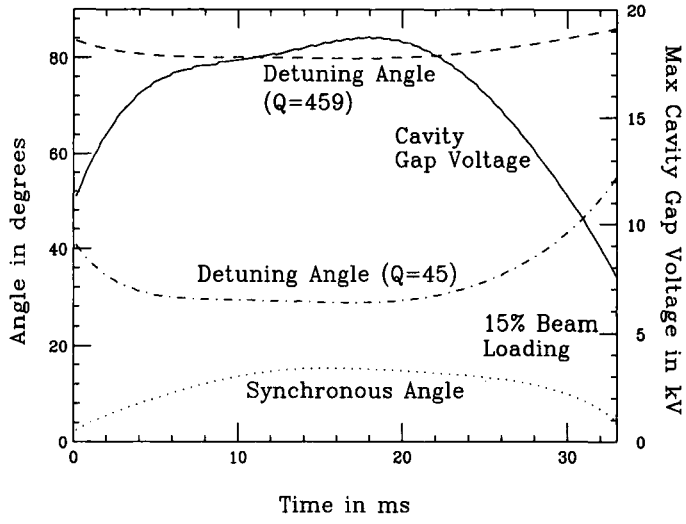


Fig. 7.22 Detuning angle for the high $Q = 459$ and low $Q_L = 45$ situations.

cooling can be very much reduced and even unnecessary. It appears that the resonant frequency of the cavity should be chosen as the rf frequency at the *end* of the ramp, or $f_r = 7.37$ MHz so that the whole ramp will be immune to Robinson's phase-oscillation instability. [8] However, the detuning will be large. For example, at the beginning of the ramp where $f_{\rm rf} = 6.64$ MHz, the detuning angle becomes $\psi = 85.2°$. Since the beam-loading voltage V_b is small, the generator voltage phasor $\tilde{V}_g$ will be very close to the gap voltage phasor $\tilde{V}_{\rm rf}$. As a result, the load angle θ_L between the gap voltage $\tilde{V}_{\rm rf}$ and the generator current phasor $\tilde{i}_g$ will be close to the detuning angle, as demonstrated in Fig. 7.23. Although the average total power delivered by the generator

$$\tfrac{1}{2}\tilde{i}_g \cdot \tilde{V}_{\rm rf} = \frac{V_{\rm rf}^2}{2R_L} + \tfrac{1}{2} i_{im} V_{\rm rf} \cos\phi_s \tag{7.115}$$

is independent of θ_L, the energy capacity of the driving tube has to be very large.

Another alternative is to choose the resonant frequency of the cavity to be the rf frequency near the *middle* of the ramp. Then the detuning angle ψ and therefore the angle θ_L between $\tilde{V}_{\rm rf}$ and $\tilde{i}_g$ will be much smaller at the middle of the ramp when the gap voltage is large. Although θ_L will remain large at both ends of the ramp, however, this is not so important because the gap voltages are relatively smaller there. The top plot of Fig. 7.24 shows the scenario of setting the cavity resonating frequency f_r equal to $f_{\rm rf}$ at the ramp time of 13.33 ms.

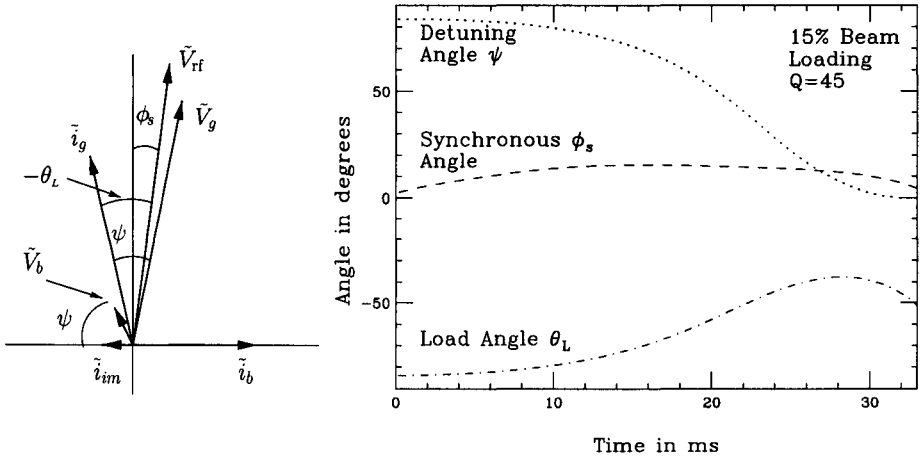


Fig. 7.23 When the cavity resonant frequency is fixed and is chosen as the rf frequency at the end of the ramp, the detuning angle ψ is fixed at each ramp time. When beam-loading is small, the load angle θ_L between the gap voltage $\tilde{V}_{rf}$ and the generator current $\tilde{i}_g$ will be close to ψ and will be large.

There is a price to pay for this choice of f_r; namely, there will be Robinson phase instability for the second half of the ramp when the rf frequency is larger than f_r. The sufficient condition for having a potential well for stable oscillation is, from Eq. (7.52), the high-intensity Robinson's criterion:

$$\frac{V_{\rm br}}{V_{\rm rf}} < \frac{\cos\phi_s}{\sin\psi\cos\psi}, \tag{7.116}$$

where $V_{\rm br} = i_{im}R_L$ is the in-phase beam-loading voltage. Below transition, the synchronous angle ϕ_s is between 0 and $\frac{1}{2}\pi$. For the second half of the ramp, the rf frequency becomes higher than the resonant frequency of the cavity, we have $\psi < 0$. The bottom plot of Fig. 7.24 illustrates the criterion for the whole ramp. It shows that the criterion is well satisfied for the first half of the ramp but not satisfied for the second half. Therefore, we must rely on control loops in the rf system to maintain phase stability. Of course a low-level feedback loop to reduce the cavity impedance helps tremendously.

Even when the beam is in an potential well for oscillatory motion, we still need to worry whether the oscillation amplitude will grow or be damped. We see that the criterion of Robinson's damping is violated as well. The instability comes from the fact that, below transition, the particles with larger energy have higher revolution frequency and see a smaller real impedance of the cavity, thus

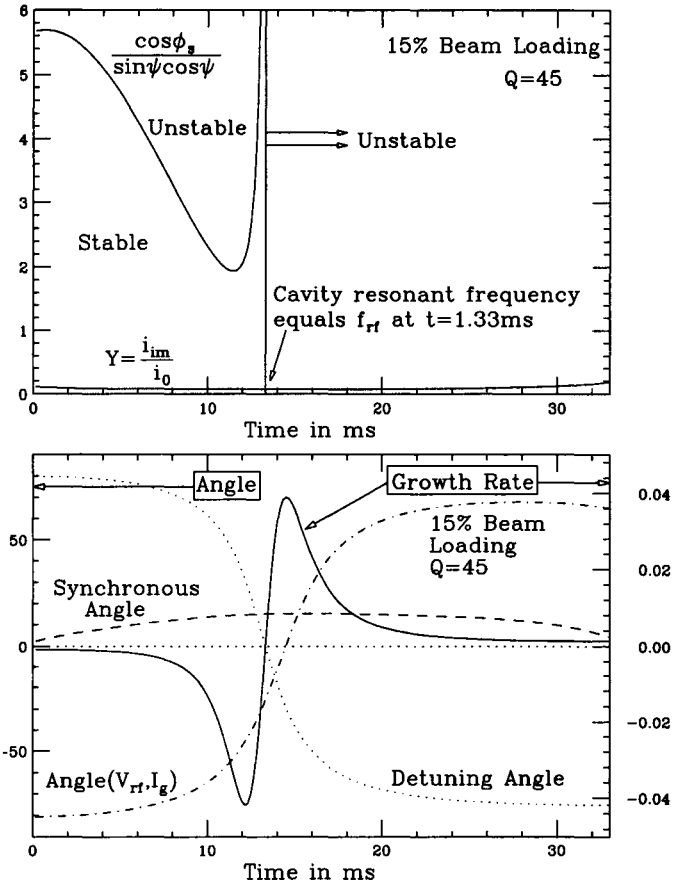


Fig. 7.24 The cavity resonant frequency is chosen as the rf frequency at the middle of the ramp at 13.33 ms. Top: The high-intensity Robinson's phase-stability criterion is satisfied in the first half of the ramp but not the second. Regions above the curve and to the left of the vertical straight line are unstable. Bottom: Although the detuning angle as well as the angle between the cavity gap voltage $\tilde{V}_{\rm rf}$ and the generator current $\tilde{I}_g$ are large at both ends of the ramp, they are relatively smaller at the middle of the ramp where the gap voltage is large.

losing less energy than particles with smaller energy. Therefore, the synchrotron oscillation amplitude will grow. In other words, the upper synchrotron sideband of the image current interacts with a smaller real impedance of the cavity resonant peak than the lower synchrotron sideband. However, since the loaded quality factor Q_L is not small, the impedance peak of the cavity is of wideband. As a result, the difference in real impedance at the two sidebands is only significant when the rf frequency is very close to the cavity resonant frequency. Thus, we expect the instability will last for only a very short time during the second half of the ramp. The growth rate of the synchrotron oscillation amplitude has been computed and is equal to [2]

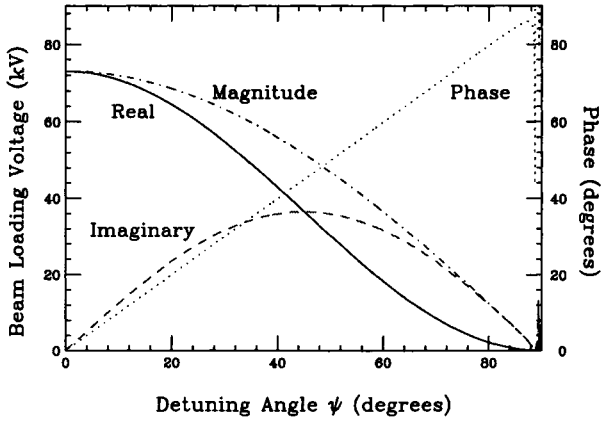
$$\frac{1}{\tau} = -\frac{i_{im}\beta\omega_s(R_+ - R_-)}{2V_{\rm rf}\cos\phi_s}, \tag{7.117}$$

where

$$R_+ - R_- = \mathcal{R}e\Big[Z_{\rm cav}(\omega_{\rm rf}+\omega_s) - Z_{\rm cav}(\omega_{\rm rf}-\omega_s)\Big], \tag{7.118}$$

i_{im} is the image current, β is the velocity with respect to light velocity, $\omega_s/(2\pi)$ is the synchrotron frequency, and $Z_{\rm cav}$ is the longitudinal impedance of the cavity as given by Eq. (7.22). Because of the small difference in the impedance at the synchrotron sidebands flanking the revolution harmonic, we see from Fig. 7.24 that the growth occurs for only a few ms and the growth time is at least ~ 25 ms. The total integrated growth increment from ramp time 13.33 ms is $\Delta G = \int \tau^{-1} dt = 0.131$ and the total growth is $e^{\Delta G} - 1 = 14.0\%$ which may be acceptable.

Finally let us compute the beam-loading voltage V_b seen by a bunch including all the effects of the previous bunch passages. In this example, $\delta_L \approx \pi h_b/Q_L = 0.0698$ for $h_b = 1$ and $Q_L = 45$. When the detuning angle $\psi = 0$, $V_b \approx V_{b0}/(2\delta_L)$. The functions F_1 and F_2 defined by Eq. (7.73) are computed at some values of the detuning ψ, which are listed and plotted in Fig. 7.25. We see that the total transient beam-loading voltage V_b falls rapidly as the detuning angle ψ increases. It vanishes approximately $\sim 88.7°$ and oscillates rapidly after that. However, the choice of a large ψ is not a good method to eliminate beam-loading, because in general the angle between the generator current phasor $\tilde{i}_g$ and the rf voltage phasor $\tilde{V}_{\rm rf}$ will be large making the rf system inefficient.



ψ	$\Psi = \delta_L \tan\psi$	F_1	F_2
0°	0°	$\sim 1/\delta_L$	0
84.9°	45°	0.12	1.2
87.5°	90°	$\sim \delta_L/2$	0.5
88.7°	180°	$\sim \delta_L/4$	0

Fig. 7.25 Left: Plot of transient beam-loading voltage including all previous bunch passages, $q(F_1 - iF_2)/C$, versus detuning angle ψ. Right: F_1 and F_2 for some values of the detuning angle ψ.

7.6 Exercises

7.1 For a Gaussian bunch with rms length σ_τ in a storage ring, find the Fourier component of the current at the rf frequency. Give the condition under which this component is equal to twice the dc current.

7.2 When the operation is at resonance, for example in a linac, show that the optimum coupling coefficient $\beta_{\rm op}$, as defined by Eq. (7.21), is also given by

$$\beta_{\rm op} = 1 + \frac{P_b}{P_c}, \tag{7.119}$$

where P_b and P_c are, respectively, the power delivered to the beam and the power dissipated in the cavities.

7.3 (1) When the beam-loading voltage V_b experienced by a point bunch happens to equal to the rf gap voltage $V_{\rm rf}$, show that the in-phase criterion implies

$$\psi + \phi_s = \frac{\pi}{2}, \tag{7.120}$$

where ψ is the detuning angle and ϕ_s is the synchronous angle. This implies that the generator voltage $\tilde{V}_g$ is in the direction of the beam and the limit of Robinson's stability is reached. Further increase in beam-loading will lead to Robinson's instability.

(2) When the optimum coupling coefficient is selected, show that

$$V_b < V_{\rm rf} \quad \text{and} \quad \psi + \phi_s < \frac{\pi}{2}, \tag{7.121}$$

or Robinson's stability criterion is always satisfied.

(3) When the optimum coupling coefficient is very large ($\beta_{\rm op} \gg 1$), for example, an rf system with superconducting cavities, show that

$$\frac{V_b}{V_{\rm rf}} \approx 1 - \frac{2\sin^2\phi_s}{\beta_{\rm op}} \quad \text{and} \quad \psi + \phi_s \approx \frac{\pi}{2} - \frac{\sin 2\phi_s}{\beta_{\rm op}}, \tag{7.122}$$

or the operation is very close to the Robinson's stability limit.

7.4 Prove the fundamental theorem of beam-loading when there are electromagnetic fields inside the lossless cavity before the passage of any charged particle.

7.5 In Sec. 7.2, rf-detuning and Robinson's stability condition have been worked out below transition. Show that above transition the detuning according the Fig. 7.4 leads to instability. Draw a new phasor diagram for the situation above transition with stable rf-detuning. Rederive Robinson's high-intensity stability criterion above transition.

7.6 Derive Eq. (7.79), the generator power delivered to the rf system with multi-passage of equally spaced bunches.

7.7 (1) Derive Eq. (7.92), the beam-loading voltage seen by a charge particle inside a Gaussian bunch of rms length σ_τ at a distance τ ahead of the bunch center.

(2) Using the property of the complex error function,

$$\lim_{\sigma_\tau \to 0} w\left(\frac{i\tau}{\sqrt{2}\sigma_\tau}\right) = \lim_{\sigma_\tau \to 0} \frac{2}{\sqrt{\pi}} e^{\tau^2/(2\sigma_\tau^2)} \int_{\frac{\tau}{\sqrt{2}\sigma_\tau}}^{\infty} e^{-t^2} dt = \begin{cases} 0 & \tau > 0, \\ 1 & \tau = 0, \\ 2 & \tau < 0, \end{cases} \tag{7.123}$$

derive Eq. (7.94), the transient beam-loading voltages seen by the head, center, and tail of the bunch as the bunch length shortens to zero.

7.8 (1) Derive Eqs. (7.96) and (7.97), the transient beam-loading voltage seen by a charge particle in a bunch with parabolic distribution at a distance T behind the head of the bunch.

(2) Derive Eqs. (7.101) and (7.101), the transient beam-loading voltage seen by a charge particle in a bunch with cosine-square distribution at a distance T behind the head of the bunch.

(3) Derive Eqs. (7.104) and (7.105), the transient beam-loading voltage seen by a charge particle in a bunch with cosine distribution at a distance T behind the head of the bunch.

7.9 For a batch with M consecutive bunches inside a ring of rf harmonic h, the steady-state beam-loading voltage experienced by the kth bunch when it crosses the cavity gap is given by Eq. (7.110).

(1) Continuing bucket by bucket, write down the beam-loading voltage experienced by the first bunch of the train when it crosses the cavity again. Since this beam-loading voltage must be equal to the one given by Eq. (7.110) with $k = 1$, determine the residual beam-loading voltage V_0 in the cavity at that time and show that it is given by Eq. (7.112).

(2) Show that the difference in beam-loading voltage ΔV_b experienced by the last and first bunch is given by Eq. (7.113).

(3) Show that ΔV_b assumes a maximum

$$\Delta V_b = V_{b0} \frac{e^{-\delta_L}\left[1 - e^{-\frac{1}{2}(h-1)\delta_L}\right]^2}{(1 - e^{-\delta_L})(1 - e^{-h\delta_L})}, \tag{7.124}$$

when $M = \frac{1}{2}(h+1)$.

7.10 For the damping ring discussed at the end of Sec. 7.2.1 and in Table 7.2, compute the variation in synchronous angle between the first and last bunch

in a train as a result of beam-loading. Consider two situations: one with normal-temperature cavities and one with superconducting cavities.

7.11 Consider a batch of 84 bunches inside the Fermilab Main Injector as described in Sec. 7.5.3.

(1) Compute the detuning angle with the requirement that the generator current is in phase with the rf voltage with respect to the middle bunch of the batch.

(2) Compute the rf phase slip between the transient beam-loading voltages of successive bunches and show that, because of the high quality factor, the accumulation for half of the batch (42 bunches) is only around 1°.

7.12 Exercise 7.9 can also be pursued in the frequency domain. Fill in the missing steps of the following derivation.

(1) Consider $M = 2m$ point bunches each with charge q inside $M = 2m$ consecutive buckets in a ring with rf harmonic h. The current is

$$I(t) = q\sum_{n=1}^{m}\delta[t-(n-\tfrac{1}{2})T_b] + q\sum_{n=1}^{m}\delta[t+(n-\tfrac{1}{2})T_b], \tag{7.125}$$

where T_b is the bucket width. In the frequency domain, the current at each revolution harmonic p is given by

$$I_p = \frac{1}{T_0}\int_{-T_0/2}^{T_0/2} I(t)e^{-i2\pi pt/T_0} = \frac{2q}{T_0}\sum_{n=1}^{m}\cos\frac{2\pi p(n-\frac{1}{2})}{h}, \tag{7.126}$$

where $T_0 = hT_b$ is the revolution period and p is an integer ranging from $-\infty$ to $+\infty$.

(2) The beam-loading voltage excited at harmonic p is $V_{bp} = I_p Z_p$ where the loaded impedance of the cavity at that harmonic is

$$Z_p = R_L\cos\psi_p e^{-i\psi_p} \qquad \text{with} \qquad \tan\psi_p = 2Q_L\left(\frac{h}{p}-\frac{p}{h}\right), \tag{7.127}$$

and R_L and Q_L are the loaded shunt impedance and quality factor.

(3) Considering the symmetry of the impedance, the beam-loading voltage in the time domain becomes

$$V_b(t) = \sum_p I_p\left(\cos^2\phi_p\cos\frac{2\pi pt}{T_0} - \cos\phi_p\sin\psi_p\sin\frac{2\pi pt}{T_0}\right). \tag{7.128}$$

(4) Using the information of the Main Injector in Sec. 7.5.3, evaluate numerically and plot I_p, V_{bp}, and $V_b(t)$.

Bibliography

[1] P. B. Wilson, Fermilab Summer School, 1981, AIP Conf. Proc., No. 87, 1982, AIP, p. 450.

[2] See for example, H. Wiedemann, *Particle Accelerator Physics II* (Springer, 1995), p. 203.

[3] D. Boussard, *Beam Loading*, Fifth Advanced CERN Accel. Physics Course (Rhodes, Greece, Sep. 20–Oct. 1, 1993), CERN Report CERN-95-06, p. 415.

[4] C. Ankenbrandt, private communication.

[5] K. Y. Ng and Z. B. Qian, *Finemet versus Ferrite—Pros and Cons*, Proc. 1999 Part. Accel. Conf., eds. A. Luccio and W. MacKay (New York, March 27–April 2, 1999), p. 874.

[6] Y. Mori, private communication; Y. Tanabe, *Evaluation of Magnetic Alloy(MA)s for JHF RF Cavity*, Mini Workshop (Tanashi, Japan, Feb. 23-25, 1998).

[7] Shekhar Mishra, David Neuffer, K. Y. Ng, Franois Ostiguy, Nikolay Solyak, Aimin Xiao, George D. Gollin, Guy Bresler, Keri Dixon, Thomas R. Junk, and Jeremy B. Williams, *Studies Pertaining to a Small Damping Ring for the International Linear Collider*, Fermilab Report FERMI-TM-2272, 2004.

[8] P. B. Robinson, *Stability of Beam in Radiofrequency System*, Cambridge Electron Accel. Report CEAL-1010, 1964.

[9] E. Raka, *RF System Considerations for a Large Hadron Collider*, AIP Conf. Proc. 184, Physics of Particle Accelerators, eds. M. Month and M. Dienes (New York, 1989), Vol. 1, p. 289.

[10] D. Boussard et al., *Longitudinal Phenomena in the CERN SPS, IEEE Trans. Nucl. Sci.* **NS-24**(3), 1399 (1977).

[11] *Conceptual Design Report of PEP-II, An Asymmetric B Factory*, June 1993, LBL-PUB-5379, SLAC-418, CALT-68-1869, UCRL-ID-114055, or UC-IIRPA-93-01.

[12] J. Dey, J. Steimel, J. Reid, *Narrowband Beam Loading Compensation in the Fermilab Main Injector Accelerating Cavities*, Proc. 2001 Part. Accel. Conf., eds. P. Lucas and S. Webber (Chicago, June 18–22, 2001), p. 876. Shekhar Shukla, John Marriner, and James Griffin, *Slip Stacking in the Fermilab Main Injector*, Proc. Summer Study on the Future of High Energy Physics, ed. N. Graf (Snowmass, June 30–July 21, 2001).

[13] J. Steimel, *Summary of RF Cavity Beam Loading Problems and Cures in the CERN PS Complex*, unpublished; D. Boussard and G. Lambert, *Reduction of the Apparent Impedance of Wide Band Accelerating Cavities by RF Feedback, IEEE Trans. Nucl. Sci.* **NS-30**(4), 2239 (1983); D. Boussard, *Control of Cavities with High Beam Loading, IEEE Trans. Nucl. Sci.* **NS-32**(5), 1852 (1985); D. Boussard, *RF Power Requirements for a High Intensity Proton Collider (Parts 1 and 2)*, CERN Report CERN-SL/91-16 (RFS), April 1991.

[14] F. Pedersen, *Beam Loading Effects in the CERN PS Booster, IEEE Trans. Nucl. Sci.* **NS-22**(3), 1906 (1975); F. Pedersen, *A Novel RF Cavity Tuning Feedback Scheme for Heavy Beam Loading, IEEE Trans. Nucl. Sci.* **NS-32**(5), 2138 (1985).

[15] J. E. Griffin, *Compensation for Beam Loading in the 400-GeV Fermilab Main Accelerator, IEEE Trans. Nucl. Sci.* **NS-22**(3), 1910 (1975); D. Wildman, *Transient Beam Loading Compensation in the Fermilab Main Ring, IEEE Trans. Nucl. Sci.*

NS-32(5), 2150 (1985).

[16] Y. Goren and T. F. Wang, *Voltage Counter-Phasing in the SSC Low Energy Booster*, Proc. 1993 Part. Accel. Conf., ed. S. T. Corneliussen (Washington, D.C., May 17–20, 1993), p.883.

[17] J. E. Griffin, *RF System Considerations for a Muon Collider Proton Driver Synchrotrons*, Fermilab Report FN-669, 1998.

[18] S. Y. Lee, K. Y. Ng and D. Trbojevic, *Phys. Rev.* **E4**, 3040 (1993); S. Y. Lee, K. Y. Ng and D. Trbojevic, Fermilab Report FN-595, 1992.

[19] K. Y. Ng and Z. B. Qian, Proc. Phys. at the First Muon Collider and at Front End of a Muon Collider, (Fermilab, Batavia, Nov. 6–9, 1997), p. 841.

[20] J. E. Griffin, K. Y. Ng, Z. B. Qian, and D. Wildman, *Experimental Study of Passive Compensation of Space Charge Potential Well Distortion at the Los Alamos National Laboratory Proton Storage Ring*, Fermilab Report FN-661, 1997.

2025 © The Author(s). This is an Open Access chapter published by World Scientific Publishing Company, licensed under the terms of the Creative Commons Attribution-NonCommercial 4.0 International License (CC BY-NC 4.0).

Chapter 8

Longitudinal Coupled-Bunch Instabilities

When the wake does not decay within the bunch spacing, bunches talk to each other. The bunches will then be coupled together and evolve into coupled-bunch instabilities if the wake is strong enough. Consider M bunches of equal intensity equally spaced in the accelerator ring. There are M coupled modes of oscillation characterized by $\mu = 0,\ 1,\ \cdots,\ M-1$, in which the center-of-mass of a bunch *lags** its predecessor by the phase $2\pi\mu/M$. In addition, an individual bunch in the μth coupled-bunch mode can oscillate in the synchrotron phase space about its center-of-mass in the mth azimuthal mode with $2m = 2,\ 4,\ \cdots$ azimuthal nodes† in the perturbed longitudinal phase-space distribution. Of course, there will also be radial modes of oscillation in the perturbed distribution.

8.1 Sacherer's Integral Equation

Because the beam particles execute synchrotron oscillations, it is more convenient to use circular coordinates (r, ϕ) in the longitudinal phase space instead of the former time advance τ and energy offset ΔE. We define

$$\begin{cases} x = r\cos\phi = \tau, \\ p_x = r\sin\phi = \dfrac{\eta}{\omega_s\beta^2}\dfrac{\Delta E}{E_0}. \end{cases} \tag{8.1}$$

The equations of motion, which can be derived from the Hamiltonian, now take

*Because of the $e^{-i\omega t}$ convention, we consider a bunch *lags* its predecessor if the phase difference is $e^{i\psi}$ with $\psi > 0$, and vice versa. More correctly, maybe we should say *lag in time*, or *lag in time-phase*. We can also formulate the problem by having the bunch *lead* its predecessor by the phase $2\pi\mu'/M$ in the μ'th coupling mode. Then mode μ' will be exactly the same as mode $M-\mu$ discussed in the text.

†For example, the dipole mode $m = 1$ can be written as $\sim \cos\phi$, which has two nodes $\phi = \pm\pi/2$.

the form,

$$\begin{cases} \dfrac{dx}{ds} = -\dfrac{\omega_s}{v} p_x, \\ \dfrac{dp_x}{ds} = \dfrac{\omega_s}{v} x + \dfrac{\eta}{E_0 \omega_s \beta^2} \langle F_0^{\parallel}(\tau; s) \rangle_{\text{dyn}}, \end{cases} \tag{8.2}$$

and become more symmetric. In the absence of the wake force $\langle F_0^{\parallel}(\tau; s) \rangle_{\text{dyn}}$, the trajectory of a beam particle is just a circle in the longitudinal phase space. In above, η is the slip factor, $v = \beta c$ is the velocity and E_0 is the energy of the synchronous particle. Here, ω_s is the potential-well perturbed incoherent angular synchrotron frequency of the beam particle under consideration and it depends on the amplitude of oscillation. Note that only the dynamic or time-dependent part of the wake force contributes.

The phase-space distribution ψ of a bunch can be separated into the unperturbed or stationary part ψ_0 and the perturbation part ψ_1 (or more correctly, the dynamic part):

$$\psi(\tau, \Delta E; s) = \psi_0(\tau, \Delta E) + \psi_1(\tau, \Delta E; s). \tag{8.3}$$

The linearized Vlasov equation becomes

$$\frac{\partial \psi_1}{\partial s} - \frac{\omega_s}{v} p_x \frac{\partial \psi_1}{\partial x} + \frac{\omega_s}{v} x \frac{\partial \psi_1}{\partial p_x} + \frac{\partial \psi_0}{\partial p_x} \frac{\eta}{E_0 \omega_s \beta^2} \langle F_0^{\parallel}(\tau; s) \rangle_{\text{dyn}} = 0. \tag{8.4}$$

Changing to the circular coordinates, the equation simplifies readily to

$$\frac{\partial \psi_1}{\partial s} + \frac{\omega_s}{v} \frac{\partial \psi_1}{\partial \phi} + \frac{\eta}{E_0 \omega_s \beta^2} \frac{d\psi_0}{dr} \sin\phi \, \langle F_0^{\parallel}(\tau; s) \rangle_{\text{dyn}} = 0. \tag{8.5}$$

The perturbation distribution can be expanded in terms of the azimuthal modes:

$$\psi_1(r, \phi; s) = \sum_m \alpha_m R_m(r) e^{im\phi - i\Omega s/v}, \tag{8.6}$$

where $R_m(r)$ are functions corresponding to the mth azimuthal, α_m are the expansion coefficients, and $\Omega/(2\pi)$ is the collective frequency to be determined. In above, $m = 0$ has been excluded because it has been included in the stationary part ψ_0, otherwise charge conservation will be violated. The Vlasov equation becomes

$$(\Omega - m\omega_s) \alpha_m R_m(r) e^{-i\Omega s/v} = -\frac{iv\eta}{E_0 \omega_s \beta^2} \frac{d\psi_0}{dr} \int_{-\pi}^{\pi} \frac{d\phi}{2\pi} e^{-im\phi} \sin\phi \langle F_0^{\parallel}(\tau; s) \rangle_{\text{dyn}}. \tag{8.7}$$

Now consider the wake force acting on a beam particle at location s, where, for example, a cavity gap is located. The particle has an arrival time τ ahead of the synchronous particle and the wake force it sees consists of the summation

of all the wakes left behind by all preceding particles passing through s at an earlier time. The dynamic part of the wake force can be expressed as

$$\langle F_0^{\parallel}(\tau;s)\rangle_{\rm dyn} = -\frac{e^2}{C_0}\sum_{k=-\infty}^{\infty}\int_{-\infty}^{\infty} d\tau' \lambda_1[\tau';s-kC_0-v(\tau'-\tau)]W_0'[kC_0+v(\tau'-\tau)], \tag{8.8}$$

where C_0 is length of the accelerator's circumference and $\lambda_1(\tau;s)$, the projection of $\psi_1(\tau,\Delta E;s)$ onto the τ axis, is the dynamic part of the linear density of the beam. The summation over k takes care of the contribution of the wake left by the charge distribution passing through the cavity gap in previous turns. Both the lower limits of the summation and the integral have been extended to $-\infty$ because the wake function satisfies causality. The expression in Eq. (8.8) is more accurate than the one in Eq. (2.7). In the latter, we have neglected the time elapse between the passage of the source particle and the passage of the test particle through the point of reference or the cavity gap. It was valid in Eq. (2.7) because the source and test particles resided in one bunch and the length of the bunch was considered short compared with the circumference of the accelerator ring. However, the problem that we face here is very different. The source and test particles may not reside inside the same bunch. Even if they do, the passage of the source particle through the point of reference may have been many revolution turns earlier than the passage of the test particle. During this time interval, the wake fields inside the cavity will have undergone tremendous changes, both in their phases and magnitudes. In addition, the longitudinal positions of the particles will have moved also in view of synchrotron oscillations. When the source particle, with arrival time τ' ahead of the test particle, passes the cavity gap k revolution turns earlier, the excitation of the cavity will have taken place at the 'time' $s-kC_0-v(\tau'-\tau)$. This is what enters into the second argument in the dynamical part of the linear density λ_1.

We now separate the total beam linear density $\lambda_1(\tau;s)$ in Eq. (8.8) into M individual linear densities representing the M bunches, so that the ℓth bunch has the linear density $\lambda_\ell(\tau;s)$ with τ measured from its synchronous particle which is located at s_ℓ. Then the witness particle in the nth bunch will experience the wake force

$$\langle F_{0n}^{\parallel}(\tau;s)\rangle_{\rm dyn} = -\frac{e^2}{C_0}\sum_{k=-\infty}^{\infty}\sum_{\ell=0}^{M-1}\int_{-\infty}^{\infty} d\tau' \times\lambda_\ell\big[\tau';s-kC_0-(s_\ell-s_n)-v(\tau'-\tau)\big]W_0'\big[kC_0+(s_\ell-s_n)+v(\tau'-\tau)\big]. \tag{8.9}$$

Unlike Eq. (8.8) where $\tau'-\tau$ denote the difference in arrival times for particles in different bunches, we have here $\tau'-\tau$ representing the difference in arrival times

for particles within the same bunch. We assume the bunches are identical and equally spaced. For the μth coupled-bunch mode, knowing the phase lag between the bunches, we can express the linear density of the ℓth bunch, $\lambda_\ell(\tau; s)$, in terms of the linear density of the nth bunch, $\lambda_n(\tau; s) = \lambda_{1n}(\tau)e^{-i\Omega s/v}$, according to

$$\lambda_\ell(\tau; s) = \lambda_{1n}(\tau)e^{i2\pi\mu(\ell-n)/M}e^{-i\Omega s/v}. \tag{8.10}$$

8.1.1 *Frequency Domain*

Next, let us go to the frequency domain using the Fourier transforms

$$W_0'(v\tau) = \frac{1}{2\pi}\int_{-\infty}^{\infty} d\omega\, Z_0^{\parallel}(\omega)e^{-i\omega\tau}, \tag{8.11}$$

$$\lambda_{1n}(\tau) = \int_{-\infty}^{\infty} d\omega\, \tilde{\lambda}_{1n}(\omega)e^{i\omega\tau}. \tag{8.12}$$

We shall neglect[†] in Eq. (8.9), the time delay $\tau'-\tau$ in λ_ℓ because this will only amount to a phase delay $\Omega(\tau'-\tau)$ where $\Omega \approx m\omega_s$, which is very much less than the phase change $\omega_r(\tau'-\tau)$ during the bunch passage, where $\omega_r/(2\pi)$ is the frequency of the driving resonant impedance, mostly originated in the rf cavities. Substituting Eqs. (8.11) and (8.12) into Eq. (8.9) and integrating over τ' and one of the ω's, the wake force for the μth coupled-bunch mode becomes

$$\langle F_{0n\mu}^{\parallel}(\tau; s)\rangle_{\rm dyn} = -\frac{e^2}{C_0}\sum_{k=-\infty}^{\infty}\sum_{\ell=0}^{M-1} e^{i2\pi\mu(\ell-n)/M}e^{i\Omega(-s+kC_0+s_\ell-s_n)/v} \times \int_{-\infty}^{\infty} d\omega\tilde{\lambda}_{1n}(\omega)Z_0^{\parallel}(\omega)e^{-i\omega(kC_0+s_\ell-s_n)/v}e^{i\omega\tau}. \tag{8.13}$$

The summation over k can now be performed using Poisson formula

$$\sum_k e^{-ik\omega C_0/v} = \sum_p 2\pi\,\delta\left(\frac{\omega C_0}{v} - 2\pi p\right) = \sum_p \omega_0\,\delta(\omega - p\omega_0). \tag{8.14}$$

This leads to

$$\langle F_{0n\mu}^{\parallel}(\tau; s)\rangle_{\rm dyn} = -\frac{e^2}{C_0}\sum_{p=-\infty}^{\infty}\sum_{\ell=0}^{M-1} \omega_0\tilde{\lambda}_{1n}(\omega_p)Z_0^{\parallel}(\omega_p) \times e^{i2\pi\mu(\ell-n)/M}e^{-i\Omega s/v+i\omega_p\tau}e^{-ip\omega_0(s_\ell-s_n)/v}, \tag{8.15}$$

[†]Without this approximation, only $Z_0^{\parallel}$ will have the argument ω_p in Eq. (8.15). The argument of $\tilde{\lambda}$ and the factor in front of τ in the exponent will be replaced by $\omega_p - \Omega$. In Eq. (8.19) below, The argument of $\tilde{\lambda}$ and the factor in front of τ in the exponent will be replaced by $\omega_q - \Omega$. This difference is too small to be of concern, because when solving the dispersion relation, such as Eq. (8.32) below, Ω is usually omitted in ω_q.

where we have used the short-hand notation

$$\omega_p = p\omega_0 + \Omega, \tag{8.16}$$

which represents the upper coherent synchrotron sideband of every revolution harmonic. We next make use of the fact that the unperturbed bunches are equally spaced, or

$$s_\ell - s_n = \frac{\ell - n}{M} C_0. \tag{8.17}$$

The summation over ℓ can be performed; the sum vanish unless $(p-\mu)/M = q$, where q is an integer:

$$\sum_{\ell=0}^{M-1} e^{i2\pi(\ell-n)(\mu-p)/M} = \begin{cases} M & \text{if } \dfrac{p-\mu}{M} = q, \\ 0 & \text{otherwise.} \end{cases} \tag{8.18}$$

The final result turns the dynamic part of the wake force in to the simple expression,

$$\langle F^{\parallel}_{0n\mu}(\tau; s)\rangle_{\text{dyn}} = -\frac{e^2 M\omega_0}{C_0} e^{-i\Omega s/v} \sum_{q=-\infty}^{\infty} \tilde{\lambda}_{1n}(\omega_q) Z_0^{\parallel}(\omega_q) e^{i\omega_q \tau}, \tag{8.19}$$

where

$$\omega_q = (qM+\mu)\omega_0 + \Omega, \tag{8.20}$$

which represents the upper coherent synchrotron sideband of every M revolution harmonics, signaling the coupling of the M bunches.

Since the left side of the Vlasov equation is expressed in terms of the radial function $R_m(r)$, we want to do the same for the wake force, hoping to arrive at an eigen-equation for $R_m(r)$ eventually. To accomplish this, let us first rewrite the perturbation density in the time domain,

$$\langle F^{\parallel}_{0n\mu}(\tau; s)\rangle_{\text{dyn}} = -\frac{e^2 M\omega_0}{C_0} e^{-i\Omega s/v} \sum_{q=-\infty}^{\infty} Z_0^{\parallel}(\omega_q) \int \frac{d\tau'}{2\pi} \lambda_{1n}(\tau') e^{i\omega_q(\tau-\tau')}. \tag{8.21}$$

Since $\lambda_{1n}(\tau')$ is the projection of the perturbed distribution onto the τ' axis, we must have

$$\begin{aligned} \lambda_{1n}(\tau')d\tau' &= \int \psi_{1n}(\tau', \Delta E')d\tau' d\Delta E' \\ &= \frac{E_0\omega_s\beta^2}{\eta} \int \psi_{1n}(r', \phi')r' dr' d\phi' \\ &= \frac{E_0\omega_s\beta^2}{\eta} \sum_{m'} \alpha_{m'} \int R_{m'}(r') e^{im'\phi'} r' dr' d\phi'. \end{aligned} \tag{8.22}$$

The wake force then takes the form

$$\langle F_{0n}^{\parallel}(\tau;s)\rangle_{\rm dyn} = -\frac{e^2\omega_0 M}{2\pi C_0}\frac{E_0\omega_s\beta^2}{\eta}\,e^{-i\Omega s/v} \times \sum_{q=-\infty}^{\infty}\sum_{m'} Z_0^{\parallel}(\omega_q)\int r'dr'd\phi'\alpha_{m'}R_{m'}(r')e^{im'\phi'}e^{i\omega_q(\tau-\tau')}, \quad (8.23)$$

This wake force is next substituted into the Vlasov equation (8.7). The integrations over ϕ and ϕ' are performed in terms of Bessel function of order m using its integral definition

$$i^m J_m(z) = \frac{1}{2\pi}\int_{-\pi}^{\pi} d\phi\, e^{\pm im\phi + iz\cos\phi}, \quad (8.24)$$

the recurrence relation

$$J_{m-1}(z) + J_{m+1}(z) = \frac{2m}{z}J_m(z), \quad (8.25)$$

and the fact that

$$J_m(-z) = (-1)^m J_m(z). \quad (8.26)$$

The result is the Sacherer's integral equation for longitudinal instability for the mth azimuthal μth coupled-bunch mode,

$$[\Omega - m\omega_s(r)]\alpha_m R_m(r) = -\frac{i2\pi e^2 M N_b\eta}{\beta^2 E_0 T_0^2\omega_s}\frac{m}{r}\frac{dg_0}{dr} \times \sum_{m'} i^{m-m'}\alpha_{m'}\int r'dr' R_{m'}(r')\sum_q \frac{Z_0^{\parallel}(\omega_q)}{\omega_q}J_{m'}(\omega_q r')J_m(\omega_q r), \quad (8.27)$$

where N_b is the number of particles per bunch and the transformation of the unperturbed longitudinal distribution

$$\psi_0(r)d\tau d\Delta E = \frac{\omega_s\beta^2 E_0}{\eta}\psi_0 dx dp_x = N_b g_0(r) r dr d\phi \quad (8.28)$$

has been made so that g_0 is normalized to unity when integrated over $rdrd\phi$.

This is an eigenfunction-eigenvalue problem, the α_m's being the eigenfunctions and Ω the corresponding eigenvalue. Notice that we have included on the left side of Eq. (8.27) explicitly the r-dependency of the incoherent synchrotron frequency ω_s, because each particle has a different amplitude of synchrotron

oscillation. To incorporate the spread, let us introduce ω_{sc} as the synchrotron frequency of those particles at the center of the bunch, and write[‡]

$$\omega_s(r) = \omega_{sc}\Big[1 + D(r)\Big], \tag{8.29}$$

with

$$D(r) = \frac{\omega_s(r)}{\omega_{sc}} - 1. \tag{8.30}$$

The term $m\omega_{sc}D(r)\delta_{mm'}$ can now be moved to the right side of the equation and becomes an additional part of the interaction matrix. The equation is then solved as an eigenfunction-eigenvalue problem with this new interaction matrix.

The solution of the eigen-equation is nontrivial. However, with some approximations, interesting results can be deduced. When the perturbation is not too strong so that the shift in frequency is much less than the synchrotron frequency, there will not be coupling between different azimuthals. The integral equation simplifies readily to

$$\begin{aligned}\big[\Omega - m\omega_s(r)\big]R_m(r) = &-\frac{i2\pi e^2 M N_b \eta}{\beta^2 E_0 T_0^2 \omega_{sc}} \frac{m}{r}\frac{dg_0}{dr} \\ &\times \int r'dr' R_m(r') \sum_q \frac{Z_0^{\parallel}(\omega_q)}{\omega_q} J_m(\omega_q r') J_m(\omega_q r).\end{aligned} \tag{8.31}$$

Moving the factor $\Omega - m\omega_s(r)$ to the right side, the radial distribution R_m can be eliminated by multiplying both sides by $rJ_m(r)$ and integrating over dr. We then arrive at the dispersion relation,

$$1 = -\frac{i2\pi e^2 M N_b m \eta}{\beta^2 E_0 T_0^2 \omega_{sc}} \sum_q \frac{Z_0^{\parallel}(\omega_q)}{\omega_q} \int dr \, \frac{dg_0}{dr} \frac{J_m^2(\omega_q r)}{\Omega_{m\mu} - m\omega_s(r)}, \tag{8.32}$$

where we have added a subscript $m\mu$ to Ω to denote the collective frequency of the μth coupled-bunch mode in the mth azimuthal mode. The dependency on μ resides in $\omega_q = (qM + \mu)\omega_0 + \Omega_{m\mu}$. Stability and growth contours can be derived from the dispersion relation of Eq. (8.32) in just the same way as in the discussion of microwave instability for a single bunch in Chapters 5 and 6. Note that so far radial modes have been neglected so that our treatment is equivalent to the employment of synthetic kernel we studied in Chapter 6.

[‡]The ω_s on the right side can simply be replaced by ω_{sc} because the synchrotron frequency spread is small compared with ω_{sc}. For simplicity, sometimes we just write ω_s instead.

8.1.2 *Synchrotron Tune Shift*

When the spread in synchrotron frequency is small and can be neglected, Eq. (8.32) leads to the frequency shift

$$\Omega_{m\mu} - m\omega_s = \frac{i2\pi e^2 M N_b m\eta}{\beta^2 E_0 T_0^2 \omega_s} \sum_q \frac{Z_0^{\parallel}(\omega_q)}{\omega_q} \left[- \int dr \, \frac{dg_0}{dr} J_m^2(\omega_q r) \right], \tag{8.33}$$

where the expression inside the square brackets, denote by F, can be viewed as a distribution dependent form factor, which is positive definite because dg_0/dr is negative. The imaginary part $\mathcal{I}m\,\Omega_{m\mu}$ gives the growth rate of the instability of the coupled-bunch mode under consideration. The real part $\mathcal{R}e(\Omega_{m\mu} - m\omega_s)$ gives the dynamic contribution to the coherent tune shift.

When the bunch length $2\hat{\tau}$ is much shorter than the wavelength of the perturbing impedance, or $\omega_q \hat{\tau} \ll 1$, the Bessel function can be substituted by its small-argument expression:

$$J_m(x) \approx \frac{1}{m!} \left(\frac{x}{2} \right)^m. \tag{8.34}$$

We are interested particularly in the synchrotron tune shift of one bunch ($M = 1$) in dipole mode ($m = 1$), and obtain

$$\Delta\Omega_1 = -\frac{e^2 N_b \eta}{2\beta^2 E_0 T_0^2 \omega_s} \sum_q \omega_q \, \mathcal{I}m \, Z_0^{\parallel}(\omega_q), \tag{8.35}$$

where $\omega_q = q\omega_0 + \omega_s$ and the bunch density normalization

$$\int g_0(r) r dr d\phi = 1 \tag{8.36}$$

has been used. In the situation that the perturbing impedance is a broadband resonance, we can make the approximation $\omega_q = q\omega_0$.

It is important to point out that Eq. (8.35) represents only the dynamic part of the synchrotron frequency shift contributed by the impedance, and the shift is from ω_s, the incoherent synchrotron frequency. There is another contribution coming from the static potential-well distortion, which is exactly the same as the incoherent shift, $\Delta\omega_{s\,\mathrm{incoh}} = \omega_s - \omega_{s0}$. The total coherent synchrotron frequency shift is therefore

$$\Omega_1 - \omega_{s0} = [\Omega_1 - \omega_s] + [\omega_s - \omega_{s0}], \tag{8.37}$$

of which the first term on the right side represents the dynamic part of the coherent shift while the second term represents the static part of the coherent shift which is the same as the incoherent shift.

8.1.2.1 *Water-Bag Model*

Take the simple case of a single bunch of length $2\hat{\tau}$ and uniform distribution in the longitudinal phase space, which is usually called the *water-bag model.* Then

$$g_0(r) = \frac{1}{\pi\hat{\tau}^2} H(\hat{\tau} - r), \tag{8.38}$$

where the Heaviside function is defined as $H(x) = 1$ when $x > 0$ and zero otherwise. The eigen-equation can be readily solved because $R_m(r) \propto \delta(r - \hat{\tau})$. The form factor, the expression inside the square brackets of Eq. (8.33), becomes

$$F = \frac{1}{\pi\hat{\tau}^2} J_m^2(\omega_q\hat{\tau}). \tag{8.39}$$

When the synchrotron frequency spread is neglected, the solution is

$$\Omega_m - m\omega_s = \frac{i2m\nu_{s0}\xi}{\hat{\tau}^2} \sum_q \frac{Z_0^{\parallel}(\omega_q)}{\omega_q} J_m^2(\omega_q\hat{\tau}), \tag{8.40}$$

where the real part is the dynamic part of the coherent synchrotron frequency shift and the imaginary part is the growth rate.

For a broadband wake that is longer than the length of the bunch ($\omega_q\hat{\tau} \ll 1$), the Bessel function can be expanded and we obtain the growth rate

$$\frac{1}{\tau_m} = \frac{\nu_{s0}\xi}{2} \frac{m}{(m!)^2} \sum_q \left(\frac{\omega_q\hat{\tau}}{2}\right)^{2m-2} \omega_q \mathcal{R}e\, Z_0^{\parallel}(\omega_q), \tag{8.41}$$

and the dynamic frequency shift

$$\mathcal{R}e\left(\Omega_m - m\omega_s\right) = -\frac{\nu_{s0}\xi}{2} \frac{m}{(m!)^2} \sum_q \left(\frac{\omega_q\hat{\tau}}{2}\right)^{2m-2} \omega_q \mathcal{I}m\, Z_0^{\parallel}(\omega_q). \tag{8.42}$$

In above, the scaling factor

$$\xi = \frac{eI_b\eta}{2\pi\beta^2 E_0\nu_{s0}^2} = \frac{e^2N_b\eta}{2\pi\beta^2 E_0T_0\nu_{s0}^2}, \tag{8.43}$$

is the same one defined in Eq. (2.90), and $\omega_q = q\omega_0 + \Omega_m$ for one bunch.

8.1.3 *Robinson's Instability*

We mentioned before that the $m = 0$ mode should be omitted because of charge conservation. In fact, we notice that putting $m = 0$ in, for example, Eq. (8.27) gives $\Omega_0 = 0$. Actually, $m = 0$ describes the potential-well distortion mode addressed in Chapter 2 and is of not much interest here where the emphasis

is on instabilities. The next azimuthal mode is $m = 1$ which describes dipole oscillations and we expect $\Omega_1 \approx \omega_s$. Consider the situation of having the driving impedance as a resonance so narrow that there is only one $q > 0$ that satisfies

$$\omega_r \approx q\omega_0 \pm \omega_s, \tag{8.44}$$

where $\omega_r/(2\pi)$ is the resonant frequency. The growth rate for a short bunch can therefore be obtained from Eq. (8.41),

$$\frac{1}{\tau_1} = \mathcal{I}m\,\Delta\omega_s = \frac{\eta e^2 N_b \omega_r}{2\beta^2 E_0 T_0^2 \omega_s}[\mathcal{R}e\,Z_0^{\parallel}(q\omega_0+\omega_s) - \mathcal{R}e\,Z_0^{\parallel}(q\omega_0-\omega_s)], \tag{8.45}$$

where the first term corresponds to positive frequency and the second negative frequency. If the resonant frequency is slightly above $q\omega_0$ as illustrated in Fig. 8.1(a), we have $\mathcal{R}e\,Z_0^{\parallel}(q\omega_0+\omega_s) > \mathcal{R}e\,Z_0^{\parallel}(q\omega_0-\omega_s)$. Above transition, the growth rate will be positive or there is instability. On the other hand, if $\omega_r < q\omega_0$ as illustrated in Fig. 8.1(b), the growth rate is negative and the system is damped. This instability criterion was first analyzed by Robinson, [1] and we have obtained exactly the same result in Sec. 7.3.3 using phasor-diagram analysis. Below transition, the reverse is true; one should tune the resonant frequency of the cavity below a revolution harmonic for stability. Note that the growth rate of Eq. (8.45) is independent of the bunch length when the bunch is

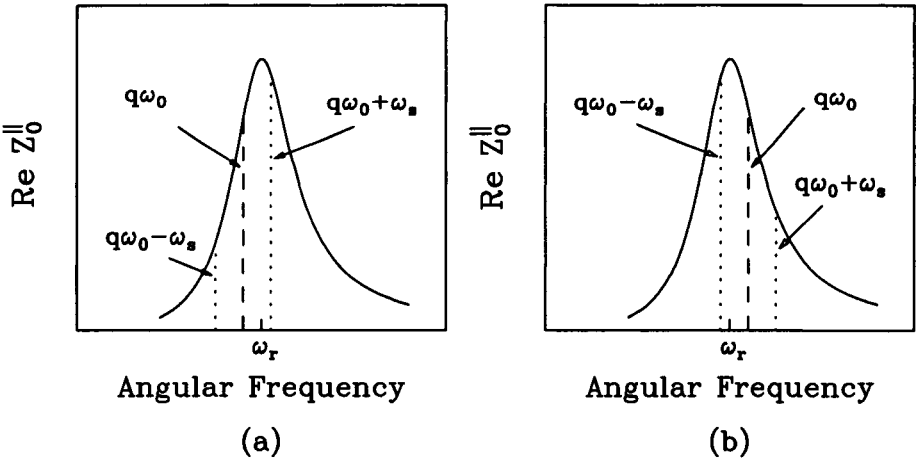


Fig. 8.1 (a) Above transition, if the resonant frequency ω_r is slightly above a revolution harmonic $q\omega_0$, $\mathcal{R}e\,Z_0^{\parallel}$ at the upper synchrotron sideband is larger than at the lower synchrotron sideband. The system is unstable. (b) Above transition, if ω_r is slightly below a harmonic line, $\mathcal{R}e\,Z_0^{\parallel}$ at the upper sideband is smaller than at the lower sideband. The system is stable.

short, implying that for the dipole mode, this is a point-bunch theory.[§] Thus, this special case should be obtainable much more easily than the complicated derivation that we have gone through, and it is worthwhile to make a digression into the easier derivation.

8.1.3.1 *Point-Bunch Theory*

Let us start from the equations of motion of a super particle with arrival time advance $\tau(s)$, carrying charge eN_b, and seeing its own wake left behind k revolutions before. We have

$$\frac{d^2\tau}{ds^2} + \frac{\omega_{s0}^2}{v^2}\tau = \frac{e^2 N_b \eta}{v\beta^2 E_0 C_0} \sum_{k=-\infty}^{\infty} W_0' \left[kT_0 + \tau(s - kC_0) - \tau(s)\right], \tag{8.46}$$

where the summation has been extended to $-\infty$ (the future) because the wake function obeys causality. The arrival time advance of each passage through the cavity gap is of the order of the synchrotron oscillation amplitude, which should be small compared with the revolution period of the ring. We can therefore expand the wake potential about kT_0 with the right side becoming

$$\begin{aligned} \text{R.S.} &= \frac{e^2 N_b \eta}{v\beta^2 E_0 C_0} \sum_{k=-\infty}^{\infty} \left[\tau(s - kC_0) - \tau(s)\right] W_0''(kT_0) \\ &= \frac{e^2 N_b \eta}{v\beta^2 E_0 C} \tau(s) \sum_{k=-\infty}^{\infty} \left[e^{-i\Omega(s/v - kT_0)} - 1\right] W_0''(kT_0), \end{aligned} \tag{8.47}$$

where we have substituted the collective-time behavior

$$\tau(s) \propto e^{-i\Omega s/v}, \tag{8.48}$$

with Ω being the collective angular frequency to be determined. Next, go to the frequency domain by introducing the longitudinal impedance $Z_0^{\parallel}$, or

$$W_0'(t) = \frac{1}{2\pi} \int d\omega Z_0^{\parallel}(\omega) e^{-i\omega t}. \tag{8.49}$$

We obtain

$$\text{R.S.} = -\frac{ie^2 N_b \eta}{v\beta^2 E_0 C_0} \sum_{k=-\infty}^{\infty} \left[e^{-i\Omega(s/v - kT_0)} - 1\right] \int \frac{d\omega}{2\pi} \omega Z_0^{\parallel}(\omega) e^{-i\omega k T_0}. \tag{8.50}$$

[§]More about Robinson's stability criterion was discussed in Chapter 7.

The summation over k can now be performed. Substituting the time behavior of τ into the left side, the equation of motion becomes

$$\Omega^2 - \omega_{s0}^2 = \frac{ie^2 N_b \eta v^2}{\beta^2 E_0 C_0^2} \sum_{p=-\infty}^{\infty} \Big[(p\omega_0 + \Omega) Z_0^{\parallel}(p\omega_0 + \Omega) - p\omega_0 Z_0^{\parallel}(p\omega_0) \Big]. \quad (8.51)$$

Finally, assuming that the perturbation is small, the result simplifies to

$$\Delta\Omega = \frac{ie^2 N_b \eta}{2\beta^2 E_0 T_0^2 \omega_s} \sum_{p=-\infty}^{\infty} \Big[(p\omega_0 + \omega_s) Z_0^{\parallel}(p\omega_0 + \omega_s) - p\omega_0 Z_0^{\parallel}(p\omega_0) \Big]. \quad (8.52)$$

The above shift in synchrotron frequency gives exactly the same growth rate as Eq. (8.45) when the driving impedance is a narrow resonance. The only difference is the second term on the right side of Eq. (8.52). To understand this term, let us go back to the original equation of motion for the point-bunch. Comparing Eq. (8.46) with Eq. (8.8), it is straightforward to find the wake force on the right side of Eq. (8.46) originate from the substitution of the linear bunch density into Eq. (8.8) by

$$\lambda(\tau'; s) = \delta\big[\tau' - \tau(s - kC)\big], \quad (8.53)$$

which includes the unperturbed linear density

$$\lambda_0(\tau') = \delta(\tau'). \quad (8.54)$$

If we trace the derivation backward, it is easy to discover that the extra second term in Eq. (8.52) originates from the unperturbed linear density $\lambda_0(\tau')$. It therefore represents the incoherent synchrotron frequency shift of the super particle, and this is exactly the same expression obtained from Eqs. (2.89) and (2.92). Notice that since the bare synchrotron frequency ω_{s0} was used in Eq. (8.46), both the static and dynamic parts of the wake force would thus be necessary on the right side. However, if the potential-well distortion problem is first solved to obtain the incoherent synchrotron frequency ω_s, which is used to replace ω_{s0}, the right side will then involve only the dynamic part of of the wake force, or only the dynamic part of the linear bunch density

$$\lambda(\tau'; s)\Big|_{\text{dyn}} = \delta\big[\tau' - \tau(s - kC_0)\big] - \delta(\tau') \quad (8.55)$$

will be required. In that case the second term, or the incoherent-frequency-shift term, in Eq. (8.52) will not be present.

Now let us come back to Eq. (8.45). For M equal bunches, the expression becomes, for coupled-bunch mode μ,

$$\frac{1}{\tau_{1\mu}} = \frac{\eta e^2 N_b M \omega_r}{2\beta^2 E_0 T_0^2 \omega_s}\left[\mathcal{R}e\, Z_0^{\parallel}(qM\omega_0+\mu\omega_0+\omega_s) - \mathcal{R}e\, Z_0^{\parallel}(q'M\omega_0-\mu\omega_0-\omega_s)\right]. \quad (8.56)$$

When $\mu = 0$, both terms will contribute with $q' = q$ and we have exactly the same Robinson's stability or instability as in the single bunch situation. This is illustrated in Fig. 8.2. When $\mu = M/2$ if M is even, both terms will contribute with $q' = q$, and the same Robinson's stability or instability will apply. For the other $M-2$ modes, only one term will be at or close to the resonant frequency and only one term will contribute. If the positive-frequency term contributes, we have instability. If the negative-frequency term contributes, we have damping instead. If one chooses to speak in the language of only positive frequencies, there will be an upper and a lower synchrotron sideband surrounding each revolution harmonic. Above transition, the coupled-bunch system will be unstable if the driving resonance leans towards the upper sideband and stable if it leans towards the lower sideband.

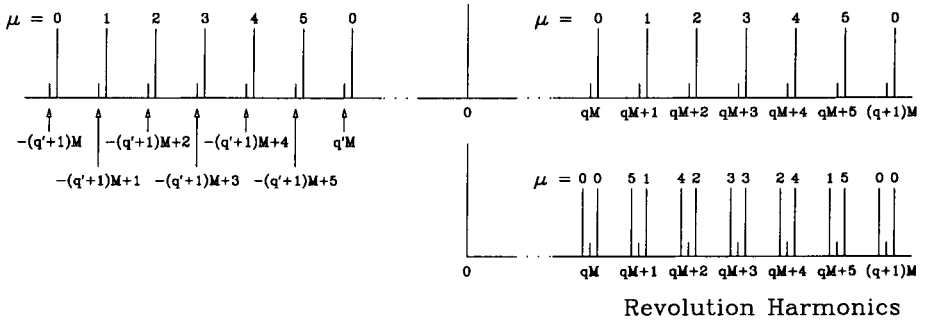


Fig. 8.2 Top plot shows the synchrotron lines for both positive and negative revolution harmonics for the situation of $M = 6$ identical equally-spaced bunches. The coupled-bunch modes $\mu = 0, 1, 2, 3, 4, 5$ are listed at the top of the synchrotron lines. Lower plot shows the negative-harmonic side folded onto the positive-harmonic side. We see upper and lower sidebands for each harmonic line.

For the higher azimuthal modes ($m > 1$) driven by a narrow resonance, we have the same Robinson's instability. The growth rates are

$$\frac{1}{\tau_{m\mu}} = \frac{\eta e^2 N_b M \omega_r}{2\beta^2 E_0 T_0^2 \omega_s}\frac{m}{(m!)^2}\left(\frac{\omega_r \hat{\tau}}{2}\right)^{2m-2} \times \left[\mathcal{R}e\, Z_0^{\parallel}(qM\omega_0+\mu\omega_0+m\omega_s) - \mathcal{R}e\, Z_0^{\parallel}(q'M\omega_0-\mu\omega_0-m\omega_s)\right], \quad (8.57)$$

which depend on the bunch length as $\hat{\tau}^{2m-2}$. As a result, higher azimuthal instabilities for short bunches will be much more difficult to excite. For long bunches, we need to evaluate the form factor F. An example will be discussed in Sec. 8.2.

Landau damping can come from the spread of the synchrotron frequency, which is the result of the nonlinear sinusoidal rf waveform. When the oscillation amplitude is small compared with the half width of the bucket, the shift in synchrotron frequency $\Delta\omega_s$ can be written analytically as (Exercise 8.5)

$$\frac{\Delta\omega_s}{\omega_s} = -\left(\frac{\pi^2}{16}\right)\left(\frac{1+\sin^2\phi_s}{1-\sin^2\phi_s}\right)(h\tau_L f_0)^2, \tag{8.58}$$

where τ_L is the total length of the bunch and ϕ_s is the synchronous angle. The mode will be stable if the growth rate without damping is smaller than the order of the synchrotron frequency spread. For the distribution $g_0(r) \propto (1-r^2)^2$, Sacherer gives the stability criterion [2]

$$\Delta\omega_{m\mu} \lesssim \frac{\sqrt{m}}{4}\Delta\omega_s. \tag{8.59}$$

where $\Delta\omega_{m\mu}$ is the dynamic part of the coherent synchrotron frequency shift. The spread in synchrotron frequency for any oscillation amplitude can be derived analytically when $\Gamma = \sin\phi_s = 0$. When the synchronous angle $\phi_s \neq 0$ or π, however, the computation becomes tedious. A numerical calculation of spread in synchrotron frequency is shown in Fig. 8.3 for various $\Gamma = \sin\phi_s$ (Exercise 8.6). The Γ-dependency in Eq. (8.58) comes from a fitting to the numerical calculation at small amplitudes.

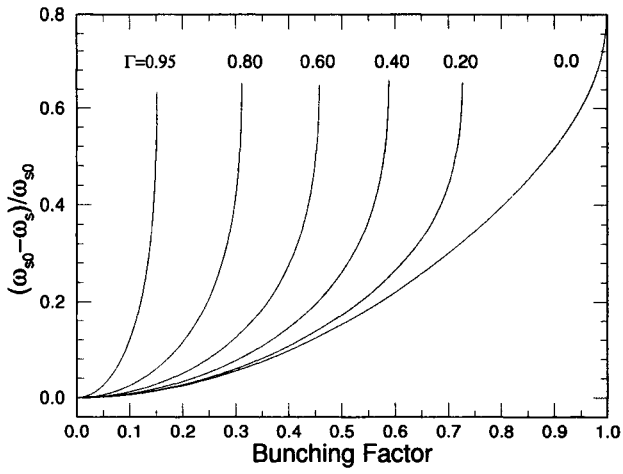


Fig. 8.3 Synchrotron frequency spread $(\omega_{s0} - \omega_s)/\omega_{s0}$ as a function of single-bucket bunching factor $B = \tau_L f_0$ for various values of $\Gamma = \sin\phi_s$. τ_L is full bunch length, f_0 is revolution frequency, ϕ_s is synchronous angle, and ω_{s0} is unperturbed angular synchrotron frequency.

8.2 Time Domain Derivation

The longitudinal coupled-bunch instabilities can also be studied without going into the frequency domain. We are employing the same Vlasov equation in Eq. (8.7), but using the wake function of a resonance in the time domain. This derivation was first given by Sacherer. [2] It is worthwhile to go through the derivation and the interpretation of the result.

The wake function for a resonance with resonant frequency $\omega_r/(2\pi)$, shunt impedance R_s and quality factor Q was given in Eq. (1.83). For a narrow resonance with $\alpha = \omega_r/(2Q) \ll \omega_r$, we can neglect the sine term[¶] and simplify the wake function to

$$W_0'(z) = \frac{\omega_r R_s}{Q} e^{-\alpha z/v} \cos\frac{\omega_r z}{v} \qquad \text{when } z > 0. \tag{8.60}$$

The wake force is then given by

$$\langle F_0^{\parallel}(\tau; s)\rangle_{\rm dyn} = -\frac{e^2\omega_r R_s N_b}{QC_0}\int_{\tau}^{\infty} d\tau'\, e^{-\alpha(\tau'-\tau)}\cos[\omega_r(\tau'-\tau)]\,\lambda_1\,[\tau'; s - v(\tau'-\tau)]\,, \tag{8.61}$$

where $\lambda_1\,[\tau'; s - v(\tau'-\tau)]$ is the dynamic part of the linear density of the beam particles passing the location s at time $\tau' - \tau$ ago. Now let $\lambda_{10}(\tau; s)$ represent the line density of the 0th bunch, which has a phase lag of $2\pi\mu/M$ for mode μ compared with the preceding bunch $\tau_{\rm sep} = T_0/M$ ahead, and is influenced by all the preceding bunches. The location argument s of λ in Eq. (8.61) becomes[‖] $s - kv\tau_{\rm sep} - v(\tau'-\tau)$, with $k = 0,\ 1,\ 2,\ \cdots$. For simplicity, we neglect the time delay $\tau'-\tau$. In the time variation $e^{-i\Omega s/v}$ where $\Omega \approx m\omega_s$, this approximation causes a phase delay $\Omega(\tau'-\tau)$ which is negligible in comparison with the phase change due to the resonator. We will also neglect the variation in the attenuation factor over one bunch $e^{-\alpha(\tau'-\tau)}$, but we retain the attenuation factor between bunches $e^{-\alpha k\tau_{\rm sep}}$. Then the wake force exerted on a particle in the μth coupled-bunch mode can be written as

$$\langle F_{0\mu}^{\parallel}(\tau; s)\rangle_{\rm dyn} = -\frac{e^2\omega_r R_s N_b}{QC_0}\sum_{k=0}^{\infty} e^{i2\pi k\mu/M - k\alpha\tau_{\rm sep}} \times \int_{\substack{\text{one}\\ \text{bunch}}} d\tau'\cos[\omega_r(\tau'-\tau+k\tau_{\rm sep})]\,\lambda_{10}(\tau')e^{-i\Omega(s/v - k\tau_{\rm sep})}, \tag{8.62}$$

[¶]The sine term can be included at the expense of a slightly more complicated derivation.

[‖]Here we include the term $k\tau_{\rm sep}$ which Sacherer had left out. This term is important to exhibit Robinson's damping criterion of stability.

where Eq. (8.10), the 'time' variations of preceding bunches in the μth coupled mode, have been used. It is worth pointing out that the lower limits of the summation and integration *cannot* be extended to $-\infty$ as before, because the explicit expression of the wake function, that does not possess the causal restriction, has been substituted.

The bunch distribution is now expanded in azimuthal harmonics in the longitudinal phase space according to Eq. (8.6). Changing the integration variables from $(\tau, \Delta E)$ to (r, ϕ) using the transformation in Eq. (8.1), the perturbed linear density of the bunch can be expressed as

$$\begin{aligned}\lambda_{10}(\tau')d\tau' &= \sum_m \int \alpha_m R_m(r') e^{im\phi'} d\tau' d\Delta E' \\ &= \sum_m \int \frac{E_0 \omega_s \beta^2}{\eta} \alpha_m R_m(r') e^{im\phi'} r' dr' d\phi'. \end{aligned} \tag{8.63}$$

Substituting λ_{10} and the wake force into Eq. (8.7) and assuming that the perturbation is small so that different azimuthals do not couple, we arrive at

$$\begin{aligned}(\Omega_{m\mu} - m\omega_s) R_m(r) = \frac{ie^2 N_b \eta \omega_r R_s}{2\pi\beta^2 E_0 Q T_0 \omega_s} \frac{dg_0}{dr} \sum_{k=0}^{\infty} e^{i2\pi k\mu/M - k(\alpha - i\Omega)\tau_{\rm sep}} \\ \times \int_0^{\infty} r' dr' R_m(r') \int_{-\pi}^{\pi} d\phi\, e^{-im\phi} \sin\phi \int_{-\pi}^{\pi} d\phi' e^{im\phi'} \cos[\omega_r(r'\cos\phi' - r\cos\phi + k\tau_{\rm sep})], \end{aligned} \tag{8.64}$$

where again we have used the unperturbed distribution $g_0(r)$ defined by Eq.(8.28) which is normalized to unity. The integrations over ϕ and ϕ' can now be performed using the properties of Bessel functions depicted in Eqs. (8.24)–(8.26), resulting the relation

$$\begin{aligned}\int_{-\pi}^{\pi} d\phi\, e^{-im\phi} \sin\phi \int_{-\pi}^{\pi} d\phi' e^{im\phi'} \cos[\omega_r(r'\cos\phi' - r\cos\phi + k\tau_{\rm sep})] \\ = i4\pi^2 \sin(k\omega_r \tau_{\rm sep}) \frac{m J_m(\omega_r r') J_m(\omega_r r)}{\omega_r r}. \end{aligned} \tag{8.65}$$

Now Eq. (8.64) has been simplified tremendously and takes the form

$$\begin{aligned}(\Omega_{m\mu} - m\omega_s) R_m(r) = -\frac{2\pi e^2 N_b R_s m\eta}{\beta^2 E_0 Q T_0 \omega_s} \frac{dg_0}{dr} \\ \times \sum_{k=0}^{\infty} e^{i2\pi k\mu/M - k(\alpha - i\Omega)\tau_{\rm sep}} \sin(k\omega_r \tau_{\rm sep}) \int_0^{\infty} dr' R_m(r') \frac{r' J_m(\omega_r r') J_m(\omega_r r)}{r}. \end{aligned} \tag{8.66}$$

Finally, we introduce Landau damping by allowing the incoherent synchrotron frequency to be a function of the radial distance from the center of the bunch in the longitudinal phase space. Moving $\Omega_{m\mu}-m\omega_s(r)$ to the right side and performing an integration over rdr, R_m can be eliminated resulting in the dispersion relation

$$1 = -\frac{i2\pi e^2 M N_b m\eta R_s}{\beta^2 E_0 T_0^2 \omega_s \omega_r} D(\alpha\tau_{\rm sep}) \int_0^\infty dr \frac{dg_0}{dr} \frac{J_m^2(\omega_r r)}{\Omega_{m\mu}-m\omega_s(r)}, \tag{8.67}$$

where we have defined the function**

$$D(\alpha\tau_{\rm sep}) = -i2\alpha\tau_{\rm sep} \sum_{k=0}^{\infty} e^{i2\pi k\mu/M - k(\alpha-i\Omega)\tau_{\rm sep}} \sin(k\omega_r\tau_{\rm sep}), \tag{8.68}$$

which contains all the information about the quality factor of the resonance and its location with respect to the revolution harmonics. It is interesting to note that Eq. (8.67) closely resembles Eq. (8.32). It will be shown below that $D = 1$ for a narrow resonance with the resonant peak located at $(qM+\mu)\omega_0 + m\omega_s$. Thus the two dispersion relations are identical. In fact, they are the same even when the resonant peak is not exactly located on top of a synchrotron line.

Let us study the function $D(\alpha\tau_{\rm sep})$. Noting that the bunch separation is $\tau_{\rm sep} = T_0/M$, the summation over k in Eq. (8.68) can be performed resulting in the function

$$D(\alpha\tau_{\rm sep}) = \alpha\tau_{\rm sep}\left(\frac{1}{1-e^{x+}} - \frac{1}{1-e^{x-}}\right), \tag{8.69}$$

where

$$x_\pm = \frac{i2\pi}{M}\left(q_\pm M + \mu + m\frac{\omega_s}{\omega_0} \mp \frac{\omega_r}{\omega_0}\right) - \alpha\tau_{\rm sep}. \tag{8.70}$$

The $q_\pm M$ term comes about because we can replace μ in Eq. (8.68) by $q_\pm M+\mu$, where $q_\pm$ are positive/negative integers and $\mu = 0,\ 1,\ \cdots,\ M-1$. When the resonance is extremely narrow, we have $\alpha\tau_{\rm sep} = \omega_r\tau_{\rm sep}/(2Q) \ll 1$. The two terms in Eq. (8.69) almost cancel each other so that $D(\alpha\tau_{\rm sep}) \approx 0$ unless $\omega_r \approx (|q_\pm|M \pm \mu)\omega_0$. For modes $\mu \neq 0$ and $\mu \neq \frac{1}{2}M$ if M is even, only one of the two terms in Eq. (8.69) contributes. If $\omega_r \approx (|q_\pm|M \pm \mu)\omega_0 \pm m\omega_s$, we have $|x_+| \ll 1$ or $|x_-| \ll 1$ and

$$D(\alpha\tau_{\rm sep}) \approx \mp\frac{\alpha\tau_{\rm sep}}{x_\pm} = \frac{-i\omega_r/(2Q)}{\omega_r - [(|q_\pm|M \pm \mu)\omega_0 \pm m\omega_s] \mp i\omega_r/(2Q)} \approx \pm 1. \tag{8.71}$$

**We would like $D = \pm 1$ when the resonance is at the upper/lower sideband. As a result, our definition of D differs from Sacherer's by a phase.

When $\mu = 0$ or $\mu = M/2$ if M is even, it is possible to choose q_+ and q_- so that both terms will contribute. We have

$$D \approx \frac{-i\omega_r/(2Q)}{\omega_r - [(q_+M+\mu)\omega_0 + m\omega_s] - i\omega_r/(2Q)} + \frac{-i\omega_r/(2Q)}{\omega_r - [(|q_-|M-\mu)\omega_0 - m\omega_s] + i\omega_r/(2Q)}, \tag{8.72}$$

where $q_+ = |q_-|$ for $\mu = 0$ and $|q_-| = q_+ + 1$ for $\mu = M/2$. Note that Eq. (8.72) is just proportional to the difference between $Z_0^{\parallel}(q_+M\omega_0 + \mu\omega_0 + m\omega_s + i\alpha)$ and $Z_0^{\parallel}(|q_-|M\omega_0 - \mu\omega_0 - m\omega_s - i\alpha)$; the Robinson's stability damping criterion derived in Eq. (8.56) is therefore recovered.

On the other hand, when the resonance is broad, $\alpha\tau_{\text{sep}} \gg 1$. The first few terms in Eq. (8.68) dominate. Since $k = 0$ does not contribute, we include here only the next term,

$$D(\alpha\tau_{\text{sep}}) \approx -i2\alpha\tau_{\text{sep}} \sin(\omega_r\tau_{\text{sep}}) e^{i2\pi\mu/M - \alpha\tau_{\text{sep}}}. \tag{8.73}$$

The magnitude $|D|$ becomes mode-independent and exhibits a maximum when $\omega_r\tau_{\text{sep}} = 2\pi\left(q + \frac{1}{4}\right)$. Thus the coupled-bunch modes near $\mu = \pm\frac{1}{4}M$ are most strongly excited, although $|D|$ will be much less than unity. Figure 8.4 plots $|D|$ versus ω_r/ω_0 for the situation of $M = 10$ bunches. The solid vertical lines show

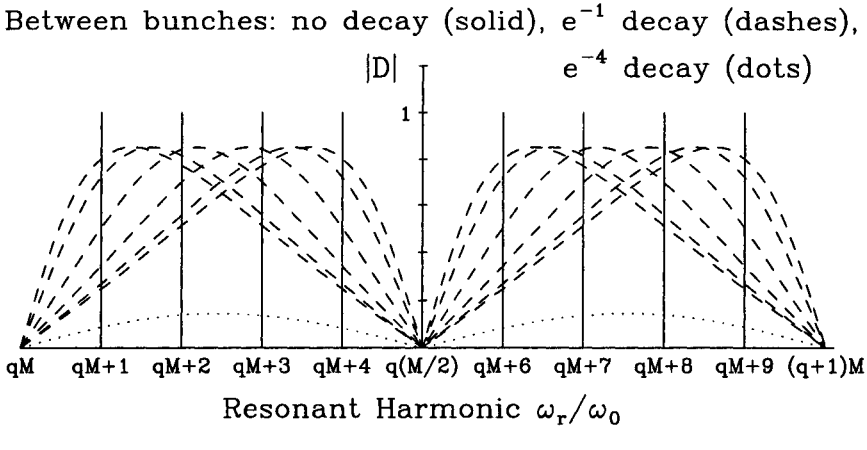


Fig. 8.4 $|D|$ as functions of resonant harmonic ω_r/ω_0 for $M = 10$ bunches when bunch-to-bunch decay decrement $\alpha\tau_{\text{sep}} \ll 1$ for narrowband resonance (solid), $\alpha\tau_{\text{sep}} = 4$ for broadband resonance (dots), and $\alpha\tau_{\text{sep}} = 1$ for resonance in between (dashes). The dashed curves from left to right represent coupled-bunch modes $\mu = 0$, 1 and 9, 2 and 8, 3 and 7, 4 and 6, 5. The excitations at $\omega_r/\omega_0 = 0$, or $M/2$ are zero, because we have set the synchrotron frequency to zero in the plot. (Courtesy Sacherer. [2])

$|D| \approx 1$ for narrow resonance. The dotted curve are for broadband resonance when the bunch-to-bunch attenuation decrement is $\alpha\tau_{\text{sep}} = 4$; the values of $|D|$ are small and appear to be mode-independent. The dashed curves correspond the intermediate case with bunch-to-bunch attenuation decrement $\alpha\tau_{\text{sep}} = 1$. From left to right, they are for modes $\mu = 0$, 1 and 9, 2 and 8, 3 and 7, 4 and 6, 5. We see that $|D|_{\max}$ is roughly the same for each mode. Note that $\alpha\tau_{\text{sep}} = 1$ translates into $(\Delta\omega_r/\omega_0)_{\text{FWHM}} = M/\pi = 3.2$ or the resonance covers more than three revolution harmonics. Apparently, the figure shows that no mode will be excited if the ω_r/ω_0 falls exactly on qM or $\frac{1}{2}qM$ if M is even. This incorrect result appears because in drawing the plot, the limit $\omega_s \to 0$ has been taken. Figure 8.5 plots $|D|_{\max}$ versus the bunch-to-bunch decrement $\alpha\tau_{\text{sep}}$, showing that it is less than 5% from unity when $\alpha\tau_{\text{sep}} < 0.55$.

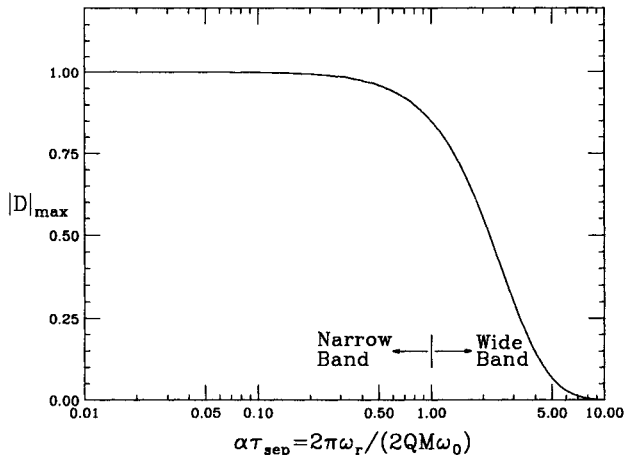


Fig. 8.5 $|D|_{\max}$ as a function of bunch-to-bunch decay decrement $\alpha\tau_{\text{sep}}$. Note that $|D|_{\max} \approx 1$ for narrow resonances but drops very rapidly as the resonance becomes broader. (Courtesy Sacherer. [2])

In the event that the spread in synchrotron frequency is small, we can obtain from Eq. (8.67) the synchrotron frequency shift

$$\Omega_{m\mu} - m\omega_s = -\frac{i2\pi e^2 N_b R_s m M \eta}{\beta^2 E_0 \omega_s \omega_r T_0^2} D(\alpha\tau_{\text{sep}}) \int_0^\infty dr \frac{dg_0}{dr} J_m^2(\omega_r r), \tag{8.74}$$

where the integral can be viewed as a form factor which is distribution-dependent. A dimensionless form factor

$$F_m(\Delta\phi) = -\frac{4\pi m \hat{\tau}}{\omega_r} \int_0^\infty dr \frac{dg_0}{dr} J_m^2(\omega_r r) \tag{8.75}$$

can now be defined for each azimuthal, where $\hat{\tau}$ is the half bunch length and $\Delta\phi = 2\omega_r\hat{\tau}$ is the change in phase of the resonator during the passage of the

whole bunch. Then the frequency shift can be rewritten as

$$\Omega_{m\mu} - m\omega_s = \frac{i\eta e^2 N_b M R_s}{4\pi\beta^2 E_0 \nu_s T_0 \hat{\tau}} D(\alpha\tau_{\rm sep}) F_m(\Delta\phi), \tag{8.76}$$

where $\nu_s = \omega_s/\omega_0$ is the synchrotron tune.

We take as an example the *parabolic* distribution in the longitudinal phase space,[††] which implies

$$g_0(r) = \frac{2}{\pi\hat{\tau}^4}(\hat{\tau}^2 - r^2) \qquad \text{and} \qquad \frac{dg_0}{dr} = -\frac{4r}{\pi\hat{\tau}^4}. \tag{8.77}$$

The integral can be performed analytically giving the form factor

$$F_m(\Delta\phi) = \frac{32m}{\Delta\phi}\int_0^1 J_m^2\left(\tfrac{1}{2}x\Delta\phi\right)x\,dx = \frac{16m}{\Delta\phi}\left[J_m^2\left(\tfrac{1}{2}\Delta\phi\right) - J_{m+1}\left(\tfrac{1}{2}\Delta\phi\right)J_{m-1}\left(\tfrac{1}{2}\Delta\phi\right)\right], \tag{8.78}$$

which is plotted in Fig. 8.6 for $m = 1$ to 6. The form factor specifies the efficiency with which the resonator can drive a given mode. We see that the maximum value of F_1 for the dipole mode occurs when $\Delta\phi \approx \pi$. This is to be expected because the head and tail of the bunch will be driven in opposite directions. Similarly, the quadrupole or breathing mode is most efficiently driven when $\Delta\phi \approx 2\pi$, and so on for the higher modes. In general, mode m is most efficiently driven when the resonator frequency is $\Delta\phi \approx m\pi$. Note also that the maximum value of F_m drops faster than $m^{-1/2}$, implying that higher azimuthal modes are harder to excite. For distributions other than the "parabolic" of Eq. (8.77), we

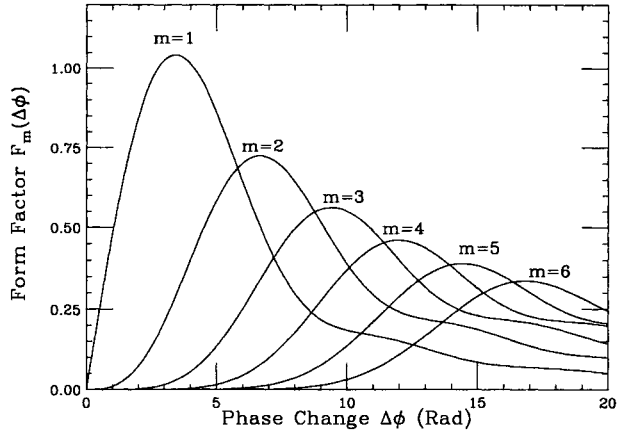


Fig. 8.6 Sacherer's form factor for longitudinal oscillation inside a bunch with azimuthal modes $m = 1$, 2, 3, 4, 5 and 6. The unperturbed parabolic distribution in the longitudinal phase space, Eq. (8.77), is assumed. (Courtesy Sacherer. [2])

[††]This is different from the so-called parabolic distribution, which is actually parabolic line density.

expect the form factors to have similar properties. However, a shorter bunch does not necessarily imply a slower growth especially for the $m = 1$ mode, although the excitation in the form factor $F_m(\Delta\phi)$ is small. According to Eq. (8.76), the growth rate is obtained from multiplying the form factor $F_m(\Delta\phi)$ with $eN_b/\hat{\tau}$, the local linear charge density or peak current. In fact, as the bunch length is shortened but with a fixed number of particles in the bunch, the local linear charge density increases, thus enhancing the growth rate. As a result, a more practical form factor should be $\bar{F}_m(\Delta\phi) = 2F_m(\Delta\phi)/\Delta\phi$ as plotted in Fig. 8.7 in logarithmic scale. It is clear that for small $\Delta\phi$, $F_1 \approx \frac{1}{2}\Delta\phi$ and $\bar{F}_1 \approx 1$. From Eq. (8.74), we obtain the growth rate for the dipole mode above transition,

$$\frac{1}{\tau_1} = \mathcal{I}m\,\Omega = \frac{\eta e^2 N_b M R_s \omega_r}{2\beta^2 E_0 \omega_s T_0^2} D(\alpha\tau_{\rm sep}), \tag{8.79}$$

which agrees with the expression in Eq. (8.56) derived for short bunches. It is also evident from Fig. 8.7 that the excitations of higher azimuthal modes will be very much smaller.

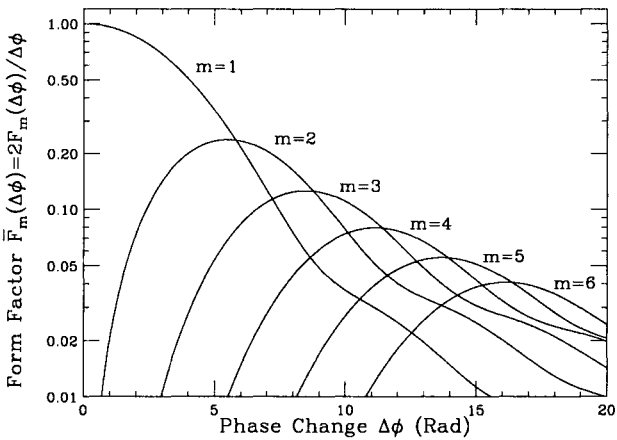


Fig. 8.7 A more useful form factor $\bar{F}(\Delta\phi)$ in logarithmic scale for longitudinal oscillation inside a bunch with azimuthal modes $m = 1$, 2, 3, 4, 5 and 6. The unperturbed parabolic distribution in the longitudinal phase space is assumed. It is related to the Sacherer's form factor of Fig. 8.6 by $\bar{F}(\Delta\phi) = 2F(\Delta\phi)/\Delta\phi$.

8.3 Observation and Cures

The easiest way to observe longitudinal coupled-bunch instability is in a mountain-range plot, where bunches oscillate in a particular pattern as time advances. Examples are shown in Fig. 8.8. Streak camera can also be used to capture the phases of adjacent bunches as functions of time. From the pattern of coupling, the coupled-mode μ can be determined. From the frequency of oscillation, the azimuthal mode m can also be determined. We can then pin down

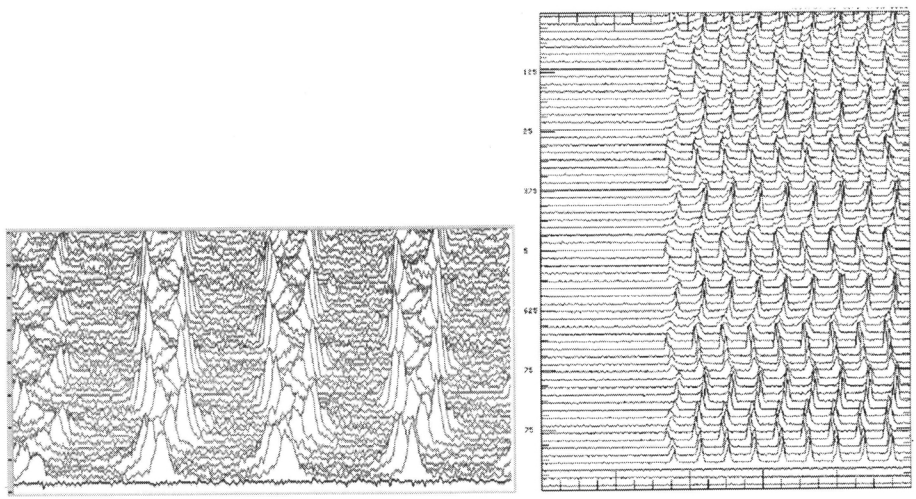


Fig. 8.8 Both mountain-range plots showing coupled-bunch instability in the Fermilab Main Injector just after injection at 8 GeV. Time goes upwards.

the frequency $\omega_r/(2\pi)$ of the offending resonance driving the instability.

Observation can also be made in the frequency domain by zooming in the excitation spectrum of the beam in the region between two rf harmonics in the way illustrated in Fig. 8.2. The coupled-bunch mode excited will be shown as a strong spectral line in between.

Longitudinal coupled-bunch instability will lead to an increase in bunch length and an increase in energy spread. For a light source, this translates into an increase in the spot size of the synchrotron light, which is usually unacceptable.

There are many ways to cure longitudinal coupled bunch instability. The driving resonances are often the higher-order modes inside the rf cavities. When the particular resonance is identified and if it is much narrower than the revolution frequency of the ring, we can try to shift its frequency so that it resides in between two revolution harmonics and becomes invisible to the beam particles. We can also study the electromagnetic field pattern of this resonance mode inside the cavity and install passive resistors and antennae to damp this particular mode. This method has been used widely in the Fermilab Booster, where longitudinal coupled-bunch instability had been very severe after the beam passed the transition energy resulting in emittance growth. At one time, the longitudinal emittance at 1.7×10^{01} per bunch grew from 0.035 eV-s around transition to more than 0.125 eV-s near extraction. The bunch area was also found to increase almost linearly with bunch intensity. Passive damping of several of-

fending modes cured this instability to such a point that the bunch area does not increase with bunch intensity anymore, even with intensity up to $3\text{–}4 \times 10^{10}$ per bunch. [3]

Longitudinal coupled-bunch instability had also been observed in the former Fermilab Main Ring. Besides passive damping of the cavity resonant modes, the instability was also reduced by lowering the rf voltage. Lowering the rf voltage will lengthen the bunch and reduce the form factor $\bar{F}_m(\Delta\phi)$. This is only possible for a proton machine where the bunches are long. It will not work for the short electron bunches for the $m = 1$ dipole mode. This is because, as mentioned before, the form factor for the dipole mode is not sensitive to the bunch length for short bunches. Even for a proton machine, the rf voltage cannot be reduced by a large amount because proton bunches are usually rather tight inside the rf bucket, especially during ramping. A lower rf voltage on a proton bunch implies lower energy spread of the beam. When the energy spread is low enough, Keil–Schnell type longitudinal single-bunch microwave instability will be induced.

If the growth turns out to be harmful, a fast bunch-by-bunch damper may be necessary to damp the dipole mode ($m = 1$). A damper for the quadrupole mode ($m = 2$) may also be necessary. This consists essentially of a wall-gap pickup monitoring the changes in bunch length and the corresponding excitation of a modulation of the rf waveform with roughly twice the synchrotron frequency. A feedback correction is then made to the rf voltage. Another way to damp the longitudinal coupled-bunch instability is to break the symmetry between the M bunches. For example, a 5% to 10% variation in the intensity of the bunches will help. The symmetry can also be broken by having bunches not placed symmetrically in the ring. Some analysis shows that the stability will be improved if some bunches in the symmetric configuration are missing. [4] Prabhakar [5] recently proposed a new way to cure longitudinal coupled-bunch instability using uneven fill in a storage ring. We are going to discuss this method in more detail in Sec. 8.3.4.

There can also be Landau damping, which comes from the spread of the synchrotron frequency. The spread due to the nonlinear sinusoidal rf wave form as given by Eq. (8.58) is usually small unless the synchronous angle is large. Electron bunches are usually much smaller in size than the rf bucket. As a result, the spread in synchrotron frequency can be very minimal and does not help much in Landau damping.

8.3.1 *Higher-Harmonic Cavity*

As we have learned, the spread of synchrotron frequency for beam particles inside a bunch comes from the nonlinearity of the sinusoidal rf wave and is therefore small. Such small spread is usually not sufficient to provide enough Landau damping to collective instabilities. More nonlinearity in the rf waveform is thus required to widen the spread in synchrotron frequency inside the bunch to ensure the damping of longitudinal coupled-bunch instabilities. One way to do this is to install a higher-harmonic cavity, sometime known as *Landau cavity*, [6] because it provides Landau damping. For example, the higher-harmonic cavity has resonant angular frequency $m\omega_{\rm rf}$ and voltage $rV_{\rm rf}$, where $\omega_{\rm rf}$ is the resonant angular frequency and $V_{\rm rf}$ the voltage of the fundamental rf cavity, and r is a parameter to be determined. The total rf voltage experienced by the beam particles becomes

$$V(\tau) = V_{\rm rf}\left[\sin(\phi_s - \omega_{\rm rf}\tau) - r\sin(\phi_m - m\omega_{\rm rf}\tau)\right] - \frac{U_s}{e}, \tag{8.80}$$

where the phase angles ϕ_s and ϕ_m are chosen to compensate for U_s, the radiation energy loss of the synchronous particle, or to provide any required acceleration. Here, the contribution of the wake force is neglected, and so is the variation of U_s with energy.

We would like the bottom of the potential well, which is the integral of $V(\tau)$, to be as flat as possible. The rf voltage seen by the synchronous particle is compensated to zero by the energy lost to synchrotron radiation. In addition, we further require

$$\left.\frac{\partial V}{\partial \tau}\right|_{\tau=0} = 0 \qquad \text{and} \qquad \left.\frac{\partial^2 V}{\partial \tau^2}\right|_{\tau=0} = 0, \tag{8.81}$$

so that the potential becomes quartic instead. We therefore have three equations in three unknowns:

$$\sin\phi_s = r\sin\phi_m + \frac{U_s}{eV_{\rm rf}}, \tag{8.82}$$

$$\cos\phi_s = rm\cos\phi_m, \tag{8.83}$$

$$\sin\phi_s = rm^2\sin\phi_m, \tag{8.84}$$

from which ϕ_m and r can be solved easily (Exercise 8.7). For small-amplitude oscillation, the potential becomes

$$-\int V(\tau)d(\omega_{\rm rf}\tau) \longrightarrow \frac{m^2-1}{24}(\omega_{\rm rf}\tau)^4 V_{\rm rf}\cos\phi_s, \tag{8.85}$$

which is quartic and the synchrotron frequency is (Exercise 8.8)

$$\frac{\omega_s(\tau)}{\omega_{s0}} = \frac{\pi}{2}\left(\frac{m^2-1}{6}\right)^{1/2} \frac{\omega_{\rm rf}|\tau|}{K\left(\frac{1}{\sqrt{2}}\right)} \left[\frac{1-\left(\dfrac{m^2}{m^2-1}\dfrac{U_s}{eV_{\rm rf}}\right)^2}{1-\left(\dfrac{U_s}{eV_{\rm rf}}\right)^2}\right]^{1/4}, \tag{8.86}$$

where the last factor can usually be neglected; its deviates from unity by only $\sim [(m^2-1)U_s/(2eV_{\rm rf})]^2$ if the synchronous angle is small. In above, ω_{s0} is the synchrotron angular frequency at zero amplitude when the higher-harmonic cavity voltage is turned off, and $K(1/\sqrt{2}) = 1.854$ is the complete elliptic integral of the first kind which is defined as

$$K(t) = \int_0^{\pi/2} \frac{d\theta}{\sqrt{1-t^2\sin^2\theta}}. \tag{8.87}$$

We see that the synchrotron frequency is zero at zero amplitude and increases linearly with amplitude. This large spread in synchrotron frequency may be able to supply ample Landau damping to the longitudinal coupled-bunch instabilities.

In the situation where there is no radiation loss and no acceleration, $U_s = 0$, the solution of Eqs. (8.82) to (8.84) simplifies, giving $\phi_s = \phi_m = 0$ and the ratio of the voltages of higher-harmonic cavity to the fundamental $r = 1/m$. Of course, it is also possible to have $r \neq 1/m$. Then the synchrotron frequency at the zero amplitude will not be zero and the spread in synchrotron frequency can still be appreciable. When $m = 2$, i.e., having a second-harmonic cavity, the mathematics simplifies. The synchrotron frequencies for various values of r are plotted in Fig. 8.9. Here, $r = 0$ implies having only the fundamental rf while $r = \frac{1}{2}$ the situation of having the synchrotron frequency linear in amplitude for small amplitudes. In between, the synchrotron frequency spread decreases as r decreases. Notice that for $0.3 \lesssim r < 0.5$, the synchrotron frequency has a maximum near the rf phase of $\sim 100°$. Particles near there will have no Landau damping at all and experience instability. Thus the size of the bunch is limited when a double cavity is used. Also the size of the bunch cannot be too small because of two reasons: first, the average synchrotron frequency may have been too low, and second, the central region of the phase space is a sea of chaos [8]

A Landau cavity increases the spread in synchrotron frequency, therefore it is ideal in damping mode-coupling instability and coupled-bunch instability. However, it may be not helpful for the Keil–Schnell type longitudinal microwave instability, which is valid for coasting beams. This method was first applied successfully with a third-harmonic cavity to increase Landau damping at the Cambridge Electron Accelerator (CEA). [9] It was later applied to the Inter-

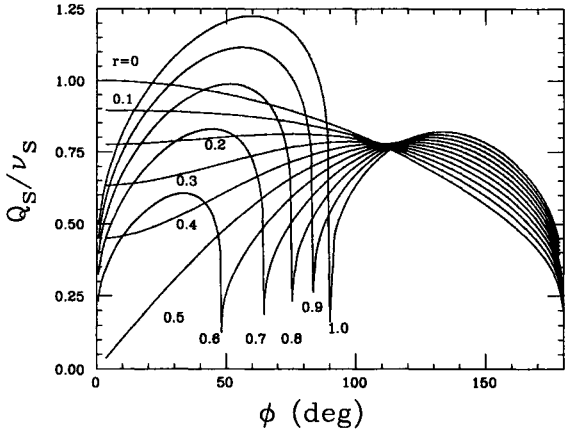


Fig. 8.9 The normalized synchrotron tune of a double rf system as a function of the peak rf phase ϕ for various voltage ratio r. Here, the higher-harmonic cavity has frequency twice that of the fundamental. When $r > \frac{1}{2}$, the center of the bucket becomes an unstable fixed point and two stable fixed points emerge. (Courtesy S. Y. Lee, *et al.* [8])

secting Storage Ring (ISR) at CERN using sixth harmonic cavity to cure mode-coupling instability. [10] Recently, a third-harmonic cavity has been reported in the SOLEIL ring in France to give a relative frequency spread of about 200%. However, since the center frequency has been dramatically decreased but not exactly to zero, the net result is a poor improvement in the stabilization. The gain in the stability threshold has been only 30%. [7]

Actually, with a higher-harmonic cavity, the bunch in the flat-bottom potential well becomes more rectangular-like in the longitudinal phase space, or particles are not so concentrated at the center of the bunch. Assuming the bunch area to be the same, the Boussard-modified Keil–Schnell threshold is proportional to the energy spread. Since the bunch becomes more flattened, the maximum energy spread at the center of the bunch is actually reduced, and so will be the instability threshold. However, spreading out the particles longitudinally does help to increase the bunching factor and decrease the incoherent self-field or space-charge tune shift. At the CERN Proton Synchrotron Booster, an rf system with higher harmonics $h = 5$ to 10 has raised the beam intensity by about 25 to 30%. [11] For the Cooler Ring at the Indiana University Cyclotron Facility, a double cavity has been able to quadruple the beam intensity [8]. As the bunch is lengthened, Landau cavities are also employed to suppress coupled-bunch instabilities and increase the Touchek lifetime. [13]

8.3.2 *Passive Landau Cavity*

Higher-harmonic cavities are useful in producing a large spread in synchrotron frequency so that single-bunch mode-mixing instability and coupled-bunch instability can be damped. However, the power source to drive this higher-harmonic

rf system can be rather costly. One way to overcome this is to do away with the power source and let the higher-harmonic cavity be driven by the beam-loading voltage of the circulating beam.

Let the ratio of the resonant frequencies of the higher-harmonic cavity to the fundamental rf cavity be m and the rf harmonic of the fundamental rf cavity be h. If the higher-harmonic cavity has a high quality factor, the beam-loading voltage is just i_b, the current component at the cavity resonant frequency, multiplied by the impedance of the cavity. Here, for a Gaussian bunch

$$i_b = 2I_0 e^{-\frac{1}{2}(mh\omega_0\sigma_\tau)^2}, \tag{8.88}$$

where σ_τ is the rms bunch length and ω_0 is the angular revolution frequency. Thus for a short bunch, $i_b \approx 2I_0$ with I_0 being the average current of the bunch.

The higher-harmonic cavity must have suitable shunt impedance R_h and quality factor Q_h, and this can be accomplished by installing necessary resistor across the cavity gap. We have used the subscript h to denote parameters for the higher-frequency cavity. Thus, R_h and Q_h can be referred to as the loaded quantities of the cavity. For a particle arriving at time τ ahead of the synchronous particle, it sees the total voltage

$$V(\tau) = V_{\rm rf}\sin(\phi_s - \omega_{\rm rf}\tau) - i_b R_h \mathcal{R}e\left[\frac{1}{1+i2Q_h\delta}e^{im\omega_{\rm rf}\tau}\right] - \frac{U_s}{e}, \tag{8.89}$$

where $\omega_{\rm rf} = h\omega_0$ is the angular rf frequency determined by the resonator in the rf klystron that drives the fundamental rf cavity and the negative sign in front of i_b indicates that this beam-loading voltage is induced by the image current and opposes the beam current. In above,

$$\delta = \frac{1}{2}\left(\frac{\omega_r}{m\omega_{\rm rf}} - \frac{m\omega_{\rm rf}}{\omega_r}\right) \approx \frac{\omega_r - m\omega_{\rm rf}}{\omega_r} \tag{8.90}$$

represents the deviation of the resonant angular frequency ω_r of the higher-harmonic cavity from the mth multiple of the rf angular frequency. Of course, this is related to the detuning angle ψ_h of the higher-harmonic cavity, which we introduce in the usual way as

$$\tan\psi_h = 2Q_h\delta. \tag{8.91}$$

Some comments are in order. We have chosen $t = 0$ as the time the synchronous particle passing through the fundamental and Landau cavity. The beam current phasor in the Landau cavity varies according to $e^{-im\omega_{\rm rf}t}$. Thus for the particle that arrives τ earlier, it sees the voltage across the Landau cavity with the extra phase $e^{im\omega_{\rm rf}\tau}$. The double-rf system is so adjusted that the synchronous

particle will not be gaining or losing energy in one revolution turn. In other words, $V_{\rm rf}\sin\phi_s$ will just cancel the radiation loss per turn U_s/e plus the beam-loading voltage in the Landau cavity $i_b R_h\,\mathcal{R}e(1+i2Q_h\delta)^{-1}$. Thus for a particle that arrives at the cavities with a time advance τ, the particle will experience an extra voltage in the fundamental cavity and an extra voltage in the Landau cavity, as represented, respectively, by the first and second terms on the right side of Eq. (8.89).

Since the beam is seeing the total rf voltage in the direction of the beam only, this voltage component evaluated from Eq. (8.89) is,

$$V_{\rm beam}(\tau) = V_{\rm rf}\sin(\phi_s - \omega_{\rm rf}\tau) - i_b R_h\cos\psi_h\cos(\psi_h - m\omega_{\rm rf}\tau) - \frac{U_s}{e}. \tag{8.92}$$

Again to acquire the largest spread in synchrotron frequency, we require

$$V_{\rm beam}(0) = 0, \quad V'_{\rm beam}(0) = 0, \quad V''_{\rm beam}(0) = 0, \tag{8.93}$$

so that the rf potential for small amplitudes becomes quartic,

$$U(\tau) = -\int V_{\rm beam}(\tau)d\tau = -\frac{\tau^4}{4!}V'''_{\rm beam}(0). \tag{8.94}$$

Since we are having exactly the same quartic potential as in an rf system with an active Landau cavity, we expect the synchrotron frequency to be exactly the same as the expression given by Eq. (8.86) when the oscillation amplitude is small.

The set of requirements, however, are different from that of the active Landau cavity system. Here, the requirements are

$$V_{\rm rf}\sin\phi_s = i_b R_h\cos^2\psi_h + U_s/e, \tag{8.95}$$

$$V_{\rm rf}\cos\phi_s = -m\,i_b R_h\cos\psi_h\sin\psi_h, \tag{8.96}$$

$$V_{\rm rf}\sin\phi_s = m^2 i_b R_h\cos^2\psi_h. \tag{8.97}$$

For an electron machine, which is mostly above transition, the synchronous angle ϕ_s is between $\frac{1}{2}\pi$ and π. Thus, from Eq. (8.96), we immediately obtain

$$\sin 2\psi_h > 0 \Longrightarrow 0 < \psi_h < \frac{\pi}{2}, \tag{8.98}$$

and from Eqs. (8.90) and (8.91), $\omega_r > m\omega_{\rm rf}$. This means that the beam in the higher-harmonic cavity is Robinson unstable, [8] as is illustrated in Fig. 8.10. Of course, the fundamental rf cavity should be Robinson stable, and it will be nice

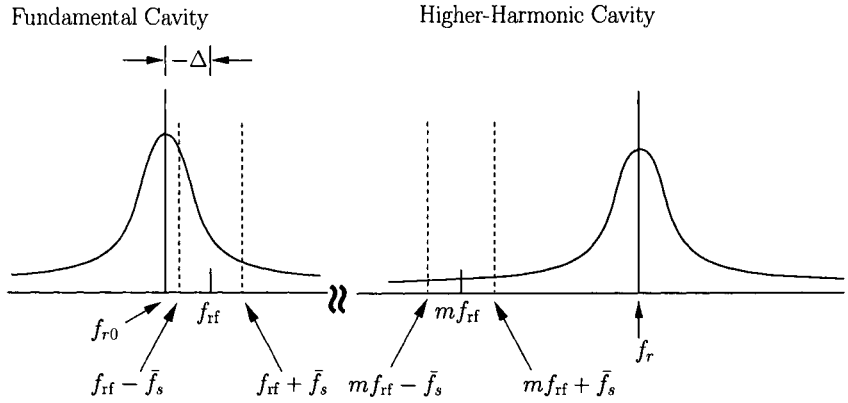


Fig. 8.10 For the higher-harmonic cavity, the resonant frequency f_r is above the mth multiple of the rf frequency $f_{\rm rf} = hf_0$. The beam will be Robinson unstable above transition. For the fundamental cavity, the resonant frequency f_{r0} is below the rf frequency $f_{\rm rf}$, and the beam will be Robinson stable. The detuning of the fundamental rf should be so chosen that the beam will be stable after traversing both cavities. The drawing is not to scale.

if the detuning is so chosen that the beam remains stable after traversing both cavities.

The synchrotron light source electron ring at LNLS, Brazil would like to install a passive Landau cavity with $m = 3$ in order to alleviate the longitudinal coupled-bunch instabilities. As an exercise, we would like to work out some estimates. The fundamental rf system has harmonic $h = 148$ or rf frequency $f_{\rm rf} = \omega_{\rm rf}/(2\pi) = 476.0$ MHz with a tuning range of ± 10 kHz, and rf voltage $V_{\rm rf} = 350$ kV. To overcome the radiation loss, the synchronous phase is set at $\phi_{s0} = 180^\circ - 19.0^\circ$. This gives a synchrotron tune at small amplitudes $\nu_s = 6.87 \times 10^{-3}$ or a synchronous frequency $f_s = 22.1$ kHz.

With the installation of the passive Landau cavity, the synchronous phase must be modified to a new ϕ_s, which is obtained by solving Eqs. (8.95) and (8.97):

$$\sin\phi_s = \left(\frac{m^2}{m^2-1}\right)\left(\frac{U_s}{eV_{\rm rf}}\right) = \frac{m^2}{m^2-1}\sin\phi_{s0}. \tag{8.99}$$

Thus,

$$\phi_{s0} = 180^\circ - 19.0^\circ \quad \Longrightarrow \quad \phi_s = 180^\circ - 21.49^\circ, \tag{8.100}$$

where $m = 3$ has been used. The detuning ψ_h of the higher-harmonic cavity can

be obtained from Eqs. (8.96) and (8.97), or

$$\tan\psi_h = -m\cot\phi_s \quad \Longrightarrow \quad \psi_h = 82.53°. \tag{8.101}$$

Finally from Eq. (8.97),

$$i_b R_h = \frac{V_{\rm rf}\sin\phi_s}{m^2\cos^2\psi_h}. \tag{8.102}$$

With $i_b = 2I_0 = 0.300$ A and $V_{\rm rf} = 350$ kV, we obtain the shunt impedance of the higher-harmonic cavity to be $R_h = 2.81$ MΩ. The power taken out from the beam is

$$P = \frac{1}{2}\frac{i_b^2 R_h}{1+\tan^2\psi_h} = 2.14 \text{ kW}, \tag{8.103}$$

which is not large when compared with the power loss due to radiation

$$P_{\rm rad} = NU_s f_0 = I_0 V_{\rm rf}\sin\phi_{s0} = 17.09 \text{ kW}, \tag{8.104}$$

where N is the total number of electrons in all the bunches. The higher-harmonic cavity has a quality factor of $Q_h = 45000$ and a resonant frequency $f_r \sim 3f_{r0} =$ 1428 MHz. From the detuning, it can be easily found that the frequency offset is $f_r - 3f_{\rm rf} = 121$ kHz.

Now let us compute the growth rate for one bunch at the coherent frequency Ω. For one particle of time advance τ, we have from Sacherer's integral equation for a short bunch, [2]

$$\Omega^2 - \omega_s(\tau)^2 = \frac{i\eta e I_0}{E_0 T_0}\sum_q (q\omega_0+\Omega)Z_0^{\parallel}(q\omega_0+\Omega). \tag{8.105}$$

where $\eta = 0.00830$ is the slip factor and we have retained the dependency of the synchrotron frequency ω_s on τ because of its large spread in the presence of the higher-harmonic cavity. From Eq. (8.86), this dependency is

$$\frac{\omega_s(\tau)}{\omega_{s0}} = \frac{\pi}{2}\left(\frac{m^2-1}{6}\right)^{1/2}\frac{\omega_{\rm rf}|\tau|}{K(\frac{1}{\sqrt{2}})}\sqrt{\frac{\cos\phi_s}{\cos\phi_{s0}}}, \tag{8.106}$$

where the last factor amounts to 0.9920 and can therefore be safely abandoned. To facilitate writing, let us denote

$$\omega_s(\tau) = \omega_{s0}\frac{|\tau|}{\bar{\tau}} \quad \text{with} \quad \frac{1}{\bar{\tau}} = \sqrt{\frac{m^2-1}{6}}\frac{\pi\omega_{\rm rf}}{2K(\frac{1}{\sqrt{2}})}. \tag{8.107}$$

Assuming a Gaussian distribution for the the arrival time τ with rms spread σ_τ, we obtain the first and second moments:

$$\langle \omega_s \rangle = \omega_{s0} \sqrt{\frac{2}{\pi}} \frac{\sigma_\tau}{\bar{\tau}} \quad \text{and} \quad \langle \omega_s^2 \rangle = \omega_{s0}^2 \frac{\sigma_\tau^2}{\bar{\tau}^2}. \tag{8.108}$$

Therefore the synchrotron angular frequency has the mean and rms spread,

$$\bar{\omega}_s = \omega_{s0} \sqrt{\frac{2}{\pi}} \frac{\sigma_\tau}{\bar{\tau}} \quad \text{and} \quad \sigma_{\omega_s} = \omega_{s0} \sqrt{\frac{\pi - 2}{\pi}} \frac{\sigma_\tau}{\bar{\tau}}. \tag{8.109}$$

With the natural rms bunch length of the Brazilian ring $\sigma_\tau = 30$ ps at the rf voltage $V_{\rm rf} = 350$ kV, we obtain $\bar{f}_s = \bar{\omega}_s/(2\pi) = 1.55$ kHz, and $\sigma_{f_s} = \sigma_{\omega_s}/(2\pi) = 1.17$ kHz. Note that $\bar{f}_s$ is very much smaller than f_{s0} when the Landau cavity is absent as a result of the small bunch length.

Since the synchrotron frequency is now a function of the offset from the stable fixed point of the rf bucket, a dispersion relation can be obtained from Eq. (8.105) by integrating over the synchrotron frequency distribution of the bunch. Here, we are interested in the growth rate without Landau damping, which is given approximately by

$$\begin{aligned} \frac{1}{\tau} = \mathcal{I}m\,\Omega \approx \frac{\eta e I_0 \omega_{\rm rf}}{2E_0 T_0 \bar{\omega}_s} \Big\{ & \Big[\mathcal{R}e\, Z_0^{\parallel}(\omega_{\rm rf} + \bar{\omega}_s) - \mathcal{R}e\, Z_0^{\parallel}(\omega_{\rm rf} - \bar{\omega}_s) \Big] \\ & + m \Big[\mathcal{R}e\, Z_0^{\parallel}(m\omega_{\rm rf} + \bar{\omega}_s) - \mathcal{R}e\, Z_0^{\parallel}(m\omega_{\rm rf} - \bar{\omega}_s) \Big] \Big\}, \end{aligned} \tag{8.110}$$

where the mean angular synchrotron frequency has been used. The growth rate can be computed easily by substituting into Eq. (8.110) the expression for $\mathcal{R}e\, Z_0^{\parallel}$. However, the differences in Eq. (8.110) can also be approximated by derivatives. For the higher-harmonic cavity, both the upper and lower synchrotron sidebands lie on the same side of the higher-harmonic resonance as indicated in Fig. 8.10. Their difference, $\sim 2\bar{f}_s = 3.00$ kHz, is also very much less than the cavity detuning $(f_r - mf_{\rm rf}) = 121$ kHz. Recalling that

$$\mathcal{R}e\, Z_0^{\parallel}(\omega) = R_h \cos^2 \psi_h, \tag{8.111}$$

where the detuning ψ_h is given by Eq. (8.91), the second term can be written as a differential,

$$\mathcal{R}e\, Z_0^{\parallel}(m\omega_{\rm rf} + \bar{\omega}_s) - \mathcal{R}e\, Z_0^{\parallel}(m\omega_{\rm rf} - \bar{\omega}_s) \approx \left[R_h \cos^2 \psi_h \sin 2\psi_h \frac{2Q_h}{\omega_r} \right] 2\bar{\omega}_s. \tag{8.112}$$

For the fundamental cavity, the resonant frequency is $\omega_{r0}/(2\pi) = 476.00$ MHz. The detuning is usually $\Delta/(2\pi) = (\omega_{r0} - \omega_{\rm rf})/(2\pi) = -10$ kHz at injection and is reduced to $\Delta/(2\pi) = -2$ kHz in storage mode when the highest

electron energy is reached. Thus, the upper and lower synchrotron sidebands also lie on one side of the resonance as illustrated in Fig. 8.10. Since $\bar{\omega}_s/\Delta$ is now not small compared with the detuning, we cannot expand in the same way as the Landau cavity. However, because $(2Q_L(-|\Delta| \pm \bar{\omega}_s)/\omega_{r0})^2$ are small, we can expand the denominator of the resonant impedance and obtain

$$\begin{aligned}
&\mathcal{R}e\, Z_0^{\parallel}(\omega_{\rm rf} + \bar{\omega}_s) - \mathcal{R}e\, Z_0^{\parallel}(\omega_{\rm rf} - \bar{\omega}_s) \\
&\approx R_{Lf}\left[\left(\frac{2Q_L\big(|\Delta|-\bar{\omega}_s\big)}{\omega_{r0}}\right)^2 - \left(\frac{2Q_L\big(|\Delta|+\bar{\omega}_s\big)}{\omega_{r0}}\right)^2\right] = -R_{Lf}\left(\frac{4Q_L}{\omega_{r0}}\right)^2 \bar{\omega}_s|\Delta|.
\end{aligned} \tag{8.113}$$

Here, for the fundamental cavity, we are given the unloaded shunt impedance $R_{sf} = 3.84\ \mathrm{M}\Omega$ and the unloaded quality factor $Q_0 = 45000$, assumed to be the same as that of the Landau cavity. The optimum coupling coefficient is found to be[†]

$$\beta_{\rm op} = 1 + \frac{i_b R_{sf} \sin\phi_s}{V_{\rm rf}} = 2.21. \tag{8.114}$$

Thus the loaded shunt impedance and the loaded quality factor are, respectively, $R_{Lf} = R_{sf}/(1+\beta_{\rm op}) = 1.20\ \mathrm{M}\Omega$ and $Q_L = Q_0/(1+\beta_{\rm op}) = 14040$. Putting things together, we arrive at the growth rate of the beam without damping for the two-cavity rf system,

$$\frac{1}{\tau} = \frac{\eta e i_b}{E_0 T_0}\left[-4Q_L^2 R_{Lf}\frac{|\Delta|}{\omega_{\rm rf}} + Q_h R_h \cos^2\psi_h \sin 2\psi_h\big|_{\rm Landau}\right]. \tag{8.115}$$

Notice that $\bar{\omega}_s$ gets cancelled out, implying that the computed growth rate will not be sensitive to the length of the bunch provided that the whole bunch is within the linear part of the $\omega_s(\tau)$, although Eq. (8.110) is valid strictly for a point bunch. Putting in numbers, we obtain the growth rate $\tau^{-1} = -20000\ \mathrm{s}^{-1}$, where the contributions from the fundamental and higher-harmonic cavities are, respectively, $-23200\ \mathrm{s}^{-1}$ and $+3220\ \mathrm{s}^{-1}$, indicating that the two-rf system turns out to be Robinson stable. However, it is important to point out that the growth rate formula given by Eq. (8.110) is valid only if the shift and spread of the synchrotron frequency are much less than some unperturbed synchrotron frequency. Here, the synchrotron frequency is linear with the offset from the

[†]We identify the LNLS-quoted shunt impedance of 3.84 MΩ as the unloaded shunt impedance R_{sf}, because the identification of $R_{Lf} = 3.84\ \mathrm{M}\Omega$ would lead to a negative optimum coupling coefficient, implying that the generator power would be less than the power delivered to the beam.

stable fixed point of the longitudinal phase space and the spread is therefore very large. As a result, Eq. (8.110) can only be viewed as an estimate.

Now let us estimate how large a Landau damping we obtain from the passive Landau cavity coming from the spread of the synchrotron frequency. The stability criterion is roughly

$$\frac{1}{\tau} \lesssim 4\sigma_{\omega_s}, \tag{8.116}$$

where the synchrotron angular frequency spread is given by Eq. (8.109), and we have taken approximately $4\sigma_{\omega_s} = 29.4$ kHz as the total spread. In other words, the higher-harmonic cavity is able to damp an instability that has a growth time longer than 0.034 ms, an improvement of about 160 folds better than when the higher-harmonic cavity is absent. Thus, theoretically, this Landau damping is large enough to alleviate the Robinson's antidamping of higher-harmonic cavity as well. We can also rewrite the growth rate of Eq. (8.115) in terms of the intrinsic properties of the higher-harmonic cavity:

$$\frac{1}{\tau} = \frac{\eta e i_b}{E_0 T_0}\left[-4Q_L^2 R_{Lf}\frac{|\Delta|}{\omega_{\rm rf}} + \frac{V_{\rm rf}^2|\sin 2\phi_s|}{m^3 i_b^3 R_h/Q_h}\right], \tag{8.117}$$

where $\sin\phi_s$ is given by Eq. (8.99).

We notice that the required shunt impedance of the passive Landau cavity $R_h = 2.81$ MΩ is large, although it is still smaller than the shunt impedance of 3.84 MΩ of the fundamental cavity. It is easy to understand why such large impedance is required. The synchronous angle for a storage ring without the Landau cavity is usually just not too much from 180°, here $\phi_{s0} = 180° - 19.0°$, because of the compensation of a small amount of radiation loss. The rf gap voltage phasor is therefore almost perpendicular to the beam current phasor. In order that the beam-loading voltage contributes significantly to the rf voltage, the detuning angle of the passive higher-harmonic cavity must therefore be large also, here $\psi_h = 82.53°$. In fact, without radiation loss to compensate, the beam-loading voltage phasor would have been exactly perpendicular to the beam current phasor.[‡] Since $\cos\psi_h = 0.130$ is small, the shunt impedance of the higher-harmonic cavity must therefore be large. In some sense, the employment of the higher-harmonic cavity is not efficient at all, because we are using only the tail of a large resonance impedance, as is depicted in Fig. 8.10. This is not a waste at all, however, because we can do away with the generator power source for this cavity. Also, the large detuning angle implies not much power will be taken out from the beam as it loads the cavity, only 2.14 kW here. On the other

[‡]With $U_s = 0$ Eqs. (8.95) and (8.97) imply $\phi_s = 0$ and $\psi_h = \pi/2$. However, Eq. (8.96) leads to $R_h \to \infty$.

hand, the detuning of the fundamental cavity need not be too large. This is because the rf gap voltage is supplied mostly by the generator voltage and only partially by the beam loading in the cavity.

The most important question here is how do we generate a large shunt impedance for the higher-harmonic cavity. Usually it is easy to lower the shunt impedance by adding a resistor across the cavity gap. Some other means will be required to raise the shunt impedance, in case it is not large enough. One way is to coat the interior of the higher-harmonic cavity with a layer of medium that has a higher conductivity. However, it is hard to think of any medium that has a conductivity very much higher than that of the copper surface of the cavity. For example, the conductivity of silver is only slightly higher. Another way to increase the conductivity significantly is the reduction of temperature to the cryogenic region. Notice that R_h/Q_h is a geometric property of the cavity. Raising R_h will raise Q_h also. However, a higher quality factor is of no concern here, because the requirements in Eqs. (8.95), (8.96), and (8.97) depend on the detuning ψ_h only and are independent of Q_h. With the same detuning ψ_h, a higher Q_h just implies a smaller frequency offset between the resonant angular frequency ω_r of the higher-harmonic cavity and the mth multiple of the rf angular frequency.

The shunt impedance of the higher-harmonic cavity determines the rf voltage to be used in the fundamental cavity. We can rewrite Eq. (8.102) as

$$\frac{i_b R_h}{V_s} = \left(\frac{m^2-1}{m^2}\right)\left(\frac{V_{\rm rf}}{V_s}\right)^2 - 1, \tag{8.118}$$

after eliminating ϕ_s and ψ_h with the aid of Eqs. (8.99) and (8.101), where $U_s = eV_s$ is the energy loss per turn due to synchrotron radiation and impedances of the vacuum chamber. Thus, for a given beam current, a small shunt impedance of the higher-harmonic cavity translates into small rf voltage. Notice that the right side is quadratic in $V_{\rm rf}$. For example, with the same radiation loss, when the shunt impedance of the higher-order cavity decreases from 6.12 to 2.81 MΩ, the rf voltage $V_{\rm rf}$ has to decrease from 500 kV to 350 kV. A low rf voltage is usually not favored because the electron bunches will become too long.

In order to maximize Landau damping, criteria must be met so that the rf potential becomes quartic. As is shown in Fig. 8.9 for a $m = 2$ double rf system, when the rf voltage ratio deviates from $r = 1/m = 0.5$ by 20% to 0.4, the spread in synchrotron frequency for a small bunch decreases tremendously to almost the same tiny value as in the single rf system. There is a big difference between an active Landau cavity and a passive Landau cavity. In an active Landau cavity, the criteria in Eqs. (8.84) to (8.84) are independent of the beam intensity. On

the other hand, the criteria for the operation of a passive cavity, Eqs. (8.95), (8.96), and (8.97), depend on the bunch intensity. What will happen when the bunch intensity changes significantly? Let us recall how we arrive at the solution of the three equations of the passive two-rf system. The new synchronous phase ϕ_s, as given by Eq. (8.99), is determined solely by the ratio of the radiation loss U_s to the rf voltage $V_{\rm rf}$. while the detuning is just given by $\psi_h = -m\cot\phi_s$. The only parameter that depends on the beam current is the shunt impedance R_h. Thus, the easiest solution is to install a variable resistor across the the gap of the higher-harmonic cavity and adjust the proper shunt impedance by monitoring the intensity of the electron bunches.

In the event that the shunt impedance is not adjustable, one can adjust instead the rf voltage so that Eq. (8.118) remains satisfied with the new current but with the preset R_h. With the new rf voltage, the synchronous phase ϕ_s has to be adjusted so that Eq. (8.99) remains satisfied. This will alter the detuning ψ_h according to Eq. (8.101). The only way to achieve the new detuning is to vary the rf frequency. This will push the beam radially inward or outward if we are outside the tuning range of the cavity. As the beam current changes by $\Delta I_0/I_0$, to maintain the criteria of the quartic rf potential, the required changes in rf voltage, synchronous angle, and detuning of the higher-harmonic cavity are, respectively,

$$\frac{\Delta V_{\rm rf}}{V_s} = \frac{1}{2}\left[\frac{m^2}{m^2-1}\frac{V_s}{V_{\rm rf}}\right]\left[\frac{m^2-1}{m^2}\frac{V_{\rm rf}^2}{V_s^2}-1\right]\frac{\Delta I_0}{I_0}, \tag{8.119}$$

$$\Delta(\pi-\phi_s) = -\left[\left(\frac{m^2-1}{m^2}\frac{V_{\rm rf}}{V_s}\right)^2-1\right]^{-1/2}\frac{\Delta V_{\rm rf}}{V_s}, \tag{8.120}$$

$$\Delta\psi_h = \frac{1}{2m}\left[\left(\frac{m^2-1}{m^2}\frac{V_{\rm rf}}{V_s}\right)^2-1\right]^{-1/2}\frac{\Delta I_0}{I_0}. \tag{8.121}$$

The change of the detuning angle ψ_h leads to a fractional change in the rf frequency and therefore a fractional change in orbit radius

$$\frac{\Delta R}{R} = -\frac{m^2-1}{4mQ}\left[\frac{m^2-1}{m^2}\frac{V_{\rm rf}^2}{V_s^2}-1\right]\left[\left(\frac{m^2-1}{m^2}\frac{V_{\rm rf}}{V_s}\right)^2-1\right]^{-1/2}\frac{\Delta I_0}{I_0}, \tag{8.122}$$

where R is the mean radius of nominal closed orbit. These changes are plotted in Fig. 8.11 for the LNLS double-rf system when he beam current varies by up to $\pm 20\%$. Because of the high quality factors Q_h of the cavities, the radial offset of the beam turns out to be very small, less than ± 0.14 mm for a $\pm 20\%$ variation of beam current.

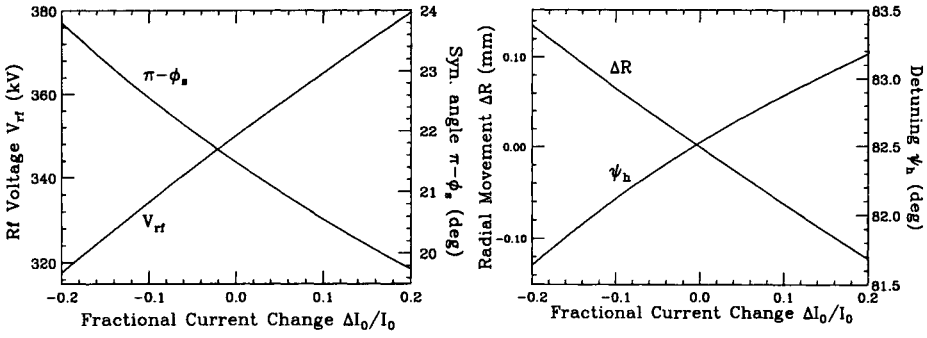


Fig. 8.11 Plots showing the required variations of rf voltage $V_{\rm rf}$, synchronous angle ϕ_s, higher-harmonic-cavity detuning ψ_h, and beam radial offset Δr to maintain the criteria of the quartic rf potential, when the beam current varies by $\pm 20\%$.

8.3.3 *Rf-Voltage Modulation*

The modulation of the rf system will create nonlinear parametric resonances, which redistribute particles in the longitudinal phase plane. The formation of islands within an rf bucket reduces the density in the bunch core and decouples the coupling between bunches. As a result, beam dynamics properties related to the bunch density, such as beam lifetime, beam collective instabilities, etc, can be improved.

Here we try to modulate the rf voltage with a frequency $\nu_m\omega_0/(2\pi)$ and amplitude ϵ, so that the energy equation becomes [12]

$$\frac{d\Delta E}{dn} = eV_{\rm rf}[1+\epsilon\sin(2\pi\nu_m n+\xi)][\sin(\phi_s-h\omega_0\tau)-\sin\phi_s]-[U_s(\delta)-U_{s0}], \quad (8.123)$$

where ξ is a randomly chosen phase, ν_m is the modulating tune, ϵ is the fractional voltage modulation amplitude, U_{s0} and $U_s(\delta)$ denote the energy loss due to synchrotron radiation for the synchronous particle and a particle with momentum offset δ. This modulation will introduce resonant-island structure in the longitudinal phase plane. There are two critical tunes. When the synchronous phase $\phi_s = 0$ or π, they are given by

$$\begin{cases} \nu_1 = 2\nu_s + \frac{1}{2}\epsilon\nu_s, \\ \nu_2 = 2\nu_s - \frac{1}{2}\epsilon\nu_s. \end{cases} \quad (8.124)$$

If we start the modulation by gradually increasing the modulating tune ν_m towards ν_2 from below, two islands appear inside the bucket from both sides, as shown in the second plot of Fig. 8.12 in the first row. The phase space showing the islands is depicted in Fig. 8.13. As ν_m is increased, these two islands come

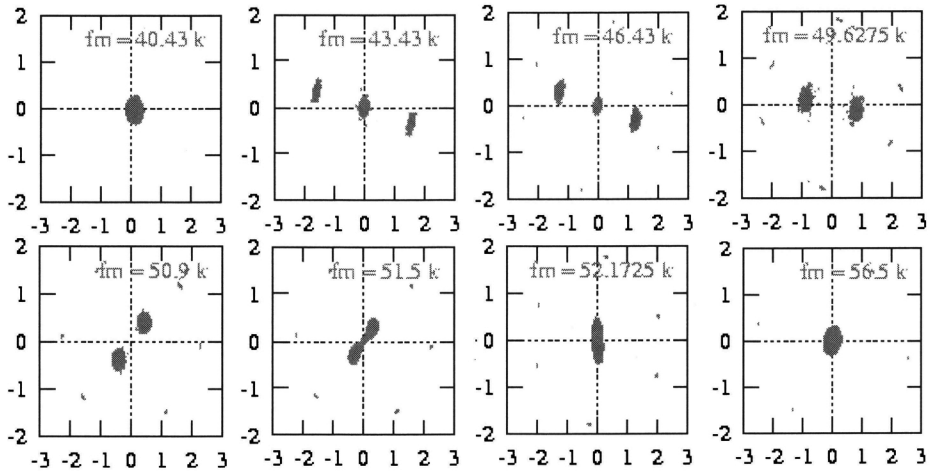


Fig. 8.12 Simulation results of rf voltage modulation. The modulation frequency is increased from left to right and top to bottom. The modulation amplitude is 10% of the cavity voltage. The fourth plot is right at critical frequency $\nu_2 f_0 = 49.6275$ kHz, the fifth plot is $2\nu_s$, and the seventh plot right at critical frequency $\nu_1 f_0 = 52.1725$ kHz. (Courtesy Wang, *et al.* [14])

closer and closer to the center of the bucket and the particles in the bunch core gradually spill into these two islands, forming three beamlets. When ν_m reaches ν_2 (fourth plot), the central core disappears and all the particles are shared by the two beamlets in the two islands. Further increase of ν_m above ν_2 moves the two beamlets closer together. When ν_m equals ν_1, the two beamlets merge into one (third plot of bottom row). Under all these situations, the two outer islands rotate around the center of the rf bucket with frequency equal to one-half the modulation frequency. Every rf bucket has the same phase space structure of having two or three islands rotating at the same angular velocity and with the roughly same phase. The only possible small phase lag is due to time-of-flight. Therefore, only coupled mode $\mu = 0$ will be allowed, unless the driving force is large enough to overcome the voltage modulation.

Rf voltage modulation has been introduced into the light source at the Synchrotron Radiation Research Center (SRRC) of Taiwan to cope with longitudinal coupled-bunch instability. [14] The synchrotron frequency was $\nu_s f_0 = 25.450$ kHz. A modulation frequency slightly below twice the synchrotron frequency with $\epsilon = 10\%$ voltage modulation was applied to the rf system. The beam spectrum measured from the beam-position monitor (BPM) sum from a HP4396A network analyzer before and after the modulation is shown in Fig. 8.14. It is evident that the intensities of the beam spectrum at the annoying frequencies have been largely reduced after the application of the modulation. The

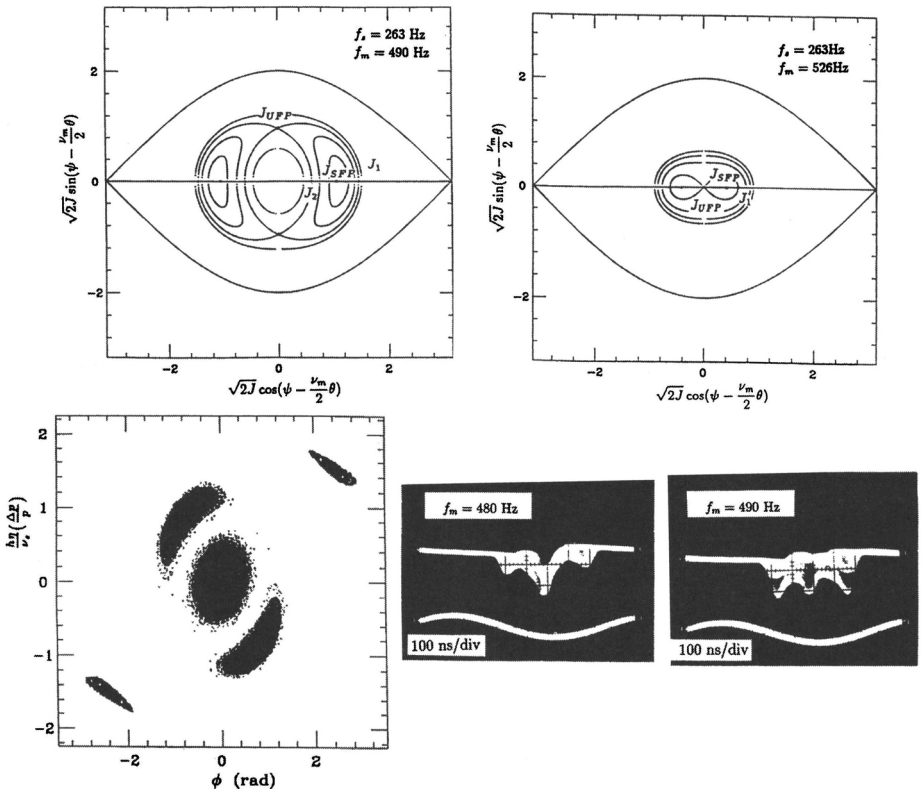


Fig. 8.13 Top figures show separatrices and tori of the time-independent Hamiltonian with voltage modulation in multi-particle simulation for an experiment at Indiana University Cyclotron Facility. The modulation tune is below ν_2 with the formation of three islands on the left, while the modulation tune is above ν_2 with the formation of two islands on the right. The lower-left plot shows the final beam distribution when there are three islands, a damping rate of 2.5 s^{-1} has been assumed. The lower-right plots show the longitudinal beam distribution from a BPM sum signal accumulated over many synchrotron periods. Note that the outer two beamlets rotate around the center beamlet at frequency equal to one-half the modulation frequency. (Courtesy Li, *et al.* [12])

sidebands around the harmonics of 587.106 Hz and 911.888 MHz are magnified in Fig. 8.15. We see that the synchrotron sidebands have been suppressed by very much. The multi-bunch beam motion under rf voltage modulation was also recorded by streak camera, which did not reveal any coupled motion of the bunches. Because of the successful damping of the longitudinal coupled-bunch instabilities, this modulation process has been incorporated into the routine operation of the light source at SRRC.

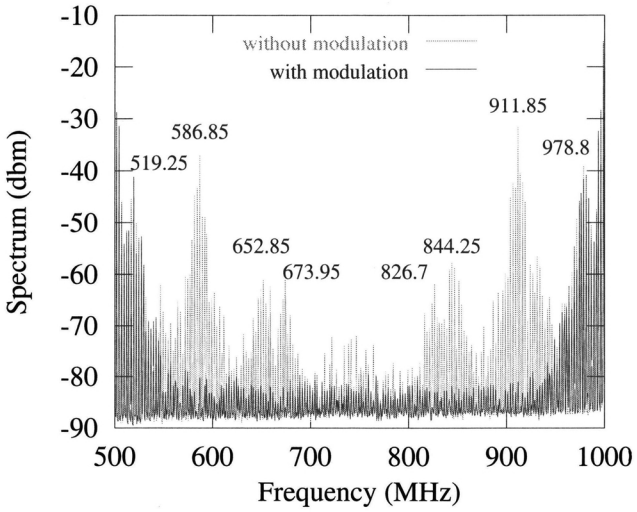


Fig. 8.14 Beam spectrum from BPM sum signal before (lighter) and after (darker) applying rf voltage modulation. The synchrotron frequency was 25.450 kHz. The voltage was modulated by 10% at 50.155 kHz. The frequency span of the spectrum is 500 MHz, which is the rf frequency. (Courtesy Wang, *et al.* [14])

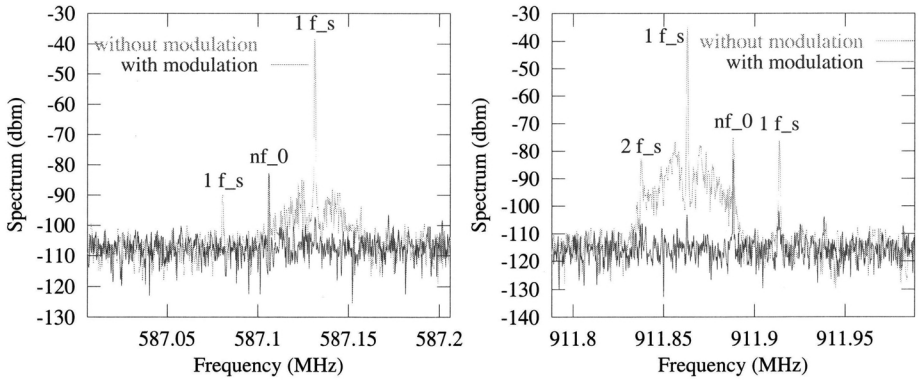


Fig. 8.15 Beam spectrum zoomed in from Fig. 8.14. The revolution harmonic frequency of the left is 587.106 MHz and the right is 911.888 MHz. The frequency span of the spectrum is 200 kHz. (Courtesy Wang, *et al.* [14])

8.3.4 *Uneven Fill*

In a storage ring with M identical bunches evenly spaced, there will be M modes of coupled-bunch oscillation, of which about half are stable and half unstable in the presence of an impedance, if all other means of damping are neglected. Take the example of having the rf harmonic $h = M = 6$ as illustrated in Fig. 8.2. If there is a narrow resonant impedance in the rf cavity located at $\omega_r \approx (qM + \mu)\omega_0$ with $\mu = 4$, coupled-bunch mode $\mu = 4$ becomes highly

unstable. At the same time, this resonant impedance also damps coupled-bunch mode $M - \mu = 2$ heavily. Usually, we only care for the mode that is unstable and pay no attention the mode that is damped. In some sense, the damping provided by the impedance is rendered useless or has been wasted. However, if there is another narrow resonant impedance located at the angular frequency $(qM + \mu')\omega_0$ with $\mu' = 2$, this impedance excites coupled-bunch mode 2, but damps coupled-bunch mode 4. If this impedance is of the same magnitude as the first one, both coupled-bunch modes 2 and 4 can become stable. Thus, having more narrow resonances in the impedance does not necessarily imply more instabilities. If they are located at the desired frequencies, they can be helping each other so that the excitation of one can be canceled by the other. This method of curing coupled-bunch instability was proposed in Ref. [15] by creating extra resonances in the impedance in the accelerator ring. However, extra resonances are difficult to create. In fact, they are not necessary, because the same purpose can also be served if we can couple the two coupled-bunch modes together, for example modes 2 and 4 in the above example, the damped mode will be helping the growth mode. If the resulting growth rates of the two coupled modes fall lower than the synchrotron radiation damping rate and the Landau damping rate in the ring, the coupled-bunch instabilities will have been cured. This method to cure coupled-bunch instabilities is called *modulating coupling* and was first proposed by Prabhakar. [5, 16] Instead of creating new resonances, the coupling of the coupled modes is accomplished with an uneven fill in the ring. We saw in Eq. (8.52) that wake field left by previous bunch passages contributes to a coherent synchrotron tune shift in the bunch. For an unevenly filled ring, these tune shifts will be different for different bunches. This provides a spread in synchrotron tune and therefore extra Landau damping, which is another idea proposed by Prabhakar.

Let us go over the uneven-fill theory briefly. Since we are going to treat the bunches as points, the derivation follows closely that performed in Sec. 8.1.3.1. Of course, it will be more involved here because of the presence of more than one bunch. Consider M point bunches evenly placed in the ring, but they may carry different charges. The arrival time advance τ_n of the nth bunch at 'time' s obeys the equation of motion,

$$\ddot{\tau}_n + 2d_r\dot{\tau}_n + \omega_{s0}^2\tau_n = \frac{e\eta}{\beta^2 E_0 T_0} V_n(\tau_n; s), \tag{8.125}$$

where d_r is the synchrotron radiation damping rate and the overdot represents derivative with respect to s/v. Here $V_n(\tau_n; s)$ is the total wake voltage seen by bunch n at time advance τ_n from the synchronous particle of its bucket, and is

given by

$$V_n(\tau_n; s) = \sum_{p=-\infty}^{\infty} \sum_{k=0}^{M-1} q_k W_0' \left[t_{n,k}^p + \tau_k(s - v t_{n,k}^p) - \tau_n(s) \right], \tag{8.126}$$

where q_k is the charge of bunch k, $t_{n,k}^p = (pM + n - k)T_b$ is the time the kth bunch is ahead of the nth bunch p turns ago, and $T_b = T_0/M$ is the bunch spacing.† Since the deviation due to synchrotron motion is small compared with the bunch spacing, Eq. (8.126) can be expanded, resulting

$$V_n(\tau_n; s) = \sum_{p=-\infty}^{\infty} \sum_{k=0}^{M-1} q_k \left[\tau_k(s - v t_{n,k}^p) - \tau_n(s) \right] W_0''(t_{n,k}^p). \tag{8.127}$$

If all bunches carry the same charge, we have the situation of even fill and we know that there are M modes for the bunches to couple; in the ℓth mode, a bunch *leads* its predecessor by the *time-phase* $2\pi\ell/M$.‡ For this reason, the solution of this ℓth coupled-bunch mode can be written in the vector form as $\tau_n \sim v_\ell$, where the M symmetric eigenmodes are, for $\ell = 0,\ 1,\ \cdots,\ M-1$,

$$v_\ell = \frac{1}{\sqrt{M}} \begin{pmatrix} 1 \\ e^{-i\ell\theta} \\ e^{-2i\ell\theta} \\ \vdots \\ e^{-i(M-1)\ell\theta} \end{pmatrix}, \qquad \theta = \frac{2\pi}{M}. \tag{8.128}$$

They form an orthonormal basis which we call the *even-fill-eigenmode* (EFEM) basis. For an uneven fill, it is natural to expand the new eigenmodes using

†In Eq. (8.9), we have $kC + (s_\ell - s_n)$ in the argument of the wake function W_0', where we are sampling the wake force on the nth bunch due to the ℓth bunch. There, s_n represent the distance along the ring measured from some reference point to the nth bunch in the *same* direction of bunch motion. Thus, the ℓth bunch is ahead of the nth bunch by the distance $s_\ell - s_n$. In Eq. (8.126), we count the number of bunch spacings instead. Thus, the kth bunch is ahead of the nth bunch by the time $(n-k)T_b$, since we number the bunches from upstream to downstream or in the *opposite* direction of bunch motion. Note that the term $v(\tau' - \tau)$ in the argument of the linear density in Eq. (8.8) has been neglected because this will only amount to a phase delay $\Omega(\tau' - \tau)$ where $\Omega \approx \omega_{s0}$ and is very much less than the phase change $\omega_\tau(\tau' - \tau)$.

‡Here, coupled-bunch mode ℓ implies the center-of-mass of a bunch *leads* its predecessor by the time-phase $2\pi\ell/M$ because of the $e^{-i\omega t}$ convention. Time-phase is phase moving in the direction of time, which is the negative of the conventional phase in the engineer's e^{jwt} language. Thus, coupled-bunch mode ℓ here is the same as coupled-bunch mode $M-\ell$ discussed in the earlier part of this Chapter. There, the center-of-mass of a bunch *lags* its predecessor by the phase $2\pi\ell/M$.

as a basis the EFEMs. The arrival time advances $\tau_n(s)$ for the M bunches in Eq. (8.125) can now be written as

$$\begin{pmatrix} \tau_0 \\ \vdots \\ \tau_{M-1} \end{pmatrix} = \varsigma^0 \boldsymbol{v}_0 + \cdots + \varsigma^{M-1} \boldsymbol{v}_{M-1} \quad \text{or} \quad \tau_n(s) = \frac{1}{\sqrt{M}} \sum_{m=0}^{M-1} \varsigma^m(s) e^{-i2\pi nm/M}, \tag{8.129}$$

where the expansion coefficients can be written inversely as

$$\varsigma^m(s) = \frac{1}{\sqrt{M}} \sum_{n=0}^{M-1} \tau_n(s) e^{i2\pi nm/M}. \tag{8.130}$$

Assuming the ansatz

$$\tau_k(s) \propto e^{-i\Omega s/v}, \tag{8.131}$$

where the collective frequency Ω is to be determined, the voltage from the wake can now be written as

$$V_n(\tau_n; s) = \frac{1}{\sqrt{M}} \sum_{p=-\infty}^{\infty} \sum_{k,m=0}^{M-1} q_k \varsigma^m(s) e^{-i2\pi nm/M} \left[e^{i(m\omega_0+\Omega)t^p_{n,k}} - 1 \right] W_0''(t^p_{n,k}), \tag{8.132}$$

where

$$\varsigma^m(s) \propto e^{-i\Omega s/v}. \tag{8.133}$$

Next project the whole Eq. (8.125) onto the ℓth EFEM, giving

$$\ddot{\varsigma}^\ell + 2d_r \dot{\varsigma}^\ell + \omega_{s0}^2 \varsigma^\ell = \frac{e\eta}{\beta^2 E_0 M} \sum_{p=-\infty}^{\infty} \sum_{n,m,k=0}^{M-1} \frac{q_k}{T_0} \varsigma^m(s) e^{i2\pi n(\ell-m)/M} \times \left[e^{i(m\omega_0+\Omega)t^p_{n.k}} - 1 \right] W_0''(t^p_{n.k}). \tag{8.134}$$

There are too many summations over bunch number. We can eliminate one by defining the integer variable $u = pM + n - k = t^p_{n.k}/T_b$. After that, $\sum_p \to \frac{1}{M} \sum_u$. The summand becomes independent of n and we have $\sum_n = M$. The right side of Eq. (8.134) simplifies to

$$\text{R.S.} = \frac{e\eta}{\beta^2 E_0 M} \sum_{u=-\infty}^{\infty} \sum_{m=0}^{M-1} I_{l-m} \varsigma^m(s) e^{i2\pi u(\ell-m)/M} \left[e^{i(m\omega_0+\Omega)uT_b} - 1 \right] W_0''(uT_b), \tag{8.135}$$

where we have introduced the complex amplitude of the pth revolution harmonic in the beam spectrum,

$$I_p = \sum_{k=0}^{M-1} i_k e^{i2\pi kp/M}, \tag{8.136}$$

with $i_k = q_k/T_0$ denoting the average current of bunch k. For an evenly filled ring, the average beam current of each bunch is the same,

$$I_p = \begin{cases} I_0 = \sum_k i_k & p = 0 \\ 0 & p \neq 0, \end{cases} \tag{8.137}$$

where I_0 is the total average current in the ring. Thus, for an evenly filled ring, Eq. (8.134) is diagonal in the sense that the different coupled-bunch modes do not couple. This just reassure us that the EFEM in Eq. (8.128) are indeed the solutions of the M coupled-bunch modes.

Let us go to the frequency space by introducing the longitudinal impedance,

$$W_0'(t) = \int \frac{d\omega}{2\pi} Z_0^{\parallel}(\omega) e^{-i\omega t}. \tag{8.138}$$

The summation over u can now be performed using Poisson formula resulting in the difference of two δ-functions, which facilitate the integration over ω resulting in

$$\text{R.S.} = -\frac{ie\eta}{\beta^2 E_0 T_0} \sum_{p=-\infty}^{\infty} \sum_{m=0}^{M-1} I_{l-m} \varsigma^m(s) \Big\{ [(pM+\ell)\omega_0+\Omega]\, Z_0^{\parallel}[(pM+\ell)\omega_0+\Omega] - [(pM+\ell-m)\omega_0]\, Z_0^{\parallel}[(pM+\ell-m)\omega_0] \Big\}. \tag{8.139}$$

This reminds us of the point-bunch model in Sec. 8.1.3.1, where we have these two similar terms on the right side of Eq. (8.52). With the introduction of the mode-coupling impedance,

$$\begin{aligned} Z_{\ell m}(\omega) &= Z_{\text{eff}}[\ell\omega_0 + \omega] - Z_{\text{eff}}[(\ell - m)\omega_0] \\ Z_{\text{eff}}(\omega) &= \frac{1}{\omega_{\text{rf}}} \sum_{p=-\infty}^{\infty} [pM\omega_0 + \omega] Z_0^{\parallel}[pM\omega_0 + \omega], \end{aligned} \tag{8.140}$$

the equation of motion for the bunches can be written in the simplified form,

$$\ddot{\varsigma}^{\ell} + 2d_r\dot{\varsigma}^{\ell} + \omega_{s0}^2\varsigma^{\ell} = -\frac{ie\eta\omega_{\text{rf}}}{\beta^2 E_0 T_0} \sum_{m=0}^{M-1} I_{l-m} Z_{\ell m}(\Omega)\varsigma^m. \tag{8.141}$$

The next simplification is to exclude all solutions when $\Omega \approx -\omega_{s0}$ and include only those near $+\omega_{s0}$. From the ansatz (8.131) or (8.133), one has

$$\ddot{\varsigma}^{\ell} + 2d_r\dot{\varsigma}^{\ell} + \omega_{s0}^2\varsigma^{\ell} \approx -2i\omega_{s0}\left[\dot{\varsigma}^{\ell} + (d_r + i\omega_{s0})\varsigma^{\ell}\right], \tag{8.142}$$

provided that $d_r \ll \omega_{s0}$ and $|\Omega - \omega_{s0}| \ll \omega_{s0}$. We finally obtain

$$\dot{\varsigma}^{\ell} + (d_r + i\omega_{s0})\varsigma^{\ell} = \sum_{m=0}^{M-1} A_{\ell m}\varsigma^{m}, \tag{8.143}$$

with

$$A_{\ell m} = \frac{e\eta\omega_{\mathrm{rf}}}{2\beta^2 E_0 T_0 \omega_{s0}} I_{\ell-m} Z_{\ell m}(\omega_{s0}). \tag{8.144}$$

This is just a M-dimensional eigenvalue problem. In the situation of an evenly filled ring, all bunch current i_k are the same so that $I_p = I_0\delta_{p0}$, the total average current in the ring. This implies no coupling between the EFEMs, as expected, and the eigenvalues are

$$\lambda_{\ell} = A_{\ell\ell} = \frac{e\eta\omega_{\mathrm{rf}}}{2\beta^2 E_0 T_0 \omega_{s0}} I_0\left[Z_{\mathrm{eff}}(\ell\omega_0 + \omega_{s0}) - Z_{\mathrm{eff}}(0)\right], \quad \ell = 1, \cdots, M-1. \tag{8.145}$$

These eigenvalues represent the growth or antidamping rates of the EFEMs. Some results are apparent:

- The sum of eigenvalues, $\sum A_{\ell\ell}$, is independent of fill shapes.
- Uneven-fill eigenvalues vary linearly as I_0.
- Radiation damping merely shifts all eigenvalues by d_r, regardless of fill shape.
- If all filled buckets have the same charge q_k, then broadband bunch-by-bunch feedback also damps all uneven-fill modes equally, since it behaves like radiation damping.
- The EFEM basis yields a sparse A-matrix because usually coupled-bunch instabilities are driven by only a few parasitic higher-order resonances in the rf cavities.

8.3.4.1 *Modulation Coupling*

The two terms on the right side of Eq. (8.141), namely $I_{\ell-m}Z_{\mathrm{eff}}[\ell\omega_0 + \Omega]$ and $I_{\ell-m}Z_{\mathrm{eff}}[(\ell - m)\omega_0]$, provide different functions. The first term couples bunch modes ℓ and m and contributes to *modulation coupling*. The second term concerns one particular mode $(\ell-m)$ only and will not couple different bunch modes.

Instead, as we will see later, it contributes to a pure synchrotron frequency tune shift and provides Landau damping.

Let us first study modulation coupling by neglecting the tune-shift term (the second term) in Eq. (8.139). We can then set[§] $I_k Z_{\text{eff}}(k\omega_0) = 0$ except for $k = 0$. This configuration implies that the modulation coupling terms are the only manifestation of fill unevenness. The problem, however, simplifies considerably. In addition, if there is only one sharp resonance in the longitudinal impedance $Z_0^{\|}$ that excites coupled-bunch instability for mode ℓ in the EFEM basis, this resonance will initiate damping for coupled-bunch mode $m = M - \ell$. Thus, the even-fill eigenvalues must satisfy $\lambda_\ell > 0$, $\lambda_m < 0$ and it is easy to show $\lambda_\ell + \lambda_m \approx 0$. We try to couple these two modes by filling the ring unevenly so that $I_{\ell-m}$ is maximized. The A-matrix is now diagonal except for the coupling between these two modes. In other words, the coupling A-matrix reduces to a two-by-two matrix. The new eigenvalues for these two modes can be solved with the result (see Exercise 8.9),

$$\lambda = \frac{1}{2}(\lambda_\ell + \lambda_m) \pm \frac{1}{2}\sqrt{(\lambda_\ell - \lambda_m)^2 + 4C_{\ell-m}^2 \lambda_\ell \lambda_m}, \tag{8.146}$$

where $C_p = |I_p|/I_0$ is called the *modulation parameter* and its value cannot exceed unity. If $C_{\ell-m} = 0$, the eigenvalues remain $\lambda = \lambda_\ell$ and λ_m, implying that there is no coupling between the two modes at all. As $C_{\ell-m}$ approaches unity, one eigenvalue approaches zero and so is its growth rate. The other eigenvalue approaches $\lambda_\ell + \lambda_m$, which also approaches zero, because the damping rate of mode m is helping the growth rate of mode ℓ.

To optimize the modulation parameter C_p, we resort to the definition of the harmonic amplitude I_p in Eq. (8.136). As an example, take a ring of $M = 900$ even-fill bunches and we wish to optimize C_p with $p = 3$. According to the definition of the harmonic amplitude I_p in Eq. (8.136), the easiest way to accomplish this is to fill the ring every $M/p = 900/3 = 300$th bucket (assuming that the total number of buckets is also $M = 900$). Since we wish to keep the same current I_0 in the ring, each of these $p = 3$ chosen buckets will be filled with bunch current $I_0/p = I_0/3$ and the modulation parameter becomes $C_3 = 1$. However, with so much charge concentrated at these three buckets, each bunch

[§]Consider a ring with $M = 84$ buckets. If there is only one sharp resonance at $\omega_r = (pM + \ell)\omega_0$ with $\ell = 79$, coupled-bunch mode $\ell = 79$ in the EFEM basis will be excited, but mode $m = M - \ell = 5$ will be damped. To couple these two modes, we need to maximize I_k or I_{-k} with $k = \ell - m = 74$. Under this situation, $I_k Z_{\text{eff}}(k\omega_0) = 0$ except for $k = 0$, because (1) although $I_{74} \neq 0$, there is no impedance at $(pM \pm 74)\omega_0$, and (2) although $Z_{\text{eff}}(k\omega_0) \neq 0$ for $k = \pm\ell$, $I_{\pm\ell}$ are zero because we maximize $I_{\ell-m}$ only. The same is true if there are a few sharp resonances. This condition, however, excludes the extra Landau damping to be studied in Sec. 8.3.4.2.

can become unstable by itself. To cope with this single-bunch instability, we can fill several adjacent buckets around each of these three chosen locations. If the maximum allowable bunch current to avoid single-bunch instability is $i_{\max}$, we need to fill up $I_0/(pi_{\max})$ adjacent buckets. For example, if $I_0 = 450$ mA and $i_{\max} = 2$ mA, we need to fill up 75 adjacent buckets at each of the three locations. So all in total $x = I_0/(Mi_{\max})$ or 25% of the buckets are filled. If $i_{\max} = 1$ mA instead, 150 adjacent buckets have to be filled in each of the three chosen locations, which makes 50% of the ring filled. These patterns are illustrated in Fig. 8.16. When a fraction x of the ring filled in this way, the

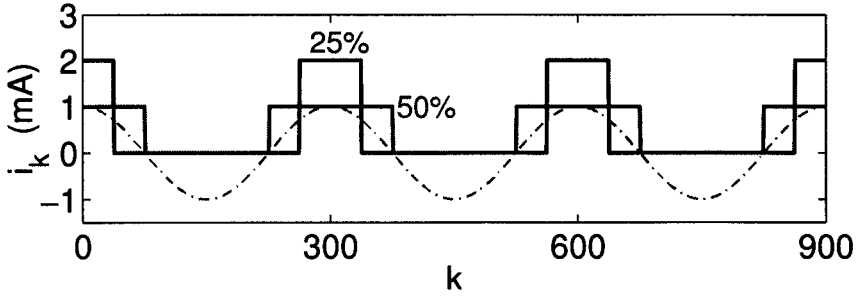


Fig. 8.16 Illustration of fill optimization for a ring with $M = 900$ bunches when evenly filled and total beam current $I_0 = 450$ mA. Solid: 50% fill and 25% fill maximize C_3 for $i_{\max} = 1$ mA and 2 mA. Dash-dot: Reference sinusoid at three times the revolution frequency. (Courtesy Prabhakar. [5])

modulation parameter C_p will be reduced, and the modulation parameter will be (Exercise 8.10)

$$C_p \approx \frac{\sin(\pi x)}{\pi x}. \tag{8.147}$$

In general, we can calculate a corresponding "weight" $\cos(2\pi pn/M)$ for bucket n and fill each "heaviest" $I_0/i_{\max}$ bucket to the same current $i_{\max}$.

8.3.4.2 *Landau Damping*

A bunch will receive a coherent synchrotron tune shift from itself[¶] and from the other bunches. For an evenly filled ring, this tune shift will be the same for all bunches. For an unevenly filled ring, however, each bunch will be seeing its predecessors in a different pattern, and therefore receive a different tune shift.

[¶]For point bunches, all shifts are coherent, in the language of particles inside a bunch. However, if we consider all the M bunches as an ensemble with the coherent excitation frequency Ω, then the tune shift of each bunch can be called incoherent.

The spread in coherent synchrotron tune shift among the bunches will provide Landau damping.

We need to be a little careful to derive the tune shifts for the bunches because, for example, Eq. (8.141) is the equation of motion for a coupled-bunch mode ℓ and not for a particular bunch. We must employ Eq. (8.129) to transform back to the equation of motion of τ_k for bunch k. Keeping only the second term on the right side of Eq. (8.141), the synchrotron frequency shift for bunch k relative to the mean synchrotron tune is found to be (Exercise 8.11)

$$\Delta\omega_{s0}^{k} = -\frac{ie\eta\omega_{\rm rf}}{2\beta^2 E_0 T_0 \omega_{s0}} \sum_{\ell=0}^{M-1} \left[Z_{\rm eff}(\ell\omega_0) I_\ell e^{-i2\pi k\ell/M} \right], \tag{8.148}$$

which is purely real because the real part of the summand is an odd function of ℓ with period M. For an evenly fill pattern, $I_\ell = 0$ unless $\ell = 0$, the tune shift for each bunch will be the same, and we reproduce the second term on the right side of Eq. (8.52) for the point-bunch model for one bunch. For $I_\ell \neq 0$ when $\ell \neq 0$, however, different bunches receive different tune shifts, creating a tune spread for Landau damping.

Consider a sharp impedance resonance at $n\omega_0$ which is not a multiple of the bunch frequency $M\omega_0$. If we design a fill optimized for C_n, a sinusoidal ringing in the wake voltage is excited at $n\omega_0$, which contributes to an uneven frequency shift according to Eq. (8.148). The best value of C_n for damping EFEM n is different from the optimum for other EFEMs: (A) Landau damping of EFEMs other than n can be calculated in the usual way, [17] if they are not coupled to other prominent EFEMs by modulation coupling or by tune-spread terms on the nth diagonal of matrix A. (B) Damping of EFEM n is larger than that of other modes, since the combination of tune spread and fill unevenness introduces coupling between ω_{s0}^{n} and ω_{s0}^{M-n}. If Landau damping and coupling to ω_{s0}^{M-n} are the only significant effects and $\lambda_n \approx -\lambda_n^*$, then the variation with fill fraction x is shown in Figure 8.17, which shows the increase in Landau damping as the fill fraction x is decreased. The figure is symmetric about both axis. Dashed lines show the evolution of λ_n from a few even-fill starting points. In the figure, $\mathcal{R}e\,\lambda$ is proportional to the growth rate while $\mathcal{I}m\,\lambda$ is proportional to the tune shift. Interestingly, eigenvalues with large imaginary parts are completely damped even by 80% fills. It appears that, in this special case, fill unevenness only seems to reduce the growth rate $\mathcal{R}e\,\lambda$, without changing the coherent tune $\mathcal{I}m\,\lambda$ very much. Thus EFEM n is best damped by maximizing C_n, i.e., by minimizing the fill fraction.

Of course, narrowband resonances are not required for producing the tune spread, though they simplify the explanation of fill-induced Landau damping.

Unlike modulation damping, there is no analog of this Landau-damping phenomenon in the transverse plane.

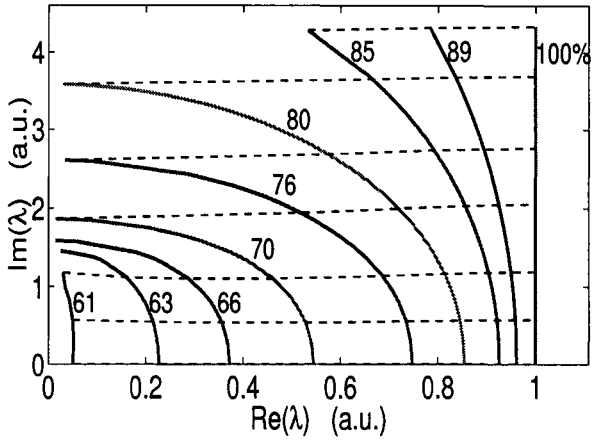


Fig. 8.17 Graphic look-up table for fill-induced damping of eigenvalue of unstable longitudinal EFEM n as C_n is increased from 0 (100% of ring filled) to 0.5 (61% filled). Dashes: Evolution of λ_n from a few even-fill starting points. (Courtesy Prabhakar. [5])

8.3.4.3 *Applications*

PEP II LER

There are longitudinal coupled-bunch instabilities in the PEP-II Low Energy Ring (LER) at $I_0 = 1$ A and $M = 873$. [16] The two largest cavity resonances are expected to drive bands of modes centered at 93.1 MHz (EFEM 683) and 105 MHz (EFEM 770) unstable. They also stabilize the corresponding bands at 25.9 MHz (EFEM 190) and 14 MHz (EFEM 103). The growth and damping rate spectrum are shown in Fig. 8.18(a). The best modulation-coupling cure is to couple the modes around 105 MHz to those near 25.9 MHz by maximizing C_{580} or C_{293} since $C_p = C_{M-p}$ $(683 - 103 = 580)$. This will automatically couples 93.1 MHz to 14 MHz. The optimization can be easily accomplished by filling every third nominally-spaced bucket, since $873/3 = 291$ is close to 293. Thus the damping parts will help the growing parts. The calculation illustrated in Fig. 8.18(b) shows that such a fill should be stable at 1 A. The above fill-pattern is equivalent to slicing the frequency range from zero to $M\omega_0$ (from 0 to 39.67 MHz, from 39.67 to 79.33 MHz, and 79.33 to 149 MHz) and placing the three parts of the growth or damping spectrum on each other. In this way, it can be easily visualized how the growth spectrum near the resonances at 93.1 MHz and 105 MHz are cancelled by the damping spectrum near 25.9 MHz and 14 MHz. Modulation coupling was expected to raise the instability threshold

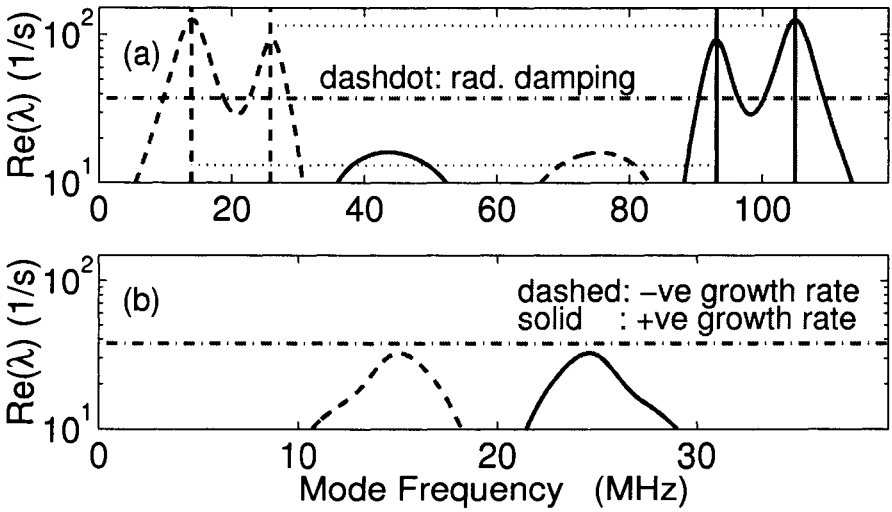


Fig. 8.18 Growth rates versus mode frequency $\ell\omega_0 + \omega_{s0}$ at $I_0 = 1$ A for PEP-II LER. Top: Even fill at normal 8.4 ns spacing with feedback required for stability. Bottom: Even fill at 3×8.4 ns spacing, stabilized by modulation coupling without feedback. The growth spectrum is sketched in solid, the damping spectrum is sketched in dashes, and the radiation damping rate is sketched in dashdots. (Courtesy Prabhakar. [5])

from 305 mA (nominal spacing) to 1.16 A (three times nominal spacing). The measured thresholds are 350 mA and 660 mA, respectively.

Advanced Light Source (ALS)

Theoretical predictions of fill-induced Landau damping were first tested at the Advanced Light Source (ALS). Only two of the 328 ALS modes were unstable: mode 204 and 233. The effective impedance at $233\omega_0$ was used to create a tune spread by maximizing C_{233}.

A baseline even-fill instability measurement was first made at $I_0 = 172$ mA. This gave the two eigenvalues $\lambda_{204} = (0.47 \pm 0.02) + i(0.05 \pm 0.03)$ ms^{-1} and $\lambda_{233} = (0.61 \pm 0.02) + i(1.16 \pm 0.03)$ ms^{-1}, assuming that the radiation damping rate $d_r = 0.074$ ms^{-1}. It is evident from Fig. 8.17 that fill fraction less than 60% will damp the target mode almost completely. Thus, any residual instability in the Landau fill must correspond to the Landau-damped mode 204. Numerical calculation gives us only one unstable mode with eigenvalue $(0.1 \pm 0.04) - i(1.62 \pm 0.06)$ ms^{-1}, whose real part is about six times less than in the even-fill case. The measured eigenvalue for a 175-mA beam with $C_{233} = 0.67$ is $(0.09 \pm 0.003) - i(1.63 \pm 0.005)$ ms^{-1}, in agreement with the theoretical prediction.

Taiwan Light Source (SRRC)

Prediction of uneven fill has also been made on the light source at SRRC of Taiwan. [18] The main source of longitudinal impedance is from the Doris type rf cavities, which have a resonance at 744.1948 MHz, loaded $Q_L = 2219$ and $R_L/Q_L = 31.95\ \Omega$. But from the observation on the real machine, the unstable mode number is 97 or resonance frequency is 742 MHz. There are $M = 200$ rf bucket in the SRRC ring. Thus, the most stable mode is 103. To couple the two modes, one must maximize C_6, or the filling pattern is in six groups of buckets. The simulations consist of using three uneven fill patterns as illustrated on the left side of Fig. 8.19 with a total beam current of 200 mA. The spectra are shown on the right side. It is evident that the growth driven by the resonance at mode 97 is no longer observed in each of the three uneven fill patterns for the maximization of C_6.

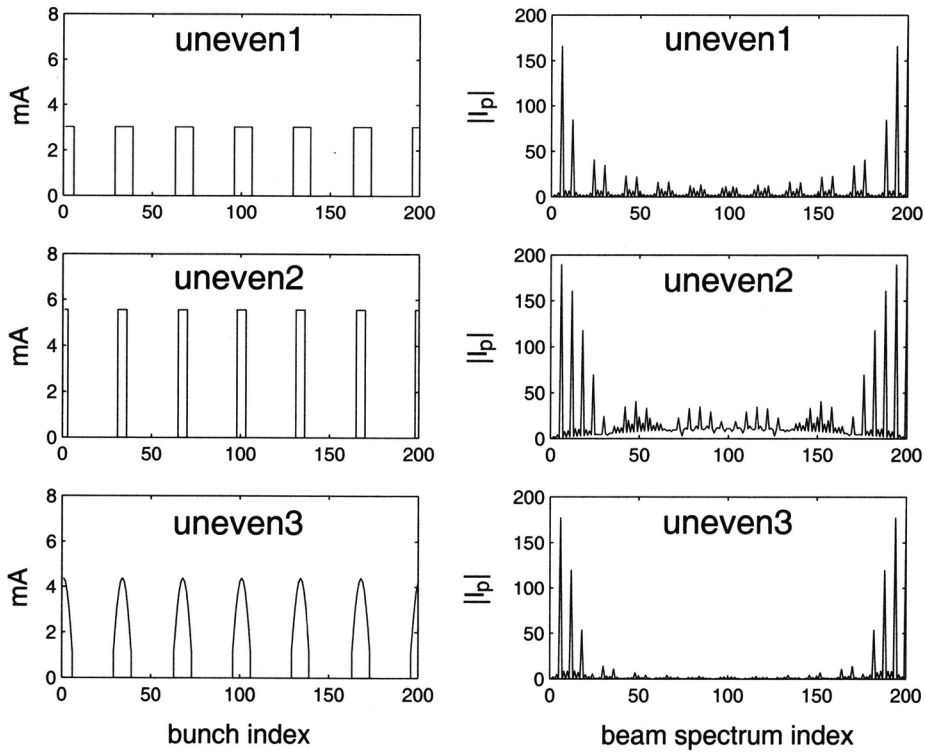


Fig. 8.19 Fill patterns used in the simulation of the Taiwan Light Source in order to maximize C_6 so that the excitation of mode 97 driven by the higher-order resonance in the cavity will be compensated by the damping at mode $200 - 97 = 103$. (Courtesy Wang, *et. al.* [18])

The growth rates for the two modes (97 and 103) are computed. The results are displayed in Fig. 8.20 and listed in Table 8.1. The plots show the smallest phase oscillation amplitude for uneven fill pattern 2. This is expected from Fig. 8.19, where, compared with the other patterns, the beam density is most

Table 8.1 Simulation results of growth rates of EFEM 97 and 103 of four fill patterns. 5 ms radiation damping time has been included.

Fill pattern	C_6	Growth rate ms^{-1} EFEM 97	EFEM 103
uniform	0	1.9399	—
uneven1	0.8302	1.0004	1.0182
uneven2	0.9476	0.4947	0.4947
uneven3	0.8855	0.8659	0.8703

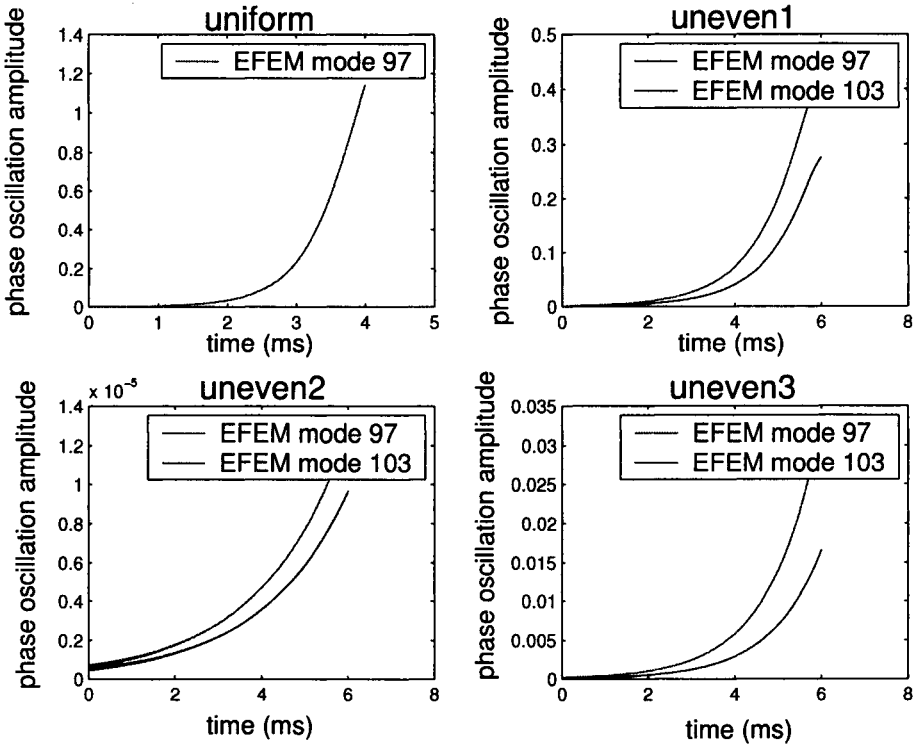


Fig. 8.20 The evolution of EFEM 97 (lighter) and EFEM 103 (darker) of four fill patterns from simulation (the even fill plus the three uneven fills). Uneven fill pattern 2 gives the smallest phase oscillation amplitudes for both EFEM modes. (Courtesy Wang, *et. al.* [18])

concentrated at the six locations. In other words, C_6 has been mostly maximized in this fill pattern. We see that the growth rates for the two EFEM modes are also the lowest in the uneven pattern 2 as tabulated in Table 8.1, where the derived growth rates include 5 ms radiation damping time. The simulation demonstrates that modulation coupling has been helping to damp the beam instability. However, the result has not been completely satisfactory because the instability has not been totally damped.

8.4 Exercises

8.1 Above/below transition, with the angular resonant frequency ω_r offset by $\Delta\omega = \pm(\omega_r - h\omega_0)$ where $\omega_{\rm rf} = h\omega_0$ is the angular rf frequency, h is the rf harmonic, and ω_0 is the revolution angular velocity, the stability of the bunch is governed by Robinson's criteria.

(1) Assuming that $\omega_s \ll |\Delta\omega| \ll \omega_{\rm rf}$ and using the expression for resonant impedance in Eq. (1.56), show that the Robinson's growth rate in Eq. (8.45) can be written as

$$\frac{1}{\tau} = -\frac{2e^2 N_b \eta R_L Q_L}{\beta^2 E_0 T_0^2} \cos^2\psi \sin 2\psi, \tag{8.149}$$

where N_b is the number of particles in the bunch, E_0 is the synchronous energy, βc is the velocity of the synchronous particle with c being the velocity of light, $T_0 = 2\pi/\omega_0$ is the revolution period, η is the slip factor, and the detuning angle ψ is defined as

$$\tan\psi = 2Q_L \frac{\omega_r - \omega_{\rm rf}}{\omega_r}$$

for the resonant impedance with shunt impedance R_L, resonant frequency $\omega_r/(2\pi)$, and quality factor Q_L.

(2) Assuming further that $|\Delta\omega|$ is much less than the resonator width $\omega_r/(2Q_L)$, which, in turn, is much less than ω_0, show that the Robinson's growth rate can be written as

$$\frac{1}{\tau} = -\frac{4e^2 N_b R_L Q_L^2 \eta \Delta\omega}{\pi\beta^2 E_0 h T_0}. \tag{8.150}$$

(3) Robinson's instability is usually more pronounced in electron than proton machines because large shunt impedance and high quality factor are often required in the rf system. Take for example a ring of circumference 180 m with slip factor $|\eta| = 0.03$. To store a typical bunch with

1×10^{11} electrons at $E_0 = 1$ GeV, one may need an rf system with $h = 240$, $R_L = 1.0$ MΩ, and $Q_L = 2000$. On the other hand, to store a bunch of 1×10^{11} protons at kinetic energy $E_0 = 1$ GeV in the same ring, one may need an rf system with $h = 4$, $R_L = 0.12$ MΩ, and $Q_L = 45$. Compare the Robinson's growth rates for the two situations when the resonant frequencies are offset in the wrong direction by $|\Delta\omega/(2\pi)| = 10$ kHz. Note that when the detuning is too large, the exact formula of the resonant impedance must be used.

8.2 (1) From Eqs. (2.89) and (2.92), show that the potential-well contribution to the incoherent synchrotron tune shift of a short bunch in the water-bag model is

$$\Delta\nu_{s\,\mathrm{incoh}} = \frac{\nu_{s0}\xi}{\omega_0\hat{\tau}} \sum_{q=-\infty}^{\infty} \mathcal{I}m\, Z_0^{\parallel}(q\omega_0) J_0(q\omega_0\hat{\tau}) J_1(q\omega_0\hat{\tau}), \tag{8.151}$$

where $\hat{\tau}$ is the half bunch length and ξ is the scale factor defined in Eq. (2.90). Hint: The Fourier transform of the linear density in the water-bag model is $\tilde{\lambda}(\omega) = J_0(\omega\hat{\tau})/(2\pi)$.

(2) Show that this static contribution to the coherent synchrotron tune shift just cancels the dynamic contribution in Eq. (8.40) when the driving wake potential is much longer than the bunch length.

8.3 Using Eqs. (2.89) and (2.92), compute the incoherent synchrotron frequency shift of a point bunch and show that it is equal to the same incoherent synchrotron frequency shift obtained in Eq. (8.52).

8.4 Using the definition in Eq. (8.75) for the form factor in the longitudinal instability growth rate, compute numerically the form factor when the unperturbed distribution is bi-Gaussian. The half bunch length can be taken as $\hat{\tau} = \sqrt{6}\sigma_\tau$, where σ_τ is the rms bunch length.

8.5 Consider a single sinusoidal rf system operating below transition at the synchronous phase angle $\phi_s = 0$.

(1) Show that the synchrotron frequency of a particle at rf phase ϕ is given by

$$\frac{f_s(\phi)}{f_{s0}} = \frac{\pi}{2K(t)}, \tag{8.152}$$

where $t = \sin\phi/2$, f_{s0} is the synchrotron frequency at zero amplitude, and $K(t)$ is the complete elliptic integral of the first kind defined in Eq. (8.87).

(2) Show that Eq. (8.152) is consistent with Eq. (8.58) at small amplitudes.

8.6 Reproduce Fig. 8.3, synchrotron frequency spread $(\omega_{s0} - \omega_s)/\omega_{s0}$ as a function of the single-bucket bunching factor at a general synchronous phase

ϕ_s, taken into account only the nonlinearity of the sinusoidal rf potential. Hint: The Hamiltonian is

$$H = \frac{\omega_{s0}\Delta\tilde{E}^2}{2} + \frac{\omega_{s0}}{\cos\phi_s}\Big[\cos\phi_s - \cos(\Delta\phi+\phi_s) + \Delta\phi\sin\phi_s\Big], \qquad (8.153)$$

where $\Delta\phi$ is the rf phase measured from the synchronous phase ϕ_s, $\Delta\tilde{E} = -2\pi\omega_{s0}\Delta E/(\omega_0 eV_{\rm rf}\cos\phi_s)$, ΔE is the energy offset of the beam particle, and $V_{\rm rf}$ is the peak rf voltage. First choose a bunch edge $\Delta\phi_1 < 0$ and determine the other edge $\Delta\phi_2 > 0$ via

$$\cos(\Delta\phi_2+\phi_s) + \Delta\phi_2\sin\phi_s = \cos(\Delta\phi_1+\phi_s) + \Delta\phi_1\sin\phi_s, \qquad (8.154)$$

from which the bunching factor $B = (\Delta\phi_2 - \Delta\phi_1)/(2\pi)$ is obtained. Next show that the synchrotron frequency ω_s of a particle at the bunch edge is given by

$$\frac{\sqrt{2}\pi\omega_{s0}}{\omega_s(B)} = \int_{\Delta\phi_1}^{\Delta\phi_2} d\Delta\phi \sqrt{\frac{\cos\phi_s}{\cos(\Delta\phi+\phi_s) - \cos(\Delta\phi_1+\phi_s) + (\Delta\phi-\Delta\phi_1)\sin\phi_s}}.$$

8.7 Solve the set of equations in Eqs. (8.82) to (8.84) to obtain the fundamental rf phase ϕ_s, the higher-harmonic rf phase ϕ_m and the voltage ratio r in terms of the harmonic ratio m, rf peak voltage $V_{\rm rf}$, and the radiation energy loss per turn U_s.
Answer:

$$\sin\phi_s = \frac{m^2}{m^2-1}\frac{U_s}{eV_{\rm rf}}, \qquad \tan\phi_m = \frac{\dfrac{m}{m^2-1}\dfrac{U_s}{eV_{\rm rf}}}{\sqrt{1-\left(\dfrac{m^2}{m^2-1}\dfrac{U_s}{eV_{\rm rf}}\right)^2}},$$

$$r = \sqrt{\frac{1}{m^2} - \frac{1}{m^2-1}\frac{U_s^2}{(eV_{\rm rf})^2}}. \qquad (8.155)$$

8.8 Derive the small-amplitude synchrotron frequency as a function of amplitude for the two-rf system as given by Eq. (8.86).

8.9 Consider the situation when $I_k Z_{\rm eff}(k\omega_0) = 0$ except for $k = 0$ and there is only one sharp resonance that can excite coupled-bunch mode ℓ and damp mode m. Fill in the steps to arrive at the new eigenmodes. We have

$$[d_r - i(\Omega-\omega_{s0})]\begin{pmatrix}\varsigma^\ell\\ \varsigma^m\end{pmatrix} = B\begin{pmatrix} I_0 Z_{\ell m} & I_{\ell-m}Z_{\ell m}\\ I_{m-\ell}Z_{m\ell} & I_0 Z_{m\ell}\end{pmatrix}\begin{pmatrix}\varsigma^\ell\\ \varsigma^m\end{pmatrix}, \qquad (8.156)$$

with

$$B = \frac{e\eta\omega_{\rm rf}}{2\beta^2 E_0 T_0 \omega_{s0}}. \tag{8.157}$$

In the above, the tune-shift term of the impedance, $Z_{\rm eff}\big[(\ell - m)\omega_0\big]$, has been neglected. Thus $Z_{\ell m}$ depends on ℓ only but not on m.
Denote the eigenvalue by $\lambda = d_r - i(\Omega - \omega_{s0})$. Then the eigenvalues for a even-fill ring are

$$\lambda_\ell = BI_0 Z_{\ell m}. \tag{8.158}$$

The eigenvalues for an uneven-fill ring are given by

$$\begin{vmatrix} \lambda - \lambda_\ell & -\dfrac{I_{\ell-m}}{I_0}\lambda_\ell \\ -\dfrac{I_{m-\ell}}{I_0}\lambda_m & \lambda - \lambda_m \end{vmatrix} = 0, \tag{8.159}$$

Noting from Eq. (8.136), the beam spectrum satisfies $I_k = I^*_{-k}$, and letting $|I_p| = C_p I_0$, the new eigenvalues for the two modes are

$$\lambda = \frac{1}{2}(\lambda_\ell + \lambda_m) \pm \frac{1}{2}\sqrt{(\lambda_\ell - \lambda_m)^2 + 4C^2_{\ell-m}\lambda_\ell\lambda_m}. \tag{8.160}$$

8.10 The modulation parameter C_p of a ring with M rf buckets can be optimized by filling evenly xN buckets in p clusters. Show that

$$C_p = \frac{p}{xM}\frac{\sin \pi x}{\sin p\pi/M}. \tag{8.161}$$

8.11 Derive Eq. (8.148), the synchrotron frequency shift of point bunches in an uneven-fill pattern. Hint: Perform the inverse Fourier transform of Eq. (8.141) to get back the equation of motion of the kth bunch in the time domain. Ignore the modulation term in Eq. (8.139) then extract the frequency shift.

Bibliography

[1] P. B. Robinson, *Stability of Beam in Radiofrequency System*, Cambridge Electron Accel. Report CEAL-1010, 1964.

[2] F. J. Sacherer, *A Longitudinal Stability Criterion for Bunched Beams*, CERN Report CERN/MPS/BR 73-1, 1973; *IEEE Trans. Nucl. Sci.* **NS 20**(3), 825 (1973).

[3] D. Wildman and K. Harkay *HOM RF Cavity Dampers for Suppressing Coupled Bunch Instabilities in the Fermilab Booster*, Proc. 1993 Part. Accel. Conf., ed. S. T. Corneliussen (Washington, D.C., May 17–20, 1993), p. 3258.

[4] R. D. Kohaupt, DESY Report DESY 85-139,1985.

[5] S. Prabhakar, *New Diagnostic and Cures for Coupled-Bunch Instabilities*, Ph.D. Thesis, Stanford University, 2000, 1999, SLAC Preprint SLAC-R-554.

[6] A. Hofmann and S. Myers, *Beam Dynamics in a Double RF System*, Proc. 11th Int. Conf. High Energy Accel. (Geneva, 1980).

[7] A. Mosnier, *Cures of Coupled Bunch Instabilities*, Proc. 1999 Part. Accel. Conf., eds. A. Luccio and W. MacKay (New York, March 27–April 2, 1999), p. 629.

[8] S. Y. Lee, D. D. Caussyn, M. Ellison, K. Hedblom, H. Huang, D. Li, J. Y. Liu, K. Y. Ng, A. Riabko, and Y. T. Yan, *Phys. Rev.* **E49**, 5717 (1994); J. Y. Liu, M. Ball, B. Brabson, J. Budnick, D D. Caussyn, G. East, M. Ellison, B. Hamilton, W. P. Jones, X. Kang, S Y. Lee, D. Li, K. Y. Ng, A. Riabko, D. Rich, T. Sloan, and L. Wang, *Phys. Rev.* **E50**, R3349 (1994); J. Y. Liu *et al.*, *Part. Accel.* **49**, 221 (1995).

[9] R. Averill, A. Hofmann, R. Little, H. Mieras, J. Paterson, K. Strauch, G-A. Voss, andd H. Winick, *Synchrotron and Betatron Instabilities of Stored Beams in CEA*, Proc. 8th Int. Conf. High Energy Accel., eds. M. H. Blewett and N. Vogt-Nilsen (CERN, Geneva, Sept. 20–24, 1971), p. 301.

[10] P. Bramham, S. Hansen, A. Hofmann, K. Hüber, and E. Peschardt, *Investigation and Cures of Longitudinal Instabilities of Bunched Beams in ISR*, Proc. 9th Int. Conf. High Energy Accel. (SLAC, Stanford, May 2–7, 1974), p. 359; P. Bramham, S. Hansen, A. Hofmann, K. Hüber, and E. Peschardt, *Investigation and Cures of Longitudinal Instabilities of Bunched Beams in ISR, IEEE Trans. Nucl. Sci.* **NS-24**(3), 1490 (1977).

[11] J. M. Baillod, L. Magnani, G. Nassibian, F. Pedersen, and W. Weissflog, *A Second Harmonic (6–16 MHz) RF System with Feedback-Reduced Gap Impedance for Accelerating Flat-Topped Bunches in the CERN PS Booster, IEEE Trans. Nucl. Sci.* **NS-30**(4), 3499 (1983); G. Gelato, L. Magnani, N. Rasmussen, H. Schnauer, and K. Schindl, Proc. 1987 IEEE Part. Accel. Conf., eds. E. R. Lindstrom and L. S. Taylor (Washington, D.C., March 16–19, 1987) p. 1298.

[12] D. Li, M. Ball, B. Brabson, J. Budnick, D. D. Caussyn, A. W. Chao, V. Derenchuk, S. Dutt, G. East, M. Ellison, D. Friesel, B. Hamilton, H. Huang, W. P. Jones, S. Y. Lee, J.Y. Liu, M. G. Minty, K. Y. Ng, X. Pei, A. Riabko, T. Sloan, M. Syphers, Y. Wang, Y. Yan, and P. L. Zhang, *Effects of Rf Voltage Modulation on Particle Motion, Nucl. Instrum. Meth.* **A364**, 205 (1995).

[13] M. Georgsson, Å. Anderson, M. Eriksson, *Landau Cavities at MAXII, Nucl. Instrum. Meth.* **A416**, 465 (1998).

[14] M. H. Wang, Peace Chang, P. J. Chou, K. T. Hsu, C. C. Kuo, J. C. Lee, and W. K. Lau, *Experiment of RF Voltage Modulation at at SRRC*, Proc. 1999 Part. Accel. Conf., eds. A. Luccio and W. MacKay (New York, March 27–April 2, 1999), p. 2837.

[15] K. Y. Ng, *Damping of Coupled-Bunch Growth by Self-Excited Cavity*, Fermilab Report FN-456, 1987; K.Y. Ng, *Longitudinal Coupled-Bunch Instability in the Fermilab Booster*, Fermilab Report FN-464, 1987 (KEK Report 87-17).

[16] S. Prabhakar, *New Diagnostic and Cures for Coupled-Bunch Instabilities*, Proc. 2001 Part. Accel. Conf., eds. P. Lucas and S. Webber (Chicago, June 18–22, 2001), p. 300.

[17] H. G. Hereward, *Landau Damping*, CERN Accelerator School—Advanced Accelerator Physics, Ed. S. Turner (Oxford, England, Sept. 16–27, 1985), p. 255; Y. H. Chin and K. Yokoya, *Landau Damping of a Multi-Bunch Instability due to Bunch-to-Bunch Tune Spread*, DESY Report DESY-86-097, 1997.

[18] M. H. Wang, P. J. Chou, and A. W. Chao, *Study of Uneven Fills to Cure the Coupled-Bunch Instability in SRRC*, Proc. 2001 Part. Accel. Conf., eds. P. Lucas and S. Webber (Chicago, June 18–22, 2001), p. 1981.

This page intentionally left blank

2025 © The Author(s). This is an Open Access chapter published by World Scientific Publishing Company, licensed under the terms of the Creative Commons Attribution-NonCommercial 4.0 International License (CC BY-NC 4.0).

Chapter 9

Transverse Instabilities

9.1 Transverse Focusing and Transverse Wake

Transverse focusing of the particle beam is necessary. If not the beam will diverge hitting the vacuum chamber and get lost. The alternating-gradient focusing scheme invented by Courant and Synder [1] employs F-quadrupoles and D-quadrupoles to provide for strong focusing of the beam in both the horizontal and vertical planes. For this reason, the transverse beam size can be made very small and so can be the size of the vacuum chamber and the aperture of the magnets. In light sources, usually the Chasman–Green lattices are used. [2] They consist of double achromats or triple achromats, which are strong focusing and give zero dispersion at both ends. Another merit of the achromats is that they can provide much smaller transverse emittances for the electron beam than the alternating gradient scheme of Courant and Synder.

Because quadrupoles can focus in only one transverse plane and defocus in the other, transverse oscillations develop in both transverse planes. These are called *betatron oscillations*, and the oscillation frequencies, $\omega_\beta/(2\pi)$, are called *betatron frequencies*, which are usually different in the two transverse planes. The number of betatron oscillations made in the vertical/horizontal direction in a revolution turn of the beam, $\nu_\beta = \omega_\beta/\omega_0$, is called the *vertical/horizontal betatron tune*. The equation of motion of a beam particle with energy E_0 in, for example, the vertical plane is given by

$$\frac{d^2y}{dn^2} + (2\pi\nu_\beta)^2 y = \frac{C_0^2\langle F_1^\perp\rangle_{\mathrm{dyn}}}{\beta^2 E_0}, \tag{9.1}$$

where C_0 is the ring circumference, βc is the particle velocity, c is the velocity of light, and n denotes turn number and the right side is the contribution due to the transverse electromagnetic wake $W_1(\tau)$. Here. ν_β on the left side is the incoherent vertical tune of the beam particle. Consider a coasting beam with

current I_0. The dynamic part of the transverse force, $\langle F_1^\perp \rangle_{\rm dyn}$, pertaining to a particular frequency, is related to the transverse impedance at that frequency through Eqs. (1.44) to (1.43) after averaging over the circumference of the ring,*

$$Z_1^\perp = -\frac{iC_0\langle F_1^\perp\rangle_{\rm dyn}}{e\beta I_0 \bar{y}}, \tag{9.2}$$

where $\bar{y}$ is the vertical displacement of the beam center. After averaging over all the beam particles, we obtain the equation of motion for the transverse motion of the beam center:

$$\frac{d^2\bar{y}}{dn^2} + (2\pi\nu_\beta)^2\bar{y} = \frac{ieI_0 Z_1^\perp C_0}{\beta E_0}\,\bar{y}. \tag{9.3}$$

Thus, the transverse wake amounts to a betatron frequency shift

$$\Delta\omega_\beta = -\frac{i\beta c^2}{2\omega_\beta E_0}\,\frac{eI_0}{C_0}\,Z_1^\perp. \tag{9.4}$$

For a coasting beam, transverse excitation comes from the transverse impedance that samples one or more of the betatron sidebands $n\omega_0 + \omega_\beta$ flanking the revolution harmonic n. The reactive part of $Z_1^\perp(\omega)$ produces a real frequency shift, which is the dynamic part of the coherent shift. The resistive part produces an imaginary frequency shift, which if positive implies instability. Since $\mathcal{R}e\, Z_1^\perp(\omega) \gtrless 0$ when $\omega \gtrless 0$, the resistive part at negative frequencies excites instability. Thus only coasting-beam modes with $n < -\nu_\beta$ can be unstable.

It is important to point out that the above derivation of betatron tune shift originates from Eq. (9.1), where smooth betatron focusing has been assumed. The more exact derivation allowing for nonuniform focusing can best be made using the Hamiltonian formalism in the action-angle variables. An example is illustrated in Exercise 3.7, where we learn that the result can be obtained partially from that of the uniform focusing simply via the substitution

$$\frac{1}{\nu_\beta} = \frac{\beta_\perp}{R}, \tag{9.5}$$

where $\beta_\perp$ is the betatron function at the location under discussion. The subscript "$\perp$" has been introduced so that one will not confuse the betatron function with the Lorentz parameter β. This subscript will be dropped only when no ambiguity exists. Thus Eq. (9.4) should be written more correctly as

$$\Delta\nu_\beta = -\frac{ieI_0}{4\pi\beta E_0}\,\left[\beta_\perp Z_1^\perp\right], \tag{9.6}$$

*The subscript is actually not necessary, because, as will be shown below in Sec. 9.4, the average transverse wake force has only a dynamic part.

where $[\beta_\perp Z_1^\perp]$ implies that the proper procedure of summing up the transverse impedance element by element should have the betatron function included as a weight. In fact, there is a physical reason for doing this; the transverse impedance is only important at a location where the transverse displacement of the beam is large. For this reason, we have

$$[\beta_\perp Z_1^\perp] = \sum_\ell (\beta_\perp Z_1^\perp)_\ell, \tag{9.7}$$

where $(Z_1^\perp)_\ell$ denotes the transverse impedance of element ℓ inside the vacuum chamber.

There is a direct parallel between the transverse dynamics and the longitudinal dynamics, as is illustrated in the equations of motion in the longitudinal phase plane and the transverse phase plane. However, there is a big difference that the betatron tune $\nu_\beta \gg 1$ while the synchrotron tune $\nu_s \ll 1$.

9.2 Betatron Fast and Slow Waves

Consider a beam particle performing vertical betatron oscillations with amplitude A and vertical betatron tune ν_β. The transverse displacement is

$$y(t) = A\cos(\nu_\beta \omega_0 t + \psi), \tag{9.8}$$

where ω_0 is the angular revolution frequency and ψ is the betatron phase at $t = 0$. Suppose that its azimuthal location along the accelerator ring is $\theta = \theta_0$ at $t = 0$. The dipole moment of the particle picked up by a beam-position monitor at location $\theta_{\rm BPM} = 0$ is the product of the transverse displacement and the longitudinal current,

$$\begin{aligned} d_e(\psi,\theta_0;t) &= e\omega_0 A\cos(\nu_\beta\omega_0 t+\psi)\sum_{p=-\infty}^{\infty}\delta(\omega_0 t-\theta+\theta_0-2p\pi) \\ &= \frac{e\omega_0 A}{2\pi}\cos(\nu_\beta\omega_0 t+\psi)\sum_{n=-\infty}^{\infty}e^{-i(n\omega_0 t-n\theta+n\theta_0)} \\ &= \frac{e\omega_0 A}{4\pi}\sum_{n=-\infty}^{\infty}\left\{e^{-i[(n+\nu_\beta)\omega_0 t-n(\theta-\theta_0)+\psi]}+e^{-i[(n-\nu_\beta)\omega_0 t-n(\theta-\theta_0)-\psi]}\right\}. \end{aligned} \tag{9.9}$$

The first term inside the curly brackets indicates upper sidebands around all the revolution harmonics, both positive and negative, while the second term indicates lower sidebands. This is illustrated in Fig. 9.1. As a result, the spectrum consists of betatron sidebands on both sides of the revolution harmonics. Notice that the second term in the curly brackets of Eq. (9.9) becomes

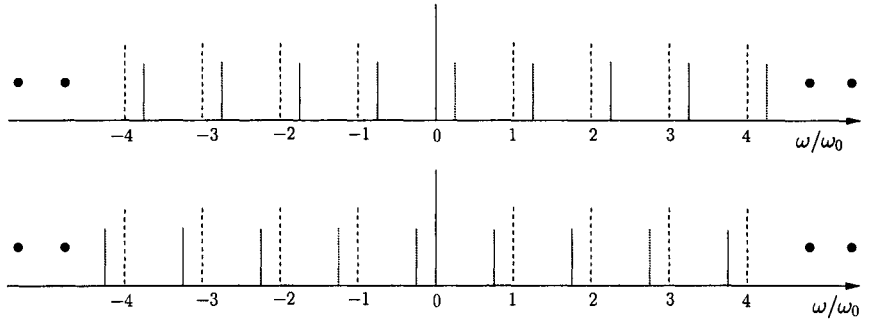


Fig. 9.1 Spectrum of a single particle executing betatron oscillations. Top: spectrum with upper betatron sidebands. Bottom: spectrum with lower betatron sidebands. Both spectra lead to exactly the same physical observation.

$e^{i[(n+\nu_\beta)\omega_0 t - n\theta + n\theta_0 - \psi]}$ if we make the substitution $n \to -n$. The dipole moment can therefore be rewritten as

$$d_e(\psi, \theta_0; t) = \frac{e\omega_0 A}{2\pi} \sum_{n=-\infty}^{\infty} \cos[(n + \nu_\beta)\omega_0 t - n\theta + \psi]. \tag{9.10}$$

Equivalently, this can also be written as

$$d_e(\psi, \theta_0; t) = \frac{e\omega_0 A}{2\pi} \sum_{n=-\infty}^{\infty} \cos[(n - \nu_\beta)\omega_0 t - n\theta - \psi]. \tag{9.11}$$

This tells us that, when both positive and negative frequencies are considered, upper sidebands and lower sidebands give the same physical picture. We therefore need to study only the top spectrum in Fig. 9.1 with upper sidebands and discard the bottom spectrum with lower sidebands, or to study only the bottom spectrum and neglect the top one. In most publications, the spectrum with the upper sidebands is chosen and we follow this convention here. However, what we observe in a network analyzer or an oscilloscope are only positive frequencies, or the spectrum with the negative frequencies folded onto the positive frequencies about the zero frequency. In other words, the upper sidebands in negative frequencies are depicted in the analyzer as the lower sidebands of the revolution harmonics.

The angular phase velocity ω_{ph} of a wave is just the ratio of the coefficient of t to the coefficient of the coordinate θ. In our case, for Eq. (9.10),

$$\omega_{\text{ph}} = \left(1 + \frac{\nu_\beta}{n}\right)\omega_0 \qquad \text{if } n \neq 0. \tag{9.12}$$

When $\nu_\beta = 0$, we see that the waves corresponding to all the revolution harmonics, positive and negative, have the same angular phase velocity ω_0, which is equal to the angular velocity of the beam particle. With a nonzero betatron tune ν_β, we may think that the waves at sidebands corresponding to $n > 0$ (upper sidebands seen in a network analyzer in an only-positive-frequency language) will travel faster and those corresponding to $n < 0$ will travel slower. The story is more complicated because the betatron tune has an integer part n_β and a noninteger part $[\nu_\beta]$, or $\nu_\beta = n_\beta + [\nu_\beta]$. An illustration is shown in Fig. 9.2 with $n_\beta = 2$ and $[\nu_\beta] = 0.25$. The illustration shows all the upper sidebands in solid and the lower sidebands, reflected from the upper sidebands that have negative frequencies, in dashes, while the revolution harmonics in dots. Because $n_\beta = 2$, the upper sideband next to $n = 0$ is actually associated with the harmonic $n = -2$, while the one next to $n = 1$ is associated with $n = -1$. Thus, these two upper sidebands correspond to waves with velocities $\omega_{\text{ph}} = -0.125\omega_0$ and $-1.25\omega_0$ according to Eq. (9.12). These waves are so slow that they go backward. The next upper sideband next to $n = 2$ is associated with $n = 0$; the wave is stationary and not moving at all [Eq. (9.12) does not apply]. The upper sidebands next to $n = 3,\ 4,\ \cdots$ are associated with positive n and they represent waves with velocities faster than ω_0. All the lower sidebands are associated with harmonics n that are negative. Thus, they represent waves with velocities slower than ω_0. Summing up

$$\frac{\omega_{\text{ph}}}{\omega_0} = 1 + \frac{\nu_\beta}{n} \quad \text{with} \quad \begin{cases} n > 0 & \text{fast wave,} \\ n < 0,\ |n| < \nu_\beta & \text{backward wave,} \\ n < 0,\ |n| > \nu_\beta & \text{slow wave,} \end{cases} \tag{9.13}$$

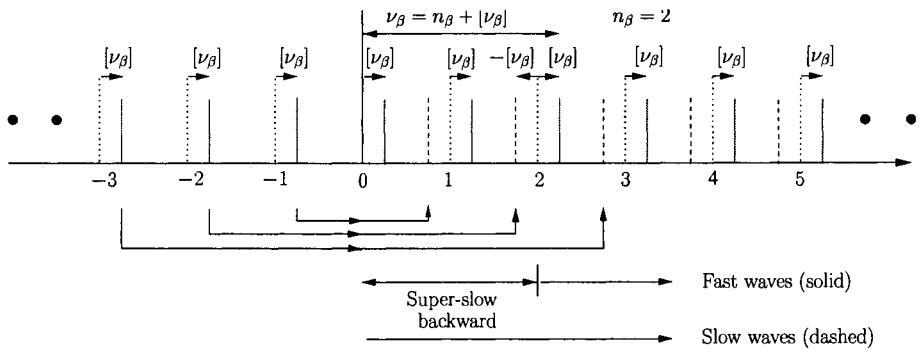


Fig. 9.2 Spectrum of a single particle executing betatron oscillations. Top: spectrum with upper betatron sidebands. Bottom: spectrum with lower betatron sidebands. Both spectra lead to exactly the same physical observation.

and $\omega_{\rm ph} = 0$ or the wave is stationary when $n = 0$. In the longitudinal spectrum we are going to study later, synchrotron sidebands correspond to waves with velocities that differ only slightly from the particle velocity, because the synchrotron tune is very much less than unity. On the other hand, we have seen that the velocities of waves corresponding to the betatron sidebands can differ very much from the particle velocity. It is important to distinguish slow waves from fast waves and backward waves, because, as we saw in Eq. (9.4) in above and later in below that only slow waves can be susceptible to instabilities. This is because $\mathcal{R}e\, Z_1^\perp(\omega) \gtrless 0$ when $\omega \gtrless 0$.

So far we have studied the betatron spectrum of a single particle. For many particles inside a beam, the transverse dipole moment is obtained by adding up the dipole moment $d_e(\psi, \theta_0; t)$ of all particles. Since the betatron phase ψ is random among the particles, the dipole moment averages to zero, meaning that all these upper and lower betatron sidebands will not be visible to an oscilloscope.† They are only visible when excited coherently by a transverse driving force, like a kicker, the transverse coupling impedance, etc. If a slow wave is excited and if there is no or not enough damping mechanism, the beam becomes unstable. For this reason, the lower betatron sidebands appear much more intense than the upper betatron sidebands. For a coasting beam, all betatron sidebands are independent and the slow-wave sidebands are excited according to the transverse impedance they sample. For a bunch beam, in addition to transverse impedance, the excitation of the slow-wave sidebands is governed by the bunch-mode spectra, like those illustrated in Fig. 6.13.

9.3 Separation of Transverse and Longitudinal Motions

Just as for synchrotron oscillations, it is more convenient to change from the rectangular coordinates (y, p_y) to the circular coordinates (r_β, θ) in the transverse betatron phase space. Following Eq. (6.1), we have

$$\begin{cases} y = r_\beta \cos\theta \\ p_y = r_\beta \sin\theta, \end{cases} \tag{9.14}$$

and Eq. (9.1) is transformed into

$$\begin{cases} \dfrac{dy}{ds} = -\dfrac{\omega_\beta}{v} p_y \\ \dfrac{dp_y}{ds} = \dfrac{\omega_\beta}{v} y - \dfrac{c}{E_0 \omega_\beta \beta} \langle F_1^\perp(\tau; s) \rangle_{\rm dyn}, \end{cases} \tag{9.15}$$

†They are visible in a Schottky scan.

where instead of turn number, the continuous variable s, denoting the distance along the designed orbit, has been used as the independent variable. In above, ω_s is the incoherent angular betatron frequency of the beam particle and is dependent on the particle's energy offset and oscillation amplitude.

For a bunched beam, longitudinal motion has to be included. For time period much less than the synchrotron damping time, Hamiltonian theory can be used. The Hamiltonian for motions in both the longitudinal phase space and transverse phase space can be written as

$$H = H_{\parallel} + H_{\perp}, \tag{9.16}$$

where $H_{\parallel}$ is the same Hamiltonian describing the longitudinal motion:

$$H_{\parallel} = -\frac{\eta(\Delta E)^2}{2v_0\beta_0^2 E_0} - \frac{eV_{\rm rf}}{C_0 h\omega_0}\left[\cos(\phi_s - h\omega_0\tau) - \cos\phi_s - h\omega_0\tau\sin\phi_s\right] + U_{\rm wake}(\tau), \tag{9.17}$$

while $H_{\perp}$ is the additional term coming from the equations of motion in the transverse phase space as given by Eq. (9.15). Note that the transverse force $\langle F_1^{\perp}(\tau; s)\rangle_{\rm dyn}$ in Eq. (9.15) depends on the longitudinal variable τ; therefore

$$[H_{\parallel}, H_{\perp}] \neq 0. \tag{9.18}$$

We assume that the perturbation is small and synchro-betatron coupling is avoided. Then

$$[H_{\parallel}, H_{\perp}] \approx 0. \tag{9.19}$$

This implies that in the transverse phase space, the azimuthal modes $m_{\perp} = 1, 2, \cdots$, and the radial modes $k_{\perp} = 1, 2, \cdots$ are good eigenmodes. In fact, this is very reasonable because at small perturbation, the transverse azimuthal modes $m_{\perp}$ correspond to frequencies $m_{\perp}\omega_{\beta}$ with separation ω_{β}. Since

$$\omega_{\beta} \gg \omega_0 \gg \omega_s, \tag{9.20}$$

the possibility for different transverse azimuthals to couple is remote. A direct result of Eq. (9.19) is the factorization of the bunch distribution Ψ in the combined longitudinal-transverse phase space; i.e.,

$$\Psi(r, \phi; r_{\beta}, \theta; s) = \psi(r, \phi; s) f(r_{\beta}, \theta; s), \tag{9.21}$$

where $\psi(r, \phi)$ is the distribution in the longitudinal phase space and $f(r_{\beta}, \theta)$ the distribution in the transverse phase space. Now decompose ψ and f into the

unperturbed parts and the perturbed parts:

$$\psi(r,\phi) = \psi_0(r) + \psi_1(r,\phi;s), \tag{9.22}$$

$$f(r_\beta,\theta) = f_0(r_\beta) + f_1(r_\beta,\theta;s). \tag{9.23}$$

The unperturbed $\psi_0(r)$, normalized to N_b, the number of beam particles, is just the stationary bunch distribution in the longitudinal phase space and the unperturbed $f_0(r_\beta)$, normalized to unity, is just the stationary transverse distribution of the bunch in the transverse phase space. When substituted into Eq. (9.21), there are four terms. The term $\psi_1 f_0$ implies only the longitudinal-mode excitations driven by the longitudinal impedance without any transverse excitations. This is what we have discussed in the previous sections and we do not want to include it again in the present discussion. The term $\psi_0 f_1$ describes the transverse excitations driven by the transverse impedance only. This term will be included in the $\psi_1 f_1$ term if we retain the azimuthal $m = 0$ longitudinal mode. For this reason, the bunch distribution Ψ in the combined longitudinal-transverse phase space contains only two terms

$$\Psi(r,\phi;r_\beta,\theta;s) = \psi_0(r)f_0(r_\beta) + \psi_1(r,\phi)f_1(r_\beta,\theta)e^{-i\Omega s/v}, \tag{9.24}$$

where $\psi_1(r,\psi)$ includes, in addition to the ψ_1 in Eq. (9.22), also the longitudinal monopole or $m = 0$ mode. We also notice that the coherent frequency Ω has been separated form $\psi_1(r,\phi;s)f_1(r_\beta,\theta;s)$.

9.4 Sacherer's Integral Equation

The linearized Vlasov equation is studied in the circular coordinates in both the longitudinal phase space and transverse phase space. However, only the transverse wake force will be included in the discussion here. After substituting the distribution of Eq. (9.24), the first-order terms of the Vlasov equation become

$$\left[-i\frac{\Omega}{v}f_1\psi_1 + \frac{\omega_s}{v}f_1\frac{\partial\psi_1}{\partial\phi} + \frac{\omega_\beta}{v}\psi_1\frac{\partial f_1}{\partial\theta}\right]e^{-i\Omega s/v} - \psi_0\frac{df_0}{dr_\beta}\sin\theta\frac{c}{E_0\omega_\beta\beta}\langle F_1^\perp(\tau;s)\rangle = 0. \tag{9.25}$$

The transverse wake force $\langle F_1^\perp(\tau;s)\rangle$ depends on the average transverse displacement of the beam. It is also a function of the longitudinal coordinate τ and should therefore contribute to the second equation of Eq. (8.2) as well, although the longitudinal wake force has been neglected here. It is, however, legitimate to drop this contribution if synchro-betatron resonance is avoided and the transverse beam size has not grown too large (see Exercise 9.3).

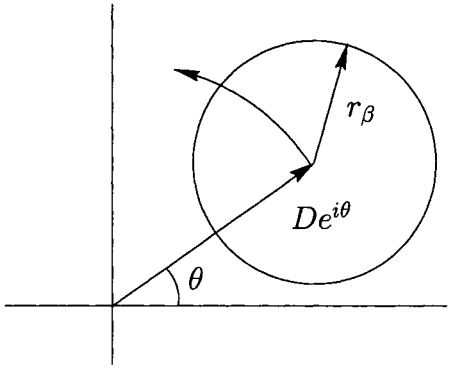


Fig. 9.3 A bunch executing betatron motion with an amplitude D in the rigid-dipole mode. In the transverse phase space, it is rotating counterclockwise rigidly with the radial offset D.

The next approximation is to consider only the rigid-dipole mode in the transverse phase space; i.e., the bunch is displaced by an infinitesimal amount D from the center of the transverse phase space and executes betatron oscillations as a rigid object by revolving at frequency $\omega_\beta/(2\pi)$ counterclockwise. Then according to the convention of Eq. (9.14) and Fig 9.3, we must have,

$$f_0(r_\beta) + f_1(\vec{r}_\beta) = f_0\left(r_\beta - De^{i\theta}\right), \tag{9.26}$$

where $\vec{r}_\beta$ is treated as a complex number in the transverse phase plane. When $D \to 0$, this becomes

$$f_1(r_\beta, \theta) = -Df_0'(r_\beta)e^{i\theta}. \tag{9.27}$$

It is easy to show that

$$D = \langle y \rangle = \int y f_1(r_\beta, \theta) r_\beta dr_\beta d\theta. \tag{9.28}$$

Thus physically D represents the dipole moment of the beam. Since we are retaining only one mode of transverse motion, all the modes that we are going to study are again synchrotron motion on top of this transverse mode. For this reason, these synchrotron modes are no longer sidebands of the revolution harmonics; they are now sidebands of the betatron sidebands. Some of the transverse modes are shown in Fig. 9.4.

Equation. (9.25) then becomes

$$\left[i(\Omega - \omega_\beta)\psi_1 - \omega_s \frac{\partial \psi_1}{\partial \phi}\right] De^{-i\Omega s/v} + \frac{ic^2}{2E_0\omega_\beta}\psi_0 \langle F_1^\perp(\tau; s)\rangle_{\text{dyn}} = 0, \tag{9.29}$$

where we have dropped the $e^{-i\theta}$ component of $\sin\theta$ because it corresponds to rotation in the transverse phase space with frequency $-\omega_\beta/(2\pi)$ which is very

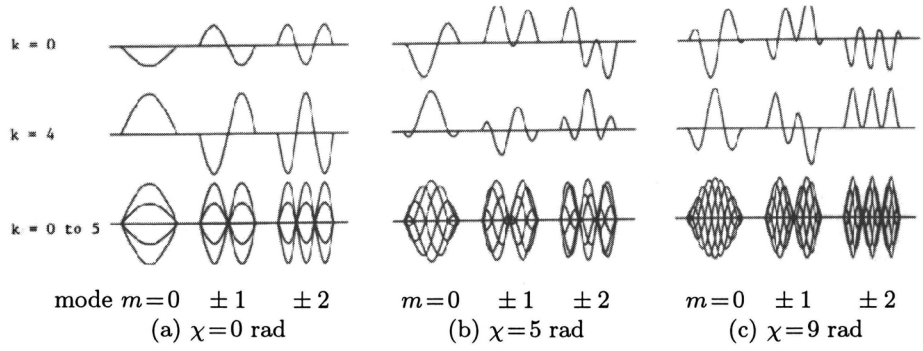


Fig. 9.4 Head-tail modes of transverse oscillation. The plots show the contortions of a single bunch on separate revolutions, and with six revolutions superimposed. Vertical axis is difference signal from beam-position monitor, horizontal axis is time, and $\nu_\beta = 4.833$. The chromaticity phases are (a) $\chi = 0$ rad, (b) $\chi = 5$ rad, and (c) $\chi = 9$ rad. Chromaticity will be introduced in Sec. 9.8. (Courtesy Zotter and Sacherer. [3])

far from $\omega_\beta/(2\pi)$ provided that the frequency shift due to the wake force is small. Notice that the transverse distribution $f_1(r_\beta, \theta)$ has been removed and the Vlasov equation involves only the longitudinal perturbed distribution function $\psi_1(r, \phi)$. This ψ_1 is the same perturbed distribution that we studied before with the exception that the azimuthal mode $m = 0$ is included.

The vertical wake force on a beam particle is given by

$$\langle F_1^\perp(\tau; s)\rangle_{\text{dyn}} = -\frac{eN_b}{C_0}\int d\tau' \langle y[\tau'; s - kC_0 - v(\tau' - \tau)]\rangle \times \lambda[\tau'; s - kC_0 - v(\tau' - \tau)] W_1[kC_0 + v(\tau' - \tau)], \quad (9.30)$$

where $\langle y(\tau'; s)\rangle$ is the average vertical displacement of the beam slice that has time advance τ' at location s along the accelerator ring, and $\lambda(\tau'; s)$ is the linear distribution. When the combined longitudinal-transverse phase space distribution $\Psi(r, \phi; r'_\beta\theta; s)$ of Eq. (9.24) is substituted into Eq. (9.30), it is clear that the static part, $\psi_0(r)f_0(r_\beta)$, gives no contribution because $\langle y(\tau'; s)\rangle = 0$ or there is no transverse displacement of the unperturbed beam center. This explains why the vertical wake force, $\langle F_1^\perp(\tau; s)\rangle$, receives contribution only from $\psi_1(r, \phi)f_1(r_\beta, \theta)e^{-i\Omega s/v}$, the dynamic or time-dependent part of the distribution. Therefore, the subscript "dyn" for the transverse wake force is not necessary. This does not mean that there is no static contribution to the coherent betatron tune shift. This just indicates that it will not be able to compute the static part of the coherent betatron tune shift simply using the transverse wake force. This also explains why when static betatron tune shifts were derived in Chapter 3,

the wake potential had not been used but instead other methods like images, etc. were employed.

Substituting the dynamic part of the beam distribution, we obtain simply $\langle y\rangle = D$, the dipole moment of the beam. Assuming M identical bunches equally spaced with the ℓth bunch at location s_ℓ, the transverse wake force on a particle in the nth bunch at a time advance τ becomes, similar to the longitudinal counterpart in Eq. (8.9),

$$\langle F_{1n}^{\perp}(\tau;s)\rangle_{\rm dyn} = -\frac{e^2 D}{C_0}\sum_{k=-\infty}^{\infty}\sum_{\ell=0}^{M-1}\int_{-\infty}^{\infty} d\tau' \times \lambda_\ell[\tau';\, s - kC_0 - (s_\ell - s_n) - v(\tau'-\tau)]W_1[kC_0 + (s_\ell - s_n) + v(\tau'-\tau)]. \tag{9.31}$$

For the μth coupled-bunch mode, we substitute in the above expression of the perturbed density of the nth bunch $\lambda_{1n}(\tau)e^{-i\Omega s/v}$ including the phase lead as given by Eq. (8.10). Now the derivation follows exactly the longitudinal counterpart in Chapter 8 and we obtain[‡]

$$\langle F_{1n\mu}^{\perp}(\tau;s)\rangle = \frac{ie^2 M D\omega_0\beta}{C}\, e^{-i\Omega s/v}\sum_{q=-\infty}^{\infty}\tilde{\lambda}_{1n}(\omega_q)Z_1^{\perp}(\omega_q)e^{i\omega_q\tau}, \tag{9.32}$$

where $\omega_q = (qM+\mu)\omega_0 + \Omega$. We next substitute the result into the linearized Vlasov equation and expand ψ_1 into azimuthals in the longitudinal phase space according to $\psi_1(r,\phi) = \sum_m \alpha_m R_m(r)e^{im\phi}$. We finally obtain Sacherer's integral equation for transverse instability

$$(\Omega - \omega_\beta - m\omega_s)\alpha_m R_m(r) = -\frac{i\pi e^2 M N_b}{\beta E_0 T_0^2}\, g_0 \sum_{m'} i^{m-m'}\alpha_{m'}\int r'dr' R_{m'}(r')\sum_q \left[\beta_\perp Z_1^{\perp}(\omega_q)\right] J_{m'}(\omega_q r')J_m(\omega_q r), \tag{9.33}$$

where N_b is the number of particles per bunch and the unperturbed distribution $g_0(r)$, which is defined in Eq. (8.28) and is normalized to unity upon integration over $rdrd\phi$, has been used instead of $\psi_0(r)$. Notice that all transverse distributions are not present in the equation and what we have are longitudinal distributions. This is not unexpected because we have retained only one transverse mode of motion, namely the rigid-dipole mode, in the transverse phase space.

[‡]Similar to Chapter 8, we neglect $v(\tau'-\tau)$ in λ_ℓ, which amounts to neglecting a phase delay $\Omega(\tau'-\tau)$, where $\Omega \sim \omega_\beta + m\omega_s$ and $|\tau'-\tau| \lesssim$ bunch length. Otherwise, $\tilde{\lambda}_{1n}(\omega_q)Z_1^{\perp}(\omega_q)$ in Eq. (9.32) will become $\tilde{\lambda}_{1n}(\omega_q - \Omega)Z_1^{\perp}(\omega_q)$ instead.

Therefore, the Sacherer's integral equation for transverse instability is almost the same as the one for longitudinal instability. There are only two differences. First, the unperturbed longitudinal distribution $g_0(r)$ appears in the former but $r^{-1}dg_0(r)/dr$ appears in the latter. Second, although the $m=0$ mode does not occur in the longitudinal equation because of violation of energy conservation, however, it is a valid azimuthal mode in the transverse equation because it describes rigid betatron oscillation. In Eq. (9.33), we have made the substitution indicated by Eq. (9.5) to allow for nonuniform betatron focusing, and we recall that $[\beta_\perp Z_1^\perp]$ implies the inclusion of the betatron function as a weight when the transverse impedance is summed element by element. Such substitution should have also been made in Eqs. (9.25) and (9.29).

9.5 Solution of Sacherer's Integral Equations for Radial Modes

Consider first the transverse integral equation, where $W(r) = g_0(r)$ is regarded to be a weight function. For each azimuthal m, find a complete set of orthonormal functions $g_{mk}(r)$ $(k = 0,\ 1,\ 2,\ \cdots)$ such that

$$\int W(r)g_{mk}(r)g_{mk'}(r)rdr = \delta_{kk'}, \tag{9.34}$$

where the subscript k represents the radial modes associated to azimuthal m. On both sides of the integral equation, perform the expansion

$$\alpha_m R_m(r)e^{im\phi} = \sum_k a_{mk}W(r)g_{mk}(r)e^{im\phi}. \tag{9.35}$$

Some comments are necessary. From Eq. (9.34), it appears that the orthonormal functions $g_{mk}(r)$ depend on the weight function $W(r)$ only and are independent of the azimuthal m. As a result, $g_{mk}(r)$ will not be uniquely defined, because the weight function $W(r) = g_0(r)$ is independent of m. In fact, this is not true. If we look into either the Sacherer's longitudinal integral equation (8.31) or the transverse integral equation (9.33) for one single azimuthal, it is easy to see that

$$R_m(r) \propto W(r)J_m(\omega_q r). \tag{9.36}$$

Therefore, for small r, we must have the behavior

$$R_m(r) \sim r^m \lim_{r\to 0} W(r). \tag{9.37}$$

Taking the bi-Gaussian distribution, $e^{-r^2/(2\sigma^2)}$, as an example, $\lim_{r\to 0} W(r)$ is a constant implying that $R_m(r) \sim r^m$. From Eq. (9.35), since $g_{mk}(r)$ is the

expansion of $R_m(r)$, the small-r behavior of $g_{mk}(r)$ will be constrained. This makes the set of orthonormal functions $g_{mk}(r)$ dependent on the azimuthal m and become, in fact, unique.

After substituting the expansion of $\alpha_m R_m$ into both sides of Eq. (9.33), multiply on both sides by $g_{mk}(r)$ and integrate over rdr. Sacherer's integral equation becomes

$$(\Omega-\omega_\beta-m\omega_s)a_{mk} = -\frac{i\pi e^2 M N_b}{\beta E_0 T_0^2}\sum_{m'k'} a_{m'k'}\sum_q \left[\beta_\perp Z_1^\perp(\omega_q)\right]\tilde{\lambda}^*_{mk}(\omega_q)\tilde{\lambda}_{m'k'}(\omega_q), \tag{9.38}$$

where we have defined

$$\tilde{\lambda}_{mk}(\omega) = \int i^{-m} W(r) J_m(\omega r) g_{mk}(r) r dr. \tag{9.39}$$

Thus, the Sacherer's integral equation has been reduced to a matrix equation,

$$(\Omega-\omega_\beta-m\omega_s)a^\perp_{mk} = \sum_{m'k'} M^\perp_{mk,m'k'}\omega_s a^\perp_{m'k'}, \tag{9.40}$$

where the beam dynamics has been embedded into the dimensionless interaction matrix

$$M^\perp_{mk,m'k'} = -\frac{i\pi e^2 M N_b}{\beta E_0 T_0^2 \omega_s}\sum_q \left[\beta_\perp Z_1^\perp(\omega_q)\right]\tilde{\lambda}^*_{mk}(\omega_q)\tilde{\lambda}_{m'k'}(\omega_q). \tag{9.41}$$

A superscript '$\perp$' has also been assigned to the expansion coefficient $a^\perp_{mk}$ to remind us that this matrix equation, developed from the Sacherer's integral equation, is for the collective motion in transverse phase space.

The $\tilde{\lambda}_{mk}(\omega)$ defined in Eq. (9.39), is the Fourier transform of the eigenmode $\lambda_{mk}(\tau)$, which can be shown to be in fact the (mk) component of the perturbed linear density $\lambda_1(\tau)$. Let us start from the Fourier transform of the linear density of the perturbed linear distribution

$$\tilde{\lambda}_1(\omega) = \frac{1}{2\pi}\int d\tau \lambda_1(\tau) e^{-i\omega\tau} = \frac{1}{2\pi}\int d\tau d\Delta E\, \psi_1(\tau,\Delta E) e^{-i\omega\tau}. \tag{9.42}$$

Now substitute the (mk)th mode of Eq. (9.35) for $\psi_1^{(mk)}$ to obtain

$$\tilde{\lambda}_1(\omega) = \frac{\omega_s\beta^2 E_0}{2\pi\eta}\sum_{mk} a_{mk}\int r dr d\phi\, W(r) g_{mk}(r) e^{im\phi-i\omega\tau}. \tag{9.43}$$

The integration over ϕ can be performed to yield a Bessel function. Finally using

the definition of $\tilde{\lambda}_{mk}(\omega)$ given in Eq. (9.39), we arrive at

$$\begin{aligned}\tilde{\lambda}_1(\omega) &= \frac{\omega_s \beta^2 E_0}{\eta} \sum_{mk} a_{mk} \int r dr\, W(r) g_{mk}(r) i^{-m} J_m(\omega r) \\ &= \frac{\omega_s \beta^2 E_0}{\eta} \sum_{mk} a_{mk} \tilde{\lambda}_{mk}(\omega). \end{aligned} \tag{9.44}$$

Taking the Fourier transform, we therefore obtain

$$\lambda_1(\tau) = \frac{\omega_s \beta^2 E_0}{\eta} \sum_{mk} a_{mk} \lambda_{mk}(\tau). \tag{9.45}$$

This demonstrates that $\lambda_{mk}(\tau)$ is the linear distribution of the excitation mode pertaining to azimuthal eigenvalue m and radial eigenvalue k, with $\tilde{\lambda}_{mk}(\omega)$ representing its frequency spectrum.

Now we are in the position to demonstrate some analytic solutions of the Sacherer's integral equation when there is no coupling among the azimuthal modes. So far, only a few of these analytic solutions are known.

9.5.1 *Chebyshev Modes*

Consider the situation when the unperturbed distribution is the air-bag distribution

$$g_0(r) = \frac{\delta(r - \hat{\tau})}{2\pi\hat{\tau}}, \tag{9.46}$$

which is normalized to unity when integrated over $r dr d\phi$. Since the weight function is $W_\perp(r) = g_0(r)$, where the superscript $\perp$ is added to remind us of the transverse phase space, we require

$$g_{mk}(\hat{\tau}) g_{mk'}(\hat{\tau}) = 2\pi \delta_{kk'}. \tag{9.47}$$

This implies that, for each azimuthal m, there can only be one radial mode, which we denote as $k = 0$. This is expected because all the particles reside at the edge of the bunch distribution in the longitudinal phase space. Thus, there is only one member in the set of orthonormal functions, namely,

$$g_{mk}(r) = \sqrt{2\pi}\delta_{k0}, \tag{9.48}$$

which is a constant. The spectrum of the linear distribution is, from Eq. (9.39),

$$\tilde{\lambda}_{m0}(\omega) = \frac{i^{-m} J_m(\omega\hat{\tau})}{\sqrt{2\pi}}, \tag{9.49}$$

and the linear distribution of the excitation is

$$\lambda_{m0}(\tau) = \int d\omega \tilde{\lambda}_{m0}(\omega) e^{i\omega\tau} = (-1)^m \sqrt{\frac{2}{\pi}} \frac{T_m(\tau/\hat{\tau})}{\sqrt{1-\tau^2/\hat{\tau}^2}}, \tag{9.50}$$

where $T_m(x) = \cos\left(m \cos^{-1} x\right)$ is the Chebyshev polynomial of order m. [6] These modes are called the *Chebyshev modes.*

9.5.2 *Legendre Modes*

The unperturbed distribution is

$$g_0(r) = \frac{1}{2\pi\hat{\tau}\sqrt{\hat{\tau}^2 - r^2}}, \tag{9.51}$$

for $r < \hat{\tau}$ and zero elsewhere. Thus the weight function is $W^{\perp}(r) = g_0(r)$. To find the orthonormal functions, we substitute $W^{\perp}(r)$ into Eq. (9.34) to get, after changing the variable of integration to $x = (r/\hat{\tau})^2$,

$$\int_0^1 \frac{x^m}{4\pi\sqrt{1-x}} f_{mk}(x) f_{mk'}(x) dx = \delta_{kk'}. \tag{9.52}$$

In above, we have introduce

$$g_{mk}(r) = \left(\frac{r}{\hat{\tau}}\right)^m f_{mk}(x), \tag{9.53}$$

because of the required behavior of $g_{mk}(x) \sim r^m$ when $r \to 0$. To transform this to a set of known orthonormal functions, substitute $u = 1 - 2x$, so that Eq. (9.52) becomes

$$\frac{1}{4\pi 2^{m+1/2}} \int_{-1}^1 \frac{(1-u)^m}{\sqrt{1+u}} \bar{f}_{mk}(u) \bar{f}_{mk'}(u) du = \delta_{kk'}, \tag{9.54}$$

where $\bar{f}_{mk}(u) = f_{mk}(x)$. Now we can readily identify $\bar{f}_{mk}(u)$ as the Jacobi polynomial $P_k^{(m,-\frac{1}{2})}(u)$ of order k, which has the normalization [6]

$$\int_{-1}^1 du(1-u)^{\alpha}(1+u)^{\beta} P_k^{(\alpha,\beta)}(u) P_{k'}^{(\alpha,\beta)}(u) = \frac{2^{\alpha+\beta+1}\Gamma(k+\alpha+1)\Gamma(k+\beta+1)}{(2k+\alpha+\beta+1)k!\Gamma(k+\alpha+\beta+1)} \delta_{kk'}. \tag{9.55}$$

From this, we can write

$$g_{mk}(r) = \sqrt{\frac{4\pi k!(m+2k+\frac{1}{2})\Gamma(m+k+\frac{1}{2})}{(m+k)!\Gamma(k+\frac{1}{2})}} \left(\frac{r}{\hat{\tau}}\right)^m P_k^{(m,-\frac{1}{2})}\left(1 - \frac{2r^2}{\hat{\tau}^2}\right). \tag{9.56}$$

The spectrum of the linear density can be obtained by integrating Eq. (9.39):

$$\tilde{\lambda}_{mk}(\omega) = \frac{i^{-m}}{\pi}\sqrt{\frac{(m+2k+\frac{1}{2})\Gamma(m+k+\frac{1}{2})\Gamma(k+\frac{1}{2})}{k!(m+k)!}}\, j_{m+2k}(\omega\hat{\tau}), \tag{9.57}$$

where $j_n(x) = \sqrt{\pi/(2x)}J_{n+\frac{1}{2}}(x)$ is the spherical Bessel function of order n. The linear density is

$$\lambda_{mk}(\tau) = (-1)^k\sqrt{\frac{(m+2k+\frac{1}{2})\Gamma(m+k+\frac{1}{2})\Gamma(k+\frac{1}{2})}{k!(m+k)!}}\, P_{m+2k}\left(\frac{\tau}{\hat{\tau}}\right), \tag{9.58}$$

which is proportional to the Legendre polynomial $P_{m+2k}(x)$ of order $m+2k$. Hence, we call these modes the *Legendre modes.*

9.5.3 *Hermite Modes*

The unperturbed distribution in the longitudinal phase space is bi-Gaussian with

$$g_0(r) = \frac{1}{2\pi\sigma}e^{-r^2/2\sigma^2}, \tag{9.59}$$

where σ is the rms length of the bunch, In order that the orthonormal function $g_{mk} \sim r^m$ as $r \to 0$, we define

$$g_{mk}(r) = \left(\frac{r}{\sqrt{2}\sigma}\right)^m f_{mk}(u), \tag{9.60}$$

where $u = r^2/(2\sigma^2)$. With the weight function $W^{\perp}(r) = g_0(r)$, the orthonormal requirement becomes

$$\frac{1}{2\pi}\int_0^\infty f_{mk}(u)f_{mk'}(u)u^m du = \delta_{kk'}. \tag{9.61}$$

We can identify the orthogonal function as the generalized Laguerre polynomial $L_k^{(m)}(u)$ of order k, which has the normalization [6]

$$\int_0^\infty L_k^{(m)}(u)L_{k'}^{(m)}(u)e^{-u}u^m du = \frac{(m+k)!}{k!}, \tag{9.62}$$

and write

$$g_{mk}(r) = \sqrt{\frac{2\pi k!}{(m+k)!}}\left(\frac{r}{\sqrt{2}\sigma}\right)^{2m} L_k^{(m)}\left(\frac{r}{\sqrt{2}\sigma}\right). \tag{9.63}$$

The spectrum of the linear distribution is found to be

$$\tilde{\lambda}_{mk}(\omega) = i^{-(m+2k)} \sqrt{\frac{1}{2\pi k!(m+k)!}} \left(\frac{\omega\sigma}{\sqrt{2}}\right)^{m+2k} e^{-\frac{1}{2}\omega^2\sigma^2}. \tag{9.64}$$

The linear density of excitation is

$$\lambda_{mk}(\tau) = \frac{1}{2^{m+2k}\sqrt{k!(m+k)!}} e^{-\tau^2/(2\sigma^2)} H_{m+2k}\left(\frac{\tau}{\sqrt{2}\sigma}\right), \tag{9.65}$$

which is proportional to the Hermite polynomial H_{m+2k} of order $m+2k$. Hence these modes are called the *Hermite modes.*

9.5.4 *Longitudinal Integral Equation*

The Sacherer's longitudinal integral equation (8.27) can be converted into a matrix equation in exactly the same way. We obtain

$$(\Omega - m\omega_s)a^{\parallel}_{mk} = \sum_{m'k'} M^{\parallel}_{mk,m'k'}\omega_s a^{\parallel}_{m'k'}, \tag{9.66}$$

where the beam dynamics has been embedded into the dimensionless interaction matrix

$$M^{\parallel}_{mk,m'k'} = \frac{ie^2 M N_b \eta m}{2\pi\beta^2 E_0 \nu_s^2} \sum_q \frac{Z_0^{\parallel}(\omega_q)}{\omega_q} \tilde{\lambda}^*_{mk}(\omega_q)\tilde{\lambda}_{m'k'}(\omega_q), \tag{9.67}$$

with $\omega_q \approx (qM+\mu)\omega_0 + m\omega_s$,

$$\tilde{\lambda}_{mk}(\omega) = \int_0^\infty i^{-m} W^{\parallel}(r) J_m(\omega r) g_{mk}(r) r dr, \tag{9.68}$$

and the weight function is identified as

$$W^{\parallel}(r) = -\frac{1}{r}\frac{dg_0(r)}{dr}, \tag{9.69}$$

with the negative sign included because $dg_0(r)/dr < 0$.

Although the dynamics inside the interaction matrix $M^{\parallel}_{mk,m'k'}$ is different from that inside the interaction matrix $M^{\perp}_{mk,m'k'}$, however, the definition of the orthonormal functions and the spectrum of the linear density excitation are exactly the same. For this reason, with the same weight function, the same set of orthonormal functions will result implying the same excitation modes.

To obtain the same weight function of the air-bag model in the transverse matrix equation, we must employ instead the water-bag model in the longitudinal matrix equation, so that the excitation modes will remain the Chebyshev modes.

Since the Legendre modes correspond to $g_0(r) \propto (\hat{\tau}^2 - r^2)^{-1/2}$ in the transverse equation, they correspond to the elliptical distribution $g_0(r) \propto (\hat{\tau}^2 - r^2)^{1/2}$ [linear density parabolic $\lambda(\tau) \propto (\hat{\tau}^2 - r^2)$] in the longitudinal equation. On the other hand, the Hermite modes correspond to the same bi-Gaussian distribution in both the transverse and longitudinal equations. These solutions are summarized in Table 9.1.

Notice that although the definition of the mode spectra $\tilde{\lambda}_{mk}(\omega)$ are exactly the same in both the transverse and longitudinal matrix equations, they carry different dimensions because the weight functions are of different dimensions. It can be easily traced that $\tilde{\lambda}_{mk}(\omega)$ is dimensionless in the transverse case but carries the dimension of $(\text{time})^{-1}$ in the longitudinal case. Thus for the same mode configuration,

$$g^{\parallel}_{mk} = \sqrt{\frac{W^{\perp}}{W^{\parallel}}}\, g^{\perp}_{mk}, \quad \tilde{\lambda}^{\parallel}_{mk} = \sqrt{\frac{W^{\parallel}}{W^{\perp}}}\, \tilde{\lambda}^{\perp}_{mk}, \quad \lambda^{\parallel}_{mk} = \sqrt{\frac{W^{\parallel}}{W^{\perp}}}\, \lambda^{\perp}_{mk}, \tag{9.70}$$

where the superscripts denote longitudinal or transverse, and they will be omitted whenever there is no ambiguity. The modes defined in Sec. 9.5.1, 9.5.2, and 9.5.3 should all carry the superscript $\perp$. It is easy to show that

$$\frac{W^{\perp}}{W^{\parallel}} = \begin{cases} \frac{1}{2}\hat{\tau}^2 & \text{Chebyshev modes,} \\ \frac{1}{3}\hat{\tau}^2 & \text{Legendre modes,} \\ \sigma & \text{Hermite modes.} \end{cases} \tag{9.71}$$

9.6 Frequency Shifts and Growth Rates

9.6.1 *Broadband Impedance*

According to the above, we deduce for a given unperturbed distribution $g_0(r)$ in the longitudinal phase space the set of orthonormal functions $g_{mk}(r)$ to be used as basis of expansion and derive the spectrum of the base excitation $\tilde{\lambda}_{mk}(\omega)$. The interaction matrix $M_{mk,mk'}$ is then computed and diagonalized to obtain the eigenvalues Ω and the corresponding eigenvector a_{mk} of the eigenmodes. The shift in frequency and growth rate are given by the real and imaginary parts of the collective frequency Ω, while the linear distribution of the excitation eigenmodes are formed by the linear combination $\sum_{mk} a_{mk}\lambda_{mk}(\tau)$.

For a general impedance, the interaction matrix must be truncated and the diagonalization performed numerically. However, some useful deduction can often be made under certain approximations. When the transverse impedance $Z^{\perp}_1(\omega)$ [or longitudinal impedance per frequency $Z^{\parallel}_0(\omega)/\omega$] in $M_{mk.m'k'}$ is purely

Table 9.1: Some solutions of the Sacherer's integral equations for longitudinal and transverse excitations. The Chebyshev, Legendre, and Hermite modes are exact solutions, while the sinusoidal modes are approximate solutions. Azimuthal modes are characterized by $m = 0,\ 1,\ 2,\ \cdots$ ($m \neq 0$ for longitudinal) and radial modes by $k = 0,\ 1,\ 2,\ \cdots$.

	Longitudinal Integral Equation		Transverse Integral Equation		Weight Function	Azimuthal & Radial Excitation Modes	
	Phase-space Distribution	Linear Distribution	Phase-space Distribution	Linear Distribution	$W(r)$ $= g_0(r)$	Linear Distribution	Spectral Distribution
	$g_0(r)$	$\lambda(\tau)$	$g_0(r)$	$\lambda(\tau)$	or $-\dfrac{g_0'(r)}{r}$	$\lambda_{mk}(\tau)$	$\tilde{\lambda}_{mk}(\omega)$
Chebyshev modes	Water-bag $H(\hat{\tau}-r)$	$\sqrt{\hat{\tau}^2-\tau^2}$	Air-bag $\delta(\hat{\tau}-r)$	$\dfrac{1}{\sqrt{\hat{\tau}^2-\tau^2}}$	$\delta(\hat{\tau}-r)$	$\dfrac{T_m(\tau/\hat{\tau})}{\sqrt{1-(\tau/\hat{\tau})^2}}$	$J_m(\omega\hat{\tau})$
Legendre modes	$\sqrt{\hat{\tau}^2-r^2}$	$\hat{\tau}^2-\tau^2$	$\dfrac{1}{\sqrt{\hat{\tau}^2-r^2}}$	constant	$\dfrac{1}{\sqrt{\hat{\tau}^2-r^2}}$	$P_{m+2k}(\tau/\hat{\tau})$	$j_{m+2k}(\omega\hat{\tau})$
Hermite modes	$e^{-\frac{r^2}{2\sigma^2}}$	$e^{-\frac{\tau^2}{2\sigma^2}}$	$e^{-\frac{r^2}{2\sigma^2}}$	$e^{-\frac{\tau^2}{2\sigma^2}}$	$e^{-\frac{r^2}{2\sigma^2}}$	$H_{m+2k}\left(\frac{\tau}{\sqrt{2}\sigma}\right)\times$ $\times e^{-r^2/(2\sigma^2)}$	$(\omega\sigma)^{m+2k}\times$ $\times e^{-\omega^2/(2\sigma^2)}$
Sinusoidal modes	$\hat{\tau}^2-r^2$	$(\hat{\tau}^2-\tau^2)^{\frac{3}{2}}$	constant	$\sqrt{\hat{\tau}^2-\tau^2}$	constant	sinusoidal	$\sqrt{h_m(\omega)}$ Eq. (9.101)

reactive and does not depend on frequency, it can be taken out of the summation sign, leaving behind $\sum_q \tilde{\lambda}^*_{mk}(\omega_q)\tilde{\lambda}_{m'k'}(\omega_q)$. When $M\omega_0\hat{\tau} \ll 1$ or the bunch is much shorter than the bunch spacing, the summation can be replaced by an integration:

$$\sum_{q=-\infty}^{\infty} \longrightarrow \frac{1}{M\omega_0\hat{\tau}} \int_{-\infty}^{\infty} d(\omega\hat{\tau}). \tag{9.72}$$

We next assume the perturbation is small so that frequency shift $|\Omega - \omega_\beta - m\omega_s| \ll \omega_s$. This implies that different azimuthal modes do not mixed and we can consider each azimuthal separately. The situation when different azimuthal modes couple together will be discussed in Chapter 11. Let us first address the transverse equation. In the Legendre modes, $\tilde{\lambda}_{mk} \propto j_{m+2k}$, the spherical Bessel function. Since

$$\int_0^\infty j_{m+2k}(x)j_{m+2k'}(x)dx = \frac{\pi\delta_{kk'}}{4\left(m+2k+\frac{1}{2}\right)}, \tag{9.73}$$

the interaction matrix is diagonal, implying that the Legendre modes are the eigenmodes. If we introduce the dimensionless parameter,

$$\Upsilon_\perp = -\frac{ie^2N_b\,\mathcal{I}m\left[\beta_\perp Z_1^\perp\right]}{8\pi\beta E_0\nu_s\hat{\tau}}, \tag{9.74}$$

the eigen-frequency-shifts are given by

$$\Omega_{mk} - \omega_\beta - m\omega_s = M^\perp_{mk,mk}\omega_s = \frac{\Gamma\left(m+k+\frac{1}{2}\right)\Gamma\left(k+\frac{1}{2}\right)}{\pi k!(m+k)!}\Upsilon_\perp\omega_s. \tag{9.75}$$

Since we are dealing here with a very broadband impedance or very short wake, the above result describes the effect of a single-bunch, although we started out the formulation of the collective motion of M equally populated and equally spaced bunches. This also explains why the factor M gets cancelled out and no longer appears in the parameter $\Upsilon_\perp$.

When the same transverse impedance is applied to the Hermite modes, $\tilde{\lambda}_{mk}(\omega) \propto \omega^{m+2k}e^{-\frac{1}{2}\omega^2\sigma^2}$. Obviously, the $\tilde{\lambda}_{mk}(\omega)$'s are not orthogonal via the replacement of Σ_q by an integral over ω when the bunch is short, and therefore the interaction matrix is not diagonal. To proceed further, one must truncate the matrix and resort to numerical diagonalization. Nevertheless, the diagonal elements can be derived in the closed form:

$$M^\perp_{mk,mk} = \frac{\Gamma\left(m+2k+\frac{1}{2}\right)}{2^{m+2k}\pi k!(m+k)!}\frac{\hat{\tau}}{\sigma}\Upsilon_\perp. \tag{9.76}$$

It can be easily seen that the most prominent radial mode is $k = 0$. We can therefore estimate the frequency shift of that mode for each azimuthal m,

$$\Omega_{m0} - \omega_\beta - m\omega_s = M^{\perp}_{m0,m0}\omega_s = \frac{\Gamma\left(m+\frac{1}{2}\right)}{2^m \pi m!}\frac{\hat{\tau}}{\sigma}\Upsilon_\perp \omega_s, \tag{9.77}$$

which depends on σ but not $\hat{\tau}$.

So far we observe only frequency shifts but no instabilities. We can therefore conclude that purely reactive transverse impedance cannot drive bunches into transverse instability. Since the transverse and longitudinal Sacherer's integral equations are exactly the same mathematically, we can also conclude that purely longitudinal impedance cannot drive a bunch into longitudinal instability. On the other hand, we know that longitudinal microwave instability does occur in a coasting beam if the reactive impedance is too capacitive/inductive above/below transition. Even in the presence of a broadband $\mathcal{R}e\, Z_1^\perp$ (or $\mathcal{R}e\, Z_0^\parallel/\omega$), however, a bunched beam cannot be driven unstable. This is because the excitation spectrum $\tilde{\lambda}_{mk}(\omega)$ is odd/even in ω depending on m is odd/even while $\mathcal{R}e\, Z_1^\perp(\omega)$ (or $\mathcal{R}e\, Z_0^\parallel/\omega$) is odd in ω. As a result, the summation $\sum_q \mathcal{R}e\, Z_1^\perp(\omega_q)\tilde{\lambda}^*_{mk}(\omega_q)\tilde{\lambda}_{m'k'}(\omega_q)$ vanishes when the summation is replaced by an integral or when the impedance is broader than $M\omega_0$ in a M-bunch configuration. A broadband impedance can only lead to instability when $\mathcal{R}e\, Z_1^\perp$ couples two azimuthal modes of different parities and we will discuss this in detail in Chapter 11.

The effect of broadband longitudinal impedance is very similar. If $\mathcal{I}m\, Z_0^\parallel/\omega$ is much broader than the full width of the excitation mode spectrum $\Delta\omega \sim 2\pi/(\hat{\tau})$, the impedance can be taken out of the summation sign in the interaction matrix. If the bunch is much shorter than the bunch spacing ($2M\omega_0\hat{\tau}/\pi \ll 1$), the summation can be replaced by an integral over frequency. We therefore obtain

$$\Omega_{mk} - m\omega_s = M^{\parallel}_{mk,mk'}\omega_s = \frac{m\Gamma(m+k+\frac{1}{2})\Gamma(k+\frac{1}{2})}{\pi k!(m+k)!}\Upsilon_\parallel \omega_s, \tag{9.78}$$

for the Legendre modes and is diagonal, where we have defined

$$\Upsilon_\parallel = -\frac{3e^2 N_b \eta}{8\pi\beta^2 E_0 \nu_s \hat{\tau}^3}\frac{\mathcal{I}m\, Z_0^\parallel(\omega)}{\omega}. \tag{9.79}$$

The diagonal elements are just the dynamic coherent synchrotron frequency shifts. Notice that for the longitudinal rigid-dipole mode ($m = 1$ and $k = 0$), this frequency shift cancels exactly the static synchrotron frequency shift computed in Eq. (2.80) if we interpret $\mathcal{L} = -\mathcal{I}m\, Z_0^\parallel/\omega$ as a generalized inductance. For a capacitive impedance below transition, this shift is upward. Thus we have just

verified the fact that the dipole mode, which is a rigid rotation of the bunch in the longitudinal phase space, is not affected by the wake fields because the latter moves with the bunch and the bunch center is not seeing any variation of the wake-field pattern.

The interaction matrix is not diagonal in the Hermite modes. However, the most prominent radial modes ($k = 0$) have the frequency shifts

$$\Omega - m\omega_s = \frac{(2m-1)!}{2^{m-1}[(m-1)!]^2}\frac{\sqrt{2}\hat{\tau}^3}{4\pi^2\sigma^3}\Upsilon_{\parallel}\omega_s. \tag{9.80}$$

The two models agree with each other in the dipole mode ($m = 1$) if we set $\hat{\tau}/\sigma = (3\pi)^{\frac{1}{3}}/2^{\frac{1}{2}}$.

9.6.2 *Narrowband Impedance*

When different azimuthal modes do not mix, collective instabilities can only occur when driven by narrowband impedances. Consider a resonant impedance that is narrower than the revolution frequency of the accelerator ring. In this case, essentially only one betatron line will be covered by the resonance at positive frequency (fast wave) and one at negative frequency (slow wave). Including only the most prominent radial mode $k = 0$, the growth rate as illustrated in Fig. 9.5 is

$$\frac{1}{\tau_{m0}} = \mathcal{I}m\, M^{\perp}_{m0,m0}\omega_s \approx -\frac{\pi e^2 M N_b \beta_{\perp}}{\beta E_0 T_0^2}\left|\tilde{\lambda}^{\perp}_{m0}(h\omega_0)\right|^2 \Delta\, \mathcal{R}e\, Z_1^{\perp}, \tag{9.81}$$

where the contributions of the two betatron sidebands are given by

$$\Delta\, \mathcal{R}e\, Z_1^{\perp} = \mathcal{R}e\, Z_1^{\perp}\left[(h+\Delta_\beta)\omega_0 + m\omega_s\right] - \mathcal{R}e\, Z_1^{\perp}\left[(h-\Delta_\beta)\omega_0 - m\omega_s\right], \tag{9.82}$$

and $\beta_{\perp}$ is the betatron function at the location of the resonant impedance. In above, $|\tilde{\lambda}_{k0}|^2$ are evaluated at the revolution harmonic $h\omega_0$ nearest to the peak of the resonance, and the betatron tune is written as $\nu_\beta = n_\beta + \Delta_\beta$ with n_β the integer nearest to ν_β and $|\Delta_\beta| < \frac{1}{2}$ is the fractional part of above or below n_β. The beam is unstable if the impedance samples more the slow-wave betatron sideband than the fast-wave betatron sideband. This is the transverse analog of Robinson stability we studied before. Of course, the imaginary part of the impedance contributes a tune shift. Specifically, for short bunches ($h\omega_0\hat{\tau} \ll 2$ or $h\omega_0\sigma \ll \sqrt{2}$), the growth rate becomes

$$\frac{1}{\tau_{m0}} = -\frac{e^2 M N_b \beta_{\perp}}{\beta E_0 T_0^2}\frac{\sqrt{\pi}}{4m!\Gamma\left(m+\frac{3}{2}\right)}\left(\frac{h\omega_0\hat{\tau}}{2}\right)^{2m}\Delta\, \mathcal{R}e\, Z_1^{\perp}, \tag{9.83}$$

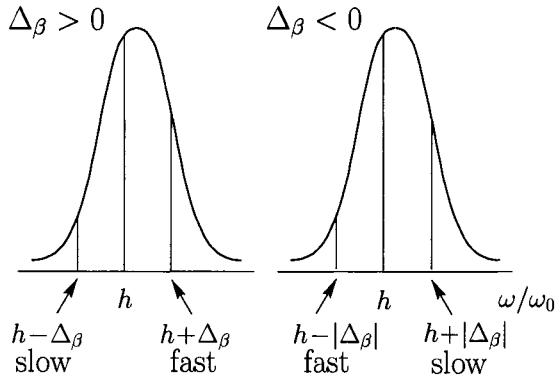


Fig. 9.5 Left: The betatron tune is above an integer. The fast-wave sideband samples more impedance than the slow-wave sideband resulting in stability. Right: The betatron tune is below an integer. The fast-wave sideband samples less impedance than the slow-wave sideband resulting in beam instability.

in the Legendre modes and

$$\frac{1}{\tau_{m0}} = -\frac{e^2 M N_b \beta_\perp}{\beta E_0 T_0^2} \frac{1}{2m!} \left(\frac{h\omega_0 \sigma}{\sqrt{2}}\right)^{2m} \Delta\, \mathcal{R}e\, Z_1^\perp, \tag{9.84}$$

in the Hermite modes. They are identical at $m = 0$, which is the growth rate for point bunches.

In the longitudinal case, the growth rate is

$$\frac{1}{\tau_{m0}} = \frac{e^2 M N_b \eta h \omega_0}{2\beta^2 E_0 T_0^2 \omega_s} \frac{3\sqrt{\pi}}{4(m-1)!\Gamma\left(m+\frac{3}{2}\right)} \left(\frac{h\omega_0}{2}\right)^{2m-2} \Delta\, \mathcal{R}e\, Z_0^\parallel, \tag{9.85}$$

for the Legendre modes and

$$\frac{1}{\tau_{m0}} = \frac{e^2 M N_b \eta h \omega_0}{2\beta^2 E_0 T_0^2 \omega_s} \frac{1}{(m-1)!} \left(\frac{h\omega_0}{\sqrt{2}}\right)^{2m-2} \Delta\, \mathcal{R}e\, Z_0^\parallel, \tag{9.86}$$

for the Hermite modes, with

$$\Delta\, \mathcal{R}e\, Z_0^\parallel = \mathcal{R}e\, Z_0^\parallel(h\omega_0 + m\omega_s) - \mathcal{R}e\, Z_0^\parallel(h\omega_0 - m\omega_s) \tag{9.87}$$

denoting the sampling of the impedance by the upper and lower synchrotron sidebands. These are exactly the Robinson's growth rates driven by narrow resonances for short bunches, and they agrees with the point-bunch result of Eq. (8.45) when $m = 1$.

9.7 Approximate Solutions and Effective Impedances

For a general impedance, the interaction matrix is not diagonal either transverse or longitudinal and either in the Legendre mode or the Hermite mode. To obtain

a solution, diagonalization must be performed numerically. However, an estimate to the collective frequency Ω_{mk} can often be obtained by computing the diagonal elements of the interaction matrix. For the transverse equation, the interaction matrix can be written in the form

$$M^{\perp}_{mk,m'k'} = -\frac{ie^2N_b}{8\pi\beta E_0\nu_s\hat{\tau}}\frac{\sum_q\left[\beta_\perp Z_1^\perp(\omega_q)\right]\tilde{\lambda}_{mk}(\omega_q)\tilde{\lambda}_{m'k'}(\omega_q)}{\sum_q|\tilde{\lambda}_{mk}(\omega_q)|^2}F_{mk}, \tag{9.88}$$

where the form factor is given by

$$F_{mk} = \frac{4\pi M\hat{\tau}}{T_0}\sum_q|\tilde{\lambda}^{\perp}_{mk}(\omega_q)|^2. \tag{9.89}$$

Since only the diagonal elements are usually desired, the above can be cast into the form

$$M^{\perp}_{mk,m'k'} = -\frac{ie^2N_b\bar{\beta}_\perp}{8\pi\beta E_0\nu_s\hat{\tau}}Z_1^\perp|^{mk}_{\text{eff}}F_{mk}, \tag{9.90}$$

where the effective transverse impedance, defined by

$$Z_1^\perp|^{mk}_{\text{eff}} = \frac{\sum_q\left[\beta_\perp Z_1^\perp(\omega_q)\right]h_{mk}(\omega_q)}{\bar{\beta}_\perp\sum_q h_{mk}(\omega_q)}, \tag{9.91}$$

represents a weighted average of the impedance over the power spectrum $h_{mk}(\omega_q) = |\tilde{\lambda}_{mk}(\omega_q)|^2$. In order that the effective impedance retains the dimension of transverse impedance, we have introduce the nominal $\bar{\beta}_\perp$, which can be R/ν_β or the betatron function at any location. Off-diagonal effective impedance can also be defined between two different bunch modes in case the growth rate, determined by the real part of the transverse impedance, is required.

There are several merits of representing the interaction matrix in terms an effective impedance: First, a rough estimate of the effective impedance and thus the interaction matrix and the frequency shift, real or imaginary, can be obtained readily by guessing at an approximate excitation power spectrum $h_{mk}(\omega)$ instead of going through a numerical diagonalization.[§] Second, there is no need to track the normalization of the power spectra before the substitution into the interaction matrix, and, as a result, we even do not need to specify the superscript "$\perp$" or "$\|$" for the mode spectrum and power spectrum in Eqs. (9.90) and (9.91). Third, the effective impedance has a physical meaning. For a coasting

[§]We remember the same perturbation in quantum mechanism, where we guess at a wavefunction with a parameter and vary that parameter to arrive at the best estimate of the eigenvalue.

beam, since all the revolution harmonics are independent, $Z_1^\perp$ is the right impedance to address because it samples individual betatron sidebands. For a bunch, $Z_1^\perp|_{\text{eff}}^{mk}$ is the more suitable approach because the impedance samples each betatron sideband according to the power spectrum of the mode of excitation under consideration, and its magnitude depends on the overlap integral between the impedance function and the excitation power spectrum.

In the smooth approximation when the summation can be converted into an integral, the form factors are[¶]

$$F_{mk} = \begin{cases} \dfrac{\Gamma(m+k+\frac{1}{2})\Gamma(k+\frac{1}{2})}{\pi k!(m+k)!} & \text{Legendre modes,} \\ \dfrac{\Gamma(m+2k+\frac{1}{2})}{2^{m+2k}\pi(m+k)!}\dfrac{\hat{\tau}}{\sigma} & \text{Hermite modes.} \end{cases} \tag{9.92}$$

The normalization in Eq. (9.89) has been so chosen that $F_{00}^\perp = 1$ for the Legendre modes. We note that $F_{00}^\perp = 1$ also in the Hermite modes if we let $\hat{\tau} = \sqrt{\pi}\sigma$.

For the longitudinal equation, we can write in the same way

$$M_{mk,m'k'}^{\parallel} = \frac{i3e^2N_b\eta m}{4\pi\beta^2E_0\omega_0\nu_s^2\hat{\tau}^3}\frac{\sum_q[Z_0^{\parallel}(\omega_q)/\omega_q]\tilde{\lambda}_{mk}(\omega_q)\tilde{\lambda}_{m'k'}(\omega_q)}{\sum_q|\tilde{\lambda}_{mk}(\omega_q)|^2}F_{mk}. \tag{9.93}$$

Although we are having the same form factor F_{mk} as given by Eq. (9.89) or (9.92) in the transverse interaction matrix, the form factor of the most prominent mode ($m = 1$ and $k = 0$) is $F_{10} = \frac{1}{2}$ for the Legendre modes and $\hat{\tau}/(4\sqrt{\pi}\sigma)$ for the Hermite modes. When only the diagonal elements are desired, we can introduce a similar effective longitudinal impedance per frequency weighted over the power spectrum of the (mk)th excitation:

$$\frac{Z_0^{\parallel}}{\omega}\bigg|_{\text{eff}}^{mk} = \frac{\sum_q Z_0^{\parallel}(\omega_q)h_{mk}(\omega_q)}{\sum_q h_{mk}(\omega_q)}. \tag{9.94}$$

The interaction matrix then takes the form

$$M_{mk,mk}^{\parallel} = \frac{i3d^2N_b\eta}{4\pi\beta^2E_0\omega_0\nu_s^2\hat{\tau}^3}\frac{Z_0^{\parallel}}{\omega}\bigg|_{\text{eff}}^{mk}F_{mk}. \tag{9.95}$$

9.7.1 *Sacherer's Sinusoidal Modes*

Assuming the perturbation is small so that only a single azimuthal mode will contribute, we learn from the Sacherer's integral equation (9.33) that the per-

[¶] F_{mk} diverges for the Chebyshev modes.

turbation excitation is

$$R_m(r)e^{im\phi} \propto W(r)J_m(\omega_q r)e^{im\phi}. \tag{9.96}$$

For a bunch of half length $\hat{\tau} = \frac{1}{2}\tau_L$, $R_m(\hat{\tau}) = 0$. So it may be reasonable to write the kth radial mode corresponding to azimuthal m as

$$R_{mk}(r)e^{im\phi} \propto W(r)J_m\left(x_{mk}\frac{r}{\hat{\tau}}\right)e^{im\phi}, \tag{9.97}$$

where x_{mk} is the $(k+1)$th zero of the Bessel function J_m.

Sacherer [5] discovered that, with a constant weight function $W(r)$ for $r < \hat{\tau}$, for example, a uniform or water-bag unperturbed distribution in the transverse plane, the projection of $R_{m0}(r)e^{im\phi}$, the most prominent radial mode, onto the τ axis

$$\lambda_{m0}(\tau) \propto \int W(r)J_m\left(x_{m0}\frac{r}{\hat{\tau}}\right)e^{im\phi}d\Delta E \tag{9.98}$$

is approximately sinusoidal as illustrated in Fig. 9.6. In fact, head-tail excitations that are sinusoidal-like had been observed in the CERN Proton Synchrotron (PS) booster. For this reason, instead of solving the integral equation, Sacherer approximated $\lambda_{mk}(\tau)$ by a linear combination of sinusoidal functions, and these modes are called *sinusoidal modes*. The linear distribution densities of the different azimuthal modes are represented by

$$\lambda_{m0}(\tau) \propto \begin{cases} \cos\dfrac{(m+1)\pi\tau}{\tau_L} & m = 0, 2, \cdots, \\ \sin\dfrac{(m+1)\pi\tau}{\tau_L} & m = 1, 3, \cdots, \end{cases} \tag{9.99}$$

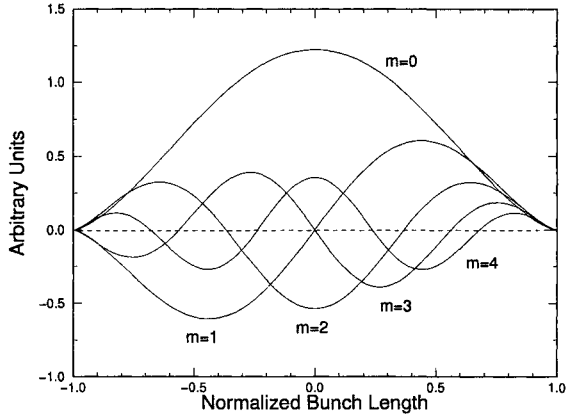


Fig. 9.6 Illustration showing that, with a constant weight function $W(r)$, the projection of $W(r)J_m(x_{m1}r/\hat{\tau})e^{im\phi}$ onto the time axis is approximately sinusoidal.

which are orthogonal to each other. Note that $\lambda_{m0}(\tau)$ has exactly m nodes along the bunch not including the two ends. The spectrum of the linear distribution $\tilde{\lambda}_{m0}$ can be readily derived and can be written as

$$\tilde{\lambda}_{m0}(\omega) = \frac{m+1}{\pi} \frac{i^m 2^{3/2}}{y^2-(m+1)^2} \begin{cases} \cos \frac{1}{2}\pi y & m = 0, 2, \cdots \\ \sin \frac{1}{2}\pi y & m = 1, 3, \cdots \end{cases} \tag{9.100}$$

where $y = \omega\tau_L/\pi$ and τ_L is the total length of the bunch in time. The normalization has been specially chosen so that the summation of the power spectra,

$$h_{m0}(\omega) = |\tilde{\lambda}_{m0}(\omega)|^2 = \frac{4(m+1)^2}{\pi^2} \frac{1+(-1)^m \cos \pi y}{[y^2-(m+1)^2]^2}, \tag{9.101}$$

has the simple property in the smooth approximation,

$$B \sum_{q=-\infty}^{+\infty} h_{m0}(\omega_q) \approx \frac{B}{M\omega_0} \int_{-\infty}^{+\infty} h_{m0}(\omega) d\omega = 1. \tag{9.102}$$

Here $B = M\omega_0\tau_L/(2\pi)$ is the bunching factor in the presence of M identical equally-spaced bunches, or the ratio of full bunch length to bunch separation. The power spectra of some lower azimuthal modes are plotted in Fig. 6.13. When the sinusoidal modes are used, the subscript zero is usually dropped because only the most prominent radial modes are included. A nonrigorous derivation by Sacherer and Laclare [4] produces the same transverse and longitudinal interaction matrices in Eqs. (9.90) and (9.95) with the form factor equal to

$$F_{m0} = \frac{1}{1+m}, \tag{9.103}$$

which is rather close to that for the Legendre modes in the low azimuthals.

The transverse growth rate obtained from the interaction matrix in Eq. (9.95) is very similar to the coasting-beam formula of Eq. (9.4). Besides the averaging over the power spectra, the coasting beam current per unit length I_0/C_0 is replaced by the average single bunch current I_b divided by the total bunch length $2\hat{\tau}\beta c$ in meters. The factor F_{m0}, which is roughly equal to $(1+m)^{-1}$, says that higher-order modes are harder to excite, and is introduced under some assumption of the unperturbed distribution in phase space. [4] It is easy to understand why the power spectrum $h_{mk}(\omega) = |\tilde{\lambda}_{mk}(\omega)|^2$ enters because $Z_1^{\perp}(\omega)\tilde{\lambda}_{mk}(\omega)$ gives the deflecting field, which must be integrated over the bunch spectrum to get the total force.

One should exercise caution when making the decision on which excitation modes to use, because the different types of modes are rather different. The power spectra of the sinusoidal modes depicted in Fig. 6.13 are plotted in units

of $\omega\tau_L/\pi$. We see that, while the $m = 0$ mode peaks at zero and has FWHM ~ 1.7 units, the other azimuthal mode m peaks roughly at $\pm(m+1)$ units and have FWHM ~ 1.59 units. The widths of the Legendre modes $j_m(\omega\hat{\tau})$ and the Hermite modes $(\omega\sigma)^{2m}e^{-(\omega\sigma)^2}$ are roughly the same as the sinusoidal modes if the half bunch length in the Legendre or sinusoidal modes are considered $\sqrt{6}\sigma$ in the Hermite modes. As is shown in Fig. 9.7, the positions of maxima of the Legendre modes do not spread out as far as the sinusoidal modes, and those of the Hermite modes are even less spread out than the Legendre modes. In fact, it is easy to show that the Hermite modes have maxima at $\omega\sigma = \pm\sqrt{m}$.

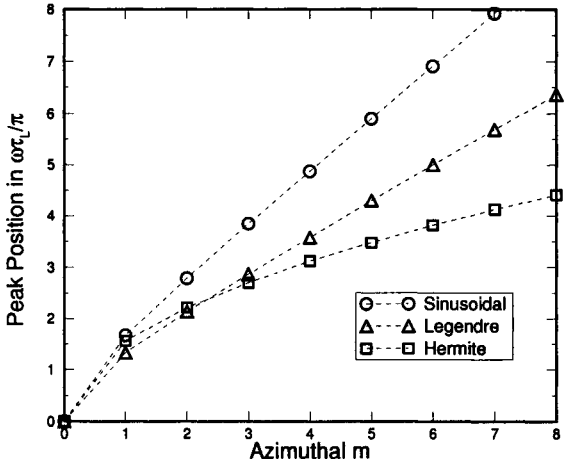


Fig. 9.7 Positions of maximum power spectra for sinusoidal modes, Legendre modes, and Hermite modes in units of $\omega\tau_L/\pi$ for each azimuthal m. For comparison, the rms bunch length σ in the Hermite modes has been taken as $1/(2\sqrt{6})$ the full bunch length τ_L.

9.8 Chromaticity Frequency Shift

The betatron tune ν_β of a beam particle depends on its momentum offset δ. The chromatic betatron tune shift is defined as

$$\Delta\nu_\beta = \xi\delta, \tag{9.104}$$

where ξ is called the *chromaticity*.[‖] Because the beam particle makes synchrotron oscillations, its betatron tune will be changing from turn to turn depending on its momentum offset. There will be a betatron phase offset which will accumulate. Consider a beam particle which is currently at the head of the bunch. It will be executing betatron oscillations with the same betatron tune

[‖]Sometimes, especially in Europe, the chromaticity ξ is also defined by $\Delta\nu_\beta = \xi\nu_\beta\delta$. We address the European definition as the *relative chromaticity*.

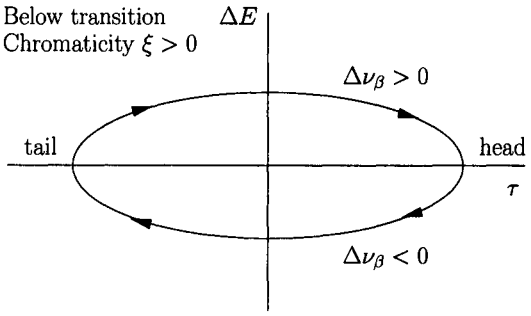


Fig. 9.8 Synchrotron motion in the longitudinal phase space below transition. If chromaticity ξ is positive, the betatron tune will be larger/smaller than that of the synchrotron particle, when the particle energy offset is positive/negative.

as the synchronous particle, because it is at the synchronous momentum. Below transition, the synchrotron oscillation is clockwise in the longitudinal phase space as indicated in Fig. 9.8, because, for example, at a positive momentum offset, the particle comes back earlier or its arrival time advance increases. Thus leaving the head of the bunch, the particle loses energy and starts to oscillate with a smaller betatron tune if the chromaticity ξ is positive. Turn by turn, the slip in betatron phase accumulates and reaches a maximum when the particle arrives at the tail of the bunch. After that the momentum offset of the second half of the synchrotron oscillation becomes positive. The betatron tune is larger than the nominal value and the accumulated betatron phase slip gradually reduces. When the particle arrives at the head, all the betatron phase slip vanishes. This phase slip is illustrated schematically in Fig. 9.9.

We would like to compute the phase slip for a particle that has a time advance τ relative to the synchronous particle that has the same betatron phase initially when $\tau = 0$. The momentum offset in Eq. (9.104) can be eliminated using the equation of motion of the phase

$$\Delta\tau = -\eta T_0 \delta, \tag{9.105}$$

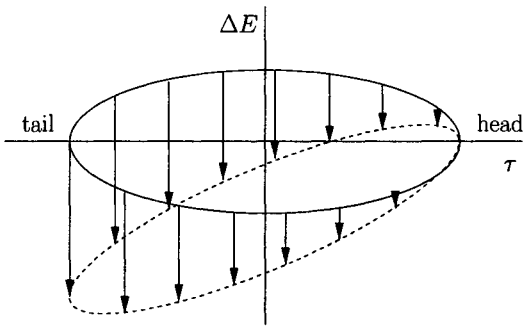


Fig. 9.9 Schematic drawing showing the lagging of the betatron phase, depicted by the arrows, from the head (right) to the tail (left) of the bunch when the chromaticity ξ and slip factor η have the different signs in this demonstration.

where η is the slip factor and $\Delta\tau$ is the change in time advance of the particle in a turn. The phase lead in a revolution turn is then

$$\int_0^\tau 2\pi\Delta\nu_\beta = -2\pi\frac{\xi}{\eta}\int_0^\tau \frac{\Delta\tau}{T_0} = -\frac{\xi\omega_0}{\eta}\tau. \tag{9.106}$$

Thus, below transition ($\eta < 0$), a particle at the bunch head ($\tau = \hat{\tau}$) has an accumulated betatron phase advance of $-\xi\omega_0\hat{\tau}/\eta$ relative to the synchronous particle, while a particle at the tail ($\tau = -\hat{\tau}$) has an accumulated betatron phase slip of $-\xi\omega_0\hat{\tau}/\eta$. Equation (9.106) indicates that the phase lag increases linearly along the bunch and is independent of the momentum offset. Relative to the synchronous particle, we write this accumulated betatron phase for a particle at arrival time advance τ as

$$-\frac{\xi\omega_0}{\eta}\tau = -\omega_\xi\tau, \tag{9.107}$$

where

$$\omega_\xi = \frac{\xi\omega_0}{\eta} \tag{9.108}$$

is called the *betatron angular frequency shift due to chromaticity.* Below transition and for positive chromaticity, ω_ξ is negative, but the accumulated betatron phase at the bunch head is positive. Thus, in all the previous derivations involving transverse motion, we should make the substitution

$$e^{i\omega_q\tau} \rightarrow e^{i(\omega_q-\omega_\xi)\tau}, \tag{9.109}$$

where $\omega_q \approx (qM+\mu)\omega_0 + m\omega_s$. For this reason, ω_ξ should be subtracted from ω_q in the argument of the power spectrum h_m but not in the argument of $\mathcal{R}e\, Z_\perp^1$ of the growth rate formula like Eq. (9.88) and also not in the argument of $\mathcal{I}m\, Z_\perp^1$ of the tune shift formula. The total *chromatic betatron phase shift* from head to tail is represented by $\chi = \omega_\xi\tau_L$, where τ_L is the total length of the bunch from head to tail. The head-tail modes for various values of χ are shown in Fig. 9.4.

For positive chromaticity above transition, $\omega_\xi > 0$, the modes of excitation in Fig. 6.13 are therefore shifted to the right by the angular frequency ω_ξ. As shown in Fig. 9.10, mode $m = 0$ sees more impedance in positive frequency than negative frequency and is therefore stable. However, it is possible that mode $m = 1$, as in the illustration of Fig. 9.10, samples more the highly negative $\mathcal{R}e\, Z_\perp^1$ at negative frequencies than positive $\mathcal{R}e\, Z_\perp^1$ at positive frequencies and becomes unstable.

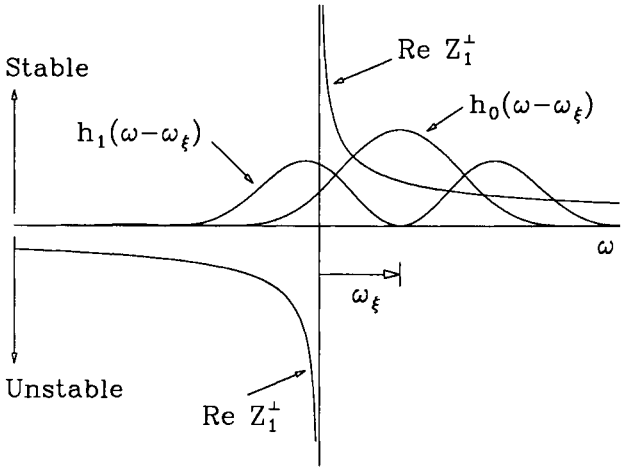


Fig. 9.10 Positive chromaticity above transition shifts the all modes of excitation towards the positive frequency side by ω_ξ. Mode $m = 0$ becomes stable, but mode $m = 1$ may be unstable because it samples more negative $\mathcal{R}e\, Z_1^\perp$ than positive $\mathcal{R}e\, Z_1^\perp$.

If the transverse impedance is sufficiently smooth, it can be removed from the summation in Eq. (9.88). The growth rate for the $m = 0$ mode becomes

$$\frac{1}{\tau_0} = -\frac{eI_b}{2\beta E_0 \tau_L}\, \mathcal{R}e\left[\beta_\perp Z_1^\perp(\omega_\xi)\right]. \tag{9.110}$$

The transverse impedance of the CERN Proton Synchrotron (PS) had been measured in this way by recording the growth rates of a bunch at different chromaticities (Exercise 9.4).

We learn in above that chromaticity is a means of shifting the overlap of the impedance function with the bunch mode power spectrum. The chromaticity is often so chosen that an instability can be avoided. However, the chromaticity is often not something that we can choose completely at will. A high chromaticity implies a large betatron tune spread and parametric resonances will be encountered. In most cases, high-strength sextupoles are required to generate such high chromaticity and the lattice of the accelerator will become so nonlinear that the aperture of the accelerator ring becomes greatly reduced.

9.9 Exercises

9.1 Fill in all the steps in the derivation of Sacherer's integral equation for transverse instabilities.

9.2 Derive the power spectra of the sinusoidal modes of excitation in Eq. (9.99), and show that they are given by Eq. (9.101) when properly normalized according to Eq. (9.102).

9.3 Redefine the longitudinal coordinates in Eq. (8.1) by $X = xv$ and $P_x = p_x v$, where v is the particle velocity, so that X carries the dimension of length. (1) Show that, for the equations of motion, Eq. (8.2) in the longitudinal phase space and Eq. (9.15) in the transverse phase space, can best be derived from the Hamiltonian

$$H = -\frac{\omega_s}{2v}(X^2 + P_x^2) - \frac{\omega_\beta}{2v}(y^2 + p_y^2) - \\ - \frac{v\eta}{E_0\omega_s\beta^2}\int_0^X dX' \langle F_0^{\parallel}(X'/v; s)\rangle + \frac{cy}{E_0\omega_\beta\beta^2}\langle F_1^{\perp}(X/v; s)\rangle. \quad (9.111)$$

(2) Show that the second equation of motion in Eq. (8.2) needs to be modified to

$$\frac{dp_x}{ds} = \frac{\omega_s}{v}x + \frac{\eta}{E_0\omega_s\beta^2}\langle F_0^{\parallel}(x; s)\rangle - \frac{y}{E_0\omega_\beta\beta^3 v}\frac{\partial}{\partial x}\langle F_1^{\perp}(x; s)\rangle, \quad (9.112)$$

where the last term is the synchro-betatron coupling term which we dropped in our discussion.

9.4 If the transverse impedance is sufficiently smooth, it can be removed from the summation in Eq. (9.88). Show that the growth rate for the $m = 0$ mode becomes

$$\frac{1}{\tau_0} = -\frac{eI_b}{2\beta E_0 \tau_L}\mathcal{R}e\left[\beta_\perp Z_1^{\perp}(\omega_\xi)\right]. \quad (9.113)$$

The transverse impedance of the CERN PS has been measured in this way by recording the growth rates of a bunch at different chromaticities. The CERN PS has a mean radius of 100 m and it can store proton bunches from 1 to 26 GeV with a transition gamma of $\gamma_t = 6$. The bunch has a spectral spread of $\sim \pm 100$ MHz, implying that each measurement of the impedance is averaged over an interval of ~ 200 MHz. If the impedance has to be measured up to ~ 2 GHz and the sextupoles in the PS can attain chromaticities in the range of ± 10, at what proton energy should this experiment be carried out?

Bibliography

[1] E. D. Courant and H. S. Synder, *Theory of the Alternating-Gradient Synchrotron*, *Annals of Physics* **3**, 1 (1958).

[2] R. Chasman, K. Green, and E. Rowe, *IEEE Trans.* **NS-22**, 1765 (1975).

[3] B. Zotter and F. Sacherer, *Transverse Instabilities of Relativistic Particle Beams in Accelerators and Storage Rings*, Proc. First Course of Int. School of Part. Accel.

of the 'Ettore Majorana' Centre for Scientific Culture, eds. A. Zichichi, K. Johnsen, and M. H. Blewett (Erice, Nov. 10–22, 1976), CERN Report CERN 77-13, p. 175.

[4] See for example, J. L. Laclare, *Bunch-Beam Instabilities, — Memorial Talk for F. J. Sacherer*, Proc. 11th Int. Conf. High-Energy Accel., (Geneva, July 7-11, 1980), p. 526.

[5] F. J. Sacherer, *Methods for Computing Bunched-Beam Instabilities*, CERN Report CERN/SI-BR/72-5, 1972.

[6] See for example, M. Abramowitz and I. Stegun, *Handbook of Mathematical Functions*, (Dover, New York, 1965), Chapter 22.

This page intentionally left blank

2025 © The Author(s). This is an Open Access chapter published by World Scientific Publishing Company, licensed under the terms of the Creative Commons Attribution-NonCommercial 4.0 International License (CC BY-NC 4.0).

Chapter 10

Transverse Coupled-Bunch Instabilities

Wake field longer than the bunch spacing can couple the motion of bunches. If there are M identical equally spaced bunches in the ring, there are M transverse coupled modes. They are characterized by $\mu = 0, \cdots, M-1$ when the center-of-mass of one bunch *lags** its predecessor by the betatron phase of $2\pi\mu/M$. The transverse growth rate for the μ-th coupled-bunch mode is given by Eq. (9.88). Including chromaticity and only the most prominent radial mode in the azimuthal m, it becomes

$$\frac{1}{\tau_{m\mu}} = -\frac{eMI_b\omega_0}{4\pi\beta E_0}\frac{\sum_q \mathcal{R}e\left[\beta_\perp Z_1^\perp(\omega_q)\right] h_m(\omega_q - \chi/\tau_L)}{B\sum_q h_m(\omega_q - \chi/\tau_L)}F_m, \tag{10.1}$$

where $\omega_q = (qM+\mu)\omega_0 + \omega_\beta + m\omega_s$, I_b is the average current per bunch, T_0/M is the bunch spacing with T_0 being the revolution period, and $\left[\beta_\perp Z_1^\perp(\omega_q)\right]$ reminds us that, when performing the element-by-element summation of $Z_1^\perp$ around the ring, the betatron function $\beta_\perp$ should be used as a weight. The form factor F_m is given by Eq. (9.89) with the radial index omitted. The bunching factor $B = M\tau_L/T_0$ is defined as the ratio of bunch length to bunch spacing and $\chi = \omega_\xi\tau_L$ is the chromaticity phase shift across the bunch of full length τ_L. Here, we assume that all the bunches are executing synchrotron oscillations in the same longitudinal azimuthal mode m.

10.1 Resistive-Wall Instabilities

The most serious transverse coupled-bunch instability that occurs in nearly all accelerator rings is the one driven by the resistive wall. [1] Since the resistive part

*In the $e^{-i\omega t}$ convention, the phase increases in the clockwise direction; i.e., $\vec{A} = Ae^{-i\phi_A}$ leads $\vec{B} = Be^{-i\phi_B}$ by ϕ implies $\phi_A - \phi_B = \phi$. More correctly, this should be called the *time-phase* instead because it increases with time.

of the transverse resistive-wall impedance behaves as† $\mathcal{R}e\, Z_1^\perp\big|_{\rm RW} \propto \omega^{-1/2}$ and is positive (or negative) when the angular frequency ω is positive (or negative), the lower betatron sideband at the lowest negative frequency acts like a narrow resonance and drives transverse coupled-bunch instabilities. Take, for example, the Fermilab Tevatron in the fixed-target mode, where there are $M = 1113$ equally spaced bunches. The betatron tune is $\nu_\beta = 19.6$. The lowest-negative-betatron-frequency sideband is at $(qM+\mu)\omega_0 + \omega_\beta = -0.4\omega_0$, for mode $\mu = 1093$ and $q = -1$, commonly known as the $(1-Q)$ line. The closest damped betatron sideband ($q = 0$) is at $(1113-0.4)\omega_0$, but $\mathcal{R}e\, Z_1^\perp\big|_{\rm RW}$ is only $-\sqrt{0.4/1112.6}$ the value at $-0.4\omega_0$. The next anti-damped betatron sideband ($q = -2$) is at $-1113.4\omega_0$, with $\mathcal{R}e\, Z_1^\perp\big|_{\rm RW}$ equal to $\sqrt{0.4/1113.4}$ the value at $-0.4\omega_0$. This is illustrated in Fig. 10.1. Thus, it is the $-0.4\omega_0$ betatron sideband that dominates. From Eq. (10.1), the growth rate for this mode can therefore be simplified to

$$\frac{1}{\tau_{m\mu}} \approx -\frac{1}{1+m}\frac{eMI_b\omega_0}{4\pi\beta E_0}\,\mathcal{R}e\left[\beta_\perp Z_1^\perp\big|_{\rm RW}(\omega_q)\right] F'_m(\omega_q\tau_L - \chi), \tag{10.2}$$

where $\chi = \omega_\xi\tau_L$ is the chromatic betatron phase shift across the length of the bunch, and the form factor is

$$F'_m(\omega\tau_L) = \frac{2\pi h_m(\omega)}{\tau_L\displaystyle\int_{-\infty}^{\infty} h_m(\omega)d\omega}, \tag{10.3}$$

which is plotted in Fig. 10.2 for Sacherer's sinusoidal modes. At zero chromaticity, only the $m = 0$ mode can be unstable because the power spectra for all the

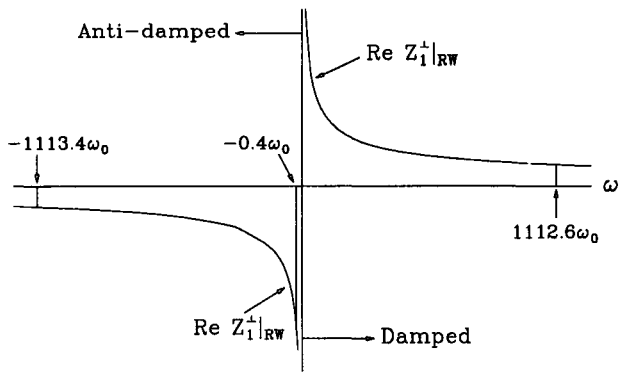


Fig. 10.1 The $-0.4\omega_0$ betatron sideband in the Tevatron dominates over all other betatron sidebands for the $\mu = 1093$ mode coupled-bunch instability driven by the resistive wall impedance.

†For illustration, here we assume that the wall is thicker than one skin depth at revolution frequency. Otherwise, $\mathcal{R}e\, Z_1^\perp \propto \omega^{-1}$, the so-called Sacherer's region. [1]

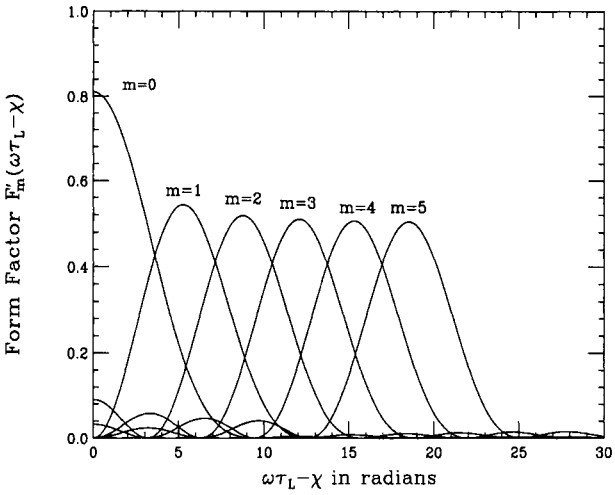


Fig. 10.2 Plot of form factor $F'_m(\omega\tau_L - \chi)$ for modes $m = 0$ to 5. With the normalization in Eq. (9.102), these are exactly the power spectra h_m.

$m \neq 0$ modes are nearly zero near zero frequency. Since the perturbing betatron sideband is at extremely low frequency, we can evaluate the form factor at zero frequency. For the sinusoidal modes, we get $F'_0(0) = 8/\pi^2 = 0.811$.

One method to make this coupled-bunch mode less unstable or even stable is by introducing positive chromaticity when the machine is above transition. For the Tevatron with slip factor $\eta = 0.0028$, total bunch length $\tau_L = 5$ ns, and revolution frequency $f_0 = 47.7$ kHz, a chromaticity of $\xi = +10$ will shift the spectra by the amount $\chi = \omega_\xi \tau_L = 2\pi f_0 \xi \tau_L/\eta = 5.4$. The form factor and thus the growth rate is reduced by more than four times. However, from Figs. 6.13 and 9.10, we see that the spectra are shifted by $\omega_\xi \tau_L/\pi = 1.7$ and the $m = 1$ mode becomes unstable. Another method for damping the instability is to introduce a betatron angular frequency spread using octupoles, with the spread larger than the growth rate. A third method is to coat the beam pipe with a layer of copper. This is especially advantageous in a superconducting ring like the Tevatron and the demised Superconducting Super Collider (SSC), because copper has a conductivity at least $\sim$ 30 times bigger at 4°K than at room temperature.

A fourth method is to employ a damper. Let us derive the displacements of consecutive bunches at a beam-position monitor (BPM). Suppose the first bunch is at the BPM with betatron phase $\phi_{\beta 0} = 0$; its displacement registered at the BPM is proportional to $\cos\phi_{\beta 0} = 1$. At that moment, the next bunch has phase $2\pi\bar{\mu}/M$ in advance, where $\bar{\mu} = qM + \mu = -20$. When this bunch arrives at the BPM, the time elapsed is T_0/M and the change in betatron phase is

$\omega_\beta T_0/M = 2\pi\nu_\beta/M$. The total betatron phase on arrival at the BPM is therefore $\phi_{\beta 1} = 2\pi\bar{\mu}/M + 2\pi\nu_\beta/M = 2\pi(\bar{\mu}+\nu_\beta)/M = (-0.4)2\pi/M$, and the displacement registered is $\cos\phi_{\beta 1}$. When the nth consecutive bunch arrives at the BPM, its phase will be $\phi_{\beta n} = n(-0.4)2\pi/M$. This is illustrated in Fig. 10.3, where only every 20th bunch is shown although the BPM has all the bunches registered. [2] What we see at the BPM is a wave of frequency -0.4 harmonic or about 19.1 kHz. Because we know that the bunches follow the pattern of such a slow wave, only a very narrow-band feedback system or a mode damper will be required to damp the instability. Usually the adjacent modes $\mu = 1092, 1091, \cdots$ will also be unstable at the $-1.4\omega_0, -2.4\omega_0, \cdots$ betatron sidebands; but the growth rates will be smaller.

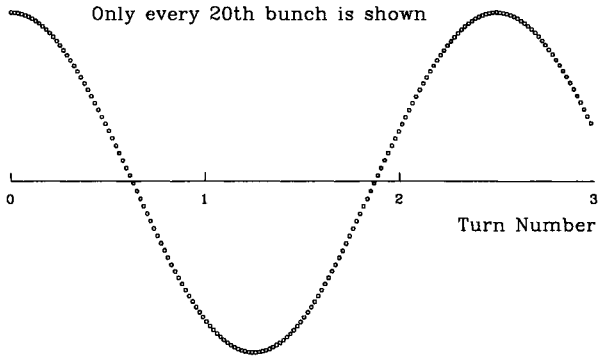


Fig. 10.3 Difference signal at a beam-position monitor recording the displacement of every 20th bunch, when the $\mu = 1093$ mode of transverse coupled-bunch is excited by the resistive-wall impedance.

To have a feeling of the growth rate, let us continue the example of the Tevatron. When all the $h = 1113$ rf buckets are filled with 6×10^{10} protons each in one scenario of the Tevatron in the fixed-target mode, the average total current is $MI_b = 0.511$ A. The stainless-steel vacuum chamber can be approximated to be cylindrical with a radius $b = 3$ cm. Let us first assume that the wall of the beam pipe is thick enough in the frequency range under discussion. The Tevatron has a mean radius of $R = 1$ km. Thus the vertical resistive-wall impedance has a real part[‡] $\mathcal{R}e\, Z_1^\perp\big|_{\rm RW} = 27.7$ MΩ/m at the revolution frequency $\omega_0/(2\pi) = 47.7$ kHz, where the conductivity of stainless-steel $\sigma_c = 1.35 \times 10^6$ $(\Omega\text{-m})^{-1}$ has been used. At the betatron tune $\nu_\beta = 19.6$, the $(1 - Q)$ line at $-0.4\omega_0$ has the impedance $\mathcal{R}e\, Z_1^\perp\big|_{\rm RW} = -43.7$ MΩ/m. At the injection energy of $E_0 = 150$ GeV and zero chromaticity, the transverse coupled-bunch growth rate driven by the resistive-wall impedance is $\tau_\mu^{-1} = 147\ \text{s}^{-1}$ and the growth

[‡]As will be shown below, the laminated Lambertson magnets will not contribute at low frequencies.

time is 6.81 ms or 325 revolution turns. In fact, this growth time is more or less the same for all accelerator rings. [3] For example, preceding the Tevatron, there are the Main Injector and the Booster. All of them have the same 53-MHz rf. The Main Injector has 588 rf buckets and the Booster has 84 rf buckets. First, if all the buckets of each ring are filled, the average total current MI_b should be the same for all the three rings. Second, the beam energy E_0 scales as the size of the ring or the mean radius R and betatron tune ν_β scales as $\sqrt{R}$. Third, the resistive-wall impedance, as given by

$$Z_1^\perp\big|_{\text{RW}}(\omega) = [1 - i\,\text{sgn}(\omega)]\frac{2Rc}{\omega b^3 \delta_c \sigma_c} \tag{10.4}$$

in Eq. (1.60), where b is the beam pipe radius and δ_c is the skin-depth defined in Eq. (1.59), scales as $R^{3/2}$ because the revolution frequency scales as R^{-1}. Substituting into Eq. (10.2), we find that the growth rate turns out to be independent of the size of the ring. Of course, usually there are differences in the vacuum chamber, and number of particles per bunch, and also the residual betatron tune. However, it is safe to say that the growth time of transverse coupled-bunch instability for every completely filled accelerator ring should be of the order of a few to a few tens of milliseconds. Although the growth time is independent of the size of the ring, the growth time in turn number is inversely proportional to the size of the ring. Thus, for the Very Large Hadron Collider (VLHC) under consideration [4] with a circumference of 233 km, the growth time will be only 5.5 revolution turns according to this scaling and assuming the residual tune to be $\frac{1}{2}$. For this reason, large machines will require powerful feedback systems, for example, criss-crossing feedback and/or one-turn correction scheme.

Actually the beam pipe of the Tevatron has a wall thickness of $t = 1.5$ mm. Thus the frequency at which the skin-depth is equal to the wall thickness is given by

$$f_c = \frac{c}{\pi Z_0 \sigma_c t^2}, \tag{10.5}$$

or 83.4 kHz, which is almost twice the revolution frequency. Below this critical frequency, the image current fills the wall of the beam pipe and the transverse resistive-wall impedance should follow the $1/\omega$-behavior instead, a phenomenon first pointed out by Sacherer. [1] Thus the resistive-wall impedance at the $(1-Q)$ line becomes $\mathcal{R}e\, Z_1^\perp\big|_{\text{RW}} = 91.5$ mΩ/m and it drives a transverse coupled-bunch instability with a growth rate of $1/\tau = 308$ s^{-1} or a growth time of 3.25 ms. In view of the $1/\omega$-behavior, the above scaling consideration will be changed. Now the transverse impedance at the revolution frequency scales as R^2 and therefore

the growth rate increases as $\sqrt{R}$. This is especially true for large ring, because the revolution frequency is low and the $(1-Q)$ line will most probably be in the Sacherer's region.

10.1.1 *Resistive-Wall Impedance at Low Frequencies*

We conclude in the previous section that resistive-wall driven transverse instabilities in the Fermilab Booster should have growth time of about a few milliseconds, if it has the same beam pipe as the Fermilab Main Injector and/or the Tevatron. The Fermilab Booster is a 15-Hz fast-cycling machine. To avoid eddy currents which can block field penetration, no beam pipe has ever been installed inside the magnets. Thus the beam particles are seeing the laminations of the combined-function magnets all the time. The coupling impedance will therefore be very much larger than that of a smooth beam pipe, because the image current has to flow into and out of each lamination, especially at low frequencies. If the $\omega^{-1/2}$-behavior were followed [Eq. (1.60)], one would expect very high transverse impedance and therefore very severe transverse coupled-bunch instabilities. However, there is no transverse damper in the Fermilab Booster and such severe transverse instabilities have never been observed.

The transverse impedance is the Fourier transform of the dipole wake and is therefore an analytic function of frequency, implying that it should not have a singularity at $\omega = 0$, whereas we see in Fig. 10.1 that it diverges to $\pm\infty$. Detailed derivation through solution of the Maxwell equations and careful bench measurements show that when the frequency is low enough $Z_1^\perp\big|_{\rm RW}$ deviates from the $\omega^{-1/2}$-behavior. The real part bends around and goes to zero at zero frequency. On the other hand, the imaginary part per unit length approaches, for a cylindrical beam pipe of radius b, a geometric constant

$$\lim_{\omega\to 0}\frac{\mathcal{I}m\, Z_1^\perp\big|_{\rm RW}}{L} = -\frac{Z_0}{2\pi b^2}, \tag{10.6}$$

which is independent of wall conductivity σ_c (dot-dashed curve in Fig. 10.4). We give it a name, the *bypass inductance* of the beam pipe. According to the general expression of the transverse resistive-wall impedance, like Eq. (1.60),

$$\frac{\mathcal{R}e\, Z_1^\perp\big|_{\rm RW}}{L}\,\mathrm{sgn}(\omega) = -\frac{\mathcal{I}m\, Z_1^\perp\big|_{\rm RW}}{L} = \frac{c}{\pi|\omega|b^3\sigma_c\delta_c}, \tag{10.7}$$

where $\delta_c = \sqrt{2/(\omega\mu\sigma_c)}$ is the skin-depth and μ is the magnetic permeability of

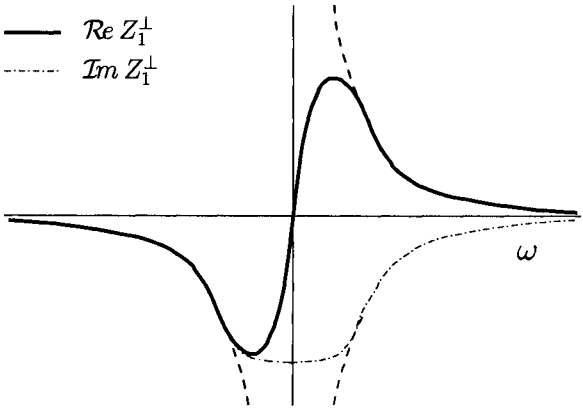


Fig. 10.4 Schematic drawing of the transverse resistive-wall impedance showing that the real part (solid) goes to zero at zero frequency and the imaginary part (dot-dashed) goes to an inductive constant. The behavior of the expression in Eq. (1.60) with $1/\sqrt{\omega}$-behavior is shown in dashes.

the beam pipe, $\mathcal{I}m\, Z_1^\parallel/L$ will exceed the geometric limit in Eq. (10.6) when

$$kb = \frac{\omega b}{c} < \frac{2}{\sigma_c b Z_0}. \tag{10.8}$$

For a stainless-steel beam pipe of radius $b = 5$ cm with $\sigma_c = 1.35 \times 10^6\ (\Omega\text{-m})^{-1}$, this occurs when $kb < 7.87 \times 10^{-8}$ or the bend-around of $\mathcal{R}e\, Z_1^\perp\big|_{\rm RW}$ must occur at the frequency $f_{\rm bend} > 75$ Hz. In reality, the wall of the beam pipe has finite thickness, electromagnetic fields leaking outside will see a much larger resistivity. When the frequency is low enough so that $\delta_c < t$, the thickness of the pipe wall, the transverse resistive-wall impedance in Eq. (10.7) must be modified by replacing δ_c with t. Now the impedance rises much faster according to $1/\omega$ (the so-called Sacherer's region [1]) and reaches the limiting value of Eq. (10.6) at the higher frequency

$$kb = \frac{2}{\sigma_c t Z_0}. \tag{10.9}$$

For the same 5-cm radius beam pipe of wall thickness $t = 1.5$ mm, this occurs when $kb = 2.62 \times 10^{-6}$ or at frequency $f = 2.50$ kHz. In other words the bend-around of $\mathcal{R}e\, Z_1^\perp\big|_{\rm RW}$ must take place at the frequency $f_{\rm bend} > 2.5$ kHz, which is very much less than the revolution frequency of most accelerator rings. Thus this low-frequency behavior of the transverse resistive-wall impedance has no influence on collective instabilities at all. It may, however, begin to have some bearing on the Large Hadron Collider (LHC) under construction at CERN, which has a circumference of 26.7 kHz and revolution frequency 11.3 kHz. This low-frequency behavior will definitely be important to the 231-km Very Large Hadron Collider (VLHC) under design, which has a revolution frequency of 1.29 kHz.

The story is quite different for laminated magnets. Because the wall impedance is very much larger, in order to have the same limiting inductive impedance[†] given by Eq. (10.6), we expect the bend-around of $\mathcal{R}e\, Z_1^{\perp}\big|_{\rm RW}$ to take place at much higher frequencies than the smooth beam pipe. If one approximates the laminations as annular rings of inner and outer radii b and d and shorted at the outer radius, an estimate of the bend-around frequency is found to be [5]

$$f_{\rm bend} \approx \frac{8c\mu'}{Z_0\sigma_c\tau}\left(\ln\frac{d}{b}\right)^2, \tag{10.10}$$

where τ is the thickness of a lamination with relative magnetic permeability μ' and conductivity σ_c. As an example, with $\tau = 0.025''$, $\mu' = 100$, $b = 1.25''$, and $d = 6''$, the bend-around frequency becomes 250 MHz (actual computation gives $\sim$ 100 MHz). The implication is that the laminated magnets do not contribute to the $\omega^{-1/2}$ behavior of the transverse impedance at low frequencies. In other words, laminated magnets will not drive transverse coupled-bunch instabilities at low frequencies. Our next task is to understand why the bend-around takes place and to have a physical understanding of the limiting wall-independent inductive impedance.

10.1.2 *Bypass Inductance*

Before going through a complicated field-theoretical derivation, let us first study the more physical understanding of the *bypass inductance* proposed by Vos. [6]

Consider a current I flowing in the z-direction displaced by $x = a$ as illustrated in Fig. 10.5(a). When the metallic wall of the cylindrical beam pipe is a perfect conductor, the image current in the wall can be computed using the method of images (see also Sec. 3.4.1). For a beam current I at an offset a on the x-axis, the magnetic field at the wall of the beam pipe can be made tangential with the positioning of an image current $-I$ on the x-axis b^2/a away from the center, as illustrated in Fig. 10.5(b). From the tangential magnetic field, the surface current density in the wall is found to be

$$K_z(\theta) = \frac{b^2 - a^2}{b^2 + a^2 - 2ba\cos\theta}\frac{i_{\rm im}}{2\pi b}, \tag{10.11}$$

where $i_{\rm im} = -I$ is the total image current in the metallic wall of the beam pipe flowing also in the *positive* z-direction. The normalization can be checked easily by integrating over the azimuthal angle θ. Since we are only interested in the

[†]This is because we expect the limiting inductance impedance to depend only on the cross-sectional geometry of the vacuum chamber and independent of its other properties.

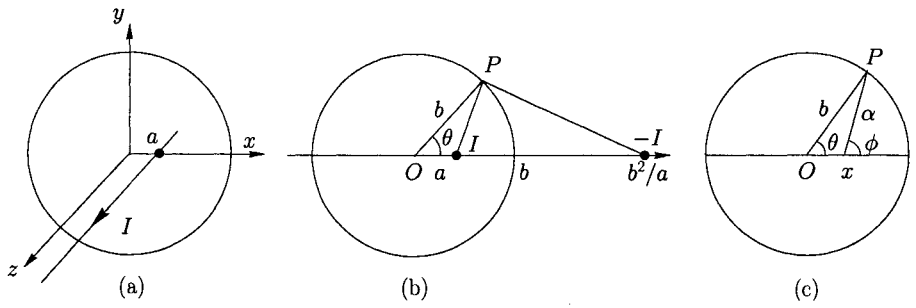


Fig. 10.5 (a) A current I at an offset a on the x-axis of a perfectly conducting cylindrical beam pipe creates surface image current $J(\theta)$ on the inner surface of the beam pipe. For the dipole-mode image current, the uniform monopole image current is subtracted. (b) An image current $-I$ at a distance b^2/a from the center is required to allow the magnetic field at any point P to be tangential to the wall surface of the cylindrical beam pipe. (c) We are after the magnetic field produced by the image current in an element $\Delta(\theta)bd\theta$ at point P at a point on the x-axis at a distance x from the origin.

dipole part of the image current, the monopole part, i.e., $K_z(\theta)$ with offset $a = 0$, must be subtracted, giving

$$K_z(\theta) - \frac{i_{\text{im}}}{2\pi b} = \frac{i_{\text{im}}}{2\pi b}\frac{2a(b\cos\theta - a)}{b^2 + a^2 - 2ba\cos\theta} \approx \frac{i_{\text{im}}a}{\pi b^2}\cos\theta, \tag{10.12}$$

where the last quantity is the dipole image current density and is denoted by $\Delta K_z(\theta)$. The total image current in one side ($-\pi/2 < \theta < \pi/2$ or the fourth and first quadrants) of the beam pipe is

$$I_d = \int_{-\pi/2}^{\pi/2} \Delta K_z(\theta) b d\theta = \frac{2i_{\text{im}}a}{\pi b}, \tag{10.13}$$

which is negative flowing in the positive z-direction. Of course, there is also a current $-I_d$ flowing in the positive z-direction between $\pi/2 < \theta < 3\pi/2$ (or the second and third quadrants). This set of currents forms a dipole loop, and we called them the *differential currents.*

The dipole image current $\Delta K_z(\theta)$ sets up a magnetic field inside the beam pipe. We are after this magnetic field on the x-axis ($-b < x < b$). By symmetry, the magnetic field there is in the vertical direction and is given by

$$H_y(x) = -\int_{-\pi}^{\pi} \frac{\Delta K_z(\theta) b d\theta}{2\pi\alpha}\cos\phi, \tag{10.14}$$

where, as illustrated in Fig. 10.5(c), α denotes the distance between the point x and the image surface current element $\Delta K_z(\theta)bd\theta$ at Point P, and ϕ is the angle

between the vector α and the x-axis. Point P is at a horizontal distance $b\cos\theta - x$ from the point of observation on the x-axis, and $\alpha^2 = b^2\sin^2\theta + (b\cos\theta - x)^2 = b^2 + x^2 - 2bx\cos\theta$. Notice that the image currents in all the four quadrants contribute to H_y in the same direction. This is expected because the image current just forms a loop. We can therefore write

$$H_y(x) = -\frac{i_{\rm im}a}{\pi^2 b}\int_0^{\pi}\frac{(b\cos\theta - x)\cos\theta}{b^2 + x^2 - 2bx\cos\theta}\,d\theta = -\frac{i_{\rm im}a}{2\pi b^2}, \tag{10.15}$$

which is independent of x as expected from a dipole source. The magnetic flux density is $B_y = \mu_0 H_y$ and the flux per longitudinal length linking the x-axis is obtained by integrating along the x-axis:

$$\Phi_y = \int_{-b}^{b} B_y dx = 2bB_y = -\frac{\mu_0 i_{\rm im}a}{\pi b} = -\frac{\mu_0}{2}I_d. \tag{10.16}$$

Thus the inductance per longitudinal length facing the loop of differential currents (I_d at one side and $-I_d$ at the other side) is

$$\mathcal{L} = \frac{\mu_0}{2}, \tag{10.17}$$

which, in fact, is the result of the geometry of the system. We can therefore consider that the image current $i_{\rm im}$ and the differential current I_d are related through a mutual inductance $\mathcal{M}$ as illustrated in equivalent circuit (a) of Fig. 10.6. From

$$-i\omega\mathcal{M}(i_{\rm im} - I_d) = -i\omega(\mathcal{L} - \mathcal{M})I_d, \tag{10.18}$$

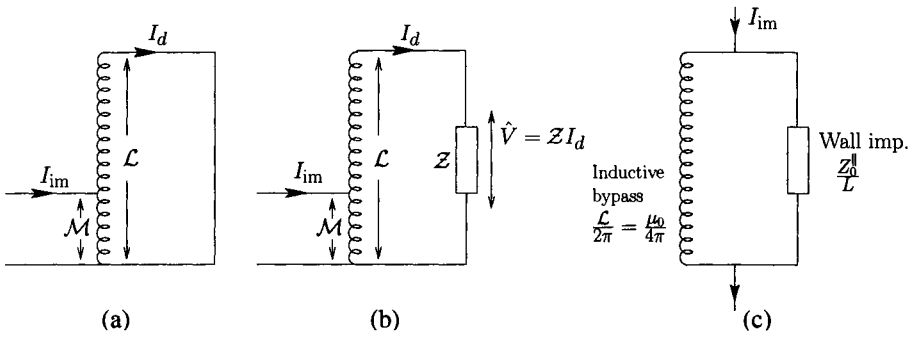


Fig. 10.6 (a) Representing by an equivalent circuit, by offsetting the beam, the image current $i_{\rm im}$ generates, through a mutual inductance $\mathcal{M}$, a differential current I_d, which sees a inductance $\mathcal{L} = \mu_0/2$. (b) When the wall of the beam pipe is not perfectly conducting, the different current sees also an impedance $\mathcal{Z}$. (c) Equivalently, the image current sees an inductive bypass per unit length $\mathcal{L}/(2\pi) = \mu_0/(4\pi)$ in parallel with the longitudinal monopole wall impedance per unit length $Z_0^{\parallel}/L$.

it is easy to solve for the mutual inductance

$$\frac{\mathcal{M}}{\mathcal{L}} = \frac{I_d}{i_{\rm im}}. \tag{10.19}$$

The horizontal force due to the image current acting on a charge in the beam is

$$F_x = e(E_x - \beta c B_y), \tag{10.20}$$

where $v = \beta c$ is the longitudinal velocity of the beam particles. The horizontal dipole impedance coming from this magnetic image is, according to Eq. (1.43),

$$\frac{Z_1^\perp}{L} = \frac{(F_x/e)_{\rm mag}}{iIa\beta} = -\frac{cB_y}{iIa} = i\frac{Z_0}{2\pi b^2}, \tag{10.21}$$

recalling that $I = -i_{\rm im}$. This represents the familiar contribution from the magnetic image. The contribution of the electric image is just the same but is of opposite sign and is multiplied by the factor β^{-2}. The sum of the electric and magnetic contributions gives

$$\frac{Z_1^\perp}{L} = -i\frac{1}{\gamma^2\beta^2}\frac{Z_0}{2\pi b^2}, \tag{10.22}$$

which is just the wall-image part of the transverse space-charge impedance derived in Sec. 3.5.2 and is inductive. We are not interested in the space-charge impedance here because it vanishes for an ultra relativistic beam. However, it is interesting to point out that the contribution of the magnetic image to the impedance in Eq. (10.21) is *capacitive.*[‡] What we want to investigate is the role it plays in the presence of resistivity in the wall of the beam pipe.

In the presence of wall resistivity, the differential currents, I_d and $-I_d$, see in addition to the inductance per length $\mathcal{L}$, an extra impedance per unit length $\mathcal{Z}$. Now Eq. (10.13) no longer holds because it is derived from the method of images in a perfectly conducting circular metallic wall. Nevertheless, Eq. (10.19), the relation between the inductance $\mathcal{L}$ and the mutual inductance $\mathcal{M}$ is still valid. Since we are still after the dipole mode,

$$\Delta K_z(\theta) = \frac{I_d}{2b}\cos\theta \quad \text{and} \quad \int_{-\pi/2}^{\pi/2} \Delta K_z(\theta) b d\theta = I_d \tag{10.23}$$

must hold. For a transverse width w and a longitudinal length L, the wall current is $w\Delta K_z(\theta)$, and the impedance is $\mathcal{R}L/w$, where $\mathcal{R}$ is called the *surface*

[‡]A charge is repelled by its own image and leads to the down-shift of the betatron tune. The image part of the impedance is inductive. A current is attracted by its own image and leads to the up-shift of the betatron tune. The impedance is therefore capacitive.

impedance,[§] and is related to the longitudinal monopole resistive-wall impedance to the lowest order of $\mathcal{R}$ by

$$\frac{Z_0^{\parallel}}{L} = \frac{\mathcal{R}}{2\pi b}. \tag{10.24}$$

For a length L in the z-direction, the voltage difference created by the resistivity of the wall is given by

$$V(\theta) = 2\frac{\mathcal{R}L}{w} w \Delta K_z(\theta), \tag{10.25}$$

or

$$V(\theta) = \frac{\mathcal{R}LI_d}{b}\cos\theta, \tag{10.26}$$

where the factor of 2 on the right side of Eq. (10.25) comes about because there is a negative surface current flowing on one side of the beam pipe and a positive surface current current flowing on the other side. The peak value occurs at $\theta = 0$, giving

$$\frac{\hat{V}}{L} = \frac{\mathcal{R}I_d}{b} = 2\pi\frac{Z_0^{\parallel}}{L} I_d. \tag{10.27}$$

In equivalent circuit (b) of Fig 10.6, this peak voltage per unit length is just equal to the differential current I_d multiplied by the impedance $\mathcal{Z}$ represented in the circuit, thus giving a relation between $\mathcal{Z}$ and $Z_0^{\parallel}$, or

$$\mathcal{Z} = 2\pi\frac{Z_0^{\parallel}}{L}. \tag{10.28}$$

On the other hand, the peak electric field at the wall of the beam pipe is

$$\hat{E}_z = -\mathcal{R}H_\theta = \mathcal{R}\Delta K_z(0) = \frac{\mathcal{R}I_d}{2b}, \tag{10.29}$$

according to the definition of surface impedance per square, where H_θ is the azimuthal component of the magnetic field at the wall of the beam pipe. The horizontal Lorentz force per unit charge acting on the beam particle turns out to be

$$\frac{F_x}{e} = E_x - vB_y = \frac{v}{i\omega}\frac{\partial E_z}{\partial x}. \tag{10.30}$$

[§]Surface impedance is usually defined by Eq. (10.24). More generally, it should be defined as the ratio of the transverse magnetic field to the longitudinal electric field at the surface like Eq. (10.29).

For the dipole mode, E_z is linear[¶] in x at $\theta = 0$; we therefore have

$$\frac{F_x}{e} = \frac{v\mathcal{R}I_d}{i2\omega b^2}. \tag{10.31}$$

The horizontal dipole resistive-wall impedance is

$$\frac{Z_1^H|_{\rm RW}}{L} = \frac{F_x/e}{iIa\beta} = -\frac{c\mathcal{R}I_d}{2\omega b^2 Ia} = -\frac{c\pi}{\omega b}\frac{I_d}{Ia}\frac{Z_0^{\parallel}}{L}. \tag{10.32}$$

We need to derive the differential current I_d as related to I in the presence of wall resistivity. From equivalent circuit (b) of Fig. 10.6, it is easy to get

$$-i\omega\mathcal{M}(i_{\rm im} - I_d) = [-i\omega(\mathcal{L} - \mathcal{M}) + \mathcal{Z}]\, I_d. \tag{10.33}$$

Using the inductance per length $\mathcal{L}$ and mutual inductance per length $\mathcal{M}$ derived in Eqs. (10.17) and (10.19), we obtain

$$\frac{I_d}{i_{\rm im}} = \frac{2a}{\pi b}\frac{-i\omega\mathcal{L}}{-i\omega\mathcal{L} + \mathcal{Z}}, \tag{10.34}$$

and the ratio approaches the perfectly-conducting-wall limit when the wall resistivity $\mathcal{Z} \to 0$. Noting that $i_{\rm im} = -I$, the horizontal dipole resistive-wall impedance is finally written as

$$\frac{Z_1^H|_{\rm RW}}{L} = \frac{2c}{\omega b^2}\frac{\dfrac{-i\omega\mathcal{L}}{2\pi}\dfrac{Z_0^{\parallel}}{L}}{\dfrac{-i\omega\mathcal{L}}{2\pi} + \dfrac{Z_0^{\parallel}}{L}} = \frac{2c}{\omega b^2}\frac{\dfrac{-i\omega\mu_0}{4\pi}\dfrac{Z_0^{\parallel}}{L}}{\dfrac{-i\omega\mu_0}{4\pi} + \dfrac{Z_0^{\parallel}}{L}}, \tag{10.35}$$

where Eq. (10.28), the relation between $\mathcal{Z}$ and $Z_0^{\parallel}$, has been used. We see that when the frequency is not too small, we recover the usual Panofsky–Wenzel-like relation

$$Z_1^H|_{\rm RW} \approx \frac{2c}{\omega b^2} Z_0^{\parallel}. \tag{10.36}$$

However, when the frequency is small, the horizontal dipole impedance approaches

$$\frac{Z_1^H|_{\rm RW}}{L} \approx -i\frac{Z_0}{2\pi b^2}, \tag{10.37}$$

[¶]we can see this linearity is obvious for the dipole mode inside a cylindrical beam pipe. But there is no such linearity for a beam pipe consisting of two parallel plates. This explains why the bypass inductance for the parallel plates cannot be derived using this method.

which agrees with our low-frequency result in the previous section. The critical frequency occurs when the two terms in the denominator of Eq. (10.35) are equal, which gives

$$\frac{\omega Z_0}{4\pi c} = \left| \frac{Z_0^{\parallel}|_{\rm RW}}{L} \right|, \tag{10.38}$$

or

$$\omega = \frac{2c}{b} \frac{|\mathcal{R}|}{Z_0}. \tag{10.39}$$

Let us try to understand the expression for the transverse dipole impedance. The transverse dipole impedance is essentially the voltage across the wall impedance $\mathcal{Z}$ in equivalent circuit (c) of Fig. 10.6 per dipole beam current Ia. The voltage across the wall resistivity is just $\mathcal{Z}I_d$. But we need to transform I_d to $i_{\rm im}$ because the impedance is defined as the voltage seen by the beam current $-i_{\rm im}$ not the differential current I_d. All the essence of the bend-around frequency lies in the transformation from the differential current I_d to the dipole beam current, and the transformation is given by Eq. (10.34). There are two ingredients to this transformation. The first one is just the ratio

$$\frac{I_d}{i_{\rm im}} \approx \frac{2a}{\pi b}, \tag{10.40}$$

at high frequencies. This is the same ratio in the absence of the wall resistivity, according to Eq. (10.13). The result is easy to understand because the differential current will be smaller if the beam offset is smaller. The second ingredient is the inductance $\mathcal{L}$ generated by the differential current. We see that the inductance $\mathcal{L}$ does not even show up at high frequencies because the current finds it difficult to flow through an inductance. The transverse impedance is therefore just $\mathcal{Z}$, the wall resistivity, multiplied by the factor $c/(\pi\omega b^2)$, exactly the same as the usual Panofsky–Wenzel-like relation, aside from a constant. The situation is quite different at low frequencies, the no-wall-resistivity transformation ratio of Eq. (10.40) needs modification, because low-frequency current finds it easier to flow through an inductance $\mathcal{L}$ rather than the wall impedance $\mathcal{Z}$. Equation (10.34) gives

$$\frac{I_d}{i_{\rm im}} \approx \frac{-i\omega\mathcal{L}}{\mathcal{Z}} \frac{2a}{\pi b}, \tag{10.41}$$

making the differential current very small. The voltage across the wall impedance $\mathcal{Z}$ is now independent of $\mathcal{Z}$, and becomes proportional to $-i\omega\mathcal{L}$. In short,

the transverse dipole impedance is given totally by the geometric effect. Nevertheless since a transformer is involved here, it can also be dependent on the relative magnetic permeability of the wall material of the beam pipe, when the penetration of the image current into the walls of the beam pipe is properly taken into account.

The above picture can be simplified by avoiding the differential current I_d and referring to the beam current I or its image $i_{\rm im}$ directly. The second factor in Eq. (10.35) represents an inductance $\mathcal{L}/(2\pi)$ in parallel with the longitudinal monopole impedance $Z_0^{\parallel}|_{\rm RW}/L$. The transverse dipole impedance per unit length is just this parallel impedance multiplied by the factor $2c/(\omega b^2)$. Thus we can imagine the dipole current flowing through this parallel circuit instead, as is illustrated in Fig. 10.6(c). We call the inductance, $\mathcal{L}/(2\pi)$, a *bypass inductance*, because, at low frequencies, the image current flows through this bypass instead of the wall impedance $\mathcal{Z}$. On the other hand, at high frequencies, the inductive bypass exhibits high reactance and the image current flows through $Z_0^{\parallel}|_{\rm RW}$ instead.

10.2 Derivation of Resistive-Wall Impedance

Because the transverse resistive-wall impedance plays an important role in the transverse coupled-bunch instabilities, it is instructive to take a detour to study this impedance. The solution of the Maxwell equation is performed in each of the regions surrounding the particle beam. The continuation of the tangential components of the electric and magnetic fields is ensured by matching them at the boundaries. Such approach has been followed by many authors, for example, Zotter, [7] Gluckstern, [8] Lambertson, [9] Vos, [10], etc. Recently, Zotter renewed his effort on this subject and some new results are obtained. [11] We follow here the derivation of Gluckstern and Zotter, but with our interpretation added from time to time.

10.2.1 *Wave Equations*

With the time dependency $e^{-i\omega t}$, Maxwell equations can be expressed as

$$\begin{aligned} \vec{\nabla}\cdot\vec{E} &= \frac{\rho}{\epsilon}, \qquad & \vec{\nabla}\cdot\vec{H} &= 0, \\ \vec{\nabla}\times\vec{E} &= i\omega\mu H, \qquad & \vec{\nabla}\times\vec{H} &= \vec{J} + \sigma_c\vec{E} - i\omega\epsilon\vec{E}, \end{aligned} \tag{10.42}$$

where ρ is the charge density of the particle beam. The three terms on the right side of the last equation represent, respectively, the current density of the particle

beam $\vec{J}$ (convection current density), the conduction current density $\sigma_c\vec{E}$ in the medium with σ_c being the conductivity, and the displacement current density $-i\omega\epsilon\vec{E}$. The last two current densities can be combined by introducing the effective electric permittivity ϵ_{eff} according to

$$-i\omega\epsilon_{\text{eff}} = -i\omega\epsilon + \sigma_c. \tag{10.43}$$

This leads to the wave equations for the longitudinal components of the electric and magnetic fields:

$$\begin{aligned} \nabla^2\vec{E} + \omega^2\epsilon_{\text{eff}}\mu\vec{E} &= \frac{1}{\epsilon}\vec{\nabla}\rho - i\omega\mu\vec{J}, \\ \nabla^2\vec{H} + \omega^2\epsilon_{\text{eff}}\mu\vec{H} &= -\vec{\nabla}\times\vec{J}. \end{aligned} \tag{10.44}$$

These two equations are solved for E_z and H_z. The transverse electric field $\vec{E}_t$ can then be obtained in terms of E_z and H_z through

$$-i\omega\epsilon_{\text{eff}}\vec{E}_t = \vec{\nabla}_t\times\vec{H}_z + \vec{\nabla}_z\times\vec{H}_t = \vec{\nabla}_t\times\vec{H}_z + \frac{1}{i\omega\mu}\vec{\nabla}_z\times(\vec{\nabla}\times\vec{E})_t, \tag{10.45}$$

or

$$\begin{aligned} \omega^2\mu\epsilon_{\text{eff}}\vec{E}_t &= i\omega\mu\vec{\nabla}_t\times\vec{H}_z + \vec{\nabla}_z\times(\vec{\nabla}_t\times\vec{E}_z) + \vec{\nabla}_z\times(\vec{\nabla}_z\times\vec{E}_t) \\ &= i\omega\mu\vec{\nabla}_t\times\vec{H}_z + \vec{\nabla}_t\frac{\partial E_z}{\partial z} - \frac{\partial^2\vec{E}_t}{\partial z^2}. \end{aligned} \tag{10.46}$$

Similarly, the transverse magnetic field $\vec{H}_t$ can be obtained via

$$\begin{aligned} i\omega\mu\vec{H}_t &= \vec{\nabla}_t\times\vec{E}_z + \vec{\nabla}_z\times\vec{E}_t \\ &= \vec{\nabla}_t\times\vec{E}_z + \frac{1}{-i\omega\epsilon_{\text{eff}}}\left[\vec{\nabla}_z\times(\vec{\nabla}_z\times\vec{H}_t) + \vec{\nabla}_z\times(\vec{\nabla}_t\times\vec{H}_z)\right], \end{aligned} \tag{10.47}$$

or

$$\omega^2\mu\epsilon_{\text{eff}}\vec{H}_t = -i\omega\epsilon_{\text{eff}}\vec{\nabla}_t\times\vec{E}_z - \frac{\partial^2\vec{H}_t}{\partial z^2} + \vec{\nabla}_t\frac{\partial H_z}{\partial z}. \tag{10.48}$$

When the solution is attempted using the separation of variables, we let

$$\frac{\partial^2\vec{E}}{\partial z^2} = -k^2\vec{E}, \quad \frac{\partial^2\vec{H}}{\partial z^2} = -k^2\vec{H}. \tag{10.49}$$

Note that the two are compatible with the same wavenumber k, which can be easily verified by applying curl to both sides. We further set

$$\frac{\partial^2\vec{E}}{\partial\theta^2} = -m^2\vec{E}, \quad \frac{\partial^2\vec{H}}{\partial\theta^2} = -m^2\vec{H}, \tag{10.50}$$

where m must be an integer because the fields are periodic in the azimuthal angle θ. Finally letting

$$\nu^2 = k^2 - \omega^2 \mu \epsilon_{\text{eff}}, \tag{10.51}$$

the wave equations for E_z and H_z become

$$\begin{aligned} \frac{1}{r}\frac{\partial}{\partial r}\left(r\frac{\partial E_z}{\partial r}\right) - \left(\frac{m^2}{r^2} + \nu^2\right) E_z &= \frac{1}{\epsilon}\nabla_z \rho - i\omega\mu J_z, \\ \frac{1}{r}\frac{\partial}{\partial r}\left(r\frac{\partial H_z}{\partial r}\right) - \left(\frac{m^2}{r^2} + \nu^2\right) H_z &= -\left[\vec{\nabla}\times\vec{J}\right]_z. \end{aligned} \tag{10.52}$$

The transverse fields are therefore

$$\nu^2 \vec{E}_t = -\vec{\nabla}_t \frac{\partial E_z}{\partial z} - i\omega\mu \vec{\nabla}_t \times \vec{H}_z, \tag{10.53}$$

$$\nu^2 \vec{H}_t = i\omega\epsilon_{\text{eff}} \vec{\nabla}_t \times \vec{E}_z - \vec{\nabla}_t \frac{\partial H_z}{\partial z}. \tag{10.54}$$

For a charged particle traveling with velocity v in the z-direction at an offset $r = a$, the charge density can be expanded as

$$\rho(r,\theta,z;t) = \frac{e}{r}\delta(r-a)\delta(\theta)\delta(z-vt) = \frac{e\delta(r-a)}{2\pi a}\sum_{m=-\infty}^{\infty}\int_{\infty}^{\infty}\frac{d\omega}{2\pi v}e^{-i\omega(t-z/v)}e^{im\theta}. \tag{10.55}$$

Thus the above consists of many longitudinal waves of different frequencies ω and azimuthal harmonics m. If we write

$$\rho(r,\theta,z;t) = \sum_{m=0}^{\infty}\int_{-\infty}^{\infty}\frac{d\omega}{2\pi}\rho_m, \tag{10.56}$$

we can pick out for our study the component corresponding to azimuthal m ($m \geq 0$ only) and frequency ω,

$$\rho_m = \frac{\mathcal{Q}_m}{(1+\delta_{m0})\pi a^{m+1} v}\delta(r-a)\cos m\theta\, e^{-i\omega(t-z/v)}, \tag{10.57}$$

which represents a forward-traveling wave $e^{i(kz-\omega t)}$ with wavenumber $k = \omega/v$. Here, $\mathcal{Q}_m = ea^m$ is the electric mth multipole of the charged particle. Correspondingly, the component of the longitudinal current density can be written as

$$J_m = \rho_m v = \frac{\mathcal{P}_m}{(1+\delta_{m0})\pi a^{m+1} v}\delta(r-a)\cos m\theta\, e^{-i\omega(t-z/v)}, \tag{10.58}$$

where $\mathcal{P}_m = \mathcal{Q}_m v = ea^m v$ is the mth multipole of the current density. Such waves for the charge density and current density will be used as the source to derive the impedances of the mth azimuthal. They represent a hollow cylindrical source with transverse distribution of azimuthal m in the cross-section. There are merits of using such a wave as the particle source. First, the phase velocity of the wave $v_{\rm ph} = \omega/k = v$ is always equal to the particle velocity. The $\vec{E}$ and $\vec{H}$ fields in all the regions will have the same $e^{-i\omega(t-z/v)}$-dependency. Thus, we can avoid going into fast and slow betatron wave velocities.‖ Second, since the wave represents a hollow cylindrical source with the appropriate $\cos m\theta$ azimuthal distribution, we only need to solve the sourceless Maxwell equation in each region and incorporate the source through boundary matching.

Thus if we write

$$E_z = \tilde{E}_z(r)\cos m\theta\, e^{ikz} \quad \text{and} \quad H_z = \tilde{H}_z(r)\sin m\theta\, e^{ikz} \tag{10.59}$$

in each region, both $\tilde{E}_z$ and $\tilde{H}_z$ are linear combination of $I_m(\nu r)$ and $K_m(\nu r)$, where I_m and K_m are modified Bessel functions of order m of the first and second kinds. Then the transverse fields can be written as

$$\begin{cases} E_\theta = \tilde{E}_\theta(r)\sin m\theta\, e^{ikz} & \text{and} \quad E_r = \tilde{E}_r(r)\cos m\theta\, e^{ikz}, \\ H_\theta = \tilde{H}_\theta(r)\cos m\theta\, e^{ikz} & \text{and} \quad H_r = \tilde{H}_r(r)\sin m\theta\, e^{ikz}, \end{cases} \tag{10.60}$$

with $\tilde{E}_\theta$, $\tilde{E}_r$, $\tilde{H}_\theta$, and $\tilde{H}_r$ derivable from

$$\begin{cases} \nu^2\tilde{E}_\theta = ik\dfrac{m}{r}\tilde{E}_z + i\omega\mu\dfrac{\partial\tilde{H}_z}{\partial r}, \\ \nu^2\tilde{E}_r = -ik\dfrac{\partial\tilde{E}_z}{\partial r} - i\omega\mu\dfrac{\tilde{H}_z}{r}, \\ \nu^2\tilde{H}_\theta = -i\omega\epsilon_{\rm eff}\dfrac{\partial\tilde{E}_z}{\partial r} - ik\dfrac{m}{r}\tilde{H}_z, \\ -\nu^2\tilde{H}_r = -i\omega\epsilon_{\rm eff}\dfrac{m}{r}\tilde{E}_z - ik\dfrac{\partial\tilde{H}_z}{\partial r}. \end{cases} \tag{10.61}$$

Thus $\tilde{E}_\theta$, $\tilde{E}_r$, $\tilde{H}_\theta$, and $\tilde{H}_r$ are linear combinations of K'_m, I'_m, K_m/r, and I_m/r.

The waves can therefore be separated into two distinct categories, i.e., transverse magnetic (TM) by specifying E_z and transverse electric (TE) by specifying H_z. For a beam particle traveling longitudinally, there is definitely longitudinal

‖In Ref. [1], Zotter employed a beam of finite cross section oscillating transversely as a source in the derivation of transverse impedance. He needed to separate the relativistic parameters γ_W and β_W corresponding to the wave velocity from γ and β corresponding to the beam velocity. However, the final result reveals that only γ and β (but not γ_W and β_W) appear in the expression for the transverse space-charge impedance [see Eq. (1.54)].

electric field, and the wake excited will therefore be TM. The situation is more complicated in the resistive-wall wake, however, in the azimuthal $m \neq 0$. Because of the nonvanishing E_θ, there will be a conducting current $\sigma_c E_\theta$ in the metallic wall of the beam pipe in the θ-direction. As a result of Ampere's law, there must exist a longitudinal magnetic field H_z. In other words, there must exist TE contribution as well.

One may wonder why we do not solve Eq. (10.44) directly for $\vec{E}_t$ and $\vec{H}_t$. The fact is that, in the cylindrical coordinates,**

$$\nabla^2 \vec{E} = \hat{r}\left[\nabla^2 E_r - \frac{E_r}{r^2} - \frac{2}{r^2}\frac{\partial E_\theta}{\partial \theta}\right] + \hat{\theta}\left[\nabla^2 E_\theta - \frac{E_\theta}{r^2} + \frac{2}{r^2}\frac{\partial E_r}{\partial \theta}\right] + \hat{z}\nabla^2 E_z. \tag{10.62}$$

Along the longitudinal direction, we get one unmixed equation for E_z, which is just Eq. (10.52). In the transverse directions, E_θ and E_r are mixed and the two equations are not easy to use. For this reason, we solve for E_z and H_z and obtain the transverse fields $\vec{E}_t$ and $\vec{H}_t$ through Eqs. (10.53) and (10.54), or Eq. (10.61). This also explains why E_z and H_z are proportional to the modified Bessel functions of order m, but not so for the transverse fields $\vec{E}_t$ and $\vec{H}_t$. The main reason of the mixing in the transverse directions comes from the curvilinear nature of the r and θ coordinates.

10.2.2 *Source Fields*

Without a beam pipe, the fields can be expressed as

$$\tilde{E}_z^{(s)}(r) = \begin{cases} -iC_m \dfrac{K_m(s)}{I_m(s)} I_m(u) & r < a, \\ -iC_m K_m(u) & r > a, \end{cases} \tag{10.63}$$

where $u = \omega r/(v\gamma)$ and $s = \omega a/(v\gamma)$. The constant C_m can be obtained by integrating the wave equation for E_z in Eq. (10.52) across the source from $r = a-$ to $r = a+$ by picking up the charges of the particle beam at $r = a$:

$$\left.\frac{d\tilde{E}_z}{dr}\right|_{a+} - \left.\frac{d\tilde{E}_z}{dr}\right|_{a-} = \frac{ie\omega}{(1+\delta_{m0})\pi a \epsilon_0 v^2 \gamma^2}, \tag{10.64}$$

or

$$C_m = \frac{\mathcal{Q}_m \omega I_m(s)}{(1+\delta_{m0})\pi a^m \epsilon_0 v^2 \gamma^2}, \tag{10.65}$$

**See, for example, P.M. Morse and H. Feshbach, *Methods of Theoretical Physics*, McGraw-Hill, New York, 1953, p.116.

where the Wronskian

$$K_m(s)I'_m(s) - I_m(s)K'_m(s) = \frac{1}{s} \tag{10.66}$$

has been used. The transverse fields in the θ-direction are, according to Eq. (10.61),

$$\tilde{E}_\theta^{(s)}(r) = \gamma C_m \frac{m}{u} K'_m(u), \qquad Z_0 \tilde{H}_\theta^{(s)}(r) = -\beta\gamma C_m K'_m(u). \tag{10.67}$$

In the presence of an enclosure at $r = b$, the fields will be reflected and we need to add solution of the sourceless wave equation. We call this region 1 ($r < b$), covering everything including the source. The fields are now

$$\begin{aligned} \tilde{E}_z^{(1)}(r) &= -iC_m F_m(u), \\ \tilde{E}_\theta^{(1)}(r) &= \gamma C_m \frac{m}{u} F_m(u), \\ Z_0 \tilde{H}_\theta^{(1)}(r) &= -\beta\gamma C_m F'_m(u), \end{aligned} \tag{10.68}$$

where

$$F_m(u) = K_m(u) - \alpha_{\text{TM}} I_m(u), \tag{10.69}$$

and the parameter α_{TM} stands for the portion of reflected wave required to satisfy the boundary condition. If the enclosure is a metallic wall, a current density $J_{m\theta} = \sigma_c \tilde{E}_\theta$ will be induced in the metallic wall in the azimuthal direction. As was stated earlier, there must exist a longitudinal magnetic field $\tilde{H}_z$. As a result, we must write

$$\begin{aligned} \tilde{E}_z^{(1)}(r) &= -iC_m F_m(u), \\ Z_0 \tilde{H}_z^{(1)}(r) &= -iC_m \alpha_{\text{TE}} I_m(u), \\ \tilde{E}_\theta^{(1)}(r) &= \gamma C_m \left[\frac{m}{u} F_m(u) + \beta \alpha_{\text{TE}} I'_m(u) \right], \\ Z_0 \tilde{H}_\theta^{(1)}(r) &= -\beta\gamma C_m \left[F'_m(u) + \alpha_{\text{TE}} \frac{m}{\beta u} I_m(u) \right], \end{aligned} \tag{10.70}$$

where α_{TE} designates the amount of TE contribution. Notice that there is only modified Bessel function of the first king, $I_m(u)$, in $Z_0 \tilde{H}_z^{(1)}(r)$. The modified Bessel function of the second kind, $K_m(u)$, is not allowed because it diverges at $r = 0$.

We learn from Eq. (1.43) in Chapter 1 that the mth-multipole transverse impedance can be expressed in terms of the longitudinal electric field[††]

$$Z_m^{\perp}(\omega) = -\frac{1}{k\beta Q_m^2}\int_0^C E_z^{(1)} J_m^* dV, \tag{10.71}$$

where $dV = rdrd\theta dz$ and the integration covers the volume inside the cylindrical vacuum chamber.

Using the small-argument expansions of the modified Bessel functions for $m \neq 0$,

$$I_m(s) = \frac{1}{m!}\left(\frac{s}{2}\right)^m \quad \text{and} \quad K_m(s) = \frac{(m-1)!}{2}\left(\frac{2}{s}\right)^m, \tag{10.72}$$

it is easy to obtain

$$Z_m^{\perp} = \frac{iZ_0R}{m\beta^2\gamma^2}\left[\frac{1}{a^{2m}} - \frac{\alpha_{\text{TM}}}{2^{2m-1}m!(m-1)!}\left(\frac{k}{\gamma}\right)^{2m}\right], \tag{10.73}$$

where $R = C_0/(2\pi)$ is the mean radius of the accelerator ring. With a perfectly conducting beam pipe of radius b, the vanishing of the longitudinal electric field at $r = b$ requires

$$\alpha_{\text{TM}} = \frac{K_m(x)}{I_m(x)}, \tag{10.74}$$

where $x = \omega b/(v\gamma)$. The coupling impedance will be completely space-charge with

$$Z_m^{\perp}\big|_{\text{SC}} = \frac{iZ_0R}{m\beta^2\gamma^2}\left[\frac{1}{a^{2m}} - \frac{1}{b^{2m}}\right], \tag{10.75}$$

where the first term comes from self-force and the second term comes from image effect in the wall of the beam pipe. The contribution due to wall resistivity is therefore

$$Z_m^{\perp}\big|_{\text{RW}} = \frac{iZ_0R}{m\beta^2\gamma^2}\left[\frac{1}{b^{2m}} - \frac{\alpha_{\text{TM}}}{2^{2m-1}m!(m-1)!}\left(\frac{k}{\gamma}\right)^{2m}\right]. \tag{10.76}$$

[††]Equations (1.43) and (10.71) are identical although they look different. In the former, $E^{\parallel}(r,\theta,z;t)$ and $J_m(r,\theta,z;t)$ are considered the longitudinal electric field and the longitudinal current density. They carry the dimension of electric field and current density, respectively. In the discussion here, $J_m(r,\theta,z;t)$ is considered a Fourier component of the current density in such a way that $\int d\omega J_m(r,\theta,z;t)$ gives the current density. Thus J_m carries the dimension of current density multiplied by time. Similarly, $E_z^{(1)}(r,\theta,z;t)$ is also a Fourier component and carries the dimension of electric field multiplied by time.

It is convenient to introduce the parameters

$$\alpha_1 = \alpha_{\text{TM}} \frac{I_m(x)}{K_m(x)} \approx \frac{\alpha_{\text{TM}} x^{2m}}{2^{2m-1} m!(m-1)!} \tag{10.77}$$

and $\bar{\alpha}_1 = 1 - \alpha_1$. Then

$$Z_m^{\perp}\big|_{\text{RW}} = \frac{iZ_0 R}{mb^{2m}} \frac{\bar{\alpha}_1}{\beta^2\gamma^2}. \tag{10.78}$$

As $\gamma \to \infty$, although the space-charge impedance goes to zero, however, the resistive-wall impedance remains finite, because $\bar{\alpha}_1 \propto \gamma^2$, as will be demonstrated below. Thus, the determination of the transverse resistive-wall impedance reduces to the derivation of the field-matching parameter $\bar{\alpha}_1$.

In the presence of many concentric regions of layers, for region p, where $a_p < r < b_p$, the fields can be written as

$$\begin{aligned}
\tilde{E}_z^{(p)}(r) &= E_p \left[\frac{K_m(u)}{K_m(x_p)} - \alpha_p \frac{I_m(u)}{I_m(x_p)} \right], \\
Z_0 \tilde{H}_z^{(p)}(r) &= G_p \left[\frac{K_m(u)}{K_m(x_p)} - \eta_p \frac{I_m(u)}{I_m(x_p)} \right], \\
\tilde{E}_\theta^{(p)}(r) &= \frac{ik}{\nu_p} \left[\frac{m\tilde{E}_z^{(p)}(r)}{u} + \beta\mu_p' \frac{dZ_0\tilde{H}_z^{(p)}(r)}{du} \right], \\
Z_0 \tilde{H}_\theta^{(p)}(r) &= -\frac{ik}{\nu_p} \left[\frac{mZ_0\tilde{H}_z^{(p)}(r)}{u} + \beta\epsilon_p' \frac{d\tilde{E}_z^{(p)}(r)}{du} \right],
\end{aligned} \tag{10.79}$$

where $u = \nu_p r$, $x_p = \nu_p b_p$, ν_p is given by Eq. (10.51), $\mu_p' = \mu_p/\mu_0$, and $\epsilon_p' = \epsilon_p/\epsilon_0$. Region 1 that includes the source is slightly different and is given by Eq. (10.70). We see that for each additional region, there are four parameters E_p, G_p, α_p, and η_p, to be determined by four new field matching conditions. Thus, the mathematics can become very messy when several regions are present. We are going to study here two special situations that can have the transverse impedances presented in rather simple expressions.

10.2.3 *Thin-Wall Model*

When the thickness t of metallic wall is much less than the skin depth δ_c, we may make the approximation that the electric field does not vary across the wall. However, the magnetic field is changed across the wall because of the conduction currents generated inside the wall.

The thin wall is described by $b < r < d = b + t$, and we designate the region outside this thin wall by region 2. Here we consider three cases: the outer region extends to (1) a perfectly conductor at $r = g$ (case PC), (2) a perfect magnet $r = g$ (case PM), and (3) to infinity (case INF). For case PC, denoting $y = kg/\gamma$, the coefficients in region 2 are

$$\alpha_2^{\text{PC}} = \frac{K_m(y)I_m(x)}{K_m(x)I_m(y)} \approx \left(\frac{b}{g}\right)^{2m}, \quad \text{and} \quad \eta_2^{\text{PC}} = \frac{K'_m(y)I_m(x)}{K_m(x)I'_m(y)} \approx -\left(\frac{b}{g}\right)^{2m}, \tag{10.80}$$

where the small-argument approximation of the Bessel functions has been used. This approximation is justified because we will take the limit $\gamma \to \infty$ eventually. For case PM, $\alpha_2^{\text{PM}} = \eta_2^{\text{PC}}$ and $\eta_2^{\text{PM}} = \alpha_2^{\text{PC}}$. For case INF, $\alpha_2^{\text{INF}} = \eta_2^{\text{INF}} = 0$ because $I_m(x)$ diverges as $x \to \infty$. Thus we have $\alpha_2 = -\eta_2$ for all the three cases, and the fields in region 2 at $r = b$ can then be written as

$$\begin{aligned}
\tilde{E}_z^{(2)}(b) &= E_2(1 - \alpha_2), \\
Z_0\tilde{H}_z^{(2)}(b) &= G_2(1 + \alpha_2), \\
\tilde{E}_\theta^{(2)}(b) &= -\frac{im\gamma}{x}(1 - \alpha_2)\big(E_2 - \beta G_2\big), \\
Z_0\tilde{H}_\theta^{(2)}(b) &= -\frac{im\gamma}{x}(1 + \alpha_2)\big(G_2 - \beta E_2\big).
\end{aligned} \tag{10.81}$$

The boundary conditions at the thin wall are

$$\begin{aligned}
\tilde{E}_z^{(2)}(d) &= \tilde{E}_z^{(1)}(b), \\
\tilde{E}_\theta^{(2)}(d) &= \tilde{E}_\theta^{(1)}(b), \\
Z_0\tilde{H}_z^{(2)}(d) &= Z_0\tilde{H}_z^{(2)}(b) - \zeta\tilde{E}_\theta^{(1)}(b), \\
Z_0\tilde{H}_\theta^{(2)}(d) &= Z_0\tilde{H}_\theta^{(2)}(b) + \zeta\tilde{E}_z^{(1)}(b),
\end{aligned} \tag{10.82}$$

where $\zeta = Z_0\sigma_c t$. With $E_1 = -iC_m K_m(x)$, this translates into four equations:

$$\begin{aligned}
(1 - \alpha_2)\frac{E_2}{E_1} &= \bar{\alpha}_1, \\
(1 - \alpha_2)\left(\frac{E_2}{E_1} - \beta\frac{G_2}{E_1}\right) &= \bar{\alpha}_1 + \beta\eta_1, \\
(1 + \alpha_2)\frac{G_2}{E_1} &= \eta_1 - \frac{im\gamma\zeta}{x}(\bar{\alpha}_1 + \beta\eta), \\
(1 + \alpha_2)\left(\frac{G_2}{E_1} - \beta\frac{E_2}{E_1}\right) &= (\eta_1 + \beta\bar{\alpha}_1 - 2\beta) + \frac{ix\zeta}{m\gamma}\bar{\alpha}_1,
\end{aligned} \tag{10.83}$$

from which the four unknowns $\bar{\alpha}_1$, η_1, E_2, and G_2 are to be determined. The second equation can be simplified to $(1-\alpha_2)G_2/E_1 = -\eta_1$ with the aid of the first. Thus, E_2 and G_2 can be eliminated in the third and fourth equations. Finally, by eliminating η_1, we obtain

$$\bar{\alpha}_1 = -\frac{\gamma^2\beta^2(1-\alpha_2) + 2ix\gamma\beta/(m\zeta)}{1 + \frac{x^2}{m^2} - \frac{ix\gamma\beta}{m}\left[\frac{2}{\zeta(1-\alpha_2)} + \frac{\zeta(1-\alpha_2)}{2}\right]}. \tag{10.84}$$

Since $x = kb/\gamma$, $\bar{\alpha}_1 \sim \gamma^2\beta^2$ as $\gamma \to \infty$, thus canceling the factor of $\gamma^2\beta^2$ in the denominator of Eq. (10.78) when the resistive-wall impedance is evaluated. Finally, the transverse resistive-wall impedance in the mth multipole can be expressed as

$$Z_m^{\perp}\big|_{\text{RW}} = -\frac{iZ_0R}{mb^{2m}} \frac{1-\alpha_2}{1 - \frac{ik\beta}{m}\left[\frac{2}{\zeta(1-\alpha_2)} + \frac{\zeta(1-\alpha_2)}{2}\right]}. \tag{10.85}$$

As frequency goes to zero, this impedance becomes inductive,

$$Z_m^{\perp}\big|_{\text{RW}} = -\frac{iZ_0R}{mb^{2m}}(1-\alpha_2), \tag{10.86}$$

which agrees with the bypass inductive impedance derived by Vos in Eq. (10.37) when $m = 1$ and $\alpha_2 = 0$ or for case INF. As mentioned before, the bypass inductance depends on the geometry of the vacuum chamber. This explains the extra factor of $1-\alpha_2$ in the presence of an exterior enclosing perfect conductor (case PC) or perfect magnet (case PM).

Let us consider the dipole impedance in case INF and take the Fermilab Tevatron as an example. The Tevatron has a mean radius of $R = 1$ km. We approximate the beam pipe as cylindrical with radius $b = 3$ cm and thickness $t = 1.5$ mm. The beam pipe is made of stainless steel with conductivity $\sigma_c = 1.35 \times 10^6$ $(\Omega\text{-m})^{-1}$. This gives $\zeta = Z_0\sigma_c t = 7.63 \times 10^5 \gg 1$. Thus the term $2/[\zeta(1-\alpha_2)]$ inside the square brackets in the denominator of Eq. (10.85) can be neglected. This is true in general for all the three cases PC, PM, and INF.[‡‡] Since the Tevatron stores proton and antiprotons from 150 GeV to 1 TeV, we can safely set $\beta = 1$. The frequency at which the skin-depth δ_c fills up the wall thickness was found to be $f_c = 83.4$ Hz in Eq. (10.5), or $kb = 5.24 \times 10^{-5}$, where we have let $\mu' = 1$. On the other hand, the revolution frequency is $f_0 = c/(2\pi R) = 47.7$ kHz. Thus the $(1-Q)$ line that drives transverse coupled-bunch instability is at frequency 19.1 kHz (betatron tune 19.6), and the resistive-

[‡‡]The only possibility that this term cannot be neglected is in case PC when the spacing between the inner and outer pipes is extremely small so that $1-\alpha_2$ is extremely small. This happens only when $(g-d)/g \lesssim 1/(m\zeta) \sim 10^{-6}$ for $m = 1$.

wall impedance is well-described by this thin-wall model. From Eq. (10.85), one obtains readily

$$\mathcal{R}e\, Z_1^{\perp}\big|_{\rm RW} = \frac{Z_0 R}{b^2}\frac{kb\zeta/2}{1+(kb\zeta/2)^2}, \tag{10.87}$$

showing that the real part of the transverse resistive-wall impedance increases linearly with frequency from zero at low frequencies. It goes through a maximum when $kb\zeta/2 = 1$ or at frequency 4.17 kHz. At this moment

$$1 = \frac{kb\zeta}{2} = \frac{kbZ_0\sigma_c t}{2} = \frac{bt}{\delta_c^2}. \tag{10.88}$$

After the maximum with $kb\zeta/2 \gg 1$,

$$\mathcal{R}e\, Z_1^{\perp}\big|_{\rm RW} \approx \frac{Z_0 R}{b^2}\frac{2}{kb\zeta}, \tag{10.89}$$

which can be written in the form of the Panofsky–Wenzel-like relation

$$\mathcal{R}e\, Z_1^{\perp}\big|_{\rm RW} \approx \frac{2c}{b^2}\frac{\mathcal{R}e\, Z_0^{\parallel}\big|_{\rm RW}}{\omega}, \tag{10.90}$$

with longitudinal monopole impedance

$$\mathcal{R}e\, Z_0^{\parallel}\Big|_{\rm RW} = \frac{R}{b\sigma_c t}, \tag{10.91}$$

or with all the image current flowing uniformly inside the wall of the beam pipe like a dc current. This is the so-called Sacherer's region, where the transverse impedance decreases as $1/k$. We also notice that there will not be any region that $\mathcal{R}e\, Z_1^{\perp}\big|_{\rm RW}$ rolls off as $1/\sqrt{k}$ no matter how high the frequency is. The reason comes from the assumption of the thin-wall model that the longitudinal electric field does not change across the thin-wall implying that the image current density must be uniform inside the wall. This assumption therefore excludes the possibility of having the image current flowing merely in the inner skin of the pipe wall. In other words, this model has to fail at higher frequencies when the wall thickness exceeds the skin-depth.

The imaginary part of the transverse resistive-wall impedance behaves as, according to Eq. (10.85),

$$\mathcal{I}m\, Z_1^{\perp}\big|_{\rm RW} = \frac{Z_0 R}{b^2}\frac{1}{1+(kb\zeta/2)^2}. \tag{10.92}$$

Thus at higher frequencies, the imaginary part falls off from the bypass inductive value as $1/k^2$, which also deviates from the usual $1/\sqrt{k}$-behavior when the wall

thickness is much larger than the skin-depth. The resistive and inductive parts of the dipole transverse resistive-wall impedance are depicted in Fig. 10.7. For the Tevatron, this thin-wall model is applicable up to $f \sim 83$ kHz or $kb \sim 5.2 \times 10^{-5}$.

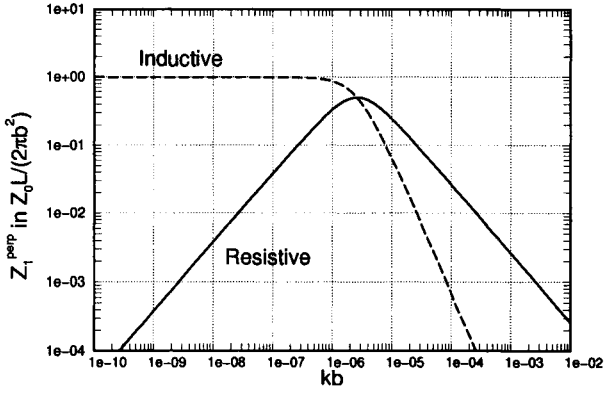


Fig. 10.7 Resistive and inductive parts of the dipole transverse impedance $Z_1^{\perp}|_{\mathrm{RW}}$ in the thin-wall model with nothing outside. For the Tevatron, the model is applicable up to $kb \sim 5.2 \times 10^{-5}$ ($f \sim 83$ kHz). The revolution frequency of 47.7 kHz corresponds to $kb = 4.0 \times 10^{-5}$, indicating that the $(1-Q)$ betatron line that drives transverse coupled-bunch instability is well-described by the $1/k$-behavior of $\mathcal{R}e\, Z_1^{\perp}|_{\mathrm{RW}}$.

10.2.4 *Thick-Wall Model*

When the wall thickness is larger than the skin-depth, the variation of the electromagnetic fields inside the metallic wall must be correctly considered. Let the wall of the beam pipe be described by $b < r < d$ and we call this region 2. The transverse propagation constant ν_2 is given by

$$\nu_2 = k^2 - \omega^2 \mu \epsilon_{\mathrm{eff}}, \tag{10.93}$$

with $\epsilon_{\mathrm{eff}} = \epsilon_0 + i\sigma_c/\omega \approx i\sigma_c/\omega$. This approximation amounts to ignoring the displacement current and is valid for frequency

$$\omega \ll \sigma_c Z_0 c, \tag{10.94}$$

or $\omega/(2\pi) \ll 2.4 \times 10^{16}$ Hz when $\sigma_c = 1.35 \times 10^6$ $(\Omega\text{-m})^{-1}$ for stainless steel is substituted. We can also neglect k^2 in Eq. (10.93) since

$$\frac{k^2}{\omega \mu \sigma_c} = \frac{\omega}{Z_0 \sigma_c c \mu' \beta^2} \ll \frac{1}{\mu' \beta^2}, \tag{10.95}$$

where the condition of displacement-current omission, Eq. (10.94), has been used. We therefore have, for the transverse wavenumber inside the metallic medium,

$$\nu_2 = \frac{1-i}{\delta_c}. \tag{10.96}$$

Inside the metallic wall (or region 2), the fields can be represented by

$$\begin{aligned}
\tilde{E}_z^{(2)}(r) &= E_2\left[\frac{K_m(u)}{K_m(x_2)} - \alpha_2\frac{I_m(u)}{I_m(x_2)}\right],\\
Z_0\tilde{H}_z^{(2)}(r) &= G_2\left[\frac{K_m(u)}{K_m(x_2)} - \eta_2\frac{I_m(u)}{I_m(x_2)}\right],\\
\tilde{E}_\theta^{(2)}(r) &= \frac{ik}{\nu_2}\left[\frac{m\tilde{E}_z^{(2)}(r)}{u} + \beta\mu'\frac{dZ_0\tilde{H}_z^{(2)}(r)}{du}\right],\\
Z_0\tilde{H}_\theta^{(2)}(r) &= -\frac{ik}{\nu_2}\left[\frac{mZ_0\tilde{H}_z^{(2)}(r)}{u} + \beta\epsilon'\frac{d\tilde{E}_z^{(2)}(r)}{du}\right],
\end{aligned} \tag{10.97}$$

where $u = \nu_2 r$ and $x_2 = \nu_2 b$. Again we consider three cases for the boundary at $r = d$, the outside surface of the pipe wall: case PC, perfect conductor at $r = d$, case PM, perfect magnet at $r = d$, and case INF when $d \to \infty$ or the metallic wall is infinitely thick. For the three cases, boundary conditions require

$$\alpha_2 = \begin{cases} \dfrac{K_m(y)I_m(x_2)}{I_m(y)K_m(x_2)}, \\ \dfrac{K'_m(y)I_m(x_2)}{I'_m(y)K_m(x_2)}, \\ 0, \end{cases} \qquad \eta_2 = \begin{cases} \dfrac{K'_m(y)I_m(x_2)}{I'_m(y)K_m(x_2)}, & \text{PC}, \\ \dfrac{K_m(y)I_m(x_2)}{I_m(y)K_m(x_2)}, & \text{PM}, \\ 0, & \text{INF}, \end{cases} \tag{10.98}$$

where $y = \nu_2 d = (1-i)d/\delta_c$. Since $|x_2|$ and $|y|$ can be large or small, there is no simply relation between α_2^{PC} and η_2^{PC} as well as between α_2^{PM} and η_2^{PM}. They are therefore treated as unrelated in the discussion below. For the sake of convenience, let us define

$$Q_2 = \frac{K'_m(x_2)}{K_m(x_2)} \quad \text{and} \quad P_2 = \frac{I'_m(x_2)}{I_m(x_2)}. \tag{10.99}$$

The fields in region 2 at $r = b$ now become

$$\begin{aligned}
\tilde{E}_z^{(2)}(b) &= E_2(1-\alpha_2),\\
Z_0\tilde{H}_z^{(2)}(b) &= G_2(1-\eta_2),\\
\tilde{E}_\theta^{(2)}(b) &= -\frac{mp}{q}E_2(1-\alpha_2) - (1-i)\frac{r}{2}G_2(Q_2 - \eta_2 P_2),\\
Z_0\tilde{H}_\theta^{(2)}(b) &= \frac{mp}{q}G_2(1-\eta_2) + \frac{1+i}{r}E_2(Q_2 - \alpha_2 P_2),
\end{aligned} \tag{10.100}$$

where the short-hand notations

$$p = \frac{k^2\delta_c^2}{2}, \qquad q = kb, \quad \text{and} \quad r = \mu'\beta k\delta_c \tag{10.101}$$

have been used. When $\tilde{E}_z$ and $\tilde{H}_z$ in regions 1 and 2 are matched at their common boundary at $r = b$, we obtain

$$E_2(1-\alpha_2) = E_1\bar{\alpha}_1 \quad \text{and} \quad G_2(1-\eta_2) = E_1\eta_1. \tag{10.102}$$

Thus E_2 and G_2 can be eliminated and the expressions for $\tilde{E}_\theta^{(2)}(x_2)$ and $\tilde{H}_\theta^{(2)}(x_2)$ can be rewritten as

$$\begin{aligned} \tilde{E}_\theta^{(2)}(b) &= \frac{E_1}{q}\left[-mp\bar{\alpha}_1 - \frac{(1-i)r}{2}\eta_1 Q_\eta\right], \\ Z_0\tilde{H}_\theta^{(2)}(b) &= \frac{E_1}{q}\left[mp\bar{\eta}_1 + \frac{1+i}{r}\bar{\alpha}_1 Q_\alpha\right], \end{aligned} \tag{10.103}$$

where

$$Q_\eta = q\frac{Q_2 - \alpha_2 P_2}{1-\alpha_2} \quad \text{and} \quad Q_\alpha = q\frac{Q_2 - \eta_2 P_2}{1-\eta_2}. \tag{10.104}$$

Finally matching $\tilde{E}_\theta$ and $\tilde{H}_\theta$, we obtain two equations in two unknowns:

$$\begin{bmatrix} \gamma^2 - ip & \beta\gamma^2 - \dfrac{(1+i)rQ_\eta}{2m} \\ \beta\gamma^2 + \dfrac{(1-i)Q_\alpha}{mr} & \gamma^2 - ip \end{bmatrix} \begin{bmatrix} \bar{\alpha}_1 \\ \eta_1 \end{bmatrix} = \begin{bmatrix} 0 \\ 2\beta\gamma^2 \end{bmatrix}. \tag{10.105}$$

The solution can be written down readily as

$$\bar{\alpha}_1 = \frac{-2\beta^2\gamma^2\left[1 - \dfrac{(1+i)rQ_\eta}{2m\beta\gamma^2}\right]}{1 - 2ip - \beta\left[\dfrac{(1-i)Q_\alpha}{mr} - \dfrac{(1+i)rQ_\eta}{2m}\right] + \dfrac{Q_\alpha Q_\eta - m^2p^2}{m^2\gamma^2}}. \tag{10.106}$$

Thus the transverse resistive-wall impedance seen by an ultra-relativistic particle results after taking the limit $\gamma \to \infty$,

$$Z_m^\perp\big|_{\text{RW}} = -\frac{i2Z_0R}{mb^{2m}}\frac{1}{1 - 2ip - \beta\left[\dfrac{(1-i)Q_\alpha}{mr} - \dfrac{(1+i)rQ_\eta}{2m}\right]}. \tag{10.107}$$

The first application is in the frequency range

$$\frac{1}{Z_0\sigma_c b\mu'\beta} \ll kb \ll \frac{Z_0\sigma_c b}{\beta}. \tag{10.108}$$

The lower limit is for $|x_2| = \sqrt{2}b/\delta_c \gg 1$ and the upper limit is due to the omission of displacement current. For a stainless-steel beam pipe of radius $b = 3$ cm, this amounts to $6.6\times10^{-8} \ll kb \ll 1.5\times10^{7}$ or 100 Hz $\ll f \ll 2.4\times10^{16}$ Hz, where we have set $\beta = 1$ and $\mu' = 1$. The large-argument expansion of the Bessel functions can be used, giving

$$Q_2 = \frac{K'_m(x_2)}{K_m(x_2)} \approx -1 \quad \text{and} \quad P_2 = \frac{I'_m(x_2)}{I_m(x_2)} \approx 1. \tag{10.109}$$

Now the denominator of the second factor in $Z_m^{\perp}\big|_{\text{RW}}$ becomes

$$\text{denom} = 1 - 2ik^2\delta_c^2 + \frac{(1-i)b}{m\delta_c\mu'}\frac{1+\alpha_2}{1-\alpha_2} - \frac{(1+i)k^2b\delta_c\mu'\beta^2}{2m}\frac{1+\eta_2}{1-\eta_2}. \tag{10.110}$$

Notice that

$$k^2\delta_c^2 = \frac{2kb}{Z_0\sigma_c b\mu'\beta} \ll \frac{2}{\mu'\beta^2}, \tag{10.111}$$

where the second inequality of Eq. (10.108) has been used. Ignoring the exterior-boundary-matching coefficients α_2 and η_2, the second term on the right side of Eq. (10.110), of $\mathcal{O}(k^2\delta_c^2)$, is much less than the fourth term, of $\mathcal{O}(k\delta_c b)$, which is in turn much less than the third term, of $\mathcal{O}(b/\delta_c)$. Since $|x_2| = \sqrt{2}/\delta_c \gg 1$, this third term dominates the denominator.

From the large-argument expansions of the Bessel functions, the exterior-boundary-matching coefficients are

$$\alpha_2 = \begin{cases} +e^{-(1-i)2t/\delta_c}, \\ -e^{-(1-i)2t/\delta_c}, \\ 0, \end{cases} \qquad \eta_2 = \begin{cases} -e^{-(1-i)2t/\delta_c}, & \text{PC}, \\ +e^{-(1-i)2t/\delta_c}, & \text{PM}, \\ 0, & \text{INF}, \end{cases} \tag{10.112}$$

where $t = d - b$ is the wall thickness. Under the morale of the thick-wall model that $t \gg \delta_c$, these coefficients have magnitudes much smaller than unity even for cases PC and PM. Thus the above argument remains valid.

The transverse resistive-wall impedance therefore becomes

$$Z_m^{\perp}\big|_{\text{RW}} = (1-i)\frac{Z_0 R\delta_c\mu'}{b^{2m+1}}\frac{1-\alpha_2}{1+\alpha_2}. \tag{10.113}$$

For the dipole mode ($m = 1$), this can be written in the more familiar form via the Panofsky–Wenzel-like relation

$$Z_1^{\perp}\big|_{\text{RW}} = \frac{2c}{b^2}\frac{Z_0^{\parallel}\big|_{\text{RW}}}{\omega}. \tag{10.114}$$

The longitudinal monopole impedance is

$$Z_0^{\parallel}\big|_{\rm RW} = (1-i)\frac{R}{b\delta_c\sigma_c}\frac{1-\alpha_2}{1+\alpha_2}, \tag{10.115}$$

indicating that, when $\alpha_2 = 0$, the real part is just the resistive impedance when the image current flows along the wall of the beam pipe up to one skin-depth. The conclusion is that the transverse resistive-wall impedance rolls off as $\omega^{-1/2}$. For case INF, this behavior remains true for the whole frequency range depicted in Eq. (10.108).

Now let us study case INF in detail. Since the wall of the beam pipe is infinitely thick, there are no field reflections and therefore $\alpha_2 = \eta_2 = 0$. Thus

$$Q_\eta = Q_\alpha = qQ_2 = kb\frac{K_m'(x_2)}{K_m(x_2)}. \tag{10.116}$$

Since $r = k\delta_c\mu'\beta \ll 1$, the Q_α-term always dominates over the Q_η-term. We can therefore write

$$Z_m^{\perp}\big|_{\rm RW} = -\frac{iZ_0R}{mb^{2m}}\frac{2}{1-\dfrac{x_2K_m'(x_2)}{m\mu'K_m(x_2)}}, \tag{10.117}$$

which is a valid solution for case INF at any frequency up to the frequency at which displacement current becomes important. The expression of the transverse impedance in Eq. (10.113) arises just from the large-argument expansions of $K_m(x_2)$ and $K_m'(x_2)$. For the low-frequency behavior, small-argument expansions are required. These expansions, however, have to be performed carefully up to the second-order terms,†

$$-\frac{x_2K_m'(x_2)}{mK_m(x_2)} = 1 + \frac{(-1)^{m+1}2}{m!(m-1)!}\left(\frac{x_2}{2}\right)^{2m}\left(1-\frac{1}{m}-2\gamma_e-2\ln\frac{x_2}{2}\right)+\cdots, \tag{10.118}$$

where $\gamma_e = 0.5772157$ is Euler's number. The necessity to include the second-order terms is obvious, because the first-order term alone does not provide any frequency dependency. Thus the transverse wall-resistive impedance for an infinitely thick beam pipe can be written as, at low frequencies,

$$Z_m^{\perp}\big|_{\rm RW} = -\frac{iZ_0R}{mb^{2m}}\frac{1}{\dfrac{1}{2}\left(1+\dfrac{1}{\mu'}\right)+\dfrac{(-1)^{m+1}}{m!(m-1)!\mu'}\left(\dfrac{x_2}{2}\right)^{2m}\left(1-\dfrac{1}{m}-2\gamma_e-2\ln\dfrac{x_2}{2}\right)}, \tag{10.119}$$

†These second-order terms which include the logarithmic term are not required for the thin-wall model, because the argument over there is $x = kb/\gamma$. Since $x\ln x \to 0$ as $\gamma \to \infty$, this term is not important. On the other hand, here $x_2 = (1-i)b/\delta_c$ is finite as $\gamma \to \infty$.

and becomes, for $m = 1$,

$$Z_1^{\perp}\big|_{\rm RW} = -\frac{iZ_0R}{b^2}\frac{1}{\frac{1}{2}\left(1+\frac{1}{\mu'}\right)+\frac{ikb^2Z_0\beta\sigma_c}{2}\left(\ln\frac{b}{2\delta_c}+\gamma_e-\frac{i\pi}{4}\right)}. \tag{10.120}$$

Thus, at low frequencies,

$$\mathcal{I}m\, Z_1^{\perp}\big|_{\rm RW} = -\frac{Z_0R}{b^2}\frac{2\mu'}{1+\mu'}, \tag{10.121}$$

and the real part increases from zero as $kb\ln(kb)$. The bypass inductive impedance agrees with that derived by Vos only when $\mu' = 1$. Since the bypass inductance is a mutual inductance between the beam and the wall of the beam pipe, its dependence on the permeability of the metallic wall is understandable. In any case, the extra magnetic-property dependent multiplicative factor for the bypass inductance varies between 1 and 2.

The $kb\ln(kb)$-behavior of the resistive part differs from the usual linear kb-behavior because we are not dealing with the situation when the skin-depth is much larger than the wall thickness. The dipole transverse wall-resistive impedance for an infinitely thick stainless-steel wall is plotted in Fig. 10.8. It is worth mentioning that there is no Sacherer's region with $1/\omega$-behavior in case INF ($\alpha_2 = 0$ and $\eta_2 = 0$), because the skin-depth can never fill up the infinitely thick wall of the beam pipe.

We stated before that the expression for $Z_m^{\perp}\big|_{\rm RW}$ in Eq. (10.113) may be incorrect for cases PC and PM, even at high frequency so that $|x_2| \gg 1$ is satisfied. The violation comes from the thickness of the wall t, which is a parameter of the model in cases PC and PM. This is because even if the frequency is high, as a model, the wall of the beam pipe can be so thin that the wall thickness t is

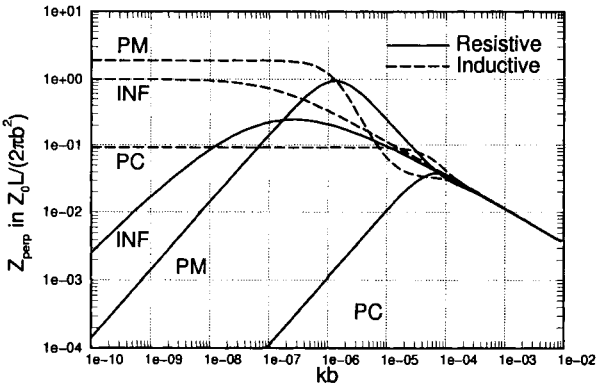


Fig. 10.8 Resistive and inductive parts of the dipole transverse impedance $Z_1^{\perp}|_{\rm RW}$ in the thick-wall model with infinite wall thickness (INF), termination by perfect conductor (PC), or termination by perfect magnet (PM). The beam pipe is of stainless steel of thickness $t = 1.5$ mm, with conductivity $\sigma_c = 1.35 \times 10^6\ (\Omega\text{-m})^{-1}$ and relative permeability $\mu' = 1$.

much less than the skin-depth δ_c.

For case PM, the boundary-field-matching coefficients in Eq. (10.112) can be approximated by

$$\alpha_2 = -\eta_2 \approx -\left[1 - 2(1-i)\frac{t}{\delta_c}\right]. \tag{10.122}$$

The denominator of the impedance, Eq. (10.110), becomes

$$\text{denom} = 1 - i2ik^2\delta_c^2 - i\frac{2bt}{m\mu'\delta_c^2} - i\frac{k^2 b\delta_c^2\mu'\beta^2}{2mt}. \tag{10.123}$$

Again, the second term, $-i2ik^2\delta_c^2$ can be neglected. The fourth term can also be neglected because it is smaller than the third term by the factor μ'^2/ζ, where $\zeta = Z_0\sigma_c t$ and is equal to 7.63×10^5 for the Tevatron. The transverse impedance then becomes

$$Z_m^{\perp}\big|_{\text{RW}} = -\frac{iR}{mb^{2m}}\frac{1}{1 - ikb\zeta/(m\mu')}. \tag{10.124}$$

This implies that after going through a maximum at $kb = m\mu'/\zeta$, $\mathcal{R}e\, Z_1^{\perp}\big|_{\text{RW}}$ rolls off as $1/\omega$. As the frequency increases to $kb = 2b/(\zeta t)$ when the skin-depth is equal to the wall thickness, the roll-off changes to $1/\sqrt{\omega}$. Since it is usually true that $b \gg t$, this Sacherer's region of $1/\omega$-behavior always exists for any beam pipe. For the example of the Tevatron, $t \sim \delta_c$ occurs when $f \sim 83$ kHz or $kb \sim 5.2 \times 10^{-5}$. As is depicted in Fig. 10.8, $\mathcal{R}e\, Z_m^{\perp}\big|_{\text{RW}}$ assumes its maximum at ~ 2.0 kHz or $kb \sim 1.3 \times 10^{-6}$ and we do see that the real part of the impedance decreases as $1/\omega$ after the maximum, and when the frequency is higher than $f \sim 83$ kHz or $kb \sim 5.2 \times 10^{-5}$, the decrease changes to the $1/\sqrt{\omega}$-behavior.

At very low frequencies so that $|x_2| \ll 1$, the small-argument expansions of the Bessel functions are required. The derivation follows identically as case INF but with the factor $(1 + \alpha_2)/(1 - \alpha_2)$ suitably inserted. Thus Eq. (10.120) becomes

$$Z_1^{\perp}\big|_{\text{RW}} = -\frac{iZ_0R}{b^2}\frac{1}{\frac{1}{2}\left(1 + \frac{1}{\mu'}\frac{1+\alpha_2}{1-\alpha_2}\right) + \frac{ikb^2Z_0\beta\sigma_c}{2}\frac{1+\alpha_2}{1-\alpha_2}\ln\frac{b}{2\delta_c}}. \tag{10.125}$$

We have also omitted the terms $\gamma_e - i\pi/4$ which contribute negligibly as compared with the logarithmic. For case PM, $\alpha_2 = -b^2/d^2$ in the dipole mode ($m = 1$). Thus when $t \ll b$,

$$\frac{1+\alpha_2}{1-\alpha_2} \approx \frac{t}{b}. \tag{10.126}$$

As a result, the bypass inductive impedance at zero frequency is

$$Z_1^{\perp}\big|_{\rm RW} \approx -\frac{i2Z_0R}{b^2}, \tag{10.127}$$

as depicted in Fig. 10.8. This is almost twice the amount derived by Vos, probably due to the strong magnetic reflection at the outer surface of the beam pipe. The real part of the transverse impedance increases from zero as $kb\ln(kb)$, in just the same way as case INF. The increase is slower, however, because of the $(1+\alpha_2)/(1-\alpha_2)$ factor.

Case PM requires the longitudinal magnetic field to vanish at the outer surface of the beam pipe, while the longitudinal and azimuthal components of the electric field remain finite. The situation resembles closely that of the thin-wall model. In fact, the impedance depicted in Fig. 10.8 agrees rather well with that in Fig. 10.7 up to the frequency when $t \approx \delta_c$.

We next turn to case PC, where the exterior of the pipe wall meets with a perfect conductor. Let us first study the regime of $|x^2| \gg 1$ but when the frequency is low enough so that the wall thickness $t = d - b$ will be much less than the skin-depth. From Eq. (10.112), the boundary-field-matching coefficients can be approximated by

$$\alpha_2 = -\eta_2 \approx 1 - 2(1-i)\frac{t}{\delta_c}. \tag{10.128}$$

The denominator of Eq. (10.110) now becomes

$$\text{denom} = 1 - i2ik^2\delta_c^2 + \frac{b}{m\mu' t} - \frac{k^2 bt\mu'\beta^2}{m}. \tag{10.129}$$

The first and last terms can be neglected as compared with the third. Thus at low frequencies, the transverse impedance behaves as

$$Z_m^{\perp}\big|_{\rm RW} = -i\frac{2Z_0Rt\mu'}{b^{2m+1}}\frac{1}{1 - i2k^2\delta_c^2 t\mu'/b}. \tag{10.130}$$

The term $-i2k^2\delta_c^2 t\mu'/b$ is small compared to unity and we keep it only because it is the term that contributes to the resistive part of the impedance. The implication is that the inductive part of the impedance reaches its constant bypass value at a much higher frequency than in the other two cases. Because of the extra factor of t/b, this bypass inductive impedance,

$$Z_m^{\perp}\big|_{\rm RW} = -i\frac{2Z_0Rt\mu'}{b^{2m+1}}, \tag{10.131}$$

is much smaller than those in the other two cases. This also implies that the resistive part of the impedance bends around at a much higher frequency.

One may have reservation about the bypass inductive impedance in case PC derived above, because so far the large-argument expansions of the Bessel functions have been employed. For verification, let use go to the regime of very low frequencies so that $|x_2| \ll 1$ and the small-argument expansions of the Bessel functions have to be used. The result is exactly Eq. (10.125), but with $\alpha_2 = b^2/d^2$ or

$$\frac{1+\alpha_2}{1-\alpha_2} \approx \frac{b}{t}, \tag{10.132}$$

when $t \ll b$. Now the $(1+\alpha_2)/(1-\alpha_2)$-term dominates, resulting in the same bypass inductive impedance at zero frequency in Eq.(10.131).

The dipole transverse impedance for case PC in the thick-wall model is depicted in Fig. 10.8. As expected, the bypass inductive impedance is much smaller than for the other two cases because it is directly proportional to the wall thickness t, and so is the maximum incurred in the resistive part of the impedance. The approach to inductive bypass of the inductive part and the bend-around of the resistive part of the transverse impedance take place at a much higher frequency than in the other two cases. We notice that the resistive part of the impedance starts to bend around near the frequency when skin-depth approaches the wall thickness ($\delta_c \sim t$) and there is no Sacherer's region of $1/\omega$-behavior.

Case PC requires the longitudinal electric field to be zero at the outer surface of the wall of the beam pipe. Therefore dipole image current inside the wall of the beam pipe has to be excluded accordingly at low frequencies when the wall is thin enough. This explains why the inductive bypass goes to zero when the wall thickness goes to zero.

10.2.5 *Layered Wall*

For storage rings that exhibit very fast transverse coupled-bunch instabilities, the inner wall of the beam pipe is often coated with a thin layer of highly conducting material like copper to reduce resistivity. This is especially beneficial for superconducting rings because the conductivity of copper at cryogenic temperatures is at least 30 times its value at room temperature.

For each layer surrounding the particle beam, there are four matchings equations for the four tangential electromagnetic field components. Thus for n layers, the derivation of the transverse impedance involves the solution of $4n$ equations in $4n$ unknowns. Computer codes have been written for numerical solutions. [7] Unfortunately, these equations are often "ill-conditioned," i.e., their determinant is close to zero making it difficult to obtain solution with sufficient accuracy. Zot-

ter recently converted his earlier code to one in MATHEMATICA [12] so that the equations can first be solved symbolically to algebraic expressions before final numerical evaluation. [11]

10.2.6 *Laminations*

Instead of going into the detail of the wall surface of a cylindrical vacuum chamber, which may be smooth or laminated,we can define the effective surface impedances per square as

$$\tilde{E}_z = -\mathcal{R}_z \tilde{H}_\theta \qquad \text{and} \qquad \tilde{E}_\theta = +\mathcal{R}_\theta \tilde{H}_z \ . \tag{10.133}$$

where $\tilde{E}_z$, $\tilde{E}_\theta$, $\tilde{H}_z$, and $\tilde{H}_\theta$ are the components of the electric and magnetic field components on the wall surface. Physically, we can imagine $\tilde{H}_\theta$ at the wall surface sets up a current per width inside the surface in the $-z$-direction and therefore a $-\tilde{E}_z$ at the wall surface. Similarly, $\tilde{H}_z$ at the surface sets up a current per width inside the surface in the θ-direction and therefore a $\tilde{E}_\theta$ at the surface. In this way, the ratios $-\tilde{E}_z/\tilde{H}_\theta$ and $\tilde{E}_\theta/\tilde{H}_z$ just give the surface impedances per square $\mathcal{R}_z$ and $\mathcal{R}_\theta$. We distinguish the surface impedances per square in the z-direction and θ-direction, because the surface may have different impedances in different direction. This is especially true for a laminated surface. The laminations are usually in the r-θ-plane perpendicular to the z-axis. The impedance is therefore large across the cracks of the laminated surface in the z-direction, and is small in the θ- direction.

Let us apply this concept to a smooth cylindrical beam pipe with a finite wall conductivity. The field equations are solved exactly as before, but with the boundary conditions at the wall surface given by Eq. (10.133) instead. It is found that if we identify $\nu_2 = x_2/b$, the transverse propagation constant inside the wall of the beam pipe according to

$$\nu_2 = -i\frac{Z_0 k}{\mathcal{R}_{z,\theta}}, \tag{10.134}$$

the solution agrees with those obtained in the previous subsections up to the next order in $|\nu_2 b|^{-1}$. The terms involving $\mathcal{R}_\theta/Z_0$ are found to belong to higher orders and can be neglected. [5] This method can also be extended to difference geometry of vacuum-chamber cross section, for example, a beam between two parallel plates.

The surface impedance per square of a laminated surface has been derived before by Snowdon, Gluckstern, and others, [13, 14, 15, 16] from which the equivalent transverse propagation constant can be obtained according to Eq. (10.134).

Then the transverse impedance of a cylindrical vacuum chamber with laminated wall surface can be evaluated using one of the impedance expressions derived previously, for example, the one given by Eq. (10.117).

We must emphasize that this is only an approximate method of evaluating the transverse impedance of the laminated vacuum chamber. Although the surface impedance is derived by solving the field equations inside the laminations and cracks, with the electric and magnetic fields matched at the boundaries, however, all the derivations by various authors have only been made with the beam in the center of vacuum chamber. In other words, the surface impedance per square has been obtained is of monopole configuration. Using a surface impedance per square of monopole configuration in an expression of a multipole configuration can be questionable. Also the method of deriving an equivalent transverse propagation constant using Eq. (10.134) may not have been the best solution. Nevertheless, we believe that the dipole impedance obtained with this procedure should serve as a good estimate.

10.3 Applications

10.3.1 *Fermilab Booster*

The Fermilab Booster consists of 48 F-magnets and 48 D-magnets. Each magnet has a length $\ell = 113.741''$. We approximate the magnets as parallel-faced, having a vertical gap of $2b = 1.64''$ for the F's and $2b = 2.25''$ for the D's. The height of the top part or bottom part of each magnet is $d = 6''$.

The vertical dipole impedance of the booster laminated magnets is computed using two models. [5] One is to approximate the laminations as annular rings of inner and outer radii $1.125''$ and $6''$, and shorted at the outer radius. Maxwell's equations are solved for the surface impedance per square [5, 13, 14] and the vertical dipole impedance is deduced using the procedure demonstrated in the last subsection. The result is shown as dashes Fig. 10.9. The other model is to approximate the magnets as parallel-faced extending to infinity horizontally. The results are shown in the same figure as solid curves. We see that, as expected, the imaginary part approaches the bypass inductive reactance

$$\mathcal{I}m\, Z_1^V \to \frac{Z_0}{2\pi}\left(\frac{L_F}{b_F^2} + \frac{L_D}{b_D^2}\right) = 29.3\ \mathrm{M\Omega/m} \tag{10.135}$$

in the annular approximation, and [5]

$$\mathcal{I}m\, Z_1^V \to \frac{\pi Z_0}{16}\left(\frac{L_F}{b_F^2} + \frac{L_D}{b_D^2}\right) = 36.2\ \mathrm{M\Omega/m} \tag{10.136}$$

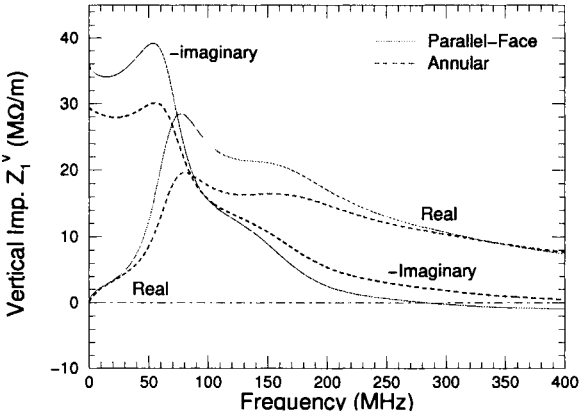


Fig. 10.9 Real and imaginary parts of the vertical dipole impedance Z_1^V of the booster laminated magnets are shown as solid curves in the parallel-plate approximation with plate. Also plotted in dashes are the real and imaginary parts of the transverse dipole impedance $Z_1^\perp$ in the annular ring approximation. The radii have been taken as half the plate-separation.

in the parallel-faced approximation[‡] at low frequencies independent of the properties of the laminations, where $2b_{F,D}$ and $L_{F,D}$ represent the pole-face gap and total length of 48 F or D magnets. The real part rolls off to zero at zero frequencies.

10.3.1.1 *Transverse Coupled-Bunch Instabilities*

Unlike the situation of a smooth beam-pipe wall, the bend-around of $\mathcal{R}e\, Z_1^V$, as depicted in Fig. 10.9, occurs at the much higher frequency around 80 MHz. This reflects the fact that the surface impedance per square is very much larger than that for a smooth beam-pipe wall, and agrees approximately with the prediction of Eq. (10.10). The bend-around of $\mathcal{R}e\, Z_1^V$ leads to a very different contribution to the transverse coupled-bunch instabilities. If it were not for this bend-around, $\mathcal{R}e\, Z_1^V$ would reach, according to the $\omega^{-1/2}$-behavior, 5340 MΩ/m at the most dangerous betatron line at the $n \approx -0.3$ harmonic or $f = -135$ kHz at injection, where we have chosen the vertical betatron tune to be $\nu_\beta \approx 6.7$. The Fermilab Booster has a circumference of 474.2 m and the injection kinetic energy is 400 MeV. At an intensity of $N_b = 6 \times 10^{10}$ per bunch and $M = 84$ bunches, the growth rate is given by

$$\frac{1}{\tau} = \frac{eMI_bc}{4\pi\nu_\beta E}\,\mathcal{R}e\, Z_1^V F' \tag{10.137}$$

in the smooth-focusing approximation, where I_b is the average current per bunch. Using the form factor $F' = 0.811$ for Sacherer's sinusoidal modes, the growth rate is $\tau^{-1} = 4.19 \times 10^6\ \mathrm{s}^{-1}$ or a growth time of 0.24 μs or 0.11 revolution turns.

[‡]The bypass inductance experienced by a beam in between two parallel plates separated by distance $2b$ is $\mathcal{I}m\, Z_1^V/L = \pi Z_0/16$. [5]

Now $\mathcal{R}e\, Z_1^V$ is bounded by its peak of 28.5 MΩ/m at 77 MHz. When this value is substituted into Eq. (10.137) instead, the growth rate drops to $\tau^{-1} = 22400\ \mathrm{s}^{-1}$ or a growth time of 0.45 μs or 20 revolution turns. The actual growth rates will be much less than this because unlike the narrow peak-like contribution of the $\omega^{-1/2}$-contribution near zero frequency, this peak of $\mathcal{R}e\, Z_1^V$ is very broad so that the damping contribution at positive frequencies will nearly cancel the growing contribution at negative frequencies. In short, $\mathcal{R}e\, Z_1^V$ of a laminated magnet will not contribute to transverse coupled-bunch instabilities because of the high bend-around frequency of $\mathcal{R}e\, Z_1^V$. In this sense, transverse coupled-bunch growths will become less in unshielded laminated magnets than if the laminated surface is shielded by a smooth metallic beam pipe. The main reason is that the image current flows through the bypass inductance at low frequencies rather than around each lamination.

Transverse coupled-bunch instabilities have been reported in the Fermilab booster, but they have never been a serious problem. This is because the laminated magnets cover only about 60% of the ring. In between the magnets there are beam pipes. The booster is 24-fold symmetric. In each period, the beam pipe in the 6-m long straight section between the D-magnets is of diameter 2.25″, the beam pipe in the 1.2-m short straight section between the F-magnets is of diameter 4.25″, and the two 0.5-m straights joining a D-magnet to a F-magnet is of radius 2.25″. Assuming these beam pipes are made of stainless steel with conductivity $\sigma_c = 1.35 \times 10^6\ (\Omega\mathrm{m})^{-1}$, they contribute to the longitudinal impedance

$$Z_0^{\parallel} = (1-i)1.38\sqrt{n}\ \Omega, \tag{10.138}$$

and vertical transverse impedance

$$Z_1^V = (1-i)\frac{0.199}{\sqrt{n}}\ \mathrm{M}\Omega/\mathrm{m}, \tag{10.139}$$

according to the parallel-faced equivalence of Eqs. (1.58) and (1.60). The $\omega^{-1/2}$-behavior is followed because for the $(1-Q)$ line at injection, the skin depth is $\delta_c \approx 1.4$ mm, still less than the 1.5-mm thickness of the beam pipe. Since $Z_0^{\parallel}/n$ rolls off with frequency, the longitudinal impedance of the beam pipe will not lead to longitudinal beam instabilities. The transverse impedance, however, will contribute to transverse coupled-bunch instabilities. The most easily excited is the lowest betatron sideband, commonly called the $(1-Q)$ line. According to Eq. (10.137), the worst vertical instability at the present vertical betatron tune 6.7 will have a growth rate of 337 s^{-1} (growth time 2.97 ms) at the injection kinetic energy of 400 MeV. The growth rate decreases in the ramp and becomes

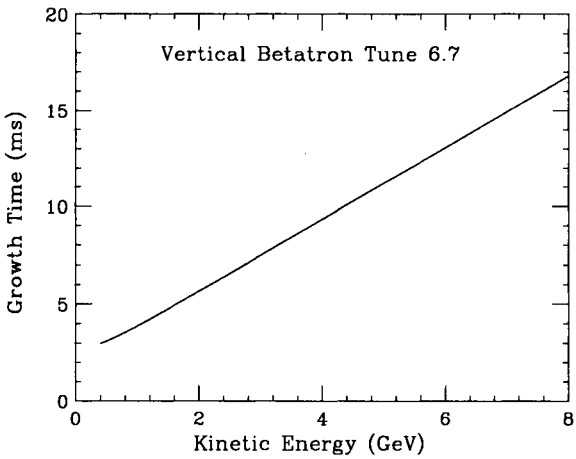


Fig. 10.10 Growth time of the worst vertical coupled-bunch instability of the Booster driven by the resistive-wall impedance of the beam pipe is shown increasing nearly linearly with the kinetic energy of the beam. The vertical betatron tune is assumed to be 6.7.

59.6 s^{-1} (growth time 16.8 ms) when reaching the extraction kinetic energy of 8 GeV. The growth time of the worst mode during the ramp is shown in Fig. 10.10. The integrated total growth during the ramp is 4.95, or a total growth in amplitude $e^{4.95} = 141$, which is still intolerably large.

Transverse coupled-bunch instabilities have been seen in the Fermilab Booster for many years. It can be monitored easily by the difference signal of a beam-position monitor. Transverse dampers have been built for each of these lower betatron sideband modes. Although they should be very effective at eliminating the resistive-wall instabilities, however, because the dampers require a fixed betatron tune throughout the acceleration cycle for the proper electronic phase shift, their function is difficult to maintain in operations. The need for the dampers has been eliminated after the upgrading the current capability of the sextupole circuits. The sextupole circuits have been operated in negative vertical chromaticity below transition and positive above transition, so that the power spectrum of the rigid-dipole mode, being shifted towards positive frequency, can sample less harmful resistive-wall impedance at the $(1-Q)$ sideband. However, the chromaticities of the Fermilab Booster have never been well-understood, possibly because of the complicated intrinsic sextupole contribution from the laminated magnets. Some measurement [17] even shows that the vertical chromaticity has always been at $\xi_y \approx +3$ to $+6$ near injection which is below transition and is of the wrong sign for stability (Fig. 10.11). In fact, we believe that a reasonable amount of chromaticity will not be sufficient to shift the power spectra of the Booster bunches near the injection kinetic energy of 400 MeV because of the rather large slip factor $\eta = -0.458$. The transition

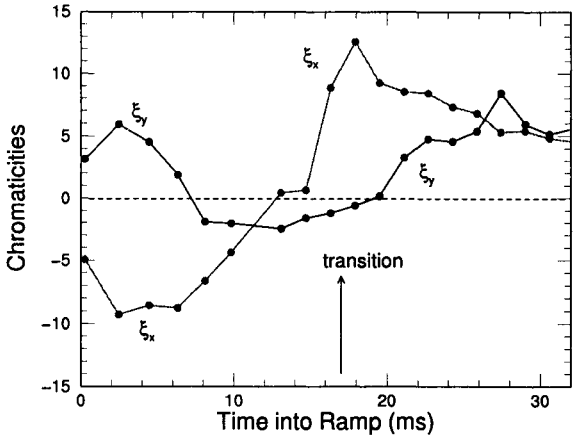


Fig. 10.11 Horizontal and vertical chromaticities $\xi_{x,y}$ of the Fermilab Booster in 2004 during the ramp cycle. Note that the chromaticities change signs near transition to reduce transverse coupled-bunch instabilities, and ξ_y is positive near injection but will not affect the instabilities much because the slip factor is relatively not small. (Courtesy Yang. [17])

gamma is $\gamma_t = 5.45$. Even for a full bunch length of $\tau_L = 10$ ns, the chromatic betatron phase shift across the bunch is $\omega_\xi \tau_L = \xi_y \omega_0 \tau_L / \eta = -0.37$ at $\xi_y = +6$. However, as seen in Fig. 6.13, the power spectrum of the rigid-dipole mode has a span of ± 2 unit of $\omega\tau_L/\pi$. The shift here from chromaticity is only $\omega_\xi \tau_L/\pi = -0.12$ and is therefore rather insignificant. However, as the energy increases, the slip factor decreases drastically, especially near transition. Over there, the chromatic betatron phase shift will be very much larger and help reducing the drive of transverse coupled-bunch instability from the resistive wall. For example, with a chromaticity of $|\xi_y| = 3$ and a total bunch length $\tau_L = 6$ ns, the chromatic betatron phase shift becomes $\omega_\xi \tau_L/\pi = 0.31$, 0.92, 4.89, and 3.33, respectively, at kinetic energy 2, 4, 6, and 8 GeV. For this reason, transverse coupled-bunch instability of the $(1-Q)$ mode grows significantly only for a short time period near injection after adiabatic capture, and becomes very insignificant later because of the chromaticity setting.

10.3.1.2 *Tune-Shift Measurement*

Turn-by-turn transverse positions of some Fermilab Booster bunches were measured by Huang [18] for 2-, 4-, 6-, 8-, and 10-turn injection, corresponding, respectively, to the intensities of 0.92, 1.85, 2.79, 3.69, and 4.66×10^{10} particles per bunch. A pinger was turned on and its voltage was ramped from 0.6 kV at injection to 3.8 kV near extraction. The pinger was fired every 0.5 ms with 2.0-μs pulse width, so that the bunches were kicked vertically every 0.5 ms. Each set of data covers 2000 turns or the whole ramping Booster cycles. Each data set is divided into small pieces, each 0.5 ms long (225 to 300 turns), so that the coherent motion induced by each pinger pulse can be analyzed. The data

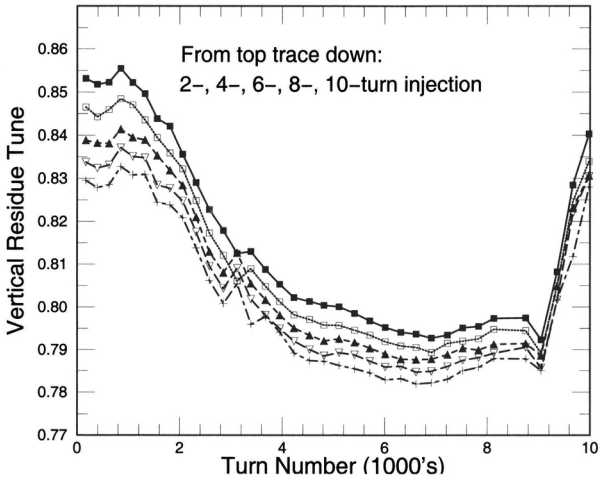


Fig. 10.12 Measured coherent vertical betatron tune shifts in the Fermilab Booster as functions of revolution turn number for 2-, 4-, 6-, 8-, and 10-turn injection, corresponding to intensity of 0.92, 1.85, 2.79, 3.69, and 4.66 $\times$ 10^{10} particles per bunch (Courtesy Huang. [18])

are supplied to an independent-component-analysis routine [19] to solve for the betatron oscillation modes and the vertical betatron tune ν_y is computed from the fast Fourier transform (FFT) of the temporal pattern. The independent-component-analysis routine increases the accuracy of tune measurement since the data of all the BPM's are used.

The vertical betatron tunes throughout the booster 15-Hz cycle had been measured. However, only those measurements up to the transition time (roughly at 17 ms or 9500 turns) were used for the present analysis. These measurements for all the data sets are plotted in Fig. 10.12. The tune depressions due to beam intensity are clearly seen at various times. The measurements near turn 3000 were found to come from errors.

The tune depression is obviously related to the transverse coupling impedance. Since the Booster bunches have roughly Gaussian linear distribution, the Sacherer's integral equation of transverse motion is solved in the Hermite mode. Following Eqs. (9.74) and (9.77), the lowest order perturbation gives, for the most easily excited rigid-dipole mode ($m = 0$ and $k = 0$), the *dynamic* betatron tune shift[†]

$$\Delta\nu_y\big|_{\rm dyn} = -\frac{e^2 N_b R}{8\pi^{3/2}\beta E_0 \nu_y \sigma_\tau}\, \mathcal{I}m\, Z_1^V\Big|_{\rm eff}, \tag{10.140}$$

[†]If one tries to approximate the betatron tune shift of a bunch by the betatron tune shift of a coasting beam, Eq. (9.4) or (9.6), with the average bunch current replaced by the peak current $I_{\rm pk} = eN_b/(\sqrt{2\pi}\sigma_\tau)$, the numerical factor in the denominator of Eq. (10.140) changes from $8\pi^{3/2}$ to $4\sqrt{2}\pi^{3/2}$.

where σ_τ is the rms bunch length and the effective transverse impedance is

$$\mathcal{I}m\, Z_1^V\Big|_{\text{eff}} = \frac{\displaystyle\int_{-\infty}^{\infty} \frac{d\omega}{2\pi} Z_1^V(\omega) e^{-\omega^2\sigma_\tau^2}}{\displaystyle\int_{-\infty}^{\infty} \frac{d\omega}{2\pi} e^{-\omega^2\sigma_\tau^2}}. \tag{10.141}$$

In above, a broadband impedance has been assumed so that the summation over the betatron sidebands can been replaced with an integral.

To obtain the *coherent betatron tune shift*, the incoherent tune shift must be added onto the dynamic tune shift. Thus one should be careful about what should be included in the transverse impedance when the coherent betatron tune shift is computed. For example, the transverse space-charge impedance can be expressed as

$$Z_1^V\Big|_{\text{sc}} = \frac{Z_0}{\pi\beta^2\gamma^2} \sum_i L_i \left[\frac{\epsilon_{sc}^V}{a_{Vi}^2} + \frac{\xi_1^V - \epsilon_1^V}{h_i^2}\right], \tag{10.142}$$

where the summation runs over each section of the vacuum chamber of length L_i, half-height h_i, and half height of the beam a_{Vi}, while ϵ_{sc}^V, ξ_1^V, and ϵ_1^V represent the appropriate space-charge coefficients and Laslett's electric image coefficients listed in Table 3.2. Only the terms involving the coherent Laslett's image coefficient ξ_1^V should be included.[‡] The beam pipes joining the magnets have such a contribution. The contribution is important at low energy, ~ 24 MΩ/m, but rolls off as $(\beta\gamma)^{-2}$ as the beam energy increases. As for the magnets, this contribution may not be appropriate, because the Laslett's coherent electric coefficient ξ_1^V is for perfectly conducting vacuum chamber only. Here, the laminated magnet pole faces are not perfectly conducting. The modification can be obtained by noticing that the term involving ξ_1^V in Eq. (10.142) can be rewritten as

$$\frac{\xi_1^V}{h_i^2\gamma^2} = \frac{\xi_1^V}{h_i^2} - \beta^2 \frac{\xi_1^V}{h_i^2}, \tag{10.143}$$

where the first term is for the electric image in the perfectly conducting walls of the vacuum chamber and the second term is for the magnetic image in the same perfectly conducting walls. For the laminated magnets, the electric image is formed at the enclosure of the magnet, which carries most of the return current at low frequencies. The magnetic image is formed at the magnetic pole faces. We therefore have instead the replacement

[‡]The tune shift corresponding to the self-force part of Eq. (10.142) is cancelled by the incoherent self-force tune shift. The tune shift corresponding to the ϵ_1^V part is cancelled by the incoherent tune shift due to images.

$$\frac{\xi_1^V}{h_i^2\gamma^2} \longrightarrow \frac{\xi_1^V}{\bar{h}_i^2} + \beta^2\frac{\xi_2^V}{h_i^2}, \tag{10.144}$$

where $\bar{h}_i^2$ stands for the radius of the magnet enclosure and $\xi_2^V = \pi^2/16$ is the Laslett's coherent magnetic coefficient derived in Sec. 3.1.2 for two horizontal parallel perfect magnetic surfaces separated by the distant $2h_i$. Attention should also be paid to the change in sign of the magnetic contribution from perfectly conducting surfaces to perfect magnetic surfaces. Since the radius of enclosure is usually much larger than the magnet half gap ($\bar{h}_i^2 \gg h_i^2$), the electric contribution is small and can be neglected. For example, if the enclosure radius is $\bar{h}_i = 8''$, the electric contribution is only 0.4 MΩ/m, where $\xi_1^V = \frac{1}{2}$ for a circular enclosure has been used. Thus the contribution of the magnets to the transverse impedance becomes with the summation goes over all the magnets,

$$Z_1^V\big|_{\mathbf{mag}} = \frac{Z_0\xi_2^V}{\pi}\sum_i \frac{L_i}{h_i^2}. \tag{10.145}$$

However, more thinking reveals that the above expression is still not quite correct, because the pole surfaces are not exactly perfectly magnetic. They are laminated instead. The effects of the laminations and cracks will become more apparent as the frequency increases. In fact, a somewhat more accurate representation of the transverse impedance of the laminated magnets is the one computed and depicted in Fig. 10.9, of which the low-frequency limit is just Eq. (10.145), the bypass inductive impedance [see Eq. (10.86) in thin-wall model PM and and Eq. (10.125) or (10.127) in thick-wall model PM]. The model of laminated magnets employed in the computed result should take care of both terms on the right side of Eq. (10.144). There are other contributions to $\mathcal{I}m\, Z_1^V$ at low frequencies, such as BPMs, bellows, steps, etc. Since they amount to only $\sim$ 0.4 MΩ/m up to 200 MHz in the Fermilab Tevatron, [2], it is safe to regard them as negligible compared with the laminated magnets in the Fermilab Booster. In short, the main contributions to the vertical coherent betatron tune shift arise from the bypass inductive impedance of the magnets plus the electric-image contribution of the pipes joining the magnets.

For each of the data piece, Huang performed a linear fit to the measured coherent vertical tune depression as a function of bunch intensity. Then following Eq. (10.140), the coherent part of the effective transverse impedance was computed and the results plotted as squares in Fig. 10.13. The exotic point at 3000 turn arises from a measurement error. The rms bunch lengths were taken from a previous measurement [20] by fitting Gaussians to the linear waveforms of the beam recorded using a wall-gap monitor. As shown in Fig. 10.14, the bunch length is almost intensity independent up to transition crossing near 17 ms.

The effective vertical dipole impedance is then evaluated according to Eq. (10.141) by including only the impedance computed for the laminated magnets as well as the contribution of the coherent Laslett's image coefficients from the beam pipes joining the magnets. The result, not exactly the same as Ref. [18], is shown as a solid curve in Fig. 10.13. The agreement is excellent after understanding that the impedance of the laminated magnets displayed in Fig. 10.9 is only an estimate using the concept of surface impedance and does not evolve rigorously from Maxwell equations. Nevertheless, the experiment appears to reproduce the right order of magnitude for the bypass inductive impedance.

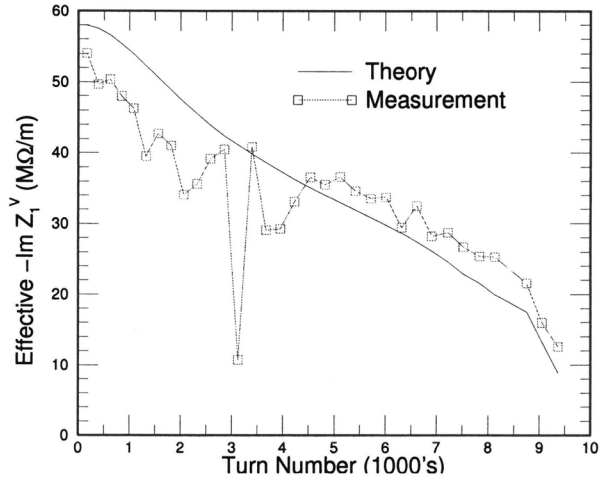


Fig. 10.13 Squares: effective coherent vertical dipole impedance in the Fermilab Booster derived from measured coherent tune shifts. The point near 3000 turns arises from an error in the measurement. Solid curve: the same from the evaluating the integrals in Eq. (10.141) using the computed impedance of the laminated magnets and the contribution from the beam pipes joining the magnets.

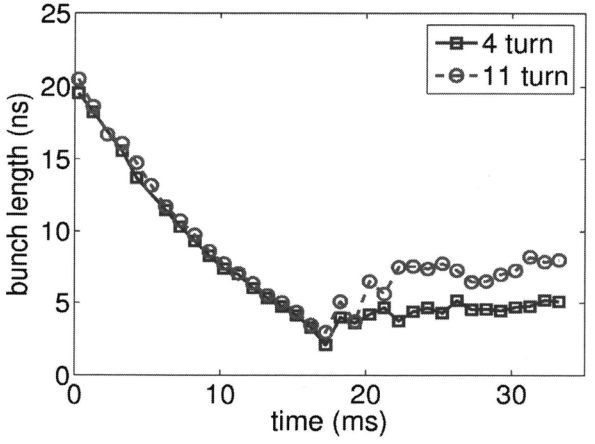


Fig. 10.14 Rms bunch length measured by Huang by fitting a Gaussian to the waveforms recorded by the wall-gap monitor for 4-turn and 11-turn injection. The measurement was made at 1-ms interval throughout the whole Booster ramping cycle. Transition crossing is at 17.5 ms. (Courtesy Huang. [20])

10.3.2 *Bench Measurement*

Because of the low revolution frequency (11.3 kHz) of the Large Hadron Collide (LHC) at CERN, careful measurements of the transverse impedances are necessary for many components of the vacuum chamber. To validate the bench-measurement technique, verification was made with theory by Mostacci, *et al.* [21] for a $L = 50$ cm stainless-steel beam pipe with radius $b = 5$ cm, wall thickness $t = 1.5$ mm, and conductivity $\sigma_c = 1.35 \times 10^6\ (\Omega/\mathrm{m})^{-1}$. The frequencies of interest had been below 1 MHz down to 100 Hz. The current I was passed into a N-turn loop $L_w = 1.25$ m long and $\Delta = 2.25$ cm wide, placed inside the beam pipe. The image current produces a magnetic field which in turn induces a voltage in the loop through the impedance Z_{pipe} of the pipe. The transverse resistive-wall impedance can then be obtained from

$$Z_1^{\perp}\Big|_{\mathrm{RW}} = \frac{c}{\omega}\frac{Z_{\mathrm{pipe}} - Z_{\mathrm{PC}}}{N^2\Delta^2}, \tag{10.146}$$

where Z_{PC} is the measured impedance of the loop placed inside a cylindrical perfectly conducting beam pipe (a copper one is good enough) of the same dimension. This method of using a loop rather than two wires can increase the signal-to-noise ratio by a factor of N^2, which is very significant considering that the measured signals are very small at low frequencies. However, there is a drawback of lowering the frequency of the loop self-resonances. The chosen number of turns = 10 is a compromise to keep the lowest self-resonance above 1 MHz. The measured results are depicted in Fig. 10.15, where the engineering

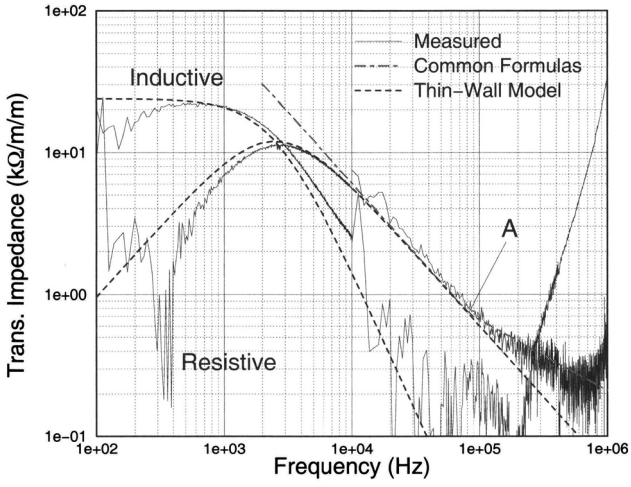


Fig. 10.15 Bench measurement of the transverse impedance of a stainless-steel beam pipe of length $L = 50$ cm, radius $b = 5$ cm, and wall-thickness $t = 1.5$ mm. Predictions using thin-wall model are shown in dashes. Point A, 0.720 kΩ/m/m at 83.4 K=kHz, is where skin-depth is equal to wall thickness. $\mathcal{R}e\, Z_1^{\perp}$ rolls off as $1/\omega$ below this frequency and $1/\sqrt{\omega}$ above this frequency (long-dashes). (Courtesy Mostacci, *et al.* [21])

convention has been used (i.e., an inductance is the positive imaginary part of the impedance). Point A, 0.720 kΩ/m/m at 84.3 kHz, is where skin-depth is equal to wall thickness, or

$$t = \delta_c = \sqrt{\frac{2c}{Z_0 \omega \mu' \sigma_c}}, \tag{10.147}$$

where the relative magnetic permeability of stainless steel $\mu' \approx 1$ has been used. Above 84.3 kHz, where the skin-depth is smaller than the wall thickness, the measured transverse impedance agrees with the $1/\sqrt{\omega}$-formula (long-dashes) very well. Below 83.4 kHz, we see the Sacherer's region, which agrees with the $1/\omega$-formula (long dashes) very well. We also see the resistive part of the impedance goes to zero linearly at lower frequencies while the inductive part approaches the constant value of 24 kΩ/m/m as expected from the expression of bypass inductive impedance $Z_0/(2\pi b^2)$. The predictions of the thin-wall model are depicted in dashes for comparison.

Now let us explain why Z_{PC} must be subtracted from Eq. (10.146). What we are after is the resistive-wall impedance experienced by a dipole particle beam. But this is different from the impedance experienced by a dipole current inside the beam pipe. In the former, the dipole particle beam sees, in additional to the resistive-wall impedance, both the magnetic and electric images in the wall of the beam pipe and the two almost cancel for an ultra-relativistic beam. A dipole current, however, sees only the magnetic image but not the electric, thus picking up, in additional to the resistive-wall impedance, a capacitive impedance, according to Eq. (10.21),

$$\left.\frac{Z_1^\perp}{L}\right|_{\substack{\text{magnetic}\\ \text{image}}} = \frac{iZ_0}{2\pi b^2}, \tag{10.148}$$

which is what the dipole current sees in a perfectly conducting beam pipe. This is what we denote by Z_{PC} in Eq. (10.146) and it must be subtracted before the resistive-wall contribution can be revealed. In fact, the measurement of the transverse impedance of the copper pipe by Mostacci, *et al.* does provide results in agreement with Eq. (10.148). As shown in Fig. 10.16, the measured real part is mostly zero while the imaginary part is 23 kΩ/m/m in the plateau and is capacitive (negative in the engineering convention). According to Mostacci, *et al.*, the low-frequency deviations are due to measurement difficulties while at high frequencies (above 200 kHz), the effect of the loop self-resonance becomes not negligible. On the other hand, the imaginary part of the transverse impedance observed by the dipole current inside the stainless-steel pipe is almost zero in the measurement before the subtraction. After the subtraction, the correct

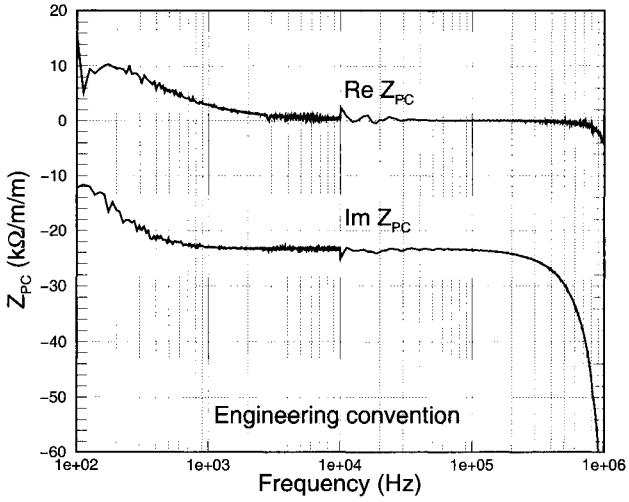


Fig. 10.16 Real and imaginary parts of the transverse dipole impedance of a copper beam pipe measured by Mostacci, *et al.* The real part is mostly zero while the imaginary part is roughly -23 kΩ/m/m and is capacitive (the engineering convention has been used. (Courtesy Mostacci, *et al.* [21])

transverse impedance for the resistive wall results. It is also possible that the deviations from the ideal values of Z_{PC} are a result of the finite conductivity of the brass pipe (Exercise 10.5).

10.4 Narrow Resonances

The narrow higher-order transverse resonant modes of the rf cavities can also drive transverse coupled-bunch instabilities. The growth rates are described by the general growth formula of Eq. (10.1). When the resonance is narrow enough, only the betatron sidebands closest to the resonant frequency $\omega_r/(2\pi)$ contribute in the summation. The growth rate is therefore given by Eq. (10.2), where two betatron sidebands are included:

$$\frac{1}{\tau_{m\mu}} \approx -\frac{1}{1+m}\frac{eMI_b\omega_0\beta_\perp}{4\pi\beta E_0}[\mathcal{R}e\, Z_1^\perp(\omega_q)F_m'(\omega_q\tau_L-\chi)-\mathcal{R}e\, Z_1^\perp(\omega_{q'})F_m'(\omega_{q'}\tau_L-\chi)], \tag{10.149}$$

where q and q' satisfy

$$\begin{cases} -\omega_r \approx \omega_q = (qM+\mu+\nu_\beta+m\nu_s)\omega_0, \\ \omega_r \approx \omega_{q'} = (q'M+\mu+\nu_\beta+m\nu_s)\omega_0, \end{cases} \tag{10.150}$$

and $\beta_\perp$ is the betatron function at the location of the resonant impedance. Similar to the situation of longitudinal coupled-bunch instabilities, mode $\mu = 0$ and mode $\mu = \frac{1}{2}M$, if M is even, receive contributions from both the positive-frequency side and negative-frequency side. In the language of only positive

frequencies, there are the upper and lower betatron sidebands flanking each revolution harmonic line. The lower sideband originates from negative frequency and is therefore anti-damped. For these two modes, both the upper and lower sidebands correspond to the same coupled-bunch mode. If the resonant frequency of the resonance leans more towards the lower sideband, there will be a growth. If the resonant frequency leans more towards the upper side band, there will be damping. This is the Robinson's stability analog in the transverse phase plane. However, sometimes it is not so easy to identify which is the lower sideband and which is the upper sideband. This is because the residual betatron tune $[\nu_\beta]$ or the noninteger part of the betatron tune can assume any value between 0 and 1. If $[\nu_\beta] > 0.5$, the upper betatron sideband of a harmonic will have a higher frequency than the lower betatron sideband of the next harmonic.

There is one important difference between transverse coupled-bunch instabilities driven by the resistive-wall impedance and by the higher-order resonant modes. The former is at very low frequency and therefore the form factor F_0' is close to 1 when the chromaticity is zero. The latter, however, is at the high frequencies of the resonances. The form factor usually assumes a much smaller value unless the bunch is very short and we sometimes refer this to "damping" from the spread of the bunch.

This instability can be observed easily in the frequency domain at the lower betatron sidebands flanking the harmonic lines. If a particular lower betatron sideband grows strongly, we subtract the betatron tune ν_β (not $[\nu_\beta]$) to find out which harmonic line it is associated with. Then from Eq. (10.150), we can determine which coupled-bunch mode μ it is. To damp this transverse coupled-bunch instability, one can identify the offending resonant modes in the cavities and damp them passively using an antenna. A tune spread due to the slip factor η or from an octupole can also contribute to the damping. When the above are not efficient enough, a transverse bunch-to-bunch damper will be required. If we can identify the annoying mode, a mode damper of narrow band will do the job. To damp coupled-bunch instabilities without knowing the annoying mode, a wideband bunch-by-bunch damper will be necessary.

Similar to longitudinal coupled-bunch instabilities, transverse coupled-bunch instabilities can also be damped by modulation coupling from an uneven fill in the ring discussed in Sec. 8.3.4.

10.5 Exercises

10.1 For the example of resistive-wall driven coupled-bunch instability of the Tevatron at the fixed target mode, try to sum up the contribution for all frequencies for the $\mu = 1093$ mode and compare the result of taking only the lowest frequency sideband.

10.2 For the same example in Exercise 10.1, compare the growth rates of mode $\mu = 1092,\ 1091,\ \cdots$, with mode 1093. How many modes do we need to include so that the growth rate drops to below $\frac{1}{4}$ of that of mode 1093?

10.3 Consider a cylindrical beam pipe of radius b with perfect magnetic wall.
(1) Show that the transverse space-charge impedance (including self-force and image effects) of azimuthal m experienced by a beam of radius a and uniform transverse distribution is

$$Z_m^{\perp}\big|_{\text{SC}} = \frac{iZ_0R}{m\beta^2\gamma^2}\left[\frac{1}{a^{2m}} + \frac{1}{b^{2m}}\right]. \tag{10.151}$$

(2) Show that the transverse resistive wall impedance is

$$Z_m^{\perp}\big|_{\text{RW}} = -\frac{iZ_0R}{m\beta^2\gamma^2}\left[\frac{1}{b^{2m}} + \frac{\alpha_{\text{TM}}}{2^{2m-1}m!(m-1)!}\left(\frac{k}{\gamma}\right)^{2m}\right], \tag{10.152}$$

where α_{TM}, defined in Eq. (10.69), represents the portion of reflected wave required to satisfy the boundary condition at the wall surface of the beam pipe. It is convenient to introduce the parameters

$$\alpha_1' = \alpha_{\text{TM}}\frac{I_m(x)}{K_m(x)} \tag{10.153}$$

and $\bar{\alpha}_1' = -1 + \alpha_1'$. Then

$$Z_m^{\perp}\big|_{\text{RW}} = \frac{iZ_0R}{mb^{2m}}\frac{\bar{\alpha}_1'}{\beta^2\gamma^2}. \tag{10.154}$$

Compare the results with expressions in Eqs. (10.75) to (10.78).

10.4 In the bench measurement of a stainless-steel beam pipe of radius 5 cm and wall thickness $t = 1.5$ mm, the impedance of a beam pipe with perfectly conducting wall has to be subtracted. Explain why, in the frequency range from 100 Hz to 1 MHz, a similar pipe made of copper with conductivity $\sigma_c = 5.99 \times 10^7\ (\Omega\text{-m})^{-1}$ can be used as a reference instead of a perfectly conducting pipe.
Hint: Compute the transverse impedance per unit length of the copper pipe at ~ 1 kHz the frequency range from 100 Hz to 1 MHz Hz and other

frequencies. Compare the result with the transverse impedance per unit length of the stainless-steel pipe in Fig. 10.15.

10.5 The deviation of $\mathcal{R}e\, Z_{\rm PC}$ from zero and the deviation of $\mathcal{I}m\, Z_{\rm PC}$ from $Z_0/(2\pi b^2)$ below $\sim$ 1 kHz in Fig. 10.16 can be explained by the finite conductivity of brass.

(1) There is a resemblance of $\mathcal{R}e\, Z_{\rm PC}$ peak in Fig. 10.16 and $\mathcal{R}e\, Z_1^\perp$ peak in Fig. 10.15. The difference is that the former is shifted to lower frequencies because of the much larger conductivity of brass. Taking the conductivity of brass as $\sigma_c = 60 \times 10^6$ $(\Omega\text{-m})^{-1}$, about 44.4 times larger than that for stainless steel, show that at 1.9 kHz, the wall thickness $t = 1.5$ mm is equal to one skin-depth. This corresponds to Point A in Fig. 10.15, where the behavior of $\mathcal{R}e\, Z_1^\perp$ changes from ω^{-1} to $\omega^{-1/2}$ at $\sim$ 84 kHz for stainless steel. We do see some changes like that in Fig. 10.16. Note that the ordinate of Fig. 10.15 is in the logarithmic scale while that of Fig. 10.16 is linear.

(2) As frequency decreases from Point A, $\mathcal{R}e\, Z_1^\perp$ increases according to ω^{-1}. A maximum is reached roughly when $\mathcal{R}e\, Z_1^\perp$ is equal to $Z_0/(2\pi b^2)$. Show that this corresponds to the frequency

$$f \sim \frac{c}{\pi Z_0 \sigma_c t b}, \tag{10.155}$$

roughly 2.5 kHz for stainless steel and 0.06 kHz for brass. The agreement of these estimates with the measurements in Fig. 2 and 4 is not too bad, considering that the thickness of the brass pipe has not been provided in Ref. [21]. The agreement would have been better if the thickness of the brass pipe is less than 1.5 mm.

(3) As for the imaginary part of the impedance, the raw measurement gives the actual $\mathcal{I}m\, Z_1^\perp$ plus the magnetic image contribution. The electric image contribution is not picked up because a current loop but not a loop of charged beam particles has been used. At zero frequency, $\mathcal{I}m\, Z_1^\perp/L = Z_0/(2\pi b^2)$, the bypass inductive contribution. But the magnetic image contribution is $-Z_0/(2\pi b^2)$, or just the negative of the bypass. Therefore raw measurement is expected to give zero at zero frequency but $-Z_0/(2\pi b^2)$ at larger frequencies. This may explain why $\mathcal{I}m\, Z_{\rm PC}$ rolls off to zero at frequencies less than $\sim$ 0.3 kHz. Only a perfectly conducting pipe will have exactly the magnetic image contribution of $-Z_0/(2\pi b^2)$. But there is no perfectly conducting pipe. So eventually the imaginary part of the raw impedance must go to zero. If the conductivity is larger, it will start to deviate from $-Z_0/(2\pi b^2)$ and go to zero at a lower frequency.

(4) $\mathcal{I}m\, Z_1^\perp$ for the stainless-steel pipe is obtained by subtracting $\mathcal{I}m\, Z_{\rm PC}$.

However, since $\mathcal{I}m\, Z_{\rm PC}$ starts rolling off to zero at ~ 0.3 kHz the subtraction is therefore not big enough below ~ 0.3 kHz. This may explain why the measured $\mathcal{I}m\, Z_1^\perp$ for stainless steel in Fig. 10.15 starts rolling off below ~ 0.3 kHz.

10.6 For a narrow resonance that has a total width larger than $2[\nu_\beta]\omega_0$ where $[\nu_\beta]$ is the residual betatron tune and the bunch power spectrum is much wider than the revolution frequency, show that the growth rate is given by

$$\frac{1}{\tau_{m\mu}} \approx \frac{eMI_b\omega_0\beta_\perp}{4\pi\beta E_0} \frac{h_m(\omega_r - \chi/\tau_L)}{B\sum_{q'} h_m(\omega_{q'} - \chi/\tau_L)} \times \left\{ \mathcal{R}e\, Z_1^\perp[(q_1 M - \mu - \nu_\beta)\omega_0 - m\omega_s] - \mathcal{R}e\, Z_1^\perp[(q_2 M + \mu + \nu_\beta)\omega_0 + m\omega_s] \right\}, \tag{10.156}$$

where q_1 and q_2 are some positive integers so that

$$\begin{aligned} (q_1 M - \mu - \nu_\beta)\omega_0 &\approx \omega_r, \\ (q_2 M + \mu + \nu_\beta)\omega_0 &\approx \omega_r. \end{aligned} \tag{10.157}$$

Such q_1 and q_2 are possible only when $\mu = 0$ or $\mu = M/2$ if M is even. Therefore whether the coupled-bunch mode is stable or unstable depends on whether the resonance is leaning more towards the upper betatron sideband or the lower betatron sideband.

Bibliography

[1] B. Zotter and F. Sacherer, *Transverse Instabilities of Relativistic Particle Beams in Accelerators and Storage Rings*, Proc. First Course of Int. School of Part. Accel. of the 'Ettore Majorana' Centre for Scientific Culture, eds. A. Zichichi, K. Johnsen, and M. H. Blewett (Erice, Nov. 10–22, 1976), CERN Report CERN 77-13, p. 175.

[2] K. Y. Ng, *Impedances and Collective Instabilities of the Tevatron at Run II*, Fermilab Report TM-2055, 1998.

[3] W. Chou and J. Griffin, *Impedance Scaling and Impedance Control*, Proc. 1997 Part. Accel. Conf., eds. M. Comyn, M. K. Craddock, M. Reiser, and J. Thomson (Vancouver, Canada, May 12–16, 1997), p.1724.

[4] The VLHC Design Study Group, *Design Study for a Staged VLHC*, Fermilab Report TM-2149, 2001.

[5] K. Y. Ng, *Coupling Impedance of Laminated Magnets*, Fermilab Report FN-0744, 2004.

[6] L. Vos, *The Transverse Impedance of a Cylindrical Pipe with Arbitrary Surface Impedance*, CERN Report CERN-AB-2003-005 ABP, 2003.

[7] B. Zotter, Part. Accel. **1**, 311 (1970).

[8] R. L. Gluckstern, *Analytic Methods for Calculating Coupling Impedances*, CERN Yellow Report 2000-011, 2000.
[9] Glen R. Lambertson, *Fields in Multilayer Beam Tubes*, LBNL Report LBNL-44454, 1999.
[10] L. Vos, *The Impedance of Multi-layer Vacuum Chamber*, CERN Report CERN-AB-2003-093 (ABP), 2003.
[11] B. Zotter *New Results on the Impedance of Resistive Metal Walls of Finite Thickness*, CERN Report CERN-AB-2005-043, 2005.
[12] S. Wolfram, *The MATHEMATICA Book* (Cambridge University Press).
[13] S. C. Snowdon, *Wave Propagation between Booster Laminations Induced by Longitudinal Motion of Beam*, Fermilab Report TM-277, 1970.
[14] R. Gluckstern, *Coupling Impedance and Energy Loss with Magnet Laminations*, Fermilab Report TM-1374, 1985.
[15] A. G. Ruggiero, *Energy Loss due to the Resistive Magnet Lamination in the NAL Booster*, Fermilab Report FN-230, 1971.
[16] R. E. Shafer, *Coupling Impedance of Laminated Magnets in the Booster*, Fermilab Report TM-1408, 1986.
[17] X. Yang, private communication.
[18] Xiaobiao Huang, *Beam Diagnosis and Lattice Modeling of the Fermilab Booster*, PhD thesis, Indiana University, 2005; X. Huang, *The Coherent Detuning of Vertical Betatron Tunes*, 2005, unpublished.
[19] X. Huang, S. Y. Lee, E. Prebys, and R. Tomlin, *Application of independent component analysis to Fermilab Booster*, *Phys. Rev. ST Accel. Beams* **8**, 064001 (2005).
[20] X. Huang, *Bunch Length Measurements at Different Intensity*, 2005, unpublished.
[21] A. Mostacci, La Sapienza, F. Casper, *Bench Measurements of Low Frequency Transverse Impedance*, Proc. 2003 Part. Accel. Conf., eds. J. Chew, P. Lucas, and S. Webber (Portland, Oregon, May 12–16, 2003, 2001), p. 1801.

2025 © The Author(s). This is an Open Access chapter published by World Scientific Publishing Company, licensed under the terms of the Creative Commons Attribution-NonCommercial 4.0 International License (CC BY-NC 4.0).

Chapter 11

Mode-Coupling Instabilities

As the beam intensity increases, the shift of each longitudinal azimuthal mode becomes so big that two adjacent modes may overlap each other. When this happens, the longitudinal azimuthal mode number m is no longer a good eigennumber, and we can no longer represent the perturbation distribution ψ_1 as a single azimuthal mode. Instead, ψ_1 should be represented by a linear combination of all azimuthal modes. This phenomenon has been referred to as "mode-mixing," "mode-coupling," "strong head-tail," and "transverse or longitudinal turbulence."

11.1 Transverse Mode-Coupling

Let us first consider transverse instability driven by a broadband impedance. This implies a single-bunch mechanism. We also set the chromaticity to zero. For the mth azimuthal mode and kth radial mode, Eq. (9.88) or (10.1) becomes

$$(\Omega - \omega_\beta - m\omega_s)\delta_{mm'}\delta_{kk'} = M^{\perp}_{mm'kk'}\omega_s, \tag{11.1}$$

where, with the aid of Eq. (9.88), the interaction matrix $M^{\perp}$ is defined as

$$M^{\perp}_{mm'kk'} = -\frac{ieI_b}{2\beta E_0 \omega_s \tau_L} \frac{\int d\omega \left[\beta_\perp Z_1^\perp(\omega)\right] \tilde{\lambda}_{m'k'}(\omega)\tilde{\lambda}^*_{mk}(\omega)}{\int d\omega \tilde{\lambda}_{mk}(\omega)\tilde{\lambda}^*_{mk}(\omega)} F_{mk}, \tag{11.2}$$

where F_{mk}, defined in Eq. (9.89), is the dimensionless form factor depending on the excitation modes under consideration, and $\left[\beta_\perp Z_1^\perp(\omega)\right]$ reminds us that when performing the element-by-element summation of the transverse impedance, the betatron function $\beta_\perp$ should be used as a weight function. The summations over discrete frequencies have been converted to integrations because the impedance

is so broadband that there is no need to distinguish the individual betatron lines. A further simplification is to keep only the first most easily excited radial modes. Then, the problem becomes coupling in the azimuthal modes. In Eq, (11.1), ω_β is the incoherent angular betatron frequency of a beam particle. The solution $\Omega - \omega_\beta$ therefore gives the dynamic part of the coherent betatron angular frequency shift.

Since $\mathcal{R}e\, Z_1^\perp(\omega)$ is odd in ω and $\mathcal{I}m\, Z_1^\perp(\omega)$ is even in ω, only $\mathcal{I}m\, Z_1^\perp(\omega)$ will contribute to the diagonal terms of the matrix $M_\perp$ giving only real frequency shifts which will not lead to instability. As the beam current becomes larger, two modes will collide and merge together, resulting in two complex eigenfrequencies, one being the complex conjugate of the other, thus introducing instability. Therefore, coupling should originate from the off-diagonal elements closest to the diagonal. We learn from Eq. (9.99) that the mth mode of excitation $\tilde{\lambda}_m(\omega)$ is even in ω when m is even, and odd in ω when m is odd. Thus, it is $\mathcal{R}e\, Z_1^\perp(\omega)$ that is responsible for the coupling and instabilities.

The eigenfrequencies are obtained from the solution of

$$\det[(\Omega - \omega_\beta - m\omega_s)I - M^\perp] = 0. \tag{11.3}$$

When only the most prominent radial mode is retained for each azimuthal, it may be simpler to start from Eq. (9.33), the original Sacherer's integral equation in Chapter 9, rather than going through the excitation modes $\tilde{\lambda}_m(\omega)$,

$$\begin{aligned}&(\Omega - \omega_\beta - m\omega_s)\alpha_m R_m(r)\\ &= -\frac{i\pi e^2 M N_b}{\beta E_0 T_0^2}\, g_0(r) \sum_{m'q} i^{m-m'} \alpha_{m'} \int r'dr' R_{m'}(r') \left[\beta_\perp Z_1^\perp(\omega_q)\right] J_{m'}(\omega_q r') J_m(\omega_q r),\end{aligned} \tag{11.4}$$

where $g_0(r)$ is the unperturbed normalized distribution in the longitudinal phase space in circular coordinate. Clearly, the equation is solvable when

$$g_0(r) = \frac{\delta(r - \hat{\tau})}{2\pi\hat{\tau}}, \tag{11.5}$$

with $\hat{\tau}$ representing the half length of the bunch, because we must have $R_m(r) \propto \delta(r - \hat{\tau})$. This is the air-bag model with beam particles residing only at the outer edge. Let us choose a simple transverse wake which is a constant $W_1(z) = -\hat{W}_1 H(z)$ $\left(\hat{W}_1 > 0\right)$, where $H(z)$ is the Heaviside step function. The corresponding transverse impedance is

$$Z_1^\perp(\omega) = \frac{\hat{W}_1/\beta}{\omega + i\epsilon} = \wp\left(\frac{\hat{W}_1}{\beta\omega}\right) - i\delta(\omega)\frac{\pi\hat{W}_1}{\beta}. \tag{11.6}$$

The Sacherer's integral equation becomes

$$\left(\frac{\Omega-\omega_\beta}{\omega_s}-m\right)\alpha_m=-\frac{\Upsilon}{\pi^2}\sum_{m'}\alpha_{m'}i^{m-m'+1}\int_{-\infty}^{\infty}d\omega\frac{J_m(\omega\hat{r})J_{m'}(\omega\hat{r})}{\omega+i\epsilon},\quad(11.7)$$

where the dimensionless current parameter is defined as

$$\Upsilon=\frac{e^2N_b\beta_\perp\hat{W}_1}{8\beta^2E_0\nu_s},\quad(11.8)$$

which is positive, and the summation over the discrete spectrum has been replaced by an integral. The $i\epsilon$, the infinitesimal imaginary part in the denominator of the integrand in Eq. (11.7), contributes only when $m=m'=0$. For the principal-value part, it is easy to see that the integral vanishes unless $m-m'$ is odd, since the Bessel functions possess definite parities. The Sacherer's equation reduces to

$$\left(\frac{\Omega-\omega_\beta}{\omega_s}-m\right)\alpha_m=\Upsilon\sum_{m'}\mathcal{W}_{mm'}\alpha_{m'},\quad(11.9)$$

with the the wake-matrix

$$\mathcal{W}_{mm'}=\begin{cases}\dfrac{4}{\pi^3(m^2-m'^2)} & m-m' \text{ odd},\\ -\dfrac{\delta_{m0}\,\delta_{m'0}}{\pi} & m-m' \text{ even}.\end{cases}\quad(11.10)$$

The infinite matrix is truncated and the eigenvalues solved numerically. The solution is shown in Fig. 11.1, where the dynamic parts of the coherent frequency

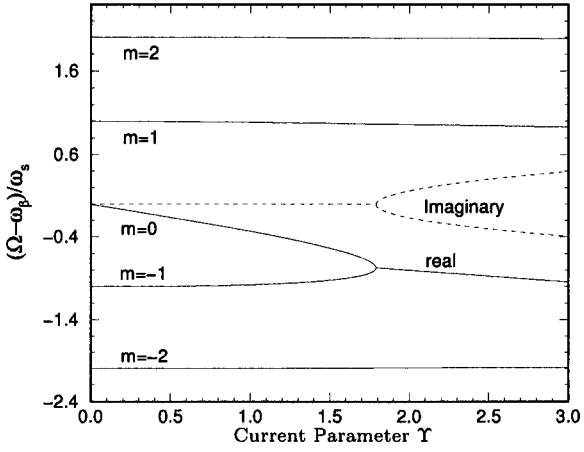


Fig. 11.1 Transverse mode frequencies $(\Omega-\omega_\beta)/\omega_s$ versus the current intensity parameter Υ for an air-bag bunch distribution perturbed by a constant wake potential $\hat{W}_1$. The instability occurs at $\Upsilon=1.79$, when the $m=0$ and $m=-1$ modes collide. The dashed curves are the imaginary part of the mode frequencies or growth/damping rate for the two colliding modes.

shifts of the azimuthal modes are plotted as functions of the current parameter. At low beam current, the azimuthal modes are good eigenmodes. As the beam current increases, mode $m = 0$ and $m = -1$ merge with each other becoming two new modes, one of which is stable and the other one unstable.

This impedance of Eq. (11.6) corresponds to a real part that falls off as frequency increases. The imaginary part is a δ-function at zero frequency, and therefore interacts with the $m = 0$ mode only, since all $m \neq 0$ modes have spectral distribution $\tilde{\lambda}_m(0) = 0$. This explains why all other modes remain almost unshifted with the exception of $m = 0$. The downward frequency shift of the $m = 0$ mode as the beam intensity increases from zero is a general behavior for short bunches. The transverse wake force produced by an off-axis beam has the polarity that deflects the beam further away from the pipe axis. This force acts as a defocusing force for the rigid-bunch mode, and therefore the frequency shifts downward. Such a downshift of the betatron frequency is routinely observed in electron accelerators and serves as an important tool of probing the impedance. Unlike the longitudinal mode-coupling described in Chapter 6 and later in this chapter, there is no symmetry of the azimuthal modes about the $m = 0$ mode, because they are now synchrotron sidebands of the betatron lines. Thus both positive and negative azimuthals must be included in the discussion.

Eventually the $m = 0$ mode shifts downwards and meets with the $m = -1$ mode, thus exciting an instability. The threshold depicted in Fig. 11.1 is at

$$\Upsilon = \frac{\pi e I_b \beta_\perp \hat{W}_1}{4\beta^2 E_0 \omega_s} = 1.79, \tag{11.11}$$

and is bunch-length independent, where $I_b = eN_b/T_0$ denotes the average bunch current. We can also obtain an approximate threshold for a general transverse wake function or transverse impedance from Eqs. (11.1) and (11.2) by equating the frequency shift to ω_s to get

$$\left| \frac{e I_b \bar{\beta}_\perp \left. Z_1^\perp \right|_{\text{eff}}^m}{2\beta E_0 \omega_s \tau_L} \right| \approx 1, \tag{11.12}$$

where

$$\left. Z_1^\perp \right|_{\text{eff}}^m = \frac{\int d\omega \left[\beta_\perp Z_1^\perp(\omega)\right] h_m(\omega)}{\bar{\beta}_\perp \int d\omega h_m(\omega)} \tag{11.13}$$

is called the *effective transverse impedance* for mode m and was defined in Eq. (9.95). In above, $\bar{\beta}_\perp$ is some reference betatron function so that $\left. Z_1^\perp \right|_{\text{eff}}^m$

retains the dimension of transverse impedance, and we can have it conveniently chosen as $\bar{\beta}_\perp = R/\nu_\beta$. Comparing Eqs. (11.11) and (11.12), we find the two thresholds are almost the same except for the bunch-length dependency, which we think should be understood as follows. The imaginary part of the impedance in Eq. (11.6) is a δ-function right at zero frequency which interacts only with the $m = 0$ mode. As the bunch length becomes shorter, the spectrum spreads out wider, so that the spectrum at zero frequency becomes smaller, and $Z_1^\perp|_{\text{eff}}^m$ also becomes smaller accordingly. In fact, if the power spectrum h_m is chosen to be dimensionless so that $h_0(0)$ is just a number, then h_m must be a function of $\omega\tau_L$ and the integral of $h_0(\omega\tau_L)$ in the denominator of Eq. (11.13) must be proportional to $1/\tau_L$ and therefore $Z_1^\perp|_{\text{eff}}^m \propto \tau_L$. Thus the coupling criterion of Eq. (11.12) becomes independent of τ_L and this explains why Υ in Eq. (11.11) is bunch-length independent in this constant-wake model. More concretely, if we work in the Sacherer's sinusoidal modes, $h_0(0) = 8/\pi^2$ from Eq. (9.101) and $\int d\omega h_0(\omega) = 2\pi/\tau_L$ from Eq. (9.102). In other words, within this model, $Z_1^\perp|_{\text{eff}}^m = -i4\hat{W}_1\tau_L/(\beta\pi^2)$. If we denote the expression on the left side of Eq. (11.12) by Υ_{appr}, we have a new current parameter $\Upsilon_{\text{appr}} = 8\Upsilon/\pi^3$. Thus the threshold criterion for the air-bag model translates into $\Upsilon_{\text{appr}} = 0.46$, which is close to the very crude estimate in Eq. (11.12).

Now consider the situation when the impedance is a broadband resonance. For a very short bunch, the $m = 0$ mode extends to very high frequencies and will cover part of the high-frequency capacitive part of the resonance. The effective impedance $Z_1^\perp|_{\text{eff}}^m$ can become small due to the cancellation of the inductive and capacitive parts. At the same time, the peak of $\mathcal{R}e\, Z_1^\perp$ is far from the peak of the $m = -1$ power spectrum, thus making the coupling between the $m = 0$ and $m = -1$ mode very weak. Since the frequency shift is small and the coupling is weak, it will take a much higher beam current for the $m = 0$ mode to meet with the $m = -1$ mode, so pushing up the threshold current. For a long bunch, the $m = 0$ mode has a small frequency spread. If it stays inside the inductive region where $\mathcal{I}m\, Z_1^\perp$ is almost constant, $\mathcal{I}m\, Z_1^\perp$ can be taken out of the integral and $Z_1^\perp|_{\text{eff}}^m$ will be almost constant. Therefore, the threshold current parameter, given by Eq. (11.12), becomes linearly with the bunch length, or the threshold increases linearly with bunch length. On the other hand, when the bunch is very long, the $m = \pm 1$ and even $m = \pm 2$ and $m = \pm 3$ modes may stay inside the constant inductive region of the impedance. This implies that the higher azimuthal modes also interact strongly with the impedance. Then the shifts will decrease with m according to the form factor F_m. Instability will first occur for the higher azimuthal modes whose power spectra reside near the peak of $\mathcal{R}e\, Z_1^\perp$. After that, several collisions may occur around a small beam-current interval

and the bunch can become very unstable suddenly.

The transverse mode-coupling instability was first observed at the DESY PETRA and later also at the SLAC PEP and the CERN LEP. The strong head-tail instability is one of the cleanest instabilities to observe in electron storage rings. [1] In particular, one may measure the threshold beam intensity when the beam becomes unstable transversely. Another approach is to measure the betatron frequency as the beam intensity is varied. From the shift of the betatron frequency per unit intensity increase, the transverse wake can be inferred. The transverse motion of the bunch across its length can also be observed easily using a streak camera.

In the longitudinal mode-mixing instability, the bunch lengthens as the beam becomes unstable essentially without losing beam particles. This does not happen in the transverse case. The instability is devastating; as soon as the threshold is reached, the bunch disappears. This strong head-tail instabilities, however, is uncommon in hadron rings. Except for the possible observation we are going to discussed in Sec. 11.5.3, they have never been reported elsewhere.

Radiation damping is too slow to damp the strong head-tail instability. A damper significantly faster than the angular synchrotron frequency ω_s is required. As shown in Fig. 11.1, it is mode $m = 0$ that is shifted downward to collide with mode $m = -1$ so as to start the instability. But mode $m = 0$ is the pure rigid dipole betatron oscillation without longitudinal excitation. Therefore, if we can introduce a positive coherent betatron tune shift, it will slow this mode from coming down and therefore push the threshold to a higher value. A conventional feedback system is resistive; i.e., the kicker is located at an odd multiple of 90° from the pickup. Here, a reactive feedback system is preferred. [2] The kicker is located at an even multiple of 90° from the pickup. In a two-particle model, where the bunch is represented by two macro-particles, the equations of motion are, in the first half of the synchrotron period,

$$\begin{aligned} \frac{d^2y_1}{dn^2} + (2\pi\nu_\beta)^2 y_1 &= \sigma(y_1 + y_2), \\ \frac{d^2y_2}{dn^2} + (2\pi\nu_\beta)^2 y_2 &= \sigma(y_1 + y_2) + \alpha y_1, \end{aligned} \tag{11.14}$$

where y_1 and y_2 are, respectively, the transverse displacements of the head and tail macro-particles, σ is the gain of the reactive feed back, and α represents the effect of the transverse wake from head to tail. Notice that the reactive feedback acts on the center of the bunch and is in phase with the particle displacements. It therefore modifies ν_β by introducing a tune shift. The instability threshold can then be raised by properly choosing the feedback strength σ. In low-energy

hadron machines, the space-charge tune shift constitutes a natural reactive feedback system which tends to shift the $m = -1$ mode downwards without affecting the $m = 0$ mode, making the two modes harder to meet with each other. We shall study this in more detail in the next section.

This instability can also be damped by Balakin–Novokhatsky–Smirnov (BNS) damping, [3] which delivers a betatron tune spread from the head of the bunch to the tail. This can be achieved by tilting the longitudinal phase space distribution of the bunch so that the tail has a lower energy relative to the head through chromaticity. Another method to implement BNS damping is to introduce a radio-frequency quadrupole magnet system, so that particles along the bunch will see a gradual shift in betatron tune.

11.2 Space-Charge and Mode-Coupling

It was reported by Blaskiewicz [4] that the space-charge tune shift can strongly damp the transverse mode-coupling instability (TMCI). The investigation was made on the basis of particle tracking. It can also be studied analytically using the solvable *square-well air-bag model*. [5] This is different from the air-bag model we used in the last section, although all the beam particles reside at the edge of the bunch. The formation of this model is sketched in Fig. 11.2. From a ring of particles in the longitudinal phase space on the left, the top semi-circle is stretched out and so is the lower semi-circle as illustrated in the right plot. The stretching continues until the top and lower semi-circles become two horizontal lines at energy offset $\pm\widehat{\Delta E}$. The lower one is described by the synchrotron phase ϕ from $-\pi$ to 0, while the upper one by ϕ from 0 to π, thus completing one synchrotron oscillation. Such a synchrotron oscillation requires, of course, a special rf potential. The bunch will be very long. The head is represented by $\phi = 0$ while the tail is represented by $\phi = \pm\pi$. We use the synchrotron phase ϕ

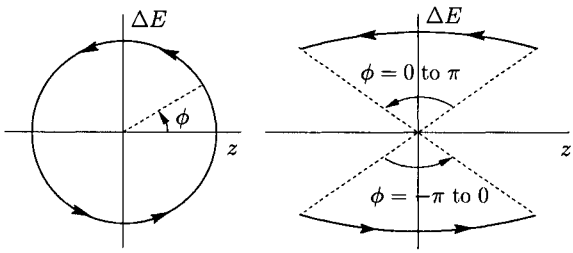


Fig. 11.2 The ordinary air-bag model (left) is transformed into the square-well air-bag model (right) by stretching out the upper and lower semi-circles until they become two infinite parallel lines at the energy spread $\pm\widehat{\Delta E}$. The longitudinal position of the particle remains specified by ϕ from $-\pi$ to 0 and from 0 to π.

and the energy offset ΔE as a set of variables for the description of the particle position in the longitudinal phase space. Although z remains the coordinate orthogonal to ΔE, the linear position of the particle can also be referenced by ϕ. The bunch particle distribution is given by

$$\psi(\phi, \Delta E) = \tfrac{1}{2}\lambda(\phi)\Big[\delta(\Delta E - \widehat{\Delta E}) + \delta(\Delta E + \widehat{\Delta E})\Big], \tag{11.15}$$

where $\lambda(\phi) = 1/(2\pi)$ is the projection onto the synchrotron phase.

What is going to be presented here is a qualitative explanation why the space-charge helps TMCI. Without space-charge, the bunch starts to be unstable when two neighboring synchro-betatron modes merge under the influence of the wake forces. Typically, the pure betatron mode (the azimuthal or synchrotron harmonic $m = 0$ mode, also known as the rigid-bunch mode) is affected by the wake force and shifts downward (from the bare betatron frequency or the incoherent betatron frequency), while the other azimuthal modes are not much affected, at least at low intensity. The transverse wake force produced by an off-axis beam has the polarity that deflects the beam further away from the pipe axis. This force acts as a defocusing force for the rigid-bunch mode, and therefore the frequency shifts downward. As a result, the instability threshold is determined by the coupling of the 0 and -1 modes as illustrated in Fig. 11.1.

The space-charge force by itself also shifts all the frequencies downward from the bare betatron frequency, as illustrated in Fig. 11.3. The only exception is the azimuthal $m = 0$ mode, which describes the motion of the bunch as a whole, and, therefore, is not influenced by the space-charge at all. Thus, in the presence of space-charge, the $m = 0$ mode will couple with the $m = -1$ mode at

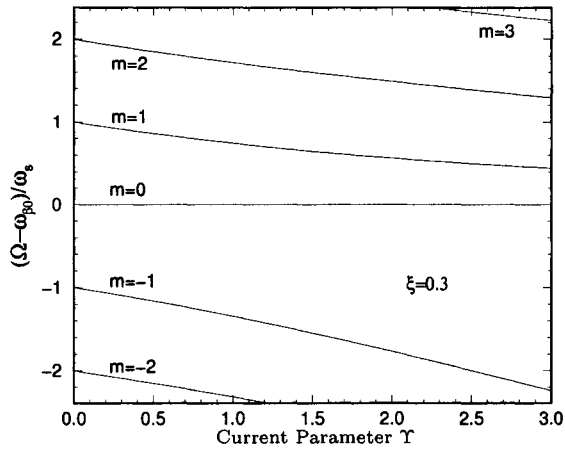


Fig. 11.3 The space-charge force in the absence of the wake forces shifts all modes downward with the exception of the $m = 0$ mode. All shifts are measured from the bare betatron frequency $\omega_{\beta 0}$.

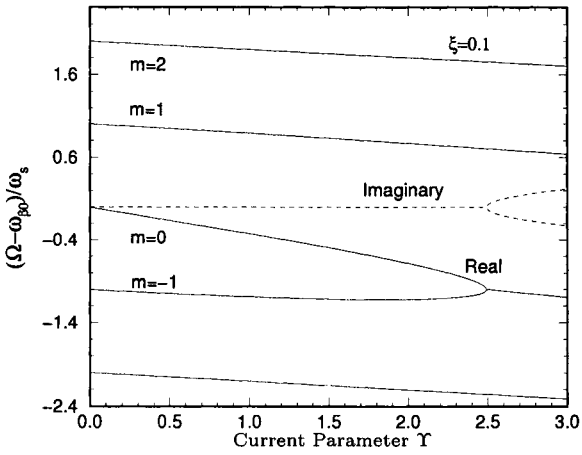


Fig. 11.4 The transverse space-charge force, added to the wake forces, shifts all azimuthal modes except the $m = 0$ mode downward, thus requiring the $m = 0$ and -1 modes to couple at a much higher current threshold $\Upsilon \approx 2.5$ (compared with $\Upsilon = 1.79$ in Fig. 11.1 where there is no space-charge). Note that the frequency shifts are measured from the bare betatron frequency $\omega_{\beta 0}$.

a higher current intensity and therefore the threshold is raised in the presence of space-charge. This is illustrated in Fig. 11.4.

Let us study the detail with mathematics. The transverse displacement $y(\phi; s)$ of a particle at the synchrotron phase ϕ satisfies the equation of motion:

$$\left[\frac{d^2}{ds^2} + k_{\beta 0}^2\right] y(\phi; s) = \langle F_1^{\perp}(\phi)\rangle + S\lambda(\phi)\big[y(\phi; s) - \bar{y}(\phi; s)\big], \tag{11.16}$$

where $k_{\beta 0} = \omega_{\beta 0}/v$ is the unperturbed or bare betatron wave number, $\omega_{\beta 0}/(2\pi)$ is the unperturbed betatron frequency, and the smooth approximation for the betatron oscillations has been applied. To incorporate synchrotron oscillation, the total time derivative takes the form

$$\frac{d}{ds} = \frac{\partial}{\partial s} + \frac{\omega_s}{v}\frac{\partial}{\partial \phi}, \tag{11.17}$$

with $\omega_s/(2\pi)$ being the synchrotron frequency. The right-hand side of Eq. (11.16) contains the transverse driving forces. The second term is the space-charge contribution. It is proportional to the linear density $\lambda(\phi)$ and the displacement relative to the local beam center, $y(\phi; s) - \bar{y}(\phi; s)$, with the constant S representing the space-charge strength. The first term is the transverse wake force

$$\langle F_1^{\perp}(\phi)\rangle = -\frac{N_b e^2}{E_0 C\beta^2}\left[\int_0^{\pi} - \int_0^{-\pi}\right] W_1[z(\phi') - z(\phi)]\lambda(\phi')\bar{y}(\phi'; s)d\phi', \tag{11.18}$$

where N_b is the number of particles in the bunch, W_1 is the transverse wake function, and $z(\phi)$ is the longitudinal position of the beam particle. The first

integral from $\phi' = 0$ to $+\pi$ is for the sampling of the particles with positive energy offset. The second integral from $\phi' = 0$ to $-\pi$ is for the sampling of the particles with negative energy offset. The negative sign before the integral signifies that the step $d\phi'$ is negative.

It is important to point out that, unlike Eqs. (11.1) and (11.4), all frequency shifts computed from Eq. (11.16) are measured from the bare betatron frequency $\omega_{\beta 0}$. Here, we have included the incoherent space-charge force $S\lambda(\phi)y(\phi;s)$ on the right side, which will generate the incoherent betatron frequency shift and also the static part of the coherent betatron frequency shift. On the other hand, the dynamic coherent space-charge force $S\lambda(\phi)\bar{y}(\phi;s)$ will generate the dynamic part of the coherent space-charge betatron frequency shift to cancel the static part. In contrast, Fig. 11.1 can also be viewed as a plot with the coherent frequency measured from the bare betatron frequency when any space-charge perturbation is omitted and the only driving force is the transverse wake force.

To solve the problem quantitatively, we expand the offset into the synchrotron harmonics (or azimuthals):

$$y(\phi;s) = \sum_{m=-\infty}^{\infty} y_m e^{i(m\phi - \Omega s/v)}, \tag{11.19}$$

where $\Omega/(2\pi)$ is the collective frequency shift to be determined. In this air-bag model, all particles reside at the edge of the bunch distribution in the longitudinal phase space. Note that because of the square-well air-bag model, these synchrotron azimuthals are slightly different from the conventional ones. The average offset at the synchrotron phase ϕ is therefore given by

$$\bar{y}(\phi;s) = \tfrac{1}{2}\Big[y(\phi;s) + y(-\phi;s)\Big] = e^{-i\Omega s/v} \sum_{m=-\infty}^{\infty} y_m \cos m\phi. \tag{11.20}$$

Now it is easy to transform the differential equation into an eigenvalue equation,

$$\left(\frac{\Omega - \omega_{\beta 0}}{\omega_s} - m\right) y_m = \Upsilon \sum_{m'=-\infty}^{\infty} y_{m'} \left(\mathcal{W}_{mm'} + \xi \mathcal{Q}_{mm'}\right), \tag{11.21}$$

where the current parameter Υ is defined in Eq. (11.8). The wake matrix elements are then given by

$$\mathcal{W}_{mm'} = -\frac{2}{\pi^3} \int_0^{\pi} d\phi \int_0^{\phi} d\phi' w[z(\phi') - z(\phi)] \cos(m\phi) \cos(m'\phi'), \tag{11.22}$$

where the wake function is presented as $W_1(z) = -\hat{W}_1 w(z)$ with $\hat{W}_1 > 0$ serving

as a normalizing constant. The space-charge parameter

$$\xi = \frac{\Delta\omega_\beta}{2\omega_s \Upsilon} \tag{11.23}$$

is the ratio of the incoherent tune shift

$$\Delta\omega_\beta = -\frac{S\lambda v^2}{2\omega_{\beta 0}} \tag{11.24}$$

to the current parameter Υ. It is therefore current independent and depends only on the transverse distribution of the beam. The space-charge matrix elements are

$$\mathcal{Q}_{mm'} = \delta_{mm'} - \delta_{m,-m'} \tag{11.25}$$

in the assumed air-bag distribution.

Again we choose the simplest step-like wake function $w(z) = H(z)$. The wake matrix can now be expressed analytically and turns out to be exactly the same as Eq. (11.10). This is to be expected because with the step-like wake, the square-well air-bag model is exactly the same as the ordinary air-bag model. The merit of this square-well air-bag model is reflected only through the simplicity of the space-charge matrix.

Without space-charge ($\xi = 0$), the mode-coupling of $m = 0$ and $m = -1$ occurs at $\Upsilon = 1.79$ as illustrated in Fig. 11.1. We recall that only mode $m = 0$ is shifted downwards and all other modes are essentially not affected. On the other hand, space-charge force in the absence of wake forces shifts all modes downwards except for mode $m = 0$, which is almost unaffected because the center of the beam does not see any charge in wake-field pattern in the rigid-dipole mode. This is illustrated in Fig. 11.3 with the space-charge parameter $\xi = 0.3$. Thus the effect of space-charge is to delay the collision of mode $m = 0$ and $m = 1$. We see in the left plot of Fig. 11.4 that the instability threshold has been pushed up to $\Upsilon = 2.49$ at $\xi = 0.1$ as compared with Fig. 11.1 where there is no space-charge.

Further increasing the space-charge parameter to $\xi = 0.16$, we see in Fig. 11.5 that modes $m = 0$ and -1 do not merge any more. The critical moment occurs at $\xi = 0.159$. What is not shown in the plot are much higher new thresholds where modes $m \geq 0$ couple in pairs. For example, at $\xi = 0.18$, mode $m = 0$ couples with mode $m = 1$, mode $m = 2$ couples with mode $m = 3$, mode $m = 4$ couples with mode $m = 5$, mode $m = 6$ couples with mode $m = 7$, etc. all near $\Upsilon \approx 35$, which implies an avalanche of instabilities. However, the threshold of the avalanche is rather sensitive to the number of modes at which the matrix is

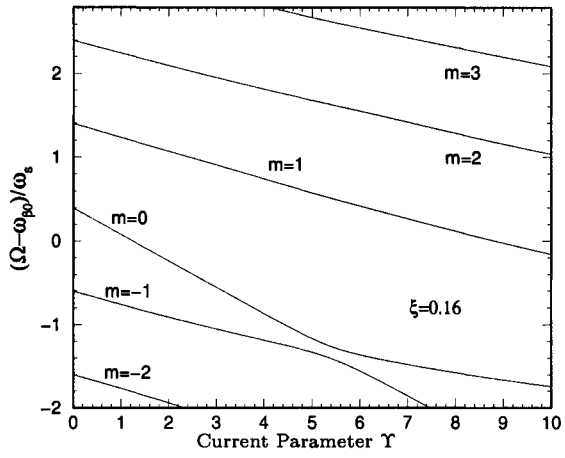


Fig. 11.5 When space-charge coefficient reaches the critical value of $\xi = 0.159$, the $m = -1$ mode is shifted away from the $m = 0$ mode by so much that they do not couple anymore. Note that the frequency shift are measured from the bare betatron frequency $\omega_{\beta 0}$.

truncated. In any case, this simplified wake-beam model illustrates how space-charge is able to increase the threshold of transverse coupled-mode instability and the increase can be an order of magnitude.

As was discussed in the previous section, a reactive feedback shifts mode $m = 0$ upwards resulting in pushing the threshold to a higher current. Here, the space-charge force shifts all the modes downwards except $m = 0$, and the result is also to have the threshold pushed towards a higher current. Therefore, the space-charge tune shift in a proton machine, as discussed above, constitutes a natural inverse reactive feedback.

11.3 Two-Particle Model

It is very informative to understand the mechanism of the mode-coupling instabilities; for example, how synchrotron oscillation helps stability and how the stability threshold arises. To do this let us consider the simple two-particle model. [6] The bunch with N_b particles is represented by two macro-particles each carrying charge $\frac{1}{2}eN_b$. First, let us consider the situation when there is no external transverse focusing nor longitudinal focusing. If the head particle has a deviation from the axis of the beam pipe, it leaves a transverse wake so that the tail particle will be kicked transversely all the time. The result is a banana-tilted bunch with the tail curling sideways more and more until it hits the beam pipe. With external transverse focusing but without longitudinal focusing, a slightly off-axis head particle will perform betatron oscillation. The wake generated will force the tail to oscillate with the same betatron frequency with its amplitude

increasing linearly until the tail hits the beam pipe. We see that the tail of the bunch will always be unstable transversely.

The picture becomes completely different when we turn on longitudinal focusing, because the particles exchange their head and tail positions. Assume that the head and tail particles are always separated by $\hat{z}$ for one half of a synchrotron period T_s and exchange position for the other half. We have during $0 < s/v < T_s/2$,

$$\begin{aligned} &\frac{d^2y_1}{ds^2} + k_\beta^2 y_1 = 0, \\ &\frac{d^2y_2}{ds^2} + k_\beta^2 y_2 = -\frac{e^2 N_b W_1(\hat{z})}{2E_0 C_0} y_1, \end{aligned} \tag{11.26}$$

where E_0 is the synchronous energy, C_0 is the ring's circumference, $W_1(\hat{z}) < 0$ is the transverse wake at $\hat{z}$ behind the source, and s is the distance along the ring, has been used as the 'time' variable. Here k_β is the incoherent betatron wavenumber. To reduce the size of the transfer matrix from 4 to 2, it is convenient to introduce the phasors of the two particles,

$$\tilde{y}_\ell = y_\ell + i\frac{y'_\ell}{k_\beta}, \qquad \ell = 1, 2. \tag{11.27}$$

The solution is (Exercise 11.1)

$$\begin{aligned} &\tilde{y}_1(s) = \tilde{y}_1(0)e^{-ik_\beta s}, \\ &\tilde{y}_2(s) = \tilde{y}_2(0)e^{-ik_\beta s} - i\frac{e^2 N_b W_1(\hat{z})}{4E_0 C_0 k_\beta}\left[\frac{\tilde{y}_1^*(0)}{k_\beta}\sin(k_\beta s) + \tilde{y}_1(0)\, s\, e^{-ik_\beta s}\right], \end{aligned} \tag{11.28}$$

where the last term grows linearly with s and is certainly much larger than the term with $\sin(k_\beta s)$ because $\omega_\beta T_s/2 = \pi\omega_\beta/\omega_s \gg 1$. Dropping the term with $\sin(k_\beta s)$, the solution can be rewritten as

$$\begin{pmatrix} \tilde{y}_1 \\ \tilde{y}_2 \end{pmatrix}_{s=vT_s/2} = e^{-i\omega_\beta T_s/2} \begin{pmatrix} 1 & 0 \\ i\Upsilon & 1 \end{pmatrix} \begin{pmatrix} \tilde{y}_1 \\ \tilde{y}_2 \end{pmatrix}_{s=0}, \tag{11.29}$$

where

$$\Upsilon = -\frac{\pi e^2 N_b W_1(\hat{z}) v^2}{4E_0 C_0 \omega_\beta \omega_s}, \tag{11.30}$$

the same as given by Eq. (11.8) in the uniform-focusing approximation, is the response of particle 2 in half a synchrotron period.

During the other half of the synchrotron period, $T_s/2 < s/v < T_s$, the equations of motion become

$$\frac{d^2y_1}{ds^2} + k_\beta^2 y_1 = \frac{e^2 N_b W_1(\hat{z})}{2E_0 C_0} y_2,$$
$$\frac{d^2y_2}{ds^2} + k_\beta^2 y_2 = 0, \tag{11.31}$$

so that for one synchrotron period,

$$\begin{pmatrix} \tilde{y}_1 \\ \tilde{y}_2 \end{pmatrix}_{s=vT_s} = e^{-i\omega_\beta T_s} \begin{pmatrix} 1 & i\Upsilon \\ 0 & 1 \end{pmatrix} \begin{pmatrix} 1 & 0 \\ i\Upsilon & 1 \end{pmatrix} \begin{pmatrix} \tilde{y}_1 \\ \tilde{y}_2 \end{pmatrix}_{s=0}. \tag{11.32}$$

The two eigenvalues are

$$\lambda_\pm = e^{\pm i\phi}, \qquad \sin\frac{\phi}{2} = \frac{\Upsilon}{2}, \tag{11.33}$$

and stability requires $\Upsilon \leq 2$.

Let us analyze the mechanism of the two-particle model and see how stability can be achieved when $\Upsilon \leq 2$. When particle 1 is at the head, it will drive particle 2 at the tail with a linear rise in betatron amplitude for half a synchrotron period, during which particle 1 leads particle 2 in betatron phase by 90°. During the second half of the synchrotron period, particle 2 is at the head position and particle 1 is at the tail position. However, the phase relationship between the two particles has not been changed and particle 2 still lags particle 1 by 90°. Thus particle 2 is forced-damping particle 1 instead. If the wake is strong enough or the half-synchrotron period is long enough, eventually the betatron amplitude of particle 1 will be damped to zero and start growing again with its betatron phase now lags that of particle 2 by 90°. Unlike a linac where the particle at the tail is driven to grow continuously by the particle at the head, here as the longitudinal positions of the two particles are exchanged, the new tail-particle will be damped to zero first before its amplitude is driven to grow. As a result, if the driving force from the wake is not large enough and/or the synchrotron period is not long enough, there can be no accumulation in amplitude growth and the two-particle bunch remains stable. A stability condition is such that both particles have the same betatron amplitudes $\hat{y}$ at the end of each half-synchrotron period with the particle at the tail lagging the particle at the head by 90°. Since the driving force of the head particle needs to damp the tail particle from amplitude $\hat{y}$ to zero first and then drive it to $\hat{y}$ again, the total growth in amplitude for each half-synchrotron period, including the damping plus growing portions, should be equal to $2\hat{y}$. Since the response of the tail particle in half a synchrotron period is Υ, we arrive at the stability

condition $\Upsilon \leq 2$, which agrees very well with $\Upsilon \lesssim 1.79$ for the air-bag model shown in Fig. 11.1.

To demonstrate the damping followed by growth during a half-synchrotron period, we perform simulation of the turn-by-turn motion of the two particles. In Fig. 11.6, we show the magnitudes of the phasors for the two particles at every time step (100 per betatron period). The current parameter has been chosen as $\Upsilon = 1.95$. Every horizontal bar represents half a synchrotron period. We see that for the first half-synchrotron period, the amplitude of particle 1 (dark) is unchanged at 1 unit,* while the phasor amplitude of particle 2 (light) is driven to more than 2 units. In the next half-synchrotron period, the amplitude of the light phasor is unchanged while the dark one is driven to about 3.5 units. In the later half-synchrotron periods, we always see the amplitude of one phasor damped to almost zero first before it increase again, in agreement with our discussion above.

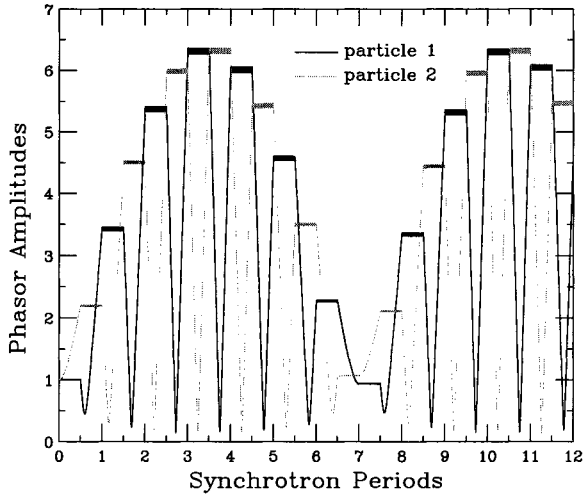


Fig. 11.6 Phasor amplitudes of the two particles in the two-particle model, starting with both particles offset by 1 unit. The simulation is performed with $\Upsilon = 1.95$. In the first half-synchrotron period, amplitude of phasor 1 (dark) at the head is unchanged, but amplitude of phasor 2 (light) at the tail is driven to more than 2 units. In the second half-synchrotron period, amplitude of phasor 1 is first damped and then grows to about 3.5 units.

11.4 Longitudinal Mode-Coupling

The azimuthal modes are not a good description of the collective motion of the bunch when the beam current is high enough. Therefore there is also mode-coupling in the longitudinal motion. Similar to the transverse coupled problem

*Actually, the amplitudes of the phasors have small fluctuations and the horizontal bars in Fig. 11.6 have a finite thickness. This is because there is a finite number of steps in each betatron period and first-order mapping has been used.

in Eqs. (11.1) and (11.2), we have here

$$(\Omega - m\omega_s)\delta_{mm'}\delta_{kk'} = M^{\parallel}_{mm'kk'}\omega_s, \tag{11.34}$$

where, with the aid of Eq. (9.93), the interaction matrix is defined as

$$M^{\parallel}_{mm'kk'} = \frac{im}{1+m}\frac{4\pi^2 eI_b\eta}{3\beta^2 E_0\omega_s^2\tau_L^3}\frac{\int d\omega \dfrac{Z_0^{\parallel}(\omega)}{\omega}\tilde{\lambda}_{m'k'}(\omega)\tilde{\lambda}^*_{mk}(\omega)}{\int d\omega\tilde{\lambda}_{mk}(\omega)\tilde{\lambda}^*_{mk}(\omega)}, \tag{11.35}$$

where we are going to use Sacherer's sinusoidal modes and only the most prominent radial modes ($k = 0$) will be retained. The impedance will be broadband so that the discrete summations over the synchrotron sidebands are replaced by integrals. This interaction matrix was originally derived by Sacherer [7] and Laclare. [8] We notice that the the numerical coefficient differs slightly from that in Eq. (9.88); however, it is only bigger by the factor $\pi^2/9$, which is not much.

Exactly the same as in the transverse situation, only $\mathcal{I}m\, Z_0^{\parallel}(\omega)/\omega$ contributes to the diagonal elements of the coupling matrix and thus to the real frequency shifts of the modes. The coupling of two modes, mostly adjacent, will give instability, which is determined by $\mathcal{R}e\, Z_0^{\parallel}(\omega)/\omega$ in the off-diagonal elements next to the diagonal ones. All the discussions about bunch-length dependency on threshold in the transverse case apply here as well. For a short bunch, the instability is caused by mode $m = 2$ shifting downward to meet with mode $m = 1$. A rough estimate of the threshold can be obtained from Eq. (11.35) by equating the frequency shift to ω_s after taken into account the factor $m/(1+m)$ with $m = 2$:

$$\frac{2}{3}\eta_2 = \frac{2}{3}\frac{4\pi^2 eI_b\eta}{3\beta^2 E_0\omega_s^2\tau_L^3}\left.\frac{Z_0^{\parallel}}{\omega}\right|^m_{\text{eff}} \approx 1, \tag{11.36}$$

where the effective longitudinal impedance for mode m is defined as

$$\left.\frac{Z_0^{\parallel}}{\omega}\right|^m_{\text{eff}} = \frac{\int d\omega \dfrac{Z_0^{\parallel}(\omega)}{\omega}h_m(\omega)}{\int d\omega\, h_m(\omega)}. \tag{11.37}$$

11.4.1 *Long Bunches*

For convenience, let us introduce the parameter $x = \omega\tau_L/\pi$, which is the unit of frequency measurement in the plot of the sinusoidal modes in Fig. 6.13. We see that with the exception of $m = 0$ which is not an allowed mode in the

longitudinal motion, the mth mode of excitation peaks at $x \approx m + 1$ and has a half width of $\Delta x \approx 1$. Now consider the Fermilab Main Ring with a revolution frequency 47.7 kHz and total bunch length $\tau_L \approx 2$ ns. Assume the impedance to be broadband centered at $x_r = 7.5$ or $f_r \sim 1.88$ GHz and quality factor $Q = 1$. The elements of the interaction matrix $M^{\parallel}_{mm'}$ can now be computed using Sacherer's sinusoidal modes. The matrix is truncated by including up to the $m = 20$ mode. Numerical diagonalization is next performed and the eigenmodes are depicted in Fig. 11.7. [10] as functions of current intensity. The collective frequencies of the azimuthal modes are plotted in a scale normalized to ω_{s0}, the bare synchrotron frequency, and the incoherent synchrotron frequency shifts have been added.

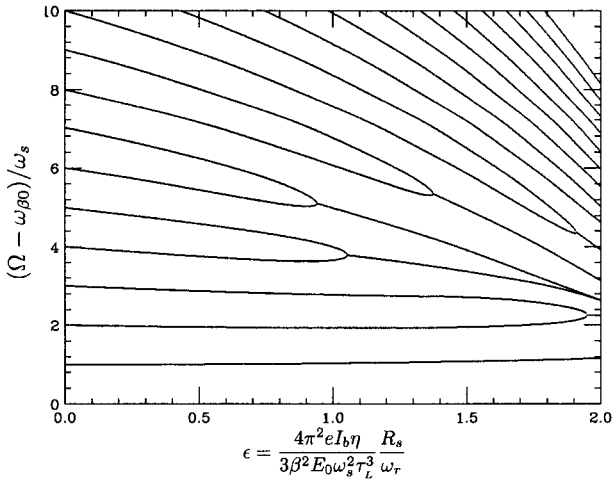


Fig. 11.7 A long bunch has its azimuthal modes $m = 6$ and 7 coupled longitudinally in the presence of a resonance at $x_r = 7.5$ and $Q = 1$ above transition. Note that the eigenfrequencies are normalized to the bare synchrotron frequency.

We see the first instability occurs when mode $m = 6$ couples with mode $m = 7$, and in the vicinity of the threshold, there are also couplings between modes $m = 4$ and 5 and modes $m = 8$ and 9. This happens because the resonance centered at $x_r = 7.5$ has a half width $\Delta x_r = x_r/(2Q) = 3.75$. Thus the $\mathcal{R}e\, Z_0^{\parallel}/\omega$ resonant peak encompasses modes $m = 4$ to 9, which peak at $x = 5$ to 10. This is a typical picture of mode-coupling instability for long bunches. From the figure, the first instability occurs at

$$\epsilon = \frac{4\pi^2 e I_b \eta}{3\beta^2 E_0 \omega_s^2 \tau_L^3} \frac{R_s}{\omega_r} \approx 0.93, \tag{11.38}$$

which agrees with the estimate of $\eta_2 \approx 1$ made in Eq. (11.36), where $m/(1+m) \approx 1$ when m is large. On the other hand, the Keil–Schnell criterion of Eq. (5.23)

gives a threshold of

$$\frac{eI_b\eta}{\beta^2 E_0\omega_s^2\tau_L^3}\frac{R_s}{\omega_r} = \frac{1}{6\pi}\frac{1}{F}, \tag{11.39}$$

where F is the Keil–Schnell form factor. This is equivalent to

$$\epsilon = \frac{2\pi}{9}\frac{1}{F}. \tag{11.40}$$

Thus, the mode-coupling threshold is very close to the Keil–Schnell threshold. However, mode-coupling instability is quite different from microwave instability. In the latter, pure reactive impedance can drive an instability; for example, the negative-mass instability just above transition is driven by the space-charge force. It can be demonstrated that pure capacitive or inductive impedance will only lead to real frequency shifts of the modes. Although two modes may cross each other, they will not be degenerate to form complex modes. Thus, there is no instability (Exercise 11.2).

The low azimuthal modes sample the inductive part of the broadband impedance and have their dynamic coherent frequencies shifted upward, while high azimuthal modes sample the capacitive part and have their dynamic coherent frequencies shifted downward. The change in shift-direction should occur around the resonant frequency of the broadband impedance. However, because of the added downward shifting static coherent frequency shifts, which equal the incoherent frequency shifts, the coherent frequencies of all modes gradually shift downward more and more with increasing azimuthal number, except for the $m = 1$ mode that does not shift, at least when the beam intensity is small.

11.4.2 *Short Bunches*

When the bunch is short, for example, electron bunches, the modes of excitation spread out to higher frequencies. Therefore, when the bunch is short enough, the resonant peak of $\mathcal{R}e\, Z_0^{\parallel}/\omega$ will encompass only modes $m = 1$ and 2. Thus, we expect these two modes will collide first to give instability. The $m = 1$ is the dipole mode and is not shifted at low beam current because the bunch center does not see any reactive impedance. The $m = 2$ is the quadrupole mode, which is shifted downward above transition. This downshift is a way to measure the reactive impedance of the ring. The rough threshold has been given by Eq. (11.36), or $\frac{2}{3}\eta_2 \approx 1$.

When the beam current is above threshold and instability starts, the energy spread increases and so does the bunch length. In an electron ring where there is radiation damping, there is no overshoot and the increase stops when the sta-

bility criterion is fulfilled again. The bunch lengthening is therefore determined by the stability criterion. If the bunch samples the impedance at a frequency range where $Z_0^{\parallel}(\omega) \propto \omega^a$, the effective impedance is

$$\left.\frac{Z_0^{\parallel}}{\omega}\right|_{\text{eff}} \propto \frac{\int d\omega\, \omega^{a-1} h_m(\omega)}{\int d\omega\, h_m(\omega)} \propto \tau_L^{1-a}, \tag{11.41}$$

where use has been made of the fact that the power spectrum h_m is a function of the dimensionless quantity $\omega\tau_L$ according to Eq. (9.101) and the result is independent of the functional form of h_m. From the threshold condition in Eq. (11.36), we have

$$\frac{4\pi^2 e I_b \eta}{3\beta^2 E_0 \omega_s^2 \tau_L^{2+a}} = \text{constant independent of } I_b,\ \eta,\ E_0,\ \omega_s,\ \tau_L. \tag{11.42}$$

Thus the bunch length obeys the scaling criterion of

$$\tau_L \propto \xi^{1/(2+a)}, \tag{11.43}$$

where

$$\xi = \frac{\eta I_b}{\nu_s^2 E_0} \tag{11.44}$$

is the scaling parameter introduced by Chao and Gareyte. [6]

Longitudinal mode-coupling is different from transverse mode-coupling. In the latter, the betatron frequency ($m = 0$) is shifted downward to meet with the $m = -1$ mode. The amount of shift is small, since $\nu_s/[\nu_\beta] \ll 1$, where $[\nu_\beta]$ is the residual betatron tune. Transverse mode-coupling has been measured in many electron rings and the results agree with theory. In the longitudinal case, the synchrotron quadrupole frequency ($m = 2$) has to be shifted downward to meet with the synchrotron dipole frequency ($m = 1$) and this shift is 100% of the synchrotron tune. At the CERN LEP which is above transition, we expect the synchrotron quadrupole mode to shift downward when the beam current increases from zero. However, it was observed that this mode shifts slightly upward instead. Since the dipole frequency is not shifted, it is hard to visualize how the two modes will be coupled. Some argue that the coupling may not be between two azimuthal modes, but instead between two radial modes that we have discarded in our discussion. But the coupling between two radial modes is generally much weaker. Some say that the actual coupling of the two modes has never been observed experimentally, and the scaling law for bunch

lengthening may have been the result of some other theories. Anyway, the theory of longitudinal mode-coupling is far from satisfactory.

11.5 TMCI for Long Bunches

11.5.1 *High Energy Accelerators*

Transverse mode-coupling instability occurs in almost all electron machines. However, except for a possibility at the CERN Super Proton Synchrotron (SPS) to be discussed later in Sec. 11.5.3, it has never been observed in hadron machines. In this section, we would like to analyze how this instability would affect the higher energy accelerators under design.

For protons, particle energy E_0 is directly proportional to the size of the accelerator. So we have

$$E_0 \propto R \quad \text{and} \quad \omega_0 \propto \frac{1}{R}. \tag{11.45}$$

The resistive-wall impedance is

$$\frac{Z_0^{\parallel}}{n} = [1 - i\,\mathrm{sgn}(\omega)]\frac{R\rho}{nb}\sqrt{\frac{\mu\omega}{2\rho}}, \tag{11.46}$$

where ρ is the resistivity and μ the magnetic permeability of the beam pipe of radius b. At a fixed frequency ω, we have

$$\frac{Z_0^{\parallel}}{n} \sim \frac{1}{b\sqrt{\omega}}, \tag{11.47}$$

$$Z_1^{\perp} \sim \frac{R}{b^3\sqrt{\omega}}. \tag{11.48}$$

For M pairs of strip-line BPMs at low frequencies $\omega \lesssim c/\ell$, where ℓ is the length of the strip lines, [11]

$$\frac{\mathcal{I}m\, Z_0^{\parallel}}{n} = -i2MZ_c\left(\frac{\phi_0}{2\pi}\right)^2\frac{\ell}{R}, \tag{11.49}$$

$$\mathcal{I}m\, Z_1^{\perp} = \frac{c}{2b^2}\left(\frac{4}{\phi_0}\right)^2 \sin^2\frac{\phi_0}{2}\frac{\mathcal{I}m\, Z_0^{\parallel}}{\omega}. \tag{11.50}$$

where Z_c is the characteristic impedance and ϕ_0/π is the fraction of the beam pipe covered by the strip lines. The betatron functions $\beta_{x,y}$ scale as $\sqrt{R}$. Thus, the betatron tunes and the number of BPMs required also scale as $\sqrt{R}$. At a

fixed frequency we have

$$\frac{\mathcal{I}m\, Z_0^{\parallel}}{n} \sim \frac{\ell}{\sqrt{R}}, \tag{11.51}$$

$$\mathcal{I}m\, Z_1^{\perp} \sim \frac{\ell}{b^2}\sqrt{R}. \tag{11.52}$$

We see that when the size of an accelerator is increased, the resistive-wall impedance will dominate over all other contributions. We also see that $Z_0^{\parallel}/n$ at a fixed frequency remains roughly independent of the size of the accelerator. From now on, we will consider resistive-wall impedance only.

The Keil–Schnell criterion for longitudinal microwave instability is

$$\left|\frac{Z_0^{\parallel}}{n}\right| < \frac{2\pi|\eta|E_0\sigma_\delta^2}{eI_{\rm pk}}. \tag{11.53}$$

For a large accelerator, the energy is usually very much larger than the transition energy. The slip factor $\eta \sim \gamma_t^{-2} \sim \nu_\beta^{-2}$ for a FODO lattice. We therefore have $\eta \sim R^{-1}$. The peak current is $I_{\rm pk} \sim N_b/\sigma_\tau$. Putting in the wall resistivity at $\omega \sim \sigma_\tau^{-1}$, the stability criterion takes the form

$$\frac{\sqrt{\sigma_\tau}}{b} \lesssim \frac{A\sigma_\delta}{N_b R}, \tag{11.54}$$

where the bunch area in eV-s is

$$A \propto E_0\sigma_\delta\sigma_\tau. \tag{11.55}$$

For an accelerator of higher energy, if we want to have roughly the same fractional energy spread and bunch length, the bunch area will scale as R. The above stability criterion becomes

$$\frac{\sqrt{\sigma_\tau}}{b} \lesssim \frac{\sigma_\tau\sigma_\delta^2}{N_b}. \tag{11.56}$$

This leads to the conclusion that longitudinal microwave instability will not worsen for higher energy accelerators.

Now let us turn to transverse mode-coupling instability and consider Eq. (11.12), which we rewrite as a stability criterion

$$Z_1^{\perp}\big|_{\rm eff} \lesssim \frac{4\pi E_0\omega_0\nu_\beta\nu_s\tau_L}{e^2N_bc}. \tag{11.57}$$

The effective impedance on the left side will be taken as the resistive-wall impedance of Eq. (11.48) multiplied by a constant. When we substitute $E_0 \sim R$,

$\omega_0 \sim 1/R$, and $\nu_\beta \sim \sqrt{R}$, we obtain

$$\frac{R\sqrt{\sigma_\tau}}{b^3} \lesssim \frac{\sqrt{R}\nu_s\sigma_\tau}{N_b}. \tag{11.58}$$

Thus, transverse mode-coupling instability will occur when the size of the accelerator becomes bigger and bigger.

According to all the accelerator rings ever built, for electron machines, particle energy scales as $E_0 \sim \sqrt{R}$ instead. This implies that there will be no $\sqrt{R}$ on the right side of Eq. (11.58), or

$$\frac{R\sqrt{\sigma_\tau}}{b^3} \lesssim \frac{\nu_s\sigma_\tau}{N_b}, \tag{11.59}$$

and the instability will come at a smaller accelerator size. This may explain why electron machines are more susceptible for transverse mode-coupling instabilities. For the longitudinal microwave instability, Eq. (11.56) becomes

$$\frac{\sqrt{\sigma_\tau}}{b} \lesssim \frac{\sigma_\tau\sigma_\delta^2}{N_b\sqrt{R}}, \tag{11.60}$$

showing that this instability will worsen as the size of the ring increases. For electron rings, because of the short bunch length, the longitudinal mode-coupling instability is more of interest. The stability condition for azimuthal modes $m = 2$ and 1 colliding is given by Eq. (6.73), or

$$\left|\frac{Z_0^\parallel}{n}\right|_{\text{ind}} \lesssim \frac{4\pi\nu_s^2\omega_0^2\hat{\tau}^3\beta^2E_0}{3e^2N_b|\eta|}. \tag{11.61}$$

Assuming again that the resistive-wall impedance dominates, we obtain

$$\frac{\sqrt{\sigma_\tau}}{b} \lesssim \frac{\nu_s^2\sigma_\tau^3}{N_b\sqrt{R}}, \tag{11.62}$$

again showing that this threshold becomes more severe for a larger ring.

In Chapter 9, we showed that for a proton ring, the growth rate for transverse coupled-bunch instability driven by the resistive-wall impedance should be more or less independent of the size of the accelerator ring. However, for electron rings we have $E_0 \propto \sqrt{R}$ instead. The growth rate for this instability now increases according to $\sqrt{R}$ for large electron rings. The growth time in revolution turns therefore decreases according to $R^{-3/2}$, making it much harder for the feedback damper to damp the instability in Very Large Lepton Colliders (VLLC) than in Very Large Hadron Colliders (VLHC).

11.5.2 *TMCI Threshold for Present Proton Machines*

For the future very large hadron machines, as was discussed above, the coupling impedance will be dominated by the resistive-wall of the vacuum chamber. However, for the hadron machines in existence, the coupling impedance is dominated by a broadband resonance centered around the cutoff frequency, which includes the contributions of BPMs, bellows, pump ports, etc. Transverse mode-coupling instability will occur when the peak of this broadband impedance couples the two azimuthal modes flanking the resonance peak, with frequencies slightly below and slightly above the resonance frequency $\omega_r/(2\pi)$, exactly in the same way in the longitudinal instability we studied before in Sec. 11.4.1. Thus the instability occurs for modes m and $m+1$ with

$$1 + m \approx \frac{\omega_r \tau_L}{\pi}, \tag{11.63}$$

if the Sacherer's sinusoidal modes are assumed. These modes will collide and initiate a transverse mode-coupling instability if they moves up or down by the amount $\alpha\omega_s$, where $0 \lesssim \alpha \lesssim 1$. According to Sacherer's integral equation (11.2), stability against transverse mode-coupling requires roughly

$$\frac{1}{|1+m|} \frac{e^2 N_b}{2\beta T_0 E_0 \tau_L} [\beta_\perp |Z_1^\perp|] \lesssim \alpha\omega_s, \tag{11.64}$$

where $|Z_1^\perp|$ is the peak value of the broadband impedance. Substituting for $|1+m|$ from Eq. (11.63) and taking the uniform focusing approximation $\beta_\perp = R/\nu_\beta$, the stability requirement becomes

$$\frac{e^2 N_b c |Z_1^\perp|}{4\alpha E_0 \nu_\beta \omega_r \omega_s \tau_L^2} \lesssim 1. \tag{11.65}$$

We can express this in terms of the longitudinal emittance

$$A = \pi \frac{\tau_L}{2} \Delta E, \tag{11.66}$$

where ΔE is the half energy spread of the bunch. Recalling that

$$\omega_s \frac{\tau_L}{2} = |\eta| \frac{\Delta E}{\beta^2 E_0}, \tag{11.67}$$

the threshold of the bunch intensity becomes

$$N_b^{\text{th}} = \frac{16\alpha}{\pi} \frac{|\eta| \omega_r \nu_\beta A}{\beta^2 e^2 c |Z_1^\perp|}. \tag{11.68}$$

Because of the form factor $F_m = (1+m)^{-1}$, the coupling of the azimuthal modes will be weaker when m is larger. Recalling that the slow waves associated with negative frequencies are responsible to drive instabilities, this can be accomplished by introducing chromaticity to shift the spectra of the the azimuthal modes to the left (higher frequencies) so that the resonant impedance at negative frequencies will couple modes of higher azimuthal. Thus above transition, positive chromaticity ξ must be applied to ensure stability, and this amounts to sifting ω_r to $\omega_r + \omega_\xi$, where the chromatic angular frequency is defined as

$$\omega_\xi = \frac{\xi \omega_0}{\eta}. \tag{11.69}$$

Correspondingly, the mode-coupling threshold increases to

$$N_b^{\text{th}} = \frac{16\alpha}{\pi} \frac{|\eta|\omega_r \nu_\beta A}{\beta^2 e^2 c |Z_1^\perp|} \left(1 + \frac{\omega_\xi}{\omega_r}\right). \tag{11.70}$$

Métral [12] derived this threshold more carefully by performing the coupling integrals for the interaction matrix. His result is the same as above but with $\alpha = \pi/4$.

11.5.3 *Possible Observation*

The absence of transverse mode-coupling instability in the hadron machines that have ever built is generally explained by the following three mechanisms: (1) the intensity threshold for the longitudinal microwave instability is generally lower than for the transverse mode-coupling instability, (2) the intensity threshold due to mode-coupling between the two lowest azimuthal modes increases with the presence of the transverse space-charge force, and (3) the intensity threshold increases with bunch area as demonstrated by Eq. (11.70). Nevertheless, a fast vertical instability reported in the CERN Super Proton Synchrotron (SPS) in 2003 may be a possible candidate.

Right after injection at 26 GeV/c, the high-intensity proton bunches ($N_b \sim 1.2 \times 10^{11}$ per bunch) with low longitudinal emittance ($A \sim 0.2$ eV-s) lost 20 to 30% their intensity after less than one synchrotron period ($T_s = 7.2$ ms). This instability, however, could be avoided by raising the vertical chromaticity ξ_y. The left plot of Fig. 11.8 shows the observed relative intensities for the first 50 ms following injection at $t = 0$ ms at nearly zero chromaticity, while the right plot shows the beam loss avoided at the chromaticity of $\xi_y = 0.8\nu_y$ with vertical betatron tune $\nu_y = 26.13$. Initially, the full bunch length was $\tau_L = 4\sigma_\tau = 2.7$ ns and the longitudinal bunch emittance was $A = \frac{1}{2}\pi\tau_L\Delta E = 0.2$ eV-s, where

ΔE is the half energy spread. The slip factor was $\eta = 6.180 \times 10^{-4}$ and the revolution frequency was $f_0 = 43.35$ kHz. A chromaticity scan was performed and the fractional beam loss was recorded. The result in the left plot of Fig. 11.9 shows the sharp drop of beam loss as vertical chromaticity increases.

The vertical dipole impedance of the SPS can be modeled by a broadband resonator with $|Z_1^{\perp}| = 20$ MΩ/m at $\omega_r/(2\pi) = 1.3$ GHz. At zero chromaticity,

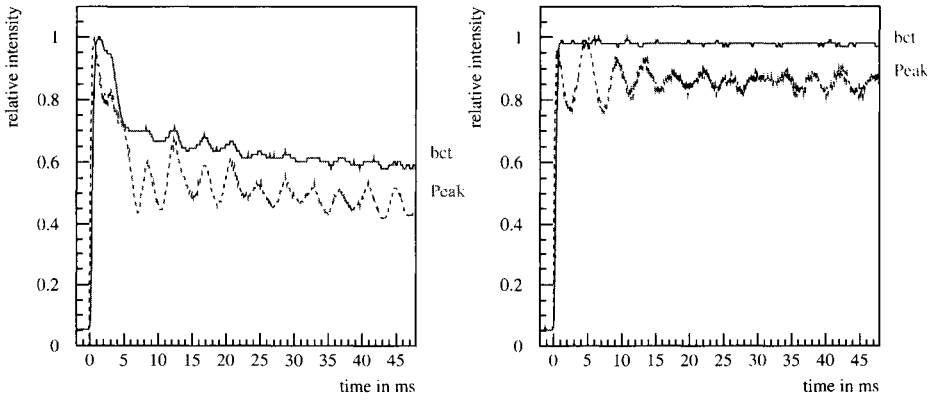


Fig. 11.8 Left: Heavy beam loss within a synchrotron period of 7.2 ms after injection into the CERN SPS at nearly zero vertical chromaticity. Right: Beam loss has been avoided when the vertical chromaticity was raised to $\xi_y = 0.8\nu_y$. Initial intensity was 1.2×10^{11} per bunch, longitudinal emittance was $A = 0.2$ eV-s, and full bunch length was $\tau_L = 4\sigma_\tau = 2.7$ ns. (Courtesy Burkhardt, *et al.* [13])

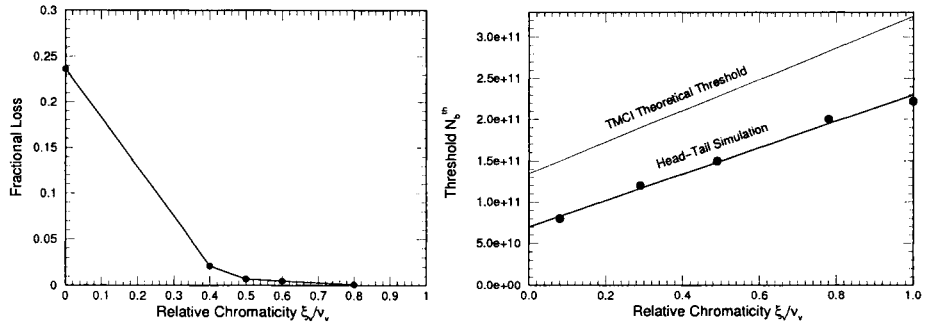


Fig. 11.9 Left: Fractional beam loss as a function of relative vertical chromaticity ξ_y/ν_y. Beam loss has been eliminated when $\xi_y/\nu_y \gtrsim 0.8$. Right: Stability threshold versus relative vertical chromaticity when analyzed as transverse head-tail. The theoretical threshold when analyzed as transverse mode-coupling using Eq. (11.70) is also shown. A slightly larger longitudinal emittance has been used. (Courtesy Burkhardt, *et al.* [13])

Eq. (11.70) gives a threshold of $N_b^{\rm th} = 1.1 \times 10^{11}$ per bunch. On the other hand, with $\xi_y = 0.8\nu_y$, the threshold is increased by the factor of 2.13. So far agreement with experimental observation has been quite satisfactory. Nevertheless, it is still too early to draw the conclusion that this has been a transverse mode-coupling instability. This is because if this observation is analyzed as transverse head-tail instability, the intensity threshold is also comparable to the theoretical threshold given by Eq. (11.70) for transverse mode-coupling instability and also increases linearly with chromaticity as depicted in the right plot of Fig. 11.9, where a slightly larger longitudinal emittance has been used. In addition, the effect of space-charge has not been included in this analysis. A more concrete verification of transverse mode-couple instability will be the monitoring of the synchrotron sidebands. By recording their frequency positions as functions of intensity, we can determine whether the transverse instability occurs when two sidebands meet each other. It will also be nice to monitor the frequency of the instability signal and determine the frequency of the driving impedance.

11.6 Exercises

11.1 In the two-particle model discussed in Sec. 11.3,
(1) Show that Eq. (11.28) constitutes the solution in the first half of the synchrotron period.
(2) Formulate the transport matrix for a synchrotron period and show that the two eigenvalues are given by Eq. (11.33). Then establish the stability condition $\Upsilon \leq 2$.

11.2 In the two-particle model in Exercise 11.1, if the beam current is slightly above threshold; i.e.,

$$\Upsilon = 2 + \epsilon, \tag{11.71}$$

where $\epsilon \ll 1$, compute the complex phase ϕ of the eigenvalues $\lambda_\pm$. Show that the growth rate is then

$$\frac{1}{\tau} = \frac{\mathcal{I}m\,\phi}{T_s} = \frac{2\sqrt{\epsilon}}{T_s}. \tag{11.72}$$

Demonstrate that for an intensity 10% above threshold, the growth time is of the order of the synchrotron period.

11.3 For longitudinal mode-coupling, the coupling matrix of Eq. (11.35) can be written as, after keeping only the lowest radial modes,

$$M_{mm'} = \epsilon\omega_s A_{mm'} \tag{11.73}$$

where ϵ is given by Eq. (11.38),

$$A_{mm'} = \frac{im}{1+m} \frac{\int d\omega \frac{\omega_r \hat{Z}_0^{\parallel}(\omega)}{\omega} \tilde{\lambda}_{m'}(\omega) \tilde{\lambda}_m^*(\omega)}{\int d\omega \tilde{\lambda}_m(\omega) \tilde{\lambda}_m^*(\omega)}, \tag{11.74}$$

and $\hat{Z}_0^{\parallel}(\omega)$ has been normalized to the shunt impedance R_s.
If the coupling is not too strong, the matrix can be truncated to 2×2 for the coupling between two modes:

$$\begin{vmatrix} \frac{\Omega}{\omega_{s0}} - m - \epsilon A_{mm} & \epsilon A_{mm'} \\ \epsilon A_{m'm} & \frac{\Omega}{\omega_s} - m' - \epsilon A_{m'm'} \end{vmatrix} = 0. \tag{11.75}$$

(1) Show that the collective frequency is given by

$$\Omega = \tfrac{1}{2}\omega_s \left[(\nu_m + \nu_{m'}) \pm \sqrt{(\nu_{m'} - \nu_m)^2 + 4\epsilon^2 A_{mm'} A_{m'm}} \right], \tag{11.76}$$

where $\nu_k = k + \epsilon A_{kk}$, $k = m$ or m'.
(2) For simplicity, let us neglect the factor $m/(1+m)$ on the right side of Eq. (11.74). For two adjacent modes ($m' = m+1$) that are coupled by a resonant peak, the higher-frequency mode samples mostly the capacitive part of the resonance while the lower-frequency mode samples the inductive part. Therefore $A_{mm} - A_{m'm'} > 0$. Show that $A_{mm'} A_{m'm} = -|A_{mm'}|^2$ and the threshold of instability ϵ_{th} is given by

$$|\epsilon_{\text{th}} A_{mm'}| = \tfrac{1}{2} |\epsilon_{\text{th}} (A_{mm} - A_{m'm'}) - 1|. \tag{11.77}$$

The solution is different depending on whether the bunch energy is above or below transition:

$$\epsilon_{\text{th}} = \frac{1}{2|A_{mm'}| + |A_{m'm'} - A_{mm}|} \qquad \text{above transition,} \tag{11.78}$$

$$|\epsilon_{\text{th}}| = \frac{1}{2|A_{mm'}| - |A_{m'm'} - A_{mm}|} \qquad \text{below transition.} \tag{11.79}$$

The above shows that the threshold will be higher when the ring is below transition. In fact, the system becomes completely stable below transition if the coupling provided by the real part of the impedance is not strong enough (or $2|A_{mm'}| < |A_{m'm'} - A_{mm}|$). For this reason, it is advantageous for the ring to be of imaginary γ_t. [14]
(3) When the impedance is purely reactive, the next-to-diagonal elements are zero. So we talk about coupling of two modes m and $m' = m + 2$

instead. Show that $A_{mm'}A_{m'm} = |A_{mm'}|^2$ and instability cannot occur. (4) Show that the same conclusions in Parts (2) and (3) can be drawn when the factor $m/(1+m)$ is not neglected in Eq. (11.74), although Eqs. (11.77) and (11.79) will be slightly modified.

Bibliography

[1] R. Kohaupt, *IEEE Trans. Nucl. Sci.* **NS-26**, 3480 (1979); D, Rice, *et al.*, *IEEE Trans. Nucl. Sci.* **NS-28**, 2446 (1981); PEP Group, Proc. 12th Int. Conf. High Energy Accel., eds. F. T. Cole and R. Donaldson (Fermilab, Batavia, Aug. 11–16, 1983), p. 209.

[2] R. Ruth, CERN Report LEP-TH/83-22 (1983); S. Myers, Proc. 1987 IEEE Part. Accel. Conf., eds. E. R. Lindstrom and L. S. Taylor (Washington, D.C., March 16–19, 1987) p. 503; B. Zotter, *IEEE Trans. Nucl. Sci.* **NS-32**, 2191 (1985); S. Myers, CERN Report LEP -523 (1984).

[3] V. Balakin, A. Novokhatsky, and V. Smirnov, Proc. 12th Int. Conf. High Energy Accel., eds. F. T. Cole and R. Donaldson (Fermilab, Batavia, Aug. 11–16, 1983), p. 11.

[4] M. Blaskiewicz, *Fast Head-tail Instability with Space Charge*, *Phys. Rev. ST Accel. Beams*, **1**, 044201 (1998).

[5] V. Danilov and E. Perevedentsev, *Strong Head-Tail Effect and Decoupled Modes in the Space-Time Domain*, Proc. XVth Int. Conf. High Energy Accel., (Hamburg, 1992), p. 1163; V. Danilov and E. Perevedentsev, *Feedback system for elimination of the TMCI*, *Nucl. Instrum. and Methods*, **A391**, 77 (1997).

[6] R. Talman, *The Influence of Finite Synchrotron Oscillation Frequency on the Transverse Head-Tail Effect*, *Nucl. Instrum. Meth.* **193**, 423 (1982).

[7] F. J. Sacherer, *Bunch Lengthening and Microwave Instability*, *IEEE Trans. Nucl. Sc.* **NS-24**, No.3, 1977.

[8] J. L. Laclare, *Bunched-Beam Instabilities*, Proc. 11th Int. Conf. High Energy Accel., ed. W. S. Newman (Geneva, Switzerland, July 7–11, 1980), p. 525.

[9] B. Chen, *The Longitudinal Collective Instabilities of Nonlinear Hamiltonian Systems in a Circular Accelerator*, Thesis, U. of Texas at Austin, May, 1995.

[10] K. Y. Ng, *Potential-Well Distortion and Mode-Mixing Instability in Proton Machines*, Fermilab Report FN-630, 1995; K. Y. Ng, *Mode-Coupling Instability and Bunch Lengthening in Proton Machines*, Proc. 1995 IEEE Part. Accel. Conf. and Int. Conf. High Energy Accel., ed. L. Gennari (Dallas, May 1–5, 1995) p. 2977.

[11] K. Y. Ng, *Impedances of Beam Position Monitors*, *Part. Accel.* **23**, 93 (1988); Fermilab Report FN-444, 1986; SSC Report SSC-N-277, 1986.

[12] E. Métral, *Stability Criteria for High-Intensity Single-Bunch Beams in Synchrotrons*, CERN Report CERN/PS 2002-022 (AE), 2002.

[13] H. Burkhardt, G. Arduini, E. Benedetto, E. Métral, and G. Rumolo, *Observation of Fast Single-Bunch Transverse Instability on Protons in the SPS*, CERN Report CERN-AB-2004-055, 2004.

[14] S. Y. Lee, K. Y. Ng, and D. Trbojevic, *Phys. Rev.* **E48**, 3040 (1993).

2025 © The Author(s). This is an Open Access chapter published by World Scientific Publishing Company, licensed under the terms of the Creative Commons Attribution-NonCommercial 4.0 International License (CC BY-NC 4.0).

Chapter 12

Head-Tail Instabilities

Head-tail instability occurs when at frequency at which the beam particle is oscillating changes as a function of energy. In the transverse space space, chromaticities are the parameters that determine the instabilities. In the longitudinal space space, it is the dependence of the slip factor on energy that plays the role. As a result, these instabilities develop without any threshold.

12.1 Transverse Head-Tail

We learn from the previous section that a bunch will not be unstable transversely in the presence of a broadband impedance when the beam current is not too large. The main reason is that, as the head and tail particles exchange positions, the new head mostly lags the new tail in betatron phase* by 90°. Thus the tail will be damped for some time first before it is driven to grow again. For this reason, there is a threshold for the strong head-tail instability, below which the beam is stable.

The above analysis is made when the chromaticity is zero. In the presence of a nonzero chromaticity, we will see below that under some condition the head of the bunch always leads the tail in betatron phase by less than 180°. Thus the bunch can become unstable without any threshold, aside from any damping mechanism like tune spread and mechanical damper.

Let us refresh ourselves about the slipping of the betatron phase in the presence of chromaticity. Figure 9.9 shows a particle synchrotron motion in the longitudinal phase space below transition with positive chromaticity ($\xi > 0$). Starting at the head, the momentum offset becomes negative, the particle betatron tune decreases, and its betatron phase ϕ_β slips. This slipping accumulates

*In the $e^{-i\omega t}$ convention, the phase increases in the clockwise direction; i.e., $\vec{A} = Ae^{-i\phi_A}$ leads $\vec{B} = Be^{-i\phi_B}$ by ϕ implies $\phi_A - \phi_B = \phi$.

and reaches a maximum when the particle arrives at the tail. After that, because the momentum offset becomes positive, the betatron tune increases and ϕ_β regains its former slippage when it arrives at the head again.

12.1.1 *Two-Particle Model*

Let us study this instability in the two-particle model. The first row of Fig. 12.1 shows the location of the two particles in longitudinal phase space below transition at start, $\frac{1}{4}$ synchrotron period, $\frac{1}{2}$ synchrotron period, and $\frac{3}{4}$ synchrotron period. The next two rows are for the σ-mode where the two particles are in phase at start. At $\frac{1}{4}$ synchrotron period, particle 1 (solid circle) is at the head and particle 2 (open circle) at the tail. Because particle 1 has been at higher energy than particle 2, particle 1 now leads/lags particle 2 if the chromaticity is positive/negative. Thus, particle 1 can forced-drive/forced-damp particle 2. In the next $\frac{1}{4}$ synchrotron period, particle 2 slips forward/backward in betatron phase because it is at a higher energy while particle 1 slips backward/forward in betatron phase because its energy is less, so that they are again in phase at $\frac{1}{2}$ synchrotron period. In the next $\frac{1}{4}$ synchrotron period, particle 2 continues to slip forward/backward in betatron phase because it is at a higher energy while particle 1 continues to slip backward/forward in betatron phase because its energy is less. At $\frac{3}{4}$ synchrotron period, particle 2 reaches the head position while particle 1 reaches the tail position. Now particle 2 leads/lags particle 1 and can drive the amplitude of particle 1 to growth/damping. Thus this σ-mode is unstable/stable below transition when the chromaticity is positive/negative.

The π-mode, where the two particles are 180° out of phase at start, is treated in the lower part of Fig. 12.1. Following their motion in a synchrotron period, this mode is found stable/unstable below transition when the chromaticity is positive/negative. Above transition, because the particles move in the opposite direction in the longitudinal phase space, opposite conclusions are obtained. The results are summarized in Table 12.1. This is known as chromaticity-driven head-tail instability which occurs without a threshold. [2, 3]

Table 12.1 The chromaticity-driven head-tail stabilities and instabilities of the σ- and π-modes in the two-particle model.

	σ-mode		π-mode	
	$\xi > 0$	$\xi < 0$	$\xi > 0$	$\xi < 0$
Below transition $\eta < 0$	unstable	stable	stable	unstable
Above transition $\eta > 0$	stable	unstable	unstable	stable

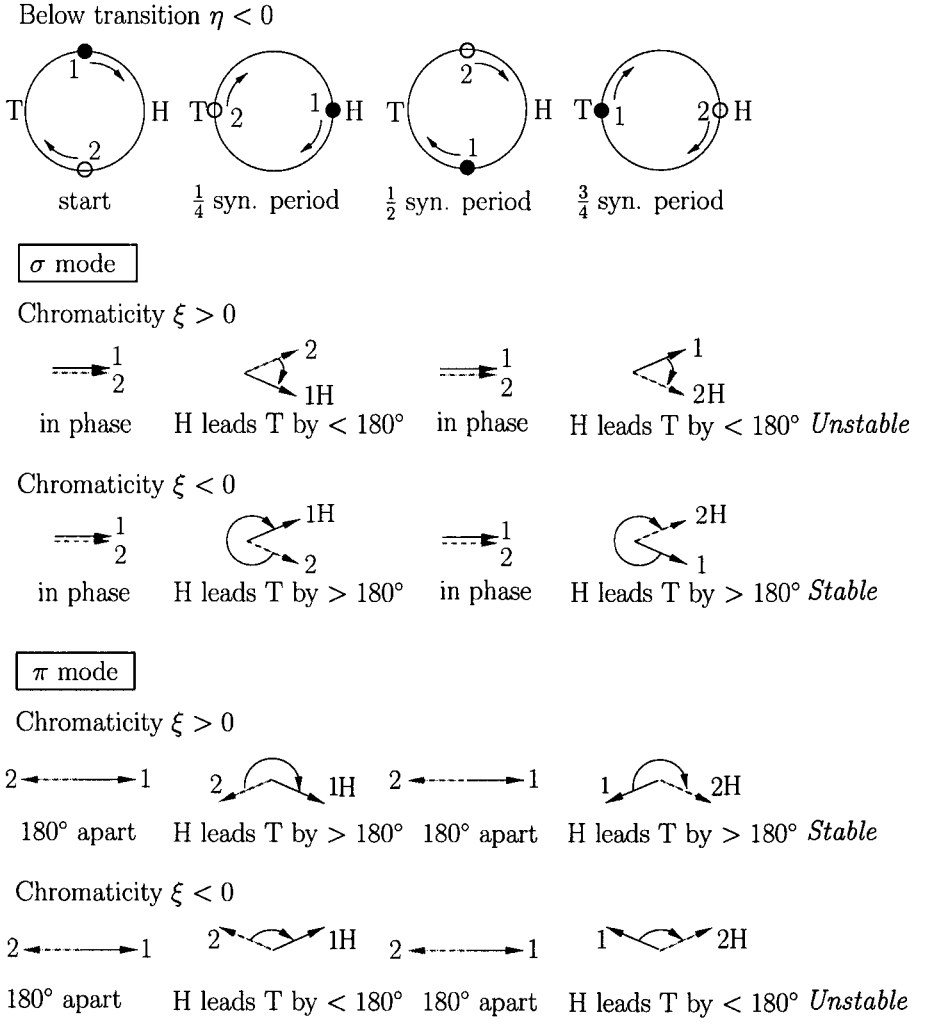


Fig. 12.1 Analysis of chromaticity-driven head-tail instabilities below transition in the two-particle model. First row shows the positions and motion of the two particles (solid circle for 1 and open circle for 2) in the longitudinal phase space, energy offset versus arrival time ahead of the synchronous particle, with bunch going to the right. Below are the analysis of their betatron phase relationship in the σ or rigid-dipole mode where the two particles are in phase, and the π-mode where the two particles are 180° out of phase (solid arrow for 1 and dashed arrow for 2). At each instance, the betatron phasors of the two particles are depicted to show their *relative* betatron phase in the $e^{-i\omega t}$ convention, but not their absolute positions in the betatron phase space.

Now let us derive the growth rate in the two-particle model by continuing the discussion of Sec. 11.3. The equation of motion is still given by Eq. (11.26) during the first half of a synchrotron oscillation and Eq. (11.31) during the second half of the synchrotron oscillation. However, the betatron frequency ω_β is no longer a constant because it oscillates in the synchrotron oscillation. Without the effect of the wake, we can write

$$\begin{aligned} y_1 &= \tilde{y}_1 \exp\Big[-i\frac{\omega_\beta s}{v} - i\phi_\xi \sin\frac{\omega_s s}{v}\Big], \\ y_2 &= \tilde{y}_2 \exp\Big[-i\frac{\omega_\beta s}{v} + i\phi_\xi \sin\frac{\omega_s s}{v}\Big], \end{aligned} \tag{12.1}$$

where

$$\phi_\xi = -\frac{2\pi\xi\hat{\tau}}{\eta T_0}, \tag{12.2}$$

with $\hat{\tau}$ representing the half bunch length, is called the *head-tail phase*, which is the betatron phase slip from the head to the center of the bunch, or the betatron phase advance of the head particle relative to the synchronous particle. The zero time corresponds to the start figure on the first row of Fig. 12.1. Thus below transition with $\xi > 0$, $\phi_\xi > 0$. We see from Eq. (12.1) that particle 1 leads particle 2 in betatron phase in the first half of the synchrotron oscillation ($0 < \omega_s s/v < \pi$), and particle 2 leads particle 1 in the second half of the synchrotron oscillation ($\pi < \omega_s s/v < 2\pi$), corresponding exactly to what was discussed in the second row of Fig. 12.1. The betatron frequencies of the two particles can be obtained by differentiating the betatron phases $\omega_\beta s/v \pm \phi_\xi \sin(\omega_s s/v)$ in Eq. (12.1), or

$$\omega_{\beta 1,2} = \omega_\beta\left[1 \pm i\frac{\phi_\xi \omega_s}{\omega_\beta}\cos\frac{\omega_s s}{v}\right]. \tag{12.3}$$

In the presence of the transverse wake, we still let the transverse displacements of the two particles be represented by Eq. (12.1), but allowing $\tilde{y}_1$ and $\tilde{y}_2$ to be slowly varying functions of time. When all these are substituted into the equation for the first half of the synchrotron oscillation, we obtain after retaining only the lowest order of the wake perturbation,

$$\tilde{y}_2' = i\frac{e^2 N_b\left[\beta_\perp \hat{W}_1\right]}{8\pi R E_0}\tilde{y}_{10} e^{-2i\phi_\xi \sin\omega_s s/v}, \tag{12.4}$$

where $-\hat{W}_1$ is the transverse wake at the distance between the two macro particles with $\hat{W}_1 > 0$ in most circumstances. In above, $\left[\beta_\perp \hat{W}_1\right]$ represents the element-by-element summation of the wake around the ring taking into account

the betatron function $\beta_\perp$ as a weight. In the uniform-focusing approximation, we can just write $\beta_\perp = R/\nu_\beta$. If the head-tail phase is small, the exponent can be expanded. An integration leads to the solution

$$\tilde{y}_2 = \tilde{y}_{20} + i\frac{e^2 N_b \left[\beta_\perp \hat{W}_1\right]}{8\pi R E_0}\tilde{y}_{10}\left[s - i\frac{2\phi_\xi v}{\omega_s}\left(1 - \cos\frac{\omega_s s}{v}\right)\right]. \tag{12.5}$$

The linearly increasing term is exactly what had been obtained in the mode-coupling solution of Eq. (11.28). Here, we have the extra head-tail term which is 90° out of phase and is responsible for the head-tail instability. We can write

$$\Upsilon = \frac{e^2 N_b \left[\beta_\perp \hat{W}_1\right]}{8RE_0\nu_s}\left(1 - i\frac{4\phi_\xi}{\pi}\right) \tag{12.6}$$

which is the response of particle 2 in half a synchrotron period ($\omega_s s/v = \pi$), and will be reduced to Eq. (11.30) in the absence of the head-tail phase. Thus after half a synchrotron oscillation, the solution of particle 2 becomes

$$\tilde{y}_2 = \tilde{y}_{20} + i\Upsilon\tilde{y}_{10}, \tag{12.7}$$

or in matrix form

$$\begin{pmatrix}\tilde{y}_1\\ \tilde{y}_2\end{pmatrix}_{s=vT_s/2} = \begin{pmatrix}1 & 0\\ i\Upsilon & 1\end{pmatrix}\begin{pmatrix}\tilde{y}_1\\ \tilde{y}_2\end{pmatrix}_{s=0}. \tag{12.8}$$

Similarly, for the second half of the synchrotron oscillation, we have

$$\begin{pmatrix}\tilde{y}_1\\ \tilde{y}_2\end{pmatrix}_{s=vT_s} = \begin{pmatrix}1 & i\Upsilon\\ 0 & 1\end{pmatrix}\begin{pmatrix}\tilde{y}_1\\ \tilde{y}_2\end{pmatrix}_{s=vT_s/2}. \tag{12.9}$$

The stability of the particles can be inferred by computing the eigenvalues $\lambda_\pm$ of the product of the two transfer matrices. The two eigenvalues are given by Eq. (11.33) and for small Υ,

$$\lambda_\pm \approx e^{\pm i\Upsilon}. \tag{12.10}$$

The growth rates of the two modes are just $\mp \mathcal{I}m\,\Upsilon$ per synchrotron oscillation, or

$$\frac{1}{\tau_\pm} = \mp\frac{e^2 N_b \omega_0^2 \xi\hat{\tau}}{4\pi^2 E_0 \eta}\left[\beta_\perp \hat{W}_1\right]. \tag{12.11}$$

We see that under any condition, below or above transition, positive or negative chromaticity, the sum of the growth rates of the σ- and π-modes is zero. Actually this sum rule remains true in a multiparticle bunch where there are many modes.

In general, the growth or damping rate of the σ or rigid-dipole mode is much larger than the growth or damping rates of all other higher modes.

12.1.2 *For a Bunch*

Let us now consider the short-range portion of the transverse impedance; i.e., $Z_1^\perp(\omega)$ when ω is large. This is equivalent to replacing the discrete line spectrum by a continuous spectrum. The summation in Eq. (10.1) can be transformed into an integration. The coherent angular frequency for the mth azimuthal mode is therefore

$$\Omega_m - m\omega_s = -\frac{i}{1+m}\frac{eI_b}{4\pi\beta E_0}\int_{-\infty}^{\infty} d\omega\ \left[\beta_\perp Z_1^\perp(\omega)\right] h_m(\omega-\omega_\xi), \tag{12.12}$$

where $\omega_\xi = \xi\omega_0/\eta$ is the betatron frequency shift due to chromaticity ξ, η is the slip factor, ω_0 is the revolution angular frequency, and E_0 is the particle energy. Note that the factor of M, the number of bunches, in the numerator and denominator cancel. This is to be expected because the perturbation mechanism is driven by the short-range wake field and the instability is therefore a single-bunch effect. This explains why we do not include the subscript μ describing phase relationship of consecutive bunches. Here, Sacherer's sinusoidal modes have been assumed. The growth rate, which is the imaginary part of Eq. (12.12) is given by

$$\frac{1}{\tau_m} = -\frac{1}{1+m}\frac{eI_b}{4\pi\beta E_0}\int_0^{\infty} d\omega\ \mathcal{R}e\left[\beta_\perp Z_1^\perp(\omega)\right]\left[h_m(\omega-\omega_\xi) - h_m(\omega+\omega_\xi)\right], \tag{12.13}$$

where use has been made of the antisymmetry of $\mathcal{R}e\, Z_1^\perp(\omega)$. It is clear that there can be no instability when the chromaticity is zero. When there is finite chromaticity, however, the growth does not have a threshold. On the other hand, the tune shift, given by

$$\Delta\Omega_m = \frac{1}{1+m}\frac{eI_b}{4\pi\beta E_0}\int_0^{\infty} d\omega\ \mathcal{I}m\left[\beta_\perp Z_1^\perp(\omega)\right]\left[h_m(\omega-\omega_\xi) + h_m(\omega+\omega_\xi)\right], \tag{12.14}$$

does not vanish when the chromaticity is zero.

Let us demonstrate this by using the resistive-wall impedance. We substitute the expression of the resistive wall impedance of Eq. (1.60) into Eq. (12.12). The result of the integration over ω is [1]

$$\frac{1}{\tau_m} = -\frac{1}{1+m}\frac{eI_b\omega_0}{4\beta E_0}\left(\frac{2}{\omega_0\tau_L}\right)^{1/2}\left[\beta_\perp\left|Z_1^\perp(\omega_0)\right|\right]\mathcal{R}e\, F_m(\chi), \tag{12.15}$$

where $\left|Z_1^{\perp}(\omega_0)\right|$ is the magnitude of the resistive wall impedance at the revolution frequency, and $\chi = \omega_\xi \tau_L$ is the total chromatic betatron phase shift from the head to the tail of the bunch. The tune shift is given by

$$\Delta\Omega_m = \frac{1}{1+m}\frac{eI_b}{4\beta E_0}\left(\frac{2}{\omega_0\tau_L}\right)^{1/2}\left[\beta_\perp\left|Z_1^{\perp}(\omega_0)\right|\right]\mathcal{I}m\, F_m(\chi), \tag{12.16}$$

The form factor can be expressed as

$$\left\{\begin{matrix}\mathcal{R}e\, F_m(\chi)\\ \mathcal{I}m\, F_m(\chi)\end{matrix}\right\} = \frac{1}{2\sqrt{\pi}}\int_0^\infty \frac{dy}{\sqrt{y}}\left[h_m(y-y_\xi) \mp (y+y_\xi)\right], \tag{12.17}$$

where h_m are power spectra of the mth excitation mode in Eq. (9.99) written as functions of $y = \omega\tau_L/\pi$ and $y_\xi = \chi/\pi = \xi\omega_0\tau_L/(\pi\eta)$. The first term in the integrand comes from contributions by positive frequencies while the second term by negative frequencies. The form factors for $m = 0$ to 5 are plotted in Fig. 12.2.

This single-bunch instability will occur in nearly all machines. The $m = 0$ mode is the rigid-bunch mode when the whole bunch oscillates transversely as a rigid unit. For the $m = 1$ mode, the head of the bunch moves transversely in one direction while the tail moves transversely in the opposite direction with the center-of-mass stationary, and is called the dipole head-tail mode. This is

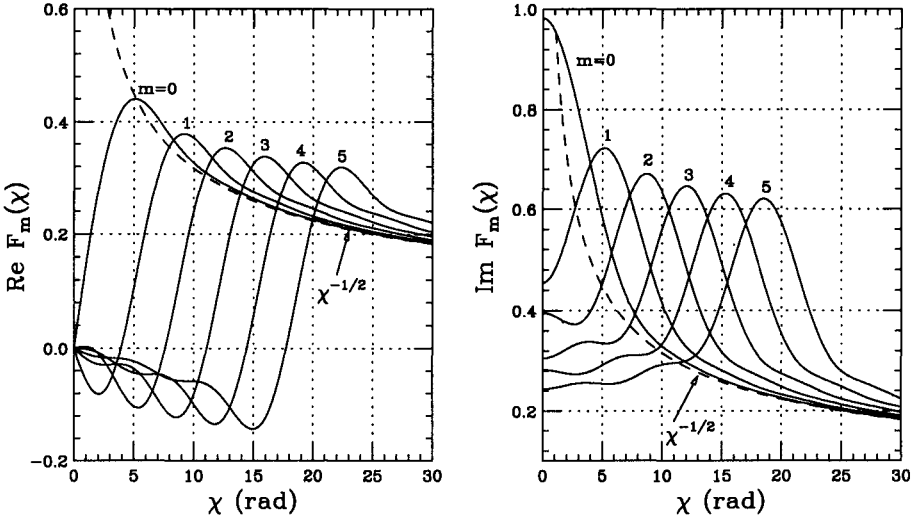


Fig. 12.2 Real and imaginary parts of the form factor $F_m(\chi)$ for head-tail instability resulting from the resistive-wall impedance, for modes $m = 0$ to 5. (Courtesy Sacherer. [1])

the head-tail instability first analyzed by Pellegrini and Sands. [2, 3]

For small chromaticity phase $\chi \lesssim 2.3$, the integrand in Eq. (12.17) can be expanded and the growth rate becomes proportional to chromaticity. The form factor has been computed and listed in Table 12.2, where positive sign implies damping. We see from Table 12.2 that mode $m=0$ is stable for positive chromaticity (above transition or $\eta > 0$). This is expected because the excitation spectrum for this mode has been pushed towards the positive-frequency side. All other modes ($m>0$) should be unstable because their spectra see relatively more negative $\mathcal{R}e\, Z_1^\perp$. Looking into the form factors in Fig. 12.2, however, the growth rate for $m = 4$ is tiny and mode $m = 2$ is even stable. This can be clarified by looking closely into the excitation spectra in Fig. 6.13. We find that while mode $m=0$ has a large maximum at zero frequency, all the other higher even m modes also have small maxima at zero frequency. As these even m spectra are pushed to the right, these small central maxima see more impedance from positive frequency than negative frequency. Since these small central maxima are near zero frequency where $|\mathcal{R}e\, Z_1^\perp|$ is large, their effect may cancel out the opposite effect from the larger maxima which interact with the impedance at much higher frequency where $|\mathcal{R}e\, Z_1^\perp|$ is smaller. This anomalous effect does not exist in the Legendre modes or the Hermite modes, because the corresponding power spectra vanish at zero frequency when $m > 0$.

Table 12.2 Linearized form factor of transverse head-tail modes driven by the resistive wall impedance when $\chi \lesssim 2.3$.

Mode m	Form Factor F_m
0	$+0.1495\,\chi$
1	$-0.0600\,\chi$
2	$+0.0053\,\chi$
3	$-0.0191\,\chi$
4	$-0.0003\,\chi$
5	$-0.0098\,\chi$

A broadband resonance can also drive the head-tail instability. However, the power spectra of the azimuthal modes must be so frequency-shifted by chromaticity that it overlaps with the resonance peak. For example, the $m = 0$ mode must be shifted by negative chromaticity (above transition) so that $\omega_\xi \approx -\omega_r$, where ω_r is the resonant angular frequency of the impedance. Mode m peaks

roughly at

$$\frac{\omega\tau_L}{\pi} \approx m + 1, \tag{12.18}$$

where τ_L is the full bunch length. Therefore, to be excited by the resonance impedance, the betatron frequency shift due to chromaticity, ω_ξ, required is roughly given by

$$\omega_\xi = -\left[\omega_\tau - \frac{\pi(m+1)}{\tau_L}\right]. \tag{12.19}$$

To avoid the strongest dipole head-tail mode at $m = 0$, an accelerator is usually operated at a slight negative chromaticity below transition. However, the higher-order modes are usually much harder to damp with a damper. If the growths of the higher-order modes are too fast to be tolerable, the machine can also be run at a slight positive chromaticity below transition so that all the high-order modes are damped. The dipole head-tail mode that is left excited can be damped with a transverse damper.

Head-tail modes of oscillations can be excited by shifting the chromaticity to the unstable direction and observed using a wideband pickup. These modes were first observed in the CERN PS Booster [4] and depicted in Fig. 12.3. These modes have also been observed in the Fermilab Main Ring. [5] Signals were measured by a quarter wavelength stripline BPM and digitized by a Tektronix digitizer RTD720 running at 2 G-sample/s. There were two damper systems in the Fermilab Main Ring to combat transverse instabilities. One was a slow damper which covered the frequencies from dc to 1.5 MHz. The other was a supper damper which was a bunch-by-bunch feedback system using digital technology. Both dampers were turned off during the measurements. The observed $m = 0$ and $m = 1$ head-tail modes are depicted in Fig. 12.4.

12.1.3 *Application to the Tevatron*

The vacuum chamber of the Tevatron is 6 cm by 6 cm square with rounded corners. Its resistive walls contribute a sizable amount of transverse impedance at low frequencies. Assuming the vacuum chamber to be made of stainless steel with resistivity 7.4×10^{-7} Ω-m, the wall impedance is found to be [6]

$$Z_1^V(\omega) = [\mathrm{sgn}(\omega) - i]27.66|n + \nu_\beta|^{-1/2}\ \mathrm{M}\Omega/\mathrm{m}, \tag{12.20}$$

for all revolution harmonics n, positive or negative.

Before the Fermilab shutdown in January of 2003, there were three C0 Lambertson magnets and 4 F0 Lambertson magnets. The C0 Lambertson magnets

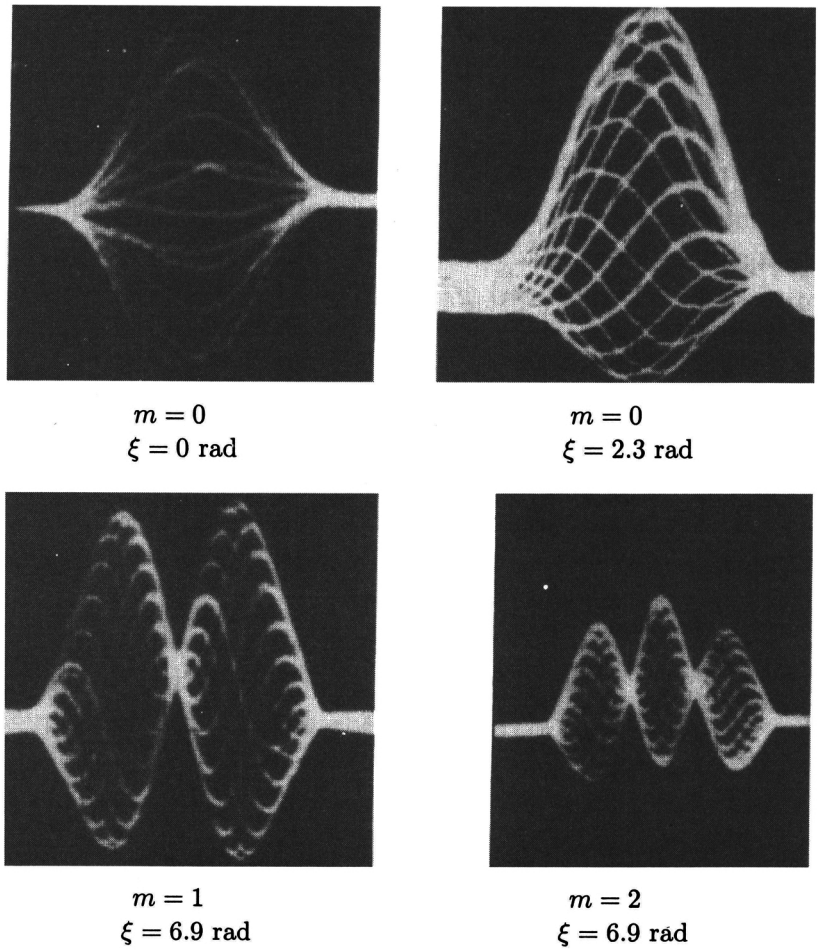


Fig. 12.3 A single bunch in the CERN PS Booster monitored in about 20 consecutive revolutions with a wideband pickup (bandwidth $\sim$ 150 MHz). Vertical axis: difference pickup signal. Horizontal axis: time (50 ns per division). The azimuthal mode number and chromaticity in each plot are as labeled. (Courtesy Gareyte and Sacherer [4].)

were of the older type and they were used for extracting the beam for fixed-target experiments. Since the fixed-target operation has been terminated, three such magnets at C0 had been removed during the shutdown. The cross-section of one such Lambertson magnet is shown in Fig. 12.5. When these Lambertson magnets were first installed, some Tevatron bending dipoles had been removed because of space limitation. To compensate the loss of bending, the Lambertson magnets had been operating in the reverse order. In normal beam circulation,

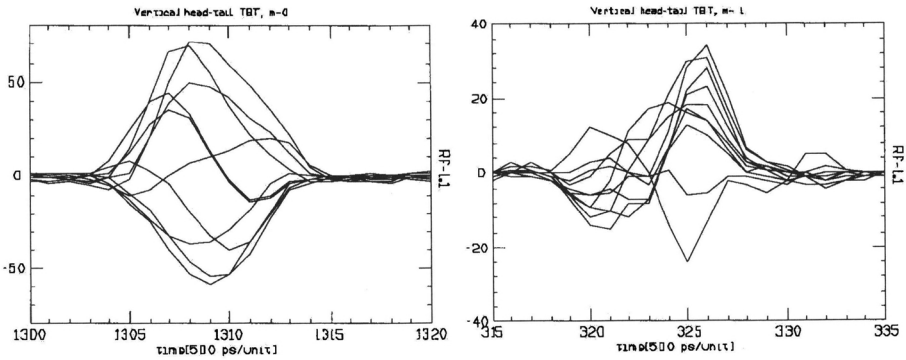


Fig. 12.4 Head-tail modes observed in a Fermilab Main Ring. Left: $m = 0$ mode with vertical chromaticity 3.6, bunch length 5 ns, and bunch intensity 1.07×10^{10}. Right: $m = 1$ mode with vertical chromaticity -40, bunch length 5 ns, and bunch intensity 1.67×10^{10}. (Courtesy Chou. [5])

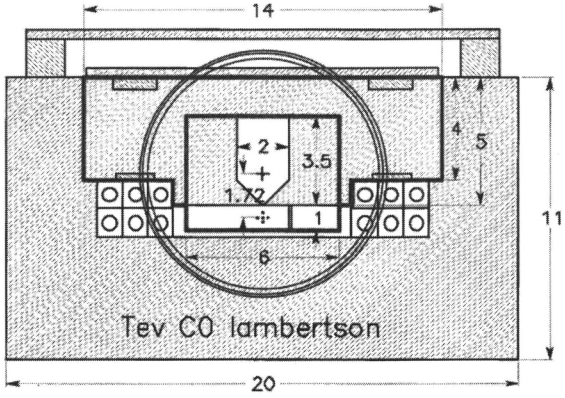


Fig. 12.5 A cross-sectional drawing of the Lambertson magnet at Tevatron C0. The measurements are in inches.

the Tevatron beam must pass through the 1″ high rectangular field region. The beam is kicked into the 2″ by 3.5″ field-free region during an extraction. This magnet can be modeled as parallel-faced with a vertical gap of $2b = 1''$ and assuming that the laminations are shorted at a distance of $d = 6''$ above and below the center line of the 1″ rectangular field region. The length of this C0 magnet is $L = 218''$ consisting of 5812 laminations each of thickness 0.0375″. The computed vertical impedance for three C0 Lambertson magnets is shown in the left plot of Fig. 12.6. Comparing with the F0 Lambertson magnets, the vertical impedance is roughly 15 times larger. This is due mainly to the smaller half gap ($b = 0.5''$) and the longer total length L of the magnets. Notice that

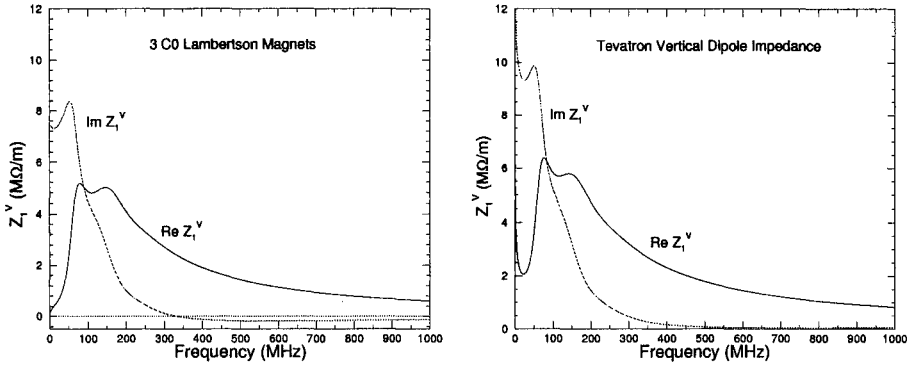


Fig. 12.6 Left: The real and imaginary parts of vertical dipole impedance experienced by a Tevatron beam in the three Lambertson magnets at C0. Right: Total vertical dipole impedance experienced in the whole Tevatron before the shutdown in January 2003, where only the contributions of the resistive wall and the Lambertson magnets have been included. Both the broadband contribution of the C0 magnets near 100 to 200 MHz and the the $\omega^{-1/2}$ contribution of the resistive wall at lower frequencies are evident.

the transverse impedance scales as L/b^3. However, as mentioned in Chapter 10, there is no $\omega^{-1/2}$-behavior at low frequencies. The measured result of Crisp and Fellenz [7] agrees with $\mathcal{I}m\, Z_1^Y$ at zero frequency and $\mathcal{R}e\, Z_1^Y$ at high frequencies. On the other hand, the computed $\mathcal{R}e\, Z_1^Y$ of the broad peak near 100 and 200 MHz is about two times larger than the corresponding measurement. Including the resistive wall and all the Lambertson magnets, the total vertical dipole impedance seen by the Tevatron beam is computed and its real and imaginary parts are shown in the right plot of Fig. 12.6. Here, we see the $\omega^{-1/2}$ behavior of the smooth beam-pipe wall at low frequencies. Around ~ 50 MHz and above, obviously the impedance of the CO Lambertson magnets dominates.

Using the power spectra depicted in Fig. 6.13, the growth and damping rates for the head-tail modes $m = 0, \pm 1, \pm 2, \pm 3, \pm 4$, and ± 5 in a Tevatron bunch of intensity $N_b = 2.6 \times 10^{11}$ at 150 GeV are computed as functions of chromaticity. The results are shown in Fig. 12.7, for rms bunch length $\sigma_\ell = 90$, 80, 70, and 60 cm. Only positive chromaticity is shown.

The transverse impedance exhibits as a broadband resonance around $\omega_r/(2\pi) = 150$ to 200 MHz plus a negative one at -150 to -200 MHz. It is the interaction of the power spectrum of the bunch with the resonance at negative frequency that brings about the observed vertical instability. For a bunch with rms length $\sigma_\ell = 90$ cm, these resonances correspond to $\omega_r \tau_L/\pi \sim 4$, the positive and negative branches of power spectra of modes $m = \pm 3$ are right on top of them at zero chromaticity. Since modes $m = \pm 4$ and ± 5 have their positive- and

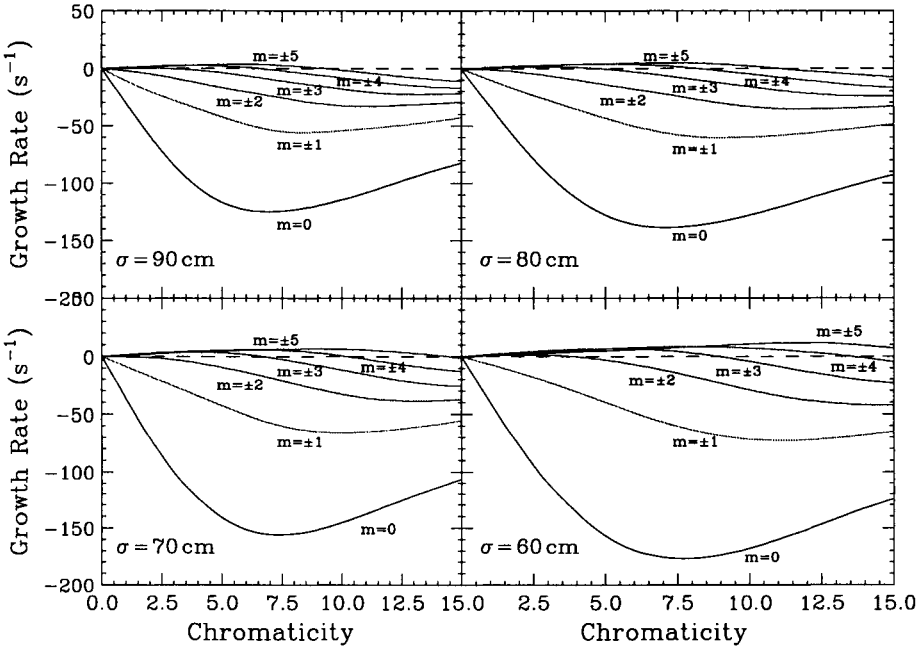


Fig. 12.7 The growth and damping rates of head-tail modes $m = 0$, 1, 2, 3, 4, and 5 are shown as functions of chromaticity. The Tevatron bunch has an intensity of $N_b = 2.6 \times 10^{11}$ at the injection energy of 150 GeV. Various rms bunch lengths, 90, 80, 70, and 60 cm, have been assumed.

negative-frequency parts of the power spectra farther apart than the impedance resonances, they become unstable when the chromaticity assumes a positive value, because the power spectra of these modes shift to the positive-frequency direction, thus sampling more of the resonance at negative frequency than the one at positive frequency. (The Tevatron operates above transition.) On the other hand, modes $m = \pm 1$ and ± 2 have their positive- and negative-frequency parts of the power spectra closer together than the resonances. They therefore become stable when the chromaticity becomes positive. When the bunch length becomes shorter, the bunch spectrum spreads out to higher frequencies. Thus positive- and negative-frequency parts of the power spectrum becomes relatively farther apart. For this reason, at $\sigma_\ell = 80$ cm, all modes $|m| \geq 3$ are unstable, while the lower modes are stable. When $\sigma_\ell = 60$ cm, modes $m = \pm 2$ have their positive- and negative-frequency parts of the power spectrum lying exactly on top of the broad resonances of $\mathcal{R}e\, Z_1^V$ at both positive and negative frequencies when the chromaticity is zero. The mode is therefore just stable when

the chromaticity changes slightly. The higher modes are unstable at positive chromaticity and the lower modes are stable.

At the bunch intensity of 2.6×10^{11}, the normalized rms emittance is $\epsilon_N = 3 \times 10^{-6}$ πm at the injection energy of 150 GeV and the rms bunch length has been $\sigma_\ell = 0.90$ cm. The linearized incoherent space-charge tune shift for a bunch with tri-Gaussian distribution is

$$\Delta\nu_{\text{spch}}^{\max} = \frac{N_b r_p R}{2\sqrt{2\pi}\gamma^2\beta\epsilon_N\sigma_\ell} = -0.0012, \tag{12.21}$$

in the smooth-focusing approximation and neglecting the contribution of dispersion. On the other hand, the coherent tune shift of the head-tail mode $m = 0$ driven by the Lambertson magnets and the resistive-wall impedance is -0.73×10^{-3} at zero chromaticity and is much smaller for the higher-order head-tail modes, especially at large chromaticity. Thus the space-charge tune spread cannot supply any Landau damping to the growth of these modes. Tune spread for Landau damping must be supplied by sextupoles or octupoles, and must be of the order of the space-charge tune shift. The synchrotron tune is 0.0018 at the rf voltage of 1 MV. However, the azimuthal head-tail modes remain as good eigenmodes because modes $m = 0$ and -1 will not merge because while the wall impedance shifts the $m = 0$ mode downward, the transverse space-charge force shifts $m = -1$ mode downwards also. In fact, no transverse coupled-mode instability has ever been reported in the Tevatron.

12.1.3.1 *Measurements by Ivanov, Burov, and Tan*

Before the January shutdown in 2003, the Tevatron did suffer from transverse single bunch instabilities, resulting in beam loss. Ivanov and Scarpine [11] made systematic measurement of the instabilities at various values of the vertical and horizontal chromaticities. The measurement data had been analyzed by Crisp, [8] Ivanov, [10], and Alexahin, *et al.* [9] In one of the data, the vertical chromaticity was reduced to $\xi_y = -2$ to induce instability. The transverse displacement of the beam was monitored by a wideband 1-m long stripline beam-position monitor (BPM) in the Tevatron during proton injection for store 1841. Figure 12.8 shows eight $A-B$ difference-signal traces in eight consecutive turns. The striplines first register at the upstream termination the difference signal of the bunch as it crosses the upstream gap and then register the negative signal of the beam after it is reflected back from the downstream end. The time lag between the positive and negative signals is 6.7 ns. In other words, for a long beam ($\tau_L \gg 6.7$ ns), the stripline termination registers the derivative of the transverse beam displacement. Thus it is not easy to interpret the difference signal, es-

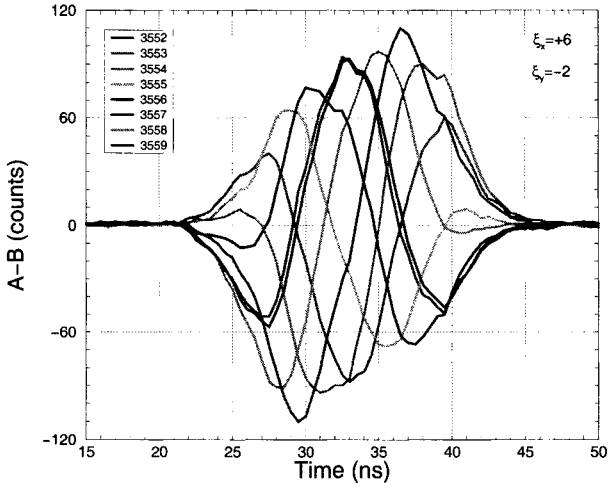


Fig. 12.8 Difference signals registered at the Tevatron 1-m stripline beam-position monitors in eight consecutive revolution turns. The signals reveal an unstable $m = 0$ head-tail mode. A contamination of the $m = \pm 1$ modes may also be present because of the left-right asymmetry of the signal envelope. (Courtesy Crisp. [8])

pecially when there is present a nonzero chromaticity. Viewed in a wideband capacitive pickup, the envelope of the difference signals exhibits m nodes for the head-tail mode m, independent of the chromaticity. This is illustrated in Fig. 12.9. Because of the differential nature of the stripline BPM, we should see one node for mode $m = 0$, 2 nodes for $m = \pm 1$, 3 nodes for $m = \pm 2$, etc. Thus definitely, the difference signals in Fig. 12.8 reveal the $m = 0$ mode. A closer examination reveals that the envelope is not exactly left-right antisymmetric, with the right side going to zero less slowly than the left side. The asymmetry appears to be real, because the sum signals during these eight consecutive turns do show an antisymmetry. A possible explanation will be the presence of more than one head-tail mode, because two head-tail modes evolve differently and they add up differently at different times. According to our analysis in Fig. 12.7, modes $m = \pm 1$ should be excited also. However, their growth rates are only about $\frac{1}{3}$ the growth rate of the $m = 0$ mode at chromaticity $\xi_y = -2$. Simulation shows

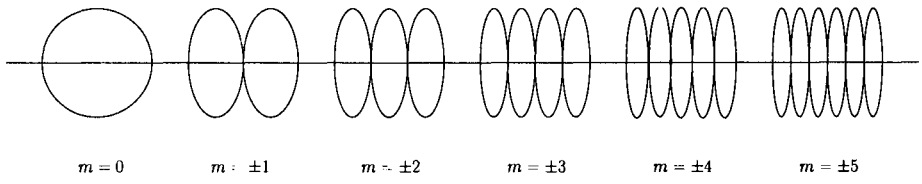


Fig. 12.9 Plot showing the envelopes of vertical oscillations of head-tail modes $m = 0$ to ± 5 of a bunch, as registered in difference signals in a wideband capacitive pickup. We see that mode m has $|m|$ nodes along the longitudinal length.

that a 5 to 10% of the $m = \pm 1$ modes will produce the asymmetric signals in Fig. 12.8.

In the experiment of Ivanov, Burov, and Tan, [11] the vertical chromaticity was lowered gradually to induce vertical instability. When the chromaticities were reduced from $\xi_x = 7.9$ and $\xi_y = 7.6$ to $\xi_x \sim \xi_y \sim 6$, the beam with an intensity of 2.6×10^{11} went unstable with about half the particles lost. The final beam with the intensity of 1.03×10^{11} had a stable longitudinal beam profile as depicted in the left plot of Fig. 12.10. The result is interpreted as

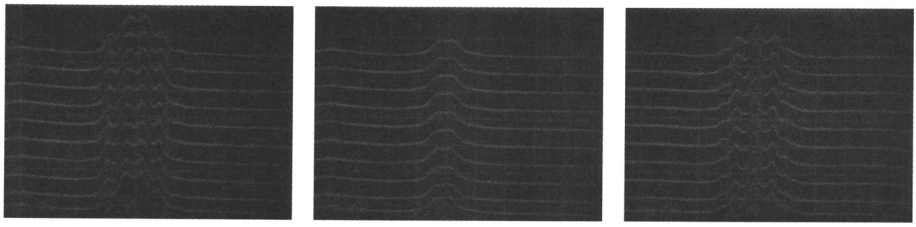


Fig. 12.10 Longitudinal beam profiles of Tevatron bunch after undergoing a vertical instability accompanied by beam loss. Left: Chromaticities reduced to $\xi_x \sim \xi_y \sim 6$, and intensity reduced from 2.6×10^{11} to 1.03×10^{11}. Particle deficiency at the beam center and also at both sides indicates an excitation with three peaks or the $m = \pm 2$ modes. Middle: Chromaticities reduced to $\xi_x = 5.8$, $\xi_y - 4.7$, and intensity reduced from 0.75×10^{11} to 0.34×10^{11}. Particle deficiency at the beam center only indicates an excitation with one peak or the $m = 0$ mode. Right: Chromaticities reduced to $\xi_x \sim 6$, $\xi_y \sim 2$ to 3, and intensity reduced from 2.65×10^{11} to 0.7×10^{11}. Particle deficiency at four locations along the beam but not at the center indicates an excitation of four peaks or the $m = \pm 3$ modes.

follows. When the bunch became unstable, it oscillated vertically as head-tail modes $m = \pm 2$. As shown in Fig. 12.9, the envelope of this mode has three peaks, which got scraped as the instability developed. Because of the particles lost at the peaks, the final stable bunch exhibits three rings in the longitudinal phase space with deficient particle density, and this is the beam profile observed. The vertical chromaticity was further reduced to $\xi_y = -4.7$, the bunch was again unstable with a sizable beam loss. The beam intensity was reduced to 0.34×10^{11} before stability was established again. The new stable beam profile is shown in the middle plot of Fig. 12.10. We can see particle density missing at the middle, implying that the instability excited belongs to the $m = 0$ mode. Similar experiment was repeated with a stable beam of intensity 2.65×10^{11}. When the chromaticities were reduced to $\xi_x \sim 6$ and $\xi_y \sim 3$, vertical instability occurred with very large amount of beam loss. The bunch regained stability when its intensity was reduced to 0.7×10^{11}. The beam profile, shown in the right plot of Fig. 12.10 exhibits particle deficiency at four locations, implying that

the mode of excitation has four peaks. According to Fig. 12.9, this corresponds to the head-tail mode $m = \pm 5$.

The C0 Lambertson magnets are no longer of any use because the Tevatron will not operate in the fixed-target mode anymore. They were removed during the January 2003 shutdown. As was mentioned before, the transverse impedance dropped by a factor of ten. The transverse impedance was further reduced in the summer of 2003, when shielding liners were installed inside the F0 Lambertson magnets so that the beam would only be seeing the laminations partially. Now the Tevatron can be operated at rather low chromaticities without encountering the transverse head-tail instabilities.

12.2 Longitudinal Head-Tail

The transverse head-tail instability comes about because of nonzero chromaticity or the betatron tune is a function of energy spread. Most important of all, the introduction of a nonzero chromaticity breaks the symmetry of the product of the transverse impedance and beam power spectrum, $Z_1^{\perp}(\omega)h_m(\omega-\omega_\xi)$, between positive and negative frequencies. There is also such an analog in the longitudinal phase space when the synchrotron tune depends on the momentum offset. This comes about because the slip factor η is momentum-offset dependent. For any lattice, we can write in general at a certain momentum-offset δ,

$$\eta = \eta_0 + \eta_1\delta + \eta_2\delta^2 + \cdots . \tag{12.22}$$

Usually, because of the small momentum spread δ, the contribution of the higher-order terms is small and this off-momentum dependency is very often ignored. However, when the operation of the ring is near transition or $\eta_0 \approx 0$, most of the contribution of the slippage factor will come from the η_1 term. When η_0 and η_1 are of the same sign, the phase drift of a particle will be larger in one half of the synchrotron oscillation where the momentum spread is positive and smaller in the second half where the momentum spread is negative. The inverse will be true when η_0 and η_1 have opposite signs. Similar to the transverse situation, this loss of symmetry can excite an instability, which we call longitudinal head-tail instability. In fact, this instability has been observed at the CERN SPS [12] and later possibly at the Fermilab Tevatron. Figure 12.11 shows the output of the rf-bunch phase detector at the CERN SPS, where the bunch length, which was 7 ns at the beginning, is seen increasing for every synchrotron oscillation. This is an instability in the dipole mode ($m = 1$) with $\sim 10^{11}$ protons in the bunch. The horizontal scale is 2 s per division or 20 s in total. Thus the growth rate is

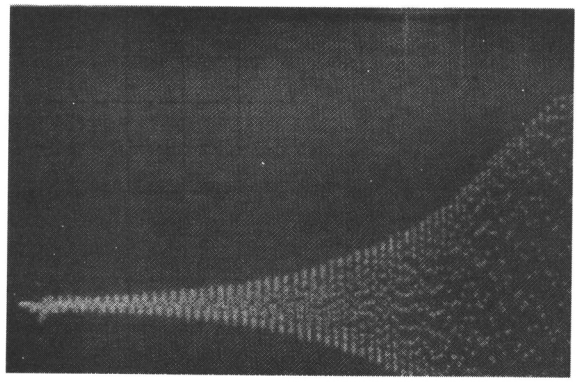


Fig. 12.11 Longitudinal head-tail growth of the dipole-synchrotron-oscillation amplitude recorded from the output of the rf phase detector at the CERN SPS for a bunch with $\sim 10^{11}$ protons. Horizontal scale is 2 s/div or 20 s total. (Courtesy Boussard and Linnecar. [12])

very slow.

To higher order in momentum spread, the off-momentum orbit length can be written as[†]

$$C(\delta) = C_0\big[1 + \alpha_0\delta(1 + \alpha_1\delta + \alpha_2\delta^2 + \cdots)\big], \tag{12.23}$$

with $C_0 = C(0)$ being the length of the on-momentum orbit. It will be proved in Sec. 16.4.1 that with the expansion of η in Eq. (12.22), the expressions for the higher-order components of the slip factor are

$$\eta_0 = \alpha_0 - \frac{1}{\gamma^2}, \tag{12.24}$$

$$\eta_1 = \alpha_0\alpha_1 + \frac{3\beta^2}{2\gamma^2} - \frac{\eta_0}{\gamma^2}, \tag{12.25}$$

$$\eta_2 = \alpha_0\alpha_2 + \frac{\alpha_0\alpha_1}{\gamma^2} - \frac{2\beta^4}{\gamma^2} + \frac{3\alpha_0\beta^2}{2\gamma^2} + \frac{\eta_0}{\gamma^4}, \tag{12.26}$$

where β and γ are the relativistic factors of the synchronous particle. For a high-energy ring like the Fermilab Tevatron, we have almost $\eta_1 = \alpha_0\alpha_1$. For a FODO lattice without special correction, α_1 is positive. Thus, the particle spends more time at positive momentum offset than at negative momentum offset. Then, the bunch becomes relatively longer at positive momentum offset than at negative momentum offset, as is illustrated in Fig. 12.12. The bunch will therefore lose more energy in the lower trajectory than in the upper trajectory. As a result, the amplitude of synchrotron oscillation grows. The energy loss by a beam particle

[†]In Europe, the coefficients α_0, α_1, α_2, etc. are usually referred to as α_1, α_2, α_3, etc. The readers should be aware of yet another common definition, where $C(\delta) = C_0(1 + \alpha_0\delta + \alpha_1\delta^2 + \alpha_2\delta^3 + \cdots)$.

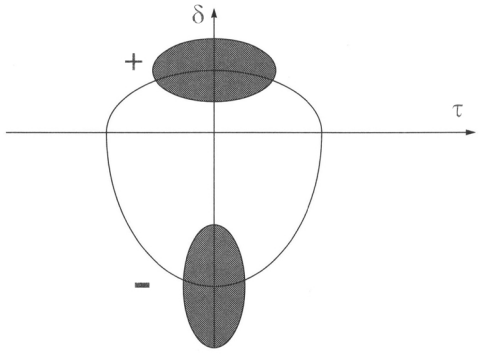


Fig. 12.12 A particle trajectory is asymmetric about the on-momentum axis when the slippage factor is not an even function of momentum offset. The bunch will be longer at positive than negative momentum offset when the first-order momentum compaction $\alpha_0\alpha_1 > 0$ and above transition. (Courtesy Bo. [13])

per turn is, according to Eq. (1.66),

$$U(\sigma_\tau) = 2\pi e^2 N_b \int d\omega \left|\tilde{\lambda}(\omega, \sigma_\tau)\right|^2 \mathcal{R}e\, Z_0^{\parallel}(\omega), \tag{12.27}$$

where N_b is the number of particles in the bunch, and

$$\tilde{\lambda}(\omega, \sigma_\tau) = \frac{1}{2\pi} \int d\tau\, \lambda(\tau, \sigma_\tau) e^{i\omega\tau} \tag{12.28}$$

is the spectrum of the bunch of rms length σ_τ with a distribution $\lambda(\tau, \sigma_\tau)$ normalized to unity. We emphasize the bunch length here because it is the difference in bunch length in each half of the synchrotron oscillation that leads to the difference in energy loss. The rms bunch length σ_τ and the rms energy spread σ_E are related by

$$\omega_s \sigma_\tau = \frac{|\eta|\sigma_E}{\beta^2 E_0}, \tag{12.29}$$

where E_0 is the synchronous energy of the beam and ω_s is the small-amplitude synchrotron angular frequency. At the onset of the growth, bunch area is still approximately constant for a proton bunch. Thus, we have

$$\sigma_\tau \propto \sqrt{\frac{|\eta|}{\omega_s}} \propto |\eta|^{1/4} \approx |\eta_0|^{1/4} \left(1 + \frac{\eta_1 \delta}{4\eta_0}\right), \tag{12.30}$$

or

$$\sigma_\tau = \sigma_{\tau 0} \left(1 + \frac{\eta_1 \delta}{4\eta_0}\right), \tag{12.31}$$

where $\sigma_{\tau 0}$ is the rms bunch length in the absence of the η_1 term. The bunch particle gains energy for half a synchrotron period when $\delta > 0$ and loses energy

for the other half synchrotron period when $\delta < 0$. Averaging over a synchrotron period, the increase in energy spread per turn is

$$\Delta E = \frac{dU}{d\sigma_\tau}\sigma_\tau\bigg|_{\delta>0} - \frac{dU}{d\sigma_\tau}\sigma_\tau\bigg|_{\delta<0} = \frac{dU}{d\sigma_\tau}\sigma_{\tau 0}\frac{\delta}{2}\chi, \tag{12.32}$$

where the asymmetry factor χ is just the fractional difference in bunch length for $\delta \gtrless 0$, and is given, from Eq. (12.31), by

$$\chi = \frac{\eta_1}{\eta_0} = \frac{\alpha_0\alpha_1 + (\frac{3}{2}\beta^2 - \eta_0)\gamma^{-2}}{\eta_0} \approx \alpha_1 + \frac{3}{2\alpha_0\gamma^2} \approx \alpha_1, \tag{12.33}$$

for a proton beam at high energies so that $\eta_0 \approx \alpha_0$. In above, Eq. (12.25) has been used. Near transition when $\alpha_0 \approx \gamma^{-2}$, however, the asymmetry factor becomes

$$\chi \approx \frac{\alpha_0\left(\alpha_1 + \dfrac{3}{2}\right)}{\eta_0}. \tag{12.34}$$

Therefore, this phenomenon is best observed near transition when η_0 is small. The time development of the energy spread is given by $\Delta E \propto e^{t/\tau}$. The growth rate of the fractional energy spread is therefore [13]

$$\frac{1}{\tau} = -\frac{f_0}{2}\frac{dU}{d\sigma_\tau}\frac{\sigma_{\tau 0}}{\beta^2 E_0}\chi, \tag{12.35}$$

where f_0 is the revolution frequency and $dU/d\sigma_\tau$ is usually negative. In parallel to the transverse head-tail instability, this instability does not have a threshold although the growth rate is intensity dependent. This instability is essentially a growth of the amplitude of the synchrotron oscillation in the dipole mode. The frequency involved will be the synchrotron frequency. The growth rate is usually very slow. For example, the photo recorded at the CERN SPS, Fig. 12.11 has a horizontal time span of 20 s.

If the driving impedance $\mathcal{R}e\, Z_0^{\parallel}$ comes from a narrow resonance with shunt impedance R_s at resonant frequency $\omega_r/(2\pi)$ and quality factor Q, we have for the energy loss per turn

$$U(\sigma_\tau) = \frac{\pi R_s \omega_r e^2 N_b}{Q}\left|\tilde{\lambda}(\omega_r, \sigma_\tau)\right|^2, \tag{12.36}$$

for a bunch containing N_b particles. For a broadband impedance, $U(\sigma_\tau)$ drops much faster with bunch length. For a general resonance, the asymmetric energy loss for a parabolic bunch distribution is found to be [14]

$$\frac{dU(\sigma_\tau)}{d\sigma_\tau}\sigma_\tau = \frac{9e^2N_b\omega_r R_s}{4sQ}\left\{\frac{2}{z^3}\left[e^{-2cz}\sin(2sz+2\theta)-\sin 2\theta\right]\right.$$
$$+\frac{4}{z^4}\left[2e^{-2cz}\sin(2sz+3\theta)+\sin 3\theta\right]+\frac{12}{z^5}e^{-2cz}\sin(2sz+4\theta)$$
$$\left.+\frac{6}{z^6}\left[e^{-2cz}\sin(2sz+5\theta)-\sin 5\theta\right]\right\}, \qquad (12.37)$$

where the notations stand for $z = \sqrt{5}\omega_r\sigma_\tau$, $c = \cos\theta = 1/(2Q)$, and $s = \sin\theta$. This differential energy loss per turn is depicted in Fig. 12.13 for the case of a sharp resonance in the left plot and for the case of a broadband with $Q = 1$ in the right plot.

As is shown in the left plot of Fig. 12.13, the asymmetric energy loss vanishes when the bunch length goes to zero, because the change in bunch length from positive momentum offset to negative momentum offset also goes to zero. On the other hand, when the bunch length is very long, the asymmetric energy loss will also be small, because the energy loss for a long bunch is small.

Let us apply the theory to the Fermilab Tevatron in the collider mode. [14] The asymmetric factor in Eq. (12.33) has been measured to be $\chi \sim +1.17$. The fundamental resonance of the eight rf cavities serves as a good driving force for this instability. Each cavity has resonant frequency $f_r = 53.1$ MHz, shunt impedance $R_s = 1.2$ MΩ, and quality factor $Q = 7000$. For Run I, where the rms bunch length was $\sigma_\tau \approx 2.684$ ns or $f_r\sigma_\tau \approx 0.1425$, $(dU/d\sigma_\tau)\sigma_\tau \sim -0.3890\, e^2N_b\omega_r R_s/Q$ is large and leads to a longitudinal head-tail growth rate of $\tau^{-1} = 1.433 \times 10^{-3}$ s^{-1} at the injection energy of $E_0 = 150$ GeV for a

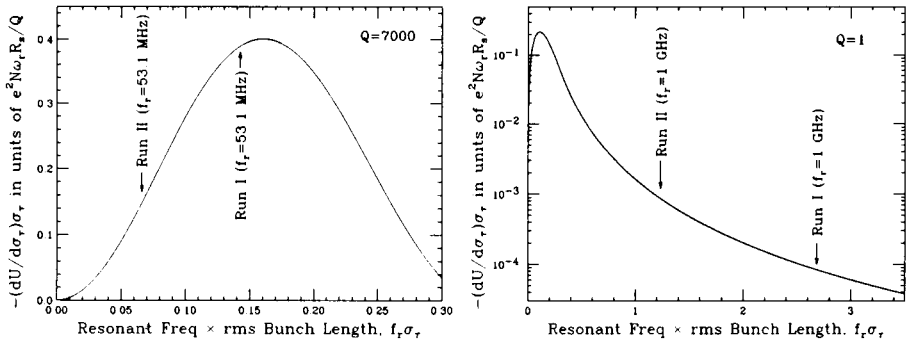


Fig. 12.13 Left: Plot of differential bunch energy loss per turn $(dU/d\sigma_\tau)\sigma_\tau$ versus $f_r\sigma_\tau$ due to a sharp resonance. Note that the effect on the Run II bunch is much less than that on the Run I bunch because of the shorter Run II bunch length. Right: The same due to a broadband resonance with $Q = 1$. Note that the effect on the Run II bunch is much more than that on the Run I bunch because of the shorter Run II bunch length.

bunch containing $N_b = 2.70 \times 10^{11}$ particles. However, for Run II, the designed bunch length will be much shorter. With $\sigma_\tau = 1.234$ ns or $f_r\sigma_\tau \approx 0.0655$, the asymmetric energy loss $(dU/d\sigma_\tau)\sigma_\tau \sim -0.1464\, e^2 N_b \omega_r R_s/Q$ is much smaller and the head-tail growth rate becomes $\tau^{-1} = 0.539 \times 10^{-3}$ s^{-1} instead. As is shown in Fig. 12.13, we are on the left side of the $(dU/d\sigma_\tau)\sigma_\tau$ peak; therefore a shorter bunch length leads to slower growth.

The broadband impedance can also have similar contributions since the resonance frequency is usually a few GHz and $\mathcal{R}e\, Z_0^{\parallel}$ is large although $Z_0^{\parallel}/n$ is just a couple of Ohms. Now $\omega_r\sigma_\tau$ falls on the right side of the $(dU/d\sigma_\tau)\sigma_\tau$ peak instead. We expect shorter bunch lengths to have faster growth rates, as is indicated in right plot of Fig. 12.13. Table 12.3 shows the longitudinal head-tail growth rates for different resonant frequencies and quality factors; $Z_0^{\parallel}/n = 2\ \Omega$ has been assumed. The growth rates driven by the fundamental rf resonance are also listed in the last row for comparison. It is obvious that the longitudinal head-tail instability for Run I is dominated by the rf narrow resonance and that for Run II by the broadband impedance instead. A slow longitudinal growth of the bunch length with growth time ~ 250 s was observed in Run I, and this might have been a longitudinal head-tail. From Table VI, it is very plausible that the growth of this head-tail instability will be at least as fast as that in Run I.

Table 12.3 Growth rates for a broadband resonance of $Z_0^{\parallel}/n = 2\ \Omega$ at various frequencies and quality factors.

f_r (GHz)	Q	Growth Rate (s^{-1})	
		Run I	Run II
1	1	0.178×10^{-3}	1.829×10^{-3}
1	3	0.022×10^{-3}	0.267×10^{-3}
2	1	0.089×10^{-3}	0.915×10^{-3}
2	2	0.023×10^{-3}	0.249×10^{-3}
1	5	0.009×10^{-3}	0.114×10^{-3}
2	3	0.011×10^{-3}	0.117×10^{-3}
2	4	0.006×10^{-3}	0.070×10^{-3}
Fundamental rf resonance		1.433×10^{-3}	0.539×10^{-3}

Let us go back to the observation at the CERN SPS. The bunch has a synchronous momentum of 26 GeV/c. The transition gamma is $\gamma_t = 23.4$, giving $\eta = 5.26 \times 10^{-4}$. For the horizontal chromaticity setting used during the observation of the longitudinal head-tail growth in Fig. 12.11, a lattice-code simulation program gives the next higher-order component of the momentum compaction to be $\alpha_1 = -0.7$. The asymmetry parameter turns out to be $\chi = +1.28$. We therefore expect an instability if $dU/d\sigma_\tau < 0$ which is normally the case. In order words, to observe such an instability, one should perform

the experiment above transition, but not too much above transition, so as to enhance the asymmetry parameter χ.

The longitudinal head-tail instability can also be driven by the resistive wall impedance. The differential energy loss in Eq (12.33) integrates to

$$\frac{dU}{d\sigma_\tau}\sigma_\tau = -\frac{3\Gamma\left(\frac{3}{4}\right)}{8\pi^2}\frac{e^2 N_b [\mathcal{R}e\, Z_0^{\parallel}]_1}{\omega_0^{1/2}\sigma_\tau^{3/2}}, \tag{12.38}$$

where

$$[\mathcal{R}e\, Z_0^{\parallel}]_1 = \frac{R\rho_c}{b\delta_1} \tag{12.39}$$

is the resistive part of the wall impedance at revolution frequency. The skin depth at revolution frequency is $\delta_1 = \sqrt{2\rho_c/(\mu_0\mu_r\omega_0)}$, where μ_r is the relative magnetic permeability, ρ_c is the electric resistivity of the beam pipe, and $\Gamma\left(\frac{3}{4}\right) = 1.225$ is the Gamma function at $\frac{3}{4}$. Because of the $\sigma_\tau^{3/2}$ in the denominator, the contribution can be important for very short bunches.

The longitudinal head-tail instability can be important in quasi-isochronous storage rings, because the the asymmetric factor as defined in Eq. (12.34) can become very large when the ring operation is close to transition. Such rings have been designed for the muon colliders. An isochronous ring is preferred because the muon bunches will be short, roughly 3 mm, which requires an rf voltage in the 50 MV range. [15] Such an rf system will be very expensive. In most of these designs, the muons only have a lifetime of about 1000 turns. If the ring is quasi-isochronous, even without rf, the debunching will be rather insignificant. In order not to degrade the luminosity of the collider, however, one must make sure that the growth time of the longitudinal head-tail instability will be much longer than 1000 turns.

12.3 Exercises

12.1 The degrees of freedom of a system are coupled internally. Some degrees of freedom continue to gain energy and grow while some lose energy and are damped. When the system is not getting energy from outside, the sum of the damping or antidamping rates of all degrees of freedom must add up to zero. If the head-tail stability or instability for all azimuthal modes do not draw energy from outside, energy must be conserved, or

$$\sum_{m=0}^{\infty}\frac{1}{\tau_m} = 0, \tag{12.40}$$

where τ_m^{-1} is given by Eq. (12.12), independent of chromaticity and the detail of the transverse impedance. Show that Eq. (12.40) is only satisfied if the factor $(1+m)^{-1}$ in Eq. (12.12) is removed. We may conclude that either the factor $(1+m)^{-1}$ should not be present in Sacherer's formula or this is not an internal system.

Hint: Show that $\sum_m |h_m(\omega)|^2$ is a constant independent of ω by performing the summation numerically. This follows from the fact that the modes of excitation $\lambda_m(\tau)$ form a complete set.

12.2 In an isochronous ring or an ultra-relativistic linac,‡ the particle at the head of the bunch will not exchange position with the particle at the tail. Thus the particle at the tail suffers from the wake of the head all the time. We can consider a macro-particle model with only two macro-particles, each carrying charge $eN_b/2$ and separated by a distance $\hat{z}$ longitudinally. The head particle executes a free betatron oscillation

$$y_1(s) = \hat{y} \cos k_\beta s, \tag{12.41}$$

while the tail sees a deflecting wake force $\langle F_1^\perp \rangle = e^2 N_b W_1(\hat{z}) y_1(s)/(2L)$ and its transverse motion is determined by

$$y_2'' + k_\beta^2 y_2 = -\frac{e^2 N_b W_1(\hat{z})}{2E_0 L}, \tag{12.42}$$

where $k_\beta = \omega_\beta/v$ is the betatron wave number, L is the length of the vacuum chamber that supplies the wake. If one prefers, one can define W_1 as the wake force integrated over one rf-cavity period; then L will be the length of the cavity period. Show that the solution of Eq. (12.42) is

$$y_2(s) = \hat{y} \left[\cos k_\beta s - \frac{e^2 N_b W_1(\hat{z})}{4k_\beta E_0 L}\, s \sin k_\beta s \right]. \tag{12.43}$$

The second term is the resonant response to the wake force and grows linearly. Show that the total growth in transverse amplitude along a length L_0 of the linac relative to the head particle is

$$\Upsilon = -\frac{e^2 N_b W_1(\hat{z}) L_0}{4k_\beta E_0 L}. \tag{12.44}$$

The above mechanism is called beam breakup.

‡For all the proton linacs in existence, the highest energy is less than 1 GeV, or proton velocity less than 0.875 of the velocity of light. Thus, normal synchrotron motion takes place, implying that head and tail of a bunch do exchange position. Therefore, Exercise 12.2 applies mostly to electron linacs.

12.3 Derive the asymmetric energy loss, $[dU(\sigma_\tau)/d\sigma_\tau]\sigma_\tau$ as given by Eq. (12.37) of a particle in a bunch with linear parabolic distribution driven by a resonance.

Bibliography

[1] B. Zotter and F. Sacherer, *Transverse Instabilities of Relativistic Particle Beams in Accelerators and Storage Rings*, Proc. First Course of Int. School of Part. Accel. of the 'Ettore Majorana' Centre for Scientific Culture, eds. A. Zichichi, K. Johnsen, and M. H. Blewett (Erice, Nov. 10–22, 1976), CERN Report CERN 77-13, p. 198.

[2] C. Pellegrini, *Nuovo Cimento* **64**, 447 (1969).

[3] M. Sands, SLAC Report SLAC-TM-69-8 (1969).

[4] J. Gareyte and F. Sacherer, *Head-tail Type Instabilities in the PS and Booster*, Proc. 9th Int. Conf. High Energy Accel. (SLAC, Stanford, May 2–7, 1974), p. 341.

[5] P. J. Chou and G. Jackson, *Experimental Studies of Transverse Beam Instabilities at Injection in the Fermilab Main Ring*, Proc. 1995 IEEE Part. Accel. Conf. and Int. Conf. High Energy Accel., ed. L. Gennari (Dallas, May 1–5, 1995) p. 3091.

[6] K. Y. Ng. *Impedances and Collective Instabilities of the Tevatron at Run II*, Fermilab Report TM-2055, 1998.

[7] J. Crisp and B. Fellenz, *Comparison of Tevatron C0 and F0 Lambertson Beam Impedance*, Fermilab Report, TM-2205, 2003.

[8] J. L. Crisp, *Tevatron Stripline Turn by Turn Data Showing Differential Head-Tail Positions*, Fermilab Report TM-2195, 2002.

[9] Yu. Alexahin, J. Annala, A. Burov, P. Ivanov, V. Shiltsev, T. Sen, and C. Y. Tan, *Tevatron Transverse Instability Studies*, Talk presented by P. Ivanov at the First Mid-West Accelerator Physics Collaboration Meeting, (Fermilab, Oct. 4–5, 2002).

[10] P. Ivanov, J. Annala, A. Burov, V. Lebedev, E. E.Lorman, V. Ranijbar, V. Scarpine, and V. Shiltsev, *Head-Tail Instability at Tevatron*, Proc. 2003 Part. Accel. Conf., eds. J. Chew, P. Lucas and S. Webber (Portland, Oregon, May 12–16, 2003, 2001), p. 3062.

[11] P. Ivanov, A. Burov, and C.Y. Tan, *Transverse Instability Studies at Low Chromaticities*, Tevatron Electronic Log Book, August 23, 2002, log-054248.

[12] D. Boussard and T. Linnecar, Proc. 2nd European Part. Accel. Conf. EPAC'90, ed. F. Marin and P. Mandrillon (Nice, France, June 12–16, 1990) p. 1560.

[13] B. Chen, *The Longitudinal Collective Instabilities of Nonlinear Hamiltonian Systems in a Circular Accelerator*, Thesis, U. of Texas at Austin, May, 1995.

[14] K. Y. Ng, *Impedances and Collective Instabilities of the Tevatron at Run II*, Fermilab Report TM-2055, 1998.

[15] K. Y. Ng *Quasi-Isochronous Buckets in Storage Rings, Nucl. Instrum. Meth.* **A404**, 199 (1988).

This page intentionally left blank

2025 © The Author(s). This is an Open Access chapter published by World Scientific Publishing Company, licensed under the terms of the Creative Commons Attribution-NonCommercial 4.0 International License (CC BY-NC 4.0).

Chapter 13

Landau Damping

As we have seen in previous chapters, collective instabilities occur in bunched and unbunched beams as a result of the interaction of the beam particles with their own wake fields. There are various ways to damp these instabilities. Aside from mechanical dampers, there is a natural stabilization mechanism against collective instabilities when the beam particles have a small spread in their frequencies, such as betatron frequency, synchrotron frequency, or revolution frequency as the situation requires. This damping mechanism is called *Landau damping*, which was first formulated by Landau. [1] Unfortunately, Landau's original paper is rather difficult to understand. Later, Jackson [2] wrote an article on longitudinal plasma oscillations and had the concept well explained. Neil, and Sessler [3] first formulated the theory of Landau damping on longitudinal instabilities of an accelerator beam, while Laslett, Neil and Sessler [4] first applied the theory to transverse instabilities. There have been quite a number of good papers written on this subject by, for example, Hereward, [5] Hofmann, [6] and Chao. [7]

We encountered Landau damping in Chapter 5 when we formulated the dispersion relation for longitudinal microwave instability using the Vlasov equation. There, we came across the ambiguity of a singularity in the denominator which is critical in determining whether the system will be stable or unstable. That ambiguity can only be avoided when the problem is treated as an initial-value problem, which will be covered in this chapter. We first study the beam response of an harmonic driving force and the beam response of shock or δ-pulse excitation. After that, we try to understand the physics of Landau damping and derive dispersion relations for bunched and unbunched beam in transverse and longitudinal instabilities. The theory of beam response is then applied to the measurement of coupling impedances. Finally, the difference between Landau damping and decoherence is discussed. Some applications to existing accelerator rings are made.

13.1 Harmonic Beam Response

Consider a particle having a natural angular frequency ω and driven by a force of angular frequency Ω. The equation describing its displacement $x(t)$ is

$$\ddot{x} + \omega^2 x = A\cos\Omega t, \tag{13.1}$$

where the overdots represent derivatives with respect to time and A denotes the amplitude of the force. The most general solution is

$$x(t) = x_0\cos\omega t + \dot{x}_0\frac{\sin\omega t}{\omega} + \frac{A}{\omega^2-\Omega^2}\left[\cos\Omega t - \cos\omega t\right], \tag{13.2}$$

where x_0 and $\dot{x}_0$ are, respectively the initial values of x and $\dot{x}$ at $t=0$. The first two terms are due to a shock or δ-pulse excitation. Although they are important, we shall postpone the discussion to the next section.

Let us pay attention to the excitation by the harmonic force. Notice that the response is well-behaved even at $\omega = \Omega$. For a large number of particles, the displacement of the center-of-mass is

$$\langle x(t)\rangle = A\int_{-\infty}^{\infty} d\omega\,\frac{\rho(\omega)}{\omega^2-\Omega^2}\left[\cos\Omega t - \cos\omega t\right]. \tag{13.3}$$

where the natural-frequency distribution $\rho(\omega)$ is normalized according to

$$\int_{-\infty}^{\infty}\rho(\omega)d\omega = 1. \tag{13.4}$$

As is the case in particle beams, the distribution is mostly a narrow one centered at angular frequency $\bar{\omega}$. For simplicity, let us assume that this distribution does not peak at any other frequency.* In order to drive this system of particles, the driving frequency must also be close to this center frequency, or $\Omega \approx \bar{\omega}$. We can therefore perform the expansion $\omega = \Omega + (\omega - \Omega)$, and Eq. (13.3) can be

*We can also assume the distribution to peak at both $\pm\bar{\omega}$ with the symmetry property $\rho(\omega) = \rho(-\omega)$. Then we obtain instead

$$\begin{aligned}\langle x(t)\rangle &= \frac{A}{2\Omega}\left[\int_{-\infty}^{\infty}d\omega\,\frac{\rho(\omega)}{\omega-\Omega} - \int_{-\infty}^{\infty}d\omega\,\frac{\rho(\omega)}{\omega+\Omega}\right]\left[\cos\Omega t - \cos\omega t\right]\\ &= \frac{A}{\Omega}\int_{-\infty}^{\infty}d\omega\,\frac{\rho(\omega)}{\omega-\Omega}\left[\cos\Omega t - \cos\omega t\right].\end{aligned} \tag{13.5}$$

However, the distributions commonly used, for example the Gaussian $\rho(\omega) = \exp[-(\omega - \bar{\omega})^2]/(2\sigma^2)$, do not possess this symmetry property.

approximated by

$$\langle x(t)\rangle = \frac{A}{2\bar{\omega}}\left[\cos\Omega t\int_{-\infty}^{\infty} d\omega\,\rho(\omega)\frac{1-\cos(\omega-\Omega)t}{\omega-\Omega} + \sin\Omega t\int_{-\infty}^{\infty} d\omega\,\rho(\omega)\frac{\sin(\omega-\Omega)t}{\omega-\Omega}\right]. \tag{13.6}$$

Notice that the fast-oscillating term of angular frequency Ω and the slow-oscillating envelope-like terms with angular frequency $\omega - \Omega$ have been separated. We also see a part, the $\cos\Omega t$ term, that is not driven *in phase*[†] by the force, and the other part, the $\sin\Omega t$ term, that is driven in phase by the force. More discussion will follow later. It is convenient to introduce two functions

$$p(\omega) = \frac{1-\cos\omega t}{\omega} \qquad \text{and} \qquad d(\omega) = \frac{\sin\omega t}{\omega}, \tag{13.7}$$

as illustrated in Fig. 13.1. The function $p(\omega)$ always vanishes at $\omega = 0$ and decays as ω^{-1} when $\omega \to \pm\infty$. It has peaks of values $\pm at$ at $\pm b/t$, where $b = 2.33$ is the root of $b = \tan(b/2)$ and $a = 2b/(1+b^2) = 0.725$. These peaks grow linearly with t^{-1} and move closer to $\omega = 0$ as t increases. When $t \to \infty$, the function approaches

$$\lim_{t\to\infty} p(\omega) = \wp\frac{1}{\omega}, \tag{13.8}$$

where $\wp$ stands for the principal value. On the other hand, $d(\omega)$ has a peak of value t at $\omega = 0$ and rolls off as ω^{-1} for large ω, having the first zeroes at $\omega = \pm\pi/t$. As $t \to \infty$, the peak at $\omega = 0$ grows linearly with t while its width also shrinks inversely with t; the area enclosed is always π. Outside the peak, the function oscillates very fast with period $\Delta\omega \approx 2\pi/t$. When $t \to \infty$, the function approaches

$$\lim_{t\to\infty} d(\omega) = \pi\delta(\omega). \tag{13.9}$$

Coming back to Eq. (13.6), as $t \gg 1/\Delta\omega$, where $\Delta\omega$ is a measure of the width of the frequency distribution $\rho(\omega)$, all the transients die, leaving us with

$$\langle x(t)\rangle = \frac{A}{2\bar{\omega}}\left[\cos\Omega t\,\wp\int_{-\infty}^{\infty} d\omega\frac{\rho(\omega)}{\omega-\Omega} + \pi\rho(\Omega)\sin\Omega t\right]. \tag{13.10}$$

Let us now repeat the derivation with the force $A\sin\Omega t$ and combine the solution with the former to get the long-term response to the force $Ae^{-i\Omega t}$:

$$\langle x(t)\rangle = \frac{Ae^{-i\Omega t}}{2\bar{\omega}}\left[\wp\int_{-\infty}^{\infty} d\omega\,\frac{\rho(\omega)}{\omega-\Omega} + i\pi\rho(\Omega)\right] = \frac{Ae^{-i\Omega t}}{2\bar{\omega}\Delta\omega}\,R(u), \tag{13.11}$$

[†]Actually, "in phase" here implies the driving phase is in phase with the velocity $\dot{x}$.

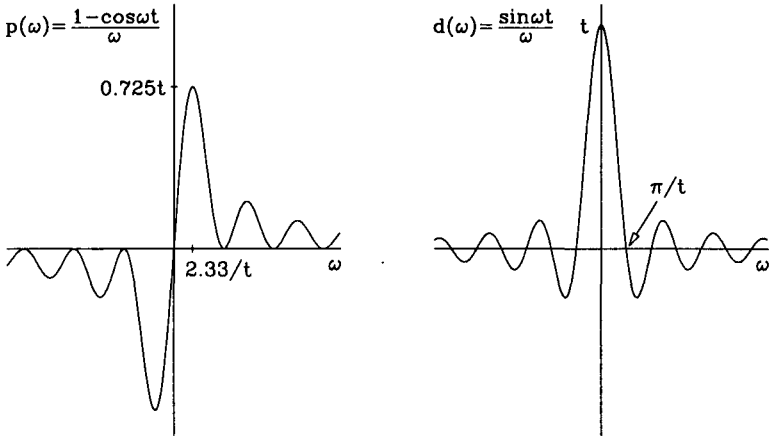


Fig. 13.1 Plots of the functions $p(\omega)$ and $d(\omega)$ with t being a parameter. As $t \to \infty$, $p(\omega) \to \wp\omega^{-1}$ and $d(\omega) \to \pi\delta(\omega)$, where $\wp$ denotes principal value.

where the *transfer function* (TF) is defined as

$$R(u) = f(u) + ig(u), \tag{13.12}$$

with

$$u = \frac{\bar{\omega} - \Omega}{\Delta\omega}, \tag{13.13}$$

and

$$f(u) = \Delta\omega\, \wp \int_{-\infty}^{\infty} d\omega\, \frac{\rho(\omega)}{\omega - \Omega} \qquad \text{and} \qquad g(u) = \pi\Delta\omega\, \rho(\bar{\omega} - u\Delta\omega). \tag{13.14}$$

Here $\Delta\omega$ is a measure of the width of the frequency distribution and the parameter u plays the role of the relative deviation of the frequency of the driving force from the mean frequency of the system. The transfer function is essentially the response of the particle per unit driving force. It is an important function, because it can be measured and it gives valuable information on the distribution function $\rho(\omega)$. As will be demonstrated below, when the driving force is acting on a beam inside a vacuum chamber, the transfer function contains also information on the coupling impedances of the vacuum chamber.

We can also combine the two expressions in Eq. (13.14) into one to obtain

$$R(u) = f(u) + ig(u) = \Delta\omega \int_{-\infty}^{\infty} d\omega\, \frac{\rho(\omega)}{\omega - \Omega - i\epsilon}. \tag{13.15}$$

There is a singularity in $R(u)$ when $\Omega = \omega - i\epsilon$ or $u\Delta\omega = \bar{\omega} - \omega + i\epsilon$. This implies that, if $\rho(\omega)$ is analytic, $R(u)$ is an analytic function with singularities only in the upper u-plane. Notice that instead of the derivation starting from the initial condition, the displacement of the center of the bunch, Eq. (13.11), can also be obtained directly by writing the force as

$$Ae^{-i(\Omega+i\epsilon)t} = Ae^{-i\Omega t}e^{\epsilon t}, \tag{13.16}$$

where ϵ is an infinitesimal positive number, so that the solution becomes

$$\langle x(t)\rangle = \frac{Ae^{-i\Omega t}}{2\bar{\omega}}\int_{-\infty}^{\infty} d\omega \frac{\rho(\omega)}{\omega - \Omega - i\epsilon} = \frac{Ae^{-i\Omega t}}{2\bar{\omega}}\left[\wp\int_{-\infty}^{\infty} d\omega \frac{\rho(\omega)}{\omega - \Omega} + i\pi\rho(\Omega)\right], \tag{13.17}$$

which is exactly the same as Eq. (13.11). The addition of the small ϵ implies that the force in Eq. (13.16) is zero at $t = -\infty$ and increases adiabatically.

13.2 Shock Response

With all the particles initially at rest, the beam is suddenly excited by a shock or a δ-pulse, imparting to the each beam particle either the same displacement x_0 or the same velocity displacement $\dot{x}_0$, but not both. From Eq. (13.2), we have the shock response either

$$\langle x(t)\rangle = x_0 H(t)\int_{-\infty}^{\infty} d\omega\, \rho(\omega)\cos\omega t, \tag{13.18}$$

or

$$\langle \dot{x}(t)\rangle = \dot{x}_0 H(t)\int_{-\infty}^{\infty} d\omega\, \rho(\omega)\cos\omega t, \tag{13.19}$$

where $H(t)$ is the Heaviside step function. We identify

$$G(t) = H(t)\int_{-\infty}^{\infty} d\omega\, \rho(\omega)\cos\omega t, \tag{13.20}$$

and call it the *transverse shock response function*, which is always real and vanishes when $t < 0$. The shock response function is important because it is an easily measured function and it can give information about the distribution function of the frequency as well as the transfer function.

It is interesting to show that there is a relation between the shock response function and the transfer function. The Fourier transform of the shock response

function is

$$\tilde{G}(\omega) = \frac{1}{2\pi}\int_0^\infty dt\, G(t) e^{i\omega t}, \tag{13.21}$$

where we notice that the integral starts from zero. The real part is

$$\begin{aligned}
\mathcal{R}e\,\tilde{G}(\omega) &= \frac{1}{2\pi}\int_0^\infty dt\, G(t)\cos\omega t = \frac{1}{2\pi}\int_0^\infty dt\, \cos\omega t \int_{-\infty}^\infty d\omega'\, \rho(\omega')\cos\omega' t \\
&= \frac{1}{4\pi}\int_{-\infty}^\infty d\omega' \rho(\omega') \int_{-\infty}^\infty dt\, \cos\omega t \cos\omega' t \\
&= \frac{1}{4}\int_{-\infty}^\infty d\omega' \rho(\omega')\big[\delta(\omega'-\omega) + \delta(\omega'+\omega)\big] = \frac{1}{4}\,\rho(\omega),
\end{aligned} \tag{13.22}$$

where $\delta(\omega'+\omega)$ has no contribution because the distribution is narrow and is centered at only one positive frequency. The imaginary part is

$$\begin{aligned}
\mathcal{I}m\,\tilde{G}(\omega) &= \frac{1}{2\pi}\int_0^\infty dt\, G(t)\sin\omega t = \frac{1}{2\pi}\int_0^\infty dt\, \sin\omega t \int_{-\infty}^\infty d\omega'\, \rho(\omega')\cos\omega' t \\
&= \frac{1}{4\pi}\int_{-\infty}^\infty d\omega' \rho(\omega') \int_0^\infty dt \left[\sin(\omega-\omega')t + \sin(\omega+\omega')t\right] \\
&= \frac{1}{4\pi}\left[\wp\int_{-\infty}^\infty d\omega' \frac{\rho(\omega')}{\omega-\omega'} + \wp\int_{-\infty}^\infty d\omega' \frac{\rho(\omega')}{\omega+\omega'}\right],
\end{aligned} \tag{13.23}$$

where again the last principal-value integral involving $\omega+\omega'$ can be neglected because of the narrow spread of the distribution ρ. We write these integrals as principal-value integrals because during the derivation, one integrand vanishes when $\omega'-\omega=0$ and the other vanishes when $\omega+\omega'=0$. Combining the result,

$$\begin{aligned}
\tilde{G}(\omega) &= \frac{-i}{2\pi}\left[\wp\int_{-\infty}^\infty d\omega' \frac{\rho(\omega')}{\omega'-\omega} + i\pi\rho(\omega)\right] \\
&= \frac{-i}{4\pi\Delta\omega}\Big[f(u) + ig(u)\Big] = \frac{-i}{4\pi\Delta\omega}R(u).
\end{aligned} \tag{13.24}$$

In other words, the Fourier transform of the shock response function is equal to the transfer function multiplied by $-i/(4\pi\Delta\omega)$. This also provides us with a way to compute the transfer function. The procedure is: compute the shock response function $G(t)$, find its Fourier transform $\tilde{G}(\omega)$, and then infer the transfer function $R(u)$. Thus we can also measure the shock response function $G(t)$ by imparting a kick to the beam and derive the transfer function $R(u)$ via Fourier transform.

As an example, take the Lorentz distribution

$$\rho(\omega) = \frac{\Delta\omega}{\pi} \frac{1}{(\omega - \bar{\omega})^2 + (\Delta\omega)^2}. \tag{13.25}$$

The shock response function is easily found to be

$$G(t) = H(t)\, \mathcal{R}e\, e^{i(\bar{\omega} + i\Delta\omega)t} = H(t) e^{-\Delta\omega t} \cos \bar{\omega} t. \tag{13.26}$$

Next the Fourier transform,

$$\begin{aligned} \tilde{G}(\omega) &= \frac{1}{2\pi} \int_0^\infty dt\, \cos \bar{\omega} t\, e^{(-\Delta\omega + i\omega)t} \\ &= \frac{1}{4\pi} \left[\frac{1}{-i(\bar{\omega} + \omega + i\Delta\omega)} + \frac{1}{i(\bar{\omega} - \omega - i\Delta\omega)} \right] = \frac{-i}{4\pi\Delta\omega} \frac{u + i}{u^2 + 1}, \end{aligned} \tag{13.27}$$

where again the smaller term involving $\omega_r + \omega$ has been removed. Thus the transfer function is

$$R(u) = f(u) + ig(u) = \frac{u + i}{u^2 + 1}, \tag{13.28}$$

which is equal to the Fourier transform of the shock response function $G(t)$ multiplied by $-i/(4\pi\Delta\omega)$. These results are depicted in Fig. 13.2. As expected, the shock excitation is the decay of the center displacement $\langle x \rangle$ or the center velocity displacement $\langle \dot{x} \rangle$. The decay comes from the distribution $\rho(\omega)$ so that each particle oscillates with a slightly different frequency. The particles will spread out and therefore the decay of the center displacement or the center velocity displacement. This is usually known as *decoherence* or *filamentation.* For the Lorentz distribution, the decay turns out to be exponential. However, it is important to point out that the center $\langle x \rangle$ decays because initially we have a nonzero x_0 but $\dot{x}_0 = 0$. In case $\dot{x}_0 \neq 0$, the Lorentz distribution *does not* give a decay of the center displacement (Exercise 13.1).

Table 13.1 lists the transfer function and shock response function for some commonly used frequency distributions (Exercise 13.2): the Lorentz distribution, the rectangular distribution, the parabolic distribution, the elliptical distribution, the bi-Lorentz distribution, and the Gaussian distribution.

Because the transfer function is the Fourier transform of shock response function, $G(t)$ is also the inverse Fourier transform of $R(u)$:

$$G(t) = \mathcal{R}e \frac{-i}{4\pi\Delta\omega} \int_{-\infty}^{\infty} d\omega\, R\left(\frac{\bar{\omega} - \omega}{\Delta\omega} \right) e^{-i\omega t}. \tag{13.29}$$

The symbol $\mathcal{R}e$ should not be there. It is there because we have consistently neglected the frequencies around $-\bar{\omega}$.

Table 13.1: Shock excitation function $G(t)$ and transfer function $R(u) = f(u) + ig(u)$ for various frequency distributions $\rho(\omega)$ with $v = (\omega_x - \omega)/\Delta\omega$.

Frequency Distribution		Shock Response	Response function	
Type	Distribution	$G(t)$	$f(u)$	$g(u)$
Lorentz	$\frac{1}{\pi\Delta\omega}\frac{1}{v^2+1}$	$e^{-\Delta\omega t}\cos\omega_x t$	$\frac{u}{u^2+1}$	$\frac{1}{u^2+1}$
rectangular	$\frac{1}{2\Delta\omega}H(1-\lvert v\rvert)$		$\frac{1}{2}\ln\left\lvert\frac{u+1}{u-1}\right\rvert$	$\frac{\pi}{2}H(1-\lvert u\rvert)$
parabolic	$\frac{3}{4\Delta\omega}(1-v^2)H(1-\lvert v\rvert)$		$\frac{3}{4}\left[(1-u^2)\ln\left\lvert\frac{u+\lvert!1}{u-1}\right\rvert+2u\right]$	$\frac{3\pi}{4}(1-u^2)H(1\lvert!-\lvert v\rvert)$
elliptical	$\frac{2}{\pi\Delta\omega}\sqrt{1-v^2}H(1-\lvert v\rvert)$		$2\left[u-\mathrm{sgn}(u)\sqrt{1-u^2}H(1-\lvert u\rvert)\right]$	$2\sqrt{1-u^2}H(1-\lvert u\rvert)$
bi-Lorentz	$\frac{2}{\pi\Delta\omega}\frac{1}{(v^2+1)^2}$		$\frac{u(u^2+3)}{(u^2+1)^2}$	$\frac{2}{(u^2+1)^2}$
Gaussian	$\frac{1}{\sqrt{2\pi}\Delta\omega}e^{-v^2/2}$	$e^{-(\Delta\omega t)^2/2}\cos\omega_x t$	$\sqrt{\frac{2}{\pi}}e^{-u^2/2}\int_0^\infty\frac{dy}{y}e^{-y^2/2}\sinh uy$	$\sqrt{\frac{\pi}{2}}e^{-u^2/2}$

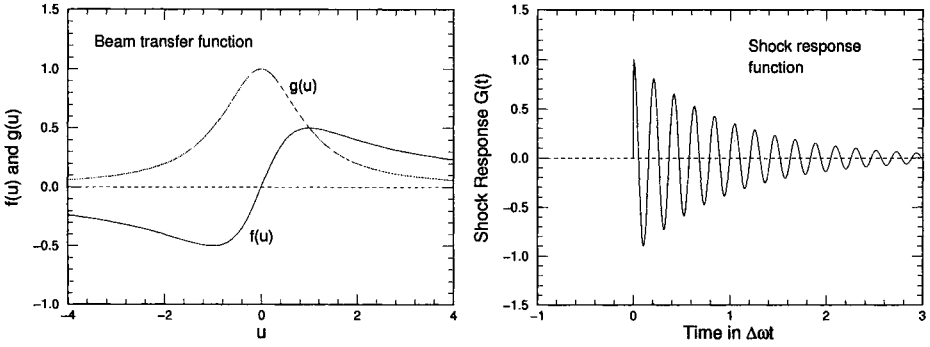


Fig. 13.2 Plots showing transfer function $R(u) = f(u) + ig(u)$ (left) and shock response function $G(t)$ (right) for Lorentz frequency distribution.

13.3 Landau Damping

After understanding the transfer function and the shock response function, let us come back to the transient response of a harmonic excitation; i.e., Eq. (13.6). The term proportional to $\sin \Omega t$ is driven in phase by the harmonic force, and the particles should be absorbing energy. Let us rewrite Eq. (13.3) in the approximation that the frequency distribution $\rho(\omega)$ is narrow around $\bar{\omega}$:

$$\langle x(t) \rangle = \frac{A \sin \bar{\omega} t}{\bar{\omega}} \int_{-\infty}^{\infty} d\omega \, \rho(\omega) \, \frac{\sin \frac{1}{2}(\omega - \Omega)t}{\omega - \Omega}. \tag{13.30}$$

Consider a component corresponding to the frequency ω, its envelope is

$$\text{Amplitude } (\omega) = \frac{A}{\bar{\omega}} \, \frac{\sin \frac{1}{2}(\omega - \Omega)t}{\omega - \Omega}. \tag{13.31}$$

This means that all particles having frequency ω are excited at $t = 0$, increase to a maximum of $A/[\bar{\omega}(\omega - \Omega)]$ at $t \approx \pi/(\omega - \Omega)$, and die down to zero again at $t = 2\pi/(\omega - \Omega)$. Thus, energy is gained but is given back to the system. For ω closer to Ω, the response amplitude rises to a larger amplitude and the energy is given back to the system at a later time. For those particles that have exactly the frequency Ω, the amplitude grows linearly with time and the energy keeps on growing. This process of ceasing to grow and transferring energy to the few particles having frequencies very close to Ω is called *Landau damping*. An illustration is shown in Fig. 13.3, where the solid curve shows a particle having exactly the same frequency as Ω and growing linearly, while the dashed curve shows a particle with frequency 95% of Ω decaying after about ten oscillations. In other words, particles with ω far away from Ω get excited, but the energy is

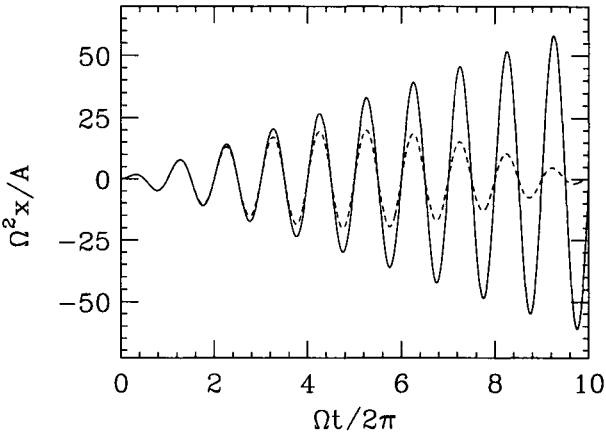


Fig. 13.3 Solid: The response of a particle having exactly the same frequency Ω as the driving force grows linearly in time. Dashes: The response of a particle having frequency 95% of Ω gives up its energy after about 10 oscillations.

returned to those particles having ω close to Ω, which are still absorbing energy. As time increases, particles with frequencies closer to Ω give up their energies to particles with frequencies much closer to Ω. Thus, as time progresses, less and less particles are still absorbing energy. As $t \to \infty$, only particles with frequency exactly equal to Ω will be absorbing energy, and there are only very few particles doing this. In practice, when these growing amplitudes hit the vacuum chamber, the process stops. This sets the time limit for Landau damping to stop. The damping process starts when the amplitude of the first particle is damped and this time is $t \approx 2\pi/\Delta\omega$.

Let us study the energy in the system. The energy is proportional to the square of the amplitude. Therefore the energy of all the particles is

$$\mathcal{E} = \frac{NA^2}{\bar{\omega}^2} \int_{-\infty}^{\infty} d\omega\, \rho(\omega)\, \frac{\sin^2(\omega - \Omega)t/2}{(\omega - \Omega)^2}, \tag{13.32}$$

where N is the total number of beam particles in the system. We see that as time progresses the amplitude square,

$$\Big[\text{Amplitude } (\omega)\Big]^2 = \frac{\sin^2(\omega - \Omega)t/2}{(\omega - \Omega)^2}, \tag{13.33}$$

becomes larger and larger while its width shrinks. This verifies that energy is being transfered by the particles having frequencies far away from Ω to particles having frequencies closer to Ω. Since the square of the amplitude always covers an area of $\pi t/2$, we have

$$\lim_{t\to\infty} \Big[\text{Amplitude}(\omega)\Big]^2 = \lim_{t\to\infty} \frac{\sin^2(\omega - \Omega)t/2}{(\omega - \Omega)^2} = \frac{\pi t}{2}\, \delta(\omega - \Omega). \tag{13.34}$$

Thus, at $t \to \infty$, the steady-state energy of the system is

$$\mathcal{E} = \frac{\pi}{2} \frac{NA^2}{\bar{\omega}^2} \rho(\Omega) t, \tag{13.35}$$

which increases linearly with time, and all this energy goes into those few particles having exactly the same frequency as Ω. However, we do see in the asymptotic solution of Eq. (13.10) that $\langle x(t) \rangle$ does not go to infinity. This is not a contradiction, because even when a few particles have very large and still growing amplitudes, the centroid will not be affected.

In our study so far, the amplitude A of the driving force is independent of the system of particles. For an instability in a particle beam, the situation is slightly different. The driving force comes from the wake fields of the beam particles interacting with the discontinuities of the vacuum chamber, and usually has an amplitude proportional to the center displacement of the beam. When there is a kick to the beam that creates a center displacement $\langle x(0) \rangle$ or a center displacement velocity $\langle \dot{x}(0) \rangle$, a force with amplitude $A \propto \langle x(0) \rangle$ or $\langle \dot{x}(0) \rangle$ is generated and drives the whole system of particles with the coherent frequency Ω. Each frequency component of the beam will receive the amount of response according to Eq. (13.31). Now two things happen. First, the particles give up their excited energy gradually to those particles having frequencies extremely close to Ω, the frequency of the driving force, and the center of displacement approaches the transfer function $R(u)$. Second, the center of displacement of the beam starts to decay according to the shock response function $G(t)$. As $\langle x(t) \rangle$ decreases, the driving force decreases also. Finally, the disturbance goes away. This is how Landau damping takes place in a beam. In fact, this process starts whenever the disturbance is of infinitesimal magnitude, implying that any disturbance will be damped as soon as it occurs. We say that there will be enough Landau damping to keep the beam stable. Notice that no frictional force has ever been introduced in the discussion. Thus, there is still conservation of energy in the presence of Landau damping, which merely redistributes energy from waves of one frequency to another.

In case the frequency spread $\Delta\omega$ is very very narrow, it will take $t \approx \pi/\Delta\omega$ for the first wave to surrender its energy to another that has frequency closer to Ω. This duration will be very long. Before this moment arrives, all frequency components continue to receive energy and $\langle x(t) \rangle$ increases and so will be the driving force. This is the picture of how an instability develops when the spread of frequency is not large enough to invoke Landau damping. However, the conservation of energy still holds. The energy that feeds the instability may be extracted from the longitudinal kinetic energy of the beam resulting in a slower speed, or from the rf system that replenishes the beam energy.

13.4 Transverse Bunched Beam Instabilities

Consider a bunch with infinitesimal longitudinal length but with finite transverse extent. We call this a slice bunch. We want to study its transverse motion. The frequency of interest here is the betatron frequency ω_β which has the incoherent tune shift included. The equation of motion of a particle with transverse displacement y is

$$\frac{d^2y}{ds^2} + \frac{\omega_\beta^2}{v^2}y = \frac{\langle F_1^\perp(\bar{y})\rangle}{\gamma m\beta^2 c^2}, \tag{13.36}$$

where $v = \beta c$ is the particle longitudinal velocity and $\bar{y}$ is the average displacement of the bunch (sometimes we use the notation $\langle y\rangle$). This is the same as Eq. (3.4) in Chapter 3, but with all the static tune shift, like the space-charge self-field tune shift, absorbed into ω_β^2. The force on the right side of Eq. (13.36) is related to the dynamic effects of the transverse wake function,‡

$$\langle F_1^\perp(\bar{y})\rangle = -\frac{e^2N_b}{C_0}\sum_{k=1}^{\infty}\bar{y}(s - kC_0)W_1(kC_0), \tag{13.37}$$

where the summation is over all previous turns and N_b is the number of particles in the bunch. The negative sign shows that the force is opposing the displacement. Because this is a slice bunch, the wake force can only come from the passage of the same bunch in previous turns. Let us denote a collective excitation of the dipole moment D of the bunch center $\bar{y}(s)$ at the collective frequency Ω by the ansatz

$$\bar{y}(s) = De^{-i\Omega s/(\beta c)}, \tag{13.38}$$

where Ω is to be determined. Expressing in terms of the transverse impedance $Z_1^\perp$, Eq. (13.36) becomes

$$\frac{d^2y}{ds^2} + \frac{\omega_\beta^2}{v^2}y = \frac{ie^2N_bD}{\gamma mcC_0^2}\sum_{p=-\infty}^{\infty}Z_1^\perp(\Omega + p\omega_0)e^{-i\Omega s/(\beta c)}. \tag{13.39}$$

When an average is made over all the particles in the bunch, Eq. (13.39) becomes one describing the center of the bunch. We obtain readily

$$\Omega - \omega_y = -\frac{ie^2N_b\beta^2 c\mathcal{Z}_\perp}{2\omega_\beta\gamma mC_0^2}, \tag{13.40}$$

‡Recall from Chapter 9 that the transverse wake force is totally dynamic and does not contain any static part. Strictly speaking, the formulation of wake potential requires $\gamma \to \infty$. Thus space-charge is not included.

where we have introduced a short-hand form for the impedance

$$\mathcal{Z}_\perp = \sum_{p=-\infty}^{\infty} Z_1^\perp(\Omega + p\omega_0). \tag{13.41}$$

Thus the transverse impedance samples the upper betatron sidebands of all revolution harmonics, positive and negative, when the beam is a point bunch. Equation (13.40) indicates that

$$(\Delta\omega_\beta)_{\text{dyn}} = -\frac{ie^2 N_b \beta^2 c \mathcal{Z}_\perp}{2\omega_\beta \gamma m C_0^2} \tag{13.42}$$

is the *dynamic part* of the *wake-induced* betatron frequency shift. It is important to understand that $(\Delta\omega_\beta)_{\text{dyn}}$ is different from the *coherent* betatron tune shift $(\Delta\omega_\beta)_{\text{coh}}$. There are two contributions to the coherent betatron tune shift: the static part $(\Delta\omega_\beta)_{\text{stat}}$ and the dynamic part $(\Delta\omega_\beta)_{\text{dyn}}$. As was demonstrated in Sec. 3.5 that in the absence of any incoherent frequency spread, $(\Delta\omega_\beta)_{\text{incoh}}$ is equal to the static part of the coherent frequency shift. As a result, we can also write[§]

$$(\Delta\omega_\beta)_{\text{dyn}} = (\Delta\omega_\beta)_{\text{coh}} - (\Delta\omega_\beta)_{\text{incoh}}\,, \tag{13.43}$$

provided there is no spread in $(\Delta\omega_\beta)_{\text{incoh}}$. Thus $(\Delta\omega_\beta)_{\text{dyn}}$ is the same as the coherent betatron tune shift only when the incoherent tune shift vanishes. The incoherent (or static coherent) frequency shift receives contributions from space-charge, image effects, etc. On the other hand, since ω_β on the left side of Eq. (13.40) is the sum of the bare betatron frequency $\omega_{\beta 0}$ and the incoherent frequency shift $(\Delta\omega_\beta)_{\text{incoh}}$, we can solve for the collective frequency Ω in the absence of betatron frequency spread with the aid of Eq. (13.43), resulting in

$$\Omega = \omega_{\beta 0} + (\Delta\omega_\beta)_{\text{coh}}\,, \tag{13.44}$$

verifying that Ω is indeed the coherent frequency of the system.

[§]For a beam inside a vacuum chamber, the incoherent betatron tune shift of a beam particle consists of space-charge tune shift represented by the space-charge coefficient ϵ_{spch} and the incoherent wall-image tune shift represented by the Laslett incoherent electric coefficient ϵ_1. This incoherent betatron tune shift is also called the static part of the coherent betatron tune shift. The dynamic part of the coherent tune shift consists of contributions from the transverse impedances: the resistive-wall impedance, space-charge impedance, etc. Note that the space-charge impedance, as detailed in Sec. 3.5, consists of two parts: the self-field part, which cancels exactly the incoherent space-charge tune shift so that space-charge does not affect the center-of-mass of the beam, and the wall-image part represented by the Laslett image coefficients $\xi_1 - \epsilon_1$, which cancels the incoherent wall-image tune shift leaving behind the coherent part represented by ξ_1. The cancellation will not happen when there is a spread in the incoherent betatron tune shift.

While the imaginary part of the impedance contributes a real betatron tune shift, the coherent tune shift has a positive imaginary part when $\mathcal{R}e\,\mathcal{Z}_\perp < 0$ leading to beam instability. If the driving impedance is narrow and covers less than one revolution harmonic centering roughly at $q\omega_0$, where q is an integer, and if the residual or decimal part of the betatron tune $[\nu_\beta] < \frac{1}{2}$, only two terms, $p = \pm q$, survive and Eq. (13.41) becomes

$$\mathcal{R}e\,\mathcal{Z}_\perp \approx \mathcal{R}e\,Z_1^\perp\Big[(q + [\nu_\beta])\omega_0\Big] - \mathcal{R}e\,Z_1^\perp\Big[(q - [\nu_\beta])\omega_0\Big]. \tag{13.45}$$

The bunch will be stable/unstable if the impedance peaks above/below $q\omega_0$. If $[\nu_\beta] > \frac{1}{2}$, however, Eq. (13.41) reduces to two other surviving terms instead:

$$\mathcal{R}e\,\mathcal{Z}_\perp \approx \mathcal{R}e\,Z_1^\perp\Big[(q - 1 + [\nu_\beta])\omega_0\Big] - \mathcal{R}e\,Z_1^\perp\Big[(q + 1 - [\nu_\beta])\omega_0\Big]. \tag{13.46}$$

The bunch will be stable/unstable if the impedance peaks below/above $q\omega_0$. This is just an example of Robinson instability in the transverse plane. The above summarizes what we have learned before without Landau damping.

Now let us introduce a distribution $\rho(\omega_\beta)$ for the betatron frequency among the beam particles. This distribution is centered at $\bar{\omega}_\beta$ with a spread $\Delta\omega$. The solution of Eq. (13.39) becomes

$$\begin{aligned}\bar{y}(s) &= \frac{ie^2 N_b D\beta^2 c\mathcal{Z}_\perp}{2\bar{\omega}_\beta\gamma m C_0^2}\, e^{-i\Omega s/(\beta c)} \int_{-\infty}^{\infty} d\omega_\beta \frac{\rho(\omega_\beta)}{\omega_\beta - \Omega - i\epsilon} \\ &= \frac{ie^2 N_b D\beta^2 c\mathcal{Z}_\perp}{2\bar{\omega}_\beta\Delta\omega\gamma m C_0^2}\, e^{-i\Omega s/(\beta c)} R(u),\end{aligned} \tag{13.47}$$

where the relation has been made to the transfer function $R(u)$ with $u = (\bar{\omega}_\beta - \Omega)/\Delta\omega$. If the ansatz of Eq. (13.38) is employed for $\bar{y}(s)$, we obtain

$$\frac{ie^2 N_b \beta^2 c\mathcal{Z}_\perp}{2\bar{\omega}_\beta\Delta\omega\gamma m C_0^2} = \frac{1}{R(u)}, \tag{13.48}$$

or

$$-\frac{(\Delta\omega_\beta)_{\rm dyn}}{\Delta\omega} = \frac{1}{R(u)}. \tag{13.49}$$

This is a dispersion relation for the coherent frequency Ω. Given the impedance $\mathcal{Z}_\perp$, the left side is a constant and Ω can be solved. More practically, we start with a fixed $\mathcal{I}m\,\Omega$, and solve for the impedance $\mathcal{Z}$ while varying $\mathcal{R}e\,\Omega$. The result plotted in the complex impedance plane will be a contour for a fixed growth rate. In particular, we are interested in the contour for the threshold when $\mathcal{I}m\,\Omega = 0+$. This will be exactly the same as the loci of $\mathcal{R}e\,u$ in the complex $1/R(u)$-plane

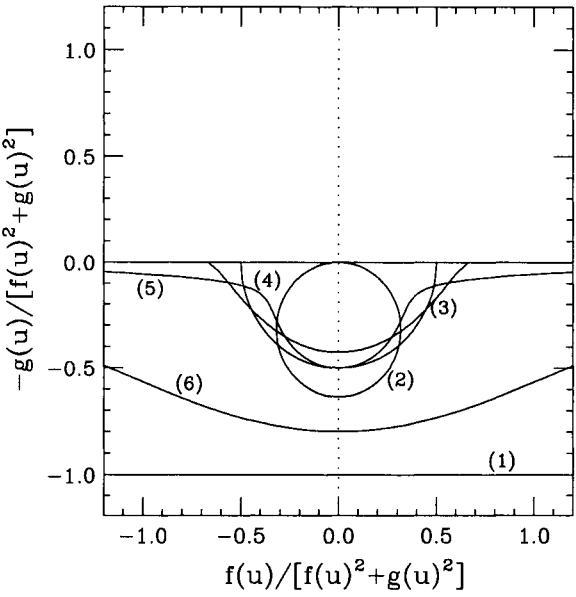


Fig. 13.4 Threshold curves in the $1/R(u)$-plane, where the stability region for every distribution is to the top of the curve and the instability region to the bottom. (1) Lorentz distribution, (2) rectangular distribution (a circle touching the horizontal axis), (3) parabolic distribution, (4) elliptical distribution (part of the dashed circle centered at origin), (5) bi-Lorentz distribution, (6) Gaussian distribution.

with $\mathcal{I}m\, u = 0$. Such threshold contours are plotted in Fig. 13.4 for various distributions. Remember that instability is generated by $\Omega \to \Omega + i\epsilon$ with ϵ real and positive. This translates into $u \to u - i\epsilon$. For the Lorentz distribution,

$$\frac{1}{R(u)} = u - i, \tag{13.50}$$

and it will be unstable if

$$\frac{1}{R(\mathcal{R}e\, u - i\epsilon)} = \mathcal{R}e\, u - i(1+\epsilon). \tag{13.51}$$

Therefore the unstable region is below $\mathcal{I}m\, R(u)^{-1} = -i$, while the stable region is above $\mathcal{I}m\, R(u)^{-1} = -i$. Since the various distributions have been introduced with all different definitions of frequency spread $\Delta\omega$, Fig. 13.4 is not a good plot for comparison. Instead, we would like to reference everything with respect to the half-width-at-half-maximum (HWHM) frequency spread $\Delta\omega_{\text{HWHM}}$. Thus, we define a new variable x to replace u:

$$u = xS \qquad \text{with} \qquad S = \frac{\Delta\omega_{\text{HWHM}}}{\Delta\omega}. \tag{13.52}$$

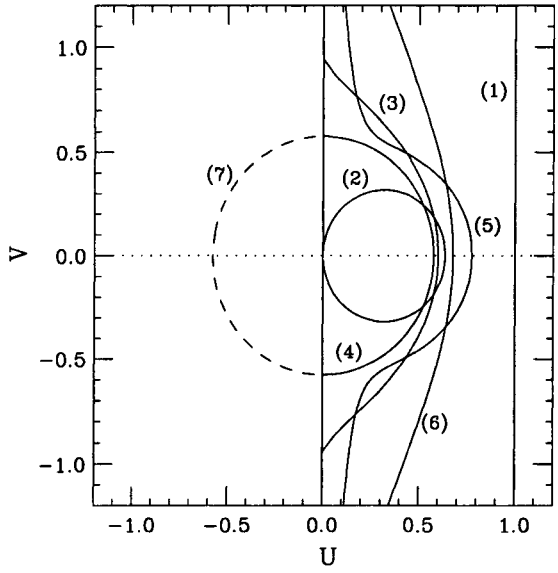


Fig. 13.5 Threshold curves in the U-V-plane plotted with reference to the HWHM frequency spread. In every case the stability region is to the left of the curve and the instability region to the right. (1) Lorentz distribution, (2) rectangular distribution (a circle touching the V-axis), (3) parabolic distribution, (4) elliptical distribution (part of the dashed circle centered at origin), (5) bi-Lorentz distribution, (6) Gaussian distribution. The Keil–Schnell type stability circle is depicted in dashes by (7).

Equation (13.49) is rewritten as

$$-\frac{(\Delta\omega_\beta)_{\text{dyn}}}{\Delta\omega_{\text{HWHM}}} = \frac{1}{\hat{R}(x)}, \tag{13.53}$$

where

$$\hat{R}(x) = \hat{f}(x) + i\hat{g}(x) = [f(u) + ig(u)]S = \int_{-\infty}^{\infty} dx' \frac{\rho(x')}{x' + x - i\epsilon}. \tag{13.54}$$

Now the frequency distribution ρ is a function of $x' = (\omega - \bar{\omega})/\Delta\omega_{\text{HWHM}}$ and is normalized to unity when integrated over x'. The normalized transfer function $\hat{R}(x)$ is now independent of $\Delta\omega$, which can have a different definition for a different distribution, and so is the normalized dispersion relation. It is customary to call the left side of Eq. (13.53) $-i(U + iV)$, following the counterpart in longitudinal microwave threshold, or

$$U + iV = \frac{i}{\hat{R}(x)} = \frac{i\hat{f}(x) + \hat{g}(x)}{\hat{f}^2(x) + \hat{g}^2(x)}, \tag{13.55}$$

so that $U \propto -\mathcal{R}e\, \mathcal{Z}_\perp$ and $V \propto -\mathcal{I}m\, \mathcal{Z}_\perp$. The threshold curves for various frequency distributions are plotted in Fig. 13.5. Thus, whatever values of (U, V) lie to the left of the locus will be stable and whatever is on the right will be unstable. Without Landau damping, any $U > 0$, which implies betatron frequency shift with a positive imaginary part, will be unstable. Now, with Landau damping,

Table 13.2 U-intercept and form factor F defined in Eq. (13.56) for various distributions.

Distribution	$\frac{1}{g(0)}$	$S=\frac{(\Delta\omega_\beta)_{\text{HWHM}}}{\Delta\omega}$	U-intercept $\frac{1}{\hat{g}(0)}=\frac{1}{g(0)S}$	Form factor $F=\frac{\sqrt{3}}{\hat{g}(0)}$
Lorentz	1	1	1	$\sqrt{3}$
rectangular	$\frac{2}{\pi}$	1	$\frac{2}{\pi}$	$\frac{2\sqrt{3}}{\pi}$
parabolic	$\frac{4}{3\pi}$	$\frac{1}{\sqrt{2}}$	$\frac{4\sqrt{2}}{3\pi}$	$\frac{4}{\pi}\sqrt{\frac{2}{3}}$
elliptical	$\frac{1}{2}$	$\frac{\sqrt{3}}{2}$	$\frac{1}{\sqrt{3}}$	1
bi-Lorentz	$\frac{1}{2}$	$\sqrt{\sqrt{2}-1}$	$\frac{1}{2\sqrt{\sqrt{2}-1}}$	$\frac{1}{2}\sqrt{\frac{3}{\sqrt{2}-1}}$
Gaussian	$\sqrt{\frac{2}{\pi}}$	$\sqrt{2\ln 2}$	$\frac{1}{\sqrt{\pi\ln 2}}$	$\sqrt{\frac{3}{\pi\ln 2}}$

the threshold has shifted to, for example, $U = 1$ for the Lorentz distribution. There is one point on the stability curve that is simple to obtain. It is the point at $x = 0$. There $\hat{f}(x) = 0$, so that $V = 0$ and $U = 1/\hat{g}(0)$. This point is important because it gives a rough idea of the threshold of instability. Similar to the Keil–Schnell stability circle for longitudinal microwave stability, we try to enclose the stability region in the U-V-plane by a circle of radius $\frac{1}{\sqrt{3}}$, which is shown in Fig. 13.5 as a dashed circle. This threshold circle coincides with the semi-circle of the elliptical distribution. Thus, the stability limit can be written as

$$\left|(\Delta\omega_\beta)_{\text{dyn}}\right| \lesssim \frac{1}{\sqrt{3}}(\Delta\omega_\beta)_{\text{HWHM}}F, \tag{13.56}$$

where F is a form factor depending on the distribution and is equal to unity for the elliptical distribution. Form factors for various distributions are tabulated in Table 13.2 (Exercise 13.3). Figure 13.5 shows how far a frequency distribution has its instability threshold deviated from the Keil–Schnell type circle of Eq. (13.56). We see that the deviation of F from unity or the threshold curve from the Keil–Schnell circle increases as the distribution goes from elliptical, parabolic, rectangular, Gaussian, bi-Lorentz, to Lorentz.

Thus, a betatron tune spread can provide Landau damping for instabilities driven by the discontinuities of the vacuum chamber, provided that the driving impedance is not too large. The transverse mode-mixing or mode-coupling instabilities that we studied in Chapter 11 have not had Landau damping in-

cluded. However, mode-coupling instability involves the coherent shifting of a betatron spectral line by as much as the synchrotron frequency. In order for Landau damping to work, a betatron tune spread of the order of the synchrotron frequency will be necessary. This amount of tune spread is quite simple for proton machines where the synchrotron tune is of the order $\nu_s \sim 0.001$. This provides for another explanation why transverse mode-mixing instabilities are usually not seen in proton machines. On the other hand, the synchrotron tunes for electron machines are usually $\nu_s \sim 0.01$. A betatron tune spread of this size is considered too large. For this reason, transverse mode-mixing instabilities in electron machines are usually alleviated by reactive dampers instead.

13.5 Longitudinal Bunched Beam Instabilities

In a bunch, Landau damping proceeds through the spread in synchrotron frequency. Consider a very short bunch consisting of N_b particles. The arrival time τ of a particle ahead of the synchronous particle is governed by the equation of motion

$$\frac{d^2\tau}{ds^2} + \frac{\omega_s^2}{v^2}\,\tau = \frac{e^2 N_b \eta}{v\beta^2 E_0 C_0} \sum_{k=-\infty}^{\infty} \Big\{ W_0'\big[kT_0 + \bar{\tau}(s - kC_0) - \bar{\tau}(s)\big] - W_0'\big[kT_0 - \bar{\tau}(s)\big] \Big\}, \tag{13.57}$$

where $v = \beta c$ is the nominal particle velocity and $\bar{\tau}$ is the arrival time of the bunch center ahead of the synchronous particle. On the left side of the equation, ω_s represents the potential-well-distorted synchrotron frequency, which is the sum of the bare synchrotron frequency ω_{s0} and the incoherent frequency shift $(\Delta\omega_s)_{\text{incoh}}$ coming from the static perturbation of the wake fields. For this reason, we should include only the dynamic part of the longitudinal wake force on the right side. We recall Eq. (8.55) in Chapter 8 that the dynamic part of the linear bunch density is

$$\lambda(\tau'; s)\Big|_{\text{dyn}} = \delta\big[\tau' - \bar{\tau}(s - kC_0)\big] - \delta(\tau'), \tag{13.58}$$

and this expression should be included in the derivation of the wake force. This explains the subtraction of the static part of the wake force on the right side of Eq. (13.57).

Since the amplitude of synchrotron oscillation of the bunch center must be very much less than the circumference of the accelerator ring, a Taylor's expan-

sion of the wake function is allowed, giving

$$\frac{d^2\tau}{ds^2} + \frac{\omega_s^2}{v^2}\tau = \frac{e^2 N_b \eta}{v\beta^2 E_0 C_0} \sum_{k=-\infty}^{\infty} \tau(s - kC_0) W_0''(kT_0). \tag{13.59}$$

Comparing with Eq. (8.46), we have ignored the wake field within the bunch because the bunch is very short, and only included the effects from the bunch passage through a fixed location of the accelerator ring in previous turns.

Introduce the ansatz

$$\bar{\tau}(s) = Be^{-i\Omega s/v}, \tag{13.60}$$

with Ω being the collective angular frequency to be determined. We next go to the frequency domain by introducing the longitudinal impedance $Z_0^{\parallel}$. Equation (13.57) can be written as

$$\frac{d^2\tau}{ds^2} + \frac{\omega_s^2}{v^2}\tau = -\frac{ie^2 N_b \eta B \omega_0 \mathcal{Z}_{\parallel}}{\beta^2 E_0 C_0^2} e^{-i\Omega s/v}, \tag{13.61}$$

where we have used the short-hand notation

$$\mathcal{Z}_{\parallel} = \sum_{p=-\infty}^{\infty} \left(p + \frac{\Omega}{\omega_0}\right) Z_0^{\parallel}(p\omega_0 + \Omega). \tag{13.62}$$

Thus the longitudinal impedance samples the upper synchrotron sidebands of all the revolution harmonics, positive and negative, when the bunch is as short as a point. Averaging Eq. (13.61) over all the particles in the bunch, the equation becomes one describing the center of the bunch. We then obtain

$$\Omega - \omega_s = (\Delta\omega_s)_{\text{dyn}}, \tag{13.63}$$

where

$$(\Delta\omega_s)_{\text{dyn}} = \frac{ie^2 N_b \omega_0 c^2 \eta \mathcal{Z}_{\parallel}}{2\omega_s E_0 C_0^2} \tag{13.64}$$

is identify as the *dynamic wake-induced* synchrotron frequency shift in the absence of spread in incoherence synchrotron frequency. The comments on the transverse situation apply here as well. We have, $(\Delta\omega_s)_{\text{dyn}} = (\Delta\omega_s)_{\text{coh}} - (\Delta\omega_s)_{\text{incoh}}$, when there is no spread in incoherent synchrotron frequency. Then $\Omega = \omega_{s0} + (\Delta\omega_s)_{\text{coh}}$ is the coherent frequency of the beam.

If the impedance is a narrow resonance centered at ω_r near $q\omega$, only two terms contribute to $\mathcal{R}e\,\mathcal{Z}_{\parallel}$:

$$\mathcal{R}e\,\mathcal{Z}_{\parallel} \approx \frac{\omega_r}{\omega_0}\left[\mathcal{R}e\,Z_0^{\parallel}(\Omega + p\omega_0) - \mathcal{R}e\,Z_0^{\parallel}(p\omega_0 - \Omega)\right], \tag{13.65}$$

where the coherent frequency Ω is close to the synchrotron frequency ω_s. Above transition ($\eta > 0$), this leads to stability/instability if the resonance peak leans towards the lower/upper synchrotron sideband, in agreement with Robinson's stability criterion. So far we have just repeated the point-bunch model studied in Chapter 8 and no Landau damping has been included.

Suppose that the particles in the bunch have a distribution $\rho(\omega_s)$ in synchrotron frequency, centering at $\bar{\omega}_s$ with spread $\Delta\omega_s$. We solve for $\tau(s)$ in Eq. (13.61). Then integrate with the distribution to get

$$\bar{\tau}(s) = -\frac{ie^2 N_b \eta B \omega_0 c^2 Z_\parallel}{2\bar{\omega}_s E_0 C_0^2} e^{-i\Omega s/v} \int d\omega_s \frac{\rho(\omega_s)}{\omega_s - \Omega - i\epsilon}. \tag{13.66}$$

With the ansatz of Eq. (13.60), self-consistency leads to the dispersion relation

$$-\frac{ie^2 N_b \omega_0 v^2 \eta Z_\parallel}{2\bar{\omega}_s \beta^2 E_0 C_0^2 \Delta\omega_s} = \frac{1}{R(u)}, \tag{13.67}$$

with $u = (\bar{\omega}_s - \Omega)/\Delta\omega_s$. Thus, using Eq. (13.64), we can again write

$$-\frac{(\Delta\omega_s)_{\rm dyn}}{\Delta\omega_s} = \frac{1}{R(u)}. \tag{13.68}$$

Therefore, we can define

$$U + iV = -i\frac{(\Delta\omega_s)_{\rm dyn}}{(\Delta\omega_s)_{\rm HWHM}} = \frac{i}{\hat{R}(x)} = \frac{\hat{g}(u) + i\hat{f}(x)}{\hat{f}^2(x) + \hat{g}^2(x)} \quad \text{with} \quad u = x\frac{(\Delta\omega_s)_{\rm HWHM}}{\Delta\omega_s}. \tag{13.69}$$

The stability threshold curve in the U-V-plane is exactly the same as in the transverse bunch instability analyzed in the previous section. The Keil–Schnell like stability circle is

$$|(\Delta\omega_s)_{\rm dyn}| \lesssim \frac{1}{\sqrt{3}}(\Delta\omega_s)_{\rm HWHM} F, \tag{13.70}$$

where $(\Delta\omega_s)_{\rm HWHM}$ is the half-width-at-half-maximum of the synchrotron frequency spread, and the form factors F for various distribution are exactly the same as given in Table 13.2.

The above example is a demonstration of Landau damping in the presence of Robinson stability or instability. Therefore, even if the rf resonant peak is shifted in the wrong way so that the beam is Robinson unstable, there is still Landau damping from the spread in synchrotron frequency that may be able to stabilize the beam. However, this will not help much usually, because the synchrotron frequency spread is mostly not large enough unless there is a higher-harmonic rf system.

13.6 Transverse Unbunched Beam Instabilities

Consider an unbunched beam containing N particles oscillating in the transverse plane. The beam has a transverse dipole $D(s,t)$ density (per unit longitudinal length) which depends on the location s along the ring and also time t. This is in fact the perturbed beam with the stationary distribution subtracted. Consider the ansatz

$$D(s,t) = \frac{eN}{C_0}\langle y(s,t)\rangle = \frac{eN\Delta}{C_0}\, e^{i(ns/R-\Omega t)}, \tag{13.71}$$

where Δ is the maximum transverse deviation, n is a revolution harmonic, $R = C_0/(2\pi)$ is the mean radius of the ring, and Ω is the coherent frequency to be determined. This is a snapshot view of the deviation of the perturbed beam and therefore must be a periodic function of the ring circumference. The ansatz in Eq. (13.71) assumes that the revolution harmonics are not related and each one can be studied independently.

A test particle at a fixed location s along the ring experiences a transverse force left by the dipole wave. At time t, this force is

$$\langle F_1^{\perp}(s,t)\rangle = -\frac{e}{C_0}\int_t^{\infty} vdt' W_1(vt'-vt)D(s,t') = \frac{iev\beta D(s,t)Z_1^{\perp}(\Omega)}{C_0}, \tag{13.72}$$

where $v = \beta c$ is the velocity of the beam particles. Since the impedance is at a fixed location, the impedance at s sees only the time variation of the dipole density of Eq. (13.71) and samples only the frequency Ω of the dipole wave. The impedance will have no knowledge about the harmonic variation of the wave around the ring. However, as will be shown below, the solution of Ω does depend on the revolution harmonic.

For a particle inside the beam, the situation is different because it moves with the beam at velocity v. Consider the specific particle which passes the location S at time $t = 0$. Its location at a later time changes according to $s = S + vt$. Its transverse displacement $y(s,t)$ is governed by the equation of motion,

$$\frac{d^2y}{dt^2} + \omega_\beta^2 y = \frac{\langle F_1^{\perp}(S+vt,t)\rangle}{\gamma m} = \frac{ie^2NcZ_1^{\perp}(\Omega)\Delta}{E_0T_0^2}\, e^{inS/R-i(\Omega-n\omega_0)t}, \tag{13.73}$$

where $E_0 = \gamma mc^2$ is the energy of the beam particle, m is its mass, and T_0 is the revolution period. Although the impedance is still sampling the frequency Ω, the transverse motion of the particle is driven by a force at the frequency $\Omega - n\omega_0$, with $\omega_0 = v/R$ denoting the revolution angular frequency of the particle around the ring. It is important to point out that the time derivative in this equation is the *total* time derivative, because we are studying the particle displacement

while traveling with the particle longitudinally. That explains why we have substituted $s = S + vt$ in the exponent on the right hand side. In order to have a clearer picture, let us travel with the particle longitudinally and at the same time count the number of transverse oscillations the particle makes in a revolution turn. The result is the incoherent tune of the particle $\nu_\beta = \omega_\beta/\omega_0$, which equals $(\Omega - n\omega_0)/\omega_0$ when the perturbation of the wake fields is minimal. On the other hand, from a beam-position monitor (BPM) at a fixed location monitoring the transverse motion of the particle, what it measures is the frequency Ω or the residual betatron tune (the fractional part of the betatron tune) of the particle.

This force-driven differential equation (13.73) can be solved easily, giving the solution

$$\left[\omega_\beta^2 - (\Omega - n\omega_0)^2\right] y(s,t) = \frac{ie^2 N c Z_1^\perp(\Omega)\Delta}{E_0 T_0^2}\, e^{inS/R - i(\Omega - n\omega_0)t}. \tag{13.74}$$

Self-consistency requires $y(s,t) = \Delta e^{i(ns/R - \Omega t)}$, which cancels the exponential on the other side. For small perturbation, there are two solutions for the coherent frequency, $\Omega \approx n\omega_0 \pm \omega_\beta$. For a coasting beam, when we are talking about positive and negative revolution harmonics, we will arrive at the same physical conclusion when we choose either $n\omega_0 + \omega_\beta$ or $n\omega_0 - \omega_\beta$. This is because (1) the beam spectra of the two choices are related by symmetry and (2) $Z_1^\perp(\omega)$ has definite symmetry about $\omega = 0$. This reminds us of a similar situation when we studied synchrotron sidebands in Chapter 6. However, one must be aware that for a bunched beam, there will be synchrotron sidebands around the betatron line and the beam spectrum will no longer possess this property. With the convention in Fig. 9.3 or Eq. (9.27), we need to choose the positive sign, or there is only upper betatron sidebands. This leads us to the dynamic part of the wake-induced betatron frequency shift of the beam

$$(\Delta\omega_\beta)_{\rm dyn} = \Omega - (n\omega_0 + \omega_\beta) \approx -\frac{ie^2 N c}{2\omega_\beta E_0 T_0^2}\, Z_1^\perp(n\omega_0 + \omega_\beta). \tag{13.75}$$

The imaginary part of the transverse impedance provides a true betatron tune shift. The real part, $\mathcal{R}e\, Z_1^\perp$, however, will lead to damping/instability if the frequency sampled by the impedance is positive/negative. In case $n\omega_0 + \omega_\beta = (n + \nu_\beta)\omega_0 < 0$, we write $n + \nu_\beta = -(|n| - \nu_\beta)$ so that the betatron line appears to be the lower sideband of the positive harmonic $|n|$. Thus, we have the conclusion that the beam is stable when a sharp resonance is driving at the upper sideband and unstable when it is driving at the lower sideband. Here, one must be careful that not all *upper* sidebands of a negative revolution harmonics will become *lower* sidebands in the language of positive frequency and hence can be unstable. This

is because the betatron tune $\nu_\beta = \nu_\beta^I + [\nu_\beta]$ has an integer part ν_β^I and a residual (or decimal) part $[\nu_\beta]$. The *upper* sideband of the harmonic n can be unstable[¶] only if $(n + \nu_\beta^I) < 0$.

To introduce Landau damping, let us allow a distribution $\rho(\omega_\beta)$ in betatron frequency among the beam particles. The distribution is centered at $\bar{\omega}_\beta$ with a narrow spread $\Delta\omega_\beta$. From Eq. (13.75) we obtain the dispersion relation

$$1 = \frac{ie^2 N c Z_1^\perp(\Omega)}{2\bar{\omega}_\beta E_0 T_0^2} \int d\omega_\beta \frac{\rho(\omega_\beta)}{\omega_\beta - (\Omega - n\omega_0)}. \tag{13.76}$$

This is a dispersion relation because it gives the relation between the wave number n/R and frequency Ω. Or

$$-\frac{(\Delta\omega_\beta)_{\text{dyn}}}{\Delta\omega_\beta} = \frac{1}{R(u)}, \tag{13.77}$$

where $u = (\bar{\omega}_\beta - \Omega - n\omega_0)/\Delta\omega_\beta$. This relation is exactly the same as Eq. (13.49). The only difference is that the dependence of the coherent betatron tune shift on impedance is different. Thus, we have also the Keil–Schnell like stability threshold

$$(\Delta\omega_\beta)_{\text{dyn}} \lesssim \frac{1}{\sqrt{3}} (\Delta\omega_\beta)_{\text{HWHM}} F. \tag{13.78}$$

Some comments are in order.

(1) In the dispersion relation of Eq. (13.76), the solution gives, for small driving impedance, $\Omega \approx (n + \nu_\beta)\omega_0$. Depending on whether $n + \nu_\beta^I$ is positive or negative, this corresponds to two different types of dipole waves, those with phase velocities higher than the particle's velocity are called *fast waves*, while those with phase velocities lower than the particle's velocity are called *slow waves*. As per the discussion above, only the slow waves will lead to beam instability. Recall Sec. 9.2 that there are also some super-slow waves which are always stable.

(2) We have introduced a spread of the betatron frequency in order to arrive at Landau damping. In fact, the revolution frequency ω_0 in the denominator of the integrand of Eq. (13.76) also has a spread and can contribute to Landau damping. Instead of the betatron frequency distribution $\rho(\omega_\beta)$, it will be more general to introduce the particle momentum distribution $\rho(\delta)$. We can develop the local betatron frequency up to the terms linear in the fractional

[¶]There is no such complexity with the synchrotron sidebands, because the synchrotron tune does not have an integer part.

momentum spread δ:

$$(n+\nu_\beta)\omega_0 = (n+\bar{\nu}_\beta)\bar{\omega}_0 + \Big[\xi - (n+\bar{\nu}_\beta)\eta\Big]\bar{\omega}_0\delta, \tag{13.79}$$

where ξ is the chromaticity and η is the slip factor in the longitudinal phase space, while $\bar{\nu}_\beta$ and $\bar{\omega}_0$ represent the nominal betatron tune and revolution frequency. The negative sign comes about because the revolution frequency becomes smaller/larger for a particle with positive momentum offset above/below transition. For the dangerous slow wave, let us denote $\hat{n} = -(n+\nu_\beta^I)$ where $\hat{n} > 0$. The above leads to

$$\Delta(n+\nu_\beta)\omega_0 = \Big[\xi + (\hat{n} - [\bar{\nu}_\beta])\eta\Big]\bar{\omega}_0\delta. \tag{13.80}$$

The integral in the dispersion relation becomes

$$\int d\omega_\beta \frac{\rho(\omega_\beta)}{\omega_\beta - (\Omega - n\omega_0)} \longrightarrow \int d\delta \frac{\rho(\delta)}{S_\beta\bar{\omega}_0\delta - \hat{\Omega}}, \tag{13.81}$$

where $\hat{\Omega} = \Omega - (n+\bar{\nu}_\beta)\bar{\omega}_0$, and

$$S_\beta = \xi + (\hat{n} - [\nu_{\bar{\beta}}])\eta \tag{13.82}$$

is usually called the *effective chromaticity*. One immediate conclusion is that when the chromaticity is negative and the ring is operating above transition ($\eta > 0$), it may happen for some $\hat{n}$ that $S_\beta = \xi + (\hat{n} - [\bar{\nu}_\beta])\eta \approx 0$. When this happens there will not be any Landau damping at all. The same is true for a positive chromaticity below transition. The dispersion relation can be rewritten as

$$-\frac{(\Delta\omega_\beta)_{\text{dyn}}}{S_\beta\bar{\omega}_0\Delta\delta} = \frac{1}{R(u)}, \tag{13.83}$$

where

$$u = \frac{1}{\Delta\delta}\left[\bar{\delta} - \frac{\hat{\Omega}}{S_\beta\bar{\omega}_0}\right], \tag{13.84}$$

$\Delta\delta$ is the spread in momentum spread, and $\bar{\delta}$ (usually zero) is the momentum spread where the distribution $\rho(\delta)$ peaks at. The Keil–Schnell like stability threshold becomes

$$(\Delta\omega_\beta)_{\text{dyn}} \lesssim \frac{1}{\sqrt{3}}\Big|S_\beta\Big|\bar{\omega}_0(\Delta\delta)_{\text{HWHM}}F, \tag{13.85}$$

which, with the help of the coherent betatron tune shift in Eq. (13.75), can be rewritten as

$$\left|Z_1^{\perp}\right| \lesssim \frac{4\pi\omega_\beta E_0}{\sqrt{3}eI_0c}\left|S_\beta\right|(\Delta\delta)_{\text{HWHM}}F. \tag{13.86}$$

Zotter [8] was the first to derive this Keil–Schnell like transverse stability criterion for a coasting beam. His numerical coefficient on the right side is 8 which is very close to our value of $4\pi/\sqrt{3}$. Of course, the spread in betatron tune can also come from the betatron oscillation amplitude, and this spread should also be included in Eq. (13.79) for a more complete description.

13.6.1 *Resistive-Wall Instabilities*

The Fermilab Recycler Ring stores and cools antiprotons at $E_0 = 8.938$ GeV for injection into the Tevatron. Starting from early 2004, sporadic transverse instabilities had been reported, with the signature of a sudden increase in both vertical and horizontal emittances accompanied by a small beam loss. The first culprit to blame was ion-trapping. [9] However, this possibility was dismissed later after two experiments. The first was a transverse instability of the similar nature induced on an antiproton beam of intensity $N_b = 28 \times 10^{10}$, full length $\tau_L = 3.5$ μs, and 95% horizontal and vertical normalized emittances 3π mm-mr by reducing the normal vertical chromaticity from $\xi_y = -2$ to zero. The difference signals of the beam were sampled with a vertical beam-position monitored at the rate of 125 MHz. The fast Fourier transform (FFT) is shown in Fig. 13.6. The tallest lines are the lower betatron sidebands. Next to their right are the revolution harmonics. The upper sidebands are to the right of the harmonics. The plot reveals excitation of the betatron sidebands rolling off very slowly until roughly at the 70th harmonic. If the instability was driven by trapped CO ions, the ion-in-beam bounce frequency (see Sec. 15.1.1) peaks at $\sim$ 100 kHz and should cluster only around the first and second harmonics (90 and 180 kHz).

The second experiment was the observation of a similar transverse instability induced on a stored proton beam which could not trap ions. The difference signal recorded during the experiment and shown in the top plot of Fig. 13.7 indicates a growth time of about 500 to 1000 turns or 11 to 56 ms. The rms energy spread was $\sigma_E = 1$ MeV and did not change throughout the instability. The FFT of the difference signals in the lower plot shows the lower betatron sidebands (tallest lines) excited very much more than the upper sidebands starting from the lowest lower betatron sideband, commonly known as the $(1 - Q)$ line or sideband. The amplifier gain is constant in the frequency range of observation down to

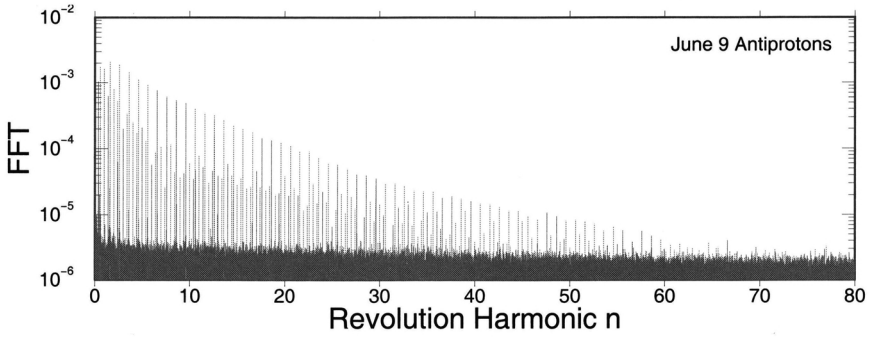


Fig. 13.6 Excitation of vertical betatron sidebands of the first 80 revolution harmonics monitored at the split-tube beam-position monitor VP522 of the Fermilab Recycler Ring during the instability induced on June 9, 2004. Note that pre-amp on VP522 has flat response from 10 kHz to 10 MHz. The tallest lines are the lower betatron sidebands. To their immediate right are the revolution harmonics. (Courtesy Crisp. [11])

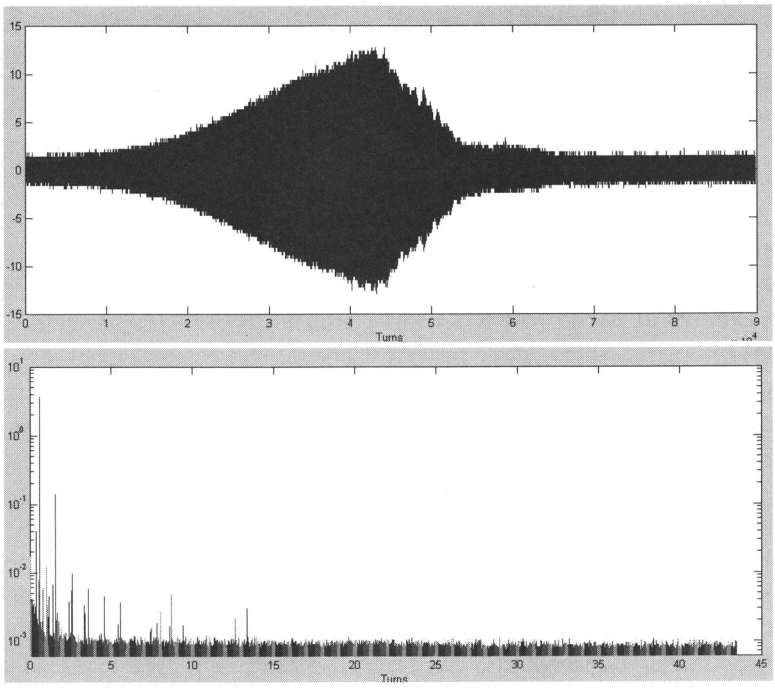


Fig. 13.7 Top: Difference signals sampling at $\sim$ 8 MHz for a period of 9×10^4 revolution turns (about 1 s) during the induction of a vertical instability in the coasting proton beam. Bottom: FFT of 1048576 samples between turn 30 to 42k. The taller lines are the lower betatron sidebands $(n - Q)$ with the harmonic lines on their immediate right. The $(1 - Q)$ line is clearly dominant and the lower betatron sidebands grows much more than the upper sidebands. (Courtesy Crisp. [12])

$\sim$ 10 kHz. The slow roll-off of the lower betatron sideband excitations gives us the clue that the instability might be driven by the resistive wall. Here, we would like to compute the growth rates and compare them with observation. [10]

13.6.1.1 *Instability of Proton Beam*

Let us concentrate on the proton beam in the second experiment. Proton beam consisting of 13 bunches was injected into the Recycler Ring from the Main Injector on July 9, 2004. [12] Initially, the total beam intensity was 79×10^{10}. The beam was debunched and scraped to 43.9×10^{10} using the collimator Top Jaw so that the 95% horizontal and vertical emittances were about $\epsilon_{N95} = 6\pi$ mm-mr. The skew quadrupole SQ408 was set to zero current to simulate the period from December 2003 to June 12, 2004 when it malfunctioned. The quadrupole-correction loop (QCL) was turned off to enhance the influence of the periodic ramping of the Main Injector which shares the same tunnel with the Recycler Ring. Finally when the vertical chromaticity was reduced from $\xi_y = -2$ to zero, a vertical instability of the beam was observed, with an about sixfold jump of vertical emittance and a 14% beam loss.

(a) Impedances

Besides space-charge, the transverse impedance receives most contribution from the resistive walls of the vacuum chamber, which is made of stainless steel with an elliptical cross-section of diameters 3.75″ by 1.75″. With $[\nu_{x,y}]$ denoting the decimal parts of the horizontal and vertical betatron tunes, the transverse resistive-wall impedances are

$$\begin{aligned} Z_1^H &= (1-i)11.79\,|n-[\nu_x]|^{-1/2}\ \mathrm{M\Omega/m}, \\ Z_1^V &= (1-i)21.92\,|n-[\nu_y]|^{-1/2}\ \mathrm{M\Omega/m}, \end{aligned} \tag{13.87}$$

with $n = 1, 2, 3, \cdots$ denoting the excitation of the lower betatron sidebands $n - [\nu_{x,y}]$, which are also commonly known as the $(n - Q)$ lines.

The proton beam had been scraped heavily leaving behind about only one-half of its initial intensity. We therefore approximate the transverse distribution as uniform with a vertical and horizontal radii

$$a_y = \sqrt{\frac{\beta_y \epsilon_{N95\%}}{\gamma\beta}}, \qquad a_x = \sqrt{\frac{\beta_x \epsilon_{N95\%}}{\gamma\beta} + (D_x\delta)^2}, \tag{13.88}$$

where $\beta_{x,y}$ are the horizontal and vertical betatron function, D_x is the horizontal dispersion and δ is the half momentum spread. The vertical self-field space-

charge impedance is given by

$$Z_1^V\Big|_{\text{self}} = i\frac{2Z_0\nu_y}{\gamma^2\beta^2}\left\langle\frac{\beta_y}{a_y(a_y+a_x)}\right\rangle. \tag{13.89}$$

At initial 95% normalized emittance $\epsilon_{N95} = 6\pi$ mm-mr in both transverse planes and integrating over the Recycler Ring using the most recent lattice, we get $Z_1^V\big|_{\text{self}} = i161.8\,\text{M}\Omega/\text{m}$. From this we subtract the inductive wall impedance and another ~ 30 MΩ/m for inductive impedance contributed by BPM's, bellows, pump ports, variation in cross-section, etc.

For the antiproton beam in the first experiment, the transverse distribution is bi-Gaussian because of stochastic cooling. The equivalent-uniform-distribution beam radii of a bi-Gaussian distribution is $a_{x,y} = \sqrt{2}\sigma_{x,y}$ with vertical rms radius given by $\sigma_y = \sqrt{\epsilon_{N95}\beta_y/(6\beta\gamma)}$ and a similar horizontal radius including dispersion. At $\epsilon_{N95} = 3\pi$ mm-mr, the space-charge impedance is $Z_1^V\big|_{\text{spch}} = i959$ MΩ/m, which is very much larger than the resistive-wall impedance in magnitude.

(b) Stability and Growth Contours

The dispersion relation governing the collective transverse motion of the beam is given by Eq. (13.76) with the spread in betatron frequency given by Eq. (13.79). Since the momentum spread of the beam has been Gaussian, the dispersion relation can be integrated in the close form to give

$$U + iV = -\frac{eI_0\beta^2cZ_1^\perp}{4\sqrt{2\pi}\nu_y\omega_0\sigma_E|S_y|} = \frac{1}{w(z_1)}, \tag{13.90}$$

where I_0 is the coasting-beam current, S_y is the vertical effective chromaticity defined in Eq. (13.82), $\eta = -0.008812$ is the slip factor, $\nu_{x,y} = 25.425/24.415$ are the nominal betatron tunes, and $w(z_1)$ is the complex error function. The collective eigen-frequency is

$$\Omega = n\omega_0 + \omega_y + \frac{\sqrt{2}\sigma_E|S_y|\omega_0}{\beta^2E}\,z_1, \tag{13.91}$$

and the imaginary part gives the growth rate. Here, ω_y/ω_0 is the bare vertical betatron tune plus the incoherent tune shift for particles at the center of the beam, n is any revolution harmonic, positive or negative.

For the experiment on the proton beam instabilities, the equi-growth contours are drawn in the U-V-plane in Fig. 13.8 along with the U-V (or $\sim -Z_1^V$) values of the lower betatron sideband excitations. This is the same type of plot as Fig. 13.5 in the Gaussian distribution with only the lower right quarter shown

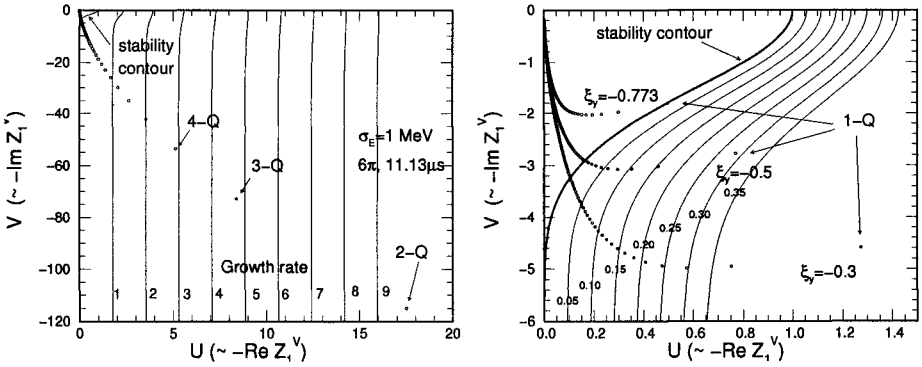


Fig. 13.8 Left: U-V values of lower sidebands of proton beam at various chromaticities along with the equi-growth contours. The $(1-Q)$ excitation is off-scale at $(U,V)=(78.0,-281)$. Right: The same for some nonzero values of ξ_y.

here. The left plot is for $\xi_y = 0$ and we see many modes lying outside the stability contour. The $(1-Q)$ excitation is off-scale at $(U,V)=(78.0,-281)$, and is on the contour of reduced growth rate $\mathcal{I}m\, z_1 = 44.0$ units, which corresponds to an actual growth rate of

$$\frac{1}{\tau} = \sqrt{2}\sigma_\delta |S_y| \omega_0\, \mathcal{I}m\, z_1 = 19.6\ \mathrm{s}^{-1}, \tag{13.92}$$

or a growth time of 51.1 ms, where $\sigma_E = 1$ MeV has been used. The $(2-Q)$ excitation has a growth rate of 11.9 s^{-1} or a growth time of 84.1 ms. They agree approximately with the observed growth times of 75 ms and 105 ms for these two modes as depicted in Fig. 13.9.

In the right plot of Fig. 13.9, we see that $(1-Q)$ is at $(U,V)=(1.27,-4.59)$ near the 0.65-unit growth contour when $\xi_y = -0.3$ and is at $(U,V) = (0.77,-2.77)$ near the 0.3-unit growth contour when $\xi_y = -0.5$. As soon as the vertical chromaticity reaches $\xi_y = -0.773$, all modes are inside the stability region. Although the (U,V) values of the $(1-Q)$ mode differ so much at $\xi_y = 0$ and -0.3, the computed growth rates are, respectively, 19.6 s^{-1} and 17.8 s^{-1}, and are comparable. The physical reason is suppression of Landau damping by the large space-charge frequency shift and this will be explained in detail later. As illustrated in Fig. 13.10, the growth rates of the low-frequency modes are nearly independent of chromaticity when the modes are highly unstable. Actually the effect of chromaticity is important only when the excitation is near stability. For example, the first stable mode at $\xi_y = 0$ is $(60-Q)$. However, $\xi_y = -0.1$ stabilizes the mode at $(50-Q)$, $\xi_y = -0.2$ stabilizes the mode at $(39-Q)$, $\xi_y = -0.3$ stabilizes the mode at $(29-Q)$.

The independence of the growth rate on chromaticity suggests that it is possible to derive a formula of the growth rate when the excitation is far from stability. The complex error function has the asymptotic behavior

$$\frac{1}{w(z_1)} = -i\sqrt{\pi} z_1 \left[1 + \mathcal{O}\left(\frac{1}{|z_1|^2}\right)\right] \tag{13.93}$$

provided that $|\arg(iz_1)| < \frac{3}{4}\pi$. This has been demonstrated obviously by the equi-growth contours in Fig. 13.8. For example, the $\mathcal{I}m\, z_1 = 1$ contour (growth rate of 1 unit) approaches $\mathcal{R}e\, w(z_1)^{-1} = \sqrt{\pi}\,\mathcal{I}m\, z_1 = \sqrt{\pi}$. Taking the real part of the dispersion relation [Eq. (13.90)] and using the definition of z_1 in Eq. (13.91), we obtain

$$-\frac{eI_0\beta^2 c\,\mathcal{R}e\, Z_1^V}{4\sqrt{2\pi}\nu_y\omega_0\sigma_E|S_y|} = \frac{\sqrt{\pi}\,\mathcal{I}m\,\Omega}{\sqrt{2}|S_y|\omega_0\sigma_\delta}. \tag{13.94}$$

We see that the chromaticity factors cancel arriving at the simple expression for the growth rate,

$$\frac{1}{\tau} = \mathcal{I}m\,\Omega = -\frac{eI_0 c\,\mathcal{R}e\, Z_1^V}{4\pi\nu_y E}. \tag{13.95}$$

This theoretical expectation is plotted in Fig. 13.10 as dashes. We see that it agrees very well with the exact numerical solution and shows significant deviations only when the excitations are close to stability. Attention should be paid to the negative sign on the right side of Eq. (13.95). It reminds us that instabilities

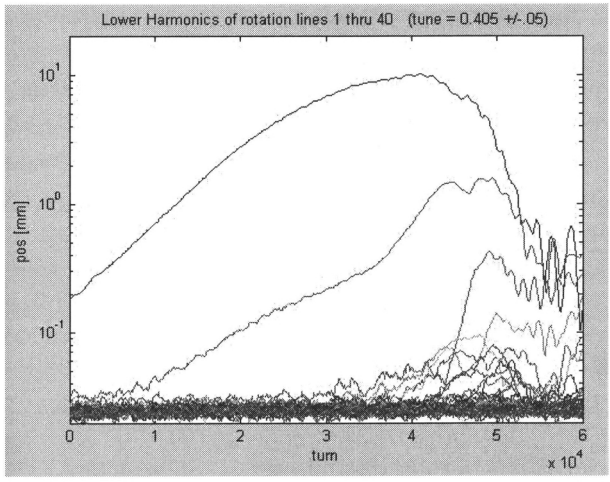


Fig. 13.9 The amplitudes of the first 40 lower betatron sidebands during the induced instability of the proton beam at the Fermilab Recycler Ring on July 9, 2004. The largest one is the $(1-Q)$ sideband and the next one is the $(2-Q)$ sideband. (Courtesy Hu and Crisp. [12])

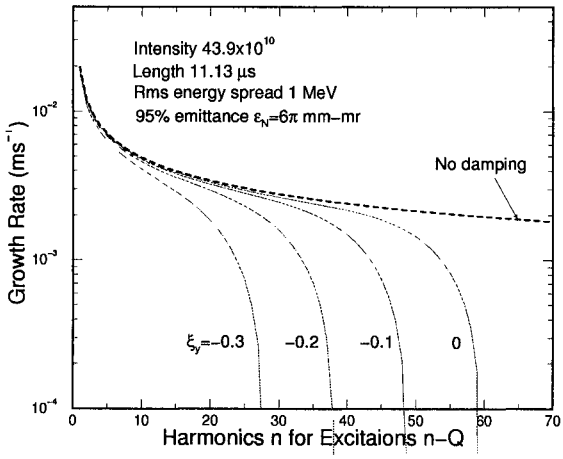


Fig. 13.10 Growth rates for excitation $(n-Q)$ at vertical chromaticity $\xi_y = 0, -0.1, -0.2,$ and -0.3. The simple theoretical expectation is shown in dashes, which is the growth rate without Landau damping, and is in excellent agreement with the growth rates at various chromaticities when the excitations are far from stability.

are driven only by the slow waves at negative frequencies where $\mathcal{R}e\, Z_1^V < 0$. Actually, the expression in Eq. (13.95) is exactly the growth rate without Landau damping, easily derivable from the dispersion relation, for example, Eq. (13.76).

(c) Space-Charge Effects

The large growth rate of 19.6 s^{-1} for the $(1-Q)$ excitation is a result of the large space-charge impedance, although it is the real part of the impedance that drives the growth. We mentioned in Fig. 13.10 that the $(1-Q)$ excitation is at $(U,V) = (1.27, -4.59)$ when the chromaticity is $\xi_y = -0.3$. If there were no space-charge impedance, this excitation would be at $(U,V) = (1.27, 0)$, where we have neglected, for convenience, the reactive part of the resistive-wall impedance. To move it inside the stability curve will only require[‖] $\xi_y \approx -0.3 \times 1.27 = -0.38$, since the V value is proportional to $\mathcal{R}e\, Z_1^V/|S_y|$. The tune spread required to Landau-damp the instability is therefore roughly $\sigma_{\Delta\nu_y} = |\xi_y \sigma_\delta| = 4.3 \times 10^{-5}$. This rms tune spread is reasonable, because it corresponds to an rms angular betatron frequency spread of $\sigma_{\omega_y} = 24$ Hz while the growth rate of the $(1-Q)$ excitation is 19.6 s^{-1} as indicated in Fig. 13.10.

Space-charge shifts the incoherent tune spread downward away from the coherent excitation and Landau damping cannot be activated. For this reason, a sizeable chromaticity is required to generate a tune spread so that the coherent excitation is again inside the incoherent spread in order that Landau damping becomes possible. The incoherent self-field space-charge tune shift is related to

[‖]For the excitation of $1-Q$, $S_y \approx \xi_y$ because the slip factor is $\eta = -0.008812$.

the transverse self-field space-charge impedance by [Eq. (3.129)]

$$\Delta\nu_y\Big|_{\text{incoh}} = -\frac{eI_0R}{4\pi\beta E\nu_y}\,\mathcal{I}m\,Z_1^V\Big|_{\text{self}}. \tag{13.96}$$

At the self-field space-charge impedance given by Eq. (13.89) with $-i28.7\ \text{M}\Omega/\text{m}$ of inductive wall impedance and about $-i30\ \text{M}\Omega/\text{m}$ inductive part from other discontinuities in the vacuum chamber subtracted, the incoherent self-field space-charge tune shift is $\Delta\nu_y = -1.26\times10^{-4}$. Because a uniform transverse distribution has been assumed, this is the self-field space-charge tune shift for every particle in the beam. According to the U-V plot, a vertical chromaticity $\xi_y = -0.773$ will be suffice to damp transverse instability. This leads to an effective chromaticity of $S_y = -0.779$ for the $(1-Q)$ mode, or an rms tune spread of

$$\sigma_{\Delta\nu_y} = |S_y|\sigma_\delta = 0.87\times10^{-4}. \tag{13.97}$$

A half spread of $\sim 2\sigma_{\Delta\nu_y} = 1.74\times10^{-4}$ is slightly larger than the incoherent self-field tune shift, and will therefore be able to cover the coherent tune line providing Landau damping. This is illustrated schematically in Fig 13.11.

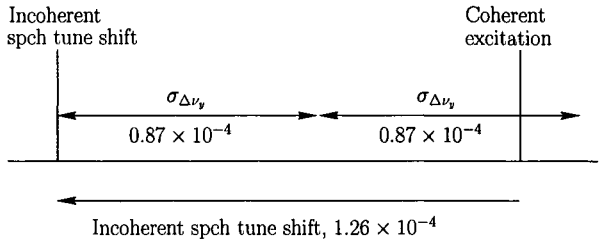


Fig. 13.11 Incoherent tune shift is 1.26×10^{-4} downward from the coherent excitation. A chromaticity of $\xi_y = -0.774$ provides an rms tune spread of $\sigma_{\Delta\nu_y} = 0.87\times10^{-4}$. A half spread of $2\sigma_{\Delta\nu_y}$ will cover the coherent excitation and enable Landau damping.

13.6.1.2 *Instabilities of Antiproton Beam*

Transverse instability was induced on June 9 of 2004 to an antiproton beam of intensity $N_b = 28\times10^{10}$, length $\tau_L = 3.5\ \mu$s, and rms energy spread $\sigma_E = 3$ MeV. When the vertical chromaticity was reduced to zero, the beam became unstable with the 95% vertical emittance jumped from $\epsilon_{N95} = 3\pi$ mm-mr to 6π mm-mr together with a small beam loss. The antiproton beam was confined between two rf squared-wave barriers at ±2 kV. The antiprotons drifted freely between the two rf barriers according to their momentum offsets and had their directions reversed after meeting one of the barriers (see Sec. 2.8). The synchrotron period was different for particle with different momentum offset and the rms value was

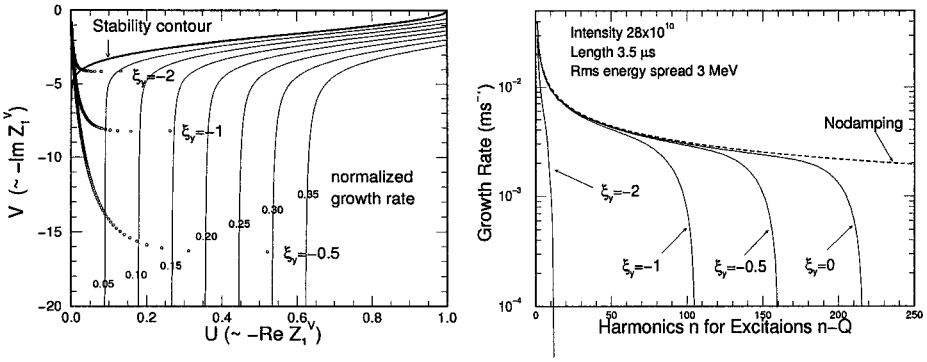


Fig. 13.12 Left: Plot showing the equi-growth contours in the U-V- (normalized $-Z_1^V$-) plane. The (U, V) values of each betatron excitation $(n - Q)$ with $n = 1, 2, 3, \cdots$ are shown as circles for $\xi_y = -2$, -1, and -0.5. Here, with $\xi_y = -2$, stability is maintained only for modes equal to or higher than $(13 - Q)$. To stabilize all the modes, a chromaticity $\xi_y = -2.26$ is required. Right: Growth rates for excitation $(n - Q)$ at vertical chromaticities $\xi_y = 0$, -0.5, -1, and -2. The simple theoretical expectation, which is the growth rate without Landau damping, is shown in dashes, and is in excellent agreement with the growth-rate curves at various chromaticities when the excitations are far from stability.

of the order of 1 s. Since the instability took place within a duration of ~ 50 ms, the antiproton beam can be well-approximated as a coasting beam.

As in the case for the proton beam, we make the stability plot in the U-V-plane. The results are shown in Fig. 13.12 for vertical chromaticity $\xi_y = -2$, -1, and -0.5. At $\xi_y = -2$, the plot shows that stability is maintained only for the betatron modes $(n - Q)$ with $n \geq 12$, which appears to be in contraction to the daily operation, because antiproton beam of this intensity, length, energy spread, and emittances has always been stable at such chromaticity. It is possible that there are other means of Landau damping that have not been considered here. According to the present dispersion relation, we require a vertical chromaticity of $\xi_y = -2.53$ to stabilize all the betatron modes.

The growth rates of the lower betatron sidebands are depicted in the right plot of Fig. 13.12. At zero chromaticity, all $(n - Q)$ with $n < 217$ are unstable. However, we see in the top plot of Fig. 13.7 that only those modes for $n \lesssim 70$ are unstable. Another indication showing that the antiproton beam was actually more stable than the theoretical prediction. Some argue that the growths of the higher sideband excitation had been buried in the background noise floor. However, noise usually promotes excitation instead. By the way, the growth rate without Landau damping for this antiproton beam is $\tau^{-1} = 40.2\ \mathrm{s}^{-1}$ agreeing with observation.

We also see in Fig. 13.7 that the $(1 - Q)$ mode has not been excited as

much as the $(2-Q)$ mode for the antiproton beam, although the resistive-wall impedance at $(1-Q)$ is $\sqrt{(2-[\nu_y])/(1-[\nu_y])} = 1.65$ times larger than the impedance at $(2-Q)$. This apparent paradox can be explained by the finite length of the beam. The beam of length $\tau_L = 3.5$ μs can support a wave of maximum half wavelength 3.5 μs. Thus the minimum frequency of excitation is $1/(2\tau_L) = 143$ kHz. The $(1-Q)$ mode is at $(1-[\nu_\beta])f_0 = 52.5$ kHz and is therefore harder to excite. On the other hand, the $(2-Q)$ mode is at 142 kHz and is therefore easier to excite.

(d) Space-Charge Effects

The large growth rate of 39.7 s^{-1} for the $(1-Q)$ excitation at zero chromaticity is a result of the large space-charge impedance, although it is the real part of the impedance that drives the growth. The impedance of the $(1-Q)$ excitation has the value $(U, V) = (52.77, -1657)$ at zero chromaticity. If there were no space-charge impedance, this excitation would be at $(U, V) = (52.77, 0)$, where we have neglected, for convenience, the reactive part of the resistive-wall impedance. To move it inside the stability curve will only require $S_y \approx 52.77\eta[\nu_\beta] = -0.27$. The tune spread required to Landau-damp the instability is therefore roughly $\sigma_{\Delta\nu_y} = |\xi_y\sigma_\delta| = 0.923 \times 10^{-4}$. This rms tune spread is reasonable, because it corresponds to an rms angular betatron frequency spread of $\sigma_{\omega_y} = 52$ Hz while without Landau damping, the growth rate of the $(1-Q)$ excitation is 40 s^{-1}.

Space-charge shifts the incoherent tune spread downward away from the coherent excitation and Landau damping cannot be activated. For this reason, a nominal chromaticity of $\xi_y \approx -2.53$ is required to generate the tune spread $\sigma_{\Delta\nu_y} = |\xi_y\sigma_\delta| = 8.59 \times 10^{-4}$ so that the coherent excitation is again inside the incoherent spread in order that Landau damping becomes possible.

The incoherent vertical betatron tune shift is

$$\Delta\nu_y\Big|_{\text{incoh}} = -\frac{eI_0R}{4\pi\beta E\nu_y}\,\mathcal{I}m\,Z_1^V = -22.4 \times 10^{-4}, \tag{13.98}$$

where we have used $\mathcal{I}m\,Z_1^V = i900$ MΩ/m, which is equal to the sum $\mathcal{I}m\,Z_1^V|_{\text{spch}} = i959$ MΩ/m, $\mathcal{I}m\,Z_1^V|_{\text{wall}} = -i28.7$ MΩ/m for the resistive wall at the $(1-Q)$ mode, and $\mathcal{I}m\,Z_1^V|_{\text{other}} = -i30.0$ MΩ/m for other inductive effects of the vacuum chamber. The above is the maximum incoherent betatron tune shift for those particles at the center of the beam. For all other particles in the beam with bi-Gaussian transverse distribution, this self-field space-charge tune shift has a distribution skewed towards the maximum. For our beam, the average incoherent tune shift is $-22.4 \times 10^{-4} \times 0.6334 = -14.2 \times 10^{-4}$ (see Sec. 3.2.2). At the chromaticity $\xi_y = -2.53$, the 2σ's point falls on the tune shift $-14.2 \times 10^{-4} + 2 \times 8.59 \times 10^{-4} = +2.98 \times 10^{-4}$. Thus the spread in tune

will definitely cover the coherent excitation line and therefore the excitation can be Landau-damped as illustrated schematically in Fig. 13.13.

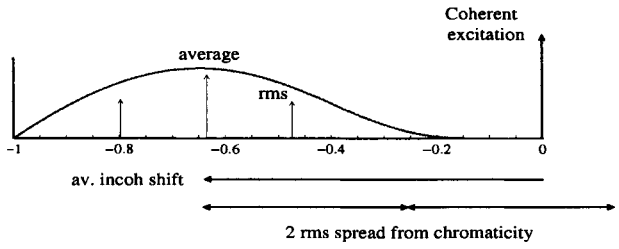


Fig. 13.13 The average incoherent vertical betatron tune shift is 14.2×10^{-4} downward from the coherent excitation. A chromaticity of $\xi_y = -2.53$ provides an rms tune spread of $\sigma_{\Delta\nu_y} = 8.59 \times 10^{-4}$. A half spread of $2\sigma_{\Delta\nu_y}$ will cover the coherent excitation and activate Landau damping.

(e) Remarks

The problem of the sporadic vertical instabilities in the Fermilab Recycler Ring cannot be considered solved yet. It appears that the resistive-wall driving force in the coasting beam theory has overestimated the growth rates, especially for the betatron sidebands of the higher harmonics. The function of the skew quadrupole SQ408 poses some mysterious issues also. All the vertical instability recorded took place when SQ408 malfunctioned with no quadrupole current flowing. After the malfunction was corrected, no more similar vertical instability has ever been reported. Usually, a vertical instability can be avoided or reduced by coupling some of the growth into the horizontal plane. Such a coupling with the aid of a sextupole improves the threshold intensity of the proton beam at the Los Alamos PSR by 25% (see Sec. 5.3.4). In the Recycler Ring, however, it is the other way around. The skew quadrupole SQ408 was used to correct vertical-horizontal coupling. Turning off SQ408 implies more vertical-horizontal coupling and the vertical instability occurs. Turning on SQ408 implies less vertical-horizontal coupling and the vertical instability is avoided.

13.7 Longitudinal Unbunched Beam Instabilities

For the last three categories, the transverse bunched beam instabilities, the transverse unbunched beam instabilities, and the longitudinal bunched beam instabilities, the treatment had been very similar. In each case, we first derived the tune shifts. Landau damping was next introduced by including the distribution of the tune. The dispersion relation derived was related to the transfer function $R(u)$, from which the stable and unstable regions in the impedance phase space could be identified. The longitudinal instabilities of an unbunched

beam is very much different, because there is no stabilizing oscillation like the betatron motion or synchrotron motion. Thus, there is no betatron frequency or synchrotron frequency, from which an incoherent frequency spread can be obtained to provide Landau damping. As a result, the derivation of the stability criterion will be very different from the last three categories. Here, the collective beam instability is the longitudinal microwave instability, and Landau damping is supplied by the spread in revolution frequency of the beam particles. The dispersion relation, Eq. (5.14), has already been discussed in Chapter 5 with the stability curves presented in Fig. 5.4. Over there, the dispersion relation was derived employing the Vlasov equation which deals with the evolution of the particle distribution. We will show another derivation in this section making use of only the equations of motion without resorting to the Vlasov equation.

Let us start from the linear distribution $\lambda(s,t)$ which has a stationary part λ_0 and a perturbation $\Delta\hat{\lambda}$. The stationary part is just a uniform distribution

$$\lambda_0 = \frac{N}{C_0}, \tag{13.99}$$

where N is the total number of particles in the unbunched beam and C_0 is the circumferential length of the ring. For the perturbation, we postulate the ansatz

$$\Delta\lambda(s,t) = \Delta\hat{\lambda} e^{ins/R - i\Omega t}, \tag{13.100}$$

where $\Delta\hat{\lambda}$ represents the maximum modulation of the longitudinal density and is assumed to be small. The harmonic $n = 0$ is excluded because of charge conservation. A snapshot view at a specific time will show the n-fold modulation of the linear density.

For a test particle at the fixed location s, the average dynamic part of the longitudinal wake force experienced from the longitudinal wave is

$$\langle F_0^{\parallel}(s,t)\rangle_{\rm dyn} = -\frac{e^2}{C_0}\int v dt'\, W_0'(vt - vt')\Delta\lambda(s,t') = -\frac{e^2 v Z_0^{\parallel}(\Omega)}{C_0}\,\Delta\lambda(s,t), \tag{13.101}$$

where the impedance only samples the collective frequency Ω.

Next consider a particle moving with the beam. It passes the location S at time $t = 0$ and is at location $s = S + vt$ at later time t. The motion of a beam particle consists of its phase drift and energy drift in the longitudinal phase space. The particle's off-momentum spread $\delta(s,t)$ increases per unit time as a result of the wake force and is governed by

$$\frac{d\delta(s,t)}{dt} = -\frac{e^2c^2}{C_0E_0} Z_0^{\parallel}(\Omega)\Delta\hat{\lambda}\, e^{ins/R - i\Omega t}, \tag{13.102}$$

while the rate of the phase drift is governed by

$$\frac{dz(s,t)}{dt} = -\eta v \delta(s,t), \tag{13.103}$$

where η is the slip parameter and we have actually employed a distance drift $z(s,t)$ rather than a phase. Here,

$$\frac{d}{dt} = \frac{\partial}{\partial t} + \frac{ds}{dt}\frac{\partial}{\partial s} \tag{13.104}$$

is the *total* time derivative. Thus, in solving Eqs. (13.102) and (13.103), we must first make the substitution $s = S + vt$. The momentum-offset equation can be integrated readily to give

$$\delta(s,t) = \frac{e^2c^2}{C_0E_0} Z_0^{\parallel}(\Omega)\Delta\hat{\lambda}\,\frac{e^{ins/R - i\Omega t}}{i(\Omega - n\omega_0)}. \tag{13.105}$$

Substituting the result into the phase-drift equation, we obtain by another integration

$$z(s,t) = -\frac{e^2\eta c^2 v}{C_0E_0} Z_0^{\parallel}(\Omega)\Delta\hat{\lambda}\,\frac{e^{inS/R - i\Omega t}}{(\Omega - n\omega_0)^2}. \tag{13.106}$$

Notice that we have retained only the contribution due to the wake field in the above solution.

If we can relate the particle longitudinal displacement $z(s,t)$ to the longitudinal density perturbation $\Delta\lambda$, the loop will be closed in Eq. (13.106) and a dispersion relation will result. There is, in fact, such a relation from the equation of continuity. The particles in the original unperturbed volume from s to $s+\Delta s$ at time t are displaced into the new perturbed volume between $s + z(s,t)$ and $s + \Delta s + z(s+\Delta s, t)$ at time t in the presence of the wake force. The number of particles in each of the volumes is

$$\lambda_0\Delta s = \big[\lambda_0 + \Delta\lambda(s,t)\big]\Big\{\big[s + \Delta s + z(s+\Delta s,t)\big] - \big[s + z(s,t)\big]\Big\}, \tag{13.107}$$

from which we obtain, for small Δs,

$$\Delta\lambda(s,t) = -\lambda_0\frac{\partial z}{\partial s} = \frac{ineI_0\eta\omega_0^2 Z_0^{\parallel}(\Omega)}{2\pi\beta^2E_0}\,\Delta\hat{\lambda}\frac{e^{ins/R - \Omega t}}{(\Omega - n\omega_0)^2}, \tag{13.108}$$

where we have introduced the average beam current $I_0 = eN\omega_0/(2\pi)$ with $\omega_0 = v/R$ being the angular revolution frequency. Self-consistency allows us to cancel

$\Delta\lambda(s,t)$ on both sides. The growth rate of the longitudinal wave ω_G is given by the imaginary part of Ω, which can be readily obtained from Eq. (13.108),

$$\omega_G = \sqrt{-\frac{ieI_0 Z_0^{\parallel}(\Omega)n\eta}{2\pi\beta^2 E_0}}\,\omega_0, \tag{13.109}$$

which is very similar to the definition of the synchrotron frequency, if we identify the rf voltage as $I_0 Z_0^{\parallel}$ and the rf harmonic as n. For this reason, the growth rate can be visualized as the synchrotron angular frequency inside a bucket created by the voltage the beam experiences from the impedance. We can draw the immediate condition that the longitudinal wave perturbation is stable above/below transition ($\eta \gtrless 0$) only if the impedance is purely inductive/capacitive.

Landau damping can now be introduced by allowing a spread in the revolution frequency inside the beam. Let $\rho(\omega_0)$ be the distribution in revolution frequency centering at $\bar{\omega}_0$ with a spread $\Delta\omega_0$. Multiplying both sides of Eq. (13.108) by $\rho(\omega_0)$ and integrating over $d\omega_0$, we obtain the dispersion relation

$$1 = \frac{ieI_0 Z_0^{\parallel}(\Omega)n\eta}{2\pi\beta^2 E_0}\int d\omega_0 \frac{\rho(\omega_0)}{(\Omega - n\omega_0 + i\epsilon)^2}. \tag{13.110}$$

The infinitesimal positive number ϵ that sneaks into the denominator of the integrand comes from the assumption that the wake force increases adiabatically from $t = -\infty$, a representation discussed in Eq. (13.16). The dispersion relation can be rewritten as

$$1 = \left[\frac{\omega_G^2}{n^2(\Delta\omega_0)^2}\right]\left[n(\Delta\omega_0)^2\int d\omega_0 \frac{\rho'(\omega_0)}{n\omega_0 - \Omega - i\epsilon}\right] = \left[\frac{\omega_G^2}{n^2(\Delta\omega_0)^2}\right] R_{\parallel}(u), \tag{13.111}$$

where an integration by part has been performed. The function $R_{\parallel}$ on the right is defined as

$$R_{\parallel}(u) = f_{\parallel}(u) + ig_{\parallel}(u) = (\Delta\omega_0)^2\left[\wp\int d\omega_0 \frac{\rho'(\omega_0)}{\omega_0 - \Omega/n} + i\pi\rho'\left(\frac{\Omega}{n}\right)\right], \tag{13.112}$$

and

$$u = \frac{\bar{\omega}_0 - \Omega/n}{\Delta\omega_0}. \tag{13.113}$$

This is the transfer function for longitudinal excitation in a coasting beam. It differs from the one we study before by having the involvement with the gradient of the distribution function rather than the distribution function itself. Usually

one writes

$$V - iU = \frac{\omega_G^2}{n^2(\Delta\omega_0)^2} = \frac{f_\parallel(u) - ig_\parallel(u)}{f_\parallel^2(u) + g_\parallel^2(u)}, \tag{13.114}$$

so that $U \propto -\mathcal{R}e\, Z_0^\parallel$ and $V \propto -\mathcal{I}m\, Z_0^\parallel$. This will give the threshold and growth curves for longitudinal microwave instability in Chapter 5. Notice that the threshold contour is now bell-shaped, because of the dependency of the transfer function on the gradient of the distribution function.

13.8 Beam Transfer Function and Impedance Measurements

The response on a beam to a kick, either longitudinal or transverse, contains a lot of information about the properties of the beam as well as the impedance properties of the vacuum chamber. Their direct measurements can be made using the methods discussed below.

Consider a coasting beam. In addition to the transverse wake, if we give an extra sinusoidal kick with harmonic n and frequency Ω, the equation of motion is

$$\ddot{y} + \omega_\beta^2 y = -2(\Delta\omega_\beta)_{\rm dyn}\omega_\beta\langle y\rangle + Ae^{ins/R - i\Omega t}, \tag{13.115}$$

where the dynamic betatron tune shift $(\Delta\omega_\beta)_{\rm dyn}$ is given by Eq. (13.75). For the particular solution, try the ansatz

$$\langle y(s,t)\rangle = Be^{ins/R - i\Omega t}. \tag{13.116}$$

As before, $s = S + vt$, and we obtain

$$y(s,t) = \frac{\left[-2(\Delta\omega_\beta)_{\rm dyn}\omega_\beta B + A\right]e^{ins/R - i\Omega t}}{\omega_\beta^2 - (n\omega_0 - \Omega)^2}. \tag{13.117}$$

Consistency requires

$$B \approx \frac{-2(\Delta\omega_\beta)_{\rm dyn}\omega_\beta B + A}{2\omega_\beta}\int d\omega\, \frac{\rho(\omega)}{\omega - (\Omega - n\omega_0)} = \frac{-2(\Delta\omega_\beta)_{\rm dyn}\omega_\beta B + A}{2\omega_\beta\Delta\omega}R(u), \tag{13.118}$$

where $\Delta\omega$ is a measure of the betatron frequency spread. After rearranging, we obtain

$$\frac{A}{2\omega_\beta\Delta\omega B} = \frac{1}{R(u)} + \frac{(\Delta\omega_\beta)_{\rm dyn}}{\Delta\omega}. \tag{13.119}$$

The ratio $2\omega_\beta \Delta\omega B/A$ is called the transverse *beam transfer function* because it records the response on the beam from a unit kick to the beam.

In a measurement, the beam is kicked at a certain harmonic but with various frequencies ω and the beam transfer function is recorded in its amplitude and phase. If the beam is of very weak intensity, the term involving the dynamic part of the coherent tune shift can be neglected and one obtains therefore the former transfer function $R(u)$, which is then plotted in the U-V-plane. Next, the beam intensity is increased to such a large value that the beam is still stable. The beam response is measured again, which, when plotted in the U-V-plane, is again the stability curve but under the influence of the coupling impedance of the vacuum chamber. In the U-V-plane, it is shifted by the amount $(\Delta\omega_\beta)_{\rm dyn}/\Delta\omega$. From the shift one can infer the impedance $Z_1^\perp$ of the vacuum chamber as illustrated in the left plot of Fig. 13.14.

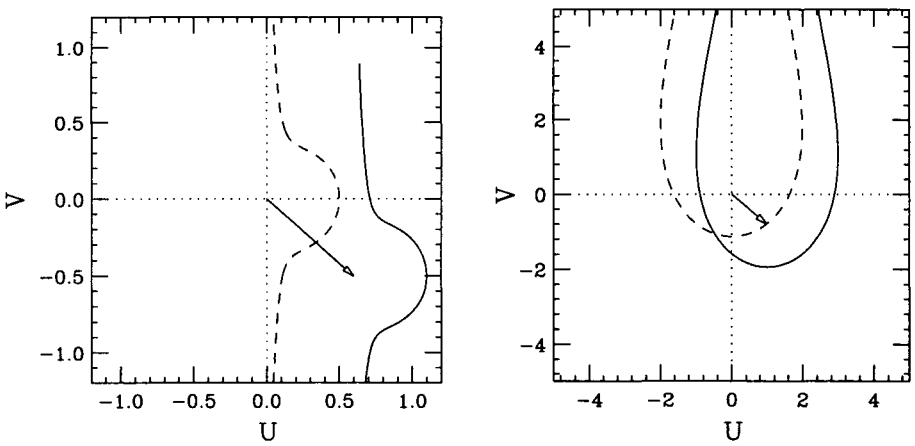


Fig. 13.14 Left: Transverse beam transfer function of a coasting beam. Dash curve is for a very low-intensity beam, thus showing the threshold curve. But it is shifted to the solid curve at high intensity. The transverse impedance can be inferred from the shift indicated by the arrow. Right: Longitudinal beam response function of a coasting beam. The dashed curve is for low intensity and is shifted to the solid curve at high intensity. The arrow is proportional to the longitudinal impedance. (Courtesy Spentzouris. [15])

It is easy to see the difference between the problem we discussed earlier in Sec. 13.1 and the one in this section. In the former, Eq. (13.1) solves for the response to a driving force or a kick on a particle, while in the latter, Eq. (13.115) solves for the the response to a kick on a beam particle in the presence of wake field inside a vacuum chamber. This explains why the former results in the

transfer function $R(u)$ which involves the frequency distribution of the particle ensemble only, while the latter results in the beam transfer function which involves the frequency distribution of the beam as well as the impedance of the vacuum chamber. Naturally, as the beam intensity goes to zero, the impedance effect goes to zero and the beam transfer function becomes the transfer function.

For the longitudinal beam response, we add a longitudinal kicking voltage per unit length, A with revolution harmonic n and frequency Ω. Then the longitudinal force seen by a particle changes from Eq. (13.101) to

$$\langle F_0^{\parallel}(s,t)\rangle_{\rm dyn} = -\frac{e^2}{C_0}\int v dt' W_0'(vt-vt')\Delta\lambda(s,t)\rho(\omega_0) + Ae^{ins/R-i\Omega t}. \quad (13.120)$$

Assume the ansatz

$$\Delta\lambda(s,t) = Be^{ins/R-i\Omega t}. \quad (13.121)$$

Then the solution of the momentum spread and longitudinal drift become

$$\delta(s,t) = \frac{\dfrac{-e^2c^2}{C_0E_0}Z_0^{\parallel}(\Omega)B + A}{-i(\Omega - n\omega_0)}e^{ins/R-i\Omega t}, \quad (13.122)$$

$$z(s,t) = \eta v\frac{\dfrac{-e^2c^2}{C_0E_0}Z_0^{\parallel}(\Omega)B + A}{(\Omega - n\omega_0)^2}e^{ins/R-i\Omega t}. \quad (13.123)$$

Doing the same as in Eq. (13.108) to Eq. (13.110), we obtain

$$B = \left[\frac{\omega_G^2}{n^2(\Delta\omega)^2}B + \frac{i2\pi\eta vN}{n^2(\Delta\omega)^2C_0^2}A\right]R_{\parallel}(u). \quad (13.124)$$

Or,

$$\frac{i2\pi\eta vN}{n^2(\Delta\omega)^2C_0^2}\frac{A}{B} = \frac{1}{R_{\parallel}(u)} - \frac{\omega_G^2}{n^2(\Delta\omega)^2}. \quad (13.125)$$

Now the ratio on the left side can be identified as the inverse of the *longitudinal beam transfer function.*

Exactly in the same way as the transverse counterpart, the longitudinal beam transfer function or the response of the kick is measured in its amplitude and phase. The inverse is then plotted in the U-V-plane. When the beam intensity is very weak, the longitudinal beam transfer function reduces to the longitudinal transfer function $R_{\parallel}(u)$ and the the threshold curve results in the U-V-plane. For an intense beam, this threshold curve will be shifted. The amount and direction

of shift will be proportional to the magnitude and phase of the longitudinal impedance. This is shown in the right plot of Fig. 13.14.

Beam transfer function and impedance measurements have been attempted by Spentzouris [15] at the Fermilab Accumulator Antiproton Storage Ring. The Accumulator stores antiprotons at $E_0 = 8.696$ GeV with an rms spread of 1–4 $\times 10^{-4}$. The ring has a revolution frequency $f_0 = 628.955$ kHz and a slip parameter $\eta = 0.023$. The operation is therefore above transition. There are three rf cavities in the ring. ARF2 and ARF3 are at rf harmonic $h = 2$. The third one, ARF1 at rf harmonic 84, has been used as a kicker. The impedance of cavity ARF3 was the target for measurement. The hardware setup for the beam-transfer-function measurement is shown in Fig. 13.15. The network analyzer excites the beam longitudinally by applying a sinusoidal wave of a fixed frequency to the broadband cavity ARF2 (quality factor $Q < 5$), and the resulting response of the beam picked up by a resistive-wall monitor is directed to the return port of the analyzer. This process is then repeated with a sinusoidal wave of a different frequency until the frequency range of the ARF3 cavity is covered.

Cavity ARF3 was first shorted mechanically and the signals of the beam response of the frequency sweep was monitored. A typical BTF measurement is shown in two left plots of Fig. 13.16, where the sweep was centered at $2f_0 = 1.25791$ MHz with a span of 100 Hz which was wide enough to encompass the frequency content of the beam. Notice that the response shows more uncertainty

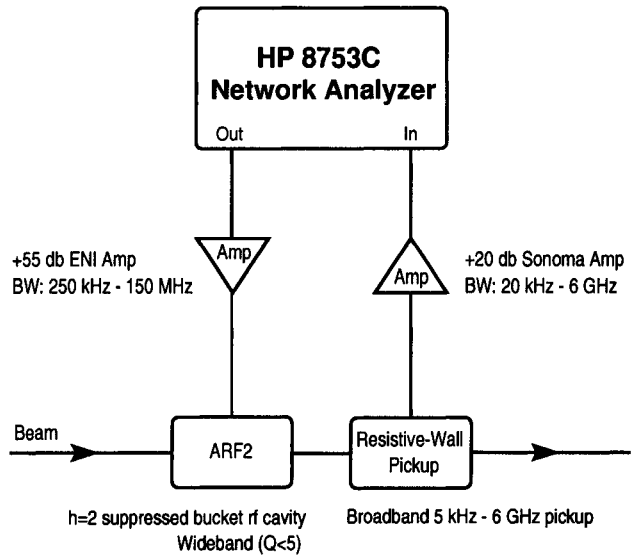


Fig. 13.15 Block diagram showing the transfer function measurement setup for the Fermilab Antiproton Accumulator. The beam is excited by the network analyzer and the response picked up by the resistive-wall monitor is returned to the analyzer. (Courtesy Spentzouris. [15])

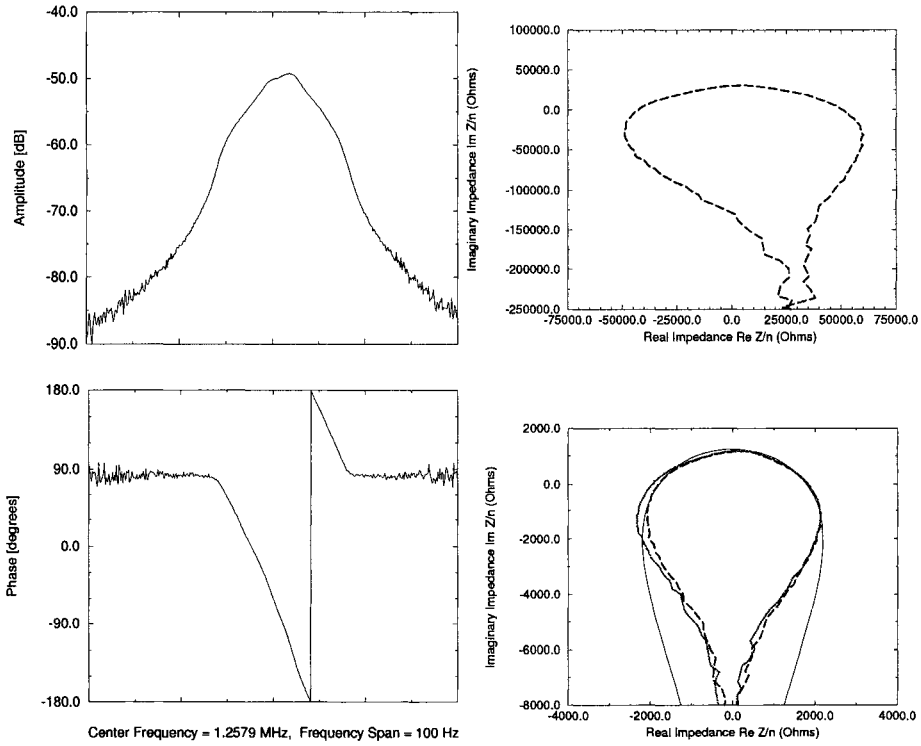


Fig. 13.16 Top left and bottom left: Amplitude and phase response of S_{21} measurement at $h = 2$ in the Accumulator with cavity ARF3 shorted mechanically. Frequency sweeps were injected at cavity ARF2. Beam parameters: intensity 68 mA and energy 8.696 GeV with rms spread 2.6 MeV. Network analyzer setup: 401 data points, sweep time 41 s, and resolution bandwidth 10 Hz. Top right: Uncalibrated stability threshold curve from data displayed at the left. Bottom right: Same stability threshold curve (dashes) as in above, but fitted to the theoretical threshold curve (solid) after scaling and rotational corrections. Dotted curve shows another set of measurement. (Courtesy Spentzouris [15].)

at both ends of the sweep because of the decreasing particle population at those outlying frequencies. The setup of the network analyzer were 401 data points, sweep time 41 s, and resolution bandwidth 10 Hz. Inverting the beam transfer function gives the stability threshold curve of the Accumulator as depicted in the top right plot of Fig. 13.16. A series of corrections was made to convert this uncalibrated threshold curve to the one in dashes in the bottom right plot. This includes scaling, rotation, and fitting to the central part of the theoretical threshold curve, which is shown as solid in the same plot. The dotted curve is the result of another set of sweep measurement.

The mechanical shorts in cavity ARF3 were removed and the beam-transfer-

function measurement repeated. The frequency response or the beam transfer function is shown in solid in the left plot of Fig. 13.17. The original beam transfer function with the ARF3 shorted (top left plot of Fig. 13.16) is also shown in dashes for comparison. The beam transfer functions are inverted and are displaced in the impedance complex plane in the right plot of Fig. 13.17. The calibrated threshold curve is shifted from the one with the mechanical shorts (dashes) to the one without the mechanical shorts (solid). The shift represented by the arrow is the impedance per unit harmonic of the ARF3 cavity: $Z_0^{\parallel}/n = 490 \pm 110\ \Omega$ with a phase angle of $-23°$, i.e., slightly inductive.

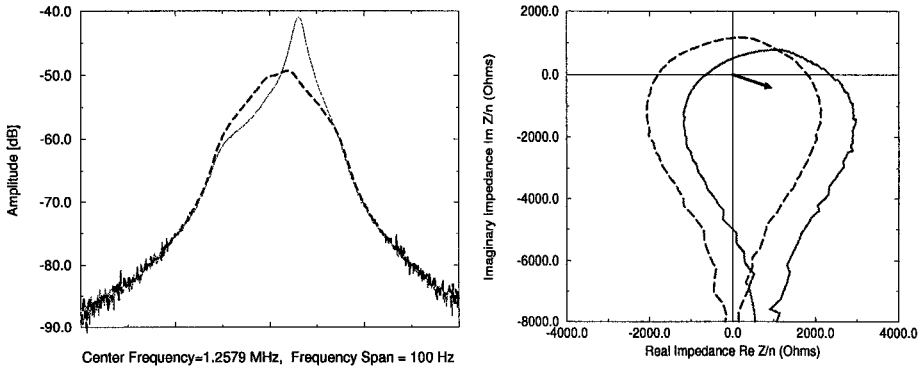


Fig. 13.17 Left: Beam-transfer-function measurements of the Fermilab Accumulator with the ARF3 cavity shorted mechanically (dashes) and with the mechanical short removed (solid). Right: Stability threshold curves in the impedance complex plane with the ARF3 cavity shorted mechanically (dashes) and with the mechanical shorts removed (solid). The shift of the stability threshold indicated by the arrow, is the impedance per harmonic of the ARF3 cavity. The origin of the threshold curve with shorts removed is shifted by approximately $(x, y) = (900, -390)\ \Omega$, which gives an ARF3 cavity impedance of $Z_0^{\parallel}/n = 490 \pm 110\ \Omega$ with a phase angle of $-23°$, i.e., slightly inductive. (Courtesy Spentzouris. [15])

There are, in general, difficulties in performing these measurements. The difference between the low-intensity and high-intensity measurements must be big enough so that the response function can be solved with sufficient accuracy from Eq. (13.119) or (13.125). Too high a beam intensity may excite beam instabilities. Too weak a beam intensity may result in having the signals submerged below the noise level. Usually the impedance to be measured cannot be simply shorted as in the ARF3 cavity. Even the sweep rate can sometimes be an important compromise in the measurement. Sweeping too fast will lose the ability to pick up accurate data. On the other hand, sweeping too slow will involve too long a measurement time, during which the properties of the beam may have been changed already.

13.9 Decoherence versus Landau damping

We learn in this chapter how Landau damping works. There is no harm in reviewing the physical picture once more. When a beam initially at rest transversely is subject to a transverse force at frequency Ω, all the particles follow the force into transverse oscillations with their oscillation amplitudes increasing. Although each particle oscillates with its own intrinsic frequency, nevertheless, their oscillations are all in phase with the driving force at the very beginning and all of them are absorbing energy from the force.** Because there is a total spread $\Delta\omega_\beta$ in betatron frequency among the particles, However, their oscillations gradually become more and more out of phase, because there is a total spread $\Delta\omega_\beta$ in betatron frequency among the particles. Assuming for simplicity that the frequency of the force Ω is at the center of the spread, after the duration $t = 2\pi/\Delta\omega_\beta$, those particles with frequencies $\Omega \pm \frac{1}{2}\Delta\omega_\beta$, which are farthest from Ω, start having their oscillation amplitudes decrease and therefore give out energy to other particles. As time goes on, more particles with intrinsic frequencies closer to Ω begin to see their oscillation amplitudes decrease and surrender energy to other particles that are still in phase with the driving force. Thus after a long time t, only very few particles that have frequencies between $\Omega \pm 2\pi/t$, which are extremely close to Ω, remain in phase with the driving force. Their oscillation amplitudes continue to increase by absorbing energy from the driving force. For all other particles, they oscillate with larger amplitudes some times and nearly zero amplitudes some other times depending on how far their frequencies are from Ω. At the beginning, the center-of-mass of the beam oscillates with an amplitude which grows from zero, because all the particles are roughly in phase. After the time $t \sim 2\pi/\Delta\omega_\beta$, since more and more particles are not oscillating in phase, the oscillation amplitude of the center-of-mass starts to decrease and displacement of the center-of-mass gradually subsides. We call the above process Landau damping. It is clear that the most important ingredient of Landau damping is a spread in the betatron frequency of the beam. In addition, the frequency Ω of the driving force must be covered by the frequency spread of the particles. Otherwise, the exchange of energy and damping described above will not happen. If the betatron frequency spread $\Delta\omega_\beta$ is too small, all the particles will have been driven in phase for a longer time period $\sim 2\pi/\Delta\omega_\beta$ before any particle starts having its amplitude reduce and returning energy to the other particles. At this time, those particles having intrinsic frequencies very close to

**'In phase' implies the driving force has a component in the direction of the particle's velocity, while 'out of phase' implies the driving force has a component in the opposite direction of the particle's velocity.

Ω will have reached an amplitude

$$\left[\text{particle amplitude}\right]_{\max} = \frac{At}{2\bar{\omega}} \approx \frac{\pi A}{\Omega \Delta\omega_\beta}, \tag{13.126}$$

according to Eq. (13.31), where A is the amplitude of the harmonic driving force. If this amplitude is larger than the aperture of the vacuum chamber, beam loss will occur. For a beam inside a vacuum chamber, the harmonic driving force is the wake force which has its magnitude proportional to the displacement of the center-of-mass of the beam. The whole instability starts when the center-of-mass is displaced transversely by whatever means. Thus, as the displacement of the center-of-mass dwindles to zero, there is no more driving force and the instability stops. Because of the dependency of the wake force on the displacement of the center-of-mass, a dispersion relation is obtained. The stability condition which results from the solution of the dispersion relation often requires the spread of the betatron frequency to be larger than the order of the growth rate in the absence of betatron frequency spread, (which is the imaginary part of the dynamical frequency shift in the absence for betatron frequency spread).

On the other hand, it is easy to understand that when there is a spread in betatron frequency $\Delta\omega_\beta$, a displacement of the center-of-mass will diminish in the time $\sim \Delta\omega_\beta^{-1}$ through *decoherence*. Thus if the beam incurs an instability with growth rate τ^{-1}, a spread in betatron frequency $\Delta\omega_\beta \sim \tau^{-1}$ can also prevent the growth from taking place because the instability cannot grow coherently in the presence of such frequency spread.

Since the required spreads in betatron frequency to curb an instability in Landau damping and in decoherence are roughly the same, we want to ask: are Landau damping and decoherence the same thing? [16] If they are not the same, we should compute the damping rate from Landau damping and the damping rate from decoherence separately, so that the sum of the two damping rates then becomes the true damping rate of the beam for a certain instability. If they are the same, this summation will lead to double counting.

In fact, we have used in the description of Landau damping the terminologies like 'frequency spread', 'in-phase oscillation', 'out-of-phase oscillation', etc., which have relation with decoherence. However, we also talk about a driving wave that excites various collective waves inside a beam. Landau damping involves the exchange of energy among the collective waves, so that after a long time only those waves with frequencies very close to the driving frequency continue to absorb energy from the driving wave. All these waves and energy exchanges do not appear to exist in the process of decoherence. Thus we may say that Landau damping involves decoherence but decoherence may not imply Lan-

dau damping. Anyway, what is decoherence? If a beam is kicked transversely, because each particle oscillates with a slightly betatron oscillation frequency, the betatron oscillations of the particles become out of phase after a while and the displacement of the center-of-mass decays. This is one form of decoherence and we call it *kinematic decoherence.* It is given such a name because only kinematics is involved and the equation of motion of each oscillator involves only its own intrinsic frequency, which may also be amplitude dependent, but is independent of any other driving force arising from other particles. This is certainly different from Landau damping, because the latter involves a harmonic driving force with an amplitude depending on, for example, the displacement of the center-of-mass of the beam as well as the coupling impedance of the vacuum chamber. However, decoherence will be affected by the dynamical force from coupling impedance, although the effect is generally small unless the beam is close to an instability. [13] We may say that decoherence with impedance effects taken into account would be the same as Landau damping, and we can also call it *dynamic decoherence.*

13.9.1 *Landau damping of a beam*

Let us consider the equation of motion governing the vertical displacement of a beam particle inside a coasting beam,

$$\ddot{y} + \omega_\beta^2 y = iA\langle y \rangle, \tag{13.127}$$

where the wake force on the right is proportional to the vertical displacement of the center-of-mass of the beam and the constant A plays the role of the transverse impedance of the vacuum chamber. More concretely, from Eq. (13.73),

$$A = \frac{eI_0\beta c^2 Z_1^\perp}{2\pi RE}, \tag{13.128}$$

where I_0 is the beam current, E the beam energy and R the mean radius of the ring. The overdots on the displacement $y(\theta, t)$ represent the second-order total time derivative

$$\frac{d^2}{dt^2} = \left(\frac{\partial}{\partial t} + \omega_0 \frac{\partial}{\partial \theta}\right)^2, \tag{13.129}$$

with θ denoting the azimuthal angle around the ring. All the particles are initially at rest with $y = 0$ and $\dot{y} = 0$. At time $t = 0$, a vertical harmonic displacement $y(\theta, t)|_{t=0} = \sum_n y_{n0} e^{in\theta}$ and transverse velocity $\partial y(\theta, t)/\partial t|_{t=0} = \sum_n \dot{y}_{n0} e^{in\theta}$ are imparted to the beam. We are going to study the time response

of the center-of-mass. Let us introduce the double Fourier transform

$$\tilde{y}_n(\omega) = \int_0^{2\pi} \frac{d\theta}{2\pi} \int_0^{\infty} \frac{dt}{2\pi} y(\theta, t) e^{-in\theta + i\omega t}. \tag{13.130}$$

The inverse Fourier transform is given by

$$y(\theta, t) = \sum_{n=-\infty}^{\infty} \int_W \tilde{y}_n(\omega) e^{in\theta - i\omega t} d\omega, \tag{13.131}$$

where the contour W is from $-\infty + i\alpha$ to $\infty + i\alpha$ with $\alpha > 0$ and chosen in such a way that the contour lies above all singularities of $\tilde{y}(\omega)$ so that causality is preserved. After the Fourier transform, Eq. (13.127) becomes

$$-\frac{\dot{y}_{n0}}{2\pi} + \frac{i(\omega - 2n\omega_0) y_{n0}}{2\pi} + (\omega_\beta^2 - \Omega^2)\tilde{y}_n(\omega) = iA\langle \tilde{y}_n(\omega) \rangle, \tag{13.132}$$

where $\Omega = \omega - n\omega_0$. In obtaining Eq, (13.132), we have made the assumption that ω lies in the upper half-plane so that the evaluation at $t = \infty$ can be performed. For simplicity, we set $\dot{y}_{n0} = 0$ and solve for

$$\tilde{y}_n(\omega) = \frac{iA\langle \tilde{y}(\omega) \rangle}{\omega_\beta^2 - \Omega^2} - \frac{i y_{n0}}{2\pi} \frac{\omega - 2n\omega_0}{\omega_\beta^2 - \Omega^2}. \tag{13.133}$$

Next integrate both sides with the distribution function $\rho(\omega_\beta)$ to obtain

$$\langle \tilde{y}_n(\omega) \rangle = \frac{-i y_{n0}(\omega - 2n\omega_0) \int_{-\infty}^{\infty} \frac{\rho(\omega_\beta)}{\omega_\beta^2 - \Omega^2} d\omega_\beta}{2\pi \mathcal{H}(\omega)} \tag{13.134}$$

where the function in the denominator is defined as

$$\mathcal{H}(\omega) = 1 - iA \int_{-\infty}^{\infty} \frac{\rho(\omega_\beta)}{\omega_\beta^2 - \Omega^2} d\omega_\beta \quad \text{when } \mathcal{I}m\, \omega > 0. \tag{13.135}$$

It will be convenient to define $\langle \tilde{y}_n(\omega) \rangle$ in the lower ω-plane as well so that contour integration can be performed later to obtain the temporal evolution of the displacement of the center-of-mass. It is easy to see that, as defined in Eq. (13.135), $\mathcal{H}(\omega)$ is discontinuous across the real ω-axis. Analytic continuation from the upper ω-plane to the lower ω-plane can be performed easily by patching the discontinuity. This can be accomplished easily by changing the contour of integration. Following Landau, this analytically-continued function can be written conveniently as [1]

$$\mathcal{H}(\omega) = 1 - iA \int_C \frac{\rho(\omega_\beta)}{\omega_\beta^2 - \Omega^2} d\omega_\beta, \tag{13.136}$$

where the contour C is the path from $\omega_\beta = -\infty$ to ∞ with the detour of going above the pole at $\omega_\beta = -\Omega$ and under the pole at $+\Omega$, as illustrated in Fig. 13.18. It is important to note that $\mathcal{H}(\omega) = 0$ is just the dispersion relation we studied before.

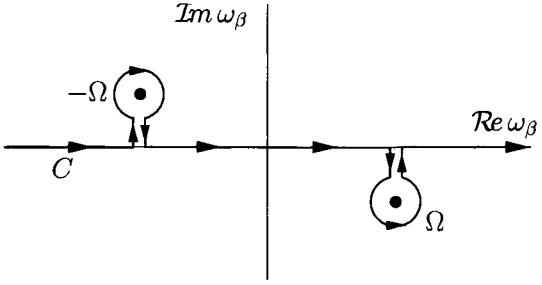


Fig. 13.18 To continue $\mathcal{H}(\omega)$ from the upper half ω-plane to the lower half ω-plane, the path of integration C in the ω_β-plane must go *above* the pole $-\Omega$ and *under* the pole $+\Omega$.

Now transforming back to the time domain, the response of the center-of-mass takes the form,

$$\langle y(\theta,t)\rangle = \sum_{n=-\infty}^{\infty} y_{n0} \int_W \frac{d\omega}{2\pi i}\, e^{in\theta - i\omega t} \frac{\int_C \frac{(\omega - 2n\omega_0)\rho(\omega_\beta)}{\omega_\beta^2 - \Omega^2} d\omega_\beta}{\mathcal{H}(\omega)}. \tag{13.137}$$

The solution consists of many waves which have frequencies that are the zeroes of $\mathcal{H}(\omega)$. These zeroes are the collective eigen-frequencies of the dispersion relation. First, let us consider the situation when there is no coupling impedance or $\mathcal{H} = 1$. The integration over ω is performed first. Remembering that the contour of integration is above all singularities so that $\langle y(t)\rangle = 0$ is obtained when $t < 0$ by completing the upper semi-circle. But for $t > 0$, one must complete the lower semi-circle picking up the two poles at $\pm\Omega$ to arrive at

$$\langle y(\theta,t)\rangle = \sum_{n=-\infty}^{\infty} y_{n0} e^{in(\theta - \omega_0 t)} \int_{-\infty}^{\infty} d\omega_\beta \rho(\omega_\beta) \left(\cos\omega_\beta t + \frac{in\omega_0}{\omega_\beta} \sin\omega_\beta t\right), \tag{13.138}$$

which is the decoherence of the center of the beam subject to a sudden harmonic displacement at time $t = 0$. If this initial sudden displacement is the same for all beam particles, or $y_{n0} = y_0 \delta_{n0}$, the above simplifies readily to

$$\langle y(\theta,t)\rangle = y_0 \int_{-\infty}^{\infty} d\omega_\beta \rho(\omega_\beta) \cos\omega_\beta t, \tag{13.139}$$

which is just the shock response function as defined in Eq. (13.20). In the presence of the coupling impedance, $\mathcal{H}$ differs from unity and the response consists of one or more collective waves instead. If the collective effect is large and the

spread in betatron frequency is not large enough for damping, there will be a growing collective wave which dominates over all other collective waves in the response $\langle y(t)\rangle$. The response will therefore have large deviation from the shock response function (or from kinematic decoherence). However, if the spread in betatron frequency is large enough so that the collective instability is Landau damped, then the collective waves will all be damped, and the response of the center-of-mass will not deviate much from the shock response function. In that sense, we may say Landau damping is not much different from kinematic decoherence. Thus there will not be double counting because the dynamical effect is small. This explains why it is not easy to reveal the impedance effects by monitoring decoherence after a sudden kick of the beam. An example is Experiment E778 performed at the Fermilab Tevatron at the design era of the Superconducting Super Collider (SSC), where the linear aperture of the lattice was pursued. [14] Since the beam in the Tevatron was very stable, the decoherence monitored received negligible contribution from the impedance of the ring. [13] If the beam were not so stable, the experiment could not have been performed. To reveal impedance effects, the beam under study must be close to the threshold of instability, but still stable subject to a transverse kick. In any case, we have demonstrated that Landau damping involves decoherence, but is much more than decoherence. On the other hand, simple decoherence is just a kinematic process and is different from the dynamic process of Landau damping, especially when collective effects are strong.

As an illustration, let us consider the Lorentzian distribution

$$\rho(\omega_\beta) = \frac{\sigma}{\pi}\frac{1}{(\omega_\beta - \bar{\omega})^2 + \sigma^2}, \tag{13.140}$$

where $\bar{\omega}$ is the mean and σ is the spread. We obtain by completing the upper semi-circle and picking up the poles at $\omega_\beta = \Omega$ and $\bar{\omega} + i\sigma$,

$$\int_C d\omega_\beta \frac{\rho(\omega_\beta)}{\omega_\beta^2 - \Omega^2} = -\frac{\Omega + i\sigma}{\Omega(\Omega - \bar{\omega} + i\sigma)(\Omega + \bar{\omega} + i\sigma)}. \tag{13.141}$$

Substituting into Eq. (13.137), we can write

$$\langle y(\theta,t)\rangle = \sum_{n=-\infty}^{\infty} y_{n0} e^{in(\theta - \omega_0 t)} \int_W \frac{d\Omega}{2\pi i} \frac{e^{-i\Omega t}(n\omega_0 - \Omega)(\Omega + i\sigma)}{\Omega(\Omega - \bar{\omega} + i\sigma)(\Omega + \bar{\omega} + i\sigma) + iA(\Omega + i\sigma)}. \tag{13.142}$$

The three poles in the denominator are exactly the same three solutions to the dispersion relation $\mathcal{H}(\omega) = 0$. This indicates that the response of the beam center consists of three harmonic waves. Recall that the $iA/(2\bar{\omega})$ is just the dynamic

part of the betatron frequency shift in the absence of betatron frequency spread. We can therefore make the approximation that

$$\frac{|A|}{2\bar{\omega}} \ll \bar{\omega}, \tag{13.143}$$

and assume that it is of the same order as σ. Physically, Eq. (13.143) states that the dynamic frequency shift or growth rate should be much less than the mean betatron frequency and is of the order of the betatron frequency spread. Thus we can write $A = 2\bar{\omega}\epsilon$ with $|\epsilon| \sim \mathcal{O}(\sigma) \ll \bar{\omega}$. Here, ϵ is nothing more than the transverse impedance $Z_1^\perp$ multiplied by a positive constant. The denominator of the integrand can be rewritten as

$$D = \Omega\,[\Omega + \bar{\omega} + i(\sigma - \epsilon)]\,[\Omega - \bar{\omega} + i(\sigma + \epsilon)] + i2\bar{\omega}\sigma\epsilon. \tag{13.144}$$

The problem will be very much simplified if the last term $i2\bar{\omega}\sigma\epsilon$ is neglected. Keeping only the lowest order terms, the result is

$$\begin{aligned}\langle y(\theta,t)\rangle = \sum_{n=-\infty}^{\infty} y_{n0}\Big[&\frac{in\omega_0\sigma}{\bar{\omega}^2}\, e^{in(\theta-\omega_0)t} \\ &+ \frac{\bar{\omega} - n\omega_0}{2\bar{\omega}}\, e^{in\theta - i(n\omega_0+\bar{\omega})t} e^{-(\sigma+\epsilon)t} \\ &+ \frac{\bar{\omega} + n\omega_0}{2\bar{\omega}}\, e^{in\theta - i(n\omega_0-\bar{\omega})t} e^{-(\sigma-\epsilon)t}\Big].\end{aligned} \tag{13.145}$$

The first term is just an harmonic wave with a small frequency perturbation $\sim -2\sigma\epsilon/\bar{\omega}$ which we have neglected.†† This term comes from those particles with $\omega_\beta = 0$, because of the peculiar behavior of $\rho(0) \neq 0$ in the Lorentzian distribution. Thus, this term should not be there in a more realistic distribution. The second term corresponds to the upper betatron sidebands of all harmonics, positive and negative, while the third term corresponds to the lower sidebands. Since upper and lower sidebands will give the same physics, we can concentrate on the second term only. When $n\omega + \bar{\omega} > 0$, the harmonic waves are either fast waves or super-slow waves and $\mathcal{R}e\, Z_1^\perp > 0$. Thus $\mathcal{R}e\,\epsilon > 0$, which enhances the kinematic decoherence rate σ. When $n\omega + \bar{\omega} < 0$, we are dealing with slow waves. Since $\mathcal{R}e\, Z_1^\perp < 0$, so is $\mathcal{R}e\,\epsilon$, implying that a transverse impedance cancels partly the decoherence rate. As the transverse impedance increases, the slow waves start to grow eventually when $\sigma + \mathcal{R}e\,\epsilon < 0$ and the beam becomes unstable.

The Lorentzian distribution has been chosen here in favor of the more common Gaussian, because the former leads to a solution with a finite number of

††Knowing that this solution for Ω is much smaller than $\bar{\omega}$, we can set the second and third Ω's on the right side of Eq. (13.144) to zero. Then it is easy to find $\Omega = i2\sigma\epsilon/\bar{\omega}$.

terms corresponding to a finite number of zeroes in the dispersion relation. On the other hand, a Gaussian distribution will lead to an infinite number of terms in the solution. Just retaining the term with the highest growth sometimes may not be meaningful because an infinite sum may lead to anything.

Let us apply the solution to Experiment E778. In 1987, E778 was performed with beam intensity $N_b = 0.5 \times 10^{10}$ per bunch, rms bunch length $\sigma_\ell \sim 15$ cm, rms momentum spread $\sigma_\delta = 1.5 \times 10^{-4}$, energy $E = 150$ GeV, and betatron tune $\nu_\beta \sim 20$. With a chromaticity of $\xi = 10$ units, the betatron tune spread is $\sigma_{\nu_\beta} = \xi\sigma_\delta = 1.5 \times 10^{-3}$, or the rms decoherence time is 670 turns. The Tevatron has a mean radius of 1 km. For an exponential decay corresponding to the Lorentzian distribution in Eq. (13.140), the rms decay time is $\sqrt{2}/\sigma$. Thus we set $\sigma = \sqrt{2}\sigma_{\nu_\beta}\omega_0 = 450$ s^{-1}. The peak current $I_0 = eN_b\beta c/(\sqrt{2\pi}\sigma_\ell) = 0.64$ A should be used in Eq. (13.128). The transverse impedance was about $Z_1^\perp = 2$ MΩ/m according to the estimation in Ref. [17] from ~ 1 MHz to ~ 1 GHz. We therefore obtain

$$\epsilon = \frac{eI_0 c Z_1^\perp}{4\pi E \nu_\beta} = 10.2 \text{ s}^{-1}, \tag{13.146}$$

or a growth time of $\omega_0/\epsilon = 2.9 \times 10^4$ revolution turns. We can therefore safely conclude that the effect of coupling impedance to the observed decoherence rate is negligible.

13.9.2 *Longitudinal Decoherence*

Now let us turn to the Landau damping of longitudinal instabilities of a coasting beam. We learn that the beam transfer function involves the derivative of the energy distribution. In other words, there will not be any Landau damping in a flat distribution. On the other hand, decoherence appears to take place via any energy distribution. It may therefore be difficult to visualize the involvement of decoherence in Landau damping. In fact, this is not true. It is easy to show that decoherence of a coasting beam also requires the derivative of the energy distribution. [18]

Let us choose as canonical variables the energy offset ΔE and the azimuthal angle around the ring $\theta = s/R$, where s is measured along the on-momentum orbit and R is the mean radius of the ring. The distribution that is normalized to unity can be written as

$$f(\theta, \Delta E; t) = f_0(\Delta E) + f_1(\theta, \Delta E; t), \tag{13.147}$$

where $f_0(\Delta E)$ is the stationary distribution which must be a function of ΔE

only. The perturbation part of the distribution can be obtained by adding a harmonic deviation

$$\delta E(\theta) = \widehat{\delta E} \cos k\theta \tag{13.148}$$

at time $t = 0$. We therefore have at $t = 0+$,

$$f(\theta, \Delta E; 0+) = f_0(\Delta E - \widehat{\delta E} \cos k\theta) = f_0(\Delta E) - \frac{df_0}{d\Delta E} \widehat{\delta E} \cos k\theta. \tag{13.149}$$

A particle moves according to $\theta = \theta' + \omega_0 t$ where θ' is the position at $t = 0$ and ω_0 is the revolution angular velocity. Thus the perturbation distribution at time $t > 0$ is

$$f_1(\theta, \Delta E; t) = -\frac{df_0}{d\Delta E} \widehat{\delta E} \cos(k\theta - k\omega_0 t). \tag{13.150}$$

The perturbation part of the current recorded at θ_0 jumps from zero at $t < 0$ to

$$I_1(\theta, t) = \frac{eN}{2\pi} \int \omega_0 f_1(\theta, \Delta E; t)\, d\Delta E = -\frac{eN\widehat{\delta E}}{2\pi} \int \frac{df_0}{d\Delta E}\, \omega_0 \cos(k\theta - k\omega_0 t) d\Delta E \tag{13.151}$$

at $t > 0$, where N is the total number of particles in the beam. We next change the variable of integration from ΔE to $\Delta\omega_0$, where $\Delta\omega_0 = \omega_0 - \bar{\omega}_0$ is the deviation from the nominal revolution angular frequency $\bar{\omega}_0$. For this, we introduce the distribution $g_0(\Delta\omega_0)$ that is normalized to unity when integrated over $\Delta\omega_0$ by

$$f_0(\Delta E) d\Delta E = g_0(\Delta\omega_0) d\Delta\omega_0. \tag{13.152}$$

Then

$$\frac{df_0}{d\Delta E}\, d\Delta E = \frac{dg_0}{d\Delta E}\, d\Delta\omega_0 = -\frac{\eta\bar{\omega}_0}{\beta^2 E_0} \frac{dg_0}{d\Delta\omega_0}\, d\Delta\omega_0, \tag{13.153}$$

where η is the slip factor, E_0 is the nominal particle energy, $\bar{\omega}_0$ is the nominal revolution angular frequency, and β is the relativistic factor. The negative sign comes about because the revolution angular frequency ω_0 is smaller at a larger energy offset ΔE above transition ($\eta > 0$). The perturbation part of the current recorded at location θ_0 as a function of time becomes

$$I_1(\theta, t) = \frac{eN\eta\bar{\omega}_0^2 \widehat{\delta E}}{2\pi\beta^2 E_0} \int_{-\infty}^{\infty} \frac{dg_0}{d\Delta\omega_0} \Big[\cos(k\theta - k\bar{\omega}_0 t) \cos k\Delta\omega_0 t + \sin(k\theta - k\bar{\omega}_0 t) \sin k\Delta\omega_0 t \Big] d\Delta\omega_0. \tag{13.154}$$

Since $f_0(\Delta E)$ is even in ΔE, $g(\Delta\omega_0)$ is even in $\Delta\omega_0$. This indicates that $dg/d\Delta\omega_0$ is odd in $\Delta\omega_0$. Thus the cosine term vanishes leaving behind

$$I_1(\theta,t) = \frac{eN\eta\bar{\omega}_0^2\widehat{\delta E}}{2\pi\beta^2 E_0}\sin(k\theta - k\bar{\omega}_0 t)\int_{-\infty}^{\infty}\frac{dg_0}{d\Delta\omega_0}\sin k\Delta\omega_0 t\, d\Delta\omega_0. \tag{13.155}$$

We can identify the longitudinal shock response function in a coasting beam as

$$G_{\parallel}(t) = H(t)\int_{-\infty}^{\infty}\frac{dg_0}{d\Delta\omega_0}\cos k\omega_0 t\, d\omega_0, \tag{13.156}$$

where $H(t)$ is the Heaviside step function, because it tells us how the perturbation in the current dies away after a disturbance at $t = 0$. We can now understand how longitudinal kinematic decoherence takes place, especially its involvement with the derivative of the distribution function just as in the transfer function $R_{\parallel}(u)$ introduced in Eq. (13.112). In fact, it can be shown easily that the Fourier transform[‡‡] of the $G_{\parallel}(t)$ just gives $R_{\parallel}(u)$.

To conclude this chapter, let us compute and plot the time evolution of the energy perturbation to the beam. With the aid of Eqs. (13.149) and (13.153), the distribution in phase space is

$$f(\theta,\Delta E;t) = f_0\left[\Delta E - \widehat{\delta E}\cos\left(k\theta - k\bar{\omega}_0 t + \frac{k\eta\bar{\omega}_0 t}{\beta^2 E_0}\Delta E\right)\right] \tag{13.158}$$

Let us normalized everything to the rms energy spread σ_E of the unperturbed beam. The distribution observed at the nth revolution turn is

$$f(\theta,\Delta E;t) = f_0\big[\varepsilon - a\cos(k\theta + k\xi\varepsilon)\big], \tag{13.159}$$

where we have used the abbreviations

$$\varepsilon = \frac{\Delta E}{\sigma_E}, \quad a = \frac{\widehat{\delta E}}{\sigma_E}, \quad \xi = \frac{2\pi n\eta\bar{\sigma}_E}{\beta^2 E_0}. \tag{13.160}$$

This distribution for the energy disturbance with second harmonic ($k = 2$) and disturbance amplitude $a = \widehat{\delta E}/\sigma_E = 0.4$ is shown in Fig. 13.19 at different 'times' $\xi = 0$, 0.31, 0.62, 0.93, and 1.24. In each plot, equi-density curves are depicted at $\varepsilon = -2.0$ to 2.0 in steps of 0.5. As an example, the equi-density

[‡‡]If we identify instead the last integral in Eq. (13.155) as the shock response function, namely

$$G_{\parallel}(t) = H(t)\int_{-\infty}^{\infty}\frac{dg_0}{d\Delta\omega_0}\sin k\Delta\omega_0 t\, d\Delta\omega_0, \tag{13.157}$$

its relation with $R_{\parallel}$ is not just simply the Fourier transformation.

curve at density x σ's $f_0(x)$ is obtained by solving for $\varepsilon(\theta)$ from the equation

$$\varepsilon - a\cos(k\theta + k\xi\varepsilon) = x. \tag{13.161}$$

On the right is shown the energy spread distribution of the beam observed at the azimuthal angle $\theta = \pi$ along the ring, where we have assumed a Gaussian for the unperturbed beam, or

$$f_0(x) = \frac{1}{\sqrt{2\pi}} e^{-x^2/2}. \tag{13.162}$$

In the bottom is the perturbed beam current at each θ obtained by integrating over ΔE, or

$$I(\theta, \xi) = \int_{-\infty}^{\infty} f_0\big[\varepsilon - a\cos(k\theta + k\xi\varepsilon)\big]\, d\varepsilon. \tag{13.163}$$

We notice that at time $\xi = 0+$ just after the introduction of the energy disturbance, the energy-spread distribution at $\theta = \pi$ is still Gaussian but shifted to a higher energy by the amount $a = \widehat{\delta E}/\sigma_E$. There is completely no change in the beam current at all because the disturbance is in the energy direction.

As time progresses, shearing occurs in the beam because of the finite slip factor η with particles having larger energy offsets shear more than those having smaller energy offsets. As a result, the equi-density curves are no longer sinusoidal and the energy distribution deviates from Gaussian. As the maxima of one equi-density curve move away from those of the others and the beam current starts exhibiting a $\cos 2\theta$ linear density, which possesses the largest amplitude at $\xi \approx 0.5$. As time goes on, however, the shearing becomes so pronounced that the modulations at the different energy deviations overlap. This reduces the modulation of the beam current and the $\cos 2\theta$-behavior slowly dies down in the last two plots. This is just the static decoherence of an energy disturbance in a coasting beam. Now it is easy to see why there will not be any decoherence if the energy distribution of the unperturbed beam is flat. In that case, we can no longer talk about equi-density curves. Instead every point in the longitudinal phase space has the same density or the whole longitudinal phase space is of equi-density. A truly flat distribution does not support any energy disturbance at all and therefore we cannot talk about decoherence either. For a water-bag energy distribution, an energy disturbance occurs at the two edges of the distribution. Decoherence occurs when the two edges shear differently.

The decay of the current modulation can be derived directly from Eq. (13.151) by integrating over the revolution-frequency offset $\Delta\omega_0$ or the energy offset ΔE. In the normalized notations, we have

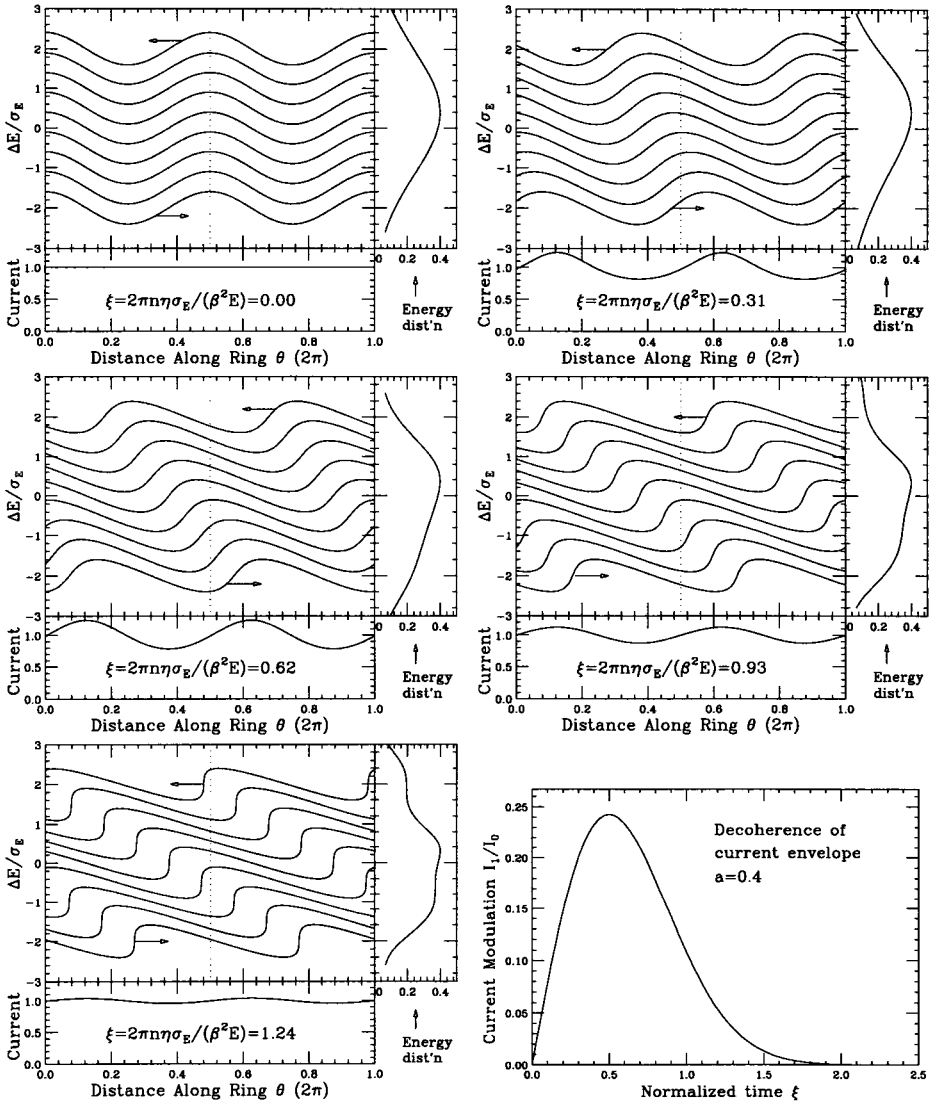


Fig. 13.19 Illustration of longitudinal decoherence of an energy disturbance of harmonic $k = 2$ and modulation amplitude $a = \widehat{\delta E}/\sigma_E = 0.4$ in a coasting beam, where σ_E is the rms energy spread of the unperturbed beam. The first five plots are at 'times' $\xi = 0+$, 0.31, 0.62, 0.93, and 1.24. Shown in each plot are equi-density curves at 0, ± 0.5, ± 1.0, ± 1.5, and $\pm 2.0\sigma_E$'s. The energy spread distribution as recorded at azimuthal angle $\theta = \pi$ along the ring is shown at the right, with Gaussian assumed for the unperturbed,. The perturbed current is shown at the bottom. The current modulation starts from zero at $\xi = 0+$, goes through a maximum at $\xi = 1/k = 0.5$, and rolls off like a Gaussian, as illustrated in the last plot.

$$\frac{I_1(\theta,\xi)}{I_0} = a\sin(k\theta - k\bar{\omega}_0 t)\int_{-\infty}^{\infty}\frac{df_0}{d\varepsilon}\sin k\xi\varepsilon\, d\varepsilon, \tag{13.164}$$

where $I_0 = eN\bar{\omega}/(2\pi)$ is the unperturbed current of the beam. For a Gaussian distribution in energy spread for the unperturbed beam, the integral can be performed exactly to give

$$\frac{I_1(\theta,\xi)}{I_0} = -a\sin(k\theta - k\bar{\omega}_0 t)k\xi e^{-k^2\xi^2/2}. \tag{13.165}$$

As monitored at location $\theta = \pi$, the envelope of the current modulation increases linearly with time, goes through a maximum at $\xi = 1/k$, and rolls off like a Gaussian, agreeing with what we observe in the numerical plots.

13.10 Exercises

13.1 A shock excitation is given to a bunch with a Lorentz frequency distribution $\rho(\omega)$ so that at $t = 0$ each particle has $\dot{x}(t) = \dot{x}_0$. Compute the response of the displacement of the center of the bunch $\langle x(t)\rangle$ and show that it does not decay to zero. Show that this is because $\rho(0) \neq 0$.

13.2 Derive the shock response function $G(t)$ and beam transfer function $R(u)$ for the various frequency distributions as listed in Table 13.1. Fill in those items that have been left blank.

13.3 Derive the U-intercept and the form factor F defined in Eq. (13.56) for various distributions as listed in Table 13.2.

13.4 Continuing the example in Exercise 8.1(3) for the electron and proton rings. When the resonant frequencies are offset in the wrong direction by $|\Delta\omega/(2\pi)| = 10$ kHz, compute the amount of spread in synchrotron tune required to Landau damp the Robinson's instability. Comment whether the spreads are feasible or not. Assume that the synchrotron tune is 0.01 for the electron ring and 0.002 for the proton ring.

13.5 Show that the longitudinal shock response function and the longitudinal transfer function in a coasting beam defined in Eqs. (13.156) and (13.112) are connected by Fourier transformation.

Bibliography

[1] L. D. Landau, *J. Phys. USSR* **10**, 25 (1946).
[2] J. D. Jackson, *Nucl. Energy Part C: Plasma physics* **1**, 171 (1960).

[3] V. K. Neil and A. M. Sessler, *Rev. Sci. Instrum.* **6**, 429 (1965).
[4] L. J.Laslett, V. K. Neil, and A. M. Sessler, *Rev. Sci. Instrum.* **6**, 46 (1965).
[5] H. G. Hereward, CERN Report 65-20 (1965).
[6] A. Hofmann, *Coherent Beam Instabilities, Frontiers of Part. Beams: Intensity Limitations*, Lecture Notes in Phys. **400**, eds. M. Dienes, M. Month, and S. Turner (Hilton Head Island, SC, Nov. 7–14, 1990) Springer-Verlag, 1990, p. 110.
[7] A. W. Chao, *Physics of Collective Beam Instabilities in High Energy Accelerators*, Wiley Interscience, 1993, Chapter 5.
[8] B. Zotter and F. Sacherer, *Transverse instabilities of Relativistic Particle Beams in Accelerator and Storage Rings*, Proc. First Course of Int. School of Part. Accel., eds. A. Zichichi, K. Johnsen, and M. H. Blewett (Erice, Nov. 10–22, 1976), p.176.
[9] K. Y. Ng, *Possible Ion Trapping in Recycler Ring*, Proc. 31st ICFA Advanced Beam Dynamics Workshop on Electron-Cloud Effect (Ecloud'04), ed. M. Furman (Napa, CA, April 19–23, 2004).
[10] K. Y. Ng, *Transverse Instability at the Recycler Ring*, Fermilab Report FERMILAB-FN-0760-AD, 2004.
[11] J. Crisp and M. Hu, *Recycler Ring Instabilities Measured on 6/9/04*, 2004, (unpublished).
[12] M. Hu and J. Crisp, *Recycler Instability Observed with Protons*, 2004, (unpublished).
[13] K. Y. Ng, *Impedance Effects on Decoherence Rate of Experiment E778*, SSC Report SSC-N-436, 1987.
[14] A. Chao, D. Johnson, S. Peggs, J. Peterson, C. Saltmarsh, and L. Schachinger, R. Meller, R. Siemann, R. Talman, P. Morton, D. Edwards, D. Finley, R. Gerig, N. Gelfand, M. Harrison, R. Johnson, N. Merminga, M. Syphers, *Experimental Investigation of Nonlinear Dynamics in the Fermilab Tevatron, Phys. Rev. Lett.* **61**, 2752 (1988); N. Merminga, D. Edwards, D. Finley, R. Gerig, N. Gelfand, M. Harrison, R. Johnson, M. Syphers, R. Meller, R. Siemann, R. Talman, P. Morton, A. Chao, T. Chen, D. Johnson, S. Peggs, J. Peterson, C. Saltmarsh, and L. Schachinger, *Nonlinear Dynamics Experiment in the Tevatron*, Proc. of 1989 IEEE Part. Accel. Conf., eds. F. Bennett and J. Kopta (Chicago, March 20–23, 1989), p. 1429.
[15] L. K. Spentzouris, *Coherent Nonlinear Longitudinal Phenomena in Unbunched Synchrotron Beams*, Phd Thesis, Northwestern University, 1996.
[16] K. Y. Ng, *Decoherence and Landau Damping*, Fermilab Report FERMILAB-FN-0763-AD, 2005.
[17] K. Y. Ng, *Impedances and Collective Instabilities of the Tevatron at Run II*, Fermilab Report TM-2055, 1998.
[18] A. Hofmann, *Landau Damping*, CERN Accelerator School 5th Advanced Accelerator Physics Course, (Hotel Paradise, Rhodes, Greece, Sept. 20–Oct. 1, 1993), p. 275, CERN Report CERN 95-06.

2025 © The Author(s). This is an Open Access chapter published by World Scientific Publishing Company, licensed under the terms of the Creative Commons Attribution-NonCommercial 4.0 International License (CC BY-NC 4.0).

Chapter 14

Beam Breakup

In a high-energy electron linac,* the relative longitudinal positions of the beam particles inside a bunch do not change. Thus, the tail particles are always affected by the head particles. We have shown that the longitudinal wake will cause the tail particles to lose energy (see Exercise 6.5). This loss, accumulated throughout the whole length of the linac, can be appreciable, leading to an undesirable spread in energy within the bunch. If the linac is the upstream part of a linear collider, this energy spread will have chromatic effect on the final focus and eventually enlarge the spot size of the beam at the interaction point. We have also discussed how this energy spread can be corrected by placing the center of the bunch at an rf phase angle where the rf voltage gradient is equal and opposite to the energy gradient along the bunch.

Here, we would like to address the effect of the transverse wake potential. A small offset of the head particles will translate into a transverse force on the particles following. The deflections of the tail particles will accumulate along the linac. When the particles hit the vacuum chamber, they will be lost. Even if the aperture is large enough, the transverse emittance will be increased to an undesirable size. This phenomenon is called *beam breakup*. This is not a collective instability, however. But beam breakup is intensity dependent.

Recently, there has been a lot of interest in isochronous or quasi-isochronous rings, where the spread in the slip factor for all the particles in the bunch is very tiny, for example, $\Delta\eta \lesssim 10^{-6}$. In some of these rings, like the muon colliders where the beam is stored to about 1000 turns, the head and tail particles hardly exchange longitudinal positions, and we have a situation very similar to linacs. Problems of beam breakup will also show up in these rings. The beam breakup discussed in this chapter does not allow particles to exchange longitudinal posi-

*All proton linacs in existence are not ultra-relativistic. The highest energy is less than 1 GeV. Therefore synchrotron oscillations occur.

tions or change their relative longitudinal positions. We therefore assume that their velocities are equal to the velocity of light.

14.1 Two-Particle Model

Take the simple two-particle model by which the bunch is represented by two macro-particles of charge $\frac{1}{2}eN_b$ each separated by a distance $\hat{z}$. The transverse displacements of the head, y_1, and the tail, y_2, satisfy

$$\frac{d^2y_1}{ds^2} + k_{\beta_1}^2 y_1 = 0, \tag{14.1}$$

$$\frac{d^2y_2}{ds^2} + k_{\beta_2}^2 y_2 = -\frac{e^2N_bW_1(\hat{z})}{2LE_0}\, y_1, \tag{14.2}$$

where E_0 is the energy of the beam particles and s is the longitudinal distance measured along the designed particle path, W_1 is the transverse wake function for one linac cavity of length L, and $k_{\beta_{1,2}}$ are the betatron wave numbers for the two particles. For an isochronous ring, L will be taken as the ring circumference $C_0 = 2\pi R$ and

$$k_{\beta_{1,2}} = \frac{\nu_{\beta_{1,2}}}{R}, \tag{14.3}$$

where $\nu_{\beta_{1,2}}$ are the betatron tunes of the two particles. We can also define the betatron tunes $\nu_{\beta_{1,2}} = Lk_{\beta_{1,2}}/(2\pi)$ for the two particles in a linac as the number of betatron oscillations they make along a length L of the linac. This model has been giving a reasonably accurate description to the beam breakup mechanism for short electron bunches when $\hat{z}$ is taken as the rms bunch length. The head makes simple harmonic motion $y_1(s) = y_{10}\cos k_{\beta_1}s$ according to Eq. (14.1), where y_{10} is its initial displacement. If the tail is initially at $y_2 = y_{10}$ with $y_2' = dy_2/ds = 0$, its displacement can be readily solved and the result is

$$y_2(s) = y_{10}\cos\bar{k}_\beta s\cos\frac{\Delta k_\beta s}{2} - y_{10}\sin\bar{k}_\beta s\left[\frac{\Delta k_\beta}{2} + \frac{e^2N_bW_1(\hat{z})}{4LE_0\bar{k}_\beta}\right]\left[\frac{\sin\Delta k_\beta s/2}{\Delta k_\beta/2}\right], \tag{14.4}$$

where $\bar{k}_\beta = \frac{1}{2}(k_{\beta_1} + k_{\beta_2})$ is the mean of the betatron wave numbers of the head and tail. When the tune difference $\Delta k_\beta = k_{\beta_2} - k_{\beta_1}$ approaches zero, the tail is driven resonantly by the head and its displacement grows linearly with s:

$$y_2(s) = y_1(s) - s\,y_{10}\sin k_{\beta_1}s\frac{e^2N_bW_1(\hat{z})}{4E_0Lk_\beta}. \tag{14.5}$$

In the length L_0, the amplitude of the tail oscillation will grow Υ_1-fold, where [3]

$$\Upsilon_1 = -\frac{e^2 N_b W_1(\hat{z}) L_0}{4E_0 L k_\beta}, \tag{14.6}$$

is the response of the tail particle. Note that $W_1(\hat{z})$ is negative for small $\hat{z}$. For the more general situation of a nonuniform-focusing channel, we learn from Exercise 3.7 that the substitution $k_\beta^{-1} \longrightarrow \beta_y$ must be made. The response parameter therefore becomes

$$\Upsilon_1 = -\frac{e^2 N_b \left[\beta_y W_1(\hat{z})\right] L_0}{4E_0 L}, \tag{14.7}$$

where $[\beta_y W_1(\hat{z})]$ implies that the average wake for one linac cavity is obtained by averaging the sum of the wake along the whole linac using the betatron function β_y as a weight. In an isochronous ring, $[\beta_y W_1(\hat{z})]$ implies that β_y serves as a weight when the wake is summed up element by element along the ring circumference. There is a physical reason for β_y to appear, because the transverse impedance initiates a kick y' of the beam and the size of the kicked displacement depends on the betatron function at the location of the impedance. This can be easily visualized in the transfer matrix.

For a broadband impedance, the transverse wake function at a distance z behind the source particle is, for $z > 0$,

$$W_1(z) = -\frac{\omega_r^2 Z_1^\perp}{Q\bar{\omega}} e^{-\alpha z/c} \sin\frac{\bar{\omega} z}{c}, \tag{14.8}$$

where $Z_1^\perp$ is the transverse impedance at the angular resonant frequency ω_r, which is shifted to $\bar{\omega} = \sqrt{\omega_r^2 - \alpha^2}$ by the decay rate $\alpha = \omega_r/(2Q)$ of the wake with Q being the quality factor. Let us introduce the dimensionless variables

$$v = \frac{\omega_r \sigma_\ell}{c}, \quad t = \frac{z}{\sigma_\ell}, \quad \text{and} \quad \phi = vt\cos\phi_0 = \frac{\bar{\omega} z}{c}, \tag{14.9}$$

where the angle ϕ_0 is defined as

$$\cos\phi_0 = \sqrt{1 - \frac{1}{4Q^2}} \quad \text{or} \quad \sin\phi_0 = \frac{1}{2Q}, \tag{14.10}$$

assuming that $Q > \frac{1}{2}$. Then, the transverse wake in Eq. (14.8) can be rewritten as, for $\phi > 0$,

$$W_1(\phi) = -2\omega_r Z_1^\perp \tan\phi_0 \sin\phi\, e^{-\phi\tan\phi_0}, \tag{14.11}$$

The wake function decreases linearly from zero when $\phi = \bar{\omega}z/c \ll 1$ and reaches a minimum

$$W_1\big|_{\min} = -2\omega_r Z_1^{\perp} \tan\phi_0 \cos\phi_0 \, e^{-\left(\frac{\pi}{2}-\phi_0\right)\tan\phi_0} \tag{14.12}$$

at

$$\phi = \frac{\pi}{2} - \phi_0 \quad \text{or} \quad \frac{\alpha z}{c} = \left(\frac{\pi}{2} - \phi_0\right)\tan\phi_0. \tag{14.13}$$

After that it oscillates with amplitude decaying at the rate of $\alpha = \omega_r/(2Q)$, crossing zero at steps of $\Delta\phi = \bar{\omega}z/c = \pi$. This is illustrated in Fig. 14.1.

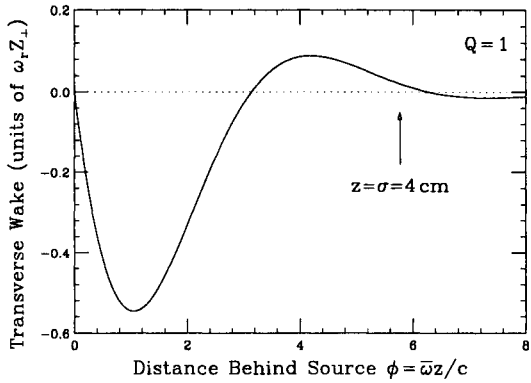


Fig. 14.1 Transverse wake function for a broadband impedance with $Q = 1$ in units of $\omega_r Z_1^{\perp}$ as a function of $\phi = \bar{\omega}z/c$ behind the source. With resonant angular frequency $\omega_r = 50$ GHz, the position for $z = \sigma_\ell$ for the 4-cm bunch is marked, which is certainly outside the linear region and the two-particle model will not apply.

Obviously, the growth expression of Eq. (14.6) does not apply to all bunch lengths. For example, if $\hat{z}$ just happens to fall on the first zero of $W_1(\hat{z})$, Eq. (14.6) says there is no growth at all. However, particles in between will be deflected and they will certainly affect the tail particle. Thus, the criterion for Eq. (14.6) to hold is the variation of the wake function along the bunch must be smooth. In other words, we must be in the linear region of the wake function, or

$$\phi = \frac{\bar{\omega}z}{c} \ll 1 \qquad \longrightarrow \qquad \sigma_\ell \ll \frac{1}{2}\frac{\lambda}{2\pi}, \tag{14.14}$$

i.e., the rms bunch length must be less than half the reduced wavelength $\lambda/(2\pi)$ of the resonant impedance. As an example, if the broadband impedance with $Q \sim 1$ has resonant frequency 7.96 GHz ($\omega_r = 50$ GHz), the two-particle model works only when the rms bunch length $\sigma_\ell \ll 3$ mm. Therefore, the model cannot be applied to the usual proton bunches. For the 50 GeV on 50 GeV

muon collider, the muon bunches have an rms length of 4 cm, and will not be able to fit into this model also. [2]

14.2 Long Bunch

For a bunch with linear density $\lambda(z)$, the transverse motion $y(z,s)$ at a distance z behind the bunch center and at position s along the linac is given by

$$\frac{d^2y(z,s)}{ds^2} + k_\beta^2 y(z,s) = -\frac{e^2N_b}{LE_0}\int_{-\infty}^{z} dz'\lambda(z')W_1(z-z')y(z',s). \qquad (14.15)$$

This equation can be solved first by letting $y(z,s)$ be a free oscillation on the right-hand side and solving for the displacement $y(z,s)$ on the left-hand side. Then, iterations are made until the solution becomes stable. Therefore, when Υ_1 is large, the growth will be proportional to powers of Υ_1 and even exponential in Υ_1. Thus, the growth of displacement can be very sensitive to $\left[\beta_y Z_1^\perp\right]$, ω_r, as well as Q.

Simulations have been performed for the 4-cm and 13-cm muon bunches in a quasi-isochronous collider ring, with a betatron tune $\nu_\beta \sim 6.24$, interacting with a broadband impedance with $Q = 1$ and $Z_1^\perp = 0.1$ MΩ/m at the angular resonant frequency $\omega_r = 50$ GHz. Initially, a bunch is populated with a vertical Gaussian spread of $\sigma_y = 3$ mm and $y' = 0$ for all particles. There is no offset for the center of the bunch. Ten thousand macro-particles are used to represent the bunch containing 4×10^{12} beam particles. The half-triangular bin size is 15 ps (or 0.45 cm). Smooth focusing has been assumed for the ring. In Fig. 14.2 we show the total growth of the *normalized* beam size $\sigma_y \equiv \langle y^2 + (\langle\beta_y\rangle y')^2\rangle^{1/2}$ relative to the initial beam size up to 1000 turns for various values of average betatron function $\langle\beta_y\rangle$, respectively, for the 13-cm and 4-cm bunches. The turn-by-turn decay of the muons has been taken into account. We see that the beam size grows very much faster for larger betatron function. Also the growths for the 4-cm bunch are much larger than those for the 13-cm bunch because the linear charge density of the former is larger.

14.2.1 *Balakin–Novokhatsky–Smirnov Damping*

Kim, Wurtele, and Sessler [3] suggested to suppress the growth of the transverse beam breakup by a small tune spread in the beam, coming either through chromaticity, amplitude dependency, or beam-beam interaction. This is because a beam particle will be resonantly driven by only a small number of particles in

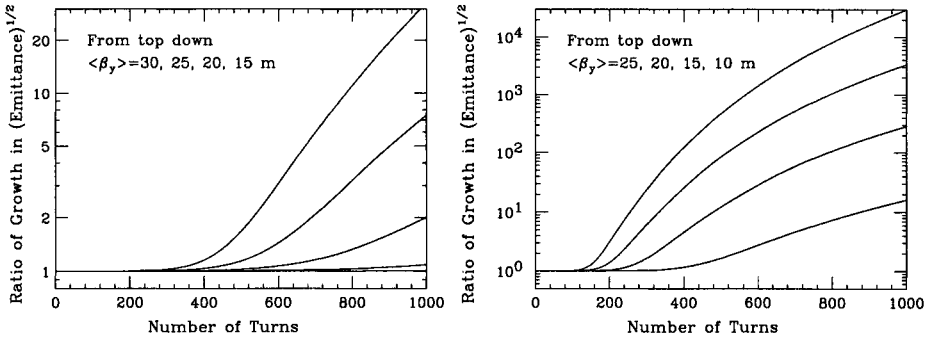


Fig. 14.2 Beam-breakup growth for 1000 turns of a muon bunch of intensity 4×10^{12} at 50 GeV interacting with a broadband impedance of $Q = 1$, $Z_1^{\perp} = 0.1$ MΩ/m at the angular resonant frequency of $\omega_r = 50$ GHz. Left: rms 13-cm bunch has total growths of 32.50, 7.4, 2.0, 1.09, 1.006, respectively for $\langle\beta_y\rangle = 30$, 25, 20, 15, 10 m. Right: rms 4-cm bunch has total growths of 29713, 3361, 287, 16.2, respectively for $\langle\beta_y\rangle = 25$, 20, 15, 10 m.

front that have the same betatron tune. This is a form of Balakin–Novokhatsky–Smirnov (BNS) damping suggested in 1983. [4]

To implement this, we add a detuning term $\Delta\nu_{\beta_i} = a[y_i^2 + (\langle\beta_y\rangle y_i')^2]$ to the ith particle, as if it is contributed by an octupole or sextupole. In Fig. 14.3, we plot the growths of the normalized beam size relative to the initial beam size with various rms tune spreads $\sigma_{\nu_\beta} = a\langle\sigma_y^2 + (\langle\beta_y\rangle\sigma_{y'})^2\rangle$. Here, an average betatron function of $\langle\beta_y\rangle = 20$ m has been used. This is because BPMs, which contribute significantly to the transverse impedance, are usually installed at locations where the betatron function is large. We see in the left plot that to damp the growth of the 13-cm bunch to less than 1%, we need an rms tune spread of $\sigma_{\nu_\beta} = 0.0008$ or a total tune spread of $\Delta\nu_\beta = 3\sigma_{\nu_\beta} = 0.0024$. On the other hand, to damp the growth of the 4-cm bunch to less than 1%, we need (right plot) an rms tune spread of $\sigma_{\nu_\beta} = 0.006$ or a total tune spread of $\Delta\nu_\beta = 3\sigma_{\nu_\beta} = 0.018$. We also see a saturation of the emittance growth for the 4-cm bunch. However, if the transverse impedance is larger, the average betatron function is larger, the resonant frequency is larger, or the quality factor is smaller, this required tune spread may become too large to be acceptable. This is because a large amplitude-dependent tune spread can lead to the reduction of dynamical aperture of the collider ring.

For the lattice of the muon collider ring designed by Trbojevic and Ng, [1] in order to allow for a large enough momentum aperture, the amplitude-dependent tune shifts are

$$\begin{aligned} \nu_{\beta x} &= 8.126 - 100\epsilon_x - 4140\epsilon_y, \\ \nu_{\beta y} &= 6.240 - 4140\epsilon_x - 50.6\epsilon_y, \end{aligned} \tag{14.16}$$

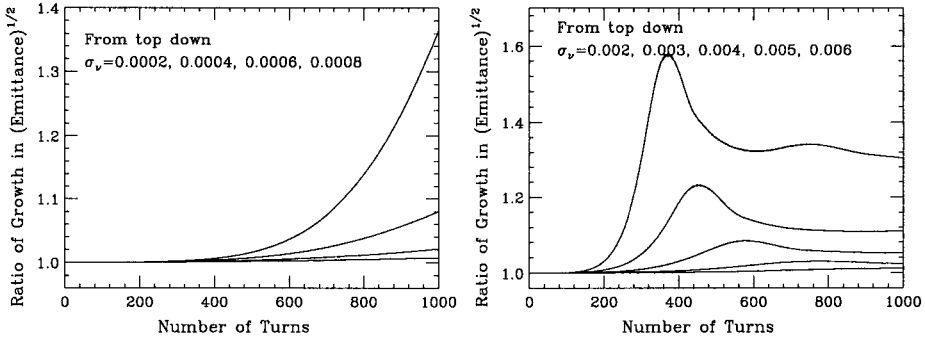


Fig. 14.3 Total growth in 1000 turns of a muon bunch of intensity 4×10^{12} at 50 GeV in the presence of an amplitude dependent tune shift, such as provided by an octupole. An average betatron function of $\langle \beta_y \rangle = 20$ m has been assumed. Left: growths of the rms 13 cm bunch are 1.36, 1.08, 1.02, 1.007, respectively for rms tune spread of $\sigma_{\nu_\beta} = 0.0002, 0.0004, 0.0006, 0.0008$. Right: growths of the rms 4 cm bunch are 1.58, 1.23, 1.08, 1.03, 1.012, respectively for rms tune spread of $\sigma_{\nu_\beta} = 0.002, 0.003, 0.004, 0.005, 0.006$.

for the on-momentum particles, where the unnormalized emittances ϵ_x and ϵ_y are measured in πm. For the 4-cm bunch, the normalized rms emittance is $\epsilon_{\text{Nrms}} = 85 \times 10^{-6}$ πm. Since the muon energy is 50 GeV, the unnormalized rms emittance is $\epsilon_{\text{rms}} = 1.80 \times 10^{-7}$ πm, and becomes 1.62×10^{-6} πm when 3σ's are taken. Thus, the allowable tune spread for the on-momentum particles is $\Delta\nu_\beta = 4140\,\epsilon_y = 0.0067$. Tune spreads larger than this will lead to much larger tune spreads for the off-momentum particles, thus reducing the momentum aperture of the collider ring. For the 4-cm bunch, to damp beam breakup to about 1% when $Z_1^\perp = 0.1$ MΩ/m and $\langle \beta_y \rangle = 20$ m, one needs $\Delta\nu_\beta = 0.018$ as mentioned above. However, we do not know exactly what $\langle \beta_y \rangle$ and $Z_1^\perp$ are. Simulations show that if $\langle \beta_y \rangle Z_1^\perp$ becomes doubled, 2.5 times, 5 times, and 10 times, the tune spreads required jump to, respectively, $\sim$ 0.054, 0.073, 0.18, and 0.54. Thus, it appears that pure tune spread may be able to damp beam breakup for the 13-cm bunch but may not work for the 4-cm bunch. Although tune spreads due to chromaticity and beam-beam interaction can also damp beam breakup, it is unclear how much the momentum aperture will be reduced due to these tune spreads.

14.2.2 *Autophasing*

The transverse beam breakup can be cured by varying the betatron tune of the beam particles along the bunch, so that resonant growth can be avoided. In the

two-particle model, if we allow

$$\Delta k_\beta = -\frac{e^2 N_b W_1(\hat{z})}{2LE_0\bar{k}_\beta} \tag{14.17}$$

in Eq. (14.4), it appears that the linear increasing term will be eliminated and the motion of the tail particle

$$y_2(s) = y_{10}\cos\bar{k}_\beta s\cos\frac{\Delta k_\beta s}{2} \tag{14.18}$$

will be bounded. We can do better, however, by requiring

$$\Delta k_\beta = -\frac{e^2 N_b W_1(\hat{z})}{4LE_0\bar{k}_\beta} = \frac{\Upsilon_1}{L_0} \tag{14.19}$$

instead, where L_0 is the length of the accelerator structure. The motion of the tail particle now becomes

$$y_2(s) = y_{10}\left[\cos\bar{k}_\beta s\cos\frac{\Delta k_\beta s}{2} - \sin\bar{k}_\beta s\sin\frac{\Delta k_\beta s}{2}\right] = y_{10}\cos k_{\beta 1}s, \tag{14.20}$$

which is exactly the same as the head particle. Being in phase all the time, the tail cannot be driven by the head at all. This is another form of BNS damping known as *autophasing.* [5] Exactly the same result will evolve if we solve Eq. (14.2) directly by enforcing $y_2(s) = y_1(s) = y_{10}\cos k_{\beta 1}s$. Thus autophasing implies

$$\frac{\Delta k_\beta}{k_\beta} = \frac{\Upsilon_1}{\bar{k}_\beta L_0}. \tag{14.21}$$

The above autophasing consideration in the two-particle model can be extended easily to a bunch with a linear distribution $\lambda(z)$. In order that all particles will perform betatron oscillation with the same frequency and same phase after the consideration of the perturbation of the transverse wake, special focusing force is required to compensate for the variation of unperturbed betatron tune along the bunch. Now the equations of motion of Eq. (14.2) in the two-particle model are generalized to

$$\frac{d^2y(z,s)}{ds^2} + \left[k_\beta + \Delta k_\beta(z)\right]^2 y(z,s) = -\frac{e^2N_b}{LE_0}\int_{-\infty}^{z} dz'\lambda(z')W_1(z-z')y(z',s), \tag{14.22}$$

where $z > 0$ denotes the tail and $z < 0$ the head, or the bunch is traveling towards the left. We need to choose the compensation $\Delta k_\beta(z)$ along the bunch

in such a way that the betatron oscillation amplitude

$$y(z,s) \sim \sin\left(k_\beta s + \varphi_0\right) \tag{14.23}$$

is independent of z, the position along the bunch, with φ_0 being some phase, because only in this way any particle will not be driven by a resonant force from any particle in front. The solution is simply

$$2k_\beta \Delta k_\beta + \Delta k_\beta^2(z) = -\frac{e^2 N_b}{LE_0}\int_{-\infty}^{z} dz'\lambda(z')W_1(z-z'), \tag{14.24}$$

or, for small compensation $\Delta k_\beta(z)$,

$$\frac{\Delta k_\beta(z)}{k_\beta} = -\frac{e^2 N_b R}{2LE_0 k_\beta^2}\int_{-\infty}^{z} dz'\lambda(z')W_1(z-z'). \tag{14.25}$$

If the linear bunch distribution $\lambda(z)$ is a Gaussian interacting with a broad-band impedance, the integration can be performed exactly to give

$$\frac{\Delta k_\beta(z)}{k_\beta} = \frac{e^2 N_b}{2LE_0 k_\beta^2}\frac{\omega_r^2 Z_1^\perp}{2\bar{\omega}Q} e^{-z^2/(2\sigma_\ell^2)}\, \mathcal{I}m\, w\left[\frac{ve^{i\phi_0}}{\sqrt{2}} - \frac{iz}{\sqrt{2}\sigma_\ell}\right], \tag{14.26}$$

where

$$w(z) = e^{-z^2}\left[1 + \frac{2i}{\sqrt{\pi}}\int_0^z e^{t^2} dt\right]. \tag{14.27}$$

is the complex error function while $\sin\phi_0 = 1/(2Q)$ and $v = \omega_r\sigma_\ell/c$ as defined in Eqs. (14.9) and (14.10). For long bunches and high resonant frequency, or $v \gg Q$, the complex error function behaves as

$$w(z) = \frac{i}{\sqrt{\pi}z} + \mathcal{O}\left(\frac{1}{|z|^3}\right). \tag{14.28}$$

This is certainly satisfied by both the 4-cm and 13-cm muon bunches, where $v = 6.67$ and 21.7, respectively, but not by the short electron bunches. Let us first discuss the long muon bunches in a storage ring. For convenience, we convert the betatron number to betatron tune by $k_\beta = \nu_\beta/R$ and the length L to the ring circumference $C_0 = 2\pi R$. Thus Δk_β, the shift in betatron wave number in a cavity length L, becomes $\Delta\nu_\beta/R$, where $\Delta\nu_\beta$ is the betatron tune shift in a turn. Then, the relative tune-shift compensation in Eq. (14.26) can be simplified to

$$\frac{\Delta\nu_\beta(z)}{\nu_\beta} \approx \frac{e^2 N_b \omega_r Z_1^\perp R}{2(2\pi)^{3/2}\nu_\beta^2 QvE_0}\left[1 + \frac{z}{vQ\sigma_\ell}\right] e^{-z^2/(2\sigma_\ell^2)}. \tag{14.29}$$

This is the situation for the autophasing of the longer muon bunches, which is very different from the autophasing for the short electron bunches. The relative tune-shift compensations required for the two long bunches are shown in the top plot of Fig. 14.4. Note that in Eq. (14.29), vQ controls the asymmetry of the tune-shift compensation curve. When $vQ \to \infty$, there is no asymmetry and the compensation curve reduces to just a Gaussian, and, at the same time, $\Delta\nu_\beta/\nu_\beta$ decreases to zero. On the other hand, when $v \ll Q$ for short bunches or low broadband resonant frequency, the relative tune shift becomes rather linear as depicted by the 1.8 mm ($v = 0.3$) curve in the bottom plot of Fig. 14.4. The curves for the 5.0 mm, 1.0 cm, and 4 cm bunch ($v = 0.83$, 1.67, and 6.67) are

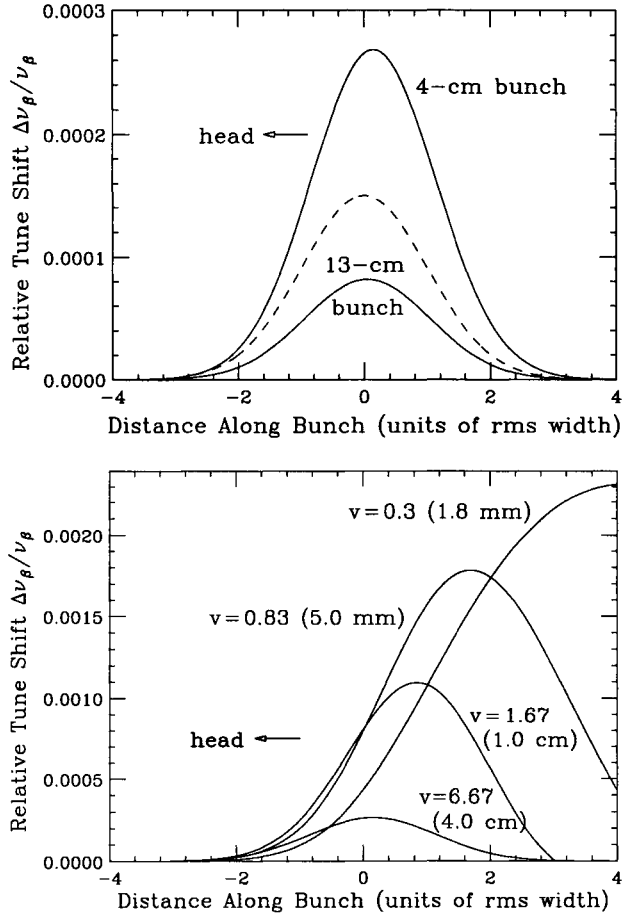


Fig. 14.4 Relative tune-shift autophasing compensation at distance z/σ_ℓ behind bunch center (bunch heading left) to cure beam breakup. Impedance is broadband resonating at $\omega_r = 50$ GHz. Top: for the rms 4-cm and 13-cm bunches, where $v = \omega_r\sigma_\ell/c = 6.67$ and 21.7 respectively, with bunch profile in dashes as a reference. Bottom: for short bunches, rms 1.8, 5.0, 10.0 mm, with $v = 0.3$, 0.83, 1.67, respectively. The curve for the 4-cm bunch is plotted as comparison. Note that when v is small, the compensation is of much lower frequencies.

also shown for comparison. Note that as the bunch length gets shorter, the the tune compensation contains components with much lower frequencies. For a very short bunch, the compensation becomes nearly linear in the region of the bunch.

To cure beam breakup with autophase damping in an electron linac, the electron bunch is usually placed off the rf wave crest so that the head and tail of the bunch will acquire slightly different energies, and therefore slightly different betatron tunes through chromaticity. For muon bunches in the collider ring, however, this method cannot be used. If one insists on having autophasing, an rf quadrupole must be installed and pulsed according to the compensation curve for each bunch as the bunch is passing through it. The variation of a quadrupole field at such high frequencies is not possible at all. Another method is to install cavities that have dipole oscillations at these frequencies, which is not simple either. For this reason, autophasing for long bunches is not practical at all.

14.3 Linac

14.3.1 *Adiabatic Damping*

Let us come back to the short electron bunches in a linac. An expression was given in Eq. (14.6) for the deflection of the tail particle in the two-particle model. In a linac, the bunches are accelerated and the energy change of the beam particles cannot be neglected. The equations of motion of the head and tail macro-particles in the two-particle model now become

$$\frac{1}{\gamma}\frac{d}{ds}\left(\gamma\frac{dy_1}{ds}\right) + k_\beta^2 y_1 = 0, \tag{14.30}$$

$$\frac{1}{\gamma}\frac{d}{ds}\left(\gamma\frac{dy_2}{ds}\right) + k_\beta^2 y_2 = -\frac{e^2 N_b W_1(\hat{z})}{2L\gamma E_{\text{rest}}}\, y_1, \tag{14.31}$$

where E_{rest} is the particle rest energy. The betatron wave number, which we have set to be the same for the two macro-particles, can have different dependency on energy. One way is to have k_β energy independent or the particle makes the same number of betatron oscillations per unit length along the linac. This is actually the operation of a synchrotron, where the quadrupole fields are ramped in the same way as the dipole field. If we further assume a constant acceleration

$$\gamma(s) = \gamma_i(1 + \alpha s), \tag{14.32}$$

where γ_i is the initial gamma and α is a constant, the equation of motion of the head becomes

$$\frac{d}{du}\left(u\frac{dy_1}{du}\right)+\frac{k_\beta^2}{\alpha^2}\,uy_1=0, \tag{14.33}$$

where $u=1+\alpha s$. Usually the acceleration gradient α is much slower than the betatron wave number k_β. For example, in the $L_0=3$ km SLAC linac where electrons are accelerated from $E_i=1$ GeV to $E_f=50$ GeV, $\alpha=0.0163\ \mathrm{m}^{-1}$, while the betatron wave number is $k_\beta=0.06\ \mathrm{m}^{-1}$. In that case, the solution is (Exercise 14.1)

$$y_1(s)=\frac{\hat{y}}{\sqrt{1+\alpha s}}\cos k_\beta s, \tag{14.34}$$

which is obtained by letting $y_1=A\cos k_\beta s$ with A a slowly varying function of u. In fact, Eq. (14.33) is the Bessel equation; Eq. (14.34) is just the asymptotic behavior of $y_1(s)=\hat{y}J_0[k_\beta(1+\alpha s)/\alpha]$.

The equation of motion of the tail becomes

$$\frac{d}{du}\left(u\frac{dy_2}{du}\right)+\frac{k_\beta^2}{\alpha^2}\,uy_2=-\frac{e^2N_bW_1(\hat{z})}{2LE_i\alpha^2}\,\frac{\hat{y}}{\sqrt{u}}\cos k_\beta s. \tag{14.35}$$

To obtain the particular solution, we try $y_2=D\sin k_\beta s/\sqrt{u}$ with D a slowly varying function of u.† The final solution is

$$y_2(s)=\frac{\hat{y}}{\sqrt{1+\alpha s}}\left[\cos k_\beta s-\frac{e^2N_bW_1(\hat{z})}{4LE_i\alpha k_\beta}\ln(1+\alpha s)\,\sin k_\beta s\right]. \tag{14.36}$$

Noticing that $E_i\alpha\approx E_f/L_0$, the growth for the whole length L_0 of the linac is

$$\Upsilon_1=-\frac{e^2N_bW_1(\hat{z})L_0}{4k_\beta E_fL}\ln\frac{E_f}{E_i}. \tag{14.37}$$

This is to be compared with Eq. (14.6), where we gain here a factor of

$$\mathcal{F}=\frac{E_i}{E_f}\ln\frac{E_f}{E_i}. \tag{14.38}$$

For the SLAC linac, this factor is $\mathcal{F}=1/12.8=0.0782$, meaning that the tail will be deflected by 12.8 less with the acceleration. This effect is called *adiabatic damping.*

†One can also try $y_2=D\sin k_\beta s$ with D a slowly varying function of u.

14.3.2 *Detuned Cavity Structure*

The dipole wake function of a cavity structure is given by

$$W_1(z) = -2\sum_n K_n \sin\frac{2\pi\nu_n z}{c}\, e^{-\pi\nu_v z/(cQ_n)} \qquad z > 0, \tag{14.39}$$

where K_n, ν_n, and Q_n are the kick factor, resonant frequency, and quality factor of the nth eigenmode in the structure, and the particle velocity has been set to c. The kick factor is defined as

$$K_n = \frac{R_n c}{Q_n}, \tag{14.40}$$

with R_n being the dipole shunt impedance of the nth mode. To reduce beam break up, it is important to reduce this dipole wake function.

One way to reduce the dipole wake is to manufacture the cavity structure with cell dimension varying gradually so that each cell has a slightly different resonant frequency. In this case, the effect of the wake due to sharp resonant peak of each individual cell will not add together and the wake of the whole structure will be reduced. Such a structure is called a *detuned cavity structure.* [6]

Let us first study the short-range part of the dipole wake. The assumption that all the cells do not couple can be made, and the wake function of Eq. (14.39) can be considered as the summation of the wake due to each individual cell. Thus, K_n, ν_n, and Q_n become the kick factor, resonant frequency, and quality factor of the nth cell. Since the variation from cell to cell is small, the summation can be replaced by an integral

$$W_1(z) \approx -2\int d\nu\, K\frac{dn}{d\nu}\sin\frac{2\pi\nu z}{c}. \tag{14.41}$$

Some comments are in order. First, the decays due to the quality factors have been neglected, because these are high-Q cavities and we are interested in the short-range wake only. Second, $K(dn/d\nu)$ is considered a function of ν and the normalization of $dn/d\nu$ is unity because $W_1(z)$ in Eq. (14.41) is referred to as the *dipole wake per cell.* Since $K(dn/d\nu)$ must be a narrow function centered about the average resonant frequency of the cells $\bar{\nu}$, the wake can be rewritten as

$$W_1(z) \approx -2\,\mathcal{I}m\left[e^{2i\pi\bar{\nu}z/c}\int dx\, K(\bar{\nu}+x)\frac{dn}{d\nu}(\bar{\nu}+x)e^{2\pi i x z/c}\right], \tag{14.42}$$

with $\nu = \bar{\nu} + x$. We see that the wake consists of a rapidly varying part, oscillating at frequency $\bar{\nu}$, and a slowly varying part, the envelope, that is given by the Fourier transform of the function $K(dn/d\nu)$ after it has been centered

about zero. For uniform frequency distribution with *full* frequency spread $\Delta\nu$, the wake is given by

$$W_1(z) \approx -2\bar{K} \sin\frac{2\pi\bar{\nu}z}{c} \frac{\sin(\pi\Delta\nu z/c)}{\pi\Delta\nu z/c}, \tag{14.43}$$

with $\bar{K}$ the average value of K. If the frequency distribution is Gaussian with rms width σ_ν, then

$$W_1(z) \approx -2\bar{K} \sin\frac{2\pi\bar{\nu}z}{c} e^{-2(\pi\sigma_\nu z/c)^2}. \tag{14.44}$$

In this case, the envelope also rolls off as a Gaussian. It seems reasonable to expect that the proper Gaussian frequency distribution is near ideal in the sense of giving a rapid drop in the wake function for a given total frequency spread, and this is the motivation for choosing the Gaussian detuning.

Take the example of the Next Linear Collider (NLC) designed in SLAC. Consider a detuned structure with $N = 206$ cells. The central frequency is $\bar{\nu} = 15.25$ GHz. The detuned frequency distribution is Gaussian with $\pm 2.5\sigma_\nu$, where the rms spread σ_ν is chosen as 2.5% of $\bar{\nu}$. It is found that the average kick factor is $\bar{K} = 40$ MV/nC/m^2. The envelope of such a wake is shown in Fig. 14.5. Notice that the wake function in fact does start from zero and has a first peak around 80 MV/nC/m^2 at $z \approx c/(4\bar{\nu}) = 4.91$ mm. It is important to point out that the dipole wake function defined in this figure differs from our usual definition; it is equal to our usual dipole wake function W_1 divided by the length of the cavity structure. The designed rms bunch length is $\sigma_\ell = 0.150$ mm which is much less than the first peak. Therefore, the detuned structure will

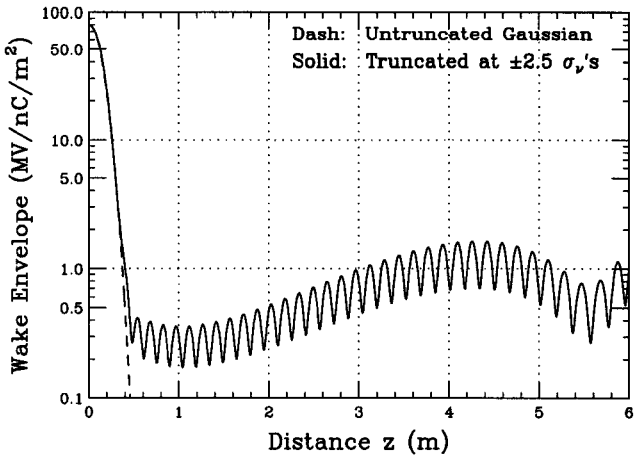


Fig. 14.5 Envelope of the dipole wake function of a Gaussian detuned structure. Coupling between cells has been ignored. The rapid Gaussian drop of the wake envelope is seen to level off after about half a meter due to the finite number of cells. (Courtesy Bane and Gluckstern [6])

not help the single-bunch breakup at all. The bunch spacing is 42 cm in one scenario and 82 cm in another. At the location of the second bunch, the wake has dropped by more than two orders of magnitude. Thus, this lowering of the wake will definitely help the multi-bunch train beam breakup.

There are some comments on the wake depicted in Fig. 14.5. First, the wake does not continue to drop as a Gaussian (the dashed curve) after about 0.4 m. Instead, it rises again having another peak around 4.2 m, although this peak is very much less than the first one. The main reason is due to the finite number of cells in the structure and the Gaussian distribution has been truncated at $\pm 2.5\sigma_\nu$. It is easy to understand the situation when we look at the uniform frequency distribution of Eq. (14.43). The envelope is dominated by the $\sin x/x$ term which gives a main peak at $x = 0$ and starts to oscillate after the first zero at $z = c/\Delta\nu$. Second, the coupling of the cells will nevertheless become important at some larger distance. Thus, the long-range part of the wake cannot be trusted at all. Bane and Gluckstern [6] devised a circuit model to represent the coupled resonators, thus giving a more realistic computation of the long-range wake. Later, Kroll, Jones, *et al.* [7] improved the model by introducing two circuits together with four damping manifolds with four holes in the cells to carry away the dipole wave generated by the beam. Their final wake is shown in Fig. 14.6.

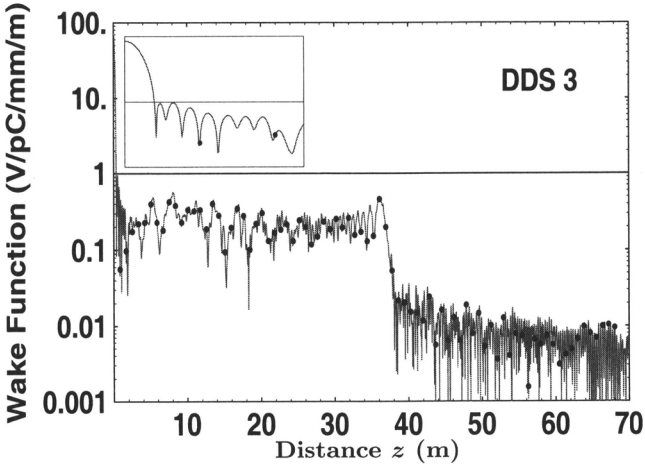


Fig. 14.6 Envelope of the dipole wake function of a detuned cavity structure consisting of 206 cells. Coupling between cells has been included using a model with two circuits coupled to four manifolds. The dots represent the 82 bunches with 84-cm bunch spacing in one scenario. (Courtesy Kroll, *et al.* [7])

We see that the short-range part of the wake is almost the same as is the computed result shown in Fig. 14.5. On the other hand, the long-range wake has been kept much below 1 MV/nC/m^2. This wake has been computed first in the frequency domain as a spectral function and is then converted to the time

or space domain via a Fourier transform. For this reason, we do not expect it to deliver the correct values at very short distances. The interested readers are referred to Refs. [6] and [7] for the detail. The dots on the plot represent the scenario of 82 bunches with 84-cm bunch spacing. The insert is a magnification of the beginning of wake covering the first two bunch spacings. A picture of the detuned structure consisting of 206 cavities coupled to four damped manifolds is shown in Fig. 14.7.

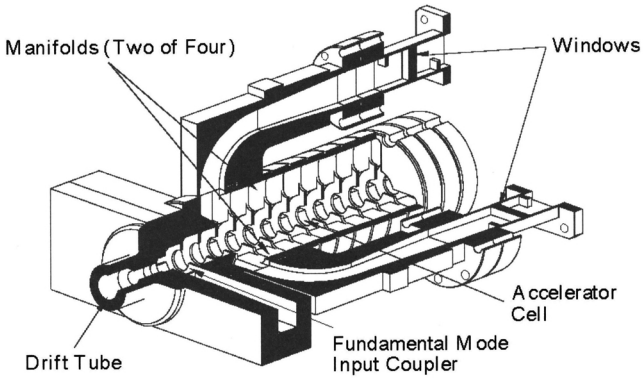


Fig. 14.7 A drawing of the detuned cavity structure consisting of 206 cavities coupled to 4 damped manifolds. (Courtesy Jones, *et al.*. [7])

For the SLAC NLC, assuming a uniform energy independent betatron focusing with 100 betatron oscillations in the linac of total length $L = 10$ km, the betatron wave number is $k_\beta = 0.06283\ \mathrm{m}^{-1}$. Initially at 10 GeV, the NLC bunch has a vertical rms beam size of $\sigma_{y0} = 4.8\ \mu$m, or the effective normalized rms vertical emittance $\epsilon_{yN} = 0.028\ \pi\mu$m. At the linac exit (500 GeV), the deflection of the tail particle in the two-particle model is multiplied only $\Upsilon_1 \sim 2.1$-fold per unit offset of the head particle (see Exercise 14.3). Assuming 1 μm initial offset of the head particle, and conservation of normalized emittance in the absence of beam breakup, the normalized rms vertical emittance becomes $\epsilon_{yN} = 0.30\ \pi\mu$m. If autophasing is to be used, assuming a *relative* chromaticity $\xi_N = -1$ defined by

$$\frac{\Delta k_\beta}{k_\beta} = \xi_N \delta, \tag{14.45}$$

an energy spread of 0.34% will be sufficient to damp the growth of the tail. These values are in close agreement of the simulations performed by Stupakov, [11] as illustrated in Fig. 14.8. The left plot shows an emittance increase up to $\sim 0.3\ \mu$m when the initial vertical offset is 1 μm. The right plot shows that the growth has been under control after the introduction of an energy spread of $\sim 0.8\%$.

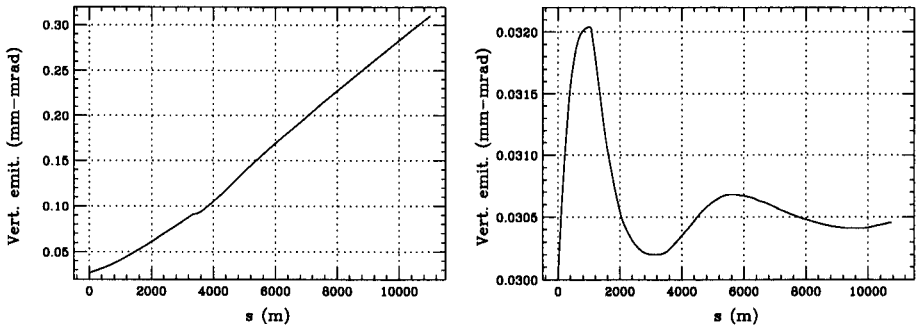


Fig. 14.8 The normalized vertical emittance of a NLC bunch from the beginning to the end of the main linac, assuming an initial vertical offset of 1 μm. Left: The emittance increases to $\sim$ 0.3 μm because of beam breakup. Right: An energy spread of $\sim$ 0.8% is added across the bunch by offsetting the rf phase. The emittance increase has been damped. (Courtesy Stupakov. [11])

14.3.3 *Multi-Bunch Breakup*

In one scenario, the NLC delivers a train of 95 bunches with bunch spacing 42 cm. Even if there is no beam breakup for a single bunch, the bunches in the train can also suffer beam breakup driven by the bunches preceding them. The first thing to do to ameliorate the instability is to design the linac cavities in such a way that the long-range dipole wake function will be as small as possible. The Gaussian detuned structure has been a way to lower the dipole wake by as much as two orders of magnitudes. According to the right plot of Fig. 14.5, at 42 cm, the dipole wake per unit length is only ~ 0.21 MV/nC/m^2.

The two-particle model can be extended to accommodate the study of multi-bunch beam breakup. Each bunch is visualized as a macro-particle containing N_b electrons. Then the equation governing the displacement of the first bunch is

$$\frac{d^2y_1}{ds^2} + k_\beta^2 y_1 = 0, \tag{14.46}$$

and that of the second bunch is

$$\frac{d^2y_2}{ds^2} + k_\beta^2 y_2 = -\frac{e^2 N_b W_1(\hat{z})}{LE}\, y_1, \tag{14.47}$$

where L is the cavity length and W_1 is the transverse wake per cavity. The first equation is the free betatron oscillation and is the same as Eq. (14.1). The second equation differs slightly from Eq. (14.2) in not having the factor 2 in the denominator. This is because, while each macro-particle contains $\frac{1}{2}N_b$ electrons

in the two-particle model of a bunch, here, in a bunch train, each macro-particle represents one bunch which is composed of N_b electrons. Also the dipole wake $W_1(\hat{z})$ in Eq. (14.47) is evaluated at the bunch spacing $\hat{z}$. Recall that the two-particle model will not work when the bunch length is too long and falls out of the linear region of the dipole wake, because some particles in between the head and the tail will suffer more beam-breakup deflections than the tail. However, this model still works for a long train of bunches, because unlike a long bunch, there are no particles between the point bunches.

Now the solution for the first bunch is

$$y_1(s) = \mathcal{R}e\, \hat{y} e^{ik_\beta s}. \tag{14.48}$$

The solution for the second bunch is

$$y_2(s) = \mathcal{R}e\, \hat{y}\, \Gamma s e^{ik_\beta s}, \tag{14.49}$$

where

$$\Gamma = \frac{ie^2 N_b W_1(\hat{z})}{2k_\beta L E_0}, \tag{14.50}$$

and we have neglected the general solution

$$y_2(s)|_{\text{general}} = \hat{y} e^{\pm ik_\beta s}, \tag{14.51}$$

which is much smaller than the particular solution in Eq. (14.49) that grows linearly as s. The equation for the deflection of the third bunch is

$$\frac{d^2 y_3}{ds^2} + k_\beta^2 y_3 = -\frac{e^2 N_b W_1(2\hat{z})}{LE_0} y_1 - \frac{e^2 N_b W_1(\hat{z})}{LE_0} y_2. \tag{14.52}$$

Here, we are going to retain only the largest driving force on the right side, meaning that the driving force from y_1 can be neglected and so is the force from the general solution of y_2. Substituting Eq. (14.49) in Eq. (14.52), we solve for the most divergent solution

$$y_3(s) = \mathcal{R}e\, \hat{y} \frac{1}{2} \Gamma^2 s^2 e^{ik_\beta s}. \tag{14.53}$$

Continuing this way, the deflection for the mth bunch will be (Exercise 14.4)

$$y_m(s) = \mathcal{R}e\, \hat{y} \frac{\Gamma^{m-1} s^{m-1}}{(m-1)!} e^{ik_\beta s}. \tag{14.54}$$

Stupakov [12] tried to estimate how much energy spread would be required to BNS damp the multi-bunch beam breakup. In order to damp the deflection

of the second bunch, the amount of tune spread required is

$$\frac{\Delta k_\beta}{k_\beta} = -\frac{e^2 N_b W_1(\hat{z})}{2k_\beta^2 E_f} \ln \frac{E_f}{E_i}, \tag{14.55}$$

taking the linac acceleration into account. It is reasonable to assume that n_b times the spread necessary for the second bunch will be required for n_b bunches. Next the natural *normalized* chromaticity for a FODO lattice of phase advance μ is

$$\xi_N = -\frac{2}{\pi} \tan \frac{\mu}{2}. \tag{14.56}$$

For 95 bunches, one gets the required energy spread of 2.7% (Exercise 14.5). The simulations by Stupakov are shown in Fig. 14.9. The initial bunch offset is 1 μm and it takes a rms energy spread of 0.8% among the bunches to damp the growth.

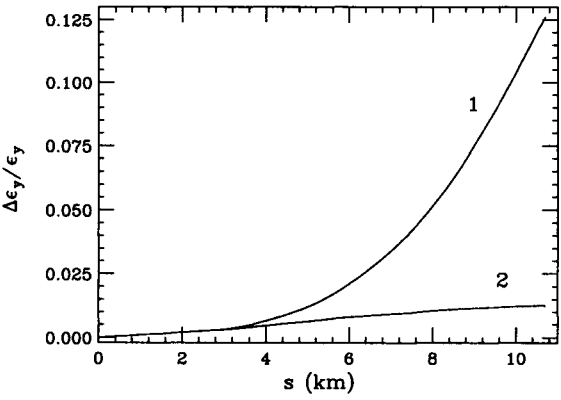


Fig. 14.9 The relative change in vertical emittance of the 95th bunch, taking the vertical size as the vertical offset of the bunch center added to the actual rms vertical size in quadrature. The initial vertical offset is 1 μm. Curve 1 shows the growth without any energy variation in the bunches. Curve 2 shows that the beam-breakup growth has been damped with a 0.8% rms energy spread varying linearly from the first to the 95th bunch. (Courtesy Stupakov. [12])

14.3.4 *Analytic Treatment*

Analytic computation of beam breakup for a bunch train has been attempted by many authors. [9, 8] In most of these papers, the dipole wake has been taken as a single dipole resonance and BNS damping has not been included. An improvement has been made by Bohn and Ng. [10] They have been able to include an energy chirp and derive analytic expressions for the BNS damping of a train of point bunches. Essentially, the energy chirp gives rise to a spread in betatron wave number among the bunches. An outline of the analytic derivation is given below.

Introduce the dimensionless *spatial* parameter $\sigma = s/L_0$ normalized to the total linac length L_0. The real time t is reduced to the dimensionless *time* parameter $\zeta = \omega_r(t - s/c)$, with ω_r being the dipole resonant angular frequency, to describe the arrival of a beam particle at position s along the linac, with $\zeta = 0$ as the arrival time of the first particle. Thus, ζ measures the longitudinal position of the particle while σ measures the position along the linac. inside the beam. The transverse displacement of a particle in the beam, represented by $y(\sigma, \zeta)$, depends on both σ and ζ and its motion is governed by[†]

$$\left[\frac{1}{\gamma}\frac{\partial}{\partial\sigma}\left(\gamma\frac{\partial}{\partial\sigma}\right) + \kappa^2(\sigma,\zeta)\right] y(\sigma,\zeta) = -\epsilon(\sigma)\int_0^\zeta d\zeta' w(\zeta-\zeta')F(\zeta')y(\sigma,\zeta'), \quad (14.57)$$

which is just another way of writing Eq. (14.15) with beam particle acceleration included as in Eq. (14.31). This equation is usually referred to as the multi-bunch cumulative beam breakup equation. Here, the normalized betatron wave number is $\kappa = k_\beta L_0$. The beam profile $F(\zeta)$ will be defined in Eq. (14.60) below. The normalized dipole wake is[‡]

$$w(\zeta) = -H(\zeta)\, e^{-\zeta/(2Q)} \sin\zeta, \quad (14.58)$$

where Q is its quality factor and $H(\zeta)$ is the Heaviside step function. All the rest is lumped into the dimensionless beam-breakup coupling strength

$$\epsilon(\sigma) = \frac{e^2 N_b w_0 L_0^2}{\gamma E_{\text{rest}} \omega_r \tau}, \quad (14.59)$$

where w_0 is the sum-wake amplitude per unit length or twice the kick factor of the dipole resonance measured in V/C/m^2 and $N_b/(\omega_r\tau)$ is the number of electrons per *longitudinal time* ζ. For a train of bunches with temporal spacing τ, N_b becomes the number per bunch. When these bunches are further considered as points, the beam profile in above is represented by

$$F(\zeta) = \sum_{n=-\infty}^{\infty} \delta\left(\frac{\zeta}{\omega_r\tau} - n\right). \quad (14.60)$$

All bunches with arrival time $\zeta < 0$ will be excluded by the causal property of the wake.

A betatron linear chirp is now introduced,

$$\kappa(\sigma,\zeta) = \kappa_0(\sigma) + \kappa_1(\sigma,0)\zeta, \quad (14.61)$$

[†]The arrival time is $\zeta = 0$ for the first particle and $\zeta > 0$ for later particles, or $\zeta > 0$ represents the arrival time *behind* the first particle.

[‡]This is also called the *sum wake* because it represents the sum of the wake fields left by all preceding particles.

where $\kappa_0(\sigma)$ is the normalized betatron wave number without the chirp and $\kappa_1(\sigma,0)$ represents the strength of a linear chirp across the bunches. With the assumption that the acceleration gradient is much less than the betatron wave number, we can introduce a new transverse offset variable

$$\xi(\sigma,\zeta) = \sqrt{\gamma(\sigma)}\, y(\sigma,\zeta)\, e^{-i\zeta\Delta(\sigma)}, \tag{14.62}$$

where

$$\Delta(\sigma) = \int_0^\sigma d\sigma' \kappa_1(\sigma',0).$$

Now Eq. (14.57) can be rewritten as[§]

$$\left[\frac{\partial^2}{\partial\sigma^2} + \kappa_0^2(\sigma)\right] \xi(\sigma,\zeta) \simeq -\epsilon(\sigma) \int_0^\zeta d\zeta' w_\Delta(\sigma,\zeta-\zeta') F(\zeta') \xi(\sigma,\zeta'), \tag{14.63}$$

where the assumption of strong focusing, $\partial\xi(\sigma,\zeta)/\partial\sigma \simeq i\kappa_0\xi(\sigma,\zeta)$, has been used. Strong focusing actually implies that the quadrupole focusing is the most important force, while the wake, the acceleration gradient, and the variation of focusing due to chirping are small. The chirped-modified wake in Eq. (14.63) is defined as

$$w_\Delta(\sigma,\zeta) = w(\zeta) e^{-i\zeta\Delta(\sigma)}, \tag{14.64}$$

where obviously the exponential comes from the definition of $\xi(\sigma,\zeta)$. This exponential, when combined with the exponential of the original wake of Eq. (14.58), gives an *effective quality factor* Q_{eff}, where

$$\frac{1}{2Q_{\text{eff}}} = \frac{1}{2Q} + i\Delta. \tag{14.65}$$

Immediately, a result can be drawn that the chirp will be important if the quality factor Q of the transverse wake is high, but will be masked if Q is sufficiently low.

The transformation into Eq. (14.63) is important, because the operator on the left side no longer depends on ζ, and the chirp has been incorporated into the dipole wake. To proceed, we Fourier transform the whole equation with respect to the variable $\zeta = n\omega_r\tau$ to obtain

$$\left[\frac{\partial^2}{\partial\sigma^2} + \kappa_0^2(\sigma)\right] \tilde{\xi}(\sigma,\theta) \simeq -\epsilon(\sigma)\omega_r\tau\tilde{w}_\Delta(\sigma,\theta)\tilde{\xi}(\sigma,\theta), \tag{14.66}$$

[§] $(\gamma')^2$ and γ'' will be neglected, where the prime implies derivative with respect to σ, but $\gamma'\xi'$ will be retained.

where

$$\tilde{\xi}(\sigma,\theta)=\sum_{m=0}^{\infty}e^{-im\theta}\xi(\sigma,m\omega_r\tau),$$

$$\tilde{w}_\Delta(\sigma,\theta)=\sum_{m=0}^{\infty}e^{-im[\theta+\omega_r\tau\Delta(\sigma)]}w(m\omega_r\tau)=\sum_{m=0}^{\infty}e^{-im\theta}w_\Delta(\sigma,m\omega_r\tau). \quad (14.67)$$

In this form, the WKB method [15] can be employed to give two independent cosine-like and sine-like functionals

$$\begin{Bmatrix}\mathcal{C}(\sigma,\theta;m)\\ \mathcal{S}(\sigma,\theta;m)\end{Bmatrix}=\sqrt{\frac{E_i\Lambda(0,\theta)}{E_\sigma\Lambda(\sigma,\theta)}}\begin{Bmatrix}\mathcal{R}e\\ \mathcal{I}m\end{Bmatrix}\exp\left[im\omega_r\tau\Delta(\sigma)+i\int_0^\sigma d\sigma'\Lambda(\sigma',\theta)\right], \quad (14.68)$$

where

$$\Lambda^2(\sigma,\theta)=\kappa_0^2(\sigma)+\epsilon(\sigma)\omega_r\tau\tilde{w}_\Delta(\sigma,\theta), \quad (14.69)$$

and we have written, for convenience, the energy of the beam particle at location σ as $E_\sigma=\gamma(\sigma)E_{\rm rest}$ and the initial energy as $E_i=\gamma(0)E_{\rm rest}$. Later we will also write the energy at linac exit as $E_f=\gamma(1)E_{\rm rest}$. Here $\Lambda(\sigma,\theta)$ is an auxiliary function reflecting the coupling between the bunch spacing and the deflecting-mode frequency, and is slowly varying with σ. When $\tilde{w}_\Delta(\sigma,\theta)$ is substituted, it takes the form

$$\Lambda(\sigma,\theta)\approx\kappa_0(\sigma)\left[1-\frac{\epsilon(\sigma)}{4\kappa_0^2(\sigma)}\,\frac{\omega_r\tau\sin\omega_r\tau}{\cos[\theta+\omega_r\tau\Delta(\sigma)-i\omega_r\tau/(2Q)]-\cos\omega_r\tau}\right]. \quad (14.70)$$

Now the solution of Eq. (14.66) can be written as

$$\tilde{\xi}(\sigma,\theta)\sqrt{\frac{E_i}{E_\sigma}}e^{im\omega_r\tau\Delta(\sigma)}=\tilde{\xi}(0,\theta)\mathcal{C}(\sigma,\theta;m)+\tilde{\xi}'(0,\theta)\frac{\mathcal{S}(\sigma,\theta;m)}{\Lambda(0,\theta)}, \quad (14.71)$$

where the prime represents derivative with respect to σ, and the assumption of strong focusing has been made. Taking the inverse Fourier transform and using Eq. (14.62), we arrive at a formal solution for the transverse offset of the $(m+1)$th bunch [9, 13]

$$y_m(\sigma)=\sum_{n=0}^{m}e^{-n\omega_r\tau/(2Q)}\int_{-\pi}^{\pi}\frac{d\theta}{2\pi}\,e^{-in\theta}\left\{y_{m-n}(0)\mathcal{C}(\sigma,\theta;m)+y'_{m-n}(0)\frac{\mathcal{S}(\sigma,\theta;m)}{\Lambda(0,\theta)}\right\}. \quad (14.72)$$

In above, the summation over n comes about when $\tilde{\xi}(0,\theta)$ and $\tilde{\xi}'(0,\theta)$ are reverted to the initial displacement $y_{m-n}(0)$ and gradient $y'_{m-n}(0)$ via inverse

Fourier transform. Physically, it tells us that the displacement of a bunch depends on all the bunches in front of it.

It is evident from Eq. (14.72) that upon taking $\theta \rightarrow -\theta$ and remembering that y_m is real, the algebraic sign of $\Delta(\sigma)$ affects only the phase of $y_m(\sigma)$ but not the envelope. This demonstrates that, as expected intuitively, the effect of a linear increase in focusing from head to tail is the same as a linear decrease.

In order for the derivation to go through analytically further, it is necessary to make the assumption that the betatron wave number decreases as $\gamma^{-1/2}$. This focusing arrangement implies that all the quadrupoles are identical and they can be on one common bus, because the focusing field gradient will be exactly the same along the linac. In other words, the focusing becomes weaker as the energy increases. In fact, the NLC quadrupoles are deployed roughly in this way, although the quadrupoles there are all on separate buses for the ease of beam alignment. With this assumption, $\epsilon(\sigma)/[4\kappa_0^2(\sigma)]$ in the defining equation of $\Lambda(\sigma, \theta)$ above will no longer be dependent on σ. This simplifies the integration to be performed later.

The linear betatron chirp required for BNS damping is best introduced via an energy spread from the first bunch to the last bunch. Let us assume that gradient of the chirp $\kappa_1(\sigma, 0)$ has exactly the same $\gamma^{-1/2}$ dependency as the normalized betatron wave number $\kappa_0(\sigma)$, or

$$\frac{\kappa_0(\sigma)}{\kappa_0(0)} = \frac{\kappa_1(\sigma, 0)}{\kappa_1(0, 0)} = \sqrt{\frac{E_i}{E_\sigma}}. \tag{14.73}$$

Thus the fractional spread in betatron focusing along the train of $M+1$ bunches

$$f_\kappa = \frac{\kappa_1(\sigma, 0)}{\kappa_0(\sigma)} M\omega_r\tau \tag{14.74}$$

becomes time-independent and is equal to one-half the fractional spread in energy f_γ.

For further discussion, let us set the initial conditions $y_m(0) = y_0$ and $y'_m(0) = 0$ for every bunch. Then the summation over n in Eq. (14.72) can be performed analytically. The summation can be decomposed into two parts: $\sum_0^m = \sum_0^\infty - \sum_m^\infty$. The first part pertains to the *steady-state* displacement y_{ss} that would arise were the deflecting wake first seeded with an infinitely long bunch train immediately preceding the actual bunch train. Given strong focusing, the steady-state displacement is

$$y_{ss}(\sigma, m\omega_r\tau) \simeq y_0 \left[\frac{E_i}{E_\sigma}\right]^{1/4} \cos\left[m\omega_r\tau\Delta(\sigma) + \int_0^\sigma d\sigma' \kappa_0(\sigma')\right], \tag{14.75}$$

which is sinusoidal along the bunches and is independent of the dipole wake, when an effective quality factor of $Q = \infty$ is assumed. A more realistic finite effective quality factor will have it damped. For this reason, the steady-state displacement should be subtracted from the transverse displacement for a practical evaluation of the transverse growth.

The second part pertains to the *transient* displacement $\delta y_m = y_m - y_{ss}$. Saddle-point integration gives a closed-form solution for δy_m, whose bounding envelope takes the form:

$$\frac{|\delta y_m|}{y_0} \simeq \left[\frac{E_i}{E_\sigma}\right]^{\frac{1}{4}} \frac{\sqrt{\mathcal{E}}\,\exp\left[q(\eta)\mathcal{E} - m\omega_r\tau/(2Q)\right]}{4m\sqrt{2\pi}\,|\sin(\omega_r\tau/2)|} \begin{cases} |1-\eta^2|^{-\frac{1}{4}} & \eta \nsim 1, \\ \left(\frac{4}{3}\right)^{\frac{1}{6}} \mathcal{E}^{\frac{1}{6}} \frac{\Gamma\left(\frac{1}{3}\right)}{\sqrt{2\pi}} & \eta = 1. \end{cases} \tag{14.76}$$

The auxiliary relations comprising Eq. (14.76) are:

$$\begin{aligned} \mathcal{E}(\sigma, m) &= \left[\frac{4mw_0e^2NL_0^2}{\bar{\kappa}_0 E_i}\right]^{1/2} \frac{\left[\left(\sqrt{E_f/E_i}-1\right)\left(\sqrt{E_\sigma/E_i}-1\right)\right]^{1/2}}{E_f/E_i - 1}, \\ \eta(\sigma, m) &= \frac{\bar{\kappa}_0|f_\gamma|}{2\mathcal{E}} \frac{m}{M} \frac{\sqrt{E_\sigma/E_i}-1}{\sqrt{E_f/E_i}-1}, \\ q(\eta) &= \begin{cases} \frac{\sqrt{1-\eta^2}}{2} + \frac{1}{4\eta}\tan^{-1}\left(\frac{2\eta\sqrt{1-\eta^2}}{1-2\eta^2}\right) & \eta < 1, \\ \frac{\pi}{4\eta} & \eta \geq 1, \end{cases} \end{aligned} \tag{14.77}$$

in which M is the total number of bunches in the train, $\bar{\kappa}_0$ is the focusing strength averaged over the linac and is related to the focusing strength at entrance $\kappa_0(0)$ by

$$\bar{\kappa}_0 = \frac{2\kappa_0(0)}{\sqrt{E_f/E_i}+1}. \tag{14.78}$$

It can also be written as $\bar{\kappa}_0 = 2\pi\nu_\beta$, where ν_β is the number of betatron oscillations a particle makes while traversing the whole length of the linac, from entry to exit.

The expression for $|\delta y_m|$ in Eq. (14.76) reflects a number of physical processes. The coefficient involving beam energy manifests adiabatic damping. The factor $|\sin(\omega_r\tau/2)|$ is a relic of a resonance function deriving from the coupling between the bunch spacing and the deflecting-mode frequency. Resonances lie near even-order wake zero-crossings; [9] they are nevertheless removed because the solution

is valid only away from zero-crossing. The focusing variation represented by $|f_\gamma|$ regulates exponential growth, and finite Q yields exponential damping. Yet "$\eta = 1$" does have special physical significance; it demarcates the onset of saturation of exponential growth and, with infinite Q, algebraic decay of the envelope. For $\eta \geq 1$ the "growth factor" $q(\eta)\mathcal{E}$ is independent of bunch number m and of linac coordinate σ; temporal "damping" then ensues through a negative power of m, and spatial "damping" ensues adiabatically as already mentioned. Therefore $\eta = 1$ corresponds to a global maximum in the envelope $|\delta y_m|$. The effect of the focusing variation is the saturation of the exponential growth, not damping; its action distinctly differs from that of a real effective Q.

We now apply the solution to designs of the SLAC NLC and DESY TESLA. Some parameters are listed in Table 14.1.

Table 14.1 Some parameters of the SLAC NLC and DESY TESLA.

	NLC†	TESLA
Linac length ℓ (km)	10.0	14.4
Number of betatron wavelengths ν_β	100	60
Entry/exit energy (GeV)	10/1000	5/250
No of bunches per train M	90	2820
Bunch charge q (nC)	−1.0	−1.6
Bunch spacing τ (ns)	2.8	377
Transverse wake:		
amplitude w_0 (V/pC/m/mm)	1	0.015
frequency $\omega_r/(2\pi)$ (GHz)	14.95	1.70
effective quality factor Q	∞	$\sim$ 125000

†The above belong to an older model of the SLAC NLC, and are chosen to illustrate multi-bunch beam breakup. The parameters w_0 and Q represent a worst-case wake.

14.3.4.1 *Amount of Energy Chirp*

The transient displacements of the 90 bunches of the NLC at the linac exit were simulated and shown in Fig. 14.10 for energy spreads $f_\gamma = 1.5$ and 3.0%. The plots are made with the scenario that the linac is $L_0 = 10$ km long, accelerating 90 bunches with bunch spacing $\tau = 2.8$ ns from 10 GeV to 1 TeV. Each bunch contains 1 nC of charges or $N_b = 6.24 \times 10^9$ electrons, making 100 betatron oscillations along the linac. The dipole wake of the SLAC NLC cavities is of resonant frequency $\omega_r/(2\pi) = 14.95$ GHz. Its long-range transverse behavior is shown in Fig. 14.5, which is computed using a circuit model. We see that the envelope of the wake is almost constant for the first 30 m or the first 36 bunch spacings. This allows us to assign an effective quality factor of $Q = \infty$ and sum-

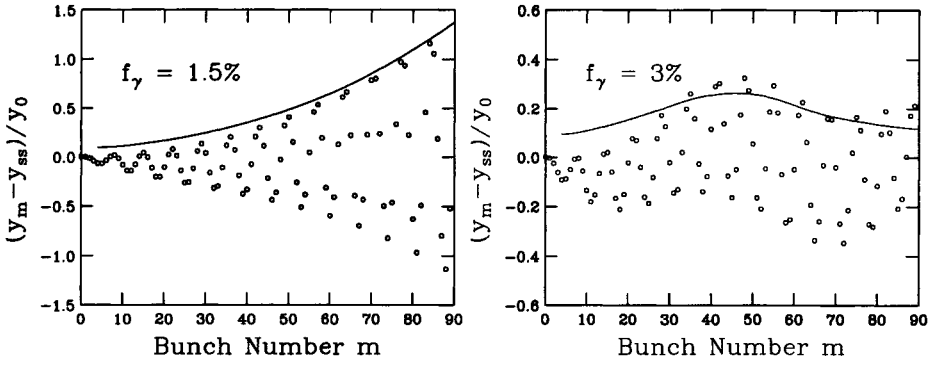


Fig. 14.10 Analytic envelope at the linac exit (solid curve) plotted against the transverse displacement of bunches calculated numerically (circles), with total energy spreads of 1.5% (left) and 3% (right).

wake amplitude[¶] $w_0 \sim 1$ MV/nC/m^2. It is clear that BNS damping is helping to control the emittance growth. The relative displacement of the 90th bunch would have been as large as 2.1 when $f_\gamma = 0$ (not shown), but was damped to ~ 1.4 with $f_\gamma = 1.5\%$ energy spread along the bunch train (left plot). We also see that when the energy spread is increased to $f_\gamma = 3.0\%$, the envelope reaches a maximum at the 48th bunch and decays algebraically afterward approaching steady state slowly (right plot).

An effective BNS damping requires an energy spread sufficient to have the maximum to reach some bunches before they leave the linac. The special significance of $\eta = 1$ translates into a criterion for the focusing variation to be effective. Specifically, one should choose a value of f_γ that ensures $\eta(1, M) > 1$, *i.e.*, that $\eta = 1$ is reached somewhere along the bunch train before it leaves the linac. According to the auxiliary relations to Eq. (14.76), the criterion for this to happen is

$$|f_\gamma| > \frac{2\mathcal{E}(1, M-1)}{\bar{\kappa}_0} = \frac{\mathcal{E}(1, M-1)}{\pi\nu_\beta}, \tag{14.79}$$

which is plotted in Fig. 14.11 versus the wake amplitude for various strengths of betatron focusing. For example, for the parameters in Table 14.1, an energy chirp of $|f_\gamma| \gtrsim 2.18\%$ in the NLC will be required. However, as will be seen in the next subsection, this amount of energy chirp can be reduced, because this is not the only criterion to control emittance growth.

[¶]The plot in Fig. 14.5 shows $w_0 \sim 0.3$ MV/nC/m^2. Here, we use $w_0 \sim 1$ MV/nC/m^2 as a reference model.

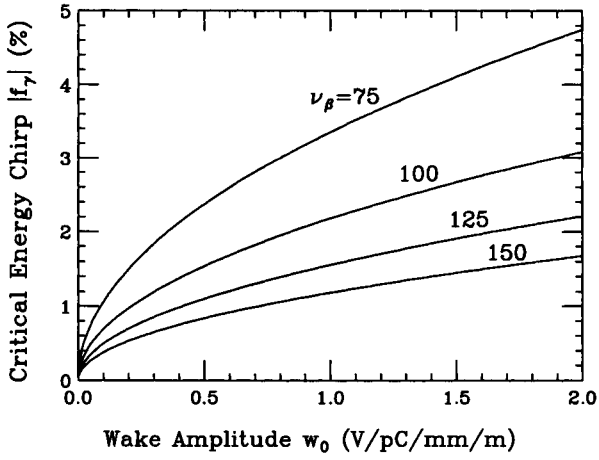


Fig. 14.11 Critical energy chirp required for BNS damping in the SLAC NLC versus deflecting wake amplitude, with number of betatron wavelengths $\nu_\beta = 75$, 100, 125, and 150.

14.3.4.2 *Emittance Growth*

The steady-state and transient displacements, being uncorrelated, comprise a measure of the total projected normalized emittance as

$$\varepsilon \equiv \left(|y_{ss}|^2 + |\delta y_m|^2_{\max}\right) \frac{\gamma\kappa_0}{L_0}, \tag{14.80}$$

wherein $|y_{ss}| = y_0[E_i/E_\sigma]^{1/4}$ per Eq. (14.75), and $|\delta y_m|_{\max}$ is the maximum value of the transient envelope reached along the bunch train. If $\eta < 1$ is always maintained, then the maximum is reached at the last bunch $m = M$. Otherwise, the maximum corresponds to the value of $|\delta y_m|$ at which $\eta = 1$. Imposing a focusing variation will reduce the transient envelope, but it will also establish a harmonic variation of y_{ss} with m and thereby introduce a nonzero steady-state emittance ε_{ss}. For this reason, the quantity of interest is the ratio

$$\frac{\varepsilon - \varepsilon_{ss}}{\varepsilon_{ss}} = \left(\frac{|\delta y_m|_{\max}}{|y_{ss}|}\right)^2, \tag{14.81}$$

from which one sees the benefit of keeping the ratio of envelopes small. This quantity, calculated from the analytic expressions given in Eqs. (14.75) and (14.76), is plotted against $|f_\gamma|$ in Fig. 14.12 for various values of the sum-wake amplitude w_0. Figure 14.12 points to the region of parameter space that, respecting multi-bunch beam breakup, admits viable linear-collider designs. In particular it shows that to achieve low multi-bunch emittance without aid from a focusing variation requires small sum-wake amplitudes, $w_0 \lesssim 0.5$ V/pC/mm/m. Otherwise, as depicted, a few-percent energy spread is necessary to relieve the

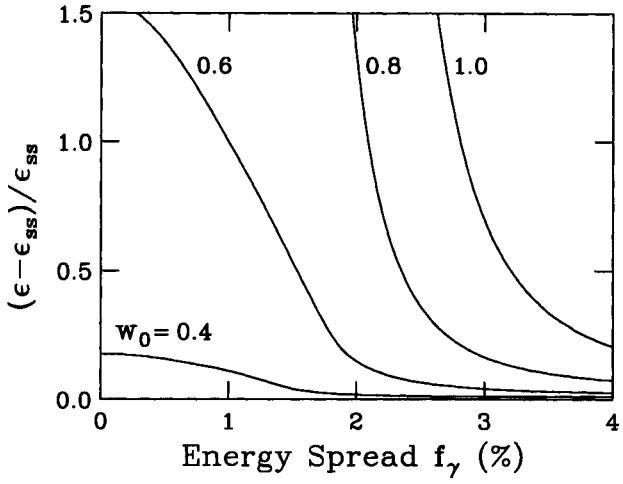


Fig. 14.12 Total normalized transverse multi-bunch emittance at the linac exit, referenced to its steady-state value, versus total energy spread across the bunch train, plotted for various sum-wake amplitudes w_0.

constraint on sum-wake amplitude. There are, of course, practical limitations on the energy spread, to include longitudinal beam requirements at the interaction point, lattice chromaticity, degradation in acceleration, etc. Nonetheless, introducing a modest energy spread constitutes a backup in case sufficiently low wake amplitudes prove generally infeasible.

It is worth mentioning that the plots in Figs. 14.10 and 14.12 have been performed with the data of the upgraded NLC. If we use the lower-energy design of accelerating the bunches up to only 500 GeV and 1.1×10^{10} particles per bunch, the reduction in adiabatic damping will increase the growths of the bunch deflections at the linac exit tremendously. To BNS damp such growths driven by the same sum-wake per length of 1 MV/nC/m^2, an energy chirp of 10 to 15% will be necessary. Certainly this is not workable because of the large momentum spread of the bunches which later translates into unacceptable transverse bunch sizes at the interaction point. The acceleration gradient will also be largely reduced. Needless to say, the linac itself will hardly have such large energy aperture for the bunches to pass through. What we actually want to point out is that BNS damping is only feasible when the actual beam breakup is not too large, because only a small amount of energy chirp is acceptable in reality.

14.3.4.3 *The Quality Factor*

Now let us apply the computed displacement envelope to the DESY TESLA design of the linear collider. If the quality factor of the deflecting wake were infinite, Eq. (14.79) would require an energy chirp of $|f_\gamma| = 9.27\%$. This chirp is

rather large because of the long bunch train of 2820 bunches. Even with such a large chirp, Eq. (14.76) predicts a normalized transient displacement envelope of $|\Delta y_m/y_0| = 296$ for the last bunch at the linac exit, and such emittance growth is totally unacceptable. Fortunately, the transverse long-range wake of the TESLA linac in Fig. 14.13 shows considerable amount of damping. [16] However, the wake does not correspond to a damped resonance of a single frequency. Assuming a resonant frequency of 1.7 GHz, one obtains a quality factor of $Q = 22400$ by comparing the wake envelope at the first and 10th bunch spacings, $Q = 69000$ by comparing the wake envelope at the first and 100th bunch spacings, and $Q = 124000$ by comparing the wake envelope at the first and 265th bunch spacings (which is the end of the wake displayed in Fig. 14.13). In the discussion below, the quality factor of $Q = 125000$ is assumed. Numerically, we find that $|\Delta y_m/y_0|$ never exceeds 0.012 and damps to less than 0.010 within the first 150 bunches, where no energy chirp has been applied. It is important to mention that the theoretical prediction of Eq. (14.76) may not apply to the TESLA linac, where multi-bunch beam breakup is not severe because of the rather small effect from the transverse wake. Instead of the method of steepest descent, the multi-bunch beam breakup equation should be solved by iteration with the coupling coefficient ϵ considered as a small quantity.

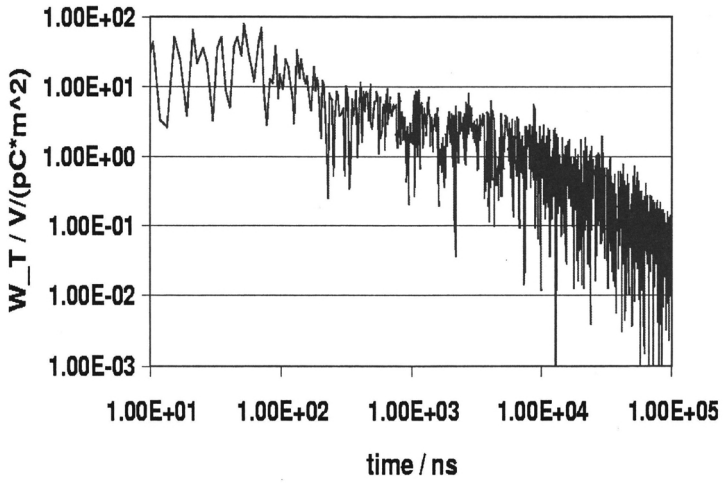


Fig. 14.13 Plot of transverse long-range dipole wake of the TESLA linac up to the 265th bunch. (Courtesy TESLA TDR. [16])

We can also visualize a finite quality factor Q of the deflecting wake as acting like an energy chirp. From the growth exponent of Eq. (14.76), it is evident that a finite quality factor will offset a certain amount of growth. [14] Setting $\eta = 1$ in the exponent, we obtain for the last bunch at the linac exit

$$|f_\gamma| = \frac{2M\omega_r\tau}{\pi^2 Q\nu_\beta}, \tag{14.82}$$

which is the equivalent amount of energy-chirp-like damping provided by the quality factor. In Fig. 14.14, we plot the normalized envelope displacement of the last bunch at the exit of the SLAC NLC linac as a function of the energy chirp $|f_\gamma|$ for various values of the quality factor. The large dots are the equivalent energy-chirp-like damping provided by the quality factor. The dashed curve joining all the large dots depicts Eq. (14.82). Notice that the displacement is approximately independent of the energy chirp until the stated threshold is exceeded, after which the displacement drops off relatively fast with increasing $|f_\gamma|$. As an illustration, recall that for a wake with an infinite quality factor, $|f_\gamma| = 2.18\%$ is required for BNS damping. However, when the quality factor is lowered to $Q = 5000$, Fig. 14.14 indicates an equivalent energy chirp of 0.96%. Thus, only $|f_\gamma| = 2.18 - 0.96 = 1.22\%$ will now be required. This is demonstrated in Fig. 14.15, where we can see the maxima of the displacement envelopes reside at the last bunch at the linac exit in both situations. A smaller quality factor not only reduces the amount of energy chirp required for BNS damping; it also helps to reduce the transient transverse displacement along the bunch train from $|\Delta y_m/y_0| = 0.76$ to a very much smaller value of 0.15. Thus, for the sake of controlling emittance growth and damping multi-bunch beam breakup, it is beneficial to have lower quality factors for the deflecting modes. Returning to the TESLA linac, Eq. (14.82) gives an "effective" energy chirp of $|f_\gamma| = 4600\%$ for the last bunch of the bunch train and 1.6% for the second bunch ($M = 1$). This explains why the transient displacement envelope was so heavily damped.

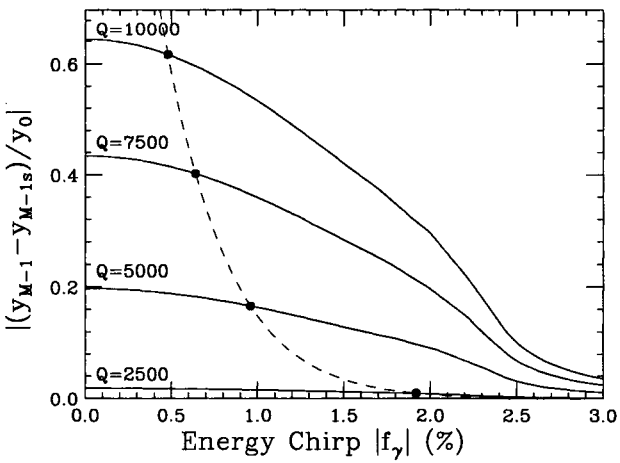


Fig. 14.14 Plot of normalized transient displacement envelope of the last bunch at the linac exit of the SLAC NLC versus energy chirp $|f_\gamma|$ for various quality factors Q of the deflecting wake. The amount of equivalent energy-chirp-like damping provided by the finite quality factor is also shown as dashes.

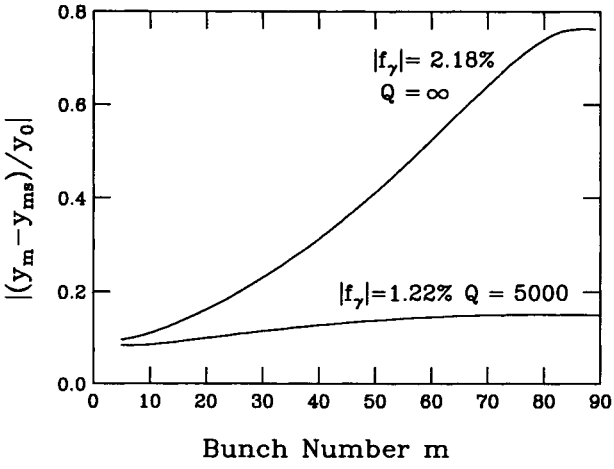


Fig. 14.15 Plot of normalized transient displacement envelope at the linac exit of the SLAC NLC when envelope maximum occurs at the last bunch. Notice that the energy chirp $|f_\gamma|$ is reduced from 2.18% to 1.22% when the quality factor is reduced from $Q = \infty$ to 5000.

14.3.5 *Misaligned Linac*

So far we have been considering linacs with perfect alignment, which is impossible in reality. The externally focusing quadruples have misalignment errors and the accelerating cavities can also be misaligned. Although most systematic misalignment errors will be corrected, some unintensional errors will remain. We would like to study how these errors will affect beam breakup and the the emittance growth of the beam.

Suppose that the quadrupole at location σ has misalignment $y_Q(\sigma)$ and the cavities have misalignment $y_C(\sigma)$ at location σ. The equation of motion governing the transverse motion of the beam will be modified from Eq. (14.57) to [17]

$$\left[\frac{1}{\gamma}\frac{\partial}{\partial\sigma}\left(\gamma\frac{\partial}{\partial\sigma}\right)+\kappa^2(\sigma,\zeta)\right][y(\sigma,\zeta)-y_Q(\sigma)]$$
$$=-\epsilon(\sigma)\int_0^\zeta d\zeta' w(\zeta-\zeta')F(\zeta')\,[y(\sigma,\zeta')-y_C(\sigma)]\,. \qquad (14.83)$$

To arrive at an analytic solution, some assumptions are necessary. Consider the linac to be comprised of girders. On each girder is an accelerating length equipped with some number of rf structures and an optical element. Assume that the structures and quadrupoles are sufficiently well-aligned on the girders, leaving the girder misalignments as the dominating offset errors. If there are a large number of girders in each betatron wavelength λ_β, the beam will experience the same large number of kicks due to the girder misalignments. Since these kicks act independently, they can be considered as *white noise* on the beam, or, for

the girders at locations σ_i and σ_j,

$$\langle y_Q(\sigma_i) y_Q(\sigma_j)\rangle = d_g^2 \delta_{ij}, \tag{14.84}$$

where d_g is the rms kick from a girder misalignment. On the other hand, the misalignment of the cavity structure is also random. Thus, for the cavity structures on the girders at locations σ_i and σ_j, we can write

$$\langle y_C(\sigma_i) y_C(\sigma_j)\rangle = d_c^2 \delta_{ij}, \tag{14.85}$$

where d_c is the rms misalignment of the cavity structure on a girder. Let us further assume that the two rms errors are the same, or $d_g = d_c$. Then with the normalized location parameter σ considered as a continuous variable, Eqs. (14.84) and (14.85) translate into (Exercise 14.6)[‖]

$$\langle y_{Q,C}(\sigma_1) y_{Q,C}(\sigma_2)\rangle = \frac{d_g^2}{N_g} \Sigma(1) \sqrt{\frac{E_\sigma}{E_i}}\, \delta(\sigma_1 - \sigma_2), \tag{14.86}$$

where N_g is the total number of girders in the linac and d_g is the rms girder misalignment, and

$$\Sigma(\sigma) = \int_0^\sigma \sqrt{\frac{E_{\sigma'}}{E_i}}\, d\sigma'. \tag{14.87}$$

When the betatron focusing is strong, the multi-bunch beam breakup equation can be solved in the same way as before when there were no misalignments. The result can be expressed analytically as

$$\frac{\langle \Delta y_m^e(\sigma)^2\rangle^{\frac{1}{2}}}{\Delta y_m(\sigma)} \approx \frac{d_g}{y_0} \frac{2\pi\nu_\beta}{\sqrt{N_g}} \begin{cases} \dfrac{1}{\sqrt{\mathcal{E}(\sigma, m)}} & \eta \le 1, \\ \sqrt{\dfrac{2}{3}} & \eta > 1, \end{cases} \tag{14.88}$$

where $\Delta y_m^e(\sigma)$ is the transient displacement of the mth bunch in the bunch train which enters the misaligned linac without any displacement errors, while $\Delta y_m(\sigma)$, given by Eq. (14.76), is the transient displacement of the mth bunch in the bunch train which enters a perfectly aligned linac with initial displacement y_0 for all the bunches. The result is remarkable. First, it is simple. Second, it is independent of the amount of energy chirp f_γ either when $\eta \le 1$ or $\eta > 1$. For $\eta = 0$, Eq. (14.88) reduces to Eq. (5.6) of Yokoya, [18] which was derived without any energy chirp. The other difference from Yokoya is that his derivation is for the square roots of the total emittances rather than the transient displacements.

[‖]There is a typo in Eq. (5) of Ref. [17] and Eq. (14.86) here is the correct expression.

14.3.5.1 *Comparison with Simulations*

In order to avoid the fluctuations due to betatron oscillation, we try to compute the transient square-root-emittance $\Delta\epsilon_m^{e\,\frac{1}{2}}$ instead of the transient displacement Δy_m^e, where the former is defined as**

$$\Delta\epsilon_m^{e\,\frac{1}{2}} = \left[(y_m^e)^2 + (\beta_y y_m'^e)^2\right]^{\frac{1}{2}} - \left[(y_{ms})^2 + (\beta y'_{ms})^2\right]^{\frac{1}{2}}, \tag{14.89}$$

with β_y being the betatron function at the location along the linac under consideration and $y_m'^e$ the divergence of the particle bunch. The subscript s denotes steady state. Thus, the left side of Eq. (14.88) is replaced by $\left|\langle\Delta\epsilon_m^e(\sigma)^{\frac{1}{2}}\rangle\right|/\Delta\epsilon_m(\sigma)^{\frac{1}{2}}$.

We performed simulations of the SLAC NLC linac and computed beam quantities at its exit ($\sigma = 1$). In order to reduce the large spreads of the bunch displacements due to the randomness of the girder misalignments, each situation was simulated with 20 seeds and the results averaged. Figure 14.16 shows the simulated results when girder numbers N_g = 2500, 10000, 40000, and 160000 were used, while the energy chirp was kept at $f_\gamma = 1.0\%$ all the time. The plot actually verifies the $N_g^{-1/2}$ dependency stated in Eq. (14.88). The theoretical predictions are also shown in dashes with the understanding that η is always less than unity. We see that Eq. (14.88) agrees with the simulated results, although

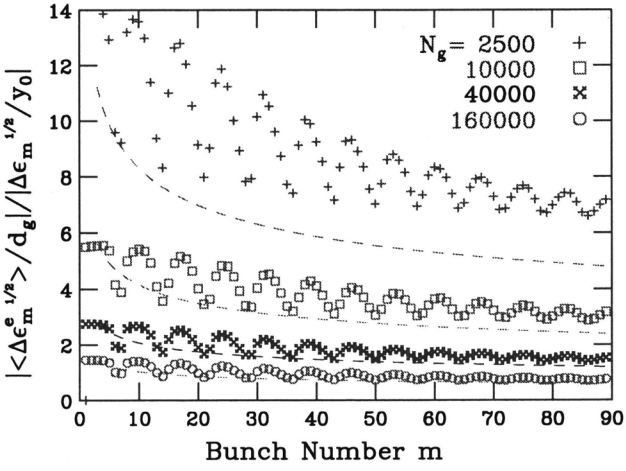


Fig. 14.16 Plot of ratio of transient square-root-emittance with girder misalignments but no beam offsets to that with beam offset but no girder misalignments at the linac exit of the SLAC NLC. The results verify the $N_g^{-1/2}$ dependency of the theoretical predictions which are shown here in dashes. The energy chirp is 1.0%.

**The emittance defined here when divided by the betatron function is the usual unnormalized emittance.

it tends to underestimate the results in general.[††] Actually, there will not be $N_g = 160000$ girders in the NLC linac. This number is created only for the purpose of checking the theoretical prediction. With a linac length of $\ell = 10$ km and $\nu_\beta = 100$ betatron wavelengths, $N_g = 2500$ may be a reasonable number, which will be used in the discussions below.

Next we vary the energy chirp to $f_\gamma = 0.5\%$, 1.0%, 1.5%, and 2.0%. In all these cases, $\eta < 1$. We see in Fig. 14.17 that the simulation results fall on each other implying that there is no dependency on f_γ. Careful examination reveals that the ratio of the emittances appears to become larger for larger energy chirp especially when $f_\gamma = 2.0\%$. This is understandable, because the parameter η is closer to unity. The theoretical prediction is also shown; it appears to underestimate the simulation results.

Now let us examine the situation when $\eta > 1$. At the linac exit, η turns unity at the 48th bunch when the energy chirp $|f_\gamma| = 3.0\%$, at the 18th bunch when $|f_\gamma| = 5.0\%$, and at the 10th bunch when $|f_\gamma| = 7.0\%$.[‡‡] Simulations for these values of energy chirp are shown in Fig. 14.18. First, these results appear to be f_γ-independent. Second, the ratios of emittances are definitely larger than those in Fig. 14.17 where $\eta < 1$. Third, these results are mostly bunch-number-independent, unlike those in Fig. 14.17. These observations lead us to conclude that the results follow the theoretical prediction for $\eta > 1$.

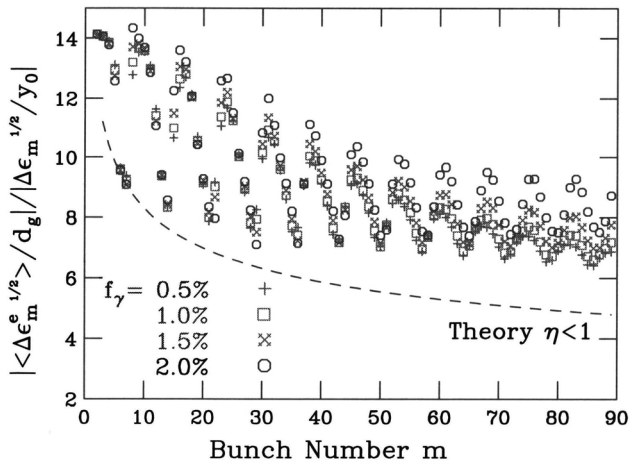


Fig. 14.17 Plot of ratio of transient square-root-emittance with girder misalignments but no beam offsets to that with beam offsets but no girder misalignments at the linac exit of the SLAC NLC with energy chirp $f_\gamma = 0.5$, 1.0, 1.5, and 2.0%. The results appears to be f_γ-independent and follow the trend of the theoretical prediction for $\eta < 1$ shown here in dashes.

[††]The agreement of theoretical predictions with simulations would be as good as in Figs. 11 and 12 of Ref. [18] if we had plotted the simulation results of all seeds instead of just the averages and also with the vertical axis in a logarithmic scale.

[‡‡]$|f_\gamma| = 5$ and 7% would be unrealistically too high to survive the dispersive regions of the linear collider; $|f_\gamma| = 3\%$ is marginal. They serve as illustrations only.

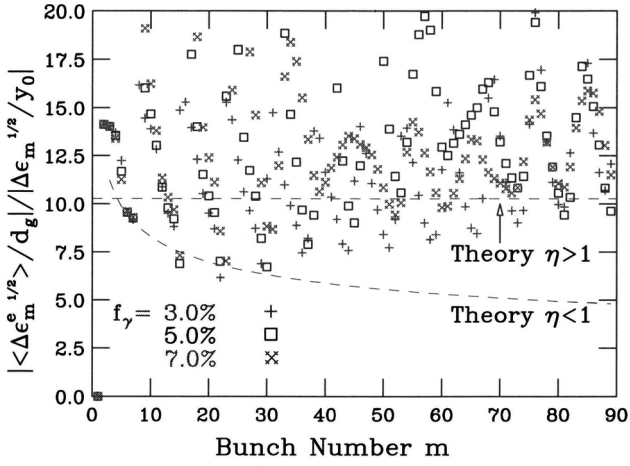


Fig. 14.18 Plot of ratio of transient emittance with girder misalignment errors but no initial displacement errors to that with initial displacement errors but no misalignment errors at the linac exit of the SLAC NLC with energy chirp f_γ = 3.0, 5.0, and 7.0%. The results appear to be f_γ-independent and follow the trend of the theoretical prediction for $\eta > 1$ shown in dashes.

14.3.5.2 *Application*

We learn from Figs. 14.17 and 14.18 that the ratios of the normalized transient square-root-emittances are, respectively, of the order 5 ($\eta < 1$) and 10 ($\eta > 1$) for the SLAC NLC linac, implying that the emittance growth from girder misalignments is much more serious than the growth from beam misalignment at linac entrance. In Fig. 14.19, we show the simulated normalized growth of transient square-root-emittance at the linac exit due to girder misalignment errors but without initial beam displacement errors. This growth is larger than the same growth of an initially displaced beam but without misalignment errors shown in Fig. 14.10. As a result, a larger energy chirp will be necessary to damp mutli-bunch beam breakup and control emittance growth. We see that although the growth saturates at an energy chirp of $f_\gamma < 3\%$, the normalized growth has been fourfold, and one needs an energy chirp of 5 to 7% to lower the growth to within twofold. On the other hand, for an initially displaced beam in a perfectly aligned linac, a 3% energy chirp controls the growth to less than 0.5 as indicated by Fig. 14.10.

Let us come back to the TESLA linac. Because of the small influence of the transverse wake, the displacements of the bunches possess rather good memory of their initial offsets when injected into the linac. As a result, in the absence of an energy chirp, the transient displacements, $\Delta y_m(\sigma)$, for all the bunches are more or less in phase during their betatron oscillations along the linac. The envelope of $\Delta y_m(\sigma)$ will become rather sensitive to the location of observation. To avoid ambiguity, the transient square-root-emittance, $\Delta\epsilon_m{}^{\frac{1}{2}}$, defined in Eq. (14.89) must be used. The top plot of Fig. 14.20 shows the simulated normalized tran-

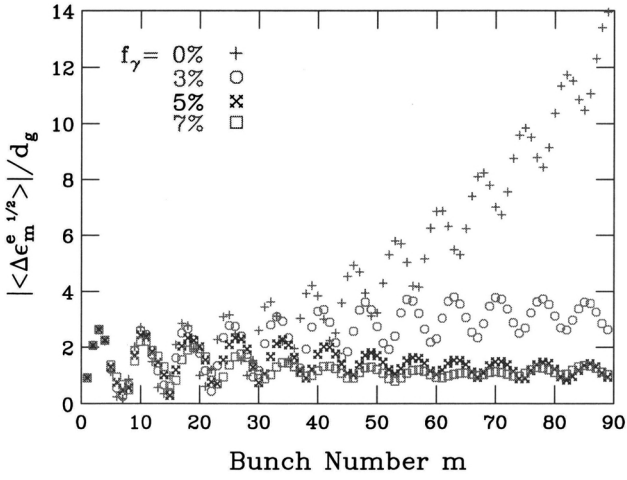


Fig. 14.19 Plot of transient square-root-emittance with girder misalignments but no beam offsets at the linac exit of the SLAC NLC with energy chirp f_γ = 0.0, 3.0, 5.0, and 7.0%. Compared with Fig. 14.10, larger energy chirp will be necessary for BNS damping.

sient square-root-emittance for a TESLA beam without energy chirp at the linac exit, where the linac elements are perfectly aligned while the beam is injected with the same offset y_0 but no divergence for all the bunches. We see that with an effective quality factor of $Q = 125000$, the maximum normalized transient square-root-emittance is small and completely acceptable, around ~ 0.012

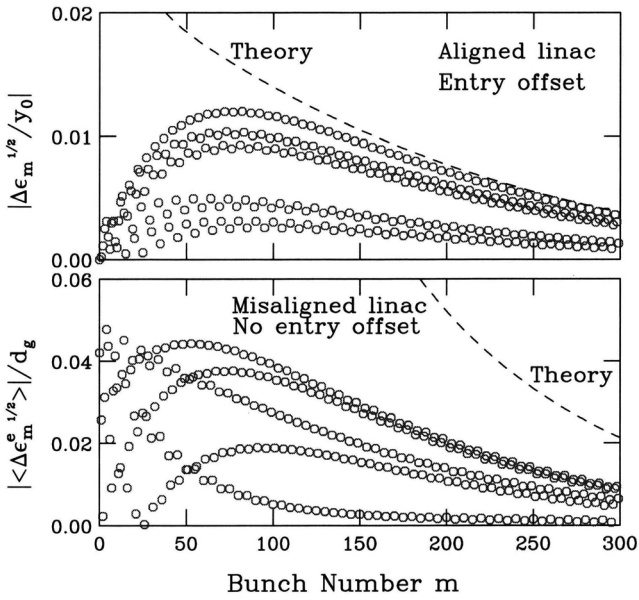


Fig. 14.20 Simulated normalized transient square-root-emittances for the first 300 TESLA bunches without energy chirp at the linac exit. Top plot is for bunches injected all with offset y_0 but no divergence in a perfectly aligned linac. Lower plot is for no injection offset, but the 2500 linac girders have rms misalignment d_g. Theoretical predictions are shown as dashes.

near the beginning of the bunch train and rolling off to ~ 0.005 near the 300th bunch. The theoretical prediction [Eq. (14.76)] is shown as dashes, and unexpectedly agrees well with simulations for bunch number $m \gtrsim 150$. The lower plot shows the beam without offset at injection into the linac, but there are random misalignment errors in the 2500 girders. (Actually, each TESLA linac has less number of girders.) Although the normalized transient square-root-emittance becomes almost 4 times larger than the top plot, starting with the maximum of ~ 0.045 and rolling off to ~ 0.012 near the 300th bunch, it is still acceptable. The theoretical prediction is shown as dashes and highly overestimates the simulation results. The disagreement is not hard to understand. Both Eqs. (14.88) and (14.83) do not apply well to the TESLA situation where the wake effect and the multi-bunch beam breakup are small. This prediction here is the product of the expressions in Eqs. (14.88) and (14.76) and therefore accumulates more uncertainty.

14.4 Quadrupole Wake

We have pointed out that the monopole wake $W_0'(z)$ leads to energy loss along the bunch and microwave instability, while the dipole wake $W_1(z)$ is responsible for beam breakup. In fact, when the transverse beam size is large, the higher-order wakes can also contribute to beam breakup. The next order to consider is the quadrupole wake $W_2(z)$, which is the $m = 2$ component in Eq. (1.22), where the transverse impulse is

$$v\Delta\vec{p}_\perp = -2ee_1x_1^2W_2(z)r\big(\hat{r}\cos 2\theta - \hat{\theta}\sin 2\theta\big). \tag{14.90}$$

Here subscript 1 stands for the source particle, which has charge e_1 and is at an offset x_1 horizontally. The unsubscripted variables are for the witness particle, which carries charge e and is at radial offset r and angle θ, measured from the positive x-axis towards the positive y-axis. Transforming back into the Cartesian coordinates via

$$\begin{aligned} \hat{r} &= \ \ \hat{x}\cos\theta + \hat{y}\sin\theta, \\ \hat{\theta} &= -\hat{x}\sin\theta + \hat{y}\cos\theta, \end{aligned} \tag{14.91}$$

we obtain

$$v\Delta\vec{p}_\perp = -2ee_1x_1^2W_2(z)(\hat{x}x - \hat{y}y), \tag{14.92}$$

which indicates that the witness particle is being kicked by the source in a quadrupole pattern. On the other hand, when the source particle is at an offset

y_1 along the y-axis, the transverse impulse is

$$v\Delta\vec{p}_\perp = -2ee_1y_1^2W_2(z)(-\hat{x}x + \hat{y}y). \tag{14.93}$$

A quadrupole implies bulging out in the x-direction and contracting in the y-direction. Thus combining the above two expressions, we arrive at

$$v\Delta\vec{p}_\perp = -2ee_1Q_nW_2(z)(\hat{x}x - \hat{y}y), \tag{14.94}$$

where

$$Q_n = \langle x_1^2\rangle - \langle y_1^2\rangle \tag{14.95}$$

is called the *normal* quadrupole moment or just *normal* quadrupole, because its bulge and contraction are in the directions of the coordinate axes. The notation $\langle\cdots\rangle$ implies averaging over all particles in the source. When the source is rotated by 45°, the bulge and contraction occur along the 45°- and 135°-axes. The normal quadrupole moment becomes a *skew* quadrupole moment

$$Q_s = 2\langle x_1y_1\rangle, \tag{14.96}$$

and, at the same time, the force pattern $\hat{x}x - \hat{y}y$ in Eq. (14.94) becomes $\hat{x}y + \hat{y}x$, or the transverse impulse,

$$v\Delta\vec{p}_\perp = -2ee_1Q_sW_2(z)(\hat{x}y + \hat{y}x). \tag{14.97}$$

A particle in a beam possessing normal and skew quadrupole moments satisfies the equations of motion:

$$\begin{aligned}
\frac{1}{\gamma}\frac{d}{ds}\left(\gamma\frac{dx}{ds}\right) + K_x(s)x &= -\frac{2e^2N_b}{\beta^2E_0L}\int dz'\lambda(z')W_2(z-z')\Big[Q_n(z')x + Q_s(z')y\Big], \\
\frac{1}{\gamma}\frac{d}{ds}\left(\gamma\frac{dy}{ds}\right) + K_y(s)y &= -\frac{2e^2N_b}{\beta^2E_0L}\int dz'\lambda(z')W_2(z-z')\Big[-Q_n(z')y + Q_s(z')x\Big],
\end{aligned} \tag{14.98}$$

where $W_2(z)$ is the quadrupole wake for one period of the linac cavity and L is the cavity period length, N_b is the number of particles in the beam, βc is the particle velocity, and $\lambda(z)$ is the linear density. The horizontal and vertical quadrupole focusing strengths are represented by $K_x(s) = (\partial B_y/\partial x)/(B\rho)$ and $K_y(s) = -(\partial B_y/\partial x)/(B\rho)$, where $B\rho$ is the magnetic rigidity of the beam and B_x and B_y are the horizontal and vertical components of the magnetic flux intensity. We see that the effect of the quadrupole wake constitutes a perturbation of the

normal and skew quadrupole focusing strengths:

$$\Delta\left[\frac{1}{B\rho}\frac{\partial B_y}{\partial x}\right] = \Delta\left[\frac{1}{B\rho}\frac{\partial B_x}{\partial y}\right] = \frac{2e^2N_b}{\beta^2E_0L}\int dz'\lambda(z')Q_n(z')W_2(z-z'),$$
$$\Delta\left[\frac{1}{B\rho}\frac{\partial B_y}{\partial y}\right] = -\Delta\left[\frac{1}{B\rho}\frac{\partial B_x}{\partial x}\right] = \frac{2e^2N_b}{\beta^2E_0L}\int dz'\lambda(z')Q_s(z')W_2(z-z'). \quad (14.99)$$

All beams in a lattice consisting of magnetic elements possess quadrupole moments even if they are injected without any offset. This is because a beam will have its horizontal and vertical sizes alternating with their maxima and minima according to the variations of the horizontal and vertical betatron functions. A *round* beam is defined as a beam with equal horizontal and vertical emittances, $\epsilon_x = \epsilon_y$. The beam is not really round in a magnetic lattice. Near a F-quadrupole, the horizontal beam radius $a_x = \sqrt{\beta_x\epsilon_x}$ is much larger than its vertical radius $a_y = \sqrt{\beta_y\epsilon_y}$ and vice versa when the beam is near a D-quadrupole. As a result, the beam exhibits a normal quadrupole moment

$$Q_n(s) = \epsilon_x\big[\beta_x(s) - \beta_y(s)\big], \quad (14.100)$$

which oscillates along the accelerator just like the betatron functions. This implies a perturbation to the betatron tune. In a lattice cell of length L_c, the horizontal and vertical tune shifts for a beam particle in the bunch at distance z behind the center (or head) are

$$\Delta\nu_{x,y}(z) = \pm\frac{e^2N_b\epsilon_x}{2\pi\beta^2L}\int dz'\lambda(z')W_2(z-z')\int_0^{L_c} ds\frac{\beta_{x,y}(s)[\beta_x(s)-\beta_y(s)]}{E_0}, \quad (14.101)$$

where the upper and lower signs are for $\Delta\nu_x$ and $\Delta\nu_y$, respectively. If the acceleration in the linac is slow or the change in energy in one cell of the lattice is small, the beam nominal energy E_0 can be taken out of the integral and we obtain

$$\Delta\nu_{x,y}(z) = \pm\frac{e^2N_b\epsilon_xL_c}{2\pi\beta^2E_0L}\int dz'\lambda(z')W_2(z-z')\big\langle\beta_{x,y}(s)\big[\beta_x(s)-\beta_y(s)\big]\big\rangle. \quad (14.102)$$

For a FODO lattice with betatron phase advance μ per cell, the average values over a cell are (Exercise 14.7)

$$\big\langle\beta_{x,y}(s)\big[\beta_x(s)-\beta_y(s)\big]\big\rangle = \pm\frac{L_c^2}{6\cos^2\frac{\mu}{2}}, \quad (14.103)$$

where the denominator just reflects the fact that a FODO lattice is unstable when the phase advance approaches 180°. The behavior of the quadrupole wake $W_2(z)$, having dimension Volts/Coulomb/m^3, is very similar to that of the dipole

wake $W_1(z)$ as illustrated in Fig. 1.6; both of them start out from zero at $z = 0$ and go negative when z is small. Thus the quadrupole wake is defocusing and the above tune shifts become more and more negative from the head to the tail of the bunch, both horizontally and vertically.

For an electron or positron beam, the horizontal emittance is often very much larger than the vertical emittance. Thus for the tune shifts along the bunch in Eq. (14.102), the averages in Eq. (14.103) should be replaced, respectively, by

$$\begin{aligned} \langle \beta_x^2(s) \rangle &= L_c^2 \frac{1 - \frac{1}{3}\sin^2\frac{\mu}{2} + \frac{2}{15}\sin^4\frac{\mu}{2}}{\sin^2\mu}, \\ \langle \beta_y(s)\beta_x(s) \rangle &= L_c^2 \frac{1 - \sin^2\frac{\mu}{2} + \frac{2}{15}\sin^4\frac{\mu}{2}}{\sin^2\mu}. \end{aligned} \tag{14.104}$$

A betatron tune shift along a bunch implies the betatron phase accumulation varies along the bunch. The result is that the head of the bunch drives the tail leading to an emittance growth of the tail. If the phase accumulation from the head to the tail is large, one must try to reduce the accumulation by lowering the strength of the quadrupole wake via detuning, for example. Otherwise, some compensation scheme must be employed. One method is to exercise BNS damping with variations of tune shifts equal to the negatives of Eq. (14.101), so that the betatron phase variations coming from the quadrupole wake are canceled.

14.4.1 *Two-Particle Model*

The two-particle model can be employed to study emittance growth driven by the quadrupole wake. More accurately, we should call this the *two-slice* model because the head needs to accommodate a quadrupole moment. The bunch is composed of a head slice and a tail slice each containing $N_b/2$ particles. The equation of motion of a particle in the head slice is

$$\frac{d^2}{ds^2}\begin{pmatrix} x \\ y \end{pmatrix} + k_\beta^2 \begin{pmatrix} x \\ y \end{pmatrix} = 0, \tag{14.105}$$

with the solution

$$\begin{pmatrix} x \\ y \end{pmatrix} = \begin{pmatrix} x_0 \\ y_0 \end{pmatrix} \cos k_\beta s + \begin{pmatrix} x_0' \\ y_0' \end{pmatrix} \frac{\sin k_\beta s}{k_\beta}, \tag{14.106}$$

where x_0 and y_0 are the initial horizontal and vertical offsets and x_0' and y_0' the horizontal and vertical divergences. In above, smooth betatron focusing has been

assumed with k_β representing the betatron wavenumber. For a round beam, we have

$$\langle x_0^2 \rangle = \frac{\langle {x_0'}^2 \rangle}{k_\beta^2} = a^2 \quad \text{and} \quad \langle y_0^2 \rangle = \frac{\langle {y_0'}^2 \rangle}{k_\beta^2} = a^2, \tag{14.107}$$

where a is the rms beam radius. It is obvious that $\langle x^2 \rangle - \langle y^2 \rangle = 0$ and $\langle 2xy \rangle = 0$, implying that there is no quadrupole moment in the beam under the assumption of smooth focusing. Quadrupole moment can be introduced by injecting the beam with its size not matching the lattice, for example,

$$x_0 \longrightarrow x_0(1+\Delta) \quad \text{and} \quad \frac{x_0'}{k_\beta} \longrightarrow \frac{x_0'}{k_\beta}(1-\Delta), \tag{14.108}$$

where Δ is small. For simplicity, assume no beam-size mismatch vertically. Substituting into Eq. (14.106) gives a normal quadrupole moment $Q_n \cos 2k_\beta s = 2a^2\Delta \cos 2k_\beta s$, where $\mathcal{O}(\Delta^2)$ has been neglected.

The equation of motion for a particle in the tail slice is

$$\frac{d^2}{ds^2}\begin{pmatrix} x \\ y \end{pmatrix} + k_\beta^2 \begin{pmatrix} x \\ y \end{pmatrix} = -\varepsilon \mathcal{Q} \begin{pmatrix} x \\ y \end{pmatrix} \cos 2k_\beta s, \tag{14.109}$$

where

$$\varepsilon = \frac{e^2 N_b W_2(\hat{z})}{\beta^2 E_0 L}, \tag{14.110}$$

with $W_2(\hat{z})$ representing the the quadrupole wake per linac cell and at distance $\hat{z} = 2\sigma_\ell$ from the source and σ_ℓ is the rms length of the bunch the two-slice model is describing, while

$$\mathcal{Q} = \begin{pmatrix} Q_n & Q_s \\ Q_s & -Q_n \end{pmatrix}, \tag{14.111}$$

with the inclusion of the skew quadrupole moment for the more general situation, although it vanishes in this example. Since the force gradient on the right side is at two times the natural frequency, the solution can be expressed in terms of Mathieu's functions. However, when the mismatch Δ is small enough, we can solve the equation by iteration. Just as for the dipole wake $W_1(\hat{z})$, there are resonant terms proportional to s, the distance along the linac. Keeping only the resonant terms, we obtain the solution for a particle in the tail slice,

$$\begin{pmatrix} x \\ y \end{pmatrix} = \begin{pmatrix} x_0 \\ y_0 \end{pmatrix} \cos k_\beta s + \begin{pmatrix} x_0' \\ y_0' \end{pmatrix} \frac{\sin k_\beta s}{k_\beta} - \frac{\varepsilon}{4k_\beta} s \mathcal{Q} \left[\begin{pmatrix} x_0 \\ y_0 \end{pmatrix} \sin k_\beta s + \begin{pmatrix} x_0' \\ y_0' \end{pmatrix} \frac{\cos k_\beta s}{k_\beta} \right]. \tag{14.112}$$

For the rms beam size and the quadrupole moment of the tail, we compute

$$\langle x^2 \rangle = a^2 + 2a^2\Delta \cos 2k_\beta s - \frac{\varepsilon}{2k_\beta} s Q_n a^2 \sin 2k_\beta s,$$
$$\langle y^2 \rangle = a^2 + \frac{\varepsilon}{2k_\beta} s Q_n a^2 \sin 2k_\beta s. \tag{14.113}$$

It is important to point out that although we start with only a horizontal mismatch at injection, the tail traveling down the linac receives contribution of a mismatch in the vertical direction. Thus even normal quadrupole moment alone will couple the horizontal motion to the vertical motion. The solution shows that the horizontal and vertical radii of the beam pulsate alternatively at twice the frequency of the betatron oscillation; while the horizontal radius increases the vertical radius decreases, and vice versa. After traversing a distance L_0, the initial fractional offset Δ increases Υ_2-fold, where

$$\Upsilon_2 = -\frac{\varepsilon a^2 L_0}{2k_\beta} = -\frac{e^2 N_b W_2(\hat{z}) a^2 L_0}{2\beta^2 E_0 k_\beta L}, \tag{14.114}$$

after substituting for $Q_n = 2a^2\Delta$. Correspondingly, the quadrupole moment of the tail increases $2\Upsilon_2$-fold. With an acceleration in the linac, we must pay attention to the fact that the beam size is inversely proportional to the square root of energy. Thus, under the assumption of a linear acceleration in the form $E_0(s) = E_i(1 + \alpha s)$, where E_i and E_f are the initial and final energies, we must make the substitution for the total length L_0 of the linac,

$$\frac{a^2 L_0}{E_0} \longrightarrow a_i^2 E_i \int_0^{L_0} \frac{ds}{E_0^2(s)} \approx \frac{a_i^2}{E_i \alpha}, \tag{14.115}$$

where a_i is the initial rms beam radius and the assumption $E_f/E_i \gg 1$ has been made. Thus the growth parameter becomes

$$\Upsilon_2 = -\frac{e^2 N_b W_2(\hat{z}) a_i^2}{\beta^2 E_i k_\beta \alpha L}. \tag{14.116}$$

In a realistic linac, the betatron focusing is nonuniform. In that case, we require the interpretation

$$\frac{W_2}{k_\beta} \longrightarrow [\beta_y W_2], \tag{14.117}$$

where the right side implies that when the quadrupole wake is summed up element-by-element, it should be multiplied by the betatron function β_y at the element.

Quadrupole moment exists whenever the beam is not round and it will oscillate along the linac in an alternating-gradient focusing lattice. The quadrupole wake it produces represents a potential limitation to high intensity linac performance. Such a study has been carried out for the SLAC linac by Chao and Cooper. [19]

14.4.2 *Observation*

The effects of quadrupole wake was first observed in the KEKB Linac. [20] This was achieved by kicking the beam, so that

$$x' \longrightarrow x' + \Delta'_x \quad \text{and} \quad y' \longrightarrow y' + \Delta'_y. \tag{14.118}$$

It is important to point out that this replacement is completely different from those in Eq. (14.108). There, the offset x of each particle is increased by an amount Δ *proportional to* its offset; but here every particle receives the *same amount* of kick $\Delta'_{x,y}$ regardless of its offset. While the former changes the size of the beam without moving its center, the latter displaces the beam without altering its size. Kicking the beam sideway will generate a dipole moment in the first order of $\Delta'_{x,y}$. As we will see below, however, the second order will generate quadrupole moments. As a result, the effects of the quadrupole wake will be masked by those of the dipole wake, and the former can manifest itself only either when the kick is large or through the characteristic of the quadrupole wake.

When the kick in Eq. (14.118) is substituted in Eq. (14.106), we obtain

$$\begin{aligned}
\langle x^2 \rangle &= \left(a^2 + \frac{{\Delta'_x}^2}{2k_\beta^2} \right) - \frac{{\Delta'_x}^2}{2k_\beta^2} \cos 2k_\beta s, \\
\langle y^2 \rangle &= \left(a^2 + \frac{{\Delta'_y}^2}{2k_\beta^2} \right) - \frac{{\Delta'_y}^2}{2k_\beta^2} \cos 2k_\beta s, \\
\langle xy \rangle &= \frac{\Delta'_x \Delta'_y}{2k_\beta^2} - \frac{\Delta'_x \Delta'_y}{2k_\beta^2} \cos 2k_\beta s,
\end{aligned} \tag{14.119}$$

where a round beam has been assumed with $\langle x_0^2 \rangle = \langle {x'_0}^2 / k_\beta^2 \rangle = a^2$ and $\langle y_0^2 \rangle = \langle {y'_0}^2 / k_\beta^2 \rangle = a^2$. Unlike the kicks in the two-particle model, here the $\mathcal{Q}(\Delta'_{x,y})$ terms vanish when averages are taken over all the particles in the bunch. The lowest kick terms are second order in $\Delta'_{x,y}$. They consist of both stationary terms and terms oscillating at twice the betatron wave number. The stationary terms enhance the transverse vertical beam size and lead to horizontal-vertical

coupling. The oscillatory terms are the normal- and skew- quadrupole moments generated:

$$Q_n \cos 2k_\beta s = -\frac{\Delta_x'^2 - \Delta_y'^2}{k_\beta^2} \cos 2k_\beta s,$$
$$Q_s \cos 2k_\beta s = -\frac{\Delta_x' \Delta_y'}{k_\beta^2} \cos 2k_\beta s. \tag{14.120}$$

Either normal or skew quadrupole moments can be studied separately by adjusting the amount of kicks in the horizontal and vertical directions. For example, with equal horizontal and vertical kicks, only skew quadrupole moment will be generated. On the other hand, with the horizontal kick very much larger than the vertical kick $\Delta_x' \gg \Delta_y'$, mostly normal quadrupole moments will be generated.

The experiment was performed with an intense electron bunch consisting of $N_b = 5 \times 10^{10}$ particles and of rms length $\sigma_\ell = 1.5$ mm. The linac has the betatron wave number $k_\beta = 2\pi/46$ m^{-1}, dipole wake per cavity length $W_1(2\sigma_\ell)/L = 4.04 \times 10^{15}$ V/(C-m^2) and quadrupole wake per cavity length $W_2(2\sigma_\ell)/L = 4.49 \times 10^{19}$ V/(C-m^4). The beam was kicked horizontally by about 0.3 mr upstream when the energy was $E_0 = 230$ MeV and the ramp rate was 20 MeV/m. The transverse motion of the beam is observed downstream. The typical horizontal betatron oscillation is shown in the left plot of Fig. 14.21. The vertical betatron oscillation in the right plot indicates the x-y coupling effects due to the quadrupole wake. The solid curves are from theoretical simulations. The agreement between observations and simulations is quite satisfactory within experimental errors, which are about ± 0.1 mm.

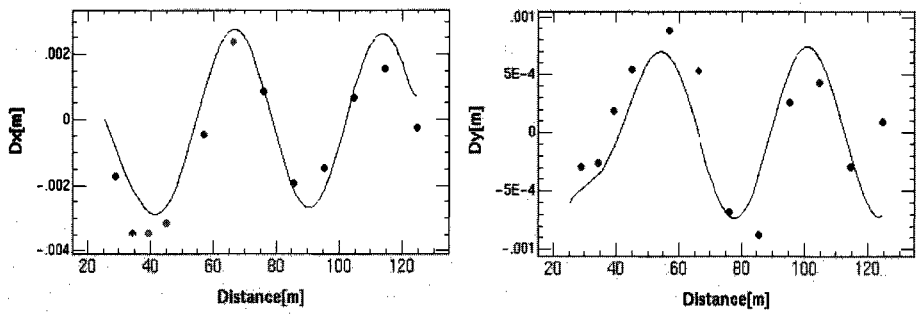


Fig. 14.21 Horizontal (left) and vertical (right) oscillations of the beam recorded downstream in the KEKB linac resulting from a horizontal kick of 0.3 mr upstream. The vertical oscillation is an indication of the x-y coupling effects of the quadrupole wake. The solid curves are simulations assuming the contribution of the quadrupole wake. (Courtesy Ogawa, *et al.* [20])

In order to check the results, the same horizontal kick was applied to a low-current beam. No vertical betatron oscillation due to x-y coupling was observed within the precision of the BPM system (< 0.1 mm). This signifies that the observed x-y coupling for the 8-nC beam is inherent in the high-intensity beam and could be of wake-field origin. The x-y coupling caused by a rotational misalignment of the steering coil used for the horizontal kick was estimated to be smaller than 0.03%. However, the coupling could be enhanced through the strong dipole wake. In order to demonstrate that the x-y coupling was the genuine effects of the quadrupole wake, the quadratic dependency of the response on the initial kick must be verified. For this, the horizontal response was measured at two locations downstream and the initial vertical kick was varied from -0.2 to 1.2 mr. The fit to the response at location B24 shown in left plot of Fig. 14.22 clearly show quadratic dependency. The linear term manifest the dipole-wake effects. The right plot in the figure also shows quadratic behavior in the vertical response at sector B7 to a vertical kick.

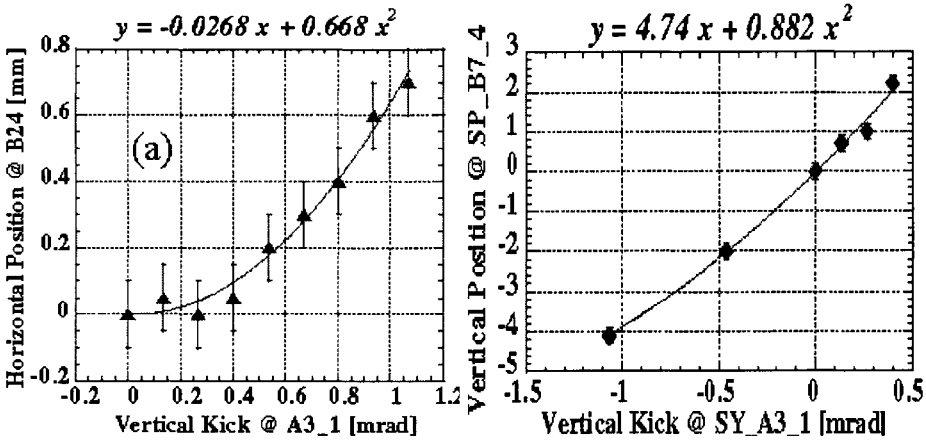


Fig. 14.22 Left: Horizontal response at location B24 to a vertical kick upstream reveals quadratic dependency on the strength of the kick. Right: Vertical response at location sector B7 to a vertical kick upstream also reveals quadratic dependency on the strength of the kick. (Courtesy Ogawa, *et. al.* [20].)

Higher-multipole wakes can also contribute to emittance growth. Similar to the growth parameter Υ_2 for the quadrupole wake, Chao and Cooper [19] derived a growth parameter Υ_m for the rms beam size in a length L_0 of the linac under the influence of the mth multipole wake in the two-slice model. It is given by

$$\Upsilon_m = -\frac{e^2 N_b W_m(\hat{z}) L_0}{4E_0 k_\beta L} m a^{2(m-1)}, \tag{14.121}$$

for a coasting beam in a linac. With constant acceleration at $E_0(s) = E_i(1+\alpha s)$, it is modified to

$$\Upsilon_m = -\frac{e^2 N_b W_m(\hat{z})}{4E_i k_\beta L\alpha} \frac{m a_i^{2(m-1)}}{m-1}, \tag{14.122}$$

where a_i and E_i are, respectively, the initial beam radius and energy. In general, the multipolar wake $W_m(\hat{z})$, having dimension Volt/Coulomb/m^{2m-1}, starts out from zero and goes negative when $\hat{z}$ is small. The multipolar wake W_m decreases as b^{2m}, where b is the beam pipe radius. Thus the growth parameter Υ_m decreases as $a^{2(m-1)}/b^{2m}$ and becomes less important when the beam size is small. Again with nonuniform betatron focusing, W_m/k_β must be interpreted as $[\beta_y W_m]$ implying that W_m must be multiplied by the local betatron function β_y when it is summed up element by element.

Quadrupole wake also plays a role in a circular accelerator ring and becomes important when the transverse beam size is large. Because of synchrotron oscillation, the head and tail of the bunch exchange position, thus suppressing the emittance growth. As a result, unlike in the linac, there is a threshold in the instability, just as in the situation of strong head-tail in the presence of a dipole wake. Here, the threshold in the two-slice model is given by

$$\Upsilon_2 = -\frac{\pi e^2 N_b W_2(\hat{z}) c^2 a^2}{2E_0 C_0 \omega_\beta \omega_s} \leq 2, \tag{14.123}$$

where C_0 is the circumference of the ring, ω_β and ω_s are the angular betatron frequency and angular synchrotron frequency. The derivation is straight forward following that for the dipole wake, and is given in detail in Ref. [21].

14.5 Exercises

14.1 (1) Assuming that the acceleration gradient is much less than the betatron wavenumber, derive the beam-breakup solutions, Eqs. (14.34) and (14.36), for the displacements of the head and tail in the two-particle model.
(2) The dipole transverse wake function of the SLAC linac per cavity cell at 1 mm is 62.9 V/pC/m. The bunch is of rms length 1 mm containing 5×10^{10} electrons. The cavity accelerating frequency is 2.856 GHz, with each cavity having the length of $\frac{1}{3}$ the rf wavelength. The betatron wavenumber is $k_\beta = 0.06$ m^{-1}. In a two-particle model, compute the ratio of the deflection of the tail particle versus that of the head particle along the whole linac of length 3 km, where the beam energy increases from 1 GeV

to 50 GeV. What would be this ratio if the linac were to stay at 1 GeV without acceleration?

14.2 A linac has a lattice consisting of N FODO cells. In between two consecutive quadrupoles, there is an acceleration structure of length ℓ, which is half of the FODO cell length. The acceleration is linear with $E_f/E_i = 1+2N\alpha\ell$ where E_i and E_f are, respectively, the initial and final energy across the N FODO cells.

(1) Show that the transverse transfer matrix across the nth acceleration structure is

$$\begin{pmatrix} 1 & \dfrac{1+n\alpha\ell}{\alpha}\ln\dfrac{1+(n+1)\alpha\ell}{1+n\alpha\ell} \\ 0 & \dfrac{1+n\alpha\ell}{1+(n+1)\alpha\ell} \end{pmatrix}. \tag{14.124}$$

(2) Is the transfer matrix symplectic? Give a physical answer.

Hint: Solve Eq. (14.33) with $k_\beta = 0$.

14.3 The proposed SLAC NLC bunch has an rms length of $\sigma_\ell = 150$ μm containing 1.1×10^{10} electrons. The linac has a length of 10 km, accelerating electrons from 10 GeV to 500 GeV. Assume a uniform betatron focusing with 100 betatron oscillations in the linac. The accelerating structure has a transverse mode at the mean frequency of $\bar{\nu} = 15.25$ GHz with an rms spread σ_ν equal to 25% of $\bar{\nu}$.

(1) Use Eq. (14.44) to compute the transverse wake function at a distance σ_ℓ, assuming that the average kick factor is $\bar{K} = 40$ MV/nC/m^2.

(2) Compute the multiplication factor of the tail particle in the two-particle model at the end of the linac.

(3) Assuming the natural chromaticity of $\xi = (\Delta k_\beta/k_\beta)/\delta \approx -1$ for the FODO-cell lattice, compute the energy spread between the head and tail of the bunch in order to damp the deflection of the tail.

14.4 (1) Complete the derivation of the beam-breakup deflection of the mth bunch as given by Eq. (14.54).

(2) For the NLC with 95 bunches with spacing 42 cm, estimate the deflection of the last bunch if the first bunch has an initial offset of 1 μm. The dipole wake at one bunch spacing is 0.21 MV/nC/m^2. An average beam energy of 250 GeV along the linac can be used in the computation.

14.5 Fill in the steps and give the estimate of the energy spread from the first to the 95th bunch in order to damp the beam breakup instability of the bunch train as outlined in Sec. 14.3.3.

14.6 (1) Across the ith girder of length $\ell_g(\sigma_i)$, the kick imparted to the beam

due to girder misalignment $y_Q(\sigma_i)$ is

$$\Delta y'_Q(\sigma_i) = \kappa^2(\sigma_i) y_Q(\sigma_i) \frac{\ell_g(\sigma_i)}{\mathcal{L}}, \tag{14.125}$$

where the prime denotes derivative with respect to the normalized distance σ, $\mathcal{L}$ is the total length of the linac, and $\kappa(\sigma_i)$ is the quadrupole strength at the girder. Show that the total kick $\Delta y'_Q$ imparted to the beam for the whole linac passage has the rms value

$$\langle (\Delta y'_Q)^2 \rangle = \sum_i d_g^2 \kappa^4(\sigma_i) \frac{\ell_g^2(\sigma_i)}{\mathcal{L}^2}, \tag{14.126}$$

where d_g is the rms girder misalignment defined in Eq. (14.84).
(2) When σ is considered as a continuous variable, we must have

$$\langle y_Q(\sigma) y_Q(\sigma') \rangle = a(\sigma) \delta(\sigma - \sigma'), \tag{14.127}$$

where the function $a(\sigma)$ is to be determined. Now the total kick imparted to the beam in passage of the whole linac is

$$\Delta y'_Q(\sigma) = \int_0^1 y_Q(\sigma) \kappa^2(\sigma) d\sigma. \tag{14.128}$$

Comparing the mean-square kick $\langle (\Delta y'_Q)^2 \rangle$ with the one computed above with the discrete-girder consideration, show that

$$a(\sigma) = d_g^2 \frac{\ell_g(\sigma)}{\mathcal{L}}. \tag{14.129}$$

(3) Since there is only one optical element on each girder, the length of a girder at location σ must be proportional to the betatron wavelength λ_β there. Using the fact the $\lambda_\beta \propto E_\sigma^{-1/2}$, show that the total number of girders is

$$N_g = \frac{\mathcal{L}}{\ell_g(\sigma)} \Sigma(1) \sqrt{\frac{E_\sigma}{E_i}}, \tag{14.130}$$

and derive Eq. (14.86).

14.7 (1) The betatron function β is defined by

$$\frac{\beta'^2}{4} - \frac{\beta''\beta}{2} - K\beta^2 + 1 = 0, \tag{14.131}$$

where K is the quadrupole focusing strength and the prime denotes derivative with respect to s, the distance along the accelerator. Show that in the absence of quadrupoles, the betatron function is a quadratic in s.

(2) Consider a half cell in a thin-lens FODO system from the exit of a F-quadrupole to the entrance of the following D-quadrupole. The horizontal and vertical betatron functions can be written as

$$\beta_{x,y}(s) = \beta^F_{x,y} - 2s\alpha^F_{x,y} + s^2\gamma, \tag{14.132}$$

where the betatron functions at the exit of the F-quadrupole are

$$\beta^F_{x,y} = L_c \frac{1 - \sin(\mu/2)}{\sin\mu}, \tag{14.133}$$

and the other Twiss parameters at the exit of the F-quadrupole are

$$\alpha^F_{x,y} = -\frac{1}{2}\frac{d\beta^F_{x,y}}{ds} = \pm\frac{1 \pm \sin(\mu/2)}{\cos(\mu/2)}, \tag{14.134}$$

and

$$\gamma = \frac{1 + (\alpha^F_{x,y})^2}{\beta^F_{x,y}}, \tag{14.135}$$

with L_c being the length and μ the betatron phase advance of one cell. Verify the expression for $\langle \beta_{x,y}(s)\,[\beta_x(s) - \beta_y(s)]\,\rangle$, $\langle \beta^2_x(s)\rangle$, and $\langle \beta_y(s)\beta_x(s)\rangle$ in Eqs. (14.103) and (14.104).

(3) A 8-nC round beam is injected into the KEKB electron linac without error and perfectly matched to the variation of the betatron functions, and has unnormalized emittances: 2.6×10^{-6} πm at 20 MeV just after the bunching sections, 3.5×10^{-7} πm at 500 MeV and 2.0×10^{-7} πm at 1.5 GeV at exit. The linac has FODO focusing of 90° per cell and the betatron wavelength is $\lambda_\beta = 46$ m. The quadrupole wake per linac cavity length is $W_2(2\sigma_\ell)/L = 4.49 \times 10^{19}$ V/(C-m^4), where σ_ℓ is the rms bunch length. Using the two-particle model, compute the betatron tune shift driven by the quadrupole wake in each of the three energy regions due to the alternating variation of the beam transverse sizes following the variation of the betatron functions.

Bibliography

[1] C. M. Ankenbrandt, *et al.* (Muon Collider Collaboration), *Phys. Rev. ST Accel. Beams* **2**, 081001 (1999).

[2] King-Yuen Ng, *Beam Instability Issues of the 50 GeV×50 GeV Muon Collider Ring*, Fermilab Report FN-678, 1999.

[3] E.-S. Kim, A, M, Sessler, and J. S. Wurtele, *Transverse Instability in a 50 GeV×50 GeV Muon Collider Ring*, Proc. 1999 Part. Accel. Conf., eds. A. Luccio and W. MacKay (New York, March 27–April 2, 1999), p. 3057.

[4] V. Balakin, A. Novokhatsky, and V. Smirnov, *VLEPP: Transverse Beam Dynamics*, Proc. 12th Int. Conf. High Energy Accel. eds. F. T. Cole and R. Donaldson (Fermilab, Batavia, Aug. 11–16, 1983), p. 119.

[5] V. E. Balakin, Proc. Int. Workshop Next Generation Linear Collider, ed. M. Riordan (SLAC, Stanford, Nov. 28–Dec. 9, 1988), p. 55.

[6] K. L. F. Bane and R. L. Gluckstern, *Part. Accel.* **42**, 123 (1993).

[7] R. Jones, K. Ko, N. M. Kroll, R. H. Miller, and K. A. Thompson, *Equivalent Circuit Analysis of the SLAC Damped Detuned Structure*, Proc. 5th European Part. Accel. Conf. EPAC'96, ed. S. Myers, R. Pascual, and J. Poole (Sitges, Barcelona, June 10–14, 1996), p. 1292; R. Jones, K. Ko, N. M. Kroll, and R. H. Miller, *Spectral Function Calculation of Angle Wakes, Wake Moments, and Misalignment Wakes for the SLAC Damped Detuned Structures (DDS)*, Proc. 1997 Part. Accel. Conf., eds. M. Comyn, M. K. Craddock, M. Reiser, and J. Thomson (Vancouver, Canada, May 12–16, 1997), p. 551; R. Jones, N.M. Kroll, and R.H. Miller, R.D. Ruth, and J.W. Wang, *Advanced Damped Detuned Structure Development at SLAC*, *ibid.*, p. 548; M. Dehler, R. M. Jones, N. M. Kroll, R. H. Miller, I. Wilson, and J. W. Wuensch, *Design of a 30 GHz Damped Accelerating Structure*, *ibid.*, p.518.

[8] K. Yokoya, *Cumulative Beam Breakup in Large-Scale Linacs*, DESY 86-084, ISSN 0418-9833, 1986.

[9] C. L. Bohn and J. R. Delayen, *Phys. Rev.* **A45**, 5964 (1992). "Multibunch Domain B" introduced in this reference is the limit of zero focusing variation away from wake zero-crossing.

[10] C. L. Bohn and K. Y. Ng, *Phys. Rev. Lett.* **85**, 984 (2000); *Preserving High Multibunch Luminosity in Linear Colliders*, Fermilab Report FERMILAB-PUB-00-072-T, 2000. Erratum p. 5010.

[11] G. Stupakov, talk given in SLAC-Fermilab Video Conference, September, 1999.

[12] G. Stupakov, *Effect of Energy Spread in the Beam Train on Beam Breakup Instability*, SLAC Report, LLC-0027, 1999.

[13] C. L. Bohn and J. R. Delayen, *Cumulative Beam Breakup in Radio-Frequency Linacs*, Proc. 1990 Linear Accelerator Conference, Los Alamos National Laboratory Report No. LA-12004-C, (Albuquerque, New Mexico, Sept. 10–14, 1990), p. 306.

[14] C. L. Bohn and K. Y. Ng, *Theory and Suppression of Multibunch Beam Breakup in Linear Colliders*, Proc. XX Int. Linac Conf., (Monterey, CA, Aug. 21–25, 2000), p. 884.

[15] The Wentzel-Kramers-Brillouin (WKB) method approximates the solution of a differential or integral equation in an inhomogeneous medium by using simple traveling waves locally and then taking into account inhomogeneity by allowing the amplitude and wavelength to vary slowly with position. Global eigenvalue problems are solved by constructing standing waves using a superposition of traveling waves that connect properly at turning (reflection) points. The method is derived in nearly any book on quantum mechanics.

[16] TESLA Technical Design Report, DESY Report 2001-011, `http://tesla.desy.de/new_pages/TDR_CD/start.html` (March, 2001).

[17] K. Y. Ng and C. L. Bohn, *Theory of Cumulative Beam-Breakup with BNS Damping*, Proc. 2nd Asian Part. Accel. Conf. (Beijing, Sep. 17–21, 2001), p. 372.

[18] K. Yokoya, *Cumulative Beam Breakup in Large-scale Linacs*, DESY Report 86-084, 1986.

[19] A. W. Chao and R. K. Cooper, *Transverse Quadrupole Wake Field Effects in High Intensity Linacs, Part. Accel.* **13**, 1 (1983).

[20] Y. Ogawa, *Quadrupole Wake-Filed Effects in the KEKB Linac*, Proc. 7th European Part. Accel. Conf. EPAC'00, ed. M. Regler (Vienna, Austria, June 26–30, 2000), p. 1161; Y. Ogawa and T. Suwada, *Observation of Quadrupole Wake-Field Effects in the KEKB Linac*, Proc. 2001 Part. Accel. Conf., eds. P. Lucas and S. Webber (Chicago, June 18–22, 2001), p. 3924.

[21] A. W. Chao, *Physics of Collective Beam Instabilities in High Energy Accelerators*, (Wiley Interscience, 1993), Section 4.4.

This page intentionally left blank

2025 © The Author(s). This is an Open Access chapter published by World Scientific Publishing Company, licensed under the terms of the Creative Commons Attribution-NonCommercial 4.0 International License (CC BY-NC 4.0).

Chapter 15

Two-Stream Instabilities

An intense particle beam forms a potential well for oppositely charged particles and will therefore trap particles of the opposite charge. These trapped particles can often accumulate to such an extent that they provide a potential well for particles of the original beam. Thus, the secondary beam can oscillate transversely in the potential well of the primary beam, while the primary beam oscillates transversely in the potential well of the external focusing quadrupoles heavily perturbed by potential of the secondary beam. This coupled-beam oscillation may grow in amplitude and lead to beam loss eventually. Instabilities involving two species of particles of opposite charges are called *two-stream instabilities*. One way to eliminate the accumulation of secondary particles of opposite charge is to leave a gap in the primary beam so that the secondary particles can be cleared. However, sometimes the accumulation of secondary particles produced by one single passage of the primary beam can be so intense that instability develops even before the clearing gap is reached.

15.1 Trapped Electrons

Proton beam trapping electrons was first observed in the Bevatron [1] and later in the CERN Intersecting Storage Ring (ISR). [2] The ISR was a collider with an intense coasting proton beam in each of the intersecting vacuum chambers. It had been observed that electrons were trapped in the potential of the proton beams with oscillation frequency around 100 MHz. The instability was intermittent. It stopped when the electrons, driven to large amplitudes, were shaken out to the walls, or out of resonance with the protons. It restarted when a sufficient number of new electrons had been accumulated. Slow beam blowup and background problems were the result.

The Proton Storage Ring (PSR) at Los Alamos (LANL) running with 2.3 to

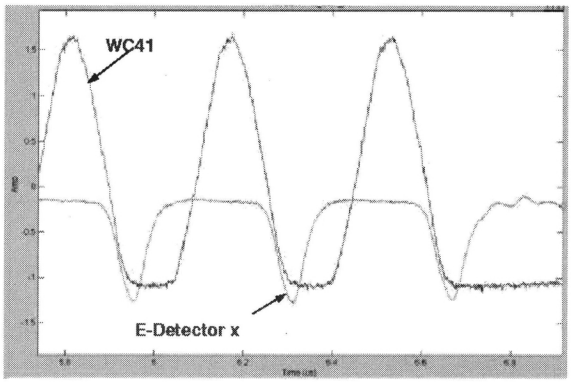


Fig. 15.1 Turn-by-turn electron signals (E-Detector x) are shown in relation to the proton beam (WC41) pulse at the LANL PSR. Electrons start to appear at the back end of the beam pulse and are cleared in the bunch gap. (Courtesy Macek. [3])

4.2×10^{13} protons has always been troubled by the electrons trapped inside the proton beam. [3] A turn-by-turn picture of the electron signal in relation to the circulating proton beam pulse at the end of a 500 μs store is shown in Fig. 15.1. The proton beam has a full width of about 240 ns. Displayed in the figure are the last three revolution turns followed by extraction. The timing between electrons and proton beam is good to a few ns. The electron detector was designed and built at Argonne National Laboratory (ANL).[4] It has a repeller grid, so that it can decouple the electron energy analysis from collection. The repeller voltage of 5 volts means that the electrons have to have a kinetic energy more than 5 eV in order to get through to the collector. Electrons start to appear after the peak of the beam pulse has passed and the peak of the electron pulse (shown as negative) appears at the end of the beam pulse. This clearly demonstrates the accumulation of electrons along the proton beam and its clearance at the gap. Higher repeller voltage shows a smaller, and narrower electron pulse. The electron flux hitting the wall is sizeable, about 25 mA/cm^2 at the peak or about 2 pC/cm^2/pulse or 60 pC/cm/pulse integrated over the circumference of the beam pipe. It is interesting to compare this with the 420 pC/cm average line density of the proton beam. Unfortunately, one cannot deduce from this one picture alone how much electron multipactoring is occurring on the backside of the beam pulse without additional data and assumptions.

An instability is clearly seen in Fig. 15.2 when beam is stored for about 300 microseconds after the end of injection. A rapidly growing vertical difference signal (top trace) can be seen shortly before beam loss occurs (lower trace), indicating beam-centroid oscillations. In Fig. 15.3, the growth of the instability can be seen turn by turn at the final $\sim$ 300 μs of the store. Here the vertical difference signal is compared to the wall-current-monitor trace probing the sum

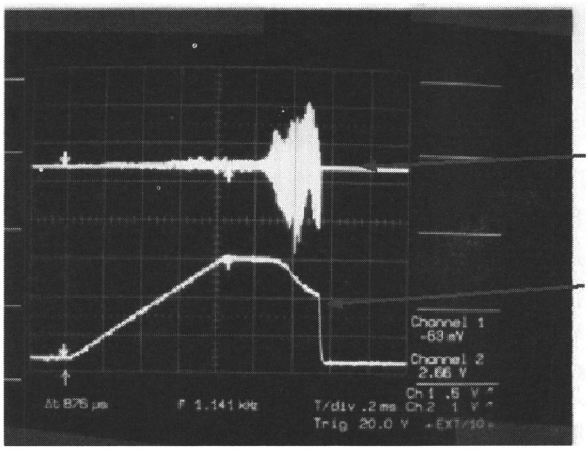


Fig. 15.2 Top trace: vertical difference signals of the beam at the LANL PSR reveal a growing instability about 300 μs after the end of injection. Lower trace: sum signals of the beam showing beam loss as the instability grows. (Courtesy Macek. [3])

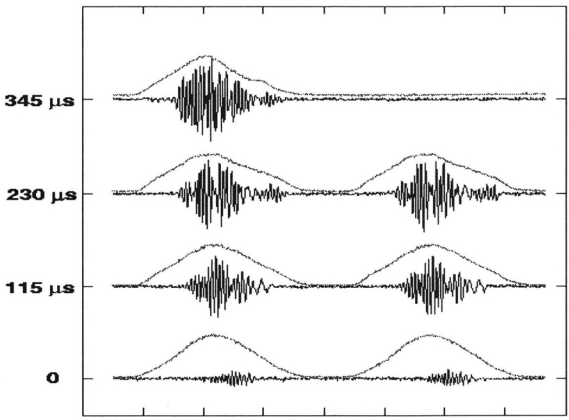


Fig. 15.3 Turn-by-turn vertical difference signals from a short stripline beam-position monitor at the final 300 μs of the store show a vertical instability starting at the back end of the bunch and spreading into the whole bunch with increasing amplitude. The bunch sum profiles from a wall-current monitor are also shown, revealing a beam loss as the instability develops. (Courtesy Macek. [3])

signal. The beam transverse instability starts on the backside of the pulse and broadens out as it grows in strength. Some beam loss is evident at the last turn before extraction.

The Brookhaven booster running in the coasting beam mode suffers sudden beam loss due to a vertical instability, [5] which cannot be identified with any reasonable amount of transverse impedance. This has been considered to be the result of two-stream instability between the proton beam and the electrons it traps. During the 2001–2003 run of the Relativistic Heavy Ion Collider (RHIC) at Brookhaven, pressure rise at the high intensity beam at injection had often been observed in the warm straight sections. [6] The pressure rise had limited

the gold beam intensity to 9×10^8 ions per bunch for the 55-bunch mode with 216 ns bunch spacing. The pressure rise was very sensitive to the bunch spacing, and the situation was much worse for the 110-bunch injection with 108 ns bunch spacing. These are illustrated in Fig. 15.4. Without any doubt, the pressure rise is an indication of the accumulation of electron cloud.

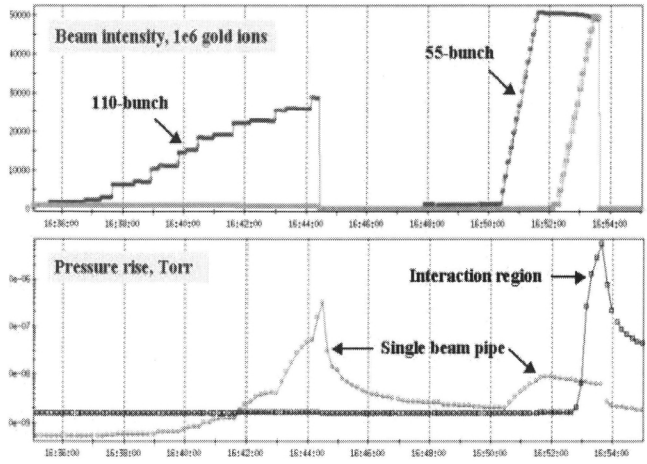


Fig. 15.4 In RHIC at BNL, vacuum-pressure increases by a hundred to a thousand times were observed at injection with gold ions of intensity 9×10^8 per bunch at the 55-bunch (216 ns bunch spacing) mode and 110-bunch (108 ns bunch spacing) mode. (Courtesy Zhang, *et al.* [6])

The Fermilab antiproton ring traps positive ions and limits the intensity of the storage. [7] The newly built Advanced Photon Source (APS) at ANL is a synchrotron light source designed for positron beams. It has been observed that electrons are trapped causing instability. [4] As a result, positron beams are abandoned and electron beams are now used instead.

15.1.1 *Single-Electron Mechanics*

15.1.2 *Electron Bounce Frequency*

Coupled-centroid oscillation of the proton beam and the trapped electrons will occur only when the amount of electrons becomes very intense. Therefore, to prevent such instability, we would like the electrons in the vacuum chamber not to accumulate. The electrons inside the vacuum chamber are supposed not to move longitudinally. As the proton bunch passes through them, they are attracted towards the central axis of the proton bunch with vertical electron *bounce frequency* $\Omega_e/(2\pi)$ given by [13]

$$\Omega_e^2 = \frac{4N_p r_e c^2}{a_V(a_V + a_H)L_b}. \tag{15.1}$$

Here, N_p is the number of protons in the bunch which has an elliptical cross section with vertical and horizontal radii a_V and a_H, L_b is the full bunch length, and r_e the electron classical radius. In the discussion below, we assume the proton beam to have uniform longitudinal and transverse distributions with a cylindrical cross section of radius a inside a cylindrical beam pipe of radius b. Thus $a_V(a_V + a_H)$ can be replaced by $2a^2$. The images of the proton beam and the electron cloud in the walls of the vacuum chamber will modify the electron bounce frequency depicted in Eq. (15.1), but their effects are neglected in this study. Only linear focusing force acting on the electrons by the proton beam will be considered. The bounce frequency in Eq. (15.1) can be derived exactly as the space-charge self-force tune shift in Chapter 3. In Eq. (3.24), for example, we make the replacement $2\nu_0^{V,H}\Delta\nu_0^{V,H}\omega_0^2 \rightarrow \Omega_e^2$ and $2a^2 \rightarrow a_V(a_V + a_H)$. We delete one factor of γ from the denominator because the trapped electrons are assumed to have no longitudinal motion. We delete the other factor of γ^2 from the denominator because the trapped electrons, having no longitudinal velocity, do not interact with the magnetic field of the proton beam.

Electron-proton instability is different from other transverse instability in that the bounce frequency of the electrons inside the proton bunch is very broad. Recall that the angular bounce frequency is defined in Eq. (15.1). Thus, the bounce frequency of the electrons depends on where they are inside the proton bunch. As an example, if the transverse distribution is the same at every longitudinal position, the trapped electrons at the longitudinal center of the proton beam will have a bounce frequency $\sqrt{2}$ times larger than the trapped electrons at the two FWHM edges of the proton beam. In other words, the spread of the electron bounce frequency will be $1/\sqrt{2}$ its mean value, which is certainly a wide spread. Another test of the *e-p* bounce oscillation is to measure the dependency of the bounce frequency on the proton beam intensity. As is given by Eq. (15.1), the bounce frequency should be proportional to the square root of the proton intensity. Such a measurement has been performed at the Los Alamos PSR and is shown in Fig. 15.5. At countdown 1 (CD 1), the longest chopped proton beam is injected from the linac. At 6.1 μC or 3.81×10^{13} protons injected, the electron bounce frequency observed is $\sim$ 200 MHz, very close to the prediction of Eq. (15.1). Next the injection is at countdown 2 (CD 2), where the chopped beam from the linac is injected into the PSR on alternate turns, thus reducing the total injection intensity by half to 3.0μC. The bounce frequency is found to peak at $\sim$ 140 MHz, very close to a reduction of $\sqrt{2}$ as predicted. The total spread of the bounce frequency at CD 1 is about 100 MHz, which is also the same order of magnitude as predicted above.

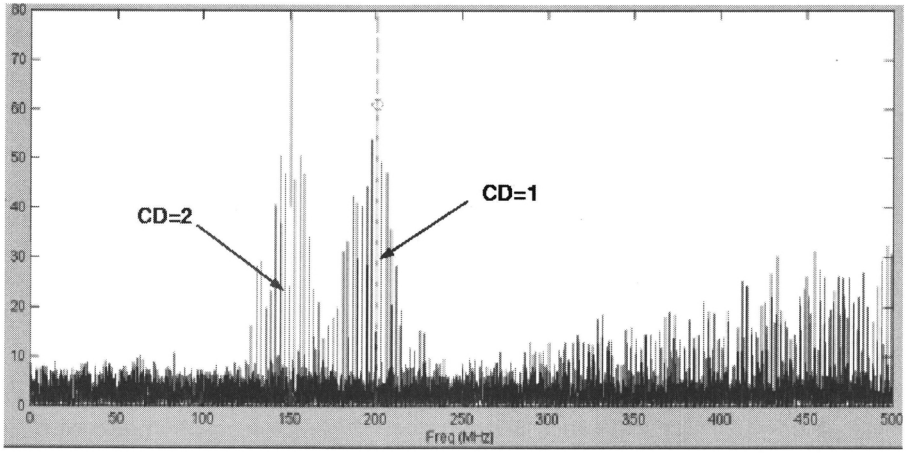


Fig. 15.5 The PSR is run at CD 1 with 6.1 μC. The electron bounce frequency measured is centered at $\sim$ 200 MHz, close to the theoretical prediction. The total spread of the bounce frequency is roughly 100 MHz, the same order of magnitude as its center value. Operated at CD 2 with 3.0 μC, the bounce frequency reduces to $\sim$ 140 MHz, roughly by $\sqrt{2}$ times as expected. (courtesy Macek. [3])

15.1.2.1 *Long bunches*

An electron trapped inside the proton beam performs betatron oscillations with an equivalent betatron function* $\beta_b = \beta c/\Omega_e$ with a total betatron phase advance $\phi_b = \Omega_e L_b/v$, where βc is the velocity of the protons. After the passage of the proton bunch, the motion of the electron in the gap is equivalent to a drift of length $L_g = \lambda_{\rm rf} - L_b$ with $\lambda_{\rm rf}$ being the rf wavelength or width of the stationary bucket. Here, we assume all rf buckets are filled. The transfer matrix for an rf wavelength is [8]

$$M = \begin{pmatrix} 1 & L_g \\ 0 & 1 \end{pmatrix} \begin{pmatrix} \cos\phi_b & \beta_b \sin\phi_b \\ -\dfrac{1}{\beta_b}\sin\phi_b & \cos\phi_b \end{pmatrix} = \begin{pmatrix} \cos\phi_b - \dfrac{L_g}{\beta_b}\sin\phi_b & \beta_b \sin\phi_b + L_g \cos\phi_b \\ -\dfrac{1}{\beta_b}\sin\phi_b & \cos\phi_b \end{pmatrix}. \tag{15.2}$$

In order that the electron will not be trapped inside the proton bunch, its motion has to be unstable or

$$\frac{1}{2}|\mathrm{Tr}M| = \left|\cos\phi_b - \frac{L_g}{2\beta_b}\sin\phi_b\right| > 1. \tag{15.3}$$

*The electron bounce tune is $Q_e = \Omega_e/\omega_0$ and the equivalent betatron function is $\beta_b = R/Q_e$, where R is the mean radius of the accelerator ring.

If the electron is unstable, we can write

$$\frac{1}{2}|\mathrm{Tr}M| = \cosh\mu, \tag{15.4}$$

where μ^{-1} is the growth of the electron oscillation amplitude in one rf bucket, and the growth rate is $\mu\beta c/\lambda_{\mathrm{rf}}$. Here, we study the effect of trapped electrons in three synchrotron rings: the storage ring of the Spallation Neutron Source (SNS) under construction at Oak Ridge National Laboratory (ORNL), the Los Alamos PSR, and the booster at Brookhaven (BNL). Some information of the three rings are listed in Table 15.1.

Table 15.1 Some data of the Oak Ridge SNS, the Los Alamos PSR, and the Brookhaven booster at injection.

	Oak Ridge SNS	Los Alamos PSR	Brookhaven Booster
Circumference C (m)	220.6880	90.2000	201.769
Injection kinetic energy (GeV)	1.000	0.797	0.200
γ	2.0658	1.8494	1.2132
β	0.8750	0.8412	0.5662
Revolution frequency f_0 (MHz)	1.1887	2.7959	0.8412
Revolution period T_0 (ns)	841.3	357.7	1189
Total number of protons N_p	2.1×10^{14}	4.2×10^{13}	2.4×10^{13}
Rf harmonic (number of bunches) h	1	1	1
Number of injection turns	1225	2000	300
Repetition rate (Hz)	60	12	7.5

Equation (15.3) appears to be a simple criterion. In fact, it is much more complex in application, because the electron bounce frequency turns out to be usually very high. Take for example the PSR, we find $\Omega_e = 1.254$ GHz, which gives an equivalent betatron function $\beta_b = \beta c/\Omega_e = 0.201$ m. With the gap length $L_g = 30.07$ m, $L_g/\beta_b = 150$. Although Ω_e is not too sensitive to L_g/β_b, it is very sensitive to $\sin\phi_b$ and $\cos\phi_b$, because the phase $\phi_b = \Omega_e L_g/v \approx 299$ rad. Thus, a very slight change in the number of protons in the beam will alter the electron bounce frequency, the betatron phase, and give rise to a large change in the trace. Since the electron bounce frequency usually has a large spread, it is more reasonable to consider the rms value of the trace instead and the corresponding untrap criterion becomes

$$\left[\frac{1}{2}\mathrm{Tr}M\right]_{\mathrm{rms}} = \sqrt{\cos^2\phi_b + \frac{L_g^2}{4\beta_b^2}\sin^2\phi_b} > 1. \tag{15.5}$$

The results of $[\frac{1}{2}\mathrm{Tr}M]_{\mathrm{rms}}$ are listed in Table 15.2. We see that for all the

three rings, the electrons trapped should be able to escape to the walls of the beam pipe in the beam gap. In fact, with such high electron bounce frequency, L_g/β_b will be large and it will not be easy to trap electrons if the gap is clean. When the intensity of the proton beam is raised, the electron bounce frequency will increase, making the electrons easier to escape at the gap.

Table 15.2 Instability and escape time through the bunch gap of a single electron trapped inside the proton bunches of the ORNL SNS, LANL PSR, and BNL booster.

	Oak Ridge SNS	Los Alamos PSR	Brookhaven Booster
Injection full bunch length (m)	143.39	60.13	100.89
Gap length (m)	77.30	30.07	100.89
Proton beam radius a (m)	0.0380	0.0150	0.0150
Bounce angular frequency Ω_e (MHz)	713.3	1253.9	462.6
Bounce betatron phase ϕ_b (rad)	309.9	299.0	435.2
$\frac{1}{2}\lvert\mathrm{Tr}M\rvert$ (rms)	52.55	37.38	108.8
Escape time in number of rf buckets	0.2148	0.2318	0.1858

15.1.2.2 *Beam Leaked into Gap*

Sometimes, the gap is not totally free of protons. The space-charge effect of the protons will distort the rf bucket reducing its momentum acceptance. As a result, some protons may leak out of the rf bucket and end up in the bunch gap. If a fraction η of the protons leaks into the gap, the electrons will oscillate with bounce frequency $\Omega_{eb}/(2\pi)$ inside the proton bunch and with bounce frequency $\Omega_{eg}/(2\pi)$ in the bunch gap. These frequencies can be neatly expressed in terms of Ω_e: [8, 11]

$$\Omega_{eb}^2 = \Omega_e^2(1-\eta) \qquad \text{and} \qquad \Omega_{eg}^2 = \Omega_e^2 \eta \frac{L_b}{L_g}. \tag{15.6}$$

Again, only linear focusing force by the proton beam is considered. The betatron phase advances in the beam and in the gap are, respectively, $\phi_b = \Omega_{eb}L_b/(\beta c)$ and $\phi_g = \Omega_{eb}L_g/(\beta c)$. The transfer matrix is therefore

$$M = \begin{pmatrix} \cos\phi_g & \beta_g \sin\phi_g \\ -\dfrac{1}{\beta_g}\sin\phi_g & \cos\phi_g \end{pmatrix} \begin{pmatrix} \cos\phi_b & \beta_b \sin\phi_b \\ -\dfrac{1}{\beta_b}\sin\phi_b & \cos\phi_b \end{pmatrix}$$

$$= \begin{pmatrix} \cos\phi_g \cos\phi_b - \dfrac{\beta_g}{\beta_b} \sin\phi_g \sin\phi_b & \beta_b \cos\phi_g \sin\phi_b + \beta_g \cos\phi_b \sin\phi_g \\ -\dfrac{1}{\beta_g} \cos\phi_b \sin\phi_g - \dfrac{1}{\beta_b} \cos\phi_g \sin\phi_b & -\dfrac{\beta_b}{\beta_g} \sin\phi_b \sin\phi_g + \cos\phi_g \cos\phi_b \end{pmatrix}, \tag{15.7}$$

where the equivalent betatron functions in the bunch and in the gap are, respectively,

$$\beta_b = \frac{\beta c}{\Omega_{eb}} \qquad \text{and} \qquad \beta_g = \frac{\beta c}{\Omega_{eg}}. \tag{15.8}$$

The condition for the electrons to escape is therefore

$$\frac{1}{2}|\mathrm{Tr}M| = \left|\cos\phi_g \cos\phi_b - \frac{1}{2}\left(\frac{\Omega_{eb}}{\Omega_{eg}} + \frac{\Omega_{eg}}{\Omega_{eb}}\right) \sin\phi_g \sin\phi_b\right| > 1. \tag{15.9}$$

It is easy to demonstrate that Eq. (15.9) reduces to Eq. (15.3) when $\eta \to 0$.

Figure 15.6 shows $[\mathrm{Tr}M]_{\mathrm{rms}}$ as a function of the fractional proton leakage η into the gap, respectively, for the ORNL SNS, LANL PSR, and BNL booster. The plots for the ORNL SNS and LANL PSR are very similar; $[\mathrm{Tr}M]_{\mathrm{rms}}$ oscillates rapidly with the fractional leakage and becomes bounded by 2 or electrons will be trapped when $\eta \gtrsim 0.1$. The situation for the BNL booster is different. Even up to $\eta = 0.20$, the oscillation of $[\mathrm{Tr}M]_{\mathrm{rms}}$ still has an amplitude larger than 2. This is mainly due to the fact of a larger gap-to-bunch-length ratio in the BNL booster. Thus, we may conclude that electrons are not so easily trapped in BNL booster as in the ORNL SNS and LANL PSR when protons are spilled into the bunch gaps. We also try to vary the electron bounce frequency in each case and find that the results remain relatively the same. The only changes in the plots are faster oscillations when the bounce frequency is increased.

15.1.2.3 *A Train of Short Bunches*

In electron or position machines, we usually have trains of short bunches with $\tau_L/\tau_{\mathrm{sep}} \ll 1$, where τ_L is the full length of a bunch and τ_{sep} is the bunch separation. Just as a proton beam traps electrons, a train of electron bunches traps ions. For a train, the peak ion bounce frequency $\Omega_{Ix,y}$ is usually defined as

$$\Omega_{Ix,y}^2 = \frac{2N_e r_u c}{\sigma_{x,y}(\sigma_x + \sigma_y) A \beta \tau_{\mathrm{sep}}}, \tag{15.10}$$

where N_e is the number of electrons in a bunch, $\sigma_{x,y}$ are it rms horizontal and vertical beam size, r_u is the classical radius of one atomic-mass-unit of ion, and A is the molecular weight of the trapped ion species. The above is just the

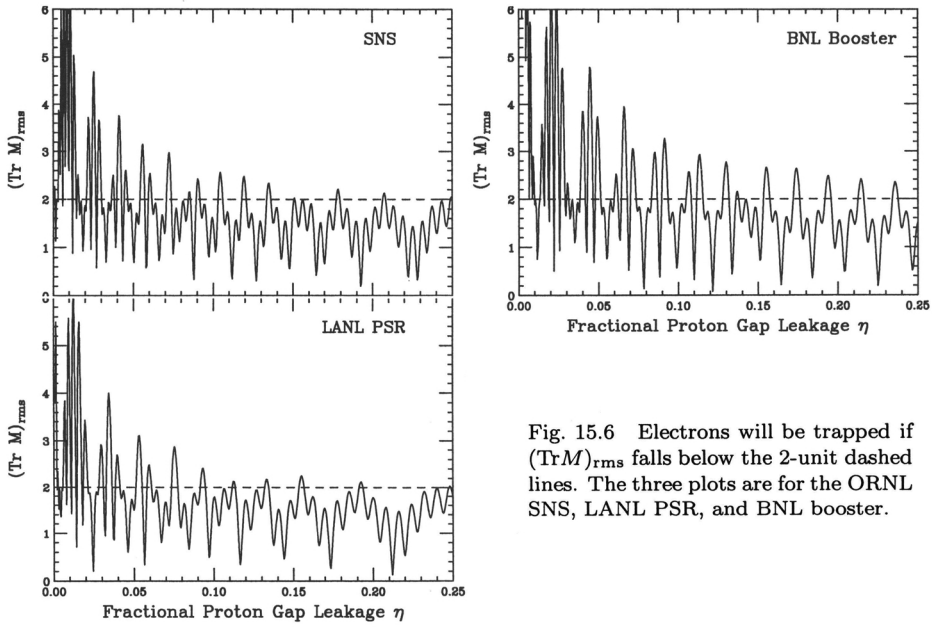


Fig. 15.6 Electrons will be trapped if $(\mathrm{Tr}M)_{\mathrm{rms}}$ falls below the 2-unit dashed lines. The three plots are for the ORNL SNS, LANL PSR, and BNL booster.

analog of the electron bounce frequency in Eq. (15.1) with the substitution of $a_{H,V} \to \sqrt{2}\sigma_{x,y}$, since the uniform transverse distribution has been changed to a bi-Gaussian one for the electron beam. The biggest different is having the bunch separation τ_{sep} in the denominator rather than the bunch length τ_L. Thus $\Omega_{Ix,y}$ serves as the ion bounce frequency averaged over the bunch separation, as if the N_e electrons were spread out uniformly within the whole bunch separation τ_{sep} forming a coasting beam. For this to hold, an important condition is that the ions will not be cleared in the bunch gaps. Since the ions oscillate at the passage of the bunch and move in hyperbolic trajectories in the bunch gaps, we must have the restriction that $\Omega_{Ix,y}\tau_{\mathrm{sep}} \lesssim 1$ in order that the ion oscillatory motion remains stable. The factor of β in the denominator of Eq. (15.10) is the relativistic factor of the electron bunches.

Although an electron bunch is short, its length is mostly very much larger than its transverse radii. Let us take the Fermilab designed damping ring as an example. The mean horizontal and vertical beam radii are, respectively, 0.34 mm and 6.6 μm, where the effect of horizontal dispersion has been included, while the rms bunch length is 6 mm. When trapped, an ion will always experience the kick from a long length of electron charges rather than just a point-like bunch. For this reason the stability criterion developed in Eqs. (15.3) and (15.9) using transfer matrices can be applied to determine whether the beam gap can trap or

clear the ions. We need to compute the ion bounce frequency inside the electron beam

$$\Omega^b_{Ix,y} = \Omega_{Ix,y}\sqrt{\frac{\tau_{\rm sep}}{\tau_L}}, \tag{15.11}$$

the phase advance when crossing the bunch $\phi_b = \Omega^b_{Ix,y}\tau_L$, and the equivalent betatron function inside the bunch $\beta_b = \beta c/\Omega^b_{Ix,y}$. Then the trace of the transfer matrix can be evaluated according to Eq. (15.3). Notice that the phase advance across the electron bunch can be written as

$$\phi_b = \left[\Omega^b_{Ix,y}\tau_{\rm sep}\right]\frac{\tau_L}{\tau_{\rm sep}}, \tag{15.12}$$

which is very much less than unity, because we expect $\Omega^b_{Ix,y}\tau_{\rm sep} \lesssim 1$. Continuing the above example of the Fermilab designed damping ring, with $N_e = 2\times 10^{10}$ per bunch at 5 GeV, full bunch length $\tau_L = 4\sigma_\tau = 0.08$ ns, bunch separation $\tau_{\rm sep} = 6$ ns, we obtain $\Omega_{Ix} = 30.3$ MHz for the trapped CO^+ ions having $A = 28$, but $\Omega^b_{Ix} = \Omega_{Ix}\sqrt{\tau_{\rm sep}/\tau_L} = 262$ MHz. Thus $\Omega_{Ix}\tau_{\rm sep} = 0.18$ and $\phi_b = 0.021$, which is much less than unity. For the vertical, although $\Omega_{Iy}\tau_{\rm sep} = 1.30$, $\phi_b = 0.15$ is still much less than unity. As a result, $\sin\phi_b$ and $\cos\phi_b$ can be expanded. We obtain from Eq. (15.3),

$$\frac{1}{2}{\rm Tr}M = \cos\phi_b - \frac{\beta c\tau_{\rm sep}}{2\beta_b}\sin\phi_b = 1 - \frac{1}{2}\left(\Omega_{Ix,y}\tau_{\rm sep}\right)^2, \tag{15.13}$$

and the condition for ion trapping is

$$\Omega_{Ix,y}\tau_{\rm sep} < \sqrt{2}. \tag{15.14}$$

We can therefore conclude that CO^+ ions will be trapped horizontally in the electron bunch train, but marginally trapped vertically. Notice that when $\Omega_{Ix}\tau_{\rm sep} \ll 1$, the right side of Eq. (15.13) can be written as $\cos\Omega_{Ix,y}\tau_{\rm sep}$. This verifies that when the ion oscillatory motion is stable inside the train (or they are well-trapped), $\Omega_{Ix,y}$, as defined in Eq. (15.10), does equal to average ion bounce frequency as if the short electron bunch were uniformly spread out longitudinally like a coasting beam.

15.1.3 *Coupled-Centroid Oscillation*

Consider coupled oscillation of the proton beam and the electron 'beam' in the vertical direction. The displacements of a proton and electron from the central axis of the vacuum chamber are denoted, respectively, by y_p and y_e. Here, we assume both the proton and electron beams are coasting beams having the same

transverse sizes and uniform distribution longitudinally and transversely. The coupled equations of motion are [13, 8, 5, 15]

$$\left(\frac{\partial}{\partial t}+\omega_0\frac{\partial}{\partial\theta}\right)^2 y_p + Q_\beta^2\omega_0^2 y_p = -Q_p^2\omega_0^2(y_p-\bar{y}_e) + Q_{ps}^2\omega_0^2(y_p-\bar{y}_p), \quad (15.15)$$

$$\frac{d^2y_e}{dt^2} = -Q_e^2\omega_0^2(y_e-\bar{y}_p) + Q_{es}^2\omega_0^2(y_e-\bar{y}_e), \quad (15.16)$$

where $\bar{y}_p$ and $\bar{y}_e$ are the vertical displacements of the centroids of, respectively, the proton and electron beams from the axis of the vacuum chamber, ω_0 is the angular revolution frequency, θ is the azimuthal angle around the ring, Q_β is the betatron tune, and Q_e, with

$$\Omega_e^2 = (Q_e\omega_0)^2 = \frac{4N_p r_e c^2}{a_V(a_H+a_V)C}, \quad (15.17)$$

is the oscillation tune of the electrons inside the proton beam. On the other hand, Q_p, with

$$\Omega_p^2 = (Q_p\omega_0)^2 = \frac{4N_p r_p c^2\chi_e}{a_V(a_H+a_V)\gamma C}, \quad (15.18)$$

would have been the oscillation tune of the protons inside the electron beam if external focusing were absent. In the presence of external focusing, Q_p becomes the perturbation to the proton betatron tune as a result of the extra potential set up by the trapped electrons. In above, χ_e is the neutralization factor, or the ratio of the electron distribution to the proton distribution, r_p is the classical proton radius, r_e the classical electron radius, and C the circumference of the accelerator ring. The negative signs on first terms on the right hand sides of Eqs. (15.15) and (15.16) indicate that the protons are focused by the electron beam and the electrons are focused by the proton beam. The factor γ in the denominator of Ω_p^2 comes about because the protons are circulating around the ring while the electrons do not. There are no magnetic force contributions because the proton, although at a high velocity, does not see a magnetic field in the stationary electron beam. On the other hand, for Ω_e, the electron has no longitudinal velocity although it sees a magnetic field from the proton beam. Again, we are considering uniformly and cylindrical-symmetrically distributed proton and electron beams of radius a; or $a_V(a_H+a_V) \to 2a^2$. Image effects in the walls of the vacuum chamber as well as nonlinear focusing forces are neglected.

The last term in the proton equation denotes the perturbation to the oscillations of the proton by the self-field of the proton beam. Here,

$$(Q_{ps}\omega_0)^2 = \frac{4N_p r_p c^2}{a_V(a_H + a_V)\gamma^3 C} \tag{15.19}$$

is proportional to the linear space-charge tune shift of the proton beam. Similarly the last term in the electron equation, with

$$Q_{es}^2 = Q_e^2 \chi_e \tag{15.20}$$

denoting the space-charge tune shift of an electron in the self-field of the electron beam.

Averaging over the proton displacements and electron displacements, we obtain the equations for the coupled motion of the proton-beam centroid $\bar{y}_p$ and the electron-beam centroid $\bar{y}_e$. The space-charge terms, Q_{ps}^2 and Q_{es}^2, drop out as expected. If there is a coherent instability occurring at the angular frequency $\Omega = Q\omega_0$, we can write

$$\bar{y}_p \sim e^{i(n\theta - \Omega t)} \qquad \text{and} \qquad \bar{y}_e \sim e^{i(n\theta - \Omega t)}, \tag{15.21}$$

where n is the longitudinal harmonic number. The coupled equations can be readily solved to give

$$(Q^2 - Q_e^2)[(n-Q)^2 - Q_\beta^2 - Q_p^2] - Q_e^2 Q_p^2 = 0, \tag{15.22}$$

which is a quartic. For a solution when Q is near Q_e, we can expand Q around Q_e. When Q_p or the neutralization factor χ_e is large enough, the solution becomes complex and an instability occurs. The limiting Q_p for stability is given by

$$Q_p \lesssim \frac{|(n-Q_e)^2 - Q_\beta^2 - Q_p^2|}{2\sqrt{Q_e|n-Q_e|}}, \tag{15.23}$$

from which the limiting neutralization factor χ_e can be obtained. Once above threshold, the growth rate, given by

$$\frac{1}{\tau} \approx \frac{Q_p\omega_0}{2}\sqrt{\frac{Q_e}{|n-Q_e|}}, \tag{15.24}$$

is very fast. Notice that Q_p^2 on the right side of Eq. (15.23) in the numerator can be neglected because usually $Q_p^2 \ll Q_\beta^2$.

A proper employment of Eq. (15.23) is important, because it can give meaningless result. For example, in the situation

$$[Q_e] = [Q_\beta] \qquad \text{or} \qquad [Q_e] + [Q_\beta] = 1, \tag{15.25}$$

where $[Q_\beta]$ and $[Q_e]$ are, respectively, the residual (or decimal part of the) betatron tune and the residual electron bounce tune, there will always exist a harmonic n which leads to $|(n - Q_e)^2 - Q_\beta^2 - Q_p^2| = 0$ and therefore an instability. However, the growth rate will go to zero also. In reality, there is always a variation in the proton linear density or the electron bounce tune Q_e usually has a sizable spread. Furthermore, the betatron tune can be suitably adjusted. To obtain something meaningful, first let us separate the numerator of the right side of Eq. (15.23) into the fast and slow waves and keep only the dangerous slow wave:

$$|(n - Q_e)^2 - Q_\beta^2 - Q_p^2| \approx 2Q_\beta|n - Q_e - Q_\beta|. \tag{15.26}$$

The electron bounce tune Q_e is computed from Eq. (15.17). Then the most offending harmonic n is determined as the integer closest to $Q_e + Q_\beta$. We next modify Q_e slightly so that

$$n - Q_e - Q_\beta = \frac{1}{2}. \tag{15.27}$$

As a result, the limiting Q_p of Eq. (15.23) is simplified, the stability condition reduces to

$$Q_p \lesssim \frac{1}{2}\sqrt{\frac{Q_\beta}{Q_e}}, \tag{15.28}$$

and the growth rate of Eq. (15.24) reduces to

$$\frac{1}{\tau} \approx \frac{Q_p\omega_0}{2}\sqrt{\frac{Q_e}{Q_\beta}}. \tag{15.29}$$

The latter becomes $\tau^{-1} \approx \omega_0/4$ when the threshold value in Eq. (15.28) is substituted. This gives a very interesting result that, once the instability threshold is reached, the growth time is always equal to $2/\pi = 0.64$ revolution turn. Because of the limitation in the evaluation of the threshold condition of Eq. (15.23), this result should be viewed as a rough estimate.

With this consideration, some computation results for the three rings under consideration are listed in Table 15.3. Here, the intensity of 4.42×10^{13} protons is used for the Brookhaven booster, where coasting beam experiments with possible e-p instabilities have been observed. We notice that the neutralization threshold

Table 15.3 Coherent centroid-oscillation instability for trapped electrons in a proton coasting beams.

	Oak Ridge SNS	Los Alamos PSR	Brookhaven Booster
Total number of protons N_p	2.10×10^{14}	4.2×10^{13}	4.42×10^{13}
Betatron tune Q_β	5.82	2.14	4.80
Proton beam radius a (m)	0.0380	0.0150	0.0150
$Q_p/\sqrt{\chi_e}$	1.2501	1.000	1.070
Most offending harmonic n	83	61	67
$Q_e = n - Q_\beta - \frac{1}{2}$	76.68	58.36	79.70
Limiting Q_p	0.1378	0.0957	0.1227
Limiting neutralization χ_e	0.0122	0.0093	0.0132
Growth rate in number of turns	0.637	0.637	0.637
Landau damping with $(\Delta Q_\beta - 2\Delta Q_{sc})/Q_\beta = 0.03$ and $\Delta Q_e/Q_e - \chi_e = 0.25$			
Limiting Q_p	0.5040	0.1853	0.4157
Limiting neutralization χ_e	0.1626	0.0343	0.151
Growth rate in number of turns	0.176	0.340	0.386

is about 1.2% for the ORNL SNS, 0.9% for the LANL PSR, and 1.3% for the BNL booster. Once the thresholds are reached, the growth rates become very fast and the corresponding growth times are less than one turn for all the four machines.

15.1.3.1 *Landau Damping*

There is another consideration of the stability of the two beam centroids, since the coherent oscillation can be stabilized by Landau damping. [14] The equation of motion of the electron, Eq. (15.16), can be viewed as an undamped oscillator driven by $\bar{y}_p$, the centroid of the proton beam. Thus, spreads in the proton betatron tune Q_β and/or proton bounce tune Q_p alone will not be able to damp the electron oscillations. To damp the electron oscillation, there must be a spread in the electron bounce tune Q_e. The same applies to the equation of motion of the proton, Eq. (15.15), driven by the centroid of the electron beam. Therefore, to provide Landau damping to the coupled-centroid oscillation, there must exist large enough spreads in both the betatron tune ΔQ_β and the electron bounce tune ΔQ_e.

First, we rewrite Eqs. (15.15) and (15.16) as

$$\left(\frac{\partial}{\partial t} + \dot{\theta}\frac{\partial}{\partial \theta}\right)^2 y_p + {Q'_p}^2 \omega_0^2 y_p = Q_p^2 \omega_0^2 \bar{y}_e - Q_{ps}^2 \omega_0^2 \bar{y}_p, \tag{15.30}$$

$$\frac{d^2 y_e}{dt^2} + {Q'_e}^2 \omega_0^2 y_e = Q_e^2 \omega_0^2 \bar{y}_p - Q_{es}^2 \omega_0^2 \bar{y}_e, \tag{15.31}$$

where the incoherent betatron tune Q'_β for the proton and incoherent bounce tune Q'_e for the electron are

$${Q'_p}^2 = Q_\beta^2 + Q_p^2 - Q_{ps}^2 \qquad \text{and} \qquad {Q'_e}^2 = Q_e^2 - Q_{es}^2. \tag{15.32}$$

Second, with the ansatz in Eq. (15.21), the coupled differential equations becomes

$$y_p = \frac{Q_p^2 \bar{y}_e - Q_{ps}^2 \bar{y}_p}{{Q'_p}^2 - \left(Q - \dfrac{n\dot{\theta}}{\omega_0}\right)^2}, \tag{15.33}$$

$$y_e = \frac{Q_e^2 \bar{y}_p - Q_{es}^2 \bar{y}_e}{{Q'_e}^2 - Q^2}. \tag{15.34}$$

Third, we need to integrate both sides with the suitable distribution functions. In doing so, two approximations are to be made: (1) only the denominators of Eqs. (15.33) and (15.34) depend on the distributions which appear in differences of squares but not the numerator, and (2) only the *slow wave* will be included. It is then easy to obtain

$$\bar{y}_p = \frac{Q_p^2}{2Q'_p \delta Q'_p} \bar{y}_e - \frac{Q_{ps}^2}{2Q'_p \delta Q'_p} \bar{y}_p, \tag{15.35}$$

$$\bar{y}_e = \frac{Q_e^2}{2Q'_e \delta Q'_e} \bar{y}_p - \frac{Q_{es}^2}{2Q'_e \delta Q'_e} \bar{y}_e, \tag{15.36}$$

where

$$\frac{1}{\delta Q'_p} = \int \frac{F_p(s)ds}{Q'_p - n + Q + \delta_p s}, \tag{15.37}$$

$$\frac{1}{\delta Q'_e} = \int \frac{F_e(s)ds}{Q'_e - Q + \delta_e s}, \tag{15.38}$$

$$\delta_p = \frac{\partial}{\partial s}\left(Q'_p(s) - \frac{n\dot{\theta}(s)}{\omega_0}\right)_{s=0}, \tag{15.39}$$

$$\delta_e = \left(\frac{\partial Q'_e(s)}{\partial s}\right)_{s=0}, \tag{15.40}$$

and Q_p, Q'_p, Q_{ps}, Q_e, Q'_e, Q_{es} in Eqs. (15.35) to (15.38) are all evaluated at $s = 0$. Here, s being a generic variable, which can represent amplitude, momentum spread, etc., while $F_p(s)$ and $F_e(s)$ are distributions normalized to unity for the protons and electrons. From Eqs. (15.35) and (15.36), it is easy to get

$$\left(2\delta Q'_p + \frac{Q_{ps}^2}{Q'_p}\right)\left(2\delta Q'_e + \frac{Q_{es}^2}{Q'_e}\right) - \frac{Q_p^2 Q_e^2}{Q'_p Q'_e} = 0. \tag{15.41}$$

Now following Laslett, *et al.*, semi-circular distributions, [14]

$$F_p(s) = \frac{2}{\pi \hat{s}_p^2}\sqrt{\hat{s}_p^2 - s^2} \qquad \text{and} \qquad F_e(s) = \frac{2}{\pi \hat{s}_e^2}\sqrt{\hat{s}_e^2 - s^2}, \tag{15.42}$$

are assumed for both the protons and electrons. One obtains

$$\begin{cases} 2\delta Q'_p = Q'_p - n + Q + i\bar{\Delta}_p, \\ 2\delta Q'_e = Q'_e - Q - i\bar{\Delta}_e, \end{cases} \tag{15.43}$$

where

$$\begin{cases} \bar{\Delta}_p = \sqrt{\Delta Q_p^2 - (Q - n + Q'_p)^2}, \\ \bar{\Delta}_e = \sqrt{\Delta Q_e^2 - (Q - Q'_e)^2}, \end{cases} \tag{15.44}$$

while ΔQ_p and ΔQ_e are the actual half spread of Q'_p and Q'_e in these distributions and are related to δ_p and δ_e in Eqs. (15.39) and (15.40) by

$$\Delta Q_p = \hat{s}_p \delta_p = \hat{s}_p \frac{\partial}{\partial s}\left(Q'_p(s) - \frac{n\dot{\theta}(s)}{\omega_0}\right)_{s=0}, \tag{15.45}$$

$$\Delta Q_e = \hat{s}_e \delta_e = \hat{s}_e \left(\frac{\partial Q'_e}{\partial s}\right)_{s=0}. \tag{15.46}$$

Equation (15.43) is obtained via the integral [10]

$$\int_{-1}^{1} \frac{\sqrt{1-x^2}\,dx}{x + x_1 - i\epsilon} = \pi\left[x_1 + i\sqrt{1 - x_1^2}\right]. \tag{15.47}$$

Substitution into Eq. (15.41) leads to a quadratic equation in the coherent coupled-oscillation tune Q, the solution of which is

$$Q = Q'_e + \frac{Q_{es}^2}{Q'_e} + d_1 - \frac{i}{2}(\bar{\Delta}_e + \bar{\Delta}_p) \pm i\left\{\frac{Q_p^2 Q_e^2}{Q'_p Q'_e} - \left[d_1 + \frac{i}{2}(\bar{\Delta}_e - \bar{\Delta}_p)\right]^2\right\}^{1/2}, \tag{15.48}$$

where

$$d_1 = \frac{1}{2}\left[\left(n - Q'_p - \frac{Q_{ps}^2}{Q'_p}\right) - \left(Q'_e + \frac{Q_{es}^2}{Q'_e}\right)\right]. \tag{15.49}$$

From Eq. (15.48), it is easy to see that stability requires

$$\mathcal{R}e\left\{\frac{Q_p^2 Q_e^2}{Q'_p Q'_e} - \left[d_1 + \frac{i}{2}\left(\bar{\Delta}_e - \bar{\Delta}_p\right)\right]^2\right\}^{1/2} \leq \frac{1}{2}\left(\bar{\Delta}_e + \bar{\Delta}_p\right). \tag{15.50}$$

This criterion is equivalent to, after considerable amount of algebra,

$$\bar{\Delta}_p \bar{\Delta}_e \geq \frac{Q_p^2 Q_e^2}{Q'_p Q'_e}\left[1 + \left(\frac{2d_1}{\bar{\Delta}_p + \bar{\Delta}_e}\right)^2\right]^{-1}. \tag{15.51}$$

Within a narrow band of instability, associated with the resonance $d_1 \approx 0$, or $n - Q'_p - Q \approx Q_{ps}^2/Q'_p$ and $|Q'_e - Q| \approx Q_{es}^2/Q'_e$, the stability limit can be simplified. With the substitution of Eq. (15.44), we finally arrive at

$$\left[\Delta Q_p^2 - \left(\frac{Q_{ps}^2}{Q'_p}\right)^2\right]^{1/2}\left[\Delta Q_e^2 - \left(\frac{Q_{es}^2}{Q'_e}\right)^2\right]^{1/2} \geq \frac{Q_p^2 Q_e^2}{Q'_p Q'_e}. \tag{15.52}$$

Because square roots are involved, we also require

$$\Delta Q_p > \left|\frac{Q_{ps}^2}{Q'_p}\right| \qquad \text{and} \qquad \Delta Q_e > \left|\frac{Q_{es}^2}{Q'_e}\right|. \tag{15.53}$$

As an approximation, $Q'_p \sim Q_\beta$ implying that $Q_{ps}^2/Q'_p \sim 2\Delta Q_{sc}$, where ΔQ_{sc} is the linear space-charge tune shift of the proton beam. Similarly, we can write $Q_{es}^2/Q'_e \sim Q_e \chi_e$, which is twice the linear space-charge tune shift of the electron beam. The stability condition then simplifies to

$$\left[\Delta Q_\beta^2 - 4\Delta Q_{sc}^2\right]^{1/2}\left[\Delta Q_e^2 - \chi_e^2 Q_e^2\right]^{1/2} \gtrsim \frac{Q_p^2 Q_e}{Q_\beta}. \tag{15.54}$$

Because of the square roots on the left side of Eq. (15.54), we also require for stability,

$$\Delta Q_\beta \geq 2\Delta Q_{sc} \qquad \text{and} \qquad \frac{\Delta Q_e}{Q_e} \geq \chi_e. \tag{15.55}$$

It is important to point out that, unlike Eq. (15.22), the space-charge self-force terms of Eqs. (15.15) and (15.16) do not drop out when averaged over the distributions. The physical reason is that finite betatron tune spread is assumed and

Landau damping is of concern here. Equation (15.55) just says that since the space-charge self-force shifts the incoherent betatron tune downward, the half spread of the betatron tune must be large enough to counteract this downward shift, so that the spread will cover the coherent excitation to achieve Landau damping. Same comment applies to the spread of the electron bounce tune.

The spread in the electron bounce frequency is difficult to measure. However, when instability occurs, the electron bounce frequency is very close to the coherent instability frequency, which is the same for the proton beam and the electron. Thus measuring the coherent transverse oscillation frequency of the proton beam, we can infer the electron bounce frequency. According to the measurement at PSR, $\Delta Q_e/Q_e \sim 0.25$. Assuming that the neutralization factor is small, we may set the half maximum fractional spread of the electron bounce tune to be $\Delta Q_e/Q_e - \chi_e \sim 0.1$, and the half maximum fractional spread of the betatron tune in excess of twice the space-charge tune shift is $(\Delta Q_\beta - 2\Delta Q_{sc})/Q_\beta \sim 0.03$. The limiting Q_p and neutralization factor χ_e can now be computed and are also listed in Table 15.3. For the ORNL SNS and the Brookhaven booster, the threshold neutralization factors have been increased to 16.3% and 15.1%, respectively, which are more than ten times. For the LANL PSR, however, the neutralization threshold χ_e becomes $\sim 3.4\%$, an increase of less than four times. Further increase in threshold requires larger spreads in Q_e and Q_β. In fact, it has been demonstrated that anti-damping can even happen unless there is a large enough overlap between ΔQ_β and ΔQ_e. [13] Notice that these stability limits of the neutralization factor can be sensitive to the distributions of the betatron tune and the electron bounce tune.

A stability condition has also been derived by Schnell and Zotter [13] assuming parabolic distributions for the betatron tune and the electron bounce tune, but without consideration of the space-charge self-forces. They obtain

$$\frac{\Delta Q_\beta}{Q_\beta}\frac{\Delta Q_e}{Q_e} \gtrsim \frac{9\pi^2}{64}\frac{Q_p^2}{Q_\beta^2}. \tag{15.56}$$

Notice that the Schnell–Zotter criterion is essentially the same as the Laslett–Sessler–Möhl criterion, if we interpret ΔQ_β of the former as the half spread of the betatron tune *in excess* of twice the space-charge tune spread of the proton beam, and ΔQ_e as the half spread of the electron bounce tune *in excess* of twice the space-charge tune spread of the electron beam. The factor $9\pi^2/64$ in Eq. (15.56) is probably a form factor of the parabolic distributions. The derivation in this section can be generalized when we notice that both Q_{ps}^2/Q_p' and Q_{es}^2/Q_e' in Eq. (15.52) come from, respectively, the $\bar{y}_e$ term in Eq. (15.15) and the $\bar{y}_p$ term in Eq. (15.16). Thus, Q_{ps}^2 and Q_{es}^2 can be extended to include

the perturbations of oscillations coming from all types of impedances of the accelerator ring including space-charge as well as wall-image effects. In that case, the Schnell–Zotter stability criterion should be valid if we interpret ΔQ_β as the half spread of the betatron tune in excess of what is necessary to cope with the instabilities of the single proton beam, and ΔQ_e as the half spread of the electron bounce tune in excess of what is necessary to cope with the instabilities of the single electron beam.

15.1.4 *Production of Electrons*

As seen in the previous section, the *e-p* coherent centroid-oscillation instability depends strongly on the neutralization factor, or the amount of electrons trapped inside the proton bunch. Thus, the next issue of importance will be the source of electron production. Electrons generated inside the vacuum chamber can be categorized into primary and secondary. Primary electrons come mainly from three sources: photoelectrons, ionization of residual gases, and electrons produced by stray beam particles striking the chamber wall. On the other hand, secondary electrons are electrons generated at the walls of the vacuum chamber when primary electrons strike the walls.

15.1.4.1 *Primary Electrons*

It is customary to quantify the generation by n'_e, which is the number of primary electrons generated by one positively-charged beam particle in one unit length of path. The rate of photo-emission may be estimated as follows. The number of radiation photons emitted per beam particle of unit charge in one unit length of dipole is [17]

$$\frac{dN_\gamma}{ds} = \frac{5\alpha\gamma}{2\sqrt{3}\rho}, \tag{15.57}$$

where $\alpha \approx 1/137$ is the fine-structure constant, γ is the Lorentz factor of the beam particle and ρ is the radius of curvature of the particle path. The rate at which photo-electrons are generated is therefore

$$n'_{e(\gamma)} = Y_\gamma \frac{dN_\gamma}{ds}, \tag{15.58}$$

where Y_γ is the photo-electron yield coefficient and is dependent on the properties of the wall surface and the photon energy. For many materials, however, Y_γ is approximately a constant of the order 0.1, over a fairly wide energy range from a few eV to tens of keV. [18] For a passage of all the bending dipoles in a revolution

turn, the total number of photo-electrons produced becomes

$$N_{e(\gamma)} = Y_\gamma \frac{5\pi\alpha\gamma}{\sqrt{3}}, \tag{15.59}$$

which is independent of the bending radius of the dipoles and is only proportional to the energy of the beam particles. Since the radius of a high-energy hadron ring is roughly proportional to beam energy, $n'_{e(\gamma)}$ becomes almost the same for all hadron rings. The largest hadron ring proposed is the 233-km Very Large Hadron Collider (VLHC) with the dipole bending radius of the bending magnets $\rho = 35$ km and beam energy 175 TeV. We obtain $n'_{e(\gamma)} \approx 5.62 \times 10^{-3}/p/\text{m}$. For the 20-TeV 82.955-km Superconducting Super Collider (SSC) that has been terminated, the dipole bending radius is $\rho = 10.1$ km, giving $n'_{e(\gamma)} \approx 2.22 \times 10^{-3}/p/\text{m}$. For the 7-TeV Large Hadron Collider (LHC) at CERN under construction, the bending radius of the dipoles is $\rho = 2804$ m and thus $n'_{e(\gamma)} \approx 2.47 \times 10^{-3}/p/\text{m}$. If we continue this estimation to the Fermilab Tevatron, which has dipole bending radius $\rho = 754.1$ m, we find $n'_{e(\gamma)} \approx 1.49 \times 10^{-3}/p/\text{m}$ for the 1-TeV proton beam. However, this Tevatron estimate is incorrect because the energy of the radiation photon will be too tiny leading to a vanishingly small secondary-electron yield Y_γ. The radiation photons has a critical value of

$$E_c = \frac{3\hbar c\gamma^3}{2\rho}, \tag{15.60}$$

where $\hbar$ is the reduced Planck constant ($\hbar c = 1.973 \times 10^{-7}$ eV-m). We obtain $E_c = 54.8$ keV for the VLHC, 284 eV for the SSC, 43.8 eV for the LHC, but only 0.48 eV for the Tevatron. Since the work function of a metallic surface is typically a few eV, it will be nearly impossible for the photons emitted from the Tevatron to release secondaries from the walls of the vacuum chamber. Photo-emission is therefore important for the VLHC and the LHC, but can be ignored for the Tevatron.

Naturally, we would like to see the radiation photons absorbed at the outside wall of the vacuum chamber near the exit ends of the dipoles so that the photo-electrons would be generated and confined by the dipole fields. Unfortunately, because of the shallow angle of impact at the wall, the radiation photons are mostly reflected instead and eventually illuminate the whole chamber. In short, this will lead the undesired situation of having photo-electrons generated and multipactored rather uniformly in any part of the chamber. To prevent such occurrence, the reflectivity of the chamber wall must be reduced. This has been accomplished at the LHC by impressing a 'sawtooth' pattern on the beam screen that forms the inner part of the chamber wall. [18] The sawtooth pattern

makes the photons impact perpendicularly to the local surface, which reduces reflectivity substantially. The measured residual reflection can be described roughly by a $\cos^2\phi$ or $\cos^3\phi$ distribution, where ϕ is the angle of the reflected photon direction with respect to the horizontal plane. For electron rings, the much larger amount of radiation photons are usually directed to an antichamber and are absorbed there.

The next source of electron production is through the collision of the protons with the residual gases in the vacuum chamber. At the vacuum pressure of 1×10^{-7} Torr (1 atm = 760 Torr) and room temperature ($T = 300°$K), there is a residual gas density of

$$\rho_I = \frac{N_A p}{RT} = 3.20 \times 10^{15} \text{ molecules/m}^3, \tag{15.61}$$

where the ideal gas law has been used, with $N_A = 6.022 \times 10^{23}$ being the Avogadro number and $R = 82.55 \times 10^{-6}$ Atm-m^{3}K^{-1} the gas constant. For singly-charged beam particles at ultrarelativistic energies, the expected average ionization cross-section is $\Sigma_I = 1$–2 Mb (or 1–2×10^{-22} m^2) for CO and N_2 and 0.2 Mb for H_2. The cross-section increases with the square of the atomic number of the ion. It also increases by several orders of magnitude for lower-energy beam particles. The number of electrons generated by one proton per meter can be written conveniently as

$$n'_{e(i)} = \rho_I \Sigma_I = 3.20 \Sigma_I[\text{Mb}] \times p[\text{Tor}] \times \frac{300}{T[\text{K}]}, \tag{15.62}$$

where p is the chamber pressure and T is the chamber temperature. Continuing the previous example at $p = 1 \times 10^{-7}$ Tor and $T = 300°$K, $n'_{e(i)} = 6.4 \times 10^{-7}/p/\text{m}$, where $\Sigma_I = 2$ Mb has been used.

Stray beam particles striking the chamber wall can release a large number of electrons, especially impinge under shallow angles, nearly parallel to the wall surface. The secondary-electron yield for beam particle or ion impact at an angle ϕ with respect to the surface normal is approximately given by

$$Y_{pl} \approx \Lambda \left(\frac{dE}{dx}\right)_e \cos^{-1}\phi, \tag{15.63}$$

where $(dE/dx)_e$ is the stopping power of the electron and $\Lambda \approx 5$–20 mg/(MeV-cm^2) for projectiles. The dependency on the incident angle is good up to $\phi = 89.8°$. A more convenient effective secondary-electron yield coefficient η_{eff} can be defined by integrating over all angles, so that the number of electrons generated generated from stray protons hitting the chamber wall is given by

$$n'_{e(pl)} = \eta_{\text{eff}} n'_{pl}, \tag{15.64}$$

where n'_{pl} is the number of lost protons per stored proton per unit length of beam traversal. At the LANL PSR, this effective electron yield coefficient has been estimated to be $\eta_{\text{eff}} \approx 100$–$200$. [19] Most of the beam loss usually takes place at injection. The SNS injection is through $n_{\text{inj}} = 1225$ revolution turns. Assuming a $f = 1.2\%$ loss, the number of lost protons per unit length per injected proton is $n'_{(pl)} = f/(n_{\text{inj}}C) = 4.44 \times 10^{-8}/p/\text{m}$, and the number of primary electrons generated is $n'_{e(pl)} = 4.44 \times 10^{-6}/p/\text{m}$, where for definiteness, the effective secondary-electron yield has been taken as $\eta_{\text{eff}} = 100$. For the PSR and the BNL Booster, this turns out to be $n'_{e(pl)} = 6.65 \times 10^{-6}/p/\text{m}$ and $1.98 \times 10^{-5}/p/\text{m}$, respectively.

15.1.4.2 *Secondary-Electron Yield*

A more important source of electron production is when an electron strikes the walls of the beam pipe and releases secondary electrons. These secondary electrons can cause multipactoring and generate an avalanche of electron cloud. Secondary emission depends on the secondary-electron yield coefficient (SEY) $\delta(\phi, E_0)$ of the chamber surface, where ϕ is the incident angle and E_0 is the incident electron energy.

The experimental measurements of secondary-electron yields $\delta(E_0)$ for an electron incident perpendicularly as functions of incident energy E_0 on some metallic surfaces are shown in Fig. 15.7. The general shape of the normal incident SEY curve can be fitted approximately by the expression [10]

$$\delta(x) = \delta_{\text{max}} 1.11 x^{-0.35} \left(1 - e^{-2.3x^{1.35}}\right), \tag{15.65}$$

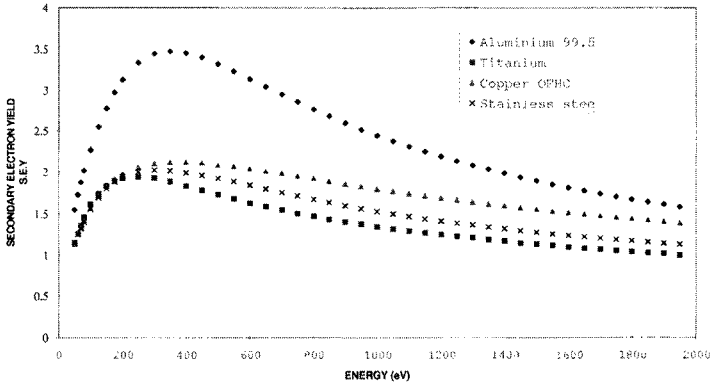


Fig. 15.7 Measured secondary-emission yields $\delta(E_0)$ for some metallic surfaces at normal incident and various electron energies. (Courtesy Hilleret [21])

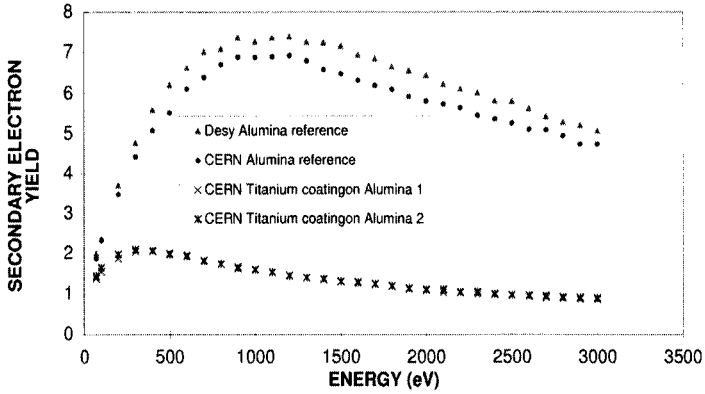


Fig. 15.8 Measured secondary-emission yields $\delta(E_0)$ for some insulator surfaces at normal incident and various electron incident energies. (courtesy Hilleret [21])

where $x = E_0/E_{\max}$ and $\delta_{\max}$ is the peak value of the SEY curve which occurs at energy $E_{\max}$. The peak value $\delta_{\max}$ is important, because it determines mostly whether an electron cloud will build up or not. The SEY depends very much on the surface chemistry. It is very sensitive to the surface roughness, its exposure to air, and how it is conditioned. For example, the peak SEY of pure aluminum is less than one. However, on samples of aluminum vacuum chambers, the measured yield has a maximum between 2.5 and 3.5, as illustrated in the measurements shown in Fig. 15.7. Both the stainless steel and copper used in the fabrication of accelerator vacuum chambers have $\delta_{\max} \sim 2$. The SEY of an insulator surface is usually very high with a maximum $\delta_{\max} \sim 7$ and peaks at the much higher incident electron energy $E_{\max} \sim 1000$ eV. However, as shown in the Fig. 15.8, the SEY can be very much reduced with a coating of Titanium. For the CERN LHC, the beam pipe is coated with non-evaporable getter (NEG) materials for their anti-multipactoring properties. Figure 15.9 shown that the maximum SEY can be reduced to $\delta_{\max} \lesssim 1.2$ after the wall surfaces coated with

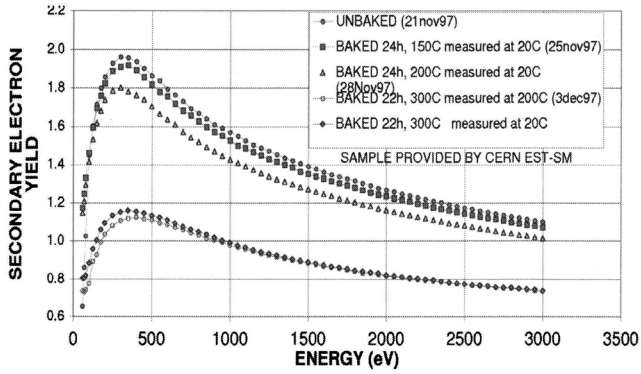


Fig. 15.9 Laboratory measurements of SEYs of TiZrV NEG coatings. It is evident that after two hours of heat treatment at 300°C, the maximum reduces to $\delta_{\max} \lesssim 1.2$. (courtesy Rossi. [23])

NEG are baked at 300°C for two hours.

Another important issue about the normal incident SEY curve is its value at almost zero incident electron energy. A nonzero value implies that there will be a substantial number of electrons of very low energies generated or reflected. Although these electrons will stay near the wall surfaces because of their very low energies, however, they can easily gain enough energy to travel to the other side of the vacuum chamber and initiate further secondary emissions upon the passage of beam bunches. Thus the simulation of electron-cloud generation using a SEY curve with zero or nonzero value at very low incident energy can lead to very different results. The measured SEY at almost zero incident electron energy is roughly 0.3–0.4 for most surfaces. Furman and Pivi provided two sets of parameters for accurately fitting two particular SEY data sets, one for stainless steel and one for copper. [24] These parameterizations are similar to Eq. (15.65) but with the correct value at zero incident electron energy taken into account.

The energy spectrum of the secondary-emitted electron has a general shape shown in Fig. 15.10. This particular plot is the measured energy spectrum for an unconditioned sample of stainless steel at normal incidence and at incident energy $E_0 = 300$ eV. The emitted electrons has an energy range of $0 \leq E \leq E_0$. [20] The spectrum exhibit three different components: the elastically scattered electrons (the narrow peak at the far right), the redifused electrons (the central region) and the true secondary-emitted electrons (the low-energy region). Accordingly, the SEY is the sum of three contributions: the elastically scattered δ_{el}, rediffused δ_{re}, and the true secondary δ_{ts}, and each component contributes differently.

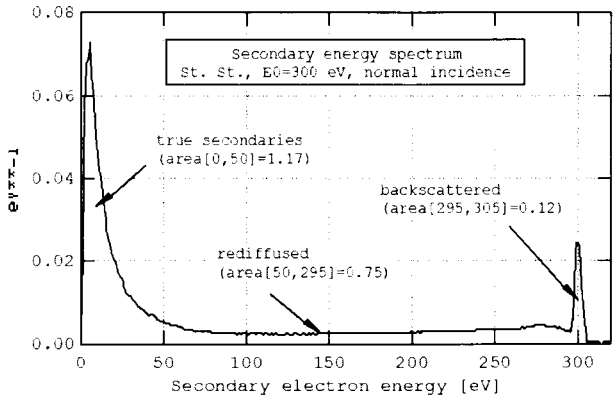


Fig. 15.10 Measured spectrum of second-emission electrons for an unconditioned stainless-steel sample at $E_0 = 300$ eV and normal incidence consists of three components: the elastically reflected electrons (narrow peak at E_0), the rediffused electrons (central flat region), and the true second-emission electrons (low-energy region). (Courtesy Kirby. [20])

The build-up of the electron cloud can be best characterized by an effective SEY coefficient δ_{eff}, which is the SEY over all angles of incidence ϕ and incident energies E_0: [28]

$$\delta_{\text{eff}} = \int dE_0 d\phi \frac{d^2N}{dE_0 d\phi} \delta(\phi, E_0). \tag{15.66}$$

Here, $d^2N/(dE_0 d\phi)$ is the differential spectrum of the incident electrons, and is also a complicated function of the bunch intensity, beam fill pattern, vacuum chamber geometry, etc. Thus δ_{eff} represents the number of secondary electrons generated by one primary electron. As a result, chamber walls with $\delta_{\text{eff}} < 1$ act as net absorbers of electrons. Primary electrons are generated during injection and the electron linear density increases linearly until the electron production is balanced by the electron absorption rate at the chamber walls. This equilibrium is reached in the time duration Δt_{tr}, which is the characteristic traversal time of an electron across the chamber from one side to the other under the influence of the beam. Thus the build-up of electron-cloud is dominated by the production of primary electrons. This situation happens mostly when the bunch intensity is low, the peak SEY is small, and/or the bunch spacing is large.

When $\delta_{\text{eff}} > 1$, the number of secondary multiplies and the chamber walls act as net generators of electrons. The build-up of the electron cloud resembles an avalanche until the electron density becomes so large that the space-charge force is strong enough to prevent any newly generated electron from leaving the chamber walls. When saturation is reached, the electron linear density will become rather insensitive to the initial primary electron density n'_e but rather comparable to the beam neutralization level. This situation happens when the bunch intensity is large, the peak SEY is large, and/or the bunch spacing is small. The growth is mostly exponential and the growth time τ is related to the effective SEY δ_{eff} by

$$\delta_{\text{eff}} = e^{\Delta t_{tr}/\tau}. \tag{15.67}$$

Since δ_{eff} is a well-defined quantity in Eq. (15.66) and the e-folding build-up time τ is also a well-defined quantity from simulation, Eq. (15.67) can be viewed as a re-definition of the less well-defined characteristic traversal time Δt_{tr} of an electron from one side of the chamber wall to the other.

15.1.4.3 *Electron-Cloud Build-up and Multipactoring*

Gröbner was the first to derive a condition for multipactoring. Consider an electron at rest on the surface of the beam pipe of radius b. [26] The momentum

it gains when a bunch of length L_b containing N_b particles each of charge Ze passes by is given by, in the transverse direction,

$$\Delta p = \frac{e\mathcal{E}_r L_b}{\beta c}, \tag{15.68}$$

where βc is the longitudinal velocity the beam bunch and

$$\mathcal{E}_r = \frac{eZN_b}{2\pi\epsilon_0 b L_b} \tag{15.69}$$

is the average radial electric field experienced by the electron, which is considered roughly not moved during the bunch passage. The transverse velocity gained by the electron is

$$v = \frac{e\mathcal{E}_r L_b}{m_e \beta c}, \tag{15.70}$$

with m_e being the electron mass. Thus the time required by the electron to move towards the opposite side of the beam-pipe wall, a distance $2b$, so as to start a second emission is

$$\Delta t_{tr} = \frac{\beta b^2}{Z r_e N_b c}, \tag{15.71}$$

where $r_e = e^2/(4\pi\epsilon_0 m_e c^2) = 2.818 \times 10^{-15}$ m is the classical electron radius. This process is repeated if this transit time Δt_{tr} happens to be exactly equal to the time $s_b/(\beta c)$ for the next bunch to pass by, with s_b representing the bunch spacing. We therefore arrive at a resonance condition

$$\frac{\beta^2 b^2}{ZN_b r_e} = s_b \tag{15.72}$$

for multipactoring to occur. This resonance process is illustrated schematically in Fig. 15.11. A Gröbner parameter,

$$G = \frac{ZN_b r_e s_b}{\beta^2 b^2}, \tag{15.73}$$

can be defined with the resonance condition given by $G = 1$. When the bunch spacing is too short so that $G < 1$, an electron is not able to reach the other side of the beam pipe within the beam gap and there will not be any multipactoring. When the bunch spacing is too long so that $G > 1$, the secondary electrons produced at the other side of the beam-pipe wall will not experience the acceleration by next bunch. They may be reabsorbed by the wall surface and not be able to multipactor again.

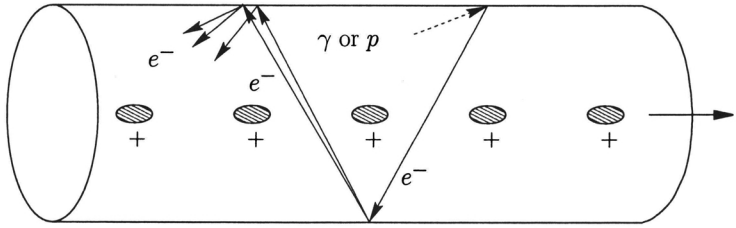


Fig. 15.11 An electron, created at the wall by a photon or a stray proton, is accelerated by a passing beam bunch. The electron receives just the right amount of energy that when it strikes the opposite side of the beam pipe at the moment the next bunch just passes by. The secondary electrons generated by this primary electron are accelerated by this bunch and the process is repeated, resulting in multipactoring. This is the Gröbner resonance condition given by Eq. (15.72). The electrons appear to move backward because the figure is drawn in the rest frame of the beam bunches.

However, the Gröbner multipactoring resonance condition suggested by Eq. (15.72) is far too stringent. Electrons coming out from secondary emission usually have very low energies. Instead of being reabsorbed immediately after the passage of the bunch, they usually stay near the chamber wall surface. Thus they can sometimes be accelerated when the next bunch comes along later and can therefore produce a new generation of secondaries. Even if the bunch spacing is too short to satisfy the resonance condition, the electrons can interact with several passing bunches to accumulate sufficient energy to arrive at the opposite side of the chamber wall to initiate secondaries.

Violation of the Gröbner condition has been reported. An example in the measurements recorded at the CERN SPS, where the thresholds for multipactoring at $s_b = 5$ ns, 25 ns, and 50 ns were found to be at bunch intensities $N_b = 8\times10^9$, 5×10^{10}, and 1×10^{11}. [27] The relationship of the threshold N_b with s_b is roughly linear rather than $1/s_b$ as suggested by Eq. (15.72). Nevertheless, Gröbner condition is important because it suggests that multipactoring depends on the bunched structure of the beam, rather than just the intensity of the beam. This concept was verified at the CERN SPS. It was found that with 20 bunches, the threshold current was about 120 mA. However, the vacuum remained stable with coasting beams of more than 25 A. [26] For a truly coasting beam at the center of a cylindrical beam pipe, an electron on the beam-pipe surface will be accelerated towards the beam. However, it will be decelerated when it leaves the beam. Thus there will not be any net gain in energy when it arrives at another part of the beam-pipe surface. As a result, for a very long proton beam, such as the one in the LANL PSR, net gain in energy is only provided significantly by the two ends of the beam. The accurate longitudinal distribution of the beam

is therefore an essential ingredient in the determination electron-cloud build-up in the beam. Of course, we are not saying that multipactoring will never take place with an intense coasting beam. When the threshold of the *e-p* coupled instability is exceeded, the electrons will be oscillating about the proton beam with increasing amplitudes. Once the electrons reach the walls of the beam pipe with sufficient energy, secondary emission will result (Exercise 15.2).

15.1.4.4 *Simulations*

As we have seen, the saturation of electron cloud is a delicate balance between the space-charge properties of the trapped electron distribution and the SEY of the chamber walls. This complicated process depends on the beam intensity, the fill pattern, the geometry of the vacuum chamber, etc., and there is no simple formula that can speculate the results. To determine whether there is a large build-up of electron cloud, one usually resorts to simulations. The first simulation code for electron-cloud build-up for short bunches was written by Ohmi, which serves to explain coupled-bunch instabilities observed with the positron beams at the KEK photon factory. [29] There are many similar codes. To mention a few, there is the code POSINST written by Furman to study electron-cloud build-up at the SLAC B-factory [30] and the code ECLOUD written by Zimmermann to analyze possible electron-cloud generation at the LHC. [32] As an illustration, we outline below the electron-cloud issues of the proposed Fermilab Main Injection upgrade simulated by POSINST following a preliminary simulation by Furman. [28]

There is a plan to upgrade the Fermilab Main Injector to a proton driver by increasing its bunch intensity fivefold from $N_b = 6 \times 10^{10}$ to 30×10^{10} per bunch. The Main Injector has a circumference of $C = 3319.4$ m. The injection will be from a 25-mA 8.938-GeV linac filling the consecutive 52-MHz rf buckets (588 buckets in total) of the Main Injector in $n_{\mathrm{inj}} = 90$ revolution turns. [31] Each bunch has an rms length of 2.52 ns (75 cm). The rf wavelength is 19.93 ns. Assuming the longitudinal distribution to be Gaussian and taking four sigmas as the total length, consecutive bunches are separated by a gap of 8.87 ns. The transverse beam size is assumed to be circular with an average radius of 5 mm. The Main Injector beam pipe is made of stainless steel with an elliptical cross-section with major and minor radii 6.15 and 2.45 cm. The peak SEY is taken to be $\delta_{\mathrm{max}} = 1.3$. The simulation consists of slicing the full bunch length into 10 slices longitudinally and the bunch gap into 9 slices. Each slice or time step is therefore roughly of length 1 ns. Transversely space-charge forces of the electron cloud are applied for every time step on a 2D transverse grid of 5 mm $\times$ 5 mm. The simulation is performed on a section of length 10 cm at 305°C and 20 nTor.

It will take too much computer time to simulate the whole injection process of $n_{\text{inj}} = 90$ turns. Instead, we just perform the simulation for the last injection turn, when the highest bunch intensity reaches $N_b = 3 \times 10^{11}$. There will be an expected injection loss of 1.2%. According to Eq. (15.64), the average number of primary electrons generated by one stray proton per unit traversal length is $n'_{e(pl)} = 4.02 \times 10^{-6}/p/\text{m}$, assuming a secondary yield of $\eta_{\text{eff}} = 100$. The average number of primary electrons generated through ionization of residual gases by one proton per unit length is $n'_{e(i)} = 1.26 \times 10^{-7}/p/\text{m}$, assuming a temperature of 305°K and ionization cross-section $\Sigma_I = 2$ Mb. Thus in a length of $L = 10$ cm, the total number of primary electrons generated by the a bunch of $N_b = 3 \times 10^{11}$ is $N_e = (n'_{e(pl)} + n'_{e(i)})LN_b = 1.24 \times 10^4$. These N_e primary electrons are represented by $M_e = 10$ macro-particles of charge $N_e/M_e = 1.24 \times 10^3$.

In the simulation, we first populate 252 consecutive rf buckets† with the present bunch intensity of 6×10^{10}. The region of simulation can be either a drift or inside a dipole of magnetic field 0.1 T. The resulting saturated linear densities of electrons are shown in the left plot of Fig. 15.12. We see that

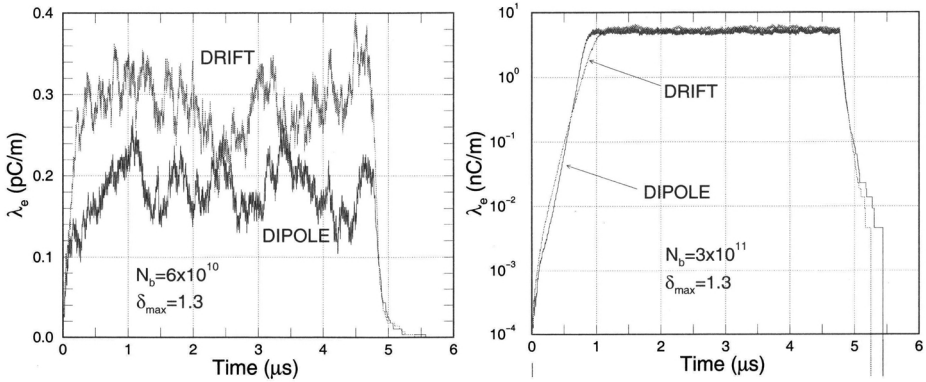


Fig. 15.12 Simulation results of POSINST showing build-up of electron-cloud linear density in the proposed upgraded Fermilab Main Injector injected with 252 bunches during one passage, each bunch containing $N_b = 6 \times 10^{10}$ protons (left) and 3×10^{11} protons (right). An elliptical stainless steel beam pipe with peak SEY $\delta_{\text{max}} = 1.3$ has been assumed. Note that the vertical scale is linear in pC/m for the left plot but logarithmic in nC/m for the right. Saturation has been reached in less than 0.5 μs for the lower-intensity beam. For the higher-intensity beam, electron build-up shows an exponential growth time of $\tau \approx 115$ ns for the drift and $\tau \approx 82$ ns inside a dipole. Saturation is reached in about 1 μs.

†We choose only 252 bunches because we find in the simulations that saturation will well be reached within 1 μs (or 53 bunch passages) when bunch intensity is $N_b = 6 \times 10^{10}$, and within 0.5 μs (or 26 bunch passages) when bunch intensity is $N_b = 3 \times 10^{11}$. However, more bunch passages will be necessary near the threshold where the electron-cloud build-up is very much slower. For example, at $N_b = 1.25 \times 10^{11}$, we need to populate up to 588 bunches.

saturation takes place within 0.5 μs or the passage of about $n_b = 26$ bunches. We learn from above that the primary electrons produced will have a linear density of $\lambda_e = e(n'_{e(pl)} + n'_{e(i)})N_b n_b = 1.0$ pC/m. Thus the saturated electron linear densities of ~ 0.3 pC/m in the drift and ~ 0.2 pC/m in the dipole just demonstrate a balance between primary-electron generation and absorption at the chamber walls. We see that the electron density at the drift is about 50% larger. The simulations also output the effective SEYs. We find them to be $\delta_{\text{eff}} \approx 0.8$ and 0.7, respectively, for the drift and the dipole. Using the effective SEY's, a more precise estimate can be obtained for the saturated electron linear densities (see Exercise 15.7).

The bunch intensity is next increased to $N_b = 3\times10^{11}$ and the simulations are repeated for both situations of in a drift and inside a dipole. The electron-cloud linear densities are shown in the right plot of Fig. 15.12. We see that the electron densities grow exponentially by many orders of magnitude and finally become saturated at $\lambda_e \sim 5.0$–5.5 nC/m, with an e-folding growth time of $\tau \approx 115$ ns for the drift and $\tau \approx 82$ ns inside a dipole. Note the different vertical scales in the two plots: logarithmic in nC/m for the right and linear in pC/m for the left. Since the linear density of the proton beam averaged over a whole bunch spacing is $\lambda_p = 8.5$ nC/m, the neutralization reached is $\chi_e = \lambda_e/\lambda_p = 0.60$–$0.65$.

In Fig. 15.13, we plot the saturated electron linear density versus bunch intensity. We see that the saturated electron increases by almost four orders of magnitude both in the drift and inside the dipole as the bunch intensity increase from $N_b = 1.0 \times 10^{11}$ to 1.5×10^{11}. Unambiguously, there is a threshold for electron-cloud build-up around $N_b \sim 1 \times 10^{11}$.

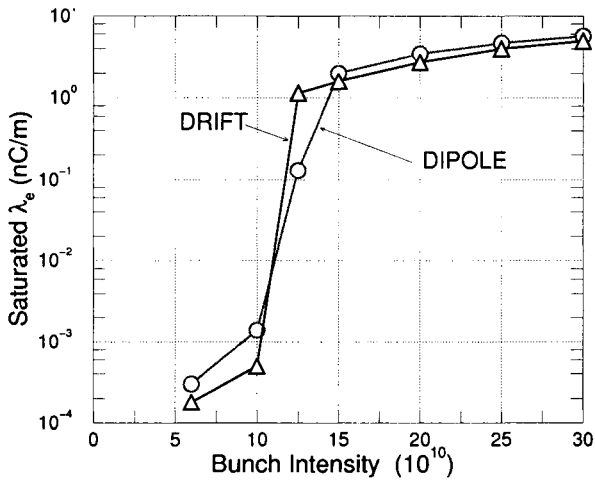


Fig. 15.13 Plot of saturated electron linear density versus bunch intensity. A threshold of electron-cloud build-up is evident around bunch intensity $N_b = 1 \times 10^{11}$ both in a drift or inside a dipole.

The current density J_e of the electron cloud striking the wall surface of the vacuum chamber were also recorded during the simulations. The energy spectra, dJ_e/dE, averaged over the passage of the 252 bunches are depicted in Fig. 15.14, for bunch intensity $N_b = 6 \times 10^{10}$ on the left and $N_b = 3 \times 10^{11}$ on the right. We see that the electron current density distributions when an avalanche growth occurs, as depicted in the right plot, are many orders of magnitude larger and extend to much higher energy than when there is no avalanche growth as depicted in the left plot. Note that the vertical scale in the right plot is very much larger. The total electron current densities striking the chamber walls are given by the areas under the distribution curves in Fig. 15.14, and they amount to $J_e = 3.40$ nA/cm^2 inside a drift and 2.24 nA/cm^2 inside a dipole, when bunch intensity is $N_b = 6 \times 10^{10}$, and $J_e = 118$ μA/cm^2 inside a drift and 141 μA/cm^2 inside a dipole, when bunch intensity is $N_b = 3 \times 10^{11}$. These would be amount of electron currents recorded if an electron collector were placed at the vacuum chamber.

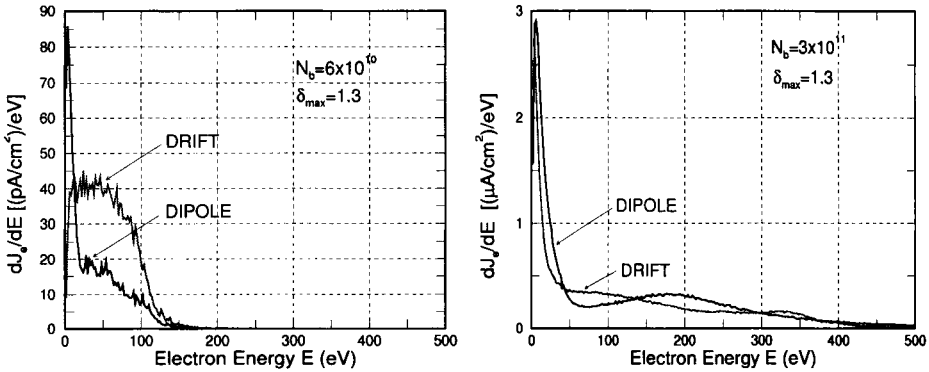


Fig. 15.14 Energy spectrum of electrons hitting the walls of the Main Injector elliptical vacuum chamber at bunch intensity $N_b = 6 \times 10^{10}$ (left) and 3×10^{11} (right). Note that the vertical scale of the right plot is very much larger than that of the left. Integration over energy results to the total electron current densities striking the walls of the beam pipe: $J_e = 3.90$ nA/cm^2 inside a drift and 2.24 pA/cm^2 inside a dipole for $N_b = 6 \times 10^{10}$, and $J_e = 118$ μA/cm^2 inside a drift and 141 μA/cm^2 inside a dipole, for $N_b = 3 \times 10^{11}$.

15.1.4.5 *Betatron Tune Shifts*

Electron cloud enhances betatron defocusing of the proton transversely and leads to a shift of the betatron tunes, both horizontal and vertical, in the upward direction. For a traversal through the electron cloud of length L, the tune shift

$\Delta\nu_\beta$ is given by (Exercise 15.8)

$$\frac{\Delta\nu_\beta}{L} = \frac{r_p \beta_\perp \rho_e}{2\gamma\beta^2}, \tag{15.74}$$

where $r_p = 1.535 \times 10^{-18}$ is the classical proton radius, γ is the relativistic factor of the proton beam, $\beta_\perp$ is the betatron function, and ρ_e is the electron density at the center of proton beam. The above simulations show that the electron densities at the center of the bunch of intensity 3×10^{11} are $\rho_e = 7.0 \times 10^{12}$ m^{-3} in the drift and 11×10^{12} m^{-3} in the dipole. Assuming 40% dipoles and 60% drifts, the average electron density is $\rho_e = 8.4 \times 10^{12}$ m^{-3}. With an average betatron function of $\beta_\perp = 25$ m, we obtain $\Delta\nu_\beta/L = 1.73 \times 10^{-5}$ m^{-1}. If we replace L by the circumference of the ring $C = 3319$ m, this betatron tune shift becomes $\Delta\nu_\beta = 0.057$, which is very big. On the other hand, around the threshold $N_b = 1 \times 10^{11}$, the electron densities are only $\rho_e \sim 0.002 \times 10^{12}$ m^{-3} in the drifts and 0.001×10^{12} m^{-3} in the dipoles. The betatron tune shift will only be $\Delta\nu_\beta \sim 1 \times 10^{-5}$.

15.1.5 *Discussion and Conclusion*

(1) In the above single-electron analysis, it appears that electrons will be cleared in the bunch gap within one rf wavelength for all the three proton rings under consideration. However, if more than $\eta \sim 10\%$ of the protons are spilled into the bunch gap, electrons will be trapped inside the proton beam in the ORNL SNS and LANL PSR. For the BNL booster, on the other hand, electrons are relatively more difficult to be trapped when there are spilled protons in the bunch gaps even if $\eta > 20\%$. This is probably due to its much larger gap-to-bunch-length ratio.

(2) For coherent centroid oscillation to become unstable, neutralization factors of $\chi_e \sim 1.2\%$, 0.9%, and 1.1% are required, respectively, for the three machines. However, spreads in the betatron frequencies and the electron bounce frequencies can provide Landau damping.

(3) The LANL PSR may accumulate protons through an injection in $\sim$ 2000 turns and the BNL booster in 300 turns. The vacuum pressures of both rings are relatively high, $\sim 1 \times 10^{-8}$ Torr for the former and $\sim 1 \times 10^{-7}$ Torr for the latter. As a result, the amount of electrons per proton produced by collision with residual gases can be as high as 1.39 and 2.33%, respectively, for the two rings. However, the electron production for the ORNL SNS via proton-ion collision is less than 1%, which is the result of a high vacuum of 1×10^{-9} Torr in the vacuum chamber.

(4) Multipactoring as a result of secondary emission is the mechanism for electron-cloud build-up. The threshold depends on the beam intensity, bunch fill pattern, geometry of the vacuum chamber cross section, maximum SEY of the chamber wall surface. Because of the complexity of the problem, the best way to investigate the possibility of electron-cloud build-up is through simulation.
(5) There is a similar proton ring called ISIS at the Rutherford Appleton Laboratory. At the injection energy of 70.4 MeV, about 2.5×10^{13} protons are stored as a continuous coasting beam, which is then captured adiabatically into two rf buckets. The protons are ramped to 0.8 GeV after which they are extracted. No *e-p* instabilities have ever been observed at ISIS either running in the bunched mode or the coasting-beam mode. This has always been a puzzle. However, when we compare ISIS with the LANL PSR, we do find some important differences. First, ISIS has a repetition rate of 50 Hz. The injection is fast, about 200 turns. On the other hand, it usually takes about 200 turns for the *e-p* instability of the PSR to develop to a point when it can be monitored. Second, ISIS has a much larger vacuum chamber, 7 cm in radius. Also the ISIS vacuum chamber is made of ceramic to limit eddy current because of the high repetition rate of 50 Hz. A wire cage is installed inside the ceramic beam pipe to carry the longitudinal return current. The wire cage does not allow transverse image current to flow, thus alleviating in some way the transverse instability. Also the cage wires have much less surface area than the walls of an ordinary metallic beam pipe. As a result, secondary emission will be reduced. The secondary emitted electrons will come out in all directions from the cage wires. The probability of them hitting another cage wire will be small, thus preventing multipactoring to occur. These may be the reasons why *e-p* instabilities have never been observed at ISIS.
(6) There are various clues to pinpoint the electron-cloud as the culprit of an instability. Some examples are direct observation of electrons using special detectors, detecting positive effect of electron-specific suppression techniques, for example, turning solenoids on and off, making correlation of vacuum pressure with beam time structure as well as instabilities, measuring betatron tune shift or beam size along bunch trains, noticing the special effect of running the ring with positron beams instead of electron beams, etc.
(7) There are a number of methods for the mitigation of the electron-cloud problems. The two main approaches are methods to suppress the electron-cloud generation and the methods to control the adverse impact of electron cloud on accelerator performance. [33] In the first category, there is the suppression of the primary or "seed" electrons, by avoiding multiple traversal of the stripping foil, by reducing the vacuum pressure, and by reducing the proton loss. The next important issue is the suppression of second emission. The vacuum cham-

ber can be coated with TiN or NEG to suppress multipactoring. Supakov and Pivi pointed out that the effective SEY can also be suppressed for a grooved metal surface. [34] Of course, increasing the transverse dimension of the vacuum chamber can also reduce the threshold of multipactoring. Both B-factories at KEK and SLAC have been able to confine the electrons to regions close to the surface of the vacuum chamber by installing low-field solenoids and thus suppress multipactoring. Unfortunately, this method is not possible for the portion of the vacuum chamber inside dipoles and quadrupoles. Beam scrubbing and installation of clearing electrodes are also able to reduce the build-up of electron cloud. Another method is the change in beam fill pattern. Increasing the spacing between consecutive bunches will certainly help. However, this will reduce the intensity of the beam. After looking into the possibility of all these, if there is still beam instabilities driven by electron cloud, we can use convention methods to deal with instabilities. Taking the LANL PSR as an example, the momentum spread of the proton beam is increased for the exchange of more Landau damping. Sextupoles and skew quadrupoles are installed to couple the more dangerous vertical beam motion into the less dangerous horizontal. Finally, the reduction of impedance, such as the cancellation of space-charge impedance by inductive inserts, will also help to push the instability threshold to higher beam intensities.

(8) At this moment, there is no simple mathematical expression that can determine the threshold for multipactoring. Computer codes have become a more and more reliable means of predicting electron-cloud issues. These codes can be divided into two categories: those that simulate electron-cloud build-up, such as the POSINST written by Furman and the ECLOUD written by Zimmermann, and those that compute beam instabilities driven by electron cloud, such as the HEADTAIL written by Rumolo [35] and the ones written by Ohmi [29] and Perevedentsev. [36] The discussion on various issues on electron cloud has become a rather forefront research topic in accelerator physics.

So far we have only given a very brief and incomplete description of electron cloud. Readers that have more interest in the subject can obtain a more thorough view by going through the proceedings of recent workshops on electron-cloud dynamics. [37]

15.2 Fast Beam-Ion Instability

In the above sections, we discuss ions trapped in an electron beam (or electrons trapped in a proton beam) causing coherent coupled ion-electron oscillation once

the intensity of the trapped ions is high enough. The best cure appears to be a gap between the consecutive bunches that is long enough for the ions to clear. If the ions are cleared in the gap, they will not accumulate inside the potential of the electron beam turn after turn and their intensity will not reach the threshold of coupled-beam instability.

However, if the linear density of the electron beam is large enough and the electron bunch is long enough, even in one pass through a region in the vacuum chamber the electron beam is able to generate and trap so many ions that coupled ion-electron occurs resulting in the emittance growth of the electron beam. This instability, called *fast-ion instability*, was first investigated by Raubenheimer and Zimmermann. [38] Instead of a long electron bunch, fast-ion instability can also occur for a long train of short electron bunches, because the gaps between consecutive bunches are usually not long enough to clear all the ions. This instability is important because of its one-pass nature and is not curable by any gap-clearing mechanism. For this reason, this instability can also happen inside a linac.

15.2.1 *The Linear Theory*

In this section, we derive the linear theory of fast-ion instability following the approach of Chao. [39] Here, we need to keep track of the gradual accumulation of ions generated.

Let $y_e(s|z)$ denotes the vertical displacement of the centroid of a slice of the electron bunch at a distance z behind the head of the bunch with s representing the location of the slice along the accelerator. If the head of the bunch passes position $s = 0$ at time $t = 0$, then s and z in $y_e(s|z)$ are related by $s = vt - z$, where v is the beam velocity. We assume that the electron beam contains N_e electrons, uniformly distribution longitudinally and transversely, has a length ℓ and horizontal and vertical radii a_H and a_V.

Let $y_I(s, t|z)$ denotes the vertical displacement of the centroid of a slice of the ions at time t and position s along the accelerator. These ions are generated by the electron slice at a distance z behind the head of the electron bunch. Since the ions are assumed to have no longitudinal velocity, s and t are not related. This explains why the argument t is needed in $y_I(s, t|z)$ but is not necessary in $y_e(s|z)$.

15.2.1.1 *The Ion Equation of motion*

Because the focusing force experienced by the ion is relative to the centroid of the electron beam, the equation of motion of the ion generated by an electron

slice z' behind the head is just

$$\frac{\partial^2}{\partial t^2} y_I(s,t|z') + \omega_I^2 \left[y_I(s,t|z') - y_e(s|vt-s) \right] = 0. \tag{15.75}$$

The second argument of the electron displacement has been substituted with $z = vt - s$ because it is the electrons in the slice of the electron bunch at $z = vt - s$ which are interacting with the ions at location s and time t. Here, only the linear force of the electron beam on the ion has been included for the linear theory in the form of the harmonic ion bounce angular frequency ω_I. All image and all image and space-charge forces are neglected. The ion bounce angular frequency ω_I is given by

$$\omega_I = \sqrt{\frac{4N_e r_u c^2}{\ell a_V (a_V + a_H) A}}, \tag{15.76}$$

where r_u is the classical radius of one atomic-mass-unit of ion (1.007276 times the proton classical radius) and A is the molecular weight of the ions. This is exactly the same as the electron bounce frequency we derived in Eq. (15.1) with the electron mass replaced by the ion mass. Although the ion is very much heavier than the electron, the electron beam size is usually very much smaller than the proton beam size. Therefore this ion bounce frequency can be very large also. For a nitrogen ion of $A = 14$ trapped inside an electron bunch containing 10^{11} particles, of total length $\ell = 1$ cm, and radius $a = 1$ mm, we find $\omega_I/(2\pi) = 70$ MHz. In case the beam transverse distribution is bi-Gaussian with rms spreads σ_H and σ_V, the following substituting should be made in Eq. (15.76),

$$a_V(a_V + a_H) \longrightarrow 2\sigma_V(\sigma_V + \sigma_H) \tag{15.77}$$

so that ω_I represents the ion bounce frequency at the center of the electron beam.

The ions described in Eq. (15.75) were produced without transverse velocity by the electron slice at location s (the head is at $s + z'$) at time $t = (s + z')/v$, and should have the same distribution as the electrons. Therefore, Eq. (15.75) has the initial conditions

$$y_I\left(s, \frac{s+z'}{v}\middle| z'\right) = y_e(s, z'),$$

$$\frac{\partial}{\partial t} y_I\,(s,t|z')\Big|_{t=\frac{s+z'}{v}} = 0. \tag{15.78}$$

These initial conditions offer a way to determine the ion distribution.

15.2.1.2 *The Trapped-Ion Distribution*

A slice of ions, when produced at time t_0, have exactly same transverse distribution as the slice of electrons. These ions have no initial transverse velocity, but they will start their transverse oscillations about the centroid of the electron slice according to $r\cos\omega_I(t-t_0)/v$, with r being the initial distance of a particular ion from the centroid of the electron slice. This implies that this slice will first contract to zero in one quarter of a betatron oscillation and expand again. Of course, we will not find all the ions contract to zero at a location at any time, because at the same location there are other slices of ions produced by other slices of electrons. These ions inside the slice will have different betatron phases than the one that we are talking about, owing to the fact that the electron slice producing them are at different z's from the head of the beam. Because of the betatron oscillation (even in the absence of coupled ion-beam oscillation), the average horizontal and vertical radii of the ion slice will be smaller than those of the electron beam. They are just $a_H/\sqrt{2}$ and $a_V/\sqrt{2}$ if the distribution of the ions is assumed to be uniform.

A derivation of the transverse distribution of the ions is as follows. For the simplicity of the derivation, we employ a model with a round electron beam with uniform distribution within the radius $a = a_H = a_V$. If Σ_I is the ionization cross section and n_g is the residual gas density in the vacuum chamber, the linear density of ions

$$\lambda_I = \Sigma_I n_g N_e \tag{15.79}$$

is produced near the tail of the electron beam, after a total of N_e electrons have passed through. Now an electron slice of width dz' at distance z' behind the head of the electron bunch of length ℓ will produce a slice of ions with linear density $\Sigma_I n_g N_e dz'/\ell$. This slice of ions will have radius a when born. These ions do not move longitudinally. When the electron slice at distance z behind the head reaches these ions, this ion slice shrinks to the radius $a\cos\omega_I(z-z')/v$. Summing up the ions produced by all the electron slices up to the slice at z, the transverse ion density within a circle of radius r is[‡]

$$\begin{aligned} n_I(r|z) &= \frac{\Sigma_I n_g N_e}{\pi a^2 \ell} \int_{0,\left(|\cos\frac{\omega_I(z-z')}{v}|<\frac{r}{a}\right)}^{z} \frac{dz'}{\cos^2\frac{\omega_I(z-z')}{v}} \\ &= \frac{\Sigma_I n_g N_e v}{\pi a^2 \ell \omega_I} \tan\frac{\omega_I z'}{v}\Big|_{0,\left(|\cos\frac{\omega_I(z')}{v}|<\frac{r}{a}\right)}^{z}. \end{aligned} \tag{15.80}$$

[‡]The integration limits imply z' from 0 to z with the condition that $|\cos\frac{\omega_I(z-z')}{v}| < \frac{r}{a}$.

Now

$$\left|\cos\frac{\omega_I(z')}{v}\right| < \frac{r}{a} \quad \text{implies} \quad \left|\tan\frac{\omega_I(z')}{v}\right| < \frac{\sqrt{a^2-r^2}}{r}. \tag{15.81}$$

Thus, in each period of π (except the first one), $\left|\tan\frac{\omega_I z'}{v}\right|$ receives the contribution of $\frac{2\sqrt{a^2-r^2}}{r}$. When $\omega_I z'/c \gg 1$, there are $\omega_I z/(v\pi)$ such periods from $z'=0$ to z. The transverse ion distribution is therefore

$$n_I(r|z) \approx \frac{2\Sigma_I n_g N_e z}{\pi^2 a^2 \ell}\frac{\sqrt{a^2-r^2}}{r}. \tag{15.82}$$

This distribution has rms radius $a/2$. However, a uniform beam of radius a has rms radius $a/\sqrt{2}$. If we approximate the ion distribution to be uniform, it corresponds to a radius of $a/\sqrt{2}$.

15.2.1.3 *The Electron Equation of Motion*

Similar to the ion oscillation in the electron beam, the electron beam also oscillates in the ions. Near the very end of the electron beam, the ions generated by the passage of the whole beam has linear density $\lambda_I = \Sigma_I n_g N_e$, The bounce angular frequency of the last slice of the electron beam in the ions in the absence of external focusing is therefore

$$\omega_e = \sqrt{\frac{8\Sigma_I n_g N_e r_e c^2}{\gamma a_V(a_V+a_H)}}. \tag{15.83}$$

Comparing with the ion bounce frequency ω_I in Eq. (15.76), the γ in the denominator indicates the longitudinal motion of the electron, and the extra factor of 2 in the numerator reminds us that the radii of the ions are smaller than those of the electron beam by $\sqrt{2}$. For bi-Gaussian distribution, the substitution $a_V(a_V+a_H) \to 2\sigma_V(\sigma_V+\sigma_H)$ should be made for the peak frequency. If the residual pressure inside the vacuum chamber is low, this electron bounce frequency is usually small. Take our previous example. If the residual pressure is $p = 10^{-9}$ Torr, the residual gas density is $n_g = 3.2\times10^{13}$ molecules/m^3 according to Eq. (15.61). For carbon monoxide, the ionization cross section is $\Sigma_I = 2.0$ Mb, ion linear density at the tail of the electron bunch is $\lambda_I = 640$ m^{-1}, and the electron-in-ion bounce frequency is $\omega_e/(2\pi) = 1.3$ kHz, which, because of the presence of external focusing, is actually a perturbation to the betatron frequency. For an electron slice at distance $z < \ell$ behind the head of the electron beam, the bounce frequency becomes $\omega_e\sqrt{z/\ell}$ because only $N_e z/\ell$ electrons have

participated in the ion production. The equation of motion for the centroid of a slice of the electron beam can therefore be written as

$$\frac{\partial^2}{\partial s^2} y_e(s|z) + \frac{\omega_\beta^2}{v^2} y_e(s|z) + \frac{\omega_e^2 z}{v^2 \ell} \left[y_e(s|z) - \frac{1}{z} \int_0^z dz'\, y_I\Big(s, \frac{s+z'}{v}\Big|z'\Big) \right] = 0, \tag{15.84}$$

where ω_β is the angular betatron frequency due to external focusing. The last term in the square brackets denotes the centroid of the ion slice produced by those electrons from the head to the length z of the electron bunch, where a uniform longitudinal distribution of the electron beam has been assumed.

15.2.1.4 *Coupled-Ion-Beam Solution*

The coupled ion-beam motion, Eqs. (15.75) and (15.84), is solved by separating the fast oscillating part and slow amplitude-evolution part. We would like to obtain the asymptotic behavior of the beam-ion system. Let us make our observation at a fixed location s when there is a resonance between the beam and ions. When the electron slice z behind the head of the electron bunch passes this location, it should have the same fast oscillating frequency as the ions at the same location. The fast oscillating part of the electron slice is

$$y_e(s|z) \sim e^{-i\omega_\beta s/v + ikz} \sim e^{-i\omega_\beta s/v + ikvt - iks}, \tag{15.85}$$

where k is to be determined and $z = vt - s$ has been substituted. The ions execute simple harmonic motion like

$$y_I(s,t|z') \sim y_I(s,t_0|z') e^{\pm i\omega_I (t-t_0)}. \tag{15.86}$$

At the time $t_0 = (s+z')/v$ when the ions were born (for any $z' < \ell$), they should have the same displacement as the electrons at z' that produce them. Therefore

$$\begin{aligned} y_I(s,t|z') &\sim y_e(s|z') e^{\pm i\omega_I (t-t_0)} \\ &\sim e^{-i\omega_\beta s/v + ikz'} e^{\pm i\omega_I t \mp i\omega_I (s+z')/v}. \end{aligned} \tag{15.87}$$

Comparing the time dependency of Eqs (15.85) and (15.87), for a resonance to occur we must have

$$k = \frac{\omega_I}{v}. \tag{15.88}$$

The other solution, $k = -\omega_I/v$, will lead to a decaying oscillatory solution which is of no interest to us (see below).

After determining the fast oscillating part of the resonance, now let

$$y_e(s|z) \sim \tilde{y}_e(s|z)e^{-i\omega_\beta s/v+i\omega_I z/v},$$

$$y_I(s,t|z') \sim \tilde{y}_I(s,t|z')e^{-i(\omega_\beta+\omega_I)s/v+i\omega_I t}, \tag{15.89}$$

where $\tilde{y}_e(s|z)$ and $\tilde{y}_I(s,t|z')$ are slowly varying in s and t, respectively. Substituting Eq. (15.89) into Eqs. (15.75) and (15.84), and neglecting second order derivatives of $\tilde{y}_e(s|z)$ and $\tilde{y}_I(s,t|z')$, we obtain

$$\frac{\partial}{\partial t}\tilde{y}_I(s,t|z') + \frac{i\omega_I}{2}\tilde{y}_e(s|vt-s) = 0, \tag{15.90}$$

$$\frac{\partial}{\partial s}\tilde{y}_e(s|z) + \frac{i\omega_e^2}{2\omega_\beta v\ell}\left[z\tilde{y}_e(s|z) - \int_0^z dz'\tilde{y}_I\Big(s, \frac{s+z}{v}\Big|z'\Big)\right] = 0, \tag{15.91}$$

with the initial condition

$$\tilde{y}_I\Big(s, \frac{s+z'}{v}\Big|z'\Big) = \tilde{y}_e(s|z'). \tag{15.92}$$

The first equation can be integrated to give

$$\begin{aligned}\tilde{y}_I(s,t|z') &= \tilde{y}_I\Big(s, \frac{s+z'}{v}\Big|z'\Big) - \frac{i\omega_I}{2}\int_{\frac{s+z}{v}}^{t} dt'\tilde{y}_e(s|vt'-s) \\ &= \tilde{y}_e(s|z') - \frac{i\omega_I}{2v}\int_{z'}^{vt-s} dz''\tilde{y}_e(s|z'').\end{aligned} \tag{15.93}$$

Substituting into the second equation, we get

$$\frac{\partial}{\partial s}\tilde{y}_e(s|z) + \frac{i\omega_e^2}{2\omega_\beta v\ell}\left[z\tilde{y}_e(s|z) - \int_0^z dz'\tilde{y}_e(s|z')\right] + \frac{i\omega_e^2}{2\omega_\beta v\ell}\frac{i\omega_I}{2v}\int_0^z dz'\int_{z'}^z dz''\tilde{y}_e(s|z'') = 0. \tag{15.94}$$

It is easy to show through integration by part that

$$z\tilde{y}_e(s|z) - \int_0^z dz'\,\tilde{y}_e(s|z') = \int_0^z dz'\,z'\frac{\partial}{\partial z'}\tilde{y}_e(s|z'),$$

$$\int_0^z dz'\int_{z'}^z dz''\,\tilde{y}_e(s|z'') = \int_0^z dz'\,z'\tilde{y}_e(s|z').$$

Then we arrive at

$$\frac{\partial}{\partial s}\tilde{y}_e(s|z) + \frac{i\omega_e^2}{2\omega_\beta v\ell}\left[\int_0^z dz'\,z'\frac{\partial}{\partial z'}\tilde{y}_e(s|z') + \frac{i\omega_I}{2v}\int_0^z dz'\,z'\tilde{y}_e(s|z')\right] = 0. \tag{15.95}$$

Another differentiating with respect to z transforms the differential-integral equation into a differential equation:

$$\frac{\partial^2}{\partial s \partial z}\tilde{y}_e(s|z) + \frac{i\omega_e^2}{2\omega_\beta v \ell} z\left[\frac{\partial}{\partial z}\tilde{y}_e(s|z) + \frac{i\omega_I}{2v}\tilde{y}_e(s|z)\right] = 0. \tag{15.96}$$

The first term inside the squared brackets is proportional to the growth rate of the transverse amplitude along the electron beam, while the second term is proportional to the ion bounce frequency. Earlier, we have estimated that the ion bounce frequency is usually very high ($\sim$ 70 MHz). Thus, for small growth rate of the electron beam envelope, we can neglect the first term in the square brackets. Then, Eq. (15.96) will be very much simplified to

$$\frac{\partial^2}{\partial s \partial z}\tilde{y}_e(s|z) + \frac{i\omega_e^2\omega_I}{4\omega_\beta v^2 \ell} z\tilde{y}_e(s|z) = 0. \tag{15.97}$$

The solution is that $\tilde{y}_e(s|z)$ depends on s and z through one dimensionless variable

$$\eta = \frac{z}{\ell}\sqrt{\frac{\omega_e^2\omega_I \ell s}{2\omega_\beta v^2}}, \tag{15.98}$$

and Eq. (15.97) becomes

$$\eta\frac{d^2\tilde{y}_e}{d\eta^2} + \frac{d\tilde{y}_e}{d\eta} - \eta\tilde{y}_e = 0. \tag{15.99}$$

which is just the modified Bessel equation. Thus, we obtain the simple solution

$$\tilde{y}_e(s,z) = y_0 I_0(\eta), \tag{15.100}$$

where I_0 is the modified Bessel function of order zero, while $y_0 = \tilde{y}_e(s|0)$ is the amplitude of oscillation of the head of the bunch if we make observation at a fixed location s, or $y_0 = \tilde{y}_e(0|z)$ is the initial amplitude of the centroid of a slice in the electron beam. In the asymptotic regime with $\eta \gg 1$, we have

$$\tilde{y}_e(s,z) = y_0\frac{e^\eta}{\sqrt{2\pi\eta}}. \tag{15.101}$$

Here, the asymptotic growth of the oscillating amplitude is exponential in z along the electron beam. However, for a fixed slice (fixed z), the growth of the amplitude is exponential in $\sqrt{s}$. If we have chosen $k = -\omega_I v$ as the resonance condition in Eq. (15.88), the solution of Eq. (15.101) would have become

$$\tilde{y}_e(s,z) \sim \frac{e^{\pm i|\eta|}}{\sqrt{2\pi|\eta|}}, \tag{15.102}$$

which is oscillatory and slowly decreasing. In fact, Eq. (15.99) becomes the Bessel equation and the solution becomes $J_0(|\eta|)$. This solution is of no interest to us and will therefore be discarded.

Observing at a fixed location s, we can define a growth length (in time) along the bunch

$$\tau_0 = \sqrt{\frac{2\omega_\beta \ell}{\omega_e^2 \omega_I s}}. \tag{15.103}$$

One may expect this growth time not dependent on the total length of the bunch. In fact, this is true, because from Eq. (15.83) ω_e^2/ℓ depends only on the linear density of the electron beam. If we are monitoring a specific slice of the electron beam (at fixed z or $\tau = z/v$ in time behind the head) as a function of time t or $s = vt$ along the accelerator, we can define an approximate e-folding growth time,

$$\text{Growth-time} = \frac{2\omega_\beta \tau_L}{\omega_e^2 \omega_I \tau^2}, \tag{15.104}$$

which is also independent of the electron bunch length $\tau_L = \ell/v$. For the tail of the beam this growth time becomes

$$t_0 = \frac{2\omega_\beta}{\omega_e^2 \omega_I \tau_L}. \tag{15.105}$$

We can now check the validity of a previous approximation of neglecting the first term in the square brackets of Eq. (15.96), which implies the necessity of

$$\left| \frac{\partial}{\partial z} \tilde{y}_e(s|z) \right| \ll \left| \frac{\omega_I}{2v} \tilde{y}_e(s|z) \right|. \tag{15.106}$$

Knowing the asymptotic behavior of the electron beam, this is equivalent to requiring

$$\frac{\eta}{z} = \sqrt{\frac{\omega_e^2 \omega_I s}{2\omega_\beta v^2 \ell}} \ll \frac{\omega_I}{2v}. \tag{15.107}$$

Using the definition of the growth time τ_0 [Eq. (15.103)] along the electron beam, this requirement is just

$$\frac{\omega_I \tau_0}{2} \gg 1. \tag{15.108}$$

In other words, the beam makes many oscillations within one growth length along the beam.

Knowing the asymptotic behavior of the amplitude of the electron bunch, we can compute the same for the ions. Substituting Eq. (15.101) into the second term on the right side of Eq. (15.93), we obtain

$$\tilde{y}_I(s,t|z') \approx -iy_0\sqrt{\frac{\omega_\beta\omega_I\ell}{2\omega_e^2 s}}\frac{e^\eta}{\sqrt{2\pi\eta}}\Big|_{z=vt-s}, \tag{15.109}$$

where the first term on the right side of Eq. (15.93) has been neglected because it is smaller by the factor $\sqrt{\omega_\beta\omega_I\ell/(2\omega_e^2 s)}$. Therefore when the ions meet the electron slice z behind the head of the electron bunch at location s, the ratio of the ion displacement to the beam displacement is

$$\frac{y_I(s,t|z')}{y_e(s|z)}\Big|_{z=vt-s} = \frac{\tilde{y}_I(s,t|z')}{\tilde{y}_e(s|z)}\Big|_{z=vt-s} \approx -i\sqrt{\frac{\omega_\beta\omega_I\ell}{2\omega_e^2 s}}. \tag{15.110}$$

Thus the ion oscillation is 90° out of phase relative to the electrons. From the restriction in Eq. (15.107), we find that the ion oscillation amplitude is very much larger than the coupled oscillation amplitude of the electron beam. We may visualize that the instability begins with ions generated inside the potential well of the electron beam and they are set into oscillation by the head of the electron beam through the dipole transverse impedance of the vacuum chamber. The oscillating ions then drive the electron beam into oscillation. The amplitude of the coupled-oscillation becomes saturated when the amplitude of the the ion oscillation is larger than the radius of the electron beam.

15.2.1.5 *A Train of Bunches*

Electron bunches are usually short and come in trains. The bunch spacing between two consecutive bunches τ_{sep} is usually large compared with the full bunch length $\tau_L \approx 4\sigma_\tau$. Thus ions generated oscillate within a bunch and move on hyperbolic paths in the gap between bunches. If the bunch gap is so large that all ions are cleared, the possibility of having a fast beam-ion instability is remote, because there will not be too many ions generated within a short electron bunch. The bunch train in the TESLA main linac falls into this category. [40] It consists of 2820 bunches with bunch spacing $\tau_{\text{sep}} = 337$ ns. Even at the separation of $\tau_{\text{sep}} = 20$ ns when injected into the dog-bone damping ring, ions with small molecular weights will be cleared at the bunch gaps.

There are also bunch trains in other electron machines with much shorter bunch spacings, like the 2-ns spacing in the Advanced Light Source (ALS), the 4-ns spacing in the SLAC PEP II HER, etc. When the ions are unable to escape in the bunch gaps, they make stable oscillatory motion along the bunch train,

and we can assume the charges in the bunches to spread uniformly along the train like a coasting beam. In that case, the *average* ion bounce frequency ω_I will be given by Eq. (15.10) or the same as Eq. (15.76) but with the electron linear density replaced by $N_e/L_{\rm sep}$ where N_e is the number of electron per bunch and $L_{\rm sep} = \beta c\tau_{\rm sep}$ is the bunch spacing. Recall in Sec. 15.1.2.3 that this introduction is valid only when $\omega_I\tau_{\rm sep} \lesssim 1$. For the electron-in-ion bounce frequency, we can continue to use the definition in Eq. (15.87), with the reminder that whenever we see ω_e^2/ℓ, ℓ should be replaced by $L_{\rm sep}$, because ω_e represents the electron-in-ion bounce frequency for electrons at the end of a length equal to $\ell = \beta c\tau_{\rm sep}$. The solution of the problem then follows closely that for a long segment of beam. The variable η will still be given by Eq. (15.98) with $\ell = \beta c\tau_{\rm sep}$, while $z = nL_{\rm sep}$ represents the position of the nth bunch. The approximate e-folding growth time for the nth bunch becomes, according to Eq. (15.105) ,

$$\left(t_0\right)_n = \frac{2\omega_\beta}{n^2\omega_e^2\omega_I\tau_{\rm sep}}. \tag{15.111}$$

After some time $s/(\beta c)$, the e-folding growth length (in time) along the bunch train becomes, according to Eq. (15.103),

$$\tau_0 = \sqrt{\frac{2\omega_\beta L_{\rm sep}}{\omega_e^2\omega_I s}}. \tag{15.112}$$

15.2.1.6 *Spectrum of Electron Beam*

Observing at location $s = 0$ through a beam-position monitor, the spectrum $\tilde{\lambda}(\Omega)$ of the electron beam is given by

$$\tilde{\lambda}(\Omega) \propto \int_0^\infty dt\, e^{-i\Omega t} \sum_{k=0}^\infty y_e(kC|vt - kC)\big|_{0<vt-kC<\ell}, \tag{15.113}$$

where $C = 2\pi R = vT_0$ is the ring circumference and k sums over multiple turns. We next transform the integration to t within one turn only. Thus

$$\begin{aligned}
\tilde{\lambda}(\Omega) &\propto \sum_{k=0}^\infty \int_0^{\ell/v} dt\, e^{-i\Omega(t+kT_0)} y_e(kC|vt) \\
&= \sum_{k=0}^\infty e^{-i(\Omega+\omega_\beta)kT_0} \int_0^{\ell/v} dt\, e^{-i(\Omega-\omega_I)t} \tilde{y}_e(kC|vt) \\
&= \sum_{k=0}^\infty e^{-i(\Omega+\omega_\beta)kT_0} \int_0^{\ell/v} dt\, e^{-i(\Omega-\omega_I)t} \frac{y_0 e^{\eta' t}}{\sqrt{2\pi\eta' t}},
\end{aligned} \tag{15.114}$$

with

$$\eta' t = t\sqrt{\frac{\omega_e^2 \omega_I k C}{2\omega_\beta \ell}}. \tag{15.115}$$

The integral can be performed exactly to give

$$\tilde{\lambda}(\Omega) \propto \sum_{k=0}^{\infty} \frac{e^{-i(\Omega+\omega_\beta)kT_0}}{\sqrt{2\pi\eta'[-\eta' + i(\Omega-\omega_I)]}} \gamma\left[\frac{1}{2}, \frac{-\eta' + i(\Omega-\omega_I)}{v/\ell}\right], \tag{15.116}$$

where

$$\gamma(\alpha, x) = \int_0^x u^{\alpha-1} e^{-x} dx \tag{15.117}$$

is the incomplete gamma function. For $|\Omega - \omega_I|\ell/v \gg 1$, we can use the asymptotic expansion $\lim_{|x|\to\infty} \gamma(\alpha, x) = -x^{\alpha-1}e^{-x}$ to obtain

$$\tilde{\lambda}(\Omega) \propto \sum_{k=0}^{\infty} \frac{e^{-i(\Omega+\omega_\beta)kT_0 + \eta'\ell/v}}{\sqrt{2\pi\eta'\ell/v}} \frac{e^{-i(\Omega-\omega_I)\ell/(2v)} \sin(\Omega-\omega_I)\ell/(2v)}{(\Omega-\omega_I)\ell/(2v)}, \tag{15.118}$$

where we have made the assumption that $|\Omega - \omega_I|\ell/v \gg \eta'\ell/v \gg 1$. The summation over k diverges because the signal itself diverges. However, if we measure in a small window around some large $k = \bar{k}$, we obtain the spectrum

$$\left|\tilde{\lambda}(\Omega)\right| \propto y_0 e^{\bar{\eta}'\ell/v} \sqrt{\frac{\ell}{2\pi\bar{\eta}'v}} \left|\frac{\sin\frac{(\Omega-\omega_I)\ell}{2v}}{\frac{(\Omega-\omega_I)\ell}{2v}}\right| \sum_{p=-\infty}^{\infty} \delta(\Omega - p\omega_0 + \omega_\beta), \tag{15.119}$$

where ω_0 is the revolution angular frequency and $\bar{\eta}'$ is the former η' when k replaced by $\bar{k}$. The spectrum observed is therefore all the lower betatron sidebands modulated by the sinc function which peaks at ω_I with a width equals to the inverse length of the electron beam.

15.2.1.7 *Possible Cures*

There are several methods to overcome this fast beam-ion instability. Simulations shows that the oscillation amplitude of the trailing beam particles saturates when it is larger than the rms beam radius due to nonlinear character of the coupling force. It is reasonable to believe that electron-ion coupling strength starts to decrease when the oscillation amplitude of the ion 'beam' is larger than the radius of the electron beam. Using the ion oscillation amplitude derived in Eq. (15.109) in the last subsection, it is easy to show that this saturation will

happen after time t into the instability, with t given by

$$\frac{e^{\sqrt{t/t_0}}}{(t/t_0)^{3/4}} = \frac{2\sqrt{2\pi}}{\omega_I \tau_L} \frac{a}{y_0}, \tag{15.120}$$

where y_0 is the initial offset of the head of the bunch and a is the radius of the beam, if assumed uniform, and t_0 is the approximate e-folding growth time given in Eq. (15.105) when observation is fixed at the last electron slice. Thus, if we can reduce the original vertical emittance by a suitable factor, the saturated emittance will be approximately what is desired. Heifets has considered saturation effects, which are expected to occur if the oscillation amplitude becomes larger than the rms beam sizes σ_x and σ_y. [41] At large amplitudes, he concluded that the oscillations grow linearly with a characteristic time,

$$\tau_H \approx t_0 \frac{\omega_I \ell}{v}. \tag{15.121}$$

This would reduce the growth rate by a factor of ~ 10 from the small amplitude exponential growth rate. Another method is to have a lattice of the accelerator ring in which the product of the horizontal and vertical betatron functions changes substantially as a function of position along the ring. The transverse beam size of the beam will have such large variation accordingly. As a result, the ion bounce frequency ω_I will vary significantly with time and no coherent oscillation can therefore develop. A third remedy is to introduce gaps within the beam if it is very long. In case of a bunch train, the introduction of additional longer bunch gaps will certainly help. As an example, an additional ten bunch gaps in PEP-II increase the instability risetime from 0.5 μs to 0.5 ms, which is inside the bandwidth of the feedback system. For linacs, the trailing bunches of a long train may be realigned by use of fast kickers and feedback.

Stupakov [42] and Bosch [43] have considered the effect of ion frequency spread, and found that the frequency spread changes the character of the instability to become more exponential:

$$\tilde{y}_e(s|z) \propto e^{sz/(v\tau_2 \ell)}, \tag{15.122}$$

where

$$\tau_2 \approx \sqrt{\frac{8}{\pi}} \frac{\ell \sigma_{\omega_I}}{v} t_0. \tag{15.123}$$

In this expression, σ_{ω_I} indicates the rms spread of the ion bounce frequency, which one expects to be some significant fraction of ω_I. For a broad frequency distribution ($\sigma_{\omega_I}/\omega_I \approx \sqrt{\pi/8}$), we find $\tau_2 \approx 2\omega_\beta/\omega_e^2$, which is the inverse of the incoherent betatron frequency shift due to the ions at $z = \ell$.

In electron storage rings, the fast-ion instability can be damped by radiation damping is the growth is not too fast. For a ring storing antiproton beams, Radiation damping is too small to be considered. For the Fermilab Recycler Ring that stores antiprotons, however, there is a transverse stochastic cooling system and an electron cooling system. If the damping time were comparable to or smaller than the beam-ion growth time, the instability could be effectively controlled.

Stupakov and Chao [44] pointed out that the fast beam-ion instability is in fact a transient phenomenon, because any damping mechanism, no matter how large the damping time τ_D is, will damp the instability. This happens because the fast beam-ion instability is a one-pass instability. Any transverse offset of the head slice will be damped in a time of order τ_D, because it is not driven by any other slices. With the first slice damped, it will not be driving the second slice, and the latter will be damped in another time interval of order τ_D. Thus one after the other, all slices of the beam will be damped. Therefore, in the simplest model, the damping mechanism is nothing more than the multiplication of the oscillation amplitude by the factor e^{-t/τ_D}.

In practice, however, the oscillation amplitude can never be damped to zero, because the noise of the feedback system produces random kicks to the beam. The final oscillation amplitude of the electron beam is then a balance between this heating noise source and the coherent damping of the damper. In a more complicated model which includes amplifier noise heating as well as damping, a critical parameter [44]

$$\eta_c = \frac{z}{\ell}\sqrt{\frac{\tau_D}{t_0}} \tag{15.124}$$

is introduced. When $\eta_c \gg 1$ or the feedback damping time is very much longer than the fast-ion growth time ($\tau_D \gg t_0$), the amplitude of the electron beam grows exponentially according to

$$\left\langle \tilde{y}_e^2(s|z) \right\rangle = \frac{(v\tau_D)^{3/2}}{8(vt_0)^{1/2}\ell}\frac{e^{\eta_c^2/2}}{\eta_c}F, \tag{15.125}$$

where F is proportional to the initial noise amplitude. For small η_c or when the feedback damping time is small compared with the fast-ion growth time ($\tau_D \ll t_0$), a cubic relationship follows:

$$\left\langle \tilde{y}_e^2(s|z) \right\rangle = \frac{(v\tau_D)^{3/2}}{48(vt_0)^{1/2}\ell}\eta_c^3 F. \tag{15.126}$$

The two asymptotic dependences are shown in Fig. 15.15. The instability re-

mains small if $\tau_D < t_0$, but grows exponentially toward the tail of the beam if $t_0 < \tau_D$. In order to control emittance growth, a successful damper should operate in the cubic region where $\tau_D < t_0$.

The "head-tail" model of the fast-ion instability can be disrupted by longitudinal beam motion. This means that, for fast-ion instability to occur, the growth time must be substantially less than the synchrotron period. The antiproton beam in the Fermilab Recycler Ring is confined between two barrier rf waves, and the synchrotron period can be as long as a few seconds. Thus, when the beam intensity is large enough, fast-ion instability should evolve with extremely small disruption from the longitudinal beam motion.

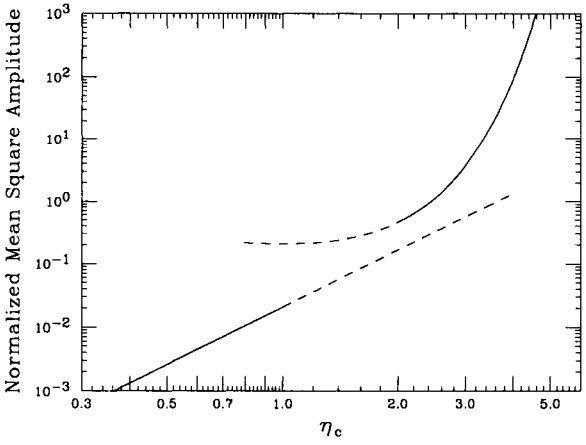


Fig. 15.15 Plot of normalized mean square amplitude $\langle \tilde{y}_e^2(z)\rangle (vt_0)^{1/2}(v\tau_D)^{-3/2}\ell/F$ versus η_c, showing the cubic behavior when $\eta \ll 1$ and the exponential behavior when $\eta_c \gg 1$. (Courtesy Stupakov and Chao. [44])

15.2.2 *Application to Electron/Positron Rings*

Raubenheimer and Zimmermann applied the linear theory of fast beam-ion instability to some existing accelerators like the SLAC Linear Collider (SLC) arc, the SLC Positron Damping Rings (DR), the LBL Advanced Light Source (ALS), the DESY HERA, the Cornell Electron Storage Ring (CESR), and the European Synchrotron Radiation Facility (ESRF). The results[§] are shown in Table 15.4.

Applications are also made to some future accelerators, like the Next Linear Collider (NLC) Electron and Positron Damping Rings (DR), the NLC Main Linac, the NLC Pre-Linac, the PEP-II Higher Energy Ring[¶] (HER), and the KEK Accelerator Test Facility (ATF) Damping Ring. The results are shown

[§]In some cases, our computed numbers are different from what are given in Ref. [38].

[¶]This ring is in operation now. But it was under construction at the time Ref. [38] was written.

Table 15.4 Parameters and oscillation growth rates for some existing accelerators.

Accelerator	SLC arc	SLC e^+ DR	ALS	HERA e^-	CESR	ESRF
ϵ_{Nx} (m)	5×10^{-5}	3×10^{-5}	1.2×10^{-5}	2×0^{-3}	2.7×10^{-3}	7.5×10^{-5}
ϵ_{Ny} (m)	5×10^{-6}	3×10^{-6}	2×10^{-7}	1.1×10^{-4}	1.2×10^{-4}	7.5×10^{-6}
n_b	1	1	328	210	7	330
N_b	3.5×10^{10}	4×10^{10}	7×10^{9}	3.7×10^{10}	4.6×10^{11}	5×10^{9}
$\beta_{x,y}$	4	1, 3	2.5, 4	25	14, 13	8, 8
$\bar{\beta}_y$	4	3	4	25	13	8
σ_x (μm)	47	113	101	991	1965	226
σ_y (μm)	15	62	17	232	399	71
ℓ or σ_z	1 mm	5.9 mm	200 m	6048 m	670 m	280 m
E (GeV)	46	1.2	1.5	26	5	6
p (Torr)	10^{-5}	10^{-8}	10^{-9}	10^{-9}	5×10^{-9}	2×10^{-9}
particle	e^+	e^+	e^-	e^-	e^-	e^-
$\omega_I/(2\pi)$ (MHz)	3.6×10^{5}	4.6×10^{4}	31	0.87	0.92	6.8
$\omega_\beta/(2\pi)$ (MHz)	11.9	15.9	11.9	1.91	3.67	5.96
$\omega_e/(2\pi)$ (MHz)	0.481	0.029	0.149	0.0054	0.0098	0.027
Single or multibunch	single	single	multi	multi	multi	multi
t_0 ($z \approx \ell$)	1.09 μs	511 μs	1.30 μs	187 μs	942 μs	65 μs

in Table 15.5. In the tables, some are data for the accelerators and some are computed numbers. For example, the beam transverse rms sizes, $\sigma_{x,y}$, are computed from the given normalized rms emittances $\epsilon_{Nx,y}$ and betatron functions $\beta_{x,y}$. In computing the ion bounce frequency $\omega_I/(2\pi)$, the beam linear density is taken at the peak density in case the beam considered is a single bunch, and as an average in case the beam considered is a train of bunches. In computing the beam particle bounce frequency $\omega_e/(2\pi)$, an ionization cross section of 2 Mb has been assumed. In computing the growth time t_0, the bunch length is taken as $\ell = 2\sigma_z$ in case the beam considered is a single bunch. With the exception of HERA and PEP-II HER, we find

$$\omega_e \ll \omega_\beta \ll \omega_I. \tag{15.127}$$

But in all cases, we do have

$$\omega_e \ll \omega_I. \tag{15.128}$$

For the existing accelerators, all the risetimes are longer than the synchrotron damping times, except for the ALS and ESRF. Transverse instabilities have been reported in the ALS; but they are not necessarily caused by ions. For the ESRF, the expected fast beam-ion instability growth time is about a factor 150 smaller than the radiation damping time. But so far there is no evidence for ion-related effects or multibunch instability at the ESRF. One possible explanation

Table 15.5 Parameters and oscillation growth rates for some future accelerators.

Accelerator	NLC e^- DR	NLC e^+ DR	NLC Pre-linac	NLC Main linac	PEP-II HER	ATF DR
ϵ_{Nx} (m)	3×10^{-6}	3×10^{-6}	3×10^{-6}	3×10^{-6}	5×10^{-4}	3×10^{-6}
ϵ_{Ny} (m)	3×10^{-8}	3×10^{-8}	3×10^{-8}	3×10^{-8}	2.5×10^{-5}	3×10^{-8}
n_b	90	90	90	90	1658	60
N_b	1.5×10^{10}	1.5×10^{10}	1.5×10^{10}	1.5×10^{10}	3×10^{10}	1×10^{10}
$\beta_{x,y}$	0.5, 5	0.5, 5	6	8	15	0.5, 5
$\bar{\beta}_y$	2	2	6	8	15	2.5
σ_x (μm)	62	62	68	35	1060	22
σ_y (μm)	3.9	3.9	6.8	3.5	169	7.1
ℓ or σ_z	38 m	4 mm	38 m	38 m	2000 m	50 m
E (GeV)	2	2	2	10	9	1.54
p (Torr)	10^{-9}	10^{-9}	10^{-8}	10^{-8}	10^{-9}	6×10^{-8}
particle	e^-	e^+	e^-	e^-	e^-	e^-
$\omega_I/(2\pi)$ (MHz)	151	2.23×10^5	108	209	4.46	98.2
$\omega_\beta/(2\pi)$ (MHz)	23.9	23.9	7.95	5.96	3.18	19.1
$\omega_e/(2\pi)$ (MHz)	0.271	0.029	0.613	0.531	0.027	1.78
Single or multibunch	multi	single	multi	multi	multi	multi
t_0 ($z \approx \ell$)	856 ns	124 μs	78 ns	40 ns	7.2 μs	19 ns

for the observed stability pertains to the distinct focusing optics: a Chasman-Green lattice, [46] in which the product of the horizontal and vertical betatron functions varies by more than a factor of 100 around the ring. This will lead to a variation of the ion bounce frequency by an order of magnitude. The decoherence of the ion motion due to this large frequency variation can effectively suppress the instability. On the other hand, this source of decoherence does not exist in a FODO lattice where the product of the transverse beam sizes is nearly constant. It is fortunate that the fast beam-ion instability was discovered when the B-factories at SLAC and KEK were still under construction. Theoretical and experimental analyses had been performed to make sure that this instability would be avoided.

15.2.2.1 *Observation at ALS*

Although so far no fast beam-ion instability has ever been reported in the operation of any accelerator ring, however, the phenomenon has been demonstrated experimentally by varying the vacuum pressure, by the injection of gases, and by varying the fill-pattern of the ring. Such experiments have been performed successfully at the LBL ALS, the Pohang Light Source (PLS), and the KEK TRISTAN. [45, 47, 48]

The ALS has 328 rf buckets. In the experiment, only up to 240 consecutive

buckets were filled so that there was a large gap to make sure that ions would not be trapped turn after turn. Unlike the experiment at the PLS, the feedback damping was turned on to suppress any coupled-bunch instabilities. Thus if any beam-ion instabilities developed, they would be due to the single-pass generated ions. The pressure in the vacuum chamber was elevated to $\sim 80 \times 10^{-9}$ Torr by injected helium gas (He). The onset of instability was carefully monitored by increasing the length of the bunch train slowly. Starting with a single bunch at 0.5 mA, consecutive bunches were filled slowly and the vertical beam size was measured. Figure 15.16 plots the rms beam size as a function of number of bunches in the train. We see that at elevated pressure with helium gas added, the beam size increases strongly with number of bunches and becomes saturated when number of bunches exceeds eight. We also see that at normal operating vacuum pressure, the beam size does not vary with the number of bunches in the train. The spectrum of the bunch train was also measured when the train contained 240 bunches, but with the total bunch intensity varied. The results in the left plots of Fig. 15.17 show the vertical betatron sidebands (the difference of the upper-sideband amplitude and the lower-sideband amplitude) clustered about 10 MHz when the total bunch current is 82 mA. As the current was raised to 142 mA and 212 mA, we see that the cluster of sidebands moves to higher frequencies. If this is the fast beam-ion instability, these sideband frequencies are just the ion bounce frequencies. The right plot of Fig. 15.17 depicts the measured ion bounce frequency as a function of beam current along with the theoretical prediction given by Eq. (15.76). We see that the theory fits the experimental data rather well.

The relative amplitude of oscillations along the bunch train was also measured indirectly. A collimator was used to scrape a train consisting of 160

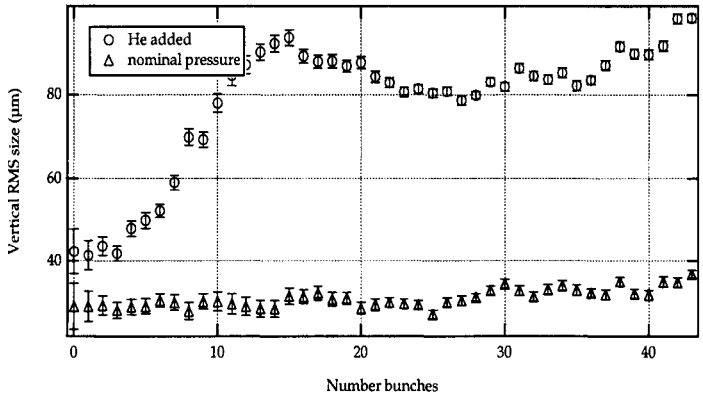


Fig. 15.16 Rms vertical beam size versus the number of bunches for nominal (triangles) and elevated (squares) pressure conditions. (Courtesy Byrd, *et al.* [45])

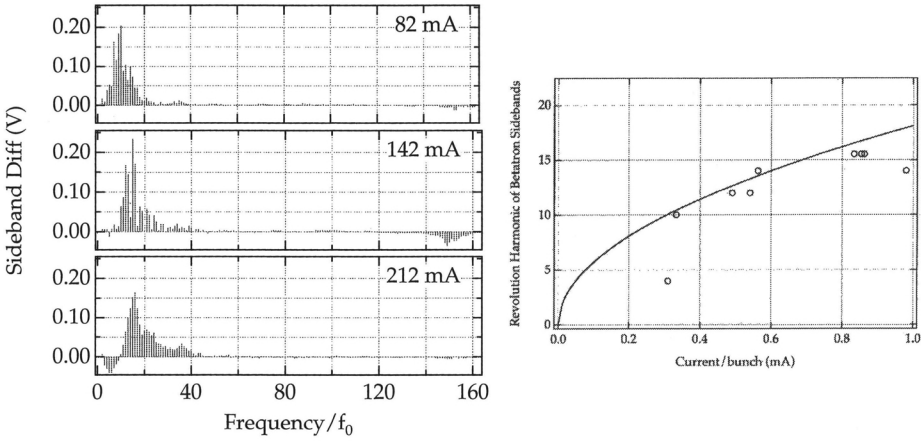


Fig. 15.17 Left: Vertical betatron sidebands measured in the 240/328 fill pattern for three different total currents of the bunch train. Right: Comparison between the measured and predicted frequency of coherent beam oscillations as a function of current per bunch for the 240/328 fill pattern. (Courtesy Byrd, *et al.* [45])

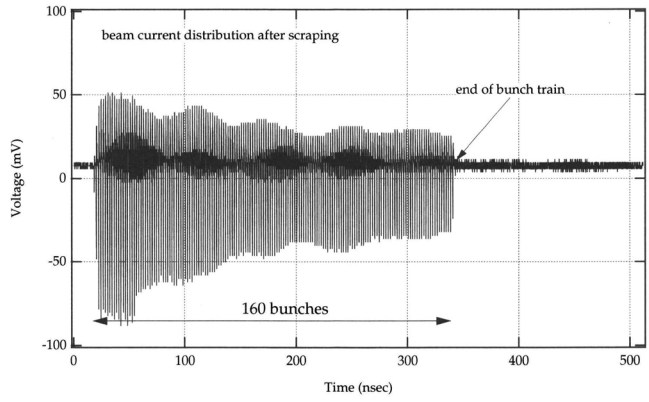


Fig. 15.18 Beam current along the bunch train for 160 bunches after scraping a vertical aperture close to the beam. The decreasing bunch current shows the increasing vertical oscillation amplitude along the bunch train before scraping. (Courtesy Byrd, *et al.* [45])

bunches. After scraping, the bunch intensity was found to be decreasing from the head of the train to the tail. In fact, the scraper reduced the bunch population in the tail about 2.5 times more than that of the leading bunches. This indicates that, before the scraping, the bunch vertical oscillating amplitudes increase along the bunch train.

The growth rate was also estimated and it agreed with the prediction of the linear theory. Thus, all evidence accumulated is qualitatively consistent with the assumption that the observed instability is the fast beam-ion instability.

15.2.3 *Application to Fermilab Linac*

Fast transverse oscillations with large amplitudes were observed [49] in the H^- beam in the 750-keV transfer line of the Fermilab linac in 1988 when the vacuum pressure was raised to 7×10^{-6} Torr to reduce the effect of space-charge on the beam [50, 51] and thereby reduce the effective emittance entering the linac. In order not to degrade the performance of the 8-GeV booster, into which the linac injects, this transverse instability has been avoided by choosing the operating vacuum pressure to be 2.65×10^{-6} Torr. The observation resembles the fast beam-ion instability, where individual ions last only for a single passage of the particle beam and need not be trapped. An experiment was performed at the 750-keV transfer line in 2000 in order to further understand the instability previously observed. [52]

Figure 15.19 shows the 750-keV transfer line into the main linac. Different gases like hydrogen, helium, nitrogen, argon, and krypton were injected through the bleeding valve. The gas pressure was controlled by adjusting the rate of flow of gas at the bleeding valve while vigorously pumping at the large ion pumps near the chopper C and the entrance into Tank 1 as well as a small ion pump near the bleeding valve. The pressure monitored near the three ion

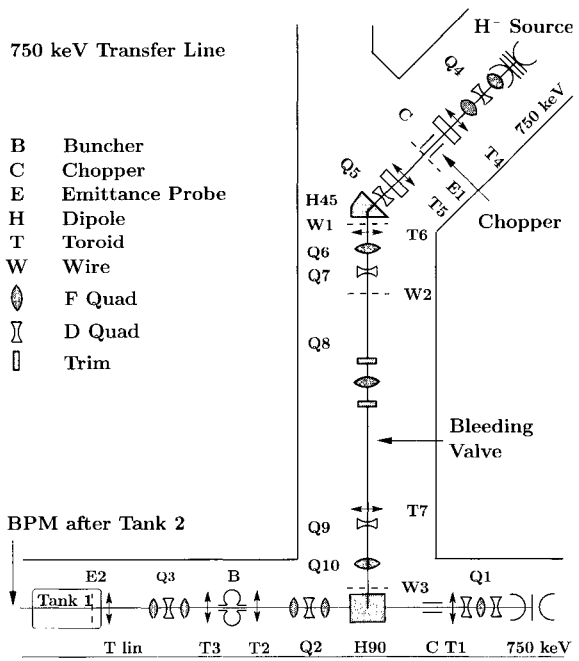


Fig. 15.19 The 750-keV transfer line of the Fermilab linac. The length is $\sim$ 10 m from the chopper C to the entry into the linac. Beam current measurements are made by a toroid monitor between Tank 1 and Tank 2, and again further downstream. (Courtesy Popovic and Sullivan. [52])

pumps showed steady readings. In this way the vacuum pressure could be varied between 1×10^{-5} and 1×10^{-4} Torr, while the normal operating vacuum pressure had been 2.65×10^{-6} Torr. A toroidal monitor near the exit of Tank 1 and entrance of Tank 2 measured the beam current. We see in Fig. 15.20 that the beam current in the transfer line (top) decreases with pressure. This is mostly due to the stripping of the electron on H^- by collision with the gas particles so that the resulting neutral H particles could not follow the dipole bend H90 into the current monitor. Another current monitor downstream measured the beam current in the linac downstream (bottom). The smaller values observed represent beam loss.

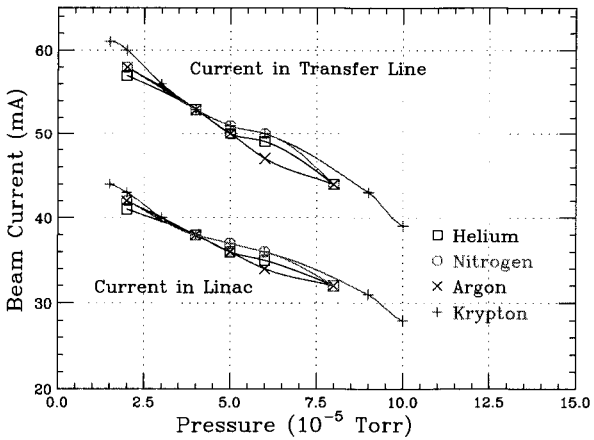


Fig. 15.20 Beam current in the transfer line (top) measured by toroids between Tank 1 and Tank 2, and further downstream in the linac (bottom). The drop in beam current at higher vacuum pressure is probably due to the stripping of the electron on the H^- by the gases injected. (Courtesy Popovic and Sullivan. [52])

A 750-keV H^- beam chopped to the length of $\tau_b = 35$ μs entered the transfer line. Its center position was picked up by the beam-position monitor after Tank 2. The signals were recorded using a LeCroy scope and the spectral content was obtained numerically using fast Fourier transform (FFT). To lower the noise level, measurements were averaged over approximately 20 beam pulses. To avoid any signal not related with the beam oscillation, only the last 20 μs of the beam pulse were Fourier analyzed. There was no noticeable difference between displacement signals in the horizontal and vertical planes, so all data were taken in the horizontal plane only.

A typical set of results for nitrogen at 3×10^{-5} Torr is shown in the top plot of Fig. 15.21, where the first two traces correspond to the beam intensity and the horizontal beam position, respectively. The fourth trace is the FFT of the beam position for the last 20 μs of the beam, while the third trace depicts the average of 23 FFT beam pulses. We can clearly see a resonant frequency of

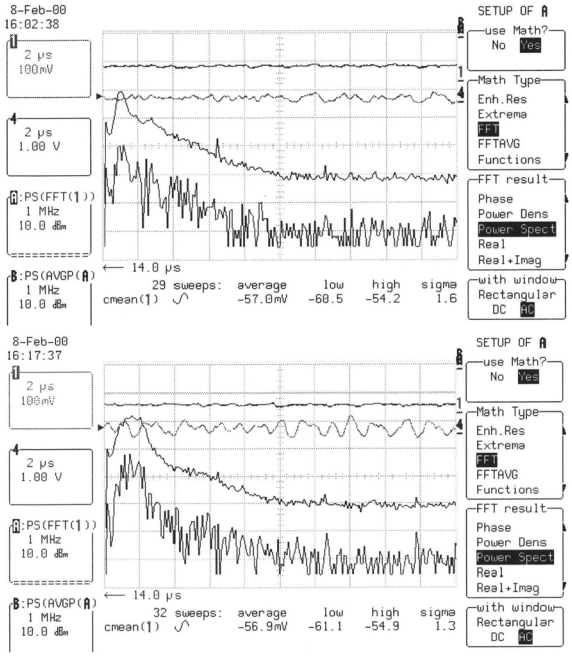


Fig. 15.21 Beam intensity (1st trace) and beam horizontal displacement (2nd trace) from the 14th μs at 2 μs per division, when the injected gas is nitrogen at 3×10^{-5} Torr (top) and 8×10^{-5} Torr (bottom). The fourth trace is the FFT at 1 MHz per division of the last 20 μs of the beam horizontal displacement. The third trace is the FFT averaged over 20 beam pulses. As pressure increases, the resonant peak becomes broadened and moves towards higher frequencies. (Courtesy Popovic and Sullivan. [52])

~ 0.5 MHz. As the gas pressure was increased to 8×10^{-5} Torr in the bottom plot of Fig. 15.21, the resonant signal is broadened and spreads out to higher frequencies. Figure 15.22 shows the BPM signals for the horizontal oscillations of a 35 μs-H^- beam when helium or argon is introduced. We see rapid growth in oscillation amplitude along the beam. The growth becomes much faster as the gas pressure is increased from 3×10^{-5} to 1×10^{-4} Torr. We also notice that saturation is reached very soon and the growth stops.

15.2.3.1 *Ionization Cross section*

To analyze the experiment, the ionization cross sections of the various gases are required. Unlike what we have studied before, the energies of the beam particles are very low here and much larger ionization cross sections are expected.

When the velocity of the incident particle is much larger than the velocity of the electron inside the target atom about to be ionized, the impulse approximation can be used. The experiment condition satisfies this criterion. The ionization energy of the electron in the outermost shell is given by

$$U = U_0 \left(\frac{Z}{n}\right)^2_{\text{eff}} \tag{15.129}$$

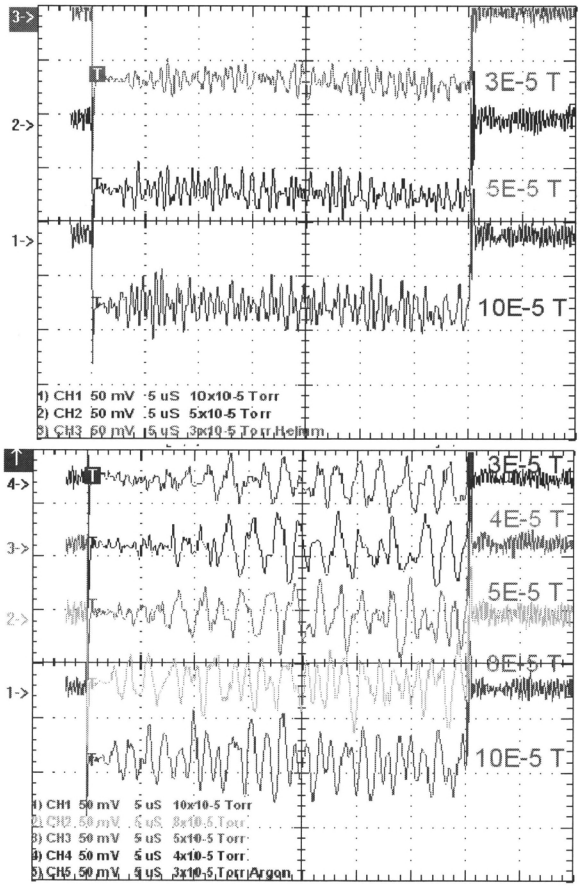


Fig. 15.22 Horizontal displacements of a 35 μs H^- beam in helium (top) and argon gas (bottom) environments at various pressures. An instability is observed and the beam displacements become saturated. The growth rate increases with gas pressure. (Courtesy Popovic and Sullivan. [52])

where Z is the atomic number of the gas element and n is the principal quantum number of the outermost shell of the gas atom. Here, $U_0 = hcR_\infty = 13.605$ eV is Rydberg energy or the ionization energy of hydrogen, $h = 6.582 \times 10^{-22}$ MeV-s is the Planck constant, and c is the velocity of light. Since the electrons in the inner shells shield the electric charges of the nucleus, the effective ratio $(Z/n)^2_{\text{eff}}$ is less than the actual $(Z/n)^2$. The effective ratios for the various gases estimated from Eq. (15.129) are listed in Table 15.6. The velocity v_e of the electron in the outermost shell is

$$v_e = v_0 \left(\frac{Z}{n}\right)_{\text{eff}} \tag{15.130}$$

where $v_0 = r_e c/\lambda\!\!\!^{-}_e = 0.0073$ is the velocity of the electron in the ground state of

Table 15.6 Ionization cross sections of various gases by 750-keV H^-. Velocities of electrons in the outermost shells of the gas atoms are estimated by an effective value of Z/n due to screening, where Z is the atomic number of the gas element and n the principal quantum number of the electron. Values of M^2 and C are from experiments. [55]

	H	He	N	Ar	Kr
Atomic number Z	1	2	7	18	36
Atomic mass number A	1	4	14	40	84
Ionization energy U (eV)	13.6	24.6	14.5	15.6	14.0
Effective ratio $(Z/n)^2_{\text{eff}}$	1.00	1.8088	1.0662	1.1618	1.029
Electron velocity in outermost shell v_e/c	0.0073	0.0098	0.0075	0.0079	0.0074
Target variable in Eq. (15.131) M^2	0.695	0.738	3.73	4.22	6.09
Target variable in Eq. (15.131) C	8.115	7.056	34.84	37.93	52.38
Ionization cross section Σ_I (Mb)	42.71	27.03	126.2	126.2	154.5

a hydrogen atom, $r_e = 2.818 \times 10^{-18}$ m is the electron classical radius, and $\lambda\!\!\!^{-}_e = \hbar/(m_e c) = 3.86159323 \times 10^{-13}$ m is the reduced electron Compton wavelength. We see that the velocities of the electron in the outermost cells of the gas atoms in this experiment are roughly $0.0073c$ to $0.0098c$, which are indeed much less than the velocity $\beta c = 0.040c$ of the 750-keV H^-.

In the impulse approximation, the bound electrons are knocked out by a sudden transfer of energy from the incident particle. Therefore, the ionization cross section does not depend very much on the ionization energy of the target atom. From the work of Bethe, [53, 54] the ionization cross section in the first Born approximation can be written as

$$\Sigma_I = 4\pi \lambda\!\!\!^{-2}_e \left[M^2 \left(\frac{\ln \beta^2\gamma^2}{\beta^2} - 1 \right) + \frac{C}{\beta^2} \right], \tag{15.131}$$

where β and γ are the Lorentz factors of the incident particle with the target at rest. The two variables M^2 and C depend on the generalized oscillator strength inside the target atom for all the transitions involved. Notice that this expression depends on the incident particle only through its *velocity*, which is an important consequence of the Born approximation and has been verified by many experiments. [55] The experimental values of M^2 and C as well as the cross sections of the gases involved are listed in Table 15.6.

15.2.3.2 *Ion Bounce Frequencies*

At the vacuum pressure of 3×10^{-5} Torr, the beam current in the transfer line is $I \sim 56.1$ mA (see Fig. 15.20). Thus the $\tau_b = 35$ μs H^- beam corresponds to a linear density of $\lambda_b = I/(e\beta c) = 2.92 \times 10^{10}$ m^{-1}. The H^- beam has a round cross section of radius $a_{H,V} = 1.0$ cm. This gives the resonant frequency

Table 15.7 Ion-beam resonant frequencies according to Ref. [38] for gases at various vacuum pressures or beam currents.

Gas	H	He	N	Ar	Kr
Mass number A	1	4	14	39	84
Resonant frequency (MHz)					
at 1×10^{-5} Torr (61.0 mA)	1.490	0.745	0.398	0.236	0.163
at 2×10^{-5} Torr (58.6 mA)	1.460	0.730	0.390	0.231	0.159
at 3×10^{-5} Torr (56.1 mA)	1.429	0.715	0.382	0.226	0.156
at 4×10^{-5} Torr (53.7 mA)	1.398	0.699	0.374	0.221	0.153
at 5×10^{-5} Torr (51.2 mA)	1.366	0.683	0.365	0.216	0.149
at 6×10^{-5} Torr (48.8 mA)	1.333	0.666	0.356	0.211	0.145
at 7×10^{-5} Torr (46.3 mA)	1.299	0.649	0.347	0.205	0.142
at 8×10^{-5} Torr (43.9 mA)	1.264	0.632	0.338	0.200	0.138
at 9×10^{-5} Torr (41.4 mA)	1.228	0.614	0.328	0.194	0.134
at 1×10^{-4} Torr (39.0 mA)	1.192	0.596	0.319	0.188	0.130

of $\omega_I/(2\pi) = 1.43/\sqrt{A}$ MHz as tabulated in Table 15.7.

The resonant frequencies computed in Table 15.7 are in the neighborhood of 1 MHz, in qualitative agreement with the experimental resonant frequencies depicted in, for example, Figs. 15.21 and 15.23. The observed resonant peaks in general have wide spreads. This may be because of the nonuniformity of the linear distribution of the H^- beam as well as the variation of its transverse radius. On the other hand, there are also disagreements with theory. Definitely, we do not see the $A^{-1/2}$ dependency predicted by Eq. (15.76) in experimental measurement, for example, in Fig. 15.24. However, in computing the resonant frequencies in Table 15.7, we have assumed only singly charged ions. Because the velocity of the incident H^- are much greater than those of the electrons in the outermost shells of the various gases, the ionization cross sections do not depend much on the ionization energy. There are, for example, six electrons in the outermost shell of an argon atom or krypton atom, it will be as easy for two or more electrons to be knocked off as for one. If there were doubly or triply charged ions produced, the resonant frequency would have been $\sqrt{2}$ and $\sqrt{3}$ times larger. It is very plausible that the deviation of the $A^{-1/2}$ dependency for argon and krypton is due to the production of multi-charged ions. The expression for ion bounce frequency in Eq. (15.76) is independent of the gas pressure. The slight decrease of the resonant frequency with rising pressure tabulated in Table 15.7 is just a reflection of the decrease in H^- current or linear density as a result of possible stripping by the gas particles.

In summary, we find that the resonant frequency is not sensitive to pressure for light gases like helium and nitrogen. However, for the heavier gases such as argon and krypton, the resonant peaks are broadened and move towards higher

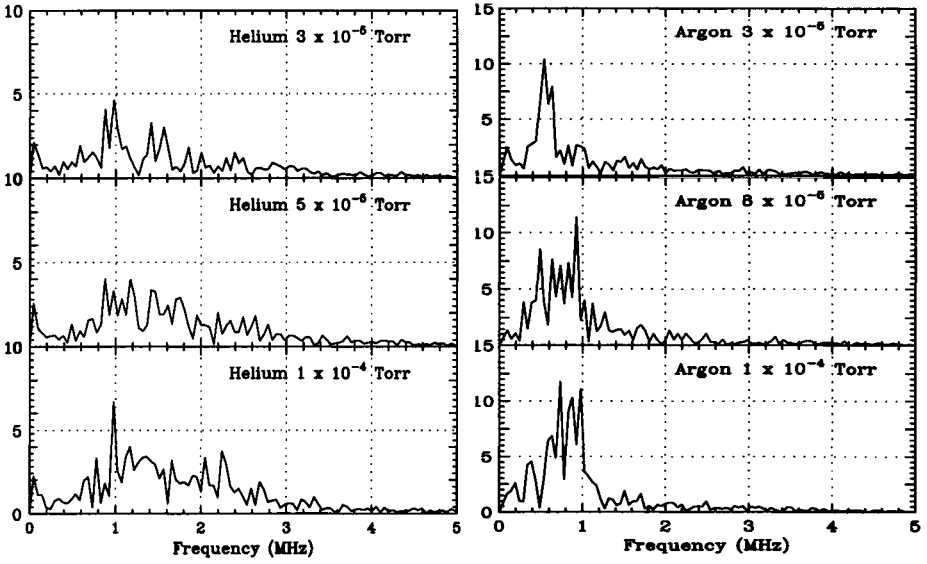


Fig. 15.23 FFT of H^- beam horizontal displacement averaged over many beam pulses. The gas environments are helium (left) and argon (right). The frequency spread does not depend much on gas pressure for helium, but does depend on pressure for argon. (Courtesy Popovic and Sullivan. [52])

frequencies when the pressure is larger than $\sim 5 \times 10^{-5}$ Torr. To conclude, we plot the spreads of the experimental resonant frequencies of the different gases for all the pressures studied in Fig. 15.24. On the same plot we also include the resonant frequencies computed in Table 15.7 from 1×10^{-5} Torr (top trace) to 1×10^{-4} Torr (bottom trace). From the figure, it is evident that the theoretical predictions, as a whole, underestimate the experimental results.

15.2.3.3 *Growth Times*

The transverse displacement of the H^- beam was measured by the BPM after Tank 2 in the linac. The excitation of transverse oscillation had been going on in the $\ell_t \sim 10$ m of the 750-keV transfer line from the chopper to the big ion pump near the entrance into the linac. Thus the time for which the beam can actually generate ions and interact with them is $t \sim \ell_t/(\beta c) = 0.835$ μs. The growth time along the beam τ_0 in Eq. (15.103) should be derived and compared with theory. For this, the betatron frequency is required. Assuming periodicity, the phase advance of the $\ell \sim 10$ m transfer line from the first large ion pump to the 90° bend into the linac are 443° in the horizontal and 110° in the vertical. Thus, an

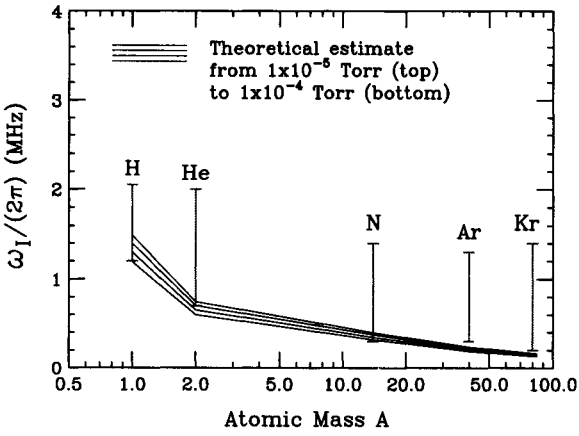


Fig. 15.24 Spreads of measured resonant frequencies of different gases at all the pressures studied. The theoretical predictions from 1×10^{-5} Torr (top trace) to 1×10^{-4} Torr (bottom trace) are also shown.

estimate of the horizontal betatron frequency is $\omega_\beta/(2\pi) = (\beta c/\ell)(443/360) = 1.47$ MHz. The growth time t_0 is then computed at a chosen reference pressure of 1×10^{-5} Torr, and the results for different gases are listed in the last row of Table 15.8.

Table 15.8 Computation of growth time along the H^- beam at 1×10^{-5} Torr. The growth time at other pressure p scales with $p^{-1/2}$.

	H	He	N	Ar	Kr
ω_b (MHz)†	10.1	8.00	20.2	17.3	19.1
Growth time along beam τ_0 (μs)	0.91	1.61	0.87	1.33	1.44

† ω_b is the same as ω_e referenced earlier in Eq. (15.83) with the classical electron radius replaced by the classical proton radius and the number of electrons in the beam replaced by number of H^- in the beam.

15.2.3.4 *Comments*

Experiments demonstrating fast-ion instability had been performed at various electron and positron rings, for example, in the LBL ALS, the Korean PLS, and the KEK TRISTAN. However, all these experiments are usually masked with electron cloud formed from secondary emission and multipactoring. This present experiment with H^- in the Fermilab linac, on the other hand, has been very much cleaner, because of the absence of electron cloud.

The beam-ion environment here is very different from that in an electron ring. Some relevant quantities are listed in Table 15.9, from which we do see

Table 15.9 Comparison of some beam and ion parameters in a typical electron ring and in the Fermilab linac, assuming that CO is the residual gas.

	Electron Ring	Fermilab Linac Experiment	
Number per bunch N_b	10^{11}	1.3×10^{13}	
Bunch length ℓ_b	0.010	419	m
Beam radius	0.001	0.010	m
Beam linear density λ_b	10^{13}	3.2×10^{10}	m^{-1}
Residual gas pressure	10^{-9}	1×10^{-5}	Torr
Gas-in-beam linear density λ_{gas}	1×10^{8}	1.0×10^{14}	m^{-1}
Ionization cross section for CO Σ_I	2	133	Mb
Maximum ion linear density λ_I	640	5.7×10^{10}	m^{-1}
CO^+ ion bounce frequency $\omega_I/(2\pi)$	64	0.40	MHz
Beam bounce frequency† $\omega_b/(2\pi)$ in absence of betatron focusing	0.00092	2.82	MHz

†10 GeV electrons are assumed for electron ring.
ω_b is the sme as ω_e referenced ealier in Eq. (15.83).

rather big differences:

(1) The ion bounce frequency in an electron ring is very much larger because of the much higher electron linear density and the much smaller transverse electron beam size.

(2) There are much more ions produced in the Fermilab linac than in an electron ring. The ion linear density in an electron ring is negligibly small compared with the beam linear density, while in the Fermilab linac the ion linear density is of the same order as the beam linear density. This is due to the much higher residual gas pressure and larger ionization cross section in the transfer line where the H^- are traveling with a low velocity. As a result, the beam bounce frequency in the ions in the absence of external focusing becomes very much smaller than in an electron ring.

(3) There are three frequencies in the fast beam-ion instability theory, the ion bounce frequency $\omega_I/(2\pi)$, the beam bounce frequency $\omega_b/(2\pi)$ in the absence of external focusing [same as ω_e referenced earlier in Eq. (15.83)], and the betatron frequency $\omega_\beta/(2\pi)$. For the two situations,

$$\begin{aligned} &\text{Electron ring} \quad \omega_I \gg \omega_\beta \gg \omega_b \\ &\text{Fermilab linac} \quad \omega_b \gtrsim \omega_\beta \gtrsim \omega_I. \end{aligned} \tag{15.132}$$

Now let us examine whether the approximation made in the derivation of the linear theory is valid in this experiment. When we are talking about growth time, we are looking in the asymptotic behavior, like Eq. (15.4), or when $\eta \gg 1$,

which is well satisfied when we are considering a position along the beam which is a few growth times behind the head. Knowing the asymptotic behavor of the H^- beam, the neglect of the first term in the square brackets of Eq. (15.96) will be justified provided that

$$\frac{\omega_I \tau_0}{2} \gg 1. \tag{15.133}$$

In Fig. 15.25, we plot $\frac{1}{2}\omega_I \tau_0$ as functions of pressure for the different gases. It is clear that criterion in Eq. (15.133) is satisfied for hydrogen and helium when the pressure is low and becomes marginal when the pressure is higher than $\sim 5 \times 10^{-5}$ Torr. For nitrogen, argon, and krypton, however, the criterion fails, since $\frac{1}{2}\omega_L \tau_0$ is consistently less than one. This implies that the concept of a growth time τ_0 given by Eq. (15.103) may not be valid for these heavier gases. Therefore, we cannot say whether the results for nitrogen, argon, and krypton agree with the linear theory of fast beam-ion instability or not. A more sophisticated solution of Eqs. (15.90) and (15.91) must be obtained without the omission of the first term in the square brackets before further comparison with experiment can be made for these heavier gases. We think, the approximation of neglecting the second derivatives in obtaining Eqs. (15.90) and (15.91) should be re-examined also.

Even for hydrogen and helium, the resonant frequency is around 1 MHz and less, and the passage time through the 10-m transfer line is 0.835 μs. This implies that the beam and the ions made less than one oscillation about each other. It is hard to visualize how a coherent instability can be established within such a short time. This is another reason why we are skeptical whether the expression for growth time could be applied to this experiment.

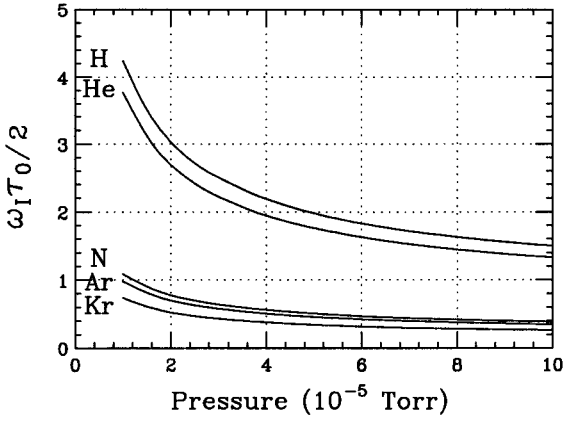


Fig. 15.25 Plot of $\frac{1}{2}\omega_I \tau_0$ versus gas pressure for various gases. When $\frac{1}{2}\omega_I \tau_0 \gg 1$, the neglect of the first term inside the square brackets of Eq. (15.96) is justified leading to the exponential asymptotic solution of Eq. (15.101). Since the requirement is not satisfied for nitrogen, argon, and krypton, the concept of the growth time given by Eq. (15.103) may not be correct.

15.2.4 *Application to Fermilab Designed Damping Ring*

In the TESLA design of the super-conducting version of the linear collider, [40] a 1-ms pulse of elelctron or positron beam contains 2820 bunches with 340 ns separation. The spacing is then reduced to 20 ns, the shortest risetime of the presently available kickers, before injecting into the damping ring, which therefore has a circumference of 17 km.[‖] There have been many attempts to minimize the ring's circumference. In the Fermilab design, the beam of the damping ring is grouped into 60 bunch trains. [56] Each train consists of 47 bunches spaced by 6.0 ns; a gap separates the tail of each train from the head of the following train. During extraction, the last bunch from each train is ejected in the course of one revolution turn. As a result, the entire extraction cycle requires 47 revolution turns. Injection is a time-reversed version of extraction: undamped bunches are delivered to the kicker every 340 ns and are kicked on-orbit as the (new) first bunch in a train. This effort can shorten the circumference of the ring by a factor of three to 6114 m. The shorter bunch spacing will lessen the efficiency of trapped ions clearance, so that fast-ion instability may pose as a problem, which we are going to investigate below. [57] Some relevant properties of the Fermilab design are listed in Table 15.10.

Ions are generated in the vacuum chamber from the residual gas and are trapped by the electron beam. In the potential well of the electron beam, the

Table 15.10 Some properties of the Fermilab designed damping ring.

Lattice	
Circumference C (m)	6113.967
Energy E (GeV)	5.066
Betatron Tune ν_x/ν_y	56.584/41.618
Momentum compaction α_p	0.001413
Maximum betatron fcn $(\beta_x)_{\max}/(\beta_y)_{\max}$ (m)	45.15/45.03
Revolution frequency f_0 (kHz)	49.034
Beam	
Extracted rms normalized emittance $\epsilon_{Nx}/\epsilon_{Ny}$ ($10^{-6}\pi$ m)	8.00/0.020
Rms energy spread	0.00150
Number of trains n_{tr}	60
Number of bunches per train n_b/n_{tr}	47
Number per bunch N_b	2×10^{10}
Bunch spacing $\tau_{\rm sep}$ (ns)	6.0
Train separation for 59 trains/last train (ns)	340/334
RMS bunch length σ_ℓ (mm)	6.00
Radiation Damping	
Energy loss per turn U_0 (MeV)	7.726
Damping times $\tau_x/\tau_y/\tau_E$ (ms)	26.7/26.7/13.4

[‖]This damping ring has two arcs joined by two very long sections in the shape of a dog-bone, and is also called the *dog-bone ring*.

trapped ions perform transverse oscillations. Treating the trains of short electron bunches as a coasting beam with the electron charges spreading out uniformly in the longitudinal direction, the ion-bounce angular frequencies are

$$\omega_{Ix,y} = \sqrt{\frac{2N_b r_u c}{\sigma_{x,y}(\sigma_x + \sigma_y)A\beta\tau_{\rm sep}}}, \tag{15.134}$$

where $r_u = 1.5459 \times 10^{-18}$ m is the classical radius of one atomic-mass-unit of ion, A is the molecular weight of the ion, $\tau_{\rm sep}$ is the bunch separation, and βc is the electron velocity. According to the analysis in Sec. 15.1.2.3, the ions will be cleared at the bunch gaps of length $\tau_{\rm sep}$ if $\omega_{Ix,y}\tau_{\rm sep} > \sqrt{2}$, otherwise they will be trapped. For CO^+ with $A = 28$, the ion-bounce angular frequencies are $\omega_{Ix} = 31.0$ MHz and $\omega_{Iy} = 220$ MHz. We obtain $\omega_{Ix,y}\tau_{\rm sep} = 0.186$ and 1.32. Thus CO^+ will be trapped. For light ions such as H_2^+ with $A = 2$, $\omega_{Ix,y}\tau_{\rm sep} = 0.696$ and 4.96. Thus H_2^+ will be trapped horizontally but not vertically. On the other hand, the bunch spacing is $\tau_{\rm sep} = 20$ ns in the TESLA dog-bone ring, very much longer. As a result, $\omega_{Ix,y}\tau_{\rm sep} = 0.635$ and 2.51 for CO^+ and 2.37 and 9.40 for H_2^+. Thus only CO^+ will be trapped horizontally.

While the ions oscillate inside the electron beam, the electrons also oscillate inside the ion 'beam'. In the absence of external transverse focusing, small-amplitude electron-in-ion bounce angular frequency is

$$\omega_{ex,y} = \sqrt{\frac{4\lambda_I r_e c^2}{\gamma\sigma_{x,y}(\sigma_x + \sigma_y)}}, \tag{15.135}$$

where λ_I is the ion linear density. Compared with the ion-bounce frequency in Eq. (15.134), there is the extra γ in the denominator because the electrons travel around the ring, and there is an extra factor of 2 in the numerator because the ions are at rest when generated by the electron, implying that the transverse radii of the ion 'beam' are a factor $\sqrt{2}$ smaller. The growth time of the last bunch in the linear theory can be expressed as

$$\tau_{x,y} = \frac{2\omega_{x,y}}{\omega_{ex,y}^2\omega_{Ix,y}\tau_{tr}}, \tag{15.136}$$

where τ_{tr} is the total length of the bunch train. Plugging in numbers gives $\tau_{x,y} = 360$ and 0.76 ms. Thus there is no worry in the horizontal direction, but some feedback device is necessary for the vertical. The results, together those for the TESLA dog-bone ring are listed in Table 15.11. This crude estimation indicates that the growth times for the TESLA dog-bone ring are so much shorter than those for the Fermilab damping ring, although the trapping test shows

Table 15.11 Possible fast-ion instabilities for trapped ions in the Fermilab damping ring and TESLA dog-bone ring at the vacuum pressure for 10^{-10} Torr.

	Fermi	Dog-bone
Bunch spacing τ_{sep} (ns)	6	20
For H_2^+		
Test for trapping $\omega_{Ix}\tau_{\text{sep}}$	0.70	2.37
$\omega_{Iy}\tau_{\text{sep}}$	4.96	9.40
For CO^+		
Test for trapping $\omega_{Ix}\tau_{\text{sep}}$	0.19	0.64
$\omega_{Iy}\tau_{\text{sep}}$	1.32	2.51
Linear Theory for CO^+		
Fast-ion growth time τ_x (ms)	360	0.133
τ_y (ms)	0.76	0.002

that CO^+ will not be trapped in the former at least vertically. The estimate also results in the horizontal growth times very much larger than the vertical ones, although the trapping test shows that trapping will be more severe in the horizontal. The reason of these puzzling conclusions is clear; the expression of the growth time in Eq. (15.136) assumes a uniform electron beam of the length of the whole train. In reality, the gaps between bunches do lower the ion trapping efficiency and therefore reduce growth. Actually, Eq. (15.136) should not be used with electrons spread out uniformly along the train when the trapping test gives a no-trapping result.

In order to study the more realistic problem, some simulations have been performed. To save time on computation, only the first 1000 revolution turns were simulated (total storage requires about 10000 turns, but the radiation damping time is about 1400 turns). The vacuum pressure was increased to 10^{-8} Torr to enhance the growth. All the bunches were considered as points and with a transverse offset randomly up to 1/100 of the rms radius. The vertical oscillation amplitudes for bunch 20 (left) and bunch 47 (right) in a train as picked up by a BPM is shown in Fig. 15.26 for the first 1000 turns. Since the vertical rms beam radius is $\sigma_y = 6.6 \times 10^{-6}$ m, the initial bunch displacements were random between $\pm 6.6 \times 10^{-8}$ m. We see in the same figure that the growths in amplitude are very rapid reaching $\pm 8 \times 10^{-4}$ m already in 1000 turns for bunch 20 and $\pm 2.5 \times 10^{-4}$ m for bunch 47 and the growths appear to continue. A feedback system with a gain of 0.2 was then applied and the simulations repeated. We see that the amplitudes of the bunches with feedback turned on have been controlled to within $\pm 150 \times 10^{-6}$ m for bunch 20 and $\pm 25 \times 10^{-6}$ m for bunch 47. However, the oscillation amplitude for bunch 20 is still very much larger than the rms bunch radius. It is interesting to see the growth of the last

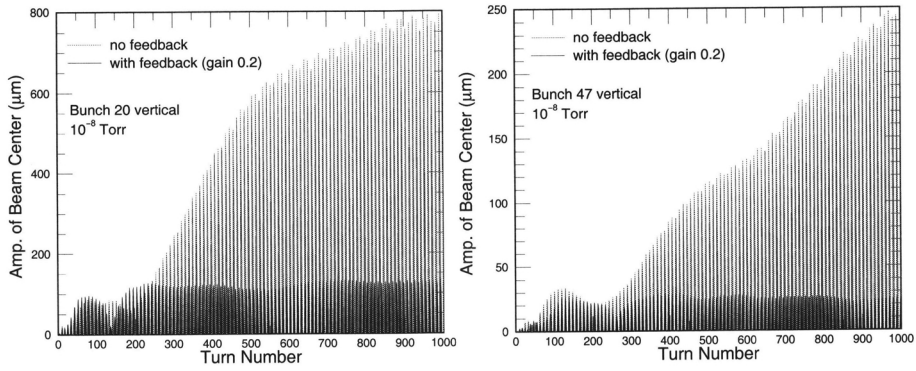


Fig. 15.26 Vertical amplitudes of the 20th bunch (left) and the 47th bunch (right) in the train for the first 1000 turns at vacuum pressure 10^{-8} Torr without and with feedback of gain 0.2. The growths have been very fast, but it is under control by the feedback system.

bunch of the train much less rapid than the 20th. The theory of fast beam-ion instability and some simulations [38] suggest that the instability growth rate increases with the square of the bunch position. On the other hand, we find in this particular train of 47 bunches that the bunches in the center of the train have much larger growths than the head and the tail bunches. We consider this peculiar observation as nothing more than the result of statistical fluctuation, because as shown below in Fig. 15.29, we do see that the later bunches in a train grow more rapidly when averages are made over all the 60 trains. However, the growth rates of the bunch displacements still do not follow the square of their locations even after the averaging.

The simulations were repeated with vacuum pressure at 1×10^{-10} Torr. The results for bunches 20 and 47 are shown in the left and right plots of Fig. 15.27. Now the growth has been very much less in the first 1000 turns and gone up to $\pm 15 \times 10^{-6}$ m for bunch 20 and $\pm 2.3 \times 10^{-6}$ m for bunch 47. Feedback of gain 0.20 stabilizes the growth to within $\pm 1.5 \times 10^{-6}$ m for bunch 20 and $\pm 0.4 \times 10^{-6}$ m for bunch 47, which are within the one sigma vertical size of the beam.

In the horizontal direction, both the betatron emittance and the dispersion contribute to the displacements of the bunches. However, only the contribution from emittance has been included in the present simulations. The horizontal emittance implies a horizontal radius of 87.8 μm. Thus the initial horizontal offset of the centers of the bunches have been offset randomly up to ± 0.88 μm. The amplitudes of oscillation of the bunches are followed for the first 1000 turns. The results for bunch 20 are shown for vacuum pressure 1×10^{-8} Torr in the left plot of Fig. 15.28 and for vacuum pressure 1×10^{-10} Torr in the right plot. Here

we see that the amplitude grows to only $\pm 50 \times 10^{-6}$ m in the first 1000 turns at the vacuum pressure of 1×10^{-8} Torr. With feedback of gain 0.2 turned on, the amplitude is damped to almost zero in 100 turns (the small dark oscillations in the left-bottom corner of the left plot). At the vacuum pressure of 1×10^{-10} Torr, there is no growth at all, the beam just oscillates with the same amplitude of 0.88 μm.

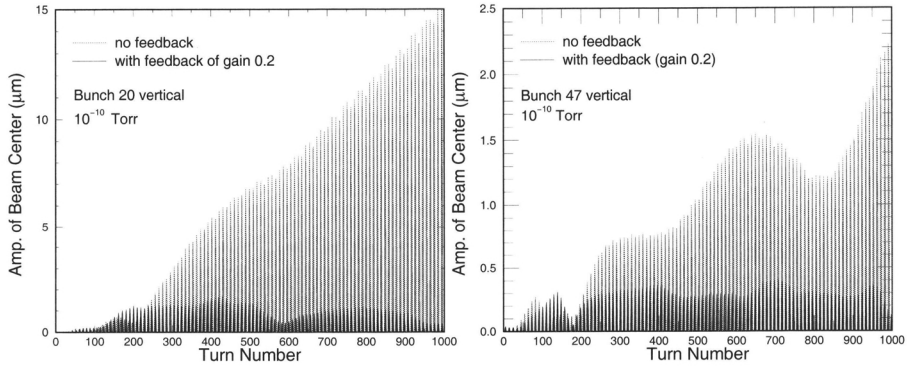


Fig. 15.27 Vertical amplitudes of the 20th bunch (left) and the 47th bunch (right) in the train for the first 1000 turns at vacuum pressure 10^{-10} Torr without and with feedback of gain 0.2. The growths have been much slower than when the pressure is 10^{-8} Torr instead. Feedback with a gain of 0.2 controls the oscillation of the bunch centers to within the rms size of the bunches.

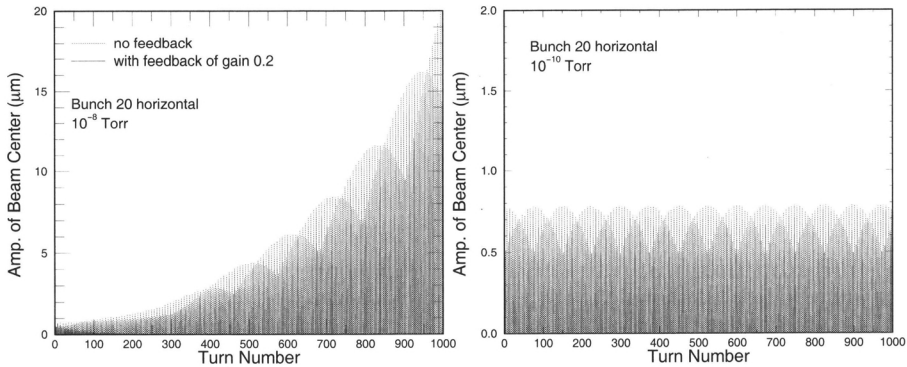


Fig. 15.28 Horizontal amplitudes of the 20th bunch in the train for the first 1000 turns at vacuum pressure 10^{-8} Torr (left) vacuum pressure 10^{-10} Torr (right). We see that the amplitude grows when the pressure is 10^{-8} Torr and is damped to almost zero with feedback of gain 0.2 (see the small dark oscillations in the left-bottom corner). At the vacuum pressure of 10^{-10} Torr, the bunch oscillation is stabilized without feedback.

So far we have been looking at only two bunches in a particlular train. In order to have better statistics, we make averages over all the 60 trains. For this we define the offset emittance

$$\epsilon_{\text{offset}} = \frac{y^2_{\text{beamcenter}}}{\beta_y}, \tag{15.137}$$

and normalized it with respect to the vertical emittance of the beam. These average normalized offset emittances over the 60 trains are shown in Fig. 15.29 for bunches 7, 14, 21, 28, 35, 42, and 46 at vacuum pressure of 0.1 nTorr in the left plot. In the right plot, we show the same but with feedback of gain 0.20 turned on. We do find that the growth without feedback increases with bunch position, but it does not scale with the square of bunch position as postulated in Ref. [58]. With feedback turned on, the offset emittance is damped to within 20% of the beam vertical emittance. Or the vertical offset is within 10% of the vertical beam size. Notice that in these simulations, radiation damping has not been included. The radiation damping time is approximately 1400 turns. Thus when radiation damping is considered, the offset emittance will be much less.

The amplitudes of oscillation of the bunches are simulated and recorded at a particular beam-position monitor (BPM) but at different time. Now let us look at the motion of all the 2820 bunches altogether at a snapshot. To convert to bunch amplitudes at a snap-shot, the BPM values for the jth bunch in the kth train must be multiplied by the betatron phase $\exp\{i2\pi[57(k-1)+(j-1)]\nu_y/N_{\text{sp}}\}$, where in the simulation we have assumed for simplicity 60 equal trains each containing 47 bunches followed by ten empty bunch spacings and

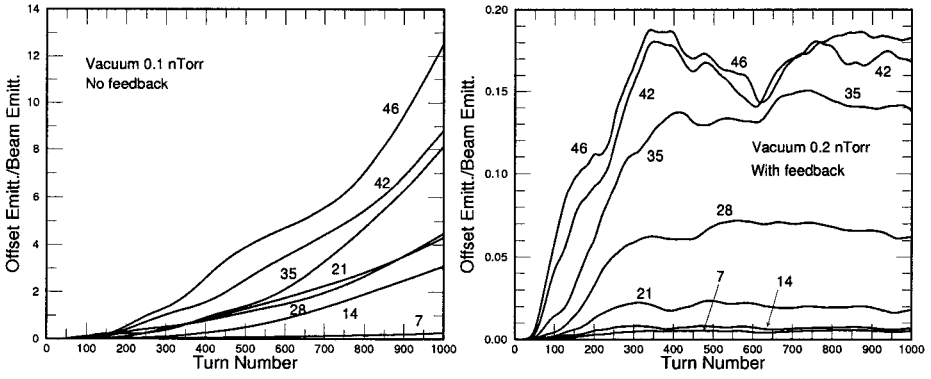


Fig. 15.29 Normalized offset emittance of bunches 7, 14, 21, 28, 35, 42, and 46 averaged over the 60 trains without/with feedback (left/right) at vacuum pressure of 0.1 nTorr. It is evident that the growth without feedback increases with bunch position. With feedback of gain 0.20, the offset emittance is controlled to within 20% of the vertical emittance of the beam.

$N_{sp} = 60 \times 57 = 3420$ is the total number of bunch spacings around the ring.

Fourier transform is made for each turn by multiplying the snapshot amplitude by** $\exp[-i2\pi\ell m/N_{sp}]$ and summed over the bunch spacing m from 0 to $N_{sp} - 1$. The results in the vertical at the 50th, 250th, 500th, 750th, and 100th turns are shown in Fig. 15.30 without (top) and with (bottom) feedback of gain 0.20. According to the analysis in Sec. 15.2.1.4, the resonant modes occur at $\ell = \nu_y - Q_{Iy}$ where $\omega_{Iy} = Q_{Iy}\omega_0$ is the angular ion bounce frequency. Because

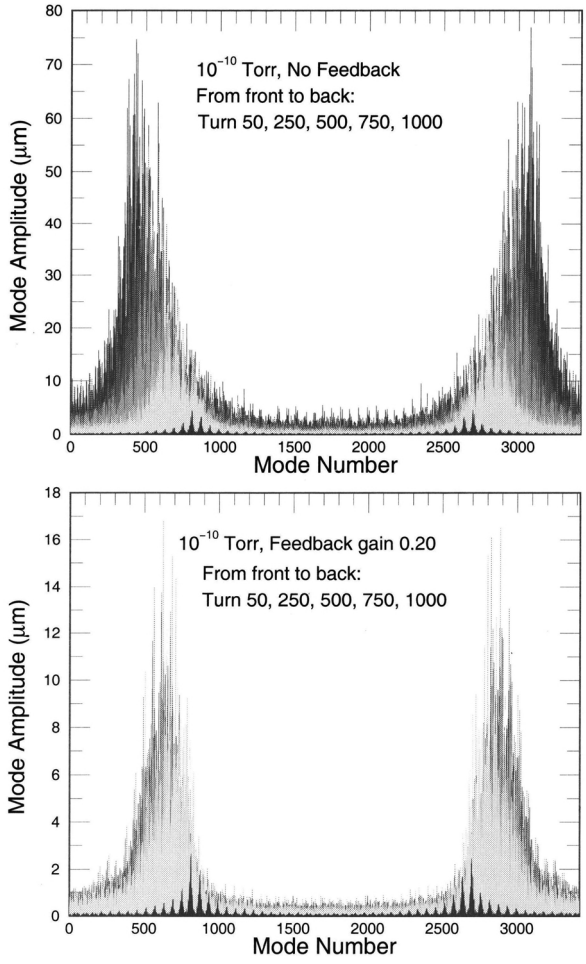


Fig. 15.30 Snapshot mode spectra are shown for the 50th, 250th, 500th, 750th, and 1000th turns at vacuum pressure 10^{-10} Torr without (top) and with (bottom) feedback of gain 0.2. The resonant modes correspond to $\ell = \nu_y + Q_{Iy}$ and $(\nu_y - Q_{Iy}) + N_{sp}$, where ν_y is the vertical betatron tune of the ring, Q_{Iy} is the vertical ion bounce tune, and $N_{sp} = 3420$ is the number of bunch spacings in the ring. Without feedback the resonant amplitudes increase in time and the ion-bounce frequency decreases indicating that the beam size increases. With feedback, both the resonant amplitudes and ion-bounce frequency reach saturation after ~ 250 turns.

**If we multiply by $\exp[+i2\pi\ell m/N_{sp}]$ instead, the two resonant modes in the mode spectrum will be at $\ell = Q_{Iy} - \nu_y$ and $N_{sp} - (\nu_y + Q_{Iy})$. Note that the two resonances in the Fourier transform correspond to the same mode.

the imaginary part of the amplitude is not monitored at the BPM, the Fourier transform results in another mirror resonance at $\ell = (\nu_y - Q_{Iy}) + N_{\rm sp}$. These two resonances do appear for each snapshot in Fig. 15.30, and their mode numbers add up to ≈ 3510, which is exactly $N_{\rm sp} + 2\nu_y$ as expected ($\nu_y = 45.1$). We identify the left resonant at $\nu_y + Q_{Iy}$ and the right at $(\nu_y - Q_{Iy}) + N_{\rm sp}$. Since they correspond to 815 and 2895 at the 50th turn, we obtain $Q_{Iy} = 775$, which agrees very well with $Q_{Iy} = 716$ using Eq. (15.134). Without feedback, as time goes on, the resonances shift to lower frequencies while their amplitudes become larger. This just reflects the evolution of the resonant beam-ion coupled oscillation with the beam size becoming larger and larger, thus lowering the ion bounce frequency. With feedback turned on, we see that the Q_{Iy} does not increase any more after 250 turns and the resonant amplitudes actually decrease after 500 turns. This reflects that an equilibrium has been reached in the presence of feedback, so that both the beam size and the oscillation amplitude do not increase anymore.

15.3 Half-Integer Stopband

Sporadic transverse instabilities were reported in the antiproton beam stored between barrier rf waves in the Fermilab Recycler Ring in the early half of 2004. The intensity of the beam varied from ~ 30 to $\sim 127 \times 10^{10}$. These instabilities had thresholds that were not a monotonic function of the beam intensity. For some time, they had been attributed to ions trapped inside the antiproton beam.

Balbekov [59] pointed out that, the observed instabilities might have been caused by the shifting of the antiproton betatron tunes by the trapped ions into the half-integer stopbands. Although it has been verified later in the year that what have been reported are actually transverse instabilities driven by the resistive wall (see Sec. 13.6.1), nevertheless, Balbekov's conjecture may still become a source of transverse instability in the future when the intensity of the antiproton beam is increased to the designed value of 600×10^{10} and the beam is cooled to small transverse emittances by the combination of stochastic cooling and electron cooling. Thus it is worthwhile to go over the theory.

The incoherent vertical space-charge tune shift of a beam particle inside the antiproton beam is

$$\Delta\nu_{sc0} = -\frac{N_{\bar{p}} r_p R}{\pi\gamma^3\beta^2 a_V (a_V + a_H)\nu_\beta}, \tag{15.138}$$

where R is the main radius of the ring, r_p is the classical antiproton radius, $N_{\bar{p}}$ is the number of antiprotons in the beam with a_V and a_H the vertical and

horizontal beam radii, and uniform transverse distribution has been assumed. The factor $1/\gamma^2$ can be written as

$$\frac{1}{\gamma^2} = 1 - \beta^2, \tag{15.139}$$

where the "1" on the right side represents the electric contribution and the β^2 represents the magnetic contribution. When ions are trapped inside the antiproton beam, they cancel the charges of the antiprotons to a certain extent and an antiproton will be seeing a smaller electric force. With χ denoting the fraction of neutralization so that the ion line density inside the beam is $\lambda_I = \chi\lambda_{\bar{p}}$, we have

$$1 - \beta^2 \longrightarrow 1 - \chi - \beta^2, \tag{15.140}$$

where $\lambda_{\bar{p}}$ is the antiproton line density, and the incoherent space-charge tune shift becomes

$$\Delta\nu_{sc} = \Delta\nu_{sc0}(1 - \chi\gamma^2), \tag{15.141}$$

where $\Delta\nu_{sc0}$, given by Eq. (15.138), is the incoherent space-charge tune shift without any trapped ions. Thus when χ is large enough, the magnetic contribution dominates over the electric contribution and $\Delta\nu_{sc}$ can even become positive. The horizontal and vertical betatron bare tunes of the Recycler Ring are, respectively, 25.425 and 25.415. With enough trapped ions, the betatron tunes may therefore be shifted into the half-integer stopbands resulting in a transverse instability.

A simple model is assumed with the antiproton beam of intensity $N_{\bar{p}}$ and length t_b having uniform transverse distribution. Assume that the ions of intensity $\chi N_{\bar{p}} T_0/t_b$ form a beam of the *same* transverse size as the antiprotons occupying all the circumference of the ring uniformly with uniform transverse distribution. For the sake of convenience, introduce a dimensionless reduced intensity

$$W = \sqrt{\frac{8\pi r_p R N_{\bar{p}}}{a_V(a_V + a_H)BA}}, \tag{15.142}$$

where $B = t_b/T_0$ is the bunching factor and $A = 28$ (40) is the molecular weight of the CO^+ (Ar^+) ion. Thus the ion bounce angular frequency is

$$\begin{cases} \omega_1 = \dfrac{W}{T_0}\sqrt{1-\chi} & \text{in beam } (0 < t < t_b), \\ \omega_2 = \dfrac{W}{T_0}\sqrt{\chi} & \text{in gap } (t_b < t < T_0). \end{cases} \tag{15.143}$$

In the gap, an ion is actually expelled by the ion beam and performs hyperbolic motion. Therefore ω_2 should be addressed more properly as the exponential growth rate. According to the transfer matrix in Eq. (15.7), the half-trace is

$$\text{Half-Trace} = \cos\phi_1 \cosh\phi_2 + \frac{1}{2}\left(\sqrt{\frac{\chi}{1-\chi}} - \sqrt{\frac{1-\chi}{\chi}}\right)\sin\phi_1 \sinh\phi_2, \quad (15.144)$$

where $\phi_1 = \omega_1 t_b = WB\sqrt{1-\chi}$ is the betatron phase advance in the antiproton beam while $\phi_2 = \omega_2(T_0 - t_b) = W(1-B)\sqrt{\chi}$ is the hyperbolic growth decrement as the ion traverses the beam gap. Again, the ion will be trapped when the half-trace falls between ± 1. The half-trace is computed for an antiproton beam of bunching factor $B = 0.8$ but of different intensities. The results are plotted in Fig. 15.31. We see that at the reduced intensity $W = 2$, the $B = 0.8$ antiproton beam can continue to accumulate trapped ions until the neutralization $\chi \approx 0.8$, whereas at the reduced intensity $W = 6$, ions can be accumulated up to $\chi \approx 0.4$ only. On the other hand, at $W = 11$, no ions cannot be trapped at all. This computation is repeated for various beam intensity W and the maximum possible neutralization is recorded in each case, thus obtaining the maximum possible neutralization as a function of W for a fixed bunching factor. The results are plotted in Fig. 15.32 when the bunching factors are $B = 0.8$, 0.6, 0.4, and 0.2. It is clear that ions can be trapped at some reduced intensity W, but not for any W. For example, a $B = 0.8$ antiproton beam can trap ions up to neutralization $\chi \approx 0.8$ when reduced intensity is $W < 3.15$ and will not trap any when $3.15 < W < 3.95$. But when $3.95 < W < 6.40$, ion-trapping is again

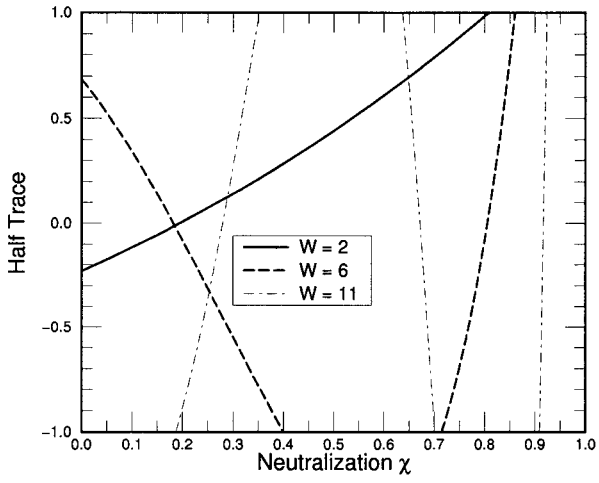


Fig. 15.31 Plot depicting the half-trace of the transport matrix versus neutralization χ at reduced intensity $W = 2$, 6, and 11, showing the corresponding maximum neutralization χ arising from trapped ions. The bunching factor is fixed at $B = 0.8$. (Courtesy Balbekov. [59])

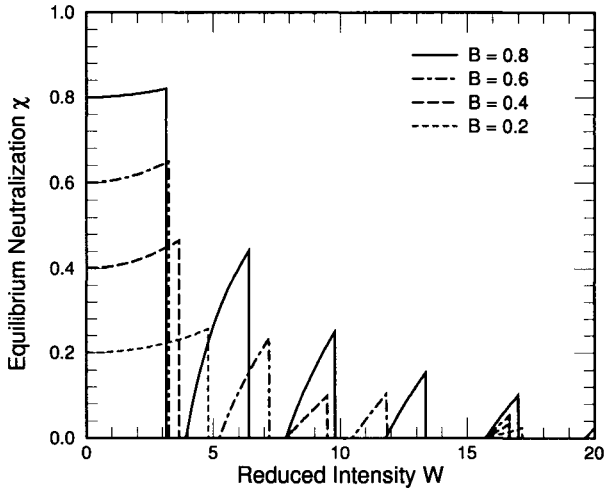


Fig. 15.32 The maximum possible neutralization from trapped ions is shown as functions of the reduced beam intensity W for bunching factors $B = 0.8$, 0.6, 0.4, and 0.2. (Courtesy Balbekov. [59])

possible. We also see that when W is small, the maximum neutralization is roughly equal to the bunching factor ($\chi \sim B$).

The incoherent space-charge tune shift of Eq. (15.138) without trapped ions can be expressed in terms of the reduced intensity W via

$$\Delta\nu_{sc0} = -\frac{AW^2}{8\pi^2\nu_\beta\gamma^3}. \tag{15.145}$$

The incoherent space-charge tune shift with neutralization $\Delta\nu_{sc}$ can now be plotted as functions of $\Delta\nu_{sc0}$ for both Ar^+ and CO^+. The plots of an antiproton beam with bunching factor $B = 0.8$ are shown in Fig. 15.33.

Every configuration of the antiproton beam corresponds to a $\Delta\nu_{sc0}$, the incoherent space-charge tune shift without trapped ions, and every $\Delta\nu_{sc0}$ corresponds to a maximum incoherent space-charge tune shift $\Delta\nu_{sc}$ neutralized by an ion species. We see in Fig. 15.33 that most values of $\Delta\nu_{sc0}$ will result in betatron tunes shifted upward towards the half-integer stopbands either due to the CO^+ ions or the Ar^+ ions. For example, consider an antiproton beam of intensity 100×10^{10} and bunching factor $B = 0.8$. At the 95% normalized transverse emittances of $\epsilon = 5\pi$ mm-mr, $\Delta\nu_{sc0} = -0.00066$ and $\Delta\nu_{sc}$ reaches 0.025 by trapping CO^+ ions. If the beam is cooled to $\epsilon = 3.5\pi$ mm-mr, $\Delta\nu_{sc0} = -0.00093$, and $\Delta\nu_{sc}$ reaches 0.036 by trapping Ar^+ ions. When the beam continues to be cooled to $\epsilon = 1.5\pi$ mm-mr, $\Delta\nu_{sc0} = -0.00219$, and $\Delta\nu_{sc}$ can be as large as 0.043 by trapping Ar^+ ions. Thus, it is quite possible that the betatron tunes will fall into the half-integer stopbands.

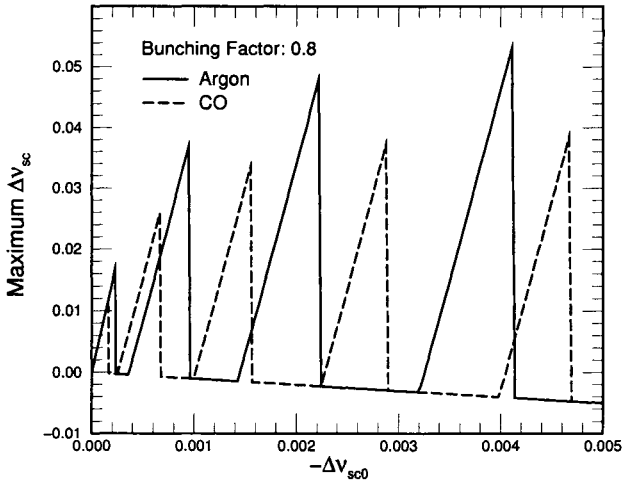


Fig. 15.33 The incoherent space-charge tune shift of an antiproton beam with maximum allowable neutralization is shown as a function of the incoherent space-charge tune shift in the absence of ion trapping. The bunching factor is $B = 0.8$. Both CO^+ (dashed) and Ar^+ (solid) ions are considered. (Courtesy Balbekov. [59])

We now summarize the main features of this theory and suggest some further investigation for verification:

(1) In this theory, the growth rate of the instability is not a monotonic function of the intensity of the antiproton beam or its transverse emittances. This is because an increase in beam intensity and/or a decrease of transverse emittances may sometimes move $\Delta\nu_{sc0}$ to a value that corresponds to a much smaller incoherent space-charge tune shift instead. In some sense, this effect resembles what has been recorded in the observed instabilities of the Recycler Ring.

(2) One way to test this theory is to change the betatron tunes of the Recycler Ring. Knowing from Fig. 15.33 that the incoherent space-charge tune shift can be as large as $\Delta\nu_{sc} \approx 0.05$, if we decrease the betatron tunes of the Recycler Ring gradually by the amount 0.05, the betatron tune will be moved to below the half integer and this type of transverse instabilities should not occur anymore. However, we must be careful that the new betatron tunes will not be in the vicinity of the stopbands of other parametric resonances.

(3) If the observed instabilities were actually the result of hitting the half-integer stopbands, there should be large changes in the incoherent betatron tunes before and after an instability. Such changes, monitored by the 1.75 GHz Schottky detector, had so far been rather small and had not been large enough to hit the half-integer tunes. For this reason, the half-integer stopbands of the Recycler Ring should be computed to see whether they are unusually large.

15.4 Exercises

15.1 Modify the coupled proton and electron equations of motion [Eqs. (15.15) and (15.16)] by including the influence of an infinitely conducting cylindrical beam pipe of radius b. Without taking into account the distributions of the various tunes, solve the equations for the threshold of coupled-centroid instability [similar to Eq. (15.23)] and the initial growth rate [similar to Eqs. (15.23) and (15.24)].

15.2 An electron is oscillating with bounce frequency $\Omega_e/(2\pi)$ inside a proton beam with amplitude increasing exponentially with an e-folding growth rate ω_I.

(1) If the electron just grazes the the wall of the beam pipe of radius b at one moment, show that the velocity when it hits the opposite wall of the beam pipe is given by

$$v = b\sqrt{2\pi\omega_I\Omega_e}\left[1 + \mathcal{O}\left(\sqrt{\frac{\omega_I}{\Omega_e}}\right)\right], \tag{15.146}$$

with the kinetic energy represented by

$$E_{\text{kin}} = \pi m_e \omega_I \Omega_e b^2, \tag{15.147}$$

where m_e is the electron mass.

(2) For single-electron motion, identify the growth rate $\omega_I = \mu\beta c/\lambda_{\text{rf}}$, where μ is given by Eq. (15.4) and λ_{rf} is the rf wavelength. Compute the kinetic energy of the electron when it hits the opposite wall of the beam pipe for the three accelerator rings, the ORNL SNS, the LANL PSR, and the BNL Booster, with some of their properties listed in Table 15.1.

(3) Identifying ω_I with the growth rate of the coherent centroid oscillation in Eq. (15.24), show that the kinetic energy of an electron hitting the other side of the beam pipe wall becomes

$$E_{\text{kin}} = \frac{\pi m_e Q_p Q_e^{3/2} \omega_0^2 b^2}{2\sqrt{|n - Q_e|}}, \tag{15.148}$$

and evaluate this kinetic energy for the above three rings. In Eq. (15.148), n is a revolution harmonic, $Q_e = \Omega_e/\omega_0$, and Q_p, defined in Eq. (15.18), is the proton bounce tune in the absence of betatron focusing.

15.3 In the experiment for measuring coupled-centroid instability at the Los Alamos PSR, the bunch occupies $\frac{2}{3}$ of the circumference of the storage ring. The coherent frequency which is close to the electron bounce frequency at CD 1 or 6.1 μC is shown in Fig. 15.5. Other information of the

PSR are listed in Table 15.1.

(1) Assuming a parabolic linear distribution of the proton bunch, and the maximum coherent or bounce frequency of 240 MHz, estimate the transverse size of the proton beam.

(2) From the peak value of the bounce frequency, estimate the location along the proton beam where the electron density is at a maximum.

15.4 Fermilab is proposing a new high intensity booster having circumference 711.304 m with rf harmonic 4. Protons are injected at the kinetic energy of 400 MeV to an intensity of 8.6×10^{12} per bunch. At the end of injection, each proton bunch has a uniform linear density but is occupying $\frac{2}{3}$ of the rf bucket. The transverse cross section of the beam is circular with a radius of 2.35 cm.

(1) Assuming the bunch gap is totally clean, show that electrons will not be trapped inside the proton beam.

(2) If a fraction χ of protons is spilled into the bunch gaps, compute the minimum χ that will lead to electron trapping.

15.5 Starting from the equations of coupled transverse motion, Eqs (15.15) and (15.16), assuming circular distributions for the protons and electrons, derive the Laslett–Sessler–Möhl stability criterion, Eq. (15.52).

15.6 In Tables 15.4 and 15.5, rows 1–6, 9–12, and 16 are inputs. Compute the output rows 7–8 and 13–15.

15.7 Consider the Fermilab Main Injector at the injection energy of 8.938 GeV with bunch intensity $N_b = 6 \times 10^{10}$ in each of the rf buckets. The circumference is $C = 3319$ m and the rf harmonic is $h = 588$. The elliptical vacuum chamber with major and minor radii $a = 6.15$ cm and $b = 2.45$ cm can be approximated as cylindrical with radius $r = \frac{1}{2}(a + b)$.

(1) Compute the bunch intensity threshold for electron-cloud multipactoring making use of Gröbner condition in Eq. (15.72).

(2) Compute the time duration Δt_{tr} for an electron to travel from one side to the vacuum chamber to the other.

Hint: $\beta c \Delta t_{tr} = \beta^2 r^2/(r_e N_b) = 10.9$ m, where βc is the longitudinal velocity of the proton beam.

(3) Assume the simple model that all the electrons, primary and secondary, strike the walls of the vacuum chamber at the end of each Δt_{tr} time interval. Show that the average saturated linear charge density of electrons is

$$\lambda_e = \frac{e n_e' N_b \beta c \Delta t_{tr}}{2 s_b} \frac{1 + \delta_{\text{eff}}}{1 - \delta_{\text{eff}}}, \tag{15.149}$$

where $n'_e = n'_{e(pl)} + n'_{e(i)}$ is the number of primary electrons generated by one proton in the beam per meter traversal and δ_{eff} is the effective SEY.
(4) The numbers of primary electrons generated by one proton per meter traversal are $n'_{e(pl)} = 4.02 \times 10^{-6}/p/\text{m}$ for stray protons and $n'_{e(i)} = 1.27 \times 10^{-7}/p/\text{m}$ for ionization. The effective SEYs from simulations are $\delta_{\text{eff}} \approx 0.8$ in the drift and 0.7 in the dipole. Evaluate λ_e and compare with the results of simulation in Fig. 15.12.
Answer: $\lambda_e = 0.34$ pC/m in the drift and 0.22 pC/m in the dipole. Note that these results are independent of the bunch intensity N_b, as demonstrated by Eq. (15.149). This estimation, however, is valid only below the threshold of multipactoring.

15.8 Derive the expression for the betatron tune shift of a proton beam in the presence of trapped electrons, as given by Eq. (15.74).
Hint: Start with Eqs. (15.15) and (15.18).

Bibliography

[1] H. Grunder and G. Lambertson, *Transverse Beams Instabilities at the Bevatron*, Proc. 8th Int. Conf. High Energy Accel., eds. M. H. Blewett and N. Vogt-Nilsen (CERN, Geneva, Sept. 20–24, 1971), p. 308.

[2] H. G. Herewards, CERN Report CERN-71-15, (1971).

[3] R. Macek, *Overview of New Developments on the PSR Instability*, Proc. 8th Advanced Beam Dynamics Mini-Workshop on Two-Stream Instabilities in Particle Accelerators and Storage Rings, (Santa Fe, Feb. 16–18, 2000),
web site: `http://www.aps.anl.gov/conferences/icfa/proceedings.html`.

[4] K. Harkay, *Electron Cloud Effects at APS*, Proc. 8th Advanced Beam Dynamics Mini-Workshop on Two-Stream Instabilities in Particle Accelerators and Storage Rings, (Santa Fe, Feb. 16–18, 2000),
web site: `http://www.aps.anl.gov/conferences/icfa/proceedings.html`.

[5] M. Blaskiewicz, *The Fast Loss Electron Proton Instability*, Proc. Workshop on Instabilities of High Intensity Hadron Beams in Rings, eds. T. Roser and S. Y. Zhang (Upton, NY, June 28–July 1, 1999), p. 321; *Estimating Electron Proton Instability Thresholds*, Proc. 8th Advanced Beam Dynamics Mini-Workshop on Two-Stream Instabilities in Particle Accelerators and Storage Rings, (Santa Fe, Feb. 16–18, 2000),
web site: `http://www.aps.anl.gov/conferences/icfa/proceedings.html`.

[6] S. Y. Zhang, M. Bai, M. Blaskiewicz, P. Cameron, A. Drees, W. Fischer, D. Gassner, J. Gullotta, P. He, H. Hseuh, H. Huang, U. Iriso-Ariz, R. C. Lee, W. W. MacKay, B. Oerter, V. Ponnaiyan, V. Ptitsyn, T. Roser, T. Satogata, L. Smart, D. Trbojevic, and K. Zeno, *RHIC Pressure Rise and Electron Cloud*,

Proc. 2003 Part. Accel. Conf., eds. J. Chew, P. Lucas, and S. Webber (Portland, Oregon, May 12–16, 2003, 2001), p. 54.

[7] J. Rosenzweig and P. Zhou, *Coherent Beam-ion Instabilities in the Fermilab Antiproton Accumulator, Ion Trapping in the Tevatron with Separated Orbits, Ion Clearing Using Cyclotron Shaking*, Proc. Fermilab III Instabilities Workshop, Fermilab, Batavia, eds. S. Peggs and M. Harvey (Fermilab, Batavia, June 25–29, 1990), p. 9, 26, and 39.

[8] D. Neuffer, E. Colton, D. Fitzgerald, T. Hardek, R. Hutson, R. Macek, M. Plum, H. Thiessen, and T.-S.Wang, *Nucl. Instrum. Meth.* **A321**, 1 (1992).

[9] In the reference below, aluminum pipe with titanium coating is mentioned: `http://www.ornl.gov/~nsns/CDRDocuments/CDRSections/CDRSections.html`. In the more recent design, however, stainless steel beam pipe with TiN coating is used.

[10] Obtainable by contour integration or see for example, I. S. Gradshteyn and I. M. Ryzhik, *Table of Integrals, Series, and Products*, Academic Press, Inc., Formula 3.644-4.

[11] A. Ruggiero and M. Blaskiewicz, *e-p Instabilities in the NSNS Accumulator Ring*, Proc. 1999 Part. Accel. Conf., eds. A. Luccio and W. MacKay (New York, March 27–April 2, 1999), p. 1581.

[12] M. Blaskiewicz, *Instabilities in the SNS*, Proc. 1999 Part. Accel. Conf., eds. A. Luccio and W. MacKay (New York, March 27–April 2, 1999), p. 1611.

[13] W. Schnell and B. Zotter, CERN Report ISR-GS-RF/76-26 (1976).

[14] L. J. Laslett, A. M. Sessler and D. Möhl, *Nucl. Instrum. Meth.* **121** 517 (1974).

[15] Tai-Sen F. Wang, *A Theoretical Study of Electron-Proton Instability I and II*, LANL Report PSR-96-004 and PSR-96-004 (1996).

[16] R. Macek, talk given at the 8th Advanced Beam Dynamics Mini-Workshop on Two-Stream Instabilities in Particle Accelerators and Storage Rings, (Santa Fe, NM, Feb. 16–18, 2000).

[17] See, for example, J. D. Jackson, *Classical Electrodynamics*, John Wiley & Sons, NY, the chapter on radiation by moving charges.

[18] F. Zimmermann, G. Rumolo, and K. Ohmi, *Electron Cloud Build Up in Machines with Short Bunches*, ICFA Beam Dynamics Newsletter No. 33, eds. K. Ohmi and M. Furman, April, 2004, p. 14.

[19] R. Macek, private communication.

[20] R. E. Kirby and F. K. King, *Nucl. Instrum. Meth. Phys. Res.* **A 469**, 1 (2001).

[21] V. Baglin, I. Collins, B. Henrist, N. Hilleret, and G. Vorlaufer, CERN LHC Project Report No. 472.

[22] O. Gröber, *Secondary Emission, Surface Effects, and Coatings*, Proc. 8th Advanced Beam Dynamics Mini-Workshop on Two-Stream Instabilities in Particle Accelerators and Storage Rings, (Santa Fe, NM, Feb. 16–18, 2000), web site: `http://www.aps.anl.gov/conferences/icfa/two-stream.html`

[23] A. Rossi, *SEY and Electron Cloud Build-Up with NEG Materials*, Proc. 31st ICFA Advanced Beam Dynamics Workshop on Electron-Cloud Effects (Ecloud'04), ed. M. A. Furman (Napa, CA, April 19–23, 2004),
web site: `http://icfa-ecloud04.web.cern.ch/icfa-ecloud04/`

[24] M. A. Furman and M. T. F. Pivi, *Probabilistic Model for the Simulation of Sec-*

ondary Electron Emission, Phys. Rev. ST AB **5** 124404, (2002)

[25] A. Rossi, G. Rumolo, and F. Zimmermann, *A Simulation Study of the Electron Cloud in the Experimental Regions of LHC*, Proc. Mini-Workshop on Electron-Cloud Simulations for Proton and Positron Beams (Ecloud'02), (CERN, Geneva, April 15–18, 2002), web site: `http://slap.cern.ch/collective.ecloud02/`

[26] O. Gröbner, *Bunch Induced Multipactoring*, Proc. 10th Int. Conf. High Energy Accel., (Protvino, July, 1977), p. 277.

[27] L. M. Jimenez, G. Arduini, P. Collier, G. Ferioli, B. Henrist, N. Hilleret, L. Jensen, K. Weiss, F. Zimmermann, *Electron Cloud with LHC-Type Beams in the SPS: a Review of Three Years of Measurement*, Proc. Mini-Workshop on Electron-Cloud Simulations for Proton and Positron Beams (Ecloud'02), (CERN, Geneva, April 15–18, 2002), web site: `http://slap.cern.ch/collective.ecloud02/`

[28] M. A. Furman, *A Preliminary Assessment of the Electron Cloud Effect for the FNAL Main Injector*, LBNL Report LBNL-57634/CBP-Note-712, 2006.

[29] K. Ohmi, *Phys. Rev. Lett.* **75**, 1526 (1995).

[30] M. A. Furman and G. R. Lambertson, *The Electron-Cloud Instability in the Arcs of the PEP-II Positron Ring*, LBNL Report LBNL-441123/CBP Notes-246, PEP-II AP Note AP 97.27, Proc. Int. Workshop on Multibunch Instabilities in Future Electron and Positron Accelerators (MBI-97), ed. Y. H. Chin (KEK, Tsukuba, Japan, July 15–18, 1997); M. A. Furman, *The Electron-Cloud Effect in the Arcs of the LHC*, LBNL Report LBNL-41482/CBP Note 247/LHC Project Report 180, May 20, 1998.

[31] *Proton Driver Study II*, eds. G. W. Foster, W. Chou, and E. Malamud, Fermilab Report Fermilab-TM-2169, 2002.

[32] F. Zimmermann, *A Simulation Study of Electron-Cloud Instability and Beam-Induced multipacting in the LHC*, LHC Project Report 95 and SLAC-PUB-7425, 1997.

[33] R. J. Macek, *Possible Cures for Electron Cloud Problems*, Proc. 31st ICFA Advanced Beam Dynamics Workshop on Electron-Cloud Effects (Ecloud'04), ed. M. A. Furman (Napa, CA, April 19–23, 2004),
web site: `http://icfa-ecloud04.web.cern.ch/icfa-ecloud04/`

[34] G. Stupakov and M. Pivi, *Suppression of the Effective Secondary Emission Yield for a Grooved Metal Surface*, Proc. 31st ICFA Advanced Beam Dynamics Workshop on Electron-Cloud Effects (Ecloud'04), ed. M. A. Furman (Napa, CA, April 19–23, 2004), web site: `http://icfa-ecloud04.web.cern.ch/icfa-ecloud04/`

[35] G. Rumolo and F. Zimmermann, *Electron Cloud Simulations: Beams Instabilities and Wake Fields*, Proc. Mini-Workshop on Electron-Cloud Simulations for Proton and Positron Beams (Ecloud'02), (CERN, Geneva, April 15–18, 2002), web site: `http://slap.cern.ch/collective.ecloud02/`

[36] E. Perevedentsev, *Head-Tail Instability Caused by Electron Cloud*, Proc. Mini-Workshop on Electron-Cloud Simulations for Proton and Positron Beams (Ecloud'02), (CERN, Geneva, April 15–18, 2002), web site:
`http://slap.cern.ch/collective.ecloud02/`

[37] Proc. 8th Advanced Beam Dynamics Mini-Workshop on Two-Stream Instabilities in Particle Accelerators and Storage Rings, (Santa Fe, NM, Feb. 16–18, 2000), web site: `http://www.aps.anl.gov/conferences/icfa/two-stream.html`;

Proc. Int. Workshop on Two-Stream Instabilities in Particle Accelerators and Storage Rings, (KEK, Tsukuba, Sep. 11–14, 2001), web site: `http://conference.kek.jp/two-stream/`; Proc. Mini-Workshop on Electron-Cloud Simulations for Proton and Positron Beams (Ecloud'02), (CERN, Geneva, April 15–18, 2002), web site: `http://slap.cern.ch/collective.ecloud02/`; Proc. 31st ICFA Advanced Beam Dynamics Workshop on Electron-Cloud Effects (Ecloud'04), ed. M. A. Furman (Napa, CA, April 19–23, 2004), web site: `http://icfa-ecloud04.web.cern.ch/icfa-ecloud04/`

[38] T. O. Raubenheimer and F. Zimmermann, *Phys. Rev.* **E52**, 5487 (1995).

[39] A. W. Chao, *Lecture Notes on Topics in Accelerator Physics*, US Particle Accelerator School (SUNY Stony Brook, NY, June 5–16, 2000), available at `http://www.slac.stanford.edu/~achao/lecturenotes.html`.

[40] TESLA Technical Design Report, Part II, *The Accelerator*, Ed. R. Brinkmann, K. Flöttmann, J. Rossbach, P. Schmüser, N. Walker, and H. Weise, March 2001; `http://tesla.desy.de/new_pages/TDR_CD/start.html`

[41] S. Heifets, Proc. Int. Workshop on Collective Effects and Impedance for B-Factories, CEIBA95, KEK Proc. 96-6, p. 270 (1996).

[42] G.V. Stupakov, Proc. Intworkshop on Collective Effects and Impedance for B-Factories, CEIBA95, KEK Proc. 96-6, p. 242 (1996).

[43] A. Bosch, *Phys. Rev. ST AB* 3, 034402 (2000).

[44] A.W. Chao and G.V. Stupakov, SLAC-PUB-7607, Proc. Int. Workshop on Multibunch Instabilities, (KEK, Tsukuba, 1997).

[45] J. Byrd, *et al.*, *Phys. Rev. Lett.* **79**, 79 (1997).

[46] R. Chasman, K. Green, and E. Rowe, *IEEE Trans.* **NS-22**, 1765 (1975).

[47] H. Fukuma, *et al.*, (unpublished).

[48] M. Kwon, *et al.*, *Phys. Rev.* **E57**, 6016 (1998).

[49] E. McCrory, G. Lee, and R. Webber, *Observation of Transverse Instabilities in FNAL 200 MeV Linac*, Proc. 1988 Int. Linac Conf., (Williamsburg, VA, Oct. 3–7, 1988), p. 182. (CEBAF-89-001).

[50] I. A. Soloshenko, *Space Charge Compensation and Collective Processes in the Intensive Beams of H^- Ions*, *AIP Conf. Proc.* **380**, 1995, p 345.

[51] M. D. Gabovich, V. P. Goretsky, D. G. Dzhabbarov, and A. P. Naĭda, *Institute of Physics of Ukrainian Science Academy* **N9**, Kiev, 1979, p 18.

[52] M. Popovic and T. Sullivan, *Observation of a H^- Beam Ion Instability*, Proc. of XX Int. Linac Conf., (Monterey, CA, Aug. 21–25, 2000), p. 848.

[53] H. Bethe, *Ann. Physik* **5**, 325 (1930).

[54] M. Inokuti, *Rev. Mod. Phys.* **43**, 297 (1971).

[55] F. F. Rieke and W. Prepejcjal, *Phys. Rew.* **A6**, 1507 (1972).

[56] Shekhar Mishra, David Neuffer, K. Y. Ng, Francǫis Ostiguy, Nikolay Solyak, Aimin Xiao, George D. Gollin , Guy Bresler, Keri Dixon, Thomas R. Junk, Jeremy B. Williams, *Studies Pertaining to a Small Damping Ring for the International Linear Collider*, Fermilab Report FERMILAB-TM-2272-AD-TD, 2004.

[57] K. Y. Ng, *Some Stability Issues of the Fermilab Damping Ring*, Fermilab Report FERMILAB-TM-2260, 2004.

[58] F. Zimmermann, *Accelerator Physics studies for KEKB: Electron Trapping, Electron Cloud in the HER, Closed-Orbit Drift, Horizontal Instability and Tune Shift,*

KEKB Commissioning Report, April 2, 2002, and CERN SL-Note-2002-017 AP (2002).

[59] V. Balbekov, private communication.

2025 © The Author(s). This is an Open Access chapter published by World Scientific Publishing Company, licensed under the terms of the Creative Commons Attribution-NonCommercial 4.0 International License (CC BY-NC 4.0).

Chapter 16

Instabilities Near and Across Transition

The slip factor has been defined as

$$\eta = \frac{1}{\gamma_t^2} - \frac{1}{\gamma^2} \tag{16.1}$$

in earlier chapters, where $E_0 = \gamma E_{\text{rest}}$ is the total energy of the synchronous particle having rest energy E_{rest}, and $\gamma_t E_{\text{rest}}$ is the transition energy of the lattice. The quantity γ_t^{-1} is also known as the lowest order of the momentum-compaction factor α_0, which was defined in Eq. (2.1). As the particle crosses transition through ramping, the slip factor passes through zero and switches sign from negative to positive. To maintain phase stability, it is also necessary for the the synchronous phase ϕ_s to jump from $0 \leq \phi_s < \frac{1}{2}\pi$ to $\frac{1}{2}\pi < \phi_s \leq \bar{\pi}$. The synchrotron angular frequency is defined as

$$\omega_s = \sqrt{-\frac{eh\eta V_{\text{rf}} \cos\phi_s}{2\pi\beta^2 E_0}}\,\omega_0, \tag{16.2}$$

where V_{rf} is the rf voltage, h is the rf harmonic, β is the velocity of the synchronous particle with respect to the velocity of light, and ω_0 is the revolution angular frequency. Because of its dependency on η, the synchrotron frequency also slows down as transition is approached. Thus, when it is close to transition, the motion of the particle eventually becomes unable to follow the rf bucket in the longitudinal phase space. Here, we first study the kinematics as the bunch is ramped through transition and the space-charge mismatch of the bunch length below and above transition. Next we study the so-called negative-mass instability, which is the dynamic effect of the wake fields across transition. Finally, the collective instabilities of isochronous rings are investigated.

16.1 Bunch Shape Near Transition

16.1.1 *Nonadiabatic Time*

Physically, η measures the amount of time or phase slip in one revolution turn per unit fractional momentum offset of a beam particle with respect to the synchronous particle. Thus, for a particle with energy deviation ΔE, its rf phase $\Delta\phi$ slips at a rate of*

$$\frac{d\Delta\phi}{dt} = \frac{h\eta\omega_0}{\beta^2 E_0}\Delta E. \tag{16.3}$$

At the same time, this off-energy particle receives additional energy from the rf cavities at the rate of

$$\frac{d\Delta E}{dt} = \frac{eV_{\rm rf}\omega_0}{2\pi}[\sin(\phi_s + \Delta\phi) - \sin\phi_s]. \tag{16.4}$$

Formerly, when we characterize the beam particle by τ, its arrival time ahead of the synchronous particle, the right side of $d\tau/ds$ in Eq. (2.10) or (2.12) is preceded by a negative sign, implying that the particle will arrive late ($\tau < 0$) above transition ($\eta > 0$) at a positive momentum offset. Here, $\Delta\phi$ is the slip in rf phase relative to the synchronous particle. When the particle arrives late at the cavity gap, the rf phase will have evolved more than $2\pi h$. Thus, the rf phase slip is positive and so is the sign preceding the right side of Eq. (16.3). Eliminating ΔE, we obtain for small $\Delta\phi$ the equation governing the motion of the phase of the particle:

$$\frac{d}{dt}\left(\frac{\beta^2 E_0}{h\eta\omega_0}\frac{d\Delta\phi}{dt}\right) - \frac{eV_{\rm rf}\cos\phi_s\omega_0}{2\pi}\Delta\phi = 0. \tag{16.5}$$

Unlike our previous discussion, β, E_0, η, and ω_0 vary with time during ramping and should not be taken out from the first derivative operator. This is especially true for η which appears in the denominator. However, as an approximation, we can neglect the slow time variations of all the parameters except η/E_0. This leads to

$$\frac{d}{dt}\left(\frac{E_0}{\eta}\frac{d\Delta\phi}{dt}\right) - \left(\frac{heV_{\rm rf}\cos\phi_s\omega_0^2}{2\pi\beta^2}\right)\Delta\phi = 0. \tag{16.6}$$

*$d\Delta\phi/dt$ is the rf phase slip in *one revolution period of the synchronous particle*, not one revolution period of the off-energy particle under consideration. Therefore, this is not equal to $-\Delta\omega/h$ where $\Delta\omega$ is the slip in angular frequency of the particle. Thus dt is equivalent to ds/v with v being the velocity of the synchronous particle and s is the distance measured along the on-energy closed orbit. This clarification is important when the higher order in energy spread is desired. See Sec. 16.4.1 for detail.

Under the approximation that the second bracketed term is considered time independent and also the variation of η/E_0 is linear in time near transition,† or

$$\frac{\eta}{E_0} = \frac{2\dot{\gamma}_t\, t}{\gamma_t^4 E_{\text{rest}}}, \tag{16.7}$$

Eq. (16.6) can be solved exactly in terms of Bessel functions of fractional orders. [1] However, all the important features of the solution can be estimated easily without going into the differential equation and Bessel functions. [3] Best of all, through the estimation, one can have a clear picture of what is going on during transition. In Eq. (16.7), the time t is measured from transition, $t < 0$ below transition and $t > 0$ above. On the other hand, the subscript t implies evaluation of the respective quantity at the moment when transition is crossed. Thus,

$$\dot{\gamma}_t = \frac{eV_{\text{rf}}\omega_0}{2\pi E_{\text{rest}}} \sin\phi_s \tag{16.8}$$

is the rate at which the relativistic factor γ of the synchrotron particle is ramped at right at the time transition is crossed.

We can also rewrite Eq. (16.6) in the form

$$\frac{d}{dt}\left(\frac{1}{\omega_s^2}\frac{d\Delta\phi}{dt}\right) + \Delta\phi = 0, \tag{16.9}$$

where ω_s is given by Eq. (16.2). However, Eq. (16.2) should be considered as a definition of ω_s only. This is because the beam particle does not follow the invariant trajectory of the Hamiltonian when it is near transition and therefore does not make synchrotron oscillations, so that ω_s, as defined by Eq. (16.2), loses its meaning of oscillation frequency.

When η^{-1} is not changing rapidly, a bucket can be defined. The bucket height is given by

$$(\Delta E)_{\text{bucket}} \propto \left(\frac{E_0}{|\eta|}\right)^{1/2}. \tag{16.10}$$

However, as the bunch particle passes through transition, η^{-1} changes rapidly. Here, we follow the assumption of a linear time variation for η/E_0 as given by Eq. (16.7), while all other parameters such as the rf voltage and the synchronous phase, aside from flipping from ϕ_s to $\pi - \phi_s$, are held fixed near transition. This means that when transition is approached, synchrotron frequency slows down to

†Some authors assume η to be linear in t instead. In that case, one also needs the additional assumption that $\dot{\gamma}_t T_c \ll 1$.

zero and the bucket height increases to infinity. In other words, when it is close enough to transition, the particle will not be able to catch up with the rapid changing of the bucket shape. This time period, from $t = -T_c$ to $t = T_c$ is called the nonadiabatic region, and T_c the *nonadiabatic time.* [2] Here, we define this region by

$$\omega_s \leq \frac{2}{(\Delta E)_{\text{bucket}}} \frac{d(\Delta E)_{\text{bucket}}}{dt}. \tag{16.11}$$

This just implies that inside this region, the rate at which the bucket height is changing is faster than the rate of executing synchrotron oscillations. The right side is, with the substitution of Eq. (16.10) and assuming the linear ramping of Eq. (16.7),

$$\frac{2}{(\Delta E)_{\text{bucket}}} \frac{d(\Delta E)_{\text{bucket}}}{dt}\bigg|_{t=-T_c} = 2\frac{d}{dt}\sqrt{\frac{T_c}{-t}}\bigg|_{t=-T_c} = \sqrt{\frac{T_c}{(-t)^3}}\bigg|_{t=-T_c} = \frac{1}{T_c}. \tag{16.12}$$

Evaluating at $t = -T_c$, the left side of Eq. (16.11) is

$$\omega_s|_{t=-T_c} = \omega_\infty \sqrt{\frac{h\dot{\gamma}_t T_c e V_{\text{rf}} \cos\phi_s}{\pi\gamma_t^4 E_{\text{rest}}}}, \tag{16.13}$$

where $\omega_\infty = \omega_0/\beta$ and is time independent. We then obtain the nonadiabatic time from Eq. (16.11):

$$T_c = \left[\left(\frac{\beta_t\gamma_t^4}{2\omega_\infty h}\right)\left(\frac{|\tan\phi_s|}{\dot{\gamma}_t^2}\right)\right]^{1/3}, \tag{16.14}$$

where the expression of $\dot{\gamma}_t$ in Eq. (16.8) has been used. Note that the nonadiabatic time is just an approximate time. The factor 2 on the right side of Eq. (16.11) was inserted for the purpose that T_c given by Eq. (16.14) is exactly the same as the adiabatic time quoted in the literature. We have written Eq. (16.14) in such a way that the factor in the first brackets contains parameters of the lattice, while $\dot{\gamma}_t$ in the second brackets is determined by the ramp curve and ϕ_s, the synchronous phase at transition, is determined by the rf-voltage table.

16.1.2 *Simple Estimation*

For the sake of simplicity, we adopt a model which states that, (1) when $|t| > T_c$, the beam particles follow the bucket with synchrotron oscillations, and (2) when $|t| < T_c$, the beam particles make no synchrotron oscillations at all.

Since the beam particle still follows the bucket at $t = -T_c$, from Eq. (16.3), the bunch length σ_ϕ is related to the rms energy spread σ_E by

$$\nu_s \sigma_\phi = \frac{h|\eta|}{\beta_t^2 \gamma_t E_{\text{rest}}} \sigma_E, \tag{16.15}$$

where η is to be evaluated at $t = -T_c$, and the energy E_0 is evaluated approximately right at transition since the change is slow. The 95% bunch area is defined as

$$S = 6\pi \sigma_\tau \sigma_E, \tag{16.16}$$

where this expression should hold in the adiabatic region. From Eqs. (16.15) and (16.16), we obtain the rms bunch length in time, $\sigma_\tau = \sigma_\phi/(h\omega_0)$, as

$$\sigma_\tau = \left(\frac{S|\eta|}{6\pi \nu_s \omega_0 \beta_t^2 \gamma_t E_{\text{rest}}} \right)^{1/2}. \tag{16.17}$$

Substituting $\eta(-T_c)$ from Eq. (16.7) and $\omega_s(-T_c)$ from Eqs. (16.11) and (16.12), we arrive at

$$\sigma_\tau = \frac{1}{\sqrt{3\pi}} \left(\frac{S T_c^2 \dot{\gamma}_t}{\beta_t^2 \gamma_t^4 E_{\text{rest}}} \right)^{1/2}. \tag{16.18}$$

Our simple model requires no synchrotron oscillation inside the nonadiabatic region. This is equivalent to having $\eta = 0$ in Eq. (16.3); or the phase of each particle will not change at all. Therefore, Eq. (16.18) is also the bunch length right at transition, where the exact expression from solving the differential equation is

$$\sigma_\tau = \frac{2}{3^{5/6}\Gamma(\frac{1}{3})} \left(\frac{S T_c^2 \dot{\gamma}_t}{\beta_t^2 \gamma_t^4 E_{\text{rest}}} \right)^{1/2}, \tag{16.19}$$

which just amounts to the replacement of $1/\sqrt{3\pi} = 0.326$ by $2/[3^{5/6}\Gamma(\frac{1}{3})] = 0.300$, where $\Gamma(\frac{1}{3}) = 2.678939$ is the Gamma function. Our estimate is about 8.8% too large because our simple model does not allow the bunch to continue to shrink in the nonadiabatic region.

On the other hand, without synchrotron oscillations, the energy of each beam particle is accelerated by the focusing rf force according to Eq. (16.4). From $t = -T_c$ to $t = 0$, a particle at a phase offset $\Delta\phi$ from the synchronous particle acquires the energy

$$\Delta E = T_c E_{\text{rest}} \frac{d\dot{\gamma}}{d\Delta\phi} \Delta\phi, \tag{16.20}$$

where, according to Eq. (16.4),

$$\frac{d\dot{\gamma}}{d\Delta\phi} \approx \frac{\dot{\gamma}_t}{\tan\phi_s}, \tag{16.21}$$

and the small phase-offset approximation has been made. At $t = -T_c$, when there are still synchrotron oscillations in our simple model, we can write the phase offset as

$$\Delta\phi = \widehat{\Delta\phi}\cos\omega_s t. \tag{16.22}$$

The energy spread of the particle is, according to the phase-drift equation [Eq. (16.4)],

$$\Delta E = -\frac{\nu_s\beta_t^2\gamma_t E_{\text{rest}}}{h\eta}\widehat{\Delta\phi}\sin\omega_s t = -\frac{\nu_s\beta_t^2\gamma_t E_{\text{rest}}}{h\eta}\sqrt{\widehat{\Delta\phi}^2 - (\Delta\phi)^2}, \tag{16.23}$$

where $\widehat{\Delta\phi} = \sqrt{6}\sigma_\tau h\omega_0$ is the half width of the bunch at $t = -T_c$ as given by Eq. (16.18). When evaluated at $t = -T_c$, it is found that the coefficient of Eq. (16.23) is equal to that of Eq. (16.20), and we denote it by

$$a = -\frac{\nu_s\beta_t^2\gamma_t E_{\text{rest}}}{h\eta} = T_c E_{\text{rest}}\frac{d\dot{\gamma}}{d\Delta\phi}. \tag{16.24}$$

Therefore, the total energy spread at transition is given by

$$(\Delta E)_{\text{total}} = a\left[\sqrt{\widehat{\Delta\phi}^2 - (\Delta\phi)^2} + \Delta\phi\right], \tag{16.25}$$

where the last term comes from the acceleration received in the nonadiabatic region. The maximum total energy spread comes out to be

$$(\Delta E)_{\text{total, max}} = \frac{1}{\sqrt{\pi}}\left(\frac{S\beta_t^2\gamma_t^4 E_{\text{rest}}}{T_c^2\dot{\gamma}_t}\right)^{1/2} \tag{16.26}$$

at $\Delta\phi = 2^{-1/2}\widehat{\Delta\phi}$. The exact value from the solution of the differential equation is

$$(\Delta E)_{\max} = \frac{\Gamma(\frac{1}{3})}{3^{1/6}2^{1/2}\pi}\left(\frac{S\beta_t^2\gamma_t^4 E_{\text{rest}}}{T_c^2\dot{\gamma}_t}\right)^{1/2}, \tag{16.27}$$

or just a replacement of $1/\sqrt{\pi} = 0.564$ by $\Gamma(\frac{1}{3})/(3^{1/6}2^{1/2}\pi) = 0.502$. By the same token, the particle at the tail of the bunch will be decelerated by the same energy. Particles in between will be accelerated accordingly. The bunch shape at transition is therefore given by Fig. 16.1, which is slanted at an angle from the ΔE-axis. Our estimate of $(\Delta E)_{\text{total}}$ is about 11% too large. This is to be

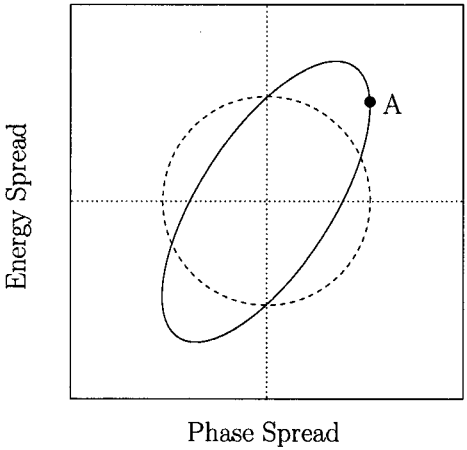


Fig. 16.1 The evolution of the bunch, according to the simple model, from $t = -T_c$ (dashes) to the time when transition is crossed (solid). In the exact solution of the differential equation, there is an additional shrinkage in the phase spread of the ellipse. Point A indicates that when the phase offset is at a maximum, the energy offset is not at a maximum.

expected because we allow pure increment in energy by the focusing rf potential in the nonadiabatic region without any motion in the phase direction.

As we recall, the maximum energy spread at transition is *not* derived via Eq. (16.16) and one should not expect Eq. (16.16) to hold in the nonadiabatic region. Here, we derive another expression for the bunch area right at transition. Using Eqs. (16.18) and (16.26) and the fact that the maximum half bunch length is $\hat{\tau} = \sqrt{6}\sigma_\tau$, we obtain the bunch area

$$S = \frac{1}{\sqrt{2}} \pi \hat{\tau} \widehat{\Delta E}. \tag{16.28}$$

If the exact solutions in Eqs. (16.19) and (16.31) are used, one gets instead

$$S = \frac{\sqrt{3}}{2} \pi \hat{\tau} \widehat{\Delta E}, \tag{16.29}$$

or the replacement of $1/\sqrt{2} = 0.707$ by $\sqrt{3}/2 = 0.866$. Notice that so far we are still within a Hamiltonian system, the bunch area should be conserved. The fact that the bunch area is now less than $\pi \hat{\tau} \widehat{\Delta E}$ indicates that the bunch ellipse has been tilted, as illustrated in Fig. 16.1. This is because phase motion in the nonadiabatic region has almost (totally in our simplified model) been frozen and the energy change has been uneven along the bunch. This problem will be studied again in the next section. We see in Fig. 16.1 that the ellipse has the same phase extend as the circle and crosses the circle when the phase spread is zero. We therefore have the bunch area

$$S = \pi \hat{\tau} \Delta E_0, \tag{16.30}$$

where $\hat{\tau}$ is the maximum phase or time spread and ΔE_0 is the half energy spread when $\tau = 0$ (not the maximum in the longitudinal phase space). The expression in Eq. (16.30) can be proved vigorously for an ellipse in any orientation (Exercise 16.5).

It is useful to write the rms time spread and rms energy spread at transition as well as the nonadiabatic time in terms of the parameters that we can control, namely, the synchronous phase ϕ_s and ramping rate $\dot{\gamma}_t$ (Exercise 16.1):

$$\sigma_\tau \propto \frac{\tan^{\frac{1}{3}} \phi_s}{\dot{\gamma}_t^{\frac{1}{6}}}, \qquad \sigma_E \propto \frac{\dot{\gamma}_t^{\frac{1}{6}}}{\tan^{\frac{1}{3}} \phi_s}, \qquad T_c \propto \frac{\tan^{\frac{1}{3}} \phi_s}{\dot{\gamma}_t^{\frac{2}{3}}}. \tag{16.31}$$

16.1.3 *More Sophisticated Approximation*

Adiabatic Region

We now discard the simple model in the previous section and come back to Eq. (16.9), the equation governing motion of small phase offset. Instead of solving the differential equation exactly, we are looking into approximates instead. In the adiabatic region, but not too far away from transition, the particle is performing synchrotron oscillations with a slowly changing frequency $\omega_s/2\pi$ given by Eq. (16.2). The solution of Eq. (16.9) is therefore of the form

$$\Delta\phi = Ae^{i\int \omega_s dt}, \tag{16.32}$$

where the amplitude A is also slowly changing with time. We then have

$$\frac{d}{dt}\left(\frac{1}{\omega_s^2}\frac{d\Delta\phi}{dt}\right) = -\Delta\phi + \left[\left(\frac{2i\dot{A}}{\omega_s} - \frac{iA\dot{\omega}_s}{\omega_s^2}\right) + \left(\frac{\ddot{A}}{\omega_s^2} - \frac{2\dot{A}\dot{\omega}_s}{\omega^3}\right)\right] e^{i\int \omega_s dt}. \tag{16.33}$$

Since $\Delta\phi$ varies much faster than A and ω_s, we can neglect $\ddot{A}$, $\ddot{\omega}_s$, and $\dot{A}\dot{\omega}_s$, and set

$$\frac{2\dot{A}}{\omega_s} = \frac{A\dot{\omega}_s}{\omega_s^2}, \tag{16.34}$$

so that Eq. (16.9) is satisfied. The relation in Eq. (16.34) leads to

$$\frac{A^2}{\omega_s} = \text{ constant}, \tag{16.35}$$

implying that the solution of Eq. (16.9) or the rf phase of a beam particle in the adiabatic region can be written as

$$\Delta\phi = B\sqrt{\omega_s}\, e^{i\int \omega_s dt}, \tag{16.36}$$

with B being a constant.

The dropping of the slowly varying terms from Eq. (16.33) is equivalent to assuming

$$\frac{\ddot{A}}{\omega_s^2} \ll \frac{A\dot{\omega}_s}{\omega_s^2}, \tag{16.37}$$

$$\frac{2\dot{A}\dot{\omega}_s}{\omega_s^3} \ll \frac{A\dot{\omega}_s}{\omega_s^2}. \tag{16.38}$$

Again, with the assumption of constant rf voltage V_{rf}, constant synchronous phase ϕ_s, and linear time variation of η/E_0 in Eq. (16.7), we can rewrite the synchrotron frequency of Eq. (16.2) in the form

$$\omega_s^2(t) = b|t| \qquad \text{with} \qquad b = \frac{\dot{\gamma}_t h e V_{\mathrm{rf}} |\cos\phi_s| \omega_\infty^2}{\pi \gamma_t^4 E_{\mathrm{rest}}}. \tag{16.39}$$

Then, together with Eq. (16.35), it is easy to show that (Exercise 16.2),

$$\text{Eq. (16.37)} \quad \Longrightarrow \quad |t| \gg \left(\frac{3}{8}\right)^{2/3} \left(\frac{1}{b}\right)^{1/3}, \tag{16.40}$$

$$\text{Eq. (16.38)} \quad \Longrightarrow \quad |t| \gg \left(\frac{1}{2}\right)^{2/3} \left(\frac{1}{b}\right)^{1/3}. \tag{16.41}$$

In other words, the adiabatic solution is only valid if Eqs. (16.40) and (16.41) hold. A nonadiabatic time T_c can therefore be defined by letting

$$T_c = \left(\frac{1}{b}\right)^{1/3}, \tag{16.42}$$

which turns out to be exactly the same expression as our former definition in Eq. (16.12). Here, we arrive at a neat way to remember the nonadiabatic time:

$$\omega_s^2 = \frac{|t|}{T_c^3} \qquad \text{or} \qquad \omega_s|_{t=-T_c} = \frac{1}{T_c}. \tag{16.43}$$

Now, let us continue the study of the bunch shape in the adiabatic region. Differentiating Eq. (16.36) and using Eq. (16.35), we get

$$\frac{d\Delta\phi}{dt} = iB\omega_s^{3/2} \left[1 - \frac{i}{4}\left(\frac{T_c}{|t|}\right)^{3/2}\right] e^{i\int \omega_s dt}, \tag{16.44}$$

or

$$\frac{d\Delta\phi}{dt} = i\omega_s \Delta\phi \left[1 + \frac{1}{16}\left(\frac{T_c}{|t|}\right)^3\right]^{1/2} e^{-i\varphi}, \tag{16.45}$$

with

$$\varphi = \tan^{-1}\frac{1}{4}\left(\frac{T_c}{|t|}\right)^{3/2}. \tag{16.46}$$

Then, using Eq. (16.3), we arrive at the energy offset of the particle

$$\Delta E = i\omega_s \Delta\phi \frac{\beta^2\gamma E_{\text{rest}}}{|\eta| h\omega_0}\left[1 + \frac{1}{16}\left(\frac{T_c}{|t|}\right)^3\right]^{1/2} e^{-i\varphi}. \tag{16.47}$$

We see from Eq. (16.36) that, as the bunch is approaching the nonadiabatic region, its width shrinks in the same way as the decrease of $\sqrt{\omega_s}$. On the other hand, from Eq. (16.47), the height of the bunch increases because of the square root term and the $t^{-1/4}$ dependency in the front factor. We also see that there is a phase advance φ of the energy offset, or a tilt in the bunch shape in the longitudinal phase space. This tells us that there is already slowing down in the phase motion in the adiabatic region when transition is approached. This reminds us again that there is no clearcut boundary between the adiabatic and nonadiabatic regions.

The next task is to relate the constant B to the bunch area. The motion of the particle described by Eqs. (16.36) and (16.47) is of the form

$$\Delta\phi = \widehat{\Delta\phi}\cos\theta, \qquad \Delta E = \widehat{\Delta E}\sin(\varphi - \theta), \tag{16.48}$$

which map out a tilted ellipse of area

$$S = \pi \frac{\widehat{\Delta\phi}}{h\omega_0}\widehat{\Delta E}\cos\varphi, \tag{16.49}$$

inscribed inside the rectangle of half-width $\widehat{\Delta\phi}/(h\omega_0)$ and half-height $\widehat{\Delta E}$, and this is the bunch area in eV-s.

The half bunch length in the adiabatic region can be read off from Eq. (16.36):

$$\widehat{\Delta\phi} = B\omega_s^{1/2}. \tag{16.50}$$

Substituting into Eq. (16.47), we obtain the half energy spread

$$\widehat{\Delta E} = \frac{\beta^2\gamma E_{\text{rest}}}{|\eta| h\omega_0}\omega_s^{3/2}\left[1 + \frac{1}{16}\left(\frac{T_c}{|t|}\right)^3\right]^{1/2}, \tag{16.51}$$

where the last square bracket term is just $\sec\varphi$, as given by Eq. (16.46). When they are substituted in the bunch area in Eq. (16.49), the constant B will be determined,

$$S = \frac{B^2 e V_{\rm rf} |\cos\phi_s|}{2h}, \tag{16.52}$$

which is time independent as anticipated.

Using the linear time dependency of ω_s^2 from Eq. (16.43) and replacing the constant B with Eq. (16.52), we obtain the time dependency of the half bunch length,

$$\widehat{\Delta\phi} = \left(\frac{2hS}{eV_{\rm rf}|\cos\phi_s|T_c}\right)^{1/2} \left(\frac{|t|}{T_c}\right)^{1/4}, \tag{16.53}$$

and also

$$\widehat{\Delta E} = \frac{\omega_0}{\pi}\left(\frac{hSeV_{\rm rf}|\cos\phi_s|T_c}{2}\right)^{1/2} \left(\frac{T_c}{|t|}\right)^{1/4} \left[1 + \frac{1}{16}\left(\frac{T_c}{|t|}\right)^3\right]^{1/2}. \tag{16.54}$$

Through the definition of the nonadiabatic time, the half bunch length and half energy spread can be written in the form that resembles the expressions in Eqs. (16.19) and (16.27):

$$\widehat{\Delta\phi} = h\omega_0 \left(\frac{2ST_c^2\dot{\gamma}_t}{\pi\beta_t^2\gamma_t^4 E_{\rm rest}}\right)^{1/2} \left(\frac{|t|}{T_c}\right)^{1/4}, \tag{16.55}$$

$$\widehat{\Delta E} = \left(\frac{S\beta_t^2\gamma_t^4 E_{\rm rest}}{2\pi T_c^2\dot{\gamma}_t}\right)^{1/2} \left(\frac{T_c}{|t|}\right)^{1/4} \left[1 + \frac{1}{16}\left(\frac{T_c}{|t|}\right)^3\right]^{1/2}. \tag{16.56}$$

Nonadiabatic Region

We can also study the nonadiabatic region from Eq. (16.9). The latter can be transformed to

$$\frac{d}{dx}\left(\frac{1}{|x|}\frac{d\Delta\phi}{dx}\right) + \Delta\phi = 0, \tag{16.57}$$

where $x = t/T_c$ and use has been made of Eq. (16.39). However, we find it easier to solve instead the differential equation governing energy offset, which reads

$$\frac{d^2\Delta E}{dx^2} + |x|\Delta E = 0. \tag{16.58}$$

We would like to introduce a *normalized* energy offset

$$\Delta p(x) = \frac{2\pi}{\omega_0 e V_{\rm rf} \cos\phi_s T_c}\,\Delta E(x) = \frac{\tan\phi_s}{\dot{\gamma}_t E_{\rm rest} T_c}\,\Delta E(x), \tag{16.59}$$

so that $\Delta p(x)$ will have the same dimension as $\Delta\phi$, the energy equation of motion becomes the simple relation

$$\Delta\phi = -\,\mathrm{sgn}(x)\frac{d\Delta p}{dx}. \tag{16.60}$$

For the sake of convenience, we concentrate on the situation above transition only when $x \geq 0$ so that the absolute-value sign can be dropped and $\mathrm{sgn}(x)$ can be ignored. At the end, we can replace x by $|x|$ everywhere in the solution so that it applies to both above and below transition. Now $\cos\phi_s$ and $\tan\phi_s$ are both negative.

To seek a solution within the nonadiabatic region where $|x| < 1$, it is natural to resort to power series:

$$\Delta p = \sum_{n=0}^{\infty} a_n x^{n+k}, \tag{16.61}$$

where k is to be determined. Substitution into of Eq. (16.58) leads to

$$\sum_{n=-3}^{\infty} a_{n+3}(n+k+3)(n+k+2)x^{n+k+1} + \sum_{n=0}^{\infty} a_n x^{n+k+1} = 0. \tag{16.62}$$

The indicial equations determine that $k = 0$ and $a_2 = 0$. The solution can be written as

$$\Delta p = \Big(a_0 + a_3 x^3 + a_6 x^6 + \cdots\Big) + \Big(a_1 x + a_4 x^4 + a_7 x^7 + \cdots\Big), \tag{16.63}$$

where the coefficients are related by the recurrence relation

$$a_{n+3} = -\frac{a_n}{(n+3)(n+2)}. \tag{16.64}$$

Thus, there are two free constants a_0 and a_1, which are to be expected from a second-order differential equation. It is more convenient to rewrite Eq. (16.63) as

$$\Delta p = a_0\Big(1 + a_3' x^3 + a_6' x^6 + \cdots\Big) + a_1\Big(x + a_4' x^4 + a_7' x^7 + \cdots\Big), \tag{16.65}$$

where we have redefined the coefficients as $a_n' = a_n/a_0$ for $n = 3, 6, 9, \cdots$, and $a_n' = a_n/a_1$ for $n = 4, 7, 8, \cdots$. They can be readily computed from the

recurrence relation:

$$\begin{cases} a'_3 = -\dfrac{1}{(3.2)},\ a'_6 = +\dfrac{1}{(6.5)(3.2)},\ a'_9 = -\dfrac{1}{(9.8)(6.5)(3.2)},\ \cdots, \\ a'_4 = -\dfrac{1}{(4.3)},\ a'_7 = +\dfrac{1}{(7.6)(4.3)},\ a'_{10} = -\dfrac{1}{(10.9)(7.6)(4.3)},\ \cdots, \end{cases} \tag{16.66}$$

where the periods or dots in above denote multiplication. The phase offset can now be obtained using Eq. (16.60):

$$\Delta\phi = -a_0\Big(3a'_3x^2 + 6a'_6x^5 + \cdots\Big) - a_1\Big(1 + 4a'_4x^3 + 7a'_7x^6 + \cdots\Big). \tag{16.67}$$

Now we are going to derive the trajectory of a particle which is at its maximum phase offset right at transition. Thus we obtain

$$-a_1 = \widehat{\Delta\phi}_0 = \frac{2^{3/2}h\omega_0}{3^{1/3}\Gamma(\frac{1}{3})}\left(\frac{ST_c^2\dot{\gamma}_t}{\beta_t^2\gamma_t^4E_{\text{rest}}}\right)^{1/2}, \tag{16.68}$$

with the aid of Eq. (16.19), where an extra subscript "0" has been added to denote "right at transition" or $x = 0$ for the sake of clarity. This position of the beam particle corresponds to Point A in Fig. 16.1, where the energy offset is *not* at its maximum, but is related to it by

$$\Delta E = \widehat{\Delta E}_0 \sin\varphi, \tag{16.69}$$

where φ is the tilde angle referenced in Eq. (16.48), and it modifies the expression of bunch area to $S = \pi\widehat{\tau}_0\widehat{\Delta E}_0\cos\varphi$. However, from Eq. (16.29), the angle is found to be $\cos\varphi = \sqrt{3}/2$. We therefore have

$$a_0 = \frac{1}{2}\widehat{\Delta p}_0 = \frac{1}{2}\frac{|\tan\phi_s|}{\dot{\gamma}_tE_{\text{rest}}T_c}\widehat{\Delta E}_0 = \frac{1}{2}\frac{3^{1/6}\Gamma^2(\frac{1}{3})}{2\pi}\widehat{\Delta\phi}_0, \tag{16.70}$$

where Eqs. (16.19) and (16.27) have been used, and obtain the relation

$$\frac{a_1}{a_0} = -\frac{2\widehat{\Delta\phi}_0}{\widehat{\Delta p}_0} = -\frac{4\pi}{3^{1/6}\Gamma^2(\frac{1}{3})}. \tag{16.71}$$

The trajectory of the beam particle is governed by

$$\Delta p(x) = \widehat{\Delta\phi}_0 \left[-x \left(1 + a_4' x^3 + a_7' x^6 + \cdots\right) - \frac{a_0}{a_1} \left(1 + a_3' x^3 + a_6' x^6 + \cdots\right) \right], \tag{16.72}$$

$$\Delta\phi(x) = \widehat{\Delta\phi}_0 \left[\left(1 + 4a_4' x^3 + 7a_7' x^6 + \cdots\right) + \frac{a_0}{a_1} \left(3a_3' x^2 + 6a_6' x^5 + 9a_9' x^8 + \cdots\right) \right]. \tag{16.73}$$

However, we are not so interested in the motion of a single particle. What we wish to derive are the half width and half energy spread of a bunch at different times. For this, we have to solve an envelope equation given by Eq. (16.91) below with the space-charge coefficient n_{spch} set to zero. However, that is a nonlinear equation which is difficult to tackle. Instead, we try to extract the bunch length and energy from the solution we obtained in Eqs. (16.72) and (16.73). To accomplish this, we introduce an ensemble of beam particles at the phase ellipse. This can be easily done by writing out the general solution of the differential equation [Eq. (16.58)] by a taking a linear combination of the Eq. (16.72) or (16.73) and another solution of the differential equation. Thus, we have

$$\begin{aligned} \Delta p(x) = \widehat{\Delta\phi}_0 \Bigg\{ & \cos\psi \left[-x\Big(1 + a_4' x^3 + a_7' x^6 + \cdots\Big) - \frac{a_0}{a_1}\Big(1 + a_3' x^3 + a_6' x^6 + \cdots\Big) \right] \\ & - \sin\psi \left[\frac{\sqrt{3}a_0}{a_1}\Big(1 + a_3' x^3 + a_6' x^6 + \cdots\Big) \right] \Bigg\}, \end{aligned} \tag{16.74}$$

$$\begin{aligned} \Delta\phi(x) = \widehat{\Delta\phi}_0 \Bigg\{ & \cos\psi \left[\Big(1 + 4a_4' x^3 + 7a_7' x^6 + \cdots\Big) + \frac{a_0}{a_1}\Big(3a_3' x^2 + 6a_6' x^5 + 9a_9' x^8 + \cdots\Big) \right] \\ & + \sin\psi \left[\frac{\sqrt{3}a_0}{a_1}\Big(3a_3' x^2 + 6a_6' x^5 + 9a_9' x^8 + \cdots\Big) \right] \Bigg\}, \end{aligned} \tag{16.75}$$

where $-\sqrt{3}a_0/a_1$ is included purely for convenience and the relation $\Delta\phi = -d\Delta p/dx$ still holds. One constant in these equation is $\widehat{\Delta\phi}_0$, the maximum phase offset of the phase ellipse at $x = 0$. In fact, it solely determines bunch area or the area of the ellipse (Exercise 16.4). The other constant is the phase angle ψ, which represents different particles on the ellipse in the longitudinal phase space.

As a first application, at $x = 0$, Eq. (16.74) becomes

$$\Delta p(x) = -\widehat{\Delta\phi}_0 \frac{a_0}{a_1}\Big(\cos\psi + \sqrt{3}\sin\psi\Big), \tag{16.76}$$

whose maximum occurs when $\psi = \pi/3$. This gives the normalized energy spread at transition

$$\widehat{\Delta p}_0 = -\frac{2a_0}{a_1}\,\widehat{\Delta\phi}_0, \tag{16.77}$$

agreeing with what we have in Eq. (16.71). The phase spread at transition is trivial because only the cosine term in Eq. (16.75) contributes.

Now let us proceed up to the order x. The energy spread in Eq. (16.74) gives

$$\Delta p(x) = -\widehat{\Delta\phi}_0 \frac{a_0}{a_1}\left[\cos\psi\left(1 + \frac{a_1}{a_0}\,x\right) + \sqrt{3}\sin\psi\right]. \tag{16.78}$$

For the maximum,

$$\cos\psi = \frac{1}{2}\left(1 + \frac{3a_1}{4a_0}\,x\right) \quad \text{and} \quad \sin\psi = \frac{\sqrt{3}}{2}\left(1 - \frac{a_1}{4a_0}\,x\right). \tag{16.79}$$

Thus, the half energy spread is

$$\widehat{\Delta p}(x) = \widehat{\Delta p}_0\left[1 + \frac{a_1}{4a_0}\,x\right] = \widehat{\Delta p}_0\left[1 - \frac{\pi}{3^{1/6}\Gamma^2\left(\frac{1}{3}\right)}\,x\right]. \tag{16.80}$$

There is no $\mathcal{O}(x)$ in the correction to the half bunch length. The next order is $\mathcal{O}(x^2)$:

$$\Delta\phi(x) = \widehat{\Delta\phi}_0\left[\cos\psi\left(1 - \frac{a_0}{2a_1}\,x^2\right) - \sin\psi\,\frac{\sqrt{3}a_0}{2a_1}\,x^2\right], \tag{16.81}$$

whose maximum occurs when $\psi = \mathcal{O}(x^2)$. Thus the half bunch length becomes

$$\widehat{\Delta\phi}(x) = \widehat{\Delta\phi}_0\left[1 - \frac{a_0}{2a_1}\,x^2\right] = \widehat{\Delta\phi}_0\left[1 + \frac{3^{1/6}\Gamma^2\left(\frac{1}{3}\right)}{8\pi}\,x^2\right]. \tag{16.82}$$

Higher orders in x of the half energy spread and half bunch length of the bunch can therefore be computed.

It is evident that from time $|t|$ in the nonadiabatic region to the time when transition is crossed, the shrinkage of the bunch length is of order $(|t|/T_c)^2$ and is therefore small, while the increase in energy spread is of order $(|t|/T_c)$ which is much larger. This explains why the simple model of Sec. 16.1.2 works so well; there we can just approximate the bunch length at transition to be the bunch

length at the nonadiabatic time. On the other hand, we have to compute the increase in energy spread within the nonadiabatic region more accurately.

There is an important comment on why that particular combination of independent solutions are used for the phase ellipse in Eq. (16.74) or (16.75). We choose the trajectory in Eqs. (16.72) and (16.73) as one of the independent solution so as to ensure that the bunch ellipse will be tilted to the correct amount at the time when transition is crossed, so that the half bunch length and half energy spread will be correct. Any other combination is also a valid solution of the differential equation, but it will lead to the bunch ellipse to be tilted differently at transition, which in turn implies the possible unphysical situation that the bunch does not fit the rf bucket when it is well below transition.

In passing, we list the exact solution for the phase offset and energy offset:

$$\Delta p(x) = A\, y^{\frac{1}{3}} \left[\cos\psi_1 J_{-\frac{1}{3}}(y) + \sin\psi_1 N_{-\frac{1}{3}}(y)\right],$$

$$\left(\frac{2}{3}\right)^{1/3} \Delta\phi(x) = A\, y^{\frac{2}{3}} \left[\cos\psi_1 J_{\frac{2}{3}}(y) + \sin\psi_1 N_{\frac{2}{3}}(y)\right], \tag{16.83}$$

where $y = \frac{2}{3}|x|^{3/2}$, and J and N are the Bessel and Neumann functions or order $\frac{2}{3}$ or $-\frac{1}{3}$. Here, A and ψ_1 are the two constants of integration. Physically, A is related to the area of the ellipse traced out by the particles and ψ_1 represents the different points on the ellipse. Unlike our solution, this solution is valid for all x. When we are very far from transition, or $|x| \gg 1$, the Bessel functions have the asymptotic expansions:

$$J_\nu(y) \approx \sqrt{\frac{2}{\pi y}} \cos\left[y - \frac{\pi}{2}\left(\nu + \frac{1}{2}\right)\right],$$

$$N_\nu(y) \approx \sqrt{\frac{2}{\pi y}} \sin\left[y - \frac{\pi}{2}\left(\nu + \frac{1}{2}\right)\right]. \tag{16.84}$$

Thus, Δp and $\Delta\phi$ are 90° out of phase, or the bunch fits the bucket as a right ellipse far from transition. Therefore, the bunch ellipse will be tilted to the right amount so that one can read off the correct half bunch length and the half energy spread at the moment when transition is crossed. This explains why we have chosen the combination of $J_{-1/3}$ and $N_{-1/3}$ for Δp in Eq. (16.83) instead of, for example, $J_{-1/3}$ and $J_{1/3}$. We can employ the half bunch length and half energy spread at $|x| \gg 1$ to compute the area of the ellipse and thus obtain its relation with the constant A. This method of asymptotic behavior cannot be applied to the power-series solution we pursuit in this section, because the power-series solution is only valid when $|x| < 1$.

In conclusion, we list the expressions for bunch length and energy spread as ratios of their values at transition (Exercise 16.7):

$$\frac{\widehat{\Delta\phi}}{\widehat{\Delta\phi}_0} = \frac{\Gamma\left(\frac{1}{3}\right)}{2^{2/3}} y^{\frac{2}{3}} \left[J^2_{\frac{2}{3}}(y) + J^2_{-\frac{2}{3}}(y) + J_{\frac{2}{3}}(y) J_{-\frac{2}{3}}(y) \right],$$

$$\frac{\widehat{\Delta p}}{\widehat{\Delta p}_0} = \frac{2^{2/3}\pi}{3^{1/2}\Gamma\left(\frac{1}{3}\right)} y^{\frac{1}{3}} \left[J^2_{\frac{1}{3}}(y) + J^2_{-\frac{1}{3}}(y) - J_{\frac{1}{3}}(y) J_{-\frac{1}{3}}(y) \right], \tag{16.85}$$

where we have expressed the Neumann functions in terms of the Bessel functions to facilitate computation. They are depicted in Fig. 16.2. The dashed curve is the product of the normalized bunch length and energy spread (the two solid curves). It approaches $\sqrt{3}/2$ as time approaches infinity, showing that the bunch is tilted near transition and becomes more and more upright when it is farther and farther from transition [see Eq. (16.29)]. We can readily read from the figure that from transition to the nonadiabatic time, the bunch length increases by 14.45% while the energy spread decreases by 23.17%.

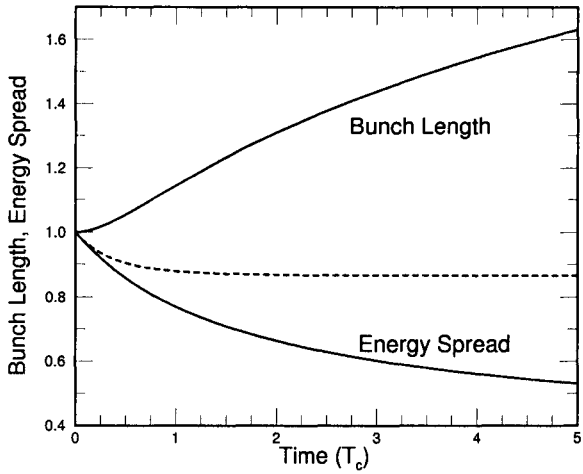


Fig. 16.2 Bunch length and energy spread normalized to their values at transition plotted as functions of time measured from transition in units of the nonadiabatic time T_c. Constant ramping rate is assumed and no wake force has been included. The dashed curve is the product of the two solid curves. It approaches $\sqrt{3}/2$ as time approaches infinity, showing that the bunch has been tilted in the longitudinal phase space near transition.

16.2 Space-Charge Mismatch

In the previous section, the equations of motion are symmetric about the transition time. This means that the bunch becomes shorter and taller while approaching transition, but restores its shape after crossing transition. Most important of all, the equilibrium bunch length is continuous across transition and the bunch

area remains constant. However, the introduction of space-charge breaks this symmetry. Below transition, the space-charge force is repulsive. The rf potential well is distorted, resulting in the lengthening of the bunch. But the situation is different above transition. With the switching of sign of the slip factor, the space-charge force also changes sign. Now it becomes attractive. It adds constructively to the rf focusing force and the equilibrium bunch length becomes shorter instead. This is illustrated in the top plot of Fig. 16.3.

A space-charge parameter can easily be defined. We have derived in Eq. (2.48) the reactive force on a beam particle due to a reactive impedance, which is proportional to the gradient of the longitudinal beam profile. If we assume a parabolic beam profile, this reactive force is linear. Thus, for a linearized

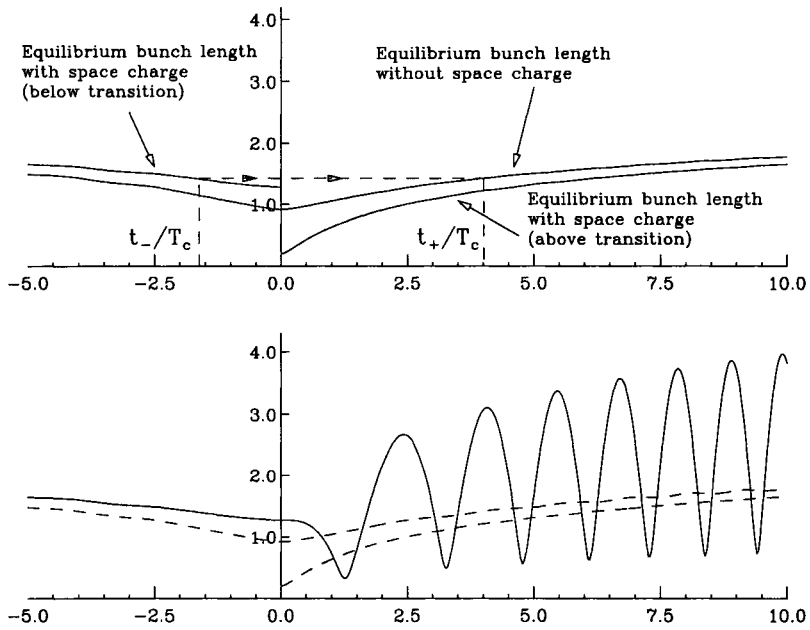


Fig. 16.3 Bunch length is plotted versus x, time normalized to the nonadiabatic time T_c, across transition. Below transition (negative time), the space-charge force is repulsive, thus giving a longer equilibrium bunch length. Above transition (positive time), the space-charge force becomes attractive and therefore shortens the equilibrium bunch length. Top plot shows the mismatch of equilibrium bunch length across transition. A possible transition jump from $x = t_-/T_c$ to $x = t_+/T_c$ should have bunch length matched from the beginning to the end of jump, and is therefore asymmetric with respect to $x = 0$. Lower plot shows the bunch that matches to the space-charge distorted bucket below transition overshoots after crossing transition and oscillates about the shorter equilibrium length.

rf voltage, the space-charge force implies the replacement,

$$\left[eV_{\rm rf}\cos\phi_s\right]\Delta\phi \longrightarrow \left[eV_{\rm rf}\cos\phi_s\right]\Delta\phi - \frac{3\pi N_b r_0 E_{\rm rest} g_0 h^2}{R\gamma_t^2 \widehat{\Delta\phi}^3}\Delta\phi, \tag{16.86}$$

where N_b is the number of particles per bunch with half width $\widehat{\Delta\phi}$ in rf radian, r_0 is the classical particle radius, and R is the mean accelerator radius. Use has been made of the fact that the reactive impedance is the space-charge impedance $Z_0^{\parallel}/n = iZ_0 g_0/(2\beta_t\gamma_t^2)$ at transition energy as given by Eq. (2.45). Notice that $\cos\phi_s$ changes sign from positive to negative on crossing transition. Thus, the space-charge force counteracts the rf force below transition and enhances the rf force above. The ratio of the space-charge force to the rf force is

$$\eta_{\rm spch} = \frac{3\pi N_b r_0 E_{\rm rest} g_0 h^2}{R\gamma_t^2 eV_{\rm rf}|\cos\phi_s|\widehat{\Delta\phi}^3}. \tag{16.87}$$

This ratio is, however, time dependent, because the bunch length changes with time. One can evaluate this ratio right at transition and called it the *space-charge parameter*. Thus

$$\eta_{\rm spch}(0) = \frac{9\Gamma^3(\frac{1}{3})}{16\sqrt{2}}\frac{N_b r_0 g_0 h}{R}\left[\frac{\beta_t E_{\rm rest}}{Sh\omega_0}\right]^{3/2}\left[\frac{h\omega_0}{\beta_t\dot{\gamma}_t}\right]^{1/2}, \tag{16.88}$$

where use has been made of Eq. (16.19). Figure 16.3 is computed according to the space-charge parameter $\eta_{\rm spch}(0) = 2$.

Thus, as soon as transition is crossed, the bunch will find itself unable to fit the rf bucket. The bunch tumbles inside the bucket performing synchrotron oscillations in the quadrupole mode. In the worst situation, there will be beam loss. Even if the bucket is large enough to hold the bunch, the bunch area will increase due to filamentation. Such phenomenon has been observed in the Fermilab Booster, Main Ring, and the present Main Injector. A longitudinal quadrupole damping has been installed in each of the rings to cope with the oscillations. Such a damper consists mainly of a pickup which sends signals of the bunch length to modify the rf voltage, which in turn damp the oscillations. Figure 16.4 shows such a mismatched oscillation at the Fermilab Main Ring. In the left plot, the quadrupole damper is turned off. The lowest trace measures the bunch length by comparing the spectral signal of the third rf harmonic to the fundamental. The bunch length goes through a minimum around 0.78 s when transition is crossed. After that it oscillates at twice the synchrotron frequency in the quadrupole mode with increasing amplitude, as a result of the space-charge mismatch of the equilibrium bunch lengths before and after transition.

Note that the quadrupole synchrotron period is diminishing away from transition due to the fact the slip factor η is increasing. In the right plot, the quadrupole damper is turned on. The lowest trace measures the bunch length. It is evident that although there are some quadrupole oscillations after transition, they are of much smaller amplitudes and are completely damped later.

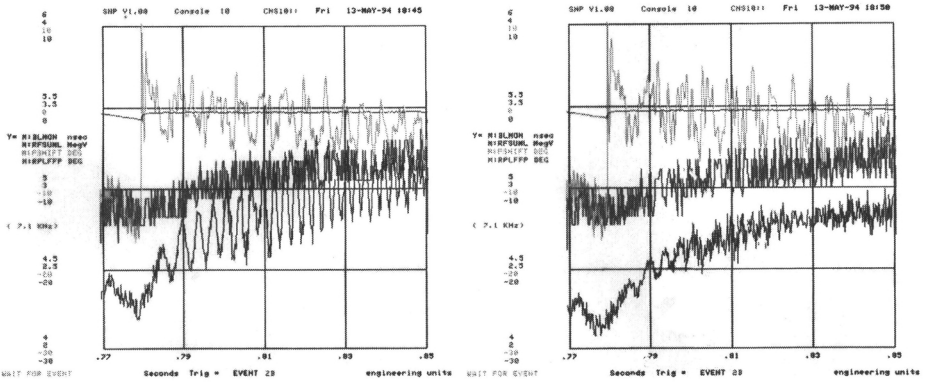


Fig. 16.4 A bunch is crossing transition at the Fermilab Main Ring. The lowest trace of the left plot measures the bunch length. It dips to a minimum at ~ 0.78 s when transition is crossed. It then oscillates at twice the synchrotron frequency with large amplitudes due to space-charge mismatch. In the right plot, the quadrupole damper is turned on. Quadrupole oscillations of small amplitudes are seen in the lowest trace after transition and are completely damped later. (Courtesy Kourbanis.)

16.2.1 *Mathematical Formulation*

Mathematically, this space-charge mismatch phenomenon can be formulated as follows. As a result of Eqs. (16.86) and (16.88), the equation of motion governing $\Delta\phi$ is modified from Eq. (16.9) to

$$\frac{d}{dt}\left[\frac{1}{\omega_s^2}\frac{d\Delta\phi}{dt}\right] + \Delta\phi + \mathrm{sgn}(t)\frac{n_{\mathrm{spch}}}{\widehat{\Delta\phi}^3}\Delta\phi = 0, \tag{16.89}$$

where $n_{\mathrm{spch}} = \eta_{\mathrm{spch}}\widehat{\Delta\phi}^3$ and is no more time dependent. Under the assumption of constant rate of ramping, the differential equation in terms of the normalized time coordinate $x = t/T_c$ becomes

$$\frac{d}{dx}\left[\frac{1}{x}\frac{d\Delta\phi}{dx}\right] + \mathrm{sgn}(x)\Delta\phi + \frac{n_{\mathrm{spch}}}{\widehat{\Delta\phi}^3}\Delta\phi = 0. \tag{16.90}$$

The half bunch length $\widehat{\Delta\phi}$, however, satisfies a slightly different differential equation,

$$\frac{d}{dx}\left[\frac{1}{x}\frac{d\widehat{\Delta\phi}}{dx}\right] + \mathrm{sgn}(x)\widehat{\Delta\phi} + \frac{n_{\mathrm{spch}}}{\widehat{\Delta\phi}^2} - x\,\frac{(S_N/\pi)^2}{\widehat{\Delta\phi}^3} = 0, \tag{16.91}$$

where S_N is a *normalized dimensionless* bunch area when the bunch ellipse is transformed to a circle. It is related to our usual bunch area S in eV-s (true area of the tilted ellipse not just π multiplied by the width and height) by

$$S_N = \frac{2h^2\omega_0^2\dot{\gamma}_t T_c^2}{\beta_t^2\gamma_t^4 E_{\mathrm{rest}}}\,S. \tag{16.92}$$

The derivation was first given by Sørenssen. [1] This is just an envelope equation in the longitudinal phase space and can be derived easily (Exercise 16.8). Comparing with the single-particle equation, Eq. (16.90), there is one extra term proportional to the square of the longitudinal emittance and inversely to the third power of the the bunch length $\widehat{\Delta\phi}$. Such an extra last term also arises in the Kapchinskij–Vladimirskij beam envelope equation for transverse oscillation. [5] In fact, it occurs also in the equation satisfied by the betatron function, where the betatron function takes the place of $\widehat{\Delta\phi}$ while the transverse emittance takes the place of $(S_N/\pi)^2$. This equation cannot be solved analytically. Nevertheless, when it is far away from transition, $|x| \gg 1$, the variation of $\widehat{\Delta\phi}$ with respect to x should be small. We can therefore neglect the derivative in Eq. (16.91), leaving behind an algebraic equation,

$$\widehat{\Delta\phi}^4 + \mathrm{sgn}(x) n_{\mathrm{spch}}\widehat{\Delta\phi} = \frac{S_N^2}{\pi^2}\,|x|. \tag{16.93}$$

In the absence of space-charge, $n_{\mathrm{spch}} = 0$, we recover the solution in Eq. (16.55), namely,

$$\widehat{\Delta\phi} = \left[\frac{S_N}{\pi}\right]^{1/2}|x|^{1/4} = h\omega_0\left[\frac{2ST_c^2\dot{\gamma}_t}{\pi\beta_t^2\gamma_t^4 E_{\mathrm{rest}}}\right]^{1/2}|x|^{1/4}. \tag{16.94}$$

If we wish, we may also consider this as a derivation of the half-bunch-length differential equation [Eq. (16.91)], since we have already derived this expression for half bunch length and we know that such a term proportional to $\left(\widehat{\Delta\phi}\right)^{-3}$ must exist in an envelope equation.

Equation (16.93), a quartic in bunch length, can be further simplified to

$$\theta^4 + \mathrm{sgn}(x)\eta_{N0}\theta = |x|, \tag{16.95}$$

where the *normalized* bunch length θ is defined as

$$\widehat{\Delta\phi} = \sqrt{\frac{S_N}{\pi}}\,\theta = h\omega_0\sqrt{\frac{2\dot{\gamma}_t T_c^2 S}{\pi\beta_t^2\gamma_t^4 E_{\rm rest}}}\,\theta = \sqrt{\frac{2h\omega_0\dot{\gamma}_t T_c^2 S_c}{\pi\beta_t\gamma_t^4}}\,\theta, \tag{16.96}$$

and the normalized space-charge parameter is

$$\begin{aligned}\eta_{N0} = n_{\rm spch}\left[\frac{\pi}{S_N}\right]^{3/2} &= \frac{3\pi^2 N_b r_0 g_0 h}{2R}\left[\frac{\beta_t E_{\rm rest}}{Sh\omega_0}\right]^{3/2}\left[\frac{h\omega_0}{2\pi\beta_t\dot{\gamma}_t}\right]^{1/2} \\ &= \frac{3\pi^2 N_b r_0 g_0 h}{2RS_c^{3/2}}\left[\frac{h\omega_0}{2\pi\beta_t\dot{\gamma}_t}\right]^{1/2},\end{aligned} \tag{16.97}$$

where the explicit expression of T_c has been used. In above, S_c is another commonly used dimensionless bunch area, which is defined as

$$S_c = \pi\widehat{\Delta(\beta\gamma)}\widehat{\Delta\phi} = \frac{h\omega_0}{\beta E_{\rm rest}}\,S. \tag{16.98}$$

Written in terms of these normalized quantities, the differential equation satisfied by the bunch length is also simplified and becomes

$$\frac{d}{dx}\left[\frac{1}{x}\frac{d\theta}{dx}\right] + \mathrm{sgn}(x)\theta + \frac{\eta_{N0}}{\theta^2} - \frac{x}{\theta^3} = 0. \tag{16.99}$$

Notice that $\widehat{\Delta\phi}/\theta$ is proportional to the bunch length at transition,

$$\widehat{\Delta\phi}_0 = \frac{2^{3/2}h\omega_0}{3^{1/3}\Gamma(\frac{1}{3})}\left[\frac{ST_c^2\dot{\gamma}_t}{\beta_t^2\gamma_t^4 E_{\rm rest}}\right]^{1/2}. \tag{16.100}$$

Thus, aside from a constant, θ can also be considered as normalized to the bunch length at transition. In fact, evaluated at transition without space-charge, $\theta = 2\pi^{1/2}3^{-1/3}/\Gamma(\frac{1}{3}) = 0.91748$ radian, as indicated in Fig. 16.3. Comparing the original space-charge parameter $\eta_{\rm spch}(0)$ in Eq. (16.88) with the normalized space-charge parameter η_{N0}, we find

$$\eta_{N0} = \frac{8\pi^{3/2}}{3\left[\Gamma(\frac{1}{3})\right]^3}\,\eta_{\rm spch}(0) = 0.77233\,\eta_{\rm spch}(0). \tag{16.101}$$

The lower plot in Fig. 16.3 is derived from solving Eq. (16.99) numerically starting with a bunch that is matched to the equilibrium bunch length far below transition.

We conclude this section by listing in Table 16.1 some transition crossing properties as well as the space-charge parameters of the Fermilab Booster, Fermilab Main Ring, and Fermilab Main Injector. We have used in the table the

the highest intensity of 6×10^{10} per bunch in operation. A rough space-charge geometric factor of $g_0 \approx 4$ has been assigned to the beam in the Booster when the space-charge impedance is evaluated, but $g_0 \approx 3$ has been assigned to the beams in the other two rings. Since the space-charge parameter $\eta_{\rm spch}(0)$ measures of amount of space-charge induced voltage on the beam relative to the rf voltage, the space-charge mismatch in bunch length after transition is appreciable in all the three rings. In addition, $\eta_{\rm spch}(0)$ for beams in the Fermilab Booster is many times those in the Main Ring and Main Injector. Thus, bunch-length oscillations can be more serious at the Booster before the installation of the quadrupole damper. In fact, this has been one of the reasons of bunch-area increase due to filamentation after crossing transition.

Table 16.1 Some transition crossing properties and the space-charge parameters of the Fermilab Booster, Main Ring, and Main Injector.

	Booster	Main Ring	Main Injector	
Circumference	474.203	6283.185	3319.419	m
Transition γ_t	5.446	18.85	21.80	
Revolution frequency f_0	621.157	47.646	90.220	kHz
Rf harmonic h	84	1113	588	
Rf voltage $V_{\rm rf}$	0.950	2.5	2.78	MV
Synchronous angle ϕ_s	44.0	60.0	37.6	degrees
Ramp rate $\dot{\gamma}_t$	437.1	109.94	163.10	s^{-1}
Nonadiabatic time T_c	0.187	3.00	2.14	ms
Number per bunch N_b	6×10^{10}	6×10^{10}	6×10^{10}	
95% bunch area S	0.05	0.20	0.13	eV-s
Rms bunch length at γ_t	0.293	0.387	0.202	ns
Space-charge g_0	4.0	3.0	3.0	
$\lvert Z_0^{\parallel}/n\rvert_{\rm spch}$	25.9	1.60	1.20	Ohms
Space-charge parameter $\eta_{\rm spch}(0)$	1.16	0.216	0.338	

16.2.2 *Transition Jump*

A transition jump is a way to go around transition crossing so that all the demise can be avoided. [6, 7, 8] It consists of the following steps. At some time $t = t_- < 0$, the currents of some quadrupoles are triggered so that γ_t of the ring is sudden raised and the beam becomes far below transition (usually $\Delta\gamma_t \approx -1$). Next, at some time $t = t_+ > 0$, these quadrupoles are triggered back to their original currents and the γ_t of the ring returns to its original value. However, at this moment the beam is far above (usually $\Delta\gamma_t \approx 1$) the original γ_t already. Because we need to avoid the bunch-length mismatch due to space-charge, we need to make sure that the equilibrium bunch lengths at t_- and t_+ are equal.

This means that $|t_-| < t_+$, or the transition jump will be asymmetric about $t = 0$. This is illustrated in the top plot of Fig. 16.3 (see also Exercise 16.9).

It is important to understand that a transition jump scheme does not really eliminate the crossing of transition. This is because when the transition gamma is returned to its original value by triggering the quadrupoles the second time, the beam particles that were below transition suddenly find themselves above transition. In other words, transition is crossed by changing suddenly the value of γ_t of the lattice instead of ramping the particles. However, crossing transition this way is much faster than ramping, usually faster by a factor of more than ten. The effective $\dot{\gamma}_t$ is therefore very large and the effective nonadiabatic time becomes very small. The manipulation of the quadrupoles at $t = t_-$ can be much slower because there is no transition crossing during that manipulation. We win here because the demise of crossing transition will not have enough time to develop. On the other hand, changing the lattice of the accelerator ring so fast can bring about other problems also. One possibility is a sudden increase in dispersion resulting in a sudden increase in the horizontal beam size which may lead to beam loss. Recently, Visnijic has been able to limit the propagation of this dispersion wave by the installation of a three-quadrupole cell. [9]

In the nonadiabatic region, the particles near the head/tail of the bunch will be gaining/losing excess energy than the synchronous particle. The momentum spread of the bunch may be increased by such an extent that the momentum acceptance will be passed and beam loss occurs. There is a suggestion to add a third or second harmonic to the rf wave so that the latter becomes flat within the length of the bunch. In this way all particles in the bunch will accelerate equally and the excess increase in momentum spread will be suppressed reducing most of the particle loss. This method had been applied to the former Fermilab Main Ring. [10]

16.3 Negative-Mass Instability

Near transition, the slip factor η decreases rapidly, thus decreasing the revolution frequency spread coming from the energy spread. Landau damping therefore diminishes and the beam is subject to instability. Below transition, most proton machines are dominated by space-charge impedance. If the resistive part of the total impedance is small, the proton bunches should be stable against microwave instability. However, as soon as transition is crossed, the space-charge force switches sign and instability becomes unavoidable once the slip factor reaches a vanishingly small value. This is called *negative-mass instability*, the name

coming from the fact that the beam particles see space-charge force attractive and inductive force repulsive above transition, as if they were having negative masses. All low-energy proton machines will suffer from negative-mass instability while crossing transition. However, this instability grows for a limited time only until the slip factor η becomes large enough to Landau-damp the instability. If the ring is well-designed so that the time interval of growth and the growth rate are both small, negative-mass instability just results in a small increase in bunch area. If the ring is not well-designed, the increase in bunch area will be so large that the momentum spread of the bunch may exceed the momentum aperture of the vacuum chamber resulting in beam loss. In a machine like the Fermilab Main Ring or the Fermilab Main Injector, where bunch coalescence is required to feed the Tevatron which is a colliding storage ring, the growth in bunch area is especially important. This is because too large a bunch area after transition will lead to undesirable large bunch area after coalescence, which will in turn lower the luminosity of the Tevatron.

As was discussed in Sec. 5.1.3, while the Landau damping rate decreases as η, the microwave instability growth rate decreases as $\sqrt{|\eta|}$ as well. The growth rate is therefore time dependent, thus complicating the calculation of the total amount of growth in bunch area.

16.3.1 *Growth at Cutoff*

In the absence of space-charge or other coupling impedances, the motion of a particle in the longitudinal phase space can be derived analytically [1] at any time near transition in terms of Bessel function $J_{\frac{2}{3}}$ and Neumann function $N_{\frac{2}{3}}$. With the introduction of space-charge, the growth rate of a small excitation amplitude can be evaluated by integrating the Vlasov equation when the bunch has either an elliptical or bi-Gaussian distribution in the longitudinal phase space. The total growth can then be tallied up by small time steps across transition. Lee and Wang [11] made such a calculation for the Relativistic Heavy Ion Collider (RHIC) at Brookhaven before the machine was built. The emittance growth was taken as two times the growth of the excitation amplitude at the cutoff frequency of the beam pipe, and the result was considered satisfactory. The choice of the cutoff frequency comes from the assumption that electromagnetic waves emitted by the bunch at higher frequencies will not bounce back from the beam pipe to interact with the bunch. This assumption has been verified to be incorrect through simulations. Wei [2] later studied the emittance growth of the Alternating Gradient Synchrotron (AGS) at Brookhaven using a similar approach. His simulation showed that the emittance blowup had been very

much overestimated. Wei pointed out that the bunch emittance had been kept constant by Lee and Wang in the computation of the growth for each time step. The bunch emittance was in fact growing and would provide more Landau damping to counteract the instability. With the emittance updated at each time step, he concluded that his numerical calculations agree with the simulations.

Simple Model

With some suitable assumptions, the model of Lee–Wang–Wei can be made analytic, resulting in some simple formulas for easy estimation. [14] First, let us begin with the dispersion relation of Eq. (5.20) derived in Chapter 5 for the revolution harmonic n:

$$1 = -\left(\frac{\Delta\Omega_0}{n}\right)^2 \int \frac{F'(\Delta\omega)}{\Delta\Omega/n - \Delta\omega}\, d\Delta\omega, \tag{16.102}$$

where $\Delta\Omega = \Omega - n\omega_0$ is the dynamic coherent angular frequency shift, Ω the coherent angular frequency of the instability, and ω_0 the angular revolution frequency of the synchronous particle of the beam or of the on-momentum particle if the beam is truly coasting. Although Eq. (16.102) is a dispersion relation for a coasting beam, however, it has been pointed out by Boussard [12] and later verified analytically by Krinsky and Wang [13] that such a dispersion relation can be applied to a long proton bunch provided that the peak current is used and the wavelength of the disturbance is much less than the bunch length.

In above, $F(\Delta\omega)$ is the distribution in offset of angular revolution frequency $\Delta\omega$ from the nominal value for a slice of the beam where the local current is maximal (usually at $\tau = 0$). The distribution is assumed to be Gaussian in this discussion:

$$F(\Delta\omega) = \frac{1}{\sqrt{2\pi}\sigma_{\omega 0}}\, e^{-\Delta\omega^2/(2\sigma_{\omega 0}^2)}, \tag{16.103}$$

with $\sigma_{\omega 0}$ being the rms spread of that slice of the beam. Since $\sigma_{\omega 0}$ is, in general, not equal to the rms angular revolution frequency spread σ_ω of the whole beam, we have introduced an extra '0' in the subscript. The rms angular revolution frequency spread is related to the rms spread in energy offset σ_{E0} of the same slice of the beam by (note the extra '0' in the subscript)

$$\sigma_{\omega 0} = \frac{|\eta|\omega_0}{\beta^2 E_0}\, \sigma_{E0}, \tag{16.104}$$

where E_0 is the energy and η is the slip factor.

In Eq. (16.102), $\Delta\Omega_0$ is the dynamic coherent frequency shift driven by the longitudinal impedance $Z_0^{\parallel}/n$ in the absence of any spread in the revolution frequency of the beam, and can be expressed as

$$\left(\frac{\Delta\Omega_0}{n}\right)^2 = \frac{ie\eta\omega_0^2 I_{\rm pk}}{2\pi\beta^2 E_0}\,\frac{Z_0^{\parallel}}{n}, \tag{16.105}$$

where $I_{\rm pk} = eN_b/(\sqrt{2\pi}\sigma_\tau)$ is the local current of the slice of the beam under discussion and should be the peak current of the beam, N_b is the number of particles in the bunch, and σ_τ is the rms bunch length.

Dimensionless variables are now introduced,

$$u = \frac{\Delta\omega}{\sigma_{\omega 0}}, \qquad z = \frac{\Delta\Omega}{n\sigma_{\omega 0}}, \tag{16.106}$$

and the dispersion relation takes the form

$$1 = -\left(\frac{\Delta\Omega_0}{n\sigma_{\omega 0}}\right)^2 \int \frac{G'(u)}{z-u}\,du, \tag{16.107}$$

with

$$G(u) = \frac{1}{\sqrt{2\pi}}\,e^{-u^2/2} \tag{16.108}$$

being the stand normal.

Again, we assume the slip factor η to be linear in time near transition as given by

$$\frac{\eta}{E_0} = \frac{2\dot{\gamma}_t}{\gamma_t^4 E_{\rm rest}}\,t = \frac{eV_{\rm rf}\omega_0 \sin\phi_s}{\pi\gamma_t^4 E_{\rm rest}^2}\,t, \tag{16.109}$$

where $E_{\rm rest}$ is the rest energy of the beam particle, t is the time measured from the moment transition is crossed, and $V_{\rm rf}$ the rf voltage. We get, from Eqs. (16.105), (16.107), and (16.109),

$$1 = -i\frac{a}{t}\int \frac{G'(u)}{z-u}du, \tag{16.110}$$

where

$$a = \frac{I_{\rm pk}(Z_0^{\parallel}/n)\beta^2\gamma_t^4 E_{\rm rest}^2}{2\omega_0\sigma_{E0}^2 eV_{\rm rf}\sin\phi_s} = \frac{I_{\rm pk}(Z_0^{\parallel}/n)\beta^2\gamma_t^4 E_{\rm rest}}{4\pi\sigma_{E0}^2\dot{\gamma}_t}, \tag{16.111}$$

is a complex number with the dimension of time. Written in the form of Eq. (16.111), all accelerator and beam parameters have been embedded in the parameter a. Thus, if we measure time with respect to $|a|$, the integral in

Eq. (16.110) becomes dependent only on the phase of the coupling impedance and is independent on all other machine and the beam properties.

We want to compute the time t_0 when η increases to such a value that stability is regained after transition is crossed. There are two simple situations. The first one is when the longitudinal impedance is purely space-charge or capacitive. The parameter a is therefore a positive imaginary number or $-ia$ is real and positive. The integral in Eq. (16.110) must therefore be real. At the edge of instability, $\Delta\Omega/n$ is replaced by $\Delta\Omega/n+i\epsilon$, where ϵ is a positive infinitesimal real number. The imaginary part of the integral is just $-i\pi G'(z) = 0$ and we obtain immediately $z = 0$. This corresponds to Point A on the threshold curve shown in Fig. 16.5. The principal value part of the integral can now be performed easily and it integrates to unity exactly. We obtain the simple solution

$$t_0 = -ia(t_0), \tag{16.112}$$

where we write $a(t_0)$ because a is a function of time through the factor $\beta^2/(\sigma_\tau\sigma_{E0}^2)$. It is obvious that both β and γ are slowly varying across transition, and can be replaced by β_t and γ_t, their values right at transition. Close to transition, the bunch is tilted in the longitudinal phase space. Recall that σ_{E0} is the rms energy spread of the slice of the bunch at $\tau = 0$ where the local current peaks and is therefore not the same as the rms energy spread of the whole bunch. However, a theorem in the geometry of ellipse states that the product $\pi\sigma_\tau\sigma_{E0}$ is the invariant rms phase space area of the beam and is time independent (Exercise 16.5). Thus, the parameter a has the same time variation as the rms bunch length σ_τ. From Fig. 16.2, we learn that the bunch length increases from its value at transition by 14.5% at one nonadiabatic time. However, we

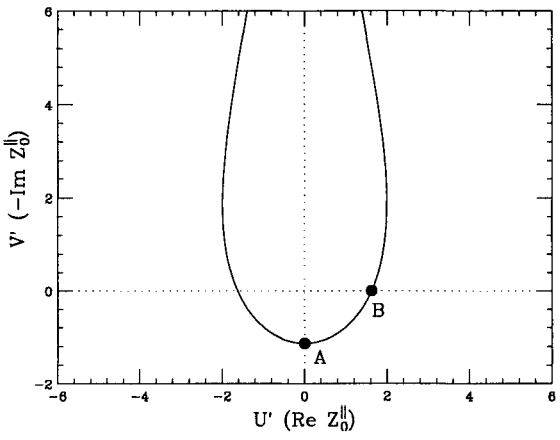


Fig. 16.5 The threshold dispersion curve for Gaussian distribution above transition. Point A corresponds to the situation where the longitudinal impedance is purely capacitive such as space-charge. Point B corresponds to the situation where the longitudinal impedance is purely real such as the peak of a broad resonance.

ignore this variation and treat the parameter a as a time-independent constant. This will be the approximation adopted in this model.

We next compute from Eq (16.110) the growth rate at other time $t = t't_0$, where $0 \le t' \le 1$. The equation to solve is

$$t' = \int \frac{G'(u)}{z-u}\, du. \tag{16.113}$$

The solution is simple because the imaginary part of the right side has to vanish, leading to $z = iy$, where y is real. We obtain[‡]

$$t' = 1 - \sqrt{\frac{\pi}{2}}\, y\, e^{y^2/2} \operatorname{erfc}\left(\frac{y}{\sqrt{2}}\right), \tag{16.114}$$

where $\operatorname{erfc}(x) = 1 - \operatorname{erf}(x)$ is the complimentary error function. The integrated growth decrement per harmonic is given by

$$\frac{S_+}{n} = \int_0^{t_0} \frac{\mathcal{I}m\, \Delta\Omega}{n}\, dt = t_0 \int_0^1 \sigma_{\omega 0}\, \mathcal{I}m\, z\, dt' = \frac{2\sigma_{E0}\dot{\gamma}_t \omega_0 t_0^2}{\beta_t^2 \gamma_t^4 E_{\text{rest}}} \int_0^1 t'\, \mathcal{I}m\, z\, dt', \tag{16.115}$$

where Eqs. (16.104) and (16.109) have been used. In Fig. 16.6(a), we plot $t'\, \mathcal{I}m\, z$ as a function of t' with the aid of Eq. (16.114). With the aid of Eqs. (16.111) and (16.112), the integrated growth per harmonic becomes

$$\frac{S_+}{n} = F_1^{\text{spch}} \frac{e\left(I_{\text{pk}} |Z_0^{\parallel}/n| \beta_t \gamma_t^2 E_{\text{rest}}\right)^2}{4\pi \sigma_{E0}^3 V_{\text{rf}} \sin\phi_s} \tag{16.116}$$

where the constant F_1^{spch}, given by

$$F_1^{\text{spch}} = \int_0^1 t'\, \mathcal{I}m\, z\, dt' = 0.236, \tag{16.117}$$

depends only on the fact that the impedance is capacitive and is independent of all other machine and beam properties. Notice that the integrated growth S_+ depends on $(N_b |Z_0^{\parallel}/n|)^2$, with one factor of $N_b |Z_0^{\parallel}/n|$ coming from the growth rate $\mathcal{I}m\, \Omega$ and the other coming from the duration of instability t_0.

Another possibility to have a simple solution to Eq. (16.110) is to assume $Z_0^{\parallel}/n$ to be purely real, for example at the peak of a broad resonance. Now the parameter a in Eq. (16.110) becomes real and positive. Therefore, we require the real part of the dispersion integral to vanish. To derive the time t_0 where

[‡]First express the right side of Eq. (16.113) in terms of the complex error function $w(iy/\sqrt{2})$ and then use another representation of the complex error function to cast the result in the form of Eq. (16.114).

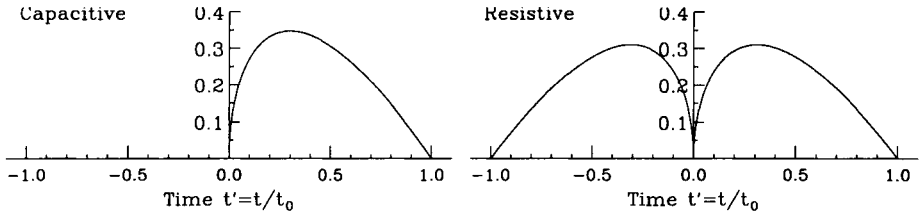


Fig. 16.6 Plot of $t' \mathcal{I}m\, z$, which is proportional to the growth rate, versus normalized time $t' = t/t_0$, where t is measured from the moment when transition is crossed ($t \gtrless 0$ above/below transition), and t_0 is the time when the slip factor η becomes large enough so that stability is achieved. Left: $Z_0^{\parallel}$ is purely capacitance like space-charge. Right: $Z_0^{\parallel}$ is purely real like the peak of a broad resonance. Note that there is no growth below transition when the impedance is purely capacitive.

the beam regains stability, we seek the solution $z = x + i\epsilon$, where ϵ is a positive infinitesimal number. We find x satisfies

$$1 - \sqrt{2}\, x\, e^{-x^2/2} \int_0^{x/\sqrt{2}} e^{t^2} dt = 0, \tag{16.118}$$

giving $x/\sqrt{2} = 0.9241$ or

$$t_0 = \sqrt{\frac{\pi}{2}}\, x\, e^{-x^2/2} = ba, \tag{16.119}$$

where $b = 0.6973$. This solution corresponds to Point B in Fig. 16.5. Substituting back into the dispersion relation, Eq. (16.110) becomes

$$bt' = -i \int \frac{G'(u)}{z-u}\, du = -i \left[1 + i\sqrt{\frac{\pi}{2}}\, z\, w\left(\frac{z}{\sqrt{2}}\right) \right], \tag{16.120}$$

where $t' = t/t_0$ and $w(z)$ is the complex error function. Next we need to relate the growth rate, which is proportional to $\mathcal{I}m\, z$, to the time t' before stability is regained. For each value of $y = \mathcal{I}m\, z$, we require

$$1 - \mathcal{I}m \left[\sqrt{\frac{\pi}{2}}\, z\, w\left(\frac{z}{\sqrt{2}}\right) \right] = 0, \tag{16.121}$$

by solving for x numerically, where $z = x + iy$. The relation of $t' \mathcal{I}m\, z$ as a function of t' is plotted in Fig. 16.6(b). The area under the growth-rate curve is 0.2118 for $0 \leq t' \leq 1$. The integrated growth above transition per harmonic S_+/n is exactly the same expression in Eq. (16.115) except that we now have $t_0^2 = (ba)^2$ instead of the former $t_0^2 = |a|^2$. Thus, we also have the same

Eq. (16.116) but with the constant F_1^{spch} replaced by another universal constant F_{1+}^{real}, which may also be called a form factor. We obtain numerically

$$F_{1+}^{\text{real}} = b^2 \int_0^1 t' \, \mathcal{I}m \, z \, dt' = 0.103. \tag{16.122}$$

Unlike the situation of a purely capacitive impedance, there is now microwave instability both after and before transition. In this particular model of a purely real impedance, the growth is symmetric about the time when transition is crossed. The integrated growth per harmonic S_-/n below transition is exactly equal to S_+/n. Thus adding up the contributions from below and above transition, the form factor becomes $F_1^{\text{real}} = F_{1-}^{\text{real}} + F_{1+}^{\text{real}} = 0.206$, which is just slightly less than F_1^{spch}.

When the condition that $Z_0^{\parallel}/n$ is purely reactive or real is relaxed, the solution of the dispersion relation can still be performed in a similar way, although more complicated, and the result can also be expressed in the form of Eq. (16.116). We can therefore conclude that the integrated growth decrement follows a scaling law [15]

$$\frac{S_-}{n} + \frac{S_+}{n} = \xi F_1, \tag{16.123}$$

where the scaling parameter, containing all the information of the accelerator and the beam except for the impedance phase, is

$$\xi = \frac{e\left(I_{\text{pk}} |Z_0^{\parallel}/n| \beta_t \gamma_t^2 E_{\text{rest}}\right)^2}{4\pi \sigma_{E0}^3 V_{\text{rf}} \sin \phi_s}, \tag{16.124}$$

and the form factor, depending on only the impedance force, is

$$F_1 = F_1^- + F_1^+, \tag{16.125}$$

with F_1^+ representing the integral similar to Eq. (16.122) above transition and F_1^- represents the integral below transition. This form factor, depicted in Fig. 16.7, has a maximum of $F_1 = 0.236$ when the impedance phase is $\phi_z = \pm\pi/2$ (purely capacitive or inductive) and a minimum of $F_1 = 0.206$ when the impedance phase is zero (purely resistive). The variation is less than 15%. The present model can also be extended to other distribution in energy offset, for example the generalized elliptic distribution

$$G(u) = A_m (1 - u^2)^m, \tag{16.126}$$

where m is a parameter and A_m is corresponding the normalization constant. Notice that $m = 1$ just corresponds to the familiar parabolic distribution.

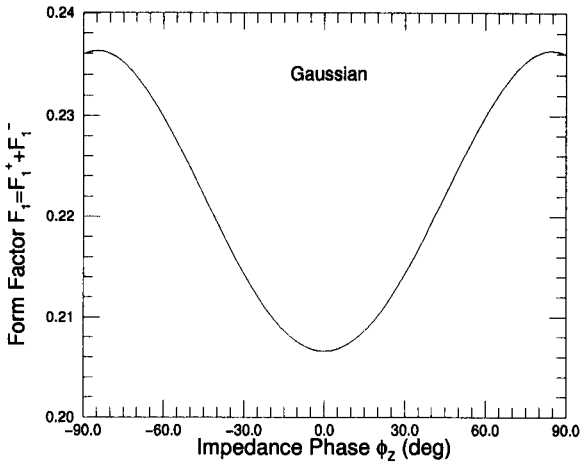


Fig. 16.7 The form factor $F_1 = F_1^- + F_1^+$ for the growth decrement or integrated growth rate across transition is shown as a function of impedance phase ϕ_Z. Variation is less than 15%.

Here, we apply these formulas to the Fermilab Booster, Main Ring, and Main Injector, as listed in Table 16.2. Since the total growth is exponential, it is very sensitive to the bunch area, impedance, number per bunch, and the growth harmonic. Even a decrease of a factor of two in the bunch area or a factor of two enhancement in one of the other quantities can increase the total

Table 16.2 Growth-at-cutoff theory applied to the Fermilab Booster, Main Ring, and Main Injector. Bunch length σ_τ and momentum spread σ_δ are evaluated at transition. However, $\sigma_{\delta 0}$ is rms momentum spread of the slice of the beam where the local current is at a maximum.

	Booster	Main Ring	Main Injector	
95% Bunch Area S	0.080	0.20	0.13	eV-s
Number per bunch N_b	6×10^{10}	6×10^{10}	6×10^{10}	
Nonadiabatic time T_c	0.187	3.00	2.14	ms
Rms bunch length σ_τ	0.370	0.387	0.202	ns
Rms mom-spread at $\tau = 0$, $\sigma_{\delta 0}$	0.00232	0.00155	0.00167	
Rms momentum spread of beam σ_δ	0.00268	0.00179	0.00193	
Cutoff harmonic n	1510	28600	19900	
Cutoff frequency	0.938	1.36	1.79	GHz
$\lvert Z_0^\parallel/n\rvert_{\rm spch}$	25.9	2.63	1.2	Ohms
$Z_0^\parallel/n\rvert_{\rm resis}$	15.0	10.0	1.6	Ohms
Impedance Phase ϕ_Z	59.9	9.06	36.7	deg
Growth duration above transition t_0	2.23	2.30	2.71	ms
σ_τ at t_0	0.292	0.387	0.202	ns
Form Factor F_1	0.230	0.207	0.217	
t_0	0.963	8.56	2.97	ms
Scaling parameter ξ	1.86×10^{-2}	1.99×10^{-3}	3.36×10^{-4}	
Total Growth	636	1.48×10^{7}	4.27	

growth tremendously. As an example, if the Booster bunch area is increased from 0.05 eV-s to 0.08 eV-s, the total growth drops from 636 to just 7.3, 87-fold. However, we should understand that what we have computed here is only the growth of a spectral component and it is not easy to relate it to the growth of the bunch area. We also learn in Chapter 5 that the linearized Vlasov equation is only valid when the initial growth rate is pursued. As soon as the growth develops to a larger value, coupling of other revolution harmonics takes place and nonlinear effects dominate. When saturation is reached, the bunch area becomes diluted and the instability stops. For this reason, the theory of growth at cutoff is not so enlightening. We will analyze all the shortcomings of the model and study the model of Hardt, [18] which may provide a more reasonable criterion of beam blowup across transition. However, this model can be meaningful if the two following conditions are fulfilled: (1) when the perturbing impedance is dominated by a narrow resonance around the cutoff frequency and (2) when the computed total growth is small. On the other hand, a huge computed total growth across transition gives us an indication that the bunch area will have a large increase across transition and beam loss will be possible.

Shortcomings

In order to discuss the shortcomings of the Lee–Wang–Wei method, let us first review some theory of the negative-mass instability. If we ignore Landau damping, the growth rate at peak current $I_{\rm pk}$ at the revolution harmonic n is simply

$$G(n,t) = n\omega_0 \left(\frac{|\eta| e I_{\rm pk} |Z_0^{\parallel}/n|_{\rm spch}}{2\pi\beta^2\gamma E_{\rm rest}} \right)^{1/2}, \tag{16.127}$$

where $E_{\rm rest}$ is the particle rest energy, η is the slip factor, t is the time measured from the moment of transition crossing, and the longitudinal space-charge impedance is given by

$$\left[\frac{Z_0^{\parallel}}{n} \right]_{\rm spch} = i \frac{Z_0 g}{2\beta\gamma^2}. \tag{16.128}$$

Here, $Z_0 \approx 377$ ohms is the free-space impedance, γ and β are the relativistic parameters of the bunch particle at or near transition. In above, g is the space-charge geometric parameter, which has already been derived in Sec. 2.4 at low frequencies with the value

$$g_0 = 1 + 2\ln\frac{b}{a}, \tag{16.129}$$

where a is the beam radius and b the beam pipe radius. A more accurate derivation which is valid for high frequencies has been given by Keil and Zotter. [19] This consists of solving the Maxwell's equations inside the vacuum chamber with boundary conditions matched. The longitudinal electric field E_z can be represented by a linear combination of modified Bessel functions $K_0(z)$ and $I_0(z)$ with $z = \omega r/(c\beta\gamma)$. The result of Eq. (16.129) arrives from the expansion of the Bessel functions at zero frequency. At frequencies of the order $\gamma c/b$, $\gamma c/a$, or higher, the space-charge geometric parameter g rolls off. When b/a is not too big, numerical fittings show that $g(n)$ can be approximated by

$$g(n) = \frac{g_0}{1 + (n/n_{\frac{1}{2}})^2}, \tag{16.130}$$

with the half-value revolution harmonic given roughly by

$$n_{\frac{1}{2}} = \gamma R \left(\frac{1.6}{b} + \frac{0.52}{a} \right), \tag{16.131}$$

where R is the radius of the accelerator ring. It is clear from Eq. (16.127) that at frequencies below the roll-off of the space-charge impedance, the growth rate for negative-mass instability is directly proportional to the harmonic n. It will be shown later in Eq. (16.162) that, when Landau damping is taken into account, the growth rate will be modified and the integrated growth becomes

$$\int_0^{t_0} G(n,t)\, dt \propto n\sqrt{g(n)}, \tag{16.132}$$

where t_0 is the time after crossing transition when the slip factor η becomes large enough so that stability is restored. Thus, the integrated growth exhibits a maximum at $n_{\max} = n_{\frac{1}{2}}/\sqrt{3}$. Taking as an example the Fermilab Main Ring, which has a radius of 1 km and transition gamma $\gamma_t = 18.8$, this corresponds to 77.6 GHz when $a = 5$ mm and $b = 35$ mm are substituted. On the other hand, the cutoff frequency is only about 1.36 GHz. For a typical cycle at an intensity of 3×10^{10} per bunch and emittance 0.15 eV-s, the total growth across transition due to the space-charge impedance for a spectral line is 1.74×10^5 times at the former frequency but only 1.23 at the latter frequency. Similarly, the maximum integrated negative-mass growths for the Fermilab Main Injector and the Fermilab Booster occur at 98.5 and 23.9 GHz, respectively. As a result, it is difficult to justify the correctness of the description of Lee–Wang–Wei. In addition, in Wei's simulation, the bunch was divided into bins with the bin width equal to the cutoff wavelength of the beam pipe. In other words, all large-growth-rate amplitudes at high frequencies had been neglected. Here, we want to point out that the first simulation across transition to exhibit negative-mass instability

was performed by Lee and Teng [16] on the Fermilab Booster, where they also divided the bunch up into cutoff wavelengths only. Later, similar simulations on the same booster were performed by Lucas and MacLachlan, [17] and they also failed to include the high-frequency amplitudes.

Measurements were made near transition for the Fermilab Main Ring. [20] The top row of Fig. 16.8 displays the observed signals around transition at frequencies 4, 5, and 6 GHz for proton bunches with initial longitudinal emittance 0.07 eV-s and 2.3×10^{10} protons. The units on the vertical axis are 5 db per division and on the horizontal axis 2 ms per division. The transition time is marked by an arrow. As seen in the figure, the signals are getting stronger and more persistent with increasing frequency as expected from the negative-mass instability. In this case, the longitudinal emittance after transition was 0.25 eV-s corresponding to a blowup of 3.6. Next a phase mismatch at injection was introduced to blowup the longitudinal emittance from 0.06 to 0.10 eV-s. The lower row of Fig. 16.8 displays the signals observed at 5.0 GHz, with two differ-

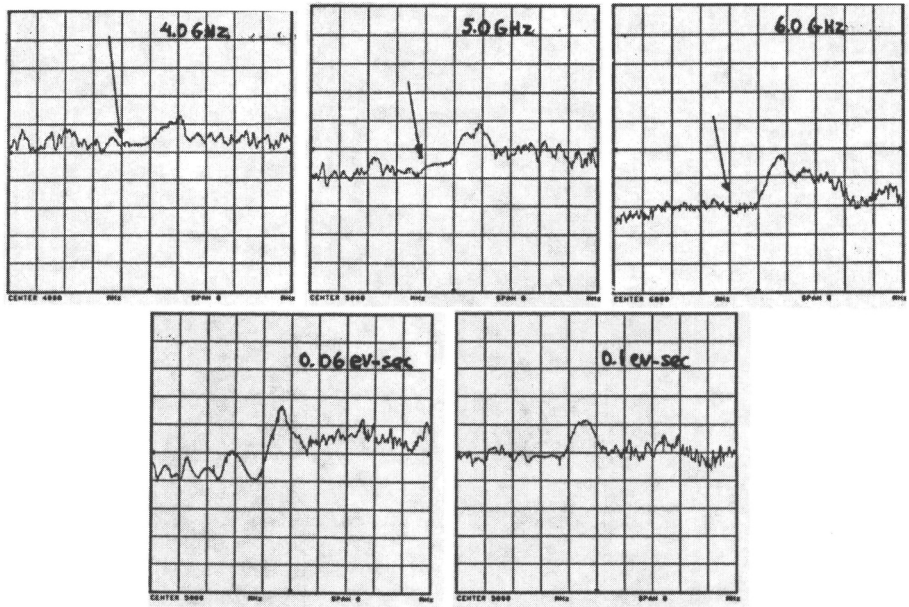


Fig. 16.8 Top row: negative-mass signals at 4.0, 5.0, and 6.0 GHz for bunches with emittance of 0.07 eV-sec and 2.2×10^{10} protons in the Fermilab Main Ring. The signals are stronger and more persistent with increasing frequencies. The arrow marks the time when transition is crossed. Lower row: negative-mass signals at 5.0 GHz for bunches with the same intensity but with longitudinal emittances 0.06 and 0.10 eV-s. The signals are smaller for the larger emittance. Vertical scale: 2db/division. Horizontal scale: 2 ms/division. [20]

ent longitudinal emittances before transition. As expected, the 5.0 GHz signal is smaller for the bigger longitudinal emittance, and dies away faster compared to the signal in the case with the smaller emittance. The emittance blowup at transition is also much smaller for the bigger initial emittance, a factor of 2 compared with 3.6.

One may raise the question that a typical proton bunch which is usually much longer than the radius of the beam pipe will have a spectrum not much higher than the cutoff frequency. Then where does the seed of the high-frequency growth near harmonic $n = n_{\max}$ or $n_{\frac{1}{2}}$ come from? The answer is Schottky noise. However, since Schottky noise is extremely small, the growth effect to the bunch at such high frequencies may or may not be significant. This question will be discussed in Sec. 16.3.2 below, after we go over the Schottky-noise model of Hardt. [18]

16.3.2 *Schottky-Noise Model*

Hardt assumed that the seeds of the negative-mass growth are provided by the statistical fluctuations of the finite number of particles N_b within the bunch on top of a smooth linear profile distribution $F(\Delta\phi)$, where $\Delta\phi$ is the rf phase offset measured from synchronous angle. The smooth distribution $F(\Delta\phi)$ has an average of unity but is normalized to $2\widehat{\Delta\phi}$, the total bunch length. The bunch is divided into M bins in the rf phase coordinate $\Delta\phi$. There are $N_b F(\Delta\phi)/M$ particles in the bin at $\Delta\phi$, and each bin has a width $2\widehat{\Delta\phi}/M$. Due to the statistical fluctuations, the mth bin contains δN_m extra particles. So a step function $f(\Delta\phi, t)$, which is a perturbation to $F(\Delta\phi)$, can be defined by

$$f(\Delta\phi, t) = \frac{\delta N_m}{\Delta N} \qquad \text{if} \quad \frac{m-1}{M} < \frac{\Delta\phi + \widehat{\Delta\phi}}{2\widehat{\Delta\phi}} < \frac{m}{M}, \tag{16.133}$$

where $\Delta N = N_b/M$ is the average number of particles in a bin. The function can be expanded in a Fourier series

$$f(\Delta\phi, t) = \sum_{k_b=-\infty}^{\infty} c_{k_b}(t) e^{i2\pi k_b \Delta\phi/(2\widehat{\Delta\phi})}, \tag{16.134}$$

where

$$c_{k_b}(t) = \frac{1}{2\widehat{\Delta\phi}} \int_{-\widehat{\Delta\phi}}^{\widehat{\Delta\phi}} f(\Delta\phi, t) e^{-i2\pi k_b \Delta\phi/(2\widehat{\Delta\phi})} d\Delta\phi, \tag{16.135}$$

and $c_0(t) = 0$ because of charge or particle conservation. Notice that the expansion has been made in bunch modes k_b, or the number of wavelengths in a

wave that can reside in a bunch with periodic boundary condition at $\pm\widehat{\Delta\phi}$. It should not be confused with the revolution harmonic n, which is the number of wavelengths in a wave around the circumference of the accelerator ring. The two are, however, related to each other by

$$\frac{k_b}{n} = \frac{2\widehat{\Delta\phi}}{2\pi h}, \tag{16.136}$$

where h is the rf harmonic. If we work with waves that vanish at the ends of the bunch or $\pm\widehat{\Delta\phi}$, we need only to include positive integer k_b which represents the number of nodes in the waves across the bunch. However, we are working here with waves that satisfy periodic boundary conditions at $\pm\widehat{\Delta\phi}$; we need to include all integers k_b, positive and negative.

Let us compute the statistical expectation

$$E\Big[|c_{k_b}(0)|^2\Big] = \frac{1}{(2\widehat{\Delta\phi})^2}\int_{-\widehat{\Delta\phi}}^{\widehat{\Delta\phi}} d\Delta\phi \int_{-\widehat{\Delta\phi}}^{\widehat{\Delta\phi}} d\Delta\phi' E\left[\frac{\delta N_m \delta N_n}{(\Delta N)^2}\right] e^{i2\pi k_b(\Delta\phi - \Delta\phi')/(2\widehat{\Delta\phi})}. \tag{16.137}$$

Initially, without any contamination of instability, the statistical fluctuations in the bins are random, or

$$E\Big[\delta N_m \delta N_n\Big] = \delta_{mn}\, \Delta N F(\Delta\phi), \tag{16.138}$$

where the right side is the expected number of particles in the mth bin, in which $F(\Delta\phi)$ is to be evaluated. This means that both $\Delta\phi$ and $\Delta\phi'$ have to be in the same bin in order to be nonvanishing. If we neglect the small fluctuation of the phase inside a bin, we can perform the integration over $d\Delta\phi'$, which just gives $2\widehat{\Delta\phi}/M$, the width of the bin.[§] What is left behind in Eq. (16.137) becomes trivial, and we readily get

$$E\Big[|c_{k_b}(0)|^2\Big] = \frac{1}{(2\widehat{\Delta\phi})^2}\int_{-\widehat{\Delta\phi}}^{\widehat{\Delta\phi}} \frac{F(\Delta\phi)}{\Delta N}\,\frac{2\widehat{\Delta\phi}}{M}\, d\Delta\phi = \frac{1}{N_b}. \tag{16.140}$$

This result is important because it is independent of mode number k_b and the number of bins M, otherwise the model will become meaningless. This also explains why $F(\Delta\phi)$ has been defined to have an average of unity. The evolution

[§]We can also transform the integral over $d\Delta\phi'$ into a summation over the bins by the replacement

$$d\Delta\phi' \to \frac{2\widehat{\Delta\phi}}{M}\sum_m. \tag{16.139}$$

of each mode amplitude c_{k_b} is

$$|c_{k_b}(t_0)| \approx \frac{1}{\sqrt{N_b}} \exp \int_0^{t_0/T_c} G(n,x)\, dx, \tag{16.141}$$

where $G(n,x)$, the growth per unit $x = t/T_c$ with T_c being the nonadiabatic time. The following derivation will be very similar to what we did in the growth-at-cutoff model. The integration is up to time t_0 when the growth rate decreases to zero as the slip factor η increases.

Hardt employed an elliptical initial particle distribution in the longitudinal phase space,¶

$$\psi(\Delta\phi, \Delta E) = \frac{3}{2\pi\widehat{\Delta\phi}\widehat{\Delta E}} \sqrt{1 - \frac{\Delta\phi^2}{\widehat{\Delta\phi}^2} - \frac{\Delta E^2}{\widehat{\Delta E}^2}}, \tag{16.142}$$

so that the linear distribution

$$\rho(\Delta\phi) = \frac{3}{4\widehat{\Delta\phi}} \left(1 - \frac{\Delta\phi^2}{\widehat{\Delta\phi}^2}\right) \tag{16.143}$$

becomes parabolic. Notice that the particle distribution in Eq. (16.142) is right-elliptic in the longitudinal phase space. The neglect of the slanting property of the distribution implies most of the microwave instability growth takes place outside the nonadiabatic region. In other words, this model will be valid only when the growth duration $t_0 \gg T_c$.

The offset of angular revolution frequency $\Delta\omega = \omega - \omega_0$ from that of the synchronous particle is related to the energy offset ΔE by

$$\Delta\omega = -\frac{\eta\omega_0}{\beta^2\gamma E_{\text{rest}}} \Delta E. \tag{16.144}$$

Therefore, at a point $\Delta\phi_1$ along the bunch profile, the distribution in $\Delta\omega$ is

$$f(\Delta\omega) = \frac{2}{\pi\widehat{\Delta\omega}} \frac{\sqrt{1 - \dfrac{\Delta\phi_1^2}{\widehat{\Delta\phi}^2} - \dfrac{\Delta\omega^2}{\widehat{\Delta\omega}^2}}}{1 - \dfrac{\Delta\phi_1^2}{\widehat{\Delta\phi}^2}}. \tag{16.145}$$

Starting from the Vlasov equation, a dispersion relation is derived and is given by Eq. (5.20). For a perturbation wave with revolution harmonic n, the dispersion

¶We outline here our understanding of the original paper of Hardt, which is very condensed and is difficult to read.

relation is

$$1 = -\left(\frac{\Delta\Omega_1}{n}\right)^2 \int \frac{df(\Delta\omega)/d\Delta\omega}{\Delta\Omega/n - \Delta\omega}\, d\Delta\omega, \tag{16.146}$$

where $\Delta\Omega$ is the deviation of coherent angular frequency Ω of the collective motion from $n\omega_0$. We are working with the revolution harmonic now and will go to bunch modes later. The factor before the integral can be written as [Eq. (5.20)]

$$\left(\frac{\Delta\Omega_1}{n}\right)^2 = \frac{ieI_{\text{local}}\eta\omega_0^2 \left[Z_0^{\parallel}(\Omega)/n\right]_{\text{spch}}}{2\pi\beta^2\gamma E_{\text{rest}}}, \tag{16.147}$$

where we substitute for the *local* beam current

$$I_{\text{local}} = \frac{3eN_b\omega_0}{4\widehat{\Delta\phi}}\left(1 - \frac{\Delta\phi_1^2}{\widehat{\Delta\phi}^2}\right), \tag{16.148}$$

and the space-charge impedance

$$\left[\frac{Z_0^{\parallel}}{n}\right]_{\text{spch}} = i\frac{Z_0 g(n)}{2\beta\gamma^2} \tag{16.149}$$

with the geometric factor $g(n)$ given by Eq. (16.130). The result is

$$\left(\frac{\Delta\Omega_1}{n}\right)^2 = -\frac{3N_b r_p g\eta h\omega_0^2}{4\beta^2\gamma^3 R\widehat{\Delta\phi}}\left(1 - \frac{\Delta\phi_1^2}{\widehat{\Delta\phi}^2}\right) = \left(\frac{\Delta\Omega_0}{n}\right)^2\left(1 - \frac{\Delta\phi_1^2}{\widehat{\Delta\phi}^2}\right), \tag{16.150}$$

where R is the radius of the accelerator ring and r_p the classical radius of the beam particle. Notice that the last factor involving $\Delta\phi_1$ will cancel the same factor in the denominator of the distribution function $f(\Delta\omega)$ in the dispersion relation.

Changing the variable of integration from $\Delta\omega$ to

$$y = \frac{\Delta\omega}{\widehat{\Delta\omega}\sqrt{1 - \dfrac{\Delta\phi_1^2}{\widehat{\Delta\phi}^2}}}, \tag{16.151}$$

the dispersion relation simplifies to

$$1 = \frac{2}{\pi}\left(\frac{\Delta\Omega_0}{n\widehat{\Delta\omega}}\right)^2 \int_{-1}^{1} \frac{y\,dy}{(\alpha - y)\sqrt{1 - y^2}}, \tag{16.152}$$

where

$$\alpha = \frac{\Delta\Omega}{n\widehat{\Delta\omega}\sqrt{1 - \dfrac{\Delta\phi_1^2}{\widehat{\Delta\phi}^2}}}. \tag{16.153}$$

The integral on the right side of Eq. (16.152) can be readily performed to give $-\pi + \pi\alpha/\sqrt{\alpha^2 - 1}$. We therefore obtain from the dispersion relation

$$\alpha = \pm\frac{a}{\sqrt{a^2 - 1}}, \qquad \text{with} \quad a = 1 + \left(\frac{n\widehat{\Delta\omega}}{\sqrt{2}\Delta\Omega_0}\right)^2. \tag{16.154}$$

Now the dispersion relation has been solved. The imaginary part of Ω gives the growth rate if positive and damping rate if negative. It is clear from Eqs. (16.153) and (16.154) that the growth rate will be largest at the center of the bunch profile where $\Delta\phi_1 = 0$. From now on we are going to concentrate on the bunch center and drop $\Delta\phi_1$.

The maximum half spread in angular revolution frequency $\widehat{\Delta\omega}$ can be written in terms of the half bunch length $\widehat{\Delta\phi}$ via

$$\widehat{\Delta\omega} = \frac{|\eta|\omega_0\widehat{\Delta E}}{\beta^2\gamma E_{\text{rest}}} = \frac{|\eta|\omega_0 S_c}{\pi\beta\gamma\widehat{\Delta\phi}}, \tag{16.155}$$

where, for convenience, the dimensionless bunch area $S_c = \pi\widehat{\beta\gamma}\widehat{\Delta\phi}$ [Eq. (16.98)] has been used. Thus,

$$\left(\frac{n\widehat{\Delta\omega}}{\sqrt{2}\Delta\Omega_0}\right)^2 = -\frac{2\eta\gamma R S_c^2}{3\pi^2 r_p g N_b h \widehat{\Delta\phi}}. \tag{16.156}$$

Notice that this is essentially the inverse of the bunch length multiplied by the space-charge force.

Since we are after the growth of each bunch mode component near transition, all quantities including the bunch length will be approximated by their values at transition. Recall that under the assumption of a linear time variation of η/E, we defined in Sec. 16.2 a normalized space-charge parameter η_{N0} in Eq. (16.97) and a normalized half bunch length θ in Eq. (16.96). Here, we want to introduce η_N which is the same as η_{N0} with the exception that the space-charge geometric parameter g_0 at zero frequency is replaced by the more general $g(n)$ which covers high frequencies. With the expression in Eq. (16.156), it just turns out that

$$\left(\frac{n\widehat{\Delta\omega}}{\sqrt{2}\Delta\Omega_0}\right)^2 = -\frac{x}{\eta_N\theta}, \tag{16.157}$$

where $x = t/T_c$ and T_c is the nonadiabatic time. The maximum half spread in angular revolution frequency can also be expressed in terms of θ via Eqs. (16.96) and (16.155) as

$$\widehat{\Delta\omega} = \frac{|\eta|\gamma_t}{\theta T_c}\sqrt{\frac{S_c\omega_0}{2\pi h\dot{\gamma}_t\beta_t}} = \frac{|x|}{\theta\gamma_t^2}\sqrt{\frac{2S_c\omega_0\dot{\gamma}_t}{\pi h\beta_t}}, \tag{16.158}$$

where the linear dependency of η near transition has been used.

With the help of Eqs. (16.153), (16.154), and (16.157), the growth rate (for $x > 0$) can be expressed as

$$\mathcal{I}m\,\Omega = n\widehat{\Delta\omega}\,\mathcal{I}m\,\alpha = n\widehat{\Delta\omega}\,\frac{\dfrac{\eta_N\theta}{x} - 1}{\sqrt{\dfrac{2\eta_N\theta}{x} - 1}}. \tag{16.159}$$

Now substitute for $\widehat{\Delta\omega}$ from Eq. (16.158) and the definition of the nonadiabatic time. We arrive at the growth per unit $x = t/T_c$,

$$G(n,x) = T_c\,\mathcal{I}m\,\Omega = \frac{n\eta_N}{h}\sqrt{\frac{S_c|\tan\phi_s|\beta_t}{\pi\dot{\gamma}_t T_c}}\,\frac{1 - \dfrac{x}{\eta_N\theta}}{\sqrt{\dfrac{2\eta_N\theta}{x} - 1}}. \tag{16.160}$$

As a reminder, on the right side of the above equation, n is the revolution harmonic while η_N is the normalized space-charge parameter. We see that this growth rate starts at zero right at transition ($x = 0$), increases to a maximum, and decreases to zero at $x = \eta_N\theta$. Thus the time when the beam regains stability is $t_0 = xT_c = \eta_N\theta T_c$. The accumulated or integrated growth decrement E_{acc} is obtained by an integration over x from $x = 0$ to $x = \eta_N\theta$,

$$E_{\text{acc}}(n) = \int_0^{\eta_N\theta} G(n,x)\,dx. \tag{16.161}$$

The integration can be performed easily with the change of variable $u = x/(2\eta_N\theta)$, and the result is

$$E_{\text{acc}}(n) = \frac{n\eta_N^2\theta}{h}\left(1 - \frac{\pi}{4}\right)\sqrt{\frac{S_c|\tan\phi_s|\beta_t}{\pi\dot{\gamma}_t T_c}}. \tag{16.162}$$

We have computed the growth decrement of a spectral line with revolution harmonic n. Since the normalized space-charge parameter η_N is linear in the

geometric parameter $g(n)$ of the space-charge impedance, the dependence on frequency is therefore

$$E_{\rm acc}(n) \propto \frac{n}{\left(1+\dfrac{n^2}{n_{\frac{1}{2}}^2}\right)^2}. \tag{16.163}$$

The maximum occurs when $n = n_{\rm max} = n_{\frac{1}{2}}/\sqrt{3}$ and is denoted by

$$E_{\rm max} = \frac{3\sqrt{3}\, n_{\frac{1}{2}} \eta_{N0}^2 \theta}{16h}\left(1-\frac{\pi}{4}\right)\sqrt{\frac{S_c|\tan\phi_s|\beta_t}{\pi\dot{\gamma}_t T_c}}, \tag{16.164}$$

where η_{N0} is the same as η_N with the exception of the replacement of $g(n)$ by g_0. The accumulated growth $E_{\rm acc}$ will be exponentiated to arrive at the total growth for a harmonic.

A criterion for negative-mass instability is required. Hardt made the assertion that there is no negative-mass blowup if

$$\sum_{k_b=-\infty}^{\infty} |c_{k_b}(t_0)|^2 \lesssim 1, \tag{16.165}$$

where t_0 is the time when stability is regained. The meaning of this criterion will be explored later. From Eq. (16.141), such a criterion is equivalent to

$$\sum_{k_b=-\infty}^{\infty} \exp\left[2E_{\rm acc}(k_b)\right] \lesssim N_b, \tag{16.166}$$

where N_b is the number of particles in the bunch and the summation is over all possible bunch modes. Because $\exp[E_{\rm acc}]$ assumes a maximum at $n = n_{\rm max}$ and falls off rapidly later, the method of steepest decent will be employed. First, we find that[‖]

$$E_{\rm acc}(n) \approx E_{\rm max}\left[1-\left(\frac{3\Delta n}{2n_{\frac{1}{2}}}\right)^2\right], \tag{16.167}$$

with $\Delta n = n - n_{\rm max}$. Next, the summation over all the bunch modes is converted

[‖]In Eq. (16.167), we obtain $[3\Delta n/(2n_{\frac{1}{2}})]^2$ for the second order term, while it is $[3\Delta n/(4n_{\frac{1}{2}})]^2$ in Ref. [18], which we think is incorrect. Therefore, we are getting slightly different results for Eqs. (16.168), (16.171), and (16.172) than in Ref. [18].

into an integral

$$\sum_{k_b=-\infty}^{\infty} \exp\Big[2E_{\rm acc}(k_b)\Big] = \exp\left[2E_{\rm max}\right] \int_{-\infty}^{\infty} \exp\left[-2\left(\frac{3\sqrt{E_{\rm max}}\Delta k_b}{2k_{b\frac{1}{2}}}\right)^2\right] d\Delta k_b, \tag{16.168}$$

where the bunch mode number k_b has been used instead of the revolution harmonic n. The relation between the two are given by Eq. (16.136). In particular the half-value bunch mode is

$$k_{b\frac{1}{2}} = \frac{\widehat{\Delta\phi}}{\pi h} n_{\frac{1}{2}}. \tag{16.169}$$

The criterion of no blowup can be written as

$$E_{\rm max} \lesssim E_{\rm crit}, \tag{16.170}$$

where the critical total growth $E_{\rm crit}$ is obtained through Eq. (16.166) by equating the right side of Eq. (16.168) to N_b; or

$$\frac{k_{b\frac{1}{2}}}{3}\sqrt{\frac{2\pi}{E_{\rm crit}}}\exp\left[2E_{\rm crit}\right] = N_b, \tag{16.171}$$

after performing the Gaussian integration. This is a transcendental equation which can be solved by iteration, giving

$$E_{\rm crit} \approx \frac{1}{2}\left[\ln N_b - \ln\left(\frac{2k_{b\frac{1}{2}}}{3}\sqrt{\frac{\pi}{\ln N_b}}\right)\right]. \tag{16.172}$$

The leading term, $\frac{1}{2}\ln N_b$, is usually an order of magnitude larger than the second term. Take for example the Fermilab Main Ring which has a radius of $R = 1$ km and transition gamma $\gamma_t = 18.8$. The beam has a radius of $a = 5$ mm and the beam pipe radius is $b = 3.5$ cm. The half-value harmonic number $n_{\frac{1}{2}} = 2.81 \times 10^6$ according to Eq. (16.131) and the half-value bunch mode is $k_{b\frac{1}{2}} = n_{\frac{1}{2}}\omega_0\widehat{\Delta\tau}/\pi = 268$ if we assume a half bunch length of $\widehat{\Delta\tau} = 1$ ns. For a bunch consisting of $N_b = 10^{11}$ particles the leading term is $\frac{1}{2}\ln N_b = 12.7$ and the second term is 0.57.

Finally, we will write out the criterion of no negative-mass blowup, Eq. (16.170), in terms of the more familiar parameters of the accelerator ring and the particle bunch. First, let us list the relevant expressions. They are the normalized space-charge parameter at zero frequency

$$\eta_{N0} = \frac{3\pi^2 N_b r_p g_0 h}{2RS_c^{3/2}}\sqrt{\frac{h\omega_0}{2\pi\beta_t\dot{\gamma}_t}} = \frac{3\pi^2 N_b r_p g_0}{2RS^{3/2}\omega_0}\sqrt{\frac{E_{\rm rest}^3\beta_t^2}{2\pi\dot{\gamma}_t}}, \tag{16.173}$$

and the normalized half bunch length at transition

$$\theta = \sqrt{\frac{\pi\beta_t\gamma_t^4}{2h\omega_0\dot{\gamma}_t T_c^2 S_c}}\,\widehat{\Delta\phi} = \frac{2\sqrt{\pi}}{3^{1/3}\Gamma\left(\frac{1}{3}\right)} = 0.91749. \tag{16.174}$$

where the conversion $S_c/S = h\omega_0/(\beta_t E_{\rm rest})$ has been used. Substituting into the expression for $E_{\max}$ in Eq. (16.164), the threshold for no negative-mass blowup [Eq. (16.170)] can be formulated by introducing a critical parameter c less than unity in the following expression:

$$\xi\, n_{\max}\left(\frac{r_p}{R}\right)^2\left(\frac{E_{\rm rest}^{5/2}\beta_t^{7/6}}{h^{1/3}\omega_0^{4/3}\gamma_t^{2/3}}\right)\left(\frac{N_b^2 g_0^2|\tan\phi_s|^{1/3}}{S^{5/2}\dot{\gamma}_t^{7/6}}\right) = cE_{\rm crit}. \tag{16.175}$$

When the critical parameter $c < 1$, there is no blowup. In above, the coefficient ξ is

$$\xi = \frac{3^{25/6}\pi^2\Gamma\left(\frac{2}{3}\right)}{2^{41/6}}\left(1-\frac{\pi}{4}\right) = 2.44656, \tag{16.176}$$

where $\Gamma\left(\frac{2}{3}\right) = 1.354118$ is the Gamma function, r_p the classical proton radius, $E_{\rm rest}$ the proton rest energy, R the ring radius, g_0 the geometric space-charge parameter at zero frequency, S bunch area in eV-s, ϕ_s the synchronized rf phase, γ_t the transition gamma, $\dot{\gamma}_t$ the rate at which transition is crossed, $n_{\max}$ the revolution harmonic at which the accumulated growth is a maximum, which is related to the half-value revolution harmonic by $n_{\max} = n_{\frac{1}{2}}/\sqrt{3}$, and $k_{b\frac{1}{2}}$ the half-value bunch mode which is given by $k_{b\frac{1}{2}} = n_{\frac{1}{2}}\widehat{\Delta\phi}/(\pi h)$. We have written Eq. (16.175) in such a way that the last factor on the left side pertains to the properties of the beam while the two factors in front pertain to the properties of the accelerator ring.

Some comments are in order:

(1) The critical condition $\sum_{k_b}|c_{k_b}(t_0)|^2 = 1$ implies, through Parseval theorem, that

$$\frac{1}{2\widehat{\Delta\phi}}\int|f(\Delta\phi,t_0)|^2 d\Delta\phi = 1. \tag{16.177}$$

From the definition of the function $f(\Delta\phi)$, the above integral can be re-written as summation over the M bins,

$$\sum_m\left(\frac{\delta N}{\Delta N}\right)_m^2\frac{(\Delta\phi)_b}{2\widehat{\Delta\phi}} = \sum_m\left(\frac{\delta N}{\Delta N}\right)_m^2\frac{1}{M}, \tag{16.178}$$

where ΔN is the average number of particles inside each bin and $(\Delta\phi)_b$ is the width of the bin. Then Eq. (16.177) becomes

$$\frac{\sum_m (\delta N)_m^2}{M} = (\Delta N)^2 . \tag{16.179}$$

The assertion of a negative-mass blowup is equivalent to the situation when the rms fluctuation in each bin is comparable to the average number of particles in each bin, which is really a large particle fluctuation or a big blowup in the bunch. This blowup implies violent changes in the bunch, such as a total bunch breakup. However, the assertion of Eq. (16.165) is a bit hand-waving, because even when the rms fluctuation is much less than ΔN, there can be a big blowup of the bunch emittance already. Hardt's paper provides no recipe to compute the increase in bunch emittance in this regime.

(2) The derivation so far has been a perturbative approach. Here, we want to examine its validity. The perturbation expansion is, in fact,

$$F(\Delta\phi) + f(\Delta\phi, t) = F(\Delta\phi) + \sum_{k_b=-\infty}^{\infty} c_{k_b}(t) e^{i2\pi k_b \Delta\phi/(2\widehat{\Delta\phi})}, \tag{16.180}$$

where $F(\Delta\phi)$ is the smooth linear profile distribution and $f(\Delta\phi, t)$ represents the fluctuation from the smooth distribution. Notice that the unperturbed distribution $F(\Delta\phi)$ has an average of unity. Since Hardt only studied the situation of no blowup or when the fluctuation function $f(\Delta\phi, t)$, as demonstrated in Eq. (16.177), has a rms of less than unity, the perturbation is therefore justified although the amount of growths of the c_{k_b}'s from $t = 0$ to $t = t_0$ are tremendous.

We are going to apply this Schottky-noise model to the Fermilab Main Ring, where many properties have been listed in Tables 16.1 and 16.2. Here, we want to study the negative-mass instability when the ramping rate across transition is $\dot{\gamma}_t = 90.0\ \text{s}^{-1}$. Table 16.3 lists and the top-left plot in Fig. 16.9 shows the computed critical parameter c for bunches of $N_b = 2.2 \times 10^{10}$ and 4.0×10^{10} protons for various bunch areas according to Eq. (16.175). The half bunch length is evaluated right at transition. We see that the parameter c increases very rapidly as the bunch area shrinks to a certain size, $S \lesssim 0.11$ eV-s for the 4.0×10^{10} bunch and $S \lesssim 0.07$ eV-s for the 2.2×10^{10} bunch. In any case, there should not be any negative-mass blowup when the bunch area is around 0.15 eV-s, as demonstrated by experiment. For the Fermilab Main Injector, the ramp rate at transition has been increased to $\dot{\gamma}_t = 160.1\ \text{s}^{-1}$. Compared with the Main Ring at $N_b = 4 \times 10^{10}$ per bunch, the blowup across transition does not occur until the bunch area is about or smaller than $S = 0.07$ eV-s (top-right plot

of Fig. 16.9). The Fermilab Booster ramps at $\dot{\gamma}_t = 406.7\ \mathrm{s}^{-1}$ across transition and can therefore accommodate bunches at much smaller areas without blowup as indicated in the lower-left plot of Fig. 16.9.

Table 16.3 Critical parameter c for negative-mass instability for a proton bunch in the Fermilab Main Ring with $N_b = 2.2 \times 10^{10}$ or 4.0×10^{10} particles. The ramp rate across transition is $\dot{\gamma}_t = 90.0\ \mathrm{s}^{-1}$. A value of $c \gtrsim 1$ implies negative-mass blowup.

Bunch area (eV-s)	Half bunch width (ns)	$N_b = 2.2 \times 10^{10}$		$N_b = 4.0 \times 10^{10}$	
		c	E_{crit}	c	E_{crit}
0.040	0.439	3.84	10.23	12.70	10.54
0.050	0.490	2.21	10.18	7.31	10.48
0.060	0.537	1.41	10.13	4.65	10.44
0.070	0.580	0.96	10.09	3.18	10.40
0.080	0.620	0.69	10.06	2.28	10.36
0.100	0.693	0.40	10.00	1.31	10.31
0.120	0.760	0.25	9.96	0.84	10.26
0.140	0.820	0.17	9.92	0.57	10.22
0.160	0.877	0.12	9.89	0.41	10.19
0.180	0.930	0.09	9.86	0.31	10.16
0.200	0.981	0.07	9.83	0.24	10.13
0.220	1.028	0.06	9.81	0.19	10.11
0.240	1.074	0.05	9.78	0.15	10.09

Growths at Cutoff and at High Frequencies

For a parabolic bunch, the unperturbed linear distribution is

$$F(\Delta\phi) = \frac{3}{4\widehat{\Delta\phi}}\left(1 - \frac{\Delta\phi^2}{\widehat{\Delta\phi}^2}\right), \tag{16.181}$$

which is normalized to have an average of unity. It is expanded in a Fourier series at $t = 0$,

$$F(\Delta\phi) = \sum_{k_b=-\infty}^{\infty} \bar{a}_{k_b}(0) e^{i2\pi k_b \Delta\phi/(2\widehat{\Delta\phi})}, \tag{16.182}$$

where the mode amplitude is, for $k_b > 0$,

$$a_{k_b}(0) = \bar{a}_{k_b}(0) + \bar{a}_{-k_b}(0) = \frac{3}{\pi^2}\frac{(-1)^{k_b+1}}{k_b^2}. \tag{16.183}$$

The bunch mode number k_b which corresponds to the cutoff harmonic $n_{\mathrm{cutoff}} = R/b$, with R and b being, respectively, the radii of the ring and the beam pipe,

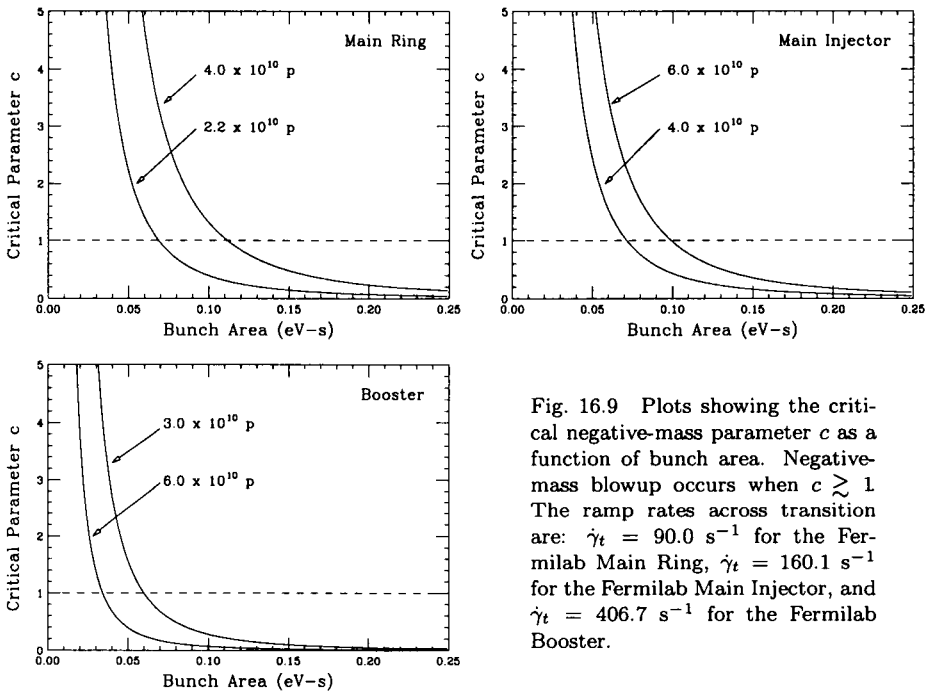


Fig. 16.9 Plots showing the critical negative-mass parameter c as a function of bunch area. Negative-mass blowup occurs when $c \gtrsim 1$ The ramp rates across transition are: $\dot{\gamma}_t = 90.0\ \mathrm{s}^{-1}$ for the Fermilab Main Ring, $\dot{\gamma}_t = 160.1\ \mathrm{s}^{-1}$ for the Fermilab Main Injector, and $\dot{\gamma}_t = 406.7\ \mathrm{s}^{-1}$ for the Fermilab Booster.

can be estimated using Eq. (16.136). Then, the final value of a power spectral line can be computed:

$$|a_{k_b}(t_0)|^2 = |a_{k_b}(0)|^2 \exp\left[\int_0^{t_0/T_c} 2G(n_{\mathrm{cutoff}}, x)dx\right]. \tag{16.184}$$

The results are listed in Table 16.4 for various run cycles of the Fermilab Main Ring. The beam pipe radius and the beam radius are kept fixed at $b = 35$ mm and $a = 5$ mm, respectively. The synchronous phase is 60°. Alongside, we have also tabulated the final size of the Schottky power spectral line at the high harmonic n_{max} according to Eq. (16.141). The sum of all the Schottky power spectral modes has been derived in Eqs. (16.141), (16.168), and (16.171) to be

$$\sum_{k_b=-\infty}^{\infty} |c_{k_b}(t_0)|^2 \approx \frac{k_{b\frac{1}{2}}}{3}\left(\frac{2\pi}{E_p}\right)^{\frac{1}{2}} |c_{k_b}(t_0)|^2_{n=n_{\mathrm{max}}}, \tag{16.185}$$

where

$$E_p = \int_0^{t_0/T_c} G(n_{\mathrm{max}}, x)dx \tag{16.186}$$

Table 16.4 Final fluctuation power spectra at cutoff and high-frequency Schottky harmonics for the Fermilab Main Ring.

$\dot{\gamma}_t$ (s^{-1})	N_b (10^{10})	Initial Bunch Emittance (eV-s)	Final Power Spectrum of Fluctuation at n_{cutoff}	at $n_{\max}$	sum
90	2.2	0.05	3.70	1.50×10^{9}	4.03×10^{10}
90	2.2	0.06	2.21	1.08×10^{2}	3.97×10^{3}
90	2.2	0.07	1.67	1.19×10^{-2}	5.74×10^{-1}
90	2.2	0.08	1.41	4.86×10^{-5}	2.93×10^{-3}
90	2.2	0.09	1.26	1.41×10^{-6}	1.06×10^{-4}
120	4.0	0.06	7.44	4.37×10^{18}	1.00×10^{20}
120	4.0	0.07	3.80	1.94×10^{9}	5.83×10^{10}
120	4.0	0.08	2.54	4.40×10^{3}	1.67×10^{5}
120	4.0	0.09	1.95	1.02×10^{0}	4.76×10^{1}
120	4.0	0.10	1.64	3.57×10^{-3}	2.00×10^{-1}

is the integrated growth at the peak harmonic $n_{\max}$ and $|c_{k_b}(t_0)|^2_{n=n_{\max}} = e^{2E_{\max}}/N_b$ is just the absolute square of the component coefficient at $n = n_{\max}$. This is also listed in the last column of the table.

We can see that the Hardt's blowup criterion of Eq. (16.165) appears to be critical, where the growth changes tremendously. When the criterion is exceeded, the Schottky modes are always larger than the mode at cutoff, showing that the inclusion only up to cutoff frequency is inadequate. On the other hand, below the blowup limit, the mode at cutoff is larger than the high-frequency Schottky modes, implying that there should be modest emittance growth below the Hardt's blowup limit. However, this does not tell us how large the emittance growth is. It will be best if we can sum up the final power spectrum of the bunch distribution:

$$\sum_{k_b} |a_{k_b}(t_0)|^2 = \sum_{k_b} \frac{9}{\pi^4 k_b^4} \exp\Big[\text{integrated growth}\Big]. \tag{16.187}$$

Unfortunately, this sum is divergent because the integrated growth is directly proportional to k_b. Even when we take into account of the space-charge roll-off, the sum still becomes unreasonably large. The reason behind this is the breakdown of the linear perturbation when the perturbed spectral mode becomes larger than the unperturbed one. As a result, it remains unclear whether the high-harmonic Schottky noise is dominating in the growth of the bunch emittance. A simulation seems to be the best solution.

Difficulties in Simulation

A simulation of the negative-mass instability is not trivial. There are two main difficulties:

(1) Inclusion of high-frequency components

The growth of the Schottky noise peaks at $n_{\max}$, which corresponds to roughly 78 GHz for the Fermilab Main Ring, while the half-value space-charge roll-off harmonic $n_{\frac{1}{2}}$ corresponds to 134 GHz. Therefore, in simulations we need a bin size of about $1/(2 \times 134)$ or 0.00373 ns. The tracking code ESME [21] developed at Fermilab divides the whole rf wavelength of 18.8 ns up into 2^n bins where n is an integer, and the number of bins will have to be at least 4096 which is too large. As a rule of thumb, the bins should have a width less than a/γ, where a is the beam radius. Simulations of the Main Ring across transition had been performed using ESME. As the bin number is increased from 128 to 256 and 512, we do see self-bunching in the phase plot corresponding to the highest frequency of 3.40, 6.81, and 13.6 GHz, respectively, in each of the situations, as illustrated in Fig. 16.10. This suggests that the negative-mass growths at the high Schottky frequencies do play a role across transition. [22] In an actual simulation, the space-charge force is usually implemented by a differentiation of the bunch profile. To maintain the same numerical accuracy, we need to follow the *three-in-one rule,* [23] which states that whenever the bin width is reduced by a factor of 2, the number of macro-particles needs to be increased by a factor of 2^3. As a result, the tracking time will increase by a factor of 2^4.

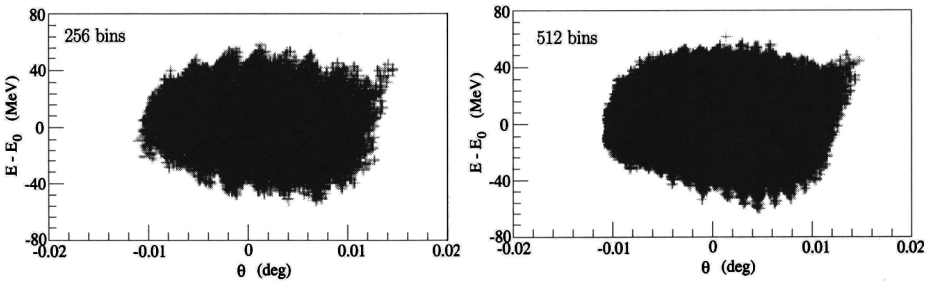


Fig. 16.10 ESME simulations of a Fermilab Main Ring bunch containing 4×10^{10} particles with initial emittance of 0.1 eV-sec just after transition with 256 bins (left) and 512 bins (right) in an rf wavelength; 20,000 and 160,000 macro-particles have been used in the two cases. Excitations of 6.81 and 13.6 GHz corresponding to the respective bin widths are clearly seen in the two longitudinal phase-space plots. (Courtesy Kourbanis.)

However, a typical Main Ring bunch has a full length of only 1 ns at transition, while the bucket width is 18.8 ns. Thus when the whole bucket is divided into bins, the majority of the bins are empty and a lot of computation will have been wasted through multiplication of zero by zero. Instead, if only two or three times the bunch region are divided into bins, there will only be 256 or 512 bins, which will reduce the tracking time drastically. Sørenssen [24] had successfully

performed simulation with a bin width of a/γ. But he did not overcome the second difficulty that we are going to discuss next.

(2) The right amount of Schottky noise

In a simulation of microwave instability, there is usually ample time for the instability to develop to saturation. Therefore, we do not care so much about the size of the initial excitation or seed of the growth. Across transition, however, the bunch is negative-mass unstable only for a short time until the frequency-flip parameter η becomes large enough to provide enough Landau damping, and this time is typically of the order of the nonadiabatic time, which is about 3 ms for the Fermilab Main Ring. Therefore, the initial excitation amplitude needs to be tailored exactly. To have the exact Schottky noise level, we need to use in the simulation micro-particles instead of macro-particles. The Fermilab Main Ring bunch has typically $N_b = 2.2 \times 10^{10}$ particles, which is certainly unrealistically too many in a simulation.

A suggestion is to populate the bunch by N_M macro-particles according to a Hammersley sequence [25] instead of randomly. This is a population according to some pattern so that the statistical fluctuation will become much less. In fact, the number of particles in each bin in excess of the smooth distribution will become $\mathcal{O}(1)$ initially, or the fluctuation function defined in Eq. (16.133) starts from $f(\Delta\phi, 0) \approx 1/\Delta N_M = M/N_M$, where M is the number of bins and $\Delta N_M = N_M/M$ is the average number of macro-particles per bin. Since $E(\delta N_n \delta N_m) = \delta_{nm}$ instead of the previous $\delta_{nm}\Delta N F(\Delta\phi)$, the expectation of the initial bunch mode amplitude turns out to be

$$E\Big[|c_{k_b}(0)|^2\Big] = \frac{M}{N_M^2}. \tag{16.188}$$

Comparing with Eq. (16.140) for a randomly distributed bunch, the number of macro-particles required in the simulation turns out to be

$$N_M = (MN_b)^{\frac{1}{2}}, \tag{16.189}$$

which is very much more reasonable (~ 2.4 to 3.6×10^6), but may be still too large to be manageable in a simulation.

There are, however, two other difficulties with the Hammersley-sequence method. In reality for a bunch containing N_b particles, at the mth bin, the step function $f(\Delta\phi_m, t)$ defined in Eq. (16.133) has an initial expectation of

$$E\Big[f^2(\Delta\phi_m, 0)\Big] = E\left[\frac{\delta N_m^2}{\Delta N^2}\right] = \frac{F(\Delta\phi_m)}{\Delta N} = \frac{M}{N_b} F(\Delta\phi_m), \tag{16.190}$$

which is proportional to the initial unperturbed bunch distribution $F(\Delta\phi_m)$.

Here, $\Delta N = N_b/M$ is the average number of micro-particles in each bin and δN_m is the excess number of particle in the mth bin because of statistically fluctuation. Now it changes to, for the Hammersley population, $E[f^2(\Delta\phi_m, 0)] = (M/N_M)^2$ which is independent of $F(\Delta\phi_m)$. Thus, the relative fluctuations in the bins cannot be made to resemble those in the randomly populated bunch, and the initial fluctuation spectrum would have been altered.

In order to have the bunch to fit the space-charge modified rf bucket before transition, we usually switch on the space-charge force adiabatically over many synchrotron periods so that the initial populated bunch emittance will be preserved. However, the favored Hammersley statistics can often be lost after several synchrotron oscillations. A test was performed with 2×10^5 particles in a truncated bi-Gaussian distribution. The bunch was projected onto one coordinate, where it was divided into 20 equal bins. To simulate synchrotron oscillation, the bunch was then rotated in phase space with an angular velocity which decreases linearly by 1% from the center to the edge of the bunch. The fluctuation or number of particles in excess of the smooth projected Gaussian distribution in each bin was recorded for every rotation, and the rms was computed. The results are plotted in Fig. 16.11 as a function of rotation number. We see that although the rms fluctuation starts from 7 initially, it increases rapidly to $\sim$ 12 after 5 rotations, $\sim$ 20 after 20 rotations, and will approach its statistical value of 100 eventually. This might have been an overestimation, because the actual decrease in synchrotron frequency is not linear and the decrease near the core of the bunch where most particles reside is very much slower. Nevertheless, this test gives us an illustration of restoration to randomness. To cope with the fast restoration to randomness, one possibility is to compute exactly the initial distribution of the bunch in the space-charge modified rf bucket right at transition and populate the bunch according to a Hammersley sequence. In this way, the tracking of the bunch particles across the negative-mass unstable period, which is usually of the order of one synchrotron period, may reveal the reliable growth from the correct Schottky noise level.

16.3.3 *Self-Bunching Model*

Microwave instability can be viewed as self-bunching. The beam current $I_{\rm pk}$, seeing the impedance $Z_0^{\|}$, gives rise to an rf voltage $I_{\rm pk}Z_0^{\|}$, and creates a self-bunching rf bucket with an energy half height

$$\frac{\Delta E}{E} = \left(\frac{2\beta^2 e I_{\rm pk} Z_0^{\|}}{\pi\eta n_z \gamma E_{\rm rest}}\right)^{\frac{1}{2}}, \tag{16.191}$$

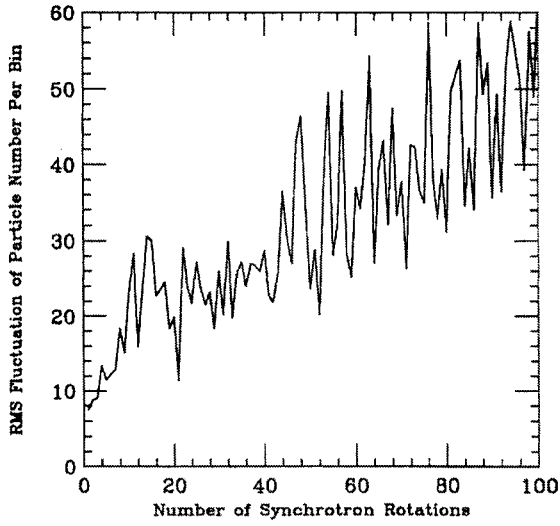


Fig. 16.11 Plot of rms fluctuation of excess particles per bunch versus number of synchrotron rotations, showing the rapid loss of Hammersley statistics and restoration to randomness.

where n_z denotes the revolution harmonic of the impedance. The beam particles will travel along their elliptical trajectories inside the bucket as synchrotron oscillations driven by the impedance. If the height of the bucket is less than the energy spread of the bunch, there will not be any extra energy spread and the bunch will appear to be stable. On the other hand, if the height of the bucket is larger than the energy spread of the bunch, the bunch particles will have to travel outside the original energy boundary of the bunch, giving rise to an emittance growth as a result of eventual filamentation. In fact, this is just another way of expressing the Keil–Schnell criterion. [26]

Here, we want to make the conjecture that this self-bunching bucket height determines the final energy spread of the bunch. Inside this bucket, the angular synchrotron frequency is given by

$$\omega_s = \left(\frac{n_z \eta I_{\rm pk} Z_0^{\parallel}}{2\pi\beta^2\gamma E_{\rm rest}} \right)^{\frac{1}{2}} \omega_0. \tag{16.192}$$

Since the slip factor η is changing rapidly at transition, we substitute, assuming constant ramping,

$$\frac{\eta}{E_0} = \frac{2\dot{\gamma}_t}{\gamma_t^4 E_{\rm rest}}\, t. \tag{16.193}$$

If we denote by $\phi_{\rm syn}$ the angle of synchrotron rotation in the longitudinal phase space, we have $\omega_s = d\phi_{\rm syn}/dt$. Integrating Eq. (16.192), we obtain the time to reach a quarter of a synchrotron oscillation ($\Delta\phi_{\rm syn} = \pi/4$) from the moment of

transition crossing as

$$T \approx \left(\frac{3\pi}{4}\right)^{\frac{2}{3}} \left(\frac{\pi E_{\text{rest}} \beta_t^2 \gamma_t^4}{n_z I_{\text{pk}} Z_0^{\parallel} \dot{\gamma}_t \omega_0^2}\right)^{\frac{1}{3}}. \tag{16.194}$$

This will be the time required for some particles to reach the top of the bucket. Of course, the height of the self-bunching bucket is also changing, and the value of $\eta\gamma$ at this moment should be substituted in Eq. (16.191). At this moment, the unperturbed energy spread of an elliptical bunch with emittance S and without space-charge distortion is, from Eq. (16.80),

$$\frac{\Delta E}{E_0} = \frac{\Gamma\left(\frac{1}{3}\right)}{2^{1/2}3^{1/6}\pi} \left(\frac{S\beta_t^2\gamma_t^2}{E_{\text{rest}} T_c^2 \dot{\gamma}_t}\right)^{\frac{1}{2}} \left(1 - \frac{\pi}{3^{1/6}\Gamma^2\left(\frac{1}{3}\right)} \frac{T}{T_c}\right), \tag{16.195}$$

where T_c is the nonadiabatic time. The correction in the second term of Eq. (16.195) is usually small. Thus, the growth in energy spread can be computed easily, and assuming filamentation the growth in emittance can be obtained. This estimate will be valid if T is less than the time to regain stability. The growths for some situations of the Fermilab Main Ring are given in Table 16.5. The corresponding growths obtained from the growth-at-cutoff model are also listed for comparison.

There is at present no reliable simulation of emittance growth. Experimental measurements are also marred by other mechanisms, such as bunch tumbling due to bunch-length mismatch, particles with different momenta crossing transition at different times, etc. Another difficulty to record emittance growth is scraping. In the Fermilab Main Ring and in many other rings, the bunch emittance usually grows to such a value near transition that scraping occurs. Therefore, it is hard to

Table 16.5 Growth of emittance for the self-bunching and growth-at-cutoff models.

$\dot{\gamma}_t$ (s^{-1})	N_b (10^{10})	Initial Bunch Emittance (eV-s)	Fractional Emittance Growth	
			Self-Bunching Model	Cutoff Model
90	2.2	0.05	4.09	4.06
90	2.2	0.06	3.03	2.43
90	2.2	0.07	2.35	1.83
90	2.2	0.08	1.89	1.54
90	2.2	0.09	1.52	1.38
120	4.0	0.06	5.32	8.16
120	4.0	0.07	4.12	4.17
120	4.0	0.08	3.31	2.78
120	4.0	0.09	2.72	2.14
120	4.0	0.10	2.29	1.80

judge at this moment the reliability of this crude model. On the other hand, this model can certainly be improved to a certain degree by including, for example, the space-charge distortion of the bunch shape, the tilt effect in phase space near transition, as well as the mechanism of overshoot when stability is regained.

16.4 Instability of Isochronous Rings

In a storage ring, sometimes there are advantages to work with a lattice having a smaller slip factor η. One reason is the achievement of shorter bunch lengths. It can be shown easily that, in electron rings where the energy spread is determined by synchrotron radiation, the bunch length is proportional to $|\eta|^{1/2}$. For proton or muon storage rings where there is negligible synchrotron radiation, the bunch length at fixed rf voltage is proportional to $|\eta|^{1/4}$. Another reason for having a small slip factor is the possible reduction of the expensive rf system. To maintain a bunch at the required rms length σ_τ and momentum spread σ_δ, the synchrotron tune is

$$\nu_s = \frac{|\eta|\sigma_\delta}{\omega_0 \sigma_\tau}, \tag{16.196}$$

and the rf voltage is therefore

$$V_{\rm rf} = \frac{2\pi|\eta|\beta^2 E_0 \sigma_\delta^2}{eh\omega_0^2\sigma_\tau^2|\cos\phi_s|} \tag{16.197}$$

which decreases linearly as $|\eta|$. In above, h is the rf harmonic, ϕ_s is the synchronous phase angle, E_0 is the total energy of the synchronous particle which has angular revolution frequency ω_0 and velocity βc where c is the velocity of light. Ideally, when $\eta = 0$, no rf will be necessary, because there will not be any drift in phase. A ring with $\eta = 0$, i.e., operating right at transition energy, is called an *isochronous* ring. However, there is always a spread in energy in the beam particles. As a result, it is not possible for every beam particle to see isochronicity. In addition, the slip factor η is a nonlinear function of the momentum spread. Usually, isochronicity is defined when the slip factor vanishes in the first order of the momentum spread. The higher-order contributions will provide a finite slippage. Thus, the ring is actually quasi-isochronous. For such a ring, the parameters of interest are (1) η for the synchronous particle and (2) the total spread in η seen by all the beam particles. It is necessary to design the lattice so that both η and the spread in η are small. When η is vanishing small, Landau damping will be far from enough and the evolution of collective instabilities will emerge as an important issue, which we are going to investigate.

16.4.1 *Higher-Order Momentum Compaction*

Transition crossing is defined as the moment when the relativistic gamma of the particle is equal to γ_t of the accelerator ring. Let us recall that the transition gamma is defined as $\gamma_t = \alpha_0^{-1/2}$, where α_0 is the momentum-compaction factor which is the fractional increment in the circumferential orbit length of a particle with fractional momentum offset δ. Hence, if $C(\delta)$ is the length of the off-momentum orbit,

$$C(\delta) = C_0(1 + \alpha_0\delta), \tag{16.198}$$

with $C_0 = C(0)$ being the length of the on-momentum orbit. Thus, the slip factor η is exactly zero at transition. However, Eq. (16.198) only gives the linear dependence of the orbit length on momentum offset. In general, this is never the case for any accelerator lattice. Therefore, Eq. (16.198) should be extended to[†]

$$C(\delta) = C_0\big[1 + \alpha_0\delta(1 + \alpha_1\delta + \alpha_2\delta^2 + \cdots)\big], \tag{16.199}$$

where α_1, α_2, etc. are called the high-order components of the momentum-compaction factor. Now the slip factor η also becomes momentum spread dependent. Its higher orders must be carefully defined so that it enters correctly into Eq. (16.3), the phase-slip equation of motion

$$\frac{d\Delta\phi}{dt} = h\omega_0\eta\delta. \tag{16.200}$$

Here, we follow a derivation of Edwards and Syphers. [27] A particle with momentum offset δ_n sees an *accumulated* rf phase ϕ_n on its nth passage of the rf cavity, which is considered to have an infinitesimal length. On its $(n+1)$th passage, at a time $T_{n+1} + \Delta T_{n+1}$ later, the accumulated rf phase seen becomes

$$\phi_{n+1} = \phi_n + \omega_{\rm rf}(T_{n+1} + \Delta T_{n+1}), \tag{16.201}$$

where $\omega_{\rm rf}/2\pi$ is the rf frequency, T_{n+1} is the revolution period of the synchronous particle during its $(n+1)$th turn and ΔT_{n+1} is the extra time taken by the off-momentum particle to complete the revolution. On the other hand, the rf phase seen by the synchronous particle accumulates according to

$$\phi_n^s = \omega_{\rm rf} t_n, \tag{16.202}$$

[†]In Europe, α_0, α_1, α_2, etc. are usually referred to, respectively, as α_1, α_2, α_3, etc. The readers should be aware of yet another definition, where $C(\delta) = C_0\big[1+\alpha_0\delta+\alpha_1\delta^2+\alpha_2\delta^3+\cdots\big]$.

where t_n is the total accumulated time up to the nth passage of the cavity. Naturally, we like to measure the rf phase seen by the off-momentum particle relative to the synchronous particle. This leads to the introduction of the rf phase offset or rf phase slip $\Delta\phi_n$ defined by

$$\Delta\phi_n = \phi_n - \phi_n^s = \phi_n - \omega_{\rm rf} t_n. \tag{16.203}$$

Substituting into Eq. (16.201) and noting that $T_{n+1} = t_{n+1} - t_n$, we arrive at

$$\Delta\phi_{n+1} = \Delta\phi_n + \omega_{\rm rf}\Delta T_{n+1}. \tag{16.204}$$

In order for the synchronous particle to be synchronized, one must adjust the rf frequency so that $\omega_{\rm rf} T_{n+1} = 2\pi h$ for all turns, where h is the rf harmonic number. Now, we can define the slip factor as the slip in revolution period at the $(n+1)$th passage of the cavity by

$$\frac{\Delta T_{n+1}}{T_{n+1}} = \eta_{n+1}\delta_{n+1}. \tag{16.205}$$

Here, the subscript of η implies its dependence on the momentum offset of the particle at the $(n+1)$th passage and *not* its higher-order expansion terms. With this definition, Eq. (16.204) becomes

$$\frac{\Delta\phi_{n+1} - \Delta\phi_n}{T_{n+1}} = \eta_{n+1}\omega_{\rm rf}\delta_{n+1}. \tag{16.206}$$

When smoothing is applied, we obtain the phase-slip equation of Eq. (16.200). The analysis demonstrates that when the phase equation is written as Eq. (16.200), the slip factor must be defined as Eq. (16.205).

Since the revolution period T can be expressed as

$$T = \frac{C}{\beta c}, \tag{16.207}$$

we can easily expand T as a Taylor series in δ, from which each higher-order of the slip factor can be identified. For example, we have

$$\frac{T_0'}{T_0} = \frac{C_0'}{C_0} - \frac{\beta_0'}{\beta_0},$$

$$\frac{T_0''}{T_0} = \frac{2C_0'^2}{C_0^2} - \frac{2\beta_0' C_0'}{\beta_0 C_0} - \frac{\beta_0''}{\beta_0} + \frac{2\beta_0'^2}{\beta_0^2},$$

$$\frac{T_0'''}{T_0} = \frac{C_0'''}{C_0} - \frac{3\beta_0' C_0''}{\beta_0 C_0} - \frac{3\beta_0'' C_0'}{\beta_0 C_0} + \frac{6\beta_0'^2 C_0'}{\beta_0^2 C_0} - \frac{\beta_0'''}{\beta_0} - \frac{\beta_0'\beta_0''}{\beta_0^2} - \frac{6\beta_0'^3}{\beta_0^3}, \tag{16.208}$$

where the *prime* denotes differentiation with respect to δ and all variables are evaluated at the synchronous particle, which explains why all the variables above carry the subscriptions zero, although these subscripts may have been suppressed in many occasions for the sake of convenience. The derivatives of C can be read off easily from Eq. (16.199). The derivatives of β can be computed straightforwardly. They are:

$$\frac{\beta_0'}{\beta_0} = \frac{1}{\gamma_0^2}, \quad \frac{\beta_0''}{\beta_0} = -\frac{3\beta_0^2}{\gamma_0^2}, \quad \frac{\beta_0'''}{\beta_0} = -\frac{3\beta_0^2(1-5\beta_0^2)}{\gamma_0^2}. \tag{16.209}$$

With the expansion of the slip factor

$$\eta = \eta_0 + \eta_1\delta + \eta_2\delta^2 + \cdots, \tag{16.210}$$

we obtain the expressions for the higher-order components of the slip factor [Exercise 16.12]:

$$\eta_0 = \alpha_0 - \frac{1}{\gamma_0^2}, \tag{16.211}$$

$$\eta_1 = \alpha_0\alpha_1 + \frac{3\beta_0^2}{2\gamma_0^2} - \frac{\eta_0}{\gamma_0^2}, \tag{16.212}$$

$$\eta_2 = \alpha_0\alpha_2 + \frac{\alpha_0\alpha_1}{\gamma_0^2} - \frac{2\beta_0^4}{\gamma_0^2} + \frac{3\alpha_0\beta_0^2}{2\gamma_0^2} + \frac{\eta_0}{\gamma_0^4}. \tag{16.213}$$

Looking at the phase-slip equation above, one may be tempted to equate $d\Delta\phi/dt$ to $-h\Delta\omega$, where $\Delta\omega$ is the slip in angular revolution frequency of the off-momentum particle relative to the synchronous particle. However, this will translate the definition of η to

$$\frac{\Delta\omega}{\omega_0} = -\eta\delta, \tag{16.214}$$

which is different from Eq. (16.205) and therefore will lead to incorrect expressions for the higher-order terms of η. This misconception comes about in the smoothing procedure from Eq. (16.206), where we divide throughout by the revolution period of the *synchronous* particle. If $\Delta\omega$ of the off-momentum particle is desired, one should divide instead by $T_{n+1} + \Delta T_{n+1}$, the revolution period of the off-momentum particle. In other words, $d\Delta\phi/dt$ in the phase equation describing the motion of an off-momentum particle does not imply the rate of change of rf phase slip of the off-momentum particle according to the clock that registers the revolution period of that particle. Instead, it is referenced to the clock that registers the revolution period of the synchronous particle. Because of

this easily-forgotten detail, it will be more convenient to use $s = v_0 t$ as the independent 'time' variable, where s is the distance measured along the closed orbit of the synchronous particle and v_0 is the velocity of the synchronous particle.

Another definition in the literature is [2]

$$\eta = -\frac{1}{\omega_0}\frac{d\omega}{d\delta}, \tag{16.215}$$

which is incompatible with the phase-slip equation in Eq. (16.200). This definition originates from the lowest order expansion in ω, [28] and is therefore insufficient when higher-orders in η are studied. This is, in fact, a variation of the incorrect definition of Eq. (16.214).

16.4.2 η_1-*Dominated Bucket*

To save the cost of rf power, suggestions have been made to make storage rings without radiation loss *isochronous* or *quasi-isochronous*, implying an operation at $\eta_0 \approx 0$. Since the drift of the longitudinal phase is small, a small rf system will be adequate. However, when η_0 is small enough, we need to include the next lowest nonlinear term of the slip factor, namely η_1. When the rf phase slip $\Delta\phi$ and the fractional momentum spread δ are used as canonical coordinates with time t being the independent variable according to the clock of the synchronous particle, the Hamiltonian describing the motion of a particle in the longitudinal phase space becomes

$$H = \left(\frac{\eta_0\delta^2}{2} + \frac{\eta_1\delta^3}{3}\right) h\omega_0 + \frac{eV_{\rm rf}\omega_0}{2\pi\beta^2 E_0}\left[\cos(\phi_s+\Delta\phi) - \cos\phi_s + \Delta\phi\sin\phi_s\right], \tag{16.216}$$

where ϕ_s is the synchronous phase. In the presence of η_1, the symmetry of the higher- and lower-momentum parts of the phase space is broken. As a result, the phase-space structure will be very much disturbed. This Hamiltonian gives stable fixed points at $(2n\pi, 0)$, $(2(n+1)\pi - 2\phi_s, -\eta_0/\eta_1)$ and unstable fixed points at $(2(n+1)\pi - 2\phi_s, 0)$, $(2n\pi, -\eta_0/\eta_1)$, where n is any integer. When the contribution of η_1 is much smaller than that of η_0, the buckets are still roughly pendulum-like as shown in Fig. 16.12(a) for the case of $\phi_s = 0$. Note that there is another series of buckets at momentum spread $-\eta_0/\eta_1$. As $|\eta_0/\eta_1|$ decreases to a point when the values of the Hamiltonian through all unstable fixed points are equal, the two series merge as illustrated in Fig. 16.12(b). This happens when

$$\left|\frac{\eta_0}{\eta_1}\right| = \left\{\frac{6eV_{\rm rf}}{\pi\beta^2 h\eta_0 E_0}\left[\left(\frac{\pi}{2} - \phi_s\right)\sin\phi_s - \cos\phi_s\right]\right\}^{1/2}. \tag{16.217}$$

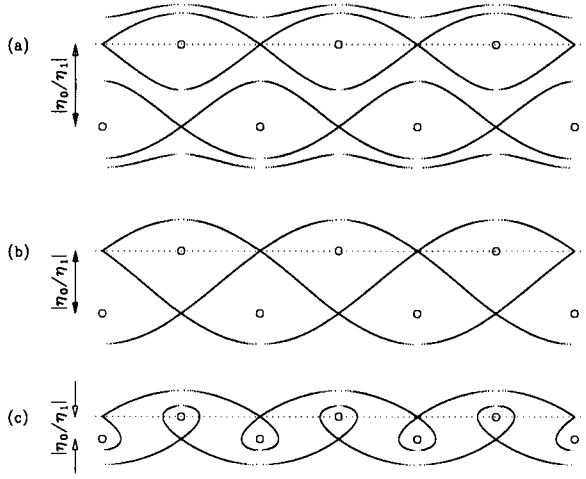


Fig. 16.12 (a) When $|\eta_0/\eta_1|$ is not too small, the longitudinal phase space shows two series of distorted pendulum-like buckets. (b) As $|\eta_0/\eta_1|$ decreases to the critical value in Eq. (16.217), the two series merge. (c) Further reduction of $|\eta_0/\eta_1|$ leads to new pairing of stable and unstable fixed points and the buckets become α-like. In each case, the dotted line is the phase axis at zero momentum spread, and the small circles are the stable fixed points.

The right side is just $\sqrt{3}$ times the half bucket height when the η_1 term in the Hamiltonian is absent. As $|\eta_0/\eta_1|$ is further reduced, the pairing of the stable and unstable fixed points is altered, and the buckets become α-like[‡] as illustrated in Fig. 16.12(c). The buckets in one series have heights given by

$$\delta_{\text{bucket}} = \begin{cases} +\left|\dfrac{\eta_0}{2\eta_1}\right| & \delta > 0, \\ -\left|\dfrac{\eta_0}{\eta_1}\right| & \delta < 0. \end{cases} \tag{16.218}$$

For the other series, the buckets are just inverted and are centered at $\delta = -|\eta_0/\eta_1|$. The heights of the buckets will vanish if the lattice approaches truly isochronous ($\eta_0 = 0$).

Let us now review some very peculiar properties of the α-like bucket.
(1) Since the height of the α-shape bucket is fixed, the bucket width $\Delta\phi$ is proportional to $V_{\text{rf}}^{-1/2}$ and so is the bucket area $\mathcal{A}$. [29] In fact,

$$\Delta\phi = \left(\frac{|\eta_0|^{3/2}}{|\eta_1|}\right)\left(\frac{2\pi\beta^2 hE_0}{3eV_{\text{rf}}|\cos\phi_s|}\right)^{1/2}, \tag{16.219}$$

$$\mathcal{A} = \frac{6}{5}\left(\frac{|\eta_0|^{5/2}}{\eta_1^2}\right)\left(\frac{2\pi\beta^2 hE_0}{eV_{\text{rf}}|\cos\phi_s|}\right)^{1/2}, \tag{16.220}$$

[‡]They are really α-like if the phase and momentum-spread axes are exchanged.

where the narrow width of the bucket has been assumed and its maximum momentum spreads of $|\eta_0/(2\eta_1)|$ and $-|\eta_0/\eta_1|$ have been used. Unlike the usual pendulum-like bucket where the bucket width is fixed and the bucket height and area increase with the rf voltage, here, this α-like bucket has fixed height while its width and area will be increased by *lowering* the rf voltage. As an example, set the bucket height to $|\eta_0/\eta_1| = k_\delta \delta_{\max}$ and the bucket half width to $\hat{\ell} = k_\ell \ell_{\max}$, where $\delta_{\max}$ and $\ell_{\max}$ are the maximum bunch momentum spread and length in m. The required rf voltage multiplied by the rf harmonic required to maintain the bunch in the bucket is, according to Eq. (16.219),

$$hV_{\rm rf} = \frac{2\pi\beta^2 E_0 R^2 |\eta_0| k_\delta^2 \delta_{\max}^2}{3ek_\ell^2 \ell_{\max}^2 |\cos\phi_s|}. \tag{16.221}$$

The maximum momentum spread and bunch length are also related by the Hamiltonian,

$$\frac{V_{\rm rf}}{h} = \frac{\pi\beta^2 E_0 |\eta_0| \delta_{\max}^2}{2e \sin^2 \frac{1}{2}\Delta\phi_{\max}} \left(1 + \frac{2}{3k_\delta}\right), \tag{16.222}$$

where we have set $\phi_s = 0$ or π. The maximum half phase spread is $\Delta\phi_{\max} = h\ell_{\max}/R$. Therefore, when the rf harmonic $h \ll 2R/\ell_{\max}$, Eqs. (16.221) and (16.222) give

$$\left(\frac{k_\delta}{k_\ell}\right)^2 = 3 + \frac{2}{k_\delta}, \tag{16.223}$$

which is universally true, independent of the bunch and lattice parameters.

(2) The asymmetry between positive and negative momentum spreads brought in by η_1 will lead to bunch length oscillations. Since the energy loss due to the resistive part of the impedance of the vacuum chamber is proportional to the bunch length, this may lead to a continuous growth of the synchrotron oscillation amplitude. This instability is called longitudinal head-tail and has been studied in detail in Chapter 12. The longitudinal head-tail instability was first observed in the CERN SPS. [30] The instability can become very strong here because η_0 has been made negligibly small.

(3) The synchrotron frequency as a function of oscillation amplitude can be computed easily. [29] As the oscillation amplitude increases, the synchrotron frequency inside the α-like bucket decreases much more slowly than that inside an ordinary pendulum-like bucket. However, it drops to zero very abruptly near the edge of the bucket. Thus, the α-like bucket resembles a resonance island more than the usual pendulum-like bucket. Because of the sudden drop of the synchrotron frequency near the separatrix, higher-order resonances due

to small jitters or modulations of the rf phase or rf voltage overlap creating a thick stochastic layer thus further reducing the stable area inside the bucket. (4) Although there are disadvantages of the α-like bucket, nevertheless, this bucket is intrinsically narrow in phase spread, as is depicted in Eq. (16.220). For a pendulum-like bucket, the bucket width is always equal to the rf wavelength, whereas for a α-like bucket, the bucket width is mostly much less than the rf wavelength. Moreover, for a bunch in an ordinary pendulum-like bucket, the bunch width varies as $(|\eta_0|/V_{\rm rf})^{1/4}$; thus reducing the momentum-compaction factor or increasing the rf voltage is not very efficient in reducing the width of the bunch. On the other hand, a bunch in the α-like bucket has a width proportional to $|\eta|^{3/2}/V_{\rm rf}^{1/2}$.

16.4.3 η_2-*Dominated Bucket*

The η_1 term will lead to a small bucket area and possibly longitudinal head-tail instability, thus limiting the beam dynamic when the machine is near isochronous. The δ-asymmetric bucket can lead to unpleasant longitudinal head-tail instability. Furthermore, α_1 can destroy the isochronicity of the ring. For example, if we want to have a 2 TeV on 2 TeV isochronous ring for the muon collider with $|\eta| \lesssim 1 \times 10^{-6}$, the α_1 term can contribute a spread of γ_t^{-2} of $\sim 70 \times 10^{-6}$ at the momentum spread of $|\delta| < 0.3\%$. [31] A large spread in γ_t^{-2} implies large slip factors for some particles, so that an unusually large rf system will be required for bunching. Therefore, η_1 should be eliminated. Then, the Hamiltonian with the next nonlinear term η_2 included becomes

$$H = \left(\frac{\eta_0\delta^2}{2} + \frac{\eta_2\delta^4}{4}\right) h\omega_0 + \frac{eV_{\rm rf}\omega_0}{2\pi\beta^2 E_0}\left[\cos(\phi_s+\Delta\phi) - \cos\phi_s + \Delta\phi\sin\phi_s\right]. \quad (16.224)$$

A quadrupole bends particles with positive and negative off-momenta in opposite directions. To the lowest order, it contributes to α_0 of the momentum-compaction factor. On the other hand, a sextupole bends particles with positive and negative off-momenta in the same direction, and therefore contributes to α_1. In fact, through first-order perturbation theory, one can show that α_2 can be corrected with octupoles, α_3 with decapoles, and so on. [32, 33] Having the ability to change α_2 with octupoles may provide a better method than the adjustment using sextupoles, because latter also affect α_1.

With the contribution of η_1 eliminated, it is possible to adjust η_0 to zero so that the Hamiltonian becomes

$$H = \frac{1}{4}h\omega_0\eta_2\delta^4 + \frac{eV_{\rm rf}\omega_0}{2\pi\beta^2 E_0}\left[\cos(\phi_s+\Delta\phi) - \cos\phi_s + \Delta\phi\sin\phi_s\right], \quad (16.225)$$

Now for $\phi_s = 0$, the bucket looks pendulum-like with the usual width of $\Delta\phi = 2\pi$. The bucket half height is $\delta_{\text{bucket}} = [4eV_{\text{rf}}/(\pi\beta^2 E_0 h|\eta_2|)]^{1/4}$. When the half bunch length $\ell_{\max}$ is short, it is related to the half momentum spread $\delta_{\max}$ by

$$\delta_{\max}^4 = \left(\frac{eV_{\text{rf}}h}{\pi\beta^2 E_0|\eta_2|}\right)\left(\frac{\ell_{\max}}{R}\right)^2. \tag{16.226}$$

If we let $\delta_{\text{bucket}} = k\delta_{\max}$, we can solve for the necessary rf voltage and rf harmonic:

$$V_{\text{rf}} = \frac{\pi\beta^2 E_0 R k^2 \Delta\eta\delta_{\max}^2}{2\ell_{\max}}, \quad h = \frac{2R}{\ell_{\max}k^2}, \tag{16.227}$$

where $\Delta\eta = |\eta_2|\delta_{\max}^2$ is the desired spread of the slip factor of the bunch. Note that the rf voltage is proportional to $\Delta\eta$, the desired spread in momentum-compaction, and $\delta_{\max}^2$, the momentum spread of the bunch squared. Thus, if we reduce the momentum-compaction spread, the rf voltage will be reduced by the same factor. On the other hand, the rf frequency is independent of the choice of $\Delta\eta$ and $\delta_{\max}$.

For small phase spread, Eq. (16.225) describes a particle oscillating in a quartic potential (with $\Delta\phi$ and δ interchanged). This is a well-known situation when a higher harmonic cavity is present and the two cavity voltages are inversely proportional to the square of their respective harmonics (see Sec. 8.3.1). For such a system, the synchrotron frequency is zero at zero oscillating amplitude and increases linearly with respect to the momentum offset $\delta_{\max}$, or the fourth root of the Hamiltonian. The synchrotron frequency increases to a maximum for larger oscillation amplitude and drops to zero again at the edge of the bucket. Simple derivation gives the synchrotron tune $\nu_s = \nu_{s0}F(H)$, where $\nu_{s0} = \sqrt{h\Delta\eta eV_{\text{rf}}/(2\pi\beta^2 E_0)}$ with $\Delta\eta = |\eta_2|\delta_{\max}^2$, just the synchrotron tune of a synchronous particle in an ordinary single rf system with a slip factor equal to $\Delta\eta$. For a constant η_2, the ν_{s0} is directly proportional to the momentum-offset excursion $\delta_{\max}$. The form factor $F(H)$ can be written as (Exercise 16.15)

$$F^{-1}(H) = \frac{\sqrt{2}}{\pi}\int_0^{\pi/2} \frac{dz}{\sqrt{\cos z}\sqrt{1 - \sin^2\frac{\Delta\phi_{\max}}{2}\sin^2 z}}. \tag{16.228}$$

The form factor is evaluated at the Hamiltonian value,

$$H = \frac{eV_{\text{rf}}\omega_0}{\pi\beta^2 E_0}\sin^2\frac{\Delta\phi_{\max}}{2} = \frac{1}{4}ah|\eta_2|\omega_0\delta_{\max}^4, \tag{16.229}$$

where $\Delta\phi_{\max}$ and $\delta_{\max}$ are equal to, respectively, the phase and momentum-offset excursions of the beam particle under investigation. A large spread in syn-

chrotron frequency can be advantageous in providing Landau damping to mode-coupling instabilities and also coupled-bunch instabilities. One obtains from Eqs. (16.227) and (16.229) $\sin^2(\Delta\phi_{\max}/2) = k^{-4}$, where $k = \delta_{\text{bucket}}/\delta_{\max}$. Thus, $\sin^2(\Delta\phi_{\max}/2) \ll 1$ for any reasonable k, and the form factor of Eq. (16.228) is roughly equal to

$$F(H) = \frac{\pi}{2K(1/\sqrt{2})} = 0.85, \tag{16.230}$$

where $K(1/\sqrt{2}) = 1.854$ is the complete elliptical function of the first kind.

16.4.4 *Microwave Instability Near Transition*

Analytic Solutions

In an operation near the transition energy ($\eta_0 \approx 0$), at least the next order, η_1, of the slip factor [Eq. (16.210)] must be included for a meaningful discussion of the beam dynamics. Holt and Colestock studied the problem of collective stability of coasting beam with Gaussian energy distribution, by including both η_0 and η_1. [35] The dispersion relation is expressed in terms of the complex error function. Their conclusion is that there is no unstable region in the complex $Z_0^{\parallel}$-plane below transition. On the other hand, there are both stable and unstable regions above transition. They also claimed that their conclusion was supported by simulations. However, they did not specify the values of η_0 and η_1 in the simulations they presented or in their stability plots in the complex $Z_0^{\parallel}$-plane. It is hard to understand at least the situation below transition. It is clear that when $|\eta_0|$ is not too small, the contribution of η_1 is irrelevant. Thus their claim as stated can be interpreted as *no microwave instability below transition*, no matter how far away it is from transition. For this reason, this claim is quite questionable. When we look into their stability plots, Fig. 16.13, we can see something that resembles a stability curve below transition. The presence of a stability curve implies the existence of both stable and unstable regions, in contradiction to their conclusion.

We performed some simulations and got different results. A coasting beam at 100 GeV was considered in a hypothetical ring of circumference 50 m, with an initial rms parabolic fractional momentum spread of 0.001, interacting with a broadband impedance of $Z_0^{\parallel}/n = 3.00\ \Omega$ at the resonance frequency of 600 MHz and quality factor $Q = 1$. This unrealistic small ring was chosen because we wanted to limit the number of longitudinal bins around the ring so that not too many macro-particles would be necessary. In the tracking, the bin size had been chosen to be 0.25 m, which was half the wavelength at 600 MHz.

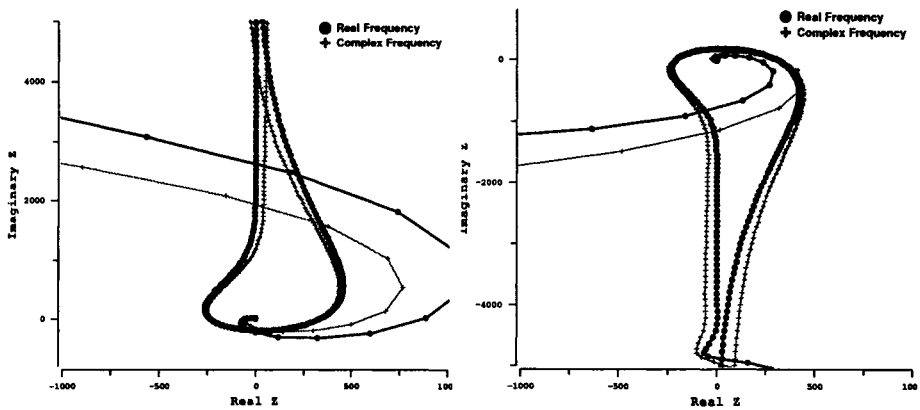


Fig. 16.13 Dispersion relation plots in the complex impedance plane. The thick curves with circles are for real frequencies and therefore should exhibit the stability boundaries. The lighter curves with +'s are for complex frequencies. Left plot is below transition and right plot is above transition. (Courtesy Holt and Colestock. [35])

With the slip factor fixed at $|\eta| = 0.005$, the beam intensity was adjusted so that the Keil–Schnell circle-approximated criterion [36] gave a stability limit of $|Z_0^{\parallel}/n| = 1.00\ \Omega$. All higher-order slip factors were set at zero. The tracking results are shown in Fig. 16.14: the top four plots for $\eta = -0.005$ (below transition) and the lower four plots for $\eta = +0.005$ (above transition) at 0, 1200, 2400, and 3600 turns. We see that below transition irregularities develop at the low-momentum edge. Ripples corresponding to the frequency of 600 MHz (wavelength = 0.5 m) are clearly seen. The momentum spread broadens at the low-momentum side until the total spread is about 1100 MeV, about 2.75 times the original total spread of about 400 MeV. This is partly because of the energy loss as a result of the resistive part of the impedance. The observation definitely confirms the occurrence of microwave instability below transition, and the eventual self-stabilization by overshooting. Above transition, irregularities also develop at the low-momentum edge and the momentum spread also broadens at the low-momentum edge. The total spread appears to be broader than below transition. In addition, we see small bomb-like droplets launched at the low-momentum side, which are not observed below transition. Instability above transition appears to be more severe than below transition. We will come back to the simulations of coasting beam near transition later in Sec. 16.4.4.

Bunched Beam Simulations

In this section, we study the stability of a bunched beam very close to transition. As an example, take a muon bunch in the proposed 50×50 GeV muon collider,

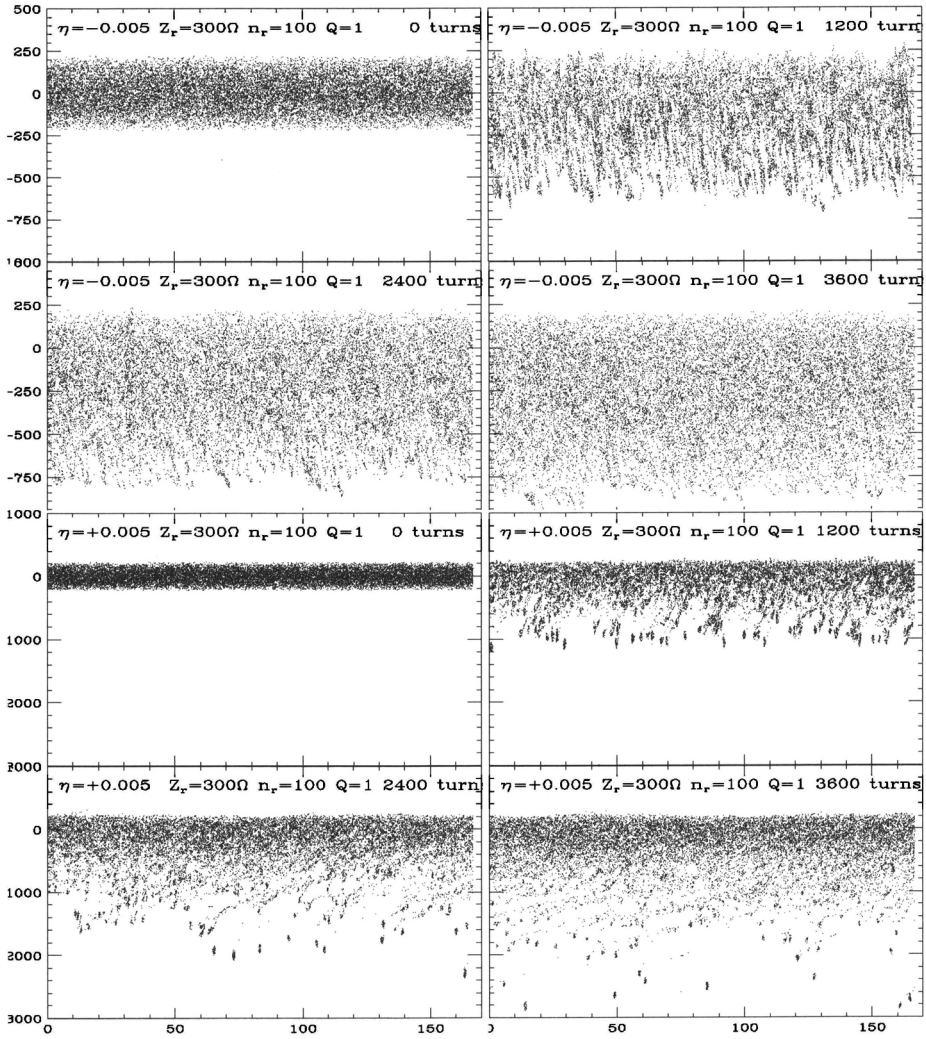


Fig. 16.14 The top four plots and lower four plots are for $\eta = -0.005$ (below transition) and $\eta = +0.005$ (above transition), respectively, at 0, 12000, 24000, and 36000 turns. The impedance is a broadband with $Q = 1$, $Z_0^{\parallel}/n = 3.0\ \Omega$ at the resonant frequency of 600 MHz.

which has a slip factor of $|\eta| = 1 \times 10^{-6}$. Everything we discuss here will apply to a proton bunch also, with the exception that the muons decay while the protons are stable. We will first discuss the situation with the decay of the muons taken into consideration, and later push the lifetime to infinity. We assume that sextupoles and octupoles are installed and adjusted so that the contributions of

η_1 and η_2 become insignificant compared with η_0. The muon bunch we consider has an intensity of $N_b = 4 \times 10^{12}$ particles, rms width $\sigma_\ell = 13$ cm and rms fractional momentum spread $\sigma_\delta = 3 \times 10^{-5}$ or $\sigma_E = 1.5$ MeV. The impedance is assumed to be broadband with $Z_0^{\|}/n = 0.5\ \Omega$ at the angular resonant frequency of $\omega_r = 50$ GHz with quality factor $Q = 1$. The muons have an e-folding lifetime of 891 turns at 50 GeV in this collider ring. During the muon lifetime, there is negligible phase motion because of ring is close to isochronous. Thus a bunching rf frequency system is not necessary. However, as will be explained below, rf systems are needed for the cancellation of potential-well distortion.

For bunched beams, there is the issue of potential-well distortion which must not be mixed up with the collective microwave instability. Potential-well distortion will change the shape of the bunch from a well-behaved bi-Gaussian distribution in the longitudinal phase space to something that looks like an N in Fig. 16.15, with the difference that the distortion of the beam does not come from the space-charge force, but mainly from the inductive part of the broadband impedance.

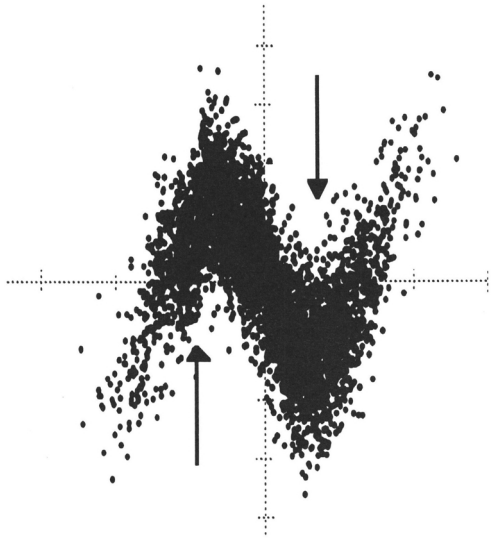


Fig. 16.15 Effects of a strong space-charge or potential-well distortion force result in a N-shape vertical shear on the bunch. The plot shows the result of simulation in the longitudinal phase space after a number of turns. The initial distribution is bi-Gaussian.

The wake potential seen by a particle inside a Gaussian bunch at a distance z behind the bunch center is shown in Fig. 16.16 and is given by

$$\begin{aligned} V(z) &= e\int_{-\infty}^{z} dz'\lambda(z')W_0(z-z') \\ &= -\frac{eN\omega_r R_\|}{2Q\cos\phi_0}\,\mathcal{R}e\, e^{i\phi_0 - z^2/(2\sigma_\ell^2)}w\left[\frac{\sigma_\ell\omega_r e^{i\phi_0}}{c\sqrt{2}} - \frac{iz}{\sqrt{2}\sigma_\ell}\right], \end{aligned} \tag{16.231}$$

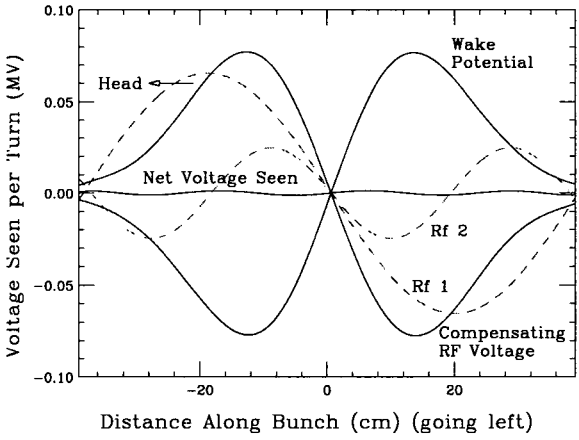


Fig. 16.16 Wake potential, compensating rf voltages, and net voltage seen by particles in the 13-cm bunch at injection. The compensating rf, shown in solid, is the sum of two rf's represented by dashes. Cancellation with the wake is incomplete with errors less than 1% of the wake potential.

where $\lambda(z)$ is the unperturbed bunch distribution, $W_0(z)$ the longitudinal monopole wake function, $\sin\phi_0 = 1/(2Q)$, and w is the complex error function. This distortion can be cancelled up to $\pm 3\sigma_\ell$ by two low-voltage rf systems, [37] which at injection are at frequencies $\omega_1/(2\pi) = 0.3854$ GHz and $\omega_2/(2\pi) = 0.7966$ GHz, with voltages $V_1 = 65.40$ kV and $V_2 = 24.74$ kV, and phases $\varphi_1 = 177.20°$ and $\varphi_2 = 174.28°$. This compensation is shown in Fig. 16.16. Since only two sinusoidal rf's are used, the cancellation is not complete; however, the error is less than 1% of the original wake potential and has been considered to be unimportant. Because of the lifetime of the muons, the beam has been tracked for only 1000 turns in the time domain using the broad-band wake function $W_0(z)$. The initial and final bunch distributions are shown in Fig. 16.17. During the simulation the compensating rf voltages were lowered turn by turn to conform with the diminishing bunch intensity due to the decay of the muons.

We see from the right plot of Fig. 16.17 that the bunch distribution has been very much distorted after 1000 turns. This comes mostly from the fact that the original distribution of the bunch in the left plot is not exactly Gaussian. It consists of 2×10^6 macro-particles randomly distributed according to a bi-Gaussian distribution. As a result, the wake potential of the actual bunch shown as a dotted curve in Fig. 16.18 deviates slightly from and wiggles around the ideal wake potential curve of a smooth Gaussian bunch shown in solid. The difference is the jitter curve in the center of the plot. The fluctuation seen in the right plot of Fig. 16.17 is the result of the accumulation of this dotted jitter curve in 1000 turns with muon decay taken into account. Although this tiny fluctuation leads to a small potential-well distortion in one turn (≤ 0.02 MeV),

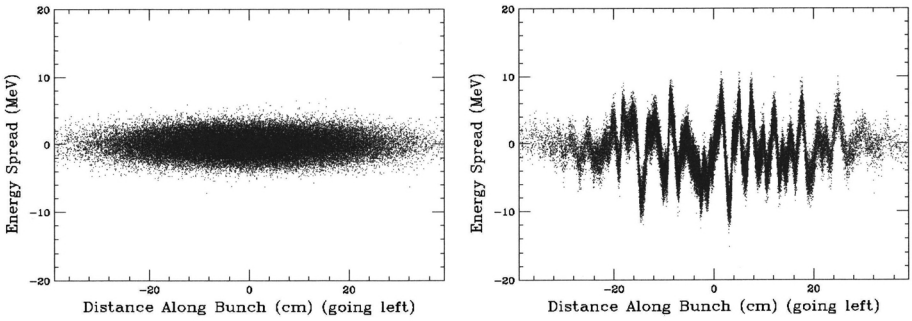


Fig. 16.17 Simulation of a 13-cm bunch of 4×10^{12} muons subject to a broadband impedance with quality factor $Q = 1$ and $Z_0^{\parallel}/n = 0.5\ \Omega$ at the resonant angular frequency $\omega_r = 50$ GHz. Half-triangular bins of width 15 ps (0.45 cm) are used with 2×10^6 macro-particles participating. Left plot shows initial distribution with $\sigma_E = 1.5$ MeV and $\sigma_\ell = 13$ cm. Right plot shows distribution after 1000 turns with compensating rf's depicted in Fig. 16.16.

it is unfortunate that this distortion accumulates turn after turn and will never reach a steady state, since the beam is so close to transition.§ (If the bunch were of electrons, this growth would stop because of radiation damping.) This accumulated distortion can be computed exactly from the the dotted jitter curve. Any growth in excess will come from collective microwave instability. Note that the uncompensated potential-well distortion is quite different from the growth due to microwave instability. For the former, the growth in energy fluctuations every turn will be exactly by the *same* amount as given by the dotted jitter curve in Fig. 16.18 (if muon decay is neglected). This is because the wake potential of particles along the bunch does not depend on the energy distribution of the bunch, but only on its linear density and the latter is essentially unchanged since the particles do not drift much during the first 1000 turns. On the other hand, the initial growth due to microwave instability at a particular turn is proportional to the actual energy fluctuation at that turn and the evolution of the growth is exponential. Thus, although the growth due to microwave instability is small at the beginning, it will grow much faster later on when the accumulated energy fluctuations become larger. It is worth mentioning that even if the wake potential of the initial bunch with statistical fluctuations has been compensated exactly by the rf's, the bunch can still be unstable against microwave instability. An infinitesimal deviation from the bunch distribution can excite the collective

§More exactly, a steady state will be reached when the momentum offset becomes so large that phase drift due to the small slip factor becomes significant. However, this will not happen in reality because of the finite momentum aperture of the storage ring.

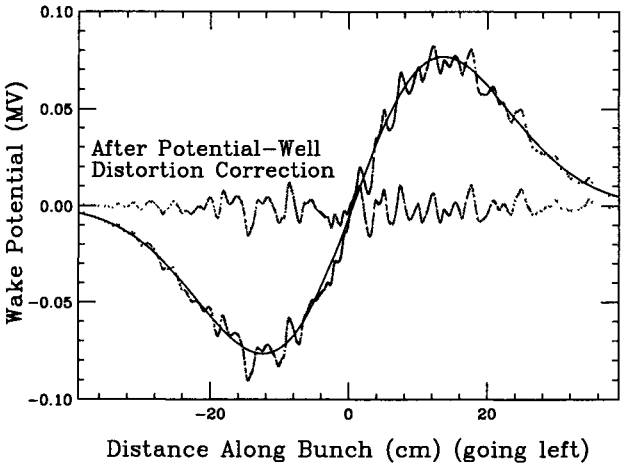


Fig. 16.18 Wake potential seen by the simulated bunch shown as dots is interlaced with the wake potential of an ideal smooth Gaussian bunch shown in solid. The difference (center curve) represents the random fluctuation of the finite number of macro-particles.

modes of instability corresponding to some eigenfrequencies. In other words, the accumulated growth due to potential-well distortion is a static solution and this static solution converges very slowly close to transition until the momentum spread is large enough for the small $|\eta|$ to smooth the distribution. Microwave instability, on the other hand, is a time-dependent solution.

In Fig. 16.19, the three plots on the left are for a 4000-turn simulation of the same muon bunch using 2×10^6 macro-particles with the decay of the muons considered. The two compensating rf systems are turned on. The first plot is for $\eta = 0$ so that microwave instability cannot develop. All the fluctuations are due to the residual potential-well distortion or the accumulation of the uncompensated jitters. The second and third plots are for, respectively, $\eta = -1 \times 10^{-6}$ (below transition) and $\eta = +1 \times 10^{-6}$ (above transition). We see that they deviate from the first plot, showing that there are growths due to microwave instability although the effect is small. The three plots on the right are the same as on the left with the exception that the muons are considered stable, or, in other words, the particles can be protons. We see that the second and third plots differ from the first one by very much (note the change in energy scale), indicating that microwave instability does play an important role for proton bunches in a quasi-isochronous ring. We also see that microwave instability is more severe above transition than below transition even when the beam is so close to transition. In the simulations, the jitters, or the statistical fluctuation around the smooth distribution might have been very much exaggerated because of the small number of macro-particles included in the tracking. In a realistic beam, these statistical fluctuations should be very much smaller. However, these jitters

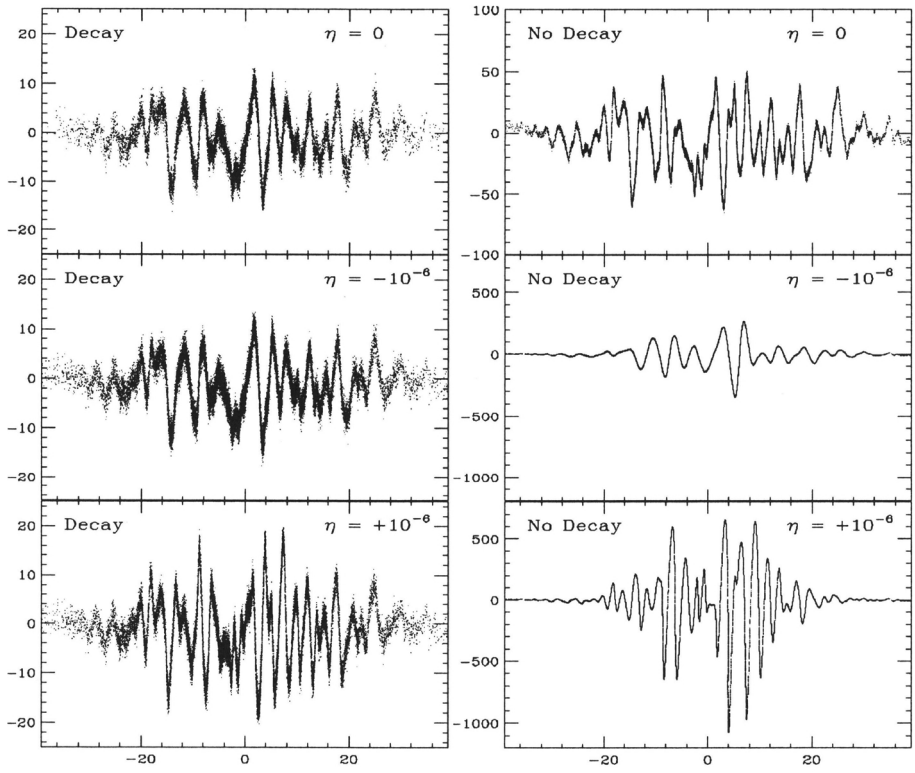


Fig. 16.19 Phase-space plots of energy spread in MeV versus distance from bunch center in cm at the end of 4000 turns. All are simulating 4×10^{12} micro-particles with 2×10^6 macro-particles. In the left three plots, the decay of the muons has been taken into account. The first left plot is for $\eta = 0$ so that it just gives the amount of potential-well distortion. The second and third plots are for, respectively, $\eta = -1 \times 10^{-6}$ and $+1 \times 10^{-6}$. The small deviations from the first plot are results of microwave instability. The right three plots are the same as the left, except that the muons are considered stable and the energy scale has been changed. Here, large microwave growths develop.

can also come from other sources, such as electronic noises, rf acceleration, rf maneuvering, etc., which may be much larger than the Schottky noise. As a result, in the design of a quasi-isochronous ring, the sources of all jitters should be carefully considered in order to estimate the growth in energy offset due to potential-well distortion or microwave instability.

Coasting Beam Simulations

For coasting beams, we do not have the inverted tilted N-shape wake potential as in Fig. 16.16. Thus, no rf compensation will be required. However, the noise

in the beam does result in a wake potential similar to the small residual wake-potential jitters in Fig. 16.16 after wake-potential compensation. Near transition where the phase motion is negligibly slow, these jitters will add up turn after turn without limit exactly in the same way as the bunched beam after having optimized the rf compensation. Thus, near transition, there is essentially no difference between a coasting beam and a bunched beam after the rf compensation. The only exception is that microwave instability develops most rapidly near the longitudinal center of the bunch where the local intensity is highest, whereas in a coasting beam, microwave instability develops with equal probability along the bunch depending on the statistical fluctuations in the macro-particles.

In Fig. 16.20, we show some coasting beam simulations near transition by having $\eta_0 = 0$ or $\pm 5 \times 10^{-5}$ and $\eta_1 = 0$ or ± 0.05. The coasting beam consists of 3.27×10^{15} protons (or nondecaying muons) having an average energy of 100 GeV in a hypothetic ring with circumference 50 m. The initial momentum spread is Gaussian with rms fractional spread $\sigma_\delta = 0.001$ or $\sigma_E = 100$ MeV. Thus, at 1σ, the contribution of $|\eta_1| = 0.05$ is the same as the contribution of $|\eta_0| = 5 \times 10^{-5}$. The simulations are performed with 8×10^5 macro-particles in 400 triangular bins. The impedance is a broadband with $Q = 1$ and $Z_0^{\|}/n = 2\ \Omega$ at the resonant frequency of $f_r = 300$ MHz.

All the plots in Fig 16.20 are illustrated in the same scale for easy comparison. The horizontal axes are longitudinal beam position from 0 to 166.7 ns, while the vertical axes are energy spread from -4000 to 3000 MeV. Plot (a) shows the initial particle distribution in the longitudinal phase space. All the other plots are simulation results at the end of 54,000 turns. Plot (b) is the result of having $\eta_0 = 0$ and $\eta_1 = 0$. It shows the accumulation of the wake-potential jitters over 54,000 turns. These jitters originate from the statistical fluctuation of the initial population of the macro-particles. Therefore, any deviation from Plot (b) implies microwave instability. Plots (c) and (d) are with $\eta_0 = 0$, but with $\eta_1 = +0.05$ and -0.05, respectively. We see the growths curl towards opposite phase directions nonlinearly. This is due to the nonlinearity in δ of the time slip given by Eq. (16.210). It appears that Plot (d) with $\eta_1 = -0.05$ exhibits a larger growth. Plots (e), (g), and (i) are for $\eta_0 = -5 \times 10^{-5}$ (below transition), but with $\eta_1 = +0.05$, -0.05, and 0, respectively. We see that the microwave instability is most severe when $\eta_1 = 0$, indicating that η_1 has the ability to curb instability. This is, in fact, easy to understand. The phase drift driven by $|\eta_1| = 0.05$ is much faster than that driven by $|\eta_0| = 5.0 \times 10^{-5}$ at larger momentum spread; for example, it will be four times faster at $2\sigma_\delta$, nine times faster at $3\sigma_\delta$, and so on. As a result, a nonvanishing $|\eta_1|$ tends to move particles away from the clumps, thus lessening the growth due to microwave instability.

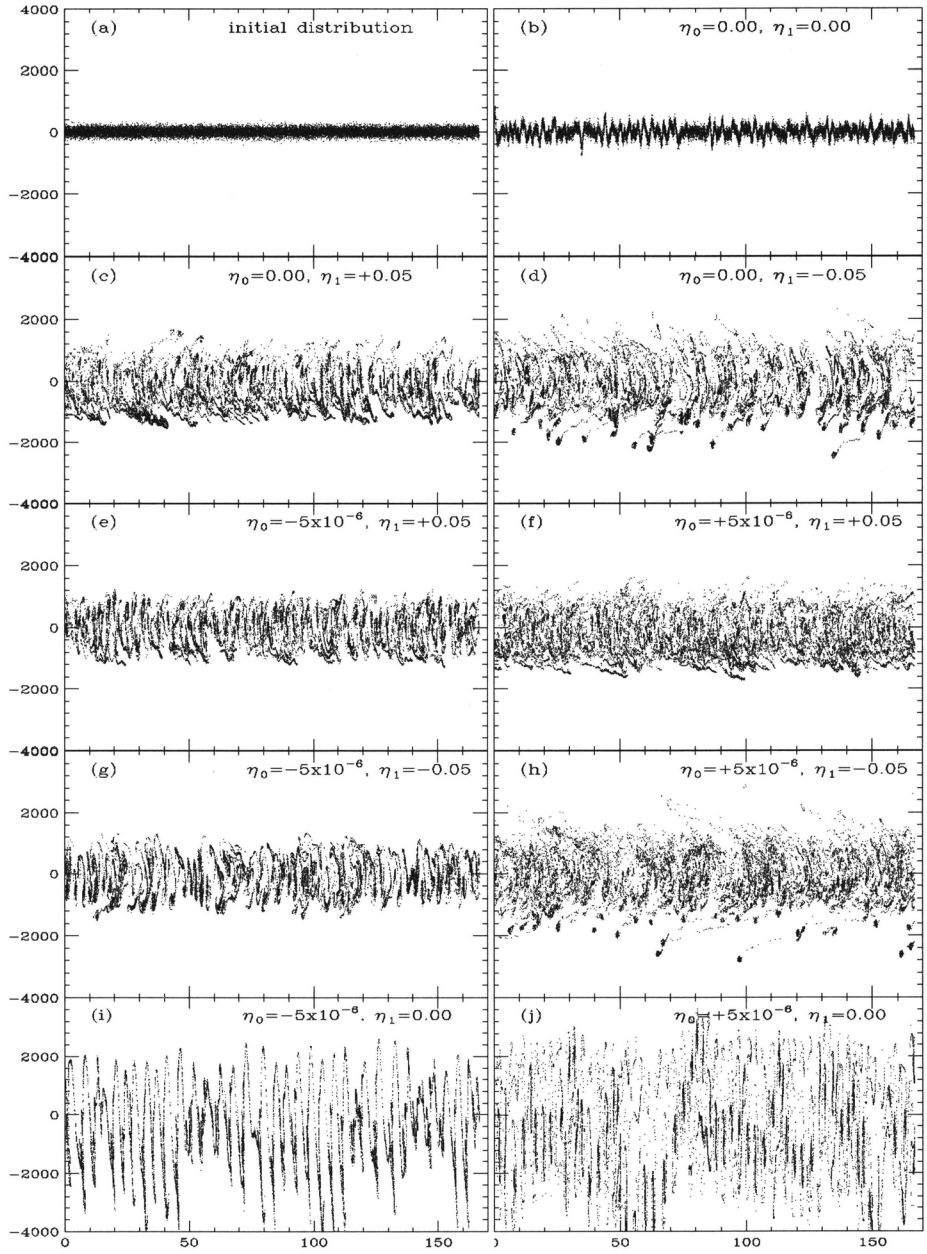


Fig. 16.20 Energy spread (MeV) versus bunch position (ns) of coasting beam simulations. See text for explanation.

Plots (f), (h), and (j) are for $\eta_0 = +5 \times 10^{-5}$ (above transition), but with $\eta_1 = +0.05$, -0.05, and 0, respectively. Again microwave instability is most severe when $\eta_1 = 0$, and η_1 does curb instability to a certain extent. Comparing Plots (e), (g), and (i) with Plots (f), (h), and (j), it is evident that the beam is more unstable against microwave instability above transition ($\eta_0 > 0$) than below transition ($\eta_0 < 0$) independent of the sign of η_1. For a fixed η_0, we also notice that negative η_1 is more unstable than positive η_1. The theoretical implications of these results are nontrivial.

Now let us come back to the analytic investigations by Holt and Colestock. [35] Their results appear to contradict the simulations presented here. Analytic analysis often starts with the Vlasov equation. The time-dependent beam distribution $\psi(\phi, \Delta E; t)$ can be separated into two parts:

$$\psi(\phi, \Delta E; t) = \psi_0(\phi, \Delta E) + \psi_1(\phi, \Delta E)\, e^{-i\Omega t}. \tag{16.232}$$

Here, ψ_0 is the *steady-state* solution of the Hamiltonian and ψ_1 describes the collective motion of the beam with the collective frequency $\Omega/(2\pi)$. After linearization, the Vlasov equation becomes an eigenequation with ψ_1 as the eigenfunction and $\Omega/(2\pi)$ the eigenfrequency. The equation also depends on ψ_0. Thus we must solve for the *steady-state* solution first before solving the eigenequation. The steady-state solution is the time-independent solution of the Hamiltonian which includes the contribution of the wake function. In other words, ψ_0 is the potential-well-distorted solution. Far away from transition, this distortion is mostly in the ϕ coordinate, for example, that brought about by the space-charge or inductive forces. Therefore, for a coasting beam, there will not be any potential-well distortion at all. The situation, however, is quite different close to transition. As was pointed out in above, the potential-well distortion is now in the ΔE coordinate. For this reason, not only bunched beams, even coasting beams will suffer from potential-well distortion as a result of the nonuniformity of the beam. In simulations, the nonuniformity arrives from the statistical fluctuation of the distribution of the macro-particles. This nonuniformity will accumulate turn by turn until the momentum spread is so large that the small $|\eta|$ is able to smooth out all nonuniformity. In other words, the steady-state distribution ψ_0 that goes into the Vlasov equation will be completely different from the original distribution in the absence of the wake and is not just a perturbation. In the analysis of Holt and Colestock, the ideal smooth Gaussian distribution in energy was substituted for ψ_0 in the Vlasov equation. However, this is a very unstable static distribution; even a small perturbation will accumulate turn by turn with extremely slow convergence. For this reason, it is hard to understand what their results really represent.

16.5 Exercises

16.1 Derive the variation of the nonadiabatic time T_c, the rms bunch length, and rms energy spread of a bunch right at transition with respect to the synchronous phase ϕ_s and the ramping rate $\dot{\gamma}_t$, as given in Eq. (16.31).

16.2 Show that the time evaluation of the phase offset,

$$\Delta\phi(t) = B\sqrt{\omega_s}e^{i\int \omega_s dt}, \quad . \tag{16.233}$$

where B is a constant, is valid only in the adiabatic region.
Hint: Show that the approximations made in Eqs. (16.37) and (16.38) are in accordance with $t \gg T_c$, where T_c is the nonadiabatic time.

16.3 Show that the half bunch length and half energy spread given by Eqs. (16.53) and (16.54) can also be obtained from the phase equation:

$$\widehat{\Delta\phi} = \frac{h|\eta|\omega_0}{\beta^2 E_0 \omega_s}\widehat{\Delta E}, \tag{16.234}$$

together with the assumption of linear time variation of η/E_0.

16.4 (1) If $f(x)$ and $g(x)$ are two independent solutions of the differential equation (16.58), show that the Wronskian $W(f,g) \equiv f(x)g'(x) - f'(x)g(x)$ is independent of x and can therefore be evaluated at any x, especially at $x = 0$.
(2) The solution can be written as

$$\begin{aligned} \Delta p &= \quad B\left[f(x)\cos\psi + g(x)\sin\psi\right], \\ \Delta\phi &= -B\left[f'(x)\cos\psi + g'(x)\sin\psi\right], \end{aligned} \tag{16.235}$$

where B is a constant. Show that these two equations trace out an ellipse by varying ψ, with the ellipse area $\mathcal{A}$ given by

$$\mathcal{A}^2 \propto (f^2 + g^2)(f'^2 + g'^2) - (ff' + gg')^2. \tag{16.236}$$

(3) Show that the right side of Eq. (16.236) is equal to the Wronskian $W(f,g)$ and the bunch area is therefore conserved and is determined only by the constant B.

16.5 The followings give an exact derivation of the bunch shape near transition under the assumption of constant ramping or η/E is directly proportional to time measured from transition. The arrival time offset $\Delta\tau$ and energy offset ΔE are the canonical variables.
(1) Similar to Eq. (16.83), show that the position of a particle at the bunch

boundary at any moment $t = xT_c$ can be written as,

$$\tau(x) = \frac{B}{h\omega_0} y^{\frac{2}{3}} \left[\cos\psi_1 J_{\frac{2}{3}}(y) + \sin\psi_1 N_{\frac{2}{3}}(y) \right], \tag{16.237}$$

$$\Delta E(x) = \frac{\dot{\gamma}_t T_c E_{\text{rest}}}{\tan\phi_s} B \left(\frac{2}{3}y\right)^{\frac{1}{3}} \left[\cos\psi_1 J_{-\frac{1}{3}}(y) + \sin\psi_1 N_{-\frac{1}{3}}(y) \right], \tag{16.238}$$

where

$$y = \frac{2}{3} x^{\frac{3}{2}}, \tag{16.239}$$

$$B^2 = \left(\frac{3}{2}\right)^{\frac{1}{3}} \frac{h^2 \omega_0^2 T_c^2 \dot{\gamma}_t S}{\beta_t^2 \gamma_t^2 E_{\text{rest}}}, \tag{16.240}$$

and S is the bunch area in eVs. Here, B and ψ_1 are the two constants of integration.

(2) Eliminating ψ_1, obtain the boundary of the bunch in the expression

$$\alpha_{\tau\tau}\tau^2 + 2\alpha_{\tau E}\tau\Delta E + \alpha_{EE}\Delta E^2 = 1, \tag{16.241}$$

which describes an ellipse with

$$\begin{aligned}
\alpha_{\tau\tau} &= \frac{h^2\omega_0^2}{\left[By^{2/3}\det\right]^2} \left[J^2_{-\frac{1}{3}}(y) + N^2_{-\frac{1}{3}}(y) \right], \\
\alpha_{\tau E} &= \left(\frac{\tan\phi_s}{\dot{\gamma}_t \tau_{\text{ad}} A E_0} \right)^2 \frac{1}{\left[B(\frac{2}{3}y)^{1/3}\det\right]^2} \left[J^2_{\frac{2}{3}}(y) + N^2_{\frac{2}{3}}(y) \right], \\
\alpha_{EE} &= \frac{h\omega_0 \tan\phi_s}{\dot{\gamma}_t \tau_{\text{ad}} A E_0} \frac{1}{B^2(\frac{2}{3})^{1/3} y \det^2} \left[J_{\frac{2}{3}}(y) J_{-\frac{1}{3}}(y) + N_{\frac{2}{3}}(y) N_{-\frac{1}{3}}(y) \right],
\end{aligned} \tag{16.242}$$

and the determinant

$$\det = J_{\frac{2}{3}}(y) N_{-\frac{1}{3}}(y) - J_{-\frac{1}{3}}(y) N_{\frac{2}{3}}(y). \tag{16.243}$$

(3) The area of the ellipse is given by the general formula

$$S = \frac{\pi}{\sqrt{\alpha_{\tau\tau}\alpha_{EE} - \alpha_{\tau E}^2}}. \tag{16.244}$$

Verify that the area is indeed the S introduced in Eq. (16.240) by substituting directly the $\alpha_{\tau\tau}$, $\alpha_{\tau E}$ and α_{EE} into Eq. (16.244). Since the area of the ellipse conserves, the verification can be very much simplified if the

substitution is made by using the asymptotic values of the Bessel and Neumann functions, or in other words, at a time far away from transition.

(4) For a bi-Gaussian distributed bunch, show that the space-charge distribution is

$$\psi(\tau, \Delta E) = \frac{3}{S} e^{-3\left(\alpha_{\tau\tau}\tau^2 + 2\alpha_{\tau E}\tau\Delta E + \alpha_{EE}\Delta E^2\right)}, \tag{16.245}$$

which is normalized to unity when integrated over τ and E. The factor of 3 in the exponent comes about because we choose the bunch area S to contain 95% of the beam particles.

(5) Show by integrating over ΔE that the linear distribution is

$$f(\tau) = \frac{\sqrt{3\pi}}{S\sqrt{\alpha_{EE}}} e^{-3\pi^2\tau^2/(\alpha_{EE}S^2)}, \tag{16.246}$$

and hence the rms length of the bunch is

$$\sigma_\tau = \frac{S\sqrt{\alpha_{EE}}}{\sqrt{6}\pi}. \tag{16.247}$$

(6) Show that the peak current I_{pk} occurs at $\tau = 0$ and is given in terms of the average current I_0 by

$$\frac{I_{\text{pk}}}{I_0} = \frac{1}{\sqrt{2\pi}\sigma_\tau f_0} = \frac{1}{f_0}\sqrt{\frac{2(\alpha_{\tau\tau}\alpha_{EE} - \alpha_{\tau E}^2)}{\pi\alpha_{EE}}} = \frac{1}{f_0}\sqrt{\frac{2}{S\,\alpha_{EE}}}, \tag{16.248}$$

where f_0 is the revolution frequency.

(7) Show that the rms energy spread of the slice of the bunch at $\tau = 0$ is

$$\sigma_{E0} = \frac{1}{\sqrt{6\alpha_{EE}}}, \tag{16.249}$$

which is different from the rms energy of the whole beam

$$\sigma_E = \frac{S\sqrt{\alpha_{\tau\tau}}}{\sqrt{6}\pi}. \tag{16.250}$$

Then verify that the bunch area is given by $S = 6\pi\sigma_\tau\sigma_{E0}$ which is time independent.

16.6 Show that the power-series expansion of $\Delta p(x)$ and $\Delta\phi(x)$ in Eq. (16.83) gives exactly the same solution as Eqs. (16.74) and (16.75). Note that ψ and ψ_1 in the two solutions can be different.

16.7 Normalized to their values at transition, show that the bunch length and energy spread of a bunch near transition are given by Eq. (16.85).
Hint: Starting from Eq. (16.83), eliminate the phase ψ_1 using the condition

of maximum bunch length, express the Neumann functions in terms of the Bessel functions through

$$N_\nu(y) = \frac{J_\nu(y)\cos\pi\nu - J_{-\nu}(y)}{\sin\pi\nu} \tag{16.251}$$

when ν is not an integer, and evaluate the bunch length right at transition. A constant ramping rate is assume and the wake force has not been included.

16.8 (1) Using as canonical coordinates,

$$\Delta\phi \quad \text{and} \quad p = \frac{h\omega_0}{\beta^2\gamma E_{\text{rest}}}\Delta E, \tag{16.252}$$

derive the envelope equation for $\tilde{\phi} = \sqrt{\langle\Delta\phi^2\rangle}$ far away from transition:

$$\ddot{\tilde{\phi}} + \omega_s^2\tilde{\phi} + \frac{\omega_s^2 n_{\text{spch}}}{\widehat{\Delta\phi}^3}\tilde{\phi} - \frac{E_0^3}{\tilde{\phi}^3} = 0, \tag{16.253}$$

where the half-length of the bunch is $\widehat{\Delta\phi} = \sqrt{5}\tilde{\phi}$ for the parabolic distribution. The symbol $n_{\text{spch}}/\widehat{\Delta\phi}^3$ is the ratio of the space-charge force to the rf force defined in Eqs. (16.87) and (16.89),

$$E_0 = \sqrt{\langle\Delta\phi^2\rangle\langle p^2\rangle - \langle p\Delta\phi\rangle^2} \tag{16.254}$$

is proportional to the longitudinal emittance, and ω_s is the angular synchrotron frequency. Then convert the envelope equation to one for the half bunch length $\widehat{\Delta\phi}$.

(2) Derive the envelope equation near transition as given by Eq. (16.91). Hint: Near transition, $\omega_s^2 = t/T_c^3 = x/T_c^2$, where T_c is the nonadiabatic time. Because of the rapidly varying ω_s^2, the substitution

$$\frac{1}{\omega_s^2}\frac{d^2\widehat{\Delta\phi}}{dx^2} \longrightarrow \frac{d}{dx}\left(\frac{1}{\omega_s^2}\frac{d\widehat{\Delta\phi}}{dx}\right) \tag{16.255}$$

is necessary.

16.9 A transition jump is to be designed for the Fermilab Main Injector with a total jump of $\Delta\gamma_t = 2.0$. Because of space-charge mismatch of the bunch length near transition, the jump will be asymmetric; i.e., $|t_-| < t_+$, where t_- is the start-jump time before transition and t_+ the end-jump time after transition. Using Eq. (16.95), compute t_-, t_+, $\Delta\gamma_{t-}$, and $\Delta\gamma_{t+}$, where the latter are, respectively, the amounts of jump from $t = t_-$ to $t = 0$ and from $t = 0$ $t = t_+$. For the Main Injector, the ramp rate across transition is $\dot{\gamma}_t = 163.1\ \text{s}^{-1}$ and the nonadiabatic time is $T_c = 2.14$ ms.

16.10 The Alternating Gradient Synchrotron (AGS) at Brookhaven is a proton ring with a circumference of 807.11 m. The beam crosses transition at $\gamma_t = 8.8$ with $\dot{\gamma}_t = 63\ \mathrm{s}^{-1}$. The rf harmonic is $h = 12$ and the synchronous phase is $\phi_s = 27.3°$.
(1) With beam pipe radius 2.356 cm and beam radius 0.5 cm, compute the space-charge impedance at transition and the frequency at which the integrated negative-mass growth is at a maximum.
(2) For a bunch with[¶] 1×10^{12} protons, compute the critical negative-mass-instability parameter c defined in Eq. (16.175) for various bunch areas. Determine the smallest bunch area to avoid negative-mass blowup. Repeat the computation with the intensity of 3×10^{12} protons.

16.11 It is possible that the AGS described in the previous problem is dominated by a broadband impedance of $Z_0^{\parallel}/n \approx 20\ \Omega$ at 1.5 GHz. Use the simplified model developed in Sec. 16.3.1 to compute the total growth across transition. The bunch area is assumed to be 6 eV-s.

16.12 (1) Derive Eqs. (16.208) and (16.209), the expansions of the revolution period T and velocity β as powers of the fractional momentum offset δ.
(2) Derive Eq. (16.214), the expansion of the slip factor.

16.13 Figure 16.12 indicates that there are two series of pendulum-like longitudinal buckets unless the energy is very close to transition.
(1) Explain why we pay attention to only one series under most condition. Use the Fermilab Main Injector as an example. The Main Injector has a $\gamma_t = 21.8$ (20.45 GeV) and $\alpha_1 = 0.50$. Compute the distance between the two series of buckets in fractional momentum spread when it is in a coasting mode at the injection energy of 8 GeV and at 18.5 GeV. (2) The rf voltage is 2.5 MV and the synchrotron phase is 0°. Compute the energy at which the two series of longitudinal buckets merge.

16.14 Retaining up to the η_1-contribution to the slip factor, for the α-like bucket,
(1) derive the relation between width and height of the bucket [Eq. (16.219)],
(2) derive the bucket area [Eq. (16.221)],
(3) derive Eq. (16.223), the universal relation between width and height of a bunch fit to the bucket.

16.15 Derive the synchrotron tune of a η_2-dominated bucket starting from the Hamiltonian of Eq. (16.225).
Answer: $\nu_s = \nu_{s0} F$, where F is given by Eq. (16.228).

[¶]The AGS is currently running at the intensity of $\sim 1 \times 10^{13}$ particles per bunch with a transition jump. Here, we are estimating the growth without transition jump.

Bibliography

[1] A. Sørenssen, *The Effect of Strong Longitudinal Space-Charge Forces at Transition,* CERN Report MPS/Int. MU/EP 67-2, 1967.

[2] J. Wei, *Longitudinal Dynamics of the Non-Adiabatic Regime on Alternating-Gradient Synchrotrons*, PhD Dissertation (SUNY, Stony Brook, 1990).

[3] K. Y. Ng *Bunch Shape Evolution Near Transition, — an Intuitive Approach*, Fermilab Report FN-644, 1996.

[4] I. Kourbanis, private communication; E. C. Raka, *Damping Bunch shape Oscillations in the Brookhaven AGS, IEEE Trans. Nucl. Sc.* **NS16**, 3, 182 (1969).

[5] I. M. Kapchinskij and V. V. Vladimirskij, *Limitations of Proton Beam Current in a strong Focusing Linear Accelerator Associated with the Beam Charge*, International Conference on High Energy Accel. and Instrum., CERN 1959, p. 274.

[6] S. Holmes, *Main Injector Transition Jump*, Fermilab Main Injector Report MI-0008, 1989.

[7] T. Risselada, CERN 4th General Accel. School, Jükuch, Germany, 1990, p.161.

[8] K. Y. Ng and A. Bogacz, *Dispersion γ_t Jump for the Main Injector*, Proc. 1995 IEEE Part. Accel. Conf., ed. L. Gennari (Dallas, May 1–5, 1995) p. 3340.

[9] V. Visnjic, *Local Dispersion Insert: the γ_t Knob for Accelerators*, Fermilab Report TM-1888, 1994.

[10] C. M. Bhat, J. Griffin, J. MacLachlan, M. Martens, K. Meisner, K. Y. Ng, *Transition Crossing in Proton Synchrotrons using a Flattened rf Wave, Phys. Rev.* **E55**, 1028 (1997).

[11] S. Y. Lee and J. M. Wang, *Microwave Instability Across the Transition Energy, IEEE Trans. Nucl. Sc.* **NS-32**, 2323 (1985).

[12] D. Boussard, CERN Report CERN-LAB II/RF/Int./75-2 (1975).

[13] S. Krinsky and J. M. Wang, *Part. Accel.* **17**, 109 (1985).

[14] K. Y. Ng, *Microwave Stability Limits for the Main Ring and Growth across Transition*, Fermilab Report TM-1383, 1986.

[15] D. Huang, S. Y. Lee, and K. Y.Ng, *Scaling Law in Microwave-Instability Growth Across Transition*, Fermilab Report FERMILAB-FN-0774-AD, 2005.

[16] W. W. Lee and L. C. Teng, *Beam-Bunch Length Matching at Transition Crossing*, Proc. 8th Int. Conf. High Energy Accel., eds. M. H. Blewett and N. Vogt-Nilsen (CERN, Geneva, Sept. 20–24, 1971), p. 327.

[17] P. Lucas and J. MacLachlan, *Simulation of Space Charge Effects and Transition Crossing in the Fermilab Booster,* Proc. 1987 IEEE Part. Accel. Conf., eds. E. R. Lindstrom and L. S. Taylor (Washington, D.C., March 16–19, 1987), p. 1114.

[18] W. Hardt, *Gamma-Transition-Jump Scheme of the CPS*, Proc. 9th Int. Conf. High Energy Accel. (SLAC, Stanford, May 2–7, 1974), p. 434.

[19] E. Keil and B. Zotter, *Part. Accel.* **3**, 11 (1972).

[20] I. Kourbanis and K. Y. Ng, *Transition Crossing in the Fermilab Main Ring, Past and Present*, Proc. 1993 Part. Accel. Conf., ed. S. T. Corneliussen (Washington, D.C., May 17–20, 1993), p. 3630.

[21] J. A. MacLachlan, *ESME: Longitudinal Phase-Space Particle Tracking—Program Documentation*, Fermilab Report TM-1274, 1984.

[22] I. Kourbanis and K. Y. Ng, unpublished.

[23] See for example Ref. 3 or I. Kourbanis and K. Y. Ng, *Main Ring Transition Crossing Simulations,* Proc. Fermilab III Instabilities Workshop, Fermilab, eds. S. Peggs and M. Harvey (Batavia, U.S., 1990), p. 151.
[24] A. Sørenssen, *What Happens Right After Phase Transition?* CERN Report CERN/MPS/DL 72-14, 1972.
[25] J. M. Hammersley and D. C. Handscomb, *Monte Carlo Methods* (Wiley, 1964).
[26] E. Keil and W. Schnell, CERN Report ISR-TH-RF/69-48, 1969.
[27] D. A. Edwards and M. J. Syphers, *An Introduction to the Physics of High Energy Accelerators* (Wiley and Sons, 1993).
[28] See for example, E. D. Courant, R. Ruth, W. Weng, L. Michelotti, D. Neuffer, and L. Teng, AIP Conf. Proc. No. 87, 36 (1982).
[29] A. Riabko, M. Bai, B. Brabson, C.M. Chu, X. Kang, D. Jeon, S.Y. Lee, and X. Zhao, *Phys. Rev.* **E54**, 815 (1996).
[30] D. Boussard and T. Linnecar, Proc. 2nd European Particle Accel. Conf., eds. P. Martin and P. Mandrillon (Nice, June 1990), p. 1560.
[31] K. Y. Ng, *Nucl. Instrum. Meth.* **A404**, 199 (1998).
[32] D. Robin, H. Hama, and A. Nadji, *Experimental Results on Low Alpha Electron-Storage Rings*, Proc. Micro Bunches Workshop, eds. E. B. Blum, M. Dienes, and J. B. Murphy (Upton, NY, Sep. 28–30, 1995), (AIP Conf. Proc. 367), p. 150; D. Robin, R. Alvis, A. Jackson, R. Holtzapple, and B. Podobedov, *Low Alpha Experiments at the ALS*, *ibib* p. 181.
[33] H. Hama, S. Takano, and G. Isoyama, *Nucl. Instrum. Meth.* **A329**, 29 (1993).
[34] A. S. Bogacz, *Microwave Instability at Transition—Stability Diagram Approach*, Proc. 1991 IEEE Part. Accel. Conf., ed. L. Lizama (San Francisco, May 6–9, 1991) p. 1815.
[35] J. A. Holt and P. I. Colestock, *Microwave Instability at Transition*, Proc. 1995 IEEE Part. Accel. Conf., ed. L. Gennari (Dallas, May 1–5, 1995) p. 3067.
[36] E. Keil and W. Schnell, CERN Report TH-RF/69-48, 1969.
[37] E.-S. Kim, A. M. Sessler, and J. S. Wurtele, *Phys. Rev. ST Accel. Beams* **2**, 051001 (1999).
[38] K. Y. Ng, *Phys. Rev. ST Accel. Beams* **2**, 091001 (1999).

2025 © The Author(s). This is an Open Access chapter published by World Scientific Publishing Company, licensed under the terms of the Creative Commons Attribution-NonCommercial 4.0 International License (CC BY-NC 4.0).

Index

g_0, space-charge geometric factor
  dependence on frequency, 724
  other distributions, 55
  rectangular beam in rectangular pipe, 56
  uniform distribution, 53

potential-well distortion
  head-tail asymmetry, 59

adiabatic damping, 567
air-bag model
  Chebyshev modes, 372
  square-well air-bag model, 451
  transverse mode-coupling, 446

Balakin–Novokhatsky–Smirnov damping
  autophasing, 563
    bunch length dependency, 565
  misalignment, 587
  mutli-bunch, 575
  transverse mode-coupling, 451
  tune spread, 561
beam breakup
  formation, 10
  long bunches, 561
  multi-bunch
    damping by energy chirp, 581
    misalignment, 587
    wake effect, 573
  single short bunch, 572
beam transfer function
  longitudinal, 539
  measurement, 540
  transverse, 537
beam-loading, 241–300
  accelerator ring, 247
  compensation by detuning, 249
  Fermilab Recycler, 79
  in-phase condition, 250
  linac, 244
  rf detuning, 247
    coupled-bunch instabilities, 282
  self-bunching, 171
  transient, 263
    compensation, 278
    Fermilab rings, 284
    for a bunch, 270
  transient to steady-state, 266
betatron tune shift
  coherent, 90
    dynamic, 360
  Hermite modes, 380
  incoherent, 90
  Legendre modes, 379
bounce frequency
  electron-in-beam, 612
    frequency spread, 612
  electron-in-trapped-ion, 647
  ion-in-beam, 645
bunch modes, 193
  convention, 199
bunch rotation, 234
bunching factor, 97, 111

bypass inductance
  bench measurement, 437
  thick-wall model, 423
  thin-wall model, 416
  tune-shift measurement, 432
  Vos derivation, 400

chromaticity
  chromatic frequency shift, 388, 468
  chromaticity phase shift, 388
  definition, 386
  effective chromaticity, 522
  head-tail phase, 476
  $Z_1^{\perp}$ measurement, 389

dc beam, 45
decoherence, 160, 505
  kinematic, 545
  longitudinal, 550
  versus Landau damping, 543
  with dynamic effects, 545
detuned cavity structure, 569
  long-range wake, 571
  short-range wake, 569

effective chromaticity, 522
effective impedance
  longitudinal, 223, 383, 463
  transverse, 383, 448
electron cloud
  ionization, 630
  mitigation and remedy, 642
  multipactoring and build-up, 634
  primary electrons, 628
  secondary electron yield, *see* secondary emission
  simulation, 637
  tune shift, 640
envelope equation
  equivalent-uniform-beam, 151
  quadrupole error on single particle, 147
  quadrupole modes
    one dimension, 144
    two dimensions, 148
  Sacherer's derivation, 137

fast and slow waves, 361
fast beam-ion instability, 643
  application, 657
    ALS, 659
    Fermilab damping ring, 672
    H^- in linac, 662
  cures, 654
  growth length along beam, 651
  growth rate, 651
  linear theory, 644
  spectrum, 653
ferrite insertion
  heated ferrite, 183
  microwave instability, 177
fundamental theorem of beam-loading, 237
  proof in lossless cavity, 264
  proof in lossy cavity, 272

Gröbner multipactoring condition, 635

Haissinski equation, *see* potential-well distortion
head-tail instability
  longitudinal, 489
    application to Tevatron, 493
    growth rate, 492
    isochronous ring, 750
    observation at SPS, 489
  transverse
    a bunch, 478
    observation, 479
    stability criteria, 474
    two-particle model, 474
higher-harmonic cavity, *see* Landau cavity

image charge/current, 1
  distribution of a particle's, 23, 27
impedances, 11–29
  definition, 12
  inductive, 17
  listing from Handbook, 29
  longitudinal
    resistive-wall, 18
    space-charge, 17

longitudinal space-charge, 54
properties, 16
relation with wake functions, 16
resistive, 17
resonances, 17
transverse
low-frequency resistive wall, 398
measurement, 432, 437
resistive-wall, 18, 407
space-charge, 17, 121, 124
impulse approximation, 3
inductive bypass, 398
interaction matrix
longitudinal, 375
transverse, 371
ion bounce frequency, 523
isochronous ring, 744
η_1-dominated bucket, 748
head-tail instability, 750
η_2-dominated bucket, 751
microwave instability, 753–763
bunched beam, 754
coasting beam, 760
potential-well distortion, 754
compensation, 757

Kapchinsky and Vladimirsky (K–V)
equation, *see* envelope equation
kick factor, 569

Landau cavity
η_2 dominated ring, 752
active, 324
passive, 326
example, 329
Landau damping, 160, 499–555
ensemble of oscillators, 499
longitudinal bunched beam, 516
longitudinal unbunched beam, 533
transverse bunched beam, 510
transverse unbunched beam, 519
versus decoherence, 543
Laslett image coefficients
bunched beams, 110
coasting beams, 109
connection with impedance, 121
convention, 96
electric, 93
geometry of beam pipe
circular, 113
elliptical, 114
parallel plates, 93
rectangular, 117
magnetic, 95
linear distribution/density, 40
Liouville theorem, 48, 81
longitudinal coupled-bunch instability,
301–352
observation and cures, 321
Landau cavity, 324
uneven fill, 339
voltage modulation, 336
Sacherer's time-domain derivation,
315
longitudinal equations of motion, 40–47
near transition, 692
longitudinal microwave instability, 159
dispersion relation, 162
ferrite insertion, 177
isochronous ring, 753–763
landau damping, 170
methods of induction, 174
methods of observation, 174
overshoot, 173
self-bunching, 9
stability curve, 166
longitudinal mode-coupling, 459
long bunches, 460
short bunches, 462
vs. Keil–Schnell instability, 462
longitudinal single-bunch instability, 203
mode coupling, 219
Robinson instability, 215
stability of a bunch, 213, 215
stability of a bunch mode
bi-Gaussian distribution, 218
dispersion, 203
elliptical distribution, 209
Landau damping, 208
longitudinal space-charge force, 54

mode-coupling, *see* longitudinal or

transverse mode-coupling
mode/particle approach, 47
momentum-compaction, 691
definition, 37
higher orders, 490, 745
negative momentum-compaction, 38

negative-mass instability, 714–744
growth at cutoff, 715
Hardt's Schottky-noise model, 726
blowup criterion, 732
self-bunching model, 741
simulation
difficulties, 738
Hammersley sequence, 740
neutralization, 110

Panofsky–Wenzel theorem, 3–7
cylindrical coordinates, 6
supplement, 5
the theorem, 5
parasitic loss, 19
coherent, 19
incoherent, 22
phase loop, 42, 257
photo-emission, 628
point-bunch model, *see* uneven fill
many bunches, 340
single bunch, 311
potential-well distortion, 2
bunch lengthening/shortening, 60, 61
compensation
ferrite insertion at PSR, 69
Finemet insertion at KEK, 73
isochronous ring, 757
Haissinski equation, 58, 59, 75, 83, 84
head-tail asymmetry in barrier bucket, 75
isochronous ring, 754
purely resistive, 59
space-charge, 54

quadrupole wake, 593
observation, 599
tune variation along beam, 595

reactive force, 52
resistive-wall instability
coasting beam, 523
coupled-bunch, 393
rf bucket
accelerating/moving, 45, 171
definition, 45
stationary, 45, 171
rf focusing, 38
rf knockout, 106
rf system
coupling coefficient, 243
optimum, 246
equivalent circuit, 241
generator power, 243
quality factor, 245
shunt impedance, 245
rigid-beam approximation, 2
Robinson's stability criteria
phase stability
high intensity, 258
low intensity, 257
superconducting cavity, 256
Robinson's damping, 262
Landau damping, 512, 518
point-bunch model, 311, 518
transverse, 380, 440, 512
water-bag model, 309

Sacherer's integral equation
approximate sinusoidal modes, 383
dynamic tune/frequency shift, 376
longitudinal, 301, 375
solution for radial modes, 370
Chebyshev modes, 372
Hermite modes, 374
Legendre modes, 373
transverse, 366
saw-tooth instability, 228
cure, 233
scaling law
bunch lengthening, 224, 463
transition growth, 721
secondary emission
at zero incident energy, 633
effective secondary emission yield, 634

electron spectrum, 633
secondary electron yield (SEY), 631
self-bunching, 170
separation of transverse and longitudinal motions, 364
shock response function
longitudinal, 552
relation with transfer function, 504, 555
transverse, 503
skin-depth, 18
slip factor
definition, 38
energy-offset dependence, 489
snap-shot view, 49
space-charge betatron tune shift
connection with space-charge impedance, 124
incoherent
Gaussian distribution, 97
tune-shift distribution, 101
uniform distribution, 96
more exact formula, 100, 130
surface impedance, 71, 404
synchrotron oscillation, 44–47
Hamiltonian, 46
synchronous particle, 40
synchronous phase, 40, 42
shift, 67
synchrotron frequency, 44
synchrotron tune, 44
tune dependence on amplitude, 44, 81
synchrotron tune/frequency shift, 64
coherent
dynamic part, 206
static part, 68
with incoherent spread, 210
dynamic, 308
incoherent, 64
synthetic kernel, 205

transfer function
definition, 502
longitudinal, 536
relation with shock response function, 504, 555
transverse, 502
transition crossing, 691–744
bunch shape variation, 694
nonadiabatic time, 692
space-charge mismatch, 707
space-charge parameter, 709
transition energy, 38
transition gamma, 38, 691
transition jump, 713
transverse coupled-bunch instability, 393
narrow resonances, 439
resistive-wall, 393
Robinson stability, 440
transverse microwave instability, 521
transverse mode-coupling, 445
air-bag model, 446
Balakin–Novokhatsky–Smirnov damping, 451
high energy accelerators, 464
long bunches
possible observation, 468
threshold, 467
reactive feedback, 450
short bunches, 446
threshold, 448
space-charge, 451
two-particle model, 456
trapped ion/electron
bounce frequency, *see* bounce frequency
half-integer stopband, 679
ion linear distribution, 646
ion transverse distribution, 646
production of electrons, 628
trapping criterion
gap with leaked beam, 616
long bunch, short gap, 614
train of short bunches, 617
two-particle model
autophasing, 563
growth with acceleration, 568
head-tail instability, 474
in linac, 558
mutli-bunch beam breakup, 573
quadrupole wake, 596
transverse mode-coupling, 456

validity, long bunches, 560
two-stream instabilities, 609–686
coupled-centroid oscillation, 619
fast beam-ion instability, 643
trapped electrons, *see* trapped ion/electron

uneven fill, 339–352
Landau damping, 346
modulation coupling, 344, 440

Vlasov equation, 48
voltage modulation, 336

wake fields/force/potential, 2
dynamical part, 44
static part, 41
wake functions
convention, 10
conversion to CGS units, 8
definition, 7
detuned cavity structure, 569
in MKS units, 8
inductive, 17
properties, 8–10
relation with impedances, 16
resistive, 17
resistive-wall, 27
resonances, 26
space-charge, 17
water-bag model, 309
Chebyshev modes, 375